

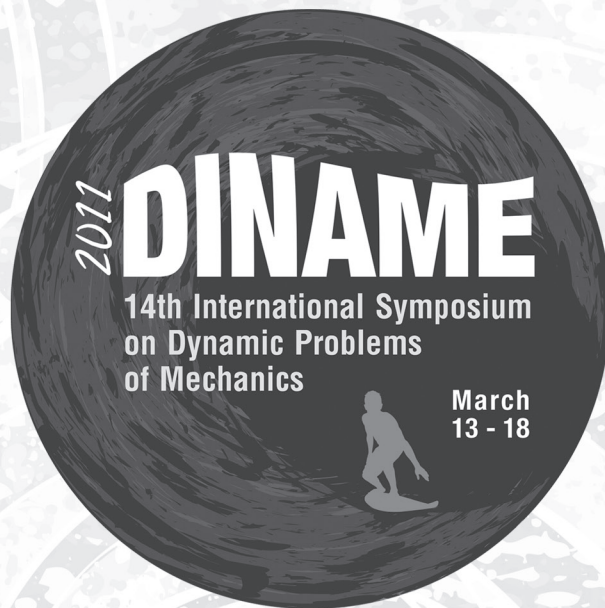
2011

DINAME

14th International Symposium
on Dynamic Problems
of Mechanics

March
13 - 18





EDITORIAL

DINAME is a biennial symposium on dynamic problems of mechanics, organized by the Committee of Dynamics of the Brazilian Society of Mechanical Sciences and Engineering, ABCM. The four and a half day, single session format of the meeting allows the participants, an intense exchange of scientific information and building of effective professional networks. The conference takes place at quite and pleasant locations with the right kind of comfort and welcoming atmosphere that contribute to the immersion regime of the meeting. DINAME 2011 is held at Maresias Beach Hotel, São Sebastião, east of the city of São Paulo. São Sebastião is located between the ocean and the largest preservation area of the Atlantic Rain Forest.

Agenor Fleury
Paulo Kurka
Diname 2011 Chairmen

COMMITTEE OF DYNAMICS OF ABCM

Agenor de Toledo Fleury

*Centro Universitário da FEI, São Paulo, Brazil
Escola Politécnica da USP, São Paulo, Brazil*

Carlos Alberto de Almeida

Pontifícia Universidade Católica, Rio de Janeiro, Brazil

Hans Ingo Weber (President)

Pontifícia Universidade Católica, Rio de Janeiro, Brazil

Ilmar Ferreira Santos

Technical University of Denmark.

José João de Espíndola

Universidade Federal de Santa Catarina, Brazil

Marcelo Amorim Savi

Universidade Federal do Rio de Janeiro, Brazil

Moyses Zindeluk

Universidade Federal do Rio de Janeiro, Brazil

Paulo Roberto G. Kurka

Universidade Estadual de Campinas, São Paulo, Brazil

Domingos Alves Rade

Universidade Federal de Uberlândia, Minas Gerais, Brazil

Paulo Sérgio Varoto

Escola de Engenharia de São Carlos, Universidade de São Paulo, Brazil

Valder Steffen Jr.

Universidade Federal de Uberlândia, Minas Gerais, Brazil

LOCAL ORGANIZING COMMITTEE

Agenor de Toledo Fleury - Chairman

Paulo Roberto G. Kurka - Chairman

Setor de Comunicação e Marketing - Centro Universitário da FEI

EDITORS OF THE PROCEEDINGS OF DINAME 2011

Agenor de Toledo Fleury

Paulo Roberto G. Kurka

Marko Ackermann (co-editor) - Centro Universitário da FEI, São Paulo, Brazil

DINAME 2011 BOARD OF REVIEWERS
Marko Ackermann, FEI
Sergio Frascino M. Almeida, ITA
Antonio Bertachini de Almeida Prado, INPE
Eduardo Aoun Tannuri, EPUSP
José Roberto França Arruda, Unicamp
José Manoel Balthazar, UNESP
Marco Antonio Luersen, UFParaná
Carlos Alberto Bavastri, UFParaná
Roberto Bortolussi, FEI
Juan F. Camino, Unicamp
João Carlos M. Carvalho, UFUberlandia
Fernando Castro Pinto, COPPE/UFRJ
Edson Cataldo, UFFluminense
Glauco Caurin, EESC/USP
Alfredo De Faria, ITA
Carlos De Marqui Junior, EESC/USP
Lázaro Donadon, UFMG
Décio Donha, EPUSP
Marcelo Braga Dos Santos, UFUberlandia
Agenor de Toledo Fleury, FEI e EPUSP
Giorgio E. O. Giacaglia, Unitau
Bob Schutz, UTexas Austin
Paulo Batista Gonçalves, PUC/RJ
Fabrizio Leonardi, FEI
Francisco P. Lepore, UFUberlandia
Raul Gonzalez Lima, EPUSP
Vicente Lopes Junior, FEIS/UNESP
Gustavo Abreu, FEIS/UNESP
Katia Lucchesi Cavalca, Unicamp
Flávio Marques, EESC/USP
Flavius P.R. Martins, EPUSP
Newton Maruyama, EPUSP

DINAME 2011 BOARD OF REVIEWERS
Luciano Menegaldo, IME/RJ
Jorge Audrin Morgado De Gois, IME/RJ
Luiz De Paula Nascimento, FEIS/UNESP
Rodrigo Nicoletti, EESC/USP
João Antonio Pereira, FEIS/UNESP
Celso P. Pesce, EPUSP
Armando Carlos Pina Filho, COPPE/UFRJ
Gustavo Ripper, INMETRO
João Mauricio Rosario, Unicamp
Rubens Sampaio, PUC/RJ
Sezimária Saramago, UFUberlandia
Adriano Siqueira, EESC/USP
Marcelo Becker, EESC/USP
Eric Conrado Souza, FEI
Marcelo Souza, INPE
Flavio Trigo, EPUSP
Marcelo Trindade, EESC/USP
Paulo Sérgio Varoto, EESC/USP
Moysés Zindeluk, COPPE/UFRJ
Eduardo Gildin, UTexas A&M
Paulo Roberto G. Kurka, Unicamp
Domingos Alves Rade, UFUberlandia
Valder Steffen Jr., UFUberlandia
Hans Ingo Weber, PUC/RJ
Luis Carlos S. Goes, ITA
Marcelo Savi, COPPE/UFRJ
Ilmar F. Santos, UTDinamarca
Carlos Alberto Almeida, PUC/RJ
João Mauricio Rosário, Unicamp
Manuel Pera, IME/USP
Bob Schutz, UTexas Austin

SUMMARY

Energy Harvesting for Wireless Applications <i>D. J. Inman</i>	11
Challenges in Modal Testing <i>D. Ewins</i>	13
Closed-Loop Reservoir Management: An Overview <i>E. Gildin</i>	14
A Bayesian Experimental Design Approach for Structural Health Monitoring <i>M. D. Todd and E. B. Flynn</i>	24
Bio-Inspired Self-Adaptive Structures <i>R. A. Shoureshi</i>	29
Experimental investigation, mathematical modeling and nonlinear analysis of an impact pendulum suspended in a vibrating structure <i>R. R. Aguiar; H. I. Weber</i>	41
Riccati Solutions for the Linear-Quadratic Optimal Control Problem of Descriptor Systems <i>P. C. Müller</i>	51
On the Analysis of Chaos Control Methods Performance Applied to Mechanical Systems <i>A. S. de Paula; M. A. Savi</i>	60
Analysis and nonlinear modeling of a dual-mass tuned vibration absorber working in electrorheological fluid <i>N. Norrick; R. Markert; R. Nicoletti</i>	70
Experimental Identification of Journal Bearing Stiffness and Damping Coefficients in Non- stationary Run-up and Run-down Processes <i>K. Baumann; P. Felscher; R. Markert; K. L. Cavalca</i>	80
Stochastic analysis of structures excited by internal flows <i>T. G. Ritto; R. Sampaio; F. A. Rochinha</i>	90
Rotor-bearing system characterization by dynamic stiffness with a magnetic actuator as source of excitation <i>H. F. de Castro; J. Bauer; N. Norrick; K. L. Cavalca; R. Markert</i>	100
A Sensitivity Analysis of Active Noise Control Applied to Ducts with Higher-Order Acoustic Modes <i>E. L. Oliveira; M. A. V. Duarte; M. A. A. Nunes</i>	110
Study of Elastic Band-Gaps in Finite Periodic Structure Using Finite Element Models <i>P. B. Silva; J. R. F. Arruda; A. L. Goldstein</i>	118
Nonlinear Modeling and Analysis of a Piezoaeroelastic Energy Harvester <i>C. De Marqui Junior; A. Erturk; M. M. Anicézio; D. J. Inman</i>	128
The Human-size Walking Robot Lola - Hardware and Control aspects <i>M. Schwienbacher; V. Favot; S. Lohmeier; T. Buschmann; H. Ulbrich</i>	138
Some Results in analyzing the dynamic behavior of blade rows coupled by shroud contacts <i>N. Bachschmid; P. Pennacchi; E. Pesatori; G. Turozzi; M. Sanvito; S. Bistolfi</i>	144
Active Vibration Control Using Actuated Air Springs <i>L. Bregant; M. Spagnol</i>	154
On The Modeling of Structural Dynamics of Risers Composed of Functionally Graded Materials <i>C.A. Almeida; J.C. Romero; I.F.M. Menezes; G.H. Paulino</i>	162

Finite Element Dynamic Analysis of Cylindrical Panels under Moving Loads A. R. de Faria.....	169
A Regularization Technique for Ill-Conditioned Linear System of Equations H. G. Moura; A. Lenzi	180
Time Domain Multivariable Subspace-Based Method for Modal Parameters Identification Using Impulse Excitation H. N. Cambraia; P. R.G. Kurka.....	186
An Application of Filtering Techniques for the Tracking Control of Mobile Robots with Slipping J. G. Iossaquí; J. F. Camino; D. E. Zampieri	194
Multi-Harmonic Adaptive Control for Roughness J.A. Mosquera Sánchez; K. Janssens; H. Van der Auweraer; L.P.R. de Oliveira.....	204
Characterization of Electromagnetic Actuator for the Control of Rotating Machinery T.S. Morais; J. Der Hagopian; V. Steffen Jr; J. Mahfoud	215
A Game-based Framework for Robotic Rehabilitation K. O. Andrade; B. Jardim; R. C. Joaquim; A. A. G. Siqueira; G. A. P. Caurin; L. M. S. Amaral.....	224
Unbalance Response of a Flexible Rotor Supported by Fluid Film Bearings with Additional Viscoelastic Damping C. C. Thomazi; M. B. Santos; F. P. Léopore Neto.....	229
Decentralized H-Infinity vibration control of a plate A. F. Mazoni; A. L. Serpa	238
Workspace Analysis of a New Cable-Based Parallel Manipulator for Rehabilitation of Shoulder Movements W. M. Nunes; J. F. Ribeiro; J. C. M. Carvalho; R. S. Gonçalves	248
Identification of Damage in Thin-Walled Curved Beams by means of Vibration Analysis F. E. Dotti; V. H. Cortínez; M. T. Piován	258
A Low Cost Electromechanical Impedance-Based SHM Architecture for Multiplexed Piezoceramic Actuators R. M. Finzi Neto; L. V. Palomino; Ti. F. Bitencourt; V. Steffen Jr; D. A. Rade; C. A. Gallo.....	268
Response of the cracked rotor under uncertain parameters via the Harmonic Balance Method and the Polynomial Chaos Expansion B. Faverjon; J-J. Sinou	277
Internal Model Control Design for Powered Below-knee Prosthesis R. Suzuki; N. Kobayashi; E. P. Hofer	284
Performance evaluation of control strategies with different Feedforward error sensors in Active Noise Control D. A. Siviero; A. L. Goldstein; J. R. F. Arruda	290
Metamodelling Studies for Flutter Prediction of Wings P. R. Caixeta Júnior; F. D. Marques.....	298
Experimental Study of the Nonlinear Hybrid Energy Harvesting System M. A. Karami; P. S. Varoto; D. J. Inman	306
Thermal and Dynamic Analysis of the Rotor/Stator Contact in Turbomachinery A. Brandão; F. Thouverez; L. Blanc	317
Development and Performance Analysis of an Autocalibration Method for Tri-axis Sensors in Attitude Estimation Systems O. Tormena Junior; F. Granziera Júnior; M. C. Tosin.....	329

Bonding influence in the electromechanical (EM) admittance of piezoelectric sensors PZT bonded to structures based on EMI technique <i>H. A. Tinoco; A. L. Serpa</i>	335
Hamiltonian Dynamics and Geometry of a Class of Mobile, Multibody Systems <i>E. C. de Souza; N. Maruyama</i>	345
A Bayesian inference approach to estimate elastic and damping parameters of a structure subjected to vibration tests <i>M. T. Lopes; D. A. Castello; C. F. T. Matt</i>	355
Development Environment for Optimized Locomotion System of Planetary Rovers <i>B. Schäfer; A. C. Leite; B. Rebele</i>	368
Testbed for Inertial PIG Sensors Calibration <i>W. E. dos Santos; C. A. Z. Pece; W. A. Kapp; G. Emmendoerfer</i>	379
Hardware-in-The-Loop Simulation of an H Controller on the Stabilization of a 2-DOF Quadrotor <i>R. Breganon; R. C. B. Sampaio; M. M. de Souza; F. T. B. de Salvi; E. M. Belo; M. Becker</i>	389
Sliding Mode Control with Adaptive Fuzzy Dead-Zone Compensation for Uncertain Nonlinear Systems <i>W. M. Bessa; A. S. de Paula; M. A. Savi</i>	398
Analysis of the Hearing Temporary Threshold Shift (TTS) of Subjects Exposed to Whole Body Vibration (WBV) Alone <i>J.G. Dornela; M.L.M. Duarte; L.V.M. Almeida; L.V. Donadon; M.C. Batista Filho; M.R.R.O. Moreira; C.H. Ferreira; B.L.C. Dantas; M.A.R. Santos</i>	408
Modeling the response in vehicular vibroacoustic systems <i>W. J. P. Casas; V. R. da Silva; R. E. Antich</i>	414
Vehicle Dynamics for Response Modeling in Freight Cars <i>W. J. P. Casas; C. H. Viganico</i>	422
Active Control of Sound Transmission with Arrays of Smart Panels using Decentralized Velocity Feedback Control <i>A. L. Goldstein</i>	432
Non linear dynamics of a structure supported by rubber mounts <i>B. Thomas; L. Manin; R. Dufour; P. Goge</i>	442
Structural Modeling of Orthotropic Thin Plates by the Spectral Element Method <i>N. B. F. Campos</i>	452
Self-Heating Effects in Viscoelastic Dampers – Modeling and Experimental Assessment <i>J. de Cazenove; A. M. G. de Lima; D. A. Rade</i>	462
Application of a Computer Vision Method to Identify the Kinematics of a Scaled-Model Riser <i>F.P.R. Martins; F.C. Trigo; H.C. Silva Jr; A.T. Fleury</i>	471
Application of the Generalized Programmed Motion Equations to Kinematic and Dynamic Task Planning for Constrained Mechanical Systems <i>Elżbieta Jarzębowska</i>	484
The Angular Kurtosis and Power: New Features for Machining Monitoring <i>M. Lamraoui; M. Thomas; M. El Badaoui; I. Zaghbani; V. songméné</i>	494
New USP Wave Basin - Mechatronic and Hydrodynamic Design Aspects <i>M. L. Carneiro; P. C. de Mello; J. C. Adamowski; K. Nishimoto; E. A. Tannuri</i>	512
Control Tuning Methods applied to Dynamic Positioning Systems <i>E. A. Tannuri; H. M. Morishita; R. R. Marangoni; F. T. Mazzilli</i>	522

Luni-solar and geopotential perturbations on a close satellite <i>Giorgio E. O. Giacaglia; Bob E. Schutz</i>	532
Modeling, identification and control of a two-link flexible manipulator <i>J. A. B. Gripp; F. L. M. Santos; C. R. Bernardo; L. C. S. Góes</i>	542
Intelligent mode shapes recognition using Fourier descriptors with application in SHM <i>J. Morlier; M. Maues; L. Mevel</i>	551
Concomitant vortex induced vibration experiments: a cantilevered flexible cylinder and a rigid cylinder mounted on a leaf-spring apparatus <i>G. R. Franzini; N. A. G. Neto; R. T. Gonçalves; C. P. Pesce; C. E.N. Mazzilli; A. L.C. Fugarra</i>	560
Motorcycle cornering behavior modeling <i>R. Donadio; R. Bortolussi</i>	574
On the Active and Semi-Active controls of the Helicopter Blade-Sailing Phenomenon in Unsteady Flow <i>K. A. L. Castão; V. Piccirillo; L. C. S. Góes; R. L. C. B. Ramos</i>	588
A Semi-Active Flutter Control Using Smart Materials <i>V. Piccirillo; K. A. L. Castão; L. C. S. Góes; J. M. Balthazar</i>	599
Multibody System Model of a Stumble in Human Gait <i>M. Ackermann; A. Forner-Cordero</i>	609
Fault Detection and Diagnosis in Sensors and Actuators of the MultiMission Platform in its Nominal Mode <i>A. C. Leite; M. L. de Oliveira e Souza</i>	614
Numerical model for modal analysis of structures subjected to post-buckling <i>M. A.s Arbelo; S. F. M. de Almeida; S. R. Rett</i>	624
Robust Control of a Large Radar Antenna under Structured Uncertainties <i>A. T. Fleury; F. Leonardi; F. Armellini</i>	634
Influence of Cable Mass on Tendon Based Parallel Manipulator <i>J. A. M. de Gois; A. Back e Travi; C. S. M. Lima</i>	642
Nonlinear study of industrial arc spring dampers <i>S. Lahiri; I. F. Santos; H. Hartmann</i>	648
Robust Modelling Using Bi-Lateral Delay Lines for High Speed Simulation of Complex Systems <i>Petter Krus</i>	659
On a simple model for the dynamics of the vertical collapse of buildings <i>C. P. Pesce; L. Casetta</i>	672
Comparing Needs of Employers to Learning Outcomes of Engineering Curricula in Europe: Preliminary Results of ECCE Project <i>N. Bachschmid; F. Cheli; A. Castelli; C. Marinoni</i>	675

Energy Harvesting for Wireless Applications

Alper Erturk and Daniel J. Inman

Department of Mechanical Engineering, Virginia Tech, Blacksburg, VA 24061 USA, erturk@vt.edu, dinman@vt.edu

Abstract: The harvesting of ambient energy to run low-power electronics has experienced a tremendous growth in activity in both universities and companies. Basically energy harvesting is an enabling technology for the wireless community providing an alternative to batteries and making remote sensing practical. Here we examine several methods of harvesting ambient vibration energy using piezoelectric and electromagnetic transduction. Both linear and nonlinear harvesting mechanisms are presented as well as the integration of harvesting and storage into structural elements. Nonlinearities are introduced to enhance the amount of power that can be harvested and to introduce broadband behavior. Harvesting of mechanical energy from flow induced vibration and its applications are also presented. Several applications are discussed from powering sensors inside wind turbine blades and bridges for structural health monitoring applications to the use of harvesting to run remote sensors in aircraft. Some of the topics from the keynote are summarized here.

Keywords: energy harvesting, nonlinearity, piezoceramics, flow-induced vibrations

INTRODUCTION

The concept of energy harvesting for powering small electronic components (such as the wireless sensors used in monitoring applications) has received growing attention over the last decade. Vibrational, solar, flow and thermal energy can be converted to usable electric energy for powering remote electronic devices autonomously (Cook-Chennault et al., 2008). This keynote lecture discusses several topics on the subject ranging from the combination of multifunctionality and energy harvesting in aircraft structures to energy harvesting for damage prognosis in bridges. Some of these topics are discussed in the following.

ENERGY HARVESTING SYSTEMS AND CONFIGURATIONS

Self-charging structures refer to structures composed of elastic substructures (usually metallic or carbon-fiber), flexible piezoceramics embedded in kapton layers, flexible solar panels and flexible thin-film battery layers (Anton et al., 2010; Gambier et al., 2010). Proof-of-concept prototypes of self-charging structures for vibrational and solar energy harvesting are shown in Fig. 1. The goal of this concept is to use these structures in load-bearing applications to improve the multifunctionality for low-power applications (e.g. for powering a wireless sensor in the vicinity of the load-bearing structure using the harvested and stored energy). If the existing load-bearing structure can be modified using flexible piezoceramics, solar panels and thin-film batteries, the electric energy can be generated from the dynamic loads and stored inside the structure itself. One of the applications of interest for self-charging structures is to use them in unmanned aerial vehicles (UAVs) as structural components. For instance, piezoceramic layers can be embedded into wing spars of the UAV while flexible solar layers can be used as surface skin to harvest solar energy in daytime. After processing in an appropriate circuitry, the combined electrical outputs can be stored in flexible thin-film battery layers.

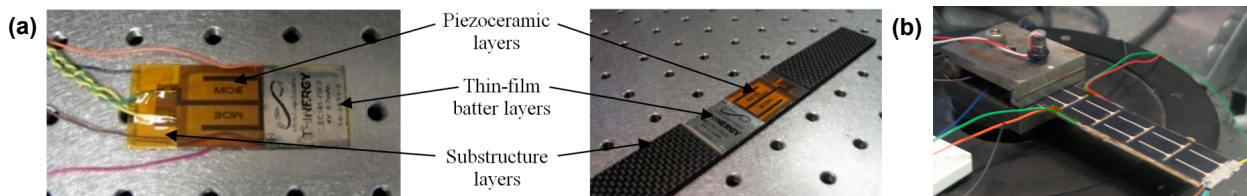


Figure 1 – Self-charging structures (a) using flexible piezoceramics and thin-film batteries and (b) using flexible piezoceramics, solar panels and thin-film batteries.

Exploiting mechanical nonlinearities for improving the electrical response in vibration-based energy harvesting is another important topic that has received significant attention over the past few years (Erturk et al., 2009; Arrieta et al., 2010). The main goal in exploiting mechanical nonlinearities is to convert linear and resonant energy harvesters into nonlinear and broadband energy harvesters. In this way, the energy harvester can respond better to excitations over a broader range of excitation frequencies. Bistable beams and plates are investigated for broadband piezoelectric power generation. A bistable piezomagnetoelastic cantilever (Erturk et al., 2009) used for nonlinear vibration-based energy harvesting is shown in Fig. 2a (which is obtained by locating two magnets near the tip of the ferromagnetic cantilever with piezoceramics) and the advantage of its broadband power frequency response due to nonlinear large-amplitude limit-cycle oscillations (LCOs) is shown in Fig. 2b. Another bistable configuration studied for bandwidth enhancement is the piezo-carbon-fiber-epoxy plate shown in Fig. 2c. Chaotic vibrations due to dynamic snap-through motion as well as large-amplitude LCOs observed in the bistable plate result in a remarkable broadband electromechanical response.

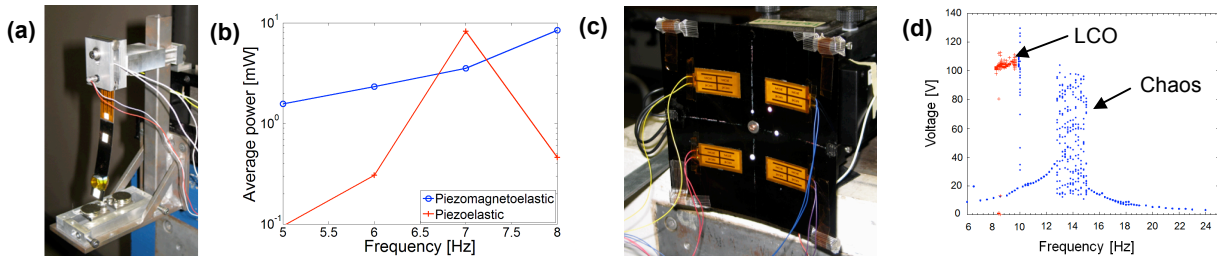


Figure 2 – (a) Bistable piezomagnetoelastic energy harvester beam and (b) its broadband power generation performance compared with the conventional (piezoelectric) configuration; (c) bistable piezo-carbon-fiber-epoxy energy harvester plate and its (d) voltage frequency response exhibiting chaos and LCO.

Converting flow (air-flow or liquid-flow) energy into electricity is another approach of generating low-power output for use in wireless sensor applications. One way of harvesting energy from airflow excitation is shown in Fig. 3. The schematic of the two-degree-of-freedom typical section shown in Fig. 3a has piezoelectric coupling in its plunge degree-of-freedom (simply due to piezoceramic patches attached to the plunge springs). If the airflow speed reaches the flutter boundary of the typical section, the piezoaeroelastic response (Fig. 3b) becomes almost persistent and the maximum power can be extracted from the system. Nonlinearities (such as free play) can be introduced to the piezoaeroelastic system to obtain bounded response (LCO) at airflow speeds below and above the linear flutter speed.

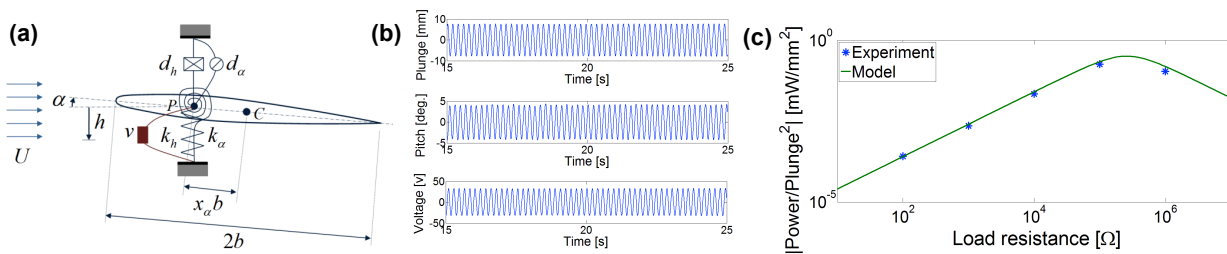


Figure 3 – (a) Schematic of a piezoaeroelastic section, (b) experimental piezoaeroelastic response at the flutter boundary and (c) the normalized piezoelectric power output at the flutter boundary for a set of resistors.

SUMMARY

Various approaches of energy harvesting for wireless applications are discussed in this keynote lecture and some of them are summarized here. Depending on the application of interest and the design limitations, multiple techniques of energy harvesting can be combined. Moreover, the energy harvester as well as the storage system can serve as a multifunctional system component. Several other techniques of energy harvesting for enabling wireless sensors are discussed in the lecture.

ACKNOWLEDGMENTS

The authors gratefully acknowledge the support from the U.S. AFOSR under the grant F9550-06-1-0326 "Energy Harvesting and Storage Systems for Future Air Force Vehicles" monitored by Dr. B. L. Lee and the U.S. Department of Commerce, NIST Technology Innovation Program, Cooperative Agreement Number 70NANB9H9007 "Self-Powered Wireless Sensor Network for Structural Health Prognosis."

REFERENCES

- Anton, S.R., Erturk, A., and Inman, D.J., 2010, "Multifunctional Self-Charging Structures Using Piezoceramics and Thin-Film Batteries," *Smart Materials and Structures*, Vol. 19, 115021.
- Cook-Chennault, K.A., Thambi, N. and Sastry, A.M., 2008, "Powering MEMS Portable Devices – a Review of Non-Regenerative and Regenerative Power Supply Systems with Emphasis on Piezoelectric Energy Harvesting Systems," *Smart Materials and Structures*, Vol. 17, 043001.
- Erturk, A., Hoffmann, J., and Inman, D.J., 2009, "A Piezomagnetoelastic Structure for Broadband Vibration Energy Harvesting," *Applied Physics Letters*, Vol. 94, 254102.
- Erturk, A., Vieira, W.G.R, De Marqui, Jr., C. and Inman, D.J., 2010, "On the Energy Harvesting Potential of Piezoaeroelastic Systems," *Applied Physics Letters*, Vol. 96, 184103.
- Gambier, P., Anton, S.R., Kong, N., Erturk, A., and Inman, D.J., 2010, "Combined Piezoelectric, Solar and Thermal Energy Harvesting for Multifunctional Structures with Thin-film Batteries," *Proceedings of the 21st International Conference on Adaptive Structures and Technologies*, State College, PA, 4-6 October 2010.

Challenges in Modal Testing

David Ewins

Imperial College London and University of Bristol, UK

Abstract: Modal Testing is approximately 50 years old. While there is no single moment when it began, there are clear signs of the underlying idea of measuring a structure's modes of vibration in the 1940s and then an upsurge of actual practice in the 1960s, the latter being fuelled by the development at that time of electronics. The advent of the microcomputer a decade later saw the development of the technology modal testing as we know it today. So, now, 40 years of continuous development provides a sophisticated and widely-used technology. Today, it is appropriate to review what further developments are sought and possible. What are the known limitations of today's methods and what improvements would really benefit the user? Three topics are selected for discussion here, and these are driven by the needs and expectations of the user: (i) Cost-effective Testing; (ii) Testing under Operating Conditions; (iii) Testing of Non-linear structures.

The first topic relates to the specific data we measure and the information we seek to extract from it, and explores the idea that this is often very inefficient at present with much more data being measured than is necessary and rather less information is obtained than is desired. This is especially true for the primary application of modal testing - for the validation of theoretical (FE) models. The essential issue centres around the numbers of frequencies and DOFs at which FRF data are measured and the discussion will draw on the latest ideas on continuous scanning to illustrate the limitations and potential benefits that should be fully appreciated and accessed, respectively.

The second area of interest addresses the growing need to be able to undertake modal testing on structures when they are in conditions closely representative of their operating configuration and environment. Increasingly, FE models used for design need to be capable of differentiating between structural behaviour at low-level, in-laboratory conditions and those which obtain in service. A good example of this is the helicopter, where vibration testing on the ground routinely encounters significantly different modes of vibration than those which apply under flying conditions. The complications which such demands introduce to the test can be significant, and especially so in respect of the excitation forcing which must be applied to generate the FRF data for modal analysis.

The third topic for detailed discussion here is an almost inevitable consequence of successful application of the previous task, and that is the increasingly common existence of non-trivial levels of nonlinear behaviour by the test structure. Although there have been significant advances in nonlinear structural dynamics techniques in recent years, they are generally an order of magnitude more complex than the linear methods upon which modal analysis and modal testing are based. As a result, the cost of fully embracing nonlinear behaviour is extremely high, and the tools for doing so are nowhere near as well developed for practical application as are conventional modal testing systems and codes. What is proposed here is the use of 'first-order' approximate nonlinear methods which will provide a useful insight into the extent and nature of many of the nonlinear features encountered in practical structures. One of the small number of methods available for modal analysis of nonlinear structures is used to illustrate this philosophy which offers a practical first step into the world of nonlinear structural dynamics while being based on exactly the same measured data that are used for conventional linear modal tests. Throughout, the talk is illustrated by practical examples, many of which are based on critical structures for which knowledge and management of the structural dynamics characteristics carries the highest priority.

RESPONSIBILITY NOTICE

The author is the only responsible for the printed material included in this paper.

Closed-Loop Reservoir Management: An Overview

Eduardo Gildin ¹

¹ Texas A&M University, Harold Vance Department of Petroleum Engineering, 3116 TAMU, College Station, TX, 77843-3116, eduardo.gildin@pe.tamu.edu

Abstract: One of the key challenges in the Oil & Gas industry is how to best manage reservoirs under different conditions, constrained by production rates based on various economic scenarios, in order to meet energy demands and maximize profit. To address the energy demand challenges, a transformation in the paradigm of the utilization of “real-time” data has to be brought to bear, as one changes from a static decision making to a dynamical and data-driven management of production in conjunction with real-time risk assessment. The use of modern methods of computational modeling and simulation may be the only means to account for the two major tasks involved in this paradigm shift: (1) large-scale computations; and (2) efficient utilization of the deluge of data streams. In recent years, reservoir simulation, parameter estimation and optimization were brought together in the oil industry into an integrated and more structured approach called optimal closed-loop reservoir management. Their applicability to a realistic field is still an open topic, as the large-scale nature of existing problems that generate complex models for controller design and real-time implementation hinders its full applicability. In this paper, I will describe the four pillars of closed-loop management: reservoir modeling, model reduction, automated parameter estimation and production optimization. In order to obtain accurate models that can be simulated within reasonable computational time and effort, reduced-order models need to be obtained. The paper will focus on model reduction using system-theoretical result and optimization approaches. Production optimization techniques and parameter estimation will be illustrated by means of the so-called Ensemble Kalman Filters.

Keywords: Porous Media, Reservoir, Optimization, Subsurface, Flow

NOMENCLATURE

$c_{\{w,o\}}$ = fluid compressibility
 g = acceleration of gravity, ft/sec²
 \mathbf{K} = permeability tensor, darcy
 $P_{o,w}$ = phase pressures, psi
 ρ = fluid density, cp (Pa.s)
 t = time, days (sec.)

ϕ = porosity, dimensionless
 q = flow rate per unit volume,
RB/day (m³/day)
 S = fluid phase saturation,
dimensionless

Subscripts

w water phase
o oil phase
i represents {o,w} phases

INTRODUCTION

In recent years, a fresh look at how real-time data could be integrated in the decision-making process and in the creation of value in the Oil & Gas industry has opened new avenues of research and, in turn, a new set of challenges were put forth. Smart wells, e-field, i-fields, among other ideas were developed based on the premise that real-time data, field-wide optimization and parameter estimation (history matching) could be put together in a somewhat structured fashion, called closed loop reservoir management. Large investments were made to deploy computers, sensors and actuators all over the field, ensuring continuous real-time influx of data. By themselves, computers and real-time data provide no benefit and are merely expenses. Value is created only when better decisions are made and implemented because of the improved knowledge and information these investments provide. The need for a substantial improvement in work processes has been noted many times in the past. Future efforts must balance acquiring additional data with developing software and work processes that can help us cope with this data flux. This continues to be the most important area of improvement.

Ensuring that reasonably right control & optimization decisions are made more rapidly so that the “real time” nature of the smart wells isn’t lost is of central issue in petroleum production processes. Engineering solutions to fluid flow problems in heterogeneous porous media require large-scale computations to effectively represent the complex physics and chemistry occurring in the subsurface. In many cases, the underlying model used to solve the forward problem in an optimization or in an inverse modeling scheme (parameter estimation) is a product of discretization of a set of partial differential equations (PDE’s). Hence, highly accurate and detailed description of the underlying models induce dynamical systems of large dimensions either in the state or parameter spaces (several millions of grid blocks are often obtained). Furthermore, with advances in sensor technology, real-time data has become routinely available in the subsurface. This deluge of data could in fact, become one of the main assets in the Oil & Gas industry, if smart ways of analysis, management and data feedback, that is, data assimilation in conjunction with optimization could be implemented in real time operations.

Recently, history matching and optimization were brought together in the oil industry into an integrated and more structured approach called optimal closed-loop reservoir management. Closed-loop control algorithms have also been applied extensively in other engineering fields, including aerospace, mechanical, electrical and chemical engineering. However, their applications to porous media flow, such as - in the current practices and improvements in oil and gas recovery, in aquifer management, in bio-landfill optimization, and in CO₂ sequestration have been minimal due to the large-scale nature of existing problems that generate complex models for controller design and real-time implementation.

In order to establish a work flow for applying the concept of closed-loop reservoir management, one needs to carefully investigate the applicability of what the author calls the four pillars of optimal reservoir management: reservoir modeling, model reduction, automated parameter estimation and production optimization. In this paper, all of this four concepts will be described and their real-time integration will be discussed. This paper is organized as follows. First, an introduction to petroleum production and porous media flow modeling is given in order to show the basic equations involved. Then, the concept of closed-loop is introduced using the smart wells technology. Finally, the four pillars of reservoir management are described in order to show the entire closed-loop framework.

PETROLEUM PRODUCTION AND POROUS MEDIA FLOW DYNAMICS

Petroleum Formation

Petroleum extraction is sometimes denominated as the only outcome of a more comprehensive energy resource matrix comprised at large of fossil fuels. In general, fossil fuels consist of oil, coal and natural gas. They have their origin in the deposition of organic matter in the bottom of the sea (and lakes) over millions of years, forming a layered structure, which under high pressure and temperature yielded a chemically modified matter known as oil shale; with increased heat, then, it transformed into liquid and gaseous hydrocarbons (Dake, 1983).

The severe geological activities that took place during this time, created faults, fractures and twists, and in turn changed the fairly homogeneous strata into a heterogeneous porous media with spatially varying rock and fluid properties (porosity, permeability, saturation, capillary effects, etc.). It should be noted that although the term porous media is used in this context, the actual rock is impermeable, and one needs to consider properties that accounts for “small openings” called pores within the formation. The two major properties are: (1) the fraction of the solid rock comprised of void spaces – porosity; (2) the distribution or connection of such pores – permeability. It is not the intention of this paper to give a comprehensive description of the petrophysical characteristic of the reservoir. The keen reader may look at (Dake, 1983; Craig 1975; Economides, 1993).

Petroleum Production

The exploration and production of petroleum reservoirs is a lengthy and delicate process. It involves not only technical questions but also economic and political issues (Dake, 1983). From the science and engineering stand point, an initial assessment by a team of geologists, geoscientist and petroleum engineers determines the probable success of finding recoverable resources. Once the study has been performed and promising regions have been detected, the exploration phase begins. Wells are drilled and core samples and logs along with wells tests data are collected and analyzed to predict roughly the reservoir reserves and potential production. The next phase consists of developing the basic structures of the potential field that is, drilling production wells and setting up the network of pipelines with surface facilities. Drilling new wells may involve a series of engineering undertaken, as drilling, cementing, casing, and completing the well may take time and lots of resources (wells can cost from 1 to 100 millions of dollars). This phase may involve the decision to adopt some kind of automation in the recovery process by using smart completions. This will be described below.

Roughly speaking, the production life-cycle of a reservoir varies from years to tens of years; systematically one can divide this cycle in three main processes, which depends on the way the hydrocarbons are extracted (Dake, 1983, Economides, 1993). Initially, the reservoir is at equilibrium, with all the phases (gas, oil and water) separated by gravity. When a production well is drilled so that it penetrates the non-permeable layer, the equilibrium is perturbed and due to the differential in pressure, the hydrocarbons flow naturally to the wellbore. By means of a set of valves, the production can be controlled until the equilibrium is reestablished. This first phase is called primary production by natural forces. Although relatively cheap and simple to be assembled, only 10-20% of the hydrocarbons present are produced. This is mainly due to the pressure drop in the reservoir.

At this stage, the operating company may start the secondary phase of the reservoir production, in which pressure is added back to the reservoir by means of injecting fluid (water or gas) into the reservoir. One of these techniques is called waterflooding, in which water is injected to counterbalance the decrease in reservoir pressure. As can be seen, injection or production wells may need to be drilled (or converted to) in addition to the ones already in place. In this phase, recovery can reach up to 50%. The main issue here is how to manage efficiently the injection of water and production of fluids (oil, gas and water) in an optimized sense, either by means of economic measures, say, the net

present value (NPV) or production measures, such as cumulative oil production. As will be seen in later sections, smart wells technologies have the potential to improve the secondary recovery.

In order to enhance even more the production of hydrocarbons, the tertiary phase of production may start. In this case, enhanced oil recovery (EOR) will deal with the injection of sophisticated fluids like polymers and foam, so that some of the fluids properties are modified to better push out the remaining oil. This paper will deal mostly with waterflooding optimization, although new initiatives are being setup to deal with optimization in the EOR framework (Economides, 193).

Smart Wells

Loosely speaking, the term smart wells have been utilized to introduce any kind of automation in the production of oil reservoirs by means of real-time reservoir characterization and control. One can also find terms such as e-field, i-field and smart fields, which may also involve automation in data analysis (data mining) and well monitoring. In this paper, we will use the term smart wells technology to signify a completion system that can monitor and control production/injection through a series of ICVs (inflow control valves) at several zones of a particular well. Therefore, using this technology, one is able to acquire data and, in turn, control independently several intervals of the well. A physical description of the smart wells can be seen in Fig. 1.

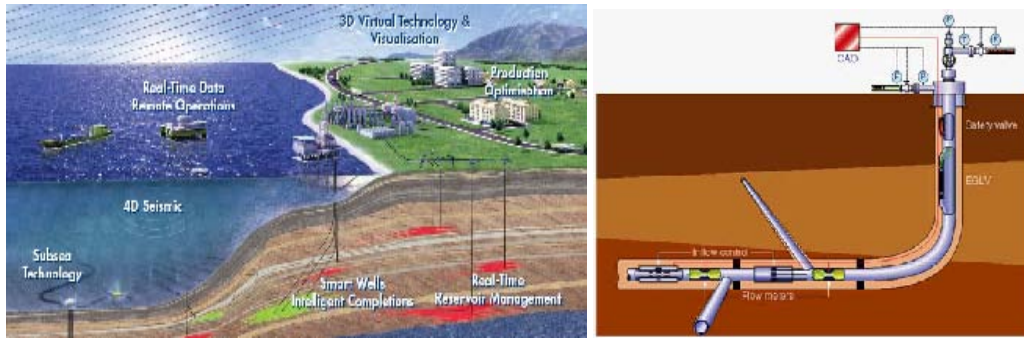


Figure 1 – Left Picture: Concept of e-field; Right Picture: Concept of Smart Wells Technology. Source: Shell

Porous Media Flow Equations

Reservoir simulation has always been one of the main components in reservoir management. Great effort has been devoted to constructing high-order reservoir models for improved oil recovery (Aziz, 1986; Peaceman, 1986). In general, the governing equations of multi-phase flow in porous media are given by a set of partial differential equations that represent conservation of mass, momentum and energy together with equations of state which describe the fluid property as a function of pressure and temperature.

As discussed in (Aziz, 1986; Peaceman, 1986), several simplifications can be taken into account such as neglected inertial effects, flow being isothermal and the use of the empirical Darcy's law. Hence, one can assume the "Black-oil" formulation, where there are two components (oil-water) and there are two phases of the hydrocarbon substance (oil and gas) present in the reservoir. In this paper, we will assume no gas in the reservoir. The mass balance equation for each phase is given by

$$\nabla \cdot (\rho_i \mathbf{v}_i) + \frac{\partial (\rho_i \phi S_i)}{\partial t} - \rho_i q_i = 0, \quad i \in \{o, w\}, \quad (1)$$

where ρ is the fluid density, \mathbf{v} is the fluid superficial velocity, t is time, $(\nabla \cdot)$ denotes the divergence operator, ϕ is the porosity, S_i is the fluid saturation of each phase, q_i is flow rate per unit volume and finally $\{o, w\}$ represents the oil and water phases, respectively. Using the empirical Darcy's law, once can write

$$\mathbf{v}_i = -\frac{k_{ri}}{\mu_i} \mathbf{K} (\nabla p_i - \rho_i g \nabla h), \quad (2)$$

where (∇) is the gradient operator, \mathbf{K} is the permeability tensor, μ fluid viscosity, k_{ri} is the relative permeability of each phase (which is a function of S_w), p_i pressure of each phase, g is the acceleration of gravity and finally h is the depth of the reservoir. Plugging Eq. 1 into Eq. 2, one writes

$$\nabla \cdot \left[-\frac{\rho_i k_{ri}}{\mu_i} \mathbf{K} (\nabla p_i - \rho_i g \nabla h) \right] + \frac{\partial (\rho_i \phi S_i)}{\partial t} - \rho_i q_i = 0. \quad (3)$$

With four unknowns p_w, p_o, S_w, S_o , four equations are required to complete the system description and solve Eq. 3. The two additional equations are given by a closure equation which states that the sum of all fractional saturations must always be equal to one, and the oil-water capillary pressure equation, which gives a relation between phase pressures as function of water saturation. They are respectively:

$$\begin{aligned} S_w + S_o &= 1, \\ p_o - p_w &= p_c(S_w) \end{aligned} \quad (4)$$

Equations 1-4 can be rearranged in such a way that the two-phase equations are formulated in terms of two state variables: p_o the oil pressure, and S_w the water saturation. In order to do that one can apply the chain rule differentiation and the definitions of oil, water and rock compressibilities as

$$c_i = \frac{1}{\rho_i} \frac{\partial \rho_i}{\partial p_i} \Big|_{TR}, \quad i \in \{o, w\}; \quad c_r = \frac{1}{\phi} \frac{\partial \phi}{\partial p_o}, \quad (5)$$

yielding

$$\begin{aligned} -\nabla \cdot \left\{ \frac{\rho_w k_{rw}}{\mu_w} \mathbf{K} \left[\left(\nabla p_o - \frac{\partial p_c}{\partial S_w} \nabla S_w \right) - \rho_w g \nabla h \right] \right\} + \\ \rho_w \phi \left[S_w (c_w + c_r) \frac{\partial p_o}{\partial t} + \frac{\partial S_w}{\partial t} \right] - \rho_w q_w &= 0, \\ -\nabla \cdot \left[\frac{\rho_o k_{ro}}{\mu_o} \mathbf{K} (\nabla p_o - \rho_o g \nabla h) \right] + \\ \rho_o \phi \left[(1 - S_w) (c_o + c_r) \frac{\partial p_o}{\partial t} - \frac{\partial S_w}{\partial t} \right] - \rho_o q_o &= 0 \end{aligned} \quad (6)$$

As can be seen from the above equations, multi-phase flow through porous media is given by a set of weakly-nonlinear parabolic PDE's that represents the dynamics of the rate of change of pressure (diffusion) coupled with a set of strongly-nonlinear parabolic-hyperbolic PDE's which describe the dynamics of the rate of change in phase saturations and component concentrations (diffusion-convection). The equations can be discretized in space yielding a set of nonlinear ordinary differential equations (Aziz, 1986; Peaceman, 1986). Most of the numerical reservoir simulators apply a spatial discretization scheme based on finite differences or finite volume formulations, using an upstream weighting in the convection dominant terms.

CLOSED-LOOP RESERVOIR MANAGEMENT

Waterflooding

As introduced before, the production of fossil fuels can be staged in three main phases. In this paper, secondary recovery by means of waterflooding will be the method of choice for optimizing the life-cycle of reservoir production. Waterflooding is the most common method used in the Oil and Gas industry, as more than 50% of the USA's production is due to this process (Craig, 1975; Dake, 1983).

Waterflooding works by injecting water so that the reservoir pressure is maintained (or even increased) in order to sweep and displace oil from the pores of the formation and replace it by water. Basically, the field is divided in two types of wells: injectors and producers. Although the concept of waterflooding is simple, the lack of independent control in all segments of the well makes the production optimization a daunting exercise. This can be visualized in Fig. 2. For homogeneous media, the water front would move uniformly from the injectors to producers. However, due to heterogeneities, and more importantly, the lack of knowledge of the true value of the rock properties, the fluid front moves in a highly non-homogeneous manner, yielding water to be produced to the point of stalling the production to a non-feasible economical setting. This is called water breakthrough, and in general, the remedy to is shut in the producers, leaving behind packets of recoverable oil (Naevdal, 2006).

Having in mind that both types of wells (injectors and producers) can be embedded with smart-wells technology, the injected water and the produced fluids (oil, water and gas) can be controlled in a feedback loop, in such a way that the optimization is done in the closed-loop fashion.

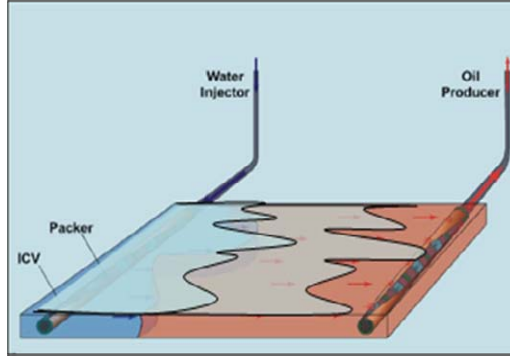


Figure 2 – Waterflooding Concept: Smart Injection Well Introduced Water to the Reservoir; Producing Wells Controls the Opening and Closing of ICV's. Source: Adapted from (Jansen, 2008)

Closed-Loop Concepts – Systems Framework

Closed-loop control is not a new subject as there has been several feedback control applications employed in the oil industry (see (Dorf, 2010) for feedback control techniques). Some of them were based on the performance optimization (percentage of oil recovery per unit volume) of a control variable (pressure and flow rates) subject to a number of constraints (Brouwer, 2002; Brouwer, 2004) However, they were basically off-line applications of optimal control theory that do not explicitly use real-time data computations. Real-time, model-based control applications have been introduced in the literature, recently for oil recovery (Jansen, 2009). One of the fundamental difficulties in designing such controllers for large-scale reservoir management stems from the fact that reservoir simulation models, given by PDE's with highly heterogeneous system parameters, yield large state-space dimensions (on the order of tens of thousands to millions) upon discretizations and, in turn, large dimensions for model-based controllers. Later in this paper, model order reduction techniques will be introduced in order to mitigate this computational cost.

The modeling of waterflooding in a systems framework starts by recasting the porous media flow equations in the so-called input-output description (Antoulas, 2005; Dorf, 2010). After discretization in space, each grid block is related to two states of the reservoir, that is, oil pressures and water saturations. Vectorizing the states of the system and denoting it $\mathbf{X} = [p_o^1 \cdots p_o^N \ S_w^1 \cdots S_w^N]^T$, and similarly for the sources terms, $\mathbf{Q} = [q_o^1 \ q_w^1 \ \cdots \ q_o^N \ q_w^N]^T$, one can write Eqs. 4-6 in the form (Jansen, 2009; Gildin, 2008):

$$\mathbf{V}(\mathbf{X})\dot{\mathbf{X}} + \mathbf{T}(\mathbf{X})\mathbf{X} = \mathbf{F}(\mathbf{X})\mathbf{Q}, \quad (7)$$

where $\mathbf{V}(\mathbf{X})$ is the accumulation matrix, which contains ϕ, c_r, c_o and c_w , $\mathbf{T}(\mathbf{X})$ is the transmissibility matrix, containing the permeabilities and viscosity parameters, and $\mathbf{F}(\mathbf{X})$ is a selection matrix representing flow rates or bottom-hole pressure measurements. The above equation, in turn, can be recast in a generalized nonlinear state-space form and linearized through an operating point, yielding, the linear time-invariant discrete state-space formulation as

$$\begin{cases} \mathbf{g}(\mathbf{u}, \mathbf{x}, \dot{\mathbf{x}}, \boldsymbol{\theta}, t) = \mathbf{0} \\ \mathbf{y}(t) = \mathbf{h}(\mathbf{u}, \mathbf{x}, \dot{\mathbf{x}}, \boldsymbol{\theta}, t) \end{cases} \Rightarrow \begin{cases} \mathbf{x}(k+1) = \mathbf{A}\mathbf{x}(k) + \mathbf{B}\mathbf{u}(k) \\ \mathbf{y}(k) = \mathbf{C}\mathbf{x}(k) + \mathbf{D}\mathbf{u}(k) \end{cases} \quad (8)$$

Designing feedback controllers for such large-scale systems become a very expensive computational task, and, in some cases where the processing time is critical, unfeasible for practical implementation (Anderson, 1989; Zhou, 1996). Furthermore, assessment of uncertainty and robustness of those complex high-order models generates an even more difficult task to be performed, since one might be interested in several runs of the full simulation model. In this manner reduced-order models, linear and nonlinear, that approximate the full-order system are desirable for either the large-scale simulation of the complex dynamical system and the design of a closed-loop control system.

Closed-Loop Block Diagram

The closed loop block diagram of optimal reservoir management, as depicted in Fig.3, would not be different from any other closed-loop system encountered in most of the feedback control systems (Dorf, 2010). The main issues in the reservoir setting, however, are the large-scale nature of the reservoir models (state and parameters spaces) and the number of uncertain parameters, which hinder its direct applicability to real-time implementations. There have been

several attempts to redraw the block diagram of Fig. 3 to a more suitable system, which can be realized in the real-time (Jansen, 2008, Gildin, 2008; Jansen, 2009; Wang 2007)

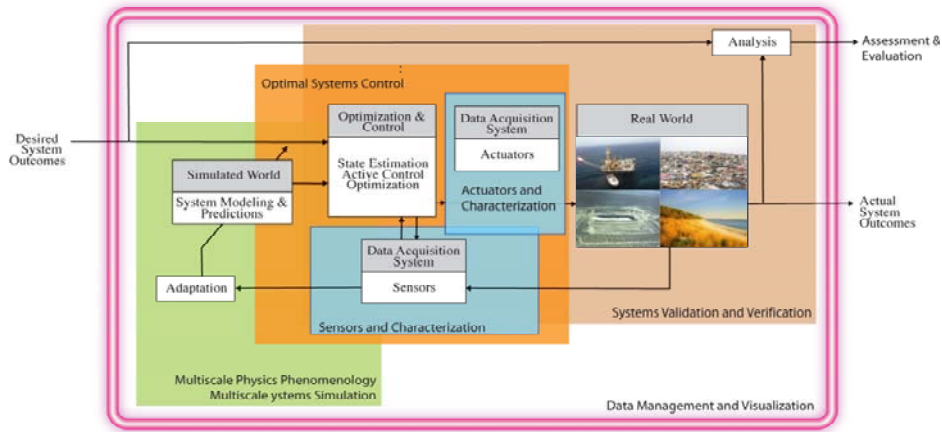


Figure 3 – Closed-Loop Reservoir Management Concept: Block Diagram Including Optimization, Parameter Estimation and Data Acquisition.

Optimization

Roughly speaking, subsurface flow optimization is concerned with the maximization of hydrocarbon production while minimizing, as in the case of waterflooding, the water production (breakthrough) of a reservoir (Jansen, 2008; Jansen 2009; Wang 2007). In general, one searches for performance indexes that relate to Net Present Value (NPV), i.e., the total oil revenues subtracted from the total injection and production costs over the life of the reservoir, multiplied by a discount factor. Mathematically one writes, for a particular instant of time, say t_k ,

$$J_k = \frac{-\sum_{i=1}^{N_{inj}} r_{wi} (q_{wi,i})_k + \sum_{j=1}^{N_{prod}} [-r_{wp} (q_{wp,j})_k + r_o q_{op,j}]_k}{(1+b)^{\frac{t_k}{\tau}}} \quad (9)$$

where, the q 's represent the control variables of water injection (wi), water production (wp) and oil production (op), in N_{inj} injection wells and N_{prod} production wells, respectively. The r 's represent the unit cost or revenue for water injection and production and oil production. The denominator represents the discount factor using the discount rate b for a reference time τ . In practice, the minimization of Eq. 9 comes together with state and input constraints, which may represent the physical restrictions with the injection and producers and economical or political decisions (Jansen, 2008; Jansen 2009; Gildin, 2009).

There are many techniques to solve the above minimization problem (Jansen, 2011). Recently, the oil industry has been paying attention to gradient-based optimization, due to the fact that gradients can be computed through the use of optimal control theory and the adjoint method (Jansen, 2011). Although adjoint-based techniques have shown to perform well in the reservoir arena, they suffer from the need of large-scale computations and the requirement to code the adjoints in the optimization software, which may not be available in several commercial off-the-shelf programs. Model predictive control theory has also been applied recently in the production optimization setting (Gildin, 2008; Jansen, 2008).

State and Parameter Estimation

A common approach to model parameter uncertainties is to append some sort of estimator (parameter and state) to the closed-loop system. In a broad sense, parameter estimation fits into the so-called data assimilation or inverse modeling framework (Oliver, 2008, Evensen, 2009). Inverse modeling can be recast in an optimization problem as one tries to minimize a well defined performance index related to the misfit between the model output (simulation) and measured data, which can be available real-time or in a batch format. In the reservoir engineering community, data assimilation is also known as assisted history matching (Oliver, 2008, Evensen, 2009). In this case, one can define an objective function as

$$J(\mathbf{x}) = \sum_{k=1}^K \left[(\mathbf{d}_k - \mathbf{y}_k)^T \mathbf{P}_\eta^{-1} (\mathbf{d}_k - \mathbf{y}_k) + (\boldsymbol{\theta}_k - \bar{\boldsymbol{\theta}}_k)^T \mathbf{Q}_\eta^{-1} (\boldsymbol{\theta}_k - \bar{\boldsymbol{\theta}}_k) \right], \quad (10)$$

where the \mathbf{P} 's are weighting matrices, usually chosen to be the error covariance matrices of measurements and prior permeability values, \mathbf{d}_k is the measure data at time k , \mathbf{y}_k is the model output, and $\boldsymbol{\theta}$ is related to the parameters to be identified, usually taken as the permeability field of the reservoir.

The estimated parameter is found by minimizing the objective function $J(\mathbf{x})$ by means of any type of optimization algorithm. It is a common practice to use adjoint-based algorithms. As exposed before, this may require great effort to code adjoints, especially for more complex problems. In this case, one can use alternatives methods based on sequential data assimilation, as in the Kalman filtering framework. The Kalman Filter (KF) and its variants would work well, except they require large-scale matrices inversion and computations, becoming infeasible for the parameter/state estimation in the reservoir setting. The most common technique employed nowadays is the so-called Ensemble Kalman Filter (EnKF) (Oliver, 2008, Evensen, 2009).

The EnKF uses Monte Carlo simulations to evaluate the a posteriori probability distribution of the state and outputs, thereby relying only on efficient matrix-vectors multiplications (Evensen, 2009, Aanonsen, 2009). The basic algorithm, starts with an initial guess of the model parameters with a given probability distribution, then it propagates the states from two instances of time (called forecast) using a reservoir simulator, and finally assimilates the production data by updating the reservoir parameters (called analysis) based on the mismatch between measurements and the corresponding predictions from the ensemble. The basic algorithm can be viewed pictorially in Fig. 4.

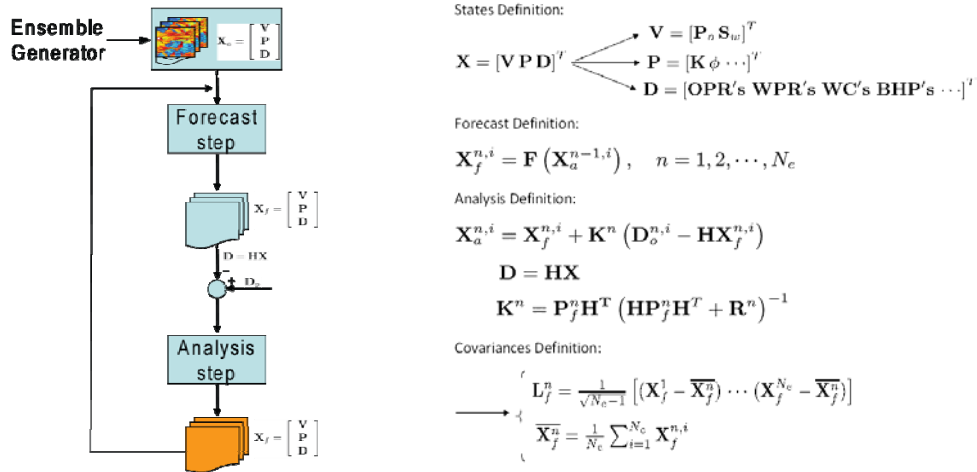


Figure 4 - The Ensemble Kalman Filter (EnKF) Algorithm – Workflow and Main Equations.

Model Reduction

As pointed out previously, the main issue in applying the closed-loop concept to the optimal reservoir management framework boils down to overcoming the large-scale nature of such models, both in the control and estimation problems. In this case, one can approximate the input-output behavior of such models in a process called model order reduction (Gildin, 2006, Cardoso, 2010, Heijn, 2004, Van Doren, 2004).

Several ways of obtaining reduced-order models were proposed in the literature (Antoulas, 2005, Gildin, 2006). In a broad sense, they can be divided in two main categories: model reduction for simulation and model reduction for control purposes. In the latter case, one should recognize the importance of the addition of the controller into the process. In this manner, the problem of controller reduction (closed-loop) is different from the problem of model reduction (open-loop) given that the ultimate goal is to accurately approximate the closed-loop performance of the dynamical system. In general, the problem of reducing the order of a large-scale model is known as the approximation of dynamical systems (Antoulas, 2005). Basically one can view the approximation methodology simply as a surrogate model, as in the case of “black box” approaches, or one can intrusively modify the equation, as in the “white-box” approaches (see Fig. 5).

In a projection framework, basically two families of model reduction may be used, as depicted in Fig. 5.: SVD-based methods and Krylov-based or moment matching methods. Several techniques have been developed in both the linear dynamical system framework, namely, the Balanced Truncation, Hankel Norm Approximation, Moment Matching by Krylov Techniques, and, in the nonlinear setting, namely the use of the Proper Orthogonal Decomposition

(POD) and its variants (Antoulas, 2005). In particular, this article describes the following methods for model reduction: modal truncation, balanced truncation, and rational Krylov.

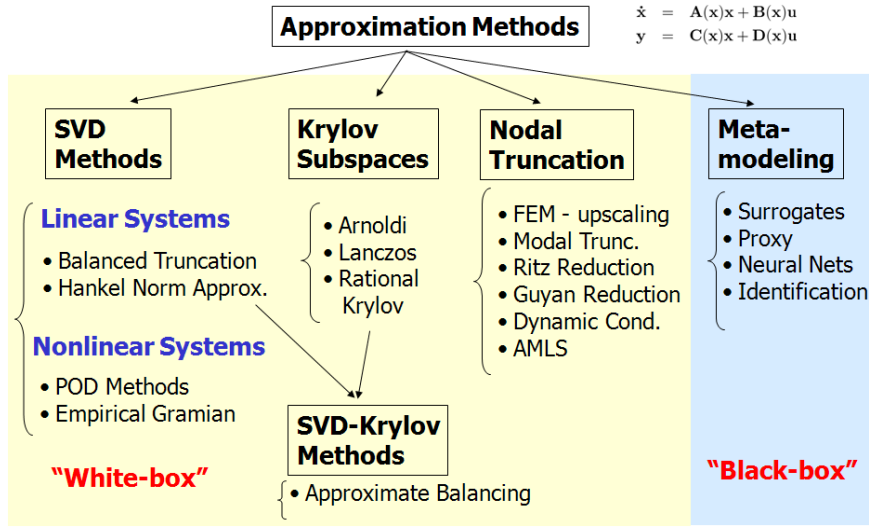


Figure 5 – Model Order Reduction Techniques. Adapted from (Antoulas, 2005).

Roughly speaking, the SVD family relies on dense matrix factorizations and preserves important theoretical properties of the original system, like stability, together with a measure of the approximation error. On the other hand, the Krylov methods rely only on matrix vector multiplications, yielding numerically efficient algorithms for large-scale applications, but they lack good theoretical properties. A combination of the best features of both families is also possible in an SVD-Krylov framework through the use of iterative methods (Antoulas, 2005). In a mathematical framework, the model and controller reduction may be posed as follows: Given a dynamical system Σ , modeled as a non-linear differential equation, or in a special case, linear time-invariant dynamical system (LTI), one seeks a reduced order approximation to Eq. 4, such that:

- the dimension of the reduced order model is $r \lll n$;
- the behavior of the reduced order model approximates the original with certain accuracy, i.e., there is a small error bound on $y(t) - y_r(t)$;
- the model reduction procedure is computationally stable and efficient, and the reduced order model is achieved by means of projection, $\Pi = VZ^T$, where $V, Z \in \mathbb{R}^{n \times r}$ with $Z^T V = I_r$, as in the following equations:

$$\Sigma_r : \begin{cases} \dot{x}_r(t) = Z^T F(Vx_r(t), u(t), t) \\ y_r(t) = Z^T H(Vx_r(t), u(t), t) \end{cases} \quad \text{or} \quad \Sigma_r : \begin{cases} \dot{x}_r(t) = Z^T A V x_r(t) + Z^T B u(t) \\ y_r(t) = C V x_r(t) + D_r u(t) \end{cases}; \quad (8)$$

In order to determine the feasibility of the application of such methods for designing low-order models and, in turn controllers, a study must be performed first at the reservoir model level, i.e., reservoir model reduction. Verification of properties, like decay rate of Hankel singular values to a linearized model and its approximation may indicate if a reduced order model will yield good results for the controller approximation problem.

CONCLUSIONS

This paper presented a general framework for realizing real-time optimal control strategies for large-scale reservoir models. As it is the case of most of oil reservoir models, uncertainty in the geological and petrophysical parameters are the main drawbacks of open-loop optimization. Closed-loop control has the potential to address issues related to production optimization given a set of unknown parameters as in any other engineering discipline taking advantage of real-time data management. However, the size of the models due to the discretization of the partial differential equations are very large (as compared with other disciplines) and are not amenable for fast implementations, or may require large amount of computational power.

Solution techniques that involve efficient numerical computations for parameter estimation and optimization are of great value in these settings. Model reduction techniques may be the only way to avoid the large scale computations that

takes place in the optimization process. It is fair to say that closed-loop reservoir management is still in its infancy and much attention and resources need to be put forth for realizing its full potential.

Research Gaps

Basically, the concept of closed-loop reservoir management has been shown to be of great value in the literature, but the introduction of such methodologies has not been fully accepted (or it has a slow pace) in practical applications in the Oil & Gas industry. The main issues are threefold:

1. Automated history matching, and in particular the use of the EnKF, has shown to provide models with good matching (past production history) and prediction capabilities, but do not result in parameters with a much geological sense. This is to say that the input-output behavior of the reservoir model is consistent to what is expected as far as production, but physically they do not represent what the geologist's may believe it is a good model. From a system theoretical point of view this is adequate as connecting blocks with the correct input-output description is what makes sense. Therefore, there should be a way of incorporating geological properties to automated history matching in as seamless manner.
2. Reduced-order models have been shown to produce reasonable approximations to the full and complex reservoir models. Thus, complex models usually have counterparts with much smaller state and parameters dimensions. This is to say that one needs to understand how much of the complexities will play a role in input-output behavior of such models. From a system theoretical point of view, controllability and observability are of central issue, and, in general, the petroleum engineering community is not aware of such properties. These may lead to simplifications on the production workflows.
3. Convince the production managers that the operation of the reservoir should be guided not only by experience, but also from "smart" decisions resulted from the closed-loop optimization. The idea is not to remove the human from the loop, but let him help on the decision process. In several occasions, as pointed out in the literature, production can be adjusted to not only produced the most of the reservoir, but to give the maximum economically, which may sounds contradictory one to another. Although one may start producing in a slower pace, over the life time of the reservoir one may recover larger amounts of oil and in turn, realize a better economic scenario. Thus, better ways of demonstrating the feasibility of the closed-loop system needs to be well thought out.

REFERENCES

- Aanonsen, S. I. , et al, 2009, "The ensemble Kalman filter in reservoir engineering – A review", SPE Journal, Vol. 14, No. 3, pp. 393-412, September 2009.
- Antoulas A.C., 2005. Approximation of Large-Scale Dynamical Systems, SIAM, Philadelphia.
- Anderson, B.D.O, and Liu, Y., 1989, "Controller Reduction: Concepts and Approaches", IEEE Trans. On Automatic Control, Vol. AC-34, No. 8, pp. 802-812, August.
- Aziz, K., and Settari, A., 1986. Petroleum Reservoir Simulation, Elsevier Applied Science Publishers.
- Brouwer, D.R, et al: "Improved Reservoir Management Through Optimal Control and Continuous Model Updating", paper SPE 90149 presented at the SPE Annual Technical Conference and Exhibition, Houston, TX, USA, September 26-29 (2004).
- Brouwer, D.R., and Jansen, J.D.: "Dynamic Optimization of Waterflooding with Smart Wells Using Optimal Control Theory", paper SPE 78278 presented at the 13th. European Petroleum Conference, Aberdeen, Scotland, UK, October 29-31 (2002).
- Cardoso, M.A., and L.J. Durlofsky., 2010. "Use of Reduced-Order Modeling Procedures for Production Optimization", SPE Reservoir Simulation Symposium, 2-4 February 2009, The Woodlands, Texas, USA.
- Craig Jr., Forrest F., 1975, "The Reservoir Engineering Aspects of Waterflooding", SPE Monograph Series, Volume , Society of Petroleum Engineers.
- Dake, L. P., 1983, "Fundamentals of Reservoir Engineering - Developments in Petroleum Science", Elsevier Science.
- Dorf, R. and R.H. Bishop, 2010. Modern Control Systems, 11/E. Prentice Hall.
- Economides, M. J., Hill, D.A. and Ehlig-Economides, C., 1993, "Petroleum Production Systems", Prentice Hall.
- Evensen, Geir, 2009. "Data assimilation, The Ensemble Kalman Filter", 2nd ed., Springer,
- Gildin, E., Klie, H., Wheeler, M.F., Rodriguez, A., and Bishop, R.H. [2006]. Projection-based Approximation Methods for the Optimal Control of Smart Fields", In Proceedings of the 10th. European Conference of the Mathematics of Oil Recovery, Amsterdam, The Netherlands, September 4-7.
- Gildin, E, and M.F. Wheeler, "Optimal Subsurface Flow Management using Model Predictive Control Techniques", in Proceedings of the European Conference on the Mathematics of Oil Recovery – ECMOR XI – Bergen, Norway, September 2008.

- Heijn, T., Markovinovic, R. and Jansen, J.D.. [2004]. "Generation of Low-Order Reservoir Models Using System-Theoretical Concepts". SPE Journal, June, Vol. 9, No. 2.
- Jansen, J.D., Bosgra, O.H. and van den Hof, P.M.J.: "Model-based control of multiphase flow in subsurface oil reservoirs". Journal of Process Control (2008) 18 (9) 846-855.
- Jansen, J.D, et al, 2009, "Closed Loop Reservoir Management", SPE Reservoir Simulation Symposium, 2-4 February 2009, The Woodlands, Texas
- Jansen, J.D., Bosgra, O.H. and van den Hof, P.M.J., 2008: "Model-based control of multiphase flow in subsurface oil reservoirs", Journal of Process Control 18 (9) 846-855. DOI: 10.1016/j.jprocont.2008.06.011.
- Jansen, J.D., 2011: "Adjoint-based optimization of multiphase flow through porous media – a review", Computers and Fluids. Published online. DOI: 10.1016/j.compfluid.2010.09.039.
- Naevdal, G., Brouwer, D.R. and Jansen, J.D.: "Water flooding using closed-loop control". Computational Geosciences (2006) 10 (1) 37-60.
- Wang, C. , Li, G. and Reynolds, A.C., 2007, "Production Optimization in Closed-Loop Reservoir Management" SPE Annual Technical Conference and Exhibition, 11-14 November 2007, Anaheim, California, U.S.A.
- Oliver, D, A. Reynolds and N. Liu: "Inverse Theory for Petroleum Reservoir Characterization and History Matching", (ix + 360 pages), Cambridge University Press, May 2008.
- Peaceman, D.W., 1977, "Fundamentals of Numerical Reservoir Simulation", Elsevier Applied Scientific Publishing Company.
- Van Doren, J., Markovinovic, R. and Jansen, J.D., 2004. "Reduced-Order Optimal Control of Waterflooding Using POD", IX ECMOR, Cannes, France.
- Zandvliet, M.J., van Doren, J.F.M., Bosgra, O.H., Jansen, J.D. and van den Hof, P.M.J., 2008: Controllability, observability and identifiability in single-phase porous media flow Computational Geosciences 12 (4) 605-622. DOI: 10.1007/s10596-008-9100-3.
- Zhou, K., Doyle, J. C., and Glover, K., 1996, "Robust and Optimal Control", Englewood Cliffs, NJ, Prentice Hall.

RESPONSIBILITY NOTICE

The author is the only responsible for the printed material included in this paper.

A Bayesian Experimental Design Approach for Structural Health Monitoring

Michael D. Todd and Eric B. Flynn

Department of Structural Engineering, University of California San Diego, 9500 Gilman Drive 0085, La Jolla CA 92093-0085 USA; email: mdtodd@ucsd.edu

Abstract: Structural health monitoring and damage prognosis together comprise a strategy for efficient life cycle management of structural components and systems. This paper provides a global framework for designing this strategy and optimizing it with regard to performance by invoking Bayesian experimental design principles. The framework shows how the design problem necessarily ties together all the required steps for implementing such a strategy. An example in the design of an ultrasonic defect detection approach for complex stiffened panels is presented.

Keywords: Bayesian design, detection theory, structural health monitoring, risk-informed decision, prognostics

NOMENCLATURE

E = Bayesian cost/loss estimate

L = cost function

p = probability

e = a given SHM system design realization

d = SHM system decision or action

c = specific cost term

Greek Symbols

θ = failure mode or damage state

δ = detector

\mathbf{v} = feature

Subscripts

j j-th damage state

k k-th decision or action

ex extrinsic cost function

in intrinsic cost function

0 null state of the variable

1 alternative state of the variable

INTRODUCTION

Structural health monitoring (SHM) is the general process of making an assessment, based on appropriate analyses of in-situ measured data, about the current ability of a structural component or system to perform its intended design function(s) successfully. Damage prognosis (DP) extends this process by considering how the SHM state assessment, when combined with probabilistic future loading and failure mode models with relevant sources of uncertainty adequately quantified, may be used to forecast remaining useful life (RUL) or similar performance-level variables in a way that facilitates efficient life cycle management. A successful SHM/DP strategy may enable significant ownership cost reduction through maintenance optimization, performance maximization during operation, and unscheduled downtime minimization, and/or enable significant life safety advantage through catastrophic failure mitigation.

In broad terms, any SHM/DP strategy inevitably must, for a well-defined application (which will be more thoroughly discussed in the next section), include in-situ data acquisition, feature extraction from the acquired data, statistical modeling of the features, and classification of the features to make risk-informed decisions. It is the authors' opinion that in general current practice, these elements are only addressed partially and/or separately without regard for what the ultimate global goal of SHM systems is: to direct economically efficient and/or safety-maximized structural health decision-making for the general purpose of long-term effective life cycle management. This paper proposes a Bayesian experimental design approach (Chaloner and Verdinelli, 1995) that facilitates the design of a DP-enabling SHM strategy in four steps: (1) Evaluation of the design space including constraints, (2) Extraction of relevant candidate features and modeling their variability as a function of free design variables, (3) Derivation of a detector, and (4) Evaluation of detector performance.

EVALUATION OF THE DESIGN SPACE

Design of an SHM system, like any system, must invariably start with a well-defined set of objectives and any constraints that may affect achieving those objectives. One does not design an aircraft without a thorough definition of the aircraft's intended usage and performance demands, computation of cost-benefit analysis for each usage/demand profile (both economic and life-safety driven), and an understanding of all constraints (physical, operational, societal, regulatory, etc.). In the case of an SHM system, essentially four groups of questions must be addressed to adequately define the design space:

Question (1): *What are the failure modes the system is being designed to monitor, and, to whatever degree possible, what are their expected probabilities of occurrence?* The first part of this question is clearly application-

dependent; on an aircraft, the most relevant failure modes might be corrosion or metal fatigue cracking, while for a concrete bridge over water, the most relevant failure modes might be pier scour or roller bearing wear. Clearly identifying the failure mode(s) of interest dictates what types of sensing and raw data might be most useful for features. It is also important to further quantify, as much as possible, both the critical level of each failure mode and the confidence that must be met in detecting and/or localizing those critical levels by the SHM system. For example, the objective “to detect 1 mm long fatigue cracks within an area of 1 m² with a detection probability of 95%” is far superior to the objective “to detect cracks” or even to the objective “to detect 1 mm cracks”. Most commonly, the objective is at least partially if not completely dictated by the regulatory laws or policies, e.g., the U.S. Federal Aviation Administration non-destructive evaluation guidelines for cracks or the U.S. Federal Highway Administration bridge inspection rules.

The second part of this question, the *a priori* probabilities of occurrence, is typically a much more difficult thing to define accurately. However, for existing structural systems that are being retrofitted with SHM systems, structural owners, operators/operating engineers, and maintenance engineers together possess significant previous experience about the system’s operation and its typical failure modes; this information may and should be exploited to formulate useful *a priori* probabilities of occurrence. It is this *a priori* information that truly permits the ultimate expression of SHM system performance in a true probabilistic formulation. Even if no such previous structural system-specific experience or information exists (as might be the case for a brand new structural system), recourse may be made to physical knowledge (e.g., general engineering experience suggests that failure often initiates at high-stress regions, such as rivets, fillets, material changes, etc.) to formulate such probabilities. One may also simply use a so-called “uninformed” probability of occurrence, such as a uniform probability, which may be updated later as new information continues to arrive.

Question (2): What specific actions will the SHM system direct in response to the failure mode(s)? Such actions vary widely depending upon the application, and often the allowable or available actions, much like the objective(s) above, are at least partially dictated by regulations. Actions can range from directing current operation status (e.g., “continue forward operation,” “reduce aircraft speed,” “close bridge”), to recommending a maintenance action (“inspect left engine pylon at next ground station,” “replace right compressor thrust bearing”), to lower-level action-precursory decisions such as “critical level of damage is present” or “critical level of damage is not present,” each of which may imply different hierarchies of higher-level actions. The clear definition of a response hierarchy is one area where SHM is different from the more basic objective of state estimation: classic estimation theory strives to achieve the optimal unbiased estimate of the current system state (and has led to the entire field of system identification, which is an important part of SHM), but with SHM, the goal is to make the most economical/safe decisions, not necessarily the most accurate state assessment. This is why the previous question (1) is so important and related to this question (2): as an example, some failure modes may be far more probable than others or far more costly if they go undetected, and the best SHM system is the one that will optimally direct action in response to this situation. The mention of “cost” leads to the next question (3), which is

Question (3): What are the costs associated with the actions/decisions that the SHM system takes/makes and with the deployment and operation of the SHM system itself? This first part of this question assigns costs to each decision/action that the SHM system is designed to direct, which will be called “extrinsic costs”. These costs include the possible consequences of these actions, e.g., what is the cost of being directed to inspect an aircraft when no damage exists (a “false positive”), what is the cost of catastrophic failure due to the target failure mode when being directed to do nothing (a “false negative”), etc. These costs are often dictated by structural asset costs, insurance costs, liability costs, possible litigation costs, and downtime leading to revenue losses. The second part of the question is the actual cost of SHM system development (research and fabrication, including testing, validation, and verification), the cost of deploying the SHM system on its host structure, and the cost(s) of operating the SHM system (power costs, SHM system self-maintenance costs, weight penalty on the structure, etc.), called “intrinsic costs.” For the construction of a meaningful cost function, the units on all terms comprising cost should be equivalent (e.g., monetary valued). The fundamental cost-benefit analysis that must be done to validate feasibility of a particular SHM system design is to determine whether the intrinsic costs are exceeded by appropriate cost-accounting of the risk reduction that the system brings to the particular application.

As a final comment on cost, for some SHM applications, particularly military ones where traditional cost sensitivities are often less important than structural asset demands (e.g., aircraft readiness for combat), the costs may be cast instead in terms of a utility loss function.

Question (4): What are the constraints present in the design space? This is a very important but often overlooked question in practical SHM system design. Constraints may take several forms: physical (a certain structural member may be inaccessible to sensors, the system cannot have more than a 0.25 m² footprint), operational (power is only available at a certain duty cycle, ambient temperatures fluctuate between -40°C and 40° C), regulatory (the SHM system outputs/actions must be compatible with existing regulations or policies), economic (a US\$1.2M budget exists for development and deployment), and even societal/aesthetic (a classic bridge may not be retrofitted with any SHM system that obscures the bridge’s aesthetic appearance). Some of these constraint types, as well as some aspects of defining the target failure modes in question (1), have been collectively referred to as “operational evaluation” (Farrar and Worden,

2007). Defining these constraints whenever possible helps to limit the SHM design space, which generally increases the likelihood of finding a global optimum design (Dechter, 2003).

Once these four groups of questions are addressed, a practical form of a Bayesian loss (cost) estimate may be defined as

$$E(L_{ex}, L_{in}; e) = \sum_{j,k} L_{ex}(d_k, \theta_j; e) p(d_k | \theta_j; e) p(\theta_j) + L_{in}(e) \quad (1)$$

This loss estimate form explicitly shows, for a given SHM system design e , all possible extrinsic costs, weighted by the probabilistic combination of events needed to incur each extrinsic cost, plus the intrinsic costs, which are assumed not to depend on extrinsic costs or upon any of the probabilities. An easily interpreted simplification of Eq. (1) occurs for any binary-decision SHM application, where the system is simply deciding whether certain damage is present at a certain critical level or not. As an example in that case, the subscript j only takes on the value 0 (damage not present) or 1 (damage present), and the subscript k only takes on the value 0 (decide there is no critical damage and do nothing) and 1 (decide there is critical damage and inspect). In this binary case, the various probabilities in Eq. (1) are then easily interpreted as

$$\begin{aligned} p(d_0 | \theta_0) p(\theta_0) &\equiv (1 - p_{\text{false alarm}})(1 - p_{\text{damage}}) & p(d_1 | \theta_0) p(\theta_0) &\equiv (p_{\text{false alarm}})(1 - p_{\text{damage}}), \\ p(d_0 | \theta_1) p(\theta_1) &\equiv (1 - p_{\text{detection}})(p_{\text{damage}}) & p(d_1 | \theta_1) p(\theta_1) &\equiv (p_{\text{detection}})(p_{\text{damage}}) \end{aligned} \quad (2)$$

and Eq. (1) may be written by inserting Eq. (2) into Eq. (1) as

$$E(L_{ex}, L_{in}; e) = c_{00}(1 - p_{\text{false alarm}})(1 - p_{\text{damage}}) + c_{01}(1 - p_{\text{detection}})(p_{\text{damage}}) + c_{10}(p_{\text{false alarm}})(1 - p_{\text{damage}}) + c_{11}(p_{\text{detection}})(p_{\text{damage}}) \quad (3)$$

In Eq. (3), c_{00} is the cost of doing nothing if no damage is actually present (probably a very low number; only the cost of continued normal operation), c_{01} is the cost of doing nothing when damage is actually present (“false negatives” cost; usually a very high cost for life-safety driven applications), c_{10} is the cost of stopping operation to inspect when no damage is actually present (“false positives” cost; usually a very high cost whenever unnecessary downtime is expensive), and c_{11} is the cost of stopping operation to inspect when damage is actually present (probably a moderately-high number, as it involves both downtime losses and repair costs).

In order to evaluate the cost of a given design e by Eq. (1) or, if appropriate, Eq. (3), one must obtain the conditional probabilities $p_{\text{detection}}$ and $p_{\text{false alarm}}$, which inherently requires extracting features \mathbf{v} from measured data, modeling the statistical variability and uncertainty in those features, designing a detector that transforms the features into the intended actions, and evaluating the detector’s performance.

FEATURE EXTRACTION AND STATISTICAL MODELING

A feature set \mathbf{v} is the final form of the reduced raw data that will ultimately be used to guide the detector’s decision-making. In most SHM literature, “features” typically refer to raw data that has been transformed in some way (e.g., from basic forms of signal processing to rather complex algorithms) (Farrar and Worden, 2007), but such transformations are really only necessary to the extent that one primary objective is sought: the final features should be as low-dimensional as possible without losing relevant information. This is where engineering/physical knowledge and/or previous experience play an important role: they guide the raw data reduction into features that capture relevant physical properties of the structural system’s behavior that indicate the targeted failure mode(s) but aren’t so high-dimensional that modeling their variability or associated uncertainty is impractical or impossible. Without applying such knowledge or experience, there is a high likelihood of generating features that are insensitive to the evolution of the failure mode (“non-sensitivity”) or highly volatile (noisy) and thus sensitive to false influences (“non-specificity”).

Once a candidate feature is identified, its variability must be statistically modeled in order to ultimately derive the required conditional probabilities, $p(d_k | \theta_j)$. This is because the probabilities associated with making the intended decisions, d_k , directly depend upon the uncertainty and variability in the features \mathbf{v} . This dependence is captured through a detector δ , which may be thought of as the probabilistic transformation of features into decision variables, or $p(\mathbf{v} | \theta_j) \xrightarrow{\delta} p(d_k | \theta_j)$. A probability model for the features observed in each of the damages states θ_j is required; this is usually also accomplished with some form of physics knowledge-inspired modeling (e.g., how a propagating ultrasonic wave’s amplitude—the feature—might scatter if it encounters a defect in its propagation path) and pure stochastic modeling to account for uncertain variables or parameters (e.g., the noise floor, thermal response variability, wave propagation attenuation factor through a complex joint, etc.).

DETECTOR DESIGN

A survey of the SHM literature indicates that detector design (although not explicitly referred to as detector design) is currently a very *ad hoc* process, with a very common practice being some form of a simple sum-of-squares (Sohn et al., 2004); this is rarely optimal, except for the (rare) case of independent, identically-distributed Gaussian-distributed features with low signal-to-noise ratio (Kay, 1998). Ignoring optimal detector design can have significant consequences on establishing the final thresholds required for making the performance-level decisions that the detector enables, leading to decreased probability of detection, increased probability of false alarms, sub-optimal cost structure, etc. The Bayes loss formulation itself may be used to find an optimal detector; the optimal detector δ_{opt} is the detector from all candidate detectors δ that minimizes the Bayes loss function conditioned on the observed features, or

$$E(L_{ex}(\delta_{opt}), L_{in}; e) < \sum_j L_{ex}(\delta(\mathbf{v}), \theta_j; e) p(\mathbf{v} | \theta_j) p(\theta_j) + L_{in}(e) \quad (4)$$

Although included for completeness in Eq. (4), the intrinsic cost function doesn't play a role in the minimization process under this formulation. In most practical, regulatory-driven SHM applications today, the detector is usually designed to command inspection or not, a binary detection process like the simplification presented in Eq. (3).

EVALUATION OF DETECTOR PERFORMANCE

Once an optimal detection process is designed, its performance must be evaluated. This fundamentally requires modeling how the statistical properties of the features transform under the detection process. Analytically, this process is accomplished by the probability change-of-variables formula (Bendat and Piersol, 2000)

$$p(\delta(\mathbf{v})) = \int \frac{p(\mathbf{v}(\delta))}{|\delta(\mathbf{v}(\delta))|} d\mathbf{v} \quad (5)$$

This integral is seldom computable in closed form due to the inverse detector functions embedded in the integrand, although linear detector transformations are sometimes excepted depending on the form of the probability density in the integrand (Kay, 1998). Recourse is made to approximation in many applications, particularly if evaluation of the Bayes cost function involves complicated, time-consuming algorithms during the optimization process. One common approximation is invocation of the central limit theorem, since for many SHM applications, the detector aggregates many summed combinations of sensor data. Chaloner and Verdinelli (1995) describe other forms of approximation. With the detector statistics now known, the SHM process executes by comparing the transformation of test features to thresholds determined from the baseline (reference) detector statistics, considering the SHM objective(s) as quantified in the first step.

OPTIMAL DESIGN

Fig. 1 presents a generalized flow architecture for the proposed SHM system design process and how the various components enable DP.

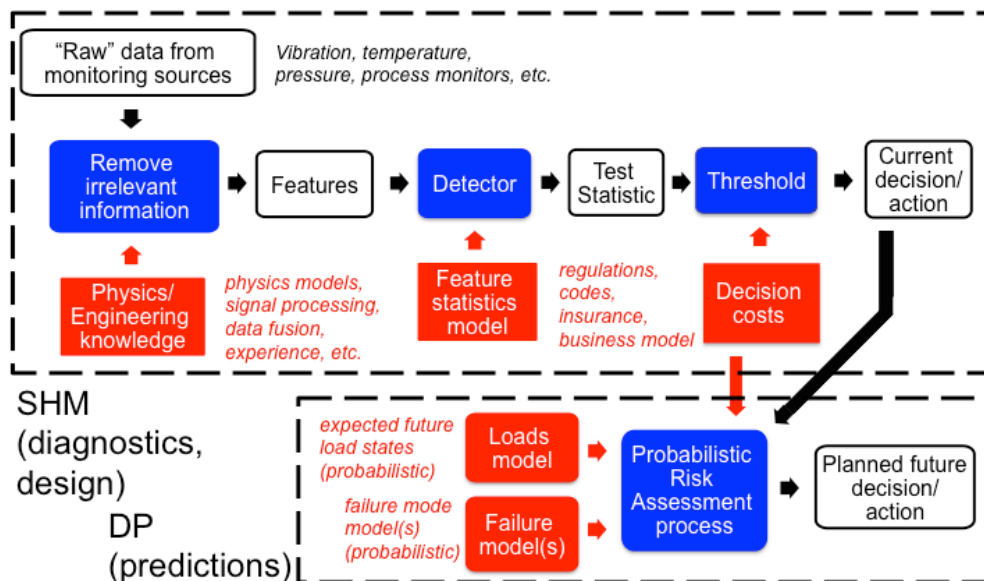


Figure 1 – Proposed SHM design process (top of figure) that enables DP processes (bottom of figure).

All of the previous steps may be done for a given SHM system design, e , to produce appropriately-quantified diagnostic results, which is a prime global objective for every SHM application. However, another very important advantage of the Bayesian experimental design approach is that a secondary optimization over the variable e may be performed as well, revealing its nature as a design procedure. Provided that appropriate models of features statistics in reference and target damage conditions are available, optimization over the constrained design space is then performed to ultimately yield the SHM system design that minimizes Bayes loss. The entire procedure from optimal design to optimal diagnosis is self-contained and consistent, as the proposed formulation integrates all aspects of the SHM process; it accomplishes both optimal SHM diagnostics (with quantified uncertainty demonstrated in a way that structural system owner/operators may make meaningful life cycle management decisions) and, if desired, optimal SHM system design (such that total risk/loss is minimized at the outset). It is the authors' opinion that this type of formulation is well-poised to enable SHM/DP technologies to make the transition to adopted industry practice. Some recent examples of this work demonstrated on ultrasonic interrogation applications, where the design space was defined to be where to optimally place a network of ultrasonic actuator/sensors, may be found in Flynn and Todd (2009) and Flynn and Todd (2010). These examples will be discussed in the conference presentation accompanying this paper.

ACKNOWLEDGMENTS

The authors acknowledge the U.S. National Science Foundation Graduate Fellowship Program, the Los Alamos National Laboratory/UC San Diego Engineering Institute, and the Benjamin F. Meaker Visiting Professor program (University of Bristol, UK) each for partially sponsoring various aspects of this work.

REFERENCES

- Bendat, J., and Piersol, A., 2000, "Random Data: Analysis and Measurement Procedures, 3rd Edition", John Wiley and Sons, New York, NY, USA, 640 p.
- Chaloner, K. and Verdinelli, I., 1995, "Bayesian Experimental Design: A Review", *Statistical Science*, Vol. 10, No. 3, pp. 273-304.
- Dechter, R., 2003, "Constraint Processing", Morgan Kaufman, San Francisco, CA, USA, 450 p.
- Farrar, C. R., and Worden, K., 2007, "An Introduction to Structural Health Monitoring", *Philosophical Transactions of the Royal Society A: Mathematical, Physical, and Engineering Sciences*, Vol. 365, pp. 303-315.
- Flynn, E., and Todd, M. D., 2009, "Optimal Placement of Piezoelectric Actuators and Sensors for Detecting Damage in Plate Structures," *Journal of Intelligent Material Structures and Systems*, Vol. 21, No. 2, pp. 265-274.
- Flynn, E., and Todd, M. D., 2010, "A Bayesian Approach to Optimal Sensor Placement for Structural Health Monitoring with Application to Active Sensing," *Mechanical Systems and Signal Processing*, Vol. 24, No. 4, pp. 891-903.
- Kay, S., 1998, "Fundamentals of Statistical Signal Processing, Volume 2: Detection Theory", Prentice-Hall PTR, Upper Saddle River, NJ, USA, 672 p.
- Sohn, H., Farrar, C. R., Hemez, F. M., Shunk, D. D., Stinemates, D. W., Nadler, B. R., and Czarnecki, J. J., 2004, "A Review of Structural Health Monitoring Literature from 1996-2001", Los Alamos National Laboratory Report LA-13976-MS (http://institute.lanl.gov/ei/shm/pubs/LA_13976_MSa.pdf).

RESPONSIBILITY NOTICE

The authors are the only ones responsible for the printed material included in this paper.

Bio-Inspired Self-Adaptive Structures

Rahmat A. Shoureshi

Intelligent Systems Lab

School of Engineering & Computer Science

University of Denver

Denver, Colorado, U.S.

rshoures@du.edu

Abstract

Evolved over millions of years, biological systems offer many exquisite examples of intelligent behavior. Many bio-organisms have sensors and actuators vastly superior to the best engineered systems. Through extensive research, we have come to realize and appreciate the fact that nature continues to reveal new and ever more interesting biomaterials that exhibit extreme, unexpected dynamic and multi-functional properties on both the component and system levels. Inspired by biological systems, new structures are being developed with thousands of sensors and actuators that enable them to perform such functions as self-adaptation, self-morphing, and even self healing. These so called Smart Structures with very large scale embedded sensors and actuators have introduced new challenges in terms of data processing, sensor fusion, and automatic control. These smart structures are dynamically classified as a large-scale system with a musculoskeletal design, analogous to the human body. In order to develop analyze, observe, diagnose, and control such structures new sensor informatics and new concepts of structural controllability and observability need to be developed. The focus of our on-going research is to develop techniques and algorithms that would utilize this musculoskeletal system effectively; thus creating the intelligence for such a large-scale autonomous structure. This paper presents our latest research results.

Keywords: bio-inspired data analysis; neuro-morphic engineering; sensor data fusion; neuro-symbolic network; transmission and distribution infrastructure

1. INTRODUCTION

Technological innovations have been the key factor in maintaining economic prosperity for the US and other developed countries. Emerging technology areas together with advances in bio, micro and nano technologies have introduced new challenges and areas of opportunity for the engineering and scientific research community. Technological evolution from macro to micro and nano scales require development of new constitutive laws, new modeling techniques and dynamic analysis, and new system analyses which would not be a simple extension of the current state-of-the-art. At the micro and nano scales, systems become very large order to the point of having million degrees-of-freedom.

Evolved over millions of years, biological systems offer many exquisite examples of intelligent behavior. Many bio-organisms have sensors and actuators vastly superior to the best engineered systems. Through extensive research, we have come to realize and appreciate the fact that nature continues to reveal new and ever more interesting biomaterials that exhibit extreme, unexpected dynamic and multi-functional properties on both the component and system level. Sensation of smell by humans and insects is achieved through a network of cells that provides a wide dynamic range. Butterfly wings exhibit shimmering color (despite having no pigments), repel water, and change pattern/shape. Muscles are capable of large deformation and large power output, with low energy consumption. Such BioSensors and BioActuators can function in noisy environments, while performing multiple functions simultaneously or sequentially on demand, with high sensitivity and large dynamic range.

The next generation of engineering systems will be more complex in unprecedented ways. Success of these systems will depend on a rich and challenging research frontier, elements of which are of common interest to many nations. In particular, the incredible momentum of the advances being made in cognitive engineering and technologies are certain to penetrate our lives and the way we live in extraordinary and, quite possibly, in unintended ways. An emerging theme in this intense period of development of new technologies will be auto-adaptive media and autonomous engineered systems with five senses information at the broader system-level of multi-complexity. An autonomous system has key distinctive capabilities such as **pre-cognition** for prediction; sensors and sensor networks for **recognition** and **detection**; **intelligence** for identification and deduction from massive, incomplete and noisy data, as well as for learning and adaptation; **reaction** for control and regulation; **functional healing** for recuperation and mitigation; and **energy harvesting** for independence and sustainability. Recognizing that biological organisms possess many sensing and actuation means that are far faster and more efficient than engineered systems, biologically inspired sensing and actuation have become vigorous research topics in recent years.

Tremendous opportunity is offered through bridging the gap between sensors and actuators occurring in biology with those used in the physical world, along with their engineering counterparts. Innovations have already resulted from initial synergistic integration of expertise and experiences from the respective disciplines. For example, ultra-sensitive flow sensors have been developed based on biomimetic research on hair cells. New cross-disciplinary efforts will result in discoveries that will enrich our understanding of biological systems, facilitate discovery of innovative materials and fabrication technologies, and increase the performance of bio-inspired sensors, actuators, and decision-support systems. These cross-disciplinary programs will open new ways to explore exciting frontiers in many scientific fields that will transcend and revolutionize the future of medicine, healthcare technologies, protection of critical infrastructures systems, and sustainability. This research addresses the challenges of recognition, detection, and intelligence associated with large-scale systems.

As new large scale and distributed sensor technologies are introduced and incorporated into structures, the need for informatics techniques that can provide effective sensor fusion and the ability to transform large volume of data into useful information has significantly increased. Thus, we have initiated a basic research that attempts to understand sensor fusion and data processing capabilities of the human brain, and attempt to develop their analogous engineered systems.

2. BRAIN SENSOR INFORMATION PROCESSING

Human brain is a highly complex system, which is capable of performing a vast range of diverse tasks. One capability of the brain is to process information coming from thousands and thousands of sensory receptors and integrating this information into a unified perception of the environment. Up to now, technical systems used for machine perception are unable to compete with their biological archetype. Having an engineered system capable of perceiving objects, events, and situations in a similar and efficient manner as the brain does, would be very valuable for a wide range of applications. To perceive objects, events, and situations in an environment, sensors of various types are necessary. This introduces the challenge of fusing data and extracting information from a variety of sensors.

The goals of sensor fusion are robustness, extended spatial and temporal coverage, increased confidence, reduced ambiguity and uncertainty, and improved resolution (Elmenreich 2002). The research field of sensor data fusion is relatively recent and dynamic. There have been several sensor fusion techniques developed. However, these techniques tend to be application dependent. Research in the neuro-science area has demonstrated that sensor fusion in the perceptual system of the human brain is of superior quality than all present engineered ones. Therefore, it seems to be particularly useful to study biological

principles of sensor fusion. Figure 1 presents an overview of the mechanisms and factors that form and influence human perception. These characteristics are derived from research results of neuroscience and neuropsychology about the perceptual system of the human brain (Luria 1973).

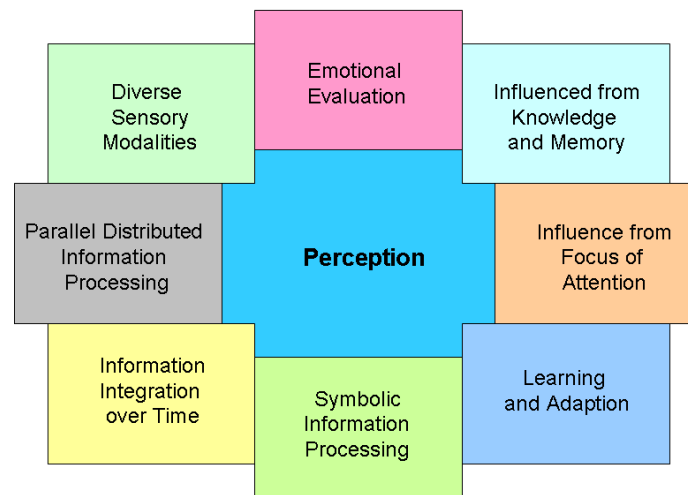


Figure 1: Characteristics of Human Perception Diverse Sensor Modalities
(Velik, Lang, Bruckner, Deutsch 2008)

To perceive the external environment, our brain uses multiple sources of sensory information derived from several different modalities including vision, touch, and audition. The combination and integration of multiple sources of sensory information is the key to robust perception (Ernst, Bühlhoff 2004).

Parallel Distributed Information Processing

The perceptual system is no unitary central unit that processes all information in one step. Instead, sensory information is processed in parallel (Luria 1973).

Information Integration over Time

To perceive objects, events, and situations in an environment, single-moment snapshots of sensory information provided by different modalities is not always sufficient for unambiguous perception. The course and the succession of sensory signals over time are of importance (Roskies, 1999).

Symbolic Information Processing

In the human brain, perceptual information from different modalities is processed by interacting neurons. However, humans do not think in terms of action potential and firing nerve cells, rather in terms of symbols. Mental processes are often considered as a process of symbol manipulation (French 1996).

Learning and Adaptation

The perceptual system of the human brain is not fully developed at birth. Although certain patterns need to be predefined by the genetic code, many concepts and correlations concerning perception are learned and adapted during life of individuals (Luria 1973).

Influence from Focus of Attention

According to the hypothesis of focused attention, what we see is determined by what we attend to. At every moment, the environment presents far more perceptual information than can be effectively processed. Attention can be used to select relevant information and to ignore irrelevant or interfering information. Instead of trying to process all objects simultaneously, processing is limited to one object in a certain area of space at a time (Hommel, Milliken 2005).

Influence from Knowledge and Memory

Perception is facilitated by knowledge. Prior knowledge is often required for interpreting ambiguous sensory signals. Much of what we take for granted as the way the world is— as we perceive it — is in fact what we have learned about the world — as we remember it. Much of what we take for perception is in fact memory. We frequently see things that are not there, simply because we expect them to be there (Goldstein 2002).

Emotional Evaluation

For perception, most often only the detection and the processing of stimuli from the external environment are considered. However, the perception of objects, events, and situations makes little sense if we do not know what influence they have on us. In the human brain, an evaluation of perceptual images is performed by emotions. The basic function of emotions in perception is to classify objects, events, and scenarios as good or bad. Emotions are necessary, to react adequately on perceived objects, events, and situations (Solms, Turnbull 2002).

3. NEURO-SYMBOLIC PROCESSING

- Considering those unique aspects of the human brain perception, it is understood that humans do not think in terms of action potentials and firing nerve cells, rather they think in terms of symbols. According to the theory of symbolic systems, the mind is a symbol system and cognition is symbolic manipulation. Examples for symbols are objects, characters, figures, sounds, or colors used to represent abstract ideas and concepts. Symbolic manipulation offers the possibility to generate complex behavior (French 1996). In summary, neurons could be regarded as basic information processing unit on a physiological basis and symbols as information processing units on a more abstract level. There are neurons in the brain which respond exclusively to certain perceptual images. For example, there have been neurons found in the secondary visual cortex that respond exclusively to the perception of faces. This fact has inspired us to use neuro-symbols, which are used for perceptual images. Figure 2 shows the concept of a neuro-symbol (Velik, Lang, Bruckner, Deutsch 2008).

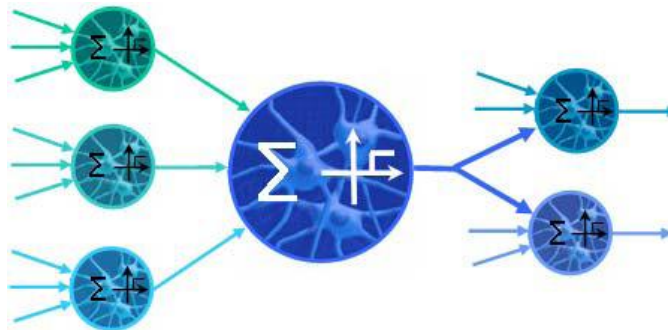


Figure 2: Principal Operation of a Neuro-Symbol

Neuro-Symbolic Networks

Based on extensive research in the neuro-science area (Luria 1973), it has been proposed that the perceptual system of the brain has a cerebral organization as depicted in Figure 3. Perception starts with information coming from sensory receptors, then this information is processed in three levels, which are referred to as primary cortex, secondary cortex, and tertiary cortex. Each sensory modality of human perception has its own primary and secondary cortex. This means that in the first two levels, information of different sensory modalities is processed separately and in parallel. In the tertiary cortex, information coming from all sensory modalities is merged.

This results in a unified multimodal perception. The tactile system of the brain comprises a whole group of sensory systems, including the cutaneous sensations, proprioception, and inesthesia. Therefore, this three level neuro-symbolic manipulation in the cortex forms a neuro-symbolic network, as shown in Figure 3 (Velik, Lang, Bruckner, Deutsch 2008).

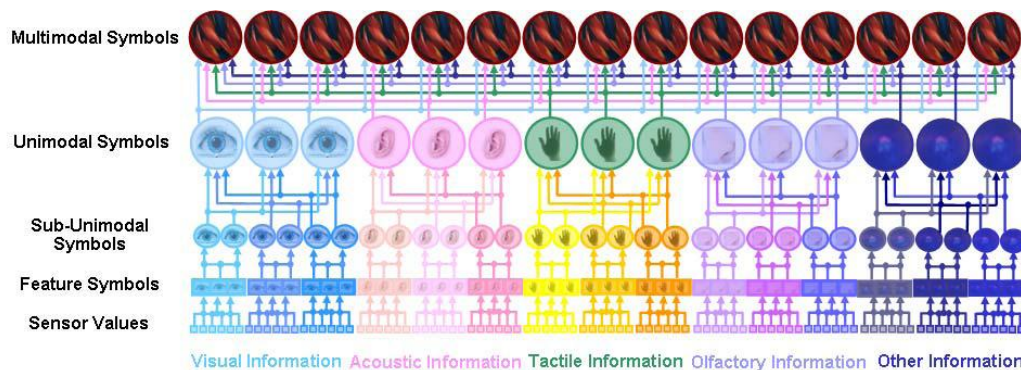


Figure 3: Neuro-Symbolic Network of Cortex (Velik, Lang, Bruckner, Deutsch 2008)

4. BIO-INSPIRED NEURO-SYMBOLIC NETWORK

Based on the understanding that neuro-science researchers have provided, as described in the previous section, and considering our previous investigations in the development of Intelligent Control systems, we have proposed the following neuro-symbolic network which integrates artificial neural network with fuzzy logic. This neuro-fuzzy system is a new approach using combination of the neural networks and symbolic systems to obtain the advantages of both without suffering from their shortcomings. It is a hybrid neural system to model cognitive functions, using a supervised learning. Input and target data have to be presented in the learning process. The neural network portion provides robustness, the ability to learn from examples, it is fault tolerant, can handle incomplete information, is able to generalize to similar input, and it is a parallel distributed systems with the potential of providing increased speed of processing. However, neural network by itself is unable to provide an explanation for the underlying reasoning mechanisms. On the other hand, symbolic processing can explain its inference process, utilizes powerful declaration languages for knowledge representation, and allows explicit control, fast initial coding, dynamic variable binding, and knowledge abstraction. Therefore, symbolic processing would complement the artificial neural networks and together, they provide a powerful system that could represent some of the features of the human cortex.

Figure 4 represents our neuro-symbolic network. This network is a combination of a fuzzy inference system (intelligent reasoning capability based on the linguistic “if/then” rule statements) and an adaptive neural network (adaptive learning capability). It uses Tsukamoto-type fuzzy reasoning for both

fuzzification and defuzzification processes; namely, its membership functions are half bell-shape functions, called monotonic nonlinear functions. It is applicable to multi-input/multi-output (MIMO) systems which employs associated hybrid learning algorithm to tune the parameters of membership functions. It utilizes Least Square Estimation in its forward processing, and Gradient Descent method in its backward processing. It updates and determines an optimal learning rate based on the changes of the error function versus the step size.

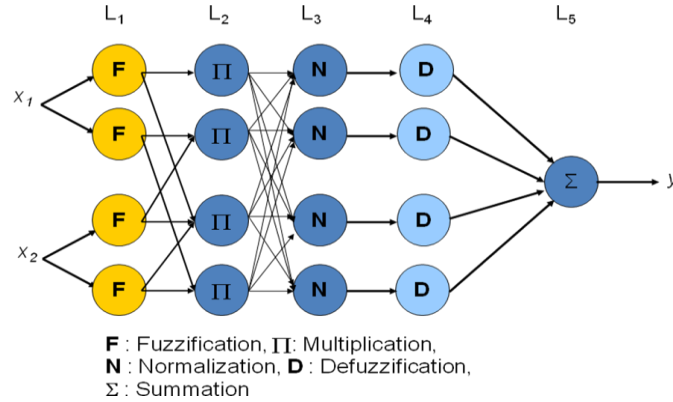


Figure 4: Architecture of Proposed Neuro-Symbolic Network

Network Information Processing Architecture

Following describes operations at each level of this network and their outputs (Shoureshi, Lim 2009).

Layer 1 (Fuzzification layer): Each node generates a membership degree of a linguistic value. The k^{th} node in this layer performs the following operation:

$$O_k^1 = \mu_{A_{ij}}(x_i) = \frac{1}{1 + \left(\frac{x_i - a_{ij}}{b_{ij}}\right)^2} \quad (1)$$

Layer 2 (Multiplication Layer): Each node calculates the firing strength of each rule by using multiplication operation.

$$O_k^2 = \prod_i O_{ij}^1(x_i) \quad (1 \leq k \leq 4) \quad (2)$$

Layer 3 (Normalization layer): The number of nodes in this layer is the same as the first layer, where the output of layer two is determined according to:

$$O_k^3 = \frac{O_k^2}{\sum_k O_k^2} \quad (1 \leq k \leq 4) \quad (3)$$

Layer 4 (Defuzzification layer): The number of nodes in this layer is equal to the number of nodes in layer one times the number of outputs. The defuzzified value for the k^{th} node is:

$$y_k = \begin{cases} c_k - d_k \sqrt{\frac{1}{O_k^3} - 1} & \text{if } k = \text{odd} \\ c_k + d_k \sqrt{\frac{1}{O_k^3} - 1} & \text{if } k = \text{even} \end{cases} \quad (1 \leq k \leq 4) \quad (4)$$

where $\{c_k, d_k\}$ are consequent parameters and are used to adjust the shape of the membership function of the consequent part. Then, the output of this layer becomes:

$$O_k^4 = O_k^3 \cdot y_k = \begin{cases} O_k^3 \cdot \left(c_k - d_k \sqrt{\frac{1}{O_k^3} - 1} \right) & \text{if } k = \text{odd} \\ O_k^3 \cdot \left(c_k + d_k \sqrt{\frac{1}{O_k^3} - 1} \right) & \text{if } k = \text{even} \end{cases} \quad (1 \leq k \leq 4) \quad (5)$$

Layer 5 (Summation layer): In this layer the number of nodes is equal to the number of outputs. There is only one connection between each node in layer four and a node in the output layer, and we have:

$$O^5 = \sum O_k^4 \quad (1 \leq k \leq 4) \quad (6)$$

In the training process, it tries to find the minimizing error function between target value and the network output. For a given training data set with P entries, the error function is defined as:

$$E = \sum_{p=1}^P E_p = \frac{1}{2} \sum_{p=1}^P (T_p - O_p^5)^2, \quad (1 \leq p \leq P) \quad (7)$$

Where O_p^5 is the p^{th} output of the network and T_p is the p^{th} desired target. The premise parameters $\{a_{ij}, b_{ij}\}$ are updated according to a gradient descent and the consequent parameters $\{c_k, d_k\}$ are updated using a LMS algorithm.

5. FIRST CASE STUDY AND ITS EXPERIMENTAL RESULTS

In order to demonstrate the ability of this network for diagnostics of structures, we consider the predicting corrosion levels on angle stubs of the portion of transmission towers below the ground (Stranovsky, Shoureshi, Kile 2011). The US transmission and distribution (T&D) infrastructure of the electric grid is deteriorating at an alarming rate. This infrastructure is subjected to significant environmental forces that can have a detrimental impact on its service life. Present inspection techniques have many short-comings, especially their inability to provide accurate and reliable information about the state of the structure below the ground without going through a costly excavation. Visual and auditory inspection and soil measurement techniques are not accurate and cannot predict the present state of the T&D infrastructure, namely tower legs, angle stubs, anchor rods, steel poles, and the conductor itself, especially for those sections below the ground, or covered by suspension assembly, shoes, or armor rods. Therefore, there is a real need for an effective, accurate, and proven non-destructive evaluation (NDE) technology that can detect and diagnose corrosion levels and the degree of damage in these structures below the ground.

Through a joint effort of the University of Denver (DU), New York Power Authority (NYPA), and Osmose Utilities Services Company, an NDE transmission tower leg inspection project was initiated. The DU NDE technology was applied to a set of NYPA towers, to inspect below the ground condition of

tower legs. Osmose conducted soil tests, excavated these legs, and verified the inspection results and diagnostic predictions. In this study, we have used two sensing modality: structural modal characteristic measurement using an on line electromagnetic sensing; and soil tests including pH measurement and soil resistivity. Figure 5 shows the principal operation of the DU NDE technology.

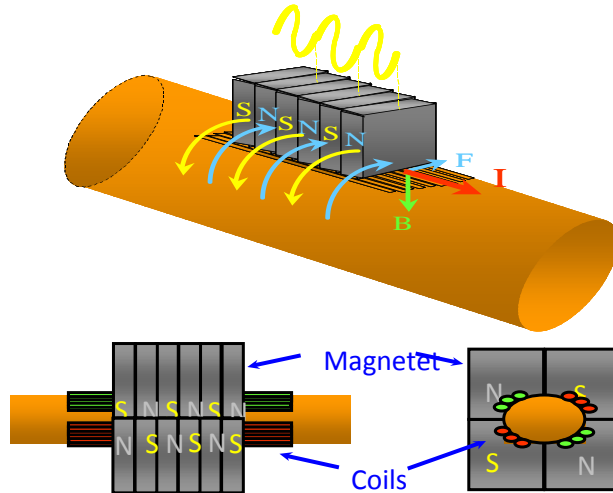


Figure 5: Structure's Electromagnetic Sensing

By a direct electromagnetic coupling between the inspection system and the structure, vibration modes of these T&D structures are excited by using our broadband excitation power electronic system. Through its receiving element, these inspection systems create vibration signatures of the T&D structure. This uniquely designed transducer applies Lorentz force on the T&D structure by the coupling of the alternated magnets and coils. This force twists the surface of the structure about its longitudinal or torsional axis. This results in excitation of the modes of these structures. Therefore, our transducer can control the vibration mode to be excited on the T&D structure, by driving a specific vibration frequency matching to the structural modal characteristics. As corrosion develops and penetrates into the structure, its modal characteristics would change, thus the signature obtained by our transducer would be able to provide information about the corrosion level of the structure. Figure 6 shows this NDE system during the actual inspection. Also shown are the actual excavation and verification of corrosion on these structures. Based on the second sensing modality, namely, soil tests, measurements presented in Figures 7 and 8 have been obtained.

Sensing results from these two modalities were given to our neuro-symbolic network. Table 1 shows the result of this network analysis and its predictions about the structural corrosion. This table also shows results of the actual corrosion measurements, obtained from the excavation of these towers. As shown, our neuro-symbolic network has produced very accurate results and decisions about the corrosion levels of these towers.



Figure 6: NDE System During Inspection of Transmission Line Stub Angle (left) and Actual Excavation and Inspection (right)

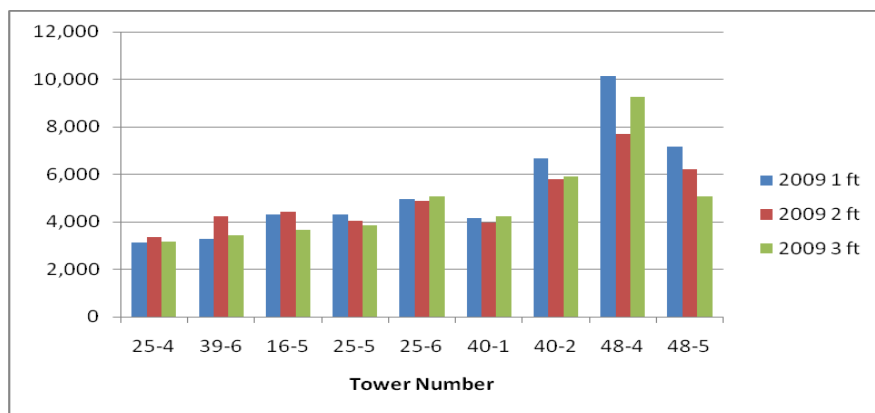


Figure 7: Soil Resistivity Measurements at different locations of Various Towers

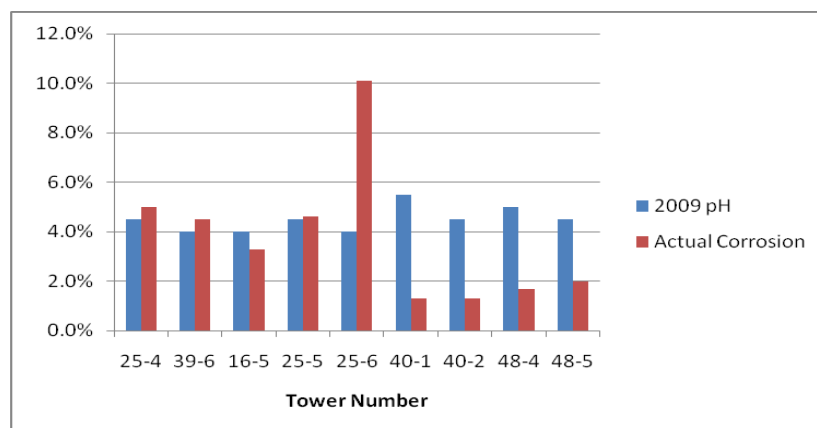


Figure 8: Soil pH measurements of Different Towers and Actual Corrosion Levels

Table 1: Corrosion Level Decision Results of Neuro-Symbolic Network

Tower Number	% of Corrosion After Excavation	Soil Measurement Results	Neuro-Symbolic Network Corrosion Level Decision
25-4	5.0%	moderate	<8%
39-6	4.5%	severe	<10%
16-5	3.3%	moderate	<7%
25-5	4.6%	mild	<10%
25-6	10.1%	mild	<15%
40-1	1.3%	moderate	<8%
40-2	1.3%	mild	<8%
48-4	1.7%	mild	<5%
48-5	2.0%	mild	<8%

6. SECOND CASE STUDY: Fly-By-Feel Autonomous Vehicle

This research is a Multidisciplinary University Research Initiative (MURI) that has several universities involved: Stanford, UCLA, DU, CU, and the University of British Columbia (UCB). Each partner university is responsible for developing different parts of this project, as highlighted below.

- Design and fabrication of “stretchable” sensory network (Stanford, UBC)
- Design of bio-inspired sensors and microelectronic devices (UCLA, Stanford, UBC, CU)
- Multi-functional material design and analysis (Stanford, DU)
- Sensing, diagnostics, recognition and state awareness (DU, Stanford)
- Integration, functionalization, prototype and validation (Stanford, UCLA, DU, UBC, CU)

Knowing the state of an aerospace vehicle in real-time is crucial for maximizing its performance, assuring its reliability, and completing successful missions. This is especially true in harsh or combat environments. Despite its importance, however, the current state-of-the-art in sensor technology for aerospace vehicles is very primitive compared to that of animals. This is because animals are equipped with a dense network of sensors that allows them to sense their state in real time, to adjust their bodies for maximal performance and to detect threats of many types from many directions. The current state-awareness technology for aircraft relies on a small number of relatively large sensors that are concentrated in small areas and are prohibitively heavy, expensive, and complex to scale to cover an entire aircraft. A departure from this traditional approach is necessary to increase the performance and capabilities of next-generation aircraft, particularly UAVs. Biological sensory systems have a remarkable ability to detect and integrate a wide variety of sensory modalities. Unlike most engineered systems, they rely on a large number of relatively simple sensors that are distributed over a large area and are

specialized for detecting specific types of stimuli. For example the mammalian skin contains between 100 and 1000 sensory receptors per square centimeter that are capable of detecting touch, vibration, stretch, temperature and chemical stimuli, and tissue damage. Biological systems use local processing to condense and extract biologically meaningful information about a stimulus. For instance tissue damage results in the activation of many receptors that relay information to a small set of sensory neurons that elicit only a single sensation. Local feedback circuits are also critical for providing a fast response to specific stimuli. Muscle stretch receptors feedback via a single synapse to regulate contractile muscle preventing muscle damage and providing rapid feedback required for behaviors such as standing or flying. Finally, biological systems can deal with large changes in size during development and are remarkably plastic, tolerating both the integration of new sensory modules and the loss of sensory modules with little loss of function. The fact that biological sensor systems have a capacity to detect and integrate a variety of types of information, are self-organizing and are tolerant to damage makes them a particularly attractive model for the design of detection systems in aircraft. While the specific biochemical systems that underlie biological detection systems are fragile and difficult to replicate and therefore unsuited for aerospace applications, there are important conceptual lessons that can be drawn from biological systems that will allow us to generate better detection systems.



Figure 9: Autonomous Aircraft with Human-Like Information Processing

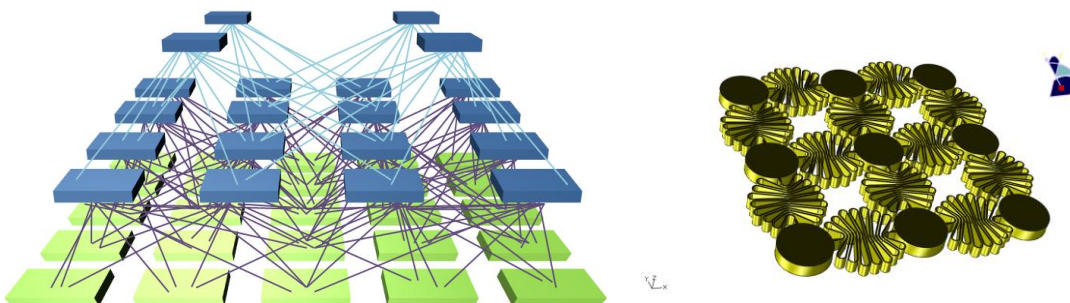


Figure 10: Schematics of Multi-Scale Information Processing and Stretchable Electronics

Figures 9 and 10 provide some of the conceptual design that are being investigated in this project. Since this is an ongoing research, further results will be included in the presentation at the conference.

7. CONCLUSIONS

This paper presented some of the results of our on-going research related to structural health monitoring and diagnostics, using bio-inspired data processing and decision-making. Based on developing some understanding of the operation of data within the human brain, using results of the neuroscience research community, we have developed a neuro-symbolic network. This network integrates key features of artificial neural networks and fuzzy logic to create an inference engine. Through a unique joint project with an electric utility company and a utility service company we were able to implement this research results on the assessment of corrosion levels of the surface of tower legs of transmission lines which are embedded below the ground. Two sensor modalities were used. One based on measurements related to the modal characteristics of the structure, the other based on soil measurements. These different sensory data were presented to our network. From this neuro-symbolic network we obtained prediction of corrosion levels with excellent accuracy, as verified by the actual excavation of these towers.

8. REFERENCES

1. Elmenreich, W., "Sensor Fusion in Time-Triggered Systems," Ph.D., dissertation, Vienna University of Technology, 2002.
2. Ernst, M.O., Bühlhoff, H.H., "Merging the Senses into a Robust Percept," *TRENDS in Cognitive Sciences*, 2004, Vol. 8, pp. 162–169.
3. French, R.M., "Review of the Engine of Reason, the Seat of the Soul," in *Minds & Machines*, 1996, Vol. 6, pp. 416–421.
4. Goldstein, E.B., "Wahrnehmungspsychologie," Spektrum Akademischer Verlag, 2002.
5. Hommel, B., Milliken, B., "Taking the Brain Serious: Introduction to, in, and across Perception and Action," *Psychological Research*, 2005.
6. Luria, A.R., "The Working Brain - An Introduction in Neuropsychology," Basic Books, 1973.
7. Roskies, A.L., "The Binding Problem," *Neuron*, Vol. 24, 1999, pp. 7-9.
8. Shoureshi, R.A., Lim, S., "Bio-Inspired Nervous System for Civil Structures," *Journal of Smart Structures and System*, Vol. 5, No. 2, 2009.
9. Solms, M., Turnbull, O., "The Brain and the Inner World – An Introduction to the Neuroscience of Subjective Experience," Other Press New York, 2002.
10. Stranovsky, G., Shoureshi, R.A., and Kile, J., "Advanced NDE Technology for Below Grade T&D Infrastructure Corrosion Detection," To be published in proceedings of IEEE-ESMO Conference, May 2011.
11. Velik, R., R. Lang, R., Bruckner, D., and Deutsch, T., "Emulating the Perceptual System of the Brain for the Purpose of Sensor Fusion," Proceedings of IEEE HSI, Krakow, Poland, May 25-27, 2008.

Experimental investigation, mathematical modeling and nonlinear analysis of an impact pendulum suspended in a vibrating structure

Romulo R. Aguiar¹ and Hans I. Weber²

¹ Department of Mechanical Engineering, COPPE - UFRJ
21941-972 Rio de Janeiro - RJ - Brazil, P.O. Box 68.503
aguiar.rr@gmail.com

² Department of Mechanical Engineering, PUC-Rio
22453-900, Rio de Janeiro - RJ - Brazil, P.O. Box 38.097
hans@puc-rio.br

Abstract: The purpose of this work is the experimental investigation and the mathematical modeling of the impact force behavior in a vibro-impact system, where an impact pendulum is mounted on a cart that moves by a prescribed displacement. By changing the impact gap, it is possible to investigate and map the impact force behavior under different excitation frequencies. The experimental data will be used to validate the mathematical model, where the system behavior is investigated in more detail. A nonlinear analysis (bifurcation diagrams, Poincaré maps and Peterka map) is performed, showing the rich response of the system, such as dynamical jumps, bifurcations and chaos.

Keywords: nonlinear dynamics, impact, vibro-impact, impact oscillator

NOMENCLATURE

m = pendulum mass, kg

l = pendulum length, m

g = acceleration of gravity, 9.81 m/s²

t = time, s

A_0 = excitation amplitude, mm

F_0 = excitation force, N

z = impact force behavior (number of impacts per excitation cycle)

F_i = impact force, N

k_i = impact stiffness, N/m

c_i = impact damping, Ns²/m

Greek Symbols

θ = generalized coordinate, rad

ω = natural frequency, rad/s or Hz

Ω = excitation frequency, rad/s or Hz

δ = impact indentation, m

Subscripts

0 = relative to excitation

i = relative to impact

INTRODUCTION

Hard rock drilling is still a great challenge for oil companies. In this context, optimum productivity is possible by combining advantages of both existing drilling techniques: rotary and percussive drilling. In conventional rotary drilling, the energy applied in the system (oil well drillstring) comes from the rotary table, located at the top of the drillstring. Such energy, supplied to drill the oil well, ends up being wasted by vibration (axial, torsional and bending), friction with borehole walls and heat. If part of the energy wasted in vibration could be reinserted into the drilling process, the rate of penetration can be increased.

The use of the already existent vibrations in the drillstring (Dareing et al. (1968)), in fact the axial vibration due to the cutting process, to generate a harmonic load on the bit and an excitation in a steel mass (hammer) which will cause impacts is the motivation of this work, see Figures 1(a) and (b). The concept of this hybrid drilling technique is to reinsert the energy wasted on axial vibration, back into the drilling process, with the use of impacts. The stress waves created by such impacts may be useful to release the system from a stick condition of stick-slip phenomena, as well as generating cracks on the rock formation, increasing the rate of penetration. The axial vibration generated by the bit/rock interaction excites a hammer. When the excitation frequency approaches the mass resonance, impacts on the bit occur, since the hammer displacement is limited by the gap. Therefore, in addition to the rotative penetration, a percussive action happens due to the impact of the hammer on the bit (Batako et al. (2003)).

The study of vibro-impact systems has been the aim of several researches, from the application of a percussive action in rotary drilling for improved performance (Franca & Weber (2004)), to ultrasonic drilling, impact dampers and vibro-safe percussion machines (Batako, et al. (2004)). The idea of combining a percussive action to rotary drilling is not new, being first developed by Hausser and Nüsse & Gräfer in 1955 (Batako et al. (2003)). In this case, the idea is to add the percussive action inside the drillstring, more precisely the bottom hole assembly, where the system is subjected to

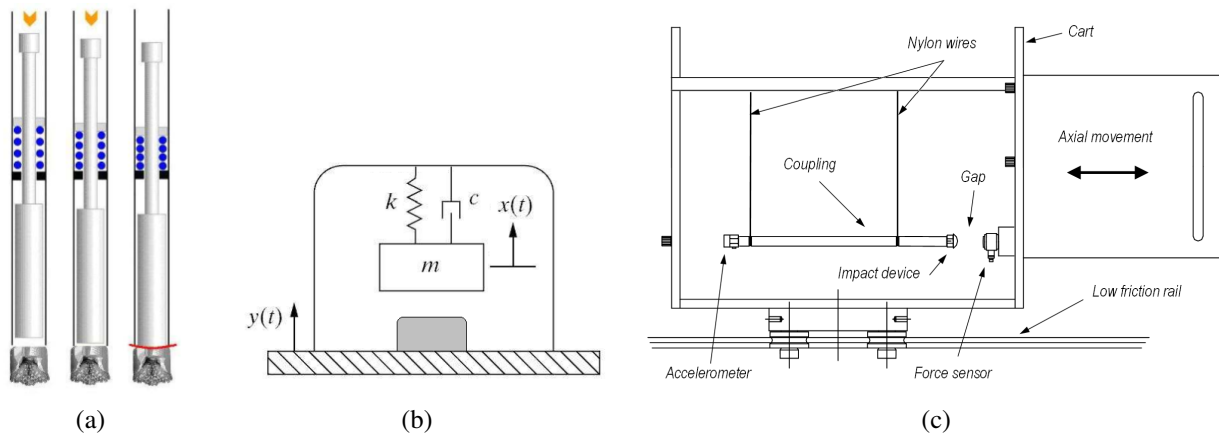


Figure 1 – (a) Resonance hammer drilling technique; (b) Vibro-impact system; (c) Test rig sketch.

a regular vibration pattern due to the rock cutting process. Although the literature shows several studies dealing with vibro-impact systems, few of them deals with embedded impacts, not to mention that there is few concern in the literature regarding the force magnitude developed by the impacts. Because the motivation of this work relies on a hybrid technique to drill hard rock formations, special attention is dedicated to the magnitude of the impact force, as well as mapping the system parameters in order to maximize the impact force.

From the theoretic point of view, vibro-impact systems are a quite interesting subject, because it presents a rich and complex dynamical response, from periodic to chaotic behavior. Since it is a nonsmooth system, bifurcations and other nonlinear phenomena may occur, where such behaviors are mostly not present in linear systems. Besides the references listed above, several other studies concerning vibro-impact systems are available in the literature, such as the works of Pavlovskaja & Wiercigroch (2001), Divenyi et al. (2006) (2007), Peterka (1996) (2003) and Peterka & Blazejczyk-Okolewska (1998).

Objectives

The main objective of this work is to understand the behavior of an impact pendulum (hammer) embedded inside a vibrating structure. The use of new hardware improved the capability of investigating the system in a shorter time scale, enhancing knowledge of contact mechanics. The study of this test rig includes defining its characteristics, like the range of possible excitation frequencies and the measurement of the impulsive forces. The experimental part of this work presents data regarding the vibro-impact system under different hammer characteristics. An experimental investigation of a single-degree of freedom subjected to impacts is considered and, despite the deceiving simplicity of this problem, its nonlinear dynamics is very rich.

From the experimental data a mathematical model is proposed and validated. Using numerical simulations the system behavior is investigated in more detail. A nonlinear analysis (bifurcation diagrams, Poincaré maps) is performed, including the mapping of regions of existence and stability of impact motions (called by the authors Peterka map). Finally, a contribution to the field of vibro-impact dynamics is proposed: the Peterka map with impact force magnitude addressed. Such a diagram can be used as design tool for this special type of devices.

EXPERIMENTAL APPARATUS

The experiment consists of a main cart, made of aluminum, which slides along the horizontal axis on a low friction rail bearing assembly, see Figure 2(a). The main cart is excited by an inverter controlled AC motor. The motor is attached to the cart through a pin that slides into a slot machined on an acrylic plate attached to the cart. The pin hole is drilled off-centered on the disk at the edge of the motor, so that rotational motor movement becomes sinusoidal cart movement. This device is used instead of an electromagnetic shaker because it can perform higher hammer amplitudes than a shaker. The device also avoids the influence of impact forces on the excitation source at higher frequencies.

The hammer is fixed inside the main cart, Figure 2(a), its weight supported by a wires set up. The entire system moves in a horizontal axis. As shown in Figure 2(a), eight wires are used, assuring that the hammer moves in the same axis as the main cart. The wires are attached to the cart structure at an angle of 30 degrees approximately from the vertical axis, minimizing the hammer rotation after impact. The hammer is composed of aluminum with a steel impact device. To vary the gap between the hammer and the cart, the impact device is composed of a screw and a knurled nut. The measurement devices on the test rig include (see Table 1):

- one accelerometer attached to the hammer;

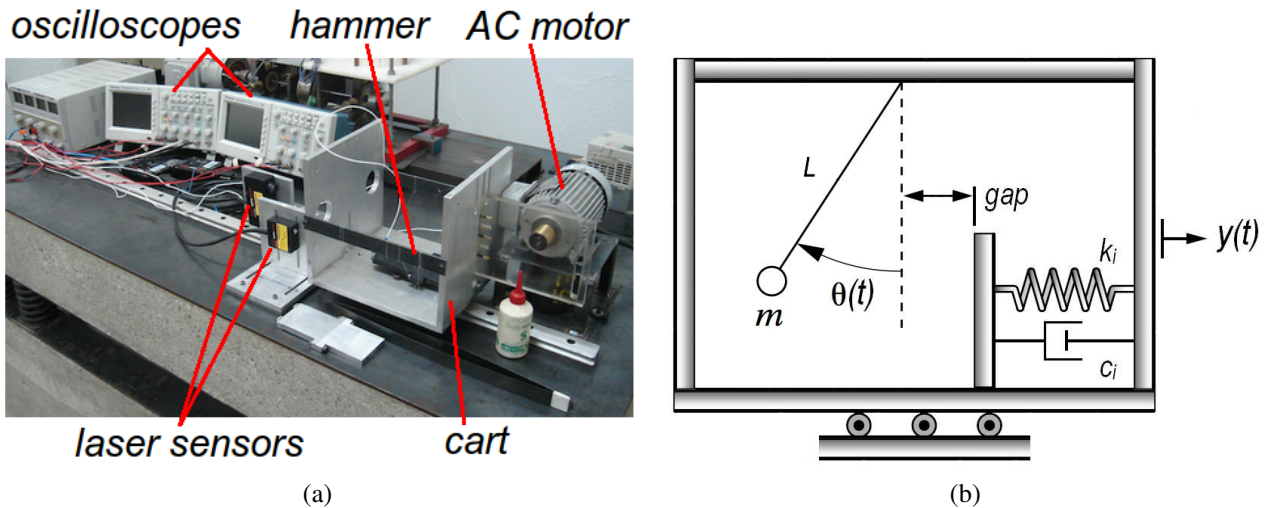


Figure 2 – (a) Picture of the entire test rig, including acquisition hardware; (b) Model of hammer supported by wires, physical representation.

Table 1 – Sensor specs.

Cart Accelerometer - 751-10 SN AC69		
Sensitivity	10.194	<i>mV/g</i>
Measure Range	± 50	<i>g</i>
Resonance frequency	50	<i>kHz</i>
Impact Force Sensor - 2311-100 SN 2471		
Sensitivity	24.41	<i>mV/N</i>
Measure Range	± 220	<i>N</i>
Resonance frequency	75	<i>kHz</i>
Cart laser displacement sensor - optoNCDT 1607-20		
Mathematical modeling and comparison between numerical simulation and experimental results Sensitivity	10	<i>V/mm</i>
Measure Range	20	<i>mm</i>
Hammer laser displacement sensor - optoNCDT 1607-100		
Sensitivity	2	<i>V/mm</i>
Measure Range	100	<i>mm</i>

- one piezoelectric force sensor fixed to the cart and located in front of the hammer impact device;
- two laser displacement sensors, both located on the side of the cart. One of the laser displacement sensors measures cart displacement and the other measures hammer displacement.

All data is acquired by two oscilloscopes using different time scales. The first oscilloscope measures the impact force and acceleration at the precise moment of impact (micro scale), after the impact force signal is triggered. The second oscilloscope measures both cart and hammer displacements using laser displacement sensors signals (macro scale).

Experimental methodology

The inputs are the gap and the excitation frequency. The length of the gap is measured using a calibrated shim. The excitation frequency is supplied by the AC motor. The outputs are: the acceleration signal from the accelerometer mounted on the top of the hammer; the impact force applied by the hammer; the cart displacement and the hammer.

As in previous experiments (Aguiar & Weber (2007) (2009)), the methodology is to observe the impact force behavior as the gap is varied. First, the natural frequency of the system without impact is determined, as well as the system parameters. After that, a study with impact is carried out. The excitation frequency is varied in order to cover the possible range of excitation frequencies. Three different gap values were chosen: 0.0 mm, 1.0 mm and 2.4 mm.

The laser displacement sensor signal presents an undesirable level of noise, which was removed using a moving average filter. Due to the nature of the moving average (a low-pass filter) the phase plane charts show a smooth effect

during the impact, which is an effect of the differentiation of low-pass filtered signal, and does not reflect the reality of the impact, as will be seen during the comparison between experimental data and numerical results.

If there is no impact, the hammer behaves as a one-degree-of-freedom system excited by a harmonic load (in this case, a base excitation). Since such system is well known and widely described in literature, it warrants no further comments.

Experimental results for gap 0.0 mm

Hammer impact force behavior can be split into frequency bands, showing similar characteristics in each frequency band, no matter which impact gap is imposed.

In a low excitation frequency range (less than 2.5 Hz), the cart movement is so slow that the hammer basically follows the prescribed excitation, generating two or three impacts per excitation cycle with low force magnitude. Due to the low impact force magnitude produced, such frequency range is not discussed in this work. In the next level of frequencies, the impact force presents a period-1 ($z = 1/1$, 1 impact per 1 excitation cycle) stable behavior. The impact force magnitude increases as the excitation frequency increases, reaching its highest value at 3.75 Hz (82.4 N) and after this frequency the impact force decreases as the frequency is raised. Figure 3 shows the impact force, hammer acceleration and both cart and hammer absolute displacements for the maximum impact force of frequency band $z = 1/1$.

The impact force transducer captures the first impulse transferred by the hammer, reaching its maximum. After the first impulse, in the micro scale time analysis, the support structure bounces back transferring energy to the hammer. The contact dynamics reacts according to its own dynamics, reaching a second peak. The accelerometer measures the hammer dynamics, because it is fixed to the opposite side of the impact device, see Figure 3(b). The existence of contact dynamics is strengthened by the results shown in the acceleration chart, because there are unexpected oscillations after the impact. Further analysis of the test rig, not presented in this work, shows that the peaks in the impact force are caused by bending flexibility of the cart plate where the impact force sensor is mounted. Also, the axial vibration of the hammer is relevant during impact, as shown in the acceleration chart.

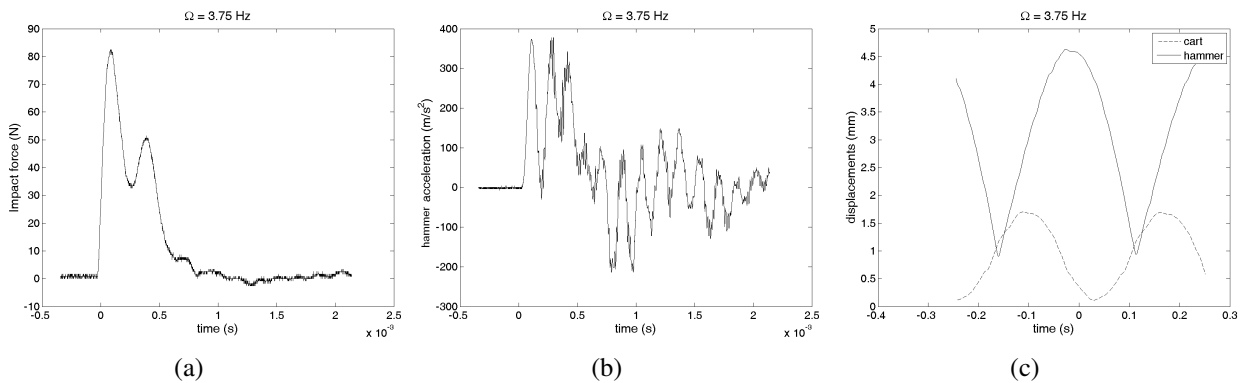


Figure 3 – Gap 0.0 mm. Excitation frequency 3.75Hz: (a) Impact force over time; (b) Hammer acceleration over time; (c) Displacements (cart and hammer) over time.

At the end of frequency band $z = 1/1$, the hammer presents a bifurcation in the impact force behavior, characterized by a period-1 impact with low magnitudes at alternate impact magnitudes, as shown in Figures 4(a) and 5(a).

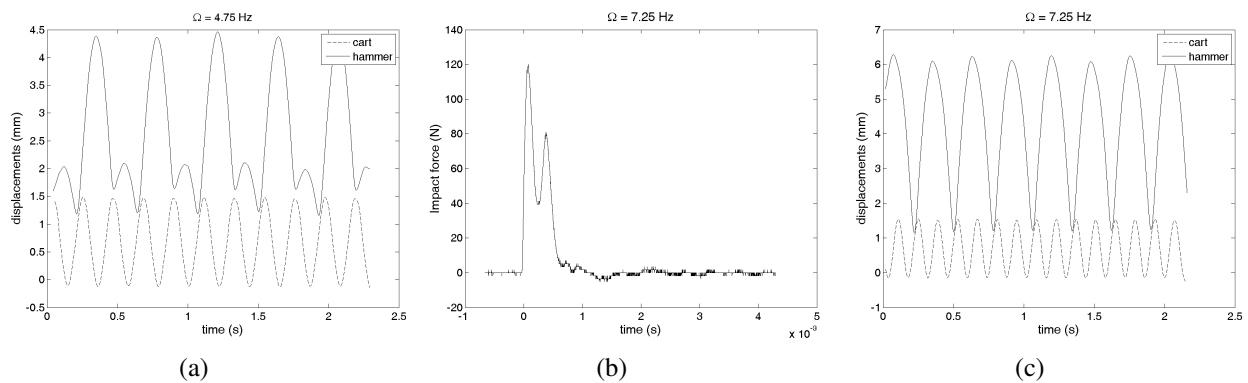


Figure 4 – Gap 0.0 mm: (a) Bifurcation at $z = 1/1$, $\Omega = 4.75$ Hz, displacements; (b) Maximum impact force on frequency band $z = 1/2$, $\Omega = 7.25$ Hz; (c) Displacements, $\Omega = 7.25$ Hz.

The second frequency band presents a similar behavior as the first one. However, in this frequency band the impact force occurs every two excitation cycles ($z = 1/2$), reaching its highest value at 7.25 Hz (120 N). The excitation frequency where the maximum impact force occurs on this frequency band ($z = 1/2$) is twice that of frequency band $z = 1/1$. Charts showing the output parameters for the maximum impact force on frequency band $z = 1/2$ are shown in Figures 4(b) and 4(c). After the activity at frequency band $z = 1/2$ the system shows another transitory behavior. See Figures 5(b) and 5(c).

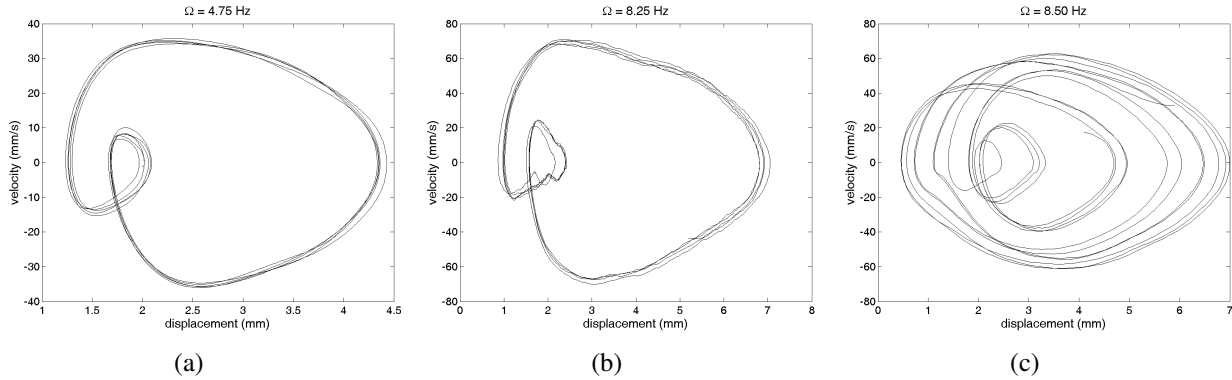


Figure 5 – Gap 0.0 mm, hammer phase planes: (a) $\Omega = 4.75$ Hz ($z = 1/1$); (b) $\Omega = 8.25$ Hz ($z = 1/1$, transition behavior); (c) $\Omega = 8.50$ Hz ($z = 1/1$, transition behavior).

Although data was not collected at higher frequencies, what appears to happen is that the frequency bands keep repeating the pattern, with the impact force behavior changing to one impact every three, four, five excitation cycles and so on, always with a bifurcation in between frequency bands. In each frequency band, the excitation frequency where the maximum impact force is found is a multiple of the frequency of the maximum impact force on period-1 ($z = 1/1$).

With this experimental data it is possible to analyze the system behavior in the frequency domain. To do so, a computational routine has been developed to determine the F_i (impact force peak). The maximum value of F_i has been extracted for each excitation frequency. Since the impact force peak does not change within each excitation frequency, except for the behavior after bifurcation, this routine seems to be quite effective. Finally, to generate a non-dimensional chart the force ratio F_i/mg is used (mg is the hammer weight), and the excitation frequency is divided by the natural frequency of the hammer without impact. The natural frequency of the hammer is experimentally identified using modal analysis. This non-dimensional chart will be useful to compare data between different hammer configurations.

Therefore, the impact force ratio chart (F_i/mg) in the frequency domain for this imposed gap is shown in Figure 6(a). Such chart shows both frequency bands ($z = 1/1$ and $z = 1/2$). Although the maximum impact force on frequency band $z = 1/2$ is higher than frequency band $z = 1/1$, is important to remember that in frequency $z = 1/2$ impacts occur every two cycles and also that energy inserted into the system increases with the square of the excitation frequency. Once the cart displacement is prescribed, it becomes that the magnitude of the excitation force F_0 is:

$$F_0 = MA_0\Omega^2, \tag{1}$$

where M is the total mass (cart and hammer combined), A_0 is the displacement amplitude of the cart and Ω is the excitation frequency.

Using a concept from the linear theory to describe a nonlinear behavior, the excitation frequency where the maximum impact force is achieved is defined as *impact resonance*. Since the hammer displacement is limited by a gap, an interesting phenomenon occurs. The occurrence of the impacts significantly changes the value of the impact resonance, as compared to the hammer resonance, as observed in Table 2. This change of resonance in the occurrence of impacts has already been studied (Aguiar & Weber (2007) (2009)) and these results were expected.

Experimental Results for gaps 1.0 mm and 2.4 mm

For these gap configurations the experimental results are similar to those observed for gap 0.0 mm. However, the non-zero gap configurations show differences from the results for 0.0 mm gap. For instance, the occurrence of nonlinear jump was observed after the impact resonance for the 2.4 mm gap configuration. Another difference includes the appearance of situations of non-impact, due to the non-zero gap (at higher frequencies, for example, where the amplitudes developed are smaller than the gap). Occurrences of nonlinear behavior were also observed and will be discussed in future section.

Table 2 – Impact resonance frequencies (experimental).

Frequency band	$z = 1/1$ (1 impact/ cycle)	$z = 1/2$ (1 impact/ 2 cycles)
gap 0.0mm	3.75Hz	7.25Hz
gap 1.0mm	3.00Hz	6.25Hz
gap 2.4mm	2.50Hz	5.25Hz
System natural frequency (gap $\rightarrow \infty$)	1.82Hz	

Comparison between gap configurations: At this point the charts showing the behavior of the impact force over the excitation for each gap are compared. According to the charts shown in Figure 6, for the frequency band $z = 1/1$, the 0.0 mm gap configuration shows the maximum force, but there was no substantial difference for the other gap configurations. For frequency band $z = 1/2$, both gap configurations 0.0 mm and 1.0 mm show the maximum impact force, with the gap 2.4 mm configuration showing the same impact force as in the previous frequency band $z = 1/1$. For possible use in the field, using this hammer set up, it is recommended that the 0.0 mm gap configuration be used, because this configuration shows higher impact force magnitudes. In addition, the 0.0 mm gap configuration shows no occurrence of nonlinear jump after the maximum impact force in each frequency band. As mentioned, a variation of impact resonance frequency is observed as the gap varies, see Table 2.

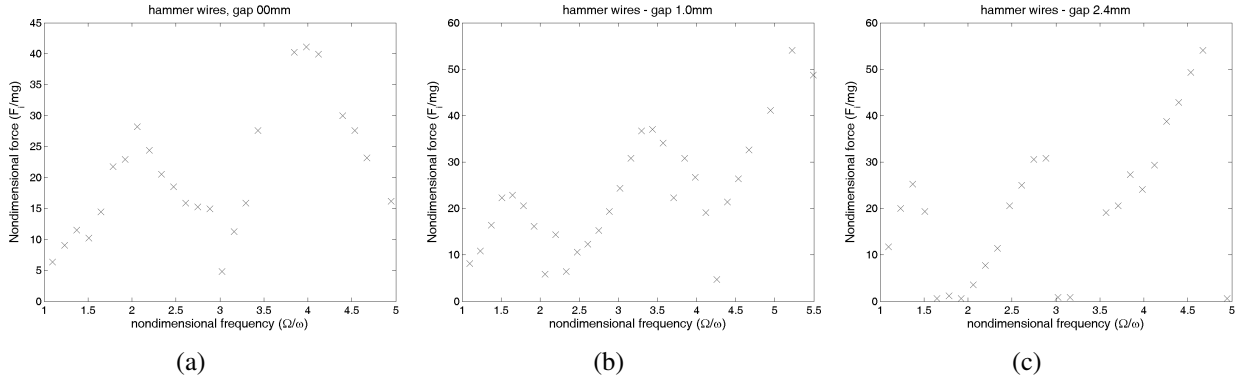


Figure 6 – Frequency domain response, non-dimensional force, F_i/mg : a) Gap 0.0 mm; b) Gap 1.0 mm; c) Gap 2.4 mm.

Experimental nonlinear behavior

The presence of impact and the gap between the hammer and the cart induces nonlinearity, and therefore nonlinear phenomena arise, specifically in the transition between frequency bands. One of these phenomena is the change of basins of attraction for certain excitation frequency/ impact gap combinations. In this situation, in which the hammer is excited within a particular frequency but is not impacting the surface, when a small impulse is inserted, the hammer starts impacting for some time and returns to the non-impact condition, as shown in Figure 7(a). However, in some cases, after the energy is inserted, the system starts impacting and continues in this condition, Figure 7(b).

MATHEMATICAL MODELING AND COMPARISON BETWEEN NUMERICAL SIMULATION AND EXPERIMENTAL RESULTS

Using the Lagrange equation, with θ as the generalized coordinate, see Figure 2(b), the hammer can be modeled as a single pendulum embedded in a cart with prescribed movement, where the impact surface is also moving within the system. For the situation of no impact, i.e., $l \sin \theta - gap > 0$, equation of motion is

$$ml^2 \ddot{\theta} - mlA_0\Omega^2 \cos \theta \sin \Omega t + mgl \sin \theta = 0. \quad (2)$$

Because impact is modeled using continuous analysis, when the hammer is impacting the cart ($l \sin \theta - gap \leq 0$), the equation of motion will slightly change to

$$ml^2 \ddot{\theta} - mlA_0\Omega^2 \cos \theta \sin \Omega t + mgl \sin \theta = -F_i l; F_i = k_i \delta + c_i \dot{\delta}, \quad (3)$$

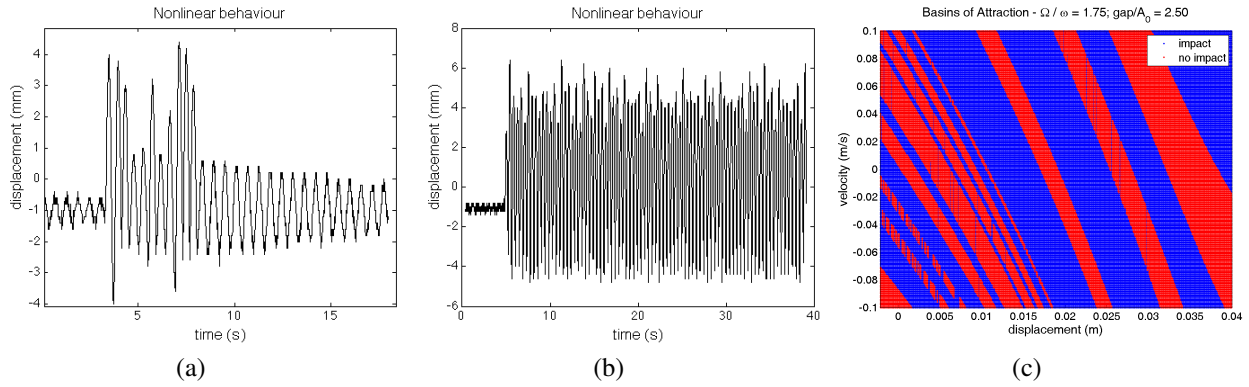


Figure 7 – Nonlinear behavior. Hammer displacement over time: a) Condition of no impact; energy inserted into the system; system impacts but return to non-impact condition; b) Condition of no impact; energy inserted into the system; system impacts and remains in the impact condition; c) basins of attraction (numerical), condition of impact (blue) / no impact (red).

Table 3 – Parameters identification.

Parameter	Value	Unit
Natural frequency, ω	1.82	Hz
Hammer mass, m	0.298	kg
Cart mass, M	5.38	kg
Wire length, l	75	mm
Excitation amplitude, A_0	0.89	mm
Parameter	Value	Unit
Impact stiffness, k_i	$5.5 \cdot 10^6$	N/m
Impact damping, c_i	$1.2 \cdot 10^3$	Ns/m

where the penetration δ and the velocity of penetration, $\dot{\delta}$ are described as

$$\begin{aligned}\delta &= l \sin \theta - \text{gap}, \\ \dot{\delta} &= l \dot{\theta} \cos \theta.\end{aligned}\quad (4)$$

It is important to emphasize that the generalized coordinate θ (and therefore $\dot{\theta}$) is embarked on the cart. To compare the numerical results with the experimental data, where the linear displacement is measured outside the cart, the following transformations must take place:

$$\begin{aligned}x &= l \sin \theta + A_0 \sin(\Omega t) \\ \dot{x} &= l \dot{\theta} \cos \theta + A_0 \Omega \cos(\Omega t)\end{aligned}\quad (5)$$

All numerical simulations were solved using the fourth order Runge-Kutta Method through the Matlab routine *ode45*. For the case with impact, according to the Filippov theory (Leine & Nijmeijer (2004)), the mathematical modeling presented is a system described by differential equation with a discontinuous right-hand side, one condition for the case where no impact is present and another one for the impact case. This mathematical modeling has been performed in previous works (Aguiar & Weber (2007) (2009)), and further information on the numerical integration of ordinary differential equations with a discontinuous right-hand side can be found in Divenyi et al. (2006) (2007).

Parameters identification

The system without impact presents some degree of damping. However, the mathematical modeling does not take this into consideration. For the system without impact, the test rig parameters are identified and the hammer natural frequency is obtained. The impact parameter identification follows previous works (Aguiar & Weber (2009)), using the spring-dashpot model (Gilardi & Sharf (2002)). These results are shown in Table 3.

Model validation and numerical results

The comparison between numerical simulation and experimental data starts with the chart of the non-dimensional force (F_i/mg) in the non-dimensional frequency domain (Ω/ω), for each gap imposed on the test rig. These results are

shown in Figure 8. The methodology applied to identify is the same as that used during the experimental analysis, where for each excitation frequency the maximum impact force is detected, regardless of the impact force behavior.

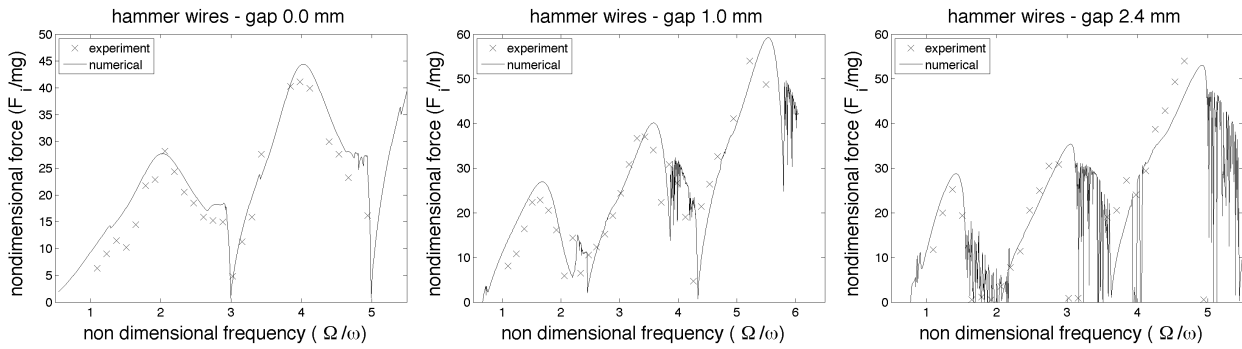


Figure 8 – Comparison between numerical simulation and experimental results. Non dimensional force versus non dimensional frequency. a) Gap 0.0 mm. b) Gap 1.0 mm. c) Gap 2.4 mm.

From the numerical analysis and the comparison between numerical simulation and experimental data shown in Figure 8, it is possible to identify, numerically, the frequency bands observed in the test rig, as the range of excitation frequencies is covered. Overall comparison shows a satisfactory agreement, especially concerning the impact resonance and the maximum impact force for the $z = 1/1$ behavior, for each gap imposed. The model validation is also addressed using the bifurcation diagram, see Figure 9.

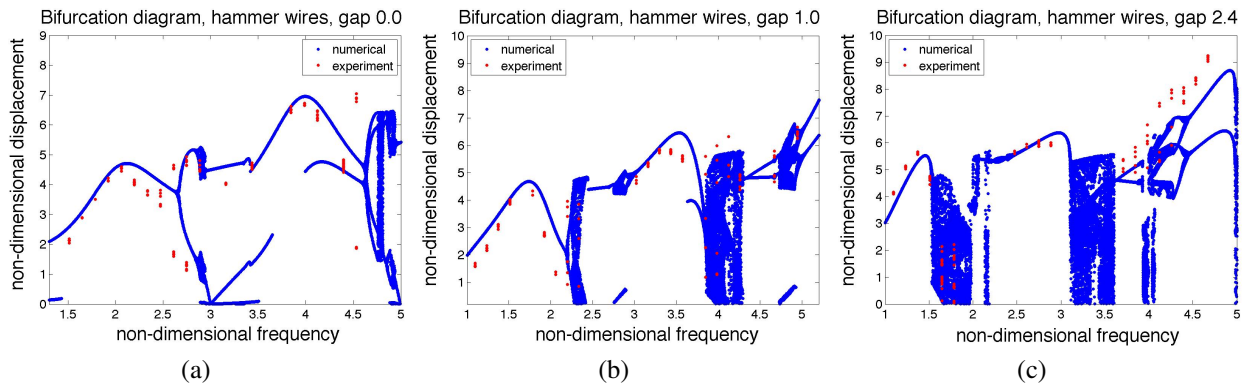


Figure 9 – Bifurcation diagram: hammer displacement, comparison between numerical simulation (blue) and experimental data (red): (a) gap 0.0 mm; (b) gap 1.0 mm; (c) gap 2.4 mm.

Although the impact force charts shown in Figure 8 give some important information regarding the impact force amplitude and the impact resonance, such charts provide neither information about the characteristics of the impact force, nor details on the transition between frequency bands. To better visualize the behavior of this dynamical system, two different tools are used. One is the map of regions of stable impact behavior, called by the authors Peterka map (Peterka (1996) and (2003), Peterka & Błażejczyk-Okolewska (1998)). This map, shown in Figure 10, provides information about the characteristic of the impact force as the gap is varied and the excitation frequency is swept. From this chart one can see the areas where the two frequencies bands occur, as noted by the red ($z = 1/1$) and green ($z = 1/2$) areas.

The Peterka map provides important information about the condition of impact, however, no information regarding the impact magnitude is given. To overcome this problem, a slight variation of the Peterka map is suggested. The relevant impact condition is $z = 1/1$. Therefore, just this area in the Peterka map is addressed. For each gap/ frequency combination, the impact force magnitude is obtained and plotted in colors, see Figure 11(a). Such methodology is also applied to impact behavior $z = 1/2$, as shown in Figure 11(b).

Chart in Figure 11(a) provides several important facts about the system behavior and it confirms some aspects observed during the experimental analysis. First, it confirms that the impact force when the hammer is excited in its natural frequency generates impact forces that are 3 times smaller in magnitude than the maximum force. It also shows that the maximum impact force for each given gap does not occur at the $z = 1/1$ boundary, except for high values of gap. Finally, the chart confirms the recommendation to operate in the field using the 0.0 mm gap, because the magnitude of the impact force is in the same value as the impact force in higher gap values. In addition, non-zero gap values are known to present nonlinear jumps.

Finally, the presence of impact and the gap between the hammer and the cart induces nonlinearities, and therefore

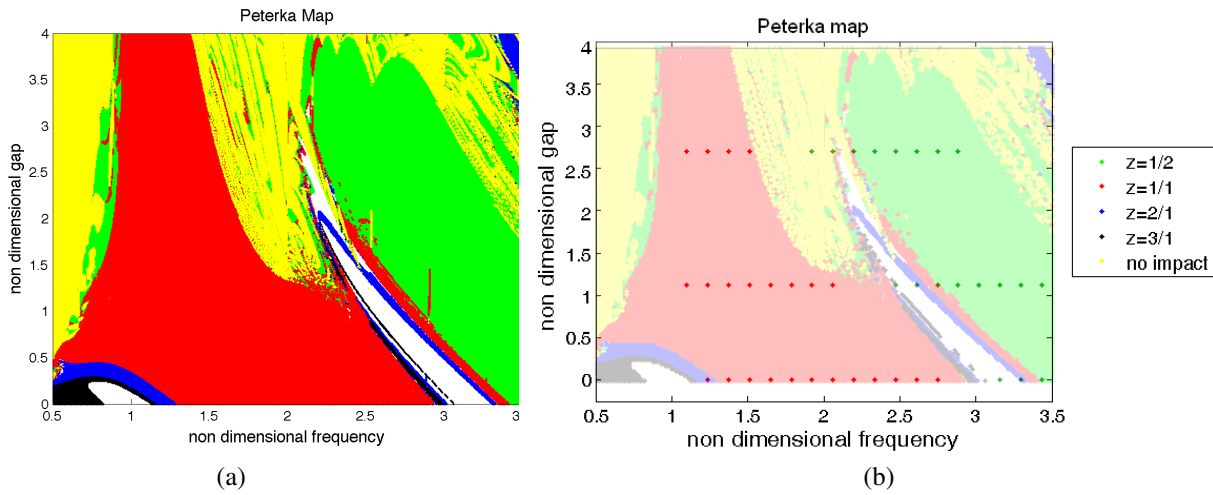


Figure 10 – Peterka map: a) Numerical; b) Numerical (bright colors) / experiment (dots) comparison.

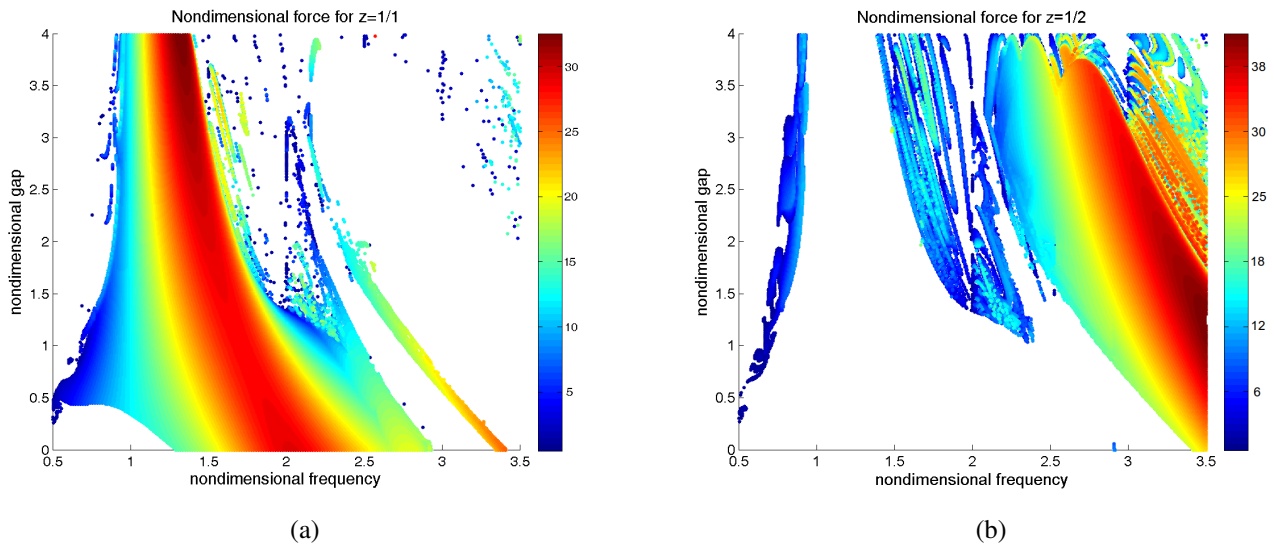


Figure 11 – Peterka map with impact force magnitude addressed: (a) impact behavior $z = 1/1$; (b) impact behavior $z = 1/2$.

nonlinear phenomena arise, specifically in the transition between frequency bands. One of these phenomena is the change of the basins of attraction for some gap conditions. In the Peterka map, Figure 10(a), for a gap condition higher than 1.5, there is an area between the $z = 1/1$ (red) and $z = 1/2$ (green) regions that are characterized by various impact conditions, which are dependent on the system initial condition, as verified by the experiment, Figure 7(a) and (b). This area in the Peterka map can be better visualized with the use of basins of attraction, defined as the set of initial conditions \mathbf{x}_0 such that $\mathbf{x}(t) \rightarrow \mathbf{x}^*$ as $t \rightarrow \infty$, see Figure 7(c).

CONCLUSIONS

This work had the purpose of an experimental investigation and mathematical modeling of the impact force behavior in a vibro-impact system, where an impact pendulum is mounted inside a cart that imposes a prescribed displacement. By changing the hammer parameters it was possible to investigate the impact force behavior under different excitation frequencies.

While studying the impact force characteristic, covering the range of excitation frequency, it was noted that there was a certain pattern of the impact force behavior. This behavior could be divided into frequency bands, presenting similar characteristics in each frequency band for all gaps imposed. In each frequency band, impact force behavior had a regular pattern, while in frequency band transitions the hammer showed nonlinear behavior, as basins of attraction, and even chaotic behavior. The presence of the gap significantly changed the impact resonance. This impact resonance differed from the hammer's natural frequency. A smoothing effect during impact was noticed in the phase plane charts, caused by the differentiation of a low-pass filtered signal, and it does not reflect the reality of the impact.

The comparison between the numerical simulation and the experimental data was satisfactory, showing the capability of the mathematical model to predict the maximum impact force and the impact resonance for all gaps imposed. Nonlinear tools were used to understand the hammer behavior, such as bifurcation diagrams, basins of attraction, Poincaré maps and Peterka maps.

Also, a new methodology was proposed to better visualize each impact force behavior in the Peterka map, plotting one impact force characteristic at a time, adding colors to the third coordinate F_i . This methodology provided important information regarding the hammer behavior and confirmed some aspects observed during the experiment analysis. By observing the experimental data and the nonlinear tools, the recommendation was made to optimize result one should operate with a 0.0 mm gap, because the magnitude of the impact forces were in the same range as the impact force in higher gap values. However, in higher gap values, nonlinear jump was observed, which did not occur in the case of 0.0 mm gap.

ACKNOWLEDGMENTS

The authors wish to thank CNPq and FAPERJ for its support of this research.

REFERENCES

- Aguiar, R.R. and Weber, H.I.: Development of a vibro-impact device for the resonance hammer drilling. Proceedings of the XII DINAME. Ilhabela, SP, Brazil (2007).
- Aguiar, R.R. and Weber, H.I.: Resonance Hammer Drilling: experimental data of an embarked impact system. Proceedings of the XIII DINAME, Angra dos Reis, RJ, Brazil (2009).
- Aguiar, R.R. and Weber, H.I.: Numerical and experimental investigation of an embarked vibro-impact system. Proceedings of COBEM 2009, 20th International Congress of Mechanical Engineering, Gramado, RS, Brazil (2009).
- Batako A.D. and Babitsky V.I. and Halliwell N.A., A self-excited system for percussive-rotary drilling, *Journal of Sound and Vibration*, (2003), Vol. 259(1), pgs 97-118.
- Batako A.D. and Babitsky V.I. and Halliwell N.A., Modelling of vibro-impact penetration of self-exciting percussive-rotary drill bit, *Journal of Sound and Vibration*, 271 (2004) 209-225.
- D.W. Dareing and F.H. Deily and G.H. Paff and J.E. Ortloff and R.D. Lynn, Downhole Measurements of Drill String Forces and Motions, *ASME Journal of Engineering for Industry*, May (1968) 217-225.
- S. Divenyi and M.A. Savi and L.F.P. Franca and H.I. Weber, *Nonlinear Dynamics and Chaos in Systems with Discontinuous Support, Shock and Vibration*, 13 (2006) 315-326.
- S. Divenyi and M.A. Savi and L.F.P. Franca and H.I. Weber, Numerical and Experimental Investigations of the Nonlinear Dynamics and Chaos in Non-Smooth Systems, *Journal of Sound and Vibration*, 301 (2007) 59-73.
- L.F.P. Franca and H.I. Weber, Experimental and Numerical Study of a new Resonance Hammer Drilling Model with Drift, *Chaos, Solitons and Fractals*, 21 (2004) 789-801.
- G. Gilardi and I. Sharf, Literature survey of contact dynamics modelling, *Mechanism and Machine Theory*, 37, (2002) 1213-1239.
- H. Lankarani and P. Nikravesh, Continuous contact force models for impact analysis in multibody systems, *Nonlinear Dynamics*, 5 (2) (1994) 193-207.
- R.I. Leine and H. Nijmeijer, *Dynamics and Bifurcations of Non-Smooth Mechanical Systems*, Springer, 2004.
- E. Pavlovskaja and M. Wiercigroch, Modeling of an impact system with a drift, *Physical review E*, 64, 056224 (2001).
- F. Peterka, Bifurcations and Transition Phenomena in an Impact Oscillator, *Chaos, Solitons and Fractals*, 7 (10) (1996) 1635-1647.
- F. Peterka and B. Blazejczyk-Okolewska, An investigation of the dynamic system with impacts, *Chaos, Solitons and Fractals*, 9 (8) (1998) 1321-1338.
- F. Peterka, More detail view on the dynamics of the impact damper, *Facta Universitatis Series: Mechanics, automatic control and robotics*, 3 (14) (2003) 907-920.

RESPONSIBILITY NOTICE

The authors are the only responsible for the printed material included in this paper.

Riccati Solutions for the Linear-Quadratic Optimal Control Problem of Descriptor Systems

Peter C. Müller¹

¹ Safety Control Engineering, University of Wuppertal, D-42097 Wuppertal, Germany

Abstract: The linear-quadratic optimal control problem for linear time-invariant descriptor systems (differential-algebraic equations) leads firstly to Hamilton's equations and secondly to the solution of Riccati equations. In this contribution it is shown that the Riccati approach only succeeds for proper descriptor systems. For improper descriptor system this approach does not hold. The results are shown explicitly by direct calculation for proper systems and by a counterexample for improper systems.

Keywords: Linear time-invariant descriptor systems, differential-algebraic equations, mechanical systems with constraints, linear-quadratic optimal control, generalized Riccati equations

INTRODUCTION

The investigation of dynamical systems in mechanical, electrical or chemical engineering usually requires a mathematical modelling of the system behavior. The increasing complexity of these processes leads on the one side to the development of computer programs automatically generating the governing system equations, cf. Schiehlen (1990) for multibody systems, or on the other side to an increase of modular subsystem modelling of which the complete model is composed. Usually, this interconnection-oriented modelling describes the dynamic behavior of the single components by differential equations and the coupling of the subsystems by algebraic equations. Allover, the mathematical model is represented by a combined set of differential and algebraic equations, i.e. by differential-algebraic equations (DAE). In mechanical systems the differential equations usually describe the dynamics of the subsystems and the algebraic equations characterize couplings by constraints such as joints. A general approach to handle mechanical systems as an interconnected set of dynamic modules has been given by Rückgauer and Schiehlen (1997).

Lagrange's equations of first and second kinds are well established in analytical mechanics. They describe the dynamical behavior of discrete systems, particularly of multibody systems. The difference of the two kinds consists in the manipulation of kinematic constraints. If a kinematic description of the system has been performed by generalized coordinates consistent with the constraints the Lagrange's equations of second kind can be applied leading to a set of differential equations only. But if a redundant set of coordinates is used to describe kinematically the system regarding still some constraints explicitly, then Lagrange's equations of first kind hold. For linear time-invariant mechanical systems with holonomic constraints we have

$$\mathbf{M}\ddot{\mathbf{q}}(t) + \mathbf{D}\dot{\mathbf{q}}(t) + \mathbf{K}\mathbf{q}(t) = \mathbf{S}_1\mathbf{u}(t) + \mathbf{F}^T\boldsymbol{\lambda}(t), \quad (1)$$

$$\mathbf{O} = \mathbf{F}\mathbf{q}(t) + \mathbf{S}_2\mathbf{u}(t). \quad (2)$$

Here, \mathbf{M} represents the matrix of inertia, \mathbf{D} characterizes damping and gyroscopic effects, and the matrix \mathbf{K} includes stiffnesses and circulatory forces. The redundant set of coordinates is represented by the vector \mathbf{q} which is constrained by the holonomic constraints (2). The effect of the constraints (2) on the dynamic behavior of system (1) is considered by Lagrange's multiplier $\boldsymbol{\lambda}$ (which is proportional to the constraint force). In both equations the control input \mathbf{u} appears; in Eq. (1) it represents a dynamic control and in Eq (2) it stands for a kinematic control. Allover, they form a DAE system with control inputs which is called a (mechanical) descriptor system.

With respect to the tasks of system modelling the descriptor system approach has many advantages. It is a very natural way to model process dynamics, cf. Müller (1995). It refers much more to the physical behavior of the system and gives more physical insight. The interpretation of results is also more simple than in case of the more abstract description by state space models. In the opposite, the state space system approach was mainly required by the mathematical tools available until 1980 to simulate, to analyse and to design such systems. But in the meantime the tools have been extended to descriptor systems (Müller, 2003). But still there are some shortcomings. In this contribution one of these shortcomings will be discussed in detail: Riccati solutions for the linear-quadratic optimal control problem of linear time-invariant descriptor systems.

DESCRIPTOR SYSTEMS

The standard notation of a linear time-invariant descriptor system is given by

$$\mathbf{E}\dot{\mathbf{x}}(t) = \mathbf{A}\mathbf{x}(t) + \mathbf{B}\mathbf{u}(t) \quad (3)$$

where \mathbf{x} is an n -dimensional generalized (or descriptor) vector, \mathbf{E} , \mathbf{A} are constant quadratic $n \times n$ -matrices, and \mathbf{B} is a constant $n \times r$ input matrix. The matrix \mathbf{E} is assumed to be singular, i.e. $\det \mathbf{E} = 0$, to represent differential and algebraic equations in Eq. (3). For the mechanical system (1,2) we have

$$\mathbf{x} = \begin{bmatrix} \mathbf{q} \\ \dot{\mathbf{q}} \\ \lambda \end{bmatrix}, \mathbf{B} = \begin{bmatrix} \mathbf{O} \\ \mathbf{S}_1 \\ \mathbf{S}_2 \end{bmatrix}, \mathbf{E} = \begin{bmatrix} \mathbf{I} & \mathbf{O} & \mathbf{O} \\ \mathbf{O} & \mathbf{M} & \mathbf{O} \\ \mathbf{O} & \mathbf{O} & \mathbf{O} \end{bmatrix}, \mathbf{A} = \begin{bmatrix} \mathbf{O} & \mathbf{I} & \mathbf{O} \\ -\mathbf{K} & -\mathbf{D} & \mathbf{F}^T \\ \mathbf{F} & \mathbf{O} & \mathbf{O} \end{bmatrix}. \quad (4)$$

Additionally, it is assumed that the matrix pencil $(\lambda\mathbf{E} - \mathbf{A})$ is regular, i.e.

$$\det(\lambda\mathbf{E} - \mathbf{A}) \not\equiv 0, \quad (5)$$

i.e. there is at least one value λ_0 with $\det(\lambda_0\mathbf{E} - \mathbf{A}) \neq 0$. An introduction into the analysis and feedback control of descriptor systems (3) is given in (Dai, 1989). There it is shown that the system (3,5) is restricted system equivalent to

$$\dot{\mathbf{x}}_1(t) = \mathbf{A}_1\mathbf{x}_1(t) + \mathbf{B}_1\mathbf{u}(t), \quad (6)$$

$$\mathbf{N}\dot{\mathbf{x}}_2(t) = \mathbf{x}_2(t) + \mathbf{B}_2\mathbf{u}(t) \quad (7)$$

where \mathbf{N} is a nilpotent matrix with index k , such that $\mathbf{N}^{k-1} \neq \mathbf{O}$, $\mathbf{N}^k = \mathbf{O}$. The system (6) is called the “slow” subsystem (representing a state-space system for \mathbf{x}_1); Eq. (7) shows the “fast” subsystem leading to the consistent solution

$$\mathbf{x}_2(t) = -\sum_{i=0}^{k-1} \mathbf{N}^i \mathbf{B}_2 \mathbf{u}^{(i)}(t) \quad (8)$$

where “consistent” means that Eq. (8) is true for initial conditions $\mathbf{x}_2(0) = \mathbf{x}_{20}$, $\mathbf{u}^{(i)}(0) = \mathbf{u}_0^{(i)}$; $\mathbf{u}^{(i)}(t)$ means the i -th time-derivative of $\mathbf{u}(t)$. The transformation from Eq. (3) to Eq. (6,7) is performed by two regular matrices \mathbf{V} , \mathbf{W} :

$$\mathbf{VEW} = \begin{bmatrix} \mathbf{I}_1 & \mathbf{O} \\ \mathbf{O} & \mathbf{N} \end{bmatrix}, \mathbf{VAW} = \begin{bmatrix} \mathbf{A}_1 & \mathbf{O} \\ \mathbf{O} & \mathbf{I}_2 \end{bmatrix}, \mathbf{VB} = \begin{bmatrix} \mathbf{B}_1 \\ \mathbf{B}_2 \end{bmatrix}. \quad (9)$$

While Eq. (6) leads to a standard state space solution with strictly proper behavior ($\mathbf{B}_2 = \mathbf{O}$), the solution (8) of the fast subsystem (7) includes time-derivatives of the control such that the solution is either proper,

$$\mathbf{x}_2(t) = -\mathbf{B}_2\mathbf{u}(t) \text{ for } \mathbf{NB}_2 = \mathbf{O}, \quad (10)$$

or improper for

$$\mathbf{NB}_2 \neq \mathbf{O}. \quad (11)$$

This distinction will be used later.

For the example of the mechanical descriptor system (3,4) Schüpphaus (1995) was able to construct the transformation matrices \mathbf{V} , \mathbf{W} and to find the representation (6,7). The system has index $k=3$ and

$$\mathbf{N} = \begin{bmatrix} \mathbf{O} & \mathbf{I} & \mathbf{O} \\ \mathbf{O} & \mathbf{O} & \mathbf{I} \\ \mathbf{O} & \mathbf{O} & \mathbf{O} \end{bmatrix}, \quad \mathbf{B}_2 = \begin{bmatrix} \mathbf{F} \mathbf{M}^{-1} \mathbf{S}_1 \\ \mathbf{O} \\ \mathbf{S}_2 \end{bmatrix} \quad (12)$$

such that

$$\mathbf{N} \mathbf{B}_2 = \begin{bmatrix} \mathbf{O} \\ \mathbf{S}_2 \\ \mathbf{O} \end{bmatrix}. \quad (13)$$

The mechanical descriptor system (1,2) with holonomic constraints is proper if and only if $\mathbf{S}_2 = \mathbf{O}$, i.e. there is no kinematic control; otherwise the system behavior is improper.

LINEAR-QUADRATIC OPTIMAL CONTROL PROBLEM

For the linear descriptor system (3) the control should be designed according to a quadratic performance criterion

$$\mathbf{J} = \frac{1}{2} \mathbf{x}^T(\mathbf{T}) \mathbf{Z} \mathbf{x}(\mathbf{T}) + \frac{1}{2} \int_0^{\mathbf{T}} \begin{bmatrix} \mathbf{x} \\ \mathbf{u} \end{bmatrix}^T \begin{bmatrix} \mathbf{Q} & \mathbf{S} \\ \mathbf{S}^T & \mathbf{R} \end{bmatrix} \begin{bmatrix} \mathbf{x} \\ \mathbf{u} \end{bmatrix} dt \rightarrow \text{minimum} \quad (14)$$

without any restriction on \mathbf{u} . The weighting matrices are constant and should satisfy the conditions

$$\mathbf{Z} = \mathbf{Z}^T \geq \mathbf{O}, \mathbf{Q} = \mathbf{Q}^T \geq \mathbf{O}, \mathbf{R} = \mathbf{R}^T > \mathbf{O}, \mathbf{Q} - \mathbf{S} \mathbf{R}^{-1} \mathbf{S}^T \geq \mathbf{O}. \quad (15)$$

One way to solve this liner-quadratic control problem is to look for Hamilton's equations and to solve them, cf. Jonckheere, 1988, and Backes, 2006. Hamilton's function is defined by

$$\mathbf{H} = \boldsymbol{\lambda}^T (\mathbf{A} \mathbf{x} + \mathbf{B} \mathbf{u}) - \frac{1}{2} \begin{bmatrix} \mathbf{x} \\ \mathbf{u} \end{bmatrix}^T \begin{bmatrix} \mathbf{Q} & \mathbf{S} \\ \mathbf{S}^T & \mathbf{R} \end{bmatrix} \begin{bmatrix} \mathbf{x} \\ \mathbf{u} \end{bmatrix}. \quad (16)$$

Then Hamilton's equation are stated by

$$\mathbf{E} \dot{\mathbf{x}} = \frac{\partial \mathbf{H}}{\partial \boldsymbol{\lambda}} = \mathbf{A} \mathbf{x} + \mathbf{B} \mathbf{u}, \quad (17a)$$

$$\mathbf{E}^T \dot{\boldsymbol{\lambda}} = -\frac{\partial \mathbf{H}}{\partial \mathbf{x}} = -\mathbf{A}^T \boldsymbol{\lambda} + \mathbf{Q} \mathbf{x} + \mathbf{S} \mathbf{u}, \quad (17b)$$

$$\mathbf{O} = \frac{\partial \mathbf{H}}{\partial \mathbf{u}} = \mathbf{B}^T \boldsymbol{\lambda} - \mathbf{S}^T \mathbf{x} - \mathbf{R} \mathbf{u}. \quad (17c)$$

Calculating \mathbf{u} by Eq. (17c) as

$$\mathbf{u} = \mathbf{R}^{-1} (\mathbf{B}^T \boldsymbol{\lambda} - \mathbf{S}^T \mathbf{x}) \quad (18)$$

the equations (17a, 17b) result in

$$\begin{bmatrix} \mathbf{E} \dot{\mathbf{x}} \\ \mathbf{E}^T \dot{\boldsymbol{\lambda}} \end{bmatrix} = \begin{bmatrix} \mathbf{A} - \mathbf{B} \mathbf{R}^{-1} \mathbf{S}^T & \mathbf{B} \mathbf{R}^{-1} \mathbf{B}^T \\ \mathbf{Q} - \mathbf{S} \mathbf{R}^{-1} \mathbf{S}^T & -(\mathbf{A} - \mathbf{B} \mathbf{R}^{-1} \mathbf{S}^T)^T \end{bmatrix} \begin{bmatrix} \mathbf{x} \\ \boldsymbol{\lambda} \end{bmatrix}. \quad (19)$$

Additionally, there are initial conditions $\mathbf{x}(0) = \mathbf{x}_0$ according to arbitrary $\mathbf{x}_1(0) = \mathbf{x}_{10}$ and special $\mathbf{x}_2(0) = \mathbf{x}_{20}$ as discussed by Eq. (6,7,8), and there is an end condition according to

$$\mathbf{E}^T \boldsymbol{\lambda}(T) = -\mathbf{Z}\mathbf{x}(T). \quad (20)$$

If Hamilton's equations and the boundary conditions are satisfied by solutions $\mathbf{x}^*(t)$, $\boldsymbol{\lambda}^*(t)$, then the related control $\mathbf{u}^*(t)$ by Eq. (18) is the optimal control according to the performance criterion (14).

The main problem consists in finding the solution of the two-point-boundary-value-problem (19,20). For the classical state-space approach the solution is determined by the Riccati matrix equation. This approach has been also extended for descriptor systems, but surprisingly there are two different approaches. The one will be called the standard approach, the other is the Kurina-März approach.

Standard approach

The standard approach to solve Eq. (19) by a Riccati equation can be found e.g. in (Bender and Laub, 1987, or Mehrmann, 1991). The approach is based on the attempt

$$\boldsymbol{\lambda}(t) = -\mathbf{P}_1(t)\mathbf{E}\mathbf{x}(t). \quad (21)$$

Inserting Eq. (21) into Eq. (19) the validity of a vector equation with respect to $\mathbf{x}(t)$ is required. Although \mathbf{x} includes redundant coordinates, in the next step it is asked for the validity of this equation for all \mathbf{x} resulting in a generalized Riccati matrix equation with respect to \mathbf{P}_1 :

$$-\mathbf{E}^T \dot{\mathbf{P}}_1 \mathbf{E} = (\mathbf{A} - \mathbf{B}\mathbf{R}^{-1}\mathbf{S}^T)^T \mathbf{P}_1 \mathbf{E} + \mathbf{E}^T \mathbf{P}_1 (\mathbf{A} - \mathbf{B}\mathbf{R}^{-1}\mathbf{S}^T) - \mathbf{E}^T \mathbf{P}_1 \mathbf{B}\mathbf{R}^{-1}\mathbf{B}^T \mathbf{P}_1 \mathbf{E} + (\mathbf{Q} - \mathbf{S}\mathbf{R}^{-1}\mathbf{S}^T). \quad (22)$$

According to the symmetric structure of Eq. (22) and the symmetric end condition according to Eq. (20) we have

$$\mathbf{E}^T \mathbf{P}_1(T)\mathbf{E} = \mathbf{Z}, \quad \mathbf{P}_1(t) = \mathbf{P}_1^T(t). \quad (23)$$

The descriptor feedback control runs as

$$\mathbf{u}(t) = -\mathbf{R}^{-1}(\mathbf{B}^T \mathbf{P}_1(t)\mathbf{E} + \mathbf{S}^T)\mathbf{x}(t). \quad (24)$$

Kurina-März-Approach

According to Kurina and März (2005) the approach is based on

$$\boldsymbol{\lambda}(t) = -\mathbf{P}_2(t)\mathbf{x}(t) \quad (25)$$

which has to satisfy Eq. (19,20). This results in the following requirements:

$$\mathbf{E}^T \mathbf{P}_2(t) = \mathbf{P}_2^T(t)\mathbf{E}, \quad (26)$$

$$-\mathbf{E}^T \dot{\mathbf{P}}_2 = (\mathbf{A} - \mathbf{B}\mathbf{R}^{-1}\mathbf{S}^T)^T \mathbf{P}_2 + \mathbf{P}_2 (\mathbf{A} - \mathbf{B}\mathbf{R}^{-1}\mathbf{S}^T) - \mathbf{P}_2^T \mathbf{B}\mathbf{R}^{-1}\mathbf{B}^T \mathbf{P}_2 + (\mathbf{Q} - \mathbf{S}\mathbf{R}^{-1}\mathbf{S}^T), \quad (27)$$

$$\mathbf{E}^T \mathbf{P}_2(T) = \mathbf{Z}. \quad (28)$$

Equation (26) represents a symmetry condition, Eq. (27) is the modified KM-Riccati matrix equation and Eq. (28) gives the end condition. The related feedback control reads as

$$\mathbf{u}(t) = -\mathbf{R}^{-1}(\mathbf{B}^T \mathbf{P}_2(t) + \mathbf{S}^T)\mathbf{x}(t). \quad (29)$$

The existence of solutions of the Riccati equations (22) and (27) will be discussed in the next section.

SOLUTIONS OF THE RICCATI EQUATIONS

Simple properties of the Riccati equations

Connection between P_1 and P_2

Immediately the following relation is proved:

If $P_1(t)$ is a solution of Eq. (22,23) then

$$P_2(t) = P_1(t)E \quad (30)$$

is a solution of Eq. (26,27,28).

The proof is done by explicit check. An opposite is not true in general: there are solutions P_2 even if P_1 does not exist.

Necessary conditions

If X is a basis for the null space of E ,

$$\text{rank } E = s : X_{n \times (n-s)} : \text{rank } X = n-s \ \& \ EX = O, \quad (31)$$

then solutions of Eq (22) or Eq. (27) do exist only if

$$(Q - SR^{-1}S^T)X = O, ZX = O, E^T P_1(A - BR^{-1}S^T)X = O \text{ for } P_1, \quad (32)$$

$$E^T P_2 X = O, ZX = O \text{ for } P_2. \quad (33)$$

Particularly, this means that the algebraic variables of the DAE must not be weighted in the sense of Eq. (32) for P_1 or in the sense of Eq. (33) for P_2 .

Standard Riccati equation for proper systems

Properties of the Riccati equation are best discussed if the descriptor system is presented by Eq. (6,7). Then the weighting matrices are given by

$$W^T Q W = [Q_{ij}], W^T Z W = [Z_{ij}], W^T S = [S_i], i,j=1,2. \quad (34)$$

For simplification of notation in the following $S = O$ is assumed. Additionally, the boundary condition (23) or (28) will not be mentioned explicitly.

In the following, the main assumption is the requirement (10), i.e. it is assumed that the system has proper behavior.

According to the separation into the slow and the fast subsystems (6,7) the matrix P_1 is written as

$$V^{-T} P_1 V^{-1} = \bar{P}_1 = \begin{bmatrix} P_{11} & P_{12} \\ P_{12}^T & P_{22} \end{bmatrix}. \quad (35)$$

The standard Riccati equation (22) splits up into

$$-\dot{P}_{11} = A_1^T P_{11} + P_{11} A_1 - (P_{11} B_1 + P_{12} B_2) R^{-1} (B_1^T P_{11} + B_2^T P_{12}^T) + Q_{11}, \quad (36)$$

$$-\dot{P}_{12} N = A_1^T P_{12} N + P_{12} - (P_{11} B_1 + P_{12} B_2) R^{-1} (B_1^T P_{12} + B_2^T P_{22}) N + Q_{12}, \quad (37)$$

$$-N^T P_{22} N = P_{22} N + N^T P_{22} - N^T (P_{12}^T B_1 + P_{22} B_2) R^{-1} (B_1^T P_{12} + B_2^T P_{22}) N + Q_{22}. \quad (38)$$

Multiplying Eq. (38) from the left by \mathbf{B}_2^T and from the right by \mathbf{B}_2 and regarding Eq. (10) the requirement $\mathbf{B}_2^T \mathbf{Q}_{22} \mathbf{B}_2 = \mathbf{O}$ is derived. Because of $\mathbf{Q} = \mathbf{Q}^T \geq \mathbf{O}$ two necessary conditions for the existence of a solution of Eq. (36,37,38) are obtained:

$$\mathbf{Q}_{12} \mathbf{B}_2 = \mathbf{O}, \mathbf{Q}_{22} \mathbf{B}_2 = \mathbf{O}. \quad (39)$$

Additionally, two properties of the solution are found from Eq. (37,38):

$$\mathbf{N}^T \mathbf{P}_{22} \mathbf{B}_2 = \mathbf{O}, \mathbf{P}_{12} \mathbf{B}_2 = \mathbf{O}. \quad (40)$$

The remaining equation (36) turns into a usual Riccati equation for the slow subsystem:

$$-\dot{\mathbf{P}}_{11} = \mathbf{A}_1^T \mathbf{P}_{11} + \mathbf{P}_{11} \mathbf{A}_1 - \mathbf{P}_{11} \mathbf{B}_1 \mathbf{R}^{-1} \mathbf{B}_1^T \mathbf{P}_{11} + \mathbf{Q}_{11}. \quad (41)$$

The feedback control for the slow subsystem reads as

$$\mathbf{u}(t) = -\mathbf{R}^{-1} \mathbf{B}_1^T \mathbf{P}_{11}(t) \mathbf{x}_1(t). \quad (42)$$

Under the necessary existence conditions (39) and the solution properties (40) the standard approach leads for proper descriptor systems to a classical ‘‘Riccati control’’ of the slow subsystem. If Eq. (39) is not satisfied then the standard approach fails.

KM-Riccati equation for proper systems

The Kurina-März-approach starts with

$$\mathbf{V}^{-T} \mathbf{P}_2 \mathbf{W} = \bar{\mathbf{P}}_2 = \begin{bmatrix} \mathbf{P}_{11} & \mathbf{P}_{12} \\ \mathbf{P}_{21} & \mathbf{P}_{22} \end{bmatrix} \quad (43)$$

according to the separation into two subsystems (the notation of \mathbf{P}_{ij} in this section will not get confused with the same notation in the previous section). The symmetry condition (26) requires

$$\mathbf{P}_{11} = \mathbf{P}_{11}^T, \mathbf{P}_{12} = \mathbf{P}_{21}^T \mathbf{N}, \mathbf{N}^T \mathbf{P}_{22} = \mathbf{P}_{22}^T \mathbf{N}. \quad (44)$$

The KM-Riccati equation (27) leads to

$$-\dot{\mathbf{P}}_{11} = \mathbf{A}_1^T \mathbf{P}_{11} + \mathbf{P}_{11} \mathbf{A}_1 - (\mathbf{P}_{11} \mathbf{B}_1 + \mathbf{P}_{21}^T \mathbf{B}_2) \mathbf{R}^{-1} (\mathbf{B}_1^T \mathbf{P}_{11} + \mathbf{B}_2^T \mathbf{P}_{21}) + \mathbf{Q}_{11}, \quad (45)$$

$$-\dot{\mathbf{P}}_{21}^T \mathbf{N} = \mathbf{P}_{21}^T + \mathbf{A}_1^T \mathbf{P}_{21}^T \mathbf{N} - (\mathbf{P}_{11} \mathbf{B}_1 + \mathbf{P}_{21}^T \mathbf{B}_2) \mathbf{R}^{-1} (\mathbf{B}_1^T \mathbf{P}_{21}^T \mathbf{N} + \mathbf{B}_2^T \mathbf{P}_{22}) + \mathbf{Q}_{12}, \quad (46)$$

$$-\dot{\mathbf{P}}_{22}^T \mathbf{N} = \mathbf{P}_{22} + \mathbf{P}_{22}^T - (\mathbf{N}^T \mathbf{P}_{21} \mathbf{B}_1 + \mathbf{P}_{22}^T \mathbf{B}_2) \mathbf{R}^{-1} (\mathbf{B}_1^T \mathbf{P}_{21}^T \mathbf{N} + \mathbf{B}_2^T \mathbf{P}_{22}) + \mathbf{Q}_{22}. \quad (47)$$

Because of Eq. (10), $\mathbf{N} \mathbf{B}_2 = \mathbf{O}$, the conditions (44) results in the necessary conditions for the solution of Eq. (44-47):

$$\mathbf{P}_{12} \mathbf{B}_2 = \mathbf{O}, \mathbf{N}^T \mathbf{P}_{22} \mathbf{B}_2 = \mathbf{O}. \quad (48)$$

Multiplying Eq. (47) by \mathbf{B}_2^T from the left and by \mathbf{B}_2 from the right the equation

$$\bar{\mathbf{P}}_{22} + \bar{\mathbf{P}}_{22}^T - \bar{\mathbf{P}}_{22}^T \mathbf{R}^{-1} \bar{\mathbf{P}}_{22} + \mathbf{B}_2^T \mathbf{Q}_{22} \mathbf{B}_2 = \mathbf{O} \quad (49)$$

is obtained for $\bar{\mathbf{P}}_{22} = \mathbf{B}_2^T \mathbf{P}_{22} \mathbf{B}_2$. The general solution of Eq. (49) is

$$\bar{\mathbf{P}}_{22} = \mathbf{R} - \mathbf{R}^{1/2} \mathbf{T} (\mathbf{R} + \mathbf{B}_2^T \mathbf{Q}_{22} \mathbf{B}_2)^{1/2} \quad (50)$$

with an arbitrary orthogonal matrix \mathbf{T} : $\mathbf{T}^T \mathbf{T} = \mathbf{I}_r = \mathbf{T} \mathbf{T}^T$. Eq. (46) leads to

$$\mathbf{P}_{21}^T \mathbf{B}_2 = \left(\mathbf{P}_{11} \mathbf{B}_1 \mathbf{R}^{-1} \bar{\mathbf{P}}_{22} - \mathbf{Q}_{12} \mathbf{B}_2 \right) \left(\mathbf{R} + \mathbf{B}_2^T \mathbf{Q}_{22} \mathbf{B}_2 \right)^{-1/2} \mathbf{T}^T \mathbf{R}^{1/2}. \quad (51)$$

Finally, Eq. (45) results in

$$\begin{aligned} -\dot{\mathbf{P}}_{11} = & \left[\mathbf{A}_1 + \mathbf{B}_1 \left(\mathbf{R} + \mathbf{B}_2^T \mathbf{Q}_{22} \mathbf{B}_2 \right)^{-1} \mathbf{B}_2^T \mathbf{Q}_{12}^T \right]^T \mathbf{P}_{11} + \mathbf{P}_{11} \left[\mathbf{A}_1 + \mathbf{B}_1 \left(\mathbf{R} + \mathbf{B}_2^T \mathbf{Q}_{22} \mathbf{B}_2 \right)^{-1} \mathbf{B}_2^T \mathbf{Q}_{12}^T \right] \\ & - \mathbf{P}_{11} \mathbf{B}_1 \left(\mathbf{R} + \mathbf{B}_2^T \mathbf{Q}_{22} \mathbf{B}_2 \right)^{-1} \mathbf{B}_1^T \mathbf{P}_{11} + \left[\mathbf{Q}_{11} - \mathbf{Q}_{12} \mathbf{B}_2 \left(\mathbf{R} + \mathbf{B}_2^T \mathbf{Q}_{22} \mathbf{B}_2 \right)^{-1} \mathbf{B}_2^T \mathbf{Q}_{12}^T \right]. \end{aligned} \quad (52)$$

Interestingly, even Eq. (45) depends on \mathbf{P}_{21} and therefore on the orthogonal matrix \mathbf{T} which is unknown, the Eq. (52) is uniquely determined. It is a classical Riccati equation for the slow subsystem determining the feedback control

$$\mathbf{u}(t) = - \left(\mathbf{R} + \mathbf{B}_2^T \mathbf{Q}_{22} \mathbf{B}_2 \right)^{-1} \left(\mathbf{B}_1^T \mathbf{P}_{11}(t) - \mathbf{B}_2^T \mathbf{Q}_{12}^T \right) \mathbf{x}_1(t). \quad (53)$$

The solution agrees with the solution of Hamilton's equations (18,19) for proper systems (without explicit proof). Therefore, the Kurina-März-approach come up with a correct solution; it is more general than the solution (41,42) of the standard Riccati approach. Here, we do not need the requirements (39) to find the solution (52,53). But in the special case of Eq. (39) the solution (52,53) coincides with the solution (41,42).

For proper descriptor systems the linear-quadratic optimal control problem can be solved by the Kurina-März-approach. The standard Riccati approach is not required; it results in the correct solution only for the special case (39).

Improper descriptor systems

In this section it is shown by a simple example that the Riccati-approaches fail for improper systems. For this, we solve the example directly and compare the result with that of KM-Riccati-approach (the standard Riccati approach is not discussed because it is weaker than the KM-Riccati approach).

The simplest index 2-problem is considered:

$$\dot{x}_2 = x_1 + b_1 u, \quad 0 = x_2 + b_2 u \quad (54)$$

$$J = \frac{1}{2} \int_0^T \left(\mathbf{x}^T \mathbf{Q} \mathbf{x} + r u^2 \right) dt \rightarrow \text{minimum}. \quad (55)$$

The solution of Eq. (54) runs as

$$x_1 = -b_1 u - b_2 \dot{u}, \quad x_2 = -b_2 u \quad (56)$$

which is improper for $b_2 \neq 0$. Inserting the solution (56) into the performance criterion (55) the direct optimization problem

$$J = \frac{1}{2} \int_0^T \left[\left(r + \mathbf{b}^T \mathbf{Q} \mathbf{b} \right) u^2 + 2 \left(q_{11} b_1 b_2 + q_{12} b_2^2 \right) u \dot{u} + q_{11} b_2^2 \dot{u}^2 \right] dt \rightarrow \text{minimum}. \quad (57)$$

is obtained. By the classical calculus of variations the Euler equation

$$\ddot{u} - \omega^2 u = 0, \quad \omega^2 = \frac{r + \mathbf{b}^T \mathbf{Q} \mathbf{b}}{q_{11} b_2^2} \quad (58)$$

appears where $q_{11} b_2^2 \neq 0$ is assumed. The solution of Eq. (58) is

$$u(t) = \frac{1}{2} \left(u_0 + \frac{\dot{u}_0}{\omega} \right) e^{\omega t} + \frac{1}{2} \left(u_0 - \frac{\dot{u}_0}{\omega} \right) e^{-\omega t} \quad (59)$$

where the initial conditions follow from Eq. (56):

$$u_0 = -\frac{1}{b_2} x_{20}, \quad \dot{u}_0 = -\frac{1}{b_2^2} (b_2 x_{10} - b_1 x_{20}). \quad (60)$$

By Eq. (56) the trajectories $x_1(t)$, $x_2(t)$ can be determined, too. The dynamics of the closed-loop control system is given by

$$\dot{x}_1 = \frac{b_1}{b_2} x_1 + \left(\omega^2 - \frac{b_1^2}{b_2^2} \right) x_2, \quad \dot{x}_2 = x_1 - \frac{b_1}{b_2} x_2. \quad (61)$$

In contrast to this direct solution, now the Kurina-März-approach will be applied to solve the optimization problem (54,55). The symmetry condition (26) leads to

$$P_2 = \begin{bmatrix} 0 & p_{12} \\ p_{21} & p_{22} \end{bmatrix}. \quad (62)$$

The KM-Riccati equation (27) splits up into

$$0 = -\frac{b_2^2}{r} p_{21}^2 + q_{11}, \quad (63)$$

$$0 = p_{21} + p_{12} - \frac{1}{r} b_2 p_{21} (b_1 p_{12} + b_2 p_{22}) + q_{12}, \quad (64)$$

$$\dot{p}_{12} = 2p_{22} - \frac{1}{r} (b_1 p_{12} + b_2 p_{22})^2 + q_{22}. \quad (65)$$

Equation (63) results in a constant solution p_{21} . Then Eq. (64) shows $p_{22} = p_{22}(p_{12})$. Finally Eq. (65) represents a scalar Riccati equation for $p_{12} = p_{12}(t)$. The correspondent feedback control (29) is

$$u = -\frac{1}{r} \left[b_2 p_{21} x_1 + (b_1 p_{12} + b_2 p_{22}) x_2 \right]. \quad (66)$$

Having in mind the second equation of Eq. (56) and Eq. (63,64), then Eq. (66) leads to the requirement

$$x_1 = -\frac{1}{q_{11}} (p_{12} + q_{12}) x_2. \quad (67)$$

Therefore, the KM-Riccati approach leads to a solution which has to satisfy the constraint (67). Particularly, the initial conditions x_{10}, x_{20} cannot be chosen arbitrarily. This is in contradiction to Eq. (61).

The KM-Riccati approach fails for this improper system (54). Because of the proportional feedback (66) it does not regard the improper behavior where the time-derivative of u , \dot{u} , has to be considered, too. This includes a dynamic feedback instead of a static feedback control.

CONCLUSION

In this paper it has been shown that the Kurina-März-Riccati equation can be successfully applied to solve the linear-quadratic optimal control problem of proper descriptor systems. The proper behavior is a strong requirement for this approach. For improper descriptor systems this approach cannot be applied. Then, the linear-quadratic optimal control problem has to be solved in a different way regarding explicitly the higher-order time-derivatives of \mathbf{u} in the solution (8) of the fast subsystem. This has been considered in (Müller, 2000). Substituting \mathbf{x}_2 by the solution (8) in the performance criterion (14) a optimization problem with respect to the slow variables \mathbf{x}_1 and the control \mathbf{u} and its time-derivatives $\dot{\mathbf{u}}, \ddot{\mathbf{u}}, \dots$ appears. This modified optimal control problem could be solved applying a extended standard Riccati equation.

Comparing the two Riccati approaches, obviously the KM-Riccati approach has to be preferred. It is clearly superior to the standard Riccati approach because it does not need the requirements (39).

To check the assumption on proper behavior, either the explicit condition (10) has to be verified or a special rank test of the matrices $\mathbf{E}, \mathbf{A}, \mathbf{B}$ has to be performed (Müller, 2011). For mechanical descriptor systems proper or improper behavior is shown explicitly by Eq. (13) according to the explicit knowledge of the transformation (9), cf. Schüpphaus (1995).

REFERENCES

- Backes, A., 2006, "Extremalbedingungen für Optimierungs-Probleme mit Algebro-Differentialgleichungen", Logos, Berlin.
- Bender, D. and Laub, A., 1987, „The Linear-Quadratic Optimal Regulator for Descriptor Systems“, IEEE Trans. Autom. Contr., Vol. 32, pp. 672-688.
- Dai, L., 1989, "Singular Control Systems", Lect. Notes Contr. Inform. Sci., Vol. 118, Springer, Berlin-Heidelberg.
- Jonckheere, E., 1988, "Variational Calculus for Descriptor Problems", IEEE Trans. Autom. Contr., Vol. 33, pp. 491-495.
- Kurina, G.A. and März, R., 2005, "Feedback Solutions of Optimal Control Problems with DAE Constraints", Institute for Mathematics, Humboldt University Berlin, Preprint 9, <http://www.mathematik.hu-berlin.de>
- Mehrmann, V.L., 1991, "The Autonomous Linear Quadratic Control Problem", Lect. Notes Contr. Inform. Sci., Vol. 163, Springer, Berlin-Heidelberg.
- Müller, P.C., 1995, "Descriptor Systems: A New Way to Model Mechatronic Systems?", Proc. 3rd Europ. Contr. Conf., Rome/Italy, Vol. 3, Part 2, pp. 2725-2729.
- Müller, P.C. 2000, "Linear-Quadratic Optimal Control of Non-Proper Descriptor Systems", CD-Proc. 14th Internat. Symp. Math. Theory of Networks and Systems (MTNS 2000), Laboratoire de Théorie des Systemes (LTS), Université de Perpignan, France.
- Müller, P.C., 2003, "Modellbildung, Identifikation und Simulation mittels Deskriptorsysteme“, VDI/VDE-GMA Congress, Session 6 C, Baden-Baden, June 3/4, 2003, <http://www.srm.uni-wuppertal.de> (Link „GMA-Kongress 2003“).
- Müller, P.C., 2011, „Characteristics of LTI Descriptor Systems“, to appear.
- Rückgauer, A. and Schiehlen, W., 1997, „Simulation of Modular Dynamic Systems“, Proc. 2nd MATHMOD, Vienna/Austria, pp. 329-334.
- Schiehlen, W., 1990, "Multibody Systems Handbook", Springer, Berlin-Heidelberg.
- Schüpphaus, R., 1995, „Regelungstechnische Analyse und Synthese von Mehrkörpersystemen in Deskriptorform“, Fortschr.-Ber. VDI, Reihe 8, Nr. 478, Düsseldorf.

On the Analysis of Chaos Control Methods Performance Applied to Mechanical Systems

Aline Souza de Paula ¹, Marcelo Amorim Savi ²

¹ Universidade de Brasília,
Department of Mechanical Engineering
70.910.900 – Brasília – DF – Brazil

² Universidade Federal do Rio de Janeiro
COPPE – Department of Mechanical Engineering
21.941.972 – Rio de Janeiro – RJ, Brazil, P.O. Box 68.503

Abstract: Chaos may be exploited in order to design dynamical systems that may quickly react to some new situation, changing conditions and their response. In this regard, the idea that chaotic behavior may be controlled by small perturbations allows this kind of behavior to be desirable in different applications. Chaos control may be understood as a two stage technique: the first one is known as learning stage where the unstable periodic orbits (UPOs) embedded in chaotic attractor are identified and system characteristics are evaluated; after that, the control stage stabilizes desired UPOs. This paper presents an overview of chaos control methods classified as follows: OGY methods – that includes discrete and semi-continuous approaches; multiparameter methods – that also includes discrete and semi-continuous approaches; and time-delayed feedback methods that are continuous approaches. These methods are employed in order to stabilize some desired UPOs establishing a comparative analysis of all methods. Essentially, a control rule is of concern and each controller needs to follow this rule. Noisy time series is treated establishing a robustness analysis of control methods. The main goal is to establish a comparative analysis of chaos control methods evaluating the capability of each method to stabilize a desired UPO analyzing its performance.

Keywords: *Chaos, control, noise, nonlinear dynamics, pendulum.*

INTRODUCTION

Nonlinearities are responsible for a great variety of possibilities in natural systems. Chaos is one of these possibilities being related to an intrinsic richness. A geometrical form to understand chaos is related to a transformation known as Smale horseshoe that establishes a sequence of contraction-expansion-folding which causes the existence of an infinity number of unstable periodic orbits (UPOs) embedded in a chaotic attractor. This set of UPO constitutes the essential structure of chaos. Besides, chaotic behavior has other important aspects as sensitive dependence to initial conditions and ergodicity.

These aspects of chaos may be exploited in order to design dynamical systems that may quickly react to some new situation, changing conditions and their response. Under this condition, a dynamical system adopting chaotic regimes becomes interesting due to the wide range of potential behaviors being related to a flexible design. The idea that chaotic behavior may be controlled by small perturbations applied in some system parameters allows this kind of behavior to be desirable in different applications.

In brief, chaos control methods may be classified as discrete and continuous methods. Semi-continuous method is a class of discrete method that lies between discrete and continuous method. The pioneer work of Ott *et al.* (1990) introduced the basic idea of chaos control proposing the discrete OGY method. Afterwards, Hübinger *et al.* (1994) proposed a variation of the OGY technique considering semi-continuous actuations in order to improve the original method capacity to stabilize unstable orbits. Pyragas (1992) proposed a continuous method that stabilizes UPOs by a feedback perturbation proportional to the difference between the present and a delayed state of the system.

This article deals with a comparative analysis of chaos control methods that are classified as follows: OGY methods, multiparameter methods and time-delayed feedback methods. Initially, a brief introduction of chaos control methods is presented. Afterwards, a comparative study is carried out by defining some control rules that should be followed by each controller. Finally, noise influence is treated showing the robustness of each controller. In order to consider a system with high instability, a nonlinear pendulum treated in other references is considered (De Paula & Savi, 2009a,b; Pereira-Pinto *et al.*, 2004). Figure 1 presents chaos control methods analyzed in this paper.

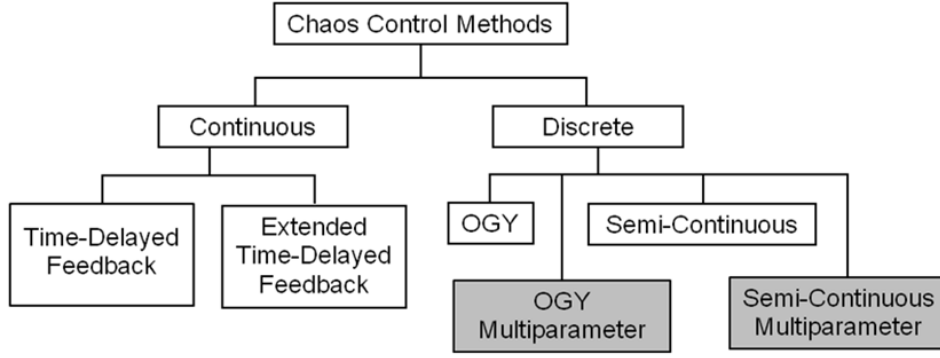


Figure 1 - Chaos control methods.

CHAOS CONTROL METHODS

The control of chaos can be treated as a two-stage process. The first stage is called learning stage where it is performed the identification of UPOs and system parameters necessary for control purposes. A good alternative for the UPO identification is the close return method (Auerbach et al., 1987). This identification is not related to the knowledge of the system dynamics details. The estimation of system parameters is done in different ways for discrete, semi-continuous and continuous methods. After the learning stage, the second stage starts promoting the UPO stabilization.

This section considers an overview of the chaos control methods, classified as follows: OGY methods – that includes discrete and semi-continuous approaches (Ott et al., 1990; Hübinger et al., 1994); multiparameter methods – that also includes discrete and semi-continuous approaches (De Paula & Savi, 2008, 2009a); and time-delayed feedback methods that are continuous approaches (Pyragas, 1992; Socolar et al., 1994).

OGY Method

The OGY method (Ott *et al.*, 1990) is described by considering a discrete system of the form of a map $\xi^{n+1} = F(\xi^n, p^n)$, where $p \in \mathfrak{R}$ is an accessible parameter for control. This is equivalent to a parameter dependent map associated with a general surface, usually a Poincaré section. Let $\xi_C^{n+1} = F(\xi_C^n, p_0)$ denote the unstable fixed point on this section corresponding to an unstable periodic orbit in the chaotic attractor that one wants to stabilize. Basically, the control idea is to monitor the system dynamics until the neighborhood of this point is reached. When this happens, a proper small change in the parameter p causes the next state ξ_{n+1} to fall into the stable direction of the fixed point. In order to find the proper variation in the control parameter, δp , it is considered a linearized version of the dynamical system in the neighborhood of the equilibrium point given by Eq.(1). The linearization has a homeomorphism with the nonlinear problem that is assured by the Hartman-Grobman theorem (Savi, 2006).

$$\delta \xi^{n+1} = J^n \delta \xi^n + w^n \delta p^n \quad (1)$$

where $\delta \xi^n = \xi^n - \xi_C^n$, $\delta \xi^{n+1} = \xi^{n+1} - \xi_C^{n+1}$, $\delta p^n = p^n - p_0$, $J^n = D_{\xi^n} F(\xi^n, p^n) \Big|_{\xi^n = \xi_C^n, p^n = p_0}$ and $w^n = D_{p^n} F(\xi^n, p^n) \Big|_{\xi^n = \xi_C^n, p^n = p_0}$.

Hübinger *et al.* (1994) verified that the linear mapping J^n deforms a sphere around ξ_C^n into an ellipsoid around ξ_C^{n+1} . Therefore, a singular value decomposition (SVD) can be employed in order to determine the unstable and stable directions, v_u^n and v_s^n , in Σ_n which are mapped onto the largest, $\sigma_u^n u_u^n$, and shortest, $\sigma_s^n u_s^n$, semi-axis of the ellipsoid in Σ_{n+1} , respectively. Here, σ_u^n and σ_s^n are the singular values of J^n .

$$J^n = U^n W^n (V^n)^T = \begin{Bmatrix} \sigma_u^n & 0 \\ 0 & \sigma_s^n \end{Bmatrix} \begin{Bmatrix} v_u^n \\ v_s^n \end{Bmatrix}^T \quad (2)$$

Korte *et al.* (1995) established the control target as being the adjustment of δp^n such that the direction v_s^{n+1} on the map $n+1$ is obtained, resulting in a maximal shrinking on map $n+2$. Therefore, it demands $\delta \xi^{n+1} = \alpha v_s^{n+1}$, where $\alpha \in \mathfrak{R}$. Hence:

$$J^n \delta \xi^n + w^n \delta p^n = \alpha v_s^{n+1} \quad (3)$$

that is a relation from which α and δp^n can be conveniently chosen.

The OGY method can be employed even in situations where a mathematical model is not available. Under this situation, all parameters can be extracted from time series analysis. The Jacobian J^n and the sensitivity vector w^n can be estimated from a time series using a least-square fit method as described in Auerbach *et al.* (1987) and Otani & Jones (1997).

An alternative to deal with some of the OGY drawbacks is the use of as many control stations as it is necessary to stabilize some orbits. This is the essential point related to semi-continuous method.

Semi-continuous Method

The semi-continuous method (SC) lies between the continuous and the discrete time control because one can introduce as many intermediate Poincaré sections, viewed as control stations, as it is necessary to achieve stabilization of a desired UPO (Hübinger *et al.*, 1994). Therefore, the SC method is based on measuring transition maps of the system. These maps relate the state of the system in one Poincaré section to the next.

In order to use N control stations per forcing period T , one introduces N equally spaced successive Poincaré sections Σ_n , $n = 0, \dots, (N-1)$. Let $\xi_C^n \in \Sigma_n$ be the intersections of the UPO with Σ_n and F be the mapping from one control station Σ_n to the next one Σ_{n+1} .

Multiparameter Method

The multiparameter chaos control method (MP) is based on the OGY approach and considers N_p different control parameters, p_i ($i = 1, \dots, N_p$). Moreover, only one of these control parameters actuates in each control station (De Paula & Savi, 2008, 2009a). Under this assumption, the map F that establishes the relation of the system behavior between the control stations Σ_n and Σ_{n+1} , depends on all control parameters. Although only one parameter actuates in each section, it is considered the influence of all control parameters based on their positions in station Σ_n . On this basis,

$$\xi^{n+1} = F(\xi^n, P^n) \quad (4)$$

where P^n is a vector with all control parameters. By using a first order Taylor expansion, one obtains the linear behavior of the map F in the neighborhood of the control point ξ_C^n and around the control parameter reference position, P_0 , is defined by.

$$\delta \xi^{n+1} = J^n \delta \xi^n + W^n \delta P^n \quad (5)$$

where $\delta \xi^{n+1} = \xi^{n+1} - \xi_C^{n+1}$, $\delta \xi^n = \xi^n - \xi_C^n$, $\delta P^n = P^n - P_0$ is related to the control actuation,

$J^n = D_{\xi^n} F(\xi^n, P^n) \Big|_{\xi^n = \xi_C^n, P^n = P_0}$ is the Jacobian matrix and $W^n = D_{P^n} F(\xi^n, P^n) \Big|_{\xi^n = \xi_C^n, P^n = P_0}$ is the sensitivity matrix

which each column is related to a control parameter. In order to evaluate the influence of all parameters actuation, it is assumed that the system response to all parameters perturbation is given by a linear combination of the system responses when each parameter actuates isolated and the others are fixed at their reference value. Therefore,

$$\delta P^n = B^n \delta p^n \quad (6)$$

where B^n is defined as a $[N_p \times N_p]$ diagonal matrix formed by the weighting parameters, *i.e.*, $diag(B^n)_i = \beta_i^n$. This can be understood considering that each parameter influence is related to a vector with components $q_i = W_i^n \delta p_i^n = W_i^n (p_i^n - p_{0i})$, and the general perturbation is given by:

$$q = \beta_1 q_1 + \beta_2 q_2 + \dots + \beta_{N_p} q_{N_p} = W^n B^n \delta p^n \quad (7)$$

Moreover, by assuming that only one parameter actuates in each control station it is possible to define active parameters, represented by subscript a , $\delta P_a^n = B_a^n \delta p_a^n$ (actuate in station Σ_n), and passive parameters, represented by subscript p , $\delta P_p^n = B_p^n \delta p_p^n$ (do not actuate in station Σ_n). At this point, it is assumed a weighting matrix for active parameter, B_a^n , and other for passive parameters, B_p^n . Therefore,

$$\delta \xi^{n+1} = J^n \delta \xi^n + W^n \delta P_a^n + W^n \delta P_p^n \quad (8)$$

Now, it is necessary to align the vector $\delta \xi^{n+1}$ with the stable direction v_s^{n+1} :

$$\delta \xi^{n+1} = \alpha v_s^{n+1} \quad (9)$$

where $\alpha \in \mathfrak{R}$ needs to be satisfied as follows:

$$J^n \delta \xi^n + W^n \delta P_a^n + W^n \delta P_p^n = \alpha v_s^{n+1} \quad (10)$$

Therefore, once the unknown variables are α and the non-vanishing term of the vector δP_a^n , one obtains the following system:

$$\begin{bmatrix} \delta P_{ai}^n \\ \alpha \end{bmatrix} = -[W_i^n - v_s^{n+1}]^{-1} [J^n W^n] \begin{bmatrix} \delta \xi^n \\ \delta P_p^n \end{bmatrix} \quad (11)$$

where δP_{ai}^n is related to the non-vanishing element of the vector δP_a^n , that consists in the active parameter in Σ_n , and W_i^n correspond to the sensitivity matrix column related to this active parameter. The solution of this system furnishes the necessary values for the system stabilization: α and δP_{ai}^n . Notice that the real perturbation is given by: $\delta P_{ai}^n = \delta P_{ai}^n / \beta_{ai}^n$.

A particular case of this control procedure has uncoupled control parameters meaning that each parameter returns to the reference value when it becomes passive. Moreover, since there is only one active parameter in each control station, the system response to parameter perturbation is the same as when it actuates alone. Under this assumption, passive influence vanishes and active vector is weighted by 1, which is represented by:

$$B_p^n = 0 \text{ and } B_a^n = I \quad (12)$$

where I is the identity matrix.

Therefore, the map F is just a function of the active parameters, $\xi^{n+1} = F(\xi^n, P_a^n)$, and the linear behavior of the map F in the neighborhood of the control point ξ_C^n and around the control parameter reference positions, P_0 , is now defined by:

$$\delta \xi^{n+1} = J^n \delta \xi^n + W^n \delta P_a^n \quad (13)$$

where the sensitivity matrix W^n is the same of the previous case. Moreover, since $B_a^n = I$, it follows that $\delta P_a^n = \delta P_{ai}^n$, thus the value of δP_{ai}^n corresponds to the real perturbation necessary to stabilize the system. In order to align the vector $\delta \xi^{n+1}$ with the stable direction, the following system is obtained:

$$\begin{bmatrix} \delta P_{ai}^n \\ \alpha \end{bmatrix} = -[W_i^n - v_s^{n+1}]^{-1} J^n \delta \xi^n \quad (14)$$

The difference between the multiparameter method (MP) (De Paula & Savi, 2008) and the semi-continuous multiparameter method (SC-MP) (De Paula & Savi, 2009a) is that the first considers only one control station per forcing period while the other considers as many control stations as necessary to stabilize the system per forcing period. Therefore, the SC-MP is the general case that can represent the MP when only one control station per period is of concern. In the same way, the OGY can be seen as a particular case when only one control station and only one control parameter are considered.

Time-delayed Feedback Methods

Continuous methods for chaos control were first proposed by Pyragas (1992) and are based on continuous-time perturbations to perform chaos control. This control technique deals with a dynamical system modeled by a set of ordinary nonlinear differential equations as follows:

$$\dot{x}(t) = Q(x, t) + B(t) \quad (15)$$

where $x(t) \in R^n$ is the state variable vector, $Q(x, t) \in R^n$ defines the system dynamics, while $B(t) \in R^n$ is associated with the control action.

Socolar *et al.* (1994) proposed a control law named as the extended time-delayed feedback control (ETDF) considering the information of time-delayed states of the system represented by the following equations:

$$\begin{aligned} B(t) &= K[(1-R)S_\tau - x] \\ S_\tau &= \sum_{m=1}^{\infty} R^{m-1} x_{m\tau} \end{aligned} \quad (16)$$

where $K \in R^{n \times n}$ is the feedback gain matrix, $0 \leq R < 1$, $S_\tau = S(t - \tau)$ and $x_{m\tau} = x(t - m\tau)$. The UPO stabilization can be achieved by a proper choice of R and K . Note that for any R and K , perturbation of Eq.(16) vanishes when the system is on the UPO since $x(t - m\tau) = x(t)$ for all m if $\tau = T_i$, where T_i is the periodicity of the i th UPO.

The controlled dynamical system consists of a set of delay differential equations (DDEs). The solution of this system is done by establishing an initial function $x_0 = x_0(t)$ over the interval $(-m\tau, 0)$. This function can be estimated by a Taylor series expansion as proposed by Cunningham (1954):

$$x_{m\tau} = x - m\tau \dot{x} \quad (17)$$

Note that DDEs contain derivatives that depend on the solution at delayed time instants. Therefore, besides the special treatment that must be given for $(t - m\tau) < 0$, it is necessary to deal with time-delayed states while integrating the system. A fourth-order Runge-Kutta method with linear interpolation on the delayed variables is employed in this work for the numerical integration of the controlled dynamical system (Mensour & Longtin, 1997).

It should be pointed out that when $R = 0$, the ETDF turns into the original time-delayed feedback control method (TDF) proposed by Pyragas (1992) where the control law is based on a feedback of the difference between the current and a delayed state given by:

$$B(t) = K[x_\tau - x] \quad (18)$$

where τ is the time delay, $x = x(t)$ and $x_\tau = x(t - \tau)$.

An important difference between continuous and discrete methods is that in continuous methods it is not necessary to wait the system to visit the neighborhood of the desired orbit. Another particular characteristic related to the learning stage is that, besides the UPO identification common to all control methods, it is necessary to establish proper values of the control parameters, K and R , for each desired orbit. This choice is done by analyzing Lyapunov exponents of the UPO, establishing negative values of the largest Lyapunov exponent. After this first stage, the control stage is performed, where the desired UPOs are stabilized. De Paula & Savi (2009b) discussed a proper procedure to evaluate the largest Lyapunov exponents necessary for the controller parameters.

COMPARATIVE ANALYSIS

As an application of the general chaos control methods, a system with high instability characteristic is of concern. A nonlinear pendulum actuated by two different control parameters is considered. The motivation of the proposed pendulum is an experimental set up discussed in De Paula *et al.* (2006) that proposed a mathematical model to describe the pendulum dynamical behavior. Basically, the pendulum consists of an aluminum disc with a lumped mass. An electric motor harmonically excites the pendulum via a string-spring device, which provides torsional stiffness to the system.

The mathematical model for the pendulum dynamics describes the time evolution of the angular position, ϕ , assuming that ω is the forcing frequency, I is the total inertia of rotating parts, k is the spring stiffness, ζ represents the viscous damping coefficient and μ the dry friction coefficient, m is the lumped mass, a defines the position of the guide of the string with respect to the motor, b is the length of the excitation arm of the motor, D is the diameter of the metallic disc and d is the diameter of the driving pulley. The equation of motion is given by (De Paula *et al.*, 2006):

$$\begin{Bmatrix} \dot{x}_1 \\ \dot{x}_2 \end{Bmatrix} = \begin{bmatrix} 0 & 1 \\ -\frac{kd^2}{2I} & -\frac{\zeta}{I} \end{bmatrix} \begin{Bmatrix} x_1 \\ x_2 \end{Bmatrix} + \begin{bmatrix} kd \\ 2I \end{bmatrix} (\Delta f(t) - \Delta l_1) - \frac{mgD \text{sen}(x_1)}{2I} - \frac{2\mu}{\pi I} \arctan(qx_2) \quad (19)$$

where $\Delta f(t) = \sqrt{a^2 + b^2 + \Delta l_2^2 - 2ab \cos(\omega t) - 2b\Delta l_2 \sin(\omega t)} - (a - b)$ and Δl_1 and Δl_2 correspond to actuations.

Numerical simulations of the pendulum dynamics are in close agreement with experimental data by assuming parameters used in De Paula *et al.* (2006): $a = 1.6 \times 10^{-1}$ m; $b = 6.0 \times 10^{-2}$ m; $d = 4.8 \times 10^{-2}$ m; $D = 9.5 \times 10^{-2}$ m; $m = 1.47 \times 10^{-2}$ kg; $I = 1.738 \times 10^{-4}$ kg m²; $k = 2.47$ N/m; $\zeta = 2.368 \times 10^{-5}$ kg m²s⁻¹; $\mu = 1.272 \times 10^{-4}$ N m; $\omega = 5.61$ rad/s.

Position and velocity time series are obtained from numerical integration of the mathematical model with $\omega = 5.61$ rad/s, a frequency related to chaotic behavior. UPOs embedded in chaotic attractor are identified by using the close return method (Auerbach *et al.*, 1987). This identification consists in the first step of the learning stage being common to all control methods.

The comparative analysis deals with four different controllers: semi-continuous (SC), semi-continuous multiparameter (SC-MP) coupled and uncoupled approaches, and extended time-delayed feedback (ETDF). The strategy of analysis considers a control rule that is followed by each controller. Noise influence is also of concern by treating noisy signals

Let us start discussing some aspects of the learning stage. Concerning discrete techniques, besides the UPO identification, it is necessary to evaluate the local dynamics expressed by the Jacobian matrix and the sensitivity vector of the transition maps in a neighborhood of the fixed points. The least-square fit method (Auerbach *et al.*, 1987; Otani & Jones, 1997) is employed to estimate Jacobian matrix. After that, the SVD technique is employed for determining stable and unstable directions near the next fixed point. The sensitivity vectors are evaluated allowing the trajectories to come close to a fixed point and then perturbing the parameters by the maximum permissible value. Multiparameter methods need to define the sensitivity matrix where each column is evaluated by the same way of the sensitivity vector of the single-parameter method. The MP has the coupled and uncoupled approaches, and the coupled approach needs to define proper values for parameters β_a and β_p . The brute-force approach is an alternative to establish values for these parameters by increasing controller efficacy as described in De Paula & Savi (2009a). This approach considers $\beta_a = 2.5$ and $\beta_p = 1.5$. On the other hand, the uncoupled approach avoids this kind of evaluation since $\beta_a = 1$ and $\beta_p = 0$. Concerning the continuous methods, the learning stage involves the determination of control parameters, R and K , which is done by evaluating the largest Lyapunov exponent of the desired UPO. The idea is to find controller parameters that are related to negative values of the maximum Lyapunov exponent, which means that the UPO becomes stable (De Paula & Savi, 2009b).

After the learning stage, the stabilization stage is initiated. Discrete methods need to wait the system to visit the neighborhood of the control orbit, when the control procedure is turned on. Single-parameter methods are employed by considering the isolated perturbation performed by the parameters ΔI_1 or ΔI_2 . Multiparameter methods assume that the first control parameter actuates in odd stations while the second actuates in even stations. Continuous methods, on the other hand, uses the first control parameter, ΔI_1 , to promote perturbations in the system. Under this assumption, K is a scalar.

Control Methods Performance

Comparative analysis evaluates the performance of the SC, the SC-MP, coupled and uncoupled approaches, and the ETDF comparing the efficacy of each one to stabilize UPOs. With this aim, a control rule is defined for the stabilization of four different UPO in the following sequence: a period-5 orbit during the first 500 periods, a period-3 from period 500 to 1000, a period-8 from 1000 to 1500 and, finally a period-1, from period 1500 to 2000. Figure 2 presents these four UPOs in one of the control sections considered by the semi-continuous methods, while Figure 3 shows the UPOs in phase space.

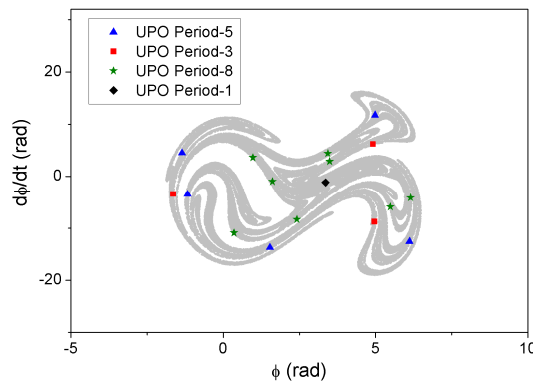


Figure 2 - UPOs of the control rule at control station #1.

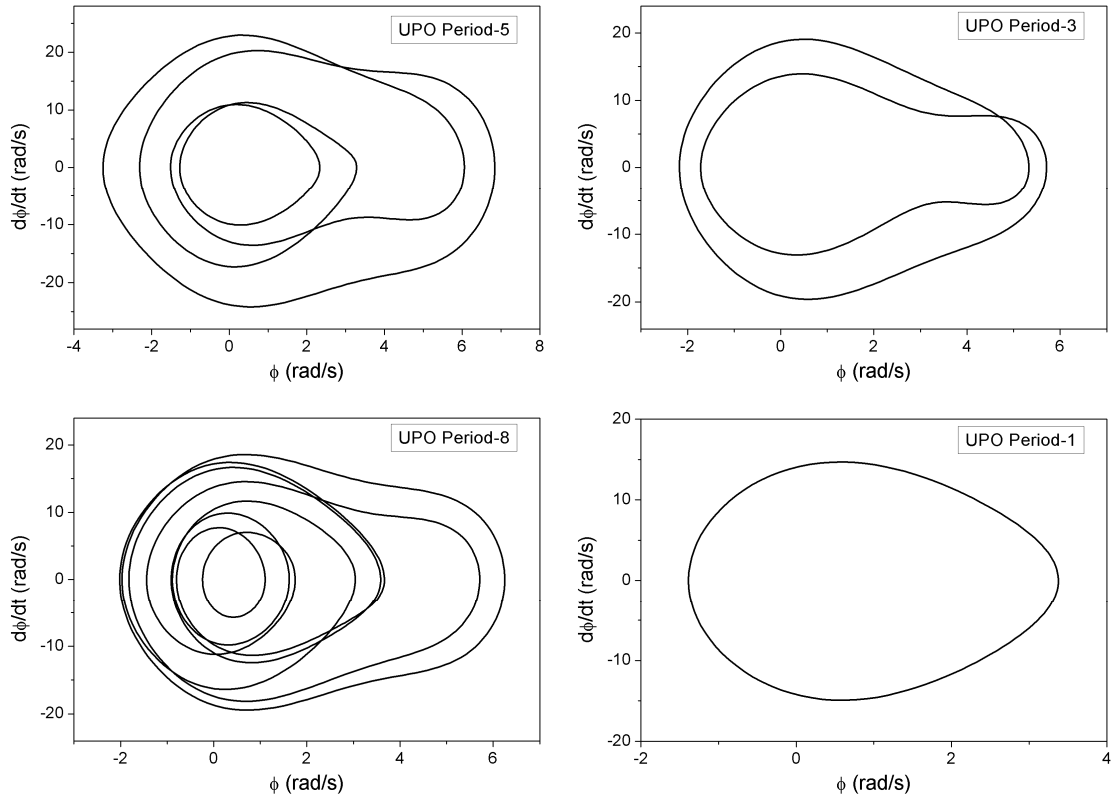


Figure 3 - UPOs of the control rule.

By employing SC method considering the isolated perturbation of each parameters Δl_1 and Δl_2 with 4 control station per forcing period, the controller is not capable to follow all control rule and only three of the four UPOs are stabilized, as showed in Figure 4. Moreover, before the stabilization of UPO is achieved it can be observed a region related to chaotic behavior that corresponds to the wait time that system dynamics takes to reach the neighborhood of desired control point.

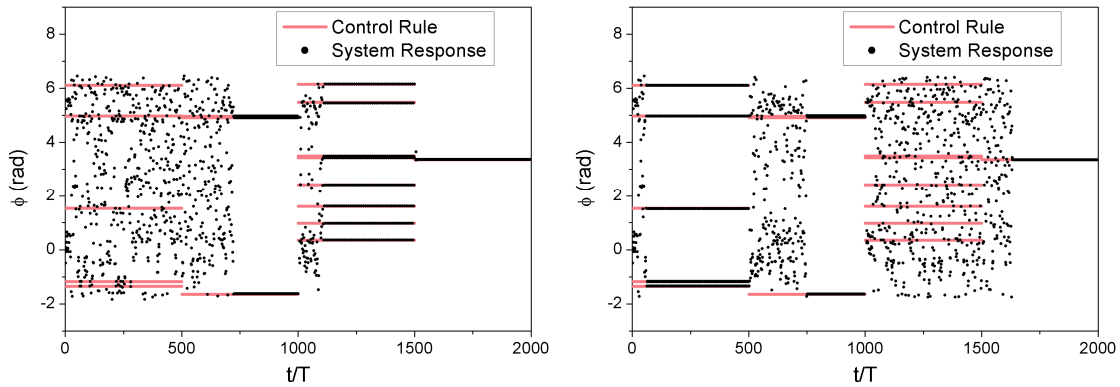


Figure 4 – System controlled at the control station #1 using SC with parameter: (a) Δl_1 ; (a) Δl_2 .

Now, by employing SC-MP method, coupled and uncoupled approaches, all orbits of the control rule are successful stabilized. Figure 5 shows the desired trajectories, imposed by the control rule, and the system time evolution at control stations #1.

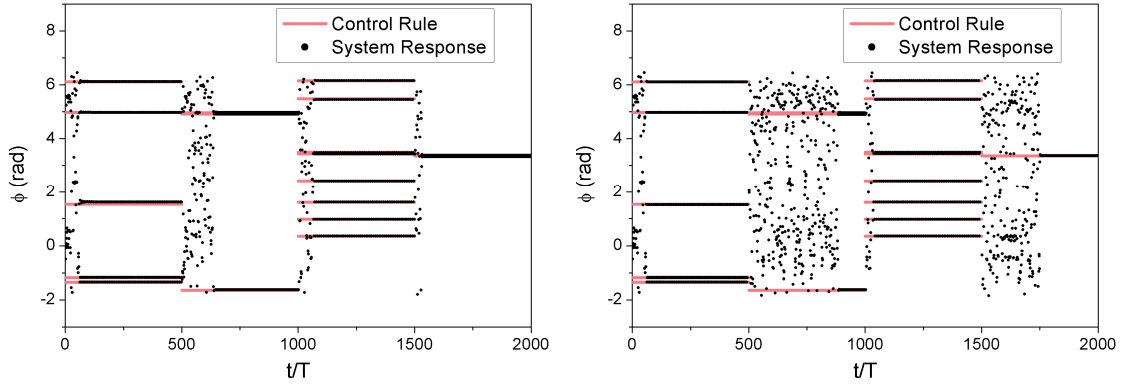


Figure 5 - System controlled at the control station #1 using SC-MP: (a) Coupled; (b) Uncoupled.

Finally, the ETDF is now employed to follow the control rule considering the use of parameter Δl_1 . The stabilization results are presented in control stations in order to establish a comparison with results obtained from the semi-continuous methods. From Figure 6 it can be noted that the ETDF is not able to stabilize the first and the third orbits of the control rule. Besides, the second orbit is different from the stabilized orbit. The stabilization of a different UPO can be explained by analyzing the values of the maximum Lyapunov exponent. Although the period-3 UPO of the control rule presents a region with negative Lyapunov exponent for some values of the control parameters, this region is small and with greater values when compared to the correspondent situation of the stabilized orbit. Concerning the first and the third UPOs of the control rule, there are no values of the control parameters that lead to negative Lyapunov exponent. Therefore, it is not possible to stabilize these orbits by employing the ETDF.

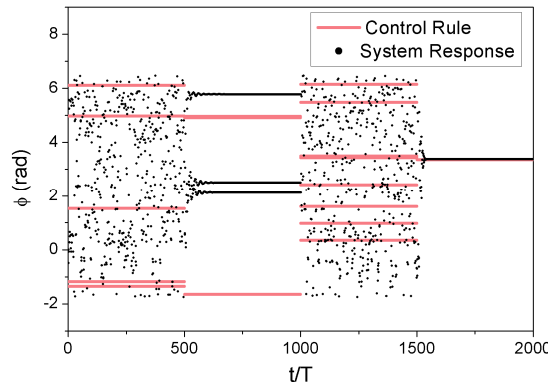


Figure 6 - System displacement controlled using ETDF at the control station #1.

Chaos Control Performance Considering Noisy Signals

Since noise contamination is unavoidable in experimental data acquisition, it is important to evaluate its effect on chaos control procedures. This section evaluates noise sensitivity of the chaos control techniques previously considered in the comparative analysis: SC, SC-MP, coupled and uncoupled approaches, and ETDF. In order to simulate noisy data sets, a white Gaussian noise is introduced in the signal, comparing results of control procedures with an ideal time series, free of noise. In general, noise can be expressed as follows,

$$\begin{cases} \dot{x} = Q(x,t) + \mu_d \\ \dot{y} = P(x,t) + \mu_o \end{cases} \quad (20)$$

where x represents state variables, y represents the observed response and $Q(x,t)$ and $P(x,t)$ are nonlinear functions. μ_d and μ_o are, respectively, dynamical and observed noises. Notice that μ_d has influence on system dynamics in contrast with μ_o . In this work, it is considered only an observed noise, simulating noise in experimental data due to instrumentation apparatus and, therefore, noise does not have influence in system dynamics.

The noise level can be expressed by the standard deviation, σ , of the system probability Gaussian distribution, that is parameterized by the standard deviation of the clean signal, σ_{signal} , as follows:

$$\eta(\%) = \frac{\sigma}{\sigma_{signal}} \times 100 \quad (21)$$

A different control rule is assumed in order to compare the control methods performance considering noisy signals. This control rule is defined in order to choose orbits that can be stabilized by all control methods for an ideal signal: a period-6 orbit during the first 500 periods, a period-2 from period 500 to 1000, a period-3 from 1000 to 1500 and, finally a period-1, from period 1500 to 2000.

A noisy signal with 1% of amplitude is now in focus. Figure 7 shows the desired trajectory, imposed by the control rule, and the system time evolution at control station #1 when the SC is employed considering the isolated actuation performed by the parameters Δl_1 and Δl_2 . Figure 8 presents the same pictures for the SC-MP, coupled and uncoupled approaches, while Figure 9 presents results for the ETDF. Note that for $\eta=1\%$, the SC with first control parameter stabilizes all UPOs of the control rule, however, sometimes system trajectory escapes from the desired orbit, returning back later. By using the second control parameter, only two of the orbits are successfully stabilized. By using the SC-MP coupled approach, the second orbit of the control rule is not satisfactory stabilized. The uncoupled approach of the SC-MP and the ETDF successfully stabilizes all orbits.

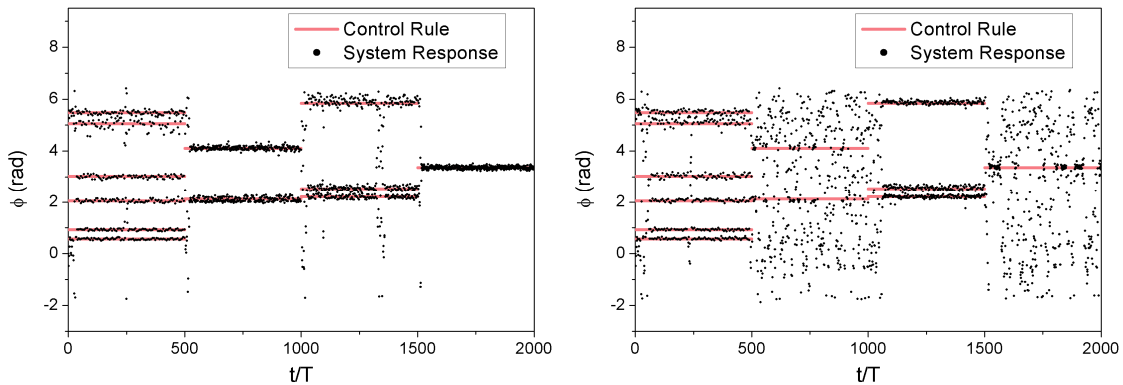


Figure 7 - System controlled using SC at the control station #1 with $\eta=1\%$: (a) Parameter Δl_1 ; (b) Parameter Δl_2 .

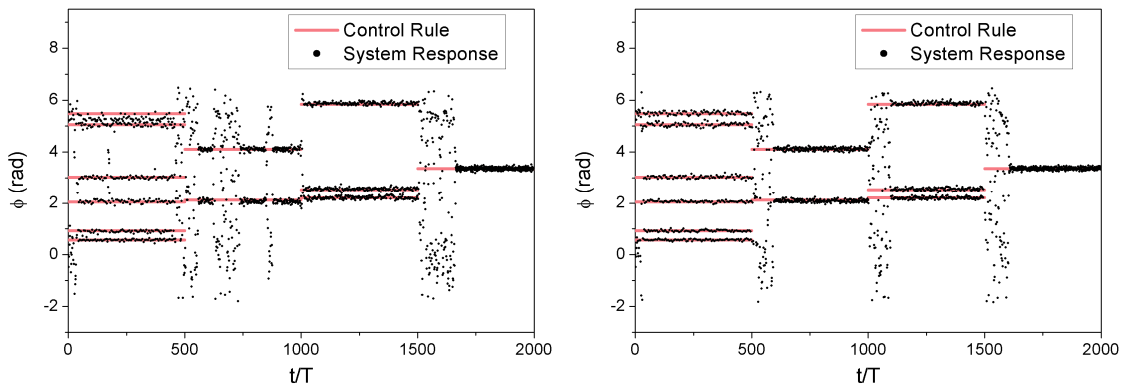


Figure 8 - System controlled using SC-MP at the control station #1 with $\eta=1\%$: (a) Coupled approach; (b) Uncoupled approach.

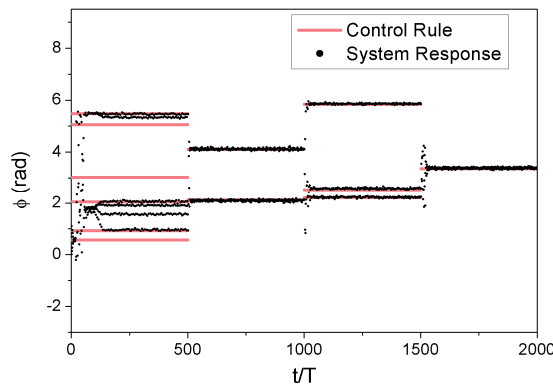


Figure 9 - System controlled using ETDF at the control station #1 with $\eta=1\%$.

A noise level of 2% is now considered. Figure 10 shows the desired trajectory imposed by the control rule and the system time evolution at control station #1 with noise level of 2% by employing SC-MP uncoupled approach and ETDF methods, which are the methods whose present the better performance for this noise level. It is important to mention that ETDF successfully stabilize all UPOs of the control rule, except for the fact that the period-6 stabilized orbit is different from the desired one.

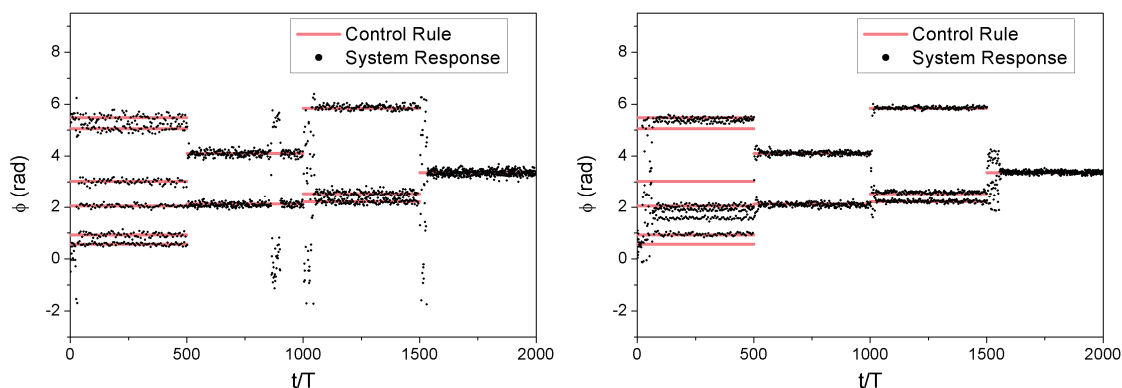


Figure 10 - System controlled at the control station #1 with $\eta=2\%$: (a) SC-MP Uncoupled; (b) ETDF.

CONCLUSIONS

This paper presents a comparative analysis of chaos control methods performances. Results point that the semi-continuous methods present good performance for ideal time series, free of noise. In this regard, it should be highlighted the good performance of the multiparameter approach. When noisy time series is of concern, continuous methods present greater robustness being associated with better performances, however, the uncoupled approach of the semi-continuous multiparameter method also presents a good performance.

ACKNOWLEDGMENTS

The authors would like to acknowledge the support of the Brazilian Research Agencies CNPq and FAPERJ and through the INCT-EIE (National Institute of Science and Technology - Smart Structures in Engineering) the CNPq and FAPEMIG. The Air Force Office of Scientific Research (AFOSR) is also acknowledged

REFERENCES

- Auerbach, D., Cvitanovic, P., Eckmann, J. -P., Gunaratne, G. & Procaccia, I., 1987, "Exploring chaotic motion through periodic orbits", *Physical Review Letters*, v.58, n.23, pp.2387-2389.
- De Paula, A. S., Savi, M. A. & Pereira-Pinto, F. H. I., 2006, "Chaos and transient chaos in an experimental nonlinear pendulum", *Journal of Sound and Vibration*, v.294, n.3, p.585-595.
- De Paula, A. S. & Savi, M. A., 2008, "A multiparameter chaos control method applied to maps", *Brazilian Journal of Physics*, v.38, n.4, pp.537-543.
- De Paula, A. S. & Savi, M. A., 2009, "A multiparameter chaos control method based on OGY approach", *Chaos, Solitons and Fractals*, v.40, n.3, pp.1376-1390.
- Hübinger, B., Doerner, R., Martienssen, W., Herdering, M., Pitka, R. & Dressler, U., 1994, "Controlling chaos experimentally in systems exhibiting large effective Lyapunov exponents", *Physical Review E*, v. 50, n. 2, pp.932-948.
- Ott, E., Grebogi, C. & Yorke, J. A., 1990, "Controlling chaos", *Physical Review Letters*, v. 64, n. 11, pp. 1196-1199.
- Pyragas, K., 1992, "Continuous control of chaos by self-controlling feedback", *Physics Letters A*, v. 170, pp. 421-428.
- Pyragas, K., 2006, "Delayed feedback control of chaos", *Philosophical Transactions of the Royal Society A*, v.364, pp.2309-2334.
- Socolar, J. E. S., Sukow, D. W. & Gauthier, D. J., 1994, "Stabilizing unstable periodic orbits in fast dynamical systems", *Physical Review E*, v.50, n.4, pp.3245-3248.

RESPONSIBILITY NOTICE

The authors are the only responsible for the printed material included in this paper.

Analysis and nonlinear modeling of a dual-mass tuned vibration absorber working in electrorheological fluid

Nicklas Norrick¹, Richard Markert¹ and Rodrigo Nicoletti²

¹ Institute of Structural Dynamics, Department of Mechanical Engineering, Technische Universität Darmstadt, Petersenstr. 30, 64287 Darmstadt, Germany, norrick@sdv.tu-darmstadt.de

² EESC Laboratory of Dynamics, São Carlos School of Engineering – USP, Av. Trabalhador São-carlense 400, São Carlos, SP, 13566-590, Brazil

Abstract: In this paper, the prototype of a dual-mass tuned vibration absorber developed together with an automotive supplier is analyzed experimentally and modeled analytically-numerically. The prototype has two independent high-voltage channels, where voltages of up to 6 kV can be applied to influence the electrorheological fluid in the system. Two test rigs are described which are used to measure the system response due to excitation of the housing. The experiments show that it is possible to continuously change the tuning frequency of a dual-mass tuned vibration absorber working in ERF. When changing the tuning frequency, the total system damping remains relatively stable. To model the dynamic effects, a mathematical model is developed and expanded in several steps, which is able to predict the dynamic system behavior for a wide range of operating states. Depending on the applied high voltages, linear or nonlinear system behavior is to be accounted for. The HILBERT-Transform of the frequency response function makes it possible to identify the type of nonlinearity. Consequently, a simple phenomenological model can be implemented, making a first nonlinear description of the system possible. By using actual measurements of the fluid properties, a more realistic description of the nonlinear damping of the ERF is plugged into the model, producing very good results. The different modeling approaches are compared and conclusions are drawn.

Keywords: Tuned vibration absorber, Vibration analysis, Nonlinear damping, Electrorheological fluid

NOMENCLATURE

a = cylinder radius, m	m = mass, kg	ω = natural frequency, 1/s
b = casing radius, m	M = mass matrix, kg	Ω = driving frequency, 1/s
b = damping coefficient, Ns/m	q = degree of freedom, m	
d = depth, m	t = time, s	
D = modal damping	u = excitation/casing motion, m	Subscripts
E = electric field, V/m		a = added mass
f = natural frequency, Hz	Greek Symbols	b = displaced fluid mass
F = force, N	γ = shear angle	F = fluid
H = transfer function	μ = dynamic viscosity, Ns/m ²	k = critical displacement
\mathcal{H} = HILBERT-transform	ρ = density, kg/m ³	max = maximum value
k = stiffness, N/m	τ = shear stress, N/m ²	r = relative coordinate
K = stiffness matrix, N/m	ψ = phase angle	y = yield

INTRODUCTION

Electrorheological fluids (ERF) make it possible to influence the natural frequencies and damping of a dual-mass tuned vibration absorber (TVA) immersed in ERF, so that this system can be used as an adaptively tuned vibration absorber or damper. More specifically, it is possible to use the change in apparent viscosity of the ERF in response to an electric field to selectively alter system parameters quickly and reversibly. It is well-known that the classical TVA can only attenuate vibration at its tuning frequency (Den Hartog, 1956). An adaptive system using ERF has the aim of vibration attenuation over a broad frequency band, which is of interest when the excitation frequencies vary during operation. A wide application area where this is the case is in motor vehicles. Typical uses are in the power train, the exhaust system and directly on the body (especially in convertibles). Due to the ever increasing demand for ergonomics and comfort in motor vehicles it is becoming increasingly attractive to use vibration attenuation systems such as TVAs in the vehicle interior, for control elements, instrument panels and screens for navigation or playing movies.

A considerable amount of publications have described the use of adjustable dampers using ERF to control system vibrations, starting as early as 1978 with Bullough and Foxon. Magnetorheological fluids (MRF), which exhibit very

similar dynamic properties, have also been studied extensively, for example in more recent work by Sims et al. (2004). In contrast, very little experimental and theoretical work has been done on tunable vibration absorbers utilizing the same effects. Janocha and Jendritza (1994) proposed a prototype TVA with adjustable damping using ERF. Both Truong and Semercigil (2001) and Sakamoto et al. (2001) carried out experiments with a sloshing-type TVA filled with ERF. Truong and Semercigil observed only a change in the TVA damping, while Sakamoto et al. showed the possibility of changing the apparent TVA mass and thereby its tuning frequency. Koo (2003) showed theoretically and experimentally that MRF dampers can be used to design a semi-active TVA with significant advantages over classical TVAs. Holdhusen (2005) used magnetorheological elastomers (MRE) to design a semi-active TVA with tunable stiffness, which also showed promising results. A number of papers have addressed the possibility of changing a sandwich beam's stiffness with ERF or MRF, for example by Choi (1991), Leng et. al (1995) and Lu and Meng (2005), but only recently (Hirunyapruk 2009) has this effect then been comprehensively studied and used for TVAs.

In this paper, a novel type of semi-actively tunable vibration absorber is considered. A prototype of a dual-mass tuned vibration absorber developed by an automotive supplier is analyzed experimentally and an analytical-numerical model is developed step-by-step to describe the system's behavior. These results can be used to further understand the behavior of tuned vibration absorbers working in ERF, thereby aiding their development for future applications.

OBJECT OF INTEREST AND MEASUREMENT SETUP

The prototype TVA consists of a closed casing, in which two bodies are suspended via helical springs. The coupling mass m_1 has about 10% of the main mass m_2 . In the narrow gaps between the coupling mass and the casing a high voltage U_1 , and in the gaps between coupling mass and main mass another high voltage U_2 , both up to 6 kV, can be applied. The casing is filled with ERF under a slight overpressure to prevent the formation of air bubbles. Figure 1 shows a schematic diagram of the prototype.

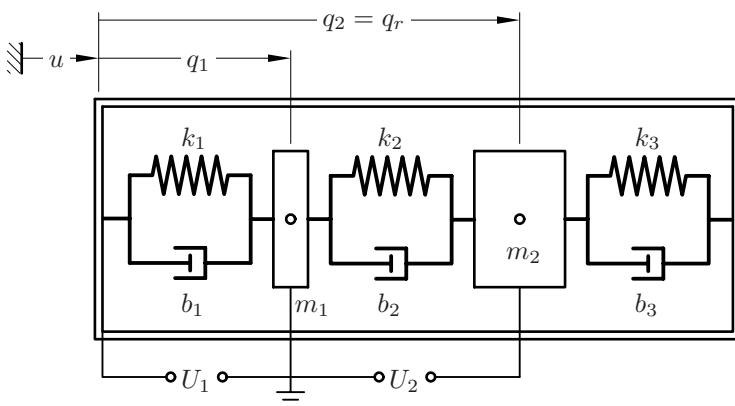


Figure 1: Sketch of the model of the dual-mass TVA

The prototype was tested on two different test rigs. The first test system consists of an electric motor-driven vibration testing table. A diagram of the test rig is shown in Fig. 2. A real-time control system is used for data acquisition and output of control signals for the high-voltage generators and the drive motor. The table path $u(t)$ and relative path $q_r(t)$ of the main absorber mass inside the housing (with its applied high voltages) are measured with eddy-current proximity probes. Additionally, a piezoelectric accelerometer on the table records the table acceleration $\ddot{u}(t)$. The actually applied high voltages U_1 and U_2 (up to 6 kV) are controlled and are logged throughout the experiments. All of the acquired signals are filtered via analog low-pass filters to eliminate aliasing errors.

The second test rig is a horizontal vibration testing table on air bearings driven by a modal exciter type 4801 from Brüel&Kjær. A diagram of this setup rig is shown in Fig. 3. The same signals are measured on this test rig with the additional advantage of measuring the excitation force F between the exciter and the vibration table.

MATHEMATICAL MODEL

Both bodies of the TVA are assumed to be rigid and are suspended only by helical springs, so that the complete system has 12 degrees of freedom. The mass matrix M is a diagonal matrix filled with the masses and principal moments of inertia of the main mass and the coupling mass. The products of inertia are all zero because the principal axes of the absorber bodies coincide with the directions of the degree of freedom used to describe the system. The stiffness matrix K has a banded structure because of the system's symmetry. The equations of motion for the undamped system can be

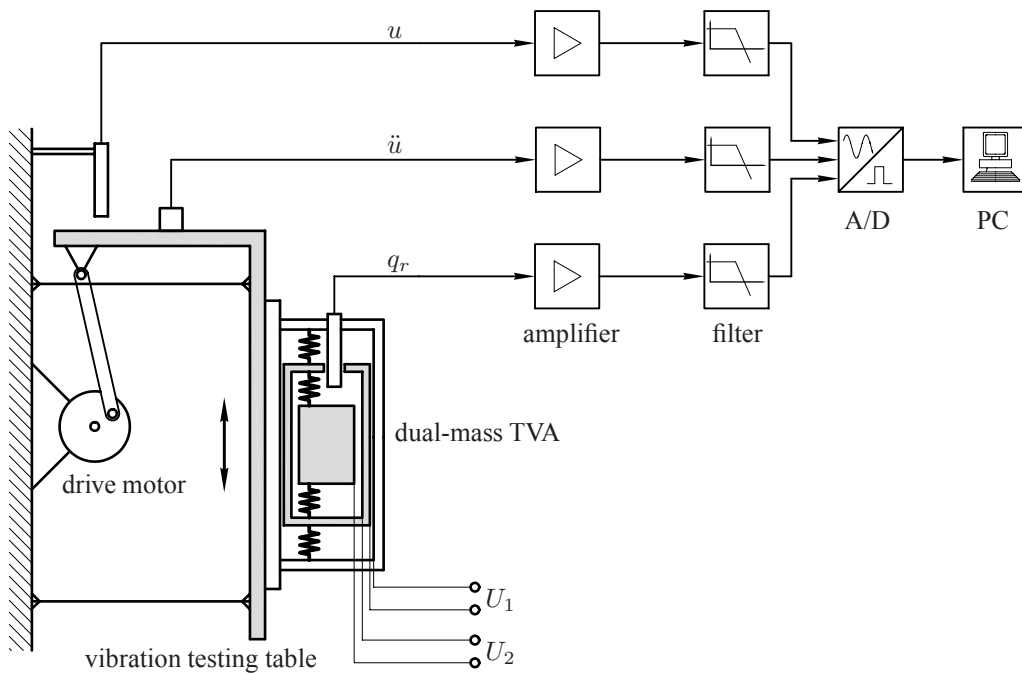


Figure 2: Vibration test rig with TVA and measuring equipment

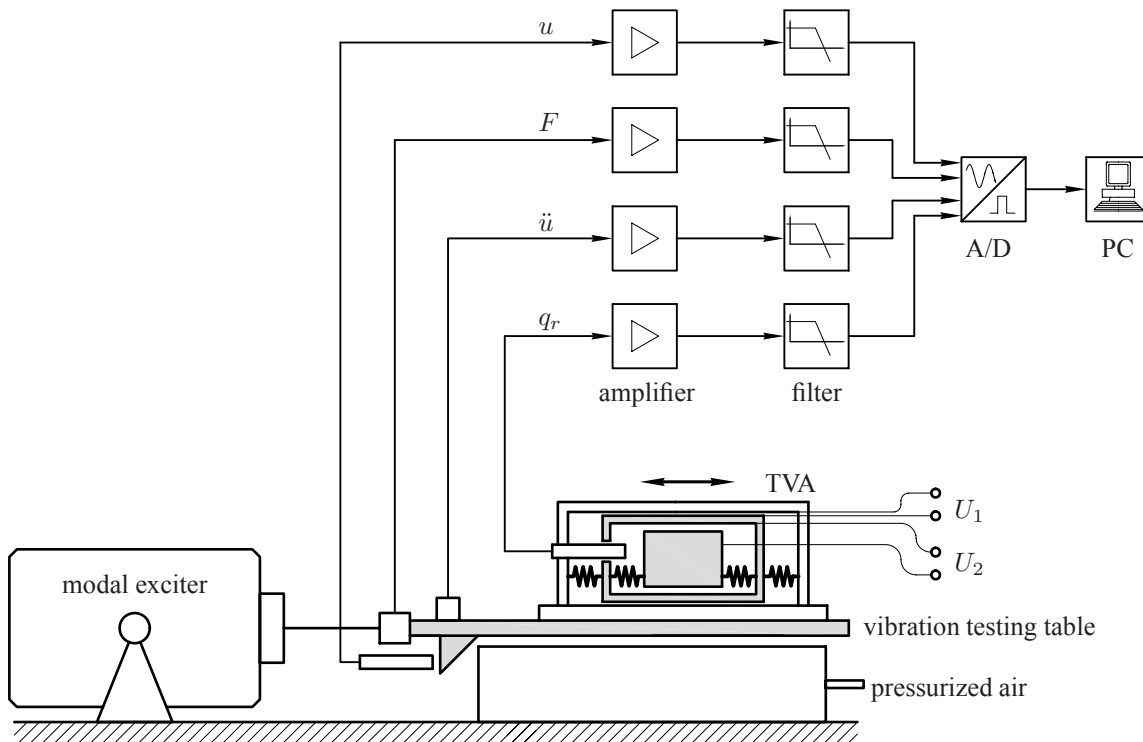


Figure 3: Vibration testing table on air bearings with TVA and measuring equipment

split into six independent two-degree-of-freedom systems because of the banded structure of the stiffness matrix. For this reason, only the two coupled transverse degrees of freedom q_1 and q_2 will be considered in the further analysis.

The masses and stiffnesses of the unfilled system were identified via static experiments. An experimental modal analysis (EMA) of the complete setup verified the results. When the tuned vibration absorber is empty, the calculated and measured natural frequencies match up very well. When the system is filled with ERF the natural frequencies drop, which is attributed to the added mass of the fluid in the system. This added mass is dependent on the outer contour of the immersed body, its speed, and the boundary conditions of the surrounding fluid volume. The added mass can be calculated exactly for certain simplified special cases. The results can be used to estimate the added mass of real systems.

An infinitely long cylinder of the radius a in a concentric cylindrical casing of the radius b was shown by Sinyavskii, Fedotovskii and Kukhtin (1980) to have the added mass per unit of depth d of

$$\frac{m_a}{d} = \rho\pi a^2 \left(\frac{b^2 + a^2}{b^2 - a^2} \right), \quad (1)$$

where ρ is the density of the surrounding fluid. For a system with moving cylindrical casing (see Fig. 4), the added mass becomes dependent on the relative motion q_r as well as the absolute motion of the casing u . This additional term corresponds to the buoyancy of the body in the accelerated reference frame caused by \ddot{u} .

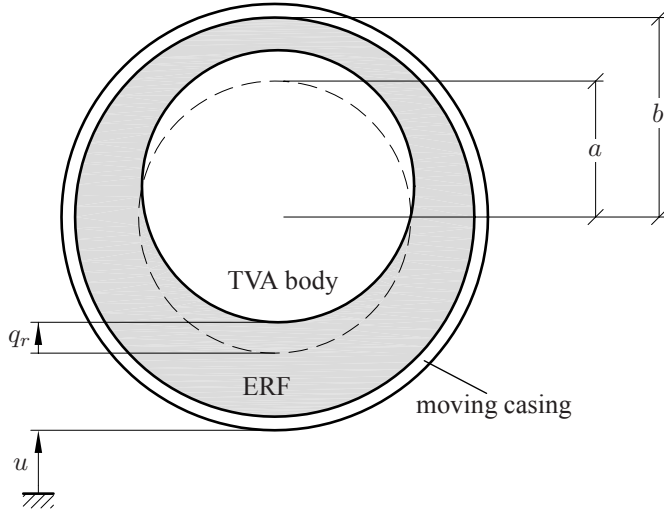


Figure 4: Sketch of the added mass configuration of a cylindrical TVA body immersed in ERF

The inertia per unit of depth is

$$\rho\pi a^2 \left(\frac{b^2 + a^2}{b^2 - a^2} \right) \ddot{q}_r - \rho\pi a^2 \ddot{u} = \frac{m_a}{d} \ddot{q}_r - \frac{m_b}{d} \ddot{u}, \quad (2)$$

where m_b/d is the mass per depth of the ERF displaced by the cylindrical tuned vibration absorber body. This approach is a good approximation for the cylindrical bodies used in the dual-mass TVA prototype and is used in the further analysis of the system.

In relative coordinates the linear equations of motion for the model fitting are

$$\begin{bmatrix} m_1 + m_{1a} & 0 \\ 0 & m_2 + m_{2a} \end{bmatrix} \begin{bmatrix} \ddot{q}_1 \\ \ddot{q}_2 \end{bmatrix} + \begin{bmatrix} b_1 + b_2 & -b_2 \\ -b_2 & b_2 + b_3 \end{bmatrix} \begin{bmatrix} \dot{q}_1 \\ \dot{q}_2 \end{bmatrix} + \begin{bmatrix} k_1 + k_2 & -k_2 \\ -k_2 & k_2 + k_3 \end{bmatrix} \begin{bmatrix} q_1 \\ q_2 \end{bmatrix} = - \begin{bmatrix} m_1 - m_{1b} \\ m_2 - m_{2b} \end{bmatrix} \ddot{u}. \quad (3)$$

At this stage, the equation has 10 free parameters: the added masses m_{1a} and m_{2a} , the buoyancy parameters m_{1b} and m_{2b} , the damping parameters b_1 , b_2 and b_3 as well as the stiffness parameters k_1 , k_2 and k_3 . Without any further knowledge of the system or the effects of the ERF, these parameters describe all possible linear influences of the fluid on the system.

LINEAR FITS

The linear fits in the frequency domain allow the extraction of the system parameters. The complex frequency response function H of the model between the excitation u and system response q_2 is fitted to the measured values via nonlinear multidimensional optimization in MATLAB. The extracted optimal values allow certain findings to be made: The stiffness parameters k_1 and k_2 coincide with the real measured values of the helical spring sets, while the stiffness parameter k_3 is set to 0 or at least very small in comparison by the optimization procedure. As a result, it is clear that the electrorheological fluid has negligible influence on the stiffness of the system, even when high voltages are applied. These results correspond with experimental results gained during the determination of material parameters for the same ERF at the Institute of Structural Dynamics at the TU Darmstadt by Pabst (2009) using algorithms developed by Dohnal (2006). To save calculation time during optimization runs, the resulting stiffnesses k_1 , k_2 and $k_3 = 0$ are eliminated from the set of free parameters in all further calculations.

Figure 5 shows the measured and fitted transfer functions corresponding to the four operating states: no voltage (a), $U_1 = 4$ kV on channel 1 (b), $U_2 = 4$ kV on channel 2 (c) and $U_1 = U_2 = 4$ kV on both channels (d). Because the relative vibration response H is very small up to about 10 Hz, the measured phase ψ is faulty in this region and suppressed in the following figures.

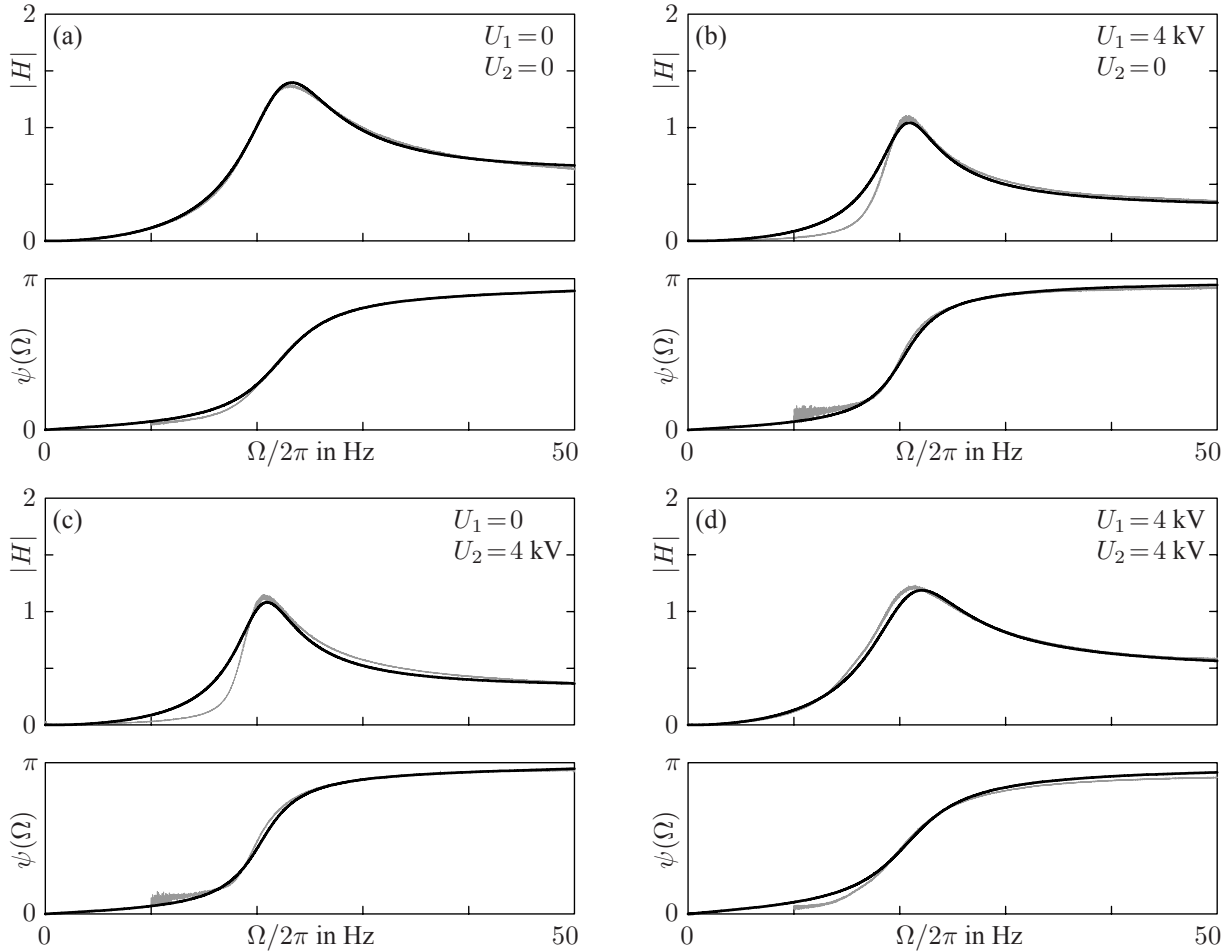


Figure 5: Frequency response functions (amplitude and phase) from measurements (grey) and linear model fits (black) for the operating states: no voltage (a), 4 kV on channel 1 (b), 4 kV on channel 2 (c) and 4 kV on both channels (d)

As long as the electrical voltages applied to both channels are similar, the system response remains linear or at least nearly linear, a fact proven by the very good coincidence of modeled and measured frequency response function (visible in the cases (a) and (d)). If the applied voltages are very different (cases (b) and (c)), the difference between the linear model and reality is insufficient. The following section will elaborate on the steps taken to fix this discrepancy.

From the identified first natural frequency f_1 depending on the applied voltages (Fig. 6), certain conclusions can be drawn: The plot is nearly symmetrical, which means that the voltage difference between the two channels is of importance. After a first drop in natural frequency, attributed to a change in added mass for small voltage differences between the two channels, the natural frequency increases with increasing voltage difference between the two channels. In this way, the first natural frequency f_1 of the system can be varied continuously between 18 and 26 Hz with the applied high voltages.

Figure 7 shows the corresponding modal damping D_1 identified by the model fitting, which also shows the symmetric traits of the system. After a first strong drop with increasing voltage difference, corresponding to the changed inertia of the system due to added mass, the damping rises gradually as the applied voltage difference increases. The single high value at the place where 6 kV are applied to channel 1 is treated as an outlier.

NONLINEAR FITS

As has been shown in the previous section, large voltage differences between the two channels make it impossible to obtain satisfactory linear model fitting results. For better results, the nonlinear system performance has to be accounted for. The HILBERT-Transform \mathcal{H} is employed in the manner of Worden and Tomlinson (2001) to identify the type of

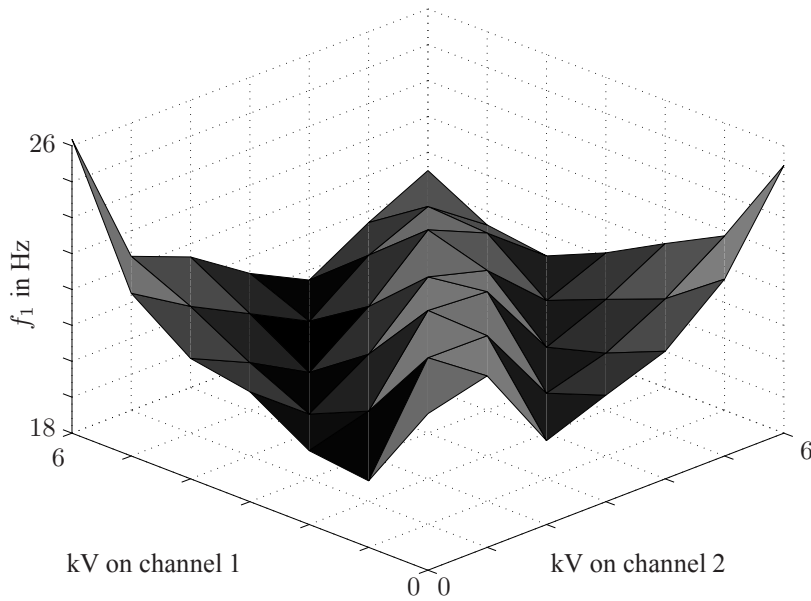


Figure 6: Identified first natural frequency f_1 as a function of the voltages applied to the ERF channels

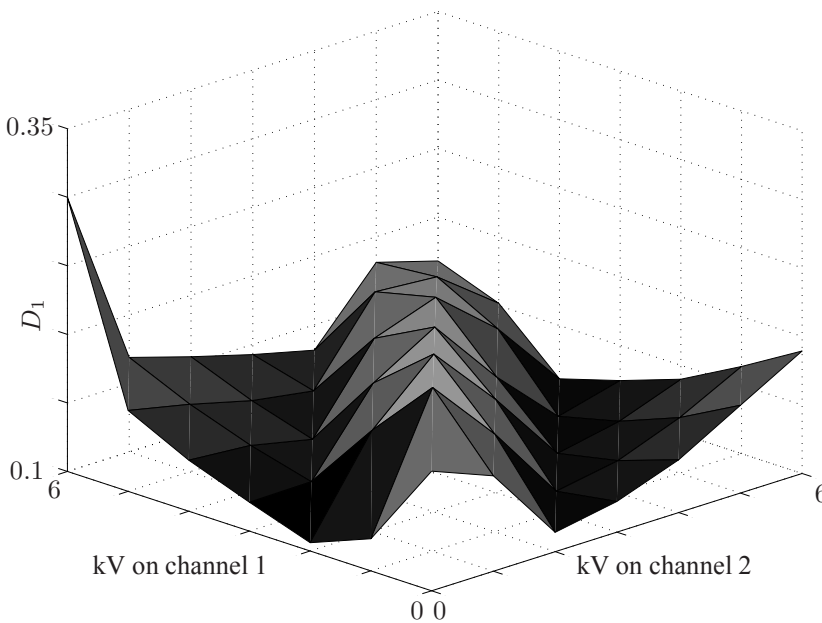


Figure 7: Identified modal damping D_1 as a function of the voltages applied to the ERF channels

nonlinearity in the system. It is well-known that the HILBERT-Transform has the ability to amplify the effects of nonlinear system behavior on the system's transfer function in such a way that characteristic deformations become visible in the NYQUIST-Plot (Fig. 8). These characteristic deformations are used to narrow down the number of possible nonlinear behaviors to be investigated.

The analysis showed that the real system behavior is similar to the behavior of a system with a softening spring characteristic with a single bend, shown in Fig. 9. This spring characteristic produced much better fitting results. It is possible to interpret this fact as follows: Up to a certain relative motion q_k of the system, one of the two serially mounted spring sets is blocked by the ERF. When this critical displacement is passed, the blockade by the ERF breaks down, and both spring sets become active, making the system softer. It is possible to say that the first modal degree of freedom has a softening spring characteristic.

The nonlinear model fitting was done with MATLAB/Simulink in the time domain. The optimum values of the linear fitting were used as starting values for the nonlinear optimization. Figure 10 shows exemplary plots of the results for the operating states $U_1 = 4$ kV on channel 1 (a) and $U_2 = 4$ kV on channel 2 (b). It is plain that the simple phenomenological model of the softening spring characteristic generates much better fits than the linear model. When interpreting the

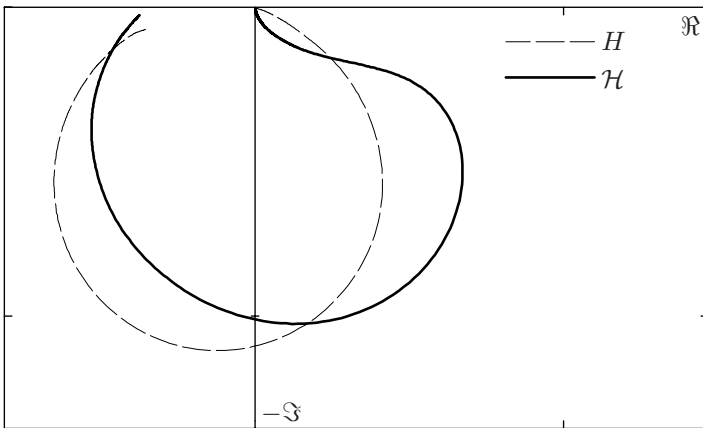


Figure 8: Measured frequency response function H and its HILBERT-transform \mathcal{H} for $U_2=4$ kV on channel 2 and $U_1=0$ kV on channel 1

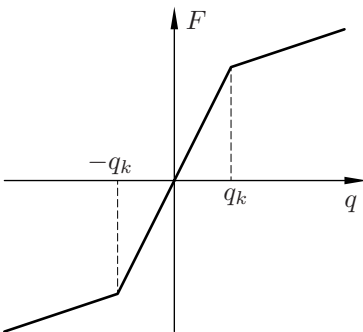


Figure 9: Softening spring characteristic diagram

phase information it also becomes clear that this model is not perfect. The actual mechanism behind the softening spring characteristic, the breakdown of the ERF blockade, is much more complex. For this reason, further steps have been taken to describe the nonlinear behavior of the system. A nonlinear BINGHAM -type damping model is employed to be able to realistically describe the effect of the ERF when subjected to high voltage.

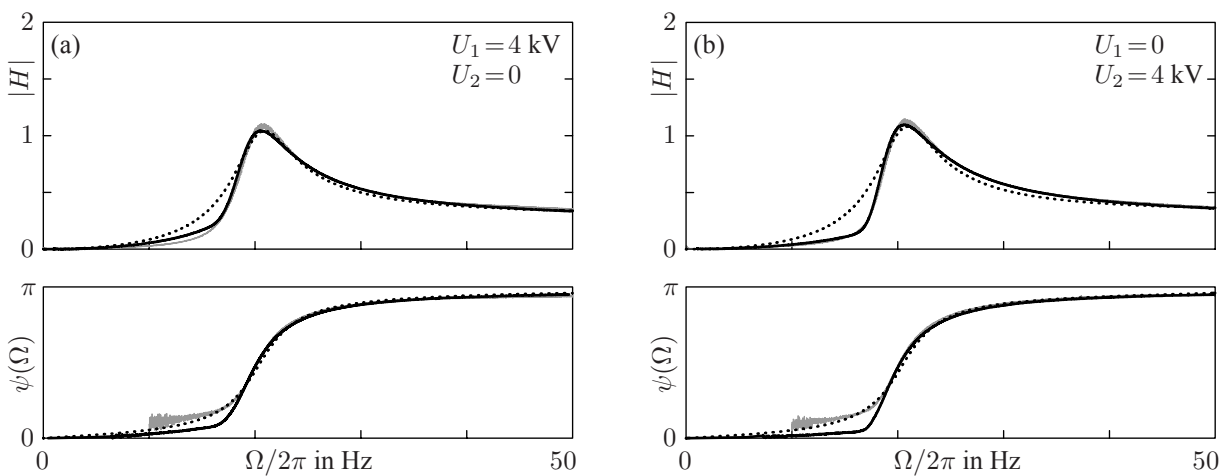


Figure 10: Frequency response functions (amplitude and phase) from measurements (grey), linear (dotted black) and nonlinear (softening spring characteristic) model fits (black) for the operating states 4 kV on channel 1 (a) and 4 kV on channel 2 (b)

Basis for this model are viscometer measurements of the real ERF obtained from the fluid manufacturer. The behavior of electrorheological fluids when high electrical fields are applied is often modeled using a BINGHAM-type model, as

stated by Coulter, Weiss and Carlson (1993), which a critical assessment of the measurements also suggest. The model parameters for the BINGHAM-type model are the electric field E and the shear rate $\dot{\gamma}$. The shear stress τ_F is calculated as the sum of the yield stress τ_y , which must be exceeded to make motion possible, and a viscous part,

$$\tau_F(E, \dot{\gamma}) = \tau_y(E) + \mu(E) \dot{\gamma}. \quad (4)$$

This model is more complex than the phenomenological model for the nonlinearity but still comparatively simple, making an implementation in MATLAB/Simulink unproblematic. To determine the values of $\tau_y(E)$ and $\mu(E)$, the viscometer measurements are used. The least-square method was used by Köhl (2010) to fit linear functions to the measurements for electrical field values from 1 to 6 kV/mm (Fig. 11 left).

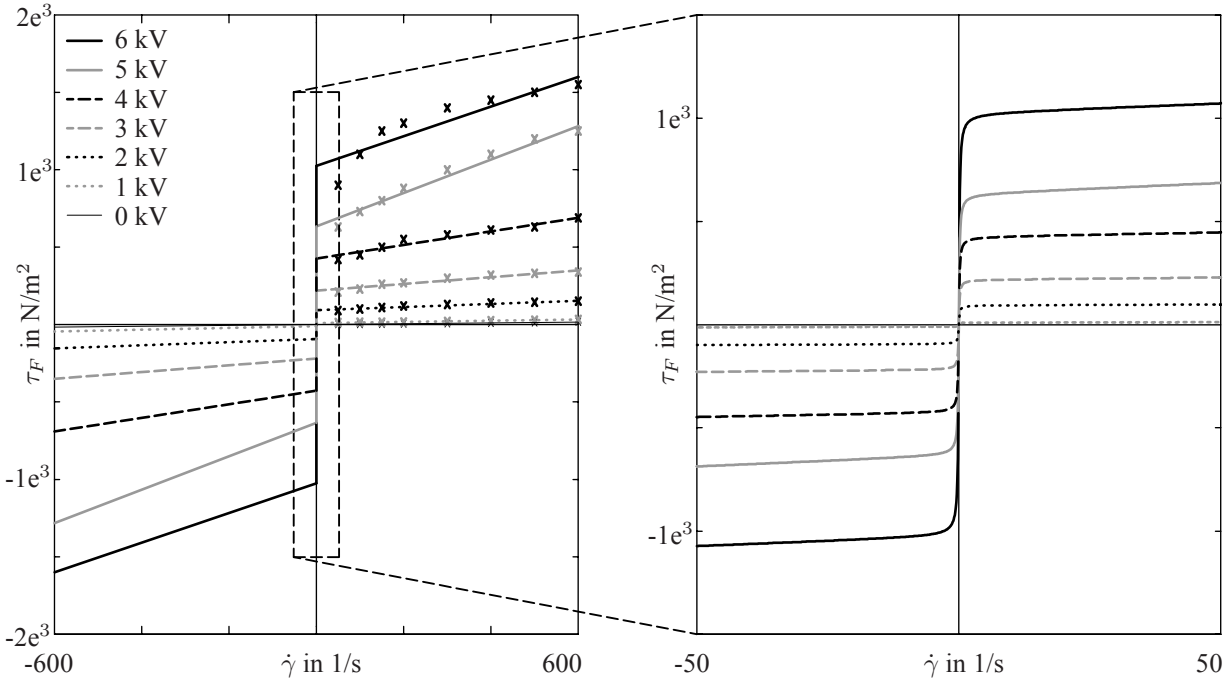


Figure 11: Shear stress due to shear rate with BINGHAM-type model and zooming in of the interesting area showing the effect of multiplication with the arctan-function (right)

For the numerical simulations it is prudent to have a continuous characteristic map, allowing the calculation of τ_F for any value of E and $\dot{\gamma}$, which is calculated with the polynomial ansatz

$$\begin{aligned} \tau_F(E, \dot{\gamma}) &= \sum_{i=0}^n \sum_{j=0}^1 a_{ij} E^i \dot{\gamma}^j \\ &= a_{00} + a_{01} \dot{\gamma} + a_{10} E + a_{11} E \dot{\gamma} + \dots + a_{n0} E^n + a_{n1} E^n \dot{\gamma}. \end{aligned} \quad (5)$$

The coefficients a_{ij} in equation (5) are in turn also identified from the linear functions in Fig. 11 using the least-square method. The shear rate is only accounted for as a linear term, while the electric field strength powers to the order seven are included. The coefficients for even higher powers are very small and can therefore be neglected.

To aid the numerical simulation across the jump from negative to positive shear rates, the arctan-function is used to force the shear stress to zero when the shear rate $\dot{\gamma}$ reaches zero. The chosen factor inside of the arctan-function is very large, resulting in a very steep rise in the shear stresses for very small shear rates,

$$\tau_F(E, \dot{\gamma}) = \frac{2}{\pi} \arctan\left(5000 \frac{\dot{\gamma}}{\dot{\gamma}_{max}}\right) (\tau_y(E) + \mu(E) \dot{\gamma}). \quad (6)$$

The shear rate can be calculated by dividing the relative speed in the ERF-filled gap by the gap height. Multiplication of the shear stress τ_F in the ERF with the surface area πa^2 affected by the electric field results in the damping force due to the ERF, which is incorporated into the nonlinear MATLAB/Simulink model as a nonlinear Embedded MATLAB function at the corresponding places. With this expansion of the model the equations of motion with the nonlinear damping force

become

$$\begin{aligned} \begin{bmatrix} m_1+m_{1a} & 0 \\ 0 & m_2+m_{2a} \end{bmatrix} \begin{bmatrix} \ddot{q}_1 \\ \ddot{q}_2 \end{bmatrix} + \begin{bmatrix} b_1(\dot{q}_1)+b_2(\dot{q}_2-\dot{q}_1) & -b_2(\dot{q}_2-\dot{q}_1) \\ -b_2(\dot{q}_2-\dot{q}_1) & b_2(\dot{q}_2-\dot{q}_1)+b_3 \end{bmatrix} \begin{bmatrix} \dot{q}_1 \\ \dot{q}_2 \end{bmatrix} + \\ + \begin{bmatrix} k_1+k_2 & -k_2 \\ -k_2 & k_2 \end{bmatrix} \begin{bmatrix} q_1 \\ q_2 \end{bmatrix} = - \begin{bmatrix} m_1-m_{1b} \\ m_2-m_{2b} \end{bmatrix} \ddot{u}. \end{aligned} \quad (7)$$

Figure 12 shows the obtained results with the nonlinear damping model described by equation 7. Note that the fits are even better than the fits with the previously shown models. This is especially evident in the phase angle $\psi(\Omega)$ of the frequency response functions between 10 and 20 Hz. The calculated phase angle is not smooth but follows the measured phase angle much more closely than the simple nonlinear model.

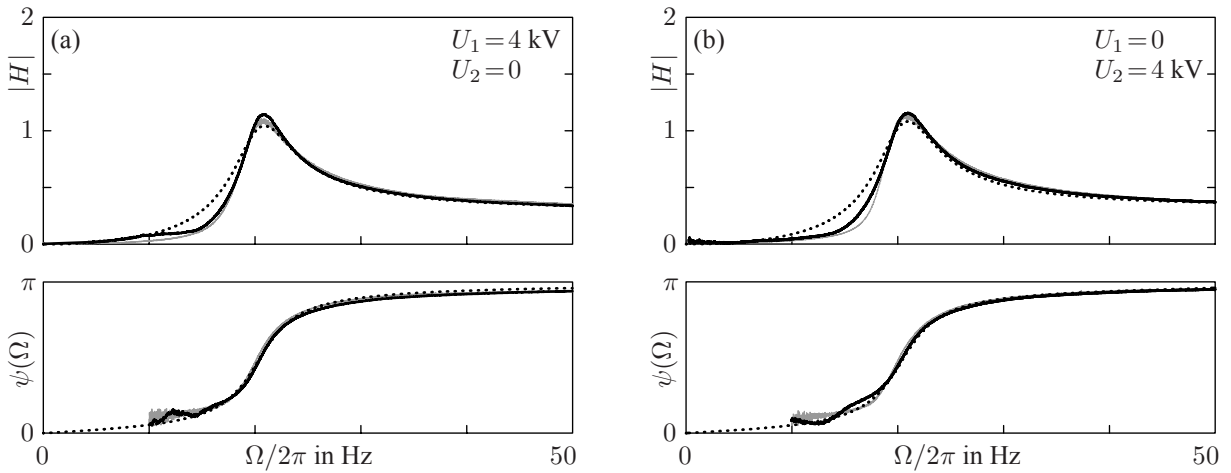


Figure 12: Frequency response functions (amplitude and phase) from measurements (grey), linear (dotted black) and BINGHAM-model fits (black) for the operating states 4 kV on channel 1 (a) and 4 kV on channel 2 (b)

It is important to remark that this model produces better results while consuming considerably more calculation time (factor of 10) than the simple phenomenological model. This fact should be considered when debating the use of this model for standard engineering applications.

CONCLUSION

The experiments showed the possibility to continuously change the tuning frequency of a dual-mass tuned vibration absorber working in ERF. When changing the tuning frequency, the total system damping remains relatively stable at a relatively high level. To model these effects, a mathematical model was developed and expanded in several steps, which is able to predict the dynamic system behavior for a wide range of operating states. Depending on the applied high voltages, linear or nonlinear system behavior is to be accounted for. The HILBERT-Transform of the frequency response function was used to identify the type of nonlinearity, so that a simple phenomenological model could be implemented, making a simple nonlinear description of the system possible. By using actual measurements of the fluid properties, a more realistic but also more complicated description of the nonlinear damping of the ERF was plugged in to the model, making it possible to obtain very good results.

ACKNOWLEDGEMENTS

The authors gratefully thank the German and Brazilian research funding agencies DAAD and CAPES for their support of this work within the PROBRAL programme.

REFERENCES

- Bullough, W. A. and Foxon, M. B., 1978: "A proportionate coulomb and viscously damped isolation system", *Journal of Sound and Vibration*, Vol. 56, pp. 35-44.
- Choi, Y. D. (2001): "Mechanical properties of a composite beam containing an electrorheological fluid", PhD Thesis, North Carolina State University.

- Coulter, J.P., Weiss, K.D. and Carlson, J.D., 1993: "Engineering Applications of Electrorheological Materials", *Journal of Intelligent Material Systems and Structures*, Vol. 4.
- Den Hartog, J.P.D., 1956: "Mechanical Vibrations", McGraw-Hill.
- Dohnal, F., 2006: "Vibration suppression of high-rise buildings by magnetorestrictive damper", technical report, College of Science and Technology, Nihon University.
- Hirunyapruk, C., Mace, B. and Brennan, M., 2008: "Vibration Control using an Adaptive Tuned Magneto-Rheological Fluid Vibration Absorber", *Proceedings of ISMA2008*, pp. 225-240.
- Holdhusen, M.H., 2005: "The State-Switched Absorber Used for Vibration Control of Continuous Systems", PhD Thesis, Georgia Institute of Technology.
- Janocha, H. and Jendritza, D.J., 1994: "Einsatzpotential von Elektrorheologischen Flüssigkeiten" (Potential uses for Electrorheological Fluids), *Konstruktion*, Vol. 46, pp. 111-115.
- Köhl, W., 2010: "Entwurf und Test verschiedener Regelungskonzepte für Dämpfer mit elektrorheologischen Flüssigkeiten" (Development and test of different control concepts for dampers with electrorheological fluids), Diploma Thesis TU Darmstadt.
- Koo, J.-H., 2003: "Using Magneto-Rheological Dampers in Semiactive Tuned Vibration Absorbers to Control Structural Vibrations", PhD Thesis, Virginia Polytechnic Institute and State University.
- Leng, J.S., Liu, Y.J., Du, S.Y., Wang, L. and Wang, D.F., 1995: "Active vibration control of smart composites featuring electro-rheological fluids", *Applied Composite Materials*, Vol. 2, pp. 59-65.
- Lu, H. and Meng, G., 2005: "An analytical investigation of a sandwich beam embedded with magnetorheological suspensions", *ERMR 2004 - Proceedings of the Ninth International Conference*, pp. 480-487.
- Pabst, C., 2009: "Experimentelle Identifizierung des dynamischen Verhaltens einer elektrorheologischen Flüssigkeit" (Experimental identification of the dynamic properties of an electrorheological fluid), Bachelor Thesis TU Darmstadt.
- Sakamoto, D., Oshima, N. and Fukuda, T., 2001: "Tuned sloshing damper using electro-rheological fluid", *Smart Materials and Structures*, Vol. 10, pp. 963-969.
- Sims, N.D., Holmes, N.J. and Stanway, R., 2004: "A unified modelling and model updating procedure for electrorheological and magnetorheological vibration dampers", *Smart Materials and Structures*, Vol. 13, pp. 100-121.
- Sinyavskii, V.F., Fedotovskii, V.S. and Kukhtin, A.B., 1980: "Oscillation of a Cylinder in a Viscous Liquid", *Prikladnaya Mekhanika*, Vol. 16, No. 1, pp. 68-75.
- Truong, T.D. and Semercigil, S.E., 2001: "A Variable Damping Tuned Absorber with Electro-Rheological Fluid for Transient Resonance of Light Structures", *Journal of Sound and Vibration*, Vol. 239, pp. 891-905.
- Worden, K. and Tomlinson, G.R., 2001: "Nonlinearity in Structural Dynamics", Institute of Physics Publishing.

RESPONSIBILITY NOTICE

The authors are the only responsible for the printed material included in this paper.

Experimental Identification of Journal Bearing Stiffness and Damping Coefficients in Non-stationary Run-up and Run-down Processes

Katrin Baumann¹, Patrick Felscher¹, Richard Markert¹, and Katia Lucchesi Cavalca²

¹ Institute of Structural Dynamics, Department of Mechanical Engineering, Technische Universität Darmstadt, Petersenstr. 30, 64287 Darmstadt, Germany. Contact: baumann@sdv.tu-darmstadt.de

² Faculdade de Engenharia Mecânica, Universidade Estadual de Campinas, Rua Mendeleev, 200, Barão Geraldo, Caixa Postal 6122, 13083-970 Campinas SP Brasil

Abstract: Within rotordynamics, the dynamic properties of journal bearings are usually taken into account by linearized stiffness and damping coefficients depending on the rotational speed. These coefficients are determined at constant rotor speeds either by experiments or calculations while neglecting all inertia forces of the fluid film flow.

In this paper, it is experimentally verified that rapidly changing rotational speeds respectively large rotational accelerations do not influence the stiffness and damping coefficients of a plain journal bearing significantly. This experimental result proves a previous theoretical investigation in which was concluded that the influence of rotational acceleration on the journal bearing dynamic properties is negligible. Therefore, the journal bearing stiffness and damping coefficients determined for constant rotor speeds may just as well be applied for non-stationary run-up and run-down processes.

Keywords: *Journal Bearings, Stiffness and Damping Properties, Non-Stationary Operation, Identification, Active Magnetic Bearings*

NOMENCLATURE

B = damping matrix, Ns/m
 b_{ij} = damping coefficient ij , Ns/m
 C = stiffness matrix, N/m
 c_{ij} = stiffness coefficient, N/m
 e = bearing eccentricity, m
 F = Kraft, N
 \mathcal{F} = Fourier transform
 i = imaginary unit, $i = \sqrt{-1}$
 $K(\bar{\Omega})$ = complex stiffness matrix, N/m
 M = mass matrix, kg
 m_{ij} = mass coefficient, kg
 N = number of measurements
 n = rotating speed, 1/min
 $R(\phi)$ = rotational matrix
 r = coordinate vector

r_G = radial coordinate
 S_{ij} = spectral density
 \mathcal{S}_{ij} = spectral density matrix
 So = Sommerfeld number
 T_{mess} = measurement duration, s
 u_G = tangential coordinate
 x = cartesian coordinate vector
 y = orthogonal coordinate of z
 z = radial coordinate

Greek Symbols

γ_0 = attitude angle, rad
 $\Delta \hat{x}$ = relative coordinate
 ε = relative bearing eccentricity
 φ = rotation angle

$\bar{\Omega}$ = excitation frequency, 1/s

Subscripts

\sim = dynamic value
 0 = stationary operation position
 G = journal bearing
 R = excitation

Other Symbols

$\dot{\hat{x}}$ = time derivative
 \hat{x} = amplitude
 \hat{x}^T = transposed matrix
 \hat{x}^* = conjugate-complex matrix

INTRODUCTION

Journal bearings strongly influence the dynamic behavior of rotor systems. Within rotordynamics, the properties of journal bearings are taken into account by linearized stiffness and damping coefficients depending on the rotational speed. These coefficients are usually determined at constant rotor speeds by either experiments or calculations; they are catalogued for several bearing types for example by Someya (1989). For the calculation of the fluid film flow and the journal bearing properties at constant rotor speeds, all inertia forces of the fluid film flow are neglected.

In the past, it has been proven that the influence of the fluid's inertia at steady-state operation on the dynamic characteristics of journal bearings is negligible. According to Lang (1978), and Pinkus (1987), the inertia forces of the fluid at constant rotor speeds are considerably smaller than the forces of viscosity as long as the modified Reynolds number of the fluid film flow in the bearing is smaller than 1. For example, Kahlert (1948) and Hahn (1957), investigated the influence of the fluid's inertia forces due to translational motion of the pin versus the bearing shell on the pressure distribution at

constant rotational speeds: Kahlert considered several fluid film flows with Reynolds numbers up to $Re = 10$, which may occur at extreme bearing conditions like high rotational speeds together with high bearing temperatures. For $Re = 10$, the pressure is increased by a maximum of 10% compared to the usual situation of $Re \ll 1$. Hahn regarded typical combustion engines and concluded that the neglect of the inertia forces is legitimated for such applications at constant rotational speeds.

But it remains to be investigated how a rapidly changing rotor speed respectively a large rotational acceleration influences the dynamic characteristics of journal bearings. This becomes quite important for fast run-up or run-down processes of rotating machines. For practical reasons and industrial purposes, it is always assumed that the inertia effects of the fluid due to rotational rotor acceleration may be neglected as well as the inertia effects due to translational motion of the pin in the bearing shell at constant rotor speeds. This assumption was confirmed theoretically in a previous paper by the authors, (Baumann et. al., 2009).

In (Baumann et. al., 2009), the influence of a rotational acceleration on the fluid film flow and thus on the journal bearing stiffness and damping coefficients was theoretically investigated for a plain journal bearing: While deducing the Reynolds Equation for non-stationary operation, several terms of inertia forces occur. Only some of them are due to the rotational acceleration; the others also occur for constant rotor speeds and have been proved to be negligible by Pinkus (1987), Kahlert (1948), Hahn (1957) and Smith (1965). So, the magnitude of the analytically derived additional terms of inertia for non-stationary rotor operation was estimated numerically by assuming reasonable rotor motion, and it was compared to the magnitude of the inertia terms occurring at constant rotor speed. Because the additional inertia terms for non-stationary operation are not bigger than the usually neglected inertia terms for stationary operation, it was concluded that the influence of a rotational acceleration respectively a time-dependent rotor speed on the pressure distribution is small and can be neglected. Therefore, the journal bearing stiffness and damping coefficients determined for constant rotor speeds may just as well be applied for fast run-up and run-down processes.

In this paper, this previous theoretical result is verified by an experimental study. For this purpose, the linearized stiffness and damping coefficients of a plain journal bearing are determined experimentally for both constant and fast changing rotor speeds. The minor influence of the rotational acceleration on the dynamic properties in real rotor-bearing systems is shown by comparing the measured stiffness and damping coefficients for stationary and non-stationary operation.

TEST RIG

For the experimental study, a journal bearing test rig (Figures 1 and 2, Table 1) was assembled. The rigid rotor runs in the centered test journal bearing and two active magnetic bearings at both rotor ends which are also actuating the rotor. The rotor is driven by an electric motor which is controlled by an external voltage signal. The driving torque is measured by a torque transducer between rotor and motor. The couplings between motor, torque transducer and rotor are torsion proof but highly flexible in lateral direction. They allow a large radial displacement of the rotor. The rotation of the rotor

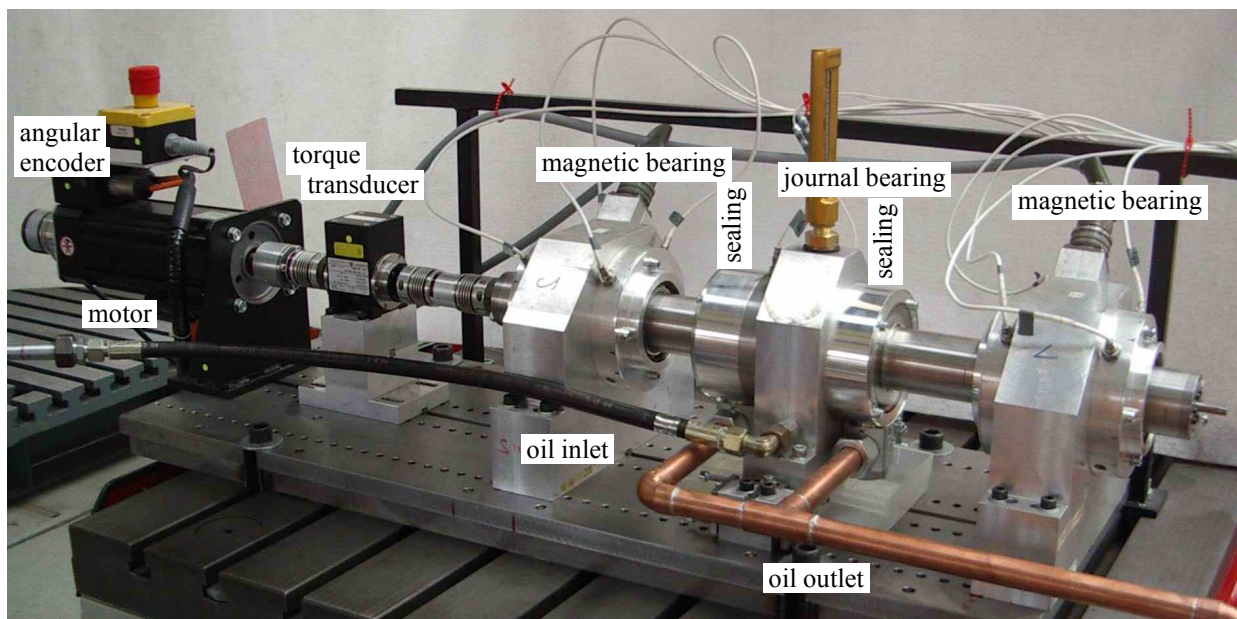


Figure 1: Journal bearing test rig in the laboratory

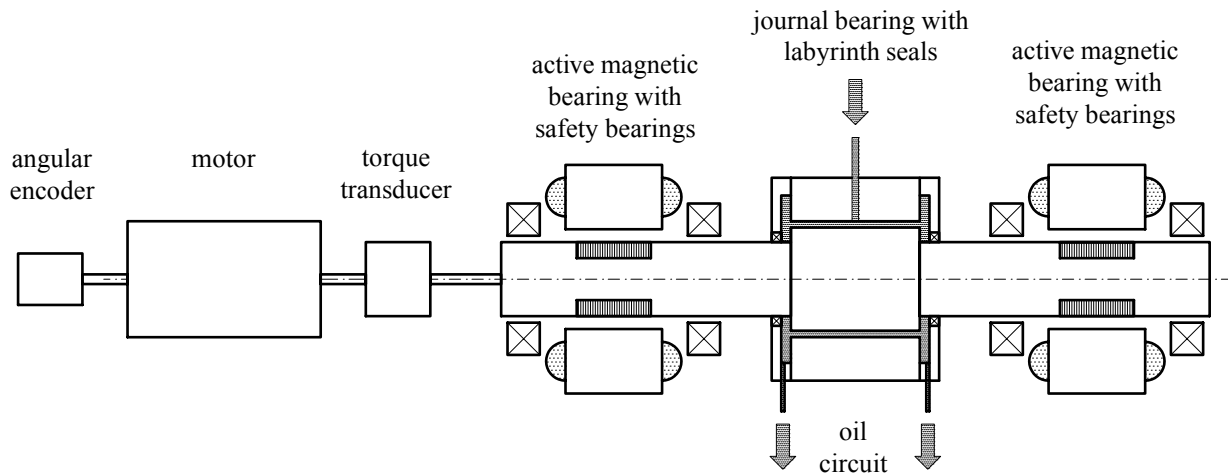


Figure 2: Sketch of the journal bearing test rig

Table 1: Characteristics of the test rig

rotor	speed	$n = 0 \dots 6000$ 1/min
	mass	$m = 13.6$ kg
journal bearing	type	cylindrical, one oil groove
	diameter	$D = 60$ mm
	width	$B = 60$ mm
	relative clearance	$\psi = 8.3$ ‰
	kinematic oil viscosity at 25 °C	$\nu = 16.5$ mm ² /s
	dynamic oil viscosity at 25 °C	$\eta = 11.4$ mPas
magnetic bearings	type	8-pole radial
	diameter (stator)	$D_{ML} = 57.6$ mm
	magnetic bearing constant	$k_{ML} = 3.63 \cdot 10^{-6}$ Vsm/A
	clearance	$s_0 = 0.78$ mm
control and data acquisition	sampling frequency	$f_s = 8192$ Hz
	low pass cut-off frequency	$f_{TP} = 3500$ Hz
	stiffness coefficient	$c_P = 10\,000$ A/m
	damping coefficient	$c_D = 6$ As/m
	integrational coefficient	$c_I = 15\,000$ A/ms

is recorded by an angular encoder at the backside of the motor. The lateral positions of the rotor in the journal bearing and in both magnetic bearings are captured by contact-free eddy-current position sensors. The magnetic bearings and all measurements are driven by a DSpace Control System.

The magnetic bearings are especially suited for experimental rotordynamic studies as they work contact-free and almost loss-free. They fulfill several functions within the rotor test system: Primarily, they allow easy positioning of the rotor at any point within the journal bearing clearance. So, different static equilibrium positions can be approached – even such which would lead to instability if the rotor was supported only by journal bearings. Besides, additional static and/or dynamic forces can be applied on the rotor and hence on the journal bearing by using the magnetic bearings as actuators. For this purpose, an additional actuator current for the magnets in addition to the the control current is provided. Last but not least, the magnetic bearings can also be used as force sensors by determining the magnetic forces on the rotor from the measured rotor position and the applied current. The magnetic force may determined either by using a idealised formula or by interpolation from a statically measured force-current-position-map, (Varun, 2007).

EXPERIMENTAL IDENTIFICATION OF JOURNAL BEARING STIFFNESS AND DAMPING COEFFICIENTS

In general, journal bearing stiffness and damping coefficients are determined experimentally by applying small excitation forces on the rotor and measuring the resulting rotor motion or vice versa. The linearized coefficients can afterwards be calculated from the relation between force and displacement respectively velocity.

Experimental procedure

The measurements for the identification of the stiffness and damping coefficients for both constant and time-varying rotor speeds differ only in the rotor driving scheme. For stationary operation, a constant speed n_0 is given. For the measurements at non-stationary operation, the motor was run up with a constant rotational acceleration over a certain speed range. These run-up measurements were carried out in the range of $n_0 - 50$ 1/min up to $n_0 + 50$ 1/min around the constant reference speed n_0 with angular accelerations of $\ddot{\varphi} = [10, 100, 500] \text{ 1/s}^2$.

As the journal bearing stiffness and damping coefficients depend on the rotor speed respectively the static equilibrium eccentricity ε_0 , different measurement positions are chosen throughout the bearing clearance. The measurement positions W_0 were chosen such that they lie on the positive axes y_j of the magnetic bearings $j = 1, 2$, see Figure 3. The magnetic bearing axes are turned through 45° against the vertical. So, the chosen measurement positions have the advantage that an uncorrelated force excitation in two orthogonal directions, namely in the directions of z_j and y_j of the magnetic bearings, can be realized very easily. During operation, the chosen measurement positions W_0 equal the static equilibrium positions of the rotor in the journal bearing. So, the usually used journal bearing coordinates z and y with z in the direction of the journal bearing load F_{G0} are turned through the angle γ_0 against the direction y_j of the magnetic bearings, see Figure 3.

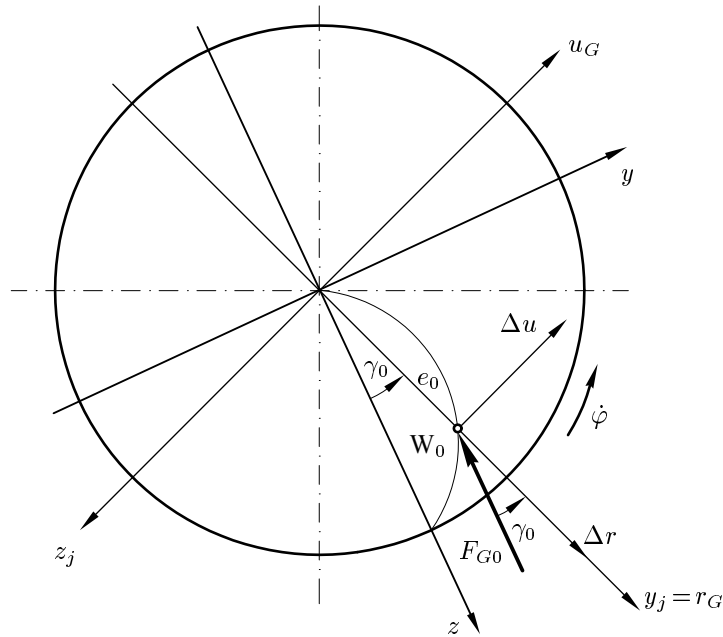


Figure 3: Static load in the journal bearing at rotated coordinates.

For realizing a force excitation of the rotor at the different equilibrium positions, additional excitation currents i_{Ry} and i_{Rz} are applied on the bearing magnets. These excitation currents are applied as uncorrelated noise in the two orthogonal directions z_j and y_j in the frequency range of 3-100 Hz. In this range, the shaft behaves rigid. The rotor responds to that excitation by carrying out small oscillations Δr_G and Δu_G around the measurement position.

The data acquisition includes the magnetic bearing currents with and without the excitation current, the rotor positions in the journal bearing and the two magnetic bearings, the angular position of the rotor and the rotational speed. The additional small oscillations $\Delta \mathbf{x}_{ru} = [\Delta r_G, \Delta u_G]^T$ around the measurement position W_0 are calculated by subtracting the stationary rotor position from the measured absolute rotor position. The stationary rotor position is determined as the

mean value of the rotor position after a 3 Hz low-pass filtering. At each measurement position 16 measurements are taken for averaging.

Due to the strong non-linearities of the magnetic bearing force, the excitation forces $\mathbf{F} = [F_{Rr}, F_{Ru}]^T$ in each coordinate direction are calculated as the difference of the overall force in the magnetic bearings and the control force. These two forces are separately interpolated from a force-current-displacement map, which was experimentally determined earlier by Varun (2007). The interpolation uses the measured magnetic bearing rotor positions and the applied currents.

Identification procedure of the journal bearing stiffness and damping coefficients from the measurement data

The calculation of the linearized stiffness and damping coefficients from the measured data is realized in the frequency domain. Regarding the run-up measurements, it has to be regarded that the frequency components resulting from the run-up and the frequency components due to the rotor excitation cannot be distinguished anymore in the frequency domain. Therefore, the small frequency range passed by the run-up frequencies is not notched out in the calculation.

For the identification of the linearized stiffness and damping coefficients c_{ij} and b_{ij} with $i, j = r, u$, the linearization of the journal bearing forces $F_{r\sim}$ and $F_{u\sim}$ around the static equilibrium position W_0 results in

$$\begin{bmatrix} F_{r\sim} \\ F_{u\sim} \end{bmatrix} = \begin{bmatrix} c_{rr} & c_{ru} \\ c_{ur} & c_{uu} \end{bmatrix} \begin{bmatrix} \Delta r_G \\ \Delta u_G \end{bmatrix} + \begin{bmatrix} b_{rr} & b_{ru} \\ b_{ur} & b_{uu} \end{bmatrix} \begin{bmatrix} \Delta \dot{r}_G \\ \Delta \dot{u}_G \end{bmatrix} + \begin{bmatrix} m_{rr} & m_{ru} \\ m_{ur} & m_{uu} \end{bmatrix} \begin{bmatrix} \Delta \ddot{r}_G \\ \Delta \ddot{u}_G \end{bmatrix}. \quad (1)$$

By transforming Equation 1 into the frequency domain $\bar{\Omega}$ by Fourier transform,

$$\begin{aligned} \hat{F}_k(\bar{\Omega}) &= \mathcal{F}\{F_{k\sim}(t)\} & \text{with} & \quad k=r, u, \\ \hat{r}(\bar{\Omega}) &= \mathcal{F}\{r_G(t)\} & \text{and} & \quad \hat{u}(\bar{\Omega}) = \mathcal{F}\{u_G(t)\}, \end{aligned} \quad (2)$$

the equation becomes

$$\begin{bmatrix} \hat{F}_r(\bar{\Omega}) \\ \hat{F}_u(\bar{\Omega}) \end{bmatrix} = \begin{bmatrix} c_{rr} + i\bar{\Omega}b_{rr} + \bar{\Omega}^2 m_{rr} & c_{ru} + i\bar{\Omega}b_{ru} + \bar{\Omega}^2 m_{ru} \\ c_{ur} + i\bar{\Omega}b_{ur} + \bar{\Omega}^2 m_{ur} & c_{uu} + i\bar{\Omega}b_{uu} + \bar{\Omega}^2 m_{uu} \end{bmatrix} \begin{bmatrix} \Delta \hat{r}(\bar{\Omega}) \\ \Delta \hat{u}(\bar{\Omega}) \end{bmatrix}, \quad (3)$$

$$\text{short: } \hat{\mathbf{F}}(\bar{\Omega}) = \mathbf{K}(\bar{\Omega}) \Delta \hat{\mathbf{r}}(\bar{\Omega}).$$

For estimating the frequency depending complex stiffness matrix $\mathbf{K}(\bar{\Omega})$ from the measured values of the excitation force $\hat{\mathbf{F}}$ and the rotor oscillations $\Delta \hat{\mathbf{r}}$, this equation is transferred into conjugate-complex variables (marked by *) and expanded to

$$\hat{\mathbf{F}}^*(\bar{\Omega}) \Delta \hat{\mathbf{r}}^T(\bar{\Omega}) = \mathbf{K}^*(\bar{\Omega}) \Delta \hat{\mathbf{r}}^*(\bar{\Omega}) \Delta \hat{\mathbf{r}}^T(\bar{\Omega}). \quad (4)$$

The transition to the spectral densities takes the Fourier transforms $\tilde{\hat{\mathbf{F}}}(\bar{\Omega}) = \hat{\mathbf{F}}(\bar{\Omega})/T_{mess}$ and $\tilde{\Delta \hat{\mathbf{r}}}(\bar{\Omega}) = \Delta \hat{\mathbf{r}}(\bar{\Omega})/T_{mess}$ into account, respecting the measurement duration T_{mess} of the $N = 16$ single measurements for averaging. This transition results in

$$\frac{1}{N} \sum_{n=1}^N \tilde{\hat{\mathbf{F}}}_n^*(\bar{\Omega}) \Delta \tilde{\hat{\mathbf{r}}}_n^T(\bar{\Omega}) = \mathbf{K}^*(\bar{\Omega}) \frac{1}{N} \sum_{n=1}^N \Delta \tilde{\hat{\mathbf{r}}}_n^*(\bar{\Omega}) \Delta \tilde{\hat{\mathbf{r}}}_n^T(\bar{\Omega}). \quad (5)$$

By summing up the spectral densities of the 16 single averaging measurements, which are carried out with different uncorrelated exciting forces, the spectral density matrix on the right hand side becomes regular and invertible, (Kühlert, 1995). So, the equation for the complex stiffness matrix is

$$\mathbf{K}^*(\bar{\Omega}) = \tilde{\mathbf{S}}_{Fr}(\bar{\Omega}) \tilde{\mathbf{S}}_{rr}^{-1}(\bar{\Omega}) \quad \text{with} \quad \tilde{S}_{ij} \bar{\Omega} = \frac{1}{N} \sum_{n=1}^N \hat{X}_{in}^*(\bar{\Omega}) \hat{X}_{jn}(\bar{\Omega}). \quad (6)$$

The stiffness and damping coefficients c_{ij} and b_{ij} and the mass parameters m_{ij} are determined by splitting the complex stiffness matrix $\mathbf{K}(\bar{\Omega})$ into its real and its imaginary part

$$\text{Re}\{k_{ij}(\bar{\Omega})\} = c_{ij}(\bar{\Omega}) + \bar{\Omega}^2 m_{ij}(\bar{\Omega}) \quad \text{and} \quad \text{Im}\{k_{ij}(\bar{\Omega})\} = \bar{\Omega} b_{ij}(\bar{\Omega}). \quad (7)$$

As this stiffness and damping coefficients are still depending on the M excitation frequencies $\bar{\Omega}_m$, they are averaged over this excitation frequency range,

$$\sum_{m=1}^M (c_{ij} + \bar{\Omega}_m^2 m_{ij} - \text{Re}\{k_{ij}\}_m)^2 \rightarrow \min \quad \text{and} \quad \sum_{m=1}^M (\bar{\Omega}_m b_{ij} - \text{Im}\{k_{ij}\}_m)^2 \rightarrow \min . \quad (8)$$

The result of these calculations are the journal bearing stiffness matrix \mathbf{C}_{ru} with the coefficients c_{ij} , the journal bearing damping matrix \mathbf{B}_{ru} with the coefficients b_{ij} and the mass matrix \mathbf{M}_{ru} of the rotor, consisting of the coefficients m_{ij} . These coefficients refer to the radial and tangential coordinates $\Delta \mathbf{x}_{ru} = [\Delta r_G, \Delta u_G]^T$. They are constant for each rotational speed n_0 ; meaning they are independent of the excitation frequency $\bar{\Omega}$. These coefficients can be transformed into the usually used journal bearing coordinates $\mathbf{x}_G = [z, y]^T$ by the rotation through the angle γ_0 ,

$$\begin{aligned} \mathbf{C}_G &= \mathbf{R}(\phi = \gamma_0) \mathbf{C}_{ru} \mathbf{R}^T(\phi = \gamma_0), \\ \mathbf{B}_G &= \mathbf{R}(\phi = \gamma_0) \mathbf{B}_{ru} \mathbf{R}^T(\phi = \gamma_0), \\ \mathbf{M}_G &= \mathbf{R}(\phi = \gamma_0) \mathbf{M}_{ru} \mathbf{R}^T(\phi = \gamma_0) \end{aligned} \quad \text{with} \quad \mathbf{R}(\phi) = \begin{bmatrix} \cos \phi & -\sin \phi \\ \sin \phi & \cos \phi \end{bmatrix}. \quad (9)$$

EXPERIMENTAL RESULTS

Figures 4 and 5 show the experimentally determined stiffness and damping coefficients for the test journal bearing at different rotational accelerations of the shaft. In general, they show a good agreement between the coefficients measured in the run-up processes and the coefficients measured at constant rotor speeds. This means, the rotational acceleration does not influence the stiffness and damping coefficients significantly. So, the conclusion of the previous theoretical investigation is confirmed experimentally. Therefore, it can be concluded that the stiffness and damping coefficients determined for constant rotor speeds are also valid for time-dependent rotor speeds such as run-up and run-down processes.

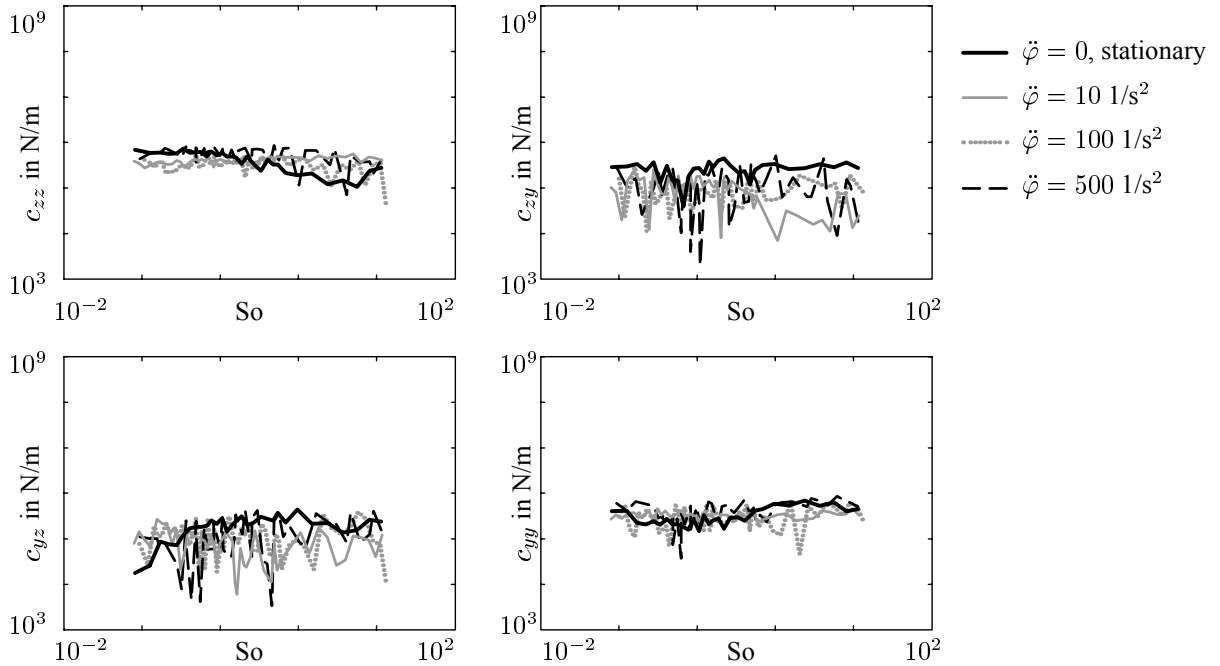


Figure 4: Comparison of the measured stiffness coefficients of the test journal bearing at stationary operation and during run-up processes with different rotational accelerations $\ddot{\phi}$ depending on the Sommerfeld number So

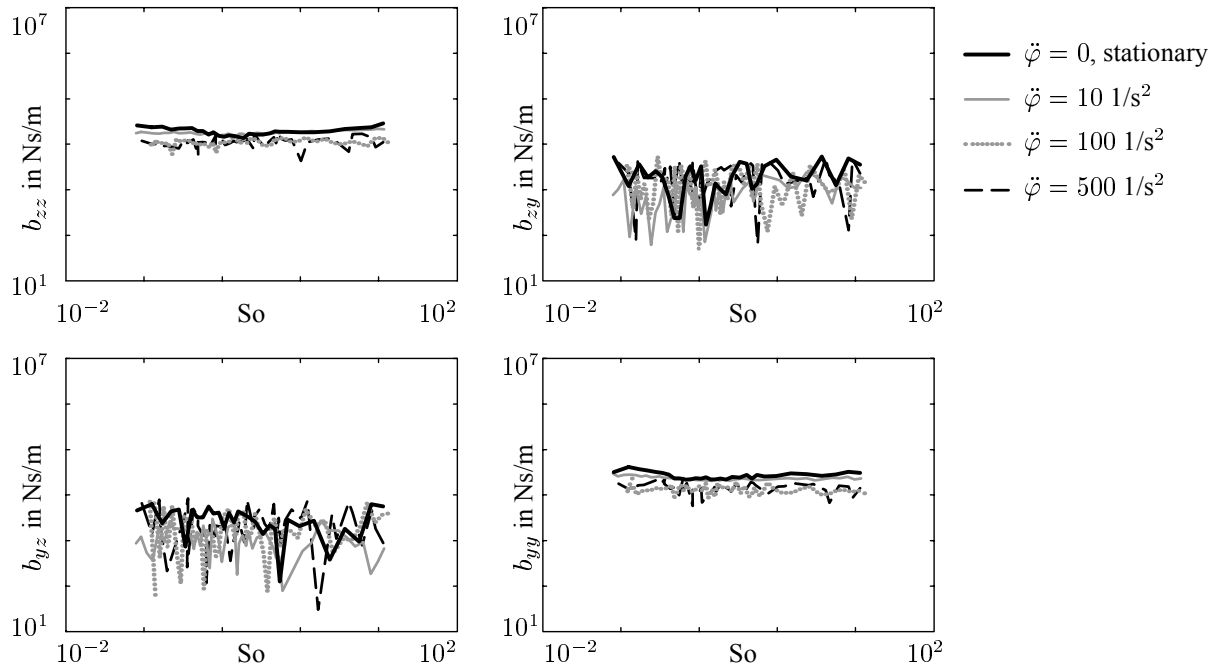


Figure 5: Comparison of the measured damping coefficients of the test journal bearing at stationary operation and during run-up processes with different rotational accelerations $\ddot{\varphi}$ depending on the Sommerfeld number So

ERROR DISCUSSION

The accuracy of the experimentally determined stiffness and damping coefficients primarily depends on the accuracy of the measurements. In particular, this includes the measurement of the magnetic excitation forces and the additional small rotor motions.

The rotor motion is measured by eddy-current position sensors. Including the measurement amplifiers, their accuracy is $<5\%$ according to the manufacturer.

The accuracy of the magnetic force measurement is composed of different parts due to the interpolation of the force from the measured force-current-position-map: To begin with, the accuracies of the measured rotor position in the magnetic bearings is again 5% and the accuracy for applying a given control or excitation current on the magnetes by using the power amplifier is 3% . These two accuracies affect the interpolation equally. But, the used force-current-position-map itself was experimentally determined by using the same eddy-current sensors, the same power amplifiers, and some additional strain gauges for measuring the force. The accuracy of this type of force measurement, being composed of the strain gauges and the measurement amplifier, is 2.7% . Regarding the law of error propagation by Gauß, the accuracy of the force-current-position-map of the magnetic bearings adds up to 6.4% . Altogether, the accuracy of the force measurement in the magnetic bearings by using this force-current-position-map amounts to 12.2% .

For estimating the consequences of those measurements inaccuracies on the calculated stiffness and damping coefficients, artificial disturbances are applied on the measurement data. These disturbances are modeled as uncorrelated white noise with a rms-value in the seize of the measurement inaccuracies; this is 5% of the rms-value of the position measurement data and 12.2% of the rms-value of the force measurement data. Then, the calculation of the stiffness and damping coefficients is performed again. To check the coincidence of the disturbances, the calculation is repeated with a second set of disturbances which is uncorrelated to the first set.

The Figures 6 to 9 show the stiffness and damping coefficients which are calculated from some disturbed measurement data in comparison to the stiffness and damping coefficients calculated from the original, undisturbed data. If the disturbances are applied either on the position measurement data or on the force measurement data, Figures 6 and 7, then it becomes clear that the errors in the force measurement affect the calculation much more than the errors in the position measurement. This is due to the larger inaccuracy for the force measurement and also due to the fact that the excitation force is calculated as the difference between measured magnetic forces. The Figures 8 and 9 show that the experimentally determined stiffness and damping coefficients have a relatively large inaccuracy in general. The variability of the stiffness and damping coefficients in Figures 4 and 5 lies within the measurement inaccuracy and are therefore not significant.

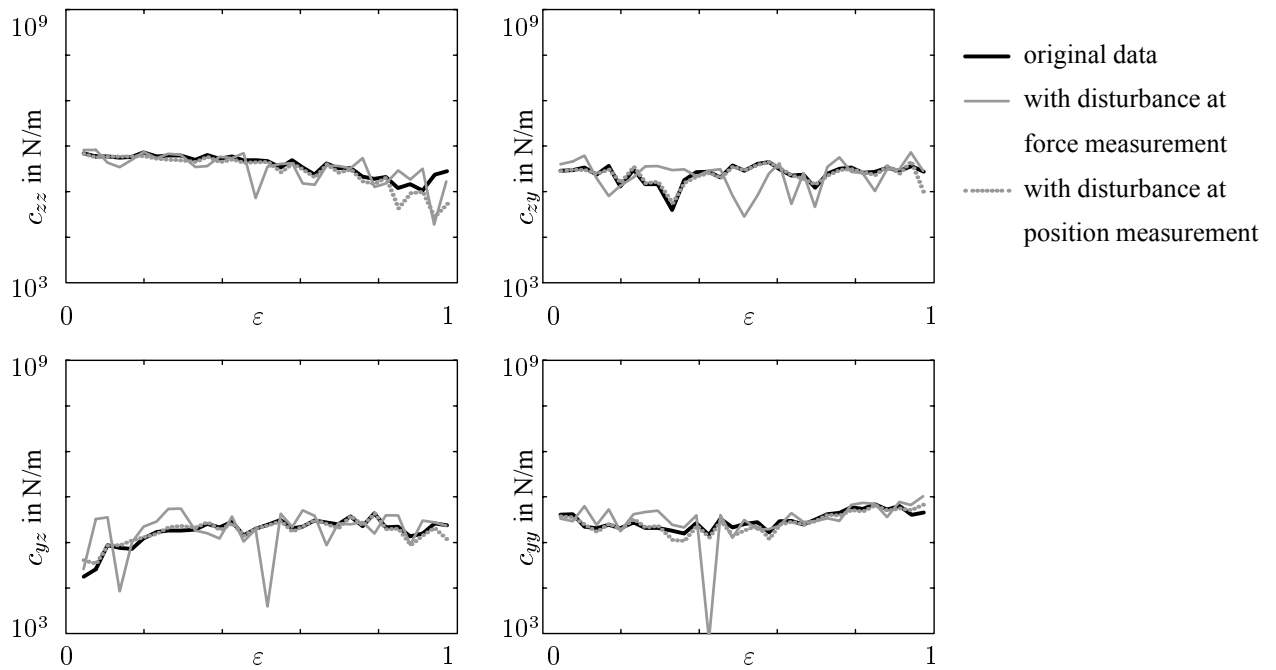


Figure 6: Stiffness coefficients c_{ij} of the test journal bearing at stationary operation depending on the relative bearing excentricity ϵ for the original measurement data and for artificially disturbed data sets: disturbances at either the position or the force measurement data

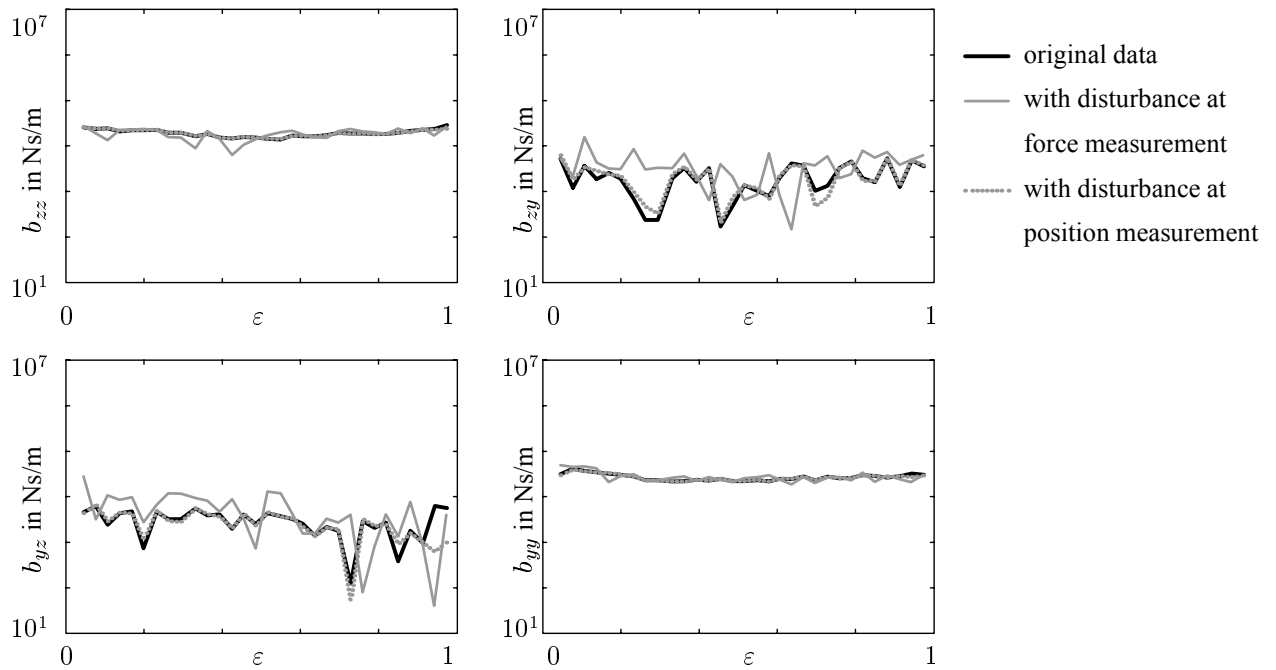


Figure 7: Damping coefficients b_{ij} of the test journal bearing at stationary operation depending on the relative bearing excentricity ϵ for the original measurement data and for artificially disturbed data sets: disturbances at either the position or the force measurement data

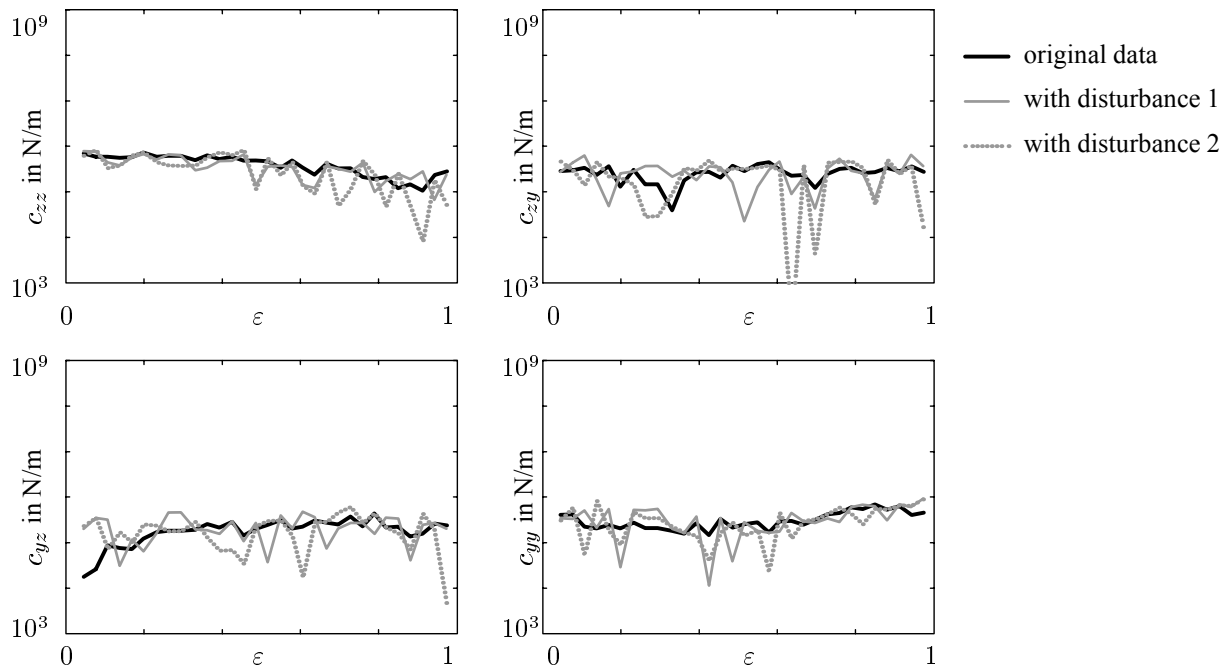


Figure 8: Stiffness coefficients c_{ij} of the test journal bearing at stationary operation depending on the relative bearing eccentricity ε for the original measurement data and for artificially disturbed data sets: different uncorrelated disturbances at the same time at the position and the force measurement data

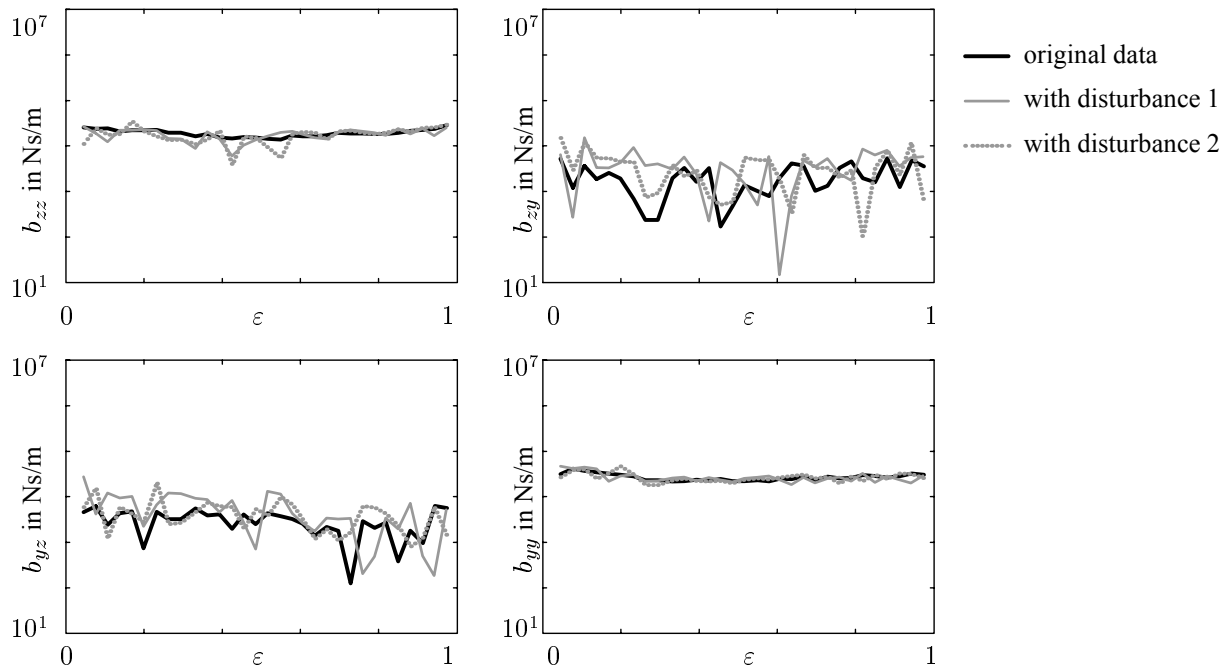


Figure 9: Damping coefficients b_{ij} of the test journal bearing at stationary operation depending on the relative bearing eccentricity ε for the original measurement data and for artificially disturbed data sets: different uncorrelated disturbances at the same time at the position and the force measurement data

CONCLUSION

In this paper, it is experimentally proven that rapidly changing rotor speeds respectively large rotational accelerations do not significantly influence the stiffness and damping coefficients of plain journal bearings. For that, the stiffness and damping coefficients of a test journal bearing were experimentally determined at stationary operation with constant rotor speeds and at non-stationary operation. The latter operational state was realized by short run-up processes around a reference speed with different rotational accelerations. The results were compared to each other and they showed good agreement for all tested rotational accelerations.

This result proves the result of a previous analytical-numerical investigation in which was shown that the inertia forces of the fluid film flow stay negligibly small also for even large rotational accelerations of the shaft. So, the known journal bearing stiffness and damping coefficients, which are determined for constant rotational speeds, may also be used for the simulation of fast run-up and run-down processes of the rotor system .

ACKNOWLEDGEMENTS

The authors gratefully thank the German and Brazilian research funding agencies DAAD and CAPES for their support of this work within the PROBRAL programme.

REFERENCES

- Baumann, K.; Markert, R.; Murmann, R., 2009, "Computergestützte Berechnung der Tragfähigkeit und des Gleitlagermomentes in hydrodynamischen Gleitlagern bei instationären An- und Auslaufvorgängen (Computer-aided Calculation of Load Capacity and Journal Bearing Moment for Hydrodynamic Bearings in Non-stationary Run-up and Run-down Procedures)", VDI-Berichte Nr. 2069, pp. 151-160.
- Hahn, H. W., 1957, "Das zylindrische Gleitlager endlicher Breite unter zeitlich veränderlicher Belastung (The Cylindric Journal Bearing of Finite Width with Time-Depending Load)", Dissertation TH Karlsruhe.
- Kahlert, G., 1948, "Der Einfluß der Trägheitskräfte bei der hydrodynamischen Schmiermitteltheorie (The Influence of the Inertia Forces within the Hydrodynamic Lubricant Theory)", Ing-Archiv 16, pp. 321-342.
- Kühlert, H.; Markert, R.; Witfeld, H., 1992, "Frequency Response Function Estimation from Multiple Input Excitation with Broadband Signals", Proc. 15th Int. Sem. on Modal Analysis, Part III, pp. 971-989.
- Lang, O. R.; Steinhilper, W., 1978, "Gleitlager." Konstruktionsbücher Bd. 32. Berlin: Springer-Verlag.
- Smith, D. M., 1965, "Journal Bearing Dynamic Characteristics - Effects of Inertia of Lubricant", Lubrication and Wear, Proceedings of the Institution of Mechanical Engineers 179 Pt 3J pp. 37-44.
- Someya, T., 1989, "Journal-Bearing Databook", Berlin: Springer-Verlag.
- Varun, S., 2007, "Force Measurement in Active Magnetic Bearings", Master-Thesis TU Darmstadt/Indian Institute of Technology Guwahati.

RESPONSIBILITY NOTICE

The authors are the only responsible for the printed material included in this paper.

Stochastic analysis of structures excited by internal flows

T. G. Ritto¹, R. Sampaio² and F. A. Rochinha¹

¹ Department of Mechanical Engineering, Federal University of Rio de Janeiro, Rio de Janeiro, Brazil
thiagoritto@gmail.com, faro@mecanica.coppe.ufrj.br

² Department of Mechanical Engineering, PUC-Rio, Rio de Janeiro, Brazil
rsampaio@puc-rio.br

Abstract: The aim of this work is to investigate model uncertainties related to structures excited by internal flow. An Euler-Bernoulli beam model is used to model the structure, and the fluid is added to the model by means of a constant mass, damping and stiffness. The nonparametric probabilistic approach is used to model the uncertainties, which are related to the stiffness of the system. An identification procedure is proposed to identify the dispersion parameter of the probabilistic model using the first natural frequency of the reference model and the fifth percentile of the stochastic system. The deterministic and stochastic responses are analyzed.

Keywords: *fluid-structure interaction, stochastic dynamical model, stochastic identification, model uncertainties*

NOMENCLATURE

E = Young Modulus, Pa

F = external force, N/m

$[\mathbf{G}]$ = random matrix

$[K_r]$ = reduced stiffness matrix, rad^2

$[\mathbf{K}_r]$ = random reduced stiffness matrix, rad^2

L = length, m

I = area moment of inertia, m^4

m = mass per unit length of the structure, kg/m

M_f = mass per unit length of the fluid, kg/m

U = velocity of the fluid, m/s

v = transversal displacement, m

INTRODUCTION

The dynamics of structures with internal axial flow has many technological applications, e.g., drill-strings [1] heat-exchanger tubes, nuclear fuel elements, towed flexible cylinders for water transportation, etc. In the present analysis the fluid-structure interaction is modeled as in [2].

The Euler-Bernoulli beam theory is used to model the structure, than the system is discretized by means of the finite element method. The analysis is done using dimensionless quantities. We assume that the stiffness contribution due to the fluid is uncertain, i.e., there is a model uncertainty related to the stiffness of the system. The nonparametric probabilistic approach [3], which is able to model both parameter and model uncertainties, is used to model these uncertainties. In this approach, the reduced stiffness matrix of the system is substituted by a random matrix.

The simplified fluid model is used as the reference model, so that the dispersion parameter related to the random matrix can be identified. A procedure that uses the first natural frequency of the reference model and the fifth percentile of the stochastic system is proposed for the identification process.

The article is organized as follows. In Section the deterministic problem is presented; the dynamic equations are introduced and the discrete system is obtained by means of the finite element method. In Section the reduced-order model, constructed with the normal modes of the structure, is presented. In Section the probabilistic model (nonparametric probabilistic approach) is quickly reviewed, and the resulting stochastic system is shown in Section ???. The numerical results are discussed in Section , and the identification procedure is explained and the stochastic system is analyzed. Finally, in Section ??, the concluding remarks are made.

DETERMINISTIC SYSTEM

Figure 1 sketches the system considered in the analysis.

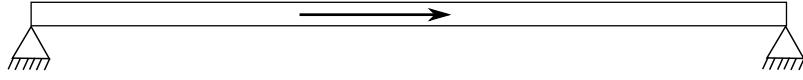


Figure 1 – Sketch of the system considered in the analysis (the arrow represents the internal fluid flow).

Using the Euler-Bernoulli beam theory, the partial differential equation governing the dynamics of the structure is written as:

$$m \frac{\partial^2 v(x,t)}{\partial t^2} + EI \frac{\partial^4 v(x,t)}{\partial x^4} = F(x,t) \quad x \in [0, L], t \in [0, T], \quad (1)$$

where v is the transversal displacement, L is the length of the beam, m is the mass per unit length, E is the elasticity modulus, I is the area moment of inertia and F is the external force. If the fluid [2] is included in the model, the above equation becomes:

$$(m + M_f) \frac{\partial^2 v}{\partial t^2} + 2M_f U \frac{\partial^2 v}{\partial x \partial t} + M_f U^2 \frac{\partial^2 v}{\partial x^2} + EI \frac{\partial^4 v}{\partial x^4} = F, \quad (2)$$

where M_f is the fluid mass per unit length and U is the axial velocity of the fluid. Using dimensionless variables, we can write:

$$\frac{\partial^2 \eta}{\partial \tau^2} + 2\beta^{1/2} u \frac{\partial^2 \eta}{\partial \zeta \partial \tau} + u^2 \frac{\partial^2 \eta}{\partial \zeta^2} + \frac{\partial^4 \eta}{\partial \zeta^4} = f, \quad (3)$$

where the dimensionless quantities are:

$$\begin{aligned} \zeta &= \frac{x}{L}, & \eta &= \frac{v}{L}, & \tau &= t \left(\frac{EI}{(m + M_f)L^4} \right)^{1/2}, \\ \beta &= \frac{M_f}{m + M_f}, & u &= U \left(\frac{M_f}{EI} \right), & f &= F \frac{L^3}{EI}. \end{aligned} \quad (4)$$

Let $\eta = \hat{\eta} \exp(i\omega\tau)$ and $f = \hat{f} \exp(i\omega\tau)$, in which ω is the dimensionless frequency, $\omega = \omega_{\text{rad}} \left(\frac{(m + M_f)L^4}{EI} \right)^{1/2}$, ω_{rad} is the frequency in rad/s and $i = \sqrt{-1}$. Substituting $\eta = \hat{\eta} \exp(i\omega\tau)$ and $f = \hat{f} \exp(i\omega\tau)$ in Eq.(3) leads to:

$$\omega^2 \eta - i\omega 2\beta^{1/2} u \frac{\partial \hat{\eta}}{\partial \zeta} + u^2 \frac{\partial^2 \hat{\eta}}{\partial \zeta^2} + \frac{\partial^4 \hat{\eta}}{\partial \zeta^4} = \hat{f}. \quad (5)$$

Equation (5) is discretized by means of the finite element method: $\hat{\eta}^{(e)}(\xi, \omega) = \mathbf{N}(\xi) \hat{\mathbf{u}}^{(e)}(\omega)$, where the shape functions, \mathbf{N} , are defined in Appendix and the element displacement vector $\hat{\mathbf{u}}^{(e)} = [\hat{\eta}_1 \quad \partial \hat{\eta}_1 / \partial \zeta \quad \hat{\eta}_2 \quad \partial \hat{\eta}_1 / \partial \zeta]$. The element matrices are the following

$$[M]^{(e)} = \int_0^1 \mathbf{N}^T \mathbf{N} l_e d\xi, \quad (6)$$

$$[C]^{(e)} = 2\beta^{1/2} u \int_0^1 \mathbf{N}^T \mathbf{N}' d\xi, \quad (7)$$

$$[K_b]^{(e)} = \int_0^1 \mathbf{N}_v'^T \mathbf{N}_v'' \frac{1}{l_e^3} d\xi, \quad (8)$$

$$[K_f]^{(e)} = -u^2 \int_0^1 \mathbf{N}'^T \mathbf{N}' \frac{1}{l_e} d\xi, \quad (9)$$

resulting in the discretized system given by:

$$\omega^2 [M] \hat{\mathbf{u}}(\omega) - i\omega [C] \hat{\mathbf{u}}(\omega) + ([K_b] + [K_f]) \hat{\mathbf{u}}(\omega) = \hat{\mathbf{f}}(\omega), \quad (10)$$

where $[M]$, $[C]$, $[K_b]$ and $[K_f] \in \mathbb{R}^{m \times m}$ are the the mass, damping and stiffness matrices (related to the bending and to the fluid), $\hat{\mathbf{u}}(\omega) \in \mathbb{C}^m$ is the response vector and $\hat{\mathbf{f}}(\omega) \in \mathbb{C}^m$ is the force vector. Matrices $[M]$ and $[K]$ are symmetric positive definite and matrix $[C]$ is not symmetric. Equation (10) can be written as

$$\hat{\mathbf{u}}(\omega) = [H(\omega)] \hat{\mathbf{f}}(\omega), \quad (11)$$

where $[H(\omega)] \in \mathbb{C}^{m \times m}$ is the frequency response function (FRF):

$$[H(\omega)] = (\omega^2[M] - i\omega[C] + ([K_b] + [K_f]))^{-1}. \quad (12)$$

REDUCED-ORDER MODEL

Let $\hat{\mathbf{u}}(\omega) = [\Phi]\hat{\mathbf{q}}(\omega)$, where $[\Phi] \in \mathbb{R}^{m \times n}$ is the matrix composed by the normal modes of the system and $\hat{\mathbf{q}}(\omega) \in \mathbb{C}^n$. The reduced-order model of the system can be written as

$$\hat{\mathbf{q}}(\omega) = (\omega^2[M_r] - i\omega[C_r] + [K_r])^{-1}[\Phi]^T \hat{\mathbf{f}}(\omega), \quad (13)$$

where the reduced-order matrices are given by $[M_r]_{ij} = \delta_{ij}$, $[C_r]_{ij} = \delta_{ij}2\xi_i\omega_i$ and $[K_r]_{ij} = \delta_{ij}\omega_i^2$. Where δ_{ij} is the Kronecker delta, which is equal to one if $i = j$ and is equal to zero otherwise, ω_i is the i -th natural frequency of the system and ξ_i is the i -th damping factor of the system.

Thus, the system was reduced from dimension m to n ($n < m$). We assume that the mass and damping do not present uncertainties and are given by

$$[M_r] = [\Phi]^T[M][\Phi] \quad , \quad [C_r] = [\Phi]^T[C][\Phi]. \quad (14)$$

We assume also that the influence of the fluid on the stiffness of the system is complex. Therefore, we do not trust matrix $[K_f]$, and we use the nonparametric probabilistic model (see next section) to model this lack of knowledge. Hence,

$$[K_r] = [\Phi]^T[K_b][\Phi]. \quad (15)$$

The natural frequencies and normal modes are computed from the following generalized eigenvalue problem:

$$(-\omega_i^2[M] + [K_b])\phi_i = \mathbf{0}. \quad (16)$$

And $[\Phi] = [\phi_1 \ \phi_2 \ \dots \ \phi_n]$.

In the numerical computations we also use the model that includes $[K_f]$. In this case,

$$[K_r] = [\Phi]^T([K_b] + [K_f])[\Phi]. \quad (17)$$

We call it reference model, and it is used to identify the dispersion parameter of the stochastic system. The natural frequencies and normal modes are computed from the following generalized eigenvalue problem:

$$(-\omega_i^2[M] + [K_b] + [K_f])\phi_i = \mathbf{0}. \quad (18)$$

And $[\Phi] = [\phi_1 \ \phi_2 \ \dots \ \phi_n]$.

PROBABILISTIC MODEL

To model our lack of knowledge about the influence of the stiffness of the fluid on the dynamical response of the system, we use the nonparametric probabilistic approach [3]. Such an approach consists in constructing a probabilistic model for the stiffness operator of the problem using intrinsic available information relative to it. The reduced random matrix is written as (note that the boldface is used for a random matrix)

$$[\mathbf{K}_r] = [\mathbf{L}]^T[\mathbf{G}][\mathbf{L}], \quad (19)$$

where $[\mathbf{L}]^T[\mathbf{L}]$ is the Cholesky decomposition of matrix $[K_r]$ (Eq. (15)), which does not include the fluid stiffness $[K_f]$. Without going into further details, the probability density function of the random matrix $[\mathbf{G}]$ can be constructed using the Maximum Entropy Principle [4] with the following available information:

1. Random matrix $[\mathbf{G}]$ is positive-definite almost surely,
2. $\mathcal{E}\{[\mathbf{G}]\} = [I]$,
3. $\mathcal{E}\{||[\mathbf{G}]^{-1}||_F^2\} = c_1$, $|c_1| < +\infty$,

where $[I]$ is the identity matrix, $\mathcal{E}\{\cdot\}$ denotes the mathematical expectation and $||[A]||_F = (\text{trace}\{[A][A]^T\})^{1/2}$ denotes the Frobenius norm. The closed form expression of the probability density function of $[\mathbf{G}]$, as well as the random generator of its independent realizations can be found in [3].

The dispersion parameter δ of matrix $[\mathbf{G}]$ is defined as:

$$\delta = \left\{ \frac{1}{n} \mathcal{E} \{ \| [\mathbf{G}] - [T] \|_F^2 \} \right\}^{\frac{1}{2}}, \quad (20)$$

where n is the size of $[\mathbf{G}]$.

NUMERICAL RESULTS

The beam is supported in both ends (i.e., $\eta = 0$ at $\zeta = 0$ and at $\zeta = 1$). It is discretized with 80 finite elements ($m = 160$) and the reduced-order model is constructed with $n = 10$. The frequency band analyzed is $[0, 30]$ Hz. The dimensionless parameter $\beta = 0.8$ is fixed and u varies from 0 to 3. For instance, for the configuration $E = 450 \times 10^6$ Pa, $d_i = 4 \times 10^{-2}$ m, $d_o = 5 \times 10^{-2}$ m, $\rho = 250$ kg/m³, $\rho_f = 1000$ kg/m³, $U = 10$ m/s, we have $\beta = 0.88$ and $u = 1.24$.

Deterministic response

Figure 2 shows the absolute value of the response $|\hat{\mathbf{u}}|$ of the deterministic system at $\zeta = 0.3$ for different flow velocities $u = \{0, 1, 2, 3\}$. It can be seen that the first natural frequency is the one that displaces the most.

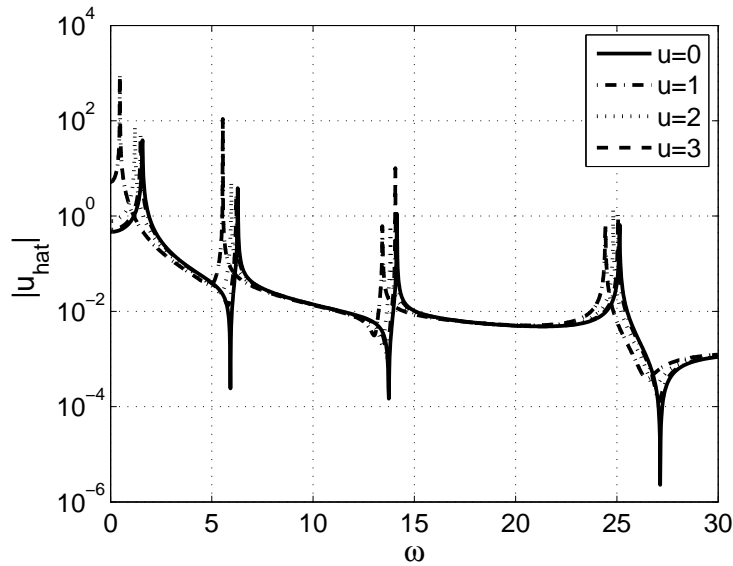


Figure 2 – Response in frequency of the deterministic system at $\zeta = 0.3$ for $u = \{0, 1, 2, 3\}$.

Figure 3 shows the distance from the reference response as the dimensionless velocity increases. It shows how the two deterministic models get apart as u increases. The distance dist is measured by:

$$\text{dist}(u) = \frac{100}{n_\omega} \sum_{j=1}^{n_\omega} \frac{\|\hat{\mathbf{u}}^{ref}(\omega_j, u) - \hat{\mathbf{u}}(\omega_j, u)\|}{\|\hat{\mathbf{u}}(\omega_j, u)\|}, \quad (21)$$

in which $\hat{\mathbf{u}}^{ref}$ is the response of the reference model (stiffness matrix given by Eq. (15)) and $\hat{\mathbf{u}}$ is the response using stiffness matrix given by Eq. (17). The frequency domain is discretized in n_ω (=1500) frequencies, and $\|\cdot\|$ is the L_2 -norm.

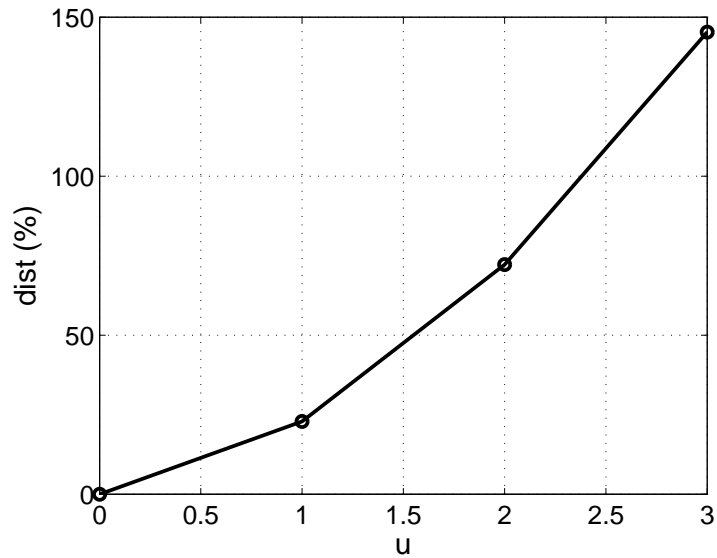


Figure 3 – Percent error as a function of the flow velocity u .

Identification of the dispersion parameter δ

Before proceeding with the identification of the dispersion parameter δ of the probabilistic model, a convergence analysis is done. As Fig. 2 shows, the first natural frequency is the one that displaces the most, as the dimensionless velocity u changes. Therefore, the first natural frequency is going to be used in the identification procedure. Let W_1 be the random variable related to the first natural frequency of the system; the convergence function is defined as

$$\text{conv}(n_s) = \frac{1}{n_s} \sum_{i=1}^{n_s} W_{1i}^2, \quad (22)$$

where n_s is the number of Monte Carlo simulations.

Figure 4(a) shows the convergence curve and Fig. 4(b) shows the histogram of W_1 for $\delta = 0.2$; the Monte Carlo simulation was done with 10000 realizations. In this case, the mean value of W_1 is 1.54 and its variance is 0.0045.

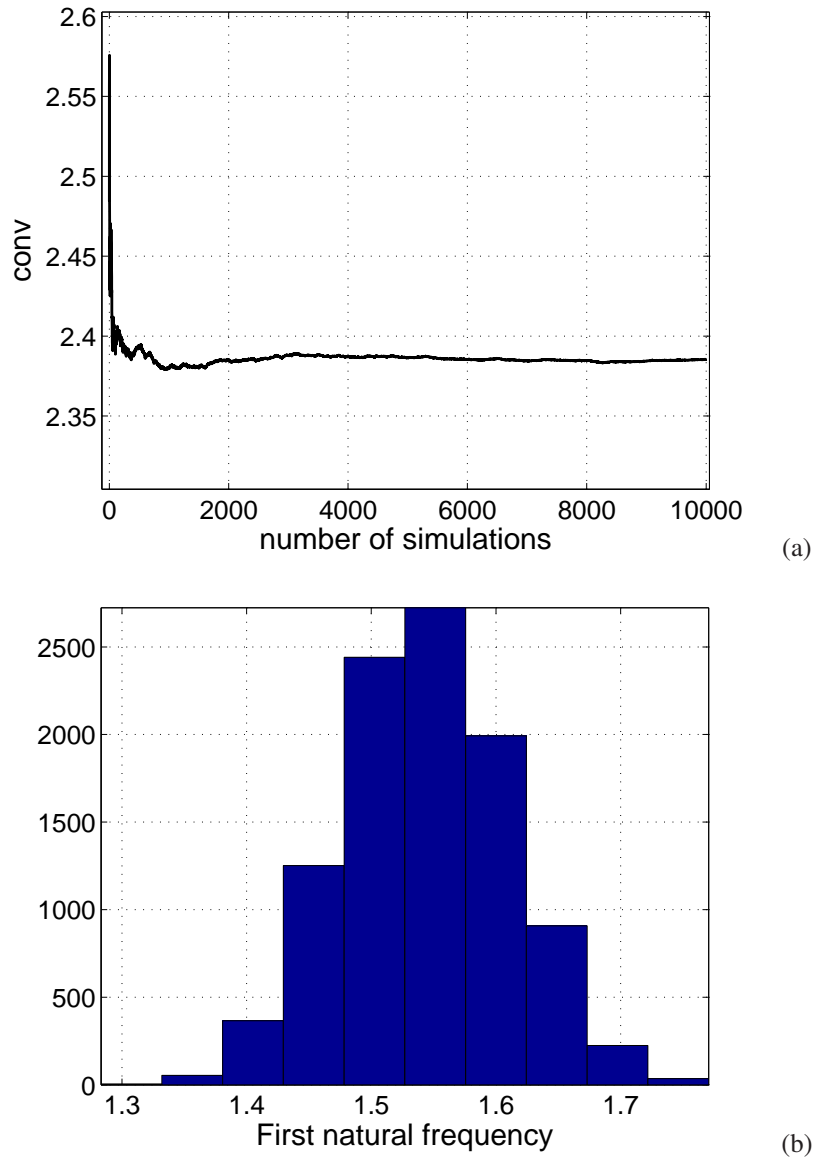


Figure 4 – (a) Mean square convergence of W_1 and (b) its histogram for $\delta = 0.2$.

Figure 5 shows how the fifth percentile varies with the dispersion parameter δ . As the value of δ increases, the value of fifth percentile decreases (the same way, when δ increases the 95th percentile increases because the standard deviation of W_1 gets greater).

The response of the system with the simplified fluid model is used as the reference model for the identification process. In a more realistic scenario, the reference model could be some experimental response. The first natural frequency for $u = \{0, 0.5, 1, 1.5, 1, 1.5, 2.0, 2.5, 3.0\}$ happens to be $\omega_1 = \{1.57, 1.55, 1.49, 1.38, 1.21, 0.95, 0.47\}$. Knowing these values and using Fig. 5, we can identify δ for different u 's; see Fig. 6. For instance, for $u = 2.5$ we have $w_1 = 0.95$; going right with the arrow until the curve is reached and then coming down, the value of δ is 0.6.

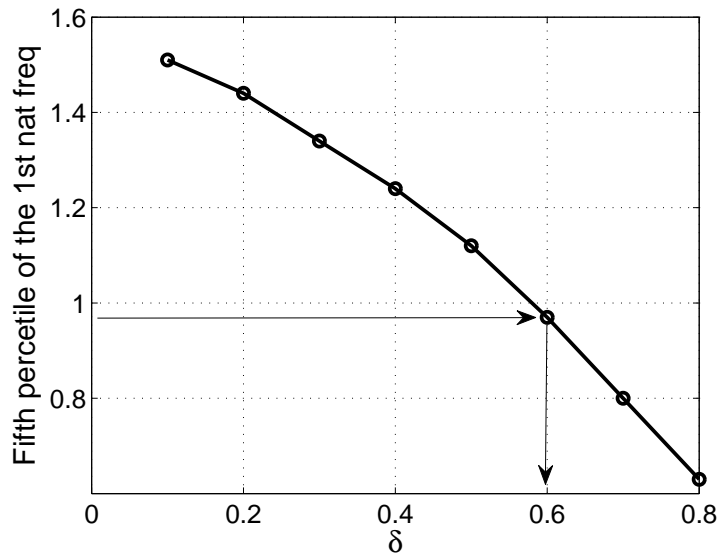


Figure 5 – Fifth percentile of W_1 as a function of δ .

Figure 6 shows the identified dispersion parameter δ as a function of the flow velocity u .

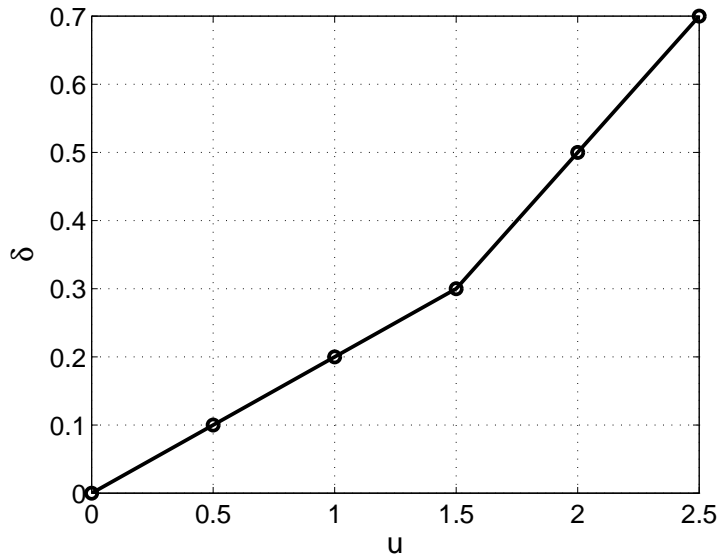


Figure 6 – Dispersion parameter δ as a function of the flow velocity u .

Stochastic response

Figure 7 shows the random response of the system at $\zeta = 0.3$ for $\delta = 0.2$. The yellow region corresponds to the 90% confidence envelope and the dashed line corresponds to the deterministic response for $u = 1$. Figure 7(b) shows how the envelope includes the response close to the first natural frequency. There are some peaks that are not inside the 90% confidence region, which is expected. To guarantee that all peaks are inside the confidence envelope it would be necessary too many Monte Carlo simulation and the confidence region would have to be constructed for a value close to one, instead of 90%.

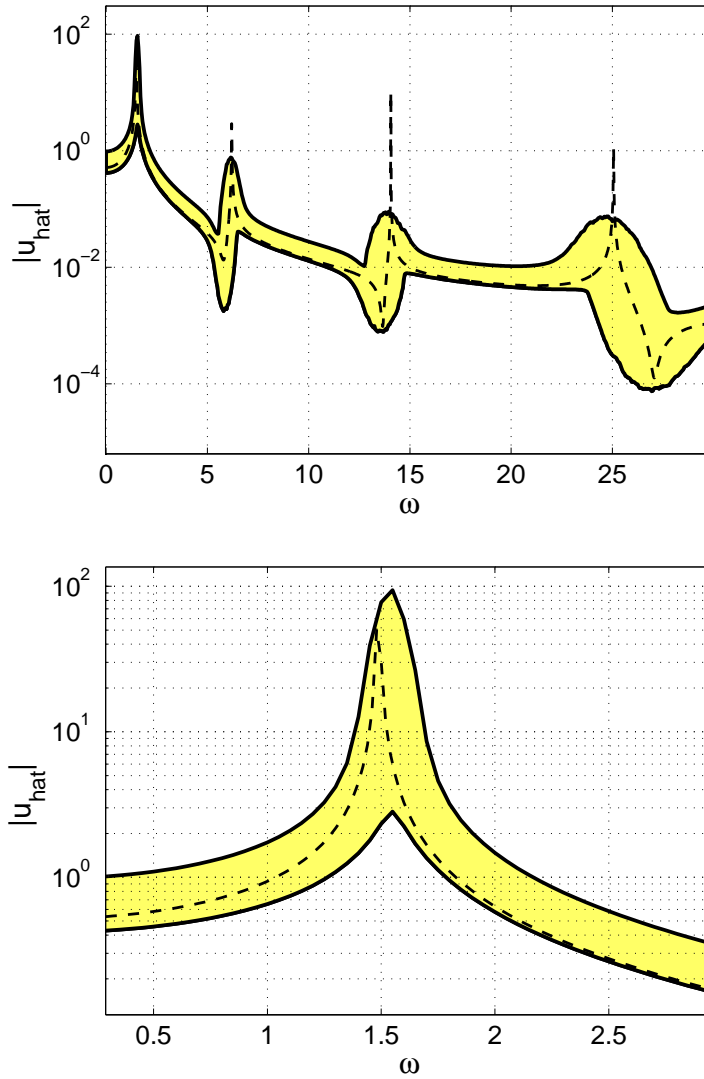


Figure 7 – Random response of the system at $\zeta = 0.3$ for $\delta = 0.2$. The yellow region corresponds to the 90% confidence envelope and the dashed line corresponds to the deterministic response for $u = 1$. (a) absolute value and (b) zoom close to the first natural frequency.

Figure 8 shows the same graphic of Fig. 7 for $\delta = 0.5$ and $u = 2$. At this point the confidence envelope is already too large, given results that might be out of our interest.

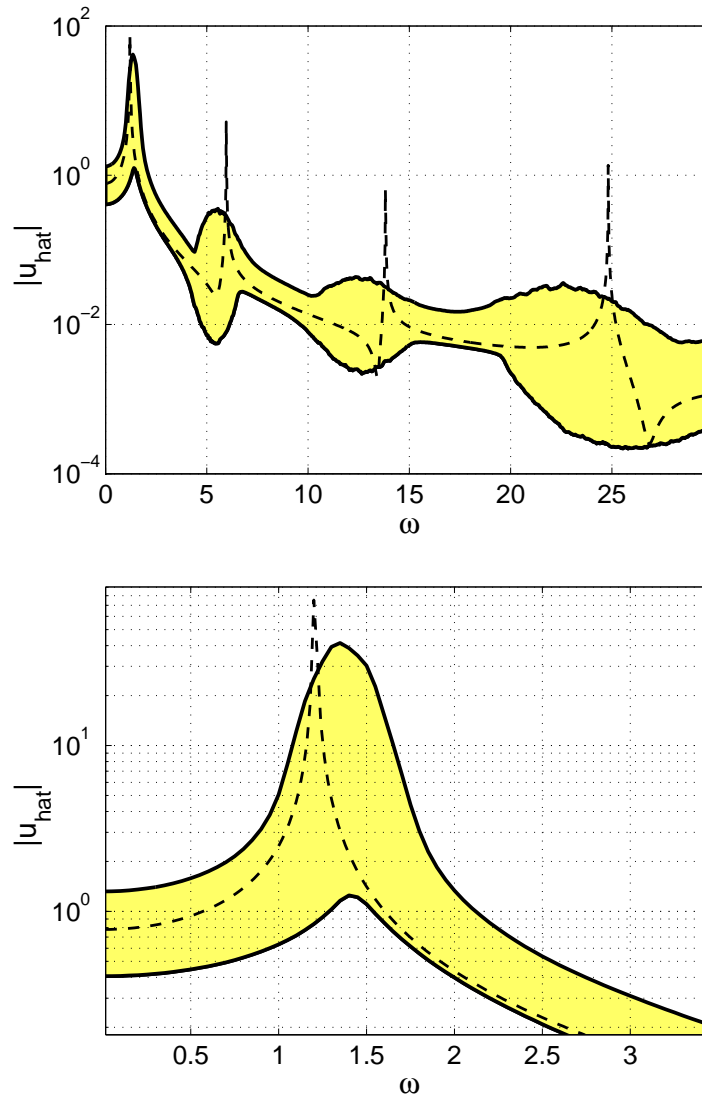


Figure 8 – FRF of the system at $\zeta = 0.3$ for $\delta = 0.5$. The yellow region corresponds to the 90% confidence envelope and the dashed line corresponds to the deterministic response for $u = 2$. (a) FRF and (b) zoom close to the first natural frequency.

CONCLUDING REMARKS

This paper has analyzed the dynamic of a structure excited by internal flow, where there are model uncertainties related to the stiffness of the system due to the lack of knowledge about the influence of the fluid on the system. These uncertainties have been modeled with the nonparametric probabilistic approach, and the stochastic system has been investigated. First, a procedure has been proposed to identify the dispersion parameter related to the probabilistic model. In such a procedure, the first natural frequency and the fifth percentile are used for the identification. Then, the spectrum of the response has been analyzed, showing how the confidence envelope changes for different values of the dispersion parameter.

REFERENCES

- [1] T. G. Ritto, C. Soize, R. Sampaio, Nonlinear dynamics of a drill-string with uncertain model of the bit-rock interaction, *International Journal of Non-Linear Mechanics* 44 (8) (2009) 865–876.
- [2] M. P. Paidoussis, *Fluid-Structure Interactions: Slender structures and Axial Flow*, Vol. 1, Academic Press, London, United Kingdom, 1998.
- [3] C. Soize, A nonparametric model of random uncertainties for reduced matrix models in structural dynamics, *Probabilistic Engineering Mechanics* 15 (2000) 277–294.
- [4] E. Jaynes, *Probability Theory: The Logic of Science*, Vol. 1, Cambridge University Press, Cambridge, UK, 2003.

RESPONSIBILITY NOTES

The authors are the only responsible for the printed material included in this paper.

ACKNOWLEDGEMENTS

The authors acknowledge the financial support of the Brazilian agencies CNPQ, CAPES, and FAPERJ.

SHAPE FUNCTIONS

The local coordinate is defined as $\xi = x/l_e$.

$$\mathbf{N} = [N_1 \ N_2 \ N_3 \ N_4], \quad (23)$$

where

$$\begin{aligned} N_1 &= 1 - 3\xi^2 + 2\xi^3, \\ N_2 &= l_e(\xi - 2\xi^2 + \xi^3), \\ N_3 &= 3\xi^2 - 2\xi^3, \\ N_4 &= l_e(-\xi^2 + \xi^3). \end{aligned} \quad (24)$$

Rotor-bearing system characterization by dynamic stiffness with a magnetic actuator as source of excitation

Helio Fiori de Castro¹, Jens Bauer², Nicklas Norrick², Katia Lucchesi Cavlaca¹ and Richard Markert²

¹ Department of Mechanical Design, Faculty of Mechanical Engineering, University of Campinas, R. Mendeleiev, 200, Cidade Universitária "Zeferino Vaz" Distrito de Barão Geraldo 13083-970 Campinas-SP Brasil

² Institute of Structural Dynamics, Department of Mechanical Engineering, Technische Universität Darmstadt, Petersenstr. 30, 64287 Darmstadt, Germany

Abstract: Important parameters in the rotating machine model, as the dynamic stiffness of the rotating system supported by journal bearings, can be determined through the dynamic system response to an excitation force (synchronous or nonsynchronous). The dynamic stiffness has direct relation with the phenomenon of fluid-induced instability, generally associated to hydrodynamic bearings of fixed geometry, because it allows determining the threshold of the instable motion. This kind of instable motion occurs due to precessional orbits in the rotor-bearing system. This instability is called "oil whirl" or "oil whip". The oil whirl phenomenon occurs when the journal bearings are lightly loaded and the shaft is whirling at a frequency close to one-half of rotor angular speed. When the rotational speed of the rotor reaches approximately twice the natural frequency (first critical speed) the oil whip phenomenon occurs and remains even if the rotor rotational speed increases. Its frequency and vibration mode corresponds to the first critical speed. The nonlinear motion due to the fluid-induced instabilities can be very harmful to the system, especially the oil whip phenomenon, what confirms the necessity to foresee the threshold of the instable motion. Therefore, the dynamic stiffness, which is defined as the machine's measure of resistance to instability, is an important parameter to preview this dynamic behaviour. This research proposes an experimental analysis of Jeffcott flexible rotor. The source of non-synchronous excitation is an electro-magnetic actuator, which means a non-contact excitation. This research presents a contribution for the rotating machine design area, as it intends to determine the threshold of instability, introducing the system dynamic stiffness as a controlled parameter in instability control.

Keywords: rotordynamics, journal bearing, dynamic stiffness, magnetic actuator

NOMENCLATURE

D = equivalent system damping, Ns/m

F = excitation force vector, N

K = dynamic stiffness vector, N/m

M = equivalent system mass, kg

R = displacement vector, m

S = equivalent system stiffness, N/m

j = imaginary constant

Greek Symbols

λ = the ratio of the mean circumferential velocity of the fluid.

Ω = shaft rotational speed, Hz

ω = excitation frequency, Hz

INTRODUCTION

The interaction between the rotating system and the oil film in a hydrodynamic bearing causes instable dynamic behaviour (see Gash et al., 2002, and Muszynska and Bently, 1989), which is characterized by a sub-synchronous forward precessional vibration. This behaviour is known as oil whirl and oil whip and was discovered by Newkirk (1924, 1925) and it has been analysed by Lund and Saibel (1967), Muszynska (1986 and 1988), Muszynska and Bently (1989), Crandall (1990), Childs (1993), Gasch et al. (2002) and Castro et al. (2006 and 2008).

The fluid-induced instabilities are known as self-exciting vibrations of a rotor-bearing system. Due to oil whirl, the shaft vibrates in a frequency close to half of the rotational speed. When the rotational speed reaches twice the first natural frequency, the oil whip instability starts, which can be severely harmful for the rotor-bearing system. In this case, the vibration frequency (or self-excitation frequency) is equal to the first natural frequency.

In order to estimate the instability threshold, Muszynska and Bently (1990) proposed the calculation of the rotor-bearing system dynamic stiffness, through a non-synchronous excitation. In that case, the system presents an instable motion when the real and the imaginary parts of the dynamics stiffness are simultaneously null.

On the other hand, mathematical models were developed in order to represent real machines with considerable confidence. Therefore, several researches were performed to determine better models for rotating machinery such as turbo generators and multi stage pumps, which are horizontal rotating machines of high load capacity. Some of these

numerical simulations were developed to study cylindrical hydrodynamic bearings by Capone (1986 and 1991), where the orbits of the shaft in the bearings were obtained, considering a nonlinear hydrodynamic force model.

Castro et al. (2006) considered this nonlinear hydrodynamic journal bearing model to simulate fluid-induced instabilities (oil whirl and oil whip), verifying that this model can numerically represent the dynamic behaviour of a rotor under fluid-induced instabilities. After that, Castro et al. (2008) analysed the nonlinear aspect of this simulation and compared it to experimental results.

Afterwards, the authors applied the concept of dynamic stiffness (see Bently et al., 1998, and Muszynska and Bently, 1990, Muszynska, 1995) to analyse fluid-induced instability considering nonlinear effects. This research proposes the analysis of a flexible rotor with a central disc, assuming unbalance excitation. An experimental analysis is accomplished on a test rig. The source of non-synchronous excitation is an electro-magnetic actuator, which means a non-contact excitation.

DYNAMIC STIFFNESS ANALYSIS IN ROTOR-BEARING SYSTEMS

The dynamic stiffness, which can be obtained by the ratio between the non-synchronous excitation force vector \mathbf{F} and the displacement (system response) vector \mathbf{R} , see Eq. (1), has direct relation with the phenomenon of fluid-induced vibration, generally associated with fixed geometry hydrodynamic bearings.

$$\mathbf{K} = \frac{\mathbf{F}}{\mathbf{R}} \quad (1)$$

The hydrodynamic force can be split into two parts: a radial force, which acts in the displacement direction of the journal into the bearing, and a tangential force that acts in the fluid flow direction. Both the forces are proportional to the displacement of the shaft into the bearing, related to the stiffness in the radial direction, because the fluid acts as a spring in this direction, and a tangential stiffness in the fluid flow direction, as can be seen in Fig. 1.

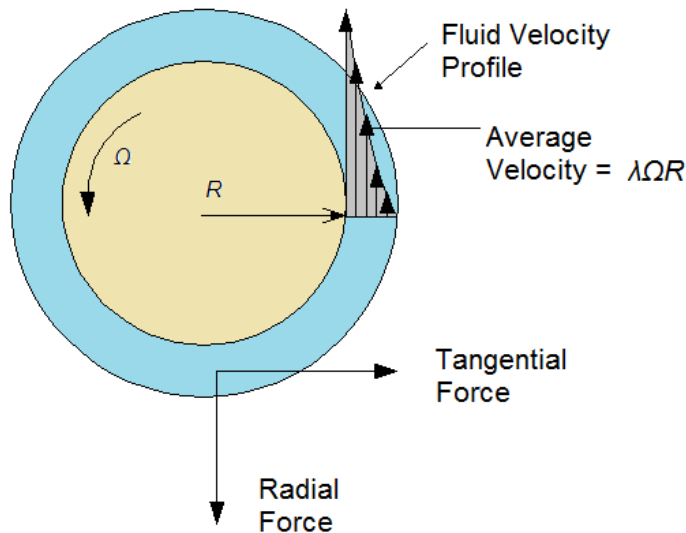


Figure 1 – Fluid Velocity Profile and hydrodynamic force components.

Due to the supporting hydrodynamic forces action, the inertia of the rotating system and of the fluid oil damping, the shaft moves around its equilibrium position, describing an orbit. The fluid-induced instability of this rotating system depends on the relation between these parameters (radial and tangential forces, inertia of the system and viscous damping of the oil).

The dynamic stiffness constitutes, therefore, a concept that allows to describe this relation regarding to the phenomena caused by each of these parameters:

$$\mathbf{K} = S - M\omega^2 + jD\omega - jD\lambda\Omega = S - M\omega^2 + jD(\omega - \lambda\Omega) \quad (2)$$

Where: S is the rotor-bearing system stiffness, $-M\omega^2$ is the mass equivalent stiffness, $jD\omega$ is the damping equivalent stiffness and $-jD\lambda\Omega$ is the tangential stiffness. M is the rotor-bearing equivalent system mass, D is the rotor-bearing equivalent damping, ω is the whirl frequency, which can be different from the shaft rotational speed Ω , j is the imaginary constant, which means that the complex terms are perpendicular to the real terms and λ is the ratio of the

mean circumferential velocity of the fluid, which is around 0.4 and 0.5, according to previous references (Muszynska, 1986, 1988, 1995).

The real part of the dynamic stiffness is the direct dynamic stiffness and the imaginary part is the quadrature dynamic stiffness. The dynamic stiffness is related to the system response by a non-synchronous perturbation. The direct dynamic stiffness is characterized by a parabolic curve, while the quadrature dynamic stiffness is characterized by a straight line.

There are some cases where the dynamic stiffness diverges from a parabolic or straight line shapes. One of the main reasons for these discrepancies is the system nonlinearity (see Muszynska and Bently, 1990 and Muszynska, 1995).

When the response of the system can be obtained from a controlled perturbation, it is possible to determine the dynamic stiffness for several constant rotational speeds. Comparing the real and imaginary parts of the dynamic stiffness, the relation that indicates whether the system is stable or not is defined or it indicates how close the system is from an instability state. When both direct and quadrature dynamic stiffness are null at together, the system motion tends to be unstable and its vibration amplitude increases significantly.

In order to obtain the dynamic stiffness, the system response needs to be filtered in the force excitation frequency. So, for a specific rotational speed, the rotor-bearing system is excited by first order harmonic wave signal, considering a excitation frequency range. In that way, the dynamic stiffness can be experimentally evaluated by the ratio between excitation and response for each excitation frequency.

EXPERIMENTAL SETUP

In rotordynamics, the application of an electro-mechanic actuator (shaker), to accomplish excitation in rotating machinery, usually causes some noise in the system response, mainly in high rotational speeds, due to the friction between the actuator journal and the rotating shaft. In order to avoid this effect, the utilization of an electromagnetic actuator is advisable. This is precisely the application of an external excitation force without contact, minimizing the excessive signal noise problem which can happen at high rotational speeds.

In this context, the electromagnetic actuator plays a significant role to solve this question, once this device generates the external excitation by electromagnetic force, without any kind of mechanical contact. Such electromagnetic forces are generated by permanent magnets or controlled electromagnets.

The electromagnetic actuator assembled in the test rig is shown in Fig. 2a. A scheme of the electro-magnetic actuator and its support is presented in Fig. 2b.

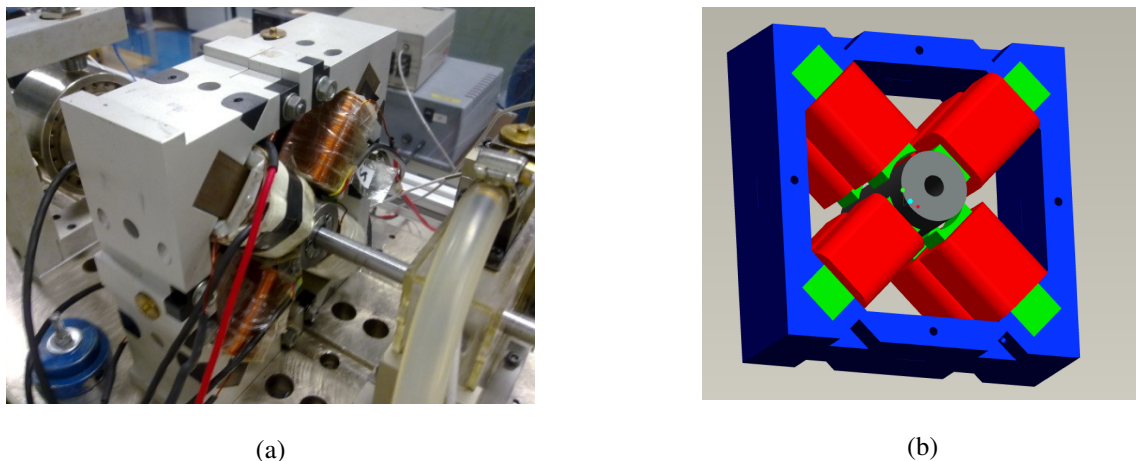


Figure 2. (a) Electromagnetic actuator assembly in the test-rig. (b) Electromagnetic actuator scheme

The experimental setup consists of two hydrodynamic bearings and one unbalanced mass assembled in the shaft middle (Fig. 3). The total length between the bearings is 600 mm. The shaft diameter is 12 mm. The concentrated mass consists of a disk of external diameter of 95 mm and length of 47 mm with mass of 2.3 kg. A pair of cylindrical hydrodynamic bearings is used to support the shaft, which are made of brass, with a radial clearance of 90 μm , bearing radius of 31 mm and bearing length of 20 mm. The bearings are lubricated with oil AWS 32.

To monitor the displacement of the shaft inside the bearings, two inductive proximity sensors are used immersed in the oil film in an angle of 45° with the horizontal direction. Other two inductive sensors are located over the lumped mass in horizontal and vertical directions. The magnetic field generated by the electromagnetic actuator is measured by hall sensors, so that it is possible to estimate the excitation force applied in the rotating system. The electromagnetic actuator directions are the same as the directions of the bearing proximity sensors. Figure 4 shows the actuator reference coordinates, which will be adopted for the tests.

In order to identify both bearings, the bearing close to the motor is called bearing 1, while the other bearing is bearing 2.

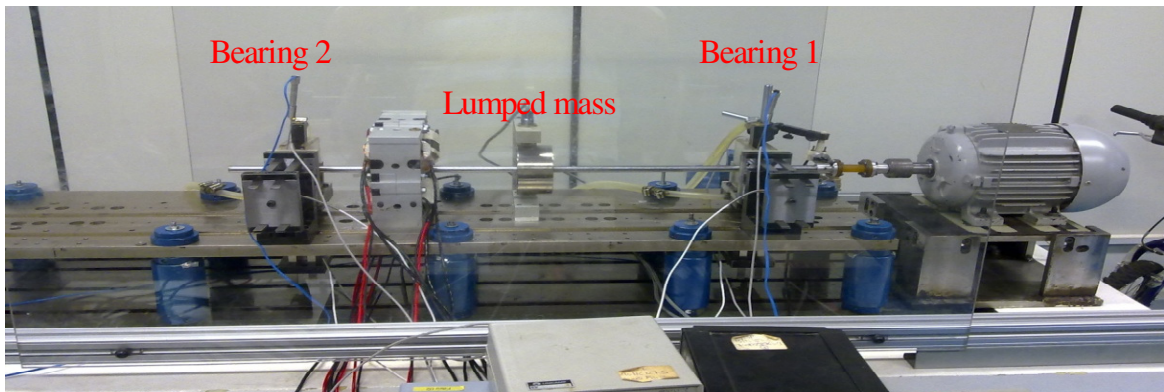


Figure 3. Experimental test-rig.

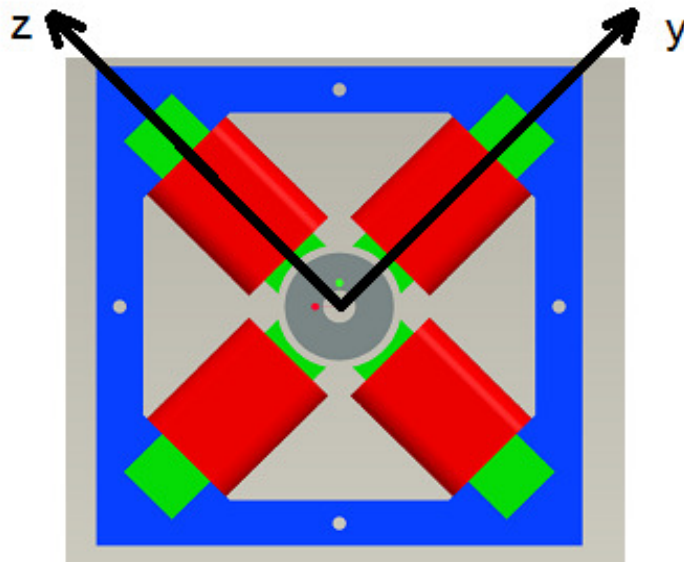


Figure 4. Actuator reference coordinates.

DYNAMIC STIFFNESS ESTIMATION

The system is tested in three different rotational speeds over the system natural frequency (22.5 Hz). These rotational frequencies are 30, 35, 40 Hz. The instability motion starts just above the rotational speed of 40 Hz, as can be seen in Fig. 5.

Therefore, the rotational speed variation considered in the tests is able to show the distance to the threshold of instability, which can be defined by the rotational speed at which both direct and quadrature dynamics stiffness cross zero at the natural frequency.

The excitation force amplitude and phase range with the excitation frequency are shown in Figs. 6 and 7 for excitation in y and z direction.

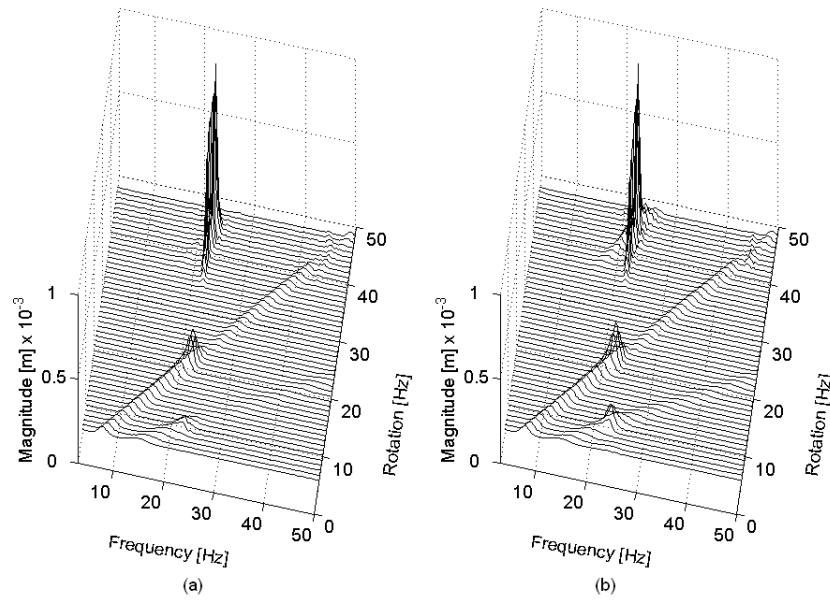


Figure 5. Waterfall plot of lumped mass precession in a run-down test through the instability region for concentrated mass: (a) horizontal displacement; (b) vertical displacement. Castro, et al (2008).

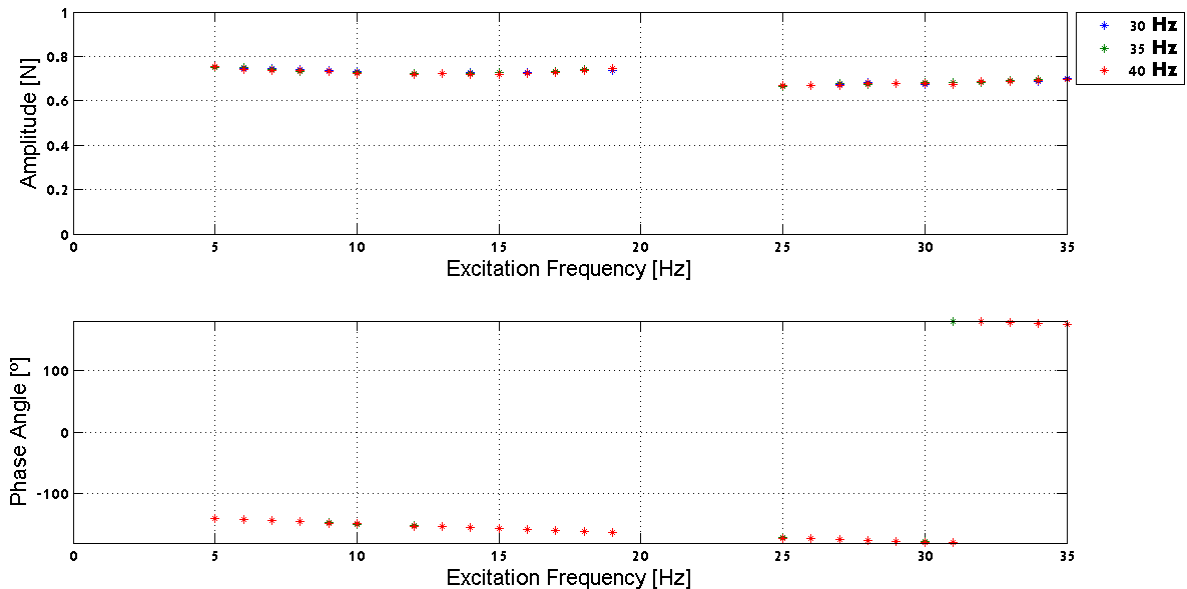


Figure 6. Excitation force amplitude and phase in y direction.

The force amplitudes and phase are constant for each excitation frequency. In this way, the system response can be analyzed for each frequency. Figure 8 presents the system response in z direction. The system responses are also carried out for both directions in each bearing and the lumped mass.

It is noted that there are small differences in the system response for different rotational speed when the excitation force approaches the first natural frequency of the rotor-bearing system (close to 22.5 Hz).

Considering all system responses and the excitation force, it is possible to estimate the dynamic stiffness for each rotational speed in both bearings and in the lumped mass for y and z direction. Figures 9, 10 and 11 show the dynamic stiffness for excitation in y direction in bearing one, two and lumped mass respectively. Similarly, Figs. 12, 13 and 14 present the dynamic stiffness in z direction.

The direct dynamic stiffness crosses the zero close to 22.5 Hz. This effect can be observed more clearly in the lumped mass dynamic stiffness in both directions. Considering Eq. 2, it can be concluded that when the direct dynamic stiffness crosses the zeros, it indicates system natural frequency.

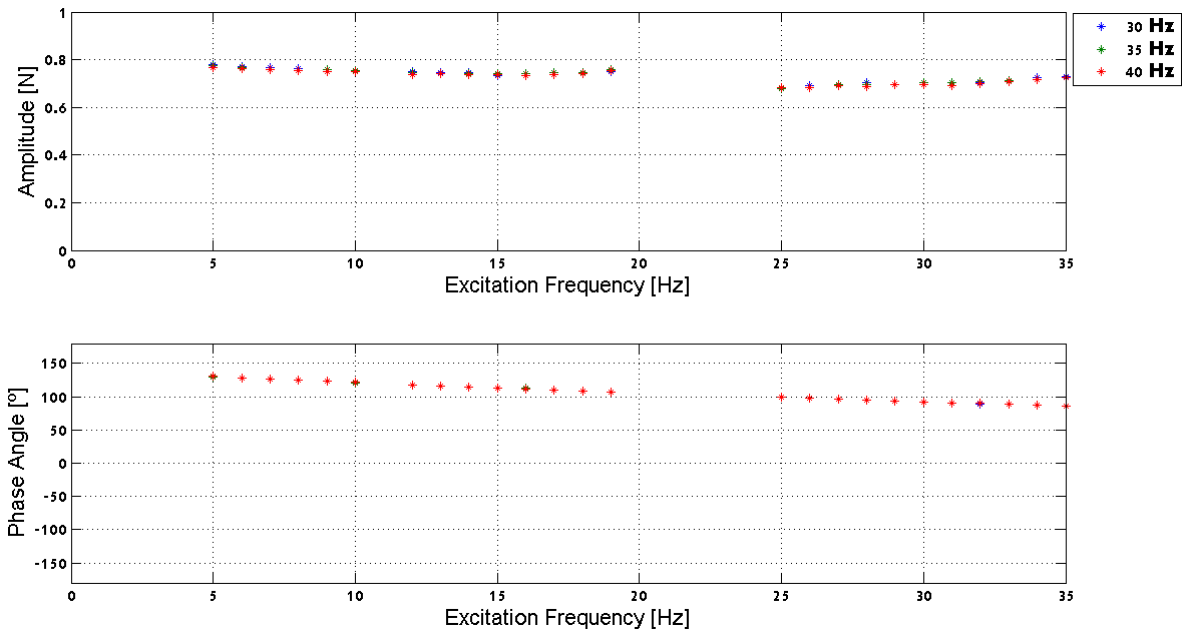


Figure 7. Excitation force amplitude and phase in z direction.

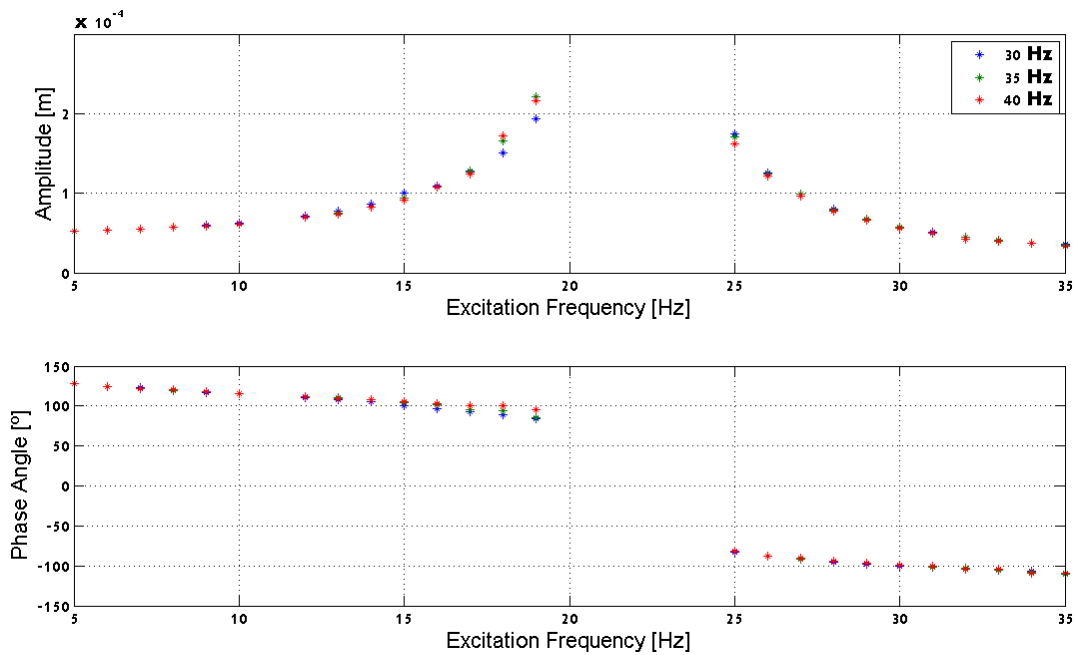


Figure 8. System response for lumped mass displacement in z direction.

It is also observed that the quadrature dynamic stiffness in the lumped mass has a similar behavior of the direct dynamic stiffness, but with significantly lower amplitude. It shows that the coupling between two orthogonal directions in the lumped mass is weak. Otherwise, the coupling in the bearing motion is important, and its quadrature dynamic stiffness has a behavior according to the imaginary part of Eq. 2.

For both excitation directions at a rotational speed of 30 Hz, the quadrature dynamic stiffness is zero for an excitation frequency close to 15 Hz (bearing 1 and 2 in y and z direction), showing that the margin of stability is close to 7.5 Hz (difference between the excitation frequencies where direct and quadrature dynamic stiffness are null). The evolution of this margin can be observed in the cases where the rotational speed increases. At a rotational speed of 35 Hz, the quadrature dynamic stiffness is null close to 17 Hz. As the direct dynamic stiffness is still null at 22.5 Hz, the margin of stability is 5.5 Hz. When the rotational speed is 40 Hz, the margin of stability is close to 3.5 Hz (the quadrature dynamics stiffness cross zero close to 19 Hz), and the system sub-synchronous motion starts to increase significantly (see Figs. 5).

Taking into account the margin of instability, the fluid circumferential average velocity ratio λ can be estimated in all cases between 0.4 and 0.5 (for rotational speed of 30 Hz λ is estimated to be 0.5, for 35 Hz it is 0.486 and for 40 Hz it is 0.475), which is in agreement with the previous literature, see Muszynska (1986, 1988, 1995).

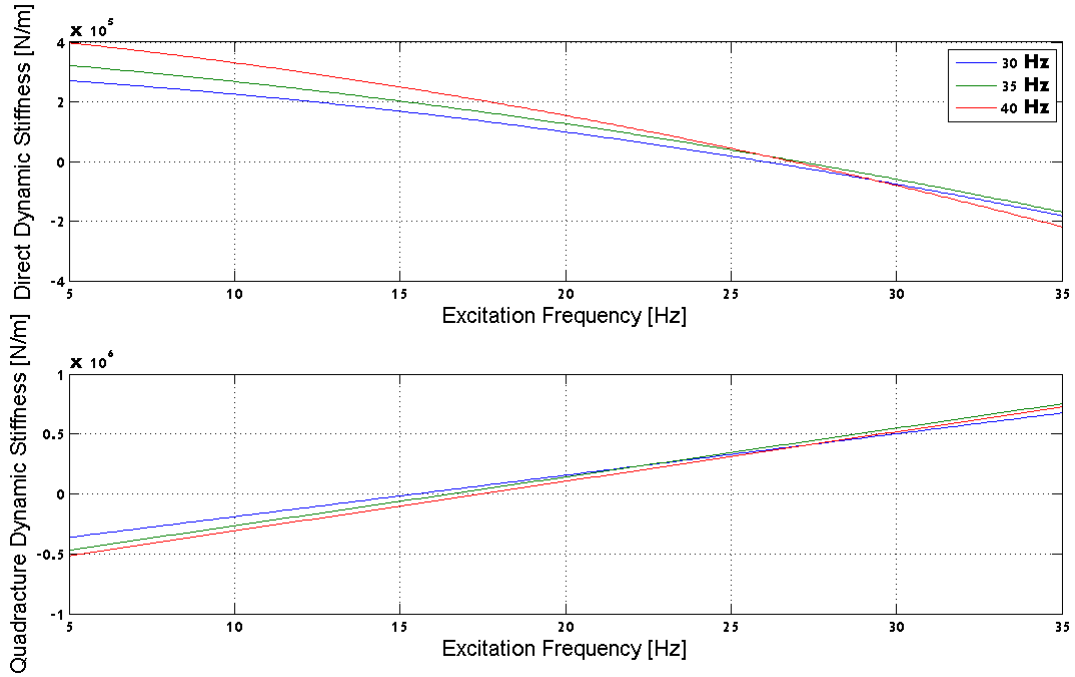


Figure 9. Dynamic stiffness for bearing 1 in y direction.

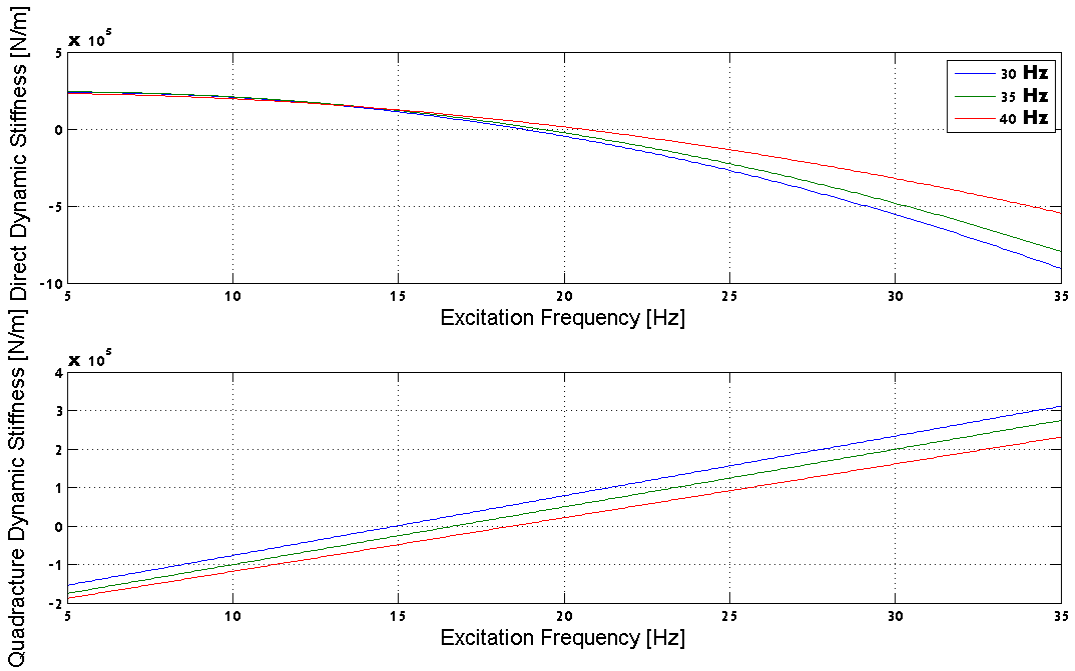


Figure 10. Dynamic stiffness for bearing 2 in y direction.

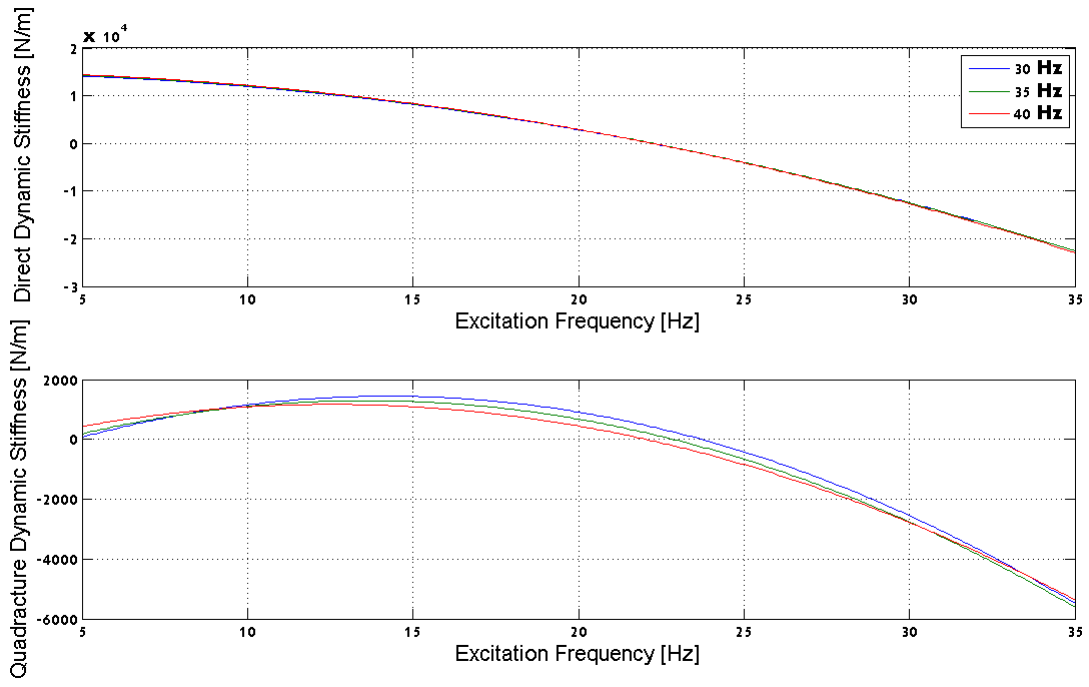


Figure 11. Dynamic stiffness for lumped mass in y direction.

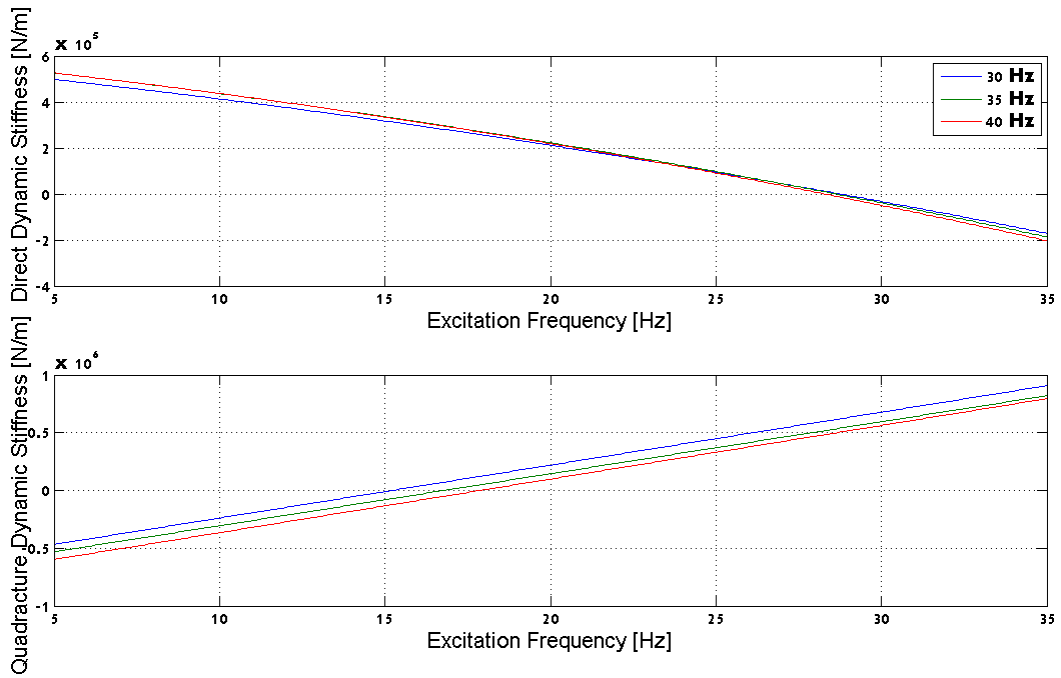


Figure 12. Dynamic stiffness for bearing 1 in z direction.

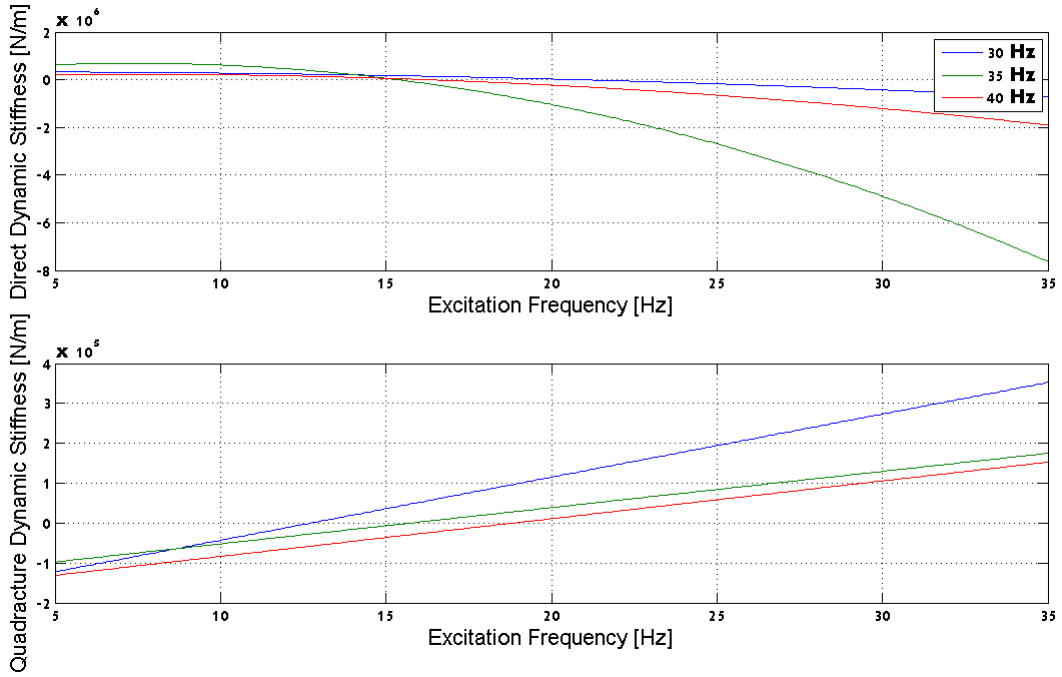


Figure 13. Dynamic stiffness for bearing 2 in z direction.

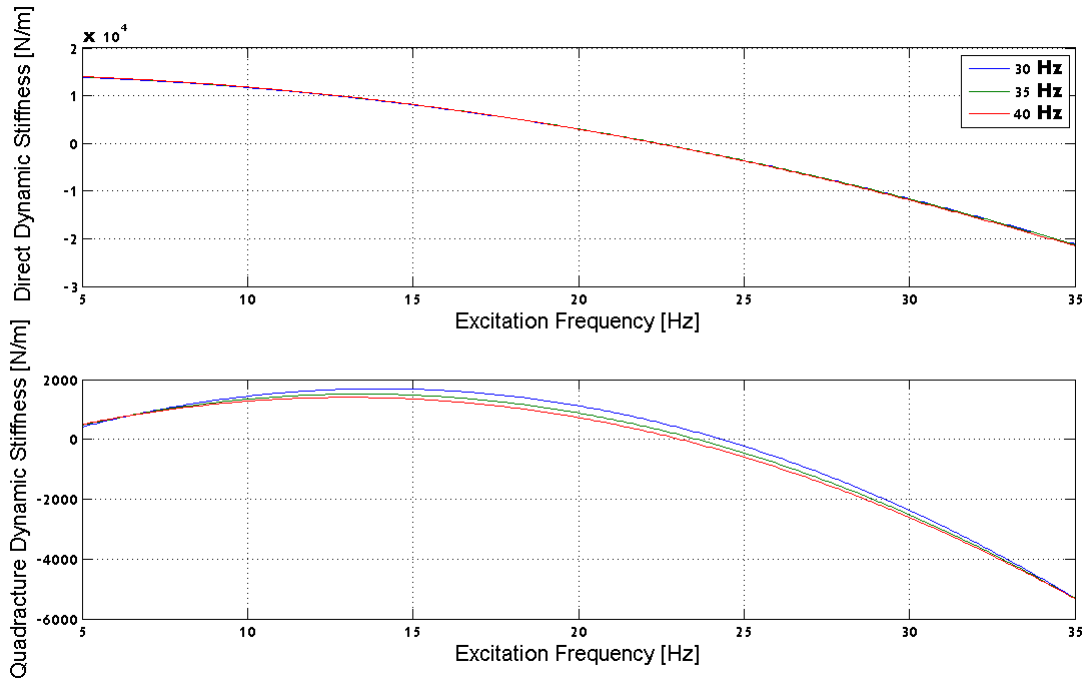


Figure 14. Dynamic stiffness for lumped mass in z direction.

CONCLUSIONS

The dynamic stiffness is estimated through the simulation of a non-synchronous perturbation in an experimental test-rig.

Considering the dynamic stiffness results, it is possible to foresee the instable motions threshold and eventually prevent this behaviour. So, the fluid circumferential average velocity ratio λ is an important parameter to determine the threshold of instability, because when both direct and quadrature dynamic stiffness cross the zero point at the same excitation frequency, the system is instable.

These tests demonstrate that the margin of stability steadily decreases as the rotor speed approaches the threshold of stability. It is also possible to estimate the fluid circumferential average velocity ratio λ , which is close to the values determined in the literature.

The paper novelty is the source of excitation as an electromagnetic actuator, avoiding contact between the rotating system and the actuator, while the rotor is running at constant speed and only the external excitation force frequency is varying.

ACKNOWLEDGMENTS

The authors gratefully thank the German and Brazilian research funding agencies DAAD and CAPES for their support of this work within the PROBRAL programme. The authors also thank CNPq and FAPESP for financial support.

REFERENCES

- Bently, D. E., Hatch, C., Jesse, R., Whiteley, J., "Dynamic Stiffness in whirl and whip", *Orbit*, first quarter, 1998, pp. 4-9.
- Castro, H F, Cavalca K L, Nordmann R., 2006, "Rotor-bearing system instabilities considering a non-linear hydrodynamic model", 7th IFToMM - Conference on Rotor Dynamics, Vienna, Austria, paper ID-136, pp. 1-10.
- Castro, H F, Cavalca K L, Nordmann R., 2008, "Whirl and whip instabilities in rotor-bearing system considering a nonlinear force model", *Journal of Sound and Vibration*, n. 317, pp. 273-293.
- Castro, F. F., Furtado, R. M., Cavalca, K. L., Pederiva, R., Butzek, N., Nordmann, R. "Experimental Performance Evaluation of Magnetic Actuator used in Rotating Machinery Analysis". *Journal of the Brazilian Society of Mechanical Sciences, ABCM – Rio de Janeiro*, v. 29 n. 1, 2007, pp. 1-10.
- Childs, D., 1993, "Turbomachinery Rotordynamics". Wiley-Intersciences, New York.
- Crandall, S., 1990, "Form Whirl to Whip in Rotordynamics", *Transactions of IFToMM 3rd International Conference on Rotordynamics*, Lyon, France, pp. 19-26.
- Gasch, R., Nordmann, R., Pfützner, H., 2002, "Rotordynamik". Springer, Berlin, 705 p.
- Lund, J. W., Saibel, E., 1967, "Oil whip whirl orbits of a rotor in sleeve bearings", *ASME Journal of Engineering for Industry*. n. 89, pp. 813-823.
- Muszynska, A., 1986, "Whirl and Whip – Rotor Bearing Stability Problems", *Journal of Sound and Vibration*, Vol. 110 n. 3, pp. 443-462.
- Muszynska, A., 1988, "Stability of Whirl and Whip in Rotor Bearing System", *Journal of Sound and Vibration*. Vol. 127 n. 1, pp. 49-64.
- Muszynska, A., Bently, D. E., 1989, "Fluid-Generated Instabilities of rotors", *Orbit*, Vol. 10, n. 1, pp. 6-14.
- Muszynska, A., Bently, D. E., 1990, "Frequency-swept rotating input perturbation techniques and identification of the fluid force models in rotor/bearing/seal systems and fluid handling machines", *Journal of Sound and Vibration*, Vol. 143 n. 1, pp. 103-124.
- Muszynska, A. , 1995, "Modal Testing of Rotors with Fluid Interactions". *International Journal of Rotating Machinery*, v. 1, n. 2, pp. 83-116.
- Newkirk, B. L., and Taylor, H. D, 1924, "Shaft Whipping", *General Electric Review*, Vol. 27, n. 3, pp. 169-178.
- Newkirk, B. L., and Taylor, H. D., 1925, "Shaft Whipping due to Oil Action in Journal Bearings", *General Electric Review*, Vol. 28, n. 8, pp. 559-568.

RESPONSIBILITY NOTICE

The author(s) is (are) the only responsible for the printed material included in this paper.

A Sensitivity Analysis of Active Noise Control Applied to Ducts with Higher-Order Acoustic Modes

Oliveira, E. L.¹, Duarte, M. A. V.², and Nunes, M. A. A.³

¹ Instituto Federal de Educação, Ciência e Tecnologia de Goiás, Rua 75, nº 46, Centro - Goiânia, GO.

² Universidade Federal de Uberlândia - Faculdade de Engenharia Mecânica, Av. João Naves de Ávila, 2121 - Campus Santa Mônica, Bloco 1M, Uberlândia - MG.

³ Universidade de Brasília - Faculdade do Gama, Área Especial 2 Lote 14, Setor Central Gama - DF.

Abstract: Active Noise Control (ANC), applied to industrial ducts, has the physical principle of destructive interference between a primary sound wave, that is generated by noise source, and a waveform of control. This results in the noise levels decrease. In ducts with large dimensions, the plane wave propagation is restricted to very low frequencies since the cutoff frequency is inversely proportional to the duct transversal dimensions. When the frequency of interest increases the propagation of plane waves disappear. This process makes acoustic modes of high order emerge. This characteristic causes an increase in the amount of acoustic sensors and actuators which are necessary to implement the active noise control. All of this makes this technique complex and very expensive. One proposed solution to this problem is the use of internal partitions in the duct in order to propagate plane sound waves, by doing that it is possible to reduce the number of sensors and actuators. As a result of this there is a large reduction in noise levels in the community (about 30 dBA at low frequencies). The aim of this work is to make a sensitivity analysis of an active control system in a duct with and without internal division. On those ducts there were some changes in their geometry and in the position of the actuators. The instrument used in this analysis was numerical simulations performed to obtain the acoustic behavior of the system with actuators located in optimal positions. After this, a technique of experimental design was used to study the effect of possible errors in the positioning of actuators and the duct geometry.

Keywords: Active noise control, higher-order acoustic modes, factorial experiments, sensitivity.

NOMENCLATURE

L = duct dimensions, m

S = cross section duct, m²

V = volume duct, m³

f = frequency, Hz

f_c = cutoff frequency, Hz

p = acoustic pressure, Pa

pos = position of source control, m

N = number of existing modes in the propagation

x(n) = input digital signal, V

y(n) = output digital signal, V

e(n) = error signal, V

c = speed of the sound in air, m/s

t = time, s

n = sample

Subscripts

x relative to duct width

y relative to duct height

z relative to duct length

d relative to duct

o relative to speed of sound

real real part f the control pressure

imag imaginary part f the control pressure

INTRODUCTION

Ducts for ventilation and exhaustion are common elements in the industries. The result is the production of noises that cause problems for employees and people living nearby. The effect of noise exposure leads to the deterioration of the sensory cells of the inner ear and it causes hearing loss in workers. In addition, there are heavy penalties for companies that generate noise to their neighborhood.

Most of the time, the sound produced by industrial ducts is composed by signal generated from the movement of the fan blades close to fixed structure. It produces a narrow-band noise (or pure tone) with the presence of harmonics. There is also aerodynamic bandwidth signal generated in regions of turbulent flow and vortices. Besides that, there is the noise of mechanical origin from the vibrations of structural components (Gerges, 2000). Most of the energy of that signal is present in the frequency range 0-500 Hz in which the systems of Active Noise Control (ANC) are efficient.

The ANC is an electroacoustic system used to attenuate a sound field through a signal of same amplitude and in opposite phase in relation to the unwanted signal. This wave produced in the ANC system is managed by an electronic unit, and it is played by control source (speaker) therefore, when it is combined with the noise generated by the primary source it results in the cancellation of both noises (Hansen et al, 2007).

The mono-channel technique has been applied to noise cancellation in ducts for decades. In these cases prevails ducts with small cross sections and wave propagation in the fundamental mode (plane wave). Figure 1 details the components of mono-channel ANC system. This process reduces the noise level and it achieves good results by using digital electronic to implement adaptive controls in real time. There are, also, sensors to adjust the control system and actuator that are used to cancel the acoustic signal (Farines, Fraga and Oliveira, 2000). It is possible to achieve a more effective application in industry, due the reduced costs of technological development nowadays.

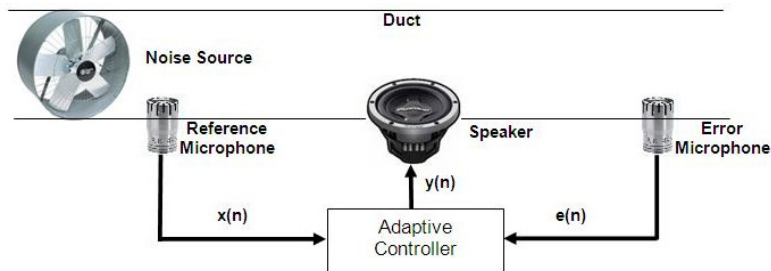


Figure 1 - Elements of a mono-channel ANC system.

Figure 1 shows the input signal $x(n)$ and the error signal $e(n)$, captured by microphones (sensors). The control signal $y(n)$ is delivered to the speaker (actuator). The function of the controller block is done by an adaptive digital filter that tries to identify the acoustic system. This filter is implemented by using a Digital Signal Processor (DSP). The aim is to ensure that the process of identification and noise cancellation happen in real time.

The design of the ANC system has a lot of variables or parameters that need to be optimized to achieve the best possible performance. Some of these variables are:

- cost function, representing the acoustic system;
- amount and location of control sources;
- quantity and location of error sensors;
- signal quality of the reference sensor;
- control algorithm;
- gain adjustment for sensors and actuators.

In addition, the ducts in industries generally have large cross sections (Zander and Hansen, 1992). This characteristic makes the propagation of sound waves in its interior, to present acoustic modes of higher-order. Thus, the ANC for industrial ducts are often developed from a multichannel control system. One of the rules says that the ANC for each mode to be controlled must be a system of control assigned to it. Thus, for each n modes exist n actuators and n sensors (Elliott, 2001). These systems use multiple sources of control (speakers) and multiple error/reference sensors (microphones). The design complexity increases even more due to greater interaction between each one of the many design variables.

Due to the difficulties of implementing a multichannel system in view the importance of exhaust systems in industries and considering that these devices are highly significant sources of noise, Nunes (2009) studied a methodology to be used in ducts with modes propagation of higher-order, where the active control is performed by mono-channel systems. Thus, the ANC was developed for plane waves to take advantage of the facilities and good results of this project. This methodology is characterized by the insertion of concentric ducts (for circular cross-section) or plate (for rectangular cross-section) inside the main duct. Thus the waves between the new internal cavities become plane.

Figure 2 shows a duct with length L_z and rectangular cross section L_y by L_x . This duct is the initial setting of the problem. In the duct of Fig. 3 the internal plate is placed so that the higher-order modes become plane within the new cavities.

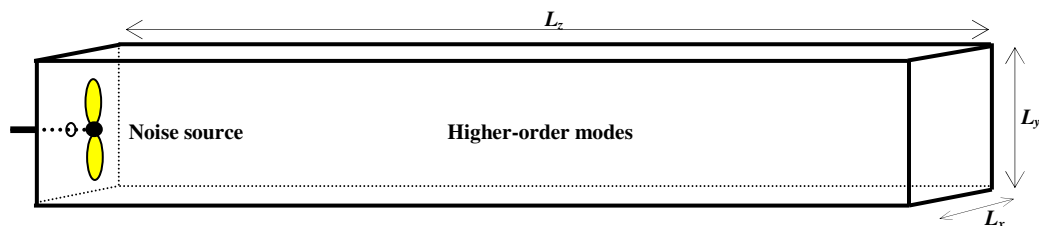


Figure 2 – Methodology for duct $L_z \times L_x \times L_y$ with rectangular cross section with duct without internal division.

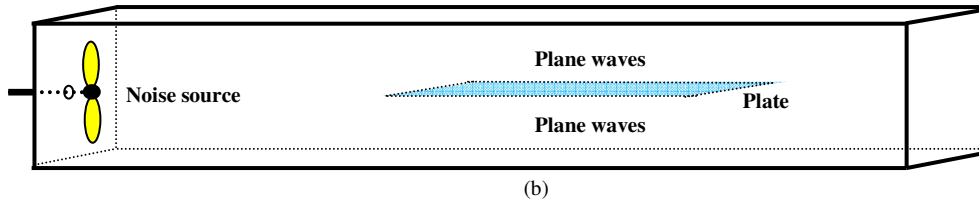


Figure 3 – Methodology for duct $L_z \times L_x \times L_y$ with rectangular cross section with internal plate division.

The ANC project (for industrial ducts) requires a large amount of sensors and actuators (working with high power due the size of the system to be controlled). The costs involved are high. Furthermore, the control efficiency is highly compromised if the position of sensors and actuators is not optimized, which requires the presence of highly specialized human resources (Snyder and Hansen, 1989). The control plane wave is already widely reported in the literature and scientific works, with most of the difficulties already overcome. Thus, applying this methodology the ANC project can provide the good cost/benefit relationship when applied to industrial ducts.

This paper used a rectangular duct to develop a few stages of the ANC project. The optimum position of the actuators were obtained with the use of tools Finite Element Method (FEM) and genetic algorithms (GA). Tests were conducted to a duct without dividing plate and a duct with dividing plate. It then attempts to verify how changes in the geometry of the duct and its cavities (which appear due to internal division) and small changes in the optimal position of actuator can influence the final attenuation of noise in the output duct. This analysis was done by using the technique experimental design, known as fractional factorial.

MODES OF SOUND WAVE PROPAGATION

The cutoff frequency of a duct defines the limit for the propagation of plane waves (fundamental mode). When the frequency of excitation of the system becomes high, its wavelength becomes comparable with the dimensions of the cross section of the duct. Then not only plane waves propagate, but also higher-order modes (Elliott, 2001).

It is given a rectangular uniform duct with length L_z and sides of the cross section L_x and L_y , as shown in Fig. 2. Noting that the largest cross sectional dimension is L_y and knowing which c_o is the speed of sound in air, it has the cutoff frequency for the duct given by:

$$f_c = \frac{c_o}{2L_y} \quad (1)$$

Using Eq. (1), the speed of sound in air (c_o) is 342 m/s in a rectangular uniform duct with length (L_z) of 6 meters and sides of 0.5 meter and 1 meters (L_x and L_y , respectively) has cutoff frequency value 171 Hz. The number of modes (N) that can propagate in a duct according to the frequency of excitation of the primary source is given in Eq. (2).

$$N = \frac{4\pi V_d}{3c_o^3} f^3 + \frac{\pi S_d}{4c_o^2} f^2 + \frac{L_d}{8c_o} f \quad (2)$$

where f is the frequency that excites the duct, S_d is the surface area of the duct walls, L_d is the sum of the lengths of the edges of the duct and V_d is the volume of the duct (Gerges, 2000).

The graph in Fig. 4 shows an exponential increase in the number of modes present in a duct as a function of excitation frequency. This behavior of the number of acoustic modes in the system increases the difficulty of the ANC project.

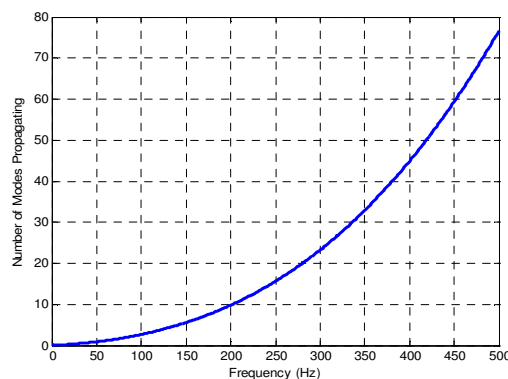


Figure 4 - Number of modes propagating in a rectangular duct with the frequency of the excitation signal.

Methodology used in system for ANC industrial ducts

Simulating such the duct using the ANSYS® can observe the form of propagation of an acoustic wave harmonic. The noise source performs the propagation of a harmonic signal. It represents a significant portion of the signal generated by industrial exhaust. The 2D simulation was performed using the acoustic element FLUID29. The excitation signal (noise source) has amplitude of 1 Pascal and frequency of 300 Hz (value above the cutoff frequency).

Can be observed through Fig. 5, the of higher-order modes. The primary source was installed in order to ensure asymmetry in acoustic system. It is more general situation.

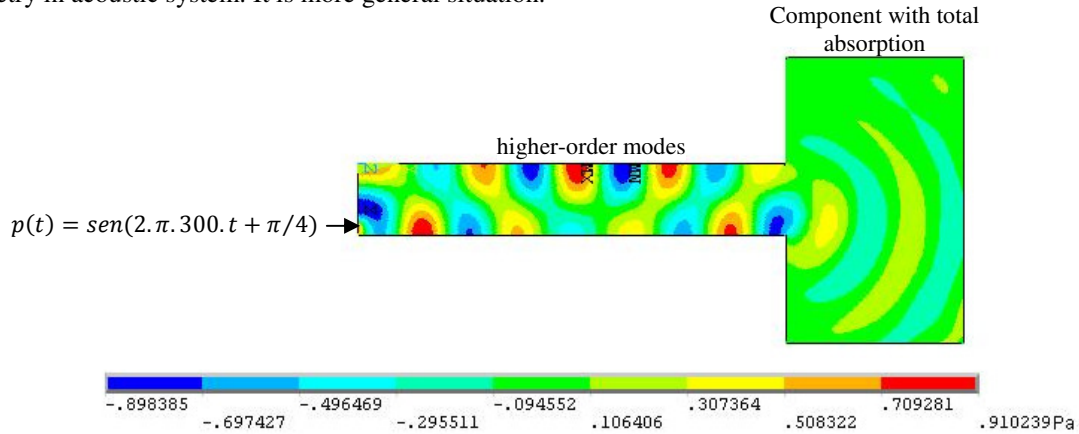


Figure 5 - Duct with excited harmonic 300 Hz presenting higher-order modes.

Starting from a duct with the wave propagation modes, the methodology will be applied to internal division and assembly of smaller cavities for the waves to become one-dimensional within them. In this case can use mono-channel active control. Figure 6 is the result of FEM simulation for the same duct. Observed plane waves in the internal cavities (internal division). The plate is 2 meters and was installed 3 meters from the primary source. The dashed rectangle shown in this figure defines the nodes to 1 meter from the duct exit. In this region it makes getting the sound pressure of the model to further define the Sound Pressure Level (SPL) in decibel (dB) for evaluation and optimization of active control system.

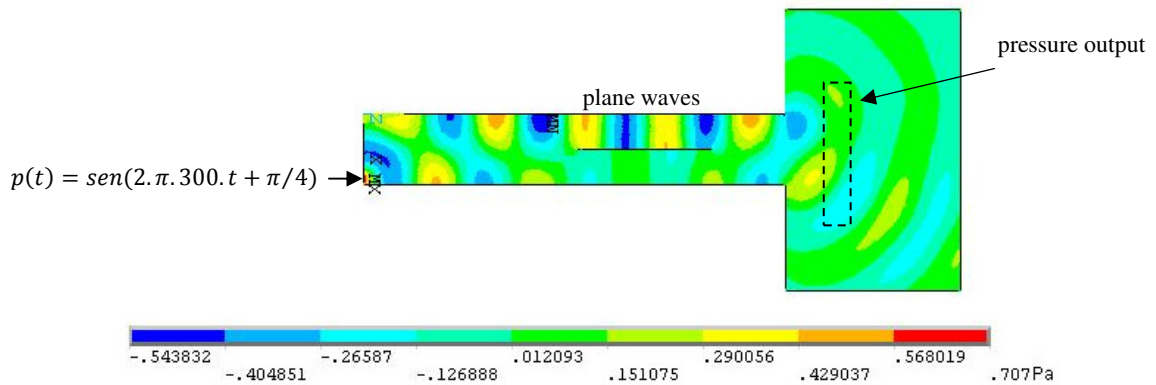


Figure 6 - Duct with excited harmonic 300 Hz presenting higher-order modes and plane waves.

SOUND PRESSURE AND LOCATION OPTIMIZATION

The first part of the study is to use the finite element model, developed for the duct mentioned above, to know the acoustic system. The next step of the ANC project is the definition of optimal position and value of control pressure to be delivered to the actuator to generate attenuated noise. The objective function in optimization is produced by using the FEM.

Nunes (2009) observed that the response surface associated with the acoustic system in question has the nonlinear behavior, with a large number of local minima. For this reason the option was to use a genetic algorithm (GA) specialist for the location of system parameters that minimize the sound pressure.

Genetic algorithms are probabilistic programs that require only local information at the point evaluated (fitness of individuals). They do not need derivatives or any other additional information (Holland, 1975). Therefore, genetic algorithms are excellent for optimizing discontinuous problems. Another great advantage of these algorithms is presented efficiency in locating the global solution.

In genetic algorithms the variables to be optimized are encoded into a chromosome of finite length. The terms individual and chromosome are synonymous and each represents a possible solution to the problem. So, being available a group of individuals (population of one generation), is set the capability of each in relation to the group, trying to select the most suitable for crossover. After performing crossover, each gene of each individual will be subject to any action of the mutation. Crossover and mutation are known as genetic operators. These genetic operators are active in individuals randomly (Serrada, 1996 and Gen, 2000).

The following will detail how each duct under study and each variable (gene) was treated in the developed genetic algorithm.

Duct without internal plate

The goal is to find the position and pressure control source that will generate the lowest sound pressure at the output duct. The average output pressure is converted into SPL and used as evaluation function (fitness) of the genetic algorithm. Figure 7 defines the elements that the genetic algorithm seeks to optimize the duct without a plate.

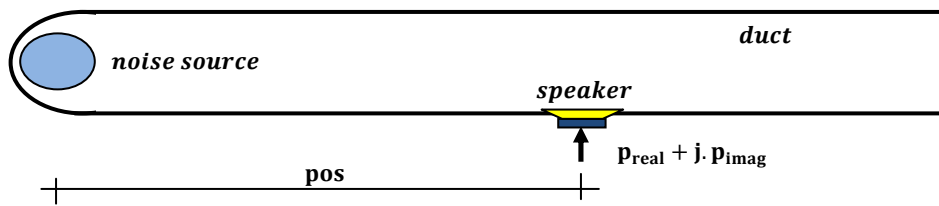


Figure 7 - Longitudinal section of simple semi-infinite duct and elements of mono-channel ANC system.

A harmonic input signal was used with frequency of 150 Hz (value below the cutoff frequency).

Table 1 shows the optimized parameters of the ANC system. The table also shows the value of SPL (one meter from the duct exit) achieved with the system operating at optimum values.

Table 1 - Parameters of the ANC system optimized with use GA - duct without division.

Description of Each Gene	Value
pos – Position control source (m)	3.201
p_{real} – Real part of the pressure control source (Pa)	0.5706181672
P_{imag} – Imaginary part of the pressure control source (Pa)	0.5749145699
SPL – Sound Pressure Level (without control) in the output duct (dB)	74
SPL_c – Sound Pressure Level (with control) in the output duct (dB)	32

Duct with internal plate

In this case are two mono-channel systems. One for each cavity of the duct. Thus, the goal is to find the source position and pressure control (real and imaginary) for each control source.

Figure 8 describes the elements that the genetic algorithm seeks to optimize the duct with internal plate.

The search range set for the optimization of the position of the sources of control was limited to position the plate in the main duct.

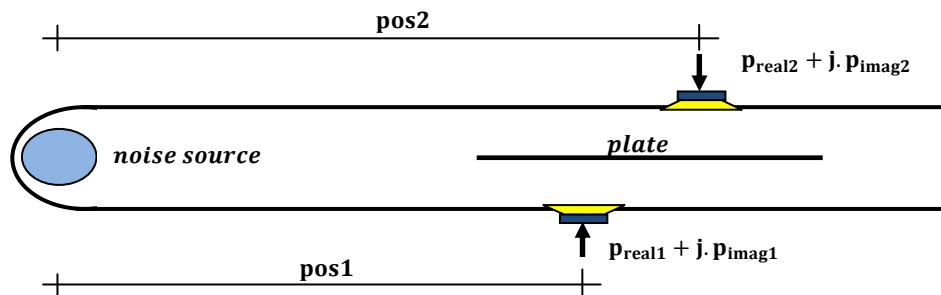


Figure 8 - Longitudinal section of semi-infinite duct with plate and elements of two mono-channel ANC systems.

A harmonic input signal was used with frequency of 210 Hz (value above the cutoff frequency). Table 2 shows the parameters of the two ANC systems. The value of SPL in dB is also shown

Table 2 - Parameters of the ANC system optimized with use GA - duct with division.

Description of Each Gene	Value
pos1 – Position control source 1 (m)	4.344
p _{real1} – Real part of the pressure control source 1 (Pa)	0.5960018889
P _{imag1} – Imaginary part of the pressure control source 1 (Pa)	0.5960018889
pos2 – Position control source 2 (m)	4.534
p _{real2} – Real part of the pressure control source 2 (Pa)	0.5732746162
P _{imag2} – Imaginary part of the pressure control source 2 (Pa)	0.5960018889
SPL – Sound Pressure Level (without control) in output duct (dB)	75
SPL _c – Sound Pressure Level (with control) in output duct (dB)	43

FRACTIONAL FACTORIAL DESIGN

In the experimental design, response is defined as the output of the system. It is the property that is interested in analyzing. In this particular case is the SPL at the exit of the duct. Factor is a variable that influences the response.

An experimental design is intended to provide information about the relationship of different factors. Want to explain what are the impacts of each factor in the response and how they relate to the level of interaction between factors. In this work we used the fractional factorial design.

According to Button (2005) and the factorial design is indicated for the initial phase of the experimental procedure when there is a need to define the most important factors and to study the effects on the response.

It is common to use only two levels for the factors of a factorial experiment. These levels are commonly represented by high (+) and low (-), and they generate 2^k experiments (Montgomery, 2001).

In a factorial design, where the number of factors is too large, the required number of experiments is too large. As the number of factors grows, the number of terms of higher orders is growing and its importance is less than the terms of lower orders. One way to solve this problem is to consider the interactions of higher order can be neglected. Thus, fewer experiments can be performed. In this case the lower order interactions are obtained. This is possible using the fractional factorial design. The fractional factorial design is among the most commonly used types of planning for product design and process improvement.

The fractional factorial design with four factors was fitted to the duct without dividing plate and the duct with plate. This design used eight experiments with two replicates. In the case of the duct without division, the replicates did not differ and was not necessary to calculate the experimental error. Tables 3 and 4 show the definition of the factors for each case studied. The factors defined as *inclination*, in fact, displacement of the plate (lateral plate or internal plate divider) vertically. Is that why these factors have units of meters.

Table 3 - Definition of levels associated with each factor for duct without internal division.

Description of Factor	-	+
A - Variation in length of duct, m	-0.100	+0.120
B - Variation in the position of the primary source, m	-0.035	+0.040
C - Variation in the position of the control source, m	-0.012	+0.015
D - Lateral inclination of the plate (bottom plate), m	-0.035	+0.025

Table 4 - Definition of levels associated with each factor for duct with internal division.

Description of Factor	-	+
A - Variation in length of duct, m	-0.100	+0.120
B - Inclination of the plate divider, m	-0.025	+0.035
C - Variation in the position of the control source, m	-0.012	+0.015
D - Lateral inclination of the plate (bottom plate), m	-0.035	+0.025

EVALUATION OF SENSITIVITY

The tools developed for acoustic analysis (FEM) and optimization (GA) of the ANC system was used to assess the sensitivity of defined factors to duct with and without dividing plates.

For each of the eight tests, the genetic algorithm needs to calculate the value of source pressure optimal control. This optimization aims at making the role of the adaptive algorithm that generates a pressure control in an ANC system. In practice this system is implemented with a dedicated processor known as DSP (Digital Signal Processor).

The experimental matrix and results for duct without partition are shown by Tab.5. Table 6 shows the matrix and results for the duct with internal plate. This table is shown the mean response given that there were three measures.

Table 5 – Experimental matrix for duct plate without division.

Test	Mean	A	B	C	D = A.B.C	Attenuation (dB)
1	+	-	-	-	-	49
2	+	+	-	-	+	44
3	+	-	+	-	+	38
4	+	+	+	-	-	50
5	+	-	-	+	+	42
6	+	+	-	+	-	53
7	+	-	+	+	-	47
8	+	+	+	+	+	42

Table 6 – Experimental matrix for duct plate with division.

Test	Mean	A	B	C	D = A.B.C	Mean Attenuation (dB)
1	+	-	-	-	-	37.33
2	+	+	-	-	+	35.00
3	+	-	+	-	+	37.00
4	+	+	+	-	-	40.33
5	+	-	-	+	+	40.33
6	+	+	-	+	-	40.33
7	+	-	+	+	-	35.33
8	+	+	+	+	+	33.33

By using the fractional factorial D factor was obtained by the product of the other three factors. The test results are presented below.

Duct without plate

Table 7 shows the result of fractional factorial design for a duct without internal plate. Through the column main effect is clear that the most significant factor is the lateral inclination of the plate (D). Factors length of duct (A) and position of the primary source (B) are also significant.

Table 7 - Results of fractional factorial design for a duct without plate (results in dB).

Mean	Main Effects				Interaction of Two Factors		
	A	B	C	D	AB	AC	BC
45.63	3.25	-2.75	-0.75	-8.25	0.25	-0.25	-0.25

In this analysis, using the input signal frequency of 150 Hz, the position of the control source (C) had less relevance. The interrelationship of effects (second order effect) was also low relevance in this analysis.

Duct with plate

Table 8 shows the result of fractional factorial design for a duct with duct partitioned. Shown are the results obtained and the standard errors due to replications. Through the columns main effects is clear that the factors inclination of the plate divider (B) and lateral inclination of the external plate (D) are the most important. However, the interaction between the factors inclination of the plate divider (B) and position of the source control (C) occurs significantly in this project.

It is important to mention that when a range of a factor (value \pm error) contains zero, it has little or no importance in the analysis. Due to the range obtained for factor A, C, AB and AC, its effects can be disregarded.

Table 8 - Results of fractional factorial design for a duct with plate (results in dB).

Mean	Main Effects				Interaction of Two Factors		
	A	B	C	D	AB	AC	BC
37.38 \pm 0.57	-0.25 \pm 1.13	-1.75 \pm 1.13	-0.08 \pm 1.13	-1.92 \pm 1.13	0.92 \pm 1.13	-0.75 \pm 1.13	-4.25 \pm 1.13

In this analysis, using the input signal frequency of 210 Hz, the position of the control source (C) had less relevance acting alone.

CONCLUSION

This study treats of some concepts used in systems ANC with the techniques and new methodologies of development of those projects. Furthermore, an evaluation of sensitivity of an ANC was made in a duct with internal plate to increase the cutoff frequency the acoustic system. Duct without plate (conventional ANC) was also analyzed. The experimental analysis was based on fractional factorial design. The following design variables: duct length, position of the actuators, position of the noise source, inclination of the external plate and inclination of the internal plate. Those variables or factors were analyzed acting alone or combined. First, numerical simulations were performed to obtain the acoustic behavior of the system with actuators installed in optimal positions. After this, a technique of fractional factorial was used to study the effect of possible changes in the positioning of actuators and the duct geometry has on noise levels measured in the community. An important conclusion of this study is the high sensitivity of two variables: inclination of external plate and inclination of the internal plate. Some results were evaluated and shown to be valuable for these control systems, serving as a starting point for an ANC project.

ACKNOWLEDGMENTS

The authors would like to thank CAPES for their financial support.

REFERENCES

- Button, S. T., 2005, "Metodologia para Planejamento Experimental e Análise de Resultado", São Paulo, Universidade Estadual de Campinas.
- Elliott, S. J., 2001, "Signal Processing for Active Control", Academic Press.
- Farines, J.M., Fraga, J. S. and Oliveira, R. S. 2000, "Sistemas de Tempo Real", Florianópolis, Universidade Federal de Santa Catarina.
- Gen, M. A., 2000, "Genetic Algorithms and Engineering Optimization", John Wiley & Sons.
- Gerges, S. N., 2000, "Ruído: Fundamentos e Controle", Editora UFSC.
- Hansen, C.H., Qiu, X., Petersen, C., Howard, C. and Singh, S., 2007, "Active Noise and Vibration Control System Design Considerations", *Mechanics*, 26(2), pp. 37-46.
- Havelock, D., Kuwano, S., and Volander, M., 2008, "Handbook of Signal Processing in Acoustics (Vol. 1)". Springer Science.
- Holland, J. H., 1975, "Adaptation in Natural and Artificial Systems", London: University of Michigan Press.
- Montgomery, D.C, 2001, "Design and Analysis of Experiments", 5 ed., John Wiley & Sons.
- Nunes, M. A. A., Duarte, M. A. V. and Teodoro, E. B., 2009, "Component Mode Synthesis Methodology in Ducts Acoustic Modal Analysis", *Proceedings of the XIII International Symposium on Dynamic Problems of Mechanics (DINAME)*, ABCM, Angra dos Reis, RJ, Brazil.
- Serrada, A. P., 1996, "Uma Introducción a la Computación Evolutiva", España: Universidade de Oviedo.
- Snyder, S. D. and Hansen C. H., 1989, "Active Noise Control in Ducts: Some Physical Insights", *Journal of the Acoustical Society of America*, 86 (1).
- Zander, A.C. and Hansen, C.H., 1992, "Active Control of Higher-Order Acoustic Modes in Ducts", *Journal of the Acoustical Society of America*, 92, pp. 244-257.

RESPONSIBILITY NOTICE

The authors are the only responsible for the printed material included in this paper.

Study of Elastic Band-Gaps in Finite Periodic Structure Using Finite Element Models

P. B. SILVA¹, J. R. F. ARRUDA¹, and A. L. GOLDSTEIN¹

¹ DMC, Faculty of Mechanical Engineering, UNICAMP. Rua Mendeleev, 200, Campinas, SP, Brazil.

Email: pri.brands@gmail.com

Abstract: Many researchers have investigated the wave propagation through periodic media and the band gap effect, in general with applications in electromagnetic and acoustic fields. This paper is primarily concerned with structural wave propagation effects in the audio frequency range. A finite element model is used to build and analyze finite periodic structures. The analytical spectral element for periodic rods is also developed and the structure dynamic response is predicted. The existence of the band gaps in the dynamic responses is observed. Finally, an experimental test is performed and the limitations of each methodology are discussed.

Keywords: *periodic structures, phononic crystals, finite element, waveguides, isolators*

NOMENCLATURE

A = cross-sectional area, m²
c = longitudinal wave speed, m/s
E = Young's module, N/m²
F = force, N
u = displacement, m
k = wavenumber, m
L = length, m
q = external load, N
[M] = mass matrix, kg
[K] = stiffness matrix, N/m
[C] = damping matrix, N.s/m
[D] = dynamic stiffness matrix, N/m
[T] = transfer matrix
{F} = force vector, N

{u} = displacement vector, m
E_{size} = element size, m
TR = Transmissibility, dB
SEM = Spectral Element Method
FEM = Finite Element Method

Greek Symbols

ε = normalized wavenumber,
dimensionless
ρ = density, kg/m³
λ = wavelength, m
η = internal loss factor,
dimensionless

ω = frequency, Hz

Subscripts

b relative to boundary
e relative to element
i relative to inclusion
m relative to matrix
n relative to n-th
1 relative to first
2 relative to second

Superscripts

a relative to applied force

INTRODUCTION

In recent years, many studies have investigated the phenomenon of wave propagation in composite materials with dielectric or elastic properties which are periodic functions of the position, with a period comparable to the wavelength of the corresponding field (Sigalas et al., 2005). This study was started by Floquet, in 1883, when he proposed analytical solutions for Mathieu's one-dimensional equation. Then, Rayleigh, in 1887, studied a continuous periodic structure considering a stretched string with a periodic and continuous variation of density along its length and undergoing transverse harmonic vibration (Mead, 1996). This work may be applied to any simple periodic structure whose wave behavior could be described by a second order differential equation, and it revealed the band gap concept.

The geometric interpretation of the wave diffraction phenomenon in periodic media came up from Brillouin's studies in 1953, when this French physicist established the concept of Brillouin zones, spatial areas where wave behavior in periodic structures is fully described (Brillouin, 1953).

Investigations concerned with the propagation of electromagnetic waves in artificial periodic structures of dielectric materials have established the concept of *photonic crystals*. The interest in such materials was to investigate the existence of forbidden frequency bands (band gaps) in which electromagnetic modes, spontaneous emissions and zero-point fluctuations are all absent. The mathematical analogy between electromagnetic waves and structural vibrations stimulated the search of corresponded band gaps produced by elastic waves propagation (Vasseur et al., 1998). There are two terms commonly used to denominate these materials with periodic configurations subjected to elastic wave propagation: *phononic crystals* and *sonic crystals*. The first is usually used for artificial crystals where the host material may be an elastic solid. In a solid host material, longitudinal waves and transversal shear waves may exist and may be coupled. In contrast, *sonic crystals* are considered to be independent of the transversal waves, although the scatterers are typically made of solid materials placed in fluids (Miyashita, 2005).

This work intends to investigate the existence of band gaps at low frequencies - in the audio range - when longitudinal waves propagate in a periodic medium, which can potentially be useful in designing noise and vibration isolators. Particularly, the behavior of longitudinal waves propagating through a finite periodic material composed of

alternated layers of two materials is investigated. Initially, this phenomenon is investigated via the spectral element method (SEM) proposed by Doyle (1997) with the help of the software MATLAB®. In this case, the structure could be simply described analytically as a rod by the elementary rod theory. Later, finite element models were developed using the commercial software ANSYS®.

In the spectral element formulation, the dynamic stiffness matrix is obtained, instead of the standard wave propagation solution (propagation modes and wavenumbers). Thus, the proposed method can be easily combined with standard finite elements using a mobility approach. Moreover, differently from the FEM, in the SEM, the dynamic stiffness matrix is computed in the frequency domain, which allows the inertia of the distributed mass to be described exactly. Therefore, refining the mesh as the wavelength decreases is no longer necessary. Doyle (1997) has shown that SEM dynamic stiffness matrix corresponds to an infinite number of finite elements.

This paper is organized as follows: initially, the formulation of the spectral element method is reviewed and the spectral element is derived using the elementary rod. Then, the mathematical formulation behind the finite element method is detailed, and details of the experiments are discussed. Using an optimization tool from the MATLAB® package, information about material properties and defining an objective function concerning the frequency range for a desired forbidden gap, the geometric characteristics of the model are found. Afterwards, the numerical methodologies discussed are used to compute the forced response of a layered rod subject to uniform longitudinal force excitation. Finally, the numerical results are compared with those from experiments, thus validating the theoretical approaches.

SPECTRAL ELEMENT ANALYSIS OF PERIODIC STRUCTURES

Elementary Rod Theory

The elementary theory is the simplest available model to describe a rod. It assumes that the rod is long and slender, and it is only subjected to one-dimensional axial stress, as shown in Figure 1 1 (Doyle, 1997).

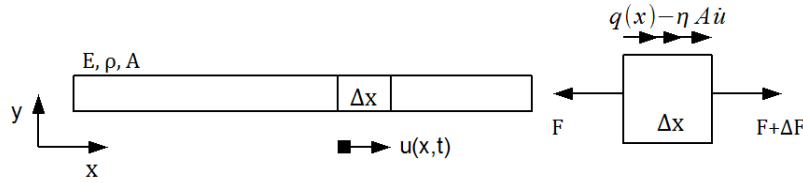


Figure 1 – Rod segment with loads.

The effect of Poisson's ratio is neglected, which implies that the displacement can be assumed as a function of the axial coordinate only. In this paper, we also consider that material properties are uniform and damping is absent. Thus, from the assumption that the material behavior is linear elastic, one-dimensional form of elastic equilibrium may be applied, yielding the following equation of motion for the rod:

$$c_0^2 \frac{\partial^2 u}{\partial x^2} - \frac{\partial^2 u}{\partial t^2} = 0, c_0 = \sqrt{\frac{EA}{\rho A}} \quad (1)$$

The spectral representation of Eq. 1 allows the corresponding solution to be written as:

$$\hat{u}(x) = Ae^{-ik_1 x} + Be^{-ik_1(L-x)} \quad (2)$$

where the coefficients A and B can be determined from the boundary conditions $\hat{u}(x=0)$, $\hat{u}(x=L)$ on the two-node element. Thus, the longitudinal displacement at the end positions can be written as:

$$\begin{aligned} \hat{u}(0) \equiv \hat{u}_1 &= A + Be^{-ik_1 L} & \hat{u}(L) \equiv \hat{u}_2 &= Ae^{-ik_1 L} + B \\ \hat{u}(x) &= \hat{g}_1(x)\hat{u}_1 + \hat{g}_2(x)\hat{u}_2 \end{aligned} \quad (3)$$

where:

$$\begin{aligned} \hat{g}_1(x) &= \frac{[e^{-ik_1 x} - e^{-ik_1(2L-x)}]}{\Delta} \\ \hat{g}_2(x) &= \frac{[-e^{-ik_1(L+x)} + e^{-ik_1(L-x)}]}{\Delta}, \Delta = [1 - e^{-i2k_1 L}] \end{aligned} \quad (4)$$

The forces and other related magnitudes could be written in function of the axial displacement or its derivatives, as follows:

$$\hat{F}(x) = EA[\hat{g}'_1(x)\hat{u}_1 + \hat{g}'_2(x)\hat{u}_2] \quad (5)$$

At each extremity of the rod, we obtain:

$$\hat{F}_1 = -\hat{F}(0) = -EA[\hat{g}'_1(0)\hat{u}_1 + \hat{g}'_2(0)\hat{u}_2]$$

$$\hat{F}_2 = +\hat{F}(L) = +EA[\hat{g}'_1(L)\hat{u}_1 + \hat{g}'_2(L)\hat{u}_2]$$

In the matrix form, we can write:

$$\begin{Bmatrix} \hat{\mathbf{F}}_1 \\ \hat{\mathbf{F}}_2 \end{Bmatrix} = EA \begin{bmatrix} -\hat{\mathbf{g}}'_1(\mathbf{0}) & -\hat{\mathbf{g}}'_2(\mathbf{0}) \\ \hat{\mathbf{g}}'_1(\mathbf{L}) & \hat{\mathbf{g}}'_2(\mathbf{L}) \end{bmatrix} \begin{Bmatrix} \hat{\mathbf{u}}_1 \\ \hat{\mathbf{u}}_2 \end{Bmatrix} = \begin{bmatrix} \hat{\mathbf{k}}_{11} & \hat{\mathbf{k}}_{12} \\ \hat{\mathbf{k}}_{21} & \hat{\mathbf{k}}_{22} \end{bmatrix} \begin{Bmatrix} \hat{\mathbf{u}}_1 \\ \hat{\mathbf{u}}_2 \end{Bmatrix} \quad (6)$$

$$\begin{Bmatrix} \hat{\mathbf{F}}_1 \\ \hat{\mathbf{F}}_2 \end{Bmatrix} = \frac{EA}{L} \frac{ik_1L}{(1-e^{-i2k_1L})} \begin{bmatrix} \mathbf{1} + e^{-i2k_1L} & e^{-i2k_1L} \\ e^{-i2k_1L} & \mathbf{1} + e^{-i2k_1L} \end{bmatrix} \begin{Bmatrix} \hat{\mathbf{u}}_1 \\ \hat{\mathbf{u}}_2 \end{Bmatrix} \quad (7)$$

That is similar to:

$$\{\hat{\mathbf{F}}\} = [\hat{\mathbf{D}}]\{\hat{\mathbf{u}}\}, \quad (8)$$

$$[\hat{\mathbf{D}}] = \frac{EA}{L} \frac{ik_1L}{(1-e^{-i2k_1L})} \begin{bmatrix} \mathbf{1} + e^{-i2k_1L} & e^{-i2k_1L} \\ e^{-i2k_1L} & \mathbf{1} + e^{-i2k_1L} \end{bmatrix} = \begin{bmatrix} \hat{\mathbf{D}}_{11} & \hat{\mathbf{D}}_{12} \\ \hat{\mathbf{D}}_{21} & \hat{\mathbf{D}}_{22} \end{bmatrix} \quad (9)$$

where $[\hat{\mathbf{D}}]$ is the dynamic stiffness matrix of the rod element.

The global dynamic stiffness matrix of a structure is obtained from the dynamic stiffness matrix of the element by the direct stiffness method proposed by Craig (1981). The boundary conditions of the modeled structure are applied to the system in the standard way. In the case of fixed degrees of freedom, the corresponding line and column of the global system dynamic matrix are suppressed.

The Transfer Matrix

The transfer matrix stands as an alternative to the solution by the dynamic stiffness matrix. Instead of relating forces to displacements, this methodology writes the values of forces and displacements at one end as a function of these values at the opposite end of the element (Arruda & Nascimento, 2009), as follows:

$$\begin{Bmatrix} \hat{\mathbf{u}}_2 \\ \hat{\mathbf{F}}_2 \end{Bmatrix} = [\mathbf{T}_{21}(\omega)] \begin{Bmatrix} \hat{\mathbf{u}}_1 \\ \hat{\mathbf{F}}_1 \end{Bmatrix} \quad (10)$$

The transfer matrix is a result of the equilibrium equations for an element, assuming that no external force is applied to the structure. By rearranging the terms of the dynamic stiffness matrix for the elementary rod and inverting the sign of $\hat{\mathbf{F}}_2$ (convention), we obtain:

$$[\mathbf{T}_{21}(\omega)] = \begin{bmatrix} -\hat{\mathbf{D}}_{12}^{-1}\hat{\mathbf{D}}_{11} & \hat{\mathbf{D}}_{12}^{-1} \\ -\hat{\mathbf{D}}_{21}^{-1} + \hat{\mathbf{D}}_{22}\hat{\mathbf{D}}_{12}^{-1}\hat{\mathbf{D}}_{11} & -\hat{\mathbf{D}}_{22}\hat{\mathbf{D}}_{12}^{-1} \end{bmatrix} = \begin{bmatrix} \cos(\mathbf{kx}_2) & \sin(\mathbf{kx}_2)/\mathbf{kEA} \\ -\mathbf{kEA}\sin(\mathbf{kx}_2) & \cos(\mathbf{kx}_2) \end{bmatrix} \quad (11)$$

where $\hat{\mathbf{D}}_{ij}$ corresponds to the element at the line i and column j of the dynamic stiffness matrix.

The global transfer matrix for the whole structure can be obtained by multiplication of the transfer matrix for each element in the respective order that they are arranged, as shown in Eq. 12 and represented in Fig. 2.

$$[\mathbf{T}(\omega)] = [\mathbf{T}_{21}(\omega)][\mathbf{T}_{32}(\omega)] \dots [\mathbf{T}_{(n-1)(n-2)}(\omega)][\mathbf{T}_{n(n-1)}(\omega)] \quad (12)$$



Figure 2 – Representation of a rod with n elements.

The Dispersion Relation

The dispersion relation describes the frequency-dependent effects in wave propagation. As it relates wavenumber with frequency, it becomes possible to know if a mode propagates or not for a given frequency.

For a periodic structure, the Bloch-Floquet theorem allows us to write the displacement as:

$$u(x, y, z, \omega) = \sum \hat{u}_n(y, z, \omega).e^{k_n x} \quad (13)$$

Thus,

$$\hat{u}_{rn} = \hat{u}_{1n}.e^{k_n \Delta} = \lambda \hat{u}_{1n} \quad \text{and} \quad \hat{F}_{rn} = \hat{F}_{1n}.e^{k_n \Delta} = \lambda \hat{F}_{1n} \quad (14)$$

Substituting Eq. 14 into Eq.10,

$$\begin{aligned} \begin{Bmatrix} \hat{\mathbf{u}}_r \\ \hat{\mathbf{F}}_r \end{Bmatrix} &= \begin{Bmatrix} \lambda \hat{\mathbf{u}}_1 \\ \lambda \hat{\mathbf{F}}_1 \end{Bmatrix} = \begin{bmatrix} \cos(kL) & \sin(kL)/kEA \\ -kEA \sin(kL) & \cos(kL) \end{bmatrix} \begin{Bmatrix} \hat{\mathbf{u}}_1 \\ \hat{\mathbf{F}}_1 \end{Bmatrix} \quad \therefore \\ \left(\lambda \begin{bmatrix} 1 & 0 \\ 0 & 1 \end{bmatrix} - \begin{bmatrix} \cos(kL) & \sin(kL)/kEA \\ -kEA \sin(kL) & \cos(kL) \end{bmatrix} \right) \begin{Bmatrix} \hat{\mathbf{u}}_1 \\ \hat{\mathbf{F}}_1 \end{Bmatrix} &= \begin{Bmatrix} 0 \\ 0 \end{Bmatrix} \end{aligned} \quad (15)$$

Solving this eigenvalue problem and applying the Cayley-Hamilton Theorem, we can easily get the wavenumber pair from the dispersion relation:

$$k_i(\omega) = \frac{\ln(\lambda_i(\omega))}{L} \quad (16)$$

FINITE ELEMENT ANALYSIS

The Finite Element Method arose as an important way for overcoming difficulties to solve problems whose analytical solution does not exist. Moreover, the range of available elements gives quite accurate solutions with this method. However, in order to guarantee consistent solutions for a structural problem from this method, it is important to satisfy the following relation for the element size (Petyt, 1996):

$$E_{size} \leq \frac{\lambda}{6} \quad (17)$$

where λ is the wavenumber. It establishes an upper limit frequency and requires mesh refinement as frequency increases, and so raising the computational cost.

Using the commercial software ANSYS® to study the wave propagation in the periodic medium via the finite element method, two types of elements were used: BEAM3 and SOLID45. The first one is a one-dimensional element consisting of two nodes with three degrees of freedom each (translations in nodal x-axis, y-axis, and rotation about nodal z-axis). The other is a three dimensional element, which presents eight nodes with three degrees of freedom each (translations in nodal x-axis, y-axis and z-axis).

For this study, the structure is evaluated by means of a forced vibration response. In this case, the equation of motion for the modeled structure can be written as:

$$[\mathbf{M}]\{\ddot{\mathbf{u}}\} + [\mathbf{C}]\{\dot{\mathbf{u}}\} + [\mathbf{K}]\{\mathbf{u}\} = \{\mathbf{F}^a\} \quad (18)$$

And it can be simplified to:

$$[\mathbf{D}_F]\{\mathbf{u}\} = \{\mathbf{F}^a\} \quad (19)$$

where $[\mathbf{M}]$ is the mass matrix, $[\mathbf{C}]$, the damping matrix, $[\mathbf{K}]$, the stiffness matrix, $\{\mathbf{u}\}$, the vector of displacements, $\{\mathbf{F}^a\}$, external load vector, and, finally, $[\mathbf{D}_F]$ is the dynamic stiffness matrix. The later equation solves the equations of motion for linear structures undergoing steady-state harmonic vibration.

DESIGN OF THE PERIODIC ROD

The existence of intervals of frequency in which waves do not propagate through a periodic structure, the so-called band gaps or stop bands, can be physically explained by Bragg and non-Bragg resonance induction. These resonances are due to the interactions between the wave propagation modes and the structural periodicity of the waveguide, which can be interpreted by the interferences of various wave modes in the waveguide and occur at crossings of different modes in the Brillouin zone (Tao, He and Wang, 2008). The existence of band gaps is closely related to the contrast between the material properties (Young's modulus and mass density) of the scatterers and the host material (Miyashita, 2005). Moreover, it is also known that the local propagation wave speed, which is dependent upon the materials properties and the periodicity of the lattice are sufficient for the estimation of the frequency around which the main band gap will occur. Based on this knowledge, a periodic rod constituted by a sequence of unit cells, each cell consisting of two layers of different materials with contrasting properties, is designed aiming a desired band gap size and frequency location.

The structure design is performed assuming a rod with fixed length L_r , and optimizing the number of cells and the thickness ratio of the two layers of different materials, which is assumed to be the same for every cell, such that a band gap (stop band) with maximum attenuation occurs at a desired frequency band. Thus, the optimization variables are:

- the number cells N_e ;
- the ratio of the thickness of each of the cell layers.

For each cell, the thicknesses of the two layers are defined as the vector $\mathbf{L} = [L_1; L_2]$, where:

$$L_1 = \frac{L_e}{(1 + L_i/L_m)}, \quad L_2 = \frac{L_e \times L_i/L_m}{(1 + L_i/L_m)} \quad \text{and} \quad L_e = \frac{L_t}{N_e}. \quad (20)$$

The periodic rod layout optimization was performed using MATLAB®'s pattern search optimization algorithm. The use of direct search algorithm is convenient as it does not require information about the gradient of the cost function and can be used to solve problems for which the objective function is not differentiable or is not even continuous. The method is based on searching a set of points, called a mesh, around the current point, looking for a point where the cost function value is lower than the value of the previous step. The point in the mesh that lowers the cost function value at the current point becomes current point at the next step of the algorithm so that a sequence of points is computed that approaches an optimal point.

The pattern search is performed by specifying a cost function, a starting point for the search and vectors representing bound constraints of the form $l_b \leq x \leq u_b$. The results are the point at which the final value is attained and the final value of the cost functions.

The cost function searches to minimize the transmissibility over a target frequency range ω_1 to ω_n , defined as:

$$feval = \sum_{i=1}^n \frac{|x_L(\omega_i)|}{|x_0(\omega_i)|} \quad (21)$$

The transmissibility was computed by using the spectral element method. The global dynamic matrix of the structure was assembled and solved for the displacements of rod excited by a uniform unit force at one end assuming free-free boundary conditions. Figure 3 below shows the layout of the optimized structure, and presents, in detail, its corresponding unit cell.

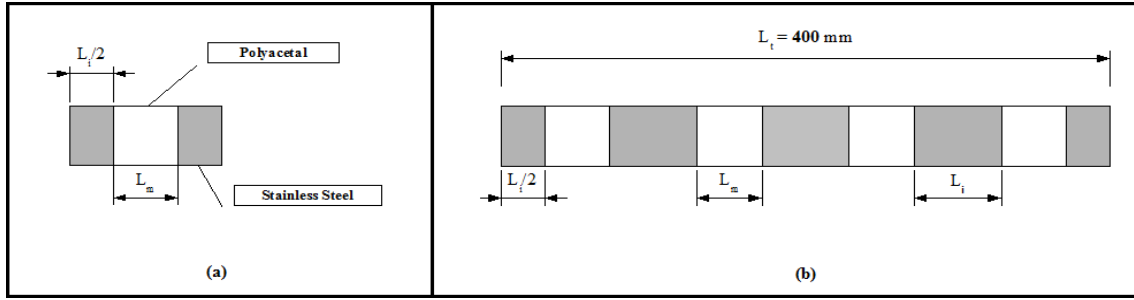


Figure 3 - (a) Unit cell of the periodic structure modeled, (b) layout of the optimized structure.

Based on the contrast between their elastic and physical properties, polyacetal ($E_m = 3.3$ GPa and $\rho_m = 1418$ Kg/m³) and stainless steel ($E_i = 193$ GPa and $\rho_i = 8030$ Kg/m³) were chosen as the materials to be used in the periodic layers. From this assumption, the following parameters are defined for the optimization process: $E_i/E_m = 58.48$ and $\rho_i/\rho_m = 5.66$.

As this work concerns the study of wave phenomena at mid-frequencies within the audible range, the interval between 6 kHz and 12 kHz was defined as the target frequency range for band gap positioning. The rod total length was fixed in 400mm and the constraints, defined as: $1 < N_e < 10$ and $0.2 < L_i/L_m < 5$.

Using these optimization parameters the design results were:

- $N_e = 4$;
- $L_i/L_m = 1.44$, i.e, $L_m = 41.06$ mm and $L_i = 58.94$ mm.

RESULTS AND DISCUSSIONS

Using the SEM formulation for an elementary rod, it was possible to find the analytical dynamic stiffness matrix for each homogeneous slice of a unit cell: two of stainless steel with $L_i/2$ of thickness, and one of polyacetal with L_m of thickness, as shown in Fig. 3(b).

By rearranging the dynamic stiffness matrices for the slices, we can easily obtain their respective transfer matrices. Thus, the transfer matrix for a unit cell is given by:

$$[\mathbf{T}_{\text{unit cell}}] = [\mathbf{T}_i] * [\mathbf{T}_m] * [\mathbf{T}_i] \quad (22)$$

Solving the eigenvalue problem for the above matrix, the wavenumbers and respective modes for longitudinal propagation through the periodic structure are obtained. These results are present in the form of dispersion curves in Fig.4, where the abscissa is given by the normalized wavenumber $\varepsilon = kL$, with L the length of a unit cell. The black and continuous curve corresponds to the imaginary wavenumbers that are associated with waves that propagate or pass band modes. The blue dashed one corresponds to the purely real wavenumbers, i.e., to evanescent waves, which do not propagate. The non-linearity of the curves indicates that the medium is dispersive. The formation of such banded frequency spectrum is directly related to mechanisms of wave interference taking place within the periodic structure (Hussein, Hulbert and Scott, 2005).

In order to compare the wave behavior of this heterogeneous structure with that of a homogeneous one having statically equivalent average Young's module, E_{avg} , Eq. 23, and average density, ρ_{avg} , Eq. 24, the dispersion curve of the homogeneous rod is plotted in Fig. 5. This analysis ratifies that wave scattering and dispersion are phenomena due to the periodical arrangement of the structure and material properties.

$$E_{avg} = \left(\frac{L_i}{L} \frac{1}{E_i} + \frac{L_m}{L} \frac{1}{E_m} \right)^{-1} \quad (23)$$

$$\rho_{avg} = \frac{1}{L} (L_i \rho_i + L_m \rho_m) \quad (24)$$

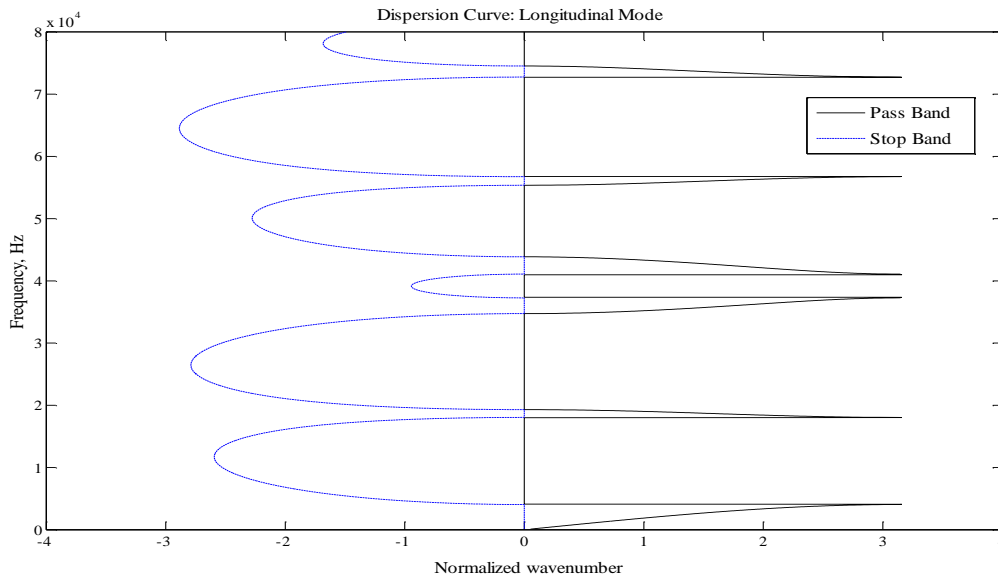


Figure 4 – Dispersion curve for longitudinal mode of the layered periodic structure by elementary SEM formulation.

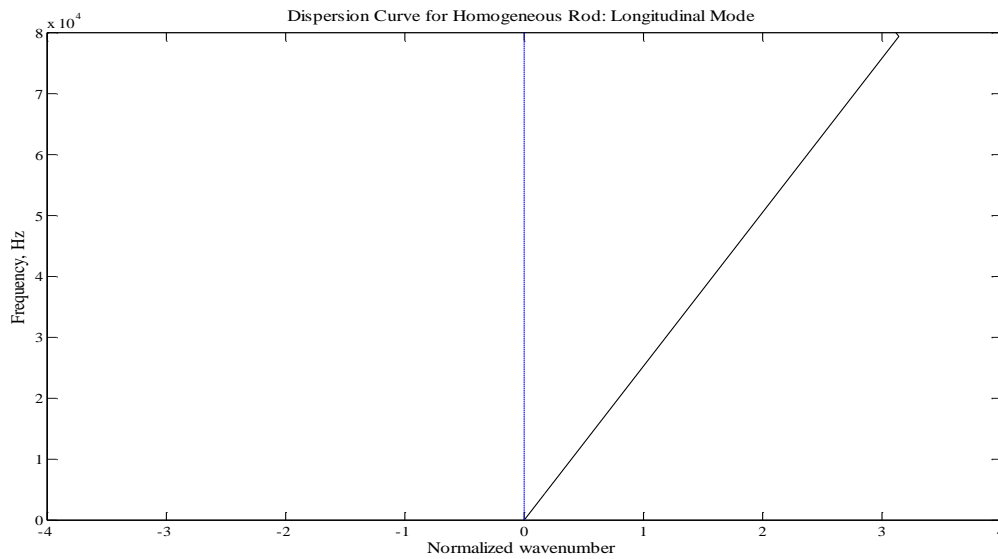


Figure 5 – Dispersion curve for longitudinal mode of a homogeneous rod whose material properties are statically equivalent averaged of the heterogeneous structure considered.

The harmonic analysis is used to analyze the forced response and longitudinal wave propagation of the periodic structure in free-free condition. A uniform force is applied at one end of the finite medium and the structure response is evaluated as a function of its transmissibility. This parameter relates axial displacement at one point along the structure with that where the force is applied, by the expression:

$$TR = 20 * \log_{10} \left(\frac{|u(x=L)|}{|u(x=0)|} \right), \quad (25)$$

where L is the structure length.

From SEM analysis, the displacement along the structure is obtained by solving the system $\{\hat{\mathbf{F}}\} = [\hat{\mathbf{D}}]\{\hat{\mathbf{u}}\}$, Eq. 8, for the global dynamic stiffness matrix of the media. The number and position of the nodes where displacement can be evaluated depend on the amount and size of the layers that compose a unit cell. Figure 6 shows the transmissibility as the ratio between the displacements measured at the ends for both periodic and equivalent homogeneous structures. This result predicts six band gaps below 80 kHz, and puts in evidence the effect of periodical organization of materials in the dynamic response.

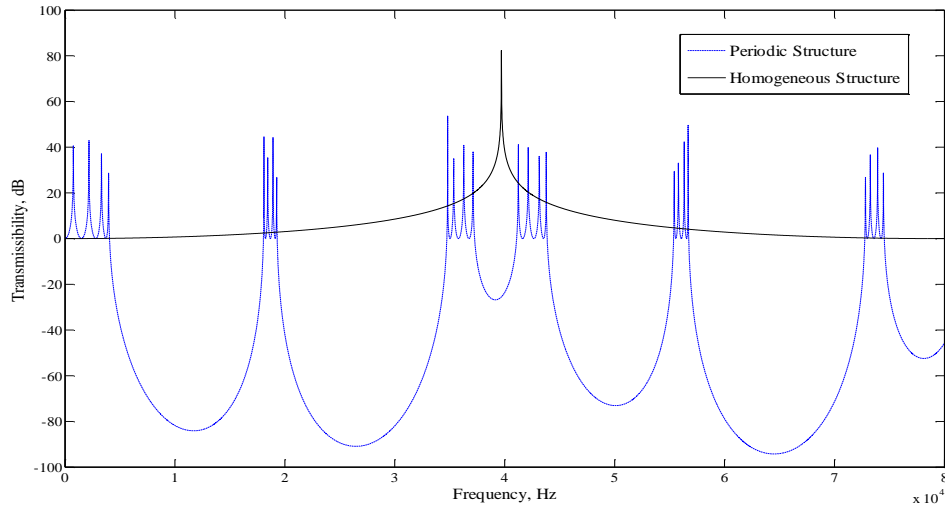


Figure 6 – Transmissibility at the ends of structure: (---) periodic structure, (—) equivalent homogeneous structure.

The same analysis was pursued using the finite element analysis. The model was meshed with elements SOLID45, Fig.7 (b), that have three degrees of freedom per node (translations in x, y, z), which produces solutions much more accurate than that based on the elementary formulation for a rod, which takes into account the axial displacement only. The model was also simulated with elements BEAM3, Fig.7 (a), a one-dimensional element which has three degrees of freedom per node (translations in x, y and rotation about nodal z-axis).

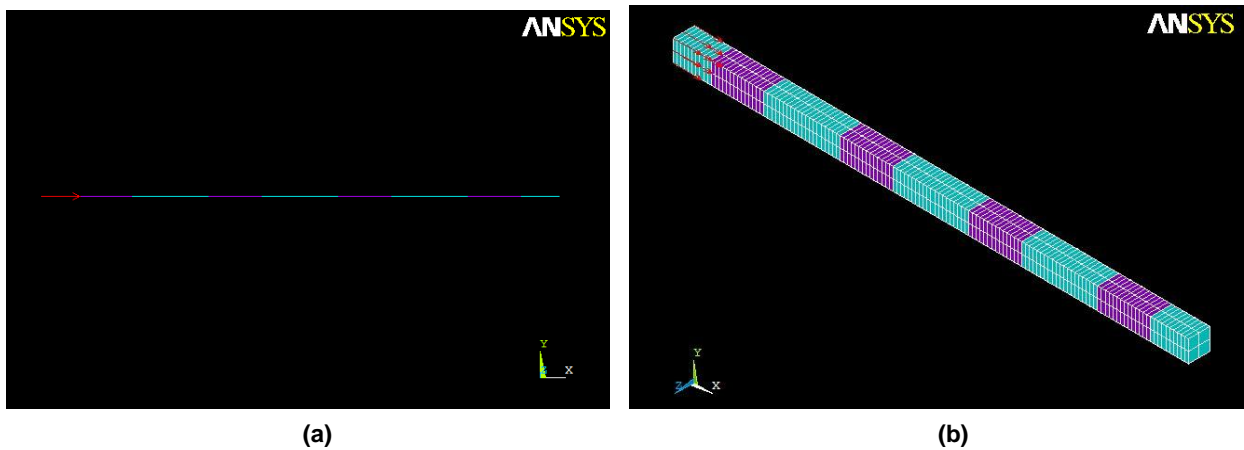


Figure 7 – (a) Model using elements BEAM3, (b) Model using elements SOLID45.

Figure 8 shows these results in terms of transmissibility for the three analyses used. The results produced by the finite element model meshed with BEAM3 elements are a better match to the ones from elementary SEM. It is clear that as frequency goes higher, the differences between results from elementary SEM and three-dimensional FEM model increases. The influences of other propagation modes that don't appear in low frequencies and which are related to higher-order modes explain these differences.

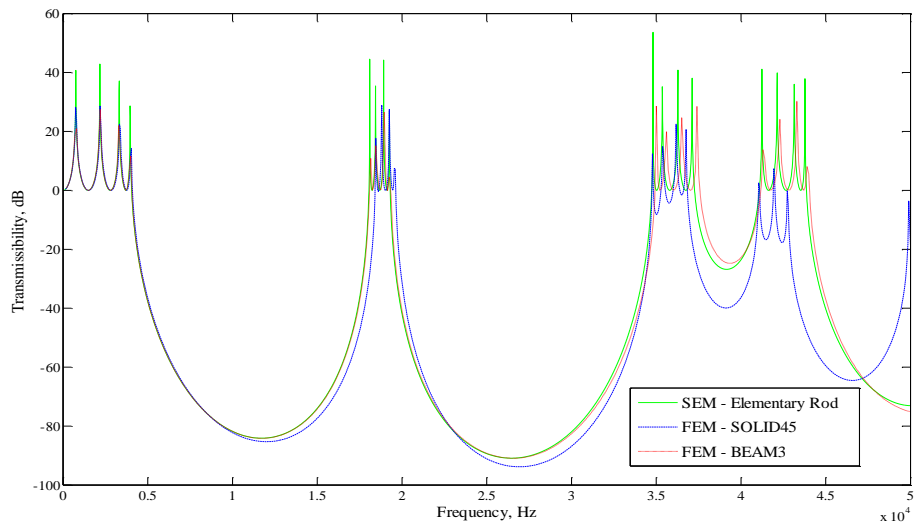


Figure 8 – Transmissibility of the periodic structure by different methodologies: (—) SEM using formulation for elementary rod, (---) FEM using SOLID45 elements and (---) FEM using BEAM3 elements.

Experimental results

The experimental analysis is an important way to validate analytical and numerical results. As this paper concerns the study of longitudinal wave propagation through periodic media, the forced vibration response analysis was chosen as the experimental method to be used.

A piezoelectric actuator, model 712A01 of PCB® Piezoelectronics, AVC, coupled with a 100g inertial mass, is used to excite longitudinally one end of the structure in the audio range. The structural response is measured using two micro-accelerometers, model 8614A500M1 of KISTLER, attached to both extremities of the structure, as represented in Fig. 9.

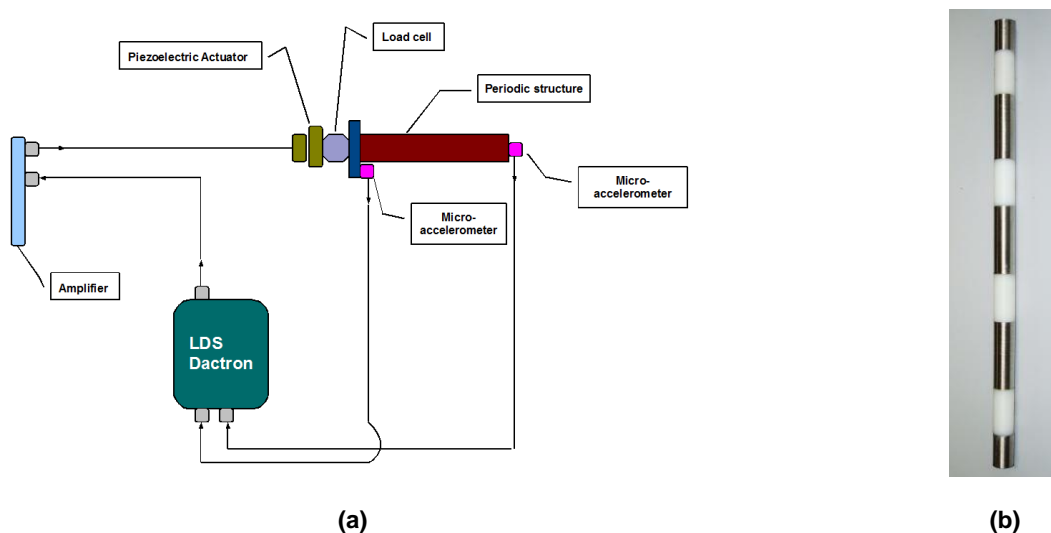


Figure 9 – (a) Experimental setup, (b) Prototype of the periodic structure.

Moreover, the acquisition system LDS Dactron PhotonII, model PHO200 and the software RT Pro Photon are used to specify the excitation signal to the piezoelectric actuator, and, also, record and treat the signals from the micro-accelerometers.

In this case, the layered periodic structure transmissibility to a white noise exciting frequencies within the range 1-20 kHz was evaluated and the result is shown in Fig. 10, superposed to that obtained via FEA using SOLID45 elements.

From Fig. 10, it can be seen that experimental results follow the simulated ones, although some noise appears in the experimental data. The noisy response for very low amplitudes is normal and due to the limited dynamic range of the accelerometers used. The divergences between experimental and numerical analysis are still being investigated, but they are probably due to the difficulty of reproducing experimentally the simulated conditions, such as the free-free boundary condition.

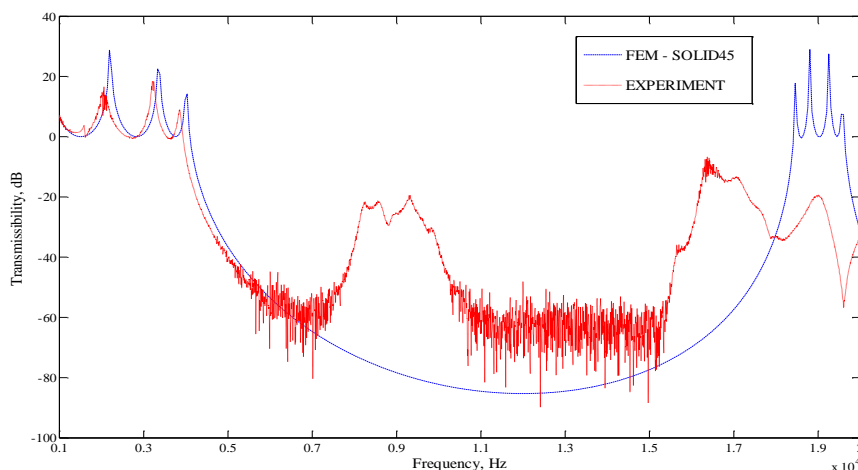


Figure 10 – Comparison between measured transmissibility by experimental test (---) and evaluated one by FEM using SOLID45 elements (---).

CONCLUSION

This paper discussed the efficiency of several methodologies in the study of elastic wave propagation in finite periodic structures. From the analytical formulation for homogenous rods, the transfer matrix method and Floquet's theorem, the dispersion curve of a multi-layered unit cell was obtained, and the transmissibility evaluated from the dynamic stiffness matrix of a periodic spectral element model. Regardless of the limitations of this one-mode analytical formulation, these results were somewhat similar to the ones obtained by FE analysis, especially those meshed with one-dimensional elements. The differences in the dynamic behavior of homogeneous and periodic structures were also elucidated. Finally, experimental tests validated the numerical results, and showed the difficulties to reproduce the simulated conditions exactly at high frequencies.

ACKNOWLEDGMENTS

The authors are grateful to the state government funding agency Fundação de Amparo à Pesquisa de São Paulo – FAPESP.

REFERENCES

- Arruda, J. R., & Nascimento, R. F. (2009). Building spectral element dynamic matrices using finite element models of waveguide slices. *Proceeding of the NOVEN 2009, Noise and Vibration: Emerging Methods*. Oxford.
- Brillouin, L. (1953). *Wave propagation in Periodic Structures*. New York: Dover.
- Craig, R. R. (1981). *Structural Dynamics: An Introduction to Computer Methods*. New York: John Wiley & Sons.
- Doyle, J. F. (1997). *Wave Propagation in Structures* (2nd ed.). Berlin, Germany: Springer-Verlag.
- Hussein, M. I., Hulbert, G. M., & Scott, R. A. (2006). Dispersive elastodynamics of 1D banded materials and structures: analysis. *Journal of Sound and Vibration*, 289, pp. 779-806.
- Mead, D. J. (1996). Wave propagation in continuous periodic structures: research contributions from Southampton, 1964-1995. *Journal of Sound and Vibration*, 190 (3), pp. 495-524.
- Miyashita, T. (2005). Sonic crystals and sonic wave-guides. *Measurement Science and Technology*, pp. R47-R63.
- Petyt, M. (1996). *Introduction to finite element vibration analysis*. Cambridge University Press.
- Sigalas, M., Kushwaha, M. S., Economou, E. N., Kafesaki, M., & Psarobas, I. E. (2005). Classical vibrational modes in phononic lattices: theory and experiment. *Z. Kristallogr.*, 220, pp. 765-809.
- Vasseur, J. O., Deymier, P. A., Frantzikonis, G., & Hong, G. (1998). Experimental evidence for the existence of absolute acoustic band gaps in two-dimensional periodic composite media. *J. Phys.: Condens. Matter*, 10, pp. 6051-6064.
- Zhi-Yong Tao, W.-Y. H. (2008). Resonance-induced band gaps in a periodic waveguide. *Journal of Sound and Vibration*, 313, pp. 830-840.

RESPONSIBILITY NOTICE

The authors are the only responsible for the printed material included in this paper.

Nonlinear Modeling and Analysis of a Piezoaeroelastic Energy Harvester

Marcela de M. Anicéio¹, Carlos De Marqui Junior¹, Alper Erturk², and Daniel J. Inman²

¹ Department of Aeronautical Engineering, Engineering School of Sao Carlos - University of Sao Paulo, Av. Trabalhador Sancarlenso 400, 13566-590, São Carlos, São Paulo

² Center for Intelligent Material Systems and Structures, Department of Mechanical Engineering, Virginia Polytechnic Institute and State University, Blacksburg, VA 24061, USA

Abstract: In this paper, a piezoaeroelastically coupled lumped-parameter model for energy harvesting from airflow excitation is presented along with experimental validations. A two-dimensional airfoil with two degrees of freedom (DOF), i.e. pitch and plunge, is investigated. Piezoelectric coupling is introduced to the plunge DOF and a resistive load is considered in the electrical domain of the problem. The unsteady aerodynamic loads are obtained from a two-dimensional lumped vortex model. The piezoaeroelastic equations are solved in a discrete state-space form. Three case studies are presented in this work. First the interaction between piezoelectric power generation and the linear aeroelastic behavior of the typical section is investigated for a set of resistive loads. Time domain predictions are compared against experimental data from wind tunnel tests. As a second case study, a free play is added to the pitch DOF. The typical section is used to investigate nonlinear limit cycle oscillations (LCO) for piezoelectric energy harvesting. Finally a combined nonlinearity is modeled in the pitch DOF. The piezoaeroelastic behavior is investigated for different nonlinear to linear stiffness ratios. Nonlinear LCO over a wide range of airflow speeds provides a useful source of electrical power.

Keywords: energy harvesting, aeroelasticity, piezoelectricity

NOMENCLATURE

m = airfoil mass per length	b_α = damping coefficient per length in the pitch DOF	N = total number of lumped vortices
m_e = fixture mass per length	R_l = load resistance	x_i = position of the i th collocation point
I_α = moment of inertia per length about the elastic axis	v_p = voltage across the resistive load	ξ_j = quarter chord position of the vortex at the i th panel
e = distance from the elastic axis to midchord position	C_p^e = equivalent capacitance of the piezoceramic layers	U = airflow speed
b = semichord of the airfoil section	θ = electromechanical coupling	U_{LF} = linear flutter speed
h = plunge displacement	M_α = aerodynamic moment per length	α = relaxation factor
α = pitch displacement	L = aerodynamic lift per length	\mathbf{x} = vector of state variables
l = the span length	w_i = downwash at the i th collocation point	\mathbf{D}_j = matrix related to the electromechanical behavior
x_α = dimensionless chord-wise offset of the elastic axis from the CG	n = discrete time	\mathbf{C}_j = matrix related to the vortices behavior
k_h = stiffness per length in the plunge DOF	Γ_j = strength of the j th vortex	\mathbf{E} = matrix relating downwashes and structural states
k_α = stiffness per length in the pitch DOF	K_{ij} = kernel function	
b_h = damping coefficient per length in the plunge DOF	M = number of lumped vortices on the airfoil	

INTRODUCTION

The conversion of aeroelastic vibrations into electrical energy is a powerful and scalable option for wind energy harvesting. A linear aeroelastic system undergoing persistent oscillations at the neutral stability condition (linear flutter speed) is the ideal linear scenario (De Marqui et al., 2010a, Erturk et al., 2010). However, persistent oscillations occurring at a specific wind speed restricts the operating envelope of such an energy harvester. On the other hand, nonlinear systems present very rich variety of dynamic behavior such as limit cycle oscillations (LCOs), internal resonances, and chaotic motions (Nayfeh and Mook, 1979). Stable aeroelastic LCO of acceptable amplitude can provide an important source of persistent electrical power over a wide range of airflow speeds. Therefore, a nonlinear aeroelastic system might be a useful configuration for energy harvesting from airflow-induced vibrations.

Many authors have examined the nonlinear behavior of aeroelastic systems. Price et al. (1994) investigated free play nonlinearities for the torsion mode of a typical section. LCO regions below the linear flutter speed, or subcritical behavior, are verified. Tang and Dowell (2006) also modeled free play nonlinearity in the pitch DOF of a typical section. In addition to the concentrated structural nonlinearity, they considered aerodynamic nonlinearities. Zhao and Yang (1990) examined LCOs when cubic nonlinearity is modeled in torsion DOF of an airfoil subjected to incompressible airflow. Zhao and Hu (2004) performed aeroelastic analysis of a two-dimensional airfoil section with combined geometric nonlinearities (free play and cubic stiffening) in torsion.

Although other transduction mechanisms exist, piezoelectric transduction has received the most attention for vibration-based energy harvesting due to the large power densities and ease of application of piezoelectric materials as summarized in the existing review articles (Sodano et al., 2004; Beeby et al., 2006; Anton and Sodano, 2007; Priya, 2007; Cook-Chennault et al., 2008). Bryant and Garcia (2009) presented time-domain modeling of a 2-DOF typical section as a piezoelectric power harvester device driven by aeroelastic vibrations. The main motivation was to have an alternative energy source for placement in urban areas. A time-domain switching energy-extracting scheme was used in order to increase the power extraction from linear aeroelastic oscillations. Erturk et al. (2010) presented a frequency-domain solution and experimental validations of a 2-DOF piezoaeroelastic airfoil for energy harvesting. An electrical power output of 10.7 mW was delivered to a 100 k Ω load at the linear flutter speed of 9.30 m/s (which was 5.1% larger than the short-circuit flutter speed). The effect of piezoelectric power generation on the linear flutter speed was also discussed in the same paper along with the possible useful consequences of having nonlinearities and subcritical LCO in the system. The literature also includes scalable configurations for wind energy harvesting. Zhu et al. (2010) present a miniature electromagnetic wind generator combining an airfoil attached to a cantilever and exposed to different flow conditions (free flow and wake a of bluff body). Kwon (2010) proposes a T-shaped piezoelectric cantilever for energy harvesting from fluid flow. The experimental results show flutter speed around 4.0 m/s, which could be achieved under natural fluid flow.

A time-domain piezoaeroelastic model of a piezoelectric generator wing with embedded piezoceramics was presented by De Marqui et al. (2010a). The model was obtained by combining an electromechanically coupled finite element (FE) model (De Marqui et al., 2009) with an unsteady vortex lattice model. At the flutter speed (which depends on the external load resistance), the aerodynamic damping vanishes and the oscillations are persistent. This condition was discussed as the simplest case for the concept demonstration of a generator wing using the linear piezoaeroelastic model. The response history with the largest instantaneous power output at the flutter speed shows a decaying behavior which is due to the shunt damping effect of power generation. The effect of using segmented electrodes on the piezoaeroelastic response of the generator wing was also investigated. The electrodes are segmented on the center line (mid-chord position) and properly combined to the electrical load to avoid the cancelation of the potential electrical output of the torsion-dominated modes (which is strongly cancelled when continuous electrodes are used). As a consequence of the improved electromechanical coupling, better power generation and shunt damping effects are obtained for the aeroelastic behavior since the piezoelectric reaction of the torsional modes in the coupled aeroelastic motions of flutter are taken into account with the segmented-electrode configuration.

Frequency-domain piezoaeroelastic modeling and analysis of a cantilevered plate-like wing with embedded piezoceramics for energy harvesting was also presented by De Marqui et al. (2010b). An electromechanical finite-element plate model was combined with the doublet-lattice method to obtain the piezoaeroelastic equations, which were solved using a p-k scheme (which takes into account the electromechanical coupling). In this way, the evolution of the aerodynamic damping and the frequency of each mode was obtained with changing airflow speeds for a given linear electrical circuit. Expressions for piezoaeroelastically coupled frequency response functions were also defined by combining flow excitation with harmonic base excitation so that the piezoaeroelastic evolution could be investigated in frequency domain at different airflow speeds and electrical boundary conditions.

In the present paper, linear and nonlinear piezoaeroelastically coupled lumped-parameter modeling of a two-dimensional airfoil with pitch and plunge DOF is presented. Piezoelectric coupling is considered for the plunge DOF. Therefore, an additional electrical degree of freedom is added to the problem. A load resistance is considered in the electrical domain. The aerodynamic loads are obtained from an unsteady lumped vortex model. Three case studies are presented for energy harvesting from aeroelastic oscillations. First the interaction between piezoelectric power generation and linear aeroelastic response of the typical section is investigated for a set of resistive loads. Time domain predictions for the pitch DOF and the plunge DOF as well as electrical power output are verified against experimental results obtained from wind tunnel tests. Later, free play nonlinearity is modeled in the pitch DOF. Model predictions are successfully verified against experimental results from wind tunnel tests. In the third case study, a combined nonlinearity is modeled in the pitch DOF. The piezoaeroelastic behavior is investigated over a range of airflow speeds for different resistive loads and a range of nonlinear - to - linear stiffness ratios. The main motivation is to obtain LCO of acceptable amplitude over a wide range of airflow speeds providing a useful broadband piezoaeroelastic harvester.

Piezoaeroelastic Model

Figure 1 shows the schematic of a linear 2-DOF typical section. The plunge and pitch displacement variables are denoted by h and α , respectively. The plunge displacement is measured at the elastic axis (positive in the downward

direction) and the pitch angle is measured at the elastic axis (positive in the clockwise direction). In addition, b is the semichord of the airfoil section, e is the distance of elastic axis from the mid-chord position, x_α is the dimensionless chord-wise offset of the elastic axis from the centroid (CG), k_h is the stiffness per length in the plunge DOF, k_α is the stiffness per length in the pitch DOF, b_h is the damping coefficient per length in the plunge DOF, b_α is the damping coefficient per length in the pitch DOF and U is the airflow speed.

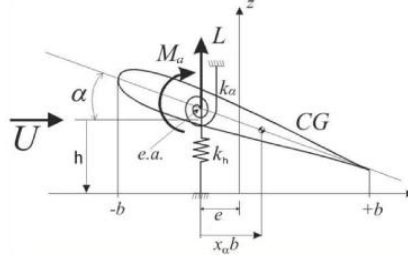


Figure 1 – 2-DOF aeroelastic typical section under airflow excitation.

In this work, piezoelectric coupling is added to the plunge DOF of the typical section. A load resistance is considered in the electrical domain of the problem. In addition, concentrated nonlinearities (free play, cubic or combined nonlinearity) are added to the pitch DOF. Therefore, by using Lagrange's equations, the modified piezoaeroelastically coupled nonlinear equations are presented here as,

$$\begin{aligned} (m + m_e)\ddot{h} + S_\alpha\ddot{\alpha} + b_h\dot{h} + k_h h - \theta v_p / l &= -L \\ S_\alpha\dot{h} + I_\alpha\ddot{\alpha} + b_\alpha\dot{\alpha} + k_\alpha\alpha + f_{fp}(\alpha) + f_c(\alpha) &= M_\alpha \\ C_p^e \dot{v}_p + \frac{v_p}{R_l} + \theta\dot{h} &= 0 \end{aligned} \quad (1)$$

where m is the airfoil mass per length (in the span direction), m_e is the fixture mass (connecting the airfoil to the plunge springs) per length, I_α is the moment of inertia per length about the elastic axis, S_α is the static moment, l is the span length, R_l is the load resistance in the electrical domain, v_p is the voltage across the resistive load, C_p^e is the equivalent capacitance of the piezoceramic layers, θ is the electromechanical coupling, M_α is the aerodynamic moment, L is the aerodynamic lift and the over-dot represents differentiation with respect to time. In Eqs. (1), $f_{fp}(\alpha)$ and $f_c(\alpha)$ are given by,

$$f_{fp}(\alpha) = \begin{cases} -k_\alpha \alpha_{fp} \\ 0 \\ k_\alpha \alpha_{fp} \end{cases} \quad f_c(\alpha) = \begin{cases} k_{n\alpha} (\alpha - \alpha_{fp})^3 & \alpha > \alpha_{fp} \\ 0 & -\alpha_{fp} \leq \alpha \leq \alpha_{fp} \\ k_{n\alpha} (\alpha + \alpha_{fp})^3 & \alpha < -\alpha_{fp} \end{cases} \quad (2)$$

and α_{fp} is the free play gap and $k_{n\alpha}$ is the nonlinear stiffness. It is important to note that when $k_{n\alpha} = 0$ the free play nonlinearity is obtained (combining the linear restoring moment and $f_{fp}(\alpha)$) whereas the $k_{n\alpha} \neq 0$ and $\alpha_{fp} \neq 0$ conditions give the combined nonlinearity (combining the linear restoring moment, $f_{fp}(\alpha)$ and $f_c(\alpha)$). The restoring moments in the pitch DOF for combined nonlinearity and free play nonlinearity are presented in Fig. 2 along with the linear case.

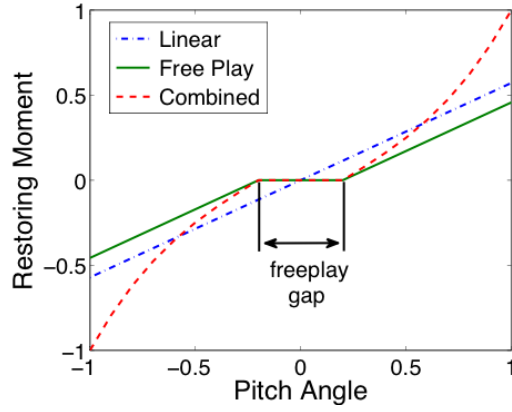


Figure 2 – Linear and nonlinear restoring moments in the pitch DOF.

Lumped Vortex Method

The unsteady aerodynamic load over the airfoil for the incompressible potential flow is solved in this work using the lumped vortex method (Hall, 1996). The airfoil and the wake are divided into elements (panels). Lumped vortex elements are placed at the quarter chord point of each panel on the airfoil and in the wake. Collocation points are placed at the three quarter chord point of each panel. The zero normal flow boundary condition (or the velocity induced by the discrete vortices is equal to the downwash arising from the unsteady motion of the airfoil at these points) has to be fulfilled at the collocation points. The boundary condition is expressed as

$$w_i^{n+1} = \sum_{j=1}^N K_{ij} \Gamma_j^{n+1} \quad i = 1, \dots, M \quad (2)$$

where w_i^{n+1} is the downwash at the i th collocation point at a time $n+1$, Γ_j is the strength of the j th vortex, and K_{ij} is the kernel function, M is the number of lumped vortices on the airfoil and N is the total number of lumped vortices (airfoil and wake). The kernel function for the flat airfoil is given by

$$K_{ij} = \frac{1}{2\pi(x_i - \xi_j)} \quad (3)$$

where x_i is the position of the i th collocation point and ξ_j the vortex at the quarter chord position of the i th panel.

Using the Kelvin condition (the strength of the unsteady vorticity shed in the wake is proportional to the time rate of change of circulation about the airfoil) the strength of the lumped vortex of the first element in the wake at the time step $n+1$ is

$$\Gamma_{M+1}^{n+1} = -\sum_{j=1}^M (\Gamma_j^{n+1} - \Gamma_j^n) \quad (4)$$

and the convection of the vorticity that has been shed into the wake with speed U is described as

$$\Gamma_i^{n+1} = \Gamma_{i-1}^n \quad i = M+2, N-1 \quad (5)$$

Hall (1996) introduced the relaxation factor α to avoid the discontinuous change in the induced wash at the airfoil body when the starting vortex reaches the end of the computational wake,

$$\Gamma_i^{n+1} = \Gamma_{i-1}^n + \alpha \Gamma_i^n \quad (6)$$

where $i = N$ for the last vortex element in the wake.

The discrete time history of the unsteady vorticity is computed by solving the following matrix equation obtained using Eqs. (2)-(6):

$$\mathbf{\Gamma}^{n+1} = \mathbf{A}^{-1}[\mathbf{w}^{n+1} - \mathbf{B}\mathbf{\Gamma}^n] \quad (7)$$

The vorticity is then used in Bernoulli's equation to calculate the aerodynamic lift and moment about the elastic axis of the typical section.

State Space Piezoaeroelastic Equations

The piezoaeroelastic equations (Eq. (1)) can be written in the discretized state-space form. The vector of state variables can be given by

$$\mathbf{x} = \{x_1 \quad x_2 \quad x_3 \quad x_4 \quad x_5\} \quad (8)$$

where $x_1 = h$, $x_2 = \dot{h}$, $x_3 = \alpha$, $x_4 = \dot{\alpha}$ and $x_5 = v_p$. The sampled version of the states is defined as,

$$x_k = \frac{(x_k^{n+1} + x_k^n)}{2} \quad \dot{x}_k = \frac{(x_k^{n+1} - x_k^n)}{\Delta t} \quad (9)$$

where Δt is the constant time increment. The state-space equation in discrete form is,

$$\mathbf{D}_1 \mathbf{x}^{n+1} + \mathbf{D}_2 \mathbf{x}^n + \mathbf{C}_1 \Gamma^{n+1} + \mathbf{C}_2 \Gamma^n = \mathbf{0} \quad (10)$$

Here, \mathbf{D}_1 and \mathbf{D}_2 are related to the electromechanical behavior and \mathbf{C}_1 and \mathbf{C}_2 describe the vortex behavior on the airfoil.

A linear relationship between the downwash \mathbf{w} at the collocation points and the structural states is defined by,

$$\mathbf{w} = \mathbf{E} \mathbf{x}_{k-1} \quad (11)$$

Using Eqs. (7), (10) and (11) the piezoaeroelastic state space equation is,

$$\begin{bmatrix} \mathbf{A} & -\mathbf{E} \\ \mathbf{C}_2 & \mathbf{D}_2 \end{bmatrix} \begin{Bmatrix} \Gamma \\ \mathbf{x} \end{Bmatrix}^{n+1} + \begin{bmatrix} \mathbf{B} & \mathbf{0} \\ \mathbf{C}_1 & \mathbf{D}_1 \end{bmatrix} \begin{Bmatrix} \Gamma \\ \mathbf{x} \end{Bmatrix}^n = \begin{Bmatrix} \mathbf{0} \\ \mathbf{0} \end{Bmatrix} \quad (12)$$

Case Studies

This section presents three case studies using the piezoaeroelastic model described in the previous section. The set of resistive loads considered here are $R_l = 10, 10^2, 10^3, 10^4, 10^5$ and $10^6 \frac{1}{2}$. In the first case study, the linear piezoaeroelastic solution is verified against experimental piezoaeroelastic responses (pitch and plunge displacements as well as voltage output) obtained from wind tunnel tests. After the linear case, bilinear structural stiffness in the pitch DOF is considered. For small airfoil rotations, the torsional stiffness is set to zero and for large rotations the systems approaches the original linear torsional stiffness (Fig. 2). The presence of such nonlinearity may result in subcritical bifurcations with LCO at airflow speeds below the linear flutter speed (Dowell and Tang, 2002). Although this type of LCO is not preferred in real aircraft, it is useful for energy harvesting. In the third case study, a combined nonlinearity is modeled in the pitch DOF. For small airfoil rotations, the torsional stiffness is set to zero and a stiffening behavior is observed for large rotations (Fig. 2). The piezoaeroelastic behavior is investigated for a set of resistive loads and also for a range nonlinear-to-linear linear pitch stiffness ratio ($\eta = k_{n\alpha} / k_\alpha$). In the first and the second case studies, LCO of acceptable amplitude is observed at a specific airflow speed and a narrow range of airflow speeds, respectively. In the third case (combined nonlinearity), the presence of LCO with acceptable amplitude is shown for a wider range of airflow speeds. This range increases as the nonlinear-to-linear stiffness ratio is increased. Hence a broadband harvester is obtained.

Figure 3 shows the experimental setup used for investigating the linear and the nonlinear piezoaeroelastic behavior of the typical section. The plunge stiffness is due the four elastic beams with clamped-clamped end conditions shown in the detailed views of Fig. 3. The free ends of the elastic beams are connected to metal plates at the top and the bottom. Therefore the experimental setup of this work slightly deviates from the ideal definition of a typical section (where springs are assumed ideal), yielding the fixture mass (m_e) defined in Eq. (1). A shaft (or pitch axis) is mounted to the upper and lower plates through a pair of bearings. The pitch stiffness is given by a spring wire clamped into the shaft (at the elastic axis). The free end of the wire is simply supported on the top plate (without a gap for the linear case and with a gap for the free play nonlinearity). Two piezoceramics (QP-10N from Mide Corporation) are attached onto the root of two bending stiffness members (symmetrically) and their electrodes are connected in parallel to a load resistance.

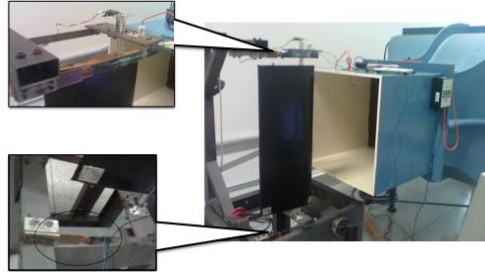


Figure 3 – Experimental typical section and detailed view of the piezoceramic patches.

The properties of the piezoaeroelastic typical section are shown in Table 1. The manufacturer’s published equivalent capacitance of $C_p^{eq} = 120nF$ is used in the piezoaeroelastic model (Eq. 12). The electromechanical coupling parameter is obtained based on distributed parameter modeling (Erturk and Inman, 2008) by considering clamped-clamped end conditions for the two beams with piezoceramics as $\theta = 1.55 mN / V$ (Erturk et al, 2010).

Table 1 – Properties of the piezoaeroelastic typical section.

b	0.125 m
l	0.5 m
$m + m_e$	4.0 kg/m
S_α	0.0524 Kg
I_α	0.0072 kg m
k_h	4200 N/m ²
k_α	5.08 N/rad
b_h	0.16 Ns/m ²
b_α	0.023 N/m rad

Linear Piezoaeroelastic Typical Section

In the first case study, the linear aeroelastic behavior of the electromechanically coupled typical section is investigated for a set of resistive loads. The experimental short-circuit ($R_l \rightarrow 0$) flutter speed is measured as 12.0 m/s. The predicted linear short-circuit flutter speed is 12.3 m/s (2.5% larger than the experimental flutter speed).¹ The load resistance of 100 k Ω gives the maximum power output among the set of resistors considered in this paper. The piezoaeroelastic time response histories (pitch, plunge and voltage output) for this load resistance with almost persistent oscillations is shown in Fig. 4. The model predicts the linear flutter speed for the optimum load (among the loads considered here) as 12.5 m/s. The experimentally verified flutter speed for the same load resistance is 12.2 m/s. Although the model overestimates the linear flutter speed (with an acceptable error) it predicts correctly the amplitudes of pitch, plunge and voltage responses as well as the frequencies.

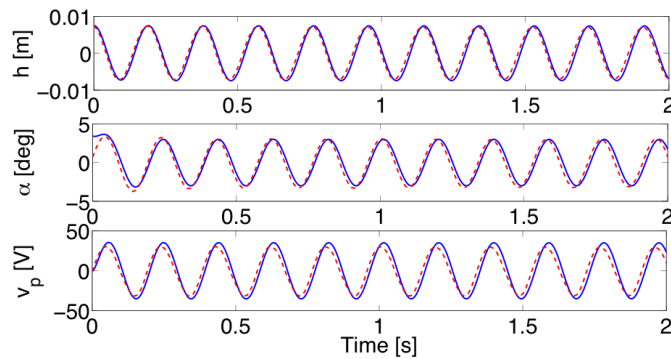


Figure 4. Experimental (continuous line) and theoretical (dashed line) piezoaeroelastic response histories for $R_l = 100 k\Omega$ at 12.2 m/s and 12.5 m/s, respectively.

¹ The model overestimates the experimental flutter speed for the entire set of resistive loads used in this work.

The variation of power output with increasing load resistance is shown in Fig. 5. The model predicts 10.2 mW for the optimum load resistance underestimating the experimental power output of 12.0 mW .

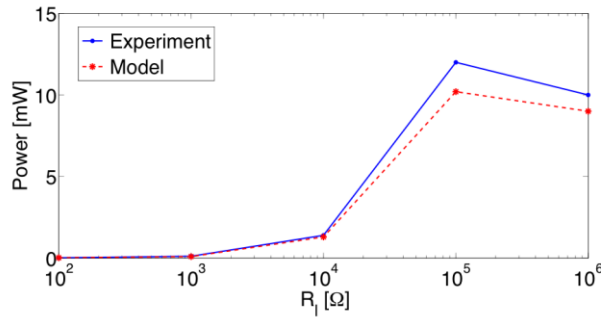


Figure 5. Experimental and theoretical power output with increasing load resistance.

Table 2 shows the variation of flutter speed (with respect to short-circuit flutter speed) for the set of resistive loads used in the experiments along with the model predictions. The resistive shunt damping effect of the maximum power generation of the optimal load causes the maximum increase of the linear flutter speed. The experimental increase in the linear flutter speed compared to the short-circuit flutter speed for this resistive load is 1.7%. The piezoaeroelastic model predicts an increase of 1.6%.

Table 2. Percentage variation of the linear flutter speed with load resistance.

Load resistance [Ω]	Experimental	Model
10^2	0 %	0 %
10^3	0 %	0 %
10^4	0.8 %	0.2 %
10^5	1.7 %	1.6 %
10^6	0.1 %	0.8 %

Piezoaeroelastic Typical Section with Free play

The experimental nonlinear piezoaeroelastic typical section with free play is presented in the second case study for energy harvesting. The nonlinear piezoaeroelastic behavior of the coupled typical section is investigated for the set of resistive loads considered in this work. The nonlinearity assumed is the bilinear structural stiffness in the pitch DOF. The free play gap in the pitch DOF is $\alpha_{fp} = \pm 1.4$ degrees. The linear pitch stiffness outside the free play gap is given by the same stiffness as the linear case study. The experimental linear elastic restoring pitch moment and free play elastic pitch moment are shown in Fig. 6.

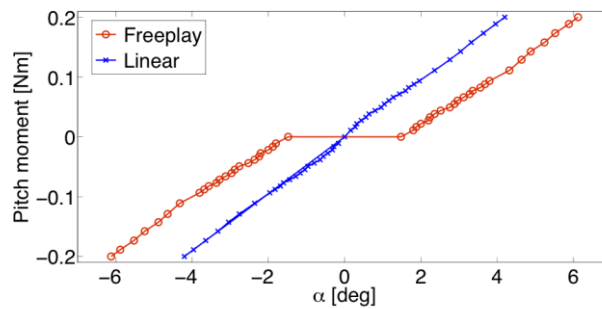


Figure 6. Experimentally measured linear and bilinear (free play) pitch moment.

The LCO mechanism observed in the experiments is the subcritical one (leading to LCOs below the linear flutter speed of each load resistance used in this work). The lowest airflow speed to have LCO is experimentally measured as 10 m/s and the model predicts this lower bound as 9.5 m/s . It is observed that, beyond 9.5 m/s the response amplitude (predicted by the present model) becomes very large for all resistive loads considered here (and eventually becomes divergent according to the theory). Therefore, no experimental testing (or simulation) was performed outside the range of 10-12 m/s.

The load resistance of 100 k Ω gives the maximum power output among the set of resistors used in this case as well. The piezoaeroelastic time histories (pitch, plunge and voltage output) for this resistive load with persistent oscillations is shown in Fig. 7. Although the model underestimates the lowest LCO speed, it predicts the amplitudes of the pitch, plunge and voltage response histories as well as the frequencies correctly.

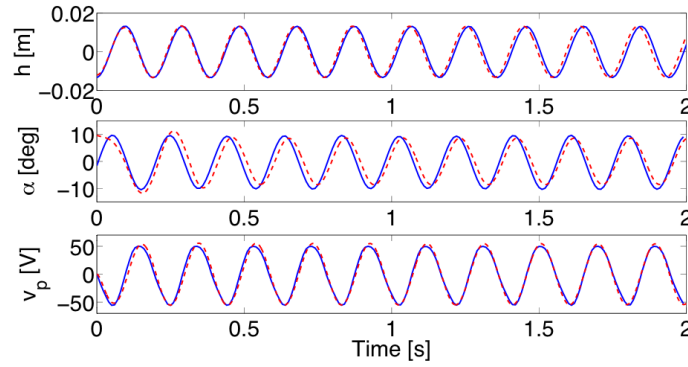


Figure 7. Experimental (continuous line) and theoretical (dashed line) nonlinear piezoaeroelastic response histories for $R_l = 100\text{ k}\Omega$ at 10.0 m/s and 9.5 m/s, respectively.

The variation of power output from the nonlinear LCO with increasing load resistance is shown in Fig. 8. Among the set of resistive loads used in the experiments and simulations, $R_l = 100\text{ k}\Omega$ gives the maximum power output. The model predicts 30.0 mW for the optimum load slightly underestimating the experiments (31.0 mW). It is important to note that the maximum power output of this nonlinear case is almost three times the power output obtained in the previous case study (linear piezoaeroelastic power harvester). Although the subcritical behavior investigated in this case study is interesting for energy harvesting, a narrow range of airflow speeds with LCO of acceptable amplitude is observed. A broadband piezoaeroelastic harvester (with LCO of acceptable amplitude over a wide range of wind speeds) would be the interesting case for practical applications.

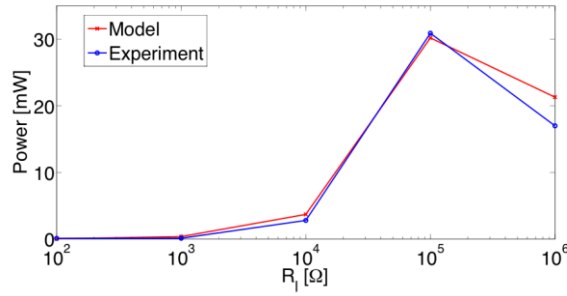


Figure 8. Experimental power output and model predictions with increasing load resistance.

Piezoaeroelastic Typical Section with Combined Nonlinearity

In the third case study, the nonlinearity modeled is the combined torsional elastic restoring moment of Eqs. (1) and (2) (recall Fig. 2). The theoretical piezoaeroelastic behavior of the electromechanically coupled typical section is investigated for different values of the nonlinear-to-linear stiffness ratio: $\eta = k_{n\alpha} / k_\alpha = 0, 50, 100$. The free play gap considered in this third case study is $\alpha_{fp} = \pm 0.4$ degrees around $\alpha = 0$. The amplitude of the mechanical outputs (h and α) and electrical power output are investigated for airflow speeds ranging from 90% of the linear flutter speed of 12 m/s to almost 1.5 times the linear flutter speed. The set of resistive loads considered in the previous case studies is used here.

Figure 9 shows the plunge amplitude with nondimensional airflow speed in short circuit condition ($R_l = 100\ \Omega$). As previously discussed in this paper, LCO of acceptable amplitude over a wide range of airflow speeds is the most interesting condition for a broadband piezoaeroelastic energy harvester. It is clear from Fig. 9 that plunge amplitude is highly sensitive to nonlinear-to-linear stiffness ratio. Clearly, when $\alpha_{fp} = 0$ and $\eta = 0$ the free play nonlinearity is achieved. One can observe from Fig. 9 that for the piezoaeroelastic harvester with free play LCO is very large beyond the nondimensional speed 0.9 (theoretically divergent above the linear flutter speed predicted in the present model) and the experimental setup cannot accept such amplitudes. However, for the configuration with combined nonlinearity ($\alpha_{fp} \neq 0$ and $\eta \neq 0$), the LCO response has acceptable amplitude over a wide airflow speed range. The amplitude of plunge displacement increases with increasing airflow speed and decreases with increasing stiffness ratio for any airflow speed.

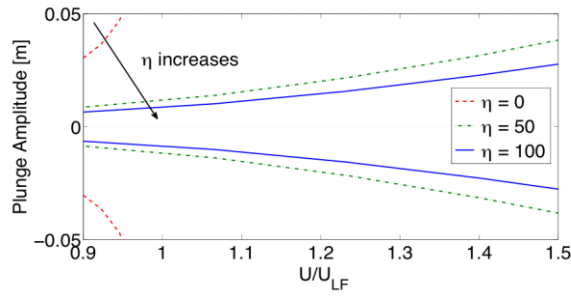


Figure 9. Plunge amplitude with increasing airflow speed for three different values of η ($R_l = 100 \Omega$).

For the case of $\eta = 100$, variation of the theoretical electrical power output with increasing airflow speed for five different values of load resistance is shown in Fig. 10a. The amplitude of power output increases with increasing airflow speed. For any airflow speed, as the value of load resistance is increased $R_l = 10^2 \Omega$ to $R_l = 10^5 \Omega$, the power output increases. When the value of load resistance is increased to $R_l = 10^6 \Omega$ (close to open-circuit condition) the power output starts decreasing. Clearly, among the set of resistive loads considered in this paper, $R_l = 10^5 \Omega$ gives the maximum power output over the entire range of airflow speeds. The maximum theoretical power of 143 mW is obtained for the optimum load resistance at $U = 22.8$ m/s. Figure 10b shows the variation of plunge amplitude (for clarity the positive amplitudes are shown) with airflow speed and $\eta = 100$ for the set of resistive load considered in this work. As can be observed from the enlarged view of Fig. 10b, the mechanical amplitude very slightly decreases as the load resistance is increased from 10^2 to $10^5 \Omega$ due to the shunt damping effect associated with the power generation.

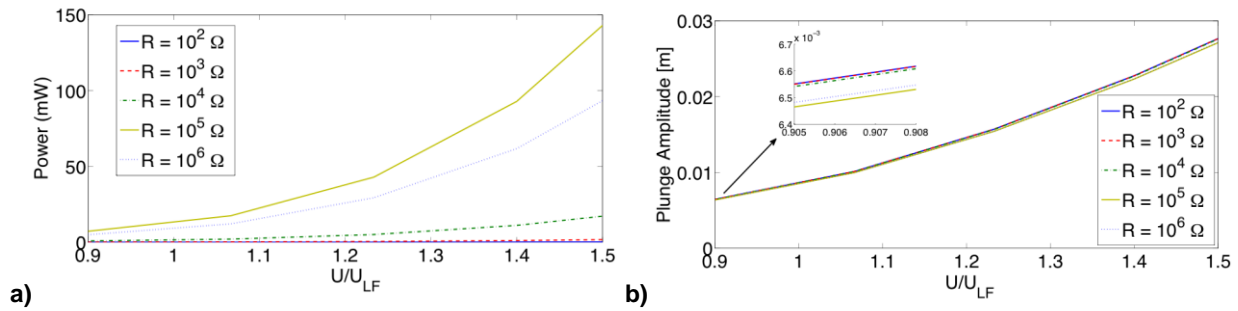


Figure 10. (a) Variation of power output and (b) variation of plunge amplitude with airflow speed for five different values of load resistance and $\eta = 100$.

Conclusions

In this paper a piezoaeroelastically coupled 2-DOF typical section with is presented for energy harvesting from linear and nonlinear aeroelastic vibrations. A discrete state space piezoaeroelastic model is derived and the unsteady aerodynamic loads are obtained using the lumped vortex model. The linear piezoaeroelastic predictions are successfully verified against experimental results obtained from wind tunnel tests. The optimum load resistance that gives the maximum power output also gives the larger flutter speed due to the resistive shunt damping effect. Although usually avoided in real aircraft, the flutter condition is the most interesting for energy harvesting from linear aeroelastic vibrations. The nonlinear piezoaeroelastic behavior of the coupled typical section is also investigated. Initially, free play nonlinearity is modeled in the pitch DOF. The predictions are successfully verified against the experimental results from wind tunnel tests. The presence of such nonlinearity results in LCO at airflow speeds below the linear flutter speed. The maximum power output is delivered to the load resistance of $R_l = 10^5 \Omega$ in the linear and nonlinear cases. However, the maximum power obtained from the nonlinear aeroelastic oscillations is 210 % larger than the maximum power obtained from the linear case. In both cases (linear and free play) divergent oscillations are observed at any airflow speed above the linear flutter speed (12 m/s).

A broadband piezoaeroelastic harvester is presented when a combined nonlinearity is modeled in the pitch DOF. The piezoaeroelastic behavior is investigated for increasing stiffness ratio and a set of resistive loads. Mechanical response amplitudes increase with increasing airflow speed and decrease with increasing stiffness ratio. Hence, LCO with acceptable amplitude over the entire range of velocities investigated ($0.9U_{FL} \leq U \leq 1.5U_{FL}$) for $\eta = 100$. Therefore, useful LCO of acceptable amplitude provides an important source of electrical power over a wide range of airflow speeds when $\eta = 100$. For the same stiffness ratio, the optimal load resistance at the largest airflow speed (of the range considered in this work) provides the maximum theoretical power output of 143 mW. Among the case studies

presented in this work, the piezoaeroelastic harvester with combined linearity is the most interesting for practical applications.

ACKNOWLEDGMENTS

The authors gratefully acknowledge CNPq and FAPEMIG for partially funding the present research work through the INCT-EIE. The authors also gratefully acknowledge the support of FAPESP (2009/10637-0). The authors gratefully acknowledge the support of the Air Force Office of Scientific Research under the grants F 9550-06-1-0326 'Energy Harvesting and Storage Systems for Future Air Force Vehicles' and F 9550-09- 1-0625 'Simultaneous Vibration Suppression and Energy Harvesting' monitored by Dr. B. L. Lee.

REFERENCES

- Anton, S.R. and Sodano, H.A. 2007, "A Review of Power Harvesting Using Piezoelectric Materials 2003-2006," *Smart Materials and Structures*, Vol. 16, pp. R1-R21.
- Beeby, S.P., Tudor, M.J. and White, N.M. 2006, "Energy Harvesting Vibration Sources for Microsystems Applications," *Measurement Science and Technology*, Vol. 13, pp. R175-R195.
- Bryant, M., Garcia, E., 2009, "Development of an Aeroelastic Vibration Power Harvester," *Proceedings of the Active and Passive Smart Structures and Integrated Systems 2009*.
- Cook-Chennault, K.A., Thambi, N. and Sastry, A.M., 2008, "Powering MEMS Portable Devices- a Review of Non-regenerative and Regenerative Power Supply Systems with Emphasis on Piezoelectric Energy Harvesting Systems," *Smart Materials and Structures*, 17:043001.
- De Marqui Jr, C., Erturk, A. and Inman, D. J., 2009, "An electromechanical finite element model for piezoelectric energy harvester plates," *Journal of Sound and Vibration*, Vol. 327, pp. 9-25.
- De Marqui, Jr., C., Erturk, A., and Inman, D. J., 2010a, "Piezoaeroelastic Modeling and Analysis of a Generator Wing with Continuous and Segmented Electrodes," *Journal of Intelligent Material Systems and Structures*, Vol. 21, No. 10, pp.983-993.
- De Marqui, Jr., C., Vieira, W.G.R., Erturk, A., and Inman, D. J., 2010b, "Modeling and Analysis of Piezoelectric Energy Harvesting from Aeroelastic Vibrations Using the Doublet-Lattice Method, *Journal of Vibration and Acoustics*, in press.
- Dowell, E.H. and Tang, D., 2002, "Nonlinear Aeroelasticity and Unsteady Aerodynamics," *AIAA Journal*, Vol. 40, pp. 1697-1707.
- Erturk, A. and Inman, D.J., 2008, "A Distributed Parameter Electromechanical Model for Cantilevered Piezoelectric Energy Harvesters," *ASME Journal of Vibration and Acoustics*, Vol.130, 041002.
- Erturk, A., Vieira, W.G.R., De Marqui, C. and Inman, D.J., 2010, "On the energy harvesting potential of piezoaeroelastic systems," *Applied Physics Letters*, Vol. 96, 184103.
- Hall, K.C., 1996, "Eigenanalysis of Unsteady Flows about Airfoils, Cascades and Wings", *AIAA Journal*, Vol. 32, No. 12, pp. 2426-2432.
- Kwon, S.D., 2010, "A T-shaped piezoelectric cantilever for fluid energy harvesting", *Applied Physics Letters*, Vol. 77, 164102.
- Nayfeh, A.H. and Mook, D.T., 1979, *Nonlinear Oscillations*, John Wiley and Sons, New York.
- Price, S.J., Lee, B.H.K. and Alighanbari, H., 1994, "Postinstability Behavior of a Two-Dimensional Airfoil with a Structural Nonlinearity", *Journal of Aircraft*, Vol. 31, pp. 1395-1401.
- Priya, S, 2007, "Advances in Energy Harvesting using Low Profile Piezoelectric Transducers," *Journal of Electroceramics*, Vol.19, pp. 167-184.
- Sodano, H.A., Inman, D.J. and Park, G. 2004, "A Review of Power Harvesting from Vibration Using Piezoelectric Materials," *The Shock and Vibration Digest*, Vol. 36, pp. 197-205.
- Tang, D. and Dowell, E.H., 2006, "Flutter and Limit-Cycle Oscillations for a Wing-Store Model with Freeplay", *Journal of Aircraft*, Vol. 43, No. 2, pp. 487-503.
- Zhang R. and Singh S.N., 2001, "Adaptive Output Feedback Control of an Aeroelastic System with Unstructured Uncertainties," *Journal of Guidance, Control, and Dynamics*, Vol. 24, No. 3, pp. 502-509.
- Zhao, L.C. and Yang, Z.C., 1990, "Chaotic Motions of an Airfoil with Nonlinear Stiffness in Incompressible Flow", *Journal of Sound and Vibration*, 138, pp.245-254.
- Zhu, D., Beeby, S., Tudor, J., White, N. and Harris, N., 2010, "A Novel Miniature Wind Generator for Wireless Sensing Applications" In: *IEEE Sensors 2010*, November 1-4, 2010, Waikoloa, Hawaii, USA.

RESPONSIBILITY NOTICE

The author(s) is (are) the only responsible for the printed material included in this paper.

The Human-size Walking Robot Lola – Hardware and Control Aspects

Markus Schwienbacher, Valerio Favot, Sebastian Lohmeier, Thomas Buschmann and Heinz Ulbrich

Institute of Applied Mechanics – Technische Universität München – Boltzmannstr. 15 – 85748 Garching, GERMANY
email: schwienbacher@amm.mw.tu-muenchen.de

Abstract: This paper presents some design and control aspects of the humanoid walking robot Lola. The robot has 25 active degrees of freedom and was developed at our institute. The main goal of this project is to realize a stable, fast and human-like walking motion with a biped robot. In order to reach the performance goal a sophisticated mechatronic hardware design combined with a robust stabilizing control is crucial. A multibody simulation of the whole system was used for design calculations and as a test-bed for the walking controller, to minimize the risk of damage during experiments. In current experiments a max. walking speed of 3.34km/h was reached, making Lola the fastest humanoid walking robot at this time.

Keywords: Robotics, Mechatronics, Walking Machine, Humanoid Robot, Control applications

INTRODUCTION

The rapid development in several technological fields such as computer technology, mechatronics and biped walking control in the last years made the realization of biped humanoid robots easier or even possible. Prominent examples are the Honda ASIMO (Hirai et al. 1998), Toyota Partner Robot (Tajima et al. 2009), HRP-2 (Kaneko et al. 2004), HRP-3 (Kaneko et al. 2008) and WABIAN-2 (Ogura et al. 2006). All these robots achieve reliable dynamic walking. But when compared to the capabilities of a human being high walking speeds and flexible motion generation still remain challenging. Many unresolved control problems exist in this field. To name a few: fast walking and running (Tajima et al. 2009), sudden turning motions, walking on rough terrain and trajectory generation in complex environments. Not only the controller, but also the mechatronic system must be designed carefully. It can not be neglected because the hardware contributes significantly to overall system performance. Both robot hardware and software must be seen as tightly coupled parts of a highly integrated mechatronic system. In the first part of this paper the mechanical and electronics design is introduced. The second part outlines the simulation environment and deals with the real-time trajectory generation and stabilizing control. Finally, first experimental results are presented.

HARDWARE OVERVIEW

Based on the research experience with our former robot Johnnie (Löffler et al. 2004), which achieved a maximum walking speed of 2.4 km/h, design considerations were derived towards a general improvement of the whole system (Lohmeier et al. 2006a;b). The speed goal for Lola is 5 km/h.

Lola is 180 cm tall and weighs approximately 60 kg. The physical dimensions are based on anthropometric data. Figure 1 shows a photograph of the fully assembled robot and the kinematic configuration with a total of 25 degrees of freedom (DoF). Simulations and experiments have shown that additional redundant DoF enable more natural and flexible gait patterns and extend the abilities of the robot in general. Therefore the legs have 7 DoF each, the pelvis has 2 and each arm has 3 DoFs. The stereo camera head has 3 DoFs, composed of a pan/tilt unit and an adjustable angle of vergence common to both cameras.

While most humanoid robots have 6DoF legs with a rigid foot, Lola has an additional actively driven joint, located between forefoot and heel, equivalent to the human toes. Other examples of humanoid robots with actuated toe joints are: H6, H7 (Nishiwaki et al. 2002) and the Toyota Partner Robot (Tajima et al. 2009).

All joints are driven by electric motors. While the sizes of gear and motor are adapted to the requirements of each link the structure of each actuator is similar. Figure 2 shows a section through the hip yaw motor as an example. We use high performance permanent magnet brushless synchronous motors (PMSM) from Parker Bayside. Except for the knee and ankle, all joints employ lightweight versions of Harmonic Drive (HD) gears as speed reducers. The knee and ankle joints consist of roller screw-based linear drives. This leads to a better mass distribution in the hip-thigh area compared to conventional HD-based designs. Each joint contains an incremental rotary encoder, an absolute angular encoder for link position sensing and a limit switch. The incremental rotary encoder mounted on the motor shaft is mainly used for motor control. The absolute angular encoder (resolution 17 bit, accuracy 0.1°) compensates elasticities and nonlinearities in the drive chain and eliminates the need for a homing routine, making startup faster and easier. To improve operational security and to prevent the robot from self-destruction each joint incorporates a limiting switch in the form of a light barrier.

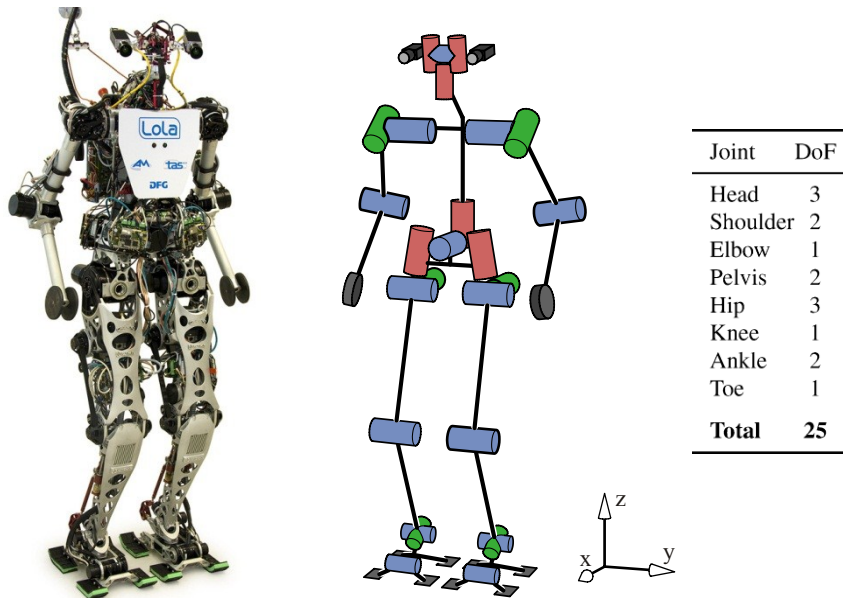


Figure 1 – Photograph of the anthropomorphic walking robot Lola and the kinematic structure of the robot with 25 DoFs.

The structural components are designed as lightweight yet stiff parts. In order to achieve good acceleration behavior of the locomotor system, the most relevant design goals for the mechanical system are: (1) minimum overall mass, (2) sufficient structural stiffness, (3) high center of mass, and (4) low moments of inertia of the leg links. The dimensioning of the robot hardware was done in an iterative process of mechanical design and multibody simulations (MBS).

Lola is equipped with two specially designed six-axes force/torque sensors mounted between the ankle and the foot. A section through the sensor is depicted in Figure 2 on the right. The sensors dimensioning and measurement range requirements were determined in MBS for a walking speed of 5 km/h. At a total weight of only 395g the sensor includes all necessary electronics and provides a digital communication interface.

The orientation and angular velocity of the upper body are estimated by an inertial measurement system (IMS). Simulations and experimental results with the robot Johnnie suggested that a sensor with high accuracy, signal quality (i.e. low noise) and bandwidth significantly improves the performance of the stabilizing controller. We are using a custom made lightweight version of the inertial measurement system iVRU-FC-C167 (from iMAR Navigation). The sensor consists of three open-loop fiber-optic gyroscopes and three MEMS accelerometers. The sensor fusion comprises internal error models and is integrated into the sensor.

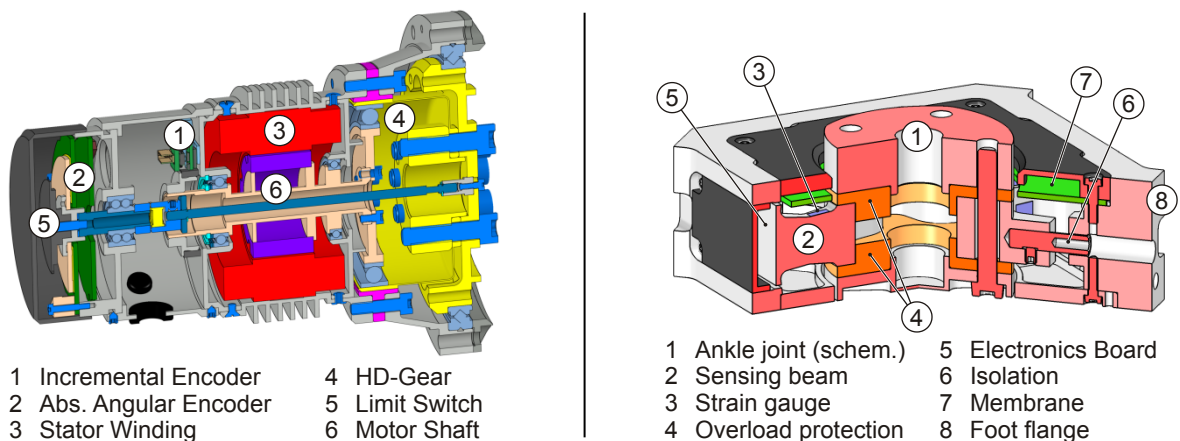


Figure 2 – CAD sections through (left) hip yaw joint and (right) force/torque sensor.

Lola is controlled by a central control unit (CCU) mounted on the back of the upper body and nine local controllers carrying out low-level tasks, such as joint control and sensor data processing. Figure 3 gives a schematic overview to the overall electronics architecture. The CCU is based on a PC platform (Intel Core 2 Duo Mobile, 2.33GHz), running the QNX real-time operating system. The local controllers are a custom development because of compactness and vari-

ous sensor/actuator interfaces. Gait pattern generation and stabilization control run on the on-board computer system without any support from outside except for power supply. An external PC is used only for monitoring purposes and to give basic operating commands if the robot is not connected to the vision system. Because of the high computational cost vision processing is done on an external PC cluster, which consists of 3 Intel Xenon based PCs.

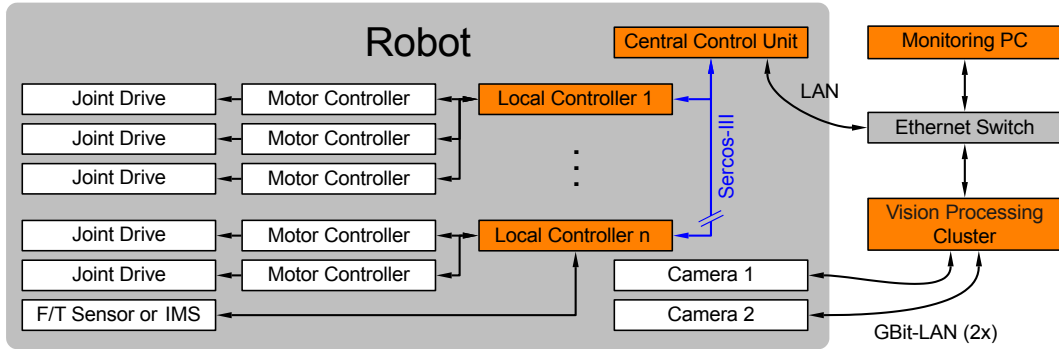


Figure 3 – Electronics architecture of Lola.

SIMULATION

The design of the robot’s hardware and control algorithms are based on simulations of the closed-loop system. During the design stage both hardware and control software are refined iteratively based on simulations of the current hardware and software design. To facilitate such a design procedure we have implemented a modular simulation system that can be used to simulate various robot configurations. The simulation model includes rigid body mechanics, gear friction models, actuator dynamics and models for the unilateral, viscoelastic foot-ground contact. This leads to the following coupled dynamical systems:

$$\mathbf{M}\ddot{\mathbf{q}} + \mathbf{h} = \mathbf{W}_\lambda \boldsymbol{\lambda} + \mathbf{W}_\tau \boldsymbol{\tau} \quad (1)$$

$$\mathbf{B}\dot{\mathbf{d}} + \mathbf{K}\mathbf{d} = \mathbf{f} \quad (2)$$

$$\mathbf{L}\dot{\mathbf{I}} + \mathbf{R}\mathbf{I} + \mathbf{k}_M \boldsymbol{\omega}_{rot} = \mathbf{U} \quad (3)$$

Equation (1) represents the equations of motion (EoM) for the rigid body dynamics. The vector \mathbf{q} consists of the generalized coordinates, \mathbf{M} is the mass matrix, and \mathbf{h} the vector of smooth forces. Finally, $\boldsymbol{\lambda}$ and $\boldsymbol{\tau}$ are the contact and actuator forces, acting on the MBS via the jacobian matrices \mathbf{W}_λ and \mathbf{W}_τ respectively.

Equation (2) describes the relationship between node forces \mathbf{f} and node displacements \mathbf{d} in the viscoelastic contact elements. The damping and stiffness matrices \mathbf{D} and \mathbf{K} can be obtained by discretizing the contact element continuum using the Finite Element Method. Drive dynamics includes the HD friction modeled as load dependent Stribeck friction and the motor dynamics shown in eq. (3). Here \mathbf{U} is the armature voltage, \mathbf{I} the current and $\boldsymbol{\omega}_{rot}$ the rotor’s angular velocity. \mathbf{L} , \mathbf{R} and \mathbf{k}_M are the inductance, resistance and motor back EMF constants, respectively. The resulting torque of a HD-based actuator is $\boldsymbol{\tau} = \mathbf{k}_M \mathbf{I} + \boldsymbol{\tau}_{HDgear}$, where $\boldsymbol{\tau}_{HDgear}$ is the friction torque.

By combining these components, different models of the robot are generated, satisfying either low calculation times or high accuracy. The simulation software has been validated against experiments with Johnnie (Buschmann et al. 2006).

CONTROL ASPECTS

In order to satisfy the high demands for real-time execution, the walking control is divided into multiple smaller processes. Based on global inputs, such as the desired walking direction and velocity, a step sequence planner plans the positions of the feet on the floor for the following three steps at the beginning of each step. A walking pattern generator calculates smooth trajectories for the feet and the center of mass (CoM). For this task the robot is modeled using a mod-

ified Inverted Pendulum Model with one additional point-mass for each leg. The simplified EoM in the coronal y-z-plane¹ is given by

$$m_b[z_b\ddot{y}_b - y_b(\ddot{z}_b + g)] = -T_x + m_l \sum_{i=1,2} [y_{l,i}(\ddot{z}_{l,i} + g) - z_{l,i}\ddot{y}_{l,i}] \quad (4)$$

where b denotes the body mass point, i is the foot index and T_x is the contact torque heading into forward direction. The values for the masses are distributed such that the upper body inclination is minimized. We solve Eq. (4) as a boundary value problem (BVP) by connecting a stable CoM trajectory solution to the current trajectory with continuity in y and \dot{y} and a desired endpoint $y_{b,E}$. In order to solve the BVP numerically in real-time we have implemented a collocation method with cubic splines as basis functions (Buschmann et al. 2007).

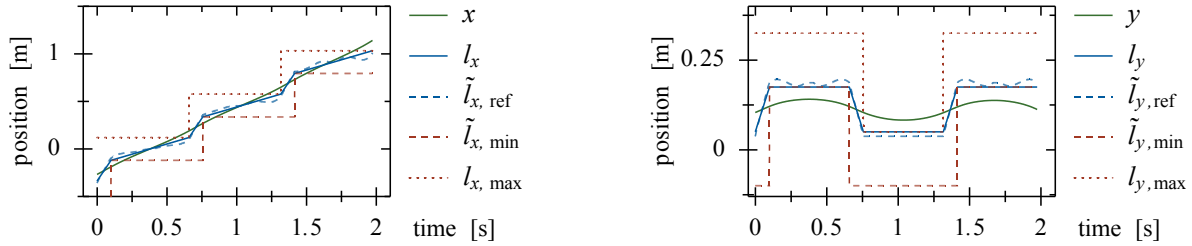


Figure 4 – Example of CoG trajectories (x and y) and center of pressure (l_x , l_y) obtained from spline collocation with 30 equally spaced control points.

Since the planned CoM and foot-torque trajectories calculated with the simplified point mass model of the robot are unstable on the real robot, a stabilizing controller must be used. The basic idea is to stabilize the upper body inclination. Similar concepts are used to control most of the existing full-size humanoid robots (Kajita et al. 2005; Löffler et al. 2004; Takenaka 2004).

The task-space trajectories, obtained from the trajectory generator, are modified using sensor data from the 6-DoF force torque sensors in the feet and the IMS in the torso. After modification the trajectories are mapped into joint space using a resolved motion rate control scheme (Whitney 1969) with null-space optimization (Liégeois 1977) of the redundant joints. The joint trajectories are then tracked using a cascaded joint position control with secondary control of velocity and motor current.

EXPERIMENTAL RESULTS AND CONCLUSION

The robot Lola is not only able to walk forwards, backwards, sideways and around curves. Small disturbances such as an uneven floor or pushing and pulling are reliably stabilized by the controller. These qualities are indispensable for higher walking speeds. Figure 5 shows a frame sequence from a recent experiment where Lola walks as fast as 3.34 km/h. In Figure 6 the motion when walking sideways can be seen.

After six years of development Lola was presented to the public in April 2010 at the Hannover Messe in Germany. During the demonstration the stability and the walking capabilities of the robot were shown. In the 5 exhibition days 25 shows were performed without major problems or failures, which show the robustness of the overall system.

¹ The EoM in the sagittal x-z-plane calculates accordingly.

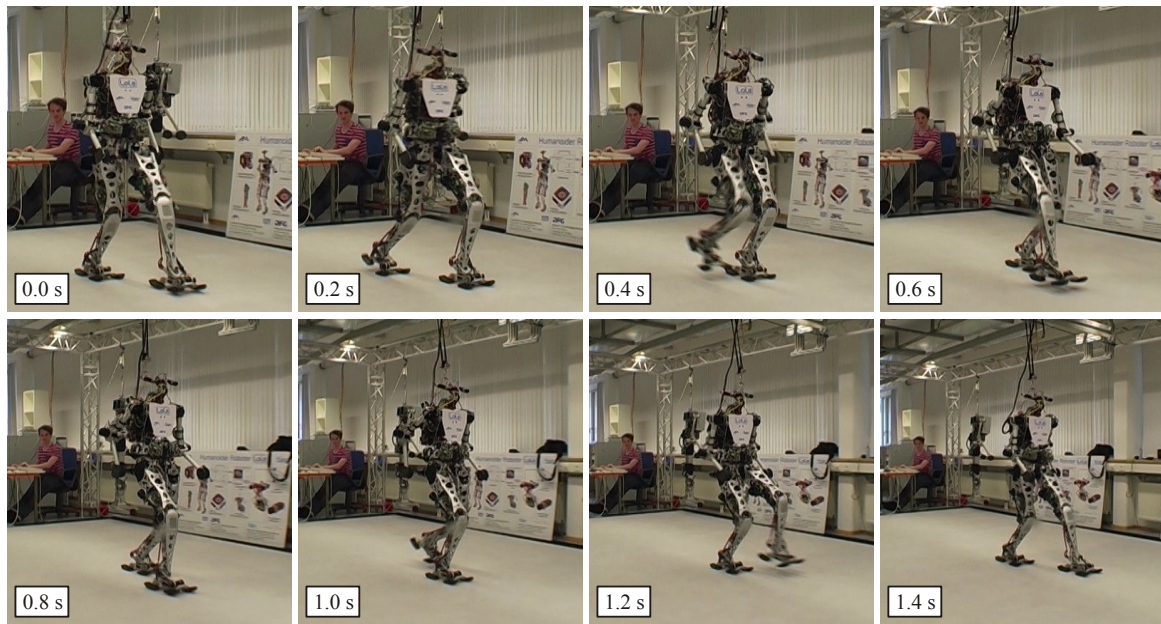


Figure 5 – Frame sequence of an experiment where Lola walks 3.34 km/h.

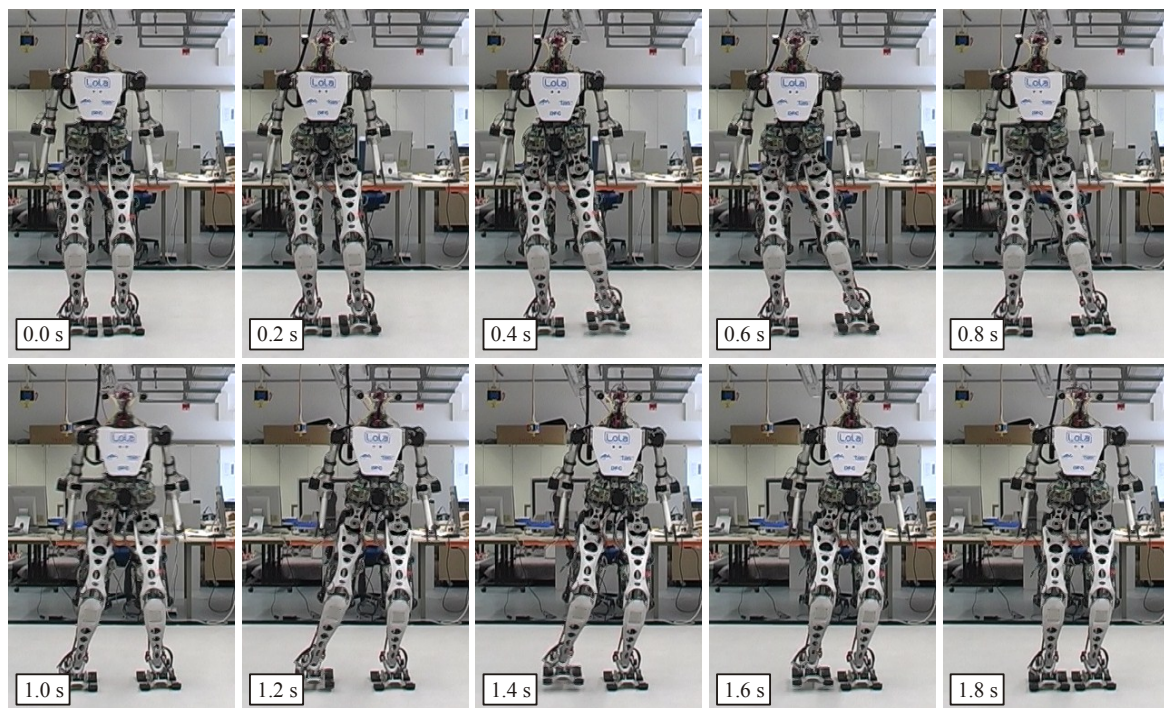


Figure 6 – Frame sequence of an experiment with Lola walking sideways.

In current walking experiments the robot is able to walk as fast as 3.34 km/h which is promising for reaching the goal of 5 km/h. While Hondas and Toyotas robots are able to run faster (Honda Asimo: 6km/h; Toyota Partner Robot: 7 km/h), their maximum walking speed is under 3 km/h (according to publicly available data). At this time (November 2010) Lola is the fastest biped robot with anthropomorphic leg structure. With the increasing system knowledge from experiments further controller improvements will be made.

ACKNOWLEDGMENTS

This work is supported by the German Research Foundation (“Deutsche Forschungsgemeinschaft” – DFG) – grant UL 105/29.

REFERENCES

- Buschmann, T., Lohmeier, S., Ulbrich, H., Pfeiffer, F., 2006, “Dynamics Simulation for a Biped Robot: Modeling and Experimental Verification”, Proc. of the IEEE Intl. Conf. on Robotics & Automation (ICRA), pp. 2673–2678.
- Buschmann, T., Lohmeier, S., Bachmayer, M., Ulbrich, H., Pfeiffer, F., 2007, “A Collocation Method for Real-Time Walking Pattern Generation”, Proc. of the IEEE-RAS Intl. Conf. on Humanoid Robots (Humanoids).
- Hirai, K., Hirose, M., Haikawa, Y., Takenaka, T., 1998, “The Development of Honda Humanoid Robot”, Proc. of the IEEE Intl. Conf. on Robotics & Automation (ICRA), Leuven, Belgium.
- Kajita, S., Nagasaki, T., Kaneko, K., Yokoi, K., Tanie, K., 2005, “A Running Controller of Humanoid Biped HRP-2LR”, Proc. of the IEEE Intl. Conf. on Robotics & Automation (ICRA).
- Kaneko, K., Kanehiro, F., Kajita, S., Hirukawa, H., Kawasaki, T., Hirata, M., Akachi, K., Isozumi, T., 2004, “Humanoid Robot HRP-2”, Proc. of the IEEE Intl. Conf. on Robotics & Automation (ICRA), New Orleans, USA.
- Kaneko, K., Harada, K., Kanehiro, F., Miyamori, G., Akachi, K., 2008, “Humanoid robot HRP-3”, International Conference on Intelligent Robots and Systems (IROS), pp. 2471–78.
- Liégeois, A., 1977, “Automatic supervisory control of the configuration and behavior of multibody mechanisms”, IEEE Intl. Transactions on Systems, Man, and Cybernetics SMC-7, pp. 63–71.
- Lohmeier, S., Buschmann, T., Ulbrich, H., Pfeiffer, F., 2006, “Modular joint Design for Performance Enhanced Humanoid Robot LOLA”, Proc. of the IEEE Intl. Conf. on Robotics & Automation (ICRA), pp. 88–93.
- Lohmeier, S., Buschmann, T., Schwienbacher, M., Ulbrich, H., Pfeiffer, F., 2006, “Leg Design for a Humanoid Walking Robot”, Proc. of the IEEE-RAS Intl. Conf. on Humanoid Robots (Humanoids), pp. 536–541.
- Löffler, K., Gienger, M., Pfeiffer, F., Ulbrich, H., 2004, “Sensors and control concept of a biped robot”, IEEE Trans. Ind. Electron. 51, pp. 972–80.
- Nishiwaki, K., Kagami, S., Kuniyoshi, Y., Inaba, M., Inoue, H., 2002, “Toe Joints that enhance Bipedal and Fullbody Motion of Humanoid Robots”, Proc. of the IEEE Intl. Conf. on Robotics & Automation (ICRA), Washington, DC, USA, pp. 3105–3110.
- Ogura, Y., Aikawa, H., Shimomura, K., Kondo, H., Morishima, A., Lim, H., Takanishi, A., 2006, “Development of a Humanoid Robot WABIAN-2”, Proc. of the IEEE Intl Conf on Robotics & Automation (ICRA), pp. 76–81.
- Tajima, R., Honda, D., Suga, K., 2009, “Fast Running Experiments Involving a Humanoid Robot”, Proc. of the IEEE Intl. Conf. on Robotics & Automation (ICRA).
- Takenaka, T., 2004, “Controller of Legged Mobile Robot”, european patent application no. EP1475198A1.
- Whitney, D.E., 1969, “Resolved Motion Rate Control of Manipulators and Human Prostheses”, IEEE Transactions on Man Machine Systems 10, pp. 47–53.

RESPONSIBILITY

The authors are the only responsible for the printed material included in this paper.

Some results in analyzing the dynamic behavior of blade rows coupled by shroud contacts

Nicolò Bachschmid^{1,2}, Simone Bistolfi², Paolo Pennacchi¹, Emanuel Pesatori², Massimiliano Sanvito², Michele Ferrante²

¹ Department of Mechanical Engineering, Politecnico di Milano, Via La Masa, 1, I-20156, Milan, Italy

² R&D Department, Franco Tosi Meccanica S.p.A., P.zza Monumento 12, I-20025, Legnano (MI), Italy

Abstract: Actual trend in steam turbine design is to use blades with integral shrouds, for high pressure and intermediate pressure steam turbine sections, as well as sometimes also for the long blades of the low pressure sections. The blades are either inserted with their root into the seat on the shaft in such a way that small clearances remain between adjacent blade shrouds, so that the relative vibration amplitude is restricted by the contact between adjacent shrouds. This mechanism is called “snubbing mechanism”. Another technology for mounting blades on the shaft is to do it in such a way that the blades are slightly forced against each other in correspondence of the shrouds: this should allow the continuity of the contact without clearances also at rated speed and full load. In this case the blades are called “pre-twisted”. Field experience has shown that these kinds of blade rows has a “robust and smooth” behavior. But there is still some lack of theoretical/numerical investigation for defining its dynamical behavior in different operating conditions, both for the blades with clearance and with pre-twist. The aim of this paper is to investigate numerically the non-linear dynamic behavior of a couple of shrouded blades, taking account of contact forces and friction. An equivalent linear model has then been developed for analyzing the behavior of the complete blade row. Also some provisional experimental results on non-rotating blade rows are presented.

Keywords: blade vibration, blades with integral shrouds, nonlinear contact.

NOMENCLATURE

g = gap between blade shrouds
h = dimensionless damping ratio
n = engine order

z = number of blades
 μ = friction coefficient
 φ = phase delay

A_{max} = max. vibration amplitude
F = pretwist contact force
f = frequency

INTRODUCTION

Blades with shrouds that restrict vibration amplitudes are commonly used by steam turbines manufacturers, see e.g. (McGuire et al.,1990) and (Hurd et al.,2005). Blade vibrations can be generated by the stationary fluid flow synchronous excitation (called engine order excitation) or by some instability mechanism like flutter or rotating stall. Also coupling with flexural and torsion vibrations of the shaft can generate blade vibrations, as specified in (McGuire et al.,1990)

Synchronous engine order excitation with the harmonics of the rotating speed, is believed to be the major excitation mechanism. The excitation comes from stationary steady state but not uniform fluid flow, which excites a backward traveling wave on the rotating blade row. Resonance occurs when the frequency of excitation equals that natural frequency of the blade row, which corresponds to a mode with a number of nodal diameters that must be equal to the engine order. The problem is that the amplitude of excitation is generally unknown since it depends on the amount of asymmetry in the pressure and velocity distribution around the blade row, where the design of the machine aims to obtain a fluid flow as much as possible axi-symmetrical.

The design of blades requires generally that resonances with engine order excitation are avoided. These blades are then called tuned blades or tuned blade rows. When resonances cannot be avoided (like in industrial steam turbines or gas turbines which must operate at different rotating speeds) then sufficient damping must be introduced by means of friction in under-platform dampers or in between shrouds or snubbers in order to reduce the vibration to acceptable levels. The design of these blades is then called resonant resistant.

In any case for the design of blades it is necessary to calculate the natural frequencies of the blade rows in which the blades are in contact or get in contact each other during vibration with the shrouds, which is not at all trivial, due to the non linear character of the contact conditions.

Further for the stress calculation of the blades it is necessary to use a rather refined mesh of the blades (30.000 elements for each blade is a good compromise for having accurate stress calculation also in the roots of the blade) and to consider the actual damping of the system which also depends on the contact conditions, on the friction and on the relative vibration amplitude in correspondence of the contacting surfaces. More refined calculation should take into account also the effects of random blade mistuning due to manufacturing tolerances.

In literature in the last decades many studies have been performed on the damping mechanism due to friction forces developing in surfaces in contact, see e.g. (Petrov et al., 2004) and (Petrov et al., 2003). As known, contact conditions between surfaces can be sticking, slipping or in separation. When contact occurs after previous separation, sharp or smooth shock can build up, as function of relative velocity and surface conditions. Accurate models consider that normal and tangential stiffness of the contact area is increasing with penetration depth as long as this is less than the sum of surface roughnesses, and become constant when penetration gets higher than surface roughness. Taking account of all these non linear effects for the analysis of the dynamic behavior of a blade row with contacting shrouds, requires or very much simplified blade models or reduced modal models (which do not allow stress evaluation in the root of the blade) and numerical time step integration, or an approximated multi-harmonic approach (harmonic balance approach) which permits quick frequency domain integration and allows the use of more complete and accurate models of the blades, as it is done e.g. in (Hohl et al., 2008) or (Petrov, 2004).

Non linear calculations with complete 3D models (with refined mesh for stress calculation) for the blade row are not practically affordable.

For studying the snubbing mechanism in (Bachschnid, 2007) the blade has been reduced (by means of modal analysis) to a single degree of freedom system, a gap between adjacent shrouds has been considered for a complete row, and when relative vibration exceeds the gap, and shrouds get in contact, then a constant contact stiffness with a non-zero threshold value is introduced combined to some damping. With this very simple model the non linear behavior of the blade row with the snubbing mechanism has been analyzed in the time domain. The dynamical behavior can generate vibrations quite different from kinematic limitation of the relative vibration amplitude: in conditions close to row resonance the vibration amplitude is even smaller than that one corresponding to the kinematic limitation, but in condition far from resonance the vibration amplitude can exceed the value obtained without contact between shrouds. The “kinematic limitation” of vibration amplitude A_{max} with reference to the gap g is shown in Figure 1, from (Bachschnid et al., 2007), as function of ratio of nodal diameter number n to number of blades z in the row. The non-linear calculated behavior with intermittent contact, an example in Fig. 1, shows reduced vibration amplitudes compared to the free standing blade amplitudes, but also that due to the rough contact conditions higher frequency components can be excited.

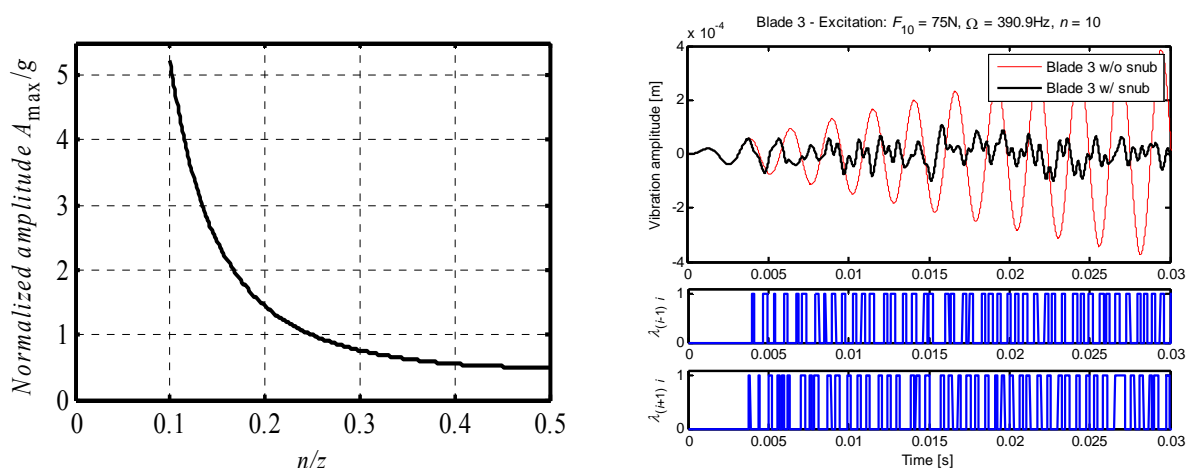


Figure 1- Kinematic vibration amplitude limitation as function of n (left) and resulting dynamic behavior (right), from (Bachschnid et al., 2007)

In the present study also these results of the snubbing mechanism will be checked with a much more refined model of the blade and of the contact conditions.

A rather complete and accurate analysis of the free and forced vibration of a shrouded blade row has been performed in (Szwedowicz et al., 2008) and compared to experimental results obtained on a test rig, showing good agreement: main concern was the definition of damping due to the contact conditions.

It is well known that also mistuning can have great influence on the dynamic behavior of blade rows. An analysis on how mistuning can combine with the snubbing mechanism made in (Bachschnid et al., 2008) with the same very simple model of the blade row and contact conditions of (Bachschnid et al., 2007) has shown that mistuning is beneficial since it is able to increase the effectiveness of the snubbing mechanism.

Interesting results of mistuning and shroud scattering are shown in (Petrov et al., 2005). In (Heinz et al., 2010) mistuning effects on a low pressure blade row (without shrouds) are measured and simulated successfully.

The aim of this paper is to present some numerical results obtained with commercial software about natural frequencies and forced response of a couple of blades in different contact conditions. Different dynamical behaviors, with continuous contact and with periodical intermittent contacts, with and without friction, with strong or weak excitation, close to resonance and far from resonance are shown. All results show a reduction of vibration amplitude with respect to the free standing blades without contact, as could be expected. From these results a linear equivalent

(with restricted validity) model of the complete blade row will be obtained which allows natural frequencies evaluation and forced vibration calculations.

DESCRIPTION OF THE MODEL

The model which has been selected for this sensitivity analysis study is the model of a blade at the first stage of a IP steam turbine. The geometry of the couple of blades and the detail of the mesh of the shrouds are shown in Figure 2. Blade row is composed by 73 blades. Only the first mode of vibration of the free standing blade has been considered, since some experimental results on a similar blade row has suggested that in this range of blade dimensions, mainly blade row vibration families are excited in which the single blade is vibrating in its first mode. Friction coefficient $\mu = 0.2$ has been considered between shrouds. The blades are fixed to the shaft at the roots. Centrifugal force and stationary static steam force are applied to the system. The amplitudes of the considered dynamical forces acting on the blades are in the range of 4% - 16% of the static steam force. Dimensionless damping $h=0.5\%$ has been considered generally in the calculations. The blades have been excited in resonance, in order to analyze the effects of the shrouds in the most critical situation when highest amplitudes are excited. In some case also higher damping has been considered, mainly for shortening the calculation time necessary for damping out the transient motion. In some other case also a condition far from resonance has been considered. In one case also some mistuning between the two blades has been introduced. In order to simulate different engine order (EO) excitations the dynamic forces are applied to the 2 blades with a phase delay φ given by

$$\varphi = 2n\pi/z \quad (1)$$

where n is the engine order and z the number of blades.

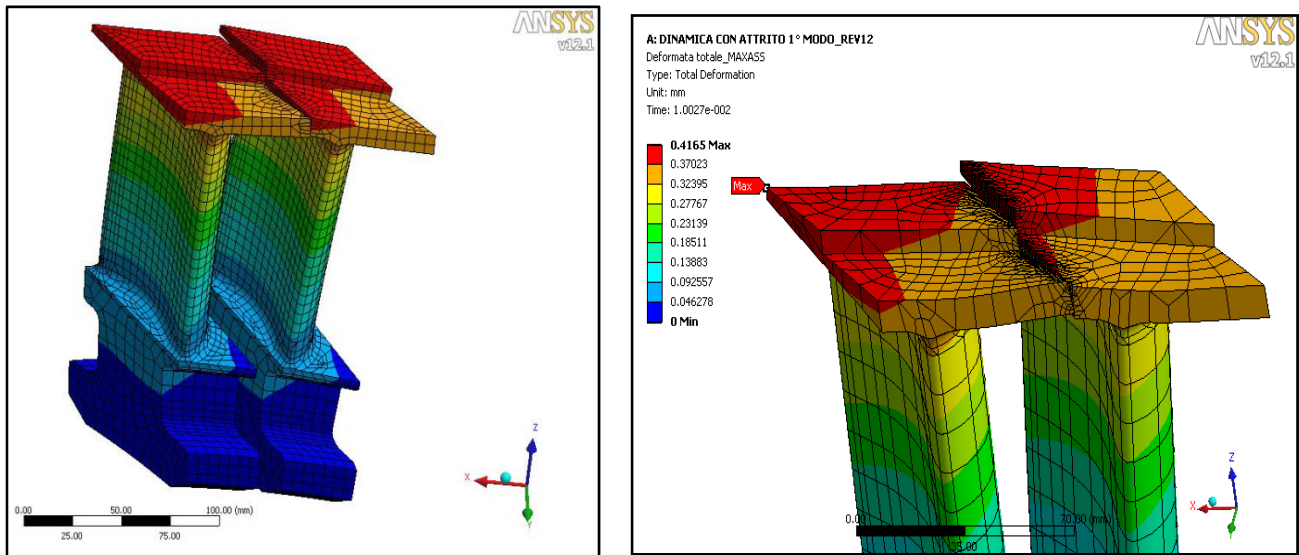


Figure 2 – a) Geometry and mesh of the couple of blades b) Detail of the shrouds

RESULTS OF THE SIMULATION

First of all the frequency response of the single free-standing blade has been calculated. The first resonance occurs at 464 Hz. The amplitude in resonance represents the upper limit of the vibration amplitude, since in this model energy loss due to friction and shocks are not considered. In order to take into account the effect of the different engine order excitations, two limit conditions have also been computed considering the following linear systems:

- a) system composed by the couple of blades in which the shrouds are connected by a *sliding* or slipping contact without friction. This condition is called “no-separation”. The resonance frequency does not change with the engine order excitation, but the vibration amplitude of the blade tip shows obviously a reduction with respect to the free standing blade which increases strongly with the engine order, reaching zero when

$$n = z/2 \quad (2)$$

This result is due to the phase difference in blade excitation as can be deduced from expression (1). The corresponding amplitude at 0 EO excitation represents the maximum amplitude and has been chosen as reference for normalizing vibration amplitudes. It should be noted that in case of a complete row the natural frequency increases with the engine order, in case of 2 blades only the contribution of the row is missed.

- b) system composed by the couple of blades bonded in correspondence of the shrouds, which corresponds to a *sticking* contact condition. In this case the natural frequency of the couple of blades increases strongly. Therefore the vibration amplitude at the frequency of 464 Hz, far below resonance, is very small and cannot be compared to the normalized amplitudes calculated in resonance and represented in Figure 3.

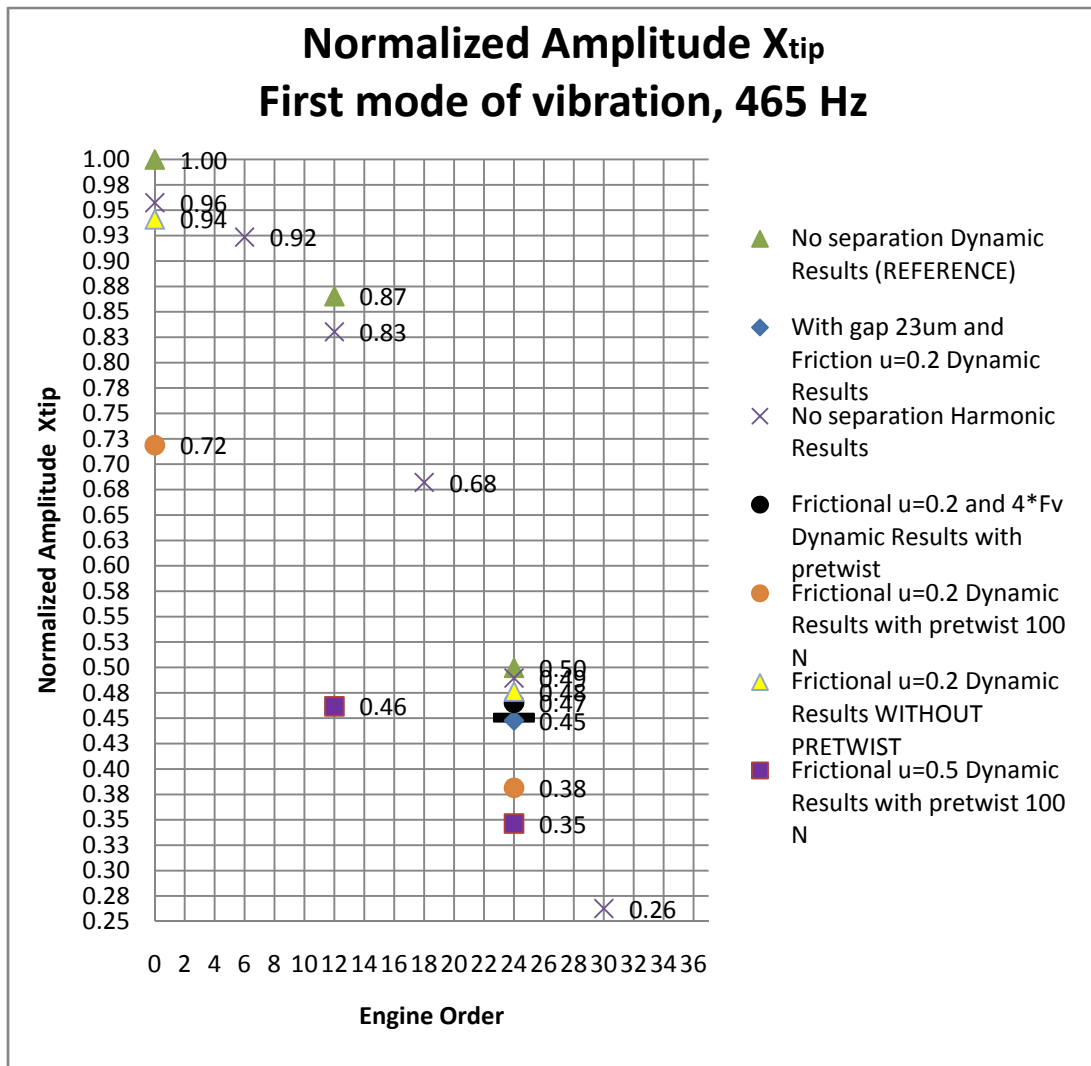


Figure 3 - Reduction of vibration amplitudes as function of engine order

The contact condition which will occur in reality is in between the two above limit conditions, because the contact conditions may include separation, slipping and sticking contact during the same load cycle.

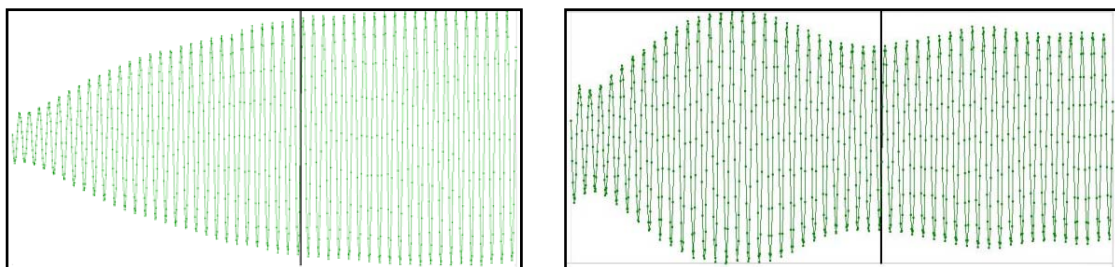


Figure 5- Transient simulation of the couple of blades in resonance (left) and out of resonance(right)

In the following the results of a series of non-linear calculations which take into account different contact conditions with friction are presented. These results are obtained as steady state vibration amplitude after a long lasting transient, due to the low damping of the blades. A huge number of cycles is needed to reach a steady state situation. Beating between natural frequency and exciting frequency occurs with excitation slightly out of resonance.

Figure 5 shows the transient vibration of the tip of the 1.st blade shroud of the couple of blades with friction, excited in resonance and slightly out of resonance: roughly 50 cycles are needed for getting a steady state situation.

In order to have a reasonable accuracy in the results of the non-linear calculation one load period has been divided in 120 load steps. Also the number of cycles has been increased to 150 for reaching true steady state situation, but only the 10 last cycles have been analyzed. Errors have been evaluated by comparing linear no-separation time step integration results (briefly called dynamic results) with harmonic analysis results (called harmonic results). These last values are given for 0, 6, 12, 24, and 30 EO excitation in Fig. 3 (indicated by crosses). Dynamic results have been instead calculated for 0, 12 and 24 EO. A maximum error in amplitude of 4% has been found, which demonstrate sufficient accuracy obtained with affordable calculation times.

No-separation results with 0 EO excitation, which are equal to single free standing blade results, have been assumed as reference situation in order to evaluate the effect of the contact conditions and the friction in terms of vibration amplitude reduction (at same frequency and same EO excitation). Steady state vibration amplitude, at the end of the transient, measured always in the same point on the shroud tip, have been divided by the reference amplitude.

A first set of calculations have been made with a low value of friction coefficient ($\mu=0.2$), assuming a rather high pretwist contact force between shrouds ($F=100\text{ N}$). Results are given in Fig. 3 for 0, 12 and 24 EO excitation showing reductions in vibration amplitudes ranging from 28% (0 EO) to 24% (24 EO). When the pretwist contact force is removed the reduction drops to 6% (0 EO) and to 4% (24 EO). When a small initial clearance (a gap of $23\ \mu\text{m}$) is left between shrouds, surprisingly a higher reduction is obtained: a 10% reduction at 24 EO excitation.

An interesting result is obtained increasing the excitation force: with a 4 times stronger excitation, and keeping constant the pretwist contact force of 100N , the vibration amplitude increases more than 4 times exceeding the proportional value by 24%. As will be shown this effect is due to the fact that continuous contact between shrouds is lost in a part of the load cycle, due to higher relative vibrations forced by the excitation.

CONTACT CONDITIONS

Regarding the type of contact (continuously sliding, intermittent sliding-separation, intermittent sliding-sticking or intermittent sticking-sliding-separation) all types can occur depending on excitation.

As an example in Figure 6 two different contact situations are shown: the case of high exciting force is compared to the case of normal (low) exciting force. The figure shows the contact conditions (2 - sliding, 3 - sticking, 1 - near and 0 - far): low excitation generates mainly sliding contact, high excitation generates separation. Therefore the energy dissipation is less in case of higher excitation.

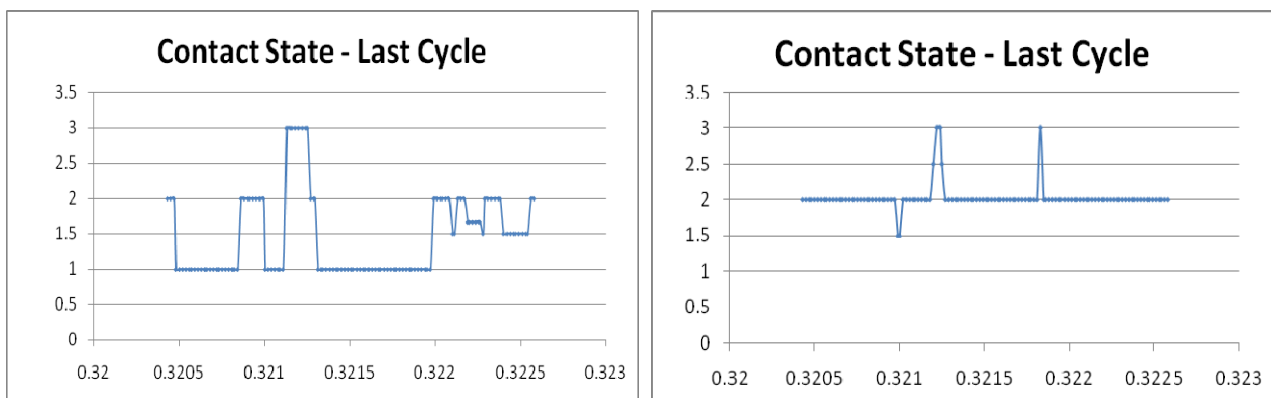


Figure 6- Contact conditions with high (left) and low (right) excitation.

For representing the contact conditions the contact stiffness has been updated automatically by the software each load step. The resulting overall contact stiffness can be evaluated dividing the resulting normal contact force by the maximum penetration depth in each step. The resulting contact stiffness is represented in Fig. 7, as well as also the contact force. The contact force ranges from 0 to 100 N for low excitation and between 0 and 600 N for high excitation, and the stiffness ranges accordingly between 0 and a maximum peak of $1.6\text{e}6\text{ N/mm}$ for low excitation and $3.0\text{e}6\text{ N/mm}$ for high excitation.

As could be expected where the contact is continuous (with low excitation) the stiffness is roughly proportional to the contact force. In fact higher contact forces generate larger contact areas and consequently higher contact stiffness.

In case of higher excitation, stiffness is defined only when contact occurs; where no contact occurs the reaction force should be 0, but its value tends towards 100N which is the effect of the external pretwist force.

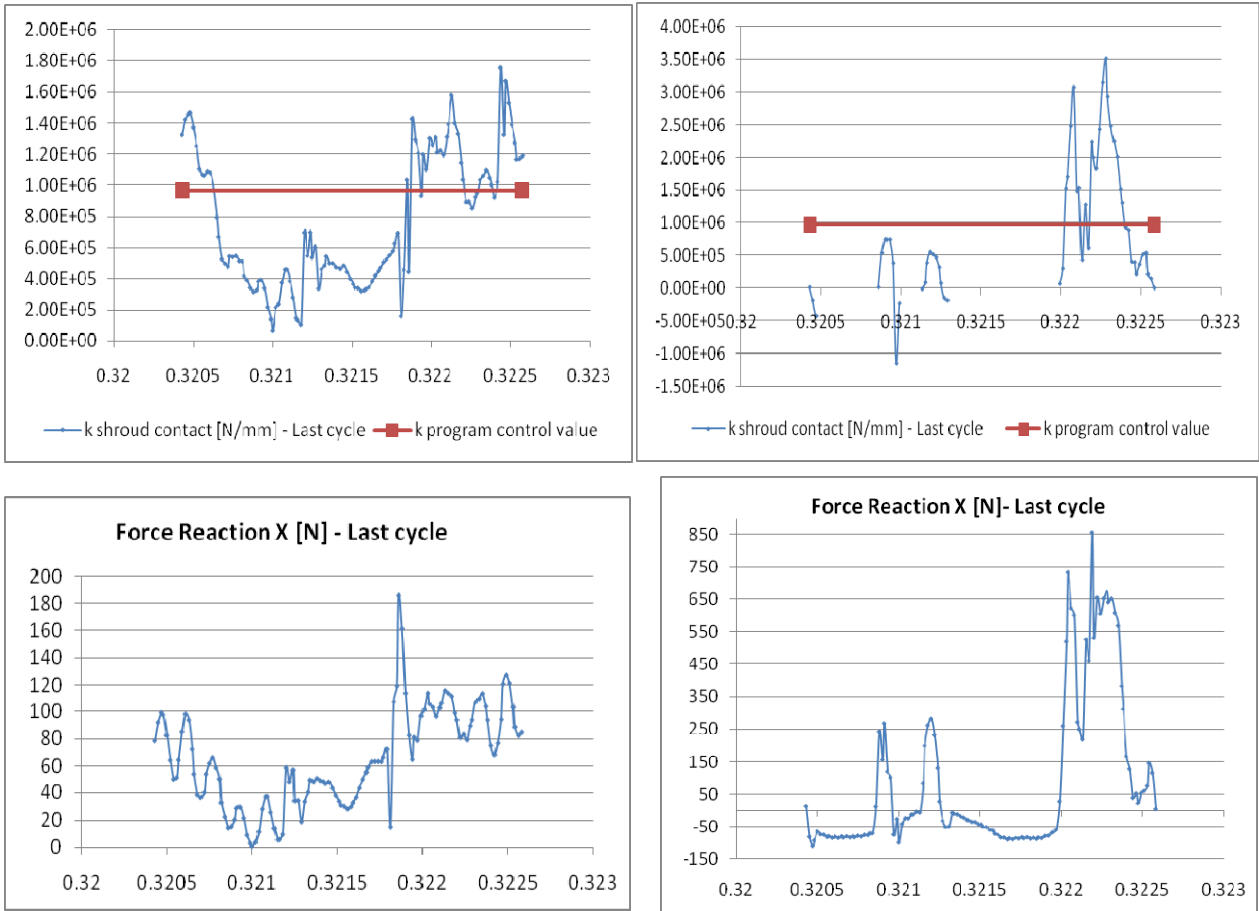


Figure 7- Contact stiffness and contact force with high (left) and low (right) excitation.

Due to the deformation of blades and shrouds caused by the centrifugal force and by the static and dynamic steam force, the contact occurs only in few elements of the contacting shroud surface. This can be seen in Fig. 8, where contact surface and contact pressures are represented. Similar results have been found in (Szwedowicz et al., 2008).

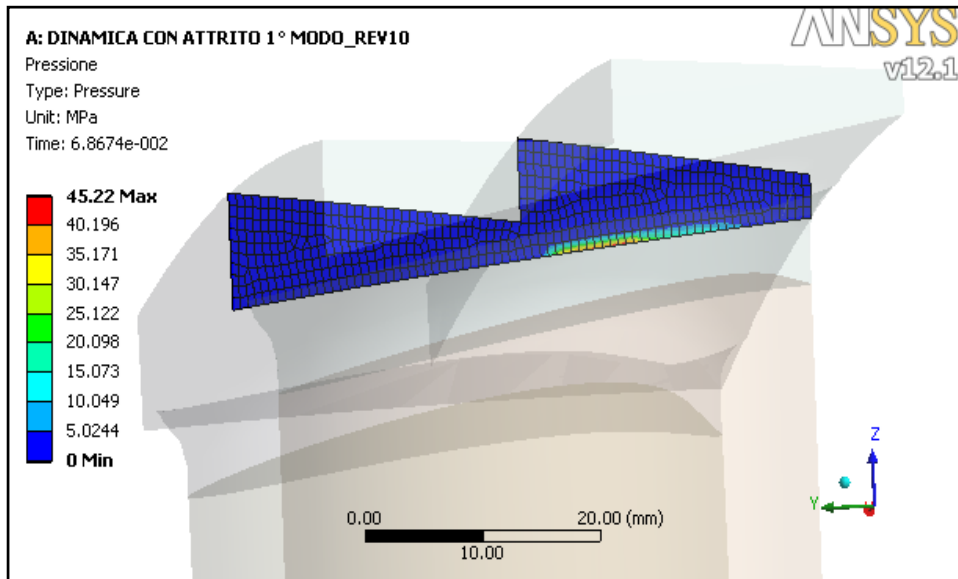


Figure 8 - Contact surface of the shrouds and contact pressure

Interesting is also the behavior of the shrouds in the case of initial gap. Figure 9 shows the gap between the shrouds during the last cycle, and the contact pressure when contact occurs. Contact occurs only during a small fraction of the

period, but is sufficient to produce higher energy dissipation with respect to the situation with 0 gap, where contact should be more continuous. The amplitude cannot be compared to the “snubbing” kinematic limitation, because here we have only 2 blades instead of the complete row. Due to the missing blades of the row, the relative vibration (gap) exceeds 100 μm , and the absolute vibration amplitude exceeds 340 μm . The vibration seems to be pure sinusoidal, no additional dynamic effects can be recognized, despite some peaks in the contact pressure. This could be different when considering the complete row, as predicted by the simple model in Fig. 1.

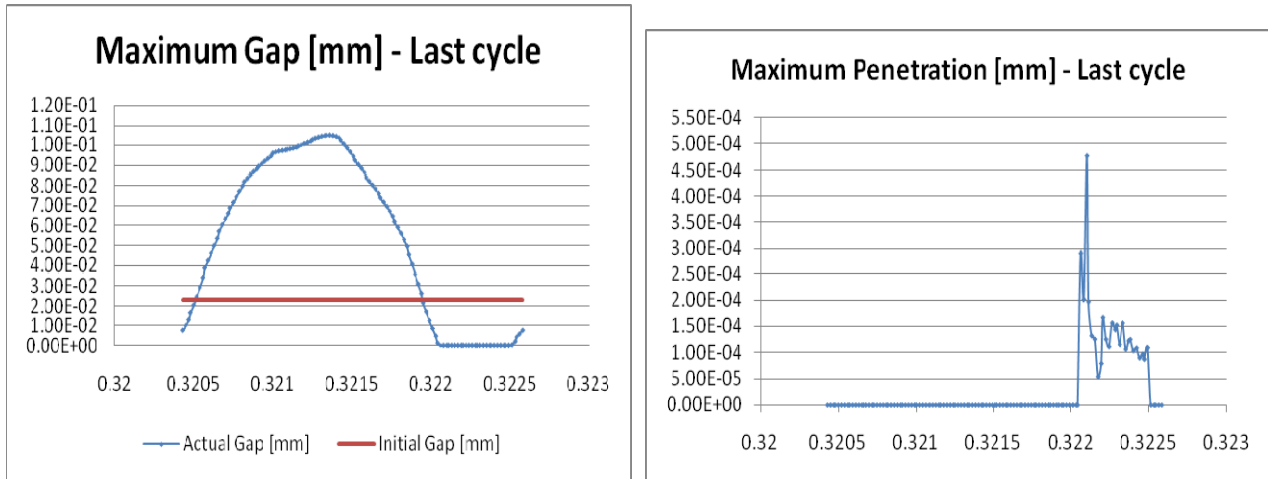


Figure 9 – Actual gap and contact pressure for shrouds with initial gap and no pretwist.

THE EQUIVALENT LINEAR MODEL

An approximated linear model of the complete blade row can be built up replacing the non linear contact forces by equivalent spring and damper forces. A linear model is required for calculating with cyclic symmetry condition the dynamical behavior of the complete row in the frequency domain, for

- a) evaluating natural frequencies corresponding to different ND (nodal diameter) row mode shapes
- b) calculating the frequency response for different EO excitation.

Non linear calculation in the time domain of the complete blade row (composed by 73 blades) are unaffordable.

The linear equivalent model of blades connected in correspondence of the shrouds by springs and dampers, has obviously only a limited validity : results will be valid in a limited range of excitation severity. The equivalent spring stiffness has been tuned for reproducing the dynamic behavior of the couple of blades in no-separation conditions (without friction).

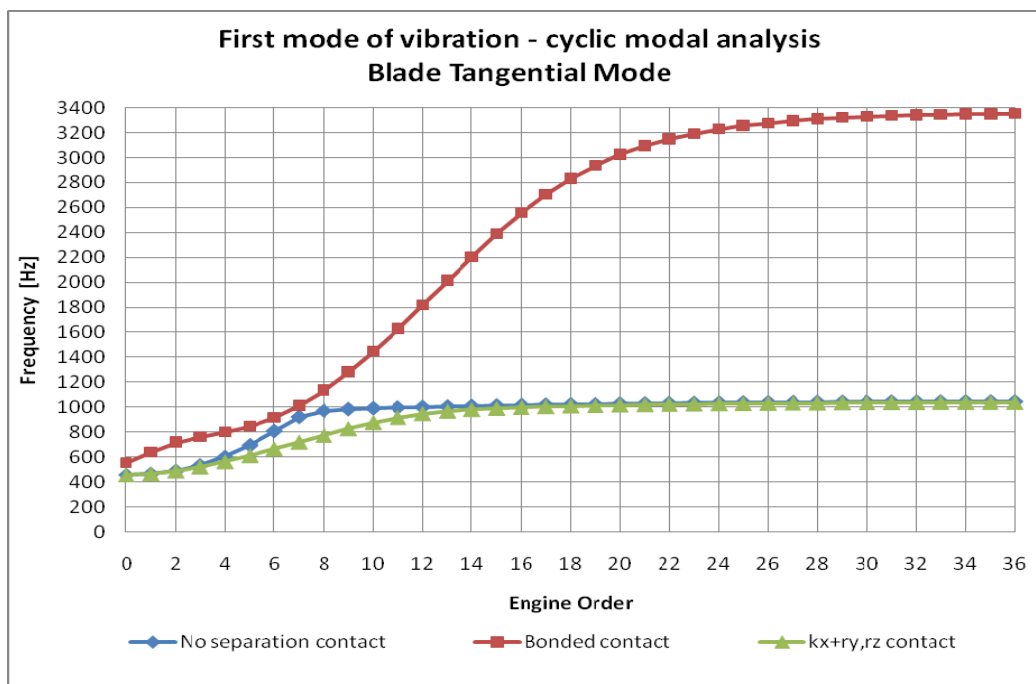


Figure 10 – Natural frequencies as function of ND number

A spring, normal to the contact face, with the mean contact stiffness reproduces accurately the dynamic behavior. Tangential springs have not been introduced. Dampers acting only in tangential directions, suitably tuned, provide the necessary vibration amplitude reduction shown in fig. 3.

With this linear model the cyclic behavior of the complete row has been calculated, and compared to the behavior of no-separation contacts between shrouds and to the behavior of bonded (sticking) contact between shrouds. Figure 10 shows the results of natural frequencies as function of the different nodal diameter (ND) mode shapes (red curve shows bonded shrouds, blue curve shows no-separation shrouds, green curve shows equivalent linear model results), and Fig. 11 one typical mode shape. No-separation results are closest to the equivalent model results, except in the range from 4 ND to 12 ND, where no separation results show much higher natural frequencies, with unrealistic shroud deformation shapes. As could be predicted the bonded contact shifts the natural frequencies to extreme high values, which are again rather unrealistic.

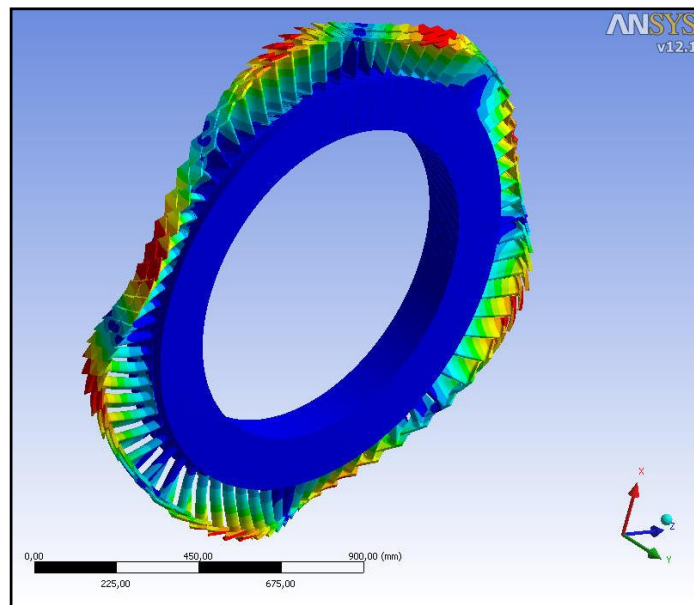


Figure 11 – Mode shape with ND4 and no-separation

Friction has only little influence on natural frequencies and mode shapes, as can be seen in above figures, but becomes extremely relevant when frequency response functions are calculated due to the assumed excitations. The results of these calculations allow then to check stresses in order to assess the blade fatigue life. Without suitable models of the shroud contacts it would be impossible to check resistance and fatigue life of blades.

EXPERIMENTAL RESULTS ON NON-ROTATING BLADE ROWS

Some experimental checks on the dynamical behavior of shrouded blade rows have been performed on a non-rotating steam turbine shaft, on which blade rows with so-called zig-zag shrouds have been mounted. One blade has been excited by a hammer in correspondence of the shroud and vibrations of the shrouds have been measured by accelerometers in correspondence of the excited blade and at different distances of the excited blade, in order to see how much the vibration was propagating along the row. Measurements have been taken at a distance of 5 blades (in both directions) and at a distance of 10 blades. Tests have been repeated in 2 different angular positions, and practically identical results have been found. Figure 12 shows the position of the 2 accelerometers. The excited blade is always the blade monitored by accelerometer 1.



Figure 12 – Position of accelerometers during impulse tests

Frequency spectra, superposed for the two accelerometers at 5 blade distance, for row 10 and 16 are shown in Fig. 13. For the longer blades (row 16) practically only one mode has been excited at 725 Hz, which propagated with roughly the same phase at the distance of 10 blades. The sharpness of the peak amplitude indicates poor damping. For a comparison the same free standing blade had following first 3 natural frequencies:

$$f_1 = 572 \text{ Hz} \quad f_2 = 973 \text{ Hz} \quad f_3 = 2873 \text{ Hz.}$$

For the shorter blades of row 10 two or three modes could be excited but these are probably different modes of the same family (related to the first mode of the blade). The first mode at 1000 Hz propagates with same phase at a distance of 10 blades. The second mode at 1175-1200 Hz showed same phase at 5 blades distance and opposition of phase at 10 blades distance. These modes show also rather good damping characteristics. For a comparison the free standing blade had following natural frequencies:

$$f_1 = 698 \text{ Hz} \quad f_2 = 1226 \text{ Hz} \quad f_3 = 3798 \text{ Hz}$$

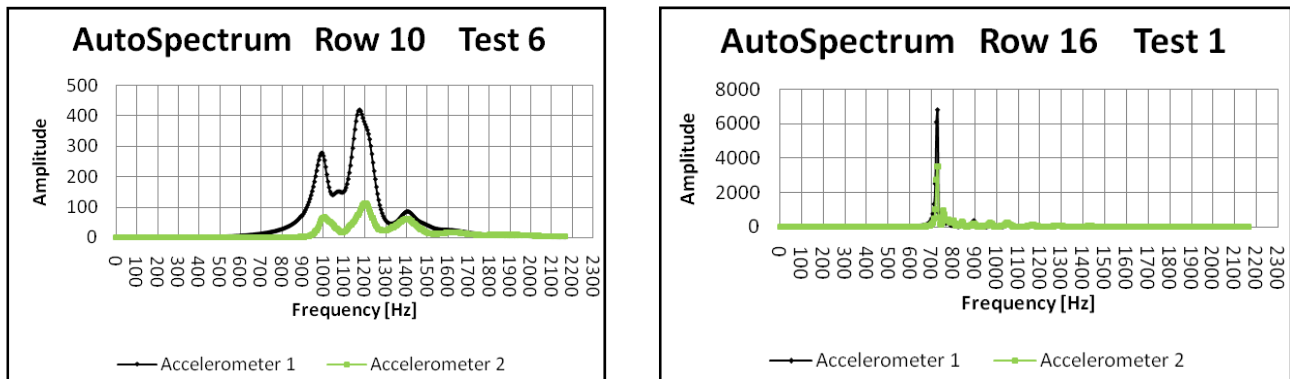


Figure 13 - Spectra obtained by impact excitation on 2 different rows of (zig-zag) shrouded blades; accelerometer 2 was at 5 blade distance from accelerometer 1, where excitation was applied.

The huge increase in natural frequencies with respect to the single standing blade and the difficulties of exciting higher modes with respect to the first mode seem to be the main results of the integrally shrouded zig-zag blades.

These results validate the assumption of considering only the first mode of vibration made for the sensitivity study of the blades coupled by shroud contacts. The equivalent linear model which will be developed can then be used also for checking these results.

CONCLUSIONS

Some numerical results in non-linear dynamic behavior of a couple of blades with shrouds which are or get in contact during vibration in different excitation conditions, are presented. Different contact conditions and their effect on vibration amplitudes are shown. These first results are part of a sensitivity analysis which will form the base of the development of linear equivalent models (with some tuning parameter), that will allow complete blade row natural frequency and forced frequency response calculations. From these results it will also be possible to evaluate also stresses for blade life prediction, therefore refined accurate meshes are needed for modeling the blades.

ACKNOWLEDGMENTS

The permission of Franco Tosi Meccanica S.p.A. to publish these results is gratefully acknowledged.

REFERENCES

- McGuire, P.M., Knipe, W.H., 1990, The development of turbine blading to achieve optimum vibration characteristics. IMECHE 1990
- Hurd, P., Thamm, N., Neef, M., Truckenmueller, F., Pollack, H., Deckers, M., 2005, Modern reaction HP/IP Turbine technology advances & experiences. ASME POWER 2005-50085.
- Petrov, E.P., Ewins, D.J., 2004, Generic friction models for time-domain vibration analysis of bladed disks, ASME Journal of Turbomachinery, vol. 126, pp. 184-192
- Petrov, E.P., Ewins, D.J., 2003, Analytical formulation of friction interface elements for analysis of nonlinear multi-harmonic vibrations of bladed disks, ASME Journal of Turbomachinery, vol. 125, pp. 364-371
- A. Hohl, C. Siewert, L. Panning, A. Kayser (2008): Non-linear vibration analysis of gas turbine bladings with shroud coupling, ASME TURBO EXPO, GT2008-50787, pp. 1-9

- Petrov, E.P., 2004, Method for direct parametric analysis of nonlinear forced response of bladed disks with friction contact interfaces, ASME Journal of Turbomachinery vol.126, pp. 654-662
- Bachschnid, N., Pennacchi, P., Pesatori, E., Turozzi, G., 2007, On the “snubbing” mechanism for reducing blade vibration, ASME Conference DETC2007/VIB-34800, pp 1-10 .
- Szwedowicz, J., Visser, R., Sextro, W., Masserey, P.A., 2008, On non linear forced vibration of shrouded turbine blades. ASME Journal of Turbomachinery vol.130, 011002, pp. 1-9
- Bachschnid, N., Pennacchi, P., Lurati, M., 2008, Combining mistuning and snubbing in bladed disks of turbomachinery, 2008 ISMA Conference Proceedings, pp. 1- 8
- Petrov, E. P., Ewins, D.J., 2005, Method for analysis of non-linear multiharmonic vibrations of mistuned bladed disks with scatter of contact interface characteristics. ASME journal of Turbomachinery, vol.127, pp. 128-136
- Heinz, C., Schatz, M., Casey, M.V., Stuer, H., 2010, Experimental and analytical investigations of a low pressure model turbine during forced response excitation, ASME TURBO EXPO, GT201-22146, pp. 1- 11

RESPONSIBILITY NOTICE

The authors are the only responsible for the printed material included in this paper.

Active Vibration Control using actuated air springs

L. Bregant, M. Spagnol

LVA, Mechanical Engineering Dept. - University of Trieste - via Valerio 10, 34127 Trieste, Italy - email: bregant@units.it

Abstract: Many engineering applications requires for the use of resilient mounts in order to decouple the source of vibration and the receiving structure. Seldom the mount manufacturers provide more than a value for the static stiffness and those devices can't perform equally well for different excitation characteristics. Air springs, on the contrary, represent a feasible and interesting alternative in all those cases, in which the source of vibration changes (amplitude and frequency alike) during operation. In this work, the full dynamic characterization of an air-spring is reported: different loads and pressures combinations are applied to determine the variation of stiffness and damping of the system, combining experimental tests and numerical simulations. The effects of the temperature is also included. With the obtained air-spring response surfaces, different active vibration control approaches on a simple SDOF system have been tested, the reported results demonstrate the good performance of the device and its applicability to more complex cases.

Keywords: air spring characteristics, active vibration control

INTRODUCTION

This report describe the results of the characterization of an air spring. This device consists of an rubber bellow with appropriate mounting elements in which compressed air can be inflated at various rates and pressure. Being able to control the airflow allows to change mainly the stiffness of the device making it suitable for Active Vibration Control (AVC) purposes. In this work a small ContiTech SK19-4 air spring Fig. 1 has been fully analyzed, on an on purpose developed testing machine, obtaining its response characteristics as function of the frequency, the pressure and the applied load. From these data, a numerical model has been derived and optimized so that numerical and experimental results would match. Such an updated model has been used to test different AVC strategies on a simple SDOF system trying to minimize the force it transmits to the foundation. The results of these numerical and experimental verifications are reported in the present paper.

AIR SPRING EXPERIMENTAL CHARACTERIZATION

The dynamic characterization of the air spring consists of finding its stiffness and damping values as function of the air pressure, the pre-load amount and the excitation frequency. These quantities are non linearly related due to the fact that the compressed air act on flexible rubber bellow as will be explained in the following section.

Air Spring Test Machine

To test the air spring, a dedicated machine has been designed and constructed Fig. 2. This is needed to apply both a constant preload and a varying force to the specimen under test, while allowing a controlled air flow and the measure of the relevant dynamics quantities. It consist of a moving mass, obtained by different elements, to change its amount to a maximum value of 40kg, sliding on three rigid columns. The mass is connected to an electro-dynamic shaker, LDS V406/8, driven by an amplifier LDS PA 100E that provide the varying force. The air flow is controlled by a proportional pressure valve REXROTH ED02, while the internal pressure in the spring is sensed by a pressure sensor SMC PSE540. The force the shaker applies on the moving mass is measured with a PCB 208A3 force-cell while the force transferred to the foundation by the air-spring is measured with a triaxial PCB 206A1 force sensor. Further details of the machine can be found the previous paper Bregant (2010).

Area and Volume estimation

The spring reaction force depends from the internal pressure and the internal volume of the air chamber. It can be expressed as:

$$F_i = p_{ri} A_{wi} \quad (1)$$

where F_i is the air spring force, p_{ri} is the relative pressure in the air spring. A_{wi} , the effective area on which the pressure acts, this being a non-linear function of the spring height. In order to calculate the internal area, a static load is applied while measuring the internal pressure with the SMC sensor.



Figure 1 – Contitech air spring SK19-4



Figure 1 – Test machine

The internal volume depends from the air mass and pressure variation inside the air spring. From thermodynamics and ideal gas flow theory:

$$p_{ri} v_i = nRT \quad (2)$$

The initial volume is $v_0 = 0.08$ L, while v_i is the generic volume at the pressure p_{ri} . In our tests, the number of moles inside the spring is kept constant closing the air circuit, to a value of about $n = 689$ mol. Once the pressure is set, no other exchange of air mass with external ambient can occur. In this case the following relation hold:

$$n = \frac{p_{r0} v_0}{RT} \quad (3)$$

$$v_i = \frac{nRT}{p_{ri}} \quad (4)$$

$v_0 = 0.08$ L $R = 0.082$ L atm K⁻¹ mol⁻¹ $T = 293.15$ K $p_{r0} = 2$ atm

The area and the volume graphs are reported in Fig. 3. These data will be used afterwards in the SIMULINK model of the air spring, through the afore mentioned formulas and to define the active control parameters.

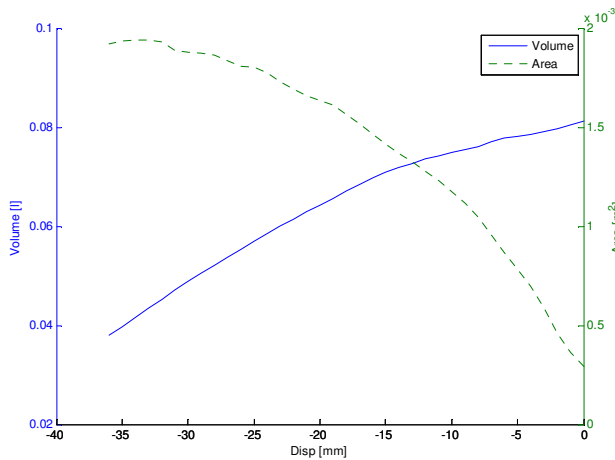


Figure 3 – Volume and Area as function of the air spring height

Stiffness and Damping evaluation

Since the air-spring will be used with different excitation frequencies it is interesting to know how the stiffness and the damping will change accordingly. The air spring is tested applying a random excitation force in the band 0-26Hz while measuring the actual force applied by the shaker, the acceleration of the moving mass, the pressure of the air inside the spring and the forces transferred by it to the foundation. From all these data it's possible to compute a FRF between the applied force and the acceleration of the mass and the transmissibility of the air spring as the ratio between the forces under and above the spring:

$$FRF = \frac{\ddot{x}}{F_{up}} \tag{5}$$

$$TR = \frac{F_{dw}}{F_{up}} \tag{6}$$

The experimentally obtained functions are fitted into a simple SIMULINK model Fig. 4, in which the mass M is known and constant while the values of C and K are optimized, Fig. 5, with the software modeFRONTIER, Fig. 6. At the end of the parameters identification phase, response surfaces of FRF and Transmissibility vs Internal Pressure and preload are created. Figure 7 shows Transmissibility function for the pre-load of 36.4 kg. It can be noticed that the natural frequency varies with pressure, between 4.0 and 6.5 Hz, in an almost linear fashion.

Figure 8 shows the trend of the stiffness and the damping for a single preload case as function of the pressure.

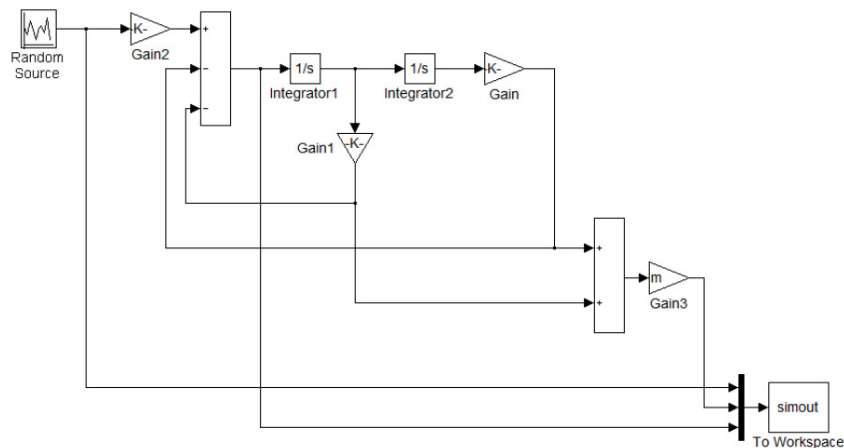


Figure 4 – SIMULINK model for C and K identification

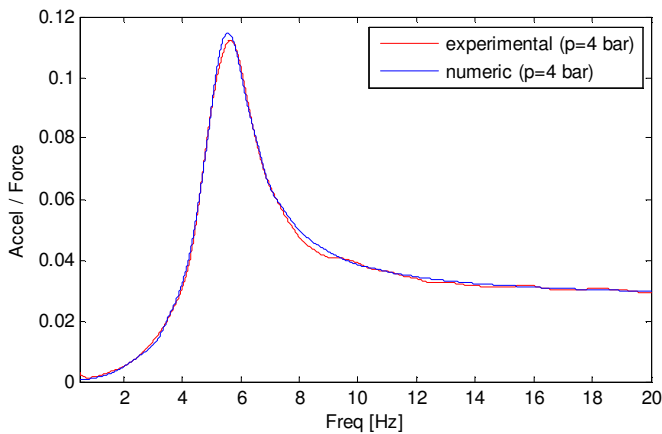


Figure 5 – Numerical and Experimental FRF

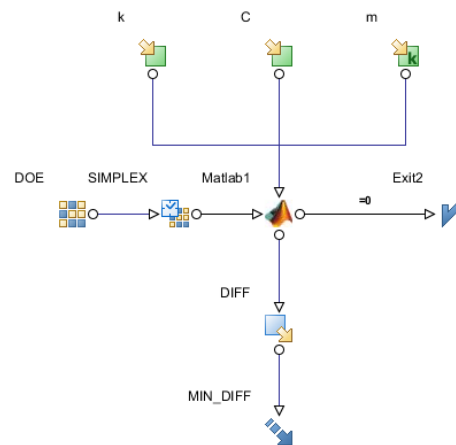


Figure 6 – Optimization/Identification Workflow

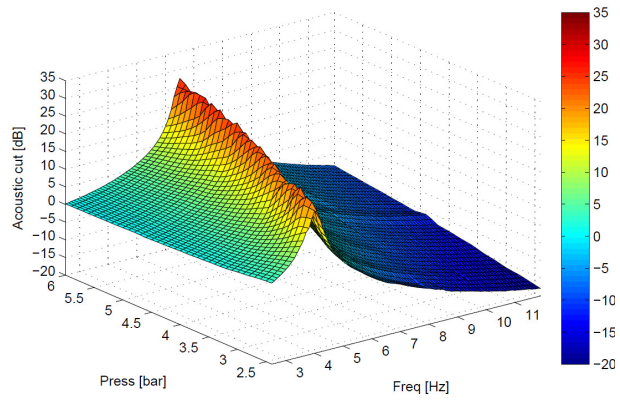


Figure 7 – Transmissibility surface

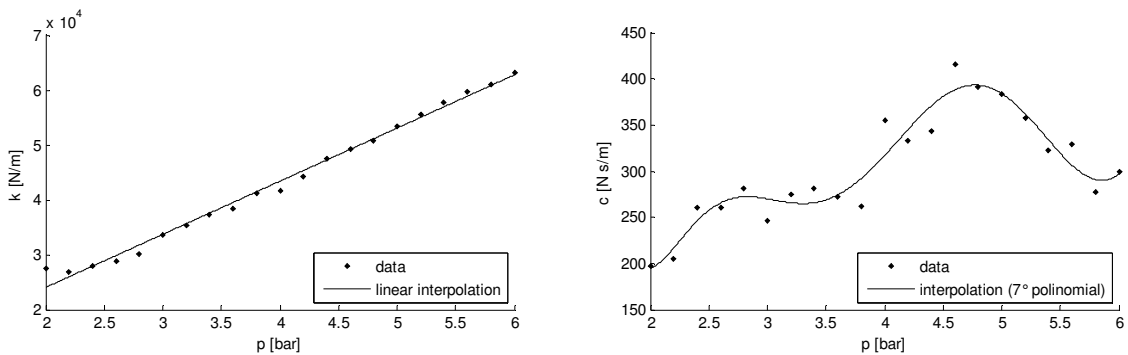


Figure 8 – Stiffness and Damping vs pressure at constant pre-load

The stiffness and damping functions (Fig. 8) can be used in the SIMULINK model according to the instantaneous pressure's values.

To validate the accuracy of the numerical model parameters' estimation, the experimental and numerical down forces were compared while the air spring pressure was set at 4 bar. The F_{up} input of the SIMULINK model is the force acquired with the upper load cell. Figure 9 compares the acquired and the computed down forces while the simulation parameters are ode1 solver with fixed-step of 0.001s.

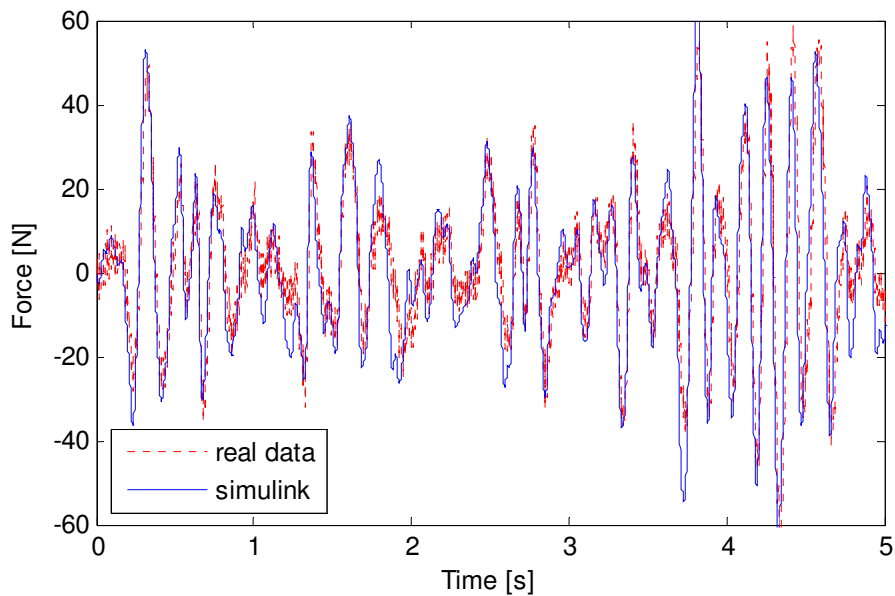


Figure 9 – Real down force vs simulated one

Temperature effect

Since the characteristics of compressed air and rubber are temperature dependent, some tests were devoted at define the relation between those quantities. Long duration tests in which the system's temperature could raise and be controlled were performed. A thermocouple was inserted in compressed air circuit and one on the exterior of the rubber bellow. The standard identification tests of FRF and Transmissibility were performed at cold conditions to have baseline function, than the system was set in operation with a simple AVC control. Each hour the FRFs and Transmissibility curves were captured. Figure 10 shows the final results after 6 hours of testing.

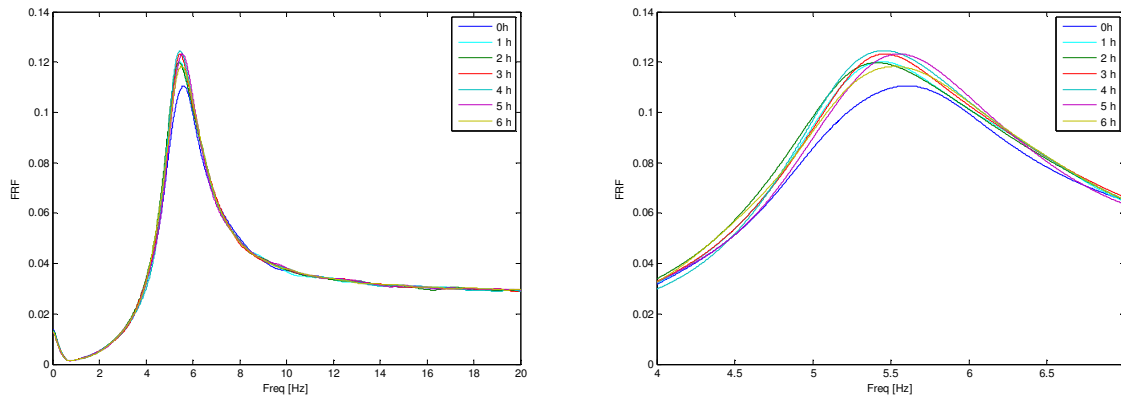


Figure 10 – FRF and Transmissibility curves as function of temperature

The peaks change visibly, but after a certain amount of time they stabilize reaching almost constant conditions. It's authors' desire to further investigate this point and distinguishing more precisely the effects of the air and the rubber heating.

ACTIVE VIBRATION CONTROL

The main purpose of this activity is to define a control strategy that allows to minimize the force transmitted from the vibrating system to the foundation. This problem is very relevant in many industrial cases where different kind of machinery are mounted on foundations that can transmit vibration to surrounding. Being able to minimize the transmitted forces will result in a minimization of structural borne noise.

In this case, a HIL approach has been adopted, combining the air-spring testing machine, SIMULINK and the dSpace testing environment. This combination allows to create a numerical model of the physical SDOF system, numerically optimise the control parameters (via modeFRONTIER) implement it in the dSpace board, perform the actual experimental test and directly compare the numerical and real data.

This loop has been tested with different parameters' combination, but the present work relates on the case in which the starting pressure is 4 bar, while the range of variation of the correction pressure is between 2 and 6 bar. Due to the design of the testing machine, it was decided to excite the system with a random signal, trying to minimize the force transmission over a certain frequency band. Two approaches will be presented here: a simple feedback control and an LQR optimal control.

Feedback retroaction

In this case the control action relays on the knowledge of the force acting on the foundation. This is not very common in real application, but can give some indication of the quality of the obtainable results. It simply requires the definition of a gain value, that act on the pressure of the air-spring, as suggested in Spanos (1995) with interesting results.

The schema of the controlled system is in Fig. 11, where the knowledge of the down force is made evident. The formulation of the control relays on the following expressions:

$$(s^2m + sc + k)X(s) = F_{up}(s) - g(sc + k)X(s) \quad (7)$$

where the gain g multiplies the F_{dw} down force.

The optimal value of the gain can be found easily with few iteration, and the down force values reduce in a evident manner. Figure 12 shows different transmissibility functions obtained with different gain values, while Fig. 13 compares the down forces of the not controlled and controlled system.

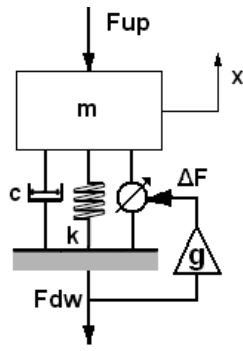


Figure 11 – Feedback controlled system

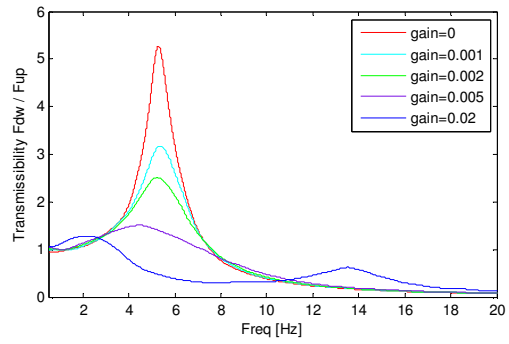


Figure 12 – Transmissibility function for different control gain values

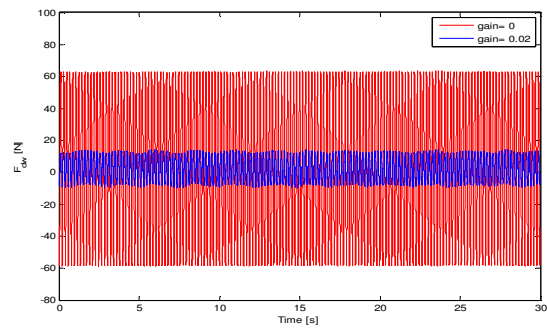
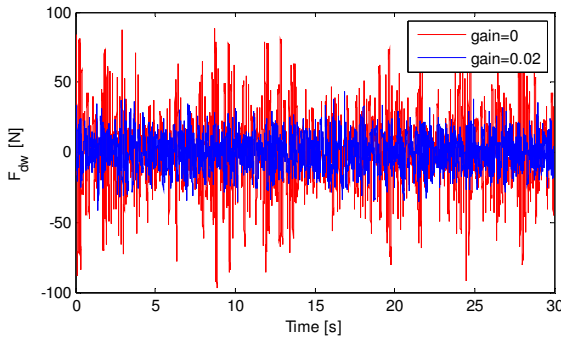


Figure 13 – Down Force comparison between not controlled and controlled system, random and sinusoidal excitation

The reduction of the RMS F_{dw} value is about 50% when the excitation is random, about 80% when the excitation is purely sinusoidal.

LQR method

The second control strategy relies on the definition of a quadratic cost function whose terms depends from the state of the system and the effort needed to control it.

Since in most of the industrial application the adopted sensors are accelerometers, to obtain the states information, single or double integrations of those signals are requested. This mathematical operation leads to some numerical problems related to the DC component, always present in the original signals, that needs to be eliminated. It's favourable to adopt a different approach in which the state vector is not formed by displacement and velocity but from velocity and acceleration. This approach, called Reciprocal State Space de facto reduces the numerical burden of the control and the instability linked to the mentioned integration, Tseng and Yedavalli (1997), Yedavalli et al. (1998), Kwak and Yedavalli (1999,2000).

In this case the basic equation linking the dynamics of the system and the pressure variation in the air spring is (8), The standard state space representation is described by equations (9), while the reciprocal state space is represented in (10) and (11). The control action is expressed by equation (12) and the quadratic cost function that need to be minimised, is in the RSS approach as equation (13). The optimal control requires for the definition of the weighting matrices Q_i and R , that are defined as function of the performance of the system and of the controller.

$$(ms^2 + cs + k)X(s) = F_{up} + \Delta p A_w \quad (8)$$

$$\begin{Bmatrix} \dot{x}_1 \\ \dot{x}_2 \end{Bmatrix} = \underbrace{\begin{bmatrix} 0 & 1 \\ -\frac{k}{m} & -\frac{c}{m} \end{bmatrix}}_{[A]} \begin{Bmatrix} x_1 \\ x_2 \end{Bmatrix} + \underbrace{\begin{bmatrix} 0 \\ 1 \end{bmatrix}}_{[B_1]} \{F_{up}\} + \underbrace{\begin{bmatrix} 0 \\ \frac{A_w}{m} \end{bmatrix}}_{[B_2]} \{\Delta p\}; \{y\} = \underbrace{\begin{bmatrix} a_1 & a_2 \end{bmatrix}}_{[C]} \begin{Bmatrix} x_1 \\ x_2 \end{Bmatrix} \quad (9)$$

$$\begin{cases} \dot{x}(t) = G\dot{x}(t) + H_1u_1(t) + H_2u_2(t) \\ y(t) = C\dot{x}(t) \end{cases} \quad (10)$$

$$G = A^{-1} ; H_1 = -A^{-1}B_1 ; H_2 = -A^{-1}B_2 \quad (11)$$

$$u = -L\dot{x} \quad (12)$$

$$J = \int_0^{\infty} (\dot{x}'(t)Q\dot{x}(t) + u'(t)Ru(t))d\tau \quad (13)$$

$$Q = \begin{bmatrix} Q_1 & Q_3 \\ Q_3 & Q_2 \end{bmatrix} R = [R_1] \quad (14)$$

Figure 14 highlight the fact that there is no direct link between the F_{dw} and control force as in the previous case. This is important because no direct feedback from the force transmitted to the foundation, but the control action relays only on the acceleration measured on the moving mass. Figure 15 shows the measured transmissibility functions without and with control. In this case only the result obtained with the optimal combination of Q and R, is shown.

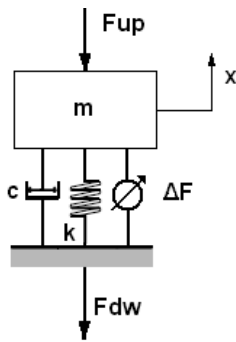


Figure 14 – LQR controlled system

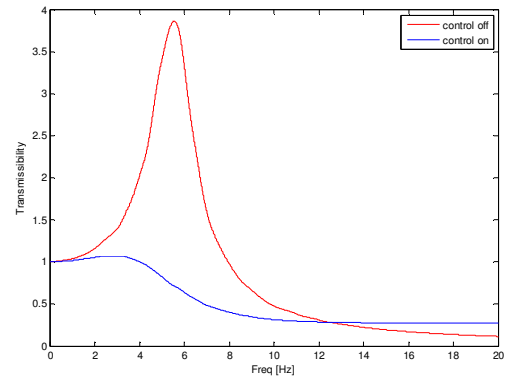


Figure 15 – Transmissibility function with control off and on

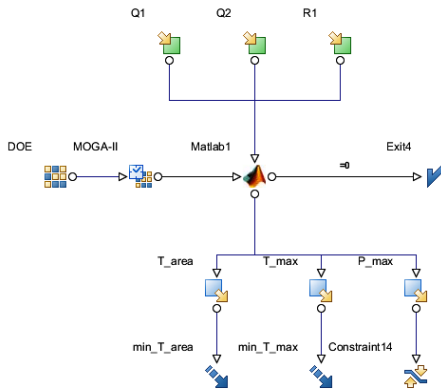


Figure 16 – Optimisation Workflow

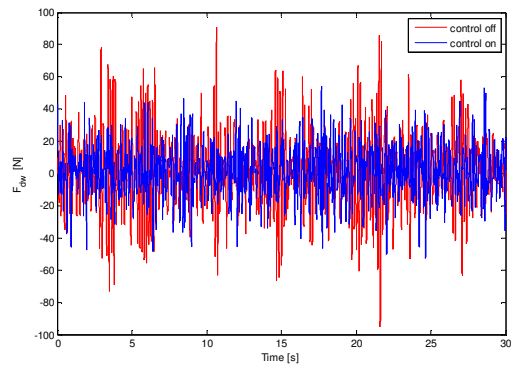


Figure 17 – Transmissibility function with control off and on

The Q and R, were obtained using modeFRONTIER; the workflow is depicted in fig. 16 where the two optimisation objectives can be seen: the minimisation of the maximum value of the Transmissibility function and the minimisation of the area underneath the Transmissibility function in the frequency range 0-20Hz.

Figure 17 compares the experimentally obtained down forces, without and with the control action. In this case the reduction for the RMS value is about 35%.

RESULTS

The present work highlight the potential of the air spring as actuator in active vibration control applications. Before being usable for this purpose air spring need to be fully characterised and considering the large amount of parameters involved, this can be a lengthy activity considering the temperature influence as well. Different pressure, pre loads, frequency ranges need do be considered, as shown in the paper, but the obtainable response surfaces can be easily adopted for designing performing controller. Two simple control strategies using this approach have been presented: a simple feedback and a RSS optimal control. Both gave interesting results, with a minimum reduction of about 35% of the transmitted RMS force.

From the author point of view, looks interesting to pursue this line of research for the multiple industrial application, for the limited industrial costs of the air spring and the control implementation. On this purpose other control strategies will be applied in the near future to more complex MDOF systems.

REFERENCES

- ANSYS, 2008, "Release 11.0 Documentation for ANSYS (Manual)".
- Bolton, 1998, "Control engineering", Longman.
- Bregant, Spagnol, Moras, 2010, "Dynamic characterization of air spring for AVC applications", Proceedings of ISMA2010, pp. 1717-1724.
- Chang F., Z-H Lu, 2008, "Dynamic model of an air spring and integration into a vehicle dynamics model", Proc. IMechE, Vol.222 Part D: J. Automobile Engineering, pp. 1813-1825.
- dSpace, 2008, "dSpace User's Guide for Release 6.4".
- Harris, 1987, "Shock and Vibration Handbook", The McGraw-Hill Companies.
- Hatch, 2001, "Vibration simulation using MATLAB and ANSYS", Chapman Hall/CRC.
- Kwak and Yedavalli, 1999, "New Modeling and Control Design Techniques for Smart Deformable Aircraft Structures with Acceleration Feedback", Proceedings of the AIAA Guidance, Navigation and Control Conference, pp 1686-1696.
- Kwak and Yedavalli, 2000, "Observer Design in Matrix Second Order System Framework: Measurement Conditions and Perspectives", Proceedings of the American Control Conference, pp 2311-2315.
- Kwak, Washington, Yedavalli, 2002, "Acceleration feedback-based active and passive vibration control of landing gear components", Journal of aerospace engineering, 15(1).
- MathWorks, 2007, "MATLAB User's Guide (Manual)".
- modeFRONTIER, 2010, "modeFRONTIER 4.0.3 user manual".
- Spanos, 1995, "A soft 6-axis active vibration isolator", Proceedings of the American Control Conference.
- Tseng, Yedavalli, 1997, "Vibration Control of a Wing Box via Reciprocal State Space Framework", Proceedings of the 1997 IEEE Conference on Control Applications.
- Tseng, Yedavalli, 1998, "Control Design via Generalized State Space System with State Derivative Measurement and Reciprocal State Space Framework", Proceedings of the 1998 American Control Conference, Philadelphia, pp 2520-2521.

RESPONSIBILITY NOTICE

The authors are the only responsible for the printed material included in this paper.

On The Modeling of Structural Dynamics of Risers Composed of Functionally Graded Materials

C.A. Almeida¹, J.C. Romero¹, I.F.M. Menezes², and G.H. Paulino³

¹ Dept. of Mech. Engng., Pontifical Catholic University of Rio de Janeiro, RJ, Brasil

² Tecgraf (Computer Graphics Technology Group), Pontifical Catholic University of Rio de Janeiro, RJ, Brazil.

³ Civil & Environmental Engrng, University of Illinois at Urbana-Champaign, IL, U.S.A.

Abstract: This work aims to provide a numerical framework for the dynamic behavior representation of riser structures, considering the use of functionally graded materials (FGM). In this respect, a new corotational finite element formulation for the numerical representation of such risers is considered, including the effects of geometric presented to show the numerical model capabilities on representing the important kinematics of a riser structure in dynamics.

Keywords: risers, functionally graded material, dynamic behavior representation, large displacement motions

NOMENCLATURE

u, v, w = displacement vector coordinates, m

x, y, z = Cartesian coordinates, m

A = element cross section area, m²

E = material Young's modulus, N/m²

G = material shear modulus, N/m²

I_y, I_z = cross section axial moment of inertia, m⁴

J = cross section polar moment of inertia, m⁴

I, J = element node numbers, dimensionless

L = element length, m

U = element strain energy

\mathbf{r} = position vector, m

\mathbf{u} = displacement vector, m

\mathbf{R} = frame transformation matrix, dimensionless

Greek Symbols

$\bar{\mathcal{G}}$ = cross-section rotation vector referred to local coordinates

$\kappa_x, \kappa_y, \kappa_z$ = curvatures w.r.t. x, y, z

\mathcal{E} = center line linear strain component

γ = shear strain component

ξ = local radial coordinate

Subscripts

C relative to corotational coordinates

G relative to global coordinates

T relative to convective coordinates

0 relative to undeformed (initial) coordinates

Superscripts

I relative to element node I

S relative to a general position along the element's length

C relative to corotational Coordinates

T relative to convective coordinates

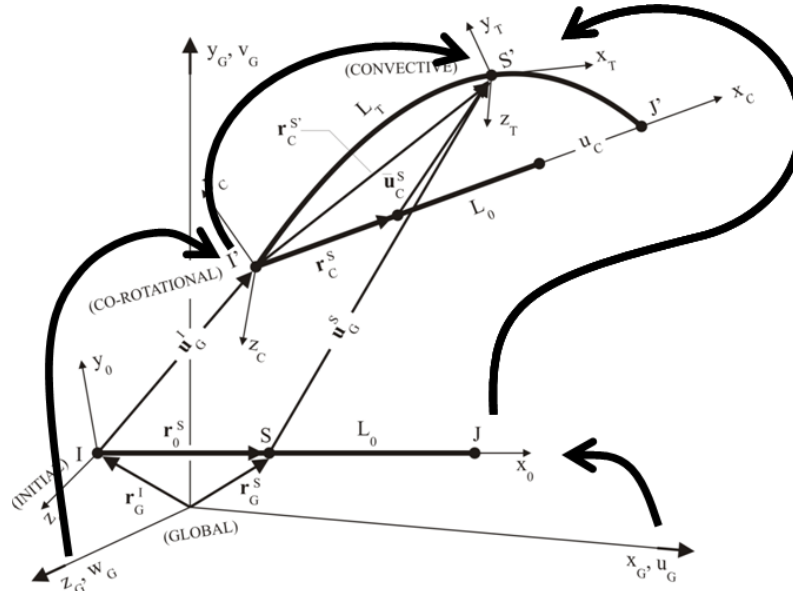
0 relative to undeformed (initial) coordinates

INTRODUCTION

The large demand for oil has brought its exploitation to more difficult and risky proven reserve areas, what has driven engineering to a significant increase for research and technological solutions - as in deep seashore waters -, requiring the development of new types of marine structures. The riser is one of the most keen and sensitive of such structures. It is basically a very long and slender pipe designed to convey oil products from deep sea to a tank placed in a floating platform. Due to adverse working conditions the riser structure should sustain, in good balance, the thermo-mechanical strength needed to accommodate thermal induced loadings, both along its length as per through the cross-section thickness, as well as general mechanical forces due to self weight - which includes the inside fluid weight -, bouyance, sea currents and waves, concentrated and distributed buoys, sea bottom contact and platform motions. Moreover, working conditions required at inner and outer surfaces of a riser are most of the time quite distinct, demanding for a material that should combine the best properties of ceramics and metals such as low density and high strength, good temperature and corrosion resistance, high toughness and good machinability, just to mention a few. To try to accomplish such demand, new materials have been formed which possess such properties, in a desired property gradation, in spatial directions. These continuous materials are able to reduce thermal stresses, residual stresses and stress concentration in the transition region, as occurring in multi-layered type risers.

THE FINITE ELEMENT FORMULATION

In this work a numerical framework for the dynamic behavior representation of such structures, considering the use of functionally graded materials (FGM), is presented. The riser is numerically represented by a corotational finite element beam formulation [1,3], including the effects of geometric nonlinearities as the structure undergoes to very large displacements and rotations. Thus, a two node finite element beam formulation that represents the important straining due to stretch, torsional and bending kinematics - all referred to the reference frame attached to the element initial node coordinates, in a Total Lagrangian formulation scheme - was employed. In the kinematics considered, as shown in Fig. 1, the element centre line moves from an initial configuration I-J to its current (final) spatial position I'-J', with the corotational coordinate system defined from the coordinates of the element nodes in the final configuration.



$$\begin{aligned} (x_G, y_G, z_G) - \mathbf{R}_G^C &\rightarrow (x_C, y_C, z_C) - \mathbf{R}_C^T \rightarrow (x_T, y_T, z_T) \\ (x_G, y_G, z_G) - \mathbf{R}_G^0 &\rightarrow (x_0, y_0, z_0) - \mathbf{R}_0^T \rightarrow (x_T, y_T, z_T) \end{aligned}$$

Figure 1 – Two node beam element coordinates and frame transformations

\mathbf{R}_G^C , \mathbf{R}_C^T , \mathbf{R}_G^0 and \mathbf{R}_0^T are frame transformations between element space coordinates from global to corotational, from corotational to convective, from global to initial and from initial to convective, respectively. Considering a typical point S at the element center line and longitudinal initial position \mathbf{r}_0^S , the associated effective displacement vector – displacement quantity measured from the corotational frame - is given, in global coordinates, by the following vector sum,

$$\bar{\mathbf{u}}_C^S = \mathbf{R}_G^C (\mathbf{r}_C^S + \mathbf{u}_C^S - \mathbf{r}_G^I - \mathbf{u}_G^I) - \mathbf{r}_0^S \quad (1)$$

with all vector quantities pictorially defined in Fig. 1. Out of the element center line the displacements are evaluated under the assumption that cross sections initially plane must remain plane after beam deformations, requiring that material global rotations - at any position point S - must be defined. This is accomplished by using the identity transformation condition,

$$\mathbf{R}_G^C \mathbf{R}_C^T = \mathbf{R}_G^0 \mathbf{R}_0^T \quad (2)$$

which results in

$$\mathbf{R}_C^T = (\mathbf{R}_G^C)^T \mathbf{R}_G^0 \mathbf{R}_0^T \quad (3)$$

with local – effective – cross-section rotation vector at S obtained from the following skew-symmetric matrix evaluation [2],

$$\bar{\mathcal{G}}_C^S = \begin{bmatrix} \bar{\mathcal{G}}_x^S & \bar{\mathcal{G}}_y^S & \bar{\mathcal{G}}_z^S \end{bmatrix} = \log_e \mathbf{R}_C^T \quad (4)$$

Equations (1) and (4) furnish a set of local corotational displacements and rotations, at any section-S, all referred to the global coordinate system considered and free from rigid body motions. Element I-J strain measures are then set from these displacements that can furnish the strain energy due to beam modes of deformation for a homogeneous material model, as in the form

$$U = \frac{1}{2} \int_0^{L_0} (EA\varepsilon^2 + GA\gamma^2 + GJ\kappa_x^2 + EI_y\kappa_y^2 + EI_z\kappa_z^2) dx_0 \quad (5)$$

where ε , γ and $\kappa_{y,z}$ are the center line ‘local’ linear and shear strain components and, curvature measures, respectively, κ_x is torsional rotation, A , $I_{y,z}$ and J are cross section geometric parameters and E and G are the material constants.

Thus, element internal forces and tangent stiffness matrix are obtained through successive differentiations of U with respect to displacements referred to co-rotational reference frame, as in the following equations (with $i,j=1,2,3$)

$$\mathbf{F}^T = \begin{bmatrix} \frac{\partial U}{\partial \bar{u}_i^S} & \frac{\partial U}{\partial \bar{\mathcal{G}}_i^S} \end{bmatrix} \quad k_{ij} = \begin{bmatrix} \frac{\partial^2 U}{\partial \bar{u}_i^S \partial \bar{u}_j^S} & \frac{\partial^2 U}{\partial \bar{u}_i^S \partial \bar{\mathcal{G}}_j^S} \\ \text{symm.} & \frac{\partial^2 U}{\partial \bar{\mathcal{G}}_i^S \partial \bar{\mathcal{G}}_j^S} \end{bmatrix} \quad (6)$$

where the following notation applies

$$\begin{aligned} \bar{u}_{1C}^S &\equiv \bar{u}_{xC}^S & \bar{u}_{2C}^S &\equiv \bar{u}_{yC}^S & \bar{u}_{3C}^S &\equiv \bar{u}_{zC}^S \\ \bar{\mathcal{G}}_1^S &\equiv \bar{\mathcal{G}}_x^S & \bar{\mathcal{G}}_2^S &\equiv \bar{\mathcal{G}}_y^S & \bar{\mathcal{G}}_3^S &\equiv \bar{\mathcal{G}}_z^S \end{aligned} \quad (7)$$

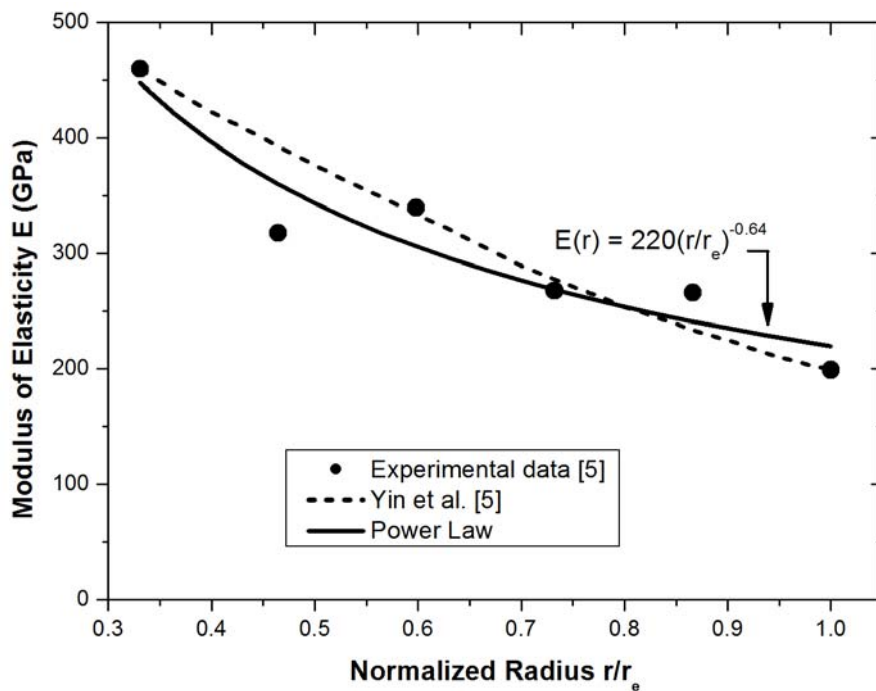


Figure 2 – Power Law Approximation of FGM Young's Modulus Variation Along Riser Thickness

In the element implementation Hermitian functions were employed in displacement representations along the length of the element. Therefore, linear functions were used for the axial displacements and torsional rotations, quadratic functions for the bending rotations and cubic functions for the element transverse displacements.

In considering the FGM non-homogeneous isotropic material model of pipe cross section risers, in its linear elastic range, a continuous variation of the elastic constants through the wall thickness were obtained from previously published experimental results, provided by Paulino, Yin et al. in [4,5], for TiC-Ni₃Al alloy. As shown in Fig. 2 published experiments were approximated by a continuous function to provide the “material law” for the Young’s Modulus r -variation through the pipe thickness, using a least square numerical approximation. In this particular, a power law equation was established and equivalent values for EA , GJ , EI_y , EI_z constants, in Eq (5), have been derived in closed form. This approach was used in the examples considered in the next section.

SAMPLE ANALYSES

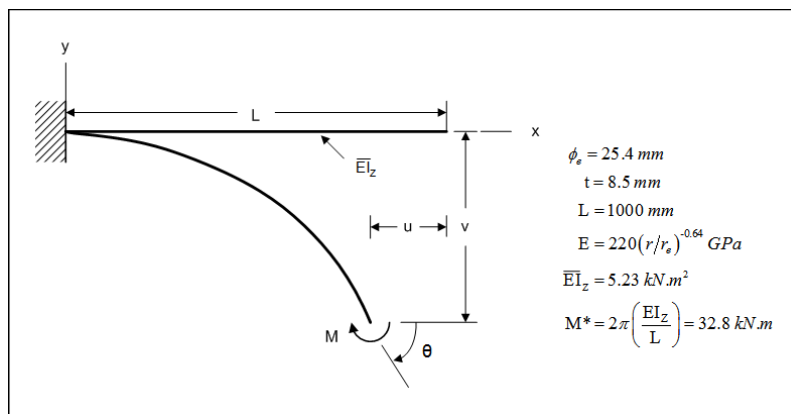


Figure 3 – The cantilever pipe beam considered in the analysis

In this first study a ten equally spaced element model of a cantilever pipe, submitted to constant bending moment is considered. Cross section geometry parameters and the material law equation used are shown in Fig. 3. M^* is the applied moment required for the beam to undergo to considerable large displacements and rotations as shown, qualitatively, in Fig. 4.

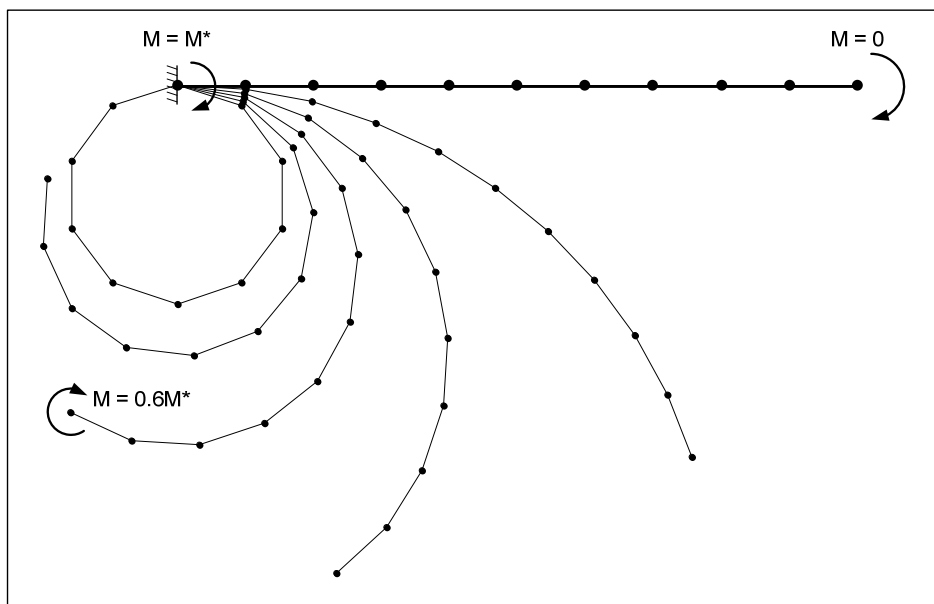


Figure 4 – Cantilever pipe beam undergoing to large displacements and rotations

Figure 5 shows comparisons of the obtained numerical results for displacements u and v and rotation θ at the tip of the beam to solutions presented in [6], for $0 \leq M \leq M^*$. The numerical results were obtained using 100 equal load steps with displacement incrementally iterative procedure, as described in [1]. A good agreement in the results can be observed. Figure 6 displays two cuts of the normal stress radial distribution at the pipe cross section, for $M = 0.6M^*$. Notice that for the FGM considered, the results are quite apart from the typical linear distribution obtained with homogeneous material beams. However, for solid section beams the two patterns cross the beam center line axis – or the neutral axis - .

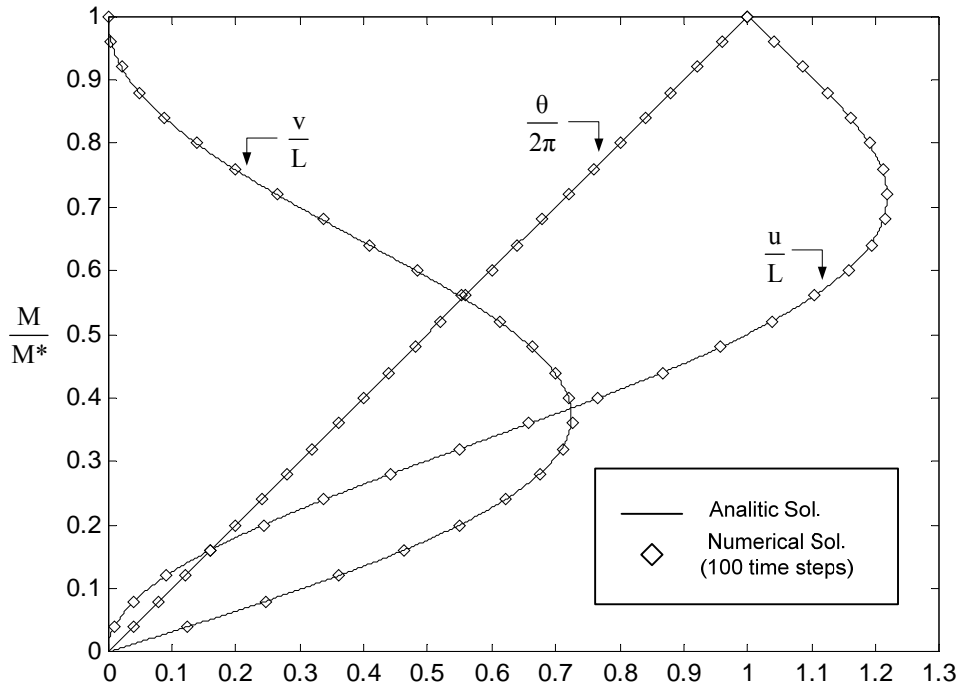


Figure 5 – Tip displacements and rotations of cantilever beam undergoing large displacements

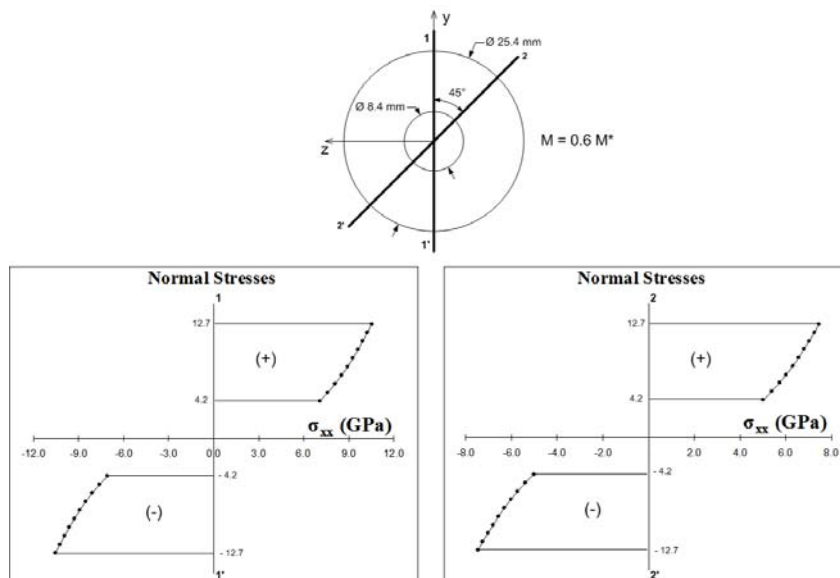


Figure 6 – Normal stresses at the cantilever pipe beam cross-section, for $M=0.6M^*$.

In a second application we use the bi-material (alumina-titanium alloy) pipe beam model where the transition is made smooth by inserting a FGM layer which thickness t_{FGM} can vary from 0% to 100% of the pipe thickness h . In all situations the FGM layer is placed at the mid-depth and the thicknesses of the alumina and the titanium are always kept equal. The objective is to evaluate their relative effects on free vibration. The FGM elastic modulus and mass density is varied according to power law, as shown in Fig. 7. Equivalent values for the beam rigidity modulus EI and line mass

distribution ρ_A are evaluated for various cross-section material configurations and the numerical values for the natural frequencies associated to bending are obtained, considering the beam under two boundary conditions: a) the cantilevered and b) the cantilever-simply supported. These frequencies values are compared to analytical results furnished in Ref. [7]. A good agreement in the results was observed when ten or more equally spaced elements are used in the model, as in the plots shown in Fig. 8. From these comparisons, it is observed quite small differences in the first two frequencies, as the FGM layer thickness is increased. However these differences are magnified when higher mode frequencies are extracted. From these plots, the amplification factors are sequentially equal to 9.0-2.77-1.96-1.65 and 3.24-2.08-1.71-1.53 for cases a) and b), respectively.

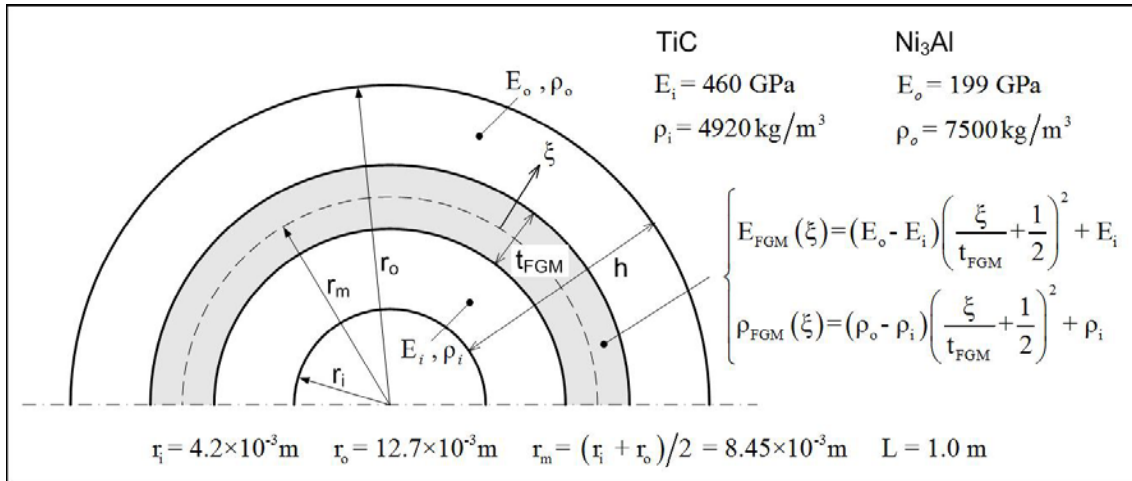


Figure 7 – Composed cross-section details as considered in the numerical analysis.

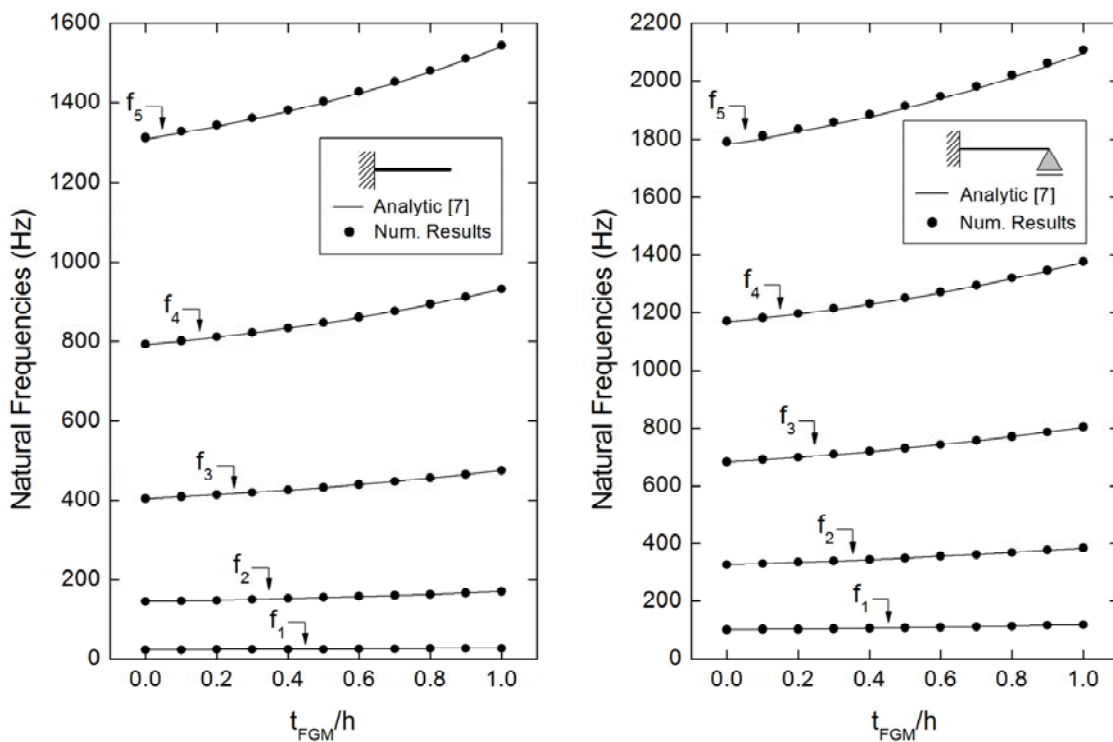


Figure 8 – First five flexure natural frequencies obtained for the composed beams considered .

CONCLUSIONS

A shear deformable two node finite element beam is presented, based on the corotational formulation referred to the spatial coordinates defined by element node. The element is based on the Timoshenko's constant transverse shear deformation theory accounting for large displacement kinematics, but in the small strain theory range. In this work, the element is used to study static and free vibration in FGM and composed risers sections, by adjusting the beam theory

rigidity parameters to the equivalent ones considering cross-section evaluations in closed form. The Hermitian's shape functions used grant the element formulation exact results only for loadings that can be represented by linear bending moments and constant shear forces. Otherwise, FEM refinement procedures for element spatial displacement convergence results must be used.

It has been found that significant difference occurs in FGM riser stress results when they are compared to its parental homogeneous material beam mainly due to rigidity parameters evaluations and, most of all, to its variation along the pipe thickness. In the analyses considered a power law was obtained from previously published experiments. It can be re-evaluated using the numerical tool employed in the analyses. Also, as it does happen in risers the use of FGM layers in the cross section can be regarded as an effective way to smoothen stress jumps in multi-metal beams.

REFERENCES

[1] Pacoste, C. and Eriksson, A. (1997), "Beam Elements in Instability Problems", *Comp. Meth. Appl. Mech. And Engrg.*, 144, 163-197.

[2] Suprunenko, D.A. (2001), "Skew-symmetric Matrix", in Hazewinkel, Michiel, *Encyclopaedia of Mathematics*, Springer, ISBN 978-1556080104.

[3] Felippa, C. A. and Haugen, B. (2005), "A Unified Formulation of Small-strain Corotational Finite Elements: I. Theory", *Comp. Meth. Appl. Mech. Engrg.*, 194, 2285-2335.

[4] Lages, E.N., Paulino G. H., Menezes, I.F.M. and Silva, R. R., (1999) *Nonlinear Finite Element Analysis Using an Object-Oriented Philosophy – Application to Beam Elements and to the Cosserat Continuum*, *Engrg. And Computers*, 15, 73-89.

[5] Yin, H. M., Paulino, G. H., Buttlar, W. G. and Sun, L. Z. (2007) "Micromechanics-based Thermoelastic Model for Functionally Graded Particulate Materials with Particle Interactions", *J. of the Mechanics and Physics of Solids*, 55, 132-160.

[6] Ramm, E. "A Plate/Shell Element for Large Deflections and Rotations", in *Formulations and Computational Algorithms in Finite Element Analysis*, Bathe, K.J., Oden, T. and Wunderlich, W. Eds. (1976) MIT-Press, ISBN 0262021277.

[7] Timoshenko, S., Young, D.H., Weaver Jr., W., *Vibration Problems in Engineering*, J. Wiley & Sons, Inc., 1974.

RESPONSIBILITY NOTICE

The author(s) is (are) the only responsible for the printed material included in this paper.

Finite Element Dynamic Analysis of Cylindrical Panels under Moving Loads

Alfredo R. de Faria¹

¹ Department of Mechanical Engineering, Instituto Tecnológico de Aeronáutica, CTA-ITA-IEM, São José dos Campos, SP 12228-900, Brazil

Abstract: The finite element method is used to investigate the dynamic response of cylindrical panels with a moving force or mass. Thin shell theory is assumed such that out-of-plane shear can be neglected and the classical shell theory can be applied. The nonlinear dynamic problem is solved using a perturbation technique that splits it into a series of simpler linear problems. It is noticed that the panel dynamics is affected by panel curvature, moving load velocity and moving mass to main structure ratio. Insensitivity to variations in the panel curvature is observed but high travel velocities and heavy traversing masses have a substantial impact on the dynamics. Critical traversing velocities for the moving concentrated force problem and safe traversing velocities for the moving mass problem are identified.

Keywords: moving loads, nonlinear dynamics, finite elements

NOMENCLATURE

\mathbf{A} = matrix of membrane stiffness, N/m

\mathbf{B} = matrix of membrane/flexural stiffness, N

\mathbf{C}_{me} = moving load element damping matrix

\mathbf{D} = matrix of flexural stiffness, Nm

\mathbf{e}_n = normal versor, m

\mathbf{e}_s = axial versor, m

\mathbf{e}_θ = circumferential versor, m

f = dummy function

\mathbf{f} = global force vector

$\bar{\mathbf{f}}$ = effective global force vector

$\bar{\mathbf{f}}_m$ = effective moving load global force vector

\mathbf{f}_e = element force vector

\mathbf{f}_{me} = moving load element force vector

\mathbf{g} = gravity acceleration, m/s²

h = panel thickness, m

\mathbf{K} = global stiffness matrix

$\bar{\mathbf{K}}$ = effective global stiffness matrix

\mathbf{K}_e = element stiffness matrix

$\bar{\mathbf{K}}_m$ = effective moving load global stiffness matrix

\mathbf{K}_{me} = moving load element stiffness matrix

m = moving mass, kg

\mathbf{M} = global mass matrix

\mathbf{M}_e = element mass matrix

\mathbf{M}_{me} = moving load element mass matrix

\mathbf{N}_1 = matrix of membrane interpolation functions, dimensionless

\mathbf{N}_2 = matrix of flexural interpolation functions, dimensionless

\mathbf{p} = position vector, m

\mathbf{q} = global vector of nodal degrees of freedom

\mathbf{q}_e = element vector of nodal degrees of freedom

\mathbf{q}_i = i -th perturbation global vector of nodal degrees of freedom

\mathbf{q}_u = u displacement nodal degrees of freedom, m

\mathbf{q}_v = v displacement nodal degrees of freedom, m

\mathbf{q}_w = flexural displacement nodal degrees of freedom

\mathbf{Q} = matrix of material stiffness, N/m²

R = cylinder radius, m

s = longitudinal coordinate, m

t = time, s

T = system kinetic energy, J

T_m = moving mass kinetic energy, J

T_p = panel kinetic energy, J

u = mid surface longitudinal displacement, m

\bar{u} = longitudinal displacement, m

U_m = gravitational potential energy of moving mass, J

U_p = cylindrical panel strain energy, J
 v = mid surface circumferential displacement, m

\bar{v} = circumferential displacement, m

w = transverse displacement, m

X = coordinate along X axis, m

Y = coordinate along Y axis, m

z = through-the-thickness coordinate, m

Z = coordinate along Z axis, m

Greek Symbols

α = aperture angle, rd

$\boldsymbol{\epsilon}$ = strain vector, dimensionless

$\boldsymbol{\epsilon}^0$ = mid surface strain vector, dimensionless

$\boldsymbol{\kappa}$ = curvature change vector, dimensionless

ν = Poisson coefficient, dimensionless

θ = circumferential coordinate, rd

ρ = mass density, kg/m³

Ω = cylindrical panel domain, dimensionless

Subscripts

i relative to i -th perturbation term

INTRODUCTION

Structures are sometimes traversed by moving loads in practical situations. For instance, a few of them are: airport runways, bridges and overhead cranes (Frýba, 1972). Usually beam or plate models are used to approximate the dynamic response of such structures (Oguamanam et al., 1998; Michaltsos et al., 1996; Hino et al., 1984). Olsson (1985) and Frýba (1972) laid the foundations to derive the dynamic governing equations of generally curved panels under moving loads but implemented only plate or beam models. Therefore, little attention has been paid to the relevant problem of shells, and particularly cylindrical panels, traversed by loads. Since these structures are frequently applied in

the aerospace, petrochemical and marine industries (de Souza and Croll, 1980; Gbadeyan and Oni, 1995) its is important to investigated the problem in deeper detail.

This article addresses the detailed dynamics of a cylindrical panel under the action of a moving concentrated load. The classical assumptions applicable to thin shells (Kraus, 1967) are adopted in the study. Governing dynamic equations are derived from the approximate energy functional computed with the aid of the R16 element (Bismarck-Nasr, 1991) that possesses six degrees of freedom per node and uses the Hermitian polynomials as interpolation functions. Static and dynamic solutions are obtained using the finite element code specially developed for this purpose.

It is shown that a system of nonsymmetric and nonlinear matrix equations is derived when dynamic effects of the moving mass are considered. Thus, an adapted forward time integration procedure should be used to numerically solve the moving load problem (Olsson, 1985). However, an alternate technique is employed based on a perturbation scheme. This technique separates the inherently nonlinear matrix equations into a series of linear matrix equations that must be sequentially solved. It is observed and proved that when the cylindrical panel mass is considerably larger than the moving mass only the initial terms in the series must be computed. Moreover, the perturbation technique naturally separates the moving mass from the moving force effects. It is observed that, whenever the moving mass problem is solved through the perturbation approach, the moving force problem is automatically solved since the moving force problem corresponds exactly the zero order term in the perturbation series of problems.

Numerical results are computed for the moving force and moving mass problems. The contribution of each term in the perturbation series is clearly identified. Three parameters that may possibly affect the dynamics of cylindrical panels under moving loads are studied: (i) panel curvature, (ii) traversing velocity magnitude and (iii) moving mass to panel mass ratio.

EQUATIONS OF MOTION

Basic geometric properties of the problem can be seen in Fig. 1. Under prescribed velocity and acceleration a moving concentrated mass m moves across the surface of a cylindrical panel. The aperture angle is α and the cylinder radius is R . The cylinder axis is aligned with the Z -axis of the inertial reference system XYZ . Versor e_x , e_y , and e_z are associated with the X , Y and Z axes respectively. Attached to the moving mass there exists a local reference system whose versors are: e_s parallel to the Z -axis, e_θ tangent to circumferential direction and e_n normal to the panel surface.

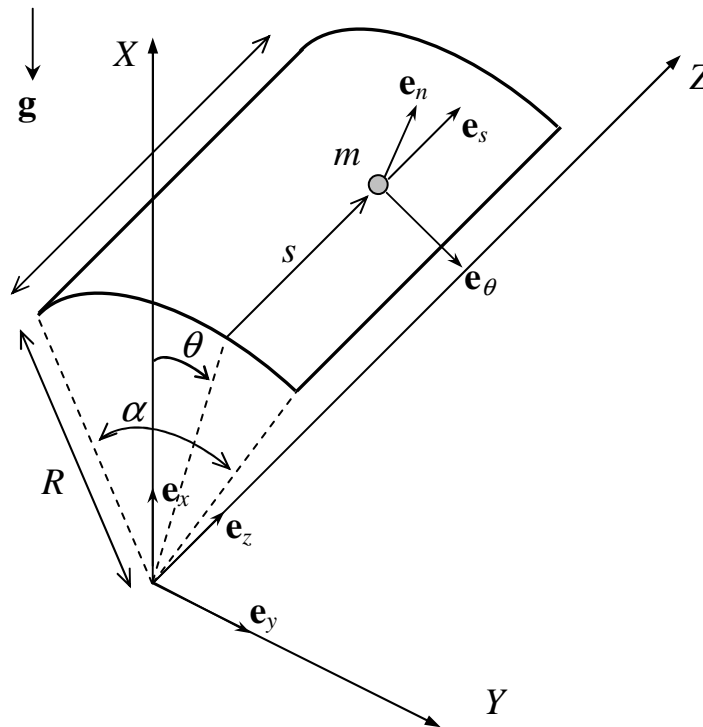


Figure 1 – Schematic of a cylindrical panel with moving load.

In accordance with the classical thin shell theory in-plane displacements \bar{u} and \bar{v} are assumed linear through the thickness and the transverse displacement \bar{w} is constant through the thickness. Hence,

$$\begin{aligned}
\bar{u}(s, \theta, z, t) &= u(s, \theta, t) - zw_{,s}(s, \theta, t), \\
\bar{v}(s, \theta, z, t) &= v(s, \theta, t) - zw_{,\theta}(s, \theta, t) / R, \\
\bar{w}(s, \theta, z, t) &= w(s, \theta, t).
\end{aligned} \tag{1}$$

Displacements \bar{u} , \bar{v} and \bar{w} are defined in the local reference system. Transformation from the local to the global reference systems and vice-versa can be accomplished with the aid of Eq. (2):

$$\mathbf{e}_s = \mathbf{e}_z, \quad \mathbf{e}_\theta = -\mathbf{e}_x \sin \theta + \mathbf{e}_y \cos \theta, \quad \mathbf{e}_n = \mathbf{e}_x \cos \theta + \mathbf{e}_y \sin \theta. \tag{2}$$

The linear strain \times displacement relations of the cylindrical panel may be written as (Novozhilov, 1953)

$$\boldsymbol{\varepsilon} = \begin{Bmatrix} u_{,s} \\ \frac{1}{R}v_{,\theta} + \frac{1}{R}w \\ \frac{1}{R}u_{,\theta} + v_{,s} \end{Bmatrix} + z \begin{Bmatrix} -w_{,ss} \\ -\frac{1}{R^2}w_{,\theta\theta} \\ -\frac{2}{R}w_{,s\theta} \end{Bmatrix} = \boldsymbol{\varepsilon}^0 + z\boldsymbol{\kappa}, \tag{3}$$

where $\boldsymbol{\varepsilon}^0$ are the mid surface strains and $\boldsymbol{\kappa}$ are the changes in curvatures. The strain energy U_p of the cylindrical panel can now be derived using the matrix of material stiffness \mathbf{Q} and Eq. (3):

$$U_p = \frac{1}{2} \int_{\Omega} \begin{Bmatrix} \boldsymbol{\varepsilon}^0 \\ \boldsymbol{\kappa} \end{Bmatrix}^T \begin{bmatrix} \mathbf{A} & \mathbf{B} \\ \mathbf{B} & \mathbf{D} \end{bmatrix} \begin{Bmatrix} \boldsymbol{\varepsilon}^0 \\ \boldsymbol{\kappa} \end{Bmatrix} d\Omega, \tag{4}$$

where

$$(\mathbf{A}, \mathbf{B}, \mathbf{D}) = \int_{-h/2}^{h/2} (1, z, z^2) \mathbf{Q} dz,$$

h is the panel thickness and Ω is the cylindrical panel domain ($d\Omega = R ds d\theta$). The gravitational potential energy of the moving mass U_m can be derived assuming that gravity is aligned with the negative direction of the X axis:

$$U_m = mg \left[\left(v - \frac{h}{2R} w_{,\theta} \right) \sin \theta - w \cos \theta \right]. \tag{5}$$

The position vector \mathbf{p} of a point on the upper surface of the cylindrical panel described in the local frame may be expressed as

$$\mathbf{p} = \left(s + u - \frac{h}{2} w_{,s} \right) \mathbf{e}_s + \left(v - \frac{h}{2R} w_{,\theta} \right) \mathbf{e}_\theta + (R + w) \mathbf{e}_n = (s + u^*) \mathbf{e}_s + (v^*) \mathbf{e}_\theta + (R + w) \mathbf{e}_n. \tag{6}$$

The kinetic energy of the system T is composed of contributions from the cylindrical panel T_p and the moving mass T_m . The former may be written as

$$T_p = \frac{1}{2} \int_V \rho \left[\left(\frac{\partial \bar{u}}{\partial t} \right)^2 + \left(\frac{\partial \bar{v}}{\partial t} \right)^2 + \left(\frac{\partial \bar{w}}{\partial t} \right)^2 \right] dV = \frac{1}{2} \int_{\Omega} \rho h \left[\dot{u}^2 + \dot{v}^2 + \dot{w}^2 + \frac{h^2}{12} \left(\dot{w}_{,s}^2 + \frac{\dot{w}_{,\theta}^2}{R^2} \right) \right] d\Omega \tag{7}$$

and the latter may be expressed as

$$T_m = \frac{m}{2} \frac{d\mathbf{p}}{dt} \cdot \frac{d\mathbf{p}}{dt}. \tag{8}$$

The position vector \mathbf{p} must be differentiated with respect to time in order to compute Eq. (8). The expression for \mathbf{p} in Eq. (6) is given in terms of unit vectors \mathbf{e}_s , \mathbf{e}_θ , \mathbf{e}_n that vary with time. Hence, derivatives of these vectors with respect to time must be obtained before an expression for $d\mathbf{p}/dt$ is calculated. Equation (2) can be differentiated to obtain

$$\frac{d\mathbf{e}_s}{dt} = \mathbf{0}, \quad \frac{d\mathbf{e}_\theta}{dt} = -\dot{\theta} \mathbf{e}_n, \quad \frac{d\mathbf{e}_n}{dt} = \dot{\theta} \mathbf{e}_\theta. \tag{9}$$

Differentiation of \mathbf{p} in Eq. (6) with respect to time, consideration of Eq. (9) and substitution into Eq. (8) yields

$$T_m = \frac{m}{2} \left[\left(\frac{du^*}{dt} \right)^2 + \left(\frac{dv^*}{dt} \right)^2 + \left(\frac{dw}{dt} \right)^2 + 2\dot{s} \frac{du^*}{dt} + 2(R+w)\dot{\theta} \frac{dv^*}{dt} - 2v^*\dot{\theta} \frac{dw}{dt} + \dot{s}^2 + \dot{\theta}^2(R+w)^2 + \dot{\theta}^2(v^*)^2 \right]. \quad (10)$$

The first variation of T_m given in Eq. (10) is taken and, integration by parts after integration in time leads to:

$$\begin{aligned} \int_{t_1}^{t_2} \delta T_m dt &= \int_{t_1}^{t_2} m \left[-\frac{d^2 u^*}{dt^2} - \ddot{s} \right] \delta u^* dt + \int_{t_1}^{t_2} m \left[-\frac{d^2 v^*}{dt^2} - \ddot{\theta}(R+w) - 2\dot{\theta} \frac{dw}{dt} + \dot{\theta}^2 v^* \right] \delta v^* dt + \\ &+ \int_{t_1}^{t_2} m \left[-\frac{d^2 w}{dt^2} + \ddot{\theta} v^* + 2\dot{\theta} \frac{dv^*}{dt} + \dot{\theta}^2(R+w) \right] \delta w dt. \end{aligned} \quad (11)$$

Differentiation with respect to time has been purposely written as d/dt in order to emphasize that these are total derivatives. Nevertheless, the position of the moving mass varies with time and, therefore, convective terms arise. First and second total derivatives are obtained as in Eq. (12):

$$\begin{aligned} \frac{df}{dt} &= \frac{\partial f}{\partial t} + \frac{\partial s}{\partial t} \frac{\partial f}{\partial s} + \frac{\partial \theta}{\partial t} \frac{\partial f}{\partial \theta} = \dot{f} + \dot{s} f_{,s} + \dot{\theta} f_{,\theta}, \\ \frac{d^2 f}{dt^2} &= \ddot{f} + 2\dot{s} \dot{f}_{,s} + 2\dot{\theta} \dot{f}_{,\theta} + \ddot{s} f_{,s} + \ddot{\theta} f_{,\theta} + \dot{s}^2 f_{,ss} + \dot{\theta}^2 f_{,\theta\theta} + 2\dot{s} \dot{\theta} f_{,s\theta}, \end{aligned} \quad (12)$$

where f is a dummy function of s and θ .

NUMERICAL PROCEDURES

Discretization of the problem is now performed. The vectors of interpolation functions are denoted by \mathbf{N}_1 and \mathbf{N}_2 where \mathbf{N}_1 has four entries that correspond to the traditional bilinear interpolation functions while \mathbf{N}_2 has sixteen entries that correspond to the R16 element interpolation functions (Bismarck-Nasr, 1991). \mathbf{q}_e is the element vector of nodal degrees of freedom such that $\mathbf{q}_e = \{ \mathbf{q}_u^T \mathbf{q}_v^T \mathbf{q}_w^T \}^T$. The exact displacements are now substituted by their finite element approximations with the aid of Eq. (13):

$$\begin{aligned} u &= [\mathbf{N}_1 \quad \mathbf{0} \quad \mathbf{0}] \mathbf{q}_e = \mathbf{N}_u \mathbf{q}_e \\ u^* &= \left[\mathbf{N}_1 \quad \mathbf{0} \quad -\frac{h}{2} \mathbf{N}_{2,s} \right] \mathbf{q}_e = \mathbf{N}_{u^*} \mathbf{q}_e \\ v &= [\mathbf{0} \quad \mathbf{N}_1 \quad \mathbf{0}] \mathbf{q}_e = \mathbf{N}_v \mathbf{q}_e \\ v^* &= \left[\mathbf{0} \quad \mathbf{N}_1 \quad -\frac{h}{2R} \mathbf{N}_{2,\theta} \right] \mathbf{q}_e = \mathbf{N}_{v^*} \mathbf{q}_e \\ w &= [\mathbf{0} \quad \mathbf{0} \quad \mathbf{N}_2] \mathbf{q}_e = \mathbf{N}_w \mathbf{q}_e \end{aligned} \quad (13)$$

Substitution of the terms u , v , w defined in Eq. (13) into Eqs. (4), (7) and (5) yields, respectively, the usual element stiffness matrix \mathbf{K}_e , element mass matrix \mathbf{M}_e and element load vector \mathbf{f}_e associated with the dynamics of the cylindrical panel. Substitution of the terms u^* , v^* , w into Eq. (11) and recalling Eq. (12) yields the moving load element stiffness matrix \mathbf{K}_{me} , moving load element mass matrix \mathbf{M}_{me} , moving load damping matrix \mathbf{C}_{me} and moving load element load vector \mathbf{f}_{me} . These element matrices are defined as:

$$\mathbf{M}_e = \int \int_{s \theta} \rho h \begin{bmatrix} \mathbf{N}_1^T \mathbf{N}_1 & \mathbf{0} & \mathbf{0} \\ \mathbf{0} & \mathbf{N}_1^T \mathbf{N}_1 & \mathbf{0} \\ \mathbf{0} & \mathbf{0} & \mathbf{N}_2^T \mathbf{N}_2 + \frac{h^2}{12} \mathbf{N}_{2,s}^T \mathbf{N}_{2,s} + \frac{h^2}{12R^2} \mathbf{N}_{2,\theta}^T \mathbf{N}_{2,\theta} \end{bmatrix} R d\theta ds, \quad (14)$$

$$\boldsymbol{\psi} = \begin{bmatrix} \mathbf{N}_{1,s}^T & \mathbf{0}^T & \frac{1}{R}\mathbf{N}_{1,\theta}^T & \mathbf{0}^T & \mathbf{0}^T & \mathbf{0}^T \\ \mathbf{0}^T & \frac{1}{R}\mathbf{N}_{1,\theta}^T & \mathbf{N}_{1,s}^T & \mathbf{0}^T & \mathbf{0}^T & \mathbf{0}^T \\ \mathbf{0}^T & \frac{1}{R}\mathbf{N}_2^T & \mathbf{0}^T & -\mathbf{N}_{2,ss}^T & -\frac{1}{R^2}\mathbf{N}_{2,\theta\theta}^T & -\frac{2}{R}\mathbf{N}_{2,s\theta}^T \end{bmatrix}^T \quad (15)$$

$$\mathbf{K}_e = \int \int_s \int_\theta \boldsymbol{\psi}^T \begin{bmatrix} \mathbf{A} & \mathbf{B} \\ \mathbf{B} & \mathbf{D} \end{bmatrix} \boldsymbol{\psi} R d\theta ds, \quad (16)$$

$$\mathbf{f}_e = \int \int_s \int_\theta \rho h g \begin{bmatrix} \mathbf{0}^T \\ \mathbf{N}_1^T \sin \theta \\ -\mathbf{N}_2^T \cos \theta - \frac{h}{2R}\mathbf{N}_{2,\theta}^T \sin \theta \end{bmatrix} R d\theta ds, \quad (17)$$

$$\mathbf{M}_{me} = m(\mathbf{N}_u^T \mathbf{N}_u + \mathbf{N}_v^T \mathbf{N}_v + \mathbf{N}_w^T \mathbf{N}_w), \quad (18)$$

$$\mathbf{C}_{me} = 2m\mathbf{N}_u^T (\dot{s}\mathbf{N}_{u,s} + \dot{\theta}\mathbf{N}_{u,\theta}) + 2m\mathbf{N}_v^T (\dot{s}\mathbf{N}_{v,s} + \dot{\theta}\mathbf{N}_{v,\theta} + \dot{\theta}\mathbf{N}_w) + 2m\mathbf{N}_w^T (\dot{s}\mathbf{N}_{w,s} + \dot{\theta}\mathbf{N}_{w,\theta} - \dot{\theta}\mathbf{N}_v), \quad (19)$$

$$\begin{aligned} \mathbf{K}_{me} = & m\mathbf{N}_u^T (\dot{s}\mathbf{N}_{u,s} + \ddot{\theta}\mathbf{N}_{u,\theta} + \dot{s}^2\mathbf{N}_{u,ss} + \dot{\theta}^2\mathbf{N}_{u,\theta\theta} + 2\dot{s}\dot{\theta}\mathbf{N}_{u,s\theta}) + \\ & m\mathbf{N}_v^T (\dot{s}\mathbf{N}_{v,s} + \ddot{\theta}\mathbf{N}_{v,\theta} + \dot{s}^2\mathbf{N}_{v,ss} + \dot{\theta}^2\mathbf{N}_{v,\theta\theta} + 2\dot{s}\dot{\theta}\mathbf{N}_{v,s\theta} + \ddot{\theta}\mathbf{N}_w + 2\dot{s}\dot{\theta}\mathbf{N}_{w,s} + 2\dot{\theta}^2\mathbf{N}_{w,\theta} - \dot{\theta}^2\mathbf{N}_v) + \\ & m\mathbf{N}_w^T (\dot{s}\mathbf{N}_{w,s} + \ddot{\theta}\mathbf{N}_{w,\theta} + \dot{s}^2\mathbf{N}_{w,ss} + \dot{\theta}^2\mathbf{N}_{w,\theta\theta} + 2\dot{s}\dot{\theta}\mathbf{N}_{w,s\theta} - \ddot{\theta}\mathbf{N}_v - 2\dot{s}\dot{\theta}\mathbf{N}_{v,s} - 2\dot{\theta}^2\mathbf{N}_{v,\theta} - \dot{\theta}^2\mathbf{N}_w), \end{aligned} \quad (20)$$

$$\mathbf{f}_{me} = m(\dot{\theta}^2 R \mathbf{N}_w^T - \dot{s} \mathbf{N}_u^T - \ddot{\theta} R \mathbf{N}_v^T). \quad (21)$$

The element arrays assembled result in the governing dynamic equations expressed below:

$$(\mathbf{M} + \mathbf{M}_m) \ddot{\mathbf{q}} + (\mathbf{C} + \mathbf{C}_m) \dot{\mathbf{q}} + (\mathbf{K} + \mathbf{K}_m) \mathbf{q} = \mathbf{f} + \mathbf{f}_m. \quad (22)$$

Equation (22) contains two kinds of arrays: (i) arrays \mathbf{K} , \mathbf{M} , \mathbf{M}_m , \mathbf{f} that are independent of s , θ , \dot{s} , $\dot{\theta}$, \ddot{s} , $\ddot{\theta}$, and (ii) arrays \mathbf{K}_m , \mathbf{C}_m , \mathbf{f}_m that dependent on s , θ and their time derivatives. A few remarks can be made about Eq. (22):

- i. The equation reduces to that of a cylindrical panel with a point mass when the moving mass velocity and acceleration components are eliminated.
- ii. The moving mass contributes to the forcing term of the motion by virtue of its velocity and acceleration.
- iii. Matrices \mathbf{K}_m , \mathbf{C}_m are nonsymmetric and depend on s , θ and their time derivatives.
- iv. The equation of motion is nonlinear in the velocity of the moving mass.

Solution of the governing dynamic matrix equation requires the use of nonlinear numerical procedures that can cope with the nonlinear character of the problem and can handle nonsymmetric matrices. Instead, a perturbation technique to solve the governing equations is proposed that requires neither nonlinear capabilities nor storage of nonsymmetric banded matrices. The technique consists in splitting the nonlinear, nonsymmetric governing equation into a series of linear, symmetric sub-problems. The total displacement is written as a summation of terms:

$$\mathbf{q} = \mathbf{q}_0 + \mathbf{q}_1 + \mathbf{q}_2 + \dots + \mathbf{q}_n, \quad (23)$$

where each term in the series is smaller than the previous ones in some norm. Hence, substituting Eq. (23) into (22), the governing equation is re-written as a sequence of matrix equations.

$$\begin{aligned} \mathbf{M}\ddot{\mathbf{q}}_0 + \mathbf{K}\mathbf{q}_0 &= \mathbf{f}, \\ \mathbf{M}\ddot{\mathbf{q}}_1 + \mathbf{K}\mathbf{q}_1 &= \mathbf{f}_m - \mathbf{M}_m\ddot{\mathbf{q}}_0 - \mathbf{C}_m\dot{\mathbf{q}}_0 - \mathbf{K}_m\mathbf{q}_0, \\ \mathbf{M}\ddot{\mathbf{q}}_2 + \mathbf{K}\mathbf{q}_2 &= -\mathbf{M}_m\ddot{\mathbf{q}}_1 - \mathbf{C}_m\dot{\mathbf{q}}_1 - \mathbf{K}_m\mathbf{q}_1, \\ &\vdots \\ \mathbf{M}\ddot{\mathbf{q}}_n + \mathbf{K}\mathbf{q}_n &= -\mathbf{M}_m\ddot{\mathbf{q}}_{n-1} - \mathbf{C}_m\dot{\mathbf{q}}_{n-1} - \mathbf{K}_m\mathbf{q}_{n-1}. \end{aligned} \quad (24)$$

Notice that the left hand side of all Eqs. (24) are written in the form $\mathbf{M}\ddot{\mathbf{q}}_i + \mathbf{K}\mathbf{q}_i$. Recalling that \mathbf{K} and \mathbf{M} are constant, symmetric matrices, a traditional time integration scheme without modifications can be used to solve each one of the Eqs. (24). Moreover, the effective stiffness matrix of the sub-problems is the same, i.e., they can be put in form $\overline{\mathbf{K}}\mathbf{q}_{i+1} = \overline{\mathbf{f}}(\mathbf{q}_i, s, \theta, \dot{s}, \dot{\theta}, \ddot{s}, \ddot{\theta})$. This can be used to advantage because only one decomposition of $\overline{\mathbf{K}}$ needs to be done for all the sub-problems which are solved sequentially from $i = 0$ to n . The number of terms n in Eq. (23) required to achieve a certain precision depends on the problem configuration. If the inertia effects of the moving mass are significantly smaller than those of the cylindrical panel then a small n is sufficient. On the other hand, as the moving mass m becomes closer to the mass of the cylindrical panel, more and more terms must be used and, in such cases, a full nonlinear numerical procedure that can handle nonsymmetric matrices may be more appropriate.

The convergence characteristics of the perturbation series (i.e. Eq. (23)) can be investigated with a modified form of the governing equation Eq. (22). This is expressed as

$$(\overline{\mathbf{K}} + \overline{\mathbf{K}}_m)\mathbf{q} = \overline{\mathbf{f}} + \overline{\mathbf{f}}_m, \quad (25)$$

where $\overline{\mathbf{K}}$ and $\overline{\mathbf{K}}_m$ represent effective matrices, and $\overline{\mathbf{f}}$ and $\overline{\mathbf{f}}_m$ denote effective vectors that are typical of forward time integration schemes such as Wilson- θ or Newmark method. The exact solution of the governing equation, Eq. (25), is given as

$$\mathbf{q} \equiv \mathbf{q}_{\text{exact}} = (\mathbf{I} + \overline{\mathbf{K}}^{-1}\overline{\mathbf{K}}_m)^{-1}\overline{\mathbf{K}}^{-1}(\overline{\mathbf{f}} + \overline{\mathbf{f}}_m) \quad (26)$$

For a series expansion with $n + 1$ terms, where $n > 1$, the solutions to the perturbed equations, i.e. Eq. (24), are:

$$\mathbf{q}_0 = \overline{\mathbf{K}}^{-1}\overline{\mathbf{f}}, \quad \mathbf{q}_1 = \overline{\mathbf{K}}^{-1}(\overline{\mathbf{f}}_m - \overline{\mathbf{K}}_m\mathbf{q}_0), \quad \mathbf{q}_2 = \overline{\mathbf{K}}^{-1}\overline{\mathbf{K}}_m\mathbf{q}_1, \quad \dots \quad \text{and} \quad \mathbf{q}_n = \overline{\mathbf{K}}^{-1}\overline{\mathbf{K}}_m\mathbf{q}_{n-1}. \quad (27)$$

The error \mathbf{e} (i.e. $\sum \mathbf{q}_i - \mathbf{q}_{\text{exact}}$) is expressed as

$$\begin{aligned} \mathbf{e} &= \mathbf{q}_0 + (\mathbf{I} + \overline{\mathbf{K}}^{-1}\overline{\mathbf{K}}_m)^{-1}[\mathbf{I} + (-\overline{\mathbf{K}}^{-1}\overline{\mathbf{K}}_m)^n]\overline{\mathbf{K}}^{-1}(\overline{\mathbf{f}}_m - \overline{\mathbf{K}}_m\mathbf{q}_0) - (\mathbf{I} + \overline{\mathbf{K}}^{-1}\overline{\mathbf{K}}_m)^{-1}\overline{\mathbf{K}}^{-1}(\overline{\mathbf{f}} + \overline{\mathbf{f}}_m) = \\ &= (\mathbf{I} + \overline{\mathbf{K}}^{-1}\overline{\mathbf{K}}_m)^{-1}(-\overline{\mathbf{K}}^{-1}\overline{\mathbf{K}}_m)^n\overline{\mathbf{K}}^{-1}(\overline{\mathbf{f}}_m - \overline{\mathbf{K}}_m\overline{\mathbf{K}}^{-1}\overline{\mathbf{f}}) \end{aligned} \quad (28)$$

This shows that the leading term in the error equation is $(\overline{\mathbf{K}}^{-1}\overline{\mathbf{K}}_m)$. If the effects of $\overline{\mathbf{K}}_m$ are very small when compared to those due to $\overline{\mathbf{K}}$, then $(\overline{\mathbf{K}}^{-1}\overline{\mathbf{K}}_m)^n$ must converge to $\mathbf{0}$ as $n \rightarrow \infty$. It is observed via numerical simulations that numerical convergence within machine precision is guaranteed with a small n .

NUMERICAL SIMULATIONS

The basic configuration to be used in the numerical simulations is reported in Tab. 1. The aperture angle and the cylinder radius are not specified in Tab. 1 because simulations are conducted for different curvatures in order to compare its effect on the dynamic response.

Table 1 – Geometry and material properties

Parameter	Value
Panel length, L	12 m
Panel thickness, h	30.0 mm
Young modulus, E	208 GPa
Poisson coefficient, ν	0.3
Mass density, ρ	7800 kg/m ³

A number of simulations demonstrate the dynamic behavior of cylindrical panels under traversing concentrated loads. In all cases the concentrated load is treated either as a concentrated force without mass or as a concentrated mass that applies force due to gravitational effects. When a concentrated force is modeled the mass inertial effects are not present such that matrices \mathbf{M}_{me} , \mathbf{C}_{me} , \mathbf{K}_{me} and vector \mathbf{f}_{me} given in Eqs. (18), (19), (20) and (21) are identically zero since $m = 0$. Equations (24) are simplified in this scenario because only the zero order sub-problem has to be solved to obtain \mathbf{q}_0 while the other terms vanish, i.e., $\mathbf{q}_1 = \mathbf{q}_2 = \dots = \mathbf{q}_n = \mathbf{0}$. On the other hand, when the mass effects are considered, perturbation terms \mathbf{q}_i with $1 \leq i \leq n$ are not zero.

A preliminary simulation is conducted to investigate the relative contribution of the perturbation series terms to the dynamic response of the cylindrical panel. The boundary conditions adopted are: two panel edges parallel to the Z axis clamped and the other two completely free. The load path selected corresponds to a trajectory where $s = L/2$ such that

the load movement is purely circumferential with $\dot{\theta} = \pi/24$ rd/s and $\ddot{\theta} = 0$ rd/s². The cylinder radius and aperture angle are $R = 45$ m and $\alpha = 30^\circ$. The concentrated force is aligned with the X axis in the negative direction and has a magnitude of 1,000 N while the moving mass is 101.94 kg, consistent with a gravitational acceleration of 9.81 m/s². The mesh used in all simulations has 30 elements in the axial direction and 60 elements in the circumferential direction.

Figure 2 presents the transverse displacements under the load obtained for the static, moving force and moving mass problems. The static problem disregards the inertial effects of both moving mass and main structure; it assumes that concentrated forces are statically applied along the load path. The moving force solution is simply the zero order component of the moving mass problem (Eq. (24)). Four terms were used in the perturbation series. Contribution of terms \mathbf{q}_2 , \mathbf{q}_3 are so small when compared to that of \mathbf{q}_0 that they are hard to be visualized in Fig. 2 because of the graph scale. In fact, the contribution of \mathbf{q}_2 and \mathbf{q}_3 are, respectively, 1,000 and 10,000 times smaller than that of \mathbf{q}_0 . Notice that the terms w_2 and w_3 oscillate about zero with very small amplitude but w_1 effectively contributes to the moving mass solution.

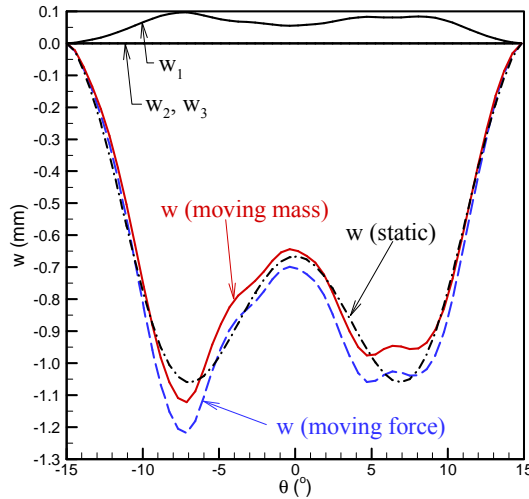


Figure 2 – Contribution of perturbation series terms.

It may be interesting to plot the transverse displacement distribution of the cylindrical panel as the load moves about. Figure 3 shows such plottings, obtained with the same parameters given above, for four different instants of time. Firstly, it can be noticed that there is symmetry about the plane $Z = L/2$ because geometry, boundary conditions and the moving load at all instants of time are symmetric about that plane. Secondly, the trends observed in Fig. 2 are confirmed in these 3D plottings, i.e., at $t = 1$ s the higher transverse displacement under the load occurs whereas it decreases as the load passes by the panel mid point and increases again at about 3/4 of the way.

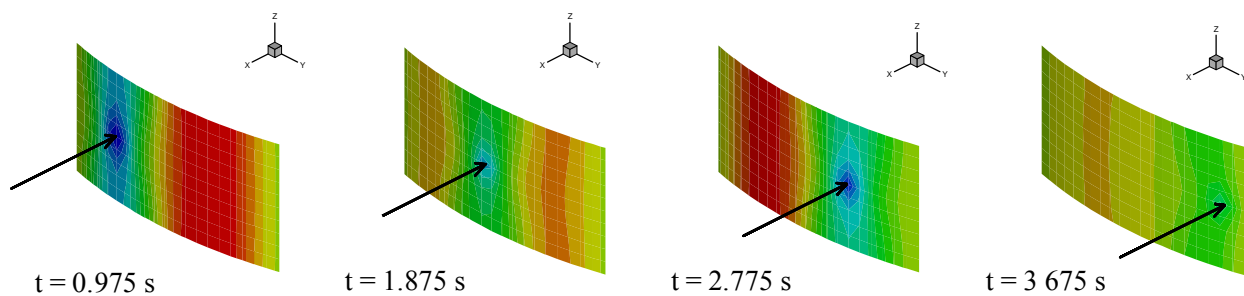


Figure 3 – Deformation plots.

The effect of the panel curvature on the dynamic response to traversing loads is investigated by varying the cylinder radius R and the aperture angle α . Four cases are considered: $R = \infty$ and $\alpha = 0^\circ$ (rectangular plate), $R = 90$ m and $\alpha = 15^\circ$, $R = 45$ m and $\alpha = 30^\circ$, and $R = 30$ m and $\alpha = 45^\circ$ such that $R\alpha$ is maintained constant. The other parameters important to the simulation are the same ones used in the preliminary analysis just presented. Results for different curvatures are presented in Fig. 4 in terms of transverse displacement under the load. Again, results for the static, moving force and moving mass problems were obtained. It can be seen that the higher the curvature, the smaller the transverse displacements. The patterns observed for finite radius ($R < \infty$) are similar but different from that associated with the flat plate case ($R = \infty$). Interesting to notice that higher curvatures imply that the moving force and the moving mass models provide distinct results what does not happen with the flat plate model, at least for the velocity $\dot{\theta}$ adopted in the simulations. Also, it is expected that the magnitude of the transverse displacements decrease with the curvature

since small curvatures (flat plate in the limit) imply predominance of bending behavior while large curvatures imply that membrane forces play a significant role, rendering stiffer the panel.

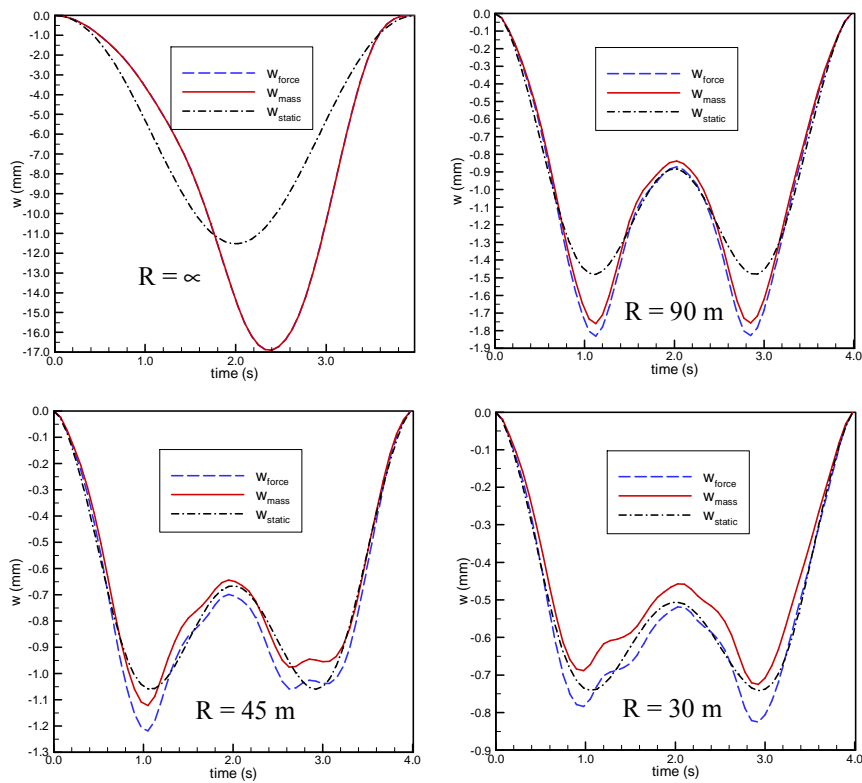


Figure 4 – Effect of panel curvature.

It is of interest to assess the influence of the traveling velocity on the panel dynamic response. For that purpose the panel with $R = 45$ m and $\alpha = 30^\circ$ is traversed by a load moving along the circumferential direction with $\dot{\theta} = \pi/48, \pi/24, \pi/12$ and $\pi/6$ rd/s. The transverse displacements presented in Fig. 5 are plotted as a function of the angle θ since it will take different times for the load to cross the panel, depending on $\dot{\theta}$.

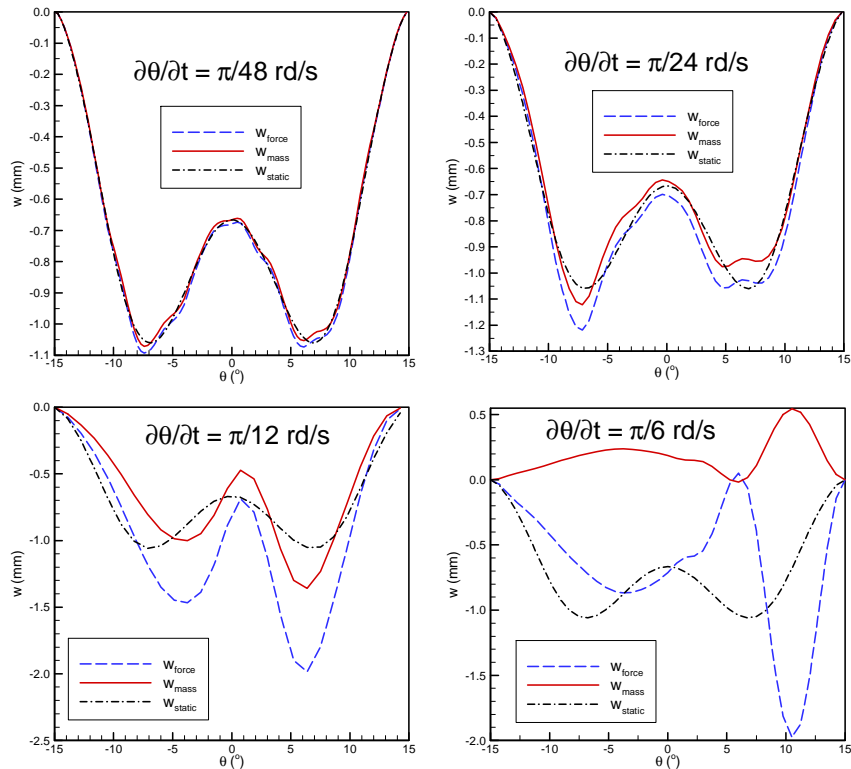


Figure 5 – Effect of traversing velocity.

The slowest velocity obviously leads to results where the static, moving force and moving mass displacements are almost equal. As the traversing velocity increases the disparity between the moving force and moving mass model becomes more and more evident. It can be seen that the highest transverse displacement shifts from $\theta \approx -7.5^\circ$ to $\theta \approx +6.5^\circ$ between the simulations where $\dot{\theta} = \pi/24$ rd/s and $\dot{\theta} = \pi/12$ rd/s. Striking is the fact that the moving mass model yields transverse displacements that are positive for $\dot{\theta} = \pi/6$ rd/s. This can be understood when vector \mathbf{f}_{me} given in Eq. (21) is inspected because it is clear that the term $m\dot{\theta}^2 R \mathbf{N}_w^T$ depends on $\dot{\theta}^2$ and implies in a transverse force pointing upwards, against that one produced by the concentrated force as observed in vector \mathbf{f}_e . The upwards force can be interpreted as the centrifugal force acting on the cylindrical panel.

Using the same data as in Fig. 5, Fig. 6 shows the transverse displacement of the panel mid point under the moving force and moving mass for different traversing velocities. The scale in the x -axis corresponds to the position where the traversing load is. The conclusion drawn from Fig. 6 is that the mid point transverse displacement may not reach its maximum magnitude necessarily when the moving load is there.

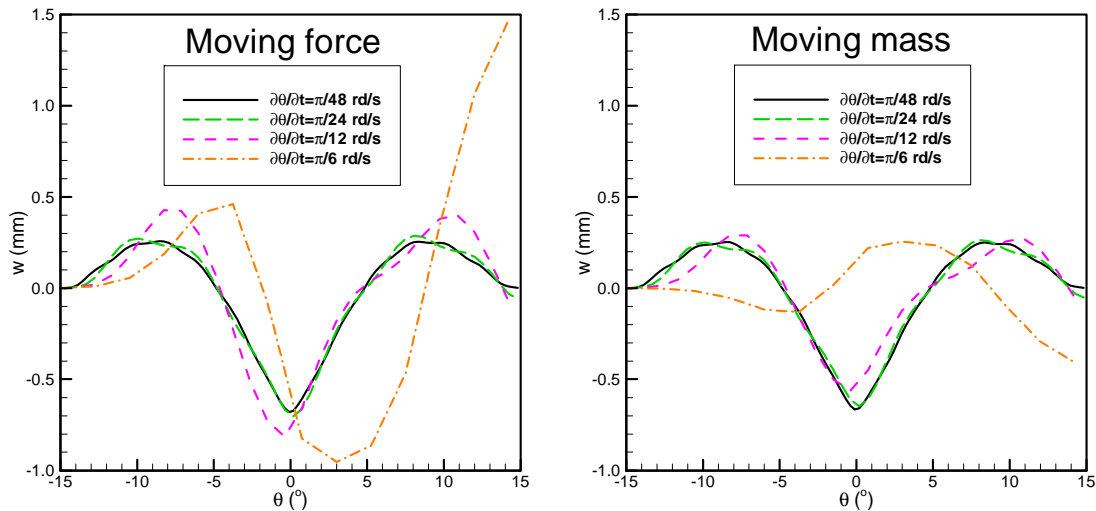


Figure 6 – Panel mid point transverse displacement.

Figure 6 reveals that the mid point displacement varies with the traversing velocity. The question of whether there is a critical velocity that induces large vibration amplitudes is investigated in Fig. 7 where the maximum mid point displacement is plotted against the moving load velocity. For small traversing velocities the moving force and moving mass models yield almost identical results. As the velocity increases it is observed that the moving force model tends to overestimate the displacement when $9\pi/96$ rd/s $\leq \dot{\theta} \leq 17\pi/96$ rd/s. Notice that when $\dot{\theta} = 14\pi/96$ rd/s the maximum mid point displacement for the moving mass problem is almost zero suggesting that this is a particularly safe traversing velocity. On the other hand, as the velocity increases ($\dot{\theta} \geq 21\pi/96$ rd/s) the moving mass model yields large displacements while the moving force model yields an underestimated result. It is observed that the moving force model points to a critical velocity of about $17\pi/96$ rd/s whereas the moving mass model indicates that there is a safe velocity of $14\pi/96$ rd/s after which the displacements tend to increase.

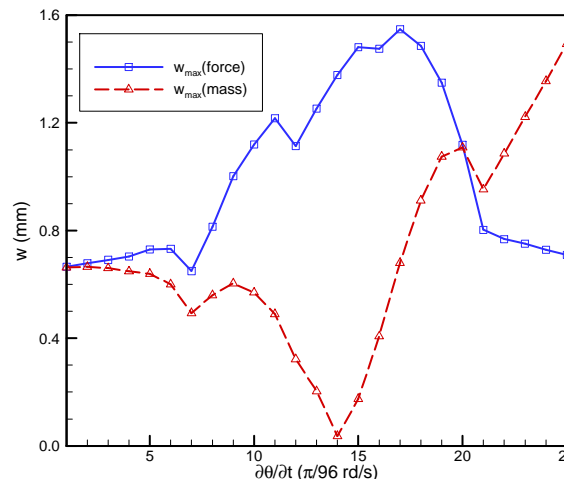


Figure 7 – Effect of traversing velocity on maximum mid point displacement.

All the simulations conducted up to here consider a constant moving mass $m = 101.94$ kg what yields $m/M = 1.54 \times 10^{-3}$ where M is the mass of the cylindrical panel. However, lighter or heavier masses may cross the panel. Hence, it is important to assess the effect of the m/M ratio on the panel dynamic response. Figure 8 presents results for the panel with $R = 45$ m and $\alpha = 30^\circ$ traversed by a load at $\dot{\theta} = \pi/24$ rd/s, $\dot{s} = 0$ m/s.

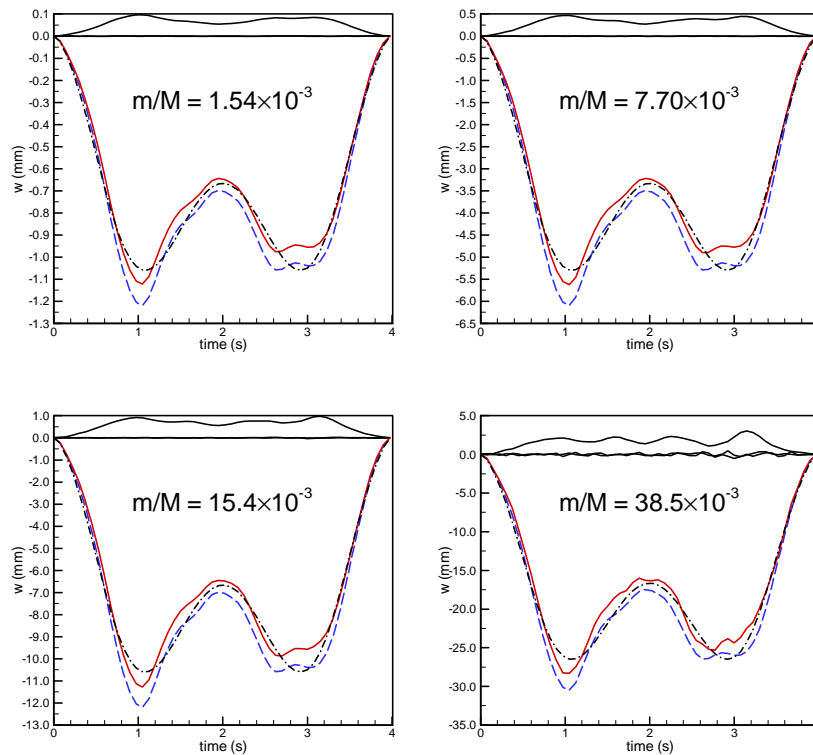


Figure 8 – Effect of m/M ratio.

Not much difference can be seen between the cases where $m/M = 1.54 \times 10^{-3}$ and $m/M = 7.70 \times 10^{-3}$ except that the magnitude of the transverse displacements are higher in the latter. Actually, the error involved in simply multiplying the displacements for $m/M = 1.54 \times 10^{-3}$ by 5 to obtain the displacements for $m/M = 7.70 \times 10^{-3}$ is negligible. It can be seen that, in both cases, the contribution of w_2 and w_3 for the dynamic response is very small but, as m/M increases, their contributions become appreciable as observed in the plottings for $m/M = 15.4 \times 10^{-3}$ and $m/M = 38.5 \times 10^{-3}$.

CONCLUSIONS

The dynamics of cylindrical panels traversed by moving concentrated loads are investigated in this paper. Effects of panel curvature, traversing velocity and relative mass (moving mass to panel mass) are observed. The numerical technique proposed to solve the problem naturally leads to a separation of the problem into moving force (zero order problem) and moving mass (complete perturbation series). This technique has the upside of splitting the effects of a purely concentrated force to inertial effects of the concentrated mass.

The perturbation series can have an arbitrary number of terms, depending on the precision required for the solution. However, it is shown that only the first few terms need to be retained in the solution sequence if the moving mass to panel mass ratio is small. Therefore, situations where heavy masses traverse lightweight structures require a large number of terms in the perturbation series. In this case it would be perhaps more effective to solve the nonlinear and nonsymmetric governing dynamic equations using a fully nonlinear solver.

Contact between moving load and base structure is assumed to exist throughout. However, this assumption may not always be observed, particularly when high velocities are considered. In this case significant centrifugal forces arise what tend to separate the moving load from the base structure. If this limitation of the model is to be overcome then a contact model must be included in the formulation. Moreover, friction is completely absent. Friction forces may be included in the simulation perhaps through a traditional Coulomb model.

ACKNOWLEDGMENTS

This work was partially financed by the Brazilian agency CNPq (grant 300236/2009-3)

REFERENCES

- Bismarck-Nasr, M.N., 1991, "On the sixteen degree of freedom rectangular plate element", *Computers & Structures*, Vol. 40, No. 4, pp. 1059-1060.
- Fryba, L., 1972, "Vibrations of Solids and Structures under Moving Loads". Groningen, Noordhoff.
- Gbadeyan, J.A. and Oni, S.T., 1995, "Dynamic behaviour of beams and rectangular plates under moving loads", *Journal of Sound and Vibration*, Vol. 182, No. 5, pp. 677-695.
- Hino, J., Yoshimura, T., Konishi, K. and Ananthanarayana, N., 1984, "A finite element method prediction of the vibration of a bridge subjected to a moving vehicle load", *Journal of Sound and Vibration*, Vol. 96, No. 1, pp. 45-53.
- Kraus, H., 1967, "Thin Elastic Shells", John Wiley & Sons, New York.
- Michaltsos, G., Sophianopoulos D. and Kounadis, N., 1996, "The effect of a moving mass and other parameters on the dynamic response of a simple supported beam", *Journal of Sound and Vibration*, Vol. 191, No. 3, pp. 357-362.
- Novozhilov, V.V., 1953, "Foundations of the Nonlinear Theory of Elasticity", Graylock, Rochester, NY.
- Oguamanam, D.C.D., Hansen, J.S. and Heppler, G.R., 1998, "Dynamic response of an overhead crane system", *Journal of Sound and Vibration*, Vol. 213, No. 5, pp. 889-906.
- Olsson, M., 1985, "Finite element, modal co-ordinate analysis of structures subjected to moving loads", *Journal of Sound and Vibration*, Vol. 99, No. 1, pp. 1-12.
- de Souza, V.C.M. and Croll, J.G.A., 1980, "An energy analysis of the free vibrations of isotropic spherical shells", *Journal of Sound and Vibration*, Vol. 73, No. 3, pp. 379-404.

RESPONSIBILITY NOTICE

The author is the only responsible for the printed material included in this paper.

A Regularization Technique for Ill-Conditioned Linear System of Equations

Henrique G. Moura ¹, Arcanjo Lenzi ¹

¹ Federal University of Santa Catarina, Laboratory of Vibration and Acoustics, 88040-900 – FLN/SC – Brazil.

Abstract: The knowledge about the input-output relations of a system can be very important in many practical situations in engineering. The linear system theory comes from applied mathematics as an efficient and simple modeling technique for input-output systems relations. Many identification problems arise from a set of linear system of equations, using known outputs only. It is a type of inverse problems, whenever systems inputs are sought by its output only. This work presents a regularization method, called random matrix (RMA) method, able to reduce errors effect over the solution of inverse problems, in presence of ill-conditionness. The presented results show the efficacy of the technique when dealing with inverse problems of high ill-conditioning levels.

Keywords: identification, regularization, random, forces.

NOMENCLATURE

Vectors and matrices

A = integro-differential matrix operation (linear system of equations).
 x = system output (displacements)
 f = system input (forces, N)

Greek Symbols

σ = eigenvalue (extract by SVD).
 ξ = error vector, (forces, N)
 δf_x = force deviation, N.
 ξ_l = force deviation, N.
 δ = random variable.
 Ω = Gaussian density function.

Subscripts

x = relative to uncertainty.
 a = relative to regularization.
 0 = relative to uncertainty.
 1 = relative to regularization.

INTRODUCTION

It is very common to face in applied mechanics a kind of identification problems when estimating a certain physical quantity of interest. Unfortunately, most of identification problems lie in the area of inverse problems, either because of the lack of appropriate measurement instruments or because any difficulties to access the measurements locations, in order to directly obtain the requested quantities. Inverse problems are characterized by determining unknown causes based on observations of their effects (Woodbury, 2008). A particular type of inverse problems found in engineering can be formulated in terms of a linear system of equations,

$$x = Af, \quad (1)$$

where y is observed effect, or output matrix, A is an integro-differential matrix operator and x is the requested quantity, or input matrix.

When there is no noise in both, the input and output data, the matrix inversion processes are computationally stables. However, if there is noise in the data, these processes may become instable, and this error can be largely amplified in the solution, so that it becomes completely meaningless. Force identification problems using accelerances matrices and transfer frequency functions are examples of such a kind of inverse problems.

When dealing with inverse problems, it is straight necessary to take an account the use of regularization techniques to better solve the problem. Regularization involves introducing additional information to the system to improve its solution in cases of ill-posedness and/or ill-conditionness. Many regularization techniques are discussed in details in the bibliography (Hansen, 1998, Sharkar, 1981).

This paper brings a new strategy to regularize ill-conditioned linear systems of equations. The whole mathematics is step by step shown in the following pages. The algorithm efficiency could be checked by a force identification problem using noisy data.

DEFINITION OF ILL-POSED AND ILL-CONDITIONED SYSTEMS

A problem is said to be well-posed if there requirements below are fulfilled: (1) there exist a unique solution to the problem; (2) the solution has a continuous dependency (smoothly) to the input data. For any negative, the problem is called ill-posed (Hansen, 1998).

The first two sentences require that the solution is not ambiguous. The second one assures the continuous dependence of this solution on the data. In simple words, a well-posed problem is one that, based on its formulation, has a consistent solution in that it could describe physical systems.

In practice, the measured data is a finite set, known with a degree of approximation, and one wants to find out a solution, as good as possible, to the problem. This process of searching of the best solution for the problem may encounter some instabilities and undesirable errors.

The last paragraph shows the difference between the non continuous dependence of the solution on the data and the instabilities of the solution, caused by uncertainties in the measured data. This instability relates an ill-conditioning situation.

Let suppose that matrix operator A is singular. It means that at least one singular value of A is zero. But, when singular values are calculated by a numerical algorithm that null value comes out as a very small number. This is called ill-conditioning and it makes the solution very sensible to small changes in the data. A measure of matrix conditionings is given by the condition number (Annalisa, 1998), defined as follow

$$CN(A) = \|A\|_2 \|A\|_2^+ = \sigma_{\max} / \sigma_{\min} \geq 1. \quad (2)$$

Note that σ_{\min} must be non zero. As the condition number increase, the system increases its ill-conditioness. Another simple way to verify matrix ill-conditioness is to calculate the matrix determinant that is close to zero whether the matrix operator is quasi-singular.

BASIC THEORY

Let's consider a linear system of equations written in the matrix form as shown in Eq. (1). If noise is added to response vector x the solution f must be compensated by ξ_0 ,

$$A(f + \xi_0) = x + \delta x = \tilde{x}. \quad (3)$$

If matrix A is ill-conditioned the error $\xi_0 = \delta f_x$ will be very large in comparison to δx . The ration $\xi_0/\delta x$ is called error amplification factor (Silva, 2005). For a regularized matrix $A(-) = A + \delta A$, applied to the exact response vector x , one would expected an error compensation δf_a . It could be written as

$$\bar{A}(f + \delta f_a) = x. \quad (4)$$

The term δf_a is called regularization error. As the exactly response x is not available, Eq. (4) must be modified to consider the noisy response.

$$\bar{A}(\bar{f} + \delta f_a) = \tilde{x}. \quad (5)$$

Now, it is possible to write the solution of the modified system as $f(-) = f + \delta f_x(-)$. Writing the vector $\xi_1 = \delta f_a + \delta f_x(-)$, as a sum of the uncertainty and regularization effects, Eq. (4) can be expressed in terms of the solution of the original problem,

$$\bar{A}(f + \xi_1) = \tilde{x}. \quad (6)$$

The two errors vectors ξ_0 and error ξ_1 show how does the solution differs for both original and regularized systems. The simple rule presented by Eq. (6) can be applied for any $x(\sim)$ to check if the regularization result is satisfactory. However, there is no analytical expression available for that, and then errors should to be numerically checked for each response of the system.

$$\|\xi_1\|_2 = \|\xi_0\|_2. \quad (7)$$

The presented regularization strategy shows that it is possible to seek, using a Monte Carlo simulation (Papoulis, 2001), a satisfactory regularized matrix $A(-)$ for the contaminated response $x(\sim)$.

THE RANDOM MATRIX METHOD

The proposed regularization aims to find a random matrix δA that, added to the original matrix A , could improve the matrix conditionness of the system, reducing the error amplification factor, and consequently, improving the inverse problem solution.

In this way, the method consists in generating a set $\{\delta A\}_{j=1,q}$ such that satisfy at least one of the rules expressed by the equations,

$$COND(A + \delta A) < COND(A). \quad (8)$$

$$DET(A + \delta A) > DET(A). \quad (9)$$

The Eq. (9) verifies the matrices determinant, and the Eq. (8) verifies the matrices conditionness whether it is non-square. The set $\{\delta A\}$ can be determined by a Monte Carlo simulation, respecting Eq. (7). For that, it is important to derive some analytical expressions to estimate the errors vectors ξ_0 and error ξ_j .

The errors vectors ξ_0 and error ξ_j can be estimated by the expressions,

$$\xi_0 = -(A)^+ \delta x. \quad (10)$$

$$\xi_j = -(\bar{A})^+ \delta A(A)^+ \tilde{x} - (\bar{A})^+ \delta x. \quad (11)$$

As it is shown, the uncertainties δx are needed to estimate the errors vectors above. In order to faithfully represent the meaning of the Eq. (7), and check perfectly the regularization efficacy by using Eq. (8) and (9), the uncertainties δx should coincide with the uncertainties in the data. As the uncertainties in the data are unknown, the regularization performed by RMA method may not be satisfactory for the contaminated data $x(\sim)$.

The problem of finding the uncertainties δx , that could be treat as sensibilities directions as well, leads to a Monte simulation, through a reasonable probability density function of $x(\sim)$. Thus, a set of uncertainties $\{\delta x\}$ can be found to control the RMA method generation in many sensibilities directions. The geometrical representation of Eq. (7) is shown in Fig. 1.

At first, it is supposed that a good estimation for δx could be provided by a Monte Carlo simulation. Thus, a set $\{\xi_{0i}\}_{i=1,p}$ can be obtained from Equations (10). For a set $\{\delta A_j\}_{j=1,q}$, respecting Eq. (8) or (9), it is possible to find a set $\{\xi_{1i}\}_j$ using Eq. (11). The set $\{\xi_{1i}\}_j$ that produce the minimum Euclidian distances, when compared to $\{\xi_{0i}\}$, relates the best δA_j . The overall computation procedure is shown below.

1. Generate a set $\{\delta x_i\}_{i=1,p}$ such that $\|\delta x_i\|_2 < \delta x_{max}$;
2. Compute a set $\{\xi_{0i}\}$ using Equation (10);
3. Generate a set $\{\delta A_j\}$ such that $\delta A = B(n)R(n)$ respecting Eq. (8) or (9); $R(n)$ is a weighted probability density function which returns a real positive matrix of order n ;
4. Compute a set $\{\xi_{1i}\}$ for each perturbation matrix $\{\delta A_j\}$ using Eq. (11);
5. Choose that set $\{\xi_{1i}\}$ that produce the minimum Euclidian distances to the set $\{\xi_{0i}\}$;
6. Adopt the modification $\{\delta A_j\}$ that related to the optimum $\{\xi_{1i}\}$;

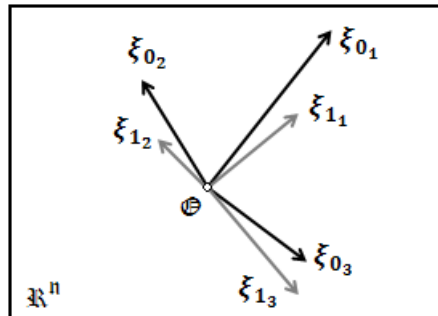


Figure 1 – Geometric representation of rule (7) for a set of three $\{\delta x\}$ and one $\{\delta A\}$.

It is important to emphasize that the method is highly dependent on the uncertainties $\{\delta x\}$ and on the matrices modifications $\{\delta A\}$. Here, both data were obtained from a normal distribution, according to the central limit theorem. Other densities probabilities functions could be applied whether some specific information is known about the stochastic responses of the system.

As it is seen, the RMA method has two main regularization parameters, δx_{max} and $B(n)$. The first one controls the amplitude of the numerical uncertainties. The numerical uncertainties must be modeled according to the expected experimental error. The second one controls the amplitude of the matrices modifications, that is, the regularization levels. The regularization error δf_a is acceptable just for small scales, which means that the regularization must be sufficient to repair the ill-conditionness only.

NUMERICAL RESULTS

The following results were obtained for a force identification process, commonly found in applied mechanics. If a response method is used, bending forces are obtained by taking the responses of the system and its frequencies response functions, according to Eq. (1).

Vector f relates excitation force, vector x relates the output responses of the system and matrix A relates the frequency response functions. Very simply stated, the frequency response functions (FRF), are the ratio of the output response to the input excitation force, in the frequency domain.

Here, the responses of the system and the FRF have been obtained by the well known analytical solution of the Euler-Bernoulli Beam (Meirovitch, 1997). Random and bias errors have been added to the responses and FRF curves. Both errors are important to simulate real data.

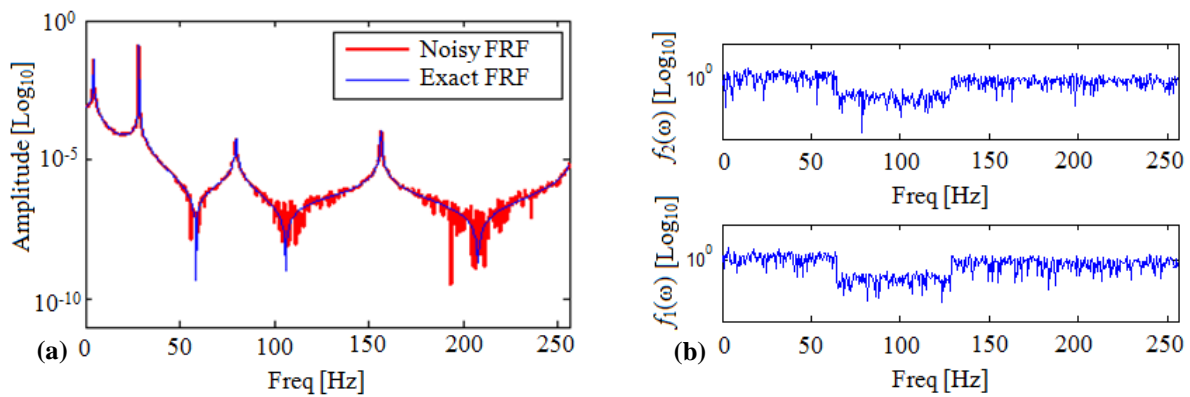


Figure 2 – (a) Noisy FRF (b) Exciting bending forces f_1 and f_2 applied upon the beam at nodes 2 and 4, respectively.

The responses of the beam were obtained at four different positions upon the beam, called nodes 1, 2, 3 and 4. Exciting bending forces have been applied to the beam at nodes 2 and 4 only. The exciting bending forces have been generated by a discrete weighted Gaussian density function, with coefficient a set to 10, $f(n) = aQ(n)$ (Papoulis, 2001). Both signals are shown in Fig. 2(b). Five hundred and twelve points (512) have been considered spaced of 0,5 Hz to simulate the spectral curves, directly in the frequency domain. The force signals have been multiplied by real constant step functions, in order to introduce significative forces variations.

The operator matrix A , or just FRF matrix, has the size 4 by 4. The RMA matrix method was applied on the FRF matrices for each frequency line. The responses of the beam refer to its measured displacements at each node. In this case, the FRF curves are called receptances. Due to the beam stiffness properties, the relation between bending forces and the respective displacements assume high ill-conditioned values, and consequently, high ill-conditioned receptances curves.

To avoid the numerical resolution of the beam equation, the responses of the beam have been obtained directly by the product between the reference FRF matrices and bending forces in the frequency domain. The results of the regularized force identification process are shown in Fig. 4.

The RMA method has been performed with a set of $p = 50$ sensibilities directions, $\{\delta x\}$, and $q = 100$ random matrices, $\{\delta A\}$. All Monte Carlo data were generated by a Gaussian density probability function. The regularization parameter δx_{max} was set to 10% of the responses levels.

The random matrices was performed by a weighted Gaussian density probability function, $R(n)$. The weight coefficients, $B(n)$, represent a modification ratio over each FRF curve. Thus, each element of $B(n)$ must assume a specially value for each correspondent FRF curve, as it is shown in Fig. 3.

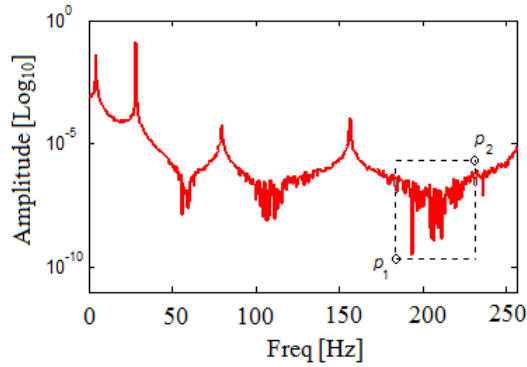


Figure 3 – Definition of element $[b_{2 \times 4}]$ thought the analysis of reacceptance $\{R(\omega)\}_{2 \times 4}$. The difference between the ordinates of point 1 and 2 defines the matrix weights.

Figure 4(a) shows the identified non-zero bending forces with and without regularization, at nodes 2 and 4. The RMA method reached satisfactory results for both rules defined by Eq. (7) and (8), reducing significantly the identification errors at frequency ranges 0 to 50 Hz and 200 to 256 Hz. The regularization results over the matrices determinants and conditioning numbers are shown in Fig. 5. The whole set of FRF matrices have been regularized by the RMA method, which means that the regularization process archive its maximum efficiency.

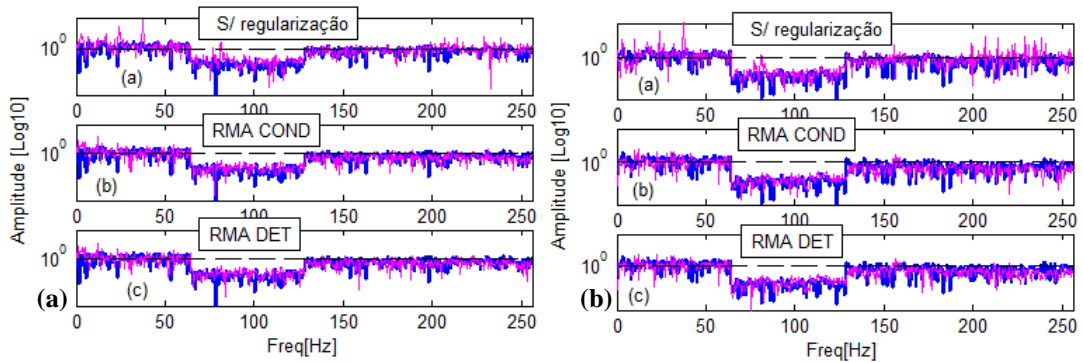


Figure 4 – Identified bending forces at nodes 2 and 4. Reference data is represented by the thick line.

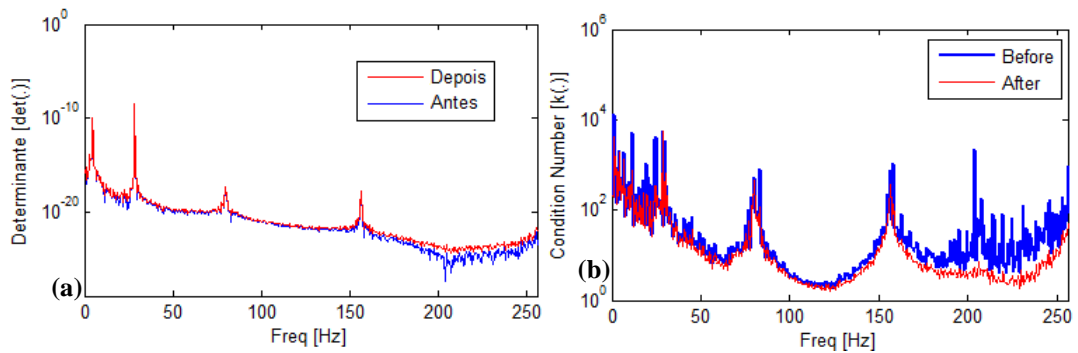


Figure 5 – (a) Matrices determinants and (b) matrices conditioning numbers before and after regularization.

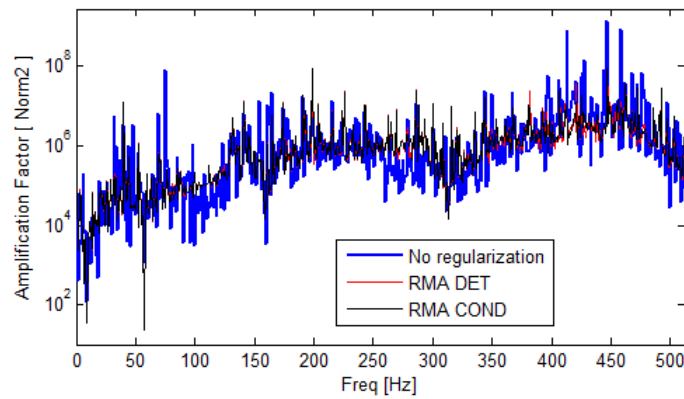


Figure 6 – Error amplification factors before and after regularization.

Figure 6 brings the amplification factor of the regularized FRF matrices. Note that the amplification factors were not totally decreased. The last results show that small variations of the amplification factors do not harm the identification results. As it was expected at the frequencies ranges 0 to 50 Hz and 200 to 256 Hz, the amplification factors were high improved.

CONCLUSIONS

The main purpose of the random matrices (RMA) method is to decrease the matrices amplification factors in order to provide a better solution for ill-conditioning linear systems inversions with noisy data. The RMA method makes possible the reduction of the amplification factors by using random matrices over the original matrix operators, with respect to two basic rules: the determinant and conditioning number of the regularized operators. These rules show in a simpler way how much ill-conditioned the matrices operators are.

Although the regularization have archived good results for the matrices determinants, conditioning numbers and identified forces, the amplification factors were not totally decreased along its operation range. Thus, others rules might be applied to better control the amplification factor reduction, and consequently improve the method efficacy.

Another comment arises about the uncertainties simulations which are very important to estimate the errors vectors before and after regularization. All priori information about the stochastic variables is very important to derive specifics probabilities densities functions and improve the overall results of the RMA regularization.

REFERENCES

- Woodbury, K. A., 2008, “What Are Inverse Problems”, Brief discussion about Inverse Problems, University of Alabama, US, available in: <http://www.me.ua.edu/inverse/whatis.html> on Out 9th.
- Hans, H. Z., 2007, “Stochastics Processes Applied To Electrical Engineering”; Lesions notes, Federal University of Santa Catarina, Electrical Engineering Department, FLN/SC, BRA.
- Silva, N. A. J., 2005, “Problemas Inversos Conceitos Fundamentais e Aplicações”, University of São Paulo, SP.
- Papoulis, A., 2001, “Probability, Random Variables and Stochastic Processes”, 4th ed., McGraw-Hill Book Company.
- Annalisa, F., 1998, “Mathematical conditioning”, An International Course on New Applications and Techniques of Experimental Modal Testing Updating, Optimization, and Damage Detection, CADIS, Jun 29 – Jul 03.
- Hansen, C., 1998, “Rank-Deficient and Discrete Ill-Posed Problems – Numerical Aspects of Linear Inversion”, SIAM Monographs on Modeling and Computation.
- Meirovitch, L., 1997, “Principles and Techniques of Vibrations”, Prentice-Hall, Upper Saddle River, NJ.
- Sharkar, T. K. et al., 1981, “Some Mathematical Considerations with the Inverse Problem”, IEEE Transactions on Antennas and Propagation, Vol.2. AP-29.

RESPONSIBILITY NOTICE

The authors are the only responsible for the printed material included in this paper.

Time Domain Multivariable Subspace-Based Method for Modal Parameters Identification Using Impulse Excitation

Heraldo Nélio Cambraia¹ and Paulo R.G. Kurka²

¹ Departamento de Engenharia Mecânica – Universidade Federal do Paraná (heraldo@ufpr.br)

² Departamento de Projeto Mecânico – Faculdade de Engenharia Mecânica – Universidade Estadual de Campinas (kurka@fem.unicamp.br)

Abstract: The paper presents a time domain multivariable subspace-based method used to identify structural modal parameters by fitting a multivariable state-space model to impulse responses data. The main characteristic of such a method consists on the determination of an extended version of the observability matrix from impulse responses data, by means of a low rank approximation process, using the singular value decomposition technique. The order of the system to be identified is estimated by inspection of the dominant singular values of the data matrix. The observable state-space realization yields an estimation of the modal parameters. A numerical simulation is used to present the main characteristics of the method in experimental modal analysis. Natural frequencies, damping factors and mode shapes are estimated.

Keywords: modal parameters identification, subspace-based method, signal processing

NOMENCLATURE

A = state matrix
B = input influence matrix
C = output influence matrix
D = direct transmission matrix
 \bar{C} = damping matrix
 f = degrees of freedom
 $\mathbf{f}(t)$ = external force
H = Hankel matrix of irf data
 $\mathbf{h}(t)$ = Markov parameters
 $h_{ij}(t)$ = impulse response function
 $\bar{\mathbf{K}}$ = stiffness matrix
 $\bar{\mathbf{M}}$ = mass matrix
 n = order of the system

$\mathbf{u}(t)$ = input vector at time
 \mathbf{U}_f = ordering input matrix
 $\mathbf{z}(t)$ = generalized displacement
 z_j = j th eigenvalue for discrete system model

Greek Symbols

Γ_i = observability matrix
 $\hat{\Gamma}_i$ = extended observability matrix
 Δt = time interval
 λ_j = j th eigenvalue for continuous system model

ξ_j = i th damping factor
 $\bar{\Lambda}$ = spectral matrix
 ϕ_j = j th mode shape
 Φ = mode shapes matrix
 Ψ = modal matrix
 Ψ_j = j th eigenvector associated to λ_j
 Ω_j = controllability matrix
 ω_j = i th natural frequency

INTRODUCTION

Mathematical modeling is an analytical approach used to describe the dynamic behavior of a phenomenon based on physical laws. System identification (sometimes referred to as system realization) is an approach, where experiments are performed on the system, and a presumed parametric model is subsequently fitted to the measured data by assigning a set of suitable numerical values to its parameters (Söderström and Stoica, 1987 and Ljung, 1999). Both approaches are important in system analysis, design and control problems.

In the control community jargon, the process of fitting a state-space model to a multivariable linear time-invariant (LTI) dynamic system from experimental data is called state-space realization (Viberg, 1995). A state-space is minimal if there exists no other realization of a lower degree to represent the system. The problem addressed in this paper deals with the application of a minimum order state-space realization technique in modal parameter identification using impulse responses data. More specifically, a time domain multivariable subspace-based parametric technique is used to identify the modal parameters of a structural system by fitting a suitable observable part of a minimal state-space model for a finite number of impulse responses data.

In the experimental modal analysis (EMA) (Maia and Silva, 1997), the multivariable modal testing has many advantages when compared to single-input and single-output techniques, especially when dealing with larger structures. The forces from multiple excitations allow a more uniform distribution of excitation energy throughout the structure, improving the accuracy of identified modal parameters and reducing the testing time. The problem has attracted much attention because of its broad application in many fields.

The time domain modal parametric identification is a problem of central importance in EMA. A number of algorithms use the impulse responses for extracting the system parameters. The Complex Exponential and Polyreference methods, for example, fit an auto-regressive (AR) model to a finite quantity of impulse response data. Similarly, the so-

called Direct Parameter Estimation method (Maia and Silva, 1997) works by fitting an auto-regressive with exogenous input (ARX) model directly to input-output data. All these methods commonly use the classical least-squares (LS) minimization technique as integral part of the step related to model coefficients estimation. It is well know that when the data is corrupted by noise, the LS approach leads to biased parameters estimation. To avoid such a problem, a large overparametrization in the order of the model is then required, adding extra difficulties to estimate the true system order and the separation of computational modes from the true system ones. Another class of identification algorithms is based on auto-regressive with moving-average (ARMA) models, for impulse response data, and the auto-regressive moving average with exogenous excitation (ARMAX), for input-output data. The above moving-average based methods try to model the presence of extraneous noise contained on the data and commonly use estimation approaches such as the maximum likelihood (ML) or other non-linear optimization schemes for the model coefficients estimation, which are of high computational cost, especially in the case of multivariable algorithms. The difficulties mentioned above, tend to limit the application of moving average methods in modal parameter estimation. A great variety of references on traditional identification methods used in EMA can be found in Maia and Silva (1997).

Alternatively, subspace-based state-space system identification (4SID) methods have been suggested to overcome the drawbacks of the traditional system identification techniques, (Viberg, 1995). The 4SID methods offer a reliable way to fit a multivariable state-space model realization, by means of a rank reduction operation upon a Hankel matrix formed from a collection of impulse responses measurements (sometimes referred to as Markov parameters) constructed from a natural ordering imposed by the state-space model, using singular value decomposition (SVD). The computational effort is relatively small in such methods. No non-linear optimization scheme is used and the order of the system can be estimated in a simpler way. In practice, due to the presence of extraneous noise in the measured data, the rank of a Hankel matrix formed by the impulse responses data is initially adopted to be greater than the order of the mechanical system to be identified. The order of the system is estimated by inspection of the dominants singular values of this Hankel data matrix. A rank reducing technique is then applied on the Hankel matrix, which leads to the calculation of the extended observability matrix and estimation of the modal parameters.

The paper is organized as follows: the basic formulation of mechanical system modeling is followed by the state-space realization of systems from impulse response data. The subspace identification algorithm is then introduced and applied into a numerical example using multivariable data, in order to illustrate the performance of present method. It will also be shown the improvement gained in the fitting of modal parameters performed by the present method as compared to AR model one, even in presence of a low signal-noise ratio. Concluding remarks are made at the end of the paper.

MATHEMATICAL MODELING OF MECHANICAL SYSTEMS

This section presents the basics of mathematical models of finite-dimensional, linear and time-invariant (LTI) mechanical systems.

The equation of motion of a f degrees of freedom LTI mechanical system is represented by the following second order matrix differential equation,

$$\bar{\mathbf{M}}\ddot{\mathbf{z}}(t) + \bar{\mathbf{C}}\dot{\mathbf{z}}(t) + \bar{\mathbf{K}}\mathbf{z}(t) = \mathbf{f}(t) \quad (1)$$

where $\bar{\mathbf{M}}$, $\bar{\mathbf{C}}$, $\bar{\mathbf{K}}$ are, respectively, the mass, damping and stiffness matrices, all of dimension $f \times f$. Vectors $\mathbf{z}(t)$ and $\mathbf{f}(t)$, of dimension $f \times 1$ represent, respectively, the generalized displacement and external forces acting on the system.

Equation (1) can be expressed in an equivalent continuous time state-space form (Gountier et al., 1993) as,

$$\dot{\mathbf{x}}(t) = \bar{\mathbf{A}}\mathbf{x}(t) + \bar{\mathbf{B}}\mathbf{u}(t) \quad (2)$$

with matrices $\bar{\mathbf{A}}$ and $\bar{\mathbf{B}}$ of dimension $n \times n$, given by,

$$\bar{\mathbf{A}} = \begin{bmatrix} \mathbf{0} & \mathbf{I}_f \\ -\bar{\mathbf{M}}^{-1}\bar{\mathbf{K}} & -\bar{\mathbf{M}}^{-1}\bar{\mathbf{C}} \end{bmatrix} \quad \text{and} \quad \bar{\mathbf{B}} = \begin{bmatrix} \mathbf{0} \\ \bar{\mathbf{M}}^{-1}\mathbf{U}_f \end{bmatrix} \quad (3)$$

where $n = 2f$ is the the state-space system model order, $\mathbf{x}(t) = \{\mathbf{z}(t) \quad \dot{\mathbf{z}}(t)\}^T$ is the generalized state vector of dimension $n \times 1$. Vector $\mathbf{u}(t)$ of dimension $m \times 1$ represents the non-null elements of the input vector $\mathbf{f}(t)$. Matrix \mathbf{U}_f of dimension $f \times m$ is the input selection matrix, such that $\mathbf{f}(t) = \mathbf{U}_f \mathbf{u}(t)$, \mathbf{I}_f is the identity matrix of dimension $f \times f$, and $\mathbf{0}$ denotes null matrices of appropriate dimensions.

Equation (2) constitutes the continuous-time state-space model for a finite n dimensional LTI mechanical system. Solution for the state vector $\mathbf{x}(t)$ at time t with an input $\mathbf{u}(t)$ and initial conditions $\mathbf{x}(t_0)$ is given by,

$$\mathbf{x}(t) = e^{\bar{\mathbf{A}}(t-t_0)} \mathbf{x}(t_0) + \int_{t_0}^t e^{\bar{\mathbf{A}}(t-\tau)} \bar{\mathbf{B}} \mathbf{u}(\tau) d\tau \quad (4)$$

Experimental input and output data in experimental modal analysis is obtained at equally spaced discrete time intervals. The continuous-time state-space model therefore needs to be rewritten in terms of a discrete-time representation. Let Δt be a constant time sampling interval. Substitution of $t = (k+1)\Delta t$ and $t_0 = k\Delta t$ into Eq. (4) yields,

$$\mathbf{x}[(k+1)\Delta t] = e^{\bar{\mathbf{A}}\Delta t} \mathbf{x}(k\Delta t) + \int_{k\Delta t}^{(k+1)\Delta t} e^{\bar{\mathbf{A}}[(k+1)\Delta t-\tau]} \bar{\mathbf{B}} \mathbf{u}(\tau) d\tau \quad (5)$$

Assuming that term $\mathbf{u}(\tau)$ of Eq. (5) has the constant value $\mathbf{u}(\tau) = \mathbf{u}(k\Delta t)$ over the interval $k\Delta t \leq \tau \leq (k+1)\Delta t$, and performing a change of variable τ by $\bar{\tau} = (k+1)\Delta t - \tau$, leads to,

$$\mathbf{x}[(k+1)\Delta t] = e^{\bar{\mathbf{A}}\Delta t} \mathbf{x}(k\Delta t) + \left[\int_0^{\Delta t} e^{\bar{\mathbf{A}}\bar{\tau}} d\bar{\tau} \bar{\mathbf{B}} \right] \mathbf{u}(k\Delta t) \quad (6)$$

Definition of the discrete quantities $\mathbf{x}[(k+1)\Delta t] = \mathbf{x}(k+1)$, $\mathbf{u}(k) = \mathbf{u}(k\Delta t)$ and matrices,

$$\mathbf{A} = e^{\bar{\mathbf{A}}\Delta t} \quad (7)$$

$$\mathbf{B} = \int_0^{\Delta t} e^{\bar{\mathbf{A}}\bar{\tau}} d\bar{\tau} \bar{\mathbf{B}}$$

allows for the description of a state-space form of the mechanical system in discrete-time through the following expression,

$$\mathbf{x}(k+1) = \mathbf{A} \mathbf{x}(k) + \mathbf{B} \mathbf{u}(k) \quad (8)$$

The set of observation variables measured during the modal testing of a structure is written in the following form,

$$\mathbf{y}(k) = \mathbf{C} \mathbf{x}(k) + \mathbf{D} \mathbf{u}(k) \quad (9)$$

where the term $\mathbf{y}(k)$ is an output vector of dimension $l \times 1$, associated with l response measurements. Matrices \mathbf{A} , \mathbf{B} , \mathbf{C} and \mathbf{D} , with appropriate dimensions, are, respectively, the state matrix, the input and output influence matrices and the direct transmission matrix (Juang, 1997).

Matrix \mathbf{A} of Eq. (8) can be expressed in terms of its n eigenvalues and eigenvectors,

$$\mathbf{A} = \mathbf{\Psi} \mathbf{\Lambda} \mathbf{\Psi}^{-1} \quad (10)$$

where matrix $\mathbf{\Lambda} = \text{diag}(z_j)$ of dimension $n \times n$, contains the eigenvalues z_j , $j = 1, \dots, n$ of \mathbf{A} . The columns of the modal matrix $\mathbf{\Psi}$ of dimension $n \times n$ are the corresponding eigenvectors.

The first line of Eq. (7) can be used, in order to calculate the modal parameters of a flexible structure, yielding also a relationship between the state matrices $\bar{\mathbf{A}}$ and \mathbf{A} of the continuous and discrete formulations. The eigenvalues in the two representations are related as,

$$\lambda_j = \log(z_j) / \Delta t \quad (11)$$

The natural frequencies ω_j and damping factors ξ_j are calculated as (Maia and Silva, 1997),

$$\omega_j = |\lambda_j| \quad \text{and} \quad \xi_j = -\text{Real}(\lambda_j) / |\lambda_j| \quad (12)$$

where symbol $|\lambda_j|$ denotes absolute value. The mode shape $\boldsymbol{\varphi}_j$, associated to the j -th eigenvalue z_j , which is the observable part of the eigenvector $\mathbf{\Psi}_j$, is then trivially calculated through Eq. (9) as,

$$\boldsymbol{\varphi}_j = \mathbf{C} \mathbf{\Psi}_j \quad (13)$$

STATE-SPACE MODEL REALIZATION FROM IMPULSE RESPONSES

The input-output relation of a causal LTI system with m input signals $\mathbf{u}(k)$ and l output signals $\mathbf{y}(k)$ can be described by the following convolution sum as,

$$\mathbf{y}(k) = \sum_{i=0}^{\infty} \mathbf{h}(i) \mathbf{u}(k-i) \quad (14)$$

where the term $\mathbf{h}(k)$ denotes the $l \times m$ matrix of impulse responses, with the element $h_{ij}(k)$ of $\mathbf{h}(k)$ representing the response in the output i at time k , to a unit impulse applied to input j at time 0.

Classical realization theory deals with the problem of finding a minimal state-space model given the collection of impulse responses referred as the Markov parameters (Viberg, 1995). For a initial condition $\mathbf{x}(k)=0$, by applying individual impulse inputs $u_i(0)=1$ ($i=1, \dots, m$) and $u_i(k)=0$ ($k=1, 2, 3, \dots$) to Eqs. (8) and (9), one finds immediately the following relation,

$$\mathbf{h}(k) = \begin{cases} \mathbf{0} & k < 0 \\ \mathbf{D} & k = 0 \\ \mathbf{CA}^{k-1}\mathbf{B} & k > 0 \end{cases} \quad (15)$$

Defining a i -block rows and j -columns $il \times jm$ Hankel matrix formed by $\mathbf{h}(k)$, it can be verified that,

$$\mathbf{H} = \begin{bmatrix} \mathbf{h}(1) & \mathbf{h}(2) & \dots & \mathbf{h}(j) \\ \mathbf{h}(2) & \mathbf{h}(3) & \dots & \mathbf{h}(j+1) \\ \vdots & \vdots & \ddots & \vdots \\ \mathbf{h}(i) & \mathbf{h}(i+1) & \dots & \mathbf{h}(i+j-1) \end{bmatrix} = \mathbf{\Gamma}_i \mathbf{\Omega}_j \quad (16)$$

where

$$\mathbf{\Gamma}_i = \begin{bmatrix} \mathbf{C} \\ \mathbf{CA} \\ \mathbf{CA}^2 \\ \vdots \\ \mathbf{CA}^{i-1} \end{bmatrix} \quad (17)$$

is the $il \times n$ observability matrix of the system, and

$$\mathbf{\Omega}_j = \begin{bmatrix} \mathbf{B} & \mathbf{AB} & \mathbf{A}^2\mathbf{B} & \dots & \mathbf{A}^{j-1}\mathbf{B} \end{bmatrix} \quad (18)$$

is the $n \times jm$ controllability matrix.

From Eq. (17), it is easy to extract an important shift-invariant structure from observability matrix $\mathbf{\Gamma}_i$ as,

$$\mathbf{\Gamma}_i^{(2)} = \mathbf{\Gamma}_i^{(1)} \mathbf{A} \quad (19)$$

where sub-matrices $\mathbf{\Gamma}_i^{(1)}$ and $\mathbf{\Gamma}_i^{(2)}$ are defined as,

$$\mathbf{\Gamma}_i = \begin{bmatrix} \mathbf{\Gamma}_i^{(1)} \\ \mathbf{CA}^{i-1} \end{bmatrix} = \begin{bmatrix} \mathbf{C} \\ \mathbf{\Gamma}_i^{(2)} \end{bmatrix} \quad (20)$$

Assuming the realization to be of minimal order n , it follows that the observability matrix $\mathbf{\Gamma}_i$ is of full rank n , then the state matrix \mathbf{A} can be derived from Eq. (19) as,

$$\mathbf{A} = \mathbf{\Gamma}_i^{(1)+} \mathbf{\Gamma}_i^{(2)} \quad (21)$$

where the symbol “+” denotes the Moore-Penrose pseudo-inverse of matrix $\mathbf{\Gamma}_i^{(1)}$.

Basically, all the necessary matrices to performing the modal parameters estimating are readily pointed out in this section. The state matrix \mathbf{A} is determined by solving Eq. (21) and matrix \mathbf{C} can be obtained from the first block row of $\mathbf{\Gamma}_i$. Next section shows a reliable way to obtaining an estimative of $\mathbf{\Gamma}_i$ from a set of impulse responses data.

MODAL PARAMETERS ESTIMATION USING SUBSPACE METHOD

This section presents an algorithm for modal parameters identification from a subspace-based system realization using the impulse responses data. Subspace method can be defined here as a technique that uses SVD to perform a rank-

reduction on the Hankel matrix \mathbf{H} formed from impulse responses data, which permits an estimate of the order of the system and an extended version of the observability matrix.

For the ideal case of noise-free data, the rank of both matrices $\mathbf{\Gamma}_i$ and $\mathbf{\Omega}_j$ is obviously n , which is also the order of the system. This enforces the product of $\mathbf{H} = \mathbf{\Gamma}_i \mathbf{\Omega}_j$ in the Eq. (16) to be also order of n . Moreover, the n columns of matrices $\mathbf{\Gamma}_i$ and $\mathbf{\Omega}_j$ span, respectively, the column and row spaces of \mathbf{H} , so that the column space of \mathbf{H} has the same shift-invariant structure as that of $\mathbf{\Gamma}_i$ pointed out by Eq. (19).

For a more realistic case where data is contaminated by noise, \mathbf{H} is full rank. However, a rank n column space of \mathbf{H} can be calculated from the following SVD partition as,

$$\mathbf{H} = \begin{bmatrix} \hat{\mathbf{Q}}_s & \hat{\mathbf{Q}}_n \end{bmatrix} \begin{bmatrix} \hat{\mathbf{S}}_s & \mathbf{0} \\ \mathbf{0} & \hat{\mathbf{S}}_n \end{bmatrix} \begin{bmatrix} \hat{\mathbf{V}}_s^T \\ \hat{\mathbf{V}}_n^T \end{bmatrix} = \hat{\mathbf{Q}}_s \hat{\mathbf{S}}_s \hat{\mathbf{V}}_s^T + \hat{\mathbf{Q}}_n \hat{\mathbf{S}}_n \hat{\mathbf{V}}_n^T \quad (22)$$

where matrices $\hat{\mathbf{Q}}_s$ and $\hat{\mathbf{V}}_s$ are orthogonal matrices with dimensions, respectively, $il \times n$ and $jm \times n$ and $\hat{\mathbf{S}}_s$ is a $n \times n$ diagonal matrix with the singular values. Obviously, in the absence of noise $\hat{\mathbf{S}}_n = 0$.

The n columns of matrix $\hat{\mathbf{Q}}_s$ span the column space of the n -order rank-reduced matrix $\hat{\mathbf{H}} \equiv \hat{\mathbf{Q}}_s \hat{\mathbf{S}}_s \hat{\mathbf{V}}_s^T$, recovered from a truncated SVD of \mathbf{H} as described by Eq. (22). Those columns contain also the n principal left singular vectors corresponding to the n principal singular values of the diagonal matrix $\hat{\mathbf{S}}_s$.

In practice, the order n of the dynamical system can be selected via inspection of the number of the most significant singular values of \mathbf{H} . An estimate of the extended observability matrix $\mathbf{\Gamma}_i$, denoted by $\hat{\mathbf{\Gamma}}_i$, is then taken as,

$$\hat{\mathbf{\Gamma}}_i = \hat{\mathbf{Q}}_s \quad \text{or} \quad \hat{\mathbf{\Gamma}}_i = \hat{\mathbf{Q}}_s \hat{\mathbf{S}}_s^{1/2} \quad (23)$$

since the theoretical observability matrix $\mathbf{\Gamma}_i$ and the extended observability matrix $\hat{\mathbf{\Gamma}}_i = \hat{\mathbf{Q}}_s$ span the column space of the data matrix \mathbf{H} , respectively, for the ideal free-noise and noise contaminated cases, for some n -order state-space realization.

The algorithm for modal parameters identification based on present sub-space method can be summarized as:

- i) estimation of the system order n via inspection of the number of the most significant singular values of \mathbf{H} as Eq. (22),
- ii) estimation of the extended observability matrix $\hat{\mathbf{\Gamma}}_i$ by Eqs. (22) and (23) and the state matrix \mathbf{A} by Eq. (21),
- iii) estimation of the eigenvalues z_j and eigenvectors $\mathbf{\Psi}_j$ of state matrix \mathbf{A} , for $j = 1, \dots, n$ (see Eq. 10),
- iv) the n system's eigenvalues λ_j are, then, calculated by Eq. (11), natural frequencies ω_j and the damping factors ξ_j are identified by Eq. (12), and
- v) finally, determination of matrix \mathbf{C} obtained from the first block row matrix $\hat{\mathbf{\Gamma}}_i$ and the mode shapes $\mathbf{\phi}_j$ are estimated by Eq. (13).

EXAMPLES OF APPLICATION

In order to show the capabilities of the presented subspace technique in modal parameters estimation, a MIMO experiment is shown. The collection of impulse responses data are obtained by numerical simulation of a seven degrees of freedom mass-spring-damper oscillator, as shown in Figure (1), using the following parameters : $m_1 = \dots = m_7 = 0.5 \text{ kg}$, $c_1 = \dots = c_7 = 5 \text{ Ns/m}$ and $k_1 = \dots = k_7 = 2000 \text{ N/m}$. Then, the matrices $\bar{\mathbf{M}}$, $\bar{\mathbf{C}}$ and $\bar{\mathbf{K}}$ take the following form,

$$\bar{\mathbf{M}} = \begin{bmatrix} m_1 & 0 & 0 & \dots & 0 \\ 0 & m_2 & 0 & \dots & 0 \\ 0 & 0 & m_3 & \dots & \vdots \\ \vdots & \vdots & \vdots & \ddots & 0 \\ 0 & 0 & 0 & 0 & m_7 \end{bmatrix} \quad (24)$$

$$\bar{\mathbf{C}} = \begin{bmatrix} c_1 + c_2 & -c_2 & 0 & \dots & 0 \\ -c_2 & c_2 + c_3 & -c_3 & \dots & 0 \\ 0 & -c_3 & c_3 + c_4 & \dots & \vdots \\ \vdots & \vdots & \vdots & \ddots & -c_7 \\ 0 & 0 & 0 & -c_7 & c_7 \end{bmatrix} \quad (25)$$

$$\bar{\mathbf{K}} = \begin{bmatrix} k_1 + k_2 & -k_2 & 0 & \dots & 0 \\ -k_2 & k_1 + k_2 & -k_3 & \dots & \vdots \\ 0 & -k_3 & k_3 + k_4 & \dots & 0 \\ \vdots & \vdots & \vdots & \ddots & -k_7 \\ 0 & 0 & 0 & -k_7 & k_7 \end{bmatrix} \quad (26)$$

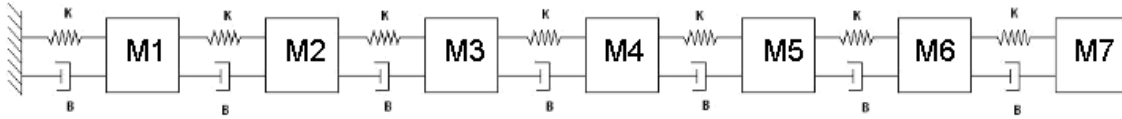


Figure 1- Seven Degrees of Freedom Oscillator System

The impulse responses $h_{ij}(k) = h_{ij}(k\Delta t)$ is the response in output i at time $k\Delta t$, due to a unit impulse applied to input j at time 0. The mathematical expression for the IRF can be easily derived from the parameters of the system as,

$$h_{ij}(k) = \sum_{l=1}^n \left[r_{ij(l)} e^{\lambda_l k \Delta t} + r_{ij(l)}^* e^{\lambda_l^* k \Delta t} \right] \quad (27)$$

where the term $r_{ij(l)} = \phi_{il} \phi_{jl}$ is the residue associated to eigenvalue λ_l (or z_l) and ϕ_{ij} is an element of the mode shapes matrix Φ . The term “*” denotes complex conjugation.

From matrices $\bar{\mathbf{M}}$, $\bar{\mathbf{C}}$ and $\bar{\mathbf{K}}$, it can be calculated the eigenvalues λ_j 's and matrix Φ . Tables 1 and 2 show the exact natural frequencies and viscous damping factors for each mode of the system. Tab. 1 shows the modal parameters identified using an AR-LS algorithm.

A multivariable 2-inputs and 7-outputs test is then simulated. Adopting $u_5(k) = \delta_5(k)$ and $u_7(k) = \delta_7(k)$ as unit impulse forces acting non-simultaneously on blocks 5 and 7, it can construct the following Markov parameters matrix formed by the impulse responses of the blocks (1)-(7) as,

$$\mathbf{h}(k) = \begin{bmatrix} h_{15}(k) & h_{17}(k) \\ h_{25}(k) & h_{27}(k) \\ h_{35}(k) & h_{37}(k) \\ h_{45}(k) & h_{47}(k) \\ h_{55}(k) & h_{57}(k) \\ h_{65}(k) & h_{67}(k) \\ h_{75}(k) & h_{77}(k) \end{bmatrix} \quad (28)$$

In the present test with $m=2$ inputs and $l=7$ outputs, it is adopted a number of 250 data samples for each term $h_{ij}(k)$ of $\mathbf{h}(k)$, disposed in a $i=211$ block rows and $j=40$ columns forming the Hankel matrix \mathbf{H} , according to Eq. (16), of dimension 1477×80 . The discretization interval Δt used is 0.020 second. A white Gaussian noise with zero mean and controlled amplitude in order to results a noise to signal ratio (NSR) around 0.0225 (or 2.25 %), is added to the impulse response signals.

The order of the system is identified by inspection of most significant singular values as discussed in the above section. Fig. 2 shows natural logarithm of singular values. Based on this criterion, successive identification with different orders, i.e. with $n=12, 14$ and 16 , are taken.

Based on the repeatability of natural frequencies, damping factors and mode shapes, it is concluded that the identified modal parameters are those shown in the Tab. 2. Tab. 1 shows the same parameters calculated using an AR-LS algorithm.

Finally, Fig. 3 shows the six identified mode shapes associated to six first natural frequencies and damping factors as compared to exact modes derived from numerical simulation.

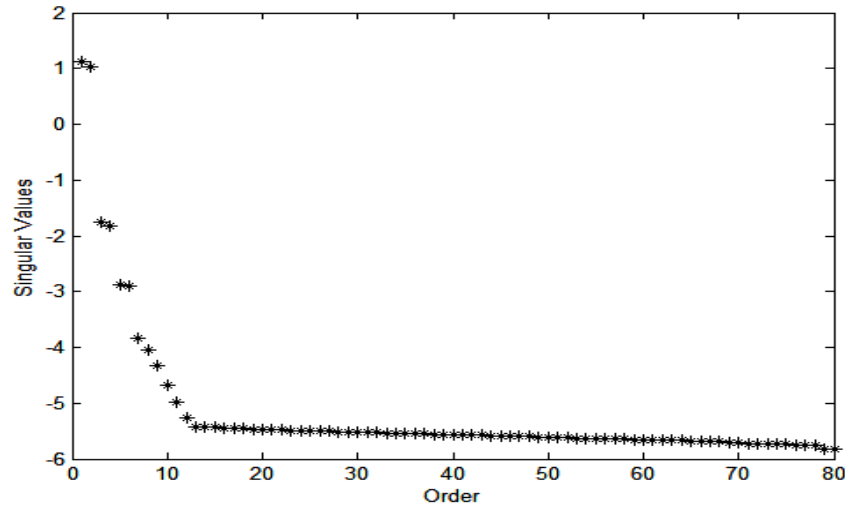


Figure 2 – Natural Logarithm of Singular Values of Matrix $Y_h V_2$

Table 1 – Exact and identified modal parameters AR method

Mode Number	Exact Natural Frequency (Hz)	Identified Natural Frequency (Hz)	Error (%)	Exact Damping Factor	Identified Damping Factor	Error (%)
1	2.1043	2.1043	0	0.0165	0.0165	0
2	6.2210	6.2228	0.0289	0.0489	0.0493	0.8180
3	10.0658	10.0865	0.2056	0.0791	0.0807	2.0228
4	13.4707	13.4266	0.3273	0.1058	0.1045	1.2287
5	16.2869	16.0780	1.2826	0.1279	0.0956	25.2541
6	18.3912	18.4267	0.1930	0.1444	0.0670	53.6011

Table 2 – Exact and identified modal parameters subspace-based method

Mode Number	Exact Natural Frequency (Hz)	Identified Natural Frequency (Hz)	Error (%)	Exact Damping Factor	Identified Damping Factor	Error (%)
1	2.1043	2.1043	0	0.0165	0.0165	0
2	6.2210	6.2202	0.0129	0.0489	0.0488	0.2045
3	10.0658	10.0843	0.1838	0.0791	0.0794	0.3792
4	13.4707	13.4457	0.1856	0.1058	0.1045	1.2287
5	16.2869	16.4163	0.7945	0.1279	0.1334	4.3002
6	18.3912	18.9567	3.0748	0.1444	0.1513	4.7784

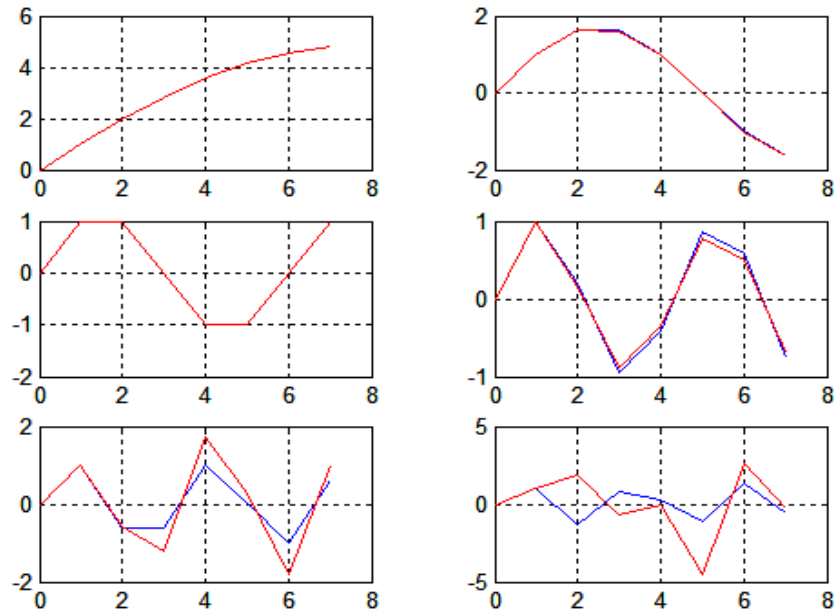


Figure 3 – Exact Mode Shapes (Blue) and Identified Mode Shapes (Red)

CONCLUSION

The paper presents a MIMO subspace-based modal identification technique valid for impulse responses data. The technique is simple, where no overparametrization and non linear search is required. The numerical reliability of the algorithm is only based on linear algebra concepts. The test based on numerical simulated data shows that the presented method can be regarded as a way to perform the modal identification –natural frequencies, damping factors and associated mode shapes, even in presence of a low signal-noise ratio.

REFERENCES

- Gontier, C., Smail, M. and Gautier, P.E., 1993, "A Time Domain Method for the Identification of Dynamic Parameters of Structures", *Mechanical Systems and Signal Processing*, vol. 7, n. 1, pp. 45-56.
- Ljung, L., 1999, "System Identification: Theory for the User", 2nd edition, Prentice Hall, 610 p.
- Maia, N.M.M. and Silva, J.M.M, 1997., "Theoretical and Experimental Modal Analysis", Research Studies Press, 468 p.
- Söderström, T. and Stoica P., 1989, "System Identification", Prentice Hall, 612 pp.
- Van der Ven, A.J., Swindlehurst, A.L. and Deprettere, E.F., 1993, "Subspace-Based Signal Analysis Using Singular Value Decomposition", *Proceedings of IEEE*, vol. 81, n. 9, 1277-1308.
- Viberg, M., 1995, "Subspace-Based Method for the Identification of Linear Time-Invariant Systems", *Automatica*, vol. 31, n. 12, pp. 1835-1851.

RESPONSIBILITY NOTICE

The authors are the only responsible for the printed material included in this paper.

An Application of Filtering Techniques For the Tracking Control of Mobile Robots with Slipping

Juliano G. Iossaqui¹, Juan F. Camino¹, and Douglas E. Zampieri¹

¹School of Mechanical Engineering, University of Campinas - UNICAMP, 13083-860, Campinas, SP, Brazil,
(jiossaqui@yahoo.com.br, camino@fem.unicamp.br, douglas@fem.unicamp.br)

Abstract: This paper presents an application of nonlinear filtering techniques for the tracking control design of tracked mobile robot under slip condition. The slip is represented only by the longitudinal wheels slip that is described by just an unknown parameter. The extended Kalman filter (EKF), the unscented Kalman filter (UKF) and the particle filter (PF) are used to estimate the states of the system, when measurements are assumed all available. Two adaptive tracking control design for tracked mobile robots are proposed. The first controller is based on the kinematic model and provides angular velocities as the control input. The second controller, based on the dynamic model, consists in a feedback control law that provides torque as control input. Numerical results show the performance of the proposed adaptive control laws using the EKF, UKF and the PF filtering techniques.

Keywords: Nonholonomic systems, tracked mobile robots, nonlinear filters, adaptive control.

NOMENCLATURE

b = distance between the wheels, m
 B = input transformation matrix
 k_i = controller gains, dimensionless
 i = longitudinal slip ratio, dimensionless
 J = moment of inertia, $kg.m^2$
 m = mass of the robot, kg

M = inertia matrix
 n = number of system states
 p = relative to slip ratio, dimensionless
 r = radius of the robot wheels, m
 α = size of the sigma point distribution

β = weighting parameter
 γ = auxiliary weighting parameter
 κ = secondary scaling parameter
 ρ = update law gain, dimensionless
 π = posterior probability density, dimensionless

INTRODUCTION

Autonomous mobile robots has received renewed attention in the last years because of its increasing use in tasks as forestry, mining, agriculture, military applications, space exploration, etc (Nourbakhsh and Siegwart, 2004). All of these applications require an efficient solution to the autonomous navigation problem, which has motivated various works in the area due to its theoretical challenges. Furthermore, these applications usually require the robot to travel across unstructured environments, where the precise localization of the robot is an important key for feedback control purposes.

Feedback control for mobile robots need knowledge of the robot's state vector. In general, the estimation of the robot's state vector from measurement system can be obtained using filtering techniques. It is well known that mobile robots are typical examples of nonlinear systems. In general, two types of filtering approaches for nonlinear systems can be found (Thrun et al., 2005). The first class, known as Gaussian filters, includes the extended Kalman filter (EKF), Gauss-Hermite filter (GHF) and unscented Kalman filter (UKF). The other class consists of the nonparametric filters, in which the main algorithm is the particle filter (PF). Several works has been developed in the literature to deal with the estimation problem applied to mobile robot motion. For instance, Jetto et al. (1999) developed the adaptive EKF for the localization of mobile robots, Kwon et al. (2005) proposed a robust localization method for mobile robot based on the combination of Kalman filter and perturbation estimator, and Rigatos (2010) compared the EKF and PF techniques for sensor fusion in motion control of mobile robots. In the same line as Rigatos (2010), this paper studies the performance of the EKF, UKF and PF algorithms applied to the proposed tracking control methods.

Morin and Samson (2006) present a review of the most recent tracking control methods for mobile robots. Other studies on tracking control designs using Lyapunov analysis can be found in Lee et al. (2009), Wu et al. (2009) and Ju et al. (2009). All these control design techniques are based on the assumption that the wheels roll without slipping. However, the slip has a critical influence on the performance of mobile robots that cannot be neglected. Thus, to attain higher performance, in addition to estimation of the state vector, the slip parameters is incorporate into the model of the robot. Many papers have addressed the slip phenomenon in the navigation of mobile robots (Matyukhin, 2007; Wang and Low, 2008). However, in such works, the slip parameters are considered as disturbance or noise (Scaglia et al., 2009) or are estimated using some filtering technique (Zhou et al., 2007). In Iossaqui et al. (2010b,a), an adaptive law is proposed to estimate the longitudinal slip parameter for two different tracked mobile robot. The first adaptive control design, taken from Iossaqui et al. (2010b), is based on the kinematic model and provides angular velocities as the control input. The

second adaptive control design, taken from Iossaqui et al. (2010a), based on the dynamic model, consists in a feedback control law that provides torque as control input. Even as in several other works in the literature these two control designs consider the perfect measurement of the states.

The main contribution of this paper is to incorporate the nonlinear filtering techniques to the adaptive control designs proposed by Iossaqui et al. (2010b,a). To address the nonlinear filtering problem, two group of filtering approaches are studied and compared: Gaussian approximation and nonparametric simulation. The former group, consisting of the EKF and UKF algorithms, uses either a single Gaussian distribution to match the first and second-order moments of the required density to different accuracy levels (Cui et al., 2005). In the EKF algorithm, the state distribution is propagated analytically through the first-order linearization of the nonlinear system. In the UKF algorithm, the state distribution is represented using a minimal set of carefully chosen sample points and propagated through the true nonlinear system. The latter group, represented by the PF algorithm, does not make any assumption on the measurement noise distribution. Instead, the nonparametric filters approximate posterior probability distribution by finite number of values, each corresponding to a region in the state space.

The paper is organized as follows. First, the adaptive controllers for a tracked mobile robot under longitudinal slip condition are reviewed. Next, the nonlinear filtering techniques used to estimate the states of the tracked mobile robot are presented. Then, the results obtained by numerical simulations of the controlled systems using the filtering techniques are showed and compared. Concluding remarks follow afterwards.

THE PROPOSED ADAPTIVE TRACKING CONTROLS

In this section, two adaptive control techniques for tracked mobile robots proposed by Iossaqui et al. (2010b,a) are presented. First, the model of the robot is presented and the equations that characterize the tracking problem are established. Then, the first adaptive control law that provides velocities as input is described. Finally, the second adaptive control law that provides torque as input is reviewed.

As presented in (Iossaqui et al., 2010b), the kinematic equation of the tracked robot under slip condition is given by

$$\begin{pmatrix} \dot{X} \\ \dot{Y} \\ \dot{\psi} \end{pmatrix} = \begin{pmatrix} r \cos \psi / 2p & r \cos \psi / 2p \\ r \sin \psi / 2p & r \sin \psi / 2p \\ -r/bp & r/bp \end{pmatrix} \begin{pmatrix} \omega_L \\ \omega_R \end{pmatrix} \Leftrightarrow \dot{q} = S(q)\xi \quad (1)$$

where $q = (X, Y, \psi)^T$ denotes the states of the robot, which is given by the robot position (X, Y) and its orientation ψ in an appropriate inertial frame. The angular velocities of the left and the right wheels are respectively ω_L and ω_R . The radius of the robot wheels is r and the distance between the wheels is b . The parameter p is defined as

$$p = \frac{1}{(1-i)}$$

with i , the longitudinal slip ratio of the two wheels, given by

$$i = \frac{(r\omega_L - v_L)}{r\omega_L} = \frac{(r\omega_R - v_R)}{r\omega_R}, \quad 0 \leq i < 1$$

where v_L and v_R are the linear velocities of the left and the right wheels with relation to the terrain.

As presented in (Iossaqui et al., 2010b), the dynamic equation of the tracked robot is given by

$$\overline{M}\dot{\xi} = \overline{B}(q)\tau \quad (2)$$

where $q = (X, Y, \psi)^T$ has been defined before, the input torque in left and right wheels is given by $\tau = (\tau_L, \tau_R)^T$, $\overline{M} = S^T(q)MS(q)$ and $\overline{B}(q) = S^T(q)B(q)$, with the matrices M and $B(q)$ given by

$$M = \begin{pmatrix} m & 0 & 0 \\ 0 & m & 0 \\ 0 & 0 & J \end{pmatrix}, \quad B(q) = \frac{1}{r} \begin{pmatrix} \cos \psi & \cos \psi \\ \sin \psi & \sin \psi \\ b/2 & b/2 \end{pmatrix}$$

where m is the total mass of the robot and J is the moment of inertia about the vertical axis through geometric center of the robot.

In order to deal with the tracking control problem, we need to define the reference trajectory, $q_r = (X_r, Y_r, \psi_r)^T$, which is generated using the kinematic model

$$\begin{pmatrix} \dot{X}_r \\ \dot{Y}_r \\ \dot{\psi}_r \end{pmatrix} = \begin{pmatrix} \cos \psi_r & 0 \\ \sin \psi_r & 0 \\ 0 & 1 \end{pmatrix} \begin{pmatrix} v_r \\ \omega_r \end{pmatrix} \Leftrightarrow \dot{q}_r = S_r(q_r)\eta_r \quad (3)$$

where v_r and ω_r are constant reference inputs. It is assumed that the signals η_r and $\dot{\eta}_r$ are bounded.

In addition, to analyze the tracking problem, the error is defined as

$$\begin{pmatrix} e_1 \\ e_2 \\ e_3 \end{pmatrix} = \begin{pmatrix} \cos \psi & \sin \psi & 0 \\ -\sin \psi & \cos \psi & 0 \\ 0 & 0 & 1 \end{pmatrix} \begin{pmatrix} X_r - X \\ Y_r - Y \\ \Psi_r - \Psi \end{pmatrix} \quad (4)$$

Adaptive velocity-based control

Figure 1 shows the scheme of the adaptive control used in Iossaqui et al. (2010b). The numbering inside the blocks in Fig. 1 indicate the corresponding equation number. Note that the state vector is composed of the three states X , Y , and ψ .

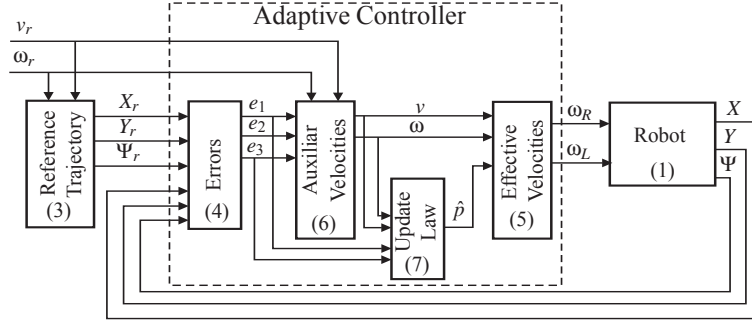


Figure 1: Adaptive velocity-based control.

The velocity control input $\xi = (\omega_L, \omega_R)^T$ is given by

$$\begin{pmatrix} \omega_L \\ \omega_R \end{pmatrix} = \frac{\hat{p}}{2r} \begin{pmatrix} 2 & -b \\ 2 & b \end{pmatrix} \begin{pmatrix} v \\ \omega \end{pmatrix} \quad (5)$$

with auxiliary velocity

$$\begin{pmatrix} v \\ \omega \end{pmatrix} = \begin{pmatrix} v_r \cos e_3 + k_1 e_1 \\ \omega_r + v_r k_2 e_2 + k_3 \sin e_3 \end{pmatrix} \quad (6)$$

and update law

$$\dot{\hat{p}} = \rho \left(v e_1 + \frac{\omega \sin e_3}{k_2} \right) \quad (7)$$

where \hat{p} is the estimation of the parameter p , $k_i > 0$ and $\rho > 0$ are controller gains.

Adaptive torque-based control

Figure 2 shows the scheme of the adaptive control used in Iossaqui et al. (2010a). The numbering inside the blocks in Fig. 2 indicate the corresponding equation number. Observe that the state vector is composed of the five states X , Y , ψ , ω_L , and ω_R .

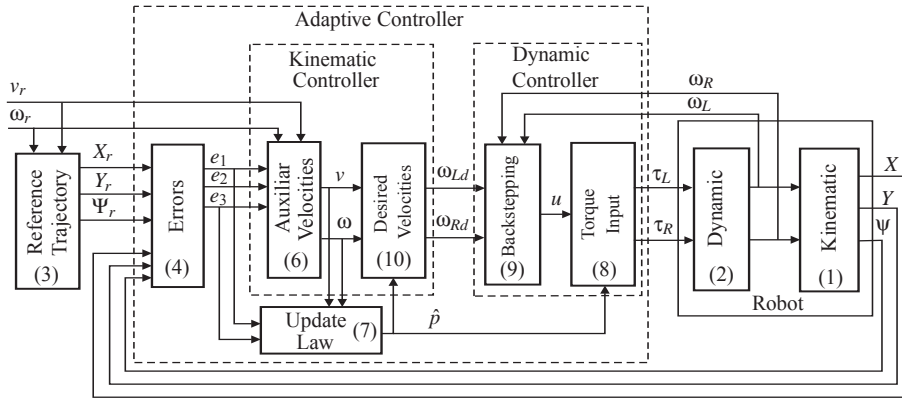


Figure 2: Adaptive torque-based control.

The torque control input $\tau = (\tau_L, \tau_R)^T$ is given by

$$\tau = \bar{B}(q)^{-1} \bar{M}u \quad (8)$$

with

$$u = \dot{\xi}_d + \begin{pmatrix} k_4 & 0 \\ 0 & k_5 \end{pmatrix} (\xi_d - \xi) \quad (9)$$

and the desired velocities ξ_d given by

$$\xi_d = \begin{pmatrix} \omega_{Ld} \\ \omega_{Rd} \end{pmatrix} = \frac{\hat{p}}{2r} \begin{pmatrix} 2 & -b \\ 2 & b \end{pmatrix} \begin{pmatrix} v \\ \omega \end{pmatrix} \quad (10)$$

where $k_i > 0$ are given constant and $(v, \omega)^T$ is given by (6). The update law that provides the estimate \hat{p} is given by (7).

NONLINEAR FILTERING TECHNIQUES

This section presents the EKF and UKF Gaussians algorithms and the nonparametric PF algorithm (Haykin, 2001). The basic structure for the EKF, UKF and for the PF involves estimation of the state of a discrete-time nonlinear dynamic system of the form

$$\begin{aligned} x_{k+1} &= f(x_k, u_k, w_k) \\ y_k &= h(x_k, v_k) \end{aligned}$$

where x_k is the state vector of the system, u_k is a control input and y_k is the measured signal. The process and measurement noises are respectively given by w_k and v_k . It is assumed that w_k and v_k are independent zero-mean Gaussian random variables with respectively covariance matrices Q and R . Note that the PF algorithm does not require any assumption on the measurement noise distribution.

The EKF algorithm

The EKF algorithm (Haykin, 2001) is based on a first order Taylor series expansion of the nonlinear functions f and h at the estimate $\hat{x}_{k|k}$ and the propagation $\hat{x}_{k+1|k}$. The EKF algorithm is given below:

Initialize with

$$\hat{x}_0 = \mathbb{E}[x_0],$$

$$P_0 = \mathbb{E}[(x_0 - \hat{x}_0)(x_0 - \hat{x}_0)^T].$$

For $k \in \{1, \dots, \infty\}$, the time-update equations are

$$\hat{x}_k^- = f(\hat{x}_{k-1}, u_{k-1}, \bar{w}_k),$$

$$P_{x_k}^- = A_{k-1} P_{x_{k-1}} A_{k-1}^T + B_k Q_k B_k^T,$$

and the measurement-update equations are

$$K_k = P_{x_k}^- C_k^T (C_k P_{x_k}^- C_k^T + D_k R_k D_k^T)^{-1},$$

$$\hat{x}_k = \hat{x}_k^- + K_k [y_k - h(\hat{x}_k^-, v_k)],$$

$$P_{x_k} = (I - K_k C_k) P_{x_k}^-,$$

with

$$A_k \triangleq \left. \frac{\partial f(x, u_k, \bar{w}_k)}{\partial x} \right|_{\hat{x}_k}, \quad B_k \triangleq \left. \frac{\partial f(\hat{x}_k^-, u_k, w_k)}{\partial w_k} \right|_{\bar{w}_k}, \quad C_k \triangleq \left. \frac{\partial h(x, v_k)}{\partial x} \right|_{\hat{x}_k}, \quad D_k \triangleq \left. \frac{\partial h(\hat{x}_k^-, v_k)}{\partial v_k} \right|_{\bar{v}_k},$$

with $\bar{w}_k = \mathbb{E}[w_k]$ and $\bar{v}_k = \mathbb{E}[v_k]$, where $\mathbb{E}[\cdot]$ is the expectation. The means \bar{w}_k and \bar{v}_k are usually zero.

The EKF can achieve satisfactory results for many applications, but may suffer from large estimate errors when systems have strong nonlinearities. As stated in Thrun et al. (2005), the EKF is a widely used technique in nonlinear state estimation and, in spite of its theoretical weakness, i.e., the lack of a formal proof of convergence, a number of applications exists, giving satisfactory results, in a large broad of technological areas.

The UKF algorithm

The UKF algorithm (Haykin, 2001) does not approximate the nonlinear process and measurement models. Instead, it uses the true nonlinear models and approximates the distribution of the state random variable. The UKF, which does not need to compute the Jacobian, uses the so-called unscented transform (UT) to obtain the sigma points. These sigma points are propagated through the nonlinear function. The UKF algorithm is given below:

Initialize with

$$\hat{x}_0 = \mathbb{E}[x_0]$$

$$P_0 = \mathbb{E}[(x_0 - \hat{x}_0)(x_0 - \hat{x}_0)^T]$$

For $k \in \{1, \dots, \infty\}$

Calculate the sigma points

$$\mathcal{X}_{k-1} = \begin{bmatrix} \hat{x}_{k-1} & \hat{x}_{k-1} + \gamma\sqrt{P_{k-1}} & \hat{x}_{k-1} - \gamma\sqrt{P_{k-1}} \end{bmatrix}$$

The time-update equations are

$$\mathcal{X}_{k|k-1}^* = f(\mathcal{X}_{k-1}, u_{k-1})$$

$$\hat{x}_k^- = \sum_{i=0}^{2L} W_i^{(m)} \mathcal{X}_{i,k|k-1}^*$$

$$P_k^- = \sum_{i=0}^{2n} W_i^{(c)} \left[\mathcal{X}_{i,k|k-1}^* - \hat{x}_k^- \right] \left[\mathcal{X}_{i,k|k-1}^* - \hat{x}_k^- \right]^T + Q_k$$

$$\mathcal{X}_{k|k-1} = \begin{bmatrix} \mathcal{X}_{k|k-1}^* & \mathcal{X}_{0,k|k-1}^* + \rho\sqrt{Q_k} & \mathcal{X}_{0,k|k-1}^* - \rho\sqrt{Q_k} \end{bmatrix}$$

$$\mathcal{Y}_{k|k-1} = h(\mathcal{X}_{k|k-1})$$

$$\hat{y}_k^- = \sum_{i=0}^{2n} W_i^{(m)} \mathcal{Y}_{i,k|k-1}$$

The measurement-update equations are

$$P_{\tilde{y}_k \tilde{y}_k} = \sum_{i=0}^{2n} W_i^{(c)} (\mathcal{Y}_{i,k|k-1} - \hat{y}_k^-) (\mathcal{Y}_{i,k|k-1} - \hat{y}_k^-)^T + R_k$$

$$P_{x_k y_k} = \sum_{i=0}^{2n} W_i^{(c)} (\mathcal{X}_{i,k|k-1} - \hat{x}_k^-) (\mathcal{Y}_{i,k|k-1} - \hat{y}_k^-)^T$$

$$K_k = P_{x_k y_k} P_{\tilde{y}_k \tilde{y}_k}^{-1}$$

$$\hat{x}_k = \hat{x}_k^- + K_k (y_k - \hat{y}_k^-)$$

$$P_k = P_k^- - K_k P_{y_k y_k} K_k^T$$

with the weights

$$W_0^{(m)} = \lambda/(n + \lambda), W_0^{(c)} = \lambda/(n + \lambda) + (1 - \alpha^2 + \beta)$$

$$W_i^{(m)} = W_i^{(c)} = 1/2(n + \lambda), \quad i = 1, 2, \dots, n$$

where $\lambda = \alpha^2(n + \kappa) - n$, $\gamma = \sqrt{n + \lambda}$ and with $\kappa \geq 0$. The dimension of the state vector is n , the size of the sigma point distribution is regularized by non-negative weighting terms α and β , which can be used to compensate for the information of the higher order moments of the distribution.

The PF algorithm

The PF algorithm (Haykin, 2001) is based on Monte Carlo simulation with sequential importance sampling. The key idea is to directly represent the required probability density function as a set of particles. These particles are propagated and updated from one discrete time to the next to represent the latest posterior density. The PF algorithm is given below:

1. Initialization: $k = 0$

- For $i = 1, \dots, N$, draw the states $x_0^{(i)}$ from prior $p(x_0)$

2. For $k = 1, 2, \dots$

(a) Importance sampling step

- For $i = 1, \dots, N$, sample $x_k^{(i)} \sim \pi(x_k | x_{0:k-1}^{(i)}, Y_0^k)$, where π represents the posterior probability density
- For $i = 1, \dots, N$, evaluate the importance weights up to a normalizing constant:

$$w_k^{(i)} = w_{k-1}^{(i)} \frac{p(y_k | x_k^{(i)}) p(x_k^{(i)} | x_{k-1}^{(i)})}{\pi(x_k^{(i)} | x_{0:k-1}^{(i)}, Y_0^k)}$$

- For $i = 1, \dots, N$, normalize the importance weights:

$$\tilde{w}_k^{(i)} = \frac{w_k^{(i)}}{\sum_{j=1}^N w_k^{(j)}}$$

(b) Selection step (resampling)

- Multiply/suppress samples $x_k^{(i)}$ with high/low importance weights $\tilde{w}_k^{(i)}$, respectively, to obtain N random samples $\tilde{x}_k^{(i)}$ approximately distributed according to $p(x_k^{(i)} | Y_0^k)$
- For $i = 1, \dots, N$, set $w_k^{(i)} = \tilde{x}_k^{(i)} = N^{-1}$

(c) Output: The output of the algorithm is a set of samples that can be used to approximate the posterior distribution as follows:

$$\hat{p}(x_k | Y_0^k) = \frac{1}{N} \sum_{i=1}^N \delta(x_k - x_k^{(i)})$$

The optimal MMSE estimator is given as

$$\hat{x}_k = \mathbb{E}(x_k, Y_0^k) \approx \frac{1}{N} \sum_{i=1}^N x_k^{(i)}$$

In general, the PF algorithm presents better accuracy of the Gaussians filters, but this occurs at the cost of greater computational effort (Thrun et al., 2005).

NUMERICAL RESULTS

Two simulation scenarios are presented in this section using the filtering techniques EKF, UKF and PF together with the adaptive velocity-based control and the adaptive torque-based control. Figure 3 shows the schematic representation of the close-loops with controller, filter and noises characterization for the two scenarios studied. Observe that the variables without subscript, with subscripts “ r ”, “ m ” and “ e ” describe respectively real, reference, measured and estimated states.

Note that in the first scenario the angular velocities are not used in the feedback control, that is, the velocities do not need to be measured. The velocities are provided directly by the control law. In the second scenario, the angular velocities need to be measured and estimated for control proposes. The velocity motion model that uses robot’s velocity to compute posterior over poses (position and orientation) is considered in the filtering implementation. The alternative solution is odometry motion model, commonly obtained by integrating wheel encoder information.

In order to applied the nonlinear filtering techniques, we discretize the continuous time equations (1) and (2) of the mobile robot with slipping using first-order difference. Then the nonlinear system dynamics at discrete time, for the first and second scenario, can be described as

$$x_k = f(x_k, u_k) + w_k$$

where w_k is a zero-mean Gaussian noise vector with covariance Q_k . The states vector for the first and second scenarios are respectively $x_k = (X, Y, \Psi)^T$ and $x_k = (X, Y, \Psi, \omega_L, \omega_R)^T$. The input vector for the first and second scenarios are respectively $u_k = (\omega_L, \omega_R)^T$ and $u_k = (\tau_L, \tau_R)^T$. The state noise w_k is considered zero for the two scenarios.

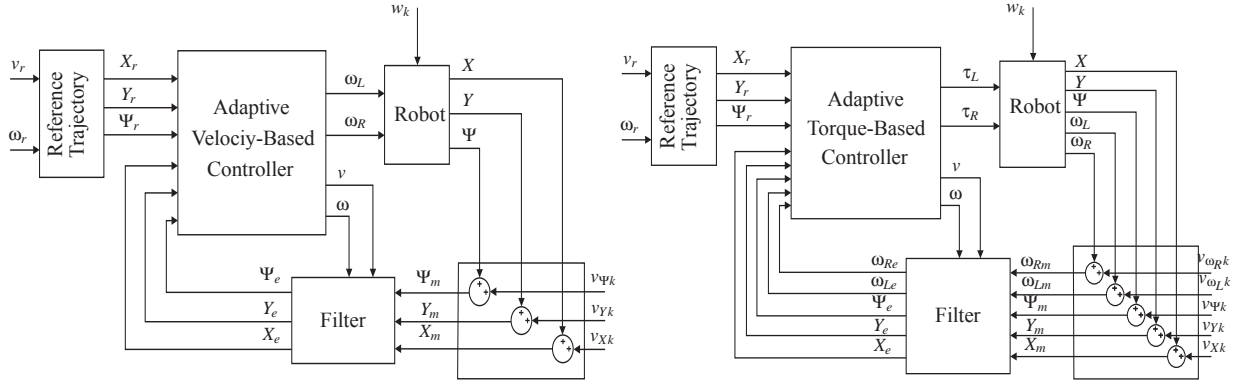


Figure 3: The representation of the close-loops studied.

For the first scenario, a simplify model used to represent the measurement model is given by

$$\begin{pmatrix} X_m \\ Y_m \\ \Psi_m \end{pmatrix} = \begin{pmatrix} X \\ Y \\ \Psi \end{pmatrix} + \begin{pmatrix} v_{Xk} \\ v_{Yk} \\ v_{\Psi k} \end{pmatrix} \Leftrightarrow y_k = f(x_k) + v_k$$

and for the second scenario by

$$\begin{pmatrix} X_m \\ Y_m \\ \Psi_m \\ \omega_{Lm} \\ \omega_{Rm} \end{pmatrix} = \begin{pmatrix} X \\ Y \\ \Psi \\ \omega_L \\ \omega_R \end{pmatrix} + \begin{pmatrix} v_{Xk} \\ v_{Yk} \\ v_{\Psi k} \\ v_{\omega_{Lk}} \\ v_{\omega_{Rk}} \end{pmatrix} \Leftrightarrow y_k = f(x_k) + v_k$$

where v_k is an additive zero-mean Gaussian noise vector with covariance R_k given respectively by

$$R_k = \begin{pmatrix} 0.1 & 0 & 0 \\ 0 & 0.1 & 0 \\ 0 & 0 & 0.2 \end{pmatrix} \quad \text{and} \quad R_k = \begin{pmatrix} 0.1 & 0 & 0 & 0 & 0 \\ 0 & 0.1 & 0 & 0 & 0 \\ 0 & 0 & 0.2 & 0 & 0 \\ 0 & 0 & 0 & 0.01 & 0 \\ 0 & 0 & 0 & 0 & 0.01 \end{pmatrix}$$

for the first and second scenarios. To perform comparison between the filtering methods, it is assumed an additive zero-mean Gaussian noise in all simulations.

The numerical simulations were performed using MATLAB. The physical parameters for the model, taken from Iossaqui et al. (2010a), are given by $b = 0.65$ m, $r = 0.35$ m, $m = 0.80$ kg and $I = 0.0608$ kg.m². The total time of the simulation is chosen as $t = 60$ s. The control parameters of the controller are chosen as $k_1 = k_3 = 6$, $k_2 = 8$ and $k_4 = k_5 = 4$. The parameter of the adaptive rule is chosen as $\rho = 3$. The initial conditions of the equations that generates the reference trajectory are taken as $q_r(0) = (0, 0, 0)^T$. The initial conditions of the adaptation law is $\hat{\rho}(0) = 1$. The initial conditions of the robot for the first and second scenario are respectively $q(0) = (0, -1.5, \pi/4)^T$ and $q(0) = (0, -1, \pi/6, 0, 0)^T$. In order to demonstrate the tracking performance, the slip parameter changes from $i = 0$ to $i = 0.25$ during the time period $22.5 \text{ s} \leq t \leq 45 \text{ s}$.

The reference inputs v_r, w_r are chosen as following

$$\begin{aligned} 0\text{s} \leq t < 15\text{s} : \quad & v_r = 0.5\text{m/s} \quad \text{and} \quad w_r = 0\text{rad/s} \\ 15\text{s} \leq t < 33\text{s} : \quad & v_r = 0.5\text{m/s} \quad \text{and} \quad w_r = -0.4\text{rad/s} \\ 33\text{s} \leq t < 51\text{s} : \quad & v_r = 0.5\text{m/s} \quad \text{and} \quad w_r = 0.4\text{rad/s} \\ 51\text{s} \leq t : \quad & v_r = 0.7\text{m/s} \quad \text{and} \quad w_r = 0\text{rad/s} \end{aligned}$$

The three constant parameters used in the UKF are chosen as $\alpha = 0.01$, $\beta = 2$ and $\kappa = 0$. The initial state covariance used in the first and second scenarios are respectively $P(0) = 10I_{3 \times 3}$ and $P(0) = 10I_{5 \times 5}$, being I the identity matrix. The number of particles, necessary in PF method, is chosen as $N = 100$.

Scenario 1: Adaptive velocity-based control

In the first scenario, the nonlinear kinematic used in the estimation is given by

$$\begin{pmatrix} x \\ y \\ \phi \end{pmatrix}_{k+1} = \begin{pmatrix} x \\ y \\ \phi \end{pmatrix}_k + h \begin{pmatrix} v \cos \phi_k \\ v \sin \phi_k \\ \omega \end{pmatrix}$$

where x_k, y_k and ϕ_k corresponds to robot pose, v and ω are respectively the linear and angular velocities. The sampling step is taken as $h = 0.005$.

Figures 4(a), 4(b) and 4(c) show the posture error $e = (e_1, e_2, e_3)^T$ obtained using the EKF, UKF and PF methods. The reference trajectory and robot trajectory in the inertial frame for each method is depicted in Fig. 4(d). All three filters methods show consistent and similar results.

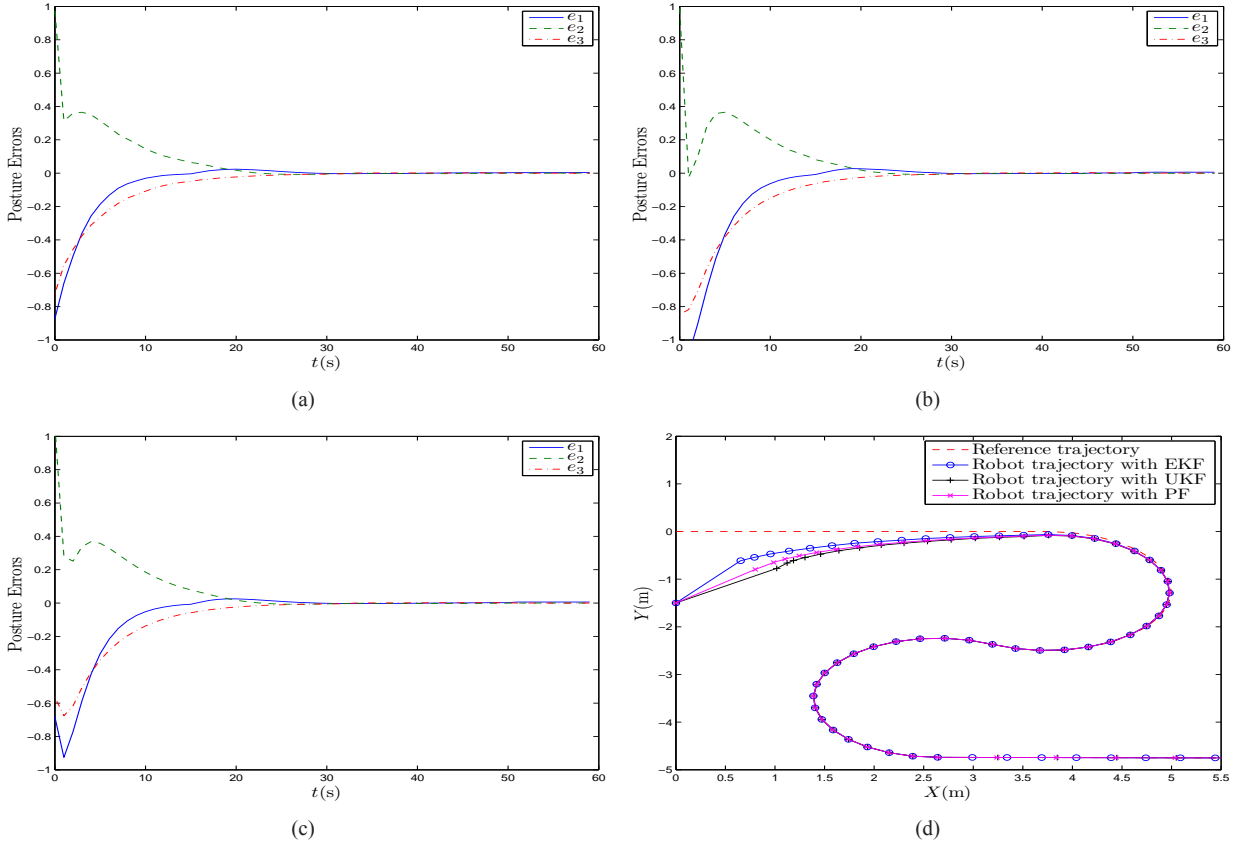


Figure 4: Posture errors (using the filters: (a) EKF; (b) UKF and (c) PF) and (d) Trajectory of the robot for 1st scenario.

Scenario 2: Adaptive torque-based control

The nonlinear kinematic used in the filter is given by

$$\begin{pmatrix} x \\ y \\ \phi \\ \omega_L \\ \omega_R \end{pmatrix}_{k+1} = \begin{pmatrix} x \\ y \\ \phi \\ \omega_L \\ \omega_R \end{pmatrix}_k + h \begin{pmatrix} v \cos \phi_k \\ v \sin \phi_k \\ \omega \\ 0 \\ 0 \end{pmatrix}$$

where x_k, y_k and ϕ_k corresponds to robot pose, w_L and w_R are respectively left and right angular velocities of the wheels, v and ω are respectively the linear and angular velocities, h is the sampling time. The sampling step is taken as $h = 0.005$.

Figures 5(a), 5(b) and 5(c) show the posture error $e = (e_1, e_2, e_3)^T$ obtained using respectively the EKF, UKF and PF methods. Figure 5(d) show the reference trajectory and comparison between robot trajectory using the EKF, UKF and PF methods. As in the first scenario, all three filters methods show consistent and similar results.

Figures 6(a), 6(b) and 6(c) show the velocity error $e = (e_4, e_5)^T$ obtained using respectively the EKF, UKF and PF filters.

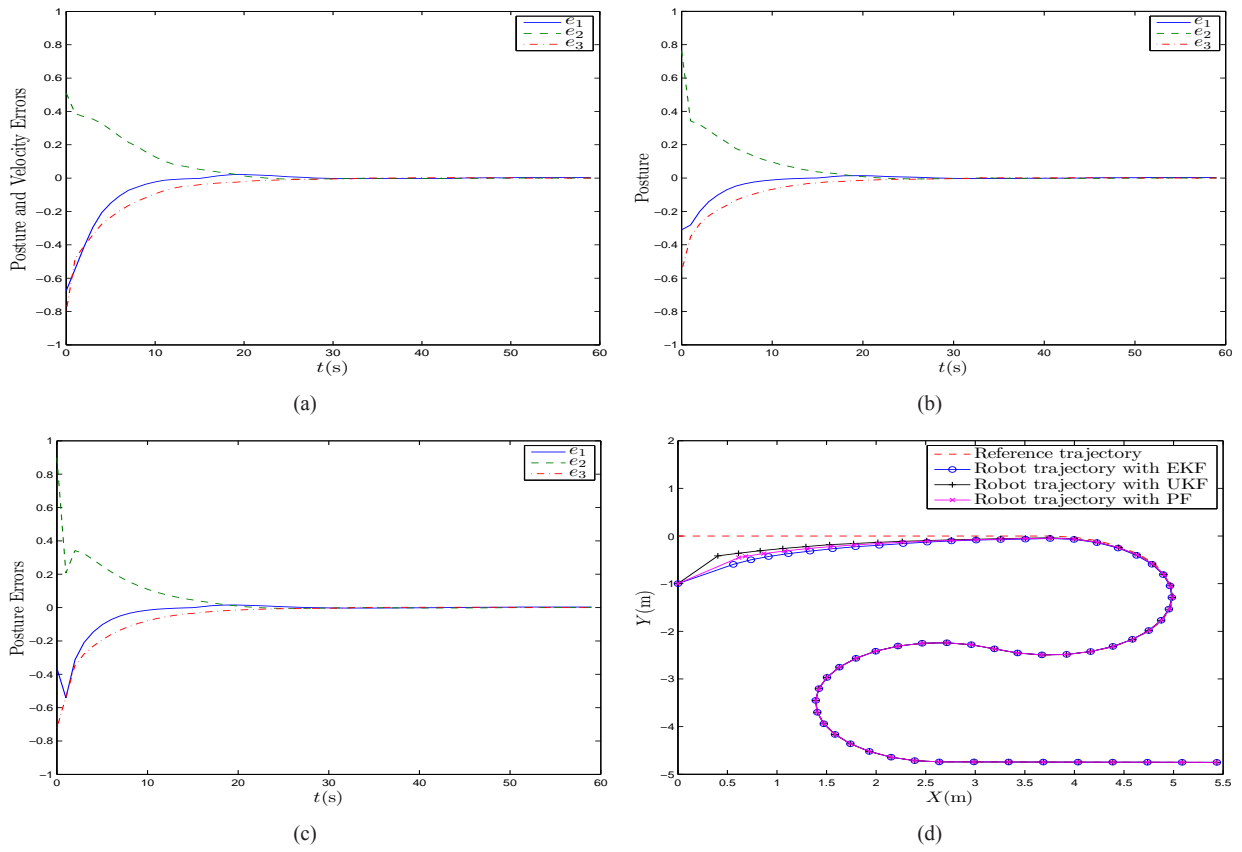


Figure 5: Posture errors (using the filters: (a) EKF; (b) UKF and (c) PF) and (d) Trajectory of the robot for 2nd scenario.

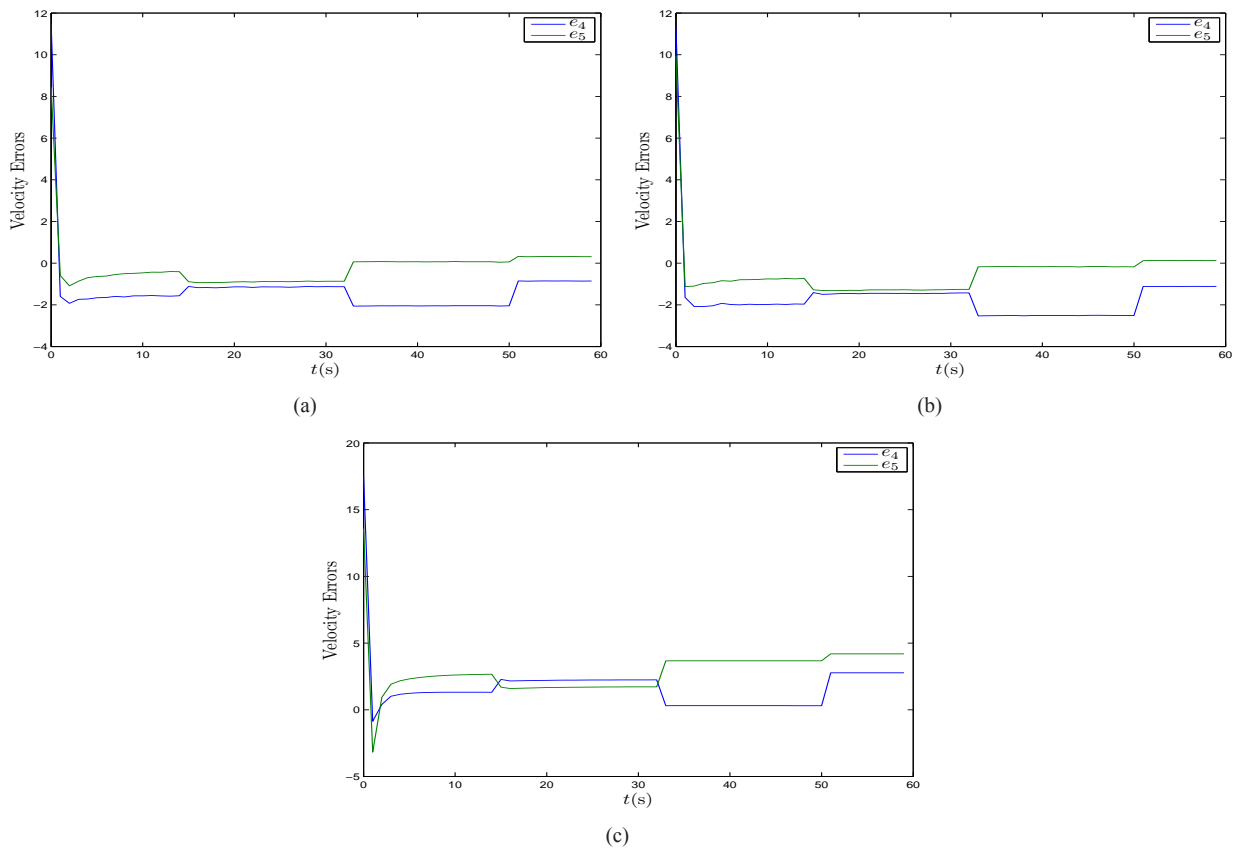


Figure 6: Velocity errors using the filters: (a) EKF, (b) UKF and (c) PF.

CONCLUSIONS

Two different adaptive tracking control for tracked mobile robot under slip condition using the extended Kalman filter (EKF), the unscented Kalman filter (UKF) and the particle filter (PF) to estimate all states of the robot are presented. The EKF, UKF and PF techniques are analyzed in two scenarios. In the first scenario, the controller is based on the kinematic model and provides angular velocities as the control input. Furthermore, the states estimates are position and orientation of the robot. In the second scenario, the controller, based on the dynamic model, consists in a feedback control law that provides torque as control input. In this case, in addition of the position and orientation the angular velocities of the wheels are estimated. Numerical results show the performance of the adaptive control laws using the EKF, UKF and PF filtering techniques. In future works, the sensors models should be included in the close-loop and the fusion datas should be studied. Others nonlinear filtering approaches will be compared.

ACKNOWLEDGMENTS

The authors are partially supported through grants from CAPES Proc. 1755/2008 and FAPESP Proc. 09/03304-5.

REFERENCES

- Cui, N., Hong, L., and Layne, J. R. (2005). A comparison of nonlinear filtering approaches with an application to ground target tracking. *Signal Processing*, 85:1469–1492.
- Haykin, S. S. (2001). *Kalman Filtering and Neural Networks*. John Wiley and Sons, New York, USA.
- Iossaqui, J. G., Camino, J. F., and Zampieri, D. E. (2010a). Adaptive torque-based control of tracked mobile robots with unknown longitudinal slip parameter. In *Proceedings of the Congresso Nacional de Engenharia Mecânica*, Campina Grande, Brasil.
- Iossaqui, J. G., Camino, J. F., and Zampieri, D. E. (2010b). Adaptive tracking control of tracked mobile robots with unknown slip parameters. In *Proceedings of the Congresso Brasileiro de Automática*, Bonito, Brasil.
- Jetto, L., Longhi, S., and Venturini, G. (1999). Development and experimental validation of an adaptive extended kalman filter for the localization of mobile robots. *IEEE Transactions on Robotics and Automation*, 15(2):219–229.
- Ju, G., Wu, Y., and Sun, W. (2009). Adaptive output feedback asymptotic stabilization of nonholonomic systems with uncertainties. *Nonlinear Analysis*, 7(1):5106–5117.
- Kwon, S., Yang, K., Park, S., and Ryuh, Y. (2005). Robust mobile robot localization with combined kalman filter-perturbation estimator. In *Intelligent Robots and Systems*, Goyang, South Korea.
- Lee, J. H., Lin, C., Lim, H., and Lee, J. M. (2009). Sliding mode control for trajectory tracking of mobile robot in the RFID sensor space. *International Journal of Control, Automation, and Systems*, 7(3):429–435.
- Matyukhin, V. I. (2007). A control of a wheeled system with account of side slip. *Journal of Computer and Systems Sciences International*, 46(4):663–673.
- Morin, P. and Samson, C. (2006). *Chapter Trajectory Tracking for Non-holonomic Vehicles*, in *Lecture Notes in Control and Information Sciences*. Springer-Verlag, London, UK.
- Nourbakhsh, I. R. and Siegwart, R. (2004). *Introduction of Autonomous Mobile Robots*. The MIT Press, London, UK.
- Rigatos, G. G. (2010). Extended kalman and particle filtering for sensor fusion in motion control of mobile robots. *Mathematics and Computers in Simulation*, In Press, Corrected Proof.
- Scaglia, G. J. E., Mut, V. A., Jordan, M., Calvo, C., and Quintero, L. (2009). Robust-control-based controller design for a mobile robot. *Journal of Engineering Mathematics*, 63(1):17–32.
- Thrun, S., Burgard, W., and Fox, D. (2005). *Probabilistic Robotics*. The MIT Press, London, UK.
- Wang, D. and Low, C. B. (2008). Modeling and analysis of skidding and slipping in wheeled mobile robots: Control design perspective. *IEEE Transactions on Robotics*, 24(3):676–687.
- Wu, J., Xu, G., and Yin, Z. (2009). Robust adaptive control for a nonholonomic mobile robot with unknown parameters. *Journal of Control Theory and Applications*, 7(2):212–218.
- Zhou, B., Peng, Y., and Han, J. (2007). UKF based estimation and tracking control of nonholonomic mobile robots with slipping. In *Proceedings of the IEEE International Conference on Robotics and Biomimetics*, pages 2058–2063, Sanya, China.

Multi-Harmonic Adaptive Control for Roughness

J.A. Mosquera Sánchez¹, K. Janssens², H. Van der Auweraer², L.P.R. de Oliveira¹

¹ Department of Mechanical Engineering, São Carlos School of Engineering, University of São Paulo.
Av. Trabalhador Sancarlenso, 400. CEP: 13566-590, São Carlos – SP, Brazil.

² LMS International, Interleuvenlaan 68, B 3001, Leuven - Belgium

Abstract: Roughness, as well as Loudness, Sharpness, and Fluctuation Strength are psychoacoustic metrics that allow correlating acoustic stimuli, e.g. of an engine, with the subjectiveness of human auditory sensation. As far as vehicle sound quality is concerned, the analysis of roughness leads to the understanding of certain types of noise inside the cabin and allows the engineer to design features that will impact heavily on the sound quality of the car and influence the global qualitative assessment a particular vehicles. This paper presents a novel approach to the control of roughness, specifically designed to tackle combustion engine noise inside vehicles, including adaptive algorithms with confirmed effectiveness, such as the NEX-LMS, and efficient procedures for calculating the aforementioned psychoacoustic metric, which are directly related to the engine orders, emphasizing the study of the multi-harmonic characteristic of the disturbance. However, for such a controller to be effective, it is necessary to understand the phenomena bearing Roughness generation and transmission, as well as the issues during control design, such as the proper choice and placement of sensors and actuators, control strategy, the natures of both transient and stationary noise sources and the various routines to be used in data processing, which, among others, might affect the system performance. As a result, engine sound quality improvement is achieved by means of an adaptive control scheme that enables the equalization of multiple harmonics.

Keywords: Active Roughness Control, Adaptive Algorithms, Multi-Harmonic Engine Disturbance, Sound Quality

NOMENCLATURE

AC = AC envelope value, Hz
 a = half-order amplitude, dB SPL
DC = DC envelope value, Hz
 d = input signal, dB SPL
 e = error signal, dB SPL
 f = frequency, hertz
 g = frequency correction, dimensionless
 k = cross-correlation, dimensionless
 m = modulation index, dimensionless
 N = scheduled gain, dimensionless
 R = roughness, asper
 r = partial roughness, asper
 S = secondary path, dimensionless

\hat{S} = secondary path estimate, dimensionless
 w = adaptive coefficients, dimensionless
 x = reference signal, dB SPL
 y = adaptive out, dimensionless
 z = critical band, bark

Greek Symbols

ΔL = temporal masking depth, dB/Bark
 β = gain factor, dimensionless
 ϕ = half-order phase, dimensionless
 μ = adaptive step size, dimensionless

Subscripts

i = relative to critical band number
 j = relative to half-order number
 k = relative to channel number in the ANC system
 mod = relative to frequency modulation
1 = relative to the first responsible half-order for roughness
2 = relative to the second responsible half-order for roughness
3 = relative to the third responsible half-order for roughness

INTRODUCTION

The majority of problems in vehicle acoustics are concerned with acoustic comfort, rather than hearing damage (Wang et al., 2007). The passenger of a vehicle has to be seen as part of a vibro-acoustic system and, consequently, the subjective judgment of pleasantness or sound comfort is influenced by both sound and vibration (Genuit, 2004). To improve the aforementioned acoustic comfort in vehicle design, researchers should first understand how to evaluate a noise sample (Wang et al., 2007) and, from this perspective, some of the many sound sources that contribute to the interior sound of a vehicle may be *tuned* to enhance the vehicle sound appreciation invoking desired emotional responses, while others should be suppressed to reduce annoyance. Active noise control systems tend to be designed with a target on sound pressure level reduction; however, the perceived control efficiency for the occupants can be more accurately assessed if psychoacoustic metrics are taken into account (de Oliveira, 2010). Hence, to go from acoustic design to sound quality design, the actual temporal and spectral signal structures from the controlled sound need to be optimized to meet sound quality targets (Van der Auweraer et al., 2007).

When dealing with sound quality (SQ) issues in a vehicle interior, it is often possible to identify four types of problems: (i) pure level harmonic problems: when only noise level is tackled and broadband noise reduction is needed, e.g., *booming*; (ii) tonal problems: similar to the aforementioned pure level problems, but strictly related to a single harmonic, i.e., with a specific sensation of frequency which may be annoying; typically related to sensations like *pitch* or *tonality* as appearing in gear whines, exhausts, etc; (iii) continuity problems: another type of harmonic level problem,

continuity problems are often related to low order levels at certain RPMs, which can affect the perception of power and sportiveness. In opposition to booming, that could be seen as a discontinuity towards higher levels, the focus here is to get the order levels to evolve as smooth as possible with respect to RPM, and (iv) multiple-harmonic problems: when amplitude and phase relation of multiple orders are responsible for the wanted (or unwanted) sound characteristics, such as in *roughness*, *muddiness*, *rumble*, etc. (de Oliveira, 2010)

As far as the active control of noise is concerned, the problems in category (i) can be dealt with linear, time-invariant broadband controllers. The same controllers can be used in (ii), although adaptive schemes could be a better alternative, as the disturbance is rather periodic and a coherent reference signal would be readily available. Problems of continuity (iii) require the controller not only to track the order, but also to drive the error to a desired level (rather than zero); which means that the controller has to be capable of matching a desired order profile either by reducing or amplifying the order level at different RPMs. Problems in category (iv) require, in addition to (iii), that the controller tracks amplitude and/or phase relation of multiple orders (de Oliveira, 2010).

The aim of this research is to address the problems in category (iv), changing the sound perception of an engine in a passenger vehicle from a psychoacoustic perspective by affecting *Roughness*. In order to do so, a variation of the NEX-LMS scheme in a multi-order implementation is used. The NEX-LMS was recently proposed by (de Oliveira, 2010), as a fast-converging order level equalization controller that has the advantage of acting on a narrowband, allowing the present multi-order implementation. The results presented here are obtained with a cabin model excited with synthesized engine sound at different RPMs. The orders responsible for the Roughness are then targeted such that the desired levels are achieved after convergence. The sound, measured at the driver’s head position, is used as an error signal in the adaptive control scheme, which works with structural actuators on the main transfer path, in this case, the firewall.

ROUGHNESS OF ENGINE NOISE

Sound quality can be defined as the degree to which the totality of the individual requirements made on an auditory event is met (Genuit, 2004). In the automotive sector, the sound quality of both the exterior and interior of the vehicle has been converted into a marketing tool to attract more consumers (Redel-Macías, Berckmans and Cubero-Atienza, 2010), due to that the acoustic characteristics of a vehicle today mean an integral part of product identity, significantly influencing customer’s decision (Genuit, 2004). Thereby, the reduction of sound pressure level often does not lead to subjectively perceived improvements. Sometimes, they are even contrary to essential characteristics of a product, i.e., if significantly low levels do not represent the power of a *sporty* car. In consequence, sound quality is an essential part of vehicle quality (Genuit, 2004).

In sound-quality engineering, basic psychoacoustic quantities like loudness, sharpness, roughness and fluctuation strength play an important role. Roughness is used in sound-quality engineering, e.g., to stress the feature of *sportiness* in a car-engine sound (Fastl, 2005). As far as combustion engines are concerned, Roughness can be understood as a result of two or more neighboring orders interacting with each other and producing modulation at a certain frequency range. It is known, from psychoacoustic literature, that the amplitude modulations related to adjacent integer and half-integer engine orders contribute to the Roughness of an engine sound (Janssens et al., 2007).

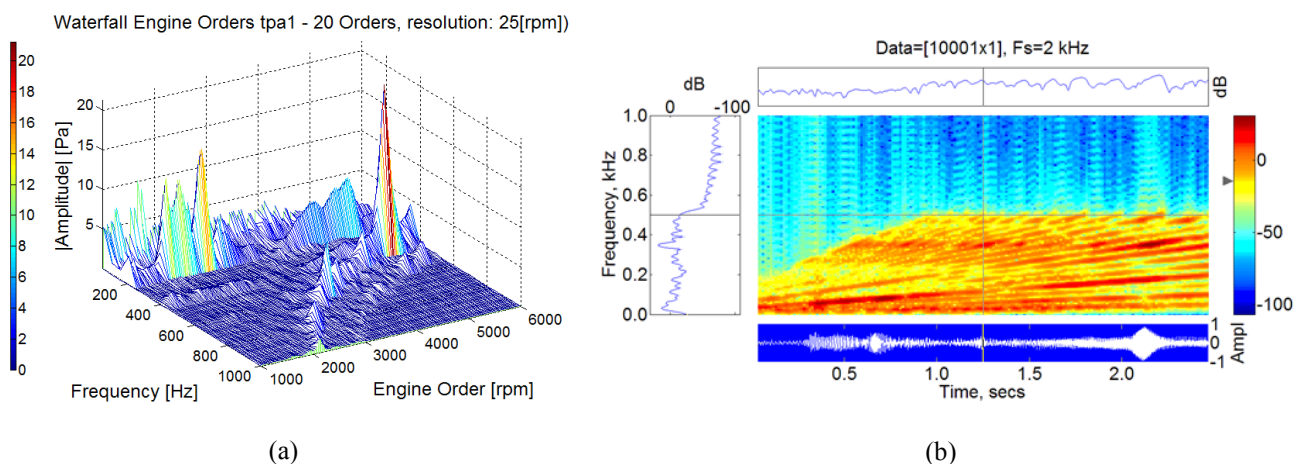


Figure 1: Waterfall and spectrogram analyses of evaluated engine noise.

Auditory Roughness is a term that was introduced by von Helmholtz in 1877 to describe the perception experienced when two sounds with proximal frequency components are heard simultaneously (Pressnitzer and McAdams, 1999). Roughness or “sensory dissonance” is also related to the perception of amplitude fluctuations and characterizes the texture of a sound in terms of impure or unpleasant qualities (de Baene et al., 2004). Roughness of signals with strong temporal structure is caused by amplitude and frequency modulations, i.e., quick changes in level and frequency and due to the filtering properties of the outer ear, each change in frequency results at the same time in a more or less strong

change in amplitude (Genuit, 2004). To define the Roughness of 1asper (In Latin, the word *asper* characterizes *rough*), it has chosen the 60dB, 1KHz tone that is 100% modulated in amplitude at a modulation frequency of 70Hz. The Roughness R of any sound can be calculated using the equation (Zwicker and Fastl, 1999):

$$(1)$$

where f_{mod} is the modulation frequency in kHz and τ is the temporal masking depth, in dB/Bark (critical bands) (Zwicker and Fastl, 1999). Using a 100% amplitude-modulated 1KHz tone and increasing the modulation frequency from low to high values, three different areas of sensation are traversed. At very low modulation frequencies the loudness changes slowly up and down. At about 15Hz, another type of sensation, Roughness, starts to increase. It reaches its maximum near modulation frequencies of 70Hz and decreases at higher modulation frequencies. As roughness decreases, the sensation of hearing three separately audible tones increases. This sensation is small for modulation frequencies near 150Hz; it increases strongly, however, for larger modulation frequencies. This behavior indicates that Roughness is created by the relatively quick changes produced by modulation frequencies in the region between about 15Hz to 300Hz. There is no need for exact periodical modulation, but the spectrum of the modulating function has to be between 15Hz and 300Hz in order to produce roughness. For this reason, most narrow-band noises sound rough even though there is no periodical change in envelope or frequency (Zwicker and Fastl, 1999).

The sound wave formed by three continuous half-order components of the engine revolution is related to the *rumbling* sound quality. In general, the degree of the rumbling sound quality is related to the magnitude of the envelope, the modulation frequency and the carrier frequency of the sound wave. When the revolution of the engine changes, the sound wave formed by three continuous half-order components is not only amplitude-modulated signal any more. In this case, the time history of this sound wave becomes the amplitude-phase-modulated signal. Mathematically, this signal can be expressed by the sum of three analytic signals, as follows (Lee, 2008):

$$(2)$$

where $A(t)$, $\phi(t)$ and $f(t)$ are the functions associated with amplitude modulation and $A(f)$, $\phi(f)$ and $f(f)$ are the functions associated with frequency modulation (Lee, 2008). It has been observed in numerous tests, concentrating on powertrain related vehicle interior roughness, which perceived roughness could be assessed by available methods only in the case of loudness differences. It seems that loudness correlates quite well with calculated roughness, which is a well-known fact from psychoacoustical literature. For noises with equal loudness however, the correlation between perceived and calculated roughness vanishes (Hoeldrich and Pflueger, 1999).

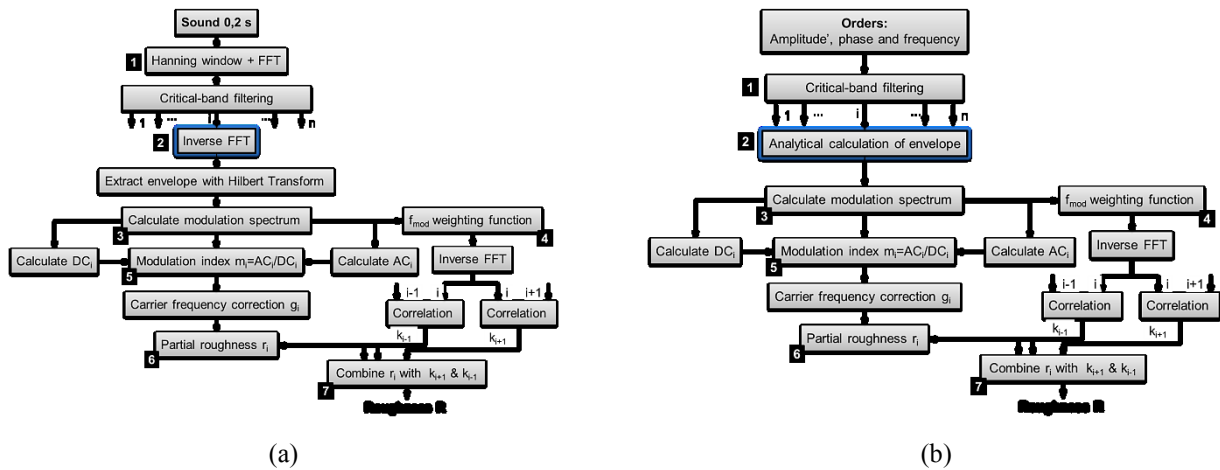


Figure 2: Roughness calculation methods: (a) Time-Domain; (b) Order-based (Janssens et al., 2007)

The roughness calculation is based on a decomposition of the sound in different critical bands. After filtering, the modulation depth is calculated per critical band and then transformed into a partial roughness by applying psychoacoustic weighting functions. The total roughness is finally obtained from the summation of weighted partial roughness values across critical bands (Hoeldrich and Pflueger, 1999) (Janssens et al., 2007). The drawbacks of this classical roughness approach are two-fold: The first one is related to the calculation speed of the algorithm. The critical band band filtering, the many FFT and inverse FFT operations and the Hilbert Transform to calculate the sound envelope for each critical band are time-demanding operations which make the algorithm slow and not applicable in real-time operation. The second disadvantage is related to the unclear relationship between the roughness and the order signature of the engine sound. For example, when the algorithm identifies a roughness problem at a certain engine RPM, it remains unclear which orders need to be modified and in which way: level decrease or increase? Phase change? (Janssens et al., 2007).

Thus, since Roughness is produced by amplitude and phase variations of certain relationships between half engine orders, it is necessary to know which orders are responsible for the Roughness. The methodology used in this research to find the orders responsible for the production of roughness perceived in the cabin of a car is based entirely on the 'order-based' algorithm summarized in Fig. 2b, which allows a direct relationship with the psychoacoustic phenomenon and the half-order amplitudes/phases that cause it. Therefore, the aforementioned methodology is summarized in the following stages:

1. Using the order-level vs. RPM profile obtained during engine run-up, shown in Fig. 1; calculate the engine Roughness signature by means of 20 interacting half-orders. The results are presented in Fig. 3a.
2. Find the critical RPMs with the highest Roughness values (red markers in Fig. 3a). The order-based Loudness calculation is presented to show that an auditory event described as *rough* may not necessarily be qualified as *loud*, as displayed in Fig. 3b.
3. Recalculate R by means of each 3-adjacent-half-orders (Janssens et al., 2007) (Lee, 2008) (de Oliveira, 2010) to obtain the orders responsible for the modulation.
4. From psychoacoustic literature it is known that Roughness is caused by amplitude and/or phase interactions of the modulating signals. Hence, in this work we have initially investigated the amplitude interactions; the next step is the construction of the 'feasible amplitude roughness-space' that can be generated by dealings with different amplitude levels of these orders. The construction of the amplitude *R-space* can display the range of possibilities that the sound quality engineer may have when designing the sound profile for that engine. The *R-space* also indicates the feasible space for the design of the ANC system presented here.

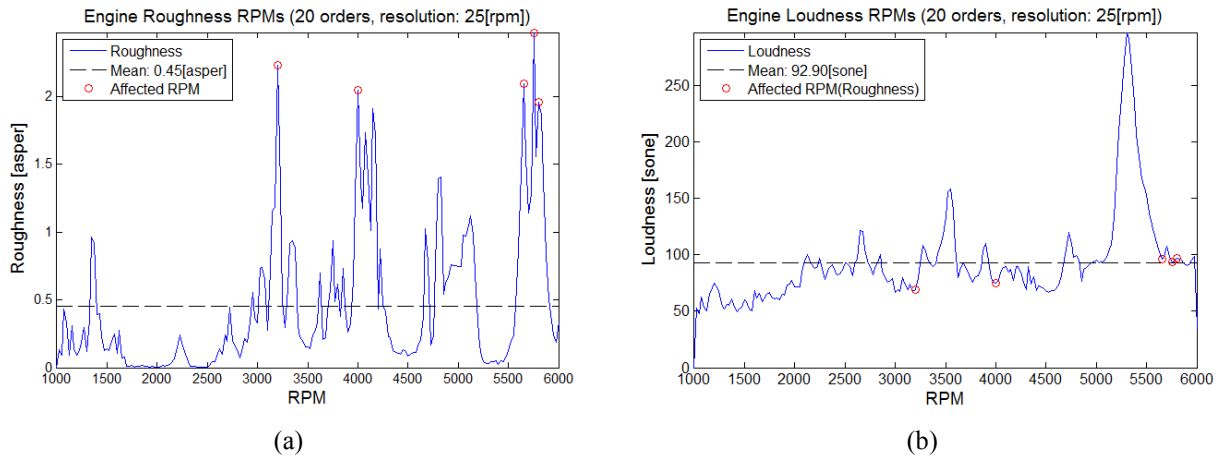


Figure 3: Order-based engine sound calculations: (a) Roughness; (b) Loudness.

MULTI-HARMONIC ADAPTIVE CONTROL FOR ROUGHNESS

Most noise sources can be classified as broadband or narrowband. Narrowband noise concentrates most of its energy at specific frequencies, and this noise is related to rotating or repetitive machines, so it is periodic or nearly periodic. For periodic noise caused by rotating machinery, narrowband techniques have been developed that are very effective in reducing repetitive noise. Since all the repetitive noise is at harmonics of the machine's basic rotational rate, the control system will cancel these known frequencies (Kuo and Morgan, 1996).

ANC is based on either *feedforward control*, where a coherent reference noise input is sensed before it propagates past the secondary source, or *feedback control*, where the active noise controller attempts to cancel the noise without the benefit of an "upstream" reference input. Feedforward ANC is generally more robust than feedback ANC, particularly when the feedforward system has a reference input isolated from the secondary anti-noise source. This technique has the following advantages: (i) undesired acoustic feedback from the cancelling loudspeaker back to the reference microphone is avoided; therefore, FIR filters can be used instead of IIR filters, thereby enabling guaranteed stability, (ii) nonlinearities and aging problems associated with the reference microphone are avoided, (iii) the periodicity of the noise removes the causality constraint, thereby allowing more flexible positioning of the secondary loudspeaker and longer controller delays, (iv) the use of an internally generated reference signal results in selectivity, specifically the ability to control each harmonic independently, and (v) it is only necessary to model the acoustic plant transfer function over frequencies in the vicinity of the harmonic tones (Kuo and Morgan, 1996).

Extending (iv), a sinusoidal signal can be used as a reference signal to cancel exact components of narrowband noise. This technique takes advantage of the correlation between the noise that contaminates the desired signal and a reference signal generated in the control (Kuo and Morgan, 1996). Thus, it is necessary to know beforehand the spectral components that request to control, in which case the roughness control implies knowledge of the responsible orders of the phenomenon.

The first active controllers aimed at SQ improvement appeared in the early 1990's by Kuo, Ji and Jiang (1993) and Eatwell (1995) and is called Active Noise Equalizer (ANE) as shown in Fig. 4(a). Designed to equalize, rather than

reduce noise levels, the ANE as first introduced by Kuo, Ji and Jiang (1993), is capable of tuning the amplitude of a sinusoidal disturbance. It works on the principle of an adaptive notch-filter, as the reference fed to the LMS algorithm is a sine wave, allowing the controller to observe and control only at that specific frequency. However, if the objective is to independently tune multiple orders, the narrowband action of the ANE is desired, as a finite number of ANEs can be cascaded, each with reference signals according to the disturbance component, without interfering with each other.

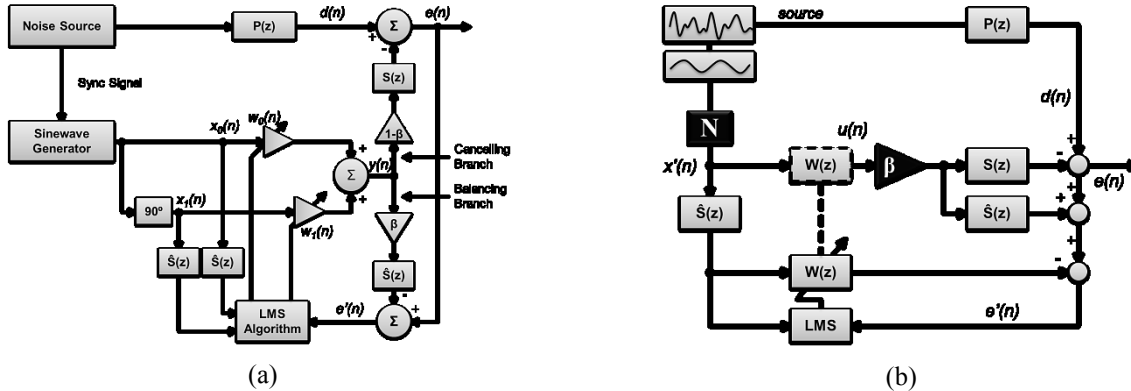


Figure 4: Single-Frequency ANEs (SFANE): (a) (Kuo, Ji and Jiang, 1993); (b) (de Oliveira, 2010)

The first implementation of such a scheme is reported in Sommerfeldt and Samuels (2001) where ANEs are cascaded to cover 8 harmonic components of the periodic disturbance signal. A similar multi-harmonic version of the ANE scheme was proposed for reshaping multi-tonal stationary noise by de Diego et al. (2000) in a setup similar to the one by Gonzalez et al. (2003), i.e. with microphones as sensors and speakers as secondary actuators in a room treated with absorbing material (passive control). In this case, the authors proposed a multi-channel implementation of the ANE and found out that the effect of such controllers was present on an area around the error sensors which were large enough to cover the listener’s head motion. The movement of the head, assessed with an instrumented human torso, did not affect the controller efficiency, nor its stability, which is a rather important conclusion as far as automotive application is concerned.

The aim of the implemented NEX-LMS control scheme is to achieve a desired sound quality target in an authentic ASQC manner (de Oliveira, 2010), by means of harmonic control of Roughness. In this control scheme, the minimization of the mean square error – the most common used performance criteria for digital filter adaptation – is achieved by means of steepest-descent methods, which results in the least mean square (LMS) algorithm. In real-life applications, the output of the filter W (see Fig. 4 and Fig. 5) is fed to the secondary actuator, therefore it is influenced by the secondary path dynamics $S(z)$ before it becomes the physical quantity $y(n)$ that superposes with the primary disturbance (de Oliveira, 2010). There are a number of possible schemes that can be used to compensate for the effect of $S(z)$. The first solution is to place an inverse filter ($1/S(z)$), in series with $S(z)$ to remove its effect. The second solution is to place an identical filter in the reference signal path to the weight update of the LMS algorithm, which realizes the filtered-X LMS (FxLMS) algorithm. Since an inverse does not necessarily exist for $S(z)$, the FxLMS algorithm is generally the most effective approach (Kuo and Morgan, 1996). An expression for the FxLMS is given by:

$$(3)$$

Where μ is the convergence coefficient, $e(n)$ the instantaneous error, i. e., the difference between the disturbance signal $d(n)$ and the controller output signal $y(n)$, $x(n)$ the reference signal, $\hat{S}(z)$ the secondary path coefficients and \otimes denotes linear convolution (Kuo and Morgan, 1996). The NEX-LMS adaptive scheme features a normalization filter in the form of the scheduled gain N , as displayed in Fig. 4b, which compensates for $S(z)$ such that the filtered signal has the same power throughout the frequency band of interest; it means that the performance is optimized for a fixed μ . For practical applications, N is kept within a safety margin (de Oliveira, 2010):

$$(4)$$

The NEX-LMS scheme uses the gain β in a way similar to the one proposed by Kuo, Ji and Jiang (1993), exposed in Fig. 4a. The difference in NEX-LMS is that, thanks to the use of the estimated primary disturbance $d'(n)$, the equalization needs to be applied only once, after the filter W (see Fig. 4b). Due to the equalization, the resulting error after convergence tends to $d(n)$, is given by (de Oliveira, 2010):

$$(5)$$

In this way, the residual error amplitude can be controlled by adjusting β . Therefore, the NEX-LMS exhibits four operating modes: $\beta = 1$ (maximum achievable reduction); $0 < \beta < 1$ (linear disturb reduction); $\beta = 0$ (neutral mode) and $\beta < 0$ (amplification mode) (de Oliveira, 2010).

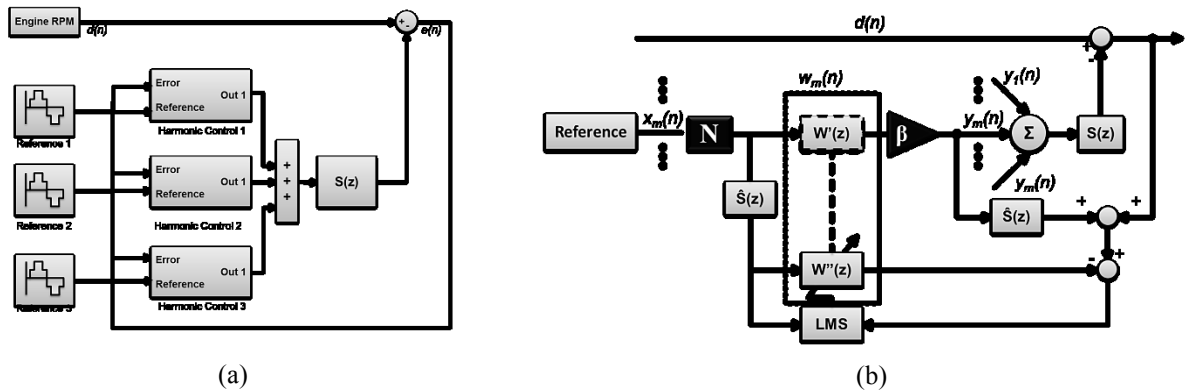


Figure 5: (a) Multi-harmonic adaptive control scheme; (b) details of the k th channel

The NEX-LMS scheme, given its characteristics and its optimized form, is suitable for harmonic-type disturbance controlling, such as those described and cataloged in the introduction as iv-type problems of SQ in vehicles. Its capability dealing with harmonic problems not only as a notch system but also as an equalizer system is very desirable in this problem, since an overall reduction of half-orders responsible by Roughness can lead to continuity – iii-type – problems, or even i-type sound quality engine problems.

As seen in Fig. 3, the problem of Roughness cannot be treated simply under the classical philosophy of ANC overall reduction, but it must be found a balance between the components that produce the sensation in order to obtain SQ of engines. However, as has been shown by various authors (Fastl, 2005) (Filippou et al., 2003) (Kuwano et al., 1997), which for a given listener may be SQ in the sense described in this document (Genuit, 2004) for another listener may not be that. Thus, the goal of proposed control system is to be able to reach *any* desired point of SQ, and not to raise the ‘minimum roughness’ as if it were the only goal that should get the control system, and therefore, knowledge of the *roughness-space* can help a sound engineer to make decisions with respect to the auditory sensation for transmitting in some listeners and the control system must be able to reach any desired roughness condition.

ROUGHNESS CALCULATIONS AND CONTROLLER SIMULATION

This section presents Roughness calculations for two stationary engine speeds, whose selection is based on the highest Roughness values obtained for the engine run-up presented in Fig. 3a. As the target of this research is to show the performance of the adopted control scheme for harmonic Roughness control, results found by computational simulation of the engine orders are presented.

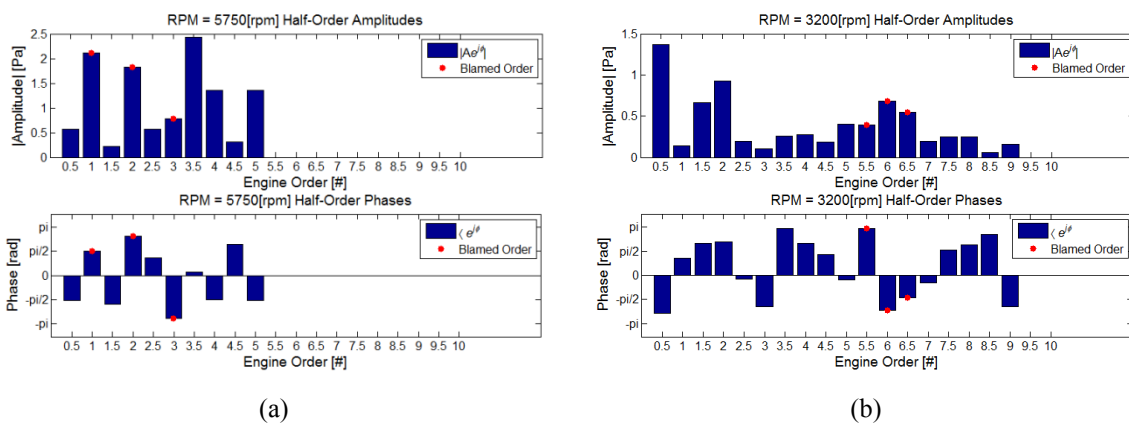


Figure 6: Order Amplitudes and Phases: (a) 5750rpm; (b) 3200rpm

Figure 6 shows the order levels and phase relations for 5750rpm and 3200rpm. Notice that, Roughness was not produced by the most powerful orders, but certain relations of amplitudes and/or phases are the cause of that auditory sensation. In this study, the target is the amplitude relations of the orders responsible for most of the modulation, leaving for future work the analyses of phase relation and its control, which as is well known from psychoacoustic literature, shows a stronger relationship with the origin of Roughness (Pressnitzer and McAdams, 1999) (Zwicker and Fastl, 1999) (Hoeldrich and Pflueger, 1999).

Order-based Roughness Calculation Results

After finding stationary engine speeds that exhibit the highest values of Roughness, we proceed to find the half-orders that cause it. The procedure adopted in this paper is to calculate the Roughness produced by interaction of 3-half-adjacent orders, once the auditory sensation produced by the interaction of distant signals in frequency does not cause the acoustic phenomenon. Taking the two stationary engine speeds with the largest Roughness values, it can be seen that the modulating orders are not necessarily those which exhibit the highest amplitude values. It must be remembered that the interactions of vibrations phase are closely related to the sensation.

Graphical methods of finding the vibrations responsible for Roughness are shown in Fig. 7a and Fig. 7c for 5750rpm and Fig. 8a and Fig. 8c in the 3200rpm situation. As explained in the section dedicated to the description of Roughness, this method involves finding the responsible half-orders by means of successive calculations of roughness for three-adjacent-half-orders whose separation in frequency does not exceed 250Hz, entirely based on the Janssens et al. (2007) algorithm. Thereby, varying the amplitudes of the involved 3-half-orders, and recalculating the roughness taking all the orders in a stationary engine speed, a *SQ-space* can be built, as shown in Fig. 7b and Fig. 7d for 5750rpm, and Fig. 8b and Fig. 8d for 3200rpm, in which there is a set of possible order amplitudes that can be achieved by the proposed active control scheme.

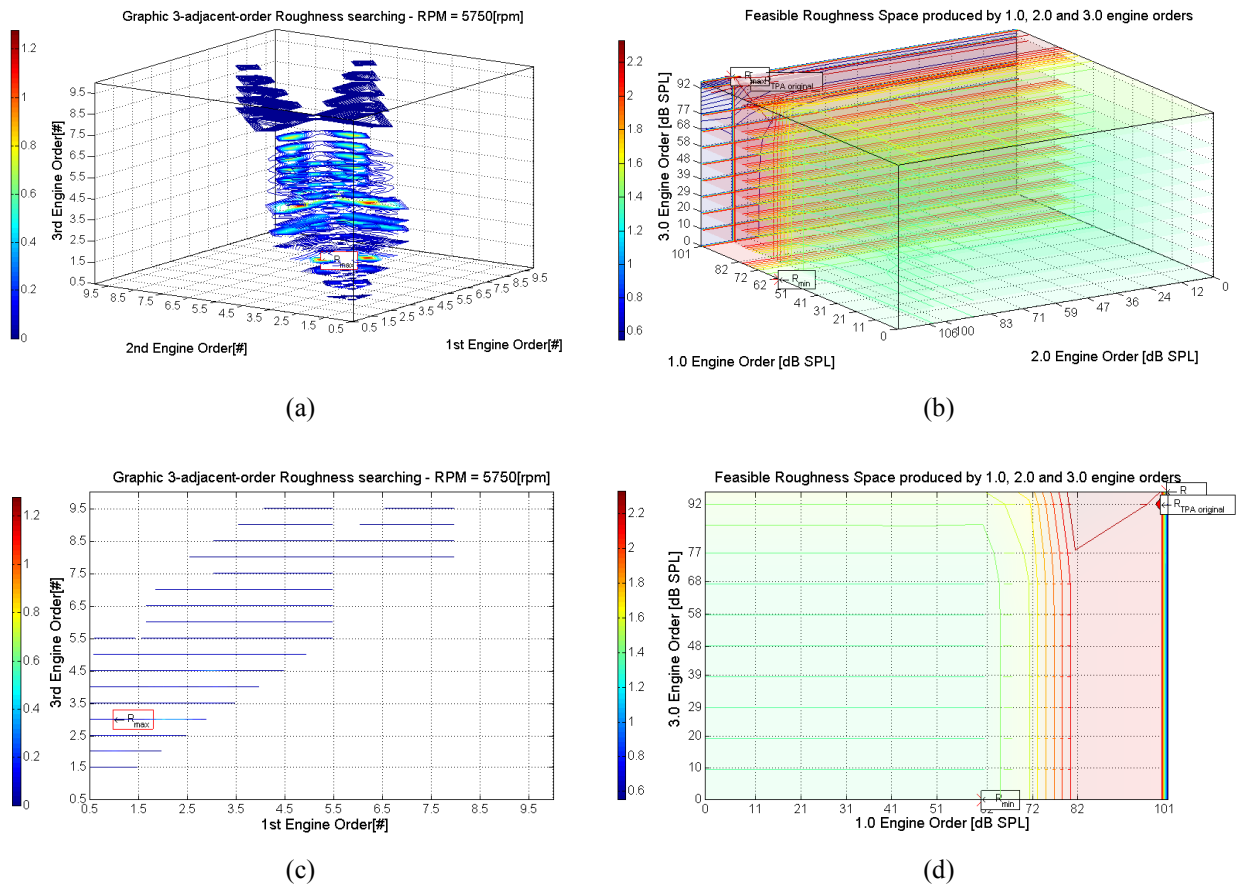


Figure 7: Roughness calculations for 5750rpm: (a) 3-D Roughness searching; (b) 3-D Roughness-space; (c) Roughness searching XZ-plane; (d) Roughness-space XZ-plane

According to psychoacoustic literature, widely in-frequency separated signals each other often do not generate any Roughness, which can be seen in Fig. 7a, Fig. 7c, Fig. 8a and Fig. 8c. Figure 7a and Fig. 7c for 5750rpm case show that the lower engine orders contribute significantly to the Roughness perception of the phenomenon: 1, 2 and 3 engine orders. The *SQ-space* generated by the variation of amplitudes of the above orders shows that there is a small area of maximum Roughness (red area in Fig. 7b and Fig. 7d) and a larger area which exhibits approximately constant Roughness (green area). This *SQ-space* shows that the total amplitude reduction of the responsible orders for Roughness does not necessarily imply the total Roughness reduction, because once made such a reduction, the perceived roughness will be produced by the other half-orders. Therefore, the philosophy of minimizing the amplitudes of the engine orders could expose other problems.

In that sense, the result for 3200rpm is revealing in terms of *SQ-space*. The responsible orders are higher (5.5, 6 and 6.5), as shown in Fig. 8a and Fig. 8c. The fact of raising the order amplitudes lies in an overall reduction in perceived Roughness (blue area in Fig. 8a and Fig. 8c), and to reduce the order amplitudes will produce higher Roughness (red area). As in the 5750rpm situation, reduction of the responsible order amplitudes will cause Roughness by other engine

orders, and this case clearly shows that reducing amplitudes of orders whose frequencies are above 250Hz (5.5, 6 and 6.5 half-orders) the Roughness caused by orders below the mentioned frequency limit becomes important, as predicted by the psychoacoustic literature.

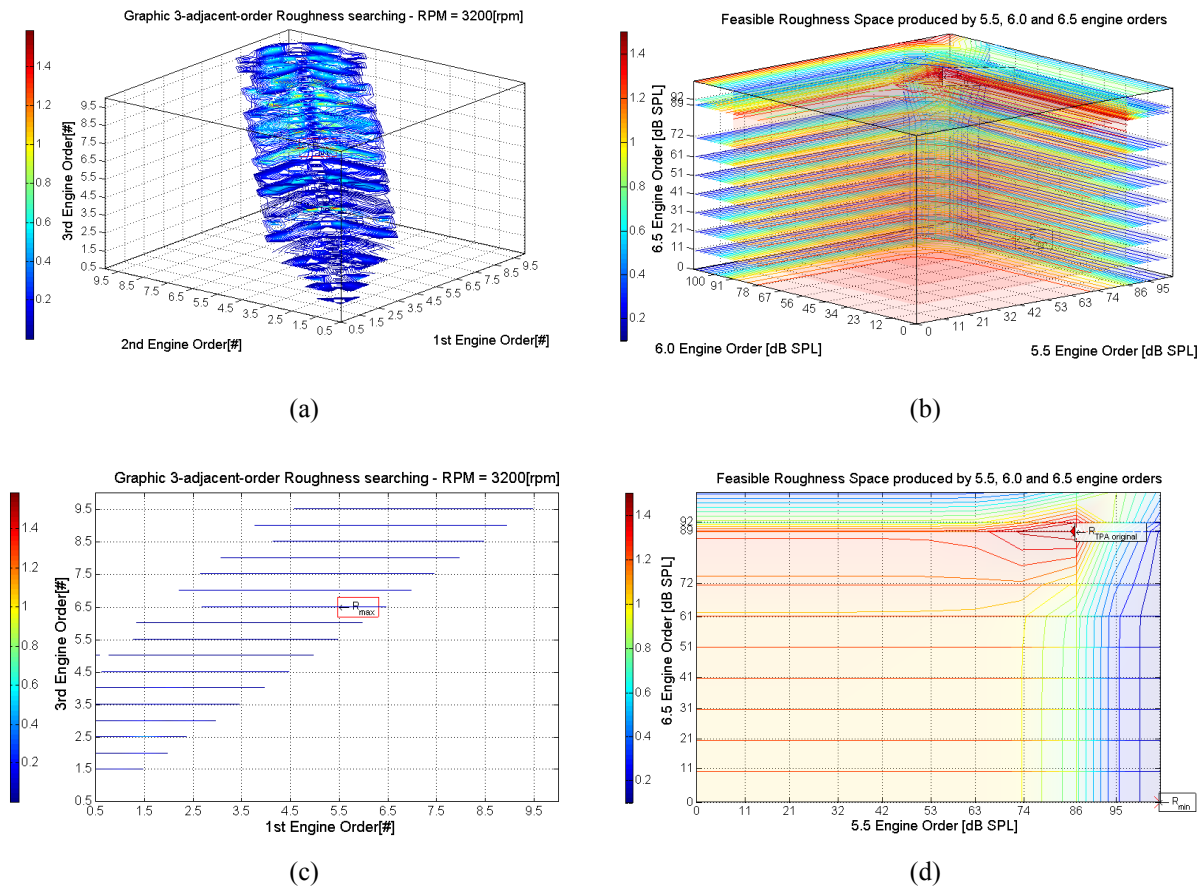


Figure 8: Roughness calculations for 3200rpm: (a) 3-D Roughness searching; (b) 3-D Roughness-space; (c) Roughness searching XZ-plane; (d) Roughness-space XZ-plane

A further analysis was done; it consists of seeking for the maximum reachable amplitude by the responsible half-orders that cause roughness during engine run-up and of calculating the roughness which could be generated if those half-orders would reach those highs. In Fig. 7b and Fig. 7d, it can be observed that, although the original Roughness situation is high (red-diamond markers), this event can be even worse if during the engine acceleration any responsible half-order would reach the aforementioned maximum amplitude. Even under these unexpected conditions, the control system scheme implemented is efficient, as shown in Table 2 and Table 3. It is worth noticing that the minimum and maximum Roughness points are listed in the charts as simple reference values, since the decision on the amount of desired roughness for the sound design of a particular engine should be made by the SQ engineer. Moreover, the target SQ does not always mean minimizing psychoacoustic metrics, as an engine that should sound *sporty* would be a perfect counterexample to that philosophy.

Characteristics of Controller Design and Simulation

Roughness control was explored by simulating the two selected stationary inputs to the system: 5750rpm and 3200rpm. Once we know the half-orders responsible for the problem, the reference of the system will be sinusoidal signals whose frequencies are equal to those of the half-orders, for each tested engine speed, with constant unit amplitude and zero phase, as the present analysis focuses on amplitude interactions. Thus, the selected control scheme, with single-input-single-output (SISO system) and with a known harmonic disturbance is implemented, gathering in parallel three adaptive control channels based on the NEX-LMS algorithm for each of the harmonics to be controlled, as exposed in Fig. 5a and Fig. 5b.

As seen in equation (3), a set of control parameters should be selected such that a rapid and accurate assessment of pseudo-error is achieved without causing instability. A fixed parameter for all channels is the size of the filter $W(z)$ which, as seen in the details of the k th channel in Fig. 5b, has two 101-order weights. From the ANC literature, it is known that a good estimate of the secondary path contributes to the successful operation of the system (Kuo and Morgan, 1996); hence, a secondary path copy of 1001 elements was realized. Finally, the success of NEX-LMS scheme lies in the neutralization of undesired effects of the paths' dynamics, which is the role of the scheduled gain as described

in Eq. 4. The system is simulated in MATLAB/Simulink under a sampling rate of 2KHz. In Table 1 a summary of the selected parameters and overall reductions achieved in responsible engine orders by means of percentages are shown for the multi-harmonic control scheme.

Table 1: Controller Simulation Summary: Characteristics and Results

Engine Speed	5750[rpm]			3200[rpm]		
Responsible Orders	1	2	3	5.5	6	6.5
μ_{ANC}	5×10^{-12}	5×10^{-12}	5×10^{-12}	5×10^{-13}	1×10^{-11}	1×10^{-9}
Order-level Reduction	99.24%	87.35%	93.59%	80.35%	94.13%	37.13%

Controller Results

The results for the control of engine orders 1, 2 and 3 responsible for the roughness at 5750rpm is shown in Figure 9 Fig. 9a, b, which shows the effectiveness of the designed system, achieving significant reductions either starting from the hypothetical situation of a roughness value even higher than the obtained during analyzed engine acceleration. A reduction of 99.24% was obtained for the half-order 1 (100 Hz) but not for the other 2 orders, although a great deal of reduction was obtained as well. Comparing these graphs with Fig. 7b and Fig. 7d, it can be noticed that it is not necessary that the controller reaches those endpoints of reduction, since as for reductions below 70dB to the 1st half-order, no better results in the roughness reduction can be obtained; Table 2 and Table 3 support this reasoning.

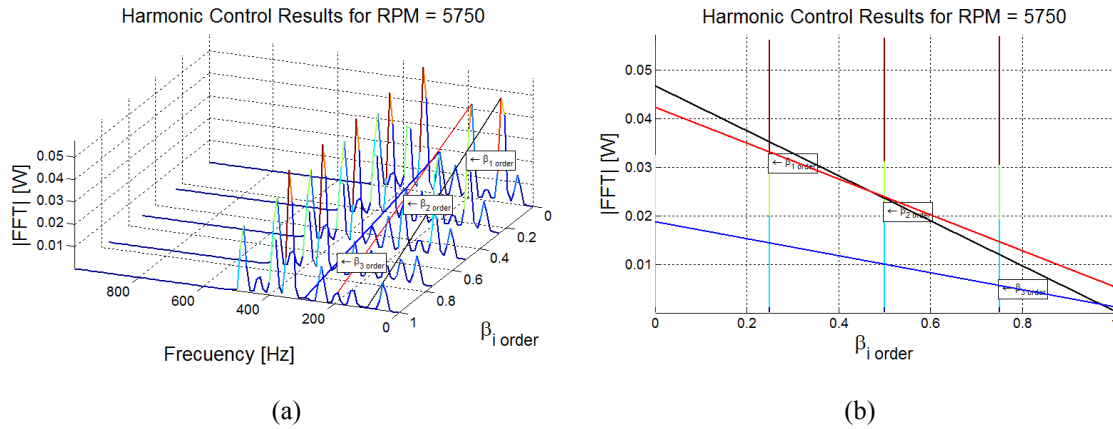


Figure 9: Controller Simulation Results for RPM = 5750: (a) 3-D waterfall; (b) Magnitude vs. $\beta_{i\text{-order}}$

Concerning the control system implemented at 3200rpm, it can be seen in Fig. 8b and Fig. 8d that, although the controller is not capable of reaching 100% reduction, the Roughness area (*SQ-space*) can be explored largely by manipulating the equalizing gain β for each channel of the proposed controller, as seen in Fig. 10a, Fig. 10b; and Fig. 9a and Fig. 9b in the 5750rpm case. It is worth noticing that the orders involved in the generation of roughness at this engine speed are closer together than in the first case, but the controller also showed effectiveness and complete independence in controlling only the three responsible half-orders without affecting the others.

Table 2: Harmonic Control Results for RPM = 5750

Engine Order	Passive ($\beta = 0$)		$\beta = 0.25$		$\beta = 0.5$		$\beta = 0.75$		$\beta = 1$	
	a_j [dB]	R[asper]	a_j [dB]	R[asper]	a_j [dB]	R[asper]	a_j [dB]	R[asper]	a_j [dB]	R[asper]
1	100.45		66.31		41.93		22.88		0.757	
2	99.2	2.4728	71.65	1.3729	48.85	1.3545	28.70	1.3531	12.54	1.3530
3	91.90		67.63		45.3		24.48		5.89	

The high rates of convergence exhibited by the system allows real-time processing, which enables sound engineers to play different conditions in *what-if* scenarios (Janssens et al., 2007) and to design accurately the engine SQ.

Table 3: Harmonic Control Results for RPM = 3200

Engine Order	Passive ($\beta = 0$)		$\beta = 0.25$		$\beta = 0.5$		$\beta = 0.75$		$\beta = 1$	
	a_j [dB]	R[asper]	a_j [dB]	R[asper]	a_j [dB]	R[asper]	a_j [dB]	R[asper]	a_j [dB]	R[asper]
5.5	85.92		66.78		46.56		27.35		16.88	
6	90.68	2.2290	69.56	1.4551	48.22	1.2821	26.77	1.3043	5.32	1.3013
6.5	88.73		77.29		67.42		59.93		55.78	

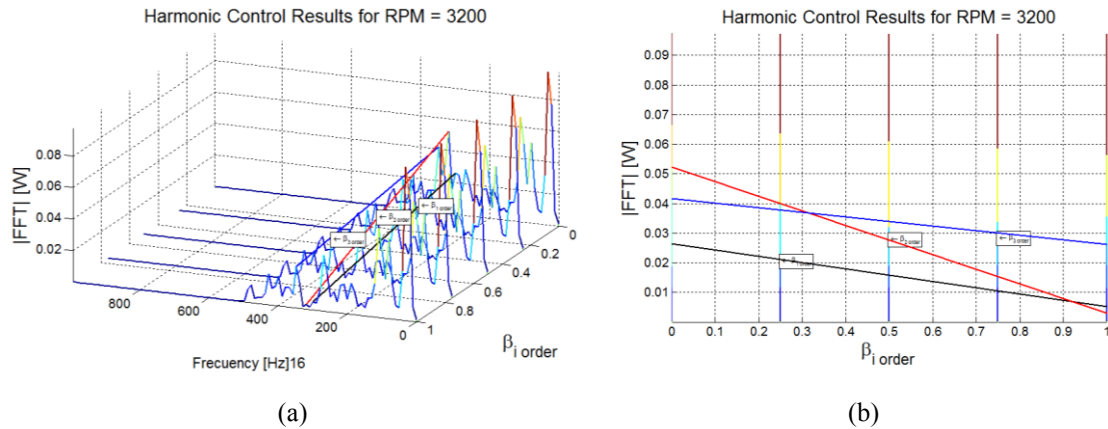


Figure 10: Controller Simulation Results for RPM = 3200: (a) 3-D waterfall; (b) Magnitude vs. $\beta_{i\text{-order}}$

CONCLUSIONS

This paper demonstrates the effectiveness of the NEX-LMS control scheme for the treatment of multi-harmonic disturbances. The metric known as psychoacoustics Roughness can be treated adequately by the implemented control scheme, since it can explore various amplitude conditions generated by the interaction of the half-orders responsible for Roughness, thus achieving the desired engine SQ attributes. The advantages of the NEX-LMS control scheme for multi-harmonic problems are demonstrated in this paper. Features such as the order-level reduction, independent tuning of distinct orders and the control performance are addressed, realizing what was predicted at the control concept design. The approach based on the identification of the half-orders responsible for Roughness is suitable for the selection of the control reference signal. As demonstrated in this paper, it is possible to significantly affect the overall roughness of a multi-harmonic noise by manipulation of the amplitude of its harmonic components. It is also successfully demonstrated that a multi-channel implementation of the NEX-LMS algorithm can perform such manipulation.

The control of non-stationary disturbance and the influence of the phase relations are currently under investigation. The next step in this research lies with the phase control of the engine orders that cause the problem.

ACKNOWLEDGMENTS

This research is supported by the São Paulo State Research Agency – FAPESP – grant # 2010/02198-4. The research of J.A. Mosquera Sánchez is supported by FAPESP - grant # 2010/03556-1.

REFERENCES

- de Baene, W., Vandierendonck, A., Leman, M., Widmann, A. and Tervaniemi, M. (2004) 'Roughness perception in sounds: behavioral and ERP evidence', *Biological Psychology*, no. 67, pp. 319-330.
- de Diego, M., Gonzalez, A., Garcia, C. and Ferrer, M. (2000) 'Some practical insights in multichannel active noise control equalization', Proceedings of the 2000 IEEE International Conference on Acoustics, Speech and Signal Processing - ICASSP, 837-840.
- de Oliveira, L.P.R. (2010) 'NEX-LMS: A novel adaptive control scheme for harmonic sound quality control', *Mechanical Systems and Signal Processing*, vol. doi: 10.1016/j.ymsp.2008.05.005.
- de Oliveira, L.P.R. (2010) 'Review and future perspectives on active sound quality control', Proceedings of the International Conference on Noise and Vibration Engineering, Leuven.
- Eatwell, G.P. (1995) 'Active control of sound quality', Proceedings of the 1995 International Congress on Noise Control Engineering - INTERNOISE'95, Newport-Beach, 521-524.
- Fastl, H. (2005) 'Psychoacoustics and Sound Quality', in Blauert, J. *Communication Acoustics*, 1st edition, Springer.
- Filippou, T.G., Fastl, H., Kuwano, S., Namba, S., Nakamura, S. and Uchida, H. (2003) 'Door sound and image of cars', DAGA'03, Oldenburg.
- Genuit, K. (2004) 'The sound quality of vehicle interior noise: a challenge for the NVH-engineers', *Int. J. Vehicle Noise and Vibration*, vol. 1, no. 1/2, pp. 158 - 168.
- Gonzalez, A., Ferrer, M., de Diego, M., Pinero, G. and Garcia-Bonito, J.J. (2003) 'Sound quality of low-frequency and car engine noises after noise control', *Journal of Sound and Vibration*, no. 265, pp. 663-679.
- Hoeldrich, R. and Pflueger, M. (1999) 'A parameterized model of psychoacoustical roughness for objective vehicle noise quality evaluation', Proc. 137th meeting of the Acoustical Society of America, Berlin.

- Janssens, K., Ahrens, S., Bertrand, A., Lanslots, J., Van der Pongseele, P., Vecchio, A. and Van der Auweraer, H. (2007) 'An on-line, order-based roughness algorithm', *SAE International*.
- Kuo, S.M., Ji, M.J. and Jiang, X.H. (1993) 'Development and experiment of narrowband active noise equalizer', *Noise Control Engineering Journal*, no. 3, pp. 281-288.
- Kuo, S.M. and Morgan, D.R. (1996) *Active Noise Control Systems: Algorithms and DSP Implementations*, New York: John Wiley & Sons.
- Kuwano, S., Namba, S., Fastl, H. and Schick, A. (1997) 'Evaluation of the impression of danger signals - comparison between Japanese and German subjects', in Schick, A. and Klatt, M. *Contributions to Psychological Acoustics*, Oldenburg: BIS.
- Lee, S.-K. (2008) 'Objective evaluation of interior sound quality in passengers cars during acceleration', *Journal of Sound and Vibration*, no. 310, pp. 149 - 168.
- Pressnitzer, D. and McAdams, S. (1999) 'Two phase effects in roughness perception', *J. Acoust. Soc. Am.*, vol. 105, no. 5, May, pp. 2773 - 2782.
- Redel-Macías, M.D., Berckmans, D. and Cubero-Atienza, A.J. (2010) 'Modelo de identificación de fuentes sonoras: Aplicación al ruido de motor de un automóvil', *Revista Iberoamericana de Automática e Informática Industrial*, vol. 7, no. 3, pp. 34 - 41, Available: 1697-7912.
- Sommerfeldt, S.D. and Samuels, T.O. (2001) 'Incorporation of loudness measures in active noise control', *J. Acoust. Soc. Am.*, no. 2, pp. 591-599.
- Van der Auweraer, H., Janssens, K., de Oliveira, L.P.R., da Silva, M. and Desmet, W. (2007) 'Virtual prototyping for sound quality design of automobiles', *Sound and Vibration*, April, pp. 26 - 30.
- Wang, Y.S., Lee, C.M., Kim, D.G. and Xu, Y. (2007) 'Sound-quality prediction for nonstationary vehicle interior noise based on wavelet pre-processing neural network model', *Journal of Sound and Vibration*, no. 299, pp. 933-947.
- Zwicker, E. and Fastl, H. (1999) *Psychoacoustics: Facts and Models*, 2nd edition, Berlin: Springer.

RESPONSIBILITY NOTICE

The author(s) is (are) the only responsible for the printed material included in this paper.

Characterization of Electromagnetic Actuator for the Control of Rotating Machinery

Morais T.S.¹, Der Hagopian J.², Steffen Jr V.¹ and Mahfoud J.²

¹ Federal University of Uberlândia, School of Mechanical Engineering, Campus Santa Monica, 38400-902 Uberlândia – MG – Brazil

² Université de Lyon, Laboratoire des Mécanique des Contacts et des Structure – LaMCoS, UMR CNRS 5259, France,

Abstract: The work deals with the design and the assessment of electromagnetic actuators (EMAs) for the control of rotating machine. The system studied has a hybrid bearing that exhibits nonlinear behavior. The system is composed of a horizontal flexible shaft supported by two ball bearings at one end and a roller bearing that is located in a squirrel cage at the other end. Four identical EMAs supplied with constant current are utilized. The EMAs associated to the squirrel cage constitutes the hybrid bearing. The aim is to develop an identification strategy to have a reliable model necessary for the control. The identification strategy consists on modeling the system with linear sub-models and the nonlinear sub-models that could be identified separately. First the EMAs were modeled by using classical equations of electromagnetism and then identified experimentally. Then, a linear model of the shaft mounted on its bearings was defined by using finite element method and was identified successfully. The model of the system was adjusted after assembling the different identified sub-models. The identification is carried out by using a pseudo-random search algorithm (Particle Swarm). The model of the system is then assessed in different configurations. The results obtained demonstrate the effectiveness of the developed strategy.

Keywords: Identification, Rotordynamics, electromagnetic actuator, Experiments.

NOMENCLATURE

a = EMA geometric parameter, mm
b = EMA geometric parameter, mm
c = EMA geometric parameter, mm
d = EMA geometric parameter, mm
e = effective air gap, mm
f = EMA geometric parameter, mm
 F_{em} = electromagnetic force, N
 F_u = external force, N
I = current, A
B = bearing
D = disc
[C] = damping matrix
[K] = stiffness matrix
[M] = mass matrix
OF = objective function
N = number of coils

{x} = vector of measured
displacements, m

Greek Symbols

α = damping factor, dimensionless
 β = damping factor, dimensionless
 γ = variable
 ω = frequency, Hz
 Ω = excitation frequency, Hz
 μ_0 = magnetic permeability of air,
H/m
 μ_r = relative magnetic permeability,
dimensionless
 ϕ = angular position
 δ_a = gap distance, m

Subscripts

0 relative to air
° derivative
a relative to actuator
b bearing
em relative to electromagnetic
g gyroscopic
r relative
s shaft
u external
x x direction
a z direction
i relative to the i^{th} sensor

INTRODUCTION

Active Magnetic Bearings (AMB) have been successfully applied in industrial applications (Schweitzer et al, 2003). They are well suited for contactless operations such as actuators and sensors in rotating machinery (Lei and Palazzolo, 2008; Kasarda et al, 2007; Mani et al, 2006 and Aenis et al, 2002). AMB technology in conjunction with conventional bearings is utilized either as an active magnetic damper (Kasarda et al, 2004), or for controlling the instability of certain supports such as journal bearings (El-Shafei and Dimitri, 2007, Sahinkaya and Burrows, 1985). In this case the AMB is considered to be an EMA.

The work presented in this paper is part of a research program aimed at controlling the dynamic behavior of rotating machinery by using EMAs when the latter crosses critical speeds and instability zones. The system studied is composed of a horizontal flexible shaft supported by two ball bearings at one end and a roller bearing that is located in a squirrel cage at the other end. Four identical electromagnetic actuators (EMA) supplied with constant current are utilized. EMA has strongly nonlinear characteristics due to the fact that the corresponding electromagnetic force is dependent on the current and armature position. The EMAs associated to the squirrel cage constitutes the hybrid bearing and exhibits nonlinear behavior. The aim of this paper is to design and to assess the EMA characteristics for control purposes. In order to achieve this task, the system (rotor with the hybrid bearing) has to be modeled and identified experimentally.

Several contributions have proposed accurate models that are identified in either the time or frequency domain, by using either optimization or curve fitting procedures (Ewins, 1984, Edwards et al., 2000 and Saldarriaga et al, 2010). In this work, an identification strategy is developed. It consists on modeling the system with different sub-models that could be identified separately. One sub-model for the linear system (Shaft and bearings) and one sub-model for the localized nonlinearity (EMA). The model of the system is then obtained by assembling the two identified sub-models and is adjusted experimentally.

In the following, we will present first the experimental set up utilized, and then the proposed identification approach will be detailed. The results obtained are first presented for the two sub-models and then for the system assembled and are discussed in the conclusion.

EXPERIMENTAL SET-UP

The system studied (Fig. 1) is a test machine composed of a horizontal flexible shaft of 0.04 m diameter containing two rigid discs. The rotor is driven by an electrical motor that can accelerate the shaft until the rotation of 10,000 rpm. The shaft is supported by bearings located at its ends, as follows: a roller bearing (B2) at one end and two ball bearings (B1) at the other end (B1). The roller bearing is located in a squirrel cage attached to the framework of the test bench by three identical flexible steel beams. The Electro-Magnetic Actuator (EMA) located on the external cage constitutes a smart active bearing and provides nonlinearity in the dynamics of the system. The displacements are measured by using four proximity sensors (Vibrometer TQ 103) arranged perpendicularly in two measurement planes located along the y axis, namely, measurement plane 1 and measurement plane 2 (fig. 1). The sensors are labeled C1 and C4 for the horizontal direction and C2 and C3 for the vertical direction.

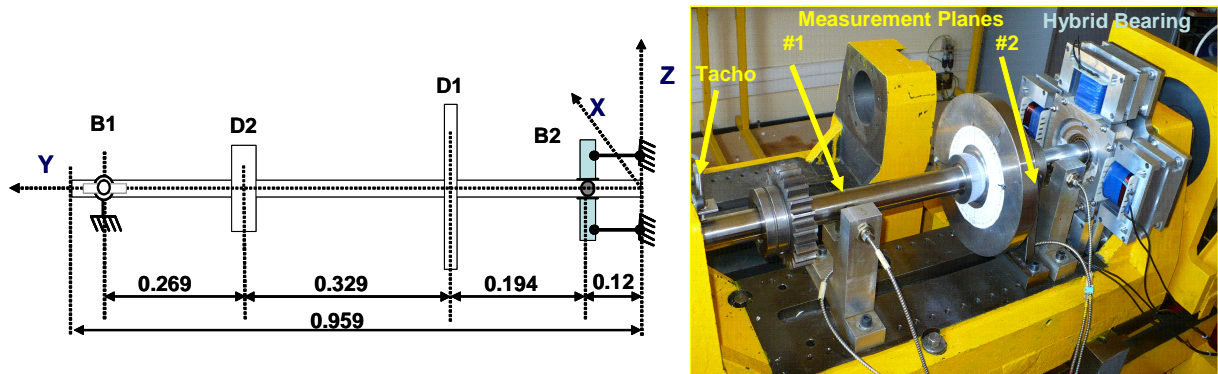


Figure 1 – Experimental test rig

Since an EMA can only produce attractive forces, Four “identical” EMA supplied by constant currents are utilized. Each EMA is composed of a ferromagnetic circuit and an electrical circuit. The ferromagnetic circuit has two parts: an (E) shape, which receives the induction coil, and an (I) shape, which is fixed to the squirrel cage. Both parts are made of sets of insulated ferromagnetic sheets. The quality of the ferromagnetic circuit alloy is considered high enough and the nominal air gap between the stator and the beam is small enough to consider magnetic loss as negligible. The geometries of the actuators are summarized in Fig. 2.

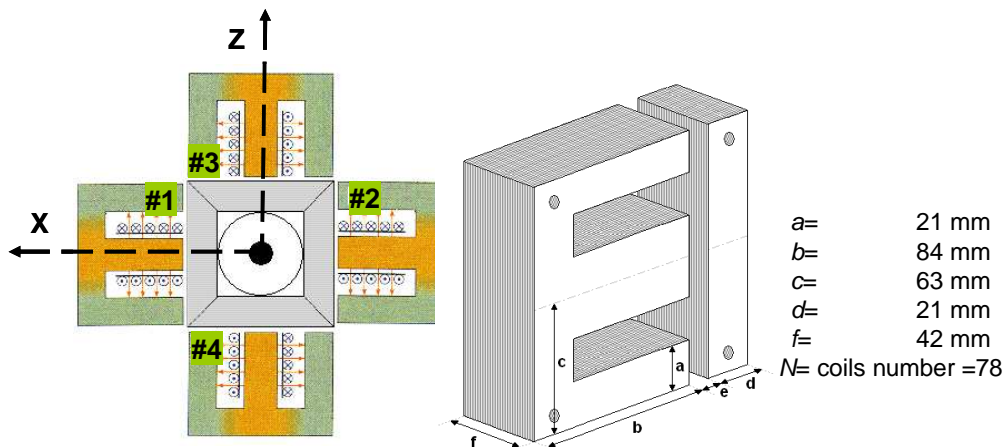


Figure 2 – EMA details

The data acquisition device used to collect experimental data was the SCADAIII interface of LMS® that enables real time data acquisition. Several codes of LMS® modal analysis software were used for data processing. The sampling frequency was 4096 Hz. A GWV20B of 110N electro-dynamic shaker provided by SS100 power amplifier of Gearing & Watson LTD, and an impact hammer Brüel & Kjaer (B&K) 8202 with a piezoelectric force sensor (B&K 8200) were used to generate the system responses to the different excitations applied. White noise inputs were used for the system identification procedures.

IDENTIFICATION APPROACH

The system studied is modeled through two sub models (Fig. 3), a rotor model and a model for the EMAs that are considered as restoring forces. The strategy developed encompasses several steps. First, a finite element model of the rotor studied is defined and identified separately then, based on magnetic circuit theory a simplified model of the EMA is defined and identified. Finally the total system (rotor plus actuators) is adjusted.

Assuming negligible eddy current effects and conservative flux, the relationship between the electromagnetic force (F_{em}), air gap (e), gap distance (δ_a) and current (I) can be expressed as (Der Hagopian and Mahfoud, 2010):

$$F_{em} = \frac{N^2 \mu_0 a f I^2}{2 \left((e \pm \delta_a) + \frac{b+c+d-2a}{\mu_r} \right)^2} \quad (1)$$

where (a , b , c , d and f) correspond to the geometrical characteristics of the actuator and μ_0 is the magnetic permeability of a vacuum ($4\pi \times 10^{-7}$ H/m). μ_r is the relative magnetic permeability (dimensionless) that is a function of the air gap and can be varied according to temperature. Its value is based on manufacturer's specifications and is generally not known with great accuracy and has to be identified.

The rotor model is composed by the following elements: rigid discs that contribute kinetic energy only; flexible shafts providing both kinetic and strain energy; and bearings with elastic and dissipation characteristics. The model obtained can be represented mathematically by a set of differential equations (Lalanne, 1998) as given by:

$$[M]\{\ddot{x}(t)\} + [C_b + \dot{\phi} C_g]\{\dot{x}(t)\} + [K + \ddot{\phi} K_g]\{x(t)\} = F_u(t) + F_{EMA}(t) \quad (2)$$

where $\{x(t)\}$ is the vector of generalized displacements; $[M]$, $[K]$, $[C_b]$, $[C_g]$ and $[K_g]$ are the well known matrices of inertia, stiffness, bearing viscous damping (that may include proportional damping), gyroscopic (with respect to the speed of rotation), and the effect of the variation of the rotation speed; $\dot{\phi}$ is the time-varying angular speed, and F_u and F_{EMA} are the forces due to the unbalance and to the electromagnetic actuator, respectively.

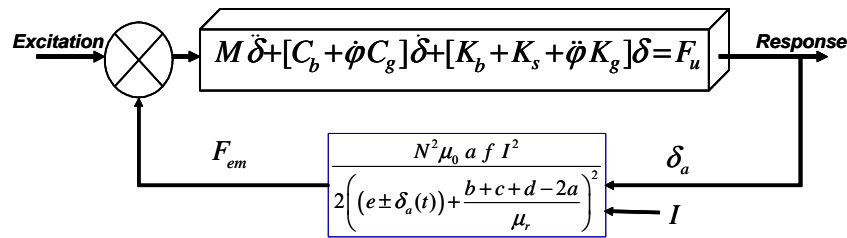


Figure 3 – Schema of the modeling process

The identification is carried out by using a pseudo-random search algorithm. These types of optimization are attracting increasingly more attention because of their capability of working successfully in complex optimization problems and also due to their robustness. In this study, Particle Swarm Optimization algorithm (PSO) was used. This technique was developed by the social psychologist James Kennedy and the electrical engineer Russel Eberhart (Kennedy and Eberhart, 1995). PSO is a global optimization technique for dealing with problems in which a best solution can be represented as a particle position in a n-dimensional space. The process is stochastic and makes use of the memory of each particle position as well as the knowledge gained by the swarm as a whole. The initial population is created by randomly distributing the particles throughout the search (design) space. For each individual a velocity vector is calculated that indicates the direction of progression. Then, the position of each particle is updated, using its previous position and the updated velocity vector. This process is repeated until convergence. The optimization tools used in the present study were previously developed by Viana (2008).

ROTOR IDENTIFICATION

The shaft is modeled by beam elements with two nodes and 4 d.o.f. per node, namely two displacements (along the directions x and z) and two rotations (around the axes x and z), respectively.

The model was discretized according to 43 nodes as shown in figure 4. The ball bearings (B1) are located at nodes # 4 and # 5 and the bearing containing the electromagnetic actuator (B2) at node # 39. The first disc (D1) is placed between the nodes # 12 and #16; the second disc (D2) is located between the nodes # 28 and #30. Finally, concentrated masses were included in the model at the position of the bearings and at the coupling between the shaft and the driving motor. It is worth mentioning that only the first eight vibration modes were taken into account in the calculation of the response.

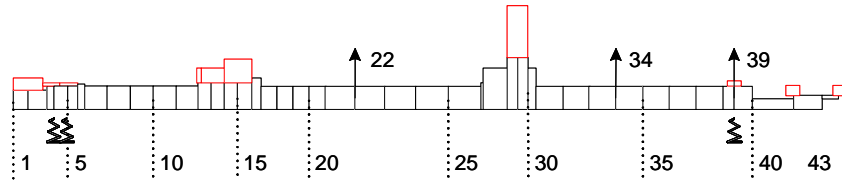


Figure 4 – Finite element model of the test rig

The identification process of the rotor model consists in updating the mathematical model with respect to experimental data. In the present case, only the bearing parameters are identified, the shaft and the disks are defined from the geometry and material properties. The stiffness K_{xx} and K_{zz} and the damping C_{xx} and C_{zz} are considered unknown as well as the coefficients α and β related to the proportional damping $C = \alpha M + \beta K$. For the identification of these parameters, white noise was inserted on the plane where D1 is localized, initially along the x-direction, then the z-direction, so that the parameters were identified separately for each direction. The cross stiffness terms were not taken into account.

The objective function is given by Eq. (3). It takes into account the norm of the difference between the experimental FRFs and those generated in the vicinity of the first two vibrating modes for each direction.

$$OF = \sum_{j=1}^2 \sum_{i=1}^2 \left(\frac{\text{norm} \left(FRF_i^{meas}(\omega_a \dots \omega_b) - FRF_i^{model}(\omega_a \dots \omega_b) \right)}{\text{norm} \left(FRF_i^{meas}(\omega_a \dots \omega_b) \right)} \right)_j \quad (3)$$

where j represents the two sensors along each direction (the planes 1 and 2 as shown in Fig. 1, and nodes #22 and #36 as shown in Fig. 4, respectively); i stands for the considered mode (two modes are taken into account for each direction); ω_a and ω_b indicate the frequency range used.

Table 1 – Design variables and optimal values for the bearings

			Design domain	Optimized values
Bearing Parameters	B1	Kxx [N/m]	1E7 to 7E8	1.167E8
		Kzz [N/m]		1.651E8
		Cxx [Ns/m]	50 to 1000	280
		Czz [Ns/m]		300
	B2	Kxx [N/m]	5E5 to 7E7	1.41E6
		Kzz [N/m]		1.43E6
		Cxx [Ns/m]	50 to 1000	120
		Czz [Ns/m]		120
Proportional Damping	C= $\alpha M + \beta K$	α	0 to 100	1.89
		β	0 to 1E-4	8.88E-6

As bearing B1 comprises two equal ball bearings, the corresponding stiffness and damping parameters are the same. Consequently, it is considered as an equivalent bearing with its 6 design variables. The design space is defined by the side constraints and the values obtained by the optimization procedures are summarized in the Tab. 1.

The measured and the calculated FRFs are compared in Fig. 5. The measured excitation was utilized in the analytical model in order to generate the FRFs at Node #22. The comparison is done at rest, consequently the non linear effects were not considered at this stage.

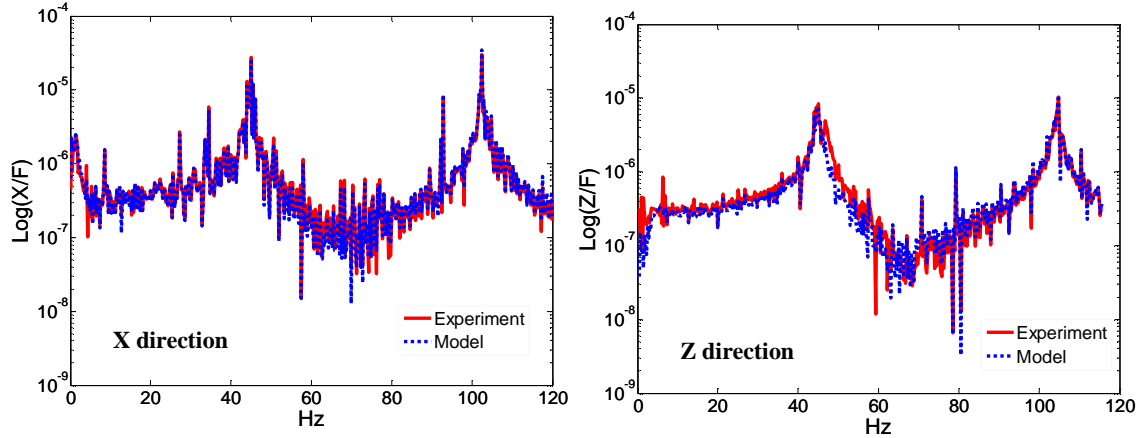


Fig. 5 – Measured and calculated FRFs, node #22, measurement plane #1

The results obtained show that the model identified describes closely the dynamic behavior of the rotor studied for the considered frequency range. The comparison of the dynamic behavior during rotation will be considered once the initial unbalance is identified.

ACTUATORS IDENTIFICATION

EMAs are designed to deliver a maximum attraction force of 300 N, and the maximum possible current is 5.0 A. The control input could be either a current or a voltage. For practical reasons, aiming at simplifying the electrical EMA model, a current control configuration was chosen as in Equ. (1).

In this model, the inputs are the current and the gap distance and the output is the force. The geometrical parameters could be measured precisely, the only unknown is the relative permeability that has to be determined experimentally. The relative permeability is determined as:

$$\mu_r = \frac{\gamma (b + c + d - 2a)}{1 - \beta e} \quad ; \quad \gamma = \sqrt{\frac{2 F_{em}}{N^2 \mu_0 a f I^2}} \quad (4)$$

A specific experimental arrangement was realized (Fig. 6). To measure the force generated by the actuator, the attraction force is measured for several air gaps for increasing and decreasing values of the input current.

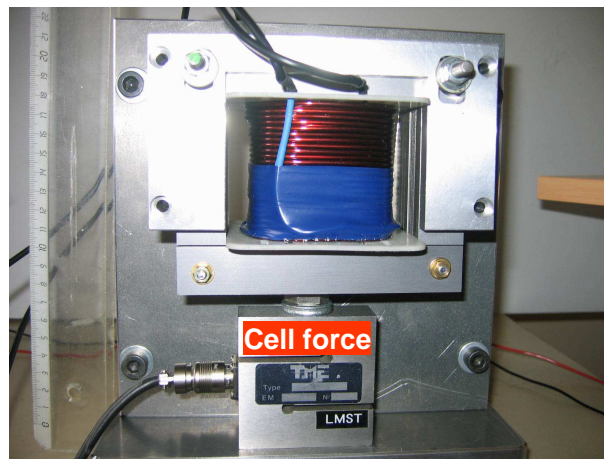


Fig 6 – Experimental arrangement for the actuator identification

The generated force due to increasing and decreasing input currents is measured for several air gaps (Fig. 7). It is worthy mentioning that without an accurate value of the gap distance between the *I* shape part fixed to the squirrel cage and the *E* shape part, it is not possible to determine the applied magnetic force with an acceptable accuracy.

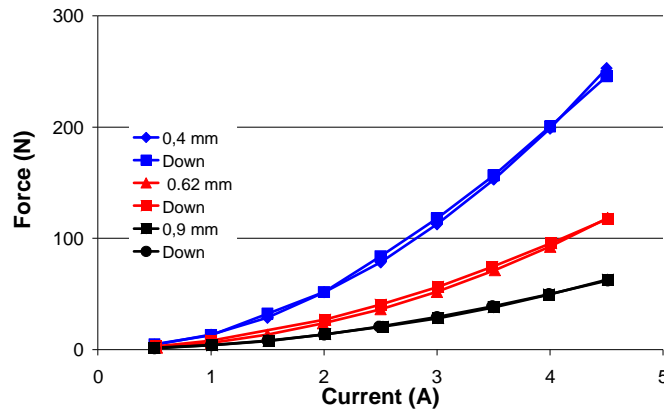


Fig. 7 – Measured forces versus current for several air gaps

The results obtained show that the hysteresis effect (due to electromagnetic flux) appears to be negligible and the generated forces are proportional to the current square value.

In the model presented here, the relative permeability is assumed to be constant for low flux density. Its variations with respect to different inputs values are presented in figure 8. The mean value determined for the model is 950.

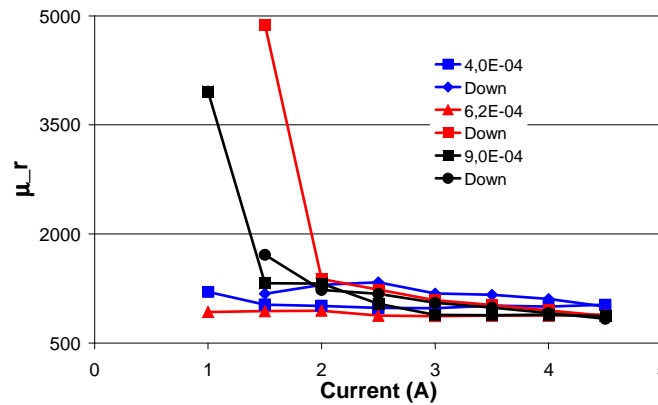


Fig. 8 – Relative magnetic permeability versus current for several air gaps

SYSTEM ASSESSMENT

After the identification of the sub-models, the assembled system is assessed for different configurations. A sinusoidal decreasing sweep is applied. The force amplitude was 30 N applied by the electromagnetic shaker on disk D2. The air gap was set to be 0.6 mm, and the actuators were supplied with a constant current of 3.5 A.

The same conditions were applied to model, the force was measured and applied to the model at node #15. The displacement measured stemming from sensor C1 and calculated by the model at node #22 are presented in Fig. 9. It is obvious that the model does not describe correctly the system studied. As mentioned before, an accurate value of the gap distance is necessary for reliable predictions.

In order to adjust the air gap value for each actuator, the PSO heuristic optimization technique is utilized. The objective function is given by Eq. 5. It takes into account the difference between the experimental measurements and those issued from the model for the frequency range utilized by the sinusoidal sweep.

$$OF = \sum_{i=1}^{nb_of_sensors} \left(\frac{(x_i^{meas}(\Omega_a \dots \Omega_b) - x_i^{model}(\Omega_a \dots \Omega_b))^2}{(x_i^{meas}(\Omega_a \dots \Omega_b))^2} \right) \quad (5)$$

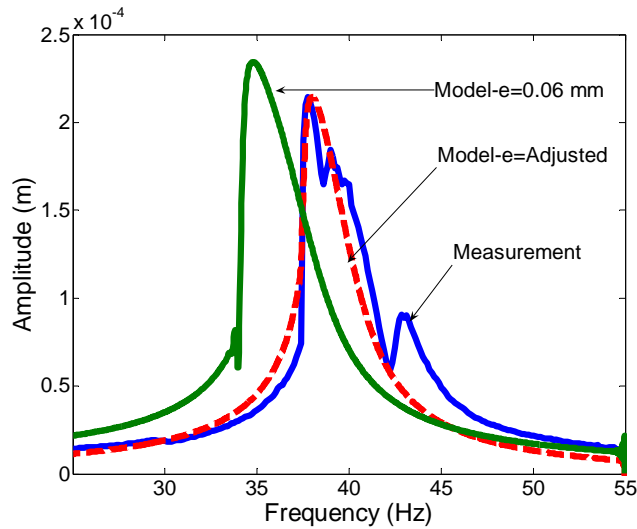


Fig.9 – System response (C1) due to sinusoidal sweep at rest

The design parameter was the air gap for each actuator. The design interval was 0.2 mm -1.2 mm. The population size used was 200 for maximum number of 100 iterations. The results obtained are summarized in table 2.

Table 2 – Optimal values for the air gap

Actuator	Design Domain	Optimized Value
#1	0.2 - 1.2 mm	0.621 mm
#2		0.666 mm
#3		0.641 mm
#4		0.715 mm

The model, when using the adjusted air gaps, describes closely the dynamic behavior of the system studied at rest (Fig. 9). In order to assess the dynamic behavior in rotation, Unbalance was added to the balanced rotor, as follows: (35.2 g.cm / 0°) at D₁ and (54.9 g.cm / -20°) at D₂, respectively.

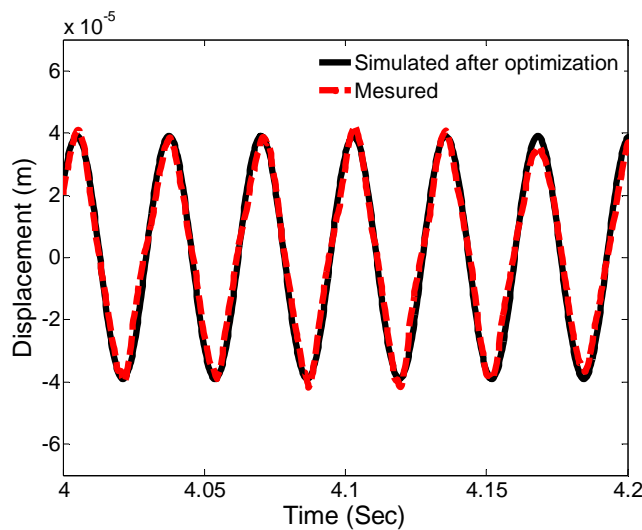


Fig.10 – System response (C1) due to unbalance, 1840 rev/min

Figure 10 shows the displacement levels measured and predicted by the model at plane #1 in the horizontal direction. It can be noticed that the model identified seems to describe closely the dynamic behavior of the test rig. Similar results are observed for the vertical direction and the measurement plane #2.

CONCLUSION

The possibility of establishing and identifying a model of a structure with a localized non linearity is assessed in this paper. The system studied is composed of a horizontal flexible shaft supported by two ball bearings at one end and a roller bearing that is located in a squirrel cage at the other end. Four identical electromagnetic actuators (EMA) supplied with constant current are utilized. The EMAs associated to the squirrel cage constitutes the hybrid bearing and exhibits nonlinear behavior.

The identification strategy consists on modeling the system with different sub-models that could be identified separately. The model of the system is adjusted after assembling the different identified sub-models. The aim is to identify separately the linear sub-models and the nonlinear sub-models. The identification is carried out by using a pseudo-random search algorithm. Particle Swarm Optimization algorithm was used in this study.

First the EMAs were modeled by using classical equations of electromagnetism. Only the relative permeability was unknown and was identified experimentally for several air gaps and different currents. A reliable model was identified. The observation of the force generated by the EMA due to increasing and decreasing input current shows that hysteresis effects are negligible. Moreover, the forces generated are obviously proportional to the current square value. It was noticed that accurate values of the gap distance are necessary for reliable predictions.

Then, a linear model of the shaft mounted on its bearings was defined by using finite element method and was identified successfully. The identification process of the rotor model consisted in updating the mathematical model with respect to experimental data, only the bearing parameters are identified, the shaft and the disks are defined from the geometry and material properties. Finally the system model was obtained by assembling the two sub-models. It was necessary to adjust the model obtained due to the high sensitivity of the air distance on the dynamic behavior of the system.

The model of the system is then assed in different configurations. The results obtained demonstrate the effectiveness of the developed model that could be used in t applications devoted to active control and/or automatic balancing

REFERENCES

- Aenis, M., Knopf, E., and Nordmann, R., 2002, "Active magnetic bearings for the identification and fault diagnosis in turbomachinery", *Mechatronics*, 12, 1011-1021.
- Der Hagopian, J. and Mahfoud, J., 2010, "Electromagnetic Actuator Design for the Control of Light Structures", *Smart Structures and Systems*, Vol. 6, No. 1, 29-38.
- Edwards, S., Lees, W. and Friswell, M., 2000, "Experimental identification of excitation and support parameters of a flexible-rotor-bearing foundation system for a single run-down", *Journal of Sound and Vibration* 232 (5) 963–992.
- El-Shafei, A., and Dimitri, A.S., 2007, "Controlling journal bearing instability using active magnetic bearings", *Proceedings of ASME Turbo Expo, GT2007-28059*, Canada.
- Ewins, D.J., 1984, "Modal Testing: Theory and Practice". Research Studies Press LTD., England.
- Kasarda, M., Mendoza, H., Kirk, R.G., and Wicks, A., 2004, "Reduction of subsynchronous vibrations in a single-disk rotor using an active magnetic damper", *Mechanics Research Communications*, 31, pp. 689-695.
- Kasarda, M., Marshall, J., and Prins, R., 2007, "Active magnetic bearing based force measurement using the multi-point technique", *Mechanics Research Communications*, 34, pp. 44-53.
- Kennedy J. and Eberhart R. C., 1995, "Particle Swarm Optimization", *IEEE International Conference on Neural Networks*; Perth, Australia;1942–1948.
- Lalanne, M. and Ferraris, G., 1998, "Rotordynamics Prediction in Engineering", John Wiley and Sons, Second Edition.
- Lei, S., and Palazzolo, A., 2008, "Control of flexible rotor systems with active magnetic bearings", *Journal of Sound and Vibration* , doi:10.1016/j.jsv.2007.12.028.
- Mani, G., Quinn, D.D., and Kasaeda, M., 2006, "Active health monitoring in a rotating cracked shaft using active magnetic bearings as force actuators", *Journal of Sound and Vibration*, 294, 454-465.
- Saldarriaga, V. M., Steffen Jr, V., Der Hagopian, J and Mahfoud J.; "Inverse Problem Approach Applied to the Balancing of Flexible Machines", *Journal of Vibration and Control* (2010), DOI: 10.1177/1077546310370669.
- Sahinkaya, M.N., and Burrows, C.R., 1985, "Control of stability and the synchronous vibration of a flexible rotor supported on oil-film bearings", *Journal of Dynamic Systems Measurement and Control*, Transactions of the ASME, vol.107, pp139-144.
- Schweitzer, G., Bleuler, H., and Traxler, A., 2003, "Active Magnetic Bearings - Basics, Properties and Applications", vdf Hochschulverlag AG, ETH, Zurich.
- Venter, G. and Sobieszczanski-Sobieski, J., 2003, "Particle Swarm Optimization", *AIAA Journal*. Vol. 41, N.8, pp.1583-1589.
- Viana, F.A.C., 2008, *Surrogate Modeling Techniques and Heuristic Optimization Methods Applied to Design and Identification Problems*, PhD Thesis, Federal University of Uberlândia, Brazil, April 2008, <http://sites.google.com/site/fchegury/>.

RESPONSIBILITY NOTICE

The authors are the only responsible for the printed material included in this paper.

A Game-Based Framework for Robotic Rehabilitation

Kléber de Oliveira Andrade¹, Bruno Jardim¹, Ricardo Cezar Joaquim¹, Adriano Almeida Gonçalves Siqueira¹,
Glaucio Augusto de Paula Caurin¹, Luiza Mesquita Sampaio do Amaral¹, Gisele Gonzalez Ito²

¹ University of São Paulo at São Carlos, Mechanical Engineering Department, Mechatronics Laboratory, Av. Trabalhador São-carlense, 400 – São Carlos, SP, Brazil, siqueira@sc.usp.br

² University of Petrolina, College of Medicine, Av. José de Sá Maniçoba, s/n – Petrolina, PE, Brazil

Abstract: In this paper a framework based on computer games is developed for rehabilitation of upper and lower limbs, considering specially designed interactive robots which deal with rehabilitation of hand and ankle movements. The Wrist Rehabilitation System, designed for Colles' Fracture patients, is an orthosis with three degrees of freedom related to the wrist's movements. The Active Ankle Foot Orthosis (AAFO) can perform exercises to improve patient skeletal muscle strength of patients recovering stroke. The interaction between the patient and the robotic system considers an impedance control. This control strategy allows the physical therapist to specify the desired behavior of the joint during the rehabilitation session.

Keywords: robotic rehabilitation, impedance control

INTRODUCTION

With a growing population of elderly, the demand for physiotherapy and occupational therapist services will rise to diagnoses associated with trauma-orthopedic lesions. Moreover, the number of recovering stroke patients has increased considerably worldwide. As a result, new rehabilitation procedures are being developed for additional home treatment, since the cost of a treatment in physiotherapy clinics is still high.

In recent years, the use of robots has generated significant advances in the medical field providing professionals new tools to treat patients. In an attempt to improve the confidence of patients with relation to a robotic rehabilitation system, an additional component very common nowadays is introduced: the computer games. This component provides a treatment focusing on the features of each individual, assisting the execution of tasks in specific contexts through visual feedback. Also, it integrates the cognitive component related to learning, which it is a necessary condition for rehabilitation of the movement (Hogan et al., n.d.).

Another crucial factor in the implementation of a robotic rehabilitation system is the contact between the patient and the robot, especially regarding the physical integrity of the user, already weakened by his/her condition. In this paper, we use impedance control (firstly developed in (Hogan 1985)) to configure how the interaction takes place between patient and robot. The impedance control applied to the robot can operate at different times during the rehabilitation process, now promoting assistance to the motion, now resisting the movement of the patient. Such a robot are called interactive robots.

In this paper, a game-based framework is developed for robotic rehabilitation of upper and lower limbs. Specifically, the proposed interactive robots deal with rehabilitation of hand and ankle movements. The Wrist Rehabilitation System is an orthosis with three degrees of freedom related to the wrist's movements. It was firstly designed for Colles' Fracture patients, which is one of the main types of fracture of the wrist, that represents one sixth of all fractures of the body (Hunter, 2002). To perform a rehabilitation process, this device can be used to implement the Indiana Hand Center Protocol (Cannon, 2001).

The Active Ankle Foot Orthosis (AAFO) was initially designed to prevent drop foot gait of patients recovering stroke. However, it can also perform exercises to improve patient skeletal muscle strength. The interaction between the patient and the robotic system considers an impedance control, implemented by a Series Elastic Actuator (SEA) attached to the ankle joint. This control strategy allows the physical therapist to specify the desired behavior of the joint during the rehabilitation session.

WRIST REHABILITATION SYSTEM

The Wrist Rehabilitation System, Fig. 1 has three degrees of freedom, flexion/extension of the wrist, ulnar/radial deviation and pronation/supination of the forearm. It considers anthropometric data to support the forearm, a handle to support the hand and a Velcro to stabilize it, if the flexion of the finger is impaired. The active movement is performed eliminating the effect of gravity, through three DC motors connected to the joints.

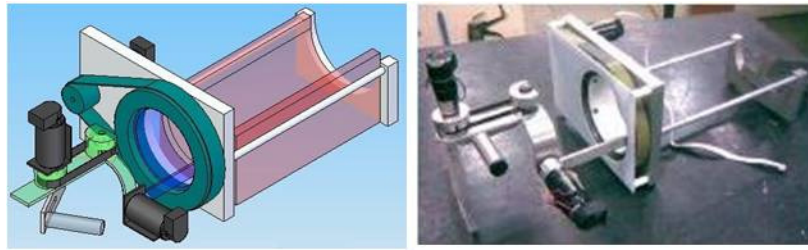


Figure 1 – Wrist Rehabilitation System

The orthosis design is inspired to perform wrist rehabilitation of Colles' Fracture patients, using the Indiana Protocol to do it. This protocol is divided in five parts:

- Start after 6 weeks: active handling (muscular contraction of the patient) to the limit of pain.
- After 1 week: active-assisted handling.
- After 2 weeks: slow passive motion (motion without muscle contraction).
- After 3 weeks: active handling resistance from 0.5 to 1kg.
- After 4 weeks: active handling with resistance above 1kg.

The exercises should be done every hour for 10 minutes. The device can measure the three angles during the activeassisted handling step by the encoder direct connected to the electrical joint motors. With the assistance of games, that motivate the patient to follow the protocol exercises, the system can store data for future analysis of the rehabilitation process.

To compare and classify the state of a patient in the rehabilitation process, the system uses the rules proposed by the Brazilian Society of Hand Therapists (Brazilian Society of Hand Therapists: Recommendations for evaluation of upper limb, 2005), comparing the optimal angles with the last patient measure, like follows: pronation/supination - $[-80\ 0]^\circ/[0\ 90]^\circ$; flexion/extension - $[0\ 80]^\circ/[0\ -70]^\circ$; and ulnar/radial deviation - $[0\ -30]^\circ/[0\ 20]^\circ$. These ranges are only a standard goal for the therapist to start the rehabilitation, being in his/her charge to select a goal variation according to his/her experience and the patient historical process.

ACTIVE AKLE FOOT ORTHOSIS

In this section the second interactive robot is described in details. The AAFO, Fig. 2, was designed considering anthropometric measures - such as limb dimensions and masses - normally observed in a healthy human. A series elastic actuator is mounted on the back of the device and moves the ankle-foot orthosis through a four-bar mechanism.

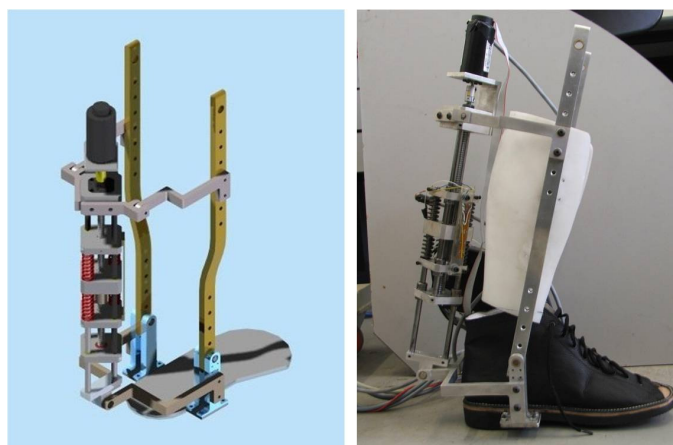


Figure 2 – Active Ankle-Foot Orthosis

The ankle joint ranges of a normal gait pattern are used as input to the actuation mechanism design. Tab. 1 shows the typical values for the human ankle during walking and the maximum values for the human ankle, the proposed AAFO and the BLEEX ankle joint (Zoss, Kazerooni and Chu, 2005). The reader can notice the higher range allowed by BLEEX ankle joint, it was designed to provide soldiers the capability to perform extreme movements.

Table 1 – Ranges of motion of the humam ankle, proposed AAFO, and BLEEX.

Ankle Movement	Walking	Humam (max.)	AAFO (max.)	BLEEX (max.)
Plantarflexion	20°	50°	25°	45°
Dorsiflexion	15°	20°	15°	45°

An analysis of a typical human walking shows that the ankle cycle of movement can be divided into four parts: swing phase (SP), controlled plantarflexion (CP), controlled dorsiflexion (CD) and powered plantarflexion (PP). According to (Au, Dilworth and Herr, 2006; B. and Herr, 2004; Walsh et al., 2006), during each subphases the ankle joint presents a specific characteristic of stiffness and damping. For example, it is showed that the ankle joint behaves as a linear spring response during CP, where joint torque is proportional to joint position. These mechanical characteristics will be useful to specify the desired stiffness and damping for the SEA during the rehabilitation session.

The series elastic actuator was reproduced according to the device developed by (Pratt and Williamson, 1995). All SEA components are shown in Fig. 3, where can be noticed the six support parts, the effector, one DC motor (maxon RE40 150W), one elastic coupling, one ball screw, one nut, and bearings to support the ball screw. The elastic series is composed by four linear springs (two for each actuation direction) with total stiffness equal, approximately, to 78.9 N/mm in each direction.

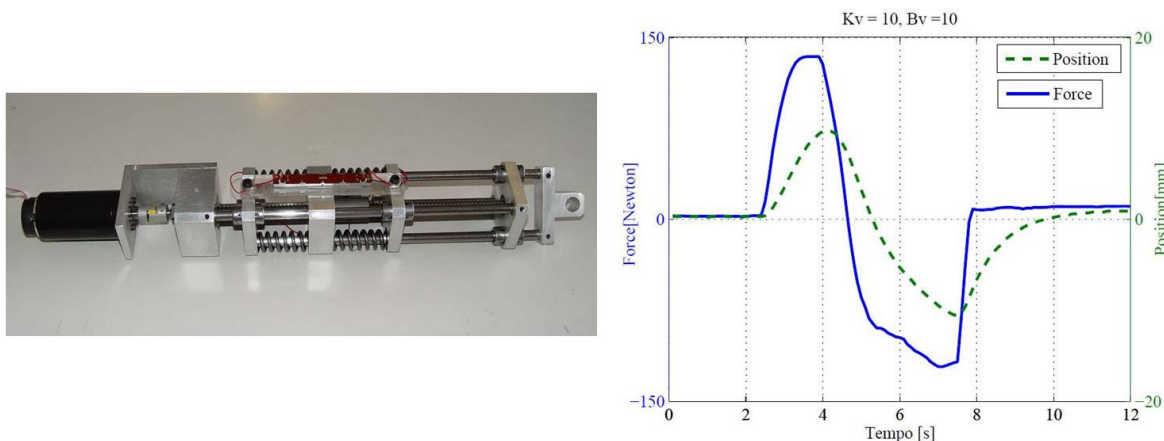


Figure 3 – Series Elastic Actuator and its spring-damper behavior

To test the ability of the SEA to simulate the behavior of a given impedance, the following experiment was considered: the device must to behave with both virtual damping ($B_v = 10$ Ns/mm) and stiffness ($K_v = 10$ N/mm). The values of K_v and B_v are introduced in the C++ program which computes the desired position for the motor and send it to the driver. The actual force value is computed considering the voltage measured through the potentiometer. For these experiments, the SEA was connected to the ankle-foot orthosis and an oscillatory force was applied in the ankle joint by the user, the results for the given behavior can be seen in Fig. 3. Note that, as expected, the spring-damper combination recovers with exponential decrement after load force is removed.

GAME-BASED FRAMEWORK STRUCTURE

In this section we present the structure of the game-based framework for robotic rehabilitation. It consists basically in the integration between the interactive robots shown in previous sections and computer games developed in XNA/C# platform. C# was the chosen language because it is an object-oriented language similar to Java language and with certain settings that come from C++, also it is the only one that works fine with XNA.

XNA (XNA's Not an Acronym) Game Studio Express is an API (Application Programming Interfaces) from the platform .Net developed by Microsoft to create games such for PC as Xbox 360 console. Although it is a recent technology, officially cast in 2006, it assembles all API's form DirectX and MDX (Managed DirectX) and others, developed only for it. Further, it allows easy access to peripherals (keyboard, mouse e Xbox 360 gamepad), grafical hardware, audio control, network access and informations housing in archives or database (Lobao et al., 2009).

The Wrist Rehabilitation System and the AAFO are both controlled by EPOS (Easy-to-use Positioning) controllers from maxon motor. This digital amplifier can perform current, position or velocity control of the motor, with set-point values set through serial or CANopen interfaces. A set of real variables, including shaft position, velocity and motor current, can be measured using these interfaces. Also, this device can measure up to 2 analog inputs. Particularly, one of these analog input channels is used to obtain the spring deflection of the SEA, computed by the measurement of the

voltage through a linear potentiometer connected between the nut support and the spring extremity. From the spring deflection, it is possible to estimate the actual torque in the ankle joint applied by the actuator and to perform the impedance control.

The basis of proposed framework for robotic rehabilitation is the communication between the EPOS controllers and XNA software. This communication is performed by the RobRehab library, specially developed for C# applications, taking as support the dll library for EPOS controller. RobRehab library provides to game developers a clear access to EPOS. Functions available by the framework are end-user ready so that the developers do not need to worry about any issue related to communication.

Figure 4 shows a specific application of the game-based framework, specially developed to demonstrate all features of the proposed system. For this setup, we connected both interactive robots to play the classical Pong game. The game purpose is to hit the ball with the racket (vertical bar) and throw it to opposite court, scoring a point when the ball goes through the racket. The pronation/supination joint of the Wrist Rehabilitation System moves up and down the left bar whereas the ankle joint of the AAFO moves up and down the right bar.

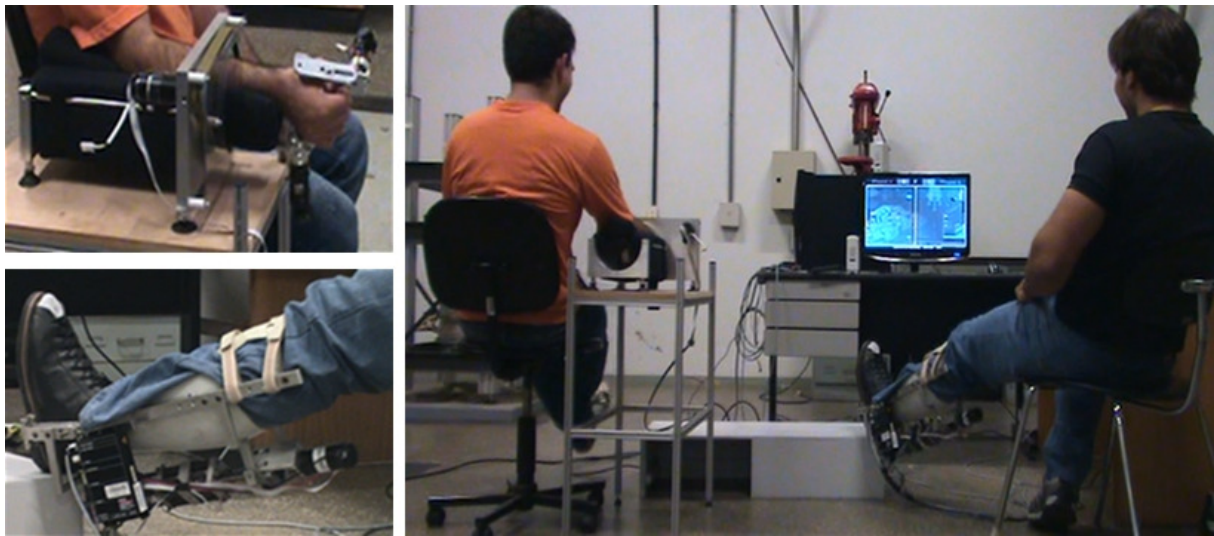


Figure 4 – Wrist Rehabilitation System and AAFO's user playing the Pong game

CONCLUSIONS

This paper presents a game-based framework for robotic rehabilitation. It presents two interactive robots which can be connected, individually or together, to a game platform using a custom robot driver library. The game system inspires the patient to fulfill a procedure, with a defined goal for the rehabilitation process and a motivating by a health competition against other person, like a regular game. This system also assists the therapist to improve the treatment, customizing the parameters to each patient. Thus, technology can help not only the individual in the treatment of fracture, but also professionals working in the area, increasing discussion about the practice and providing data for this.

ACKNOWLEDGEMENTS

This work was supported by CNPq (Master scholarship) and FAPESP (Grant no. 2008/09530-4).

REFERENCES

- Au, S. K., Dilworth, P. & Herr, H. (2006). An ankle-foot emulation system for the study of human walking biomechanics, Proc. IEEE Int. Conf. on Robotics and Automation., Orlando, Florida.
- B., B. J. & Herr, H. (2004). Adaptative control of a variable-impedance ankle-foot orthosis to assist drop-foot gait, IEEE Transactions on Neural Systems and Rehabilitation Engineering 12(1).
- Brazilian Society of Hand Therapists: Recommendations for evaluation of upper limb. (2005). 2nd ed. São Paulo.
- Cannon, N. M. (2001). Indiana Hand Center. Diagnosis and Treatment Manual for Physicians and Therapists. 4th ed., Indiana.
- Hogan, N. (1985). Impedance control: An approach to manipulation. parts 1-3., Dynamic Syst Measure Control pp. 1–24.

- Kléber de O. Andrade, Bruno Jardim, Ricardo C. Joaquim, Adriano A. A. G. Siqueira, Glauco A. de P. Caurin, Luiza M. S. do Amaral, Gisele G. Ito*
- Hogan, N., Krebs, H. I., Rohrer, B., Palazzolo, J. J., Dipietro, L., Fasoli, S. E., Stein, J., Frontera, W. R. & Volpe, B. T. (n.d.). Motions or muscles? Some behavioral factors underlying robotic assistance of motor recovery, *Journal of Rehabilitation Research and Development* 43(5): 605.
- Hunter, J. M. (2002). *Rehabilitation of the hand and upper extremity*. 5th ed., Mosby.
- Lobao, A. S., Evangelista, B. P., Farias, J. A. L. & Grootjans, R. (2009). *Beginning XNA 3.0 Game Programming: From Novice to Professional*, Ed. Apress.
- Pratt, G. & Williamson, M. (1995). Series elastic actuators, *Proceedings of the 1995 IEEE/RSJ International Conference on Intelligent Robots and Systems*, Vol. 1, Pittsburgh, pp. 399 – 406.
- Walsh, C. J., Paluska, D. J., Pasch, K., Grand, W., Valiente, A. & Herr, H. (2006). Development of a lightweight, underactuated exoskeleton for load-carrying augmentation, *Proceedings of the 2006 IEEE International Conference on Robotics and Automation*, Orlando, Florida, pp. 3485–3491.
- Zoss, A., Kazerooni, H. & Chu, A. (2005). On the mechanical design of the Berkeley Lower Extremity Exoskeleton (BLEEX), *Proceedings of the 2005 IEEE/RSJ International Conference on Intelligent Robots and Systems*, Edmonton, Canada, pp. 3465 – 3472.

RESPONSIBILITY NOTICE

The authors are the only responsible for the printed material included in this paper.

Unbalance Response of a Flexible Rotor Supported by Fluid Film Bearings with Additional Viscoelastic Damping

Thomazi C. C. ¹, Santos M. B. ², and Léopore Neto, F. P. ³

^{1,2,3} Federal University of Uberlândia, School of Mechanical Engineering, João Naves de Avila Avenue, 2121 - 1M, Santa Mônica Campus, Uberlândia – MG, Brazil.

Abstract: Finite Element analyses are carried out to investigate the effect of viscoelastic damping provided by double disc damper devices on the unbalance response of a flexible rotor supported by fluid film bearings. The performance of three different materials in minimizing the amplitude of synchronous whirl is presented. The influence of the dimensions of the viscoelastic disc is discussed. The viscoelasticity is implemented through the use of Prony series. The dynamic characteristics of the fluid film are obtained considering the short bearing theory. The results obtained from simulations allow to state, with some optimism, that the viscoelastic dampers may be good alternative in the mitigation of harmful consequences caused by unbalance forces on high-speed and light-weight rotating machines.

Keywords: flexible rotor, unbalance response, fluid film bearings, viscoelastic damping

NOMENCLATURE

c = radial clearance, mm
 d = diameter, mm
 g = material parameter on Prony series
 h = width, mm
 l = length, mm
 t = thickness, mm or time, s
 C = damping coefficient, N·s/m
 E = modulus of elasticity, N/m²
 F = force, N

G = shear relaxation modulus, dimensionless
 K = stiffness coefficient, N/m

Greek Symbols

γ = density, kg/m³
 ν = Poisson's ratio
 η = absolute viscosity, Pa·s
 τ = material parameter on Prony series

Subscripts

b relative to bearing dimensions
 d relative to disc dimensions
 e relative to elastomer
 j relative to journal dimensions
 s relative to shaft dimensions
 y relative to the y direction
 z relative to the z direction

INTRODUCTION

Fluid film bearings are commonly used to support rotating parts of machinery and have strong influence on the dynamic behavior of such equipment. With the increasing need for high-speed and light-weight rotating machines, continuous efforts are being made to enhance the performance of this type of bearings in a sense to reduce vibration amplitudes, excessive shaft whirling and dynamic instabilities that may arise at elevated running speeds.

Lund (1965) showed that flexible and damped supports may improve the stability of high-speed rotors that run on journal bearings. Lee et al. (2004) state that is necessary to develop more efficient bearings for turbomachinery that operate in super-bending-critical speeds. This task could be achieved increasing the load carrying capacity and the damping of the bearings.

Bearing support damping is desirable in many applications because it can suppress instabilities and attenuate rotor whirl amplitude at the critical speeds (Vance, 1988). Rotating machines show a more or less pronounced vibration peak at the critical speed. To reduce its amplitude, the designer must increase non-rotating damping (Genta, 2005).

There are different ways to incorporate damping on the rotor supports: using fluid film bearings, making use of squeeze film damper, through hydraulic dampers, applying special mountings, or introducing viscoelastic dampers (Vance, 1988).

Lee et al. (2004) used a viscoelastic foil bearing, while Choudhry (2003) applied a wire mesh as a bearing damper. These authors had distinct solutions to achieve the common objective of reduce the rotor orbits using convenient compact dampers. Lee et al (2004) attribute the orbit reduction to the mechanical energy dissipation due to the viscoelastic hysteresis. The friction among the steel wires is the cause of the mechanical energy dissipation and, consequently, the reducing of the rotor orbits, on the Choudhry's device.

Shabaneh and Zu (2000) investigated the dynamic behavior of a rotor supported by linear elastic bearings mounted on viscoelastic suspension. They verified that increasing the loss factor, the natural frequency of the system increases and vibration decay occurs quickly. As the stiffness of the viscoelastic material increases, the natural frequency also increases until it reaches the value of a rigid bearing support. However, the vibration decay may occur faster or slower, depending on the stiffness of the material.

Panda e Dutt (1999) found optimum characteristics for a rotor system mounted on rolling element bearings and plain cylindrical journal bearings at the ends having polymeric supports, minimizing the unbalance response and maximizing the stability limit speed.

Synchronous vibration due to unbalance is usually controlled through rotor balancing. This is the most effective mean to minimize shaft synchronous whirling because it attacks directly the cause of the unbalance. However, rotor balancing by itself is often insufficient to compensate the unbalance and consequently reduce synchronous rotor vibration. Adding external damping to the supports in combination with rotor balancing may be a well suited solution in order to limit the vibration to tolerable magnitudes.

Viscoelastic polymers are considered good support elements for rotating machines, due their efficiency dissipating vibratory energy. Elastomers are viscoelastic materials capable of relative large strains with essentially full recovery. Elastomeric materials provide energy dissipation converting mechanical energy into heat energy, thereby damping.

In the present work, analyses have been carried out on the dynamic behavior of a flexible rotor system supported by fluid film journal bearings with additional passive damping provided by elastomeric dampers introduced between the bearings and their housings. The finite element method was used to model the system. The influence of the viscoelastic properties, as well as the dimensions of the elastomeric damper on the forced response due to mass unbalance is presented.

The choice for elastomeric materials was taken based in the fact that dampers made with them are easy to manufacture and assembly. Moreover, elastomers permit compact designs which may be a great advantage in terms of costs compared to other types of dampers.

FINITE ELEMENT MODELLING

A steel shaft, on which two rigid steel discs are attached by means of steel hubs, is supported by two bronze short bearings. The overall dimensions of the rotor-bearing-damper system are presented in Fig. 1. The shaft is 2100 mm long, with a diameter $d_s = 20$ mm. The diameter of the journals is $d_j = 60$ mm. The diameter of the discs is $d_d = 200$ mm. The first disc (from left to right in Fig. 1) has thickness $t_d = 19.75$ mm, and the other has $t_d = 19.65$ mm. These dimensions were taken from a test facility installed in the Laboratory of Mechanical Systems of the School of Mechanical Engineering of the Federal University of Uberlândia.

The mechanical properties of steel ($E = 207 \times 10^9$ N/m², $\nu = 0.29$ and $\gamma = 7800$ kg/m³) and bronze ($E = 75.8 \times 10^9$ N/m², $\nu = 0.33$ and $\gamma = 8950$ kg/m³) were adopted for the rotor (shaft, discs and hubs) and for the bearing shell, respectively.

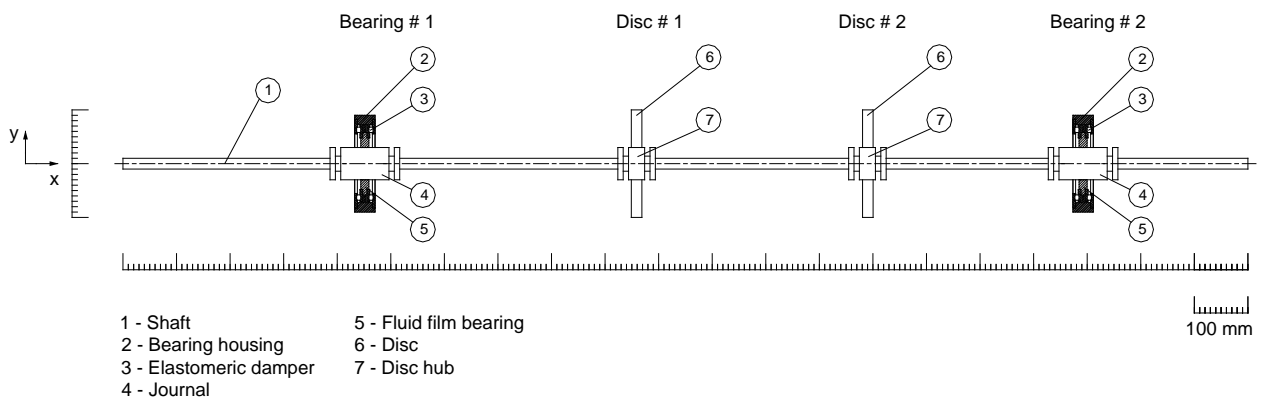


Figure 1 – Dimensions of the rotor-bearing-damper system.

The damper idealized in this work consists in two elastomeric hollow discs mounted on the outer edges of the flat faces of the bearing shell, so its inner diameter is equal to the bearing shell outer diameter. This shear continuous cartridge configuration is shown in Fig. 2.

The Finite Element program ANSYS[®], version 12, was used to model the system. The rotor was meshed with 73 elements. The bearing shells were meshed with 4 x 2 x 92 (axial x radial x circumferential direction, respectively) elements and each elastomeric disc was meshed with 16 x 2 x 92 (thickness, t_e x annulus width, h_e x circumferential direction, respectively) elements, as shown in Fig. 3. This meshing was adopted after running successive refinements and no significant changes in the amplitude of synchronous response were observed.

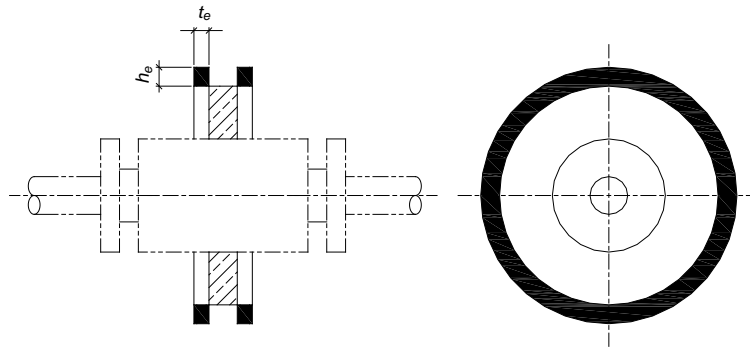


Figure 2 – Geometry of the elastomeric damper device.

Two-node, linear beam elements, based on the Timoshenko theory, Beam188, were used to model the rotor. The axial displacement and the rotation about the longitudinal axis of the shaft were constrained in a manner that axial motion and torsion are suppressed.

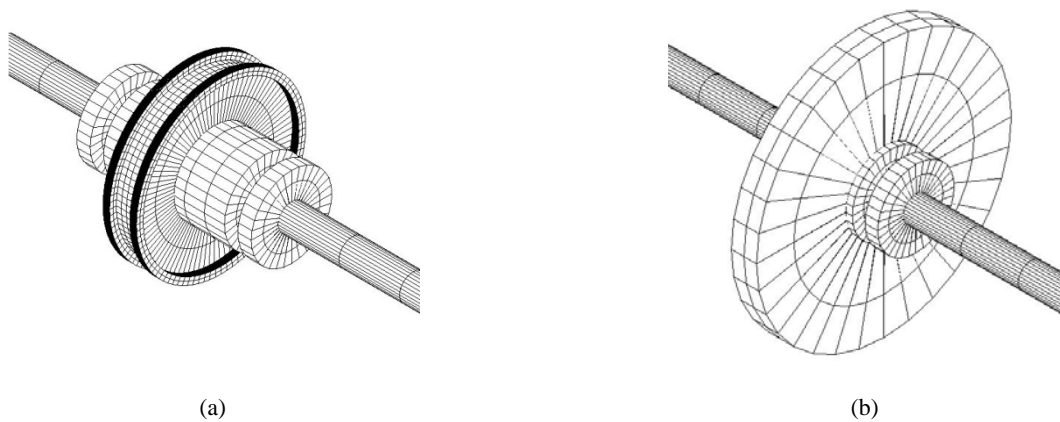


Figure 3 – Details of the Finite element mesh: (a) bearing shell, elastomeric damper and journal; (b) disc and disc hub.

The dynamic characteristics of the bearings were represented by spring-damper elements, Combi214. Each bearing is model with one element. The stiffness and damping coefficients of the fluid film were evaluated based on the short bearing assumption (Vance, 1988). Table 1 presents these coefficients for six different rotating speeds. Figure 4 helps to identify each parameter. The bearings are orthotropic with the following data: bearing #1: length $l_b = 15$ mm, nominal inner diameter $d_b = 60$ mm, radial clearance $c = 65 \mu\text{m}$, shell thickness $t_b = 28$ mm, oil viscosity $\eta = 32$ mPa·s, and is subjected to a static load $F = 98.52$ N; bearing #2 has the same constructive characteristics of the first bearing and is subjected to a load, $F = 101.47$ N.

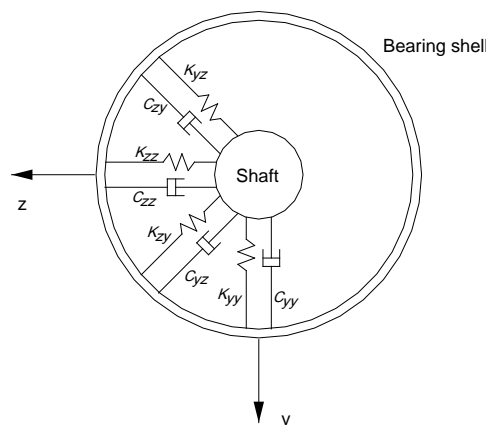


Figure 4 – The eight stiffness and damping parameters.

Table 1 – Dynamic characteristics of the bearings.

	Speed	Kzz	Kzy	Kyz	Kyy	Czz	Czy	Cyz	Cyy
	rpm	N/m	N/m	N/m	N/m	N·s/m	N·s/m	N·s/m	N·s/m
Bearing #1	200	7.780E5	-5.740E4	1.604E6	1.664E6	3.668E4	3.805E4	3.805E4	1.220E5
	1000	3.182E6	-5.147E5	6.246E6	5.866E6	3.306E4	3.105E4	3.105E4	9.606E4
	2000	3.421E6	-1.710E6	6.024E6	3.955E6	2.521E4	1.655E4	1.655E4	4.864E4
	3000	3.558E6	-2.768E6	6.251E6	3.184E6	2.244E4	1.143E4	1.143E4	3.498E4
	4000	3.644E6	-3.782E6	6.691E6	2.777E6	2.109E4	8.754E3	8.754E3	2.891E4
	5000	3.700E6	-4.777E6	7.263E6	2.537E6	2.033E4	7.099E3	7.099E3	2.566E4
Bearing #2	200	7.991E5	-5.003E4	1.659E6	1.743E6	3.721E4	3.909E4	3.909E4	1.260E5
	1000	3.268E6	-4.892E5	6.454E6	6.143E6	3.351E4	3.189E4	3.189E4	9.910E4
	2000	3.512E6	-1.695E6	6.201E6	4.142E6	2.546E4	1.700E4	1.700E4	4.995E4
	3000	3.655E6	-2.758E6	6.407E6	3.328E6	2.261E4	1.174E4	1.174E4	3.575E4
	4000	3.745E6	-3.775E6	6.830E6	2.898E6	2.121E4	8.999E3	8.999E3	2.943E4
	5000	3.804E6	-4.772E6	7.388E6	2.642E6	2.042E4	7.300E3	7.300E3	2.603E4

To model the bearing shell, eight-node, solid elements, Solid185, were employed.

The elastomeric damper was also modeled with Solid 185 elements. The outer flat faces of the elastomeric discs were constrained in all directions, while the inner faces have their displacement constrained only in the axial direction. The viscoelasticity is implemented through the use of two pairs of Prony series [Eq. (1)] defined for shear behavior (Bergström, 2005).

$$G(t) = 1 - \sum_{i=1}^N g_i \left[1 - e^{-t/\tau_i} \right] \quad (1)$$

where G is the dimensionless relaxation modulus and g_i and τ_i are material parameters. These parameters were obtained from tests conducted on a test rig developed in the Laboratory of Mechanical Systems of the School of Mechanical Engineering of the Federal University of Uberlandia (Léporo Neto and Braga, 2008). The viscoelastic properties of the elastomers are presented in the next section.

RESULTS

Unbalance forces can be described as a vector rotating with the same angular speed as the rotor and whose components in the fixed reference frame vary harmonically in time with circular frequency equal to the rotational speed (Genta, 2005). The amplitude of these forces is proportional to the square of the rotational speed. Unbalance response analysis is a powerful tool to verify whether or not a rotor system design will successfully overcome critical speeds without damages caused by excessive vibrations.

Two models were taken as reference for comparing results: a simply supported rotor (SSR) and a rotor supported by fluid film bearings mounted in rigid housings (FFBRH). For all the models presented in this work an unbalance of 0.005 kg·m was introduced in the disc #1 (see Fig. 1). The analyses cover 5000 rpm range. The displacement of the node in which the unbalance force was applied is presented in Fig. 5.

The SSR model presented peaks of 3.45 mm, 8.31 mm and 7.52 mm for the first, second and third critical speeds, respectively. The correspondent magnitudes for the FFBRH model were 2.18 mm, 6.62 mm and 1.06 mm.

One feature of fluid film bearings is to provide damping to rotor system. As can be seen in Fig. 5, the amplitude of the synchronous response of the FFBRH model is lower for all critical speeds when compared to the SSR model. For the third critical speed this reduction is of the order of seven times.

These sets of curves indicate that the second and third critical speeds should be the most troubles for the simply supported condition and although the amplitude for the second critical diminished with the use of fluid film bearing, it still remained higher, compared to the first and third critical speeds.

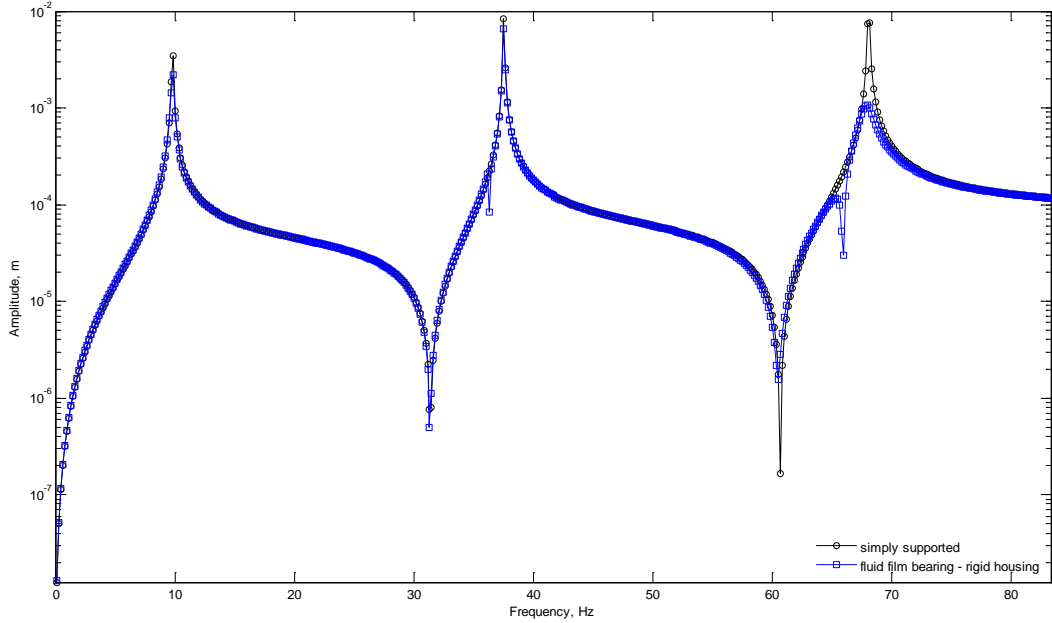


Figure 5 – Unbalance response for the simply supported rotor and for the rotor supported by film fluid bearings on rigid housings.

Influence of the viscoelastic properties

Three different elastomeric materials, named “Sample 30”, “Sample 50” and “Sample 70”, were tested. The properties of these materials are shown on Tab. 2.

Table 2 – Properties of the viscoelastic materials.

	Modulus of elasticity (N/m ²)	Poisson ratio	Density (kg/m ³)	g_1	τ_1	g_2	τ_2
Sample 30	1.658E6		1100	0.4168	0.1994	0.5832	0.0045
Sample 50	2.329E6	0.4998	1150	0.3362	0.0986	0.6638	0.0034
Sample 70	2.810E6		1200	0.3140	0.0935	0.6860	0.0031

In the analysis it was adopted elastomeric disc thickness, $t_e = 5.0$ mm, and width of annulus, $h_e = 5$ mm. The synchronous responses are presented in Fig. 6.

Comparing results for the FFBRH model and the elastomeric dampers models, one can observe that: (1) with the elastomeric dampers more critical speeds appeared in the analyzed frequency range. (2) For the surroundings of the first critical speed the synchronous response of the Samples 30 and 50 suffered a reduction of approximately 50 percent compared to the FFBRH model, while the response of Sample 70 was 65 percent higher. (3) From the 28 Hz to 45 Hz range, the responses of the samples were, at least, 2/3 lower compared to the response on the second critical speed of the FFBRH model. The Sample 70 model presented the lower amplitudes for this range. (4) For higher frequencies, the Sample 30 model presented a higher peak (maximum 2.77 mm) than the other two samples.

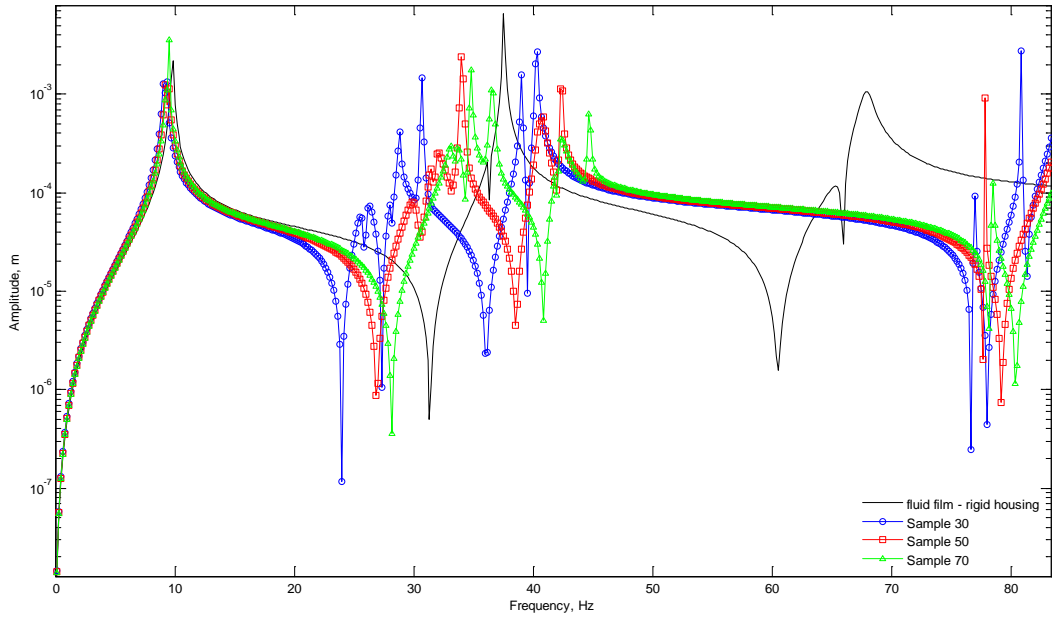


Figure 6 – Influence of the type of elastomer.

Influence of the thickness of the elastomer

In the analysis to investigate the influence of the thickness of the elastomeric discs on the unbalance response, the width of the annulus was kept constant, $h_e = 5.0$ mm. Four different thicknesses were adopted, $t_e = 2.5$ mm, $t_e = 5.0$ mm, $t_e = 7.5$ mm and $t_e = 10.0$ mm. Figures 7 and 8 illustrate the unbalance responses for these different thickness.

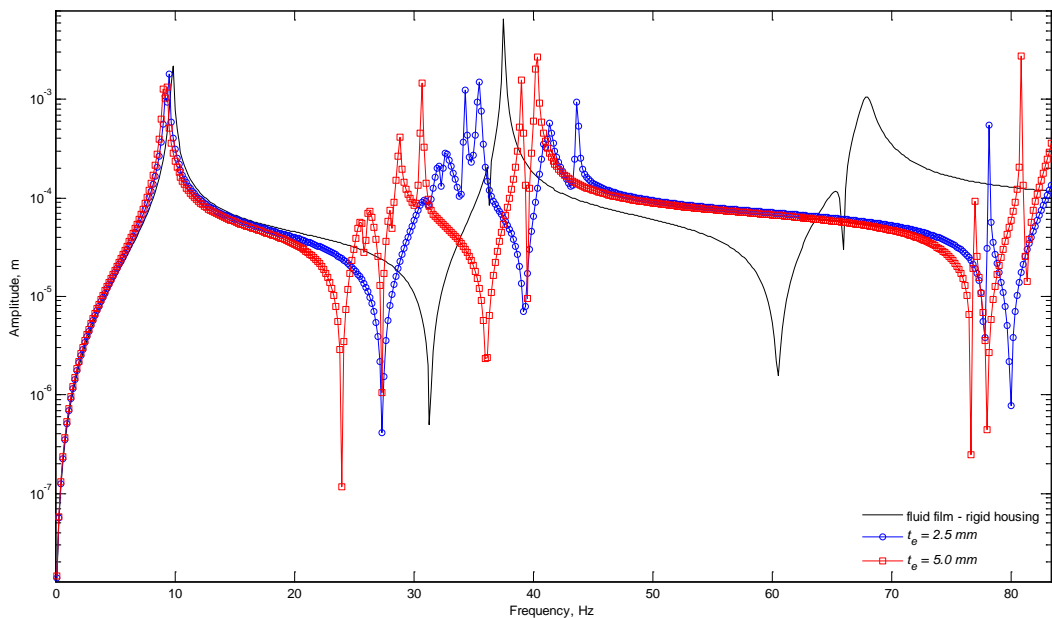


Figure 7 – Influence of the thickness of the elastomer ($t_e = 2.5$ mm and 5.0 mm).

From these results two facts emerged: (1) with the 2.5 mm thick discs a substantial reduction in synchronous response occurred in all frequency ranges of the critical speeds of the FFBRH. (2) For the 5.0 mm thick dampers, the synchronous response was lower for almost the entire frequency range when compared to the FFBRH model, except for the higher frequencies, where a peak of 2.77 mm appeared.

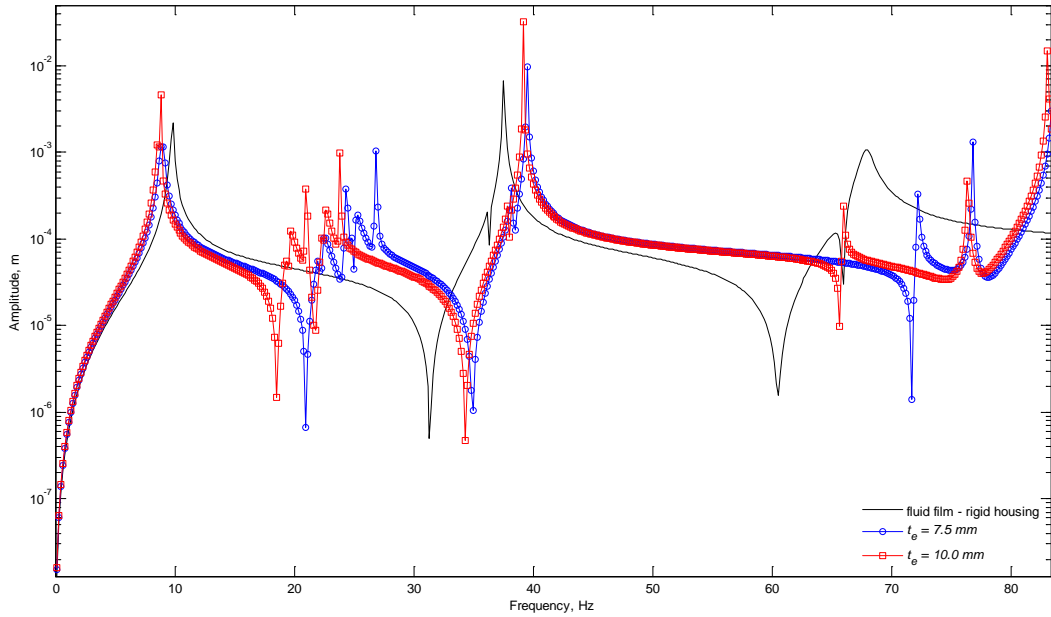


Figure 8 – Influence of the thickness of the elastomer ($t_e = 7.5$ mm and 10.0 mm).

In contrast to the results presented for 2.5 mm and 5.0 mm, the response for the dampers with 7.5 mm and 10.0 mm thick were worse compared to the FFBRH model for almost the entire 5000 rpm range. It can be noted that thicker discs have lower performance when compared to the ones with thinner thickness. In fact, the damper with 7.5 mm thick discs presented lower amplitudes than FFBRH model only for the vicinity of the first critical speed, while the model with 10.0 mm thick discs presented higher amplitudes for all the frequency range. The results for the 10.0 mm thick discs model are worse even when compared to the SSR model.

Influence of the width of the annulus

To investigate the influence of the width of the annulus, the disc thickness was kept constant, $t_e = 2.5$ mm. Three different widths were adopted, $h_e = 2.5$ mm, $h_e = 5.0$ mm, $h_e = 7.5$ mm. The unbalance responses for these cases are shown in Fig 9.

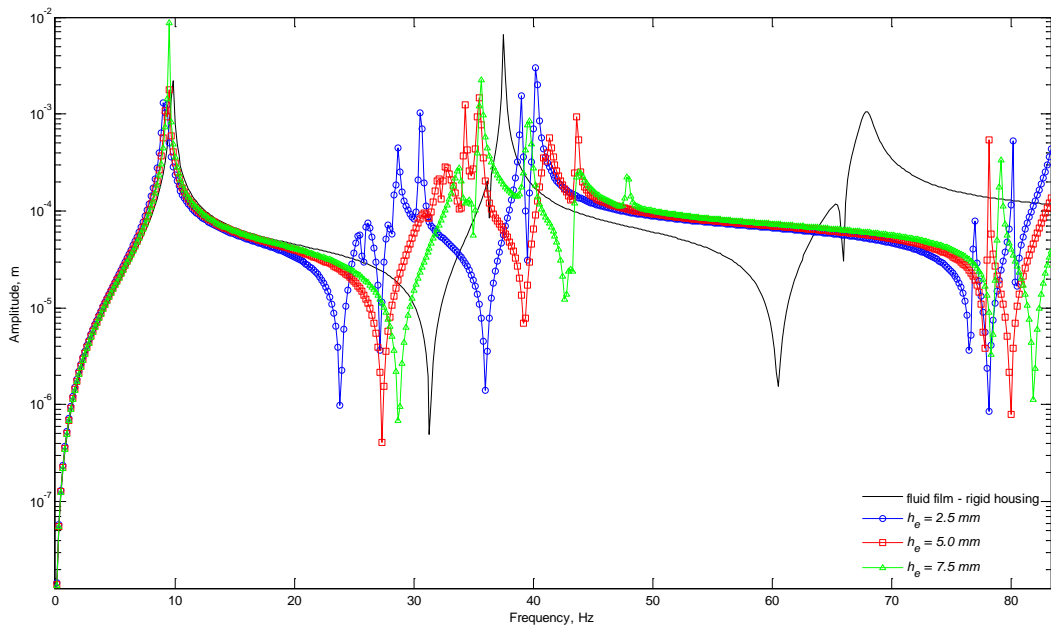


Figure 9 – Influence of the width of the elastomer.

For the surroundings of the first critical speed the models with $h_e = 2.5$ mm and $h_e = 5.0$ mm presented lower amplitudes when compared with the FFBRH model. However the response of the $h_e = 7.5$ mm was four times higher. For the other regions of interest all the models with elastomeric dampers present lower responses than the FFBRH model.

From the above results one can say that the use of elastomeric dampers generally present benefits in order to minimize the unbalance response. However, a judicious choice for the dimensions of the elastomeric discs must be made depending on the operating frequencies, since the effects may be contrary to the reduction of the amplitudes. It must be kept in mind when considering the geometry of the elastomeric damper that effect of column height may be important when considering compressible loads and that bending effects may significantly modify the behavior of elastomers in shear.

DISCUSSIONS

A two-disc rotor supported by fluid film journal bearings was analyzed using the Finite Element Method to verify the influence of the use of elastomeric dampers on the unbalance response of the system. The results presented in this paper give some indication of the influence that the dimensions of the elastomeric discs, as well as the viscoelastic properties may have on the unbalance response.

Elastomers are generally restricted to applications where the temperature is less than 200°C. Even more, these materials are prone to chemical degradation and aging. It should be stressed that these factors were not accounted for in this work. The viscoelastic properties implemented by means of Prony series were obtained through laboratory tests conducted on “moderate” environment at constant temperature.

The static strain preload is another important factor not considered in the analyses herein. Depending on the level of the preload, the stiffness and damping characteristics may suffer significant changes. The influence of this type of loading deserves further investigation.

CONCLUSIONS

Harmonic analyses have been carried out on a flexible rotor supported by fluid film bearings with additional damping provided by elastomeric dampers to study the unbalance response of the system.

Within the scope of the present work, some general remarks may be outlined:

- (i) Improving damping of fluid film bearings with viscoelastic dampers may substantially reduces the unbalance response. The reduction reached eight times lower values when compared to the fluid film bearings mounted on rigid housing on the same region of interest.
- (ii) Care must be taken when choosing the thickness to width ratios for the elastomer, in order to avoid poor responses on certain operating ranges. The worst configuration showed amplitudes almost 9 times higher than the fluid film bearing mounted on rigid housing. The same advice is valid for the choice of viscoelastic material and its properties.
- (iii) The combination of elastomeric damping with rotor balancing can produce good results in controlling synchronous whirling.

For further works, it will be evaluate elastomeric dampers geometries to sustain rotor transients and analyze the effects of the static preload. Future efforts will also be dispended to establish better relationships between the geometry and viscoelastic properties to achieve optimized compact low-cost damping systems for rotordynamics applications.

ACKNOWLEDGMENTS

The authors would like to acknowledge the financial support received from FAPEMIG.

REFERENCES

- Bergström, J. S., 2005, “Calculation of Prony Series Parameters from Dynamic Frequency data”.
- Choudhry, V. V., 2003, “Experimental evaluation of wire mesh for design as a bearing damper”, in Office of Graduate Studies, Texas A&M University, p. 98.
- Genta, G., 2005, “Dynamic of Rotating Systems”, Springer.
- Lee, Y. B. et al., 2004, “Dynamic characteristics of a flexible rotor system supported by a viscoelastic foil bearing (VEFB)”, *Tribology International*, 37(9), p. 679-687.
- Lépore Neto, F. P. and Santos, M. B., 2008, “Parametric analysis of the performance of a viscoelastic damper device”, *Proceedings of the 5th National Congress of Mechanical Engineering, V CONEM, Salvador, Brazil, (in Portuguese)*.
- Lund, J. W., 1965, “The stability of an elastic rotor in journal bearings with flexible, damped supports”, *Journal of Applied Mechanics*, Vol. 32, Transactions ASME, Series E 87, p. 911-920.

- Panda, K. C. e Dutt, J. K., 1999, "Design of optimum support parameters for minimum rotor response and maximum stability limit", *Journal of Sound and Vibration*, 223(1), p. 1-21.
- Shabaneh, N. H. e Zu, J. W., 2000, "Dynamic analysis of rotor-shaft systems with viscoelastic supported bearings", *Mechanism and Machinery Theory*, 35, p. 1313-1330.
- Vance, J. M., 1988, "Rotordynamics of Turbomachinery", John Wiley & Sons.

RESPONSIBILITY NOTICE

The authors are the only responsible for the printed material included in this paper.

DECENTRALIZED H-INFINITY VIBRATION CONTROL OF A PLATE

Alysson Fernandes Mazoni and Alberto Luiz Serpa

Department of Computational Mechanics, Faculty of Mechanical Engineering,
University of Campinas - UNICAMP, Campinas, São Paulo, Brazil
mazoni@fem.unicamp.br, serpa@fem.unicamp.br

Abstract. Robust vibration control has been studied by considering piezoelectric transducers as instrumentation in several works. Depending on the number of sensors and actuators and depending on the structures' size, it is convenient that actuators and sensors work in a decentralized way, in order to have less wiring and a control system that can be robust to faults of transducers. In this work, some \mathcal{H}_∞ controllers are designed to control the vibration of a plate in a decentralized fashion. It is verified through simulations which ones from the set of decentralized controllers are more effective according to various positions of the disturbance signal. The structural model is obtained using finite elements and the control design solution applies the concepts of semidefinite programming through linear matrix inequalities.

Keywords: *Vibration control, H-infinity control, Decentralized control.*

INTRODUCTION

In the vibration control of panels, there is no consensus in literature regarding which control design technique can be considered the most suitable. Several techniques appear to give similar or equivalent results, as shown in the works [Baz and Chen, 2000, Bhattacharya et al., 2002, Hurlebaus et al., 2008]. The computational tractability of techniques based in the theory of robust control, [Zhou and Doyle, 1997], and linear matrix inequalities, [Boyd et al., 1994], give them a slight predominance. Some works that use this computational approach are [Barrault et al., 2007, Barrault et al., 2008, Cheung and Wong, 2009, Halim et al., 2008].

A possible approach for vibration control is the decentralized control, which consists of a control architecture where the control system is composed of several controllers. Each controller accesses a subset of inputs and outputs. Usually the inputs and outputs of a particular controller are spatially close, in order to simplify connections and wiring.

Decentralized control is used for sound irradiation control of plates in [Bianchi et al., 2004], with semi-active control in [Casadei et al., 2010], using an optimal controller with static feedback in [Jiang and Li, 2010] and with decentralized velocity feedback in [Zilletti et al., 2010].

The immediate advantage of a decentralized system is its constructive robustness, since the controllers can be implemented using independent processing systems and the system can continue working suboptimally when an actuator or sensor fails. Another advantage is the numerical simplicity of the controllers, since each one deals with a smaller number of inputs and outputs.

The purpose of this work is to investigate some aspects of the plate vibration control problem for the cases of centralized and decentralized approaches using the \mathcal{H}_∞ control technique. For the solution of this control problem the MATLAB software is employed [Balas et al., 2006].

\mathcal{H}_∞ CONTROL - GLOBAL DESIGN

The \mathcal{H}_∞ control design consists of designing a controller transfer function $K(s)$ in a closed loop with a plant $P(s)$ in order to minimize the \mathcal{H}_∞ norm of the closed loop transfer function $T(s)$ from the disturbance w to the performance z in the frequency domain ω . The loop is usually represented as in Figure 1.

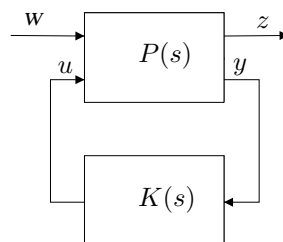


Figure 1: \mathcal{H}_∞ closed loop diagram - w is the disturbance, z is the performance, y is the measured signal and u is the control signal

The \mathcal{H}_∞ norm is obtained as

$$\|T(s)\|_\infty = \sup_{\omega} \bar{\sigma}(T(j\omega)),$$

where $\bar{\sigma}$ is the maximum singular value of the transfer function $T(s)$. This is a measure of the peak frequency response of $T(s)$.

The weighting filters, common in \mathcal{H}_∞ control design as in [Zhou and Doyle, 1997], can be used in the design to weight the performance output and control inputs. A low-pass weighting filter $W_z(s)$ can be used to weight the performance and a high-pass filter $W_u(s)$ can be used to weight the control forces. The common weighting filters transfer functions are:

$$W_p(s) = \left(\frac{s \sqrt[k]{M} + \omega_c}{s + \omega_c \sqrt[k]{\epsilon}} \right)^k, \quad W_u(s) = \left(\frac{s + \omega_c \sqrt[k]{M}}{s \sqrt[k]{\epsilon} + \omega_c} \right)^k,$$

where ω_c is the cut frequency, k is the filter order, M is the gain at pass band and ϵ is the gain at rejection band.

An \mathcal{H}_∞ controller design problem can be written as an optimization problem. The controller $K(s)$ can be obtained by the minimization of the \mathcal{H}_∞ norm of the closed-loop $T(s)$, i.e.,

$$\begin{aligned} & \min_{K(s)} && \|T(s)\|_\infty \\ & \text{subjected to} && K(s) \text{ stable} \\ & && T(s) \text{ stable.} \end{aligned}$$

This optimization problem can be considered a global design, since it involves all the inputs and outputs of the plant. The solution of this optimization problem can be obtained by the solution of the Riccati equations or by the solution of a linear matrix inequality problem [Zhou and Doyle, 1997, Boyd et al., 1994] and it can be obtained using MATLAB Robust Control Toolbox with the `hinfsyn` function, [Balas et al., 2006].

DECENTRALIZED \mathcal{H}_∞ CONTROL

The decentralized control design problem can be obtained by imposing a block-diagonal structure to the controller. If the order of inputs and outputs in the transfer function respects physical proximity, a block diagonal structure for the controller can be obtained such as:

$$K(s) = \begin{bmatrix} K_1(s) & & & \\ & K_2(s) & & \\ & & \ddots & \\ & & & K_p(s) \end{bmatrix},$$

where $K_i(s)$ are the local controllers.

It is difficult to formulate the decentralized control design with a problem structure that can be solved easily. When the optimization problem is formulated through linear matrix inequalities, the requirement to impose a particular structure in the decision variable $K(s)$ represents a mathematical difficulty that can lead to a non-convex problem. This difficulty motivates the investigation of other approaches for the decentralized control.

One alternative is that the original plant can be divided in several local plants with their own inputs and outputs and with spatially close actuators and sensors. In this case, it is possible to design local controllers corresponding to each plant subdivision. The closed-loop can be generated by employing these controllers along with the original plant in all its input and output signals, i.e., it is possible to solve several optimization problems such as

$$\begin{aligned} & \min_{K_i(s)} && \|H_i(s)\|_\infty \\ & \text{subjected to} && K_i(s) \text{ stable} \\ & && H_i(s) \text{ stable.} \end{aligned}$$

where the controllers $K_i(s)$ are obtained. In this case, the closed-loop is a function of all controllers and of the global plant.

Through this approach no additional mathematical development is necessary, since the solution is taken as a combination of solutions of several simultaneous optimization problems.

STRUCTURAL AND CONTROL MODELS

It is considered in this work a finite element model of a plate. The MATLAB codes given in [Ferreira, 2008] were employed to obtain the mass and stiffness matrices. The mesh is shown in Figure 2 and Table 1 shows the physical parameters used in the finite element model of the plate.

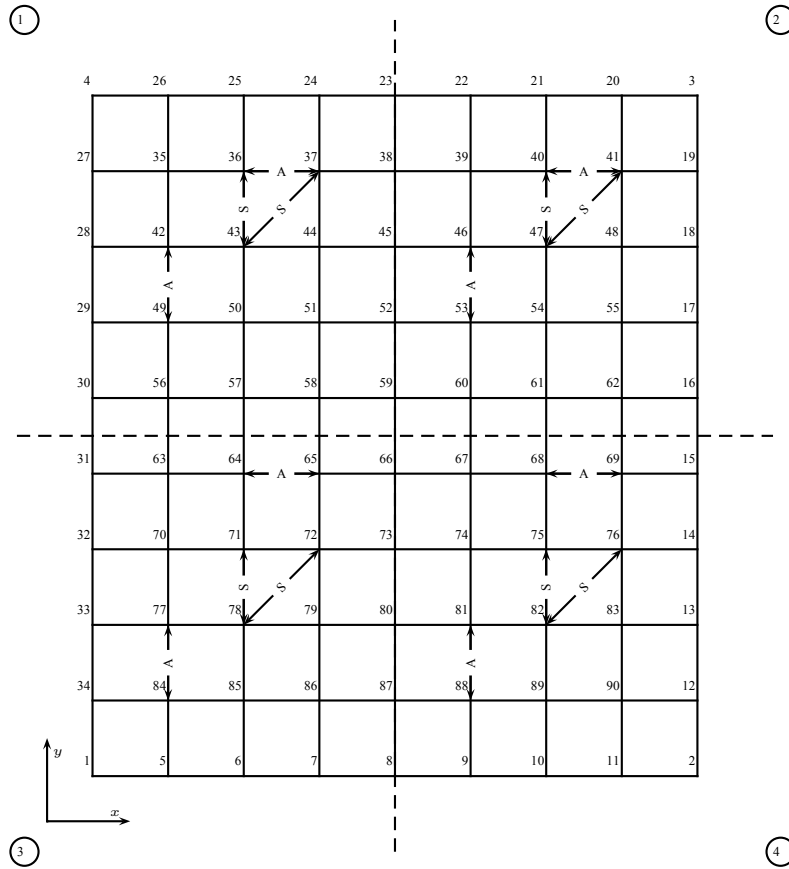


Figure 2: Finite element mesh for the plate with four partitions - A denotes actuators and S denotes sensors

Table 1: Physical properties of the plate

Height	1 m
Width	1 m
Thickness	2 mm
Density	2710 kg/m ³
Poisson Modulus	0.33
Young Modulus	70 GPa

Table 2: Definition and placement of actuators and sensors for the mesh in the Figure 2.

	Actuators			Sensors		
	Number	DOF	Nodes	Number	DOF	Nodes
Disturbance	1 (w)	\odot	86			
Partition 1	2 (u_1)	\leftrightarrow	36 - 37	1 (z_1)	\nearrow	43 - 37
	3 (u_2)	\updownarrow	49 - 42	2 (y_1)	\updownarrow	43 - 36
Partition 2	4 (u_3)	\leftrightarrow	40 - 41	3 (z_2)	\nearrow	47 - 41
	5 (u_4)	\updownarrow	53 - 46	4 (y_2)	\updownarrow	47 - 40
Partition 3	6 (u_5)	\leftrightarrow	64 - 65	5 (z_3)	\nearrow	78 - 72
	7 (u_6)	\updownarrow	84 - 77	6 (y_3)	\updownarrow	78 - 71
Partition 4	8 (u_7)	\leftrightarrow	68 - 69	7 (z_4)	\nearrow	82 - 76
	9 (u_8)	\updownarrow	88 - 81	8 (y_4)	\updownarrow	82 - 75

The Mindlin plate formulation was used in this work [Ferreira, 2008]. The plate finite element has four nodes and three degrees of freedom in each node: rotations in axes x and y and displacement in axis z . The plate in this work was considered with all boundaries free.

In order to have a more realistic dynamic system in the simulations, damping should be taken into account. In this case, it was included a modal damping of 3×10^{-6} to all vibration modes of the plate.

Inputs and outputs

Using \mathcal{H}_∞ control, centralized and decentralized designs are compared with the same configuration of actuators and sensors. It is considered that the actuators and sensors are piezoelectric (PZT).

The actuator receives a voltage and apply a pair of opposite moments in nearby nodes. The sensor generates a voltage proportional to its deformations, i.e., proportional to the difference between angles in nearby nodes. Figure 3 shows schematically the actuator and sensor representation used in this work.

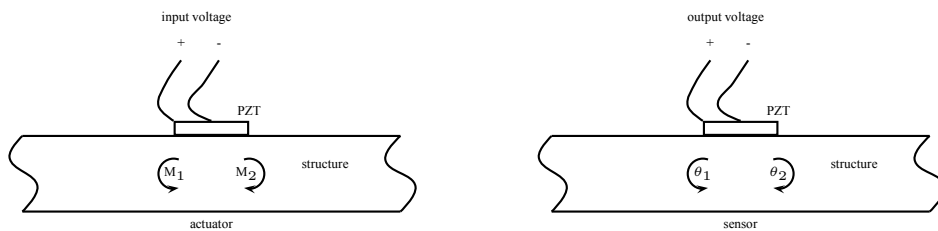


Figure 3: PZT actuator and sensor relations to the respective degrees-of-freedom

There are, in this simplified plate model, three convenient orientations for the transducers: horizontal, vertical and with an orientation of 45 degrees (representing identical actuation in the degrees of freedom in x and y directions of the same node).

CENTRALIZED AND DECENTRALIZED CONTROL SIMULATIONS

The Table 2 shows actuators, sensors and nodes location for the mesh of Figure 2. The arrows indicate the respective degrees of freedom. The partition reveals which actuators and sensors are used in each local model for the decentralized control. The disturbance is considered a force in the z direction applied in the node 86. Actuators numbered from 2 to 9 are chosen as control inputs. Sensors 2, 4, 6 and 8 are measuring outputs. The performance parameters are the sensors numbered as 1, 3, 5 and 7. The uncontrolled system was normalized to have an \mathcal{H}_∞ norm equal to 1 (normalized plant).

The control design is performed using the linear matrix inequalities formulation for the \mathcal{H}_∞ controller design using the function `hinfsyn` of MATLAB 7.2 (default parameters).

The parameters of the weighting filters used in this work are shown in Table 3. The same filters were employed in all simulations of this work.

A simulation test is performed according to the above configuration of inputs and outputs. A linear sine sweep of 7 s from 0 to 1.5 KHz is used as a disturbance signal. Results are shown in figures 4, 5, 6 and 7. The centralized controlled systems has an \mathcal{H}_∞ norm of 0.21. The decentralized controlled system has an \mathcal{H}_∞ norm of 0.35.

Table 3: Weighting filters parameters

	ω_c	k	M	ϵ
$W_z(s)$ - low-pass weight for performance	1500	1	0.1	0.001
$W_u(s)$ - high-pass weight for control force	2000	1	0.1	0.001

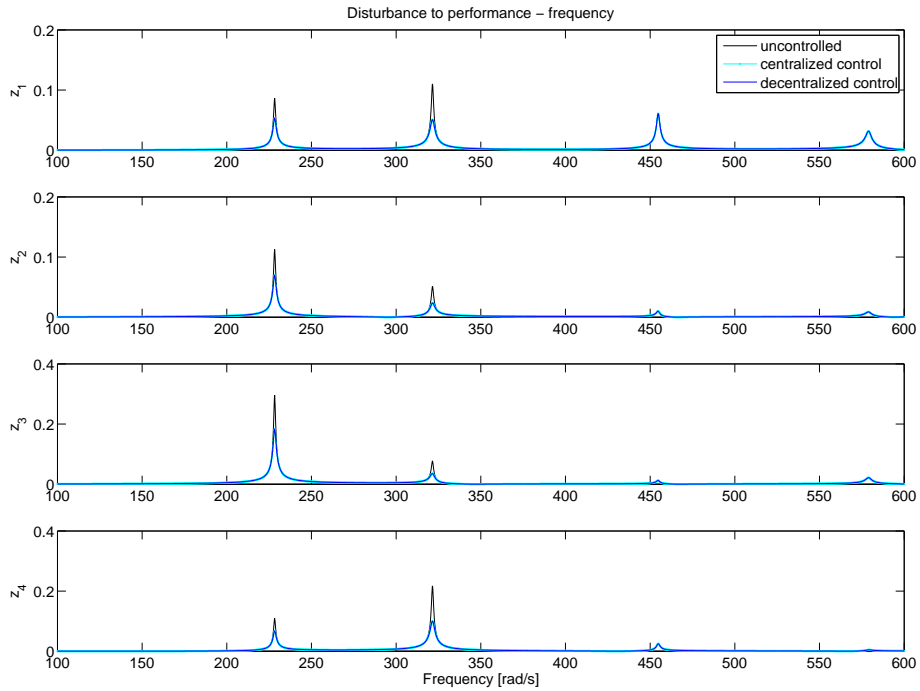


Figure 4: Frequency response from disturbance signal to performance output

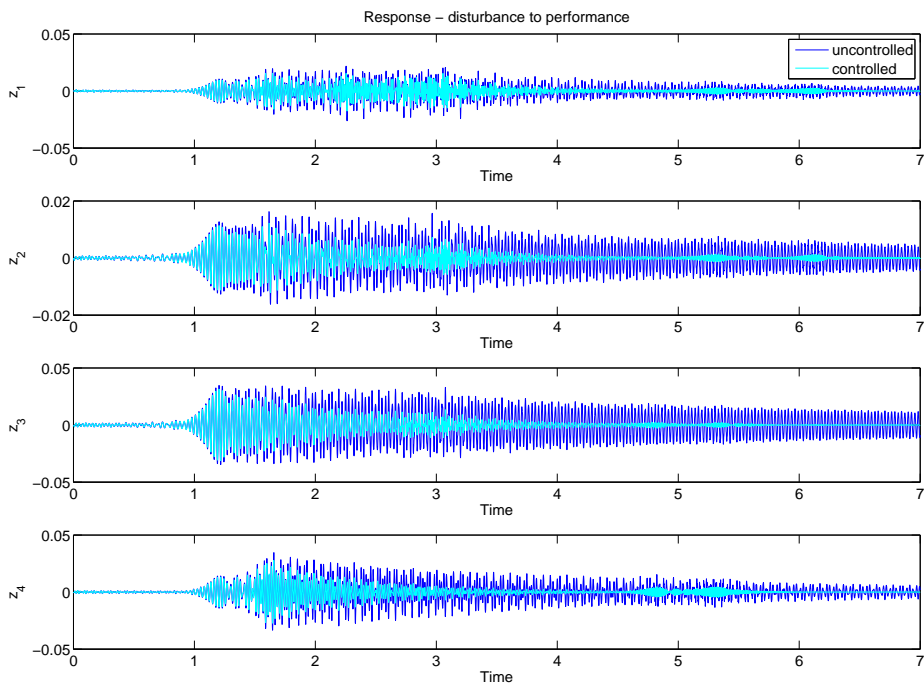


Figure 5: Uncontrolled and centralized control - time response from disturbance signal to performance output

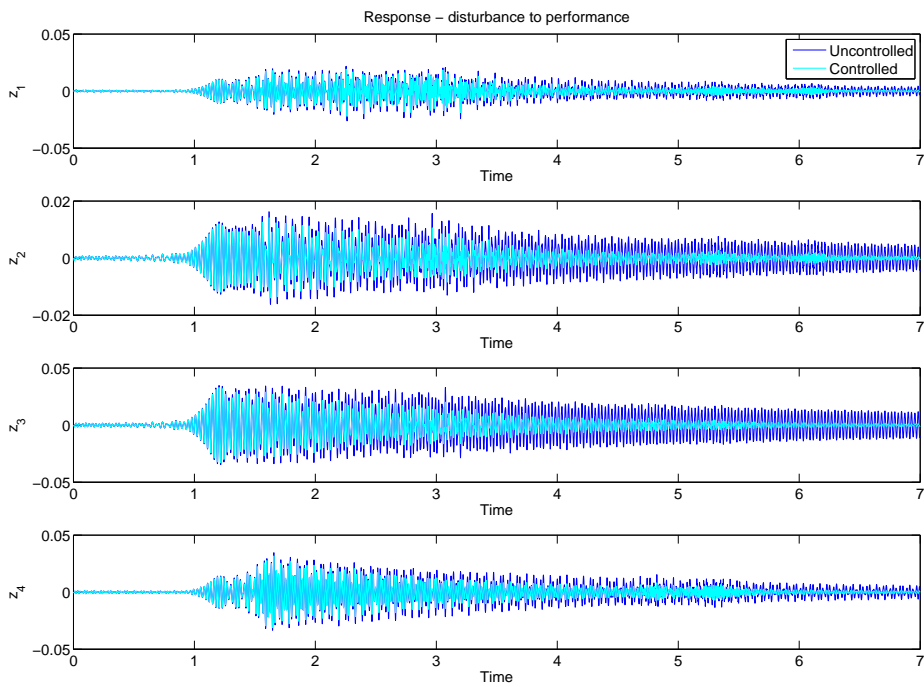


Figure 6: Uncontrolled and decentralized control - time response from disturbance signal to performance output

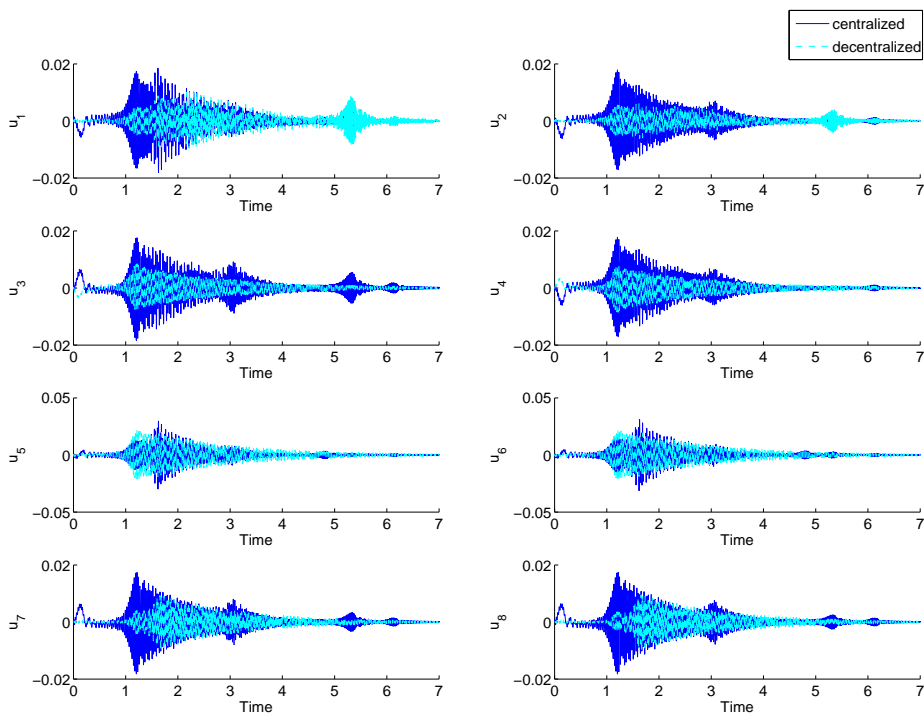


Figure 7: Centralized and decentralized control - control signal

EFFECTS OF DISTURBANCE PLACEMENT

Using the previous problem configuration, but changing only the node where the disturbance force is applied, a simulation can be conducted to evaluate the effect of the disturbance placement in the centralized and decentralized control approaches. In the following simulated cases, the disturbance position, always in z direction, was changed from node 35 to 90. Figure 8 show two-dimensional plots where the coordinate pair (x, y) stands for a position of the disturbance in the plate and the z axis indicates the \mathcal{H}_∞ norm achieved.

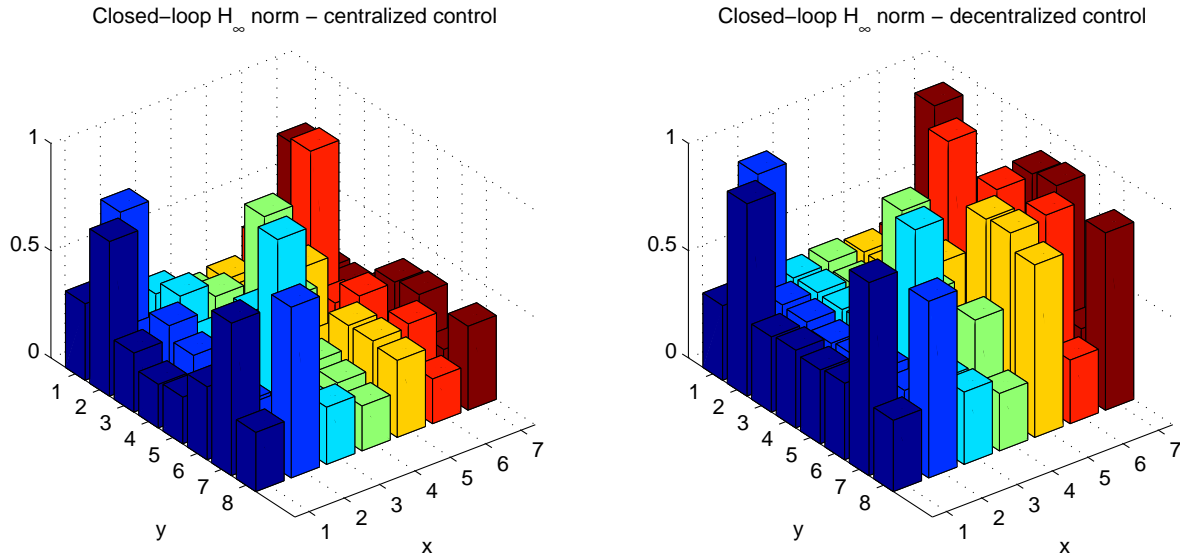


Figure 8: Centralized and decentralized control - \mathcal{H}_∞ norm for each position of the disturbance

Figure 8 shows that the centralized control produces a larger norm reduction than the decentralized case, however with a small difference. It is possible to see that the decentralized control can be considered a viable approach in terms of the \mathcal{H}_∞ norm reduction, allowing to exploit the advantages of the decentralized approach. Notice that the uncontrolled plate presents \mathcal{H}_∞ norm equal to 1 (normalized system).

A comparison of the control signal energy is given for each of the eight actuators in figures 9 and 10. This signal is calculated based on the time response as $\sum_i u_i^2$, where i denotes time instant. The control signal energy shows that decentralized control uses, in general, less control energy in majority of actuators, except for those which are very close to the disturbance application point.

CONCLUSIONS

For the case of the vibration control of plate with four decentralized controllers, the results show that decentralized control presents comparable results to centralized control, which allows its practical application. Centralized control can demand more complex equipment and can be considered less robust in case of failures when compared to the decentralized approach. Decentralized control can be a potentially simpler configuration and can lead to a more robust implementation. In the case of the example considered in this work, the decentralized control used less control energy in most cases. The aspect of energy distribution requires a more detailed investigation, considering also other decentralized control placement distribution.

A future investigation is related to the stability of the decentralized case, since each decentralized control can affect the others. In this work, this aspect was checked by the direct verification of the closed-loop stability, but only for the specific configuration of the four decentralized controllers considered here.

ACKNOWLEDGMENTS

The authors thank to CAPES (Coordenação de Aperfeiçoamento de Pessoal de Nível Superior, Ministério da Educação, Brazil) for the financial support.

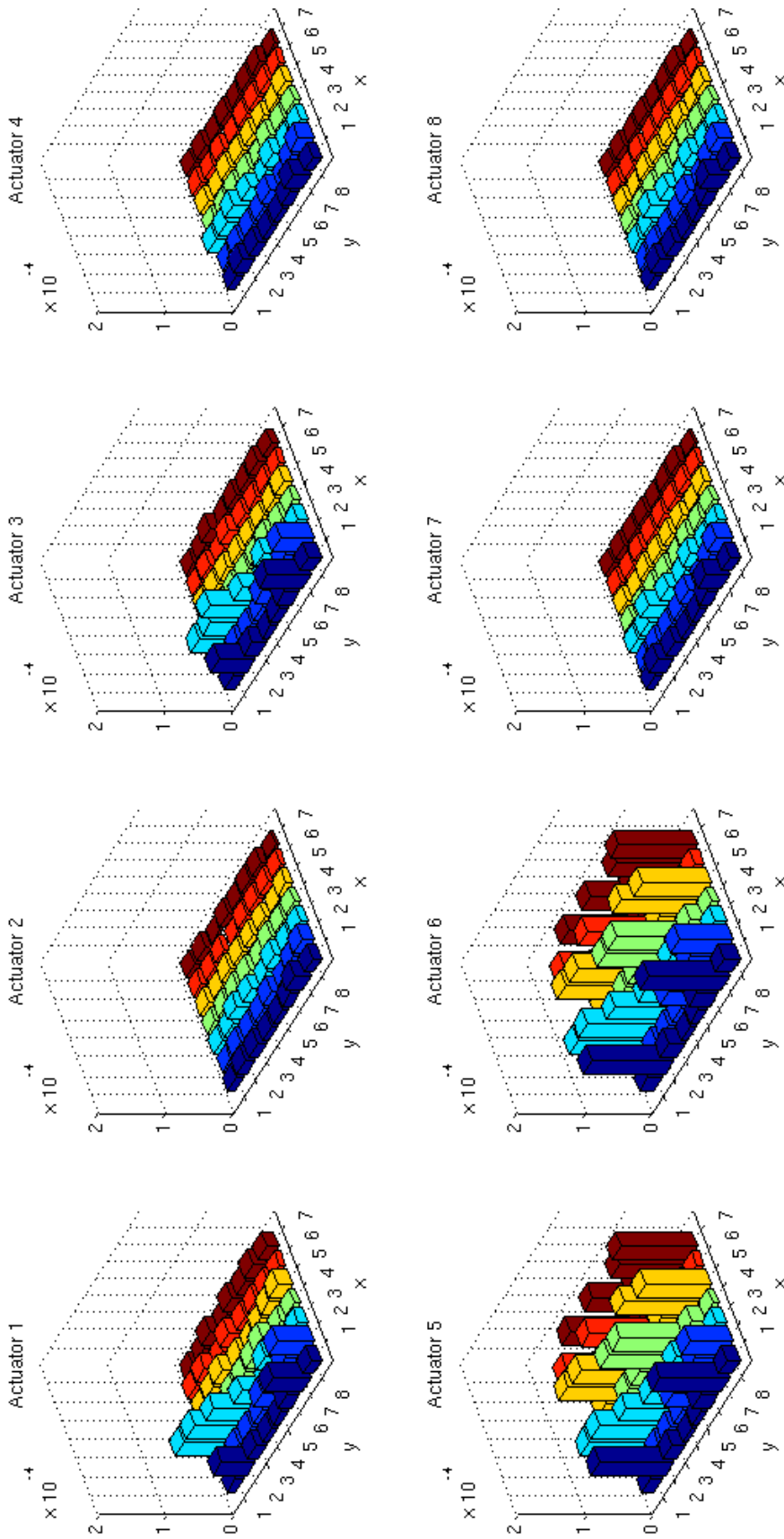


Figure 9: Centralized control - control energy for each actuator related to each position of the disturbance.

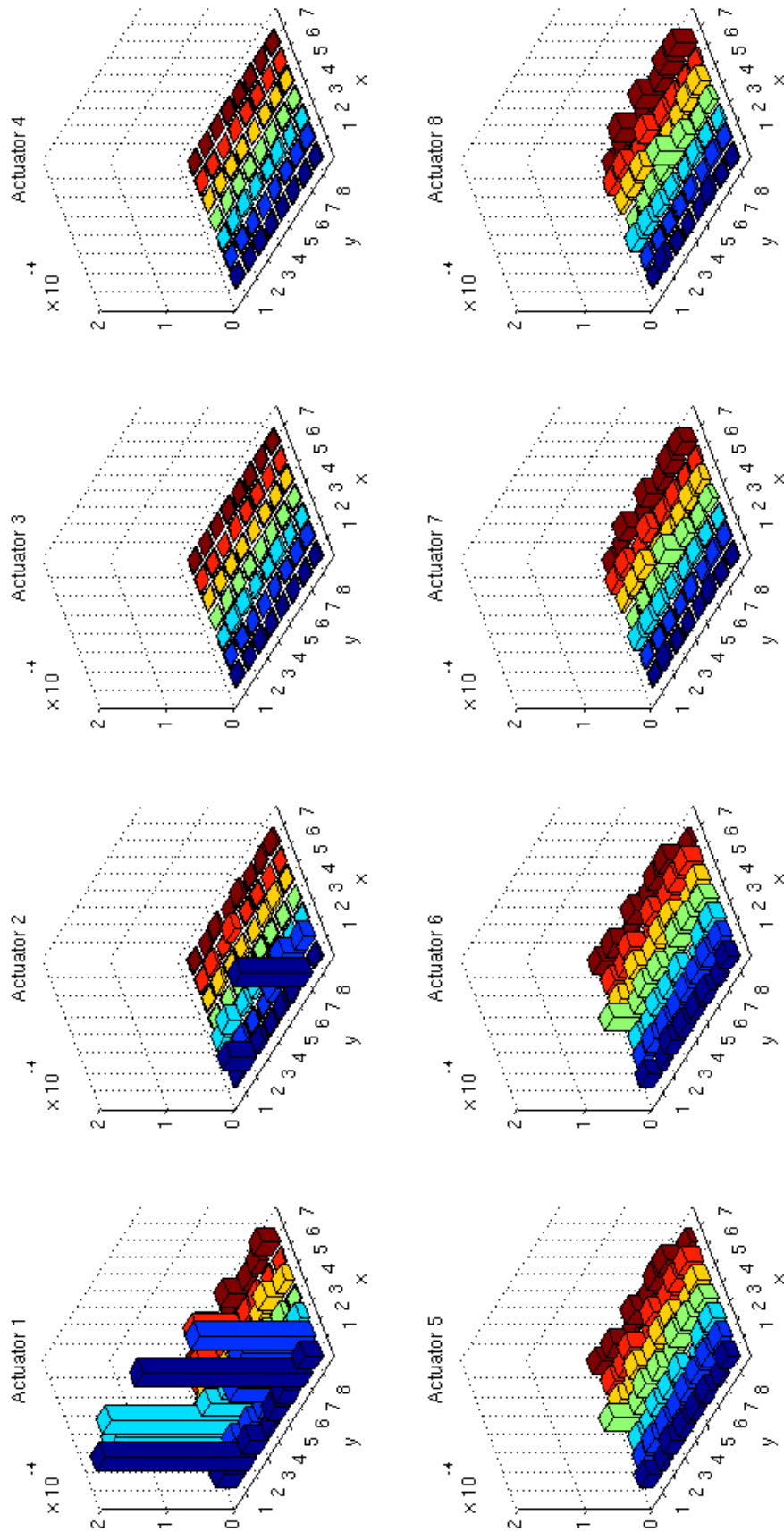


Figure 10: Decentralized control - control energy for each actuator related to each position of the disturbance.

References

- [Balas et al., 2006] Balas, G., Chiang, R., Packard, A., and Safonov, M. (2006). *Robust Control Toolbox: User's Guide*. The Mathworks.
- [Barrault et al., 2007] Barrault, G., Halim, D., Hansen, C., and Lenzi, A. (2007). Optimal truncated model for vibration control design within a specified bandwidth. *International Journal of Solids and Structures*, 44(14-15):4673 – 4689.
- [Barrault et al., 2008] Barrault, G., Halim, D., Hansen, C., and Lenzi, A. (2008). High frequency spatial vibration control for complex structures. *Applied Acoustics*, 69(11):933 – 944.
- [Baz and Chen, 2000] Baz, A. and Chen, T. (2000). Control of axi-symmetric vibrations of cylindrical shells using active constrained layer damping. *Thin-Walled Structures*, 36(1):1 – 20.
- [Bhattacharya et al., 2002] Bhattacharya, P., Suhail, H., and Sinha, P. K. (2002). Finite element analysis and distributed control of laminated composite shells using lqr/imsc approach. *Aerospace Science and Technology*, 6(4):273 – 281.
- [Bianchi et al., 2004] Bianchi, E., Gardonio, P., and Elliott, S. J. (2004). Smart panel with multiple decentralized units for the control of sound transmission. part iii: control system implementation. *Journal of Sound and Vibration*, 274(1-2):215 – 232.
- [Boyd et al., 1994] Boyd, S., El Ghaoui, L., Feron, E., and Balakrishnan, V. (1994). *Linear Matrix Inequalities in System and Control Theory*, volume 15 of *Studies in Applied Mathematics*. SIAM, Philadelphia, PA.
- [Casadei et al., 2010] Casadei, F., Ruzzene, M., Dozio, L., and Cunefare, K. A. (2010). Broadband vibration control through periodic arrays of resonant shunts: experimento investigation on plates. *Smart materials and structures*, 19.
- [Cheung and Wong, 2009] Cheung, Y. and Wong, W. (2009). H_∞ and H_2 optimizations of a dynamic vibration absorber for suppressing vibrations in plates. *Journal of Sound and Vibration*, 320(1-2):29 – 42.
- [Ferreira, 2008] Ferreira, A. (2008). *MATLAB Codes for Finite Element Analysis: Solids and Structures*. Springer Publishing Company, Incorporated.
- [Halim et al., 2008] Halim, D., Barrault, G., and Cazzolato, B. S. (2008). Active control experiments on a panel structure using a spatially weighted objective method with multiple sensors. *Journal of Sound and Vibration*, 315(1-2):1 – 21.
- [Hurlebaus et al., 2008] Hurlebaus, S., Stöbener, U., and Gaul, L. (2008). Vibration reduction of curved panels by active modal control. *Comput. Struct.*, 86(3-5):251–257.
- [Jiang and Li, 2010] Jiang, J. and Li, D. (2010). Decentralized guaranteed cost static output feedback vibration control for piezoelectric smart structures. *Smart Materials and Structures*, 19(1):015018.
- [Zhou and Doyle, 1997] Zhou, K. and Doyle, J. C. (1997). *Essentials of Robust Control*. Prentice Hall.
- [Zilletti et al., 2010] Zilletti, M., Elliott, S. J., and Gardonio, P. (2010). Self-tuning control systems of decentralised velocity feedback. *Journal of Sound and Vibration*, 329(14):2738 – 2750.

Workspace Analysis of a Cable-Based Parallel Manipulator for Rehabilitation of Shoulder Movements

Wilgo Moreira Nunes¹, José Francisco Ribeiro², João Carlos Mendes de Carvalho³, and Rogério Sales Gonçalves⁴

¹ Federal University of Uberlândia, Uberlândia, Brazil, wilgomoreira@gmail.com

² Federal University of Uberlândia, Uberlândia, Brazil, jribeiro@mecanica.ufu.br

³ Federal University of Uberlândia, Uberlândia, Brazil, jcmendes@mecanica.ufu.br

⁴ Federal University of Uberlândia, Uberlândia, Brazil, rsgoncalves@mecanica.ufu.br

Abstract: This paper presents a new cable driven parallel structure for rehabilitation of the movements of the human shoulder. The robotics structure consists of four cables that allow the movement of vertical flexion-extension, abduction-adduction and horizontal flexion-extension with different limits of movement and speed. The development of this robotic device is justified by the large number of people with shoulder problems. These problems are due of stroke, polio, arthritis, disaster recovery and can be applied to movements of physical therapy. The kinematics model of cable-base parallel robots is obtained similarly to the model obtained from traditional parallel structures. The static force analysis is made using the Jacobian matrix. The analysis of the workspace of the proposed structure is performed considering the circumduction motion of the human arm. Finally the numerical simulations of the cable-base parallel structure for rehabilitation of the movements of the human shoulder are presented.

Keywords: Shoulder, Rehabilitation, Cable-base parallel manipulator, Workspace

INTRODUCTION

The science of rehabilitation showed in most cases that repeated movements of human members can help the patient regain the functions of the member injury. Robots for these tasks can be more efficient in performing these exercises than humans. Robotic systems for rehabilitation can be generally used to record information like position, trajectory, force and velocity exploiting the motor performance during active movements, and to guide the movement of a patient limb attached to the device. All the data can be archived and then compared to check the progress of patients on therapy.

Different robotic architectures have been developed and applied in rehabilitation. The most successful example of a robot designed for neuro rehabilitation is probably the MIT-Manus (Krebs et al., 2004), developed at Massachusetts Institute of Technology (MIT). The MIT-Manus robot consists of two degrees of freedom serial robot that may influence or interact with the patient's arm over a working plan. Despite the effectiveness of the MIT-Manus has been proven by clinical trials this robot can not provide all types of motion required by conventional therapy, especially the outlaws of the plan, besides the high cost of US\$ 60,000.

A three-dimensional workspace is usually obtained by serial robots with multiple degrees of freedom. Some examples are: ARM (Assisted Rehabilitation and Measurement), despite this robot allow three-dimensional movements its structure is heavy and the quality of movement is affected by the high inertia of the system (Kahn et al., 2006); the MIME (Mirror-Image Movement Enabler) is a Puma robot model 562 with 6 degrees of freedom which is attached to the patient's arm by moving it into pre-trajectories programmed (Lum et al., 2002) but due to its characteristic of producing high forces and speeds and to need an operator industrial robots this structure does not represent a viable tool for rehabilitation assistance, in addition to high cost; Armin is an exoskeleton with 6 degrees of freedom (Nef and Riener, 2005) that can be fixed around the patient's arm and provide all the physiotherapy movements, the main disadvantage of this robot is the complexity of adjusting the parameters of the arm for different patients and complex construction due to the high number of mechanical components; another robotic system applied to rehabilitation is REHAROB (Rehabilitation Robot), a robotic system based on two industrial robots from ABB (Fazekas et al., 2007) that allow three-dimensional movements by moving the forearm and arm, but this system has disadvantages such as the inability to transport and the prohibitive cost around US\$ 150,000.

These serial robots are heavy machines that are not easily transportable, have high prices, pose risks to patients with fractures, but their major drawback is the resistance of patients to use these systems. Due to the problems presented in the use of industrial robots in the treatment of rehabilitation, the cables-based parallel manipulators are an alternative.

The cable-based parallel manipulator consists of a moving platform, which can carry an end-effector and a base. These two elements are connected by multiple cables that can extend or retract, Fig. 1. A cable-based manipulator can

move the end-effector by changing the cables lengths while preventing any cables becoming slack. Therefore, feasible tasks are limited due to main static, or dynamic, characteristics of the cables because they can only pull the end-effector but do not push it (Cannella et al., 2008). A classification of cable-driven parallel manipulators is given for a manipulator “fully-constrained” and “underconstrained”. A scheme for these two types is shown in Fig. 1. The first class, Fig. 1(a), the pose of the end-effector can be completely determined by the cables configuration. For the second class, Fig. 1(b), the position and orientation of the end-effector can not be completely defined by cables configurations and the gravity effect can be considered (Hiller et al., 2009).

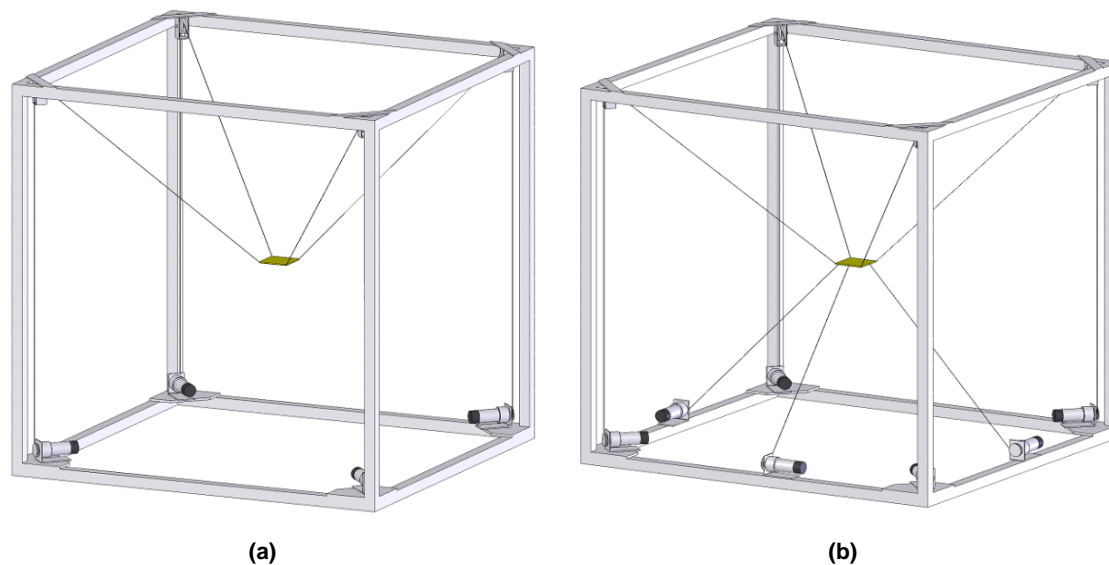


Figure 1 – Types of cables-based parallel manipulators. (a) underconstrained; (b) fully-constrained (Cannella et al., 2008).

These structures have characteristics that make them suitable for rehabilitation purposes. They have large workspace which may be adapted to different patient and different training. The mechanical structure is easy to assembly and disassembly and can be reconfigured in order to perform different therapies and can be easy to transportation, the actuators are often located on the fixed base and the structure can be reconfigured only by changing the actuators positions or the attachment points of the cables. The structures are modularity and have good inertial behavior as due to the fact that this kind of systems has small moving masses consisting of cables and end-effector. Such kinds of manipulators have low cost and simple maintenance which are relevant characteristics for possible commercial system to be used by patients at home. In the clinical point the use of cables instead to rigid links makes the patient feel less constrained and is important because it helps the acceptance of a new technology. These characteristic makes the cable driven parallel structures ideal for rehabilitation (Homma et al., 2002). The drawbacks related to the use of cable driven parallel structure are the physical nature of cables that can only pull and not push and the workspace evaluation becomes forces dependent and can have a complex and irregular shape (Hiller et al., 2009).

Some examples of these structures are described. The Calowi (Cassino Wire Low-cost robot) has architecture 4-4, four cables connected to the end-effector in four different transmission system with pulleys. The cables are actuated by four DC motors which can extend and retract the cables. This structure is intended as low cost manufacturing applications with different purposes as: helping the elderly and patients with lower limb problems in operations to sit and get up; rescue in disaster areas, or transportation of persons in hospital rooms (Cannella et al., 2008). Mayhew et al. (2005) developed the MACARM (Multi-Axis Cartesian-based Arm Rehabilitation Machine), a robot that is actuated by cables for rehabilitation of human upper limbs. The NeReBot (NeuroRehabilitation robot) have three degrees of freedom and is designed for rehabilitation of patients with upper limb problems. Its operating principle is simple: once the patient's forearm is fixed in splint (or orthosis) the machine can produce stimuli in the upper limbs by pulling three cables of nylon (Fanin et al., 2003, Rosati et al., 2005). MariBot (Marisa robot) is an evolution of NeReBot and have five degrees of freedom. It is a hybrid formed by a plan serial robot manipulator with 2 degrees of freedom used to position the cables on the plan, and a parallel structure actuated by cables with three degrees of freedom that allows the movements of the upper limb of patients in rehabilitation treatments (Rosati et al., 2005).

Thus, this paper presents a new cable driven parallel structure for rehabilitation of the movements of the human shoulder. The robotics structure consists of four cables that allow the movements of vertical flexion-extension, abduction-adduction and horizontal flexion-extension with different limits of movement and speed. The development of this robotic device is justified by the large number of people with shoulder problems. These problems are due of stroke, polio, arthritis, disaster recovery, and can be applied to movements of physical therapy. First the shoulder movements are presented. After, the kinematics model of cable-base parallel robots is obtained similarly to the model obtained from traditional parallel structures. The static force analysis is made using the Jacobian matrix. The analysis of the workspace

of the proposed structure is performed considering the circumduction motion of the human arm. Finally the numerical simulations of the cable driven parallel structure for rehabilitation of the movements of the human shoulder are presented.

SHOULDER MOVEMENTS

The shoulder is the proximal joint of the upper limb that has three degrees of freedom (Kapanji, 2000). It is the articulation of the human body that promotes the arm movements in the three planes of space: Plan A - Sagittal; Plan B - Front and Plan C - Horizontal, Fig. 2(a), in for three main axes: Cross Axis (1), anterior-posterior Axis (2) and Vertical Axis (3), Fig. 2(b).

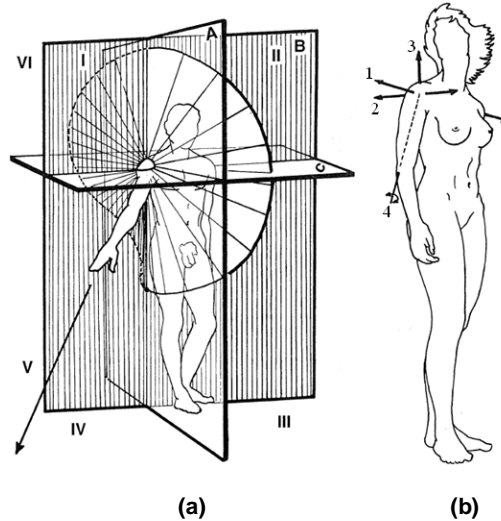


Figure 2 – (a) Plans for analysis of shoulder movements; (b) axes of movement of shoulder (Kapanji, 2000).

The shoulder joint has the following movements: horizontal Flexion and Extension, Adduction/Abduction, vertical Flexion and Extension and Medial Rotation. A scheme for shoulder movements is shown in Fig. 3. The range shoulder are: vertical flexion 0° to 180°; vertical extension 0° to -45/-50°, abduction 0° to 180°; adduction 180° to 0°; horizontal flexion 0° to 140° and horizontal extension 0° to -30/-40° (Kapanji, 2000).

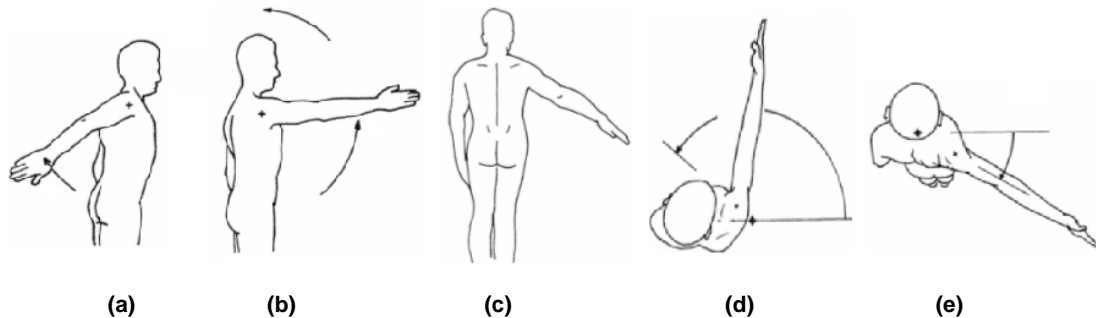


Figure 3 – Shoulder movements. (a) Vertical Extension; (b) Vertical Flexion; (c) Abduction; (d) Horizontal Flexion; (e) Horizontal Extension (Kapanji, 2000).

KINETOSTATIC MODELING

The cable-based parallel manipulator 4-2, proposed in this paper, is formed by four cables arranged in a rigid structure (fixed platform) having two attachment points on the splint (moving platform), Fig. 4(a). The cables are represented by the lengths ρ_1, ρ_2, ρ_3 and ρ_4 and are connected to motors attached to pulleys at points P_1, P_2, P_3 and P_4 respectively. The points $v_1 = v_3$ and $v_2 = v_4$ correspond to the connection points of cables ρ_1, ρ_3, ρ_2 and ρ_4 in the splint respectively, Fig. 4(b). The distances between the points P_1 and P_2, V_1 and V_2 are adjustable depending on the size of the patient's arm. The cable-based parallel manipulator 4-2 allows three-dimensional motion of the arm from a desired trajectory. Figure 4(c) shows the prototype built at the Laboratory of Robotics and Automation at Federal University of Uberlândia. Figures 4(a) and 4(c) show the elements of the cable-based parallel manipulator 4-2, consisting of four sets formed by DC motor 24 volts and 45 Nm torque, encoder 500 pulses per revolution and pulley. In this first step toward implementation of graphic simulations and future experimental tests will be used a wooden puppet anthropometric from 1.80 m to simulate human body, Fig. (4c).

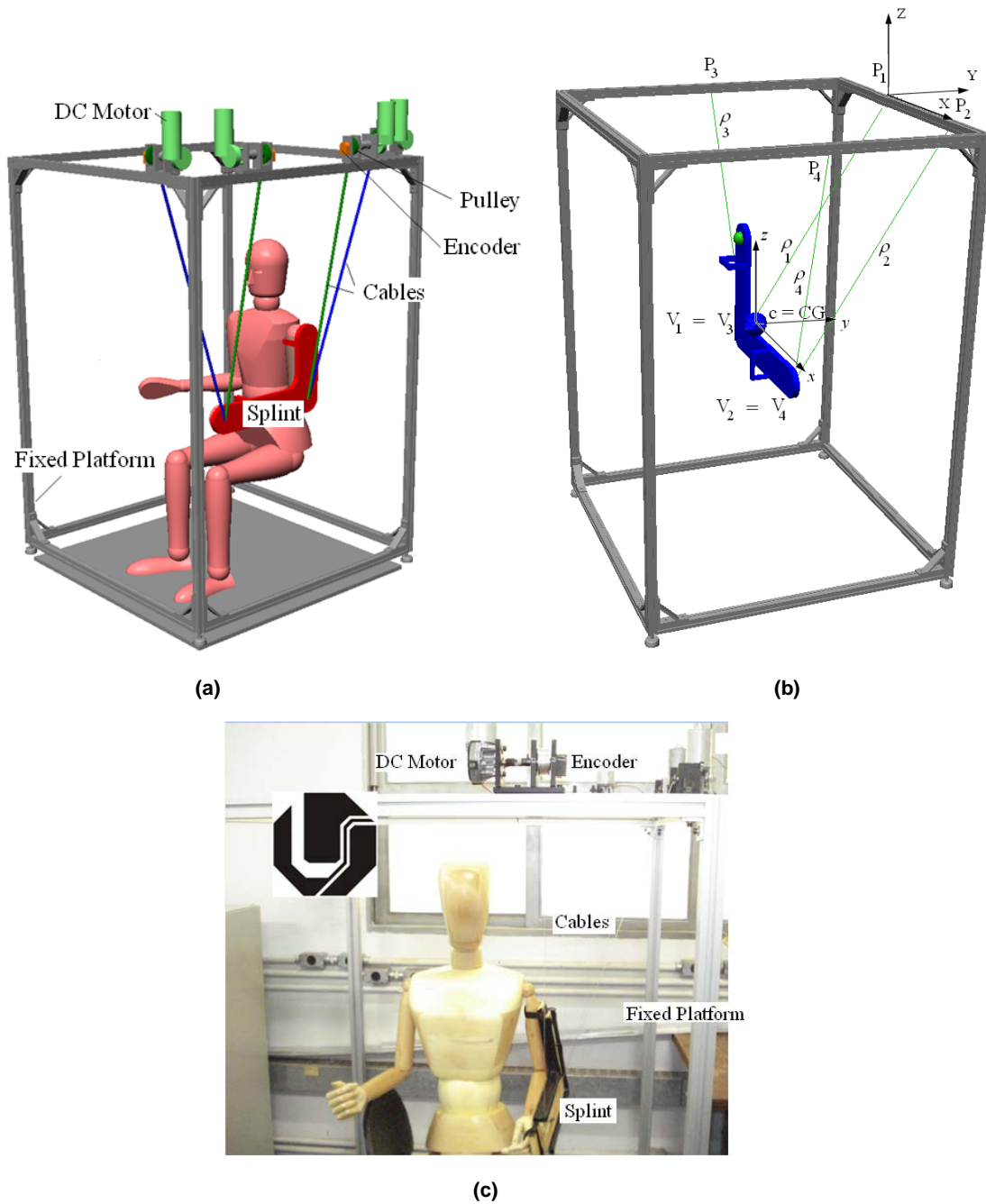


Figure 4 – (a) Scheme of the proposed parallel structure 4-2; (b) Parameters of parallel structure 4-2; (c) Prototype build.

The kinematics model of cable-base parallel robots is obtained similarly to the model obtained from traditional parallel structures (Côté, 2003). The inverse kinematic problem consists in finding the cables lengths, ρ_i , as function of the end-effector pose. The forward kinematic problem consists of finding the end-effector poses for a given set of cables lengths ρ_i . For the kinematic model, the used parameters are shown in Fig. 4(b) and 5. The kinematic variables are the cables lengths ρ_i .

The inverse kinematic model of the proposed parallel structure 4-2 can be found by

$$\begin{aligned}
 \rho_i &= \|c + Qv_i - p_i\| \\
 \rho_i^2 &= (c + Qv_i - p_i)^T (c + Qv_i - p_i) \\
 \rho_i^2 &= c^T c + 2c^T Qv_i - 2c^T p_i + v_i^T v_i - 2p_i^T Qv_i + p_i^T p_i
 \end{aligned} \tag{1}$$

$$Q = \begin{bmatrix} \cos \beta \cos \gamma & -\cos \beta \sin \gamma & \sin \beta \\ \sin \theta \sin \beta \cos \gamma + \cos \theta \sin \gamma & -\sin \theta \sin \beta \sin \gamma + \cos \theta \cos \gamma & -\sin \theta \cos \beta \\ -\cos \theta \sin \beta \cos \gamma + \sin \theta \sin \gamma & \cos \theta \sin \beta \sin \gamma + \sin \theta \cos \gamma & \cos \theta \cos \beta \end{bmatrix} \quad (2)$$

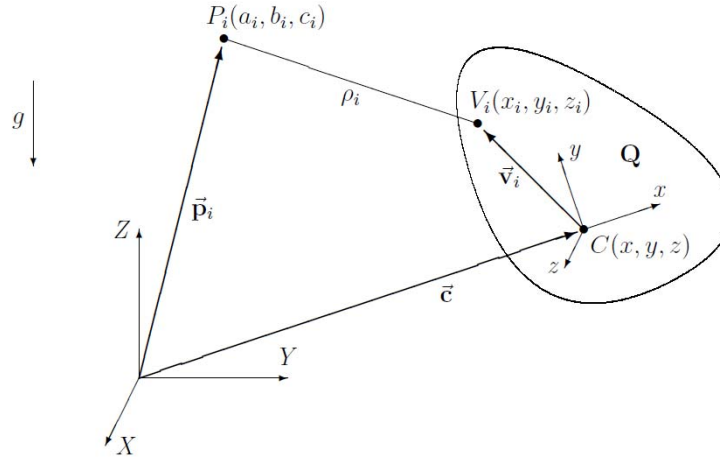


Figure 5 – Kinematic variables (Côté, 2003).

With i varying from 1 to n (number of cables), where: p_i is the position vector of point P_i with components a_i , b_i and c_i in relation to fixed reference point, v_i is the position vector of point V_i with components x_i , y_i and z_i for the moving frame, $C(c_x, c_y, c_z)$ is the position vector of center of gravity of the moving platform, Q is the rotation matrix between fixed and moving frame obtained by a rotation of θ about x-axis followed by a second rotation β about the new y-axis and a third rotation γ about the new z-axis and ρ_i is the distance between points P_i and V_i (cable length i) (Gonçalves and Carvalho, 2010).

Static Force Analysis

The static force analysis is made considering that all cables must remain in tension under any load. When a manipulator performs a given task, the end-effector exerts force and moment on the external environment in the case of cable driven parallel structure forces are transmitted by extending and retracting cables and by ensuring the condition of pulling cables. The static force analysis is important in order to determine the quality of force transmission which is a fundamental aspect of the energetic efficiency of the manipulator and in the case of cable driven parallel structure is necessary to determination of the feasible workspace.

As the speed of cable is low, in the proposed cable-based parallel manipulator 4-2, the analysis can be based on a static model of forces. For this analysis, it is necessary to calculate the Jacobian. The Jacobian is the matrix composed of the partial derivatives of each cable with the design variables, which in the case are the coordinates and angles of the mobile platform relative to inertial reference. For the proposed cable-driven parallel manipulator the Jacobian matrix can be obtain by Eq. 3 which is a 4x6 matrix, because there are four actuated joints. The Jacobian matrix is therefore rectangular and to calculate its inverse a numerical technique must be used to find the pseudo-inverse.

$$J = \begin{bmatrix} \frac{\partial \rho_1}{\partial c_x} & \frac{\partial \rho_1}{\partial c_y} & \frac{\partial \rho_1}{\partial c_z} & \frac{\partial \rho_1}{\partial \theta} & \frac{\partial \rho_1}{\partial \beta} & \frac{\partial \rho_1}{\partial \gamma} \\ \frac{\partial \rho_2}{\partial c_x} & \frac{\partial \rho_2}{\partial c_y} & \frac{\partial \rho_2}{\partial c_z} & \frac{\partial \rho_2}{\partial \theta} & \frac{\partial \rho_2}{\partial \beta} & \frac{\partial \rho_2}{\partial \gamma} \\ \frac{\partial \rho_3}{\partial c_x} & \frac{\partial \rho_3}{\partial c_y} & \frac{\partial \rho_3}{\partial c_z} & \frac{\partial \rho_3}{\partial \theta} & \frac{\partial \rho_3}{\partial \beta} & \frac{\partial \rho_3}{\partial \gamma} \\ \frac{\partial \rho_4}{\partial c_x} & \frac{\partial \rho_4}{\partial c_y} & \frac{\partial \rho_4}{\partial c_z} & \frac{\partial \rho_4}{\partial \theta} & \frac{\partial \rho_4}{\partial \beta} & \frac{\partial \rho_4}{\partial \gamma} \end{bmatrix} \quad (3)$$

Soon after the calculation of the Jacobian, we use the equation of virtual work to determine the forces acting on the actuator from external forces applied to the system.

$$\delta W = F \delta x + F_a \delta \rho = 0 \quad (4)$$

F is the force caused by external agents, δx is the virtual displacement of the design variables (displacement and angle of the mobile platform), F_a is the force of the actuator and $\delta \rho$ is virtual displacement of the cable. For analysis of static forces, virtual work is zero, so this expression is equal to zero.

The virtual displacement are related through the Jacobian matrix (Alp A. and Chou T., 2001)

$$\delta \rho = J \delta x \quad (5)$$

Substituting the Eq. (5) on Eq. (4):

$$F_a = \text{inv}(-J).F \quad (6)$$

Then, to determine the force that will act on the actuator, it is necessary to make the calculation of the inverse Jacobian matrix and then make the product with the external forces acting on the system.

WORKSPACE

One of the most important characteristics of manipulators is the workspace. The workspace is the set of position and orientations configurations in which the end-effector is controllable, tensions in cables are positive, forces values lie between a minimum and maximum in order to maintain cables in tension and to avoid the cables break, the end-effector is far from singularities and cables wrapping is avoided (Hiller et al., 2009; Merlet, 2004; Barrette and Gosselin, 2005).

The initial workspace is defined by movement circumduction. The movement circumduction reunites rotation for the three axes, Fig. 2(a). When this circumduction amplitude reaches its maximum, the arm in space describes an irregular cone: the cone circumduction. This cone delimits the sphere whose center is the shoulder and whose radius is the length of the upper limb, a spherical sector of accessibility, within which the hand can grasp objects without moving the trunk, eventually leads them to the mouth. In Fig. 2(a), the curve represents the base of the cone circumduction (trajectory of the fingertips), covering the different sectors of space determined by the planes of reference of the joint: A) Sagittal Plane (vertical flexion-extension); B) Frontal Plane (Abduction-Adduction); C) Horizontal Plane (Horizontal Flexion-Horizontal Extension). The curve passes (to the right upper limb) by sectors: III - below the front and the left; II - above, front and left; IV - above, behind and right; V - below, behind and right; VIII - below, behind and left a path is very short, because the extension-adduction amplitude is low, Fig. 2(a), the sector VIII is located below the plane C, behind the sector III and left the sector V. Sector VII is not visible, lies on top. Therefore, the study of the workspace will be based on the cone formed by the movement circumduction, Fig. 2(a).

Figure 6 shows the workspace for the structure developed, Fig. 4(c), taking into account the motion circumduction with limits of movements $\theta = 0^\circ$ to 180° and $\beta = -50^\circ$ to 50° .

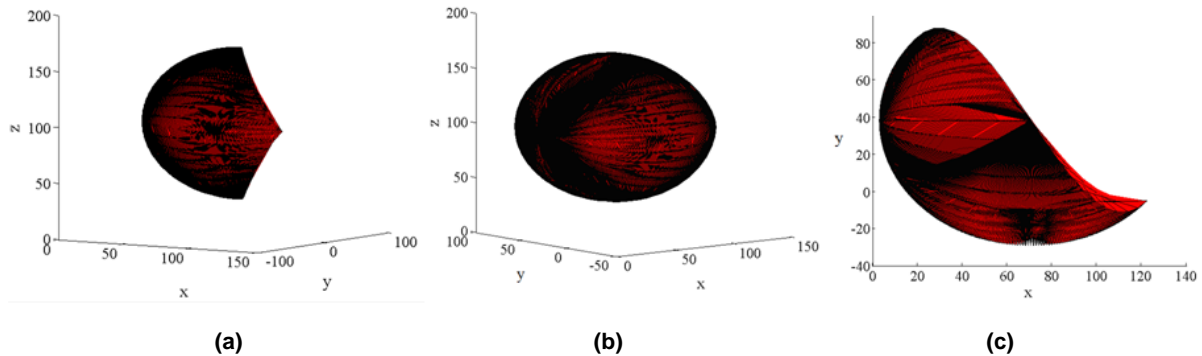


Figure 6 – Workspace of cable-based parallel manipulator proposed. (a) Three-dimensional view; Perspective view; (c) Top view, units in [cm].

NUMERICAL ANALYSIS

In the numerical analysis was developed a graphical model of the cable-based parallel manipulator 4-2, with the implementation of the control system according to Eqs. (1) to (6), using the software MatLab[®]. Figures 7 and 10 show the shoulder movement of abduction obtained from the cable-based parallel manipulator 4-2 developed and the displacement of the center gravity of the splint $c(c_x, c_y, c_z)$, the angle of displacement of the splint (θ, β, γ) and the length of the cables ρ_1, ρ_2, ρ_3 and ρ_4 related to the simulation time. The same analyses are done for the shoulder movement of the vertical flexion/extension, Figs. 8 and 11, horizontal flexion/extension, Figs. 9 and 12. The shoulder movement of circumduction is showed in Figs. 13 and 14 and the full motion describes a cone in space. From the numerical analysis, the proposed structure can reproduce the movements of the shoulder.

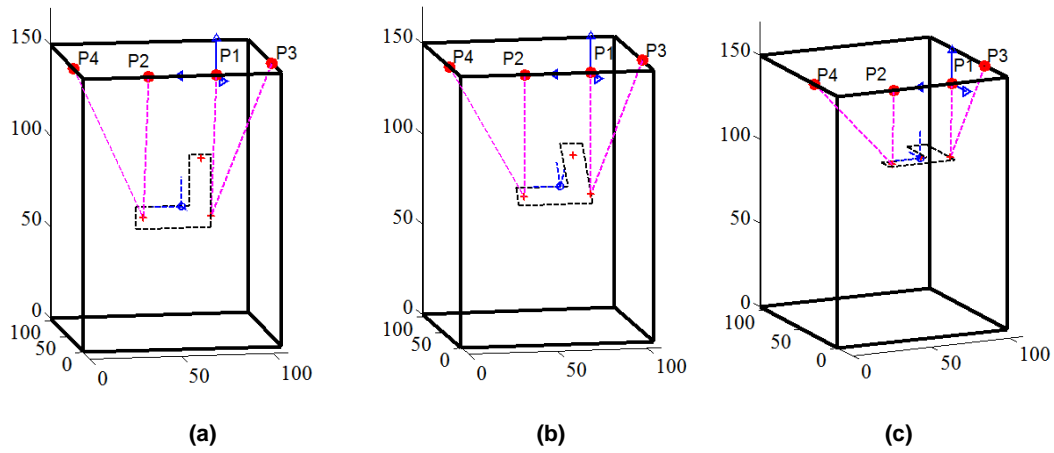


Figure 7 – (a) Splint the initial position; (b) Abduction 45°; (c) Abduction 90°.

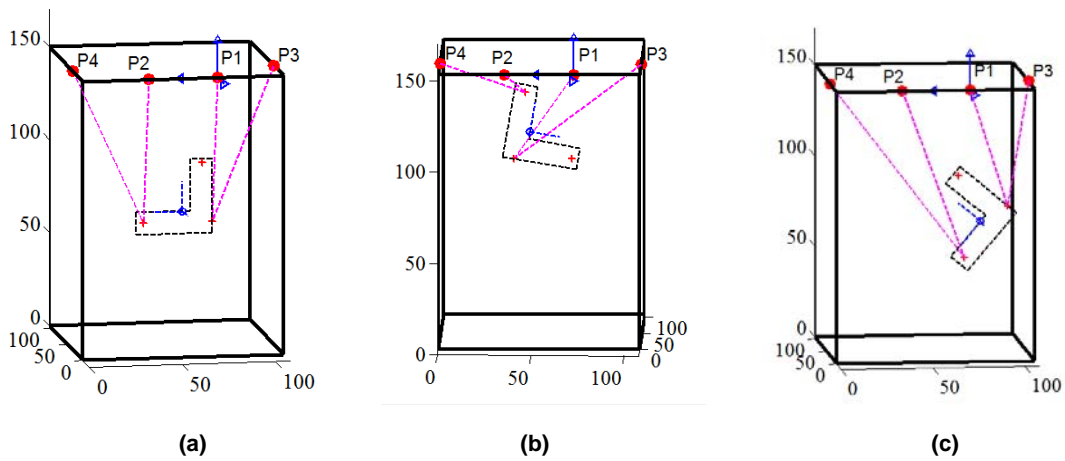


Figure 8 – (a) Splint the initial position 0°; (b) Vertical Flexion -100°; (c) Vertical Extension 50°.

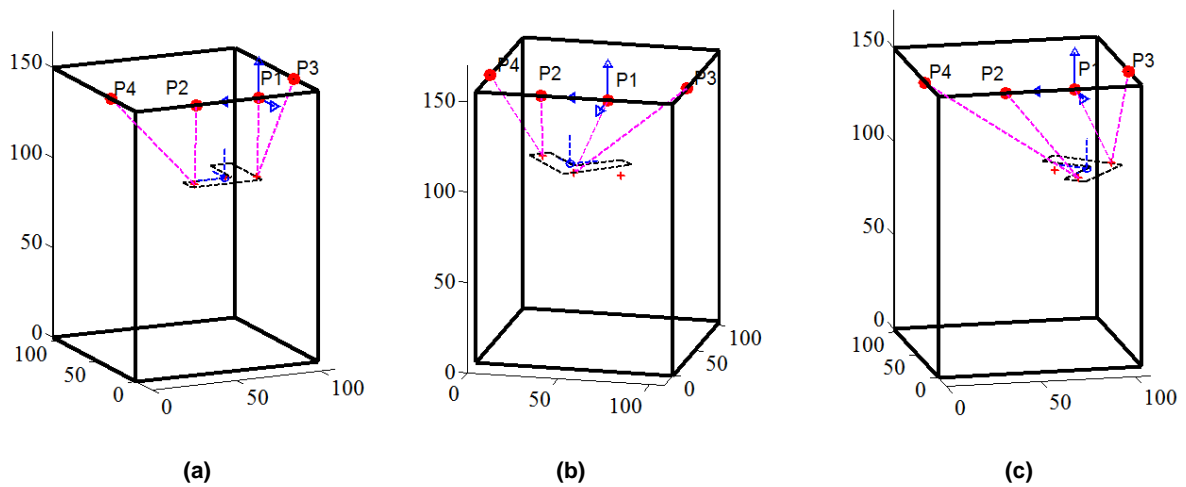


Figure 9 – (a) Splint the initial position (90° abduction); (b) Horizontal Flexion -50°; (c) Horizontal Extension 50°.

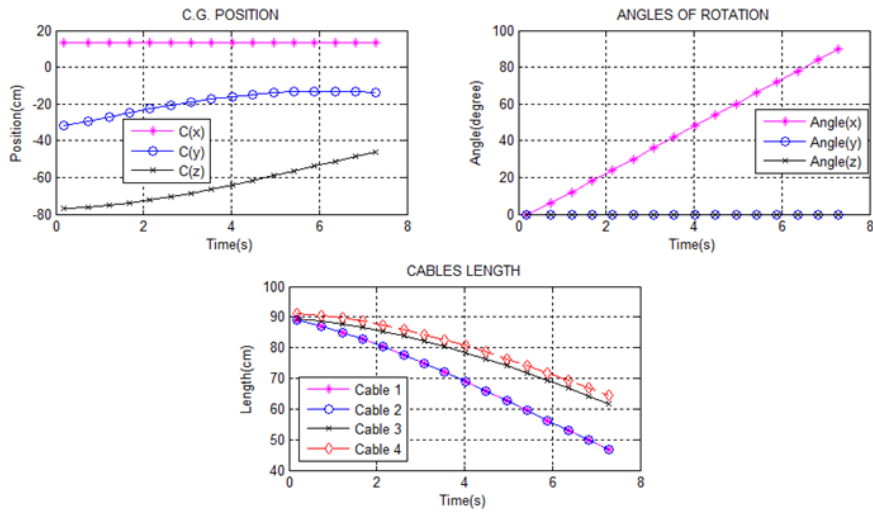


Figure 10 – Graphs of the movement of abduction and adduction (0 to 90°), Fig. 7.

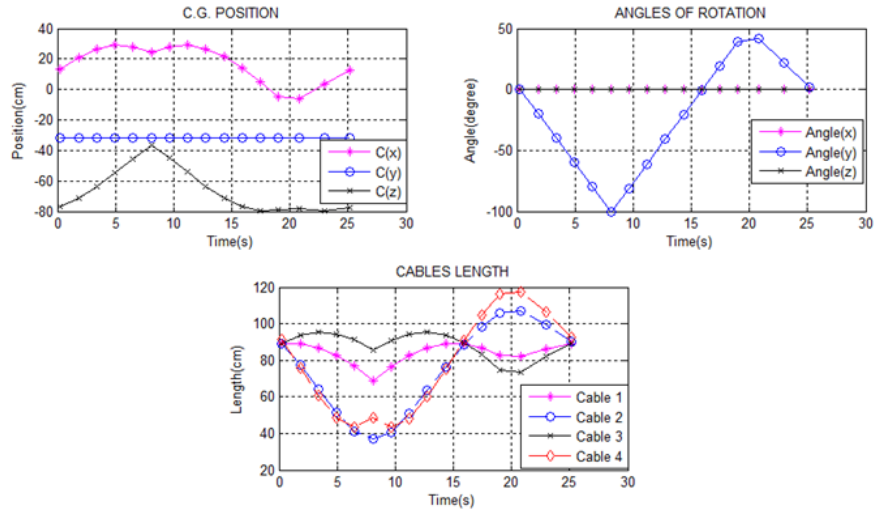


Figure 11 – Graphs of the movement of Vertical flexion and extension (-100 to 50°), Fig. 8.

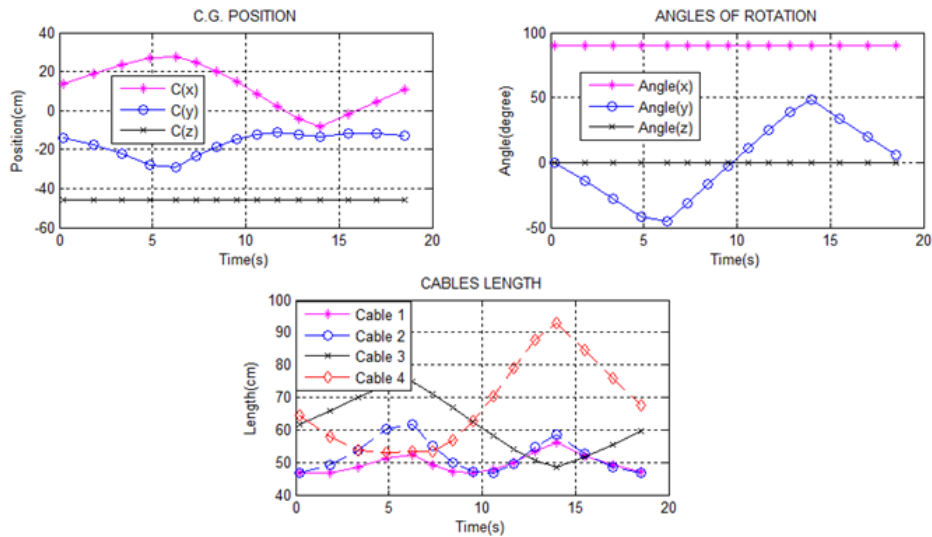


Figure 12 – Graphs of the movement of Horizontal flexion and Horizontal extension (-50 to 50°), Fig. 9.

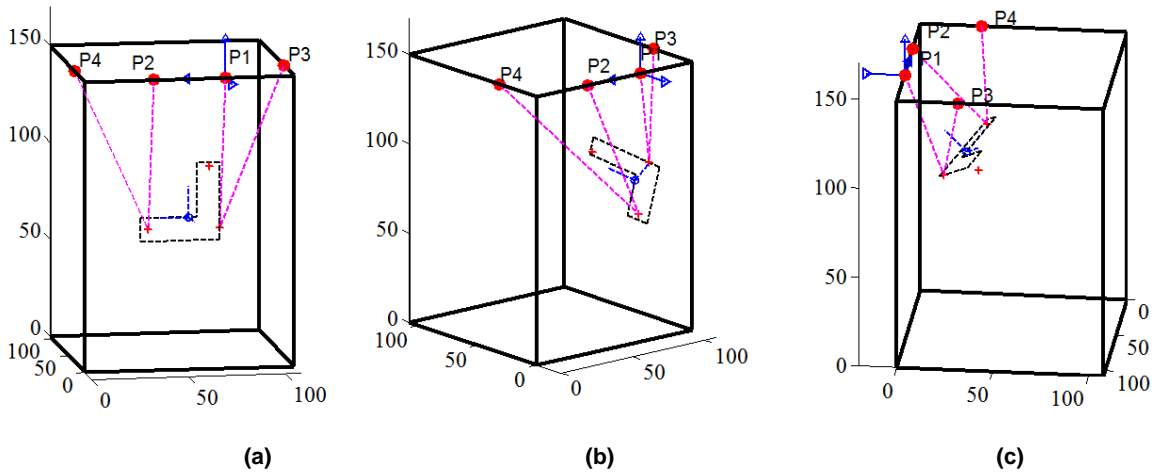


Figure 13 – Combination of Movements of Flexion-Extension with Abduction-Adduction; (a) Splint the initial position; (b) Abduction of 45° with Extension of 50°; (c) Adduction of 45° with Flexion of -50°.

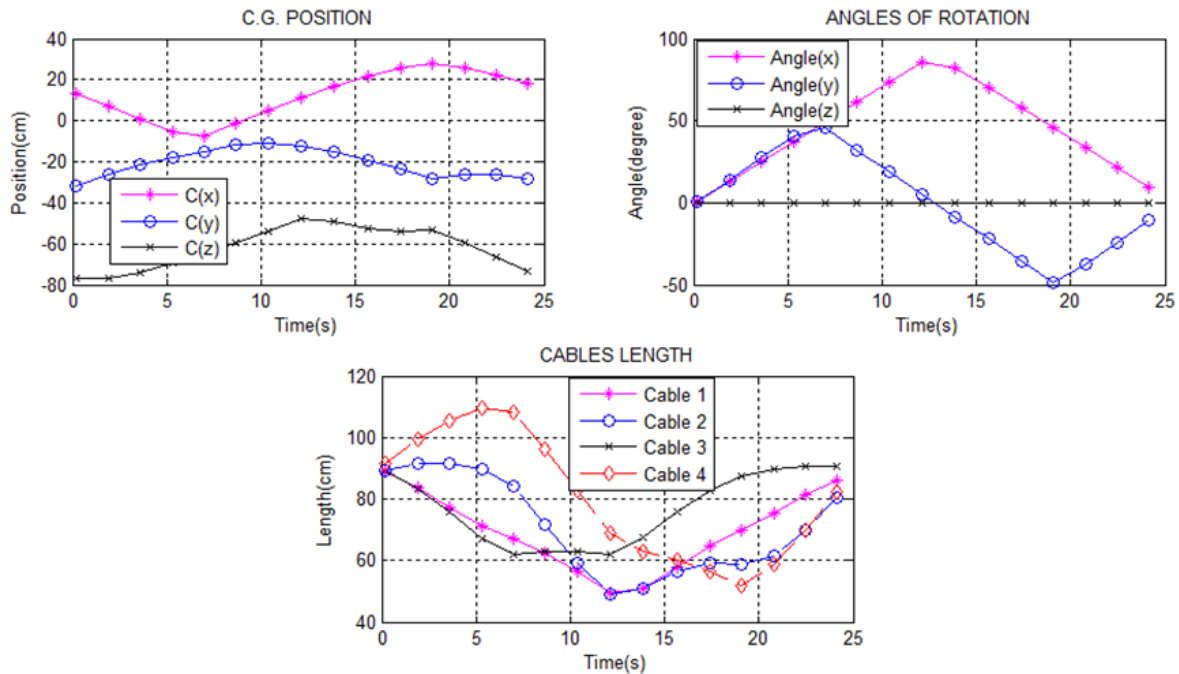


Figure 14 – Graphs of the Combined Movements of Flexion-Extension with Abduction-Adduction, Fig. 13.

CONCLUSIONS

In this paper a cable-based parallel manipulator for rehabilitation of the shoulder movements has been presented. The development of this robotic device is justified by the large number of people with shoulder problems. These problems are due of stroke, polio, arthritis, disaster recovery and can be applied to movements of physical therapy.

The developed cable-based parallel manipulator structure 4-2 is formed by four cables that connect the fixed platform and mobile platform (splint), allowing the realization of the major movements of the shoulder: vertical flexion-extension; abduction-adduction and horizontal flexion-extension. The Kinetostatic model was obtained for the proposed structure.

The analysis of the workspace of the proposed structure is performed considering the circumduction motion of the human arm.

Finally, the presented numerical simulations show the feasibility of the proposed structure that can reproduce the shoulder movements.

The optimization of the workspace and experimental tests are still undergoing to validate the proposed structure.

ACKNOWLEDGMENTS

The authors are thankful to CNPq (process 471968/2009-9), PROPP/UFU, CAPES and FAPEMIG for the partial financing support of this research work.

REFERENCES

- Alp A. B, Chou T., Kaler E., Gemesaw C., 2001, "Cable-Suspended Parallel Robots", Thesis the Faculty of the University of Delaware.
- Barrette, G., Gosselin, C. M., 2005 "Determination of the Dynamic Workspace of Cable Driven Planar Parallel Mechanisms", *Journal of Mechanical Design, Transactions of the ASME*, Vol. 127, No 2, pp. 242-248.
- Cannella, G.; Ottaviano, E.; Castelli, G., 2008, "A Cable-Based System for Aiding Elderly People in Sit to Stand Transfer", *MUSME 2008, The International Symposium on Multibody Systems and Mechatronics*, San Juan (Argentina), 8-12.
- Côté, G., 2003, "Analyse et Conception de Mécanismes Parallèles Actonnés par Câbles", Dissertation (in French).
- Fanin, C., Gallina, P., Rossi, A., Zanatta, U., Masiero, S., 2003, "Nerebot: a wire-based robot for neurorehabilitation", in *Proceedings of the IEEE 8th International Conference on Rehabilitation Robotics ICORR2003*, Daejeon, Republic of Korea.
- Fazekas, G., Horvath, M., Troznai, T., Toth, A., 2007, "Robot-Medated Upper Limb Physiotherapy for Patients with Spastic Hemiparesis: A preliminary Study", *Journal of Rehabil Med*, V. 39, p. 580-582.
- Gonçalves, R. S., Carvalho, J. C. M., 2010, "Desenvolvimento de uma Estrutura Robótica Paralela Atuada por Cabos para Reabilitação dos Movimentos do Ombro". In: *VI Congresso Nacional de Engenharia Mecânica*, 2010, Campina Grande, PB.
- Hiller, M., Hirsch, K., Bruckmann, T., Brandt, T., Schramm, D., 2009, "Common Aspects in Methods for the Design of Mechatronic Systems - Applications in Automotive and Robotic Systems U. of Duisburg-Essen", Germany, XII International Symposium on Dynamic Problems of Mechanics, Angra dos Reis, RJ.
- Homma, K., Fukuda, O., Nagata, Y., 2002, "Study of a wire-driven leg rehabilitation system", in *Proceedings of the IEEE International Conference on Intelligent Robots and Systems*, vol. 2, Lausanne, Switzerland, pp. 1451-1456.
- Kahn, L. E., Zygmant, M. L., Rymer, W. Z., Reinkensmeyer, D. J., 2006, "Robot-assisted reaching exercise promotes arm movement recovery in chronic hemiparetic stroke: a randomized controlled pilot study", *Journal of NeuroEngineering and Rehabilitation*, pp. 1-13.
- Kapandji, A. I, 2000, "Fisiologia Articular – Membro Superior", 5^a edition, Editorial Médica Panamericana.
- Krebs, H. I., Finley, M. A., Dipietro, L., Ohlhofer, J., Whittall, J., Bever, C. T., 2004, "Does MIT-MANUS Upper Extremity Robot Testing Create a Learning Effect in Healthy Adults?".
- Lum, P.S., Burgar, C.G., Shor, P.C., Majmundar, M., Van der Loos, M., 2002, "Robot assisted movement training compared with conventional therapy techniques for the rehabilitation of upper-limb motor function after stroke". *Archives of Physical Medicine & Rehabilitation*, 83(7):952-959.
- Mayhew, D., Bachrach, B., Rymer, W. Z., Beer, R. F., 2005, "Development of the MACARM – a Novel Cable Robot for Upper Limb Neurorehabilitation", *Proceedings of the 2005 IEEE, 9th International Conference on Rehabilitation Robotics*, Chicago, USA.
- Merlet, J-P., 2004, "Analysis of the Influence of Wires Interference on the Workspace of Wire Robots", *On Advances in Robot Kinematics*, Kluwer Academic Publishers, pp. 211-218.
- Nef, T., Riener, R., 2005, "ARMin: Design of a novel arm rehabilitation robot", in *Proc. IEEE 9th Int. Conf. Rehabilitation Robotics ICORR2005*, Chicago, IL, Jun. 2005, pp. 57-60.
- Rosati, G., Gallina, P., Masiero, S., Rossi, A., 2005, "Design of a new 5 d.o.f. wire-based robot for rehabilitation", *Proceedings of the 2005 IEEE 9th International Conference on Rehabilitation Robotics*, Chicago, USA.

RESPONSIBILITY NOTICE

The authors are the only responsible for the printed material included in this paper.

Identification of Damage in Thin-Walled Curved Beams by means of Vibration Analysis

Franco E. Dotti^{1,2}, Víctor H. Cortínez^{1,2}, and Marcelo T. Piovan^{1,2}

¹ Centro de Investigaciones de Mecánica Teórica y Aplicada, Universidad Tecnológica Nacional FRBB. 11 de Abril 461, B8000LMI, Bahía Blanca. Argentina

² Consejo Nacional de Investigaciones Científicas y Tecnológicas. Argentina

Abstract: A theoretical model for the dynamic analysis of damaged thin-walled curved beams is presented. This model incorporates bending and warping effects of shear flexibility by means of a linearized formulation based on the principle of virtual work. A beam iso-parametric finite element with five nodes and seven degrees-of-freedom per node is employed to solve the governing equations. Damage is considered in the model by modifying the sectional properties of a single finite element having an appropriate length. In order to perform identification of failure parameters, damage is treated as a fatigue crack located in a boundary of the beam cross-section. Location and depth of the crack are identified by means of the minimization of a target function. This function is defined in terms of differences of certain dynamic parameters among numerical and experimental values. As dynamic indices of damage, forced response and natural frequencies are employed. Two different optimization algorithms –Differential Evolution and Simulated Annealing– are employed to perform the optimization and their results are compared. Numerical results and comparisons with shell models illustrates that the present beam model is accurate enough to perform damage detection in thin-walled curved beams by means of frequency analysis.

Keywords: thin-walled, curved beams, damage detection, forced vibration, optimization

INTRODUCTION

Structural damage in engineering systems leads to changes in dynamic parameters such as natural frequencies, modal shapes, modal damping, forced response. These changes depend on nature, location and severity of the imperfection. Reviews of structural damage detection based on modal parameters and frequency changes are given in the works of Farrar and Doebling (1997) and Salawu (1997), respectively. A review of damage detection by mechanical vibration analysis can be found in the work of Dimarogonas (1996) and an interesting comparison between natural frequencies and modal shapes approaches can be found in the article of Kim et al. (2003).

In previous works, the effects of structural damage corresponding to bending modes were taken into account for Euler-Bernoulli curved and straight beams (Chondros and Dimarogonas, 1997; Cheeseman et al., 1996; Saavedra and Cuitiño, 1996). Thin-walled beams present a more complex behavior than Euler-Bernoulli beams since, in general, bending, torsional and axial movements are coupled. According to the knowledge of the authors, recent works presented by Cortínez et al. (2007), Dotti et al. (2010) and Cortínez and Dotti (2010) are the first articles to deal with the problem of cracked thin-walled beams' dynamics, despite of their intensive application on several areas of engineering.

After the early dynamic theory presented by Vlasov (1961) for curved thin-walled beams, the free vibration frequencies of horizontally curved beams have been determined, among other works, by Culver (1967) and Shore and Chaudhuri (1977) by means of analytical solutions of the equations of motion proposed. Yoo and Feherenbach (1981) have determined natural frequencies of vibrations of curved beams by means of a finite element formulation. Among other works, Gendy and Saleeb (1994), Cortínez et al. (1999) and Piovan et al. (2000) considered shear flexibility in a complete form. Recently, Piovan and Cortínez (2007) studied the mechanics of anisotropic curved thin-walled beams. All the works mentioned before considering thin-walled curved beams dynamics do not regard the presence of structural damage.

In the present article, the dynamic behavior of cracked thin-walled curved beams is analyzed by means of a beam model formulation accounting for shear flexibility due to bending and warping, originally introduced by Cortínez and Rossi (1998) for undamaged straight beams. An iso-parametric curvilinear non-locking element with seven degrees-of-freedom per node, previously formulated by Piovan and Cortínez (2007), is used to discretize the governing equations. Damage is taken into account as a fatigue crack located at a boundary of the beam cross-section since it represents a common failure in beam like structures. This kind of flaw is introduced by modifying the sectional properties of a single finite element, i.e. the presence of damage is modeled as a geometrical imperfection. The length of the modified element is obtained by elastic energy comparisons between the present beam model and a Fracture Mechanics model recently developed by Cortínez et al. (2009).

The capability of the model to replicate natural and forced responses of curved thin-walled-beams is evaluated by numerical experiments: a comparative study with shell finite element solutions is carried out.

Location and depth of this fatigue crack are identified by minimizing a target function defined by differences between results of the present beam model and results of numerical experiments, with an ABAQUS' shell model. The mentioned results can be natural frequencies, but also amplitudes, velocities and accelerations, generated by natural or forced response. Differential Evolution (Storn and Price, 1997) and Simulated Annealing (Kirkpatrick et al., 1983) are employed to perform the optimization and their results are compared.

THEORY

Displacement and strain fields

Figure 1 shows a sketch of a curved thin-walled beam with the presence of damage. The reference point C is coincident with the center of gravity while the point O corresponds to the shear center of the undamaged cross-section. B is a generic point in the middle line of the cross-sectional wall. The coordinates corresponding to points lying on this middle line are denoted as $\bar{Y}(s)$ and $\bar{Z}(s)$ (or $Y(s)$ and $Z(s)$). See also Fig. 2. The present thin-walled beam theory is based on the following two assumptions: 1) The cross-section contour is rigid in its own plane, although it is free to warp out of it, and 2) The torsional warping distribution is assumed to be given by the Saint-Venant function. According to these hypotheses, the displacement field is assumed (Cortínez et al., 1999) to be in the following form

$$u_x = u - \bar{y} \left(\theta_z - \frac{u}{R} \right) - \bar{z} \theta_y + \omega \left(\theta_x - \frac{\theta_y}{R} \right) \quad (1)$$

$$u_y = v - z \phi_x \quad (2)$$

$$u_z = w + y \phi_x \quad (3)$$

where ω is the warping function (See Cortínez and Piovan, 2002, for more details), u , v and w are the displacements of the center of gravity in the x , y and z directions, respectively, θ_y and θ_z are bending twists, ϕ_x is the torsional twist and θ_x , the warping variable.

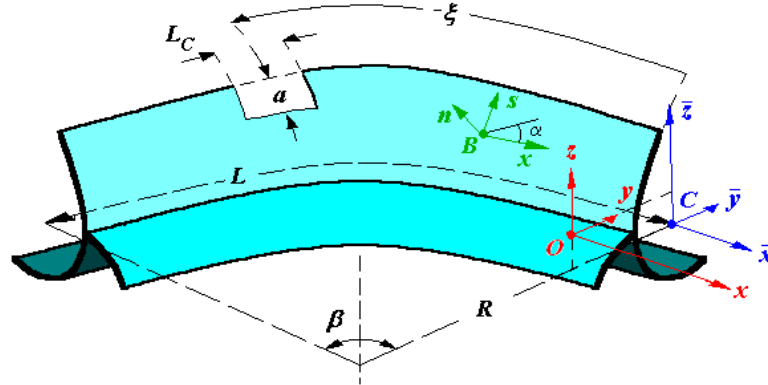


Figure 1 – Generic curved thin-walled beam with damage and basic associated coordinate systems.

For the present case, there are only three non-zero strain components. The well-known expressions for these strains are given by

$$\varepsilon_{xx} = \left(\frac{\partial u_x}{\partial x} + \frac{u_y}{R} \right), \quad \varepsilon_{xy} = \left(\frac{\partial u_y}{\partial x} - \frac{u_x}{R} \right) + \frac{\partial u_x}{\partial y}, \quad \varepsilon_{xz} = \frac{\partial u_z}{\partial x} + \frac{\partial u_x}{\partial z} \quad (4)$$

Note that the displacement field of a straight thin-walled beam can be obtained setting R as infinity.

One-dimensional variational equation of motion

Substituting expressions (1-4) into general expression of virtual work principle produces

$$L_K + L_M + L_P = 0 \quad (5)$$

where

$$L_K = \int_V \left[\sigma_{xx} \delta \varepsilon_{xx} + 2 \sigma_{xy} \delta \varepsilon_{xy} + 2 \sigma_{xz} \delta \varepsilon_{xz} \right] dydzdx \quad (6)$$

$$L_M = \int_V \rho \left[\ddot{u}_x \delta u_x + \ddot{u}_y \delta u_y + \ddot{u}_z \delta u_z \right] dydzdx \quad (7)$$

$$L_P = -\int_V \left[\bar{X}_x \delta u_x + \bar{X}_y \delta u_y + \bar{X}_z \delta u_z \right] dydzdx - \int_{S_1} \left[\bar{T}_x \delta u_x + \bar{T}_y \delta u_y + \bar{T}_z \delta u_z \right] dydz \quad (8)$$

In previous equations, the non-zero components of the stress tensor are denoted as σ_{xx} , σ_{xy} and σ_{xz} , and ρ represents the material density. \bar{X}_i and \bar{T}_i with $i = x, y, z$ correspond to volume forces and external forces acting on the ends of the beam, respectively. Integrating (5) with respect to y and z and neglecting high order terms, one can obtain the one-dimensional variational equation of motion (See Cortínez et al, 1999).

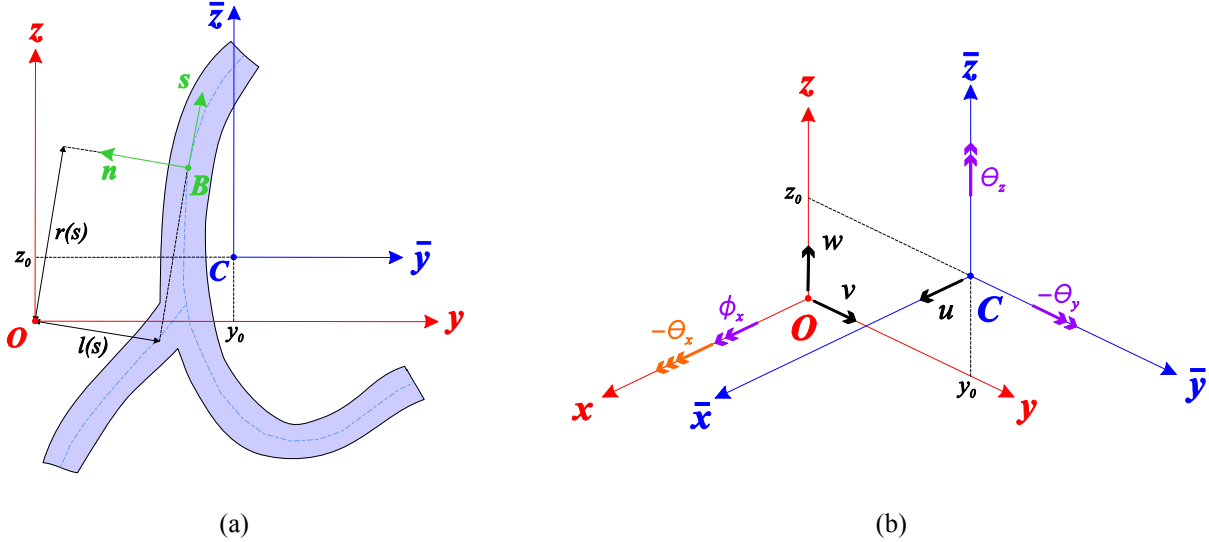


Figure 2 – (a) Geometrical entities of the cross-section and coordinate systems. (b) Definition of the generalized displacements.

Constitutive equations

Structural damage is regarded as a geometrical imperfection. Therefore, the cross-section of a segment of length L_C is modified as shown in Fig. 1, in order to consider the presence of damage. In this case, the origins of the considered coordinate systems are not coincident with the center of gravity and the shear center of the damaged cross-section. Taking this into account, the constitutive equations for the damaged segment of the beam can be obtained from the constitutive functional of the principle of virtual work as

$$N^{(c)} = E \left[A^{(c)} \left(u' + \frac{v}{R} \right) - S_y^{(c)} \left(\theta'_y + \frac{\phi_x}{R} \right) - S_z^{(c)} \left(\theta'_z - \frac{u'}{R} \right) + S_\omega^{(c)} \left(\theta'_x - \frac{\theta'_y}{R} \right) \right] \quad (9)$$

$$M_y^{(c)} = E \left[S_y^{(c)} \left(u' + \frac{v}{R} \right) - I_y^{(c)} \left(\theta'_y + \frac{\phi_x}{R} \right) - I_{yz}^{(c)} \left(\theta'_z - \frac{u'}{R} \right) + I_{y\omega}^{(c)} \left(\theta'_x - \frac{\theta'_y}{R} \right) \right] \quad (10)$$

$$M_z^{(c)} = E \left[S_z^{(c)} \left(u' + \frac{v}{R} \right) - I_{yz}^{(c)} \left(\theta'_y + \frac{\phi_x}{R} \right) - I_z^{(c)} \left(\theta'_z - \frac{u'}{R} \right) + I_{z\omega}^{(c)} \left(\theta'_x - \frac{\theta'_y}{R} \right) \right] \quad (11)$$

$$B^{(c)} = E \left[S_\omega^{(c)} \left(u' + \frac{v}{R} \right) - I_{y\omega}^{(c)} \left(\theta'_y + \frac{\phi_x}{R} \right) - I_{z\omega}^{(c)} \left(\theta'_z - \frac{u'}{R} \right) + C_w^{(c)} \left(\theta'_x - \frac{\theta'_y}{R} \right) \right] \quad (12)$$

$$T_{sv}^{(c)} = GJ^{(c)} \left(\phi'_x - \frac{\theta'_y}{R} \right) \quad (13)$$

$$\begin{Bmatrix} Q_y^{(c)} \\ Q_z^{(c)} \\ T_w^{(c)} \end{Bmatrix} = G[S] \begin{Bmatrix} v' - \theta_z \\ w' - \theta_y \\ \phi'_x - \theta_x \end{Bmatrix} \quad (14)$$

where N , Q_y , Q_z , M_y , M_z , B , T_w and T_{sv} are the beam forces. Besides, A , S_y , S_z , S_ω , I_y , I_z , C_w , I_{yz} , $I_{y\omega}$, $I_{z\omega}$, and J are inertia properties of the cross section, E is the Young modulus and G is the shear modulus. The superscript $\bullet^{(c)}$ in beam forces and inertia constants refer to the damaged section of the beam. No superscript indicates beam forces and inertia constants for the undamaged cross-section.

It is worthwhile to note that constitutive expressions for the undamaged cross-section can be obtained from (9-14) as a particular case in which some of the inertia constants vanish. The matrix $[S]$ in equation (14) is obtained as

$$[S] = e \begin{bmatrix} \int_s \left[\left(\frac{dY}{dS} \right)^2 + \left(\frac{dZ}{dS} \right)^2 \right] ds & 0 & \int_s \left[r \left(\frac{dY}{dS} \right)^2 - l \left(\frac{dZ}{dS} \right)^2 \right] ds \\ 0 & \int_s \left[\left(\frac{dY}{dS} \right)^2 + \left(\frac{dZ}{dS} \right)^2 \right] ds & \int_s \left[l \left(\frac{dY}{dS} \right)^2 + r \left(\frac{dZ}{dS} \right)^2 \right] ds \\ \int_s \left[r \left(\frac{dY}{dS} \right)^2 - l \left(\frac{dZ}{dS} \right)^2 \right] ds & \int_s \left[l \left(\frac{dY}{dS} \right)^2 + r \left(\frac{dZ}{dS} \right)^2 \right] ds & \int_s (r^2 + l^2) ds \end{bmatrix} \quad (15)$$

being r and l geometrical magnitudes of the undamaged cross-section, defined in Fig. 2.

FATIGUE DAMAGE MODELING

The length L_C (Fig. 1) must be chosen appropriately in order to produce a behavior analog to the presence of a real damage. Although this approach is able to reproduce different damage scenarios, for the case of a fatigue crack, L_C is chosen in order to represent the behavior of the beam with the presence of a crack with depth a and location ξ .

In the following, L_C is determined for the case of a fatigue crack by elastic energy comparisons between the present beam model and a Fracture Mechanics model recently developed by Cortínez et al. (2009). Constitutive equations may be expressed as

$$\{Q_E\} = [J_E] \{\Delta\}, \quad \{Q_E^{(c)}\} = [J_E^{(c)}] \{\Delta\} \quad (16)$$

where the vectors of generalized beam forces, $\{Q_E\}$ and $\{Q_E^{(c)}\}$, and the vector of generalized displacements, $\{\Delta\}$, are defined as

$$\{Q_E\} = \{N, M_y, M_z, B, Q_y, Q_z, T_w, T_{sv}\} \quad (17)$$

$$\{Q_E^{(c)}\} = \{N^{(c)}, M_y^{(c)}, M_z^{(c)}, B^{(c)}, Q_y^{(c)}, Q_z^{(c)}, T_w^{(c)}, T_{sv}^{(c)}\} \quad (18)$$

$$\{\Delta\} = \{u', \theta'_y, \theta'_z, \theta'_x, v' - \theta_z, w' - \theta_y, \phi'_x - \theta_x, \phi'_x\} \quad (19)$$

The inertia properties of the beam are contained into the beam constitutive matrices, $[J_E]$ and $[J_E^{(c)}]$.

The strain energy of the curved thin-walled beam of Fig. 1 is given by

$$U = \frac{I}{2} \int_0^{\xi - \frac{L_C}{2}} \left(\{Q_E\}^T [J_E]^{-1} \{Q_E\} \right) dx + \frac{I}{2} \int_{\xi - \frac{L_C}{2}}^{\xi + \frac{L_C}{2}} \left(\{Q_E^{(c)}\}^T [J_E^{(c)}]^{-1} \{Q_E^{(c)}\} \right) dx + \frac{I}{2} \int_{\xi + \frac{L_C}{2}}^L \left(\{Q_E\}^T [J_E]^{-1} \{Q_E\} \right) dx \quad (20)$$

Evaluating the corresponding integrals with respect to the variable x , Eq. (20) may be rewritten as

$$U = U_I + U_{II} + U_{III} \quad (21)$$

where U_I is the strain energy associated to the mode I of fracture and therefore to the axial force N , bending moments M_y , M_z and bimoment B . U_{II} is associated to mode II, and therefore to shear forces Q_y , Q_z and to Vlasov torque T_w ; and U_{III} is associated to mode III, that is related to the Saint-Venant torque T_{sv} . In this way, Griffith's criterion allows expressing the stress intensity factor of mode I, K_I , as (also K_{II} and K_{III} can be obtained)

$$K_I(a, \xi, L_C) = \sqrt{\frac{eE}{1-\nu^2} \frac{\partial U_I}{\partial a}} \quad (22)$$

The factor K_I predicted by the model depends on the severity of damage, a , but also depends on its equivalent length L_C and its location ξ . On the other hand, the theoretical expression of K_I introduced by Cortínez et al. (2009) for a cracked thin-walled beam is given by

$$K_I'(a, \xi) = \sqrt{\frac{2\pi}{(1-\nu^2)e}} \left(\chi_1 N^2 + \chi_2 M_z^2 + \chi_3 M_y^2 + \chi_4 B^2 + \chi_5 N M_y + \chi_6 N M_z + \right. \\ \left. \chi_7 M_y M_z + \chi_8 N B + \chi_9 M_y B + \chi_{10} M_z B \right)^{\frac{1}{2}} \quad (23)$$

being e the thickness of the beam. Taking into account the expressions of Eq. (22) and (23), the equivalent length L_C can be obtained by minimizing a discrete target function, F_K , given by the quadratic differences between the two expressions of K_I , that is

$$\min \left[F_K = \sum_{j=1}^{n_\xi} \sum_{i=1}^{n_a} \sqrt{\left(\frac{K_I(a_i, \xi_j, L_C) - K_I'(a_i, \xi_j)}{K_I'(a_i, \xi_j)} \right)^2} \right] \quad (24)$$

where n_a and n_ξ are the number of depths and locations employed in the optimization calculation. The coefficients χ_i from Eq. (23) depend on crack depth, since they depend on the cross-sectional constants of the damaged cross-section. Refer to the work of Cortínez et al. (2009) for more details.

FINITE ELEMENT FORMULATION

In order to solve the dynamic problem of a curved thin-walled beam with the presence of damage, an iso-parametric finite element with five nodes (quartic order approximation) and thirty five degrees-of-freedom is employed. This finite element, called ISOP5N, was originally introduced by Piovan and Cortínez (2007). The presence of damage in the beam is taking into account by means of a single finite element with length L_C and constitutive properties given by expressions (9) to (14). Undamaged zones of the beam are modeled in a conventional fashion.

By means of standard finite element procedures, the general finite element equation can be obtained as

$$[M]\{\ddot{U}\} + [C]\{\dot{U}\} + [K]\{U\} = \{R\} \quad (25)$$

where $[K]$, $[M]$ and $[C]$ are global matrices of elastic stiffness, mass and structural damping, respectively; whereas $\{U\}$ and $\{P\}$ are the global vectors of nodal displacements and nodal forces. The problem of forced vibration is solved by standard modal superposition (Bathe, 1996).

For the case of free vibration analysis, Eq. (25) can be reduced to the following eigenvalue problem, where damping effects are neglected and harmonic motion is prescribed

$$([K] - \Omega^2[M])\{U\}^* = 0 \quad (26)$$

where $\Omega = 2\pi f$, being f the natural frequency measured in Hertz. The vector $\{U\}^*$ arises from supposing that $\{U\} = \{U\}^* e^{i\Omega t}$. The eigensystem (26) allows obtaining the natural frequencies of the beam as well as its corresponding modal shapes.

DAMAGE IDENTIFICATION

Identification by comparisons of natural frequencies

With the purpose of damage detection, natural frequencies obtained by solving Eq. (26), associated to discrete depths and locations of damage, are interpolated by means of spline interpolations in order to obtain continuous functions of the frequencies. These functions are given by $F^{(k)}(X,\Lambda)$, for the generic case of a natural frequency k . Normalized depth and location are defined as

$$\Lambda = a/b, \quad X = \xi/L \quad (27)$$

The inverse problem of identifying X and Λ is given by the minimization of a target function $T(X,\Lambda)$, defined in terms of the difference between model results and experimental measurements, that is

$$\min \left[T(X, \Lambda) = \frac{100}{q} \sum_{k=1}^q \sqrt{\left(\frac{F^{(k)}(X, \Lambda) - f^{(k)}}{f^{(k)}} \right)^2} \right] \quad (28)$$

where q is the number of natural frequencies employed in the calculation and $f^{(k)}$ represents an experimental measurement of the natural frequency k .

Identification by comparison of amplitudes generated by forced vibrations

Identification by forced vibration analysis is performed by comparison between stationary amplitudes of displacements predicted by the model and measured experimentally. Amplitudes considered in the identification may correspond to displacements u_x , u_y and/or u_z of any point of the beam, for sinusoidal loads in the closeness of resonance. In general terms, other displacements excepting the mentioned before are not utilized because of their difficulty to measure in practice. For each measurement point in the beam $P_i = (\bar{x}_i, \bar{y}_i, \bar{z}_i)$, spline interpolations are employed to convert the discrete results of amplitudes given by the model into continuous functions of X and Λ . These functions are given by $\Psi_{i,j}^{(1)}(X,\Lambda)$, $\Psi_{i,j}^{(2)}(X,\Lambda)$ and $\Psi_{i,j}^{(3)}(X,\Lambda)$, associated to the displacements u_x , u_y and u_z , respectively. Sub-index j relates to a load case Q_j .

According to the previous exposition, identification of X and Λ corresponds to the following optimization problem

$$\min \left[S(X, \Lambda) = \sum_k^3 \sum_{j=1}^{n_Q} \sum_{i=1}^{n_P} \sqrt{\left(\frac{\Psi_{i,j}^{(k)}(X, \Lambda) - \delta_{i,j}^{(k)}}{\delta_{i,j}^{(k)}} \right)^2} \right] \quad (29)$$

where $\delta_{i,j}^{(k)}$ represent a stationary amplitude of displacement k measured experimentally at the point P_i , while the beam is subjected to a load case Q_j . Each load case is constituted by known sinusoidal loads. n_Q represents the total number of load cases considered in the detection and n_P , the total points of amplitude measurements.

NUMERICAL RESULTS AND DISCUSSION

Accuracy of the beam model

In this section the capability of the beam model to reproduce the dynamic behavior of a curved thin-walled beam is evaluated. Experimental measurements are simulated numerically with shell finite element models, programmed in the ABAQUS 7 ® code. Comparisons of natural frequencies and forced response are performed for steel beams with the following properties: $E = 210$ GPa, $G = 80.76$ GPa, $\nu = 0.3$ y $\rho = 7830$ kg/m³.

Table 1 – Values of the target function $T(X,\Lambda)$ with $q = 3$, for a curved cantilever thin-walled U beam. Dimensions: $b = 0.2$ m, $h = 0.2$ m, $e = 0.01$ m, $L = 4.71$ m, $R = 3$ m. Optimal $L_c = L/42$.

	$\Lambda = 0.25$		$\Lambda = 0.50$		$\Lambda = 0.75$		$\Lambda = 1.00$	
	$L/L_c = 42$	$L/L_c = 50$	$L/L_c = 42$	$L/L_c = 50$	$L/L_c = 42$	$L/L_c = 50$	$L/L_c = 42$	$L/L_c = 50$
$X = 0.15$	0.05	0.10	0.21	0.61	0.19	0.40	1.56	2.01
$X = 0.30$	0.05	0.11	0.37	0.59	0.24	0.46	2.12	2.85
$X = 0.45$	0.04	0.03	0.20	0.31	0.23	0.31	3.35	3.32
$X = 0.60$	0.01	0.02	0.10	0.13	0.13	0.25	3.21	3.48
$X = 0.75$	0.00	0.01	0.07	0.08	0.16	0.19	3.01	3.54

With the purpose of testing the capability of the model in estimating natural frequencies, Tab. 1 presents values of the target function $T(X,\Lambda)$, employing the first three natural frequencies, for a curved cantilever thin-walled U beam, with flange b , height h , thickness e , and flanges oriented to the center of curvature. This kind of beam corresponds to a sufficiently general case, involving bending-torsional couplings. It is worthwhile to note that $T(X,\Lambda)$ represents an average error function of results with respect to experimental ones. One can see that average errors are sufficiently small to detect damage, taking into account a threshold of 5% in frequency error for a good detection (see Salawu, 1997 and Dotti et al., 2009).

In addition, Fig. 3 shows the good agreement with respect to experimental results of the first two natural frequencies of the mentioned beam, for fixed damage location.

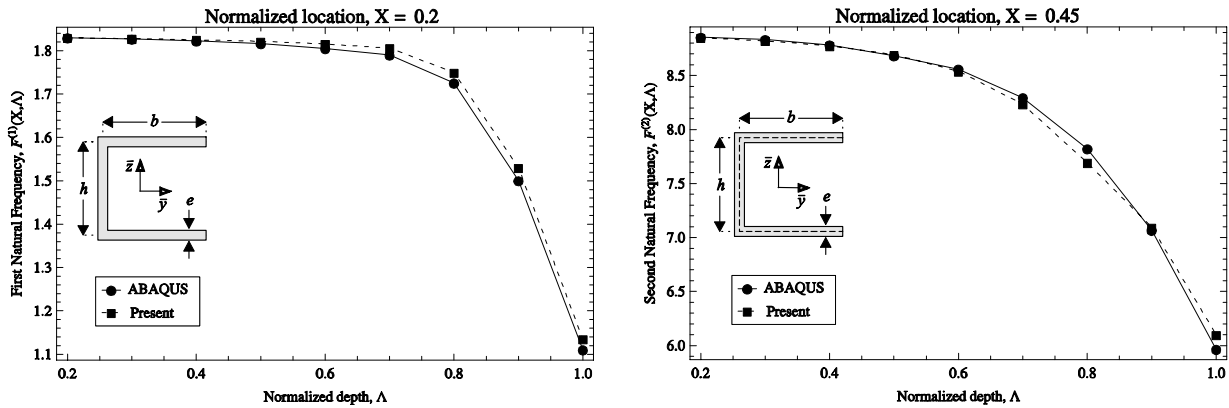


Figure 3 – First two natural frequencies of a curved cantilever thin-walled U beam for fixed damage location. Dimensions: $b = 0.2$ m, $h = 0.2$ m, $e = 0.01$ m, $L = 4.71$ m, $R = 3$ m. Damage length $L_c = L/42$. Frequencies in Hz. Mode 1: Flexural-Torsional ($z-\phi$). Mode 2: Flexural (y).

Stationary forced response is also tested against experimental results for a U beam. Two load cases, Q_1 and Q_2 , consisting in shear forces are considered in this analysis. They are given by

$$Q_1 : \left\{ Q_y(L) = 200N \sin(\Omega_f t) \right\} \tag{30}$$

$$Q_2 : \left\{ Q_z(L) = 10N \sin(\Omega_f t) \right\} \tag{31}$$

with variable excitation frequency Ω_f , and point of application at the free end of the beam, as can be seen in Fig. 4. For all the calculations, a total of five modes are employed in the modal superposition analysis. Classic Rayleigh damping is employed, being 2% of critical damping, considering five natural frequencies. The comparison between model results and numerical experiments is illustrated by means of curves representing stationary amplitude vs. excitation frequency. Displacements are measured at the free end of the beam, over the middle of the web. Figures 5 and 6 show, for a known damage, the amplitudes of displacements u_y and u_z , for the load cases Q_1 and Q_2 , respectively. One can see that the model is able to reproduce successfully the coupling generated by the presence of damage as well as couplings proper of thin-walled beams. Axial displacement can also be reproduced satisfactorily, being u_x considerably smaller than transverse displacements.



Figure 4 – Configuration of load cases in forced frequency analysis of a cantilever thin-walled curved U beam.

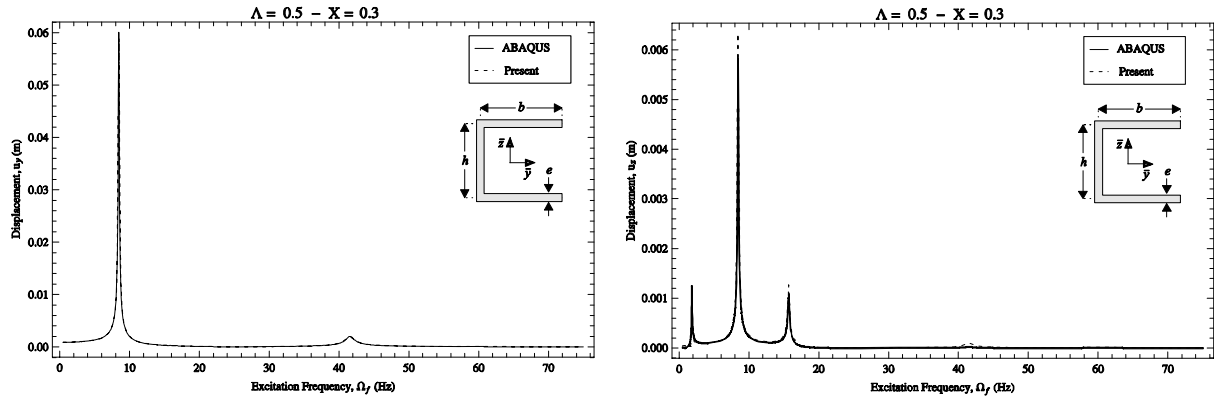


Figure 5 – Displacement amplitudes vs. excitation frequency. Dimensions: $b = 0.2$ m, $h = 0.2$ m, $e = 0.01$ m, $L = 4.71$ m, $R = 3$ m. Load Case: Q_7 . Damage Length: $L_C = L/42$.

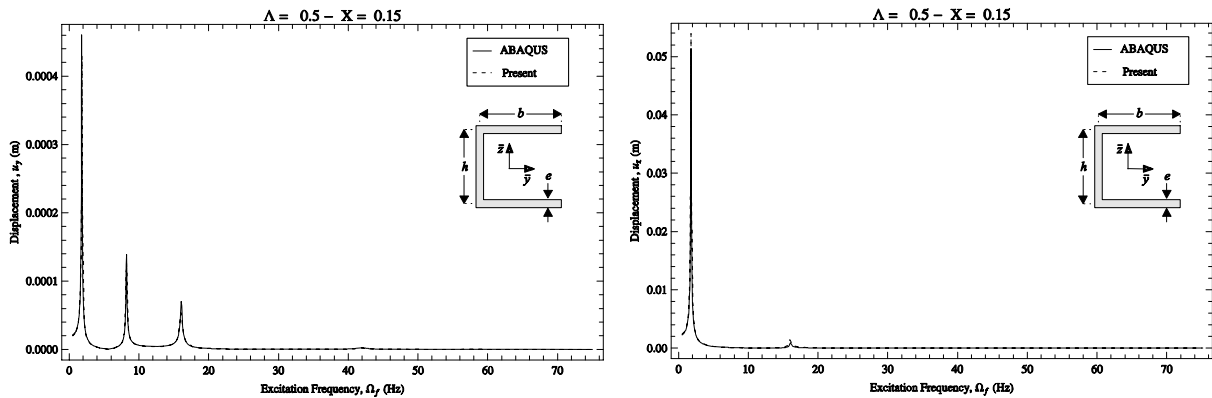


Figure 6 – Displacement amplitudes vs. excitation frequency. Dimensions: $b = 0.2$ m, $h = 0.2$ m, $e = 0.01$ m, $L = 4.71$ m, $R = 3$ m. Load Case: Q_2 . Damage Length: $L_C = L/42$.

Identification by comparisons of natural frequencies

Minimization of a target function $T(X,\Lambda)$ in order to identify damage parameters X and Λ is performed by two different optimization methods: Differential Evolution (DE) and Simulated Annealing (SA). In both cases, the three first natural frequencies are employed ($q = 3$), and the variables are set with the following restrictions: $0 \leq X \leq 1$, $0 \leq \Lambda \leq 1$. The spread constant and the cross probability employed in calculations with DE are set to 0.6 and 0.5, respectively. In calculations with SA, an acceptance rule of $\exp\{10[-\Delta T(X,\Lambda) \log(i+1)]\}$ is employed. Minimal values of $T(X,\Lambda)$ employed are the best of 20 optimization calculations, with different random initial points.

Table 2 – Identification of X and Λ employing natural frequencies ($q = 3$), for a curved cantilever thin-walled U beam. Dimensions: $b = 0.2$ m, $h = 0.2$ m, $e = 0.01$ m, $L = 4.71$ m, $R = 3$ m. $L_C = L/42$.

Experimental		Estimation				Error (%)			
Location, X	Depth, Λ	Location, \bar{X}		Depth, Λ		Error in Location		Error in Depth	
		DE	SA	DE	SA	DE	SA	DE	SA
0.15	0.25	0.200	0.198	0.294	0.292	5.00	4.80	4.40	4.20
	0.50	0.170	0.179	0.542	0.564	2.00	2.90	4.20	6.40
	0.75	0.175	0.185	0.747	0.745	2.50	3.50	-0.30	-0.50
	1.00	0.160	0.168	1.000	1.000	1.00	1.80	0.00	0.00
0.30	0.25	0.335	0.334	0.285	0.282	3.50	3.40	3.50	3.20
	0.50	0.294	0.294	0.532	0.529	-0.60	-0.60	3.20	2.90
	0.75	0.298	0.298	0.747	0.745	-0.20	-0.20	-0.30	-0.50
	1.00	0.284	0.284	1.000	1.000	-1.60	-1.60	0.00	0.00
0.60	0.25	0.606	0.606	0.289	0.286	0.60	0.60	3.90	3.60
	0.50	0.598	0.599	0.551	0.548	-0.20	-0.10	5.10	4.80
	0.75	0.598	0.598	0.759	0.757	-0.20	-0.20	0.90	0.70
	1.00	0.544	0.620	1.000	0.999	-5.60	2.00	0.00	-0.10
0.75	0.25	0.842	0.831	0.281	0.278	9.20	8.10	3.10	2.80
	0.50	0.701	0.828	0.569	0.567	-4.90	7.80	6.90	6.70
	0.75	0.785	0.681	0.765	0.763	3.50	-6.90	1.50	1.30
	1.00	0.698	0.676	0.987	0.998	-5.20	-7.42	-1.30	-0.20

Results are shown in Table 2. Average absolute error in estimation of location (DE: 2.86%; SA: 3.24%) is similar than average error in estimation of depth (DE: 2.41%; SA: 2.37%). Errors are generally slightly smaller employing DE algorithm. Comparing computation time, SA takes advantage with average times of 0.6 s against 6.5 s corresponding to DE. Calculations are performed with an AMD Athlon 64 5200+ processor, 3 Gb of RAM and ASUS M2N-MX-SE+ motherboard.

Identification by comparison of stationary amplitudes generated by forced vibrations

Minimization of a target function $S(X,\Lambda)$ is performed employing DE and SA algorithms, with similar settings of previous calculation. Minimal values are the best of 20 optimization calculations with different random initial points. Load cases Q_1 and Q_2 are considered. For Q_1 , stationary amplitudes of displacement u_y , with Ω_f near the second resonance are compared. For Q_2 , idem amplitudes of u_z are employed with Ω_f near the first resonance. Results are shown in Table 3. Depth and location are both slightly better estimated by DE. Average absolute errors in depth are the following: DE: 2.52%, SA: 3.32%; while those corresponding to location are DE: 2.85% and SA: 3.41%.

Table 3 – Identification of X and Λ employing forced vibration amplitudes, for a curved cantilever thin-walled U beam. Dimensions: $b = 0.2$ m, $h = 0.2$ m, $e = 0.01$ m, $L = 4.71$ m, $R = 3$ m. $L_c = L/42$.

Experimental		Estimation				Error (%)			
Location, X	Depth, Λ	Location, X		Depth, Λ		Error in Location		Error in Depth	
		DE	SA	DE	SA	DE	SA	DE	SA
0.15	0.25	0.154	0.166	0.355	0.321	0.40	1.60	10.50	7.10
	0.50	0.159	0.160	0.504	0.504	0.90	1.00	0.40	0.40
	0.75	0.155	0.225	0.743	0.685	0.50	7.50	-0.70	-6.50
	1.00	0.150	0.150	0.997	0.997	0.00	0.00	-0.30	-0.30
0.30	0.25	0.220	0.360	0.259	0.315	-8.00	6.00	0.90	6.50
	0.50	0.303	0.359	0.519	0.614	0.30	5.90	1.90	11.40
	0.75	0.299	0.299	0.763	0.763	-0.10	-0.10	1.30	1.30
	1.00	0.297	0.297	1.000	1.000	-0.30	-0.30	0.00	0.00
0.60	0.25	0.700	0.650	0.361	0.261	10.00	5.00	11.10	1.10
	0.50	0.516	0.458	0.467	0.494	-8.40	-14.20	-3.30	-0.60
	0.75	0.642	0.612	0.741	0.729	4.20	1.20	-0.90	-2.10
	1.00	0.579	0.581	0.997	0.998	-2.10	-1.90	-0.30	-0.20
0.75	0.25	0.797	0.797	0.250	0.334	4.70	4.70	0.00	8.40
	0.50	0.784	0.692	0.498	0.476	3.40	-5.80	-0.20	-2.40
	0.75	0.745	0.745	0.744	0.748	-0.50	-0.50	-0.60	-0.20
	1.00	0.732	0.732	0.921	0.954	-1.80	-1.80	-7.90	-4.60

CONCLUSIONS

In this article, a simplified theoretical beam model that simulates the dynamic behavior of thin-walled damaged beams is presented. Damage is considered by modifying the sectional properties of a single finite element having an appropriate length. This length can be estimated in terms of elastic energy comparisons between the present beam model and a Fracture Mechanics model. The present approach is consistent with numerical results obtained from higher order models: natural frequencies, forced vibration amplitudes and vibratory couplings generated by the presence of a geometrical imperfection are generally well reproduced.

The model is also employed in the identification of damage, by comparisons with experimental measures. Two indicators, natural frequencies and forced vibration stationary amplitudes, are considered separately for detection, showing both acceptable results. Similar identification errors are obtained with both indicators, but it is important to note that three frequencies are employed in damage detection by natural frequencies, while two amplitudes are used in detection with forced vibrations. This may signify that the indicator consisting of stationary amplitudes generated by forced vibrations has better capability of damage detection.

Identification is performed by means of two known algorithms: Differential Evolution (DE) and Simulated Annealing (SA). In general terms, DE calculations are slightly more accurate, while SA calculations take less computation time.

ACKNOWLEDGMENTS

The authors would like to thank the support of Secretaría de Ciencia y Tecnología of Universidad Tecnológica Nacional and CONICET. The present article is part of the doctoral thesis by Franco Dotti, under the direction of Víctor Cortínez and Marcelo Piovan, at the Engineering Department of Universidad Nacional del Sur.

REFERENCES

- Bathe, K.-J., 1996, "Finite Element Procedures", Prentice Hall, New Jersey.
- Chaudhuri, S.K. and Shore, S., 1977, "Dynamic Analysis of Horizontally Curved I Girders Bridges", *Journal of the Structural Division (ASCE)*, Vol. 103, pp. 1589-1604.
- Cheeseman, B.A., Santare, M.H. and O'Toole, B.J., 1996, "Flexural Failure of Notched Curved Composite Beams", *Engineering Fracture Mechanics*, Vol. 54, No. 4, pp. 479-498.
- Chondros, T.G. and Dimarogonas, A.D., 1997, "A Consistent Cracked Bar Vibration Theory", *Journal of Sound and Vibration*, Vol. 200, No. 3, pp. 303-313.
- Cortínez, V.H. and Dotti, F.E., 2010, "Un Modelo Numérico para la Dinámica de Vigas de Pared Delgada Fracturadas por Fatiga: Aplicación a la Identificación de Daños", *Mecánica Computacional*, Vol. 29, Accepted.
- Cortínez, V.H., Dotti, F.E. and Piovan, M.T., 2009, "Factor de Intensidad de Tensiones del Modo I para Vigas Abiertas de Pared Delgada", *Mecánica Computacional*, Vol. 28, pp. 955-971.
- Cortínez, V.H., Piovan, M.T. and Rossi, R.E., 1999, "Out-of-Plane Vibrations of Thin-Walled Curved Beams Considering Shear Flexibility", *Structural Engineering and Mechanics*, Vol. 8, pp. 257-272.
- Cortínez, V.H., Piovan, M.T. and Dotti, F.E., 2007, "Dynamics of Cracked Thin-Walled Beams", *Proceedings of the 19th COBEM. 19th International Congress of Mechanical Engineering. Brasilia, DF, Brasil*.
- Cortínez, V.H. and Rossi, R.E., 1998, "Dynamics of Shear Deformable Thin-Walled Open Beams Subjected to Initial Stresses", *Revista Internacional de Métodos Numéricos para Cálculo y Diseño en Ingeniería*, Vol. 14, No. 3, pp. 293-316.
- Culver, C.G., (1967), "Natural Frequencies of Horizontally Curved Beams", *Journal of the Structural Division (ASCE)*, Vol. 93, pp. 189-203.
- Dimarogonas, A.D., 1996, "Vibration of Cracked Structures: a State of the Art Review", *Engineering Fracture Mechanics*, Vol. 55, No. 5, pp. 831-857.
- Dotti, F.E., Piovan, M.T. and Cortínez, V.H., 2009, "Vibrations of Damaged Thin-Walled Beams", Submitted.
- Farrar, C.R. and Doebling, S.W., 1997, "An Overview of Modal-Based Damage Identification Methods", *EUROMECH 365 International Workshop: DAMAS 97, Structural Damage Assessment using Advanced Signal Processing Procedures*.
- Gendy, A.S. and Saleeb, A.F., 1994, "Vibrations of Coupled Extensional/Flexional/Torsional Modes of Curved Beams with Arbitrary Thin-Walled Sections", *Journal of Sound and Vibration*, Vol. 174, No. 2, pp. 261-274.
- Kim, J.-T., Ryu, Y.-S., Cho, H.-M and Stubbs, N., 2003, "Damage Identification in Beam-Type Structures: Frequency-Based Method vs. Mode-Shape-Based Method", *Engineering Structures*, Vol. 25, pp. 57-67.
- Kirkpatrick, S., Gelatt, C.D. and Vecchi, M.P., 1983, "Optimization by Simulated Annealing", *Science*, Vol. 220, No. 4598, pp. 671-680.
- Piovan, M.T. and Cortínez, V.H., 2007, "Mechanics of Thin-Walled Curved Beams made of Composite Materials, allowing for Shear Deformability", *Thin-Walled Structures*, Vol. 45, pp. 759-789.
- Piovan, M.T., Cortínez, V.H. and Rossi, R.E., 2000, "Out-of Plane Vibrations of Shear Deformable Continuous Horizontally Thin-Walled Curved Beams", *Journal of Sound and Vibration*, Vol. 237, No. 1, pp. 101-118.
- Saavedra, P.N. and Cuitiño, L.A., 2001, "Crack Detection and Vibration Behavior of Cracked Beams", *Computer & Structures*, Vol. 79, pp. 1451-1459.
- Salawu, O.S., 1997, "Detection of Structural Damage in Frequency: Through Changes a Review", *Engineering Structures*, Vol. 19, No. 9, pp. 718-723.
- Storn, R. and Price, K., 1997, "Differential Evolution – A Simple and Efficient Heuristic for Global Optimization Over Continuous Spaces", *Journal of Global Optimization*, Vol. 11, pp. 341-359.
- Vlasov, V.Z., 1961, "Thin-Walled Elastic Beams", 2° National Science Foundation, Washington DC.
- Yoo, C.H. and Feherenbach, J.P., 1981, "Natural Frequencies of Curved Girders", *Journal of the Engineering Mechanics Division (ASCE)*, Vol. 107, No. 2, pp. 339-353.

RESPONSIBILITY NOTICE

The authors are the only responsible for the printed material included in this paper.

A Low Cost Electromechanical Impedance-Based SHM Architecture for Multiplexed Piezoceramic Actuators

Roberto Mendes Finzi Neto ¹, Lizeth Vargas Palomino ², Tiago Fernandes Bitencourt ², Valder Steffen Jr ², Domingos Alves Rade ² and Carlos Alberto Gallo ²

¹ Federal University of Goiás – Campus Catalão Av. Dr. Lamartine P. Avelar 1120, Setor Universitário – Catalão – Brazil.

² Federal University of Uberlândia – School of Mechanical Engineering – Campus Santa Mônica, Av. João Naves de Avila 2121, Bloco 1M – Uberlândia – Brazil.

Abstract: The Electromechanical Impedance (EMI) method has been considered as a promising tool for Structural Health Monitoring (SHM) in real time. Usually, massive, high-cost, single-channel impedance analyzers are used to process the time domain data to obtain the complex frequency-dependent electromechanical impedance functions, from which features related to the presence, position and extent of damage can be extracted. However, for large structures, it is desirable to deploy an array of piezoelectric transducers over the area to be monitored and measure these transducers successively so as to increase the probability of successful detection of damage in an early phase. In this context, a miniaturized, low cost, highly expandable SHM architecture for monitoring an array of multiplexed piezoelectric transducers is proposed. Each logical block of the proposed architecture is presented in detail. The proposed architecture neither uses costly Fast Fourier Transform (FFT) analyzers/algorithms nor requires a digital computer for processing. A personal computer is only necessary for user interfacing. It has been verified that the system can work for frequencies ranging from 0 to 400 kHz with high accuracy and stability. A prototype using inexpensive integrated circuits and a Digital Signal Processor (DSP) was built and tested for an aluminium beam. Simulated damages were introduced to each structure and the detection performance of the prototype was tested. The actual prototype uses a Universal Serial Bus (USB) connection to communicate with a personal computer; however, a WiFi® connection is also available.

Keywords: Electromechanical impedance, piezoelectric transducer, structural health monitoring, DSP.

INTRODUCTION

The development of in-service structural health monitoring and damage detection techniques has attracted a large number of academic and industrial researchers. The ultimate goal is to monitor the structure integrity in operation conditions, during its entire working life. The reduction of maintenance costs by minimizing explicit preemptory maintenance and prevention of catastrophic failures are highly desirable.

Among the various existing SHM methods, the so-called Electromechanical Impedance technique has been regarded as one of the most promising ones for use in industrial engineering structures, as reported in a number of studies (Chaudhry et al., 1995; Giurgiutiu et al, 1999; Lalande et al, 1996; Liang et al, 1994, Park et al, 1999, Peirs et al, 2004; Sun et al, 1995). Basically, the method identifies failures by monitoring the structure mechanical impedance that will exhibit variations in the presence of structural damage. Since the structure mechanical impedance is difficult to obtain directly, a piezoelectric transducer, most frequently a PZT (lead-zirconate-titanate) ceramic patch bonded to the monitored structure (or embedded into it) is used as a sensor-actuator device. The electric impedance of the PZT is directly related to the mechanical impedance of the host structure (Park and Inman, 2001).

Figure 1 shows the well-known one-dimensional model representation of a mechanical system containing an integrated sensor-actuator piezoelectric patch (Raju, 1997).

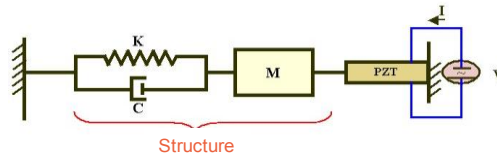


Figure 1. One-dimensional electromechanical coupling model.

The solution of the wave equation for the PZT patch connected to the structure leads to frequency-dependent electrical admittance given by Eq. (1) (Liang et al, 1994):

$$Y(\omega) = i\omega a \left[\bar{\epsilon}_{33}^T (1 - i\delta) - \frac{Z_s(\omega)}{Z_s(\omega) + Z_a(\omega)} d_{31}^2 \hat{Y}_{11}^2 \right] \quad (1)$$

where $Y(\omega)$ is the electrical admittance (inverse of the electrical impedance), Z_a and Z_s are the PZT's and the structure's mechanical impedances, respectively, \hat{Y}_{11}^2 is the complex Young's modulus of the PZT in direction 1 under zero electric field, d_{31} is the piezoelectric coupling constant at zero stress, $\bar{\epsilon}_{33}^T$ is the dielectric constant at zero stress, δ is the dielectric loss

tangent of the piezoelectric patch, and a is a geometric constant of the PZT patch. This equation indicates that the electrical impedance of the PZT wafer bonded onto the structure is directly related to the mechanical impedance of the host structure.

Damage causes direct changes in the structural stiffness and/or damping and alters the local dynamic characteristics of the system. As a result, the mechanical impedance is modified by structural damage. Assuming that the PZT patch's properties remain constant (Chaudhry et al., 1995). Therefore, any change in the electromechanical impedance signature is considered as an indication of structural change, which can be induced by various types of damage.

By monitoring the measured electromechanical impedance and comparing it to a baseline measurement that corresponds to the pristine condition, one can qualitatively determine that incipient structural damage has occurred. The sensitivity of the Non Destructive Evaluation (NDE) technique in detecting damage is closely related to the frequency band selected in the excitation signal of the PZT (Moura Jr and Steffen Jr., 2006). Usually, the PZT is excited with a sinusoidal waveform, with low amplitude (typically of the order of 1 Volt) at frequencies varying from 30 kHz to 250 kHz (Raju, 1997) and up to 1000 kHz for some structures and applications (Giurgiutiu and Zagrai, 2005). The optimum frequency band for pristine conditions under practical applications remains a subject of study for the EMI-based method. Some of the most recent papers working on this issue are those by Peairs et al. (2004).

Structural Health Monitoring (SHM) can play an important role in maintaining safety of in-service structures. The development of an integrated sensory system able to monitor, collect, and deliver the information necessary for structural health monitoring becomes an important issue in this context. One of the proposed approaches is to utilize arrays of PZT patches attached to the surface of a metallic structure or embedded in a composite material. When attached to the structure and connected to the electronics, the PZT patches become active sensors that can perform both as actuators and sensors. The high-frequency response is not affected by the global structural vibration modes and external conditions such as flight loads and ambient vibrations, (Giurgiutiu and Zagrai, 2005). Thus, the impedance method allows for monitoring incipient local damage, like cracks, which produces only imperceptible or hardly noticeable changes to the large-scale dynamics of the entire structure. For this reason, the high-frequency impedance method can detect localized small damage that is otherwise undetectable through conventional vibration testing.

While the impedance response plots provide a qualitative approach for damage identification, the quantitative assessment of damage is traditionally made by using a scalar damage metric. In an earlier work (Sun et al., 1995), a simple statistical algorithm, which is based on frequency-by-frequency comparisons, referred to as Root Mean Square Deviation (RMSD), has been used to quantify damage.

Temperature changes, among all other ambient conditions, may affect the electric impedance signatures measured by a PZT patch. Many experiments from various case studies have shown that the real part of the PZT electromechanical impedance is more sensitive to damage and other changes in the structure features than the magnitude or the imaginary part (Giurgiutiu et al., 1999). Then, the proposed monitoring system discards the imaginary part and only the real part of the electromechanical impedance is used to assess the monitored structures aiming at minimizing the effect of temperature change.

MODELING THE IMPEDANCE OF THE PZT

The EMI expresses a complex valued function dependent on frequency. For each corresponding frequency, it can be represented in terms of its real and imaginary parts or, alternatively, magnitude and phase. The easiest way to calculate the corresponding impedance, for a given excitation frequency f_{ex} , is using Eq. (2) and Eq.(3), where $V_{ex}(\omega)$ and $I_{PZT}(\omega)$ are the excitation voltage and the current at the PZT patch, respectively.

$$Z(\omega) = \frac{V_{ex}(\omega)}{I_{PZT}(\omega)} \quad (2)$$

$$\omega = 2 \pi f_{ex} \quad (3)$$

Equations (4) and (5) are used to calculate both the real and imaginary parts of the electromechanical impedance at a given excitation frequency ω and phase lag θ .

$$Z_{Re}(\omega) = \frac{V_{ex\ peak}}{I_{PZT\ peak}} * \cos(\theta) \quad (4)$$

$$Z_{Im}(\omega) = \frac{V_{ex\ peak}}{I_{PZT\ peak}} * \sin(\theta) \quad (5)$$

In general, $I_{PZT}(\omega, t)$ is not measured directly. A shunt resistor is used for this purpose. Fig. 2 presents two possible circuits for measuring the current.

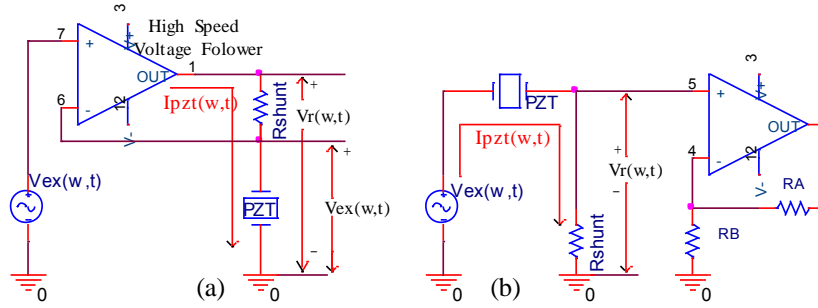


Figure 2. Circuits used to measure the PZT current.

The circuit presented in Fig. 2 (a) is commonly used in applications where many PZT patches are bonded to a metallic structure. The voltage amplitude applied to the PZT patch is kept constant independently from the PZT impedance variation and the R_{shunt} value. Eq. (6) and Eq.(7) describe how the real and imaginary parts of the PZT impedance are calculated.

$$Z_{Re}(\omega) = \frac{R_{shunt} * V_{ex\ peak}}{V_r\ peak - V_{ex\ peak}} * \cos(\theta) \quad (6)$$

$$Z_{Im}(\omega) = \frac{R_{shunt} * V_{ex\ peak}}{V_r\ peak - V_{ex\ peak}} * \sin(\theta) \quad (7)$$

The circuit presented in Fig. 2 (b) is chosen for applications where the monitored structure is not a metallic one, due to the ground reference problem (Wang and You, 2008). A second stage containing a gain amplifier is necessary for the circuit, due to the small value of R_{shunt} (typically between 100Ω – 200Ω for better results). The real and imaginary parts of the PZT impedance are calculated as follows (Eq.8 and Eq.9).

$$Z_{Re}(\omega) = \frac{R_{shunt} * V_{ex\ peak}}{V_r\ peak} * \frac{R_A + R_B}{R_B} \cos(\theta) \quad (8)$$

$$Z_{Im}(\omega) = \frac{R_{shunt} * V_{ex\ peak}}{V_r\ peak} * \frac{R_A + R_B}{R_B} \sin(\theta) \quad (9)$$

The bandwidth and gain accuracy of the topology illustrated in Fig. 2(b) is limited by the OA and resistors RA and RB . Precautions, such as the use of low tolerance resistors and high speed OA , must be taken to avoid measurement errors in $I_{PZT}(\omega, t)$.

The majority of the techniques used to measure the real and/or imaginary parts of the electromechanical impedance will need the three following parameters: $V_{ex\ peak}$, $I_{pzt\ peak}$ and θ . According to some software-based techniques, θ can be calculated from $V_{ex}(\omega, t)$ and $I_{PZT}(\omega, t)$ using a curve fitting technique (Radil et al., 2008; Ramos, 2009).

THE IMPEDANCE MEASUREMENT PROBLEM

Complex frequency-dependent impedance values are usually measured at low power levels with an impedance network analyzer. However, the cost of this type of equipment is in the order of tens of thousands of U.S. dollars. Besides, classical impedance analyzers are quite heavy and cumbersome. Cheaper impedance measurement instruments usually cover only a fixed set of frequencies at low frequency ranges and are limited to less than ten different frequencies. The hardware issues related to the EMI technique were first investigated by Peairs and Inman (2004), who proposed a low-cost version of the EMI technique using a FFT signal analyzer and a shunt resistor associated to an operational amplifier to measure the current of the PZT. Peairs and Inman's work has been further extended by several research groups during the recent years. Xu and Giurgiutiu (2005) proposed a clever way to improve time processing and the data acquisition requirements by developing a frequency swept excitation signal with a constant energy spectrum. Filho and Baptista (2008) continued in the same direction but, as an alternative, they have chosen to use a chirp excitation signal, leading to good results.

All these solutions for a low cost version of the EMI technique are based on FFT algorithms implemented in signal analyzers or in personal computers with a DAQ board (the cost ranges from US\$ 5,000 to US\$10,000). Implementations using DSP with FFT capabilities are less costly though less efficient with respect to the processing time required, when compared to solutions implemented using personal computers or signal analyzers.

Besides the FFT based techniques for impedance analyzes one finds the curve fitting algorithms. The sine fitting algorithm is a well known example as presented by Radil et al (2008). They proposed a very precise method for measuring the impedance. At a low sampling rate, the authors were able to reconstruct the excitation voltage and the current applied to the

impedance. Then, the phase and amplitude of the impedance were extracted with high accuracy (less than 1% error) and stability. The authors selected a fixed-point DSP working at 40 MHz, 80 MIPS capacity. Their system takes 1.7s to calculate amplitude and phase at each frequency point. Consequently, to construct a baseline with 400 frequency points 680s are required. Ramos et al (2009) proposed an ellipse-fitting algorithm, which is more precise, stable and faster than the sine fitting algorithms. However, the processing time remains a major issue.

Techniques based only on software (curve fitting algorithms) are more precise but the processing time tends to be unaffordable. Techniques based on Digital Signal Analyzers (DSAs) are more expensive but they are much faster (Witczak et al., 2009). DSPs implementing FFT algorithms are less expensive and faster but are limited to the DSP performance. Next section describes the proposed architecture for a SHM system using a hybrid solution.

THE ARCHITECTURE OF THE PROPOSED SYSTEM

The alternative is to use a hybrid topology, first proposed by Finzi Neto et al. (2010), in which hardware and software approaches are combined together to measure amplitude and phase of the impedance from each PZT. Fig. 3 illustrates the proposed architecture.

The idea expressed in Fig. 3 measures the phase θ and the current I_{PZT} using hardware. The impedance $Z_{Re}(\omega)$ is calculated by software. The main advantages for this method are: (a) The computational complexity of the software is reduced to N (where N is the number of frequency points); (b) I_{PZT} can be sampled at lower rates with a sampling rate independent of f_{ex} ; (c) Phase θ is digitally measured using a Two Edge Counter, which is found in every DSP. A minimum resolution of 16 bits is required, for better results.

Three main circuit blocks are illustrated in Fig. 3: The switching system, the signal conditioning and the measurement and DSP hardware.

The developed DSP software is intended to work standalone. Only a few working parameters can be recorded directly on flash memory or externally defined by a PC or other computer system through a USB connection. Fig. 4 presents the flowchart of this computer code.

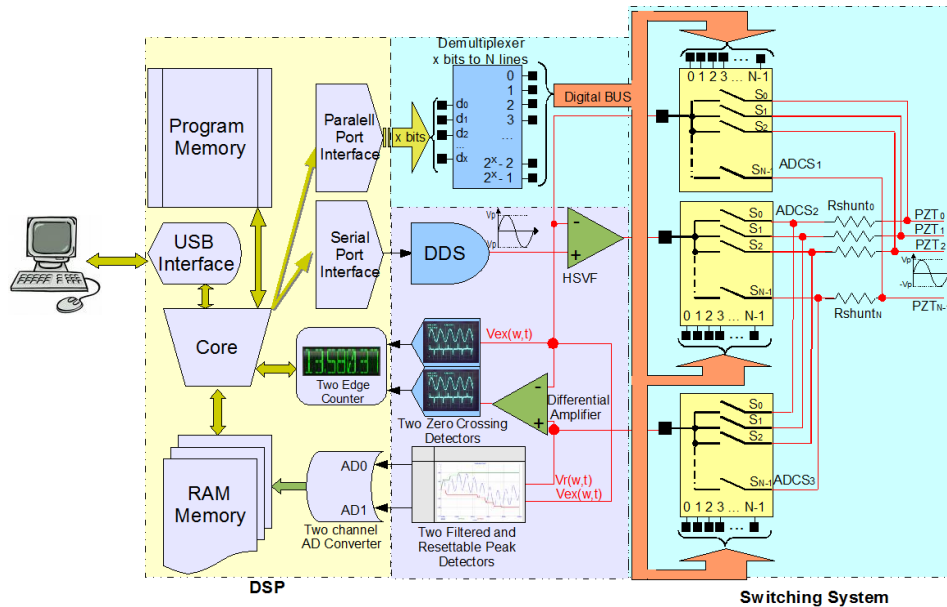


Figure 3 – Proposed SHM system using a hybrid impedance measuring architecture

THE PROTOTYPE AND EXPERIMENTAL RESULTS

A prototype for 16 PZT patches was built for testing and validating the proposed architecture. A TMDSEZS2808 eZdsp Starter Kit from Texas Instruments was used to store the data and run the DSP program. This kit is based on the TMS320F2808, working at 100 MHz. All the required peripherals (ADC, TEC, PPI, SPI, USB, etc) are available in an “easy to use” platform. Three ADG526 from Analog Devices were used as ADCS1, ADCS2 and ADCS3. Sixteen low tolerance (less than 1%) shunt resistors of 100 Ω were used to sample the PZT current. The DDS was implemented with a single AD9834, also from Analog Devices. The HSVP uses only a LM318 operational amplifier from NEC. The differential amplifier was implemented by using the ADA4922-1, the two FRPD used the PKD01, and the two ZCD used the AD8564, all from Analog Devices. A personal computer running interface software based on Labview® was used to communicate with the prototype. When the baseline measurements are made, the software can store all the baselines for further analysis.

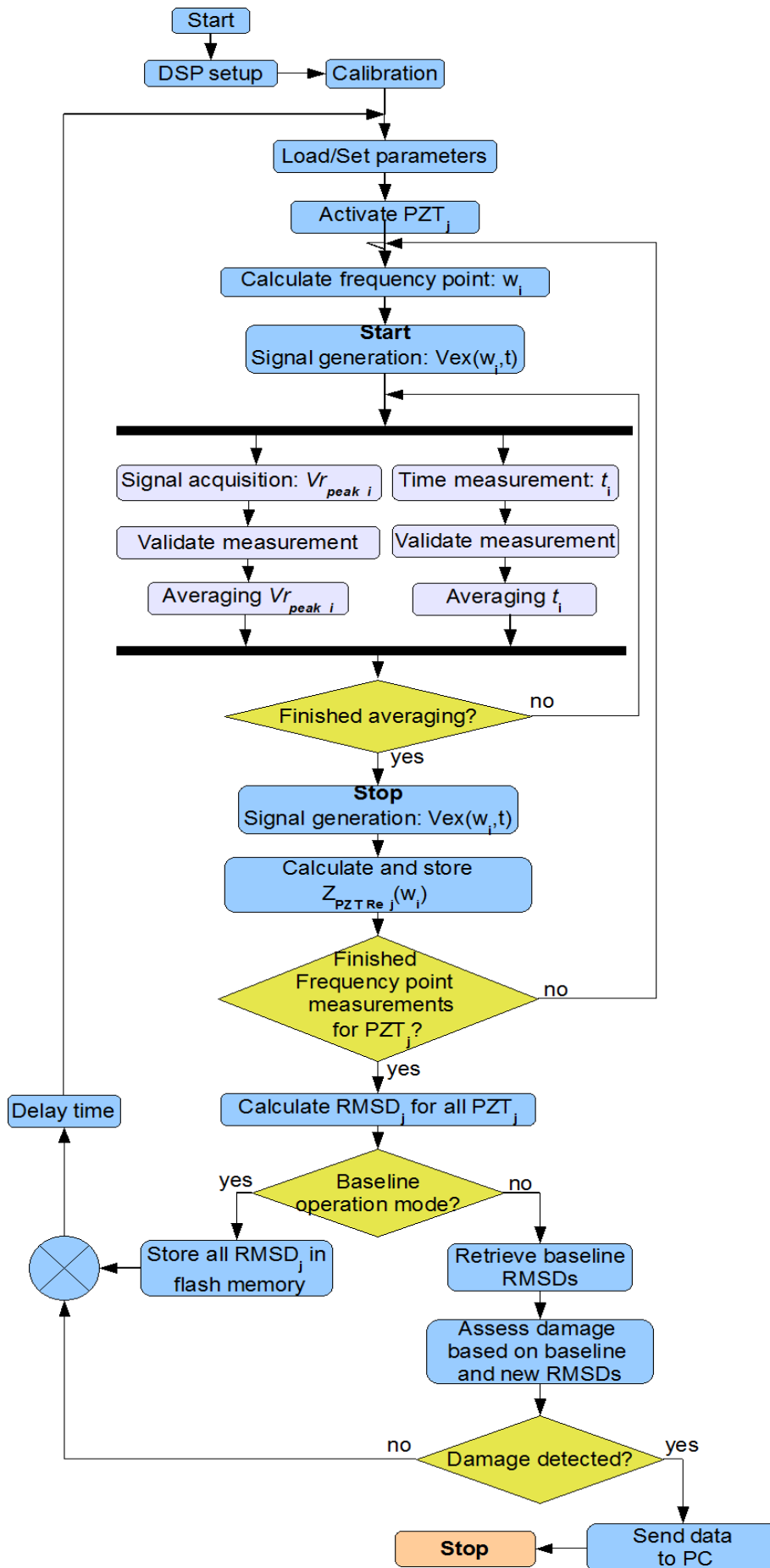


Figure 4 – Flow chart of the DSP program

A HP4194A impedance analyzer was used as a reference to verify the stability, accuracy and sensitivity of the prototype. Using a specimen, a set of impedance measurements (containing 401 frequency lines), for PZT1 and PZT2 patches were obtained by using both systems, which are configured to calculate each frequency line sixteen times and then compute their mean value. The calculated RMSD values quantify the largest difference between the reference impedance (HP4194) and the counterpart obtained from the prototype during three days of repeated measurements. The results are presented in Fig. 5.

From the results presented in Fig. 5 it can be seen that, qualitatively, the impedances obtained from the impedance analyzer and the proposed system are very close to each other. Quantitatively, the low RMSD values indicate a good accuracy and stability of the prototype results.

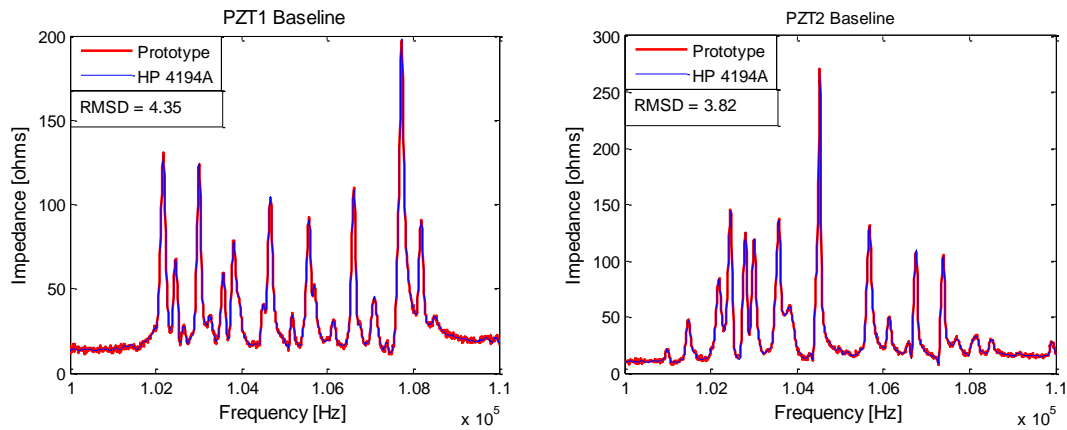


Figure 5 – Baseline FRF obtained using the impedance analyzer and the prototype for the aluminium beam under pristine conditions.

As the accuracy and stability of the system were demonstrated, further experiments were performed by using the prototype, as presented in the following sections for illustration purposes.

Case study # 1: aluminium beam

The experiment was conducted at room temperature using a 500 mm x 25 mm x 4 mm aluminium beam as shown in Fig. 6a. A metallic rivet, inserted at point D, was used to simulate damage when extracted, and two PZT patches, having dimensions 15 x 15 mm² and 10 x 15 mm², were bonded to the beam. The structure was suspended by elastic cords to simulate free boundary conditions, as shown in Fig. 6(b). The frequency range between 100 kHz and 110 kHz (containing 401 frequency lines) has shown to be more sensitive to the type of damage, as resulted from a trial and error approach.

The experiment was conducted in two steps using both the proposed system and the impedance analyzer, with these measuring devices configured to calculate each frequency line sixteen times and then use the corresponding mean value:

1. Baseline FRF and RMSD, for PZT1 and PZT2, were obtained and calculated. Fig.7 presents the corresponding results.
2. The metallic rivet at point D was extracted from the beam and a new set of impedances and RMSD were measured and calculated for each PZT patch.

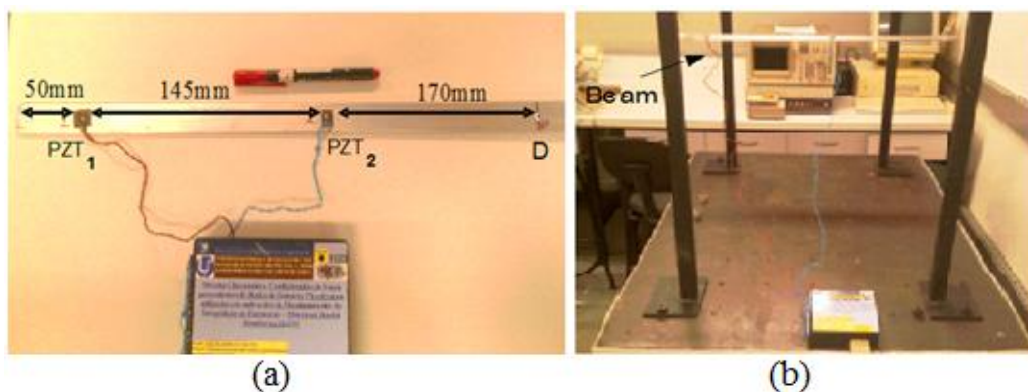


Figure 6 – Aluminium beam used in the experiment: (a) Configuration of the beam; (b) Free-free set.

Figure 7 presents the impedances for PZT1 and PZT2, after the damage, measured both by the prototype and the impedance analyzer. The low RMSD values confirm the high accuracy and stability of the measurements.

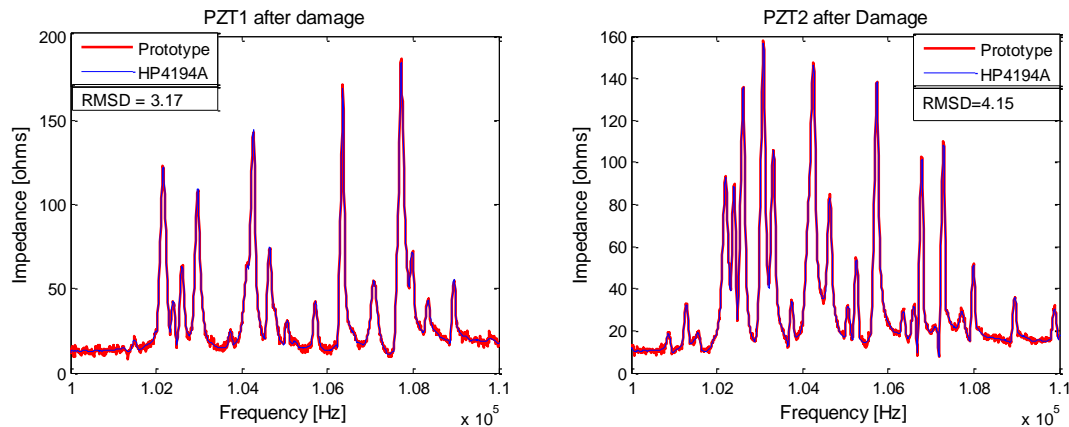


Figure 7. Amplitudes of the electromechanical impedances obtained using the HP4194A impedance analyzer and the prototype for the damaged aluminium beam

To assess the damage, the impedances before and after the damage, obtained by using the prototype, are compared in Fig.8.

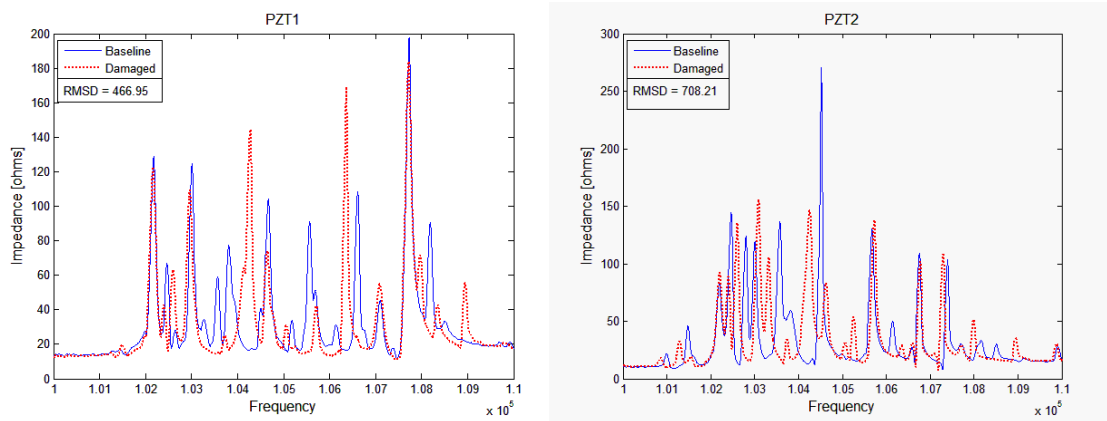


Figure 8. Amplitude of the impedances before and after the metallic rivet was extracted from the beam.

Qualitatively, it can be clearly seen that the impedances for both PZT patches have changed significantly after the occurrence of damage. Quantitatively, the high values found for the RMSD metric suggest how serious the damage is.

Case study # 2: aluminium aircraft panel

The second experiment was conducted at room temperature considering the aircraft panel presented in Fig. 9. Due to the size and complexity of the structure (0.8 m x 0.8 m), six PZT patches of 18 mm x 18 mm were used in the experiment. To simulate the damage the metallic rivet outlined in Fig. 9(b) was extracted. The number of PZT patches used was arbitrary (no preliminary study was done to optimize the number of PZT patches).

The experiment followed the same protocol described above with the exception of the frequencies ranged from 100 kHz to 110 kHz.

The set of impedance signals is presented in Fig.10. The same small impedance variations, seen in the Fig.10, are observed for all the impedance signals. The RMSD values from PZTs #1, #2, #3 and #5 presented low RMSD values as compared to those from PZT #4 and PZT #6. A higher value for PZT #4 was expected due to its position with respect to the damage. However, for the PZT #6, the high RMSD value indicates a structural change that was detected by this PZT patch.



Figure 9. Aircraft panel: (a) 6 PZT patches bonded to the structure; (b) metallic rivet.

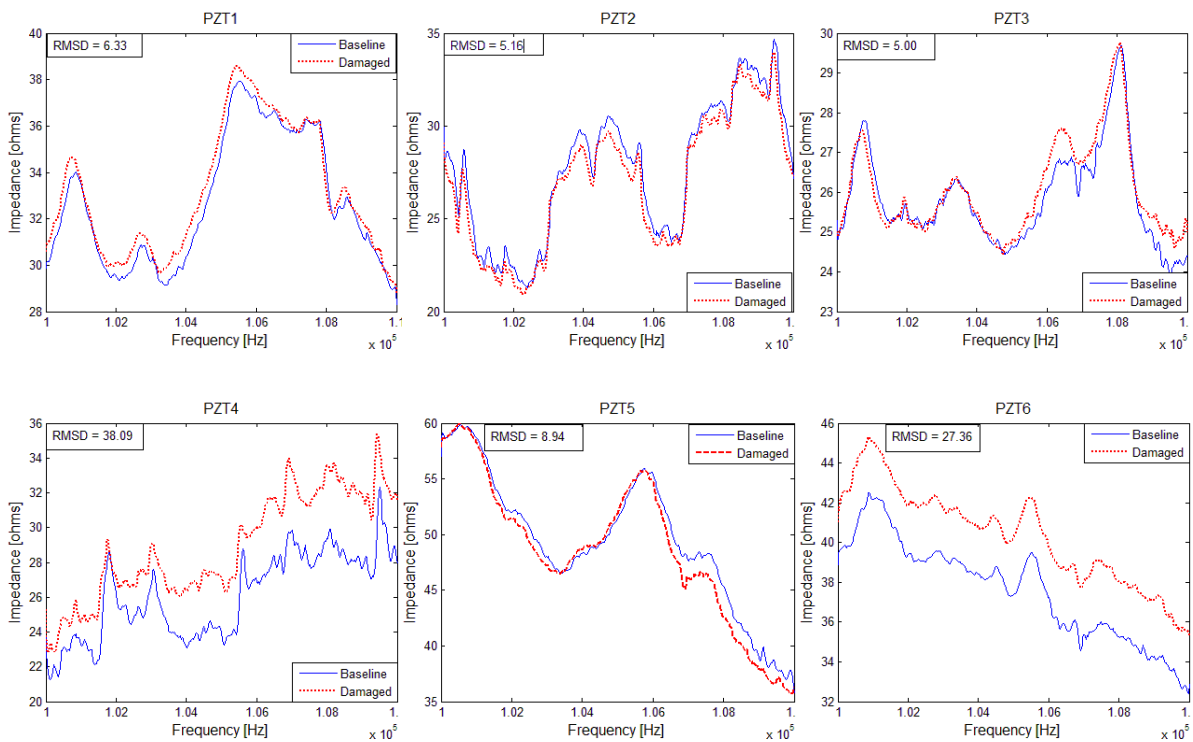


Figure 10. Impedances in the range (100kHz - 110kHz) before and after the metallic rivet was extracted from the aircraft panel.

CONCLUSIONS

This paper presented alternative electromechanical impedance based architecture for multiplexed piezoceramic sensors/actuators used in SHM applications. The proposed architecture offers stability, readability, low cost and scalability. Almost any kind, size and complexity of a structure can be monitored by using the proposed system.

The impedance signals obtained from the presented architecture were shown to be similar to those obtained from a classical impedance analyzer. As the proposed architecture leads to much lower costs, it seems to be better adapted for industrial applications.

ACKNOWLEDGEMENTS

The authors are thankful to FAPEMIG and CNPq (research agencies in Brazil) for providing financial support to this work through Proc. Nb. 574001/2008-5 - (INCT-EIE).

REFERENCES

- Chaudhry, Z., Lalande, F., Ganino, F., Rogers, C.A., and Chung, J. (1995). Monitoring the Integrity of Composite Patch Structural Repair Via Piezoelectric Actuators/Sensors. *Proceedings of AIAA/ASME/ASCE/AHS/ASC 36th Structures, Structural Dynamics and Materials Conference, Adaptive Structures Forum, AIAA Publishing*, pp. 2243-2248.
- Filho, J. and Baptista, F.A. (2008). "New Impedance Measurement System for PZT Based Structural Health Monitoring." *IEEE Transactions on Instrumentation & Measurements*. VOL. 58, NO. 10, PP. 3602-3608.
- Finzi Neto, R. M.; Steffen Jr., V.; Rade, D. A.; Gallo, C. A..(2010). Proposal of a solid State Switching and Signal Conditioning System for Structural Health Monitoring Based on Piezoelectric sensors/actuators. PACAM XI - 11th Pan-American Congress of Applied Mechanics, 2010, Foz do Iguaçu, PR – Brazil
- Giurgiutiu, V., Reynolds, A., and Rogers, C.A., (1999). Experimental investigation of E/M impedance health monitoring of spot-welded structural joints. *Journal of Intelligent Material Systems and Structures*, vol. 10, 802-812.
- Giurgiutiu, V. and Zagari, A.N. (2005). Damage Detection in Thin Plates and Aerospace Structures with the Electro-Mechanical Impedance Method. *Journal of Structural Health Monitoring*, vol. 4: pp. 99 - 118.
- Lalande, F., Childs, B., Chaudhry, Z., and Rogers, C.A. (1996). High-Frequency Impedance Analysis for NDE of Complex Precision Parts. *Proceedings of SPIE Conference on Smart Structures and Materials*, SPIE Publishing, V. 2717, pp.237-245.
- Liang, C., Sun, F.P., and Rogers, C.A., (1994). *Coupled Electromechanical Analysis of Adaptive Material Systems – Determination of the Actuator Power Consumption and System Energy Transfer*?. *Journal of Intelligent Material Systems and Structures*, vol. 5, pp. 12–20.
- Moura Jr, J. R. V., Steffen Jr., V. (2006), Impedance-based Health Monitoring for aeronautic Structures using Statistical Meta-modeling. *Journal of Intelligent Materials Systems and Structures*. vol:17, no:11, pp:1023-1036.
- Park, G., Kabeya, K., Cudney, H.H. and Inman, D.J. (1999). Impedance-based structural health monitoring for temperature varying applications. *JSME International Journal, Series A*, 42(2): 249–258.
- Park, G. and Inman, D.J. (2001). Impedance-based structural health monitoring, monograph: In: Woo, S.C. (ed), *Nondestructive Testing and Evaluation Methods for Infrastructure Condition Assessment*, New York, NY: Kluwer Academic Publishers.
- Peairs, D.M., Park, G. and Inman, D.J. (2004). Improving Accessibility of the Impedance-Based Structural Health Monitoring Method. *Journal of Intelligent Material Systems and Structures*, 15(2):129–139.
- Radil, T., Ramos, P.M., Serra, A.C. (2008). Impedance Measurement With Sine-Fitting Algorithms Implemented in a DSP Portable Device. *IEEE Transactions on Instrumentation and Measurement*. vol. 57, no. 1.
- Raju, V. (1997), Implementing Impedance-Based Health Monitoring, MSc Thesis, Virginia Tech, USA.
- Ramos, P.M., Janeiro, F.M., Tlemçani, M.(2009). Recent Developments on Impedance Measurements With DSP-Based Ellipse-Fitting Algorithms. *IEEE Transactions on Instrumentation and Measurement*, vol. 58, no. 5.
- Sun, F., Chaudhry, Z., Liang, C., and Rogers, C.A. (1995). Truss Structure Integrity Identification Using PZT Sensor-Actuator. *Journal of Intelligent Material Systems and Structure*, vol.6, pp. 134-139.
- Wang, S., You, C (2008). A Circuit Design for Impedance-based Structural Health Monitoring. *Journal of Intelligent Material Systems and Structures*, vol. 19, pp. 1029 - 1040.
- Witczak, M., Rybski, R., Kaczmarek, J. (2009). Impedance Measurement With the D-Optimum Experimental Conditions. *IEEE Transaction on Instrumentation and Measurement*, vol. 58, no. 8.
- Xu, B. and Giurgiutiu, V. (2005). A Low-Cost and Field Portable Electromechanical (E/M) Impedance Analyzer for Active Structural Health Monitoring. in: *Proc. 5th International Workshop on Structural Health Monitoring*, Stanford University, September 15–17.

Response of the cracked rotor under uncertain parameters via the Harmonic Balance Method and the Polynomial Chaos Expansion

Béatrice Faverjon¹ and Jean-Jacques Sinou²

¹ Laboratoire de Mécanique des Contacts et des Structures UMR-CNRS 5259
INSA-Lyon, 18-20, rue des Sciences
69621 Villeurbanne Cedex France

² Laboratoire de Tribologie et Dynamique des Systèmes UMR-CNRS 5513
Ecole Centrale de Lyon, 36 avenue Guy de Collongue
69134 Ecully Cedex, France

Abstract: This paper is dedicated to study the effects of the presence of a transverse crack in a rotating shaft under uncertain physical parameters to obtain useful informations in detecting the presence of a crack in rotating system. The non linear response, that is calculated by the Harmonic Balance Method in a deterministic way is here expanded in more in the Polynomial Chaos. The results of the random non linear response is analyzed and the Harmonic Balance Method combined with the Stochastic Finite Element Method is compared with the reference method associating the Harmonic Balance Method and the Monte Carlo Simulations.

Keywords: cracked rotor, uncertainties, Harmonic Balance Method, Polynomial Chaos Expansion

INTRODUCTION

Characterizing the behavior of cracks is of great importance in rotor-dynamics and health monitoring domain, and is made through non-destructive testing (Wauer, 1990; Gasch, 1993). Lots of researches have been focused on the detection of transverse cracks mostly done by caring out the changes at the level of the natural frequencies or studying the evolution of the nonlinear behavior of the system at the super harmonics. When considering a cracked rotor, one phenomenon clearly identified is the breathing of the crack that is time-dependent and that changes the stiffness of the system. Previous researches carried out that: one signature for detecting cracks can be found through the evolution of the $2\times$ amplitudes at one-half resonance speeds and the associated distortion of the orbit; a great information for the detection can be given by the presence of the $3\times$ super harmonic frequency components. One real problem is that some parameters vary and unfortunately distort the nonlinear dynamic behavior of the rotor system and the detection of the crack. Moreover, these variations are usually unknown that brings uncertainties in the modeling. Very frequently, the uncertain quantities are the material parameters of the rotor, the unbalance excitation force and the boundary conditions. The model has then to be taken as random.

There exist few methods to obtain a correct modeling of the uncertainties. Some methods being able to be used in rotor-dynamics are the Monte Carlo simulations (Shinozuka and Astill, 1972), one of the most straightforward but computationally expensive tools; the perturbation method (Nakagiri and Hisada, 1982) and the Neumann expansion (Adomian and Malakian, 1980) which are efficient in the case of small perturbations; the Polynomial Chaos Expansion in conjunction with a Galerkin procedure that is the Stochastic Finite Element Method (Ghanem and Spanos, 1991; Ghanem and Kruger, 1996). The polynomial chaos basis is an orthogonal basis set of random variables, represented in a mean-square convergent expansion in terms of multidimensional Hermite polynomials of normalized Gaussian variables. This last method, even if technically the dimension of the system to solve is bigger, yields to a smaller computing time for a good accurate of the random response of the system. This paper aims to show the effect of the uncertainties of input parameters on the response of the cracked rotor using the Stochastic Finite Element Method.

An efficient deterministic way to obtain the non-linear response of a cracked rotor is to use the Harmonic Balance Method. Here, we present the combination of the Harmonic Balance Method and the Stochastic Finite Element Method to calculate the response of a cracked rotor under uncertain parameters.

Firstly, we will focus ourselves on the rotor and on the modeling of the crack. The rotor system consists in a shaft with one disc at the mid-span. The crack section is defined by the reduction of the second moment of area of the element at the location of the crack as previously suggested by Mayes and Davies (Davies and Mayes, 1984; Mayes and Davies, 1984). Secondly, to quantify the effects of uncertainties on the response variability in the cracked rotor systems, the stochastic response obtained via the combination of the Harmonic Balance Method (in this particular case, see (J-J. Sinou and Lees, 2005; J-J. Sinou and Lees, 2007) and the Polynomial Chaos Expansion procedure will be described and studied.

Finally, the results obtained from the alternative approach via the Harmonic Balance Method and the Polynomial Chaos Expansion are compared with computations using the reference Monte Carlo method that is done by calculating the response of the rotor for many samples and using the deterministic calculation from the Harmonic Balance Method.

MODEL OF THE CRACKED ROTOR

The layout of the cracked rotor system under consideration is shown in Fig. 1. The rotor is composed of a shaft of length 0.5m with one disc at the mid-span. The material properties and dimensions of the rotor are given in Table 1. It is discretized into Timoshenko beam finite elements, with four degrees of freedoms at each node, the axial and torsional degrees of freedom being not considered. After assembling the various shaft elements and the rigid disc, the equations of the uncracked rotor can be written as

$$\mathbf{M}\ddot{\mathbf{x}} + \mathbf{D}\dot{\mathbf{x}} + (\mathbf{K} - g(t)\mathbf{K}_c)\mathbf{x} = \mathbf{f} + \mathbf{q} \quad (1)$$

where $\ddot{\mathbf{x}}$, $\dot{\mathbf{x}}$ and \mathbf{x} are the acceleration, velocity and displacement vectors. \mathbf{M} and \mathbf{K} are the mass and stiffness matrices of the complete uncracked rotor, that is : \mathbf{M} includes the mass matrices of the shaft and the rigid disc; \mathbf{K} includes the stiffness matrices of the shaft and the supports, together with the circulatory matrix which accounts for the shaft's internal damping. Matrix \mathbf{D} combines the effects of the shaft's internal damping, damping of the supports, and gyroscopic moments. Plus, \mathbf{f} and \mathbf{q} contain the gravitational and balance forces, respectively. The function $g(t)$ describing a simple crack breathing phenomenon such as discussed by Sinou and Lees (Sinou and Lees, 2005; Sinou, 2006), typical in weight dominated systems, may be approximated by a cosine function $g(t)$

$$g(t) = \frac{1 - \cos\omega t}{2} \quad (2)$$

where ω defines the rotational speed of the rotor. If $g(t) = 0$, the crack is closed and has no effect on the dynamic behavior of the rotor (i.e. the rotor may be treated as uncracked). If $g(t) = 1$, the crack is fully open.

The crack section is defined by the reduction of the second moment of area ΔI of the element at the location of the crack (see the paper of Mayes and Davies (Davis and Mayes,1984; Mayes and Davis,1984) for more details). By using Rayleigh's method, they obtained that the change in ΔI satisfied

$$\Delta I = I_0 \left(\frac{\frac{R}{l} (1 - \nu^2) F(\mu)}{1 + \frac{R}{l} (1 - \nu^2) F(\mu)} \right), \quad (3)$$

where I_0 , R , l , and ν are the second moments of area, beam radius, length of the section and Poisson's ratio, respectively. μ is the non-dimensional crack depth and is given by $\mu = \frac{h}{R}$ where h defines the crack depth of the beam, as shown in Figure . $F(\mu)$ defines the non-linear compliance as a function of variations in non-dimensional crack depth μ , which can be derived from a series of experiments using chordal cracks (see Mayes and Davies (Davis and Mayes,1984; Mayes and Davis,1984)).

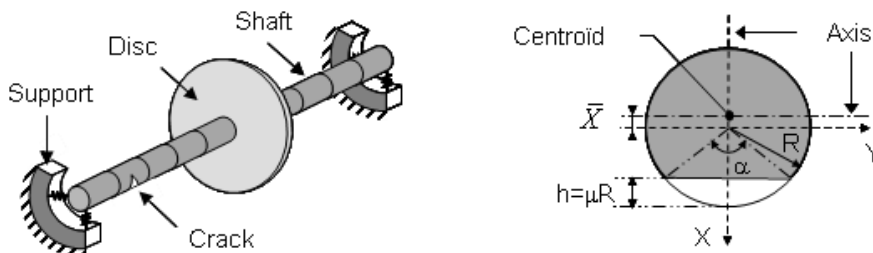


Figure 1: Finite-element model of the rotor and the cracked-beam section

Equation 7 becomes

$$(\mathbf{\Lambda}(\tau) + \mathbf{\Lambda}_c) \mathbf{\Theta}(\tau) = \mathbf{\Gamma}(\tau) \quad (10)$$

We consider that $\mathbf{K}(\tau) = \mathbf{K}_b + \tilde{\mathbf{K}}(\tau)$ with \mathbf{K}_b the support boundary conditions taken as deterministic and $\tilde{\mathbf{K}}(\tau)$ obtained from the Karhunen-Loeve expansion implemented in the Galerkin formulation of the finite element method (Ghanem and Spanos, 1991) with a gaussian law for the stiffness of the rotor and given by

$$\tilde{\mathbf{K}}(\tau) = \overline{\tilde{\mathbf{K}}} (1 + \delta^K \xi^K(\tau)) . \quad (11)$$

in which $\{\xi_i\}$, $i = 1$ to L , is a set of orthonormal random variables, $\overline{\bullet}$ is the mean of one random quantity and δ^\bullet is its variation coefficient. It should be noted that the normal distribution assumed has been truncated to avoid negative values of the parameter, since it is physically strictly positive. Then, the random expression of $\mathbf{\Lambda}$ is given by

$$\mathbf{\Lambda}(\tau) = \mathbf{\Lambda}_d + \mathbf{\Lambda}_r(\tau) \quad (12)$$

$$\text{where } \mathbf{\Lambda}_d = \begin{bmatrix} \mathbf{K}_b & & & \\ & \mathbf{\Lambda}_1^d & & \\ & & \ddots & \\ & & & \mathbf{\Lambda}_m^d \end{bmatrix} \quad \text{with } \mathbf{\Lambda}_k^d = \begin{bmatrix} \mathbf{K}_b - k^2 \omega^2 \mathbf{M} & k\omega \mathbf{D} \\ -k\omega \mathbf{D} & \mathbf{K}_b - k^2 \omega^2 \mathbf{M} \end{bmatrix} \quad (13)$$

where $\mathbf{\Lambda}_d$ stays deterministic and

$$\mathbf{\Lambda}_r(\tau) = \begin{bmatrix} \tilde{\mathbf{K}}(\tau) & & \\ & \ddots & \\ & & \tilde{\mathbf{K}}(\tau) \end{bmatrix} \quad (14)$$

The unknown solution $\mathbf{\Theta}(\tau)$ is expanded with polynomial chaoses

$$\mathbf{\Theta}(\tau) = \sum_{j=0}^{\infty} \mathbf{Y}_j \Psi_j(\underline{\xi}(\tau)) \quad (15)$$

where $\Psi_j(\underline{\xi}(\tau))$ refers to a rearrangement of the p-order finite dimensional orthogonal polynomials with respect to the gaussian function which constitute a complete basis in the space of second-order random variables ; \mathbf{Y}_j is the unknown deterministic j^{th} vector associated with $\Psi_j(\underline{\xi}(\tau))$ and $\underline{\xi} = \{\xi_r\}$, set of orthonormal random variables (Ghanem and Spanos, 1991).

Besides, for the force term, we have

$$\mathbf{\Gamma} = \mathbf{\Gamma}_g + \mathbf{\Gamma}_u(\tau) \quad (16)$$

$$\text{with } \mathbf{\Gamma}_g = \begin{bmatrix} \mathbf{C}_0^f & \mathbf{0} & \dots & \mathbf{0} \end{bmatrix}^T \quad \text{and } \mathbf{\Gamma}_u(\tau) = \begin{bmatrix} \mathbf{0} & \mathbf{C}_1^q(\tau) & \mathbf{S}_1^q(\tau) & \mathbf{0} & \dots & \mathbf{0} \end{bmatrix}^T \quad (17)$$

where gravity component $\mathbf{\Gamma}_g$ is deterministic and unbalance component $\mathbf{\Gamma}_u(\tau)$ is random and modeled reasonably by one truncated polynomial chaos expansion to order 1

$$\tilde{\mathbf{\Gamma}}_u(\tau) = \overline{\tilde{\mathbf{\Gamma}}_u} (1 + \delta^{\Gamma_u} \xi^{\Gamma_u}(\tau)) , \quad (18)$$

After projection on the chaos polynomial basis, we obtain the following stochastic system to solve

$$\mathbf{A} \mathbf{Y} = \mathbf{F} \quad (19)$$

with each component $[\mathbf{A}]_{ij}$ of \mathbf{A} given by

$$[\tilde{\mathbf{A}}]_{ij} = \left[\left(\mathbf{\Lambda}_c + \mathbf{\Lambda}_d + \overline{\mathbf{\Lambda}_r} \right) \langle \Psi_i^2 \rangle \delta_{ij} + \overline{\mathbf{\Lambda}_r} \delta^K c_{ij1\kappa} \right] \quad (20)$$

and where $\langle \bullet \rangle$ corresponds to the mathematical expectation, δ_{ij} is the Kronecker symbol and $c_{ijk\kappa} = \langle \xi_k^K \Psi_i \Psi_j \rangle$ (Ghanem and Spanos, 1991). Vector $\mathbf{F}(\tau)$ of forces projected on the polynomial chaos basis has polynomial chaos vector terms given by

$$\tilde{\mathbf{F}}_j(\tau) = \mathbf{\Gamma}_g \delta_{0j} \langle \Psi_i^2 \rangle \delta_{ij} + \overline{\tilde{\mathbf{F}}_{u_j}} \left[\langle \Psi_i^2 \rangle \delta_{0j} \delta_{ij} + \delta^{\Gamma_u} \langle \Psi_i \rangle \xi^{\Gamma_u} \right] \quad (21)$$

where $\underline{\xi} = \{\xi^K, \xi^{\Gamma_u}\}$.

NUMERICAL RESULTS

This section is dedicated first to show the robustness of the method combining the Harmonic Balance Method and the Polynomial Chaos Expansion and secondly to construct and study the random aspect of the non-linear response of a cracked rotor due to the uncertain external forces and stiffness properties. The random aspect will be presented through the mean and the standard deviation of the response.

In a computational context, the summations in the previous expressions are truncated after some term P . Then, response $\Theta(\tau)$ (see Equation 15) becomes

$$\tilde{\Theta}(\tau) = \sum_{j=0}^P \mathbf{Y}_j \Psi_j(\underline{\xi}(\tau)) \quad (22)$$

where P , the total number of polynomial chaoses used in the expansion (excluding the 0^{th} -order term), can be determined by $P = 1 + \sum_{s=1}^p \frac{1}{s!} \prod_{r=0}^{s-1} (L+r)$, p being the order of the homogeneous chaos being used (Ghanem and Spanos, 1991). The standard deviation $\sigma_r = \sqrt{\langle (\Theta(\tau) - \Theta_0)^2 \rangle}$, given the orthogonality of the polynomial chaoses and considering the P^{th} truncation, becomes

$$\sigma_r = \sqrt{\sum_{j=1}^P \Theta_j^2(\tau) \langle \Psi_j^2 \rangle} \quad (23)$$

First, let us show the efficiency of the HBM-PCE method compared to the classical Harmonic Balance Method-Monte Carlo Simulations (HBM-MCS) method. The reference solution is obtained with the HBM-MCS method computed with 5000 samples. We compute the non-linear vertical response at the middle of the cracked rotor, for one non-dimensional crack depth μ equal to 1 (corresponding to the loss of half the shaft's area) and with variations for both shaft stiffness of the rotor system and the excitation forces of 2%. Several orders in the polynomial chaos expansion are considered $p = 5, 10$ and 20 . Here, for a better clearness of presentation, we present the random non linear response for harmonic 2 alone, that is its mean (Figure) and standard deviation (Figure). For both figures, we have : (a) the response on the whole frequency range studied and (b) a zoom for example on the resonance second peak. Regarding the mean or the standard deviation, both methods have globally close results in the whole frequency range, most highest discrepancies locating at each sub-critical speed. At this location, the HBM-PCE gets better with p and after a convergence study, order 20 seems sufficient. These variations, however still present, are only due to the very small damping taken in the present study. It should be noted that the same conclusions have been made for the others harmonics.

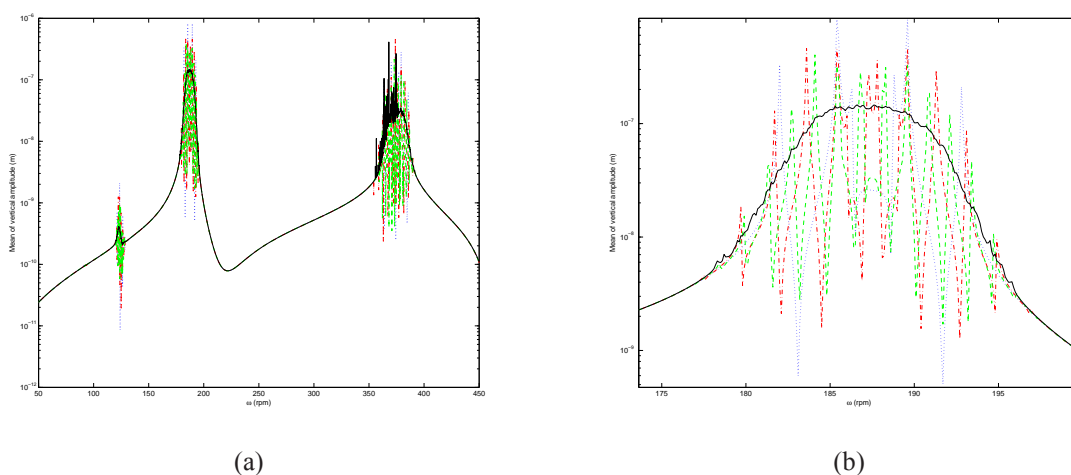


Figure 2: Mean of the second harmonic order computed by the MCS (solid line) and by the PCE of several orders : order 5 (dotted lines), order 10 (dotted-dashed lines), order 20 (dashed lines). (a) : whole frequency range, (b) : zoom on the second peak of resonance

Secondly, let us analyze the random non linear response due to the uncertain parameters : stiffness and external forces. Results are presented on Figures that show the mean value and the standard deviation of the non-linear vertical response at the middle of the cracked rotor for variation of 2%. First of all, it appears that variations of the mean value and of the

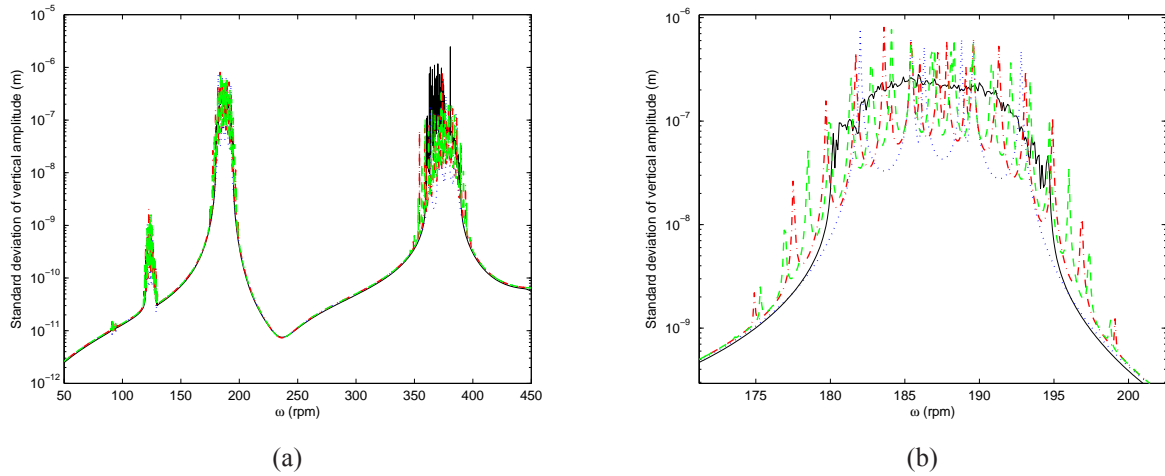


Figure 3: Standard deviation of the second harmonic order computed by the MCS (solid line) and by the PCE of several orders : order 5 (dotted lines), order 10 (dotted-dashed lines), order 20 (dashed lines). (a) : whole frequency range, (b) : zoom on the second peak of resonance

standard deviation increase when the rotor is passing through $\frac{1}{n}$ sub-critical speeds. For example, variations of the mean value and of the standard deviation for the $2\times$ resonances are observed when the running speed is approximately one-half the critical speed, one-half and $\frac{1}{3}$ of the first critical speed. Then, variations of the mean value and of the standard deviation of the $3\times$ harmonic component of the system response are predominant at one-third of the first resonance frequency. Finally, the $4\times$ vertical responses increase at $\frac{1}{4}$ of the first critical speed. A small decrease in the critical speed and the $n\times$ resonances of the rotor system is also observed, due to the reduction in system stiffness resulting from the presence of the crack. The range of speed where the non-linear amplitudes of the rotor system is large due to uncertainties. This observation clearly demonstrates that basic methods based on linear condition monitoring techniques (such as the changes in frequencies and modes shapes) can be rendered ineffective in the case of specific configurations taking into account uncertainties for the detection of cracks in rotor systems. However, it is observed the emergences and variations in $n\times$ harmonic components of the system in the frequency domain are key indicators for the detection of transverse cracks in a rotating shaft.

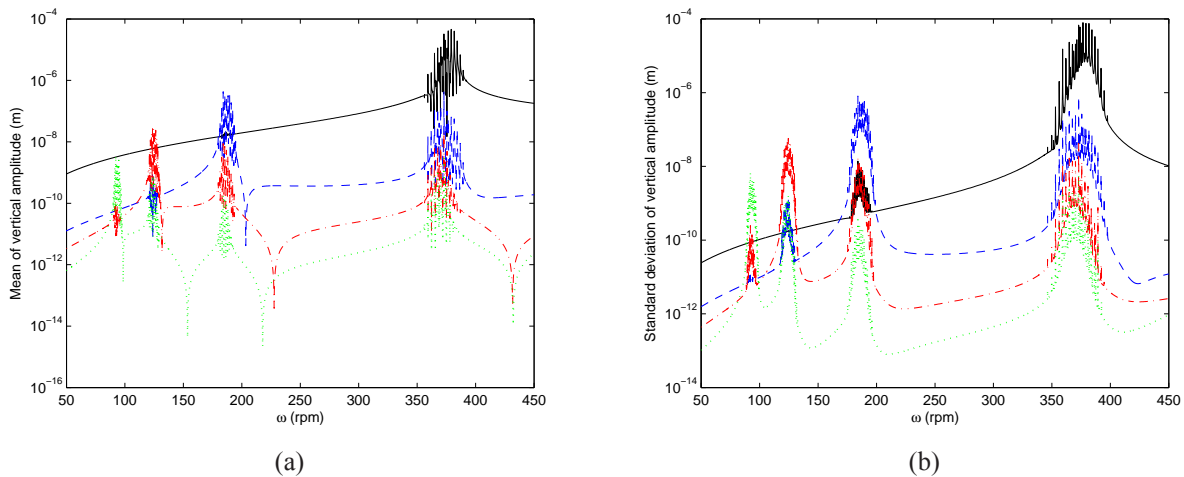


Figure 4: Evolution of the vertical $n\times$ displacements at the middle of the shaft for a non-dimensional crack depth $\mu = 1$ with variations of the Young modulus and the excitation forces (black=order 1, -- blue=order 2, -.red=order 3, ... green=order 4) (a) mean, (b) standard deviation for variation coefficient of 2%

CONCLUSION

This paper wants to show the effects of the presence of a transverse crack in a rotating shaft under uncertain physical

parameters in order to outline some robust indicators for detecting damage in rotating system. In this case, uncertainties appear at the level of the stiffness properties or of the excitation forces. The non linear response has then to be considered as random that is done using the Polynomial Chaos Expansion (PCE). The deterministic problem is solved using the Harmonic Balance Method (HBM) and one reference random solution is computed associating this last method with the Monte Carlo Simulations (MCS). The HBM-PCE method is then compared with the HBM-MCS method and finally validated. A complete analysis is done for a variation of 2% for both the stiffness properties and the excitation forces, an important observation is the recognition of the appearances of the $n \times$ harmonic components when the running speed reaches $\frac{1}{n}$ of the critical speeds.

REFERENCES

- Adomian G. and Malakian K., 1980, "Inversion of stochastic partial differential operators ? the linear case", *J. Math. Anal. Appl.*, Vol.77, pp.309-327.
- Davies W. G. R. and Mayes I. W., 1984, "The vibrational behaviour of a multi-shaft, multi-bearing system in the presence of a propagating transverse crack", *Transactions of the ASME Journal of Vibration, Acoustics, Stress, and Reliability in Design*, Vol.106, pp.146-153.
- Gasch R., 1993, "A survey of the dynamic behaviour of a simple rotating shaft with a transverse crack", *Journal of Sound and Vibration*, Vol.160.No.2, pp.313-332.
- Ghanem R. G. and Spanos P. D., 1991, "Stochastic Finite Elements: A Spectral Approach", Springer-Verlag.
- Ghanem R. G. and Kruger R., 1996, "Numerical solution of spectral stochastic finite element systems", *Computer methods in applied mechanics and engineering*, Vol.129, pp. 289-303.
- Mayes I. W. and Davies W. G. R., 1984, "Analysis of the response of a multi-rotor-bearing system containing a transverse crack in a rotor", *Transactions of the ASME Journal of Vibration, Acoustics, Stress, and Reliability in Design*, Vol.106, pp.139-145.
- Nakagiri S. and Hisada T., 1982, "Stochastic finite element method applied to structural analysis with uncertain parameters", *Proc. Intl. Conference on FEM*, pp.206-211.
- Shinozuka M. and Astill J., 1972, "Random eigenvalue problems in structural dynamics", *AIAA Journal*, Vol.10.No.4, pp.456-462.
- Sinou J.-J., 2007, "Effects of a crack on the stability of a non-linear rotor system", *International Journal of Non-Linear Mechanics*, Vol.42, pp.959-972.
- Sinou J.-J. and Lees A. W., 2005, "Influence of cracks in rotating shafts", *Journal of Sound and Vibration*, Vol.285.No.4-5, pp. 1015-1037.
- Sinou J.-J. and Lees A. W., 2007, "A non-linear study of a cracked rotor", *European Journal of Mechanics A/Solids*, Vol.26.No.1, pp.152-170.
- Wauer J., 1990, "Dynamics of cracked rotors: literature survey", *Appl. Mech. Rev.* Vol.43, pp.13-17.

Internal Model Control Design for Powered Below-knee Prosthesis

Ryoichi Suzuki¹, Takayuki Sawada¹, Nobuaki Kobayashi¹, and Eberhard P. Hofer²

¹ Kanazawa Institute of Technology, 7-1 Ohgigaoka, Nonoichi, Ishikawa 921-8501, JAPAN

² University of Ulm, Albert-Einstein-Allee 41, 89081 Ulm, Germany

Abstract: This paper proposes a control method for robotic below-knee prostheses. The main goal of this research is to determine the feasibility of generating adequate plantar flexion force by using the internal model control design. The prototype of the powered below-knee prosthesis is developed to evaluate proposed controllers. The paper shows that the prototype is able to provide a more natural gait than a conventional passive prosthesis.

Keywords: Internal model control, powered below-knee prosthesis, biomechanics

INTRODUCTION

This paper focuses on control methods for powered below-knee prostheses. Powered ankle-foot prostheses have been developed and studied to improve quality of life for disabilities (Au and Herr, 2008). Although conventional prostheses are able to provide assistance, control problems to generate more mechanical energy still remain. On the other hand, below-knee prosthesis with elastic foets are also good assistive devices to generate plantar flexion force. Power of force depends on a store of elastic energy for toe-off. However, it is often difficult for children or elderly to store adequate energy.

The main goal of this research is to determine the feasibility of generating adequate plantar flexion force by using the internal model control design. The prototype of the powered below-knee prosthesis shown in Figure 1 is developed. The tendon-driven mechanism is applied to generate flexion force. The prototype consists of a DC motor, a rotary encoder, wires, a motor driver, a microcomputer, and batteries. Force sensors or pressure sensors are out of use to generate flexion force. The weight is 2.0kg.

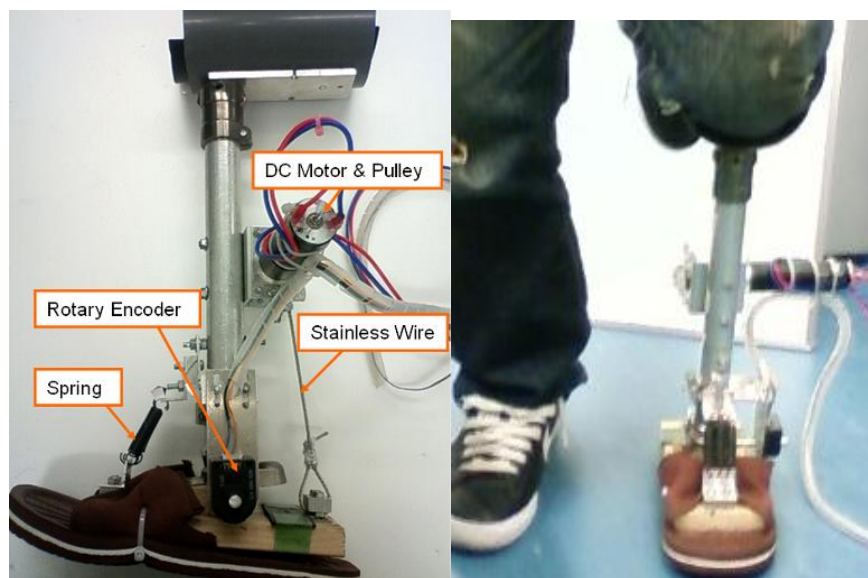


Figure 1 – A prototype of the powered below-knee prosthesis

A level ground walking gait cycle is able to define its start with the heel strike of one foot and its end when at the next heel strike of the same foot. This cycle can be decomposed by two phases, stance and swing. The stance phase begins at heel strike and ends when the toe of the same foot loses contact with the ground, and the swing phase is the portion of the cycle when the foot is off the ground after toe-off until heel strike. Our purpose is to contribute to assist on this stance phase.

The stance phase is divided into the following three more sub-stages (Au et al., 2008).

Controlled plantar flexion (Mode 1): begins at heel-strike and ends at foot-flat on the ground surface.

Controlled dorsal flexion (Mode 2): begins at foot-flat and continues until the ankle reaches a state of maximum dorsal flexion. The main function of the human ankle during Mode 2 is to store the elastic energy necessary to propel the body upwards and forwards during the Mode 3.

Powered plantar flexion (Mode 3): begins after Mode 2 and ends at the instant of toe-off from the ground surface. In this phase, the ankle releases the elastic energy stored during the controlled dorsal flexion phase to achieve the high plantar flexion power.

The powered plantar flexion phase is important to build powered below-knee prostheses. It is well known that maximum power is required during Mode 3 in a gait cycle. The purpose of the research is to control the angle of talocrural (or ankle) joint and to generate adequate plantar flexion force during Mode 3 by using the internal model control design. Figure 2 shows the definition of the talocrural joint and the observation data (Takashima et al., 2003).

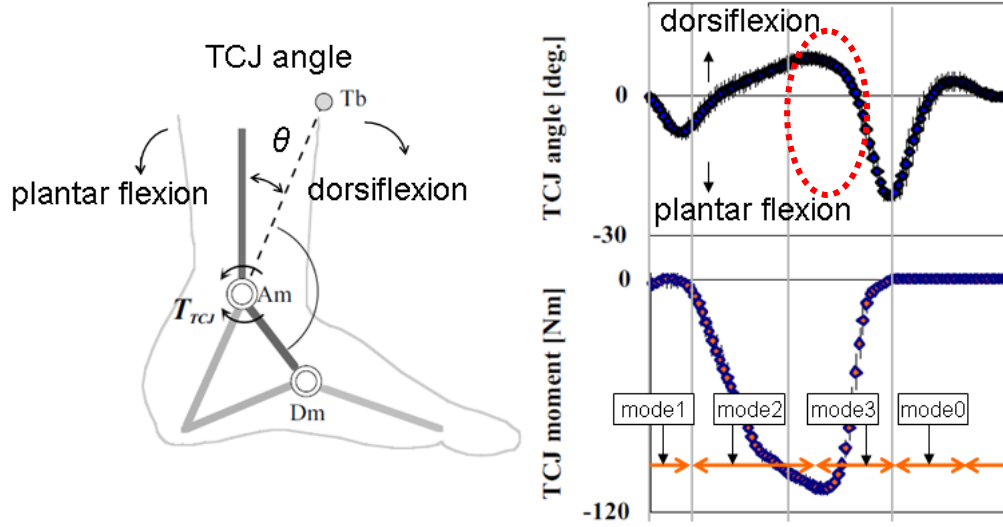


Figure 2 – Definition of talocrural joint (TCJ) angle, and observation data (82kg in weight) of TCJ angle, moment in a gait cycle (Takashima et al., 2003)

INTERNAL MODEL CONTROL DESIGN

We apply the IMC scheme to control talocrural joint angle of the prototype of the powered below-knee prosthesis. The internal model control (IMC) scheme is shown in Figure 3. Here Σ_f is a control object with feedback (stable system), $\bar{\Sigma}_f$ is a mathematical model of the control object, and $\bar{\Sigma}_{f\tau}^{-1}$ is an approximate inverse system of $\bar{\Sigma}_f$. Although the synthetic structure is simple, it is satisfactory for the functions of disturbance rejection and trajectory tracking. The scheme has also disturbance estimation property (Suzuki et al., 2007).

We consider the following single input single output (SISO) system.

$$\dot{x} = Ax + bu + b\xi, \quad y = cx \quad (1)$$

where x is the state, u is the input, ξ is the disturbance, and y is the output. The feedback gain $f = -b^T P_\varepsilon$ in a sense of LQ optimal control is obtained by the following riccati equation as $\varepsilon \rightarrow 0$.

$$A^T P_\varepsilon + P_\varepsilon A - P_\varepsilon b b^T P_\varepsilon + \frac{1}{\varepsilon^2} c^T c = 0 \quad (2)$$

The approximate inverse system $\bar{\Sigma}_{f\tau}^{-1}$ is calculated by the following statement.

$$\bar{\Sigma}_{f\tau}^{-1}(s) \bar{\Sigma}_f(s) = (\tau s + 1)^{-d} \quad (3)$$

where $\tau \ll 1$ and d is a minimal integral index. The transfer functions Σ_{yr} and $\Sigma_{\hat{\xi}\xi}$ are satisfied the following statements by choosing $\tau \rightarrow 0$.

$$\Sigma_{yr}(s) = \bar{\Sigma}_f \bar{\Sigma}_{f\tau}^{-1} \rightarrow 1 \quad (4)$$

$$\Sigma_{\hat{\xi}\xi}(s) = \bar{\Sigma}_{f\tau}^{-1} \bar{\Sigma}_f \rightarrow 1 \quad (5)$$

These two statements mean that the IMC scheme has a trajectory tracking property and a disturbance estimation property. The disturbance ξ added to the input channel is able to estimate as $\hat{\xi}$ in Figure 3.

Figure 4 shows the block diagram of the simplified internal model control scheme. The scheme shown in Figure 4 has also same properties of the scheme shown in Figure 3. The controller is constructed by a gain g .

$$g = \left\{ c(-A - bf)^{-1} b \right\}^{-1} \quad (6)$$

The advantage of the scheme in Figure 4 is to reduce the order of controllers. The IMC scheme shown in Figure 4 has also the trajectory tracking property and the disturbance estimation property.

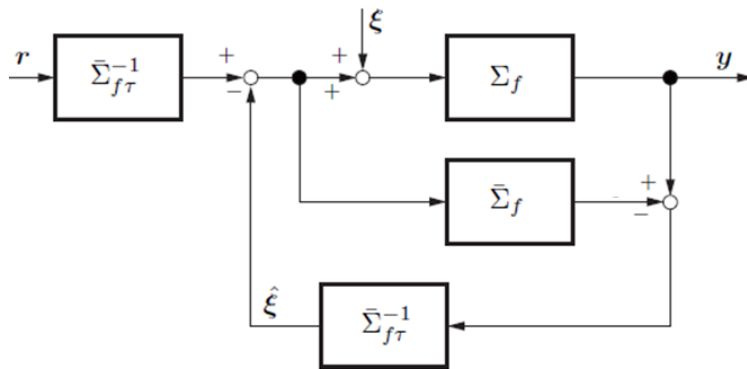


Figure 3 – Block diagram of the internal model control scheme

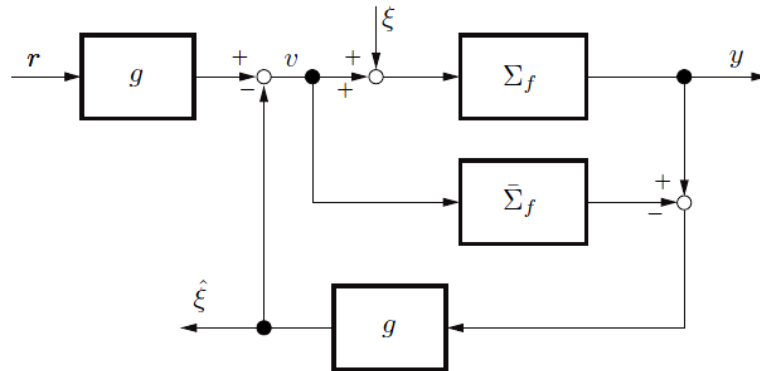


Figure 4 – Block diagram of the simplified internal model control scheme

These two controllers are implemented to microcomputers. The control performance of each controller is evaluated by comparative experiments.

A PROTOTYPE OF POWERED BELOW-KNEE PROSTHESIS

The system configuration of the prototype is shown in Figure 5. The prototype is rigidly attached to the leg. The users are limited to persons with knee flexion.

The mathematical model of the prototype is obtained as follows,

$$c_m r_2 \dot{\theta} + k r_3 \theta = \frac{\tau_m}{r_1} \quad (7)$$

where c_m is the damping coefficient, k is the spring constant, τ_m is the input torque to the motor, and θ is the angular value of the ankle joint. r_1, r_2, r_3 is lengths of components. The state space model is represented as follows.

$$\dot{\theta} = -\frac{kr_3}{c_m r_2} \theta + \frac{1}{c_m r_2 r_1} \tau_m, \quad y = \theta \quad (8)$$

Here, the input is τ_m and the output is θ . The ankle joint is controlled by using the tendon-driven mechanism with the IMC based controller shown in Figure 3 and Figure 4. Then the powered below-knee prosthesis generates adequate plantar flexion force during the end of Mode 2 and Mode 3.

The set point r is the angle of the ankle joint. The desired set point has been determined by observing non-handicapped persons in gait cycles. Motions of ankle joints have been captured by a video camera. As a result of the observation, the set point r is settled to $r = (0.4/0.5)t$ [rad] in this study. If we put another sensor on the unaffected side, then the set point will be variable as to a speed of the unaffected leg.

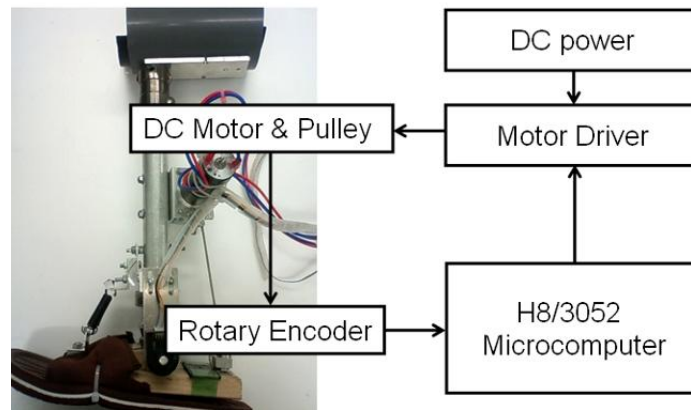


Figure 5 – System configuration of the prototype of the powered below-knee prosthesis

EXPERIMENTAL RESULTS

Figure 6 shows an experimental overview in Mode 1, Mode 2, and Mode 3. The rotary encoder measures the joint angle, and then the prototype recognizes the stance phase (dorsal flexion or plantar flexion) and calculates the control input for the powered plantar flexion phase.

The joint angle of ankle and the moment are shown in Figure 7. The green line shows the result of a conventional passive prosthesis. The purple line shows the results of the prototype implemented the controller in Figure 3, and the pink line shows the result of the prototype implemented the controller in Figure 4. The subject is 68kg in weight.

At first, we compare the experimental results with Figure 2. We can see that the prototype control the joint angle and generate adequate plantar flexion force during Mode 3. The passive prosthesis is not able to generate adequate force after the phase of Mode 2. Next, we compare the performance of two controllers. The simplified controller in Figure 4 has time delay before the swing phase (Mode 0). Although the tracking performance is poor a little bit than the controller in Figure 3, the control performance of the simplified controller is generally acceptable.

Figure 8 shows the experimental result of different subjects for 68kg and 48kg. We can see that the prototype provides adequate plantar flexion angle during Mode 3.

We verified the feasibility of generating adequate plantar flexion force by using the internal model control design. This is the initial experimental study for control the powered below-knee prosthesis. Another experiments and assessments are required to improve the control performance of the prototype.

CONCLUSIONS

This paper proposed a control method for robotic below-knee prostheses by using the internal model control design. The prototype of the powered below-knee prosthesis was developed to evaluate proposed controllers and to determine the feasibility of generating adequate plantar flexion force. The prototype was able to provide a more natural gait than a conventional passive prosthesis by experiments.

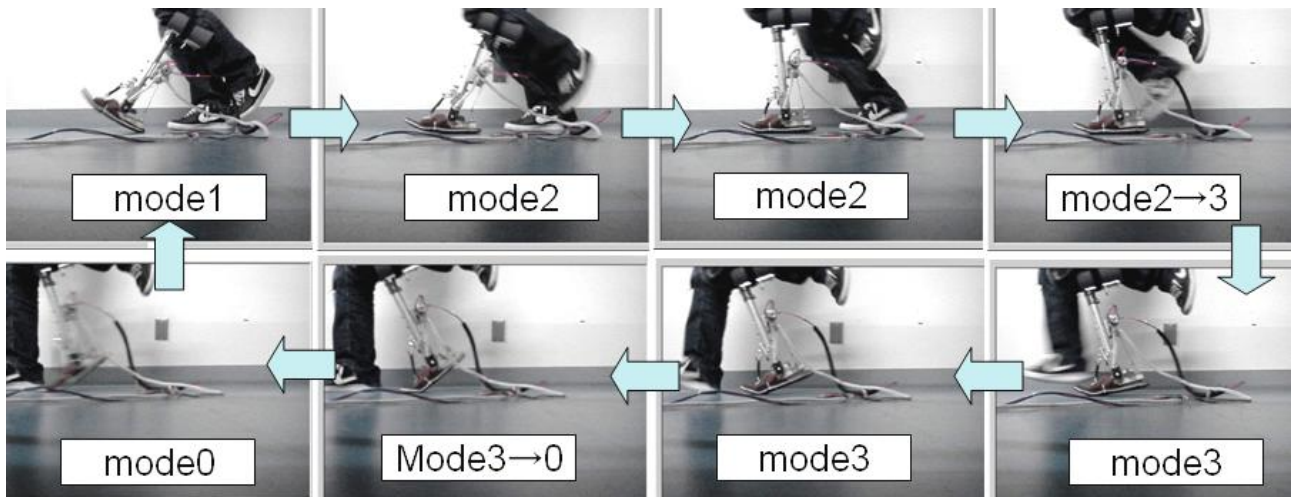


Figure 6 – Experimental overview on control during walking

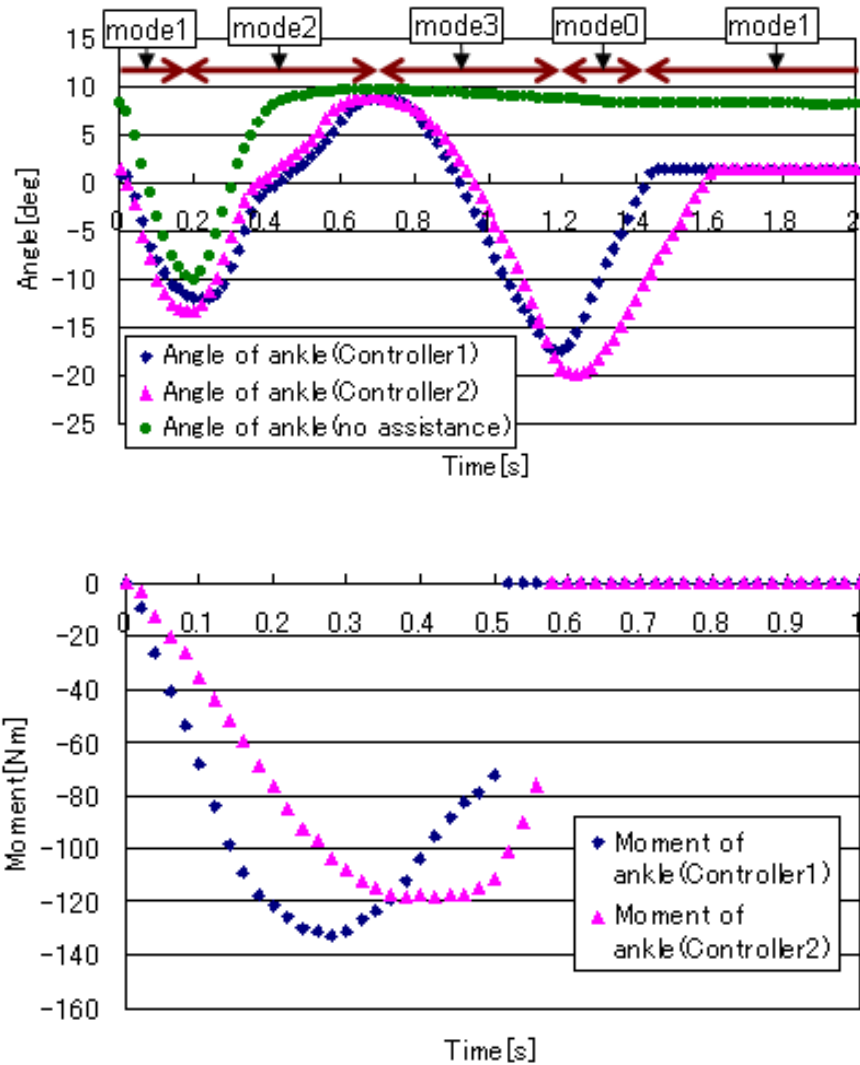


Figure 7 – Experimental results (ordinary person): the joint angle and moment of ankle

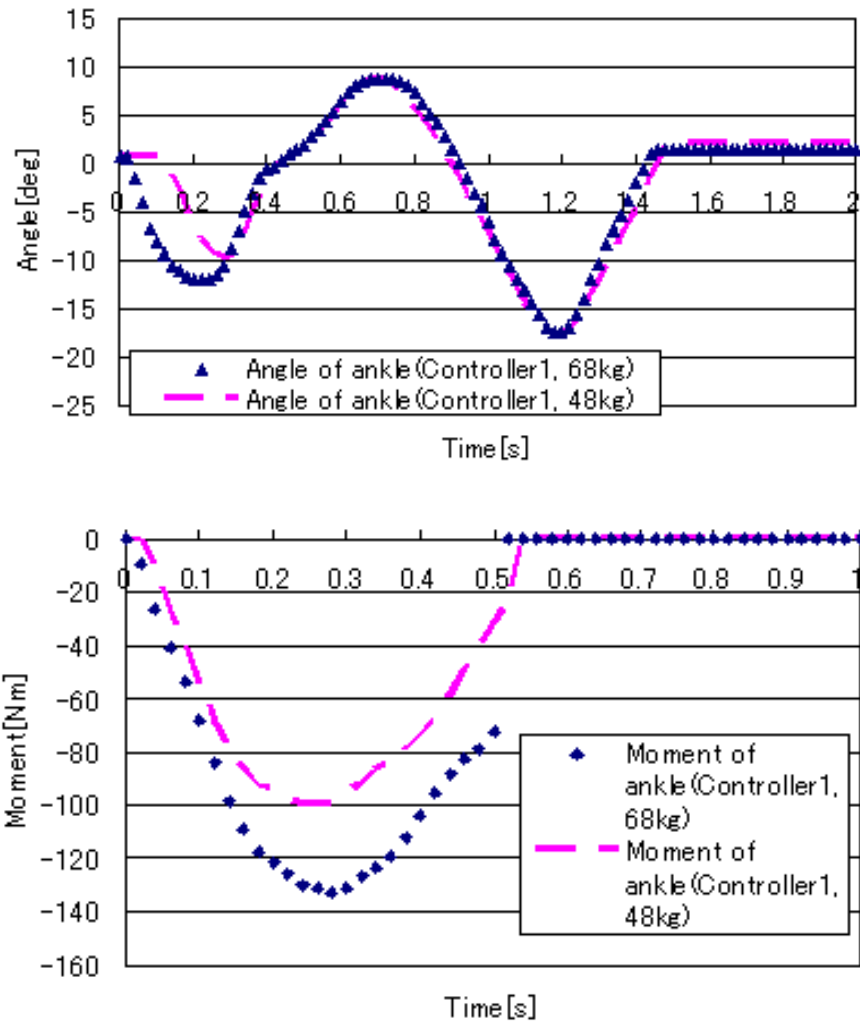


Figure 8 – Comparison of subjects (ordinary persons) for 68kg and 48kg in weight

ACKNOWLEDGMENTS

This research was partially supported by the Ministry of Education, Science, Sports and Culture, Grant-in-Aid for Scientific Research (C), No. 21560476, 2010.

REFERENCES

- Au, S. K. and Herr, H. M., 2008, "Powered Ankle-Foot Prosthesis", *IEEE Robotics & Automation Magazine*, pp. 52-59.
- Au, S., Berniker, M. and Herr, H., 2008, "Powered Ankle foot prosthesis to assist level-ground and stair-descent gaits", *Neural Networks*, Vol. 21, pp. 654-666.
- Suzuki, R., Fujiki, N., Sugawara, A., Kobayashi, N. and Ito, K., 2007, "State and Disturbance Estimation Based on Internal Model Control Structure and Its Application to Sensorless Grasping Control", *Proceedings of the 33rd Annual Conference of the IEEE Industrial Electronics Society (IECON)*, Taipei, Taiwan, pp. 2846-2851.
- Takashima, T., Fujimoto, H., Kakihana, W. and Takanashi, A., 2003, "Model Analysis of the Human Foot Include Subtalar Joint, Talocrural Joint, and Foot Arch (in Japanese)", *Transaction of the Japan Society of Mechanical Engineers, C*, Vol. 69, No. 688, pp. 111-116.

RESPONSIBILITY NOTICE

The authors are the only responsible for the printed material included in this paper.

Performance evaluation of control strategies with different feedforward error sensors in active noise control

Siviero, D. A.¹, Goldenstein, A. L.¹, and Arruda, J. R. F.¹

¹ Universidade Estadual de Campinas, Departamento de Mecânica Computacional, Rua Mendeleev, 200, Campinas, SP, Brasil

Abstract: One of the problems faced today in the implementation of active noise control (ANC) applications is the choice of error sensors to provide the best control performance for a given target noise abatement, for example, in an airplane, where to place error sensors and which type of sensors to use to improve aircraft panel transmission loss at given frequencies. Following these lines, this work shows the performance comparison of feedforward controllers in both time and frequency domain with different error sensors, namely a pressure sensor (microphone), widely used in this type of application and a particle velocity sensor (Microflown[®], mod. Standard PU), which is believed to be less subject to ambient noise not correlated with the noise to be abated (e.g., boundary layer noise). Tests have been conducted in a plane wave tube using as control actuator a smart-foam under development, which uses a piezoelectric actuator. The controller performances were evaluated by the gain in sound transmission loss when the active noise control was on.

Keywords: Acoustic Noise Control, Transmission Loss, Adaptive Filtering, Smart Foam

INTRODUCTION

Feedforward control algorithms based on adaptive filtering are widely used and tested in different areas due to the simplicity of design and ease of application. (Kuo and Morgan, 1996; Widrow and Stearns, 1985). In ANC problems, many studies have used the Filtered-X LMS, FX-LMS, (Siviero *et al*, 2010, Donadon *et al*, 2006; Kim, Kim, Roh, 2002; Guigou and Fuller, 1998; Gentry, Guigou and Fuller, 1997), where the control signal which is sent to the acoustic actuator is obtained through an adaptive filtering of a reference signal that must to be highly correlated with the primary disturbance (noise to be controlled) and preferably not affected by the control signal (otherwise this influence must be filtered out). The adaptation of this filter is performed based on the instantaneous error signal, which is the sum of the plant response when it is excited by an exogenous signal and the plant response to the control signal

The well known equation that adjusts the FX-LMS controller filter weights which works with a reference signal, a control signal and an error signal can be written as:

$$\mathbf{w}(n+1) = \mathbf{w}(n) + \frac{\mu \mathbf{x}'(n) \mathbf{e}(n)}{|\mathbf{x}'(n)|^2} \quad (1)$$

where $\mathbf{x}'(n)$ is the reference signal, filtered by the estimated secondary plant obtained from an offline (or online) identification, $\mathbf{e}(n)$ is the instantaneous error signal, $\mathbf{w}(n)$ is a vector with the gain values of the FIR filters, $\mathbf{w}(n+1)$ is a vector with the future values of FIR filter, before the adaptation step and μ represents the size of adaptation step, which must be between 0 and 1 to ensure the normalized algorithm stability (Widrow and Stearns, 1985).

As the control strategy tested is adaptive and attempts to minimize the instantaneous error, the more the error signal is correlated with the sum of plant responses to excitation and the control signal, the better is the performance of the controller, or, in other words, if the sensors capture less noise uncorrelated with the signals of interest the controller will have better performance. This fact motivates the attempt to use of particle velocity sensors. The sound pressure and particle velocity have a different physical nature. While the sound pressure has omnidirectional sensitivity, the particle velocity is a vector, and, therefore, is directional. Thus, the particle velocity sensor will only capture the particle velocity in the direction that the sensor is aligned with. Thus, the external noise should produce fewer disturbances in this type of measurement.

In this work, we have used two different error sensors, a GRAS[®] microphone model MCE212 and a Microflown[®] standard model PU.

The configuration used in the FX-LMS controller in frequency domain is very similar to the time domain configuration (Kuo and Morgan, 1996). The basic difference is that signals are fed to the adaptive filter in a different way. They are accumulated in a buffer, of which the size is numerically equal to the number of frequency lines that are to be controlled and these buffered sequences are converted to the frequency domain via the Fast Fourier Transform (FFT) algorithm. The estimate of the secondary path becomes the frequency response of the actuator control signal to

the error sensor signal, with same number of points as the buffer mentioned before. A greater computational cost is required in this kind of controller. However, when the primary noise source is periodic, a better control performance is expected at the harmonics of the periodic signal, as the controller efforts are concentrated to minimize the system response at these specific frequencies only. Before it is applied to the plant, the control signal must be converted back to the time domain through an inverse Fourier Transform (iFFT).

Figure 1 shows a block diagram of a frequency domain FX-LMS controller.

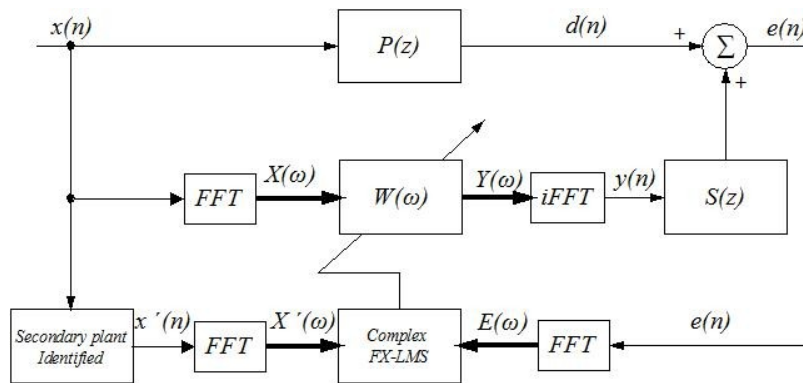


Figure 1: Frequency domain FX-LMS controller diagram.

ERROR SENSORS

The error signal used to feed the adaptive algorithm filters consisted, as previously described, of two different types of sensors: a pressure sensor and a particle velocity sensor, positioned at 10mm along the duct part downstream from the sample. Thus, two different instantaneous error signals have been selected: the pressure signal and the particle velocity signal. The purpose of this approach is to determine at which frequencies it is better to measure the pressure in the near field for TL control purposes and at which frequencies it is better to measure the particle velocity.

THE ACTUATOR

The hybrid acoustic actuator consists of a 2mm-thick curved acrylic plate, with a piezoelectric transducers (Face International® 7R Thunder®) attached to its external surface. The Thunder actuator was selected, as it produces comparatively higher forces and larger displacements compared to other traditional piezoelectric patch actuators. It consists of a thin wafer of piezoceramics bonded to an electrically conductive substrate and a superstrate with a high performance bonding material. The bond between layers makes possible the induced pre-stress during manufacturing and keeps the ceramic in compression allowing the Thunder to deflected far more and then standard piezoceramics without cracking. The pre-stress also yields Thunder's unique, natural "pumping" motion, increasing or decreasing the radius of curvature depending on the polarity of the applied voltage. The acrylic plate was positioned between the middle the two pieces of foam. Figure 2 shows an exploded view of the actuator.

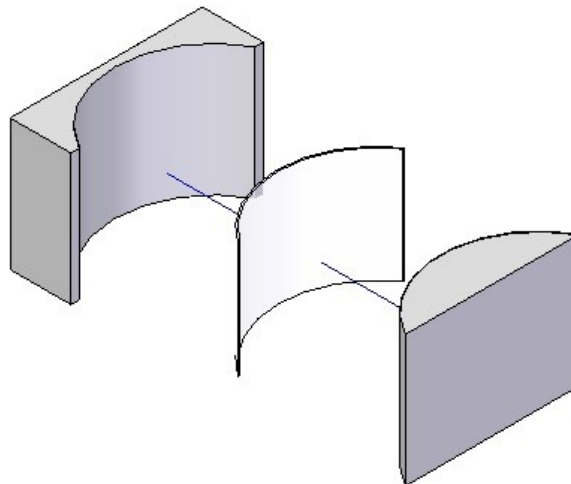


Figure 2: Exploded view of the actuator. The gray parts indicate the foam.

The acrylic plate shape was designed to maximize the air displacement when the piezoelectric actuator positioned in the center shrinks or expands. This curved shape has been applied in several studies of this type of actuator (Olivieri, Bolton and Yoo, 2006; Song and Bolton, 2000), where a PVDF film (a polymeric material with piezoelectric characteristics) was used. In tests conducted in the present investigation piezoelectric patches were bonded to an acrylic plate in order to increase the acoustic actuator efficiency (largest area). It also has the effect of improving the passive panel transmission loss. Further studies are still needed in the comparison between the PVDF film and actuators like the one used here, with piezoceramic patches bonded to larger structural supports.

The acrylic plate dimensions were based on a foam pad used in commercial aircraft panels. After completing the tests with the actuator in a plane wave tube, it will be fixed in a fuselage panel for TL tests in a suite of acoustic chambers (reverberant / anechoic). The plate curvature was such that it fits the Thunder ® 7R perfectly. The thinner acrylic plate commercially available has been used.

The actuator, which was attached to the central region of the plate was fed by maximum voltage amplitude of 140Vpp. The actuator and acrylic plate are shown in Figure 3.

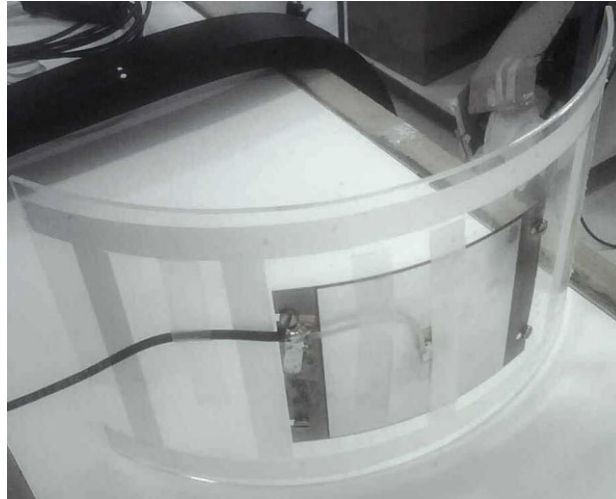


Figure 3: Acrylic plate with Thunder 7R.

SYSTEM IDENTIFICATION

The identification of the secondary discrete plant $\hat{S}(n)$ was performed using an offline identification algorithm called ERA (Juang and Pappa, 1985), which can use the impulse response obtained from the frequency response function between the control actuator and the error sensor to estimate a discrete state space system that produces a frequency response similar to the one measured experimentally. Figure 4 shows two comparisons between the system responses estimated and measured, one using a microphone and the other using a particle velocity sensor. Measurements are presented with foam added to the termination of the plane wave duct to improve its anechoic behavior.

The identified secondary plants have order 72, using a sampling time of 1.5e-3s. The frequency band identified for control was from 80Hz to 240Hz. The work focused on this frequency band due to the interest in using active control to improve the sound TL at low frequencies, and due to limitations of the control hardware used.

SOUND TRANSMISSION LOSS MEASUREMENT

The measurement of sound TL was performed in a plane wave tube of rectangular cross section. The tube was specifically built to test the pad under investigation. The dimensions of the duct are illustrated in Figure 5. The duct termination includes a flare with an internal angle of 30° to create a less abrupt impedance change, reducing the reflection of sound waves at the tube end. The tube dimensions, as well as the positioning of the microphones, were based on standard ASTM1030/98.

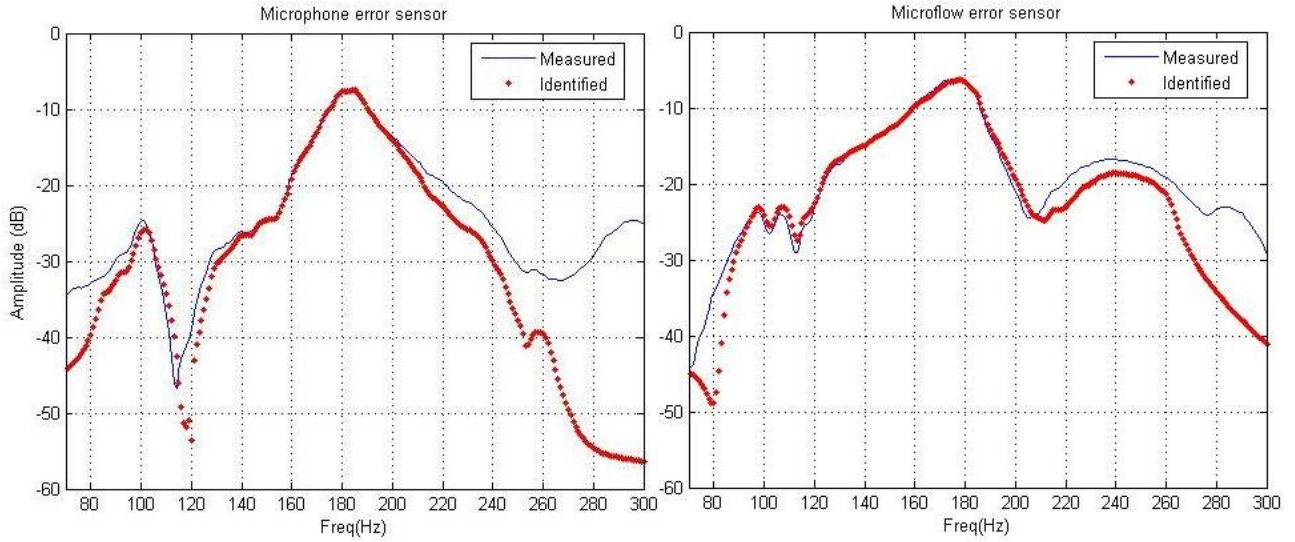


Figure 4: Identification of secondary path. Left: microphone; right: particle velocity sensor

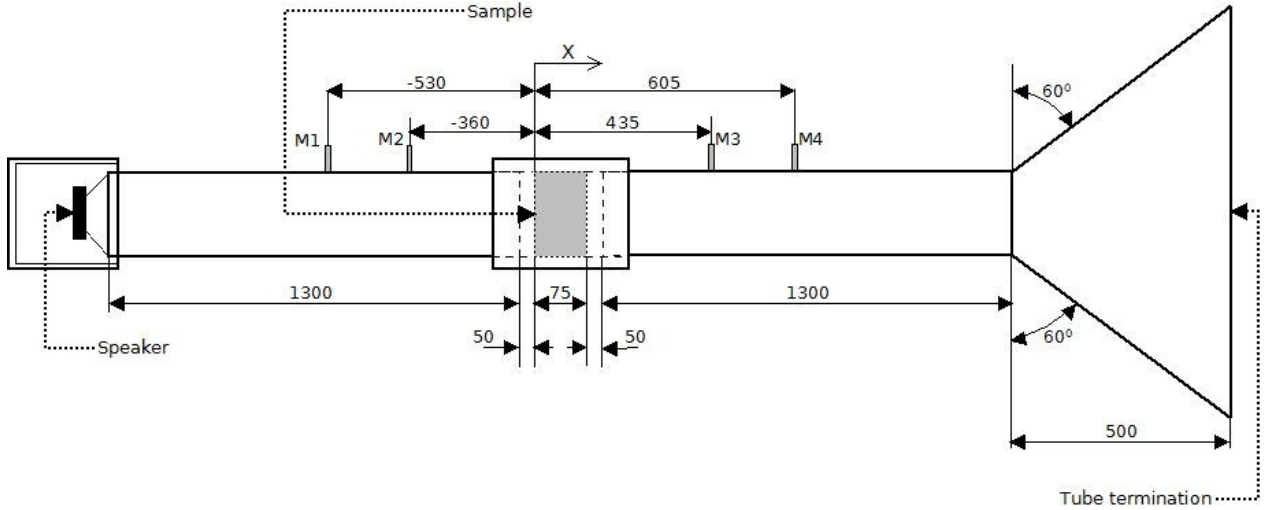


Figure 5: Duct for the measurement of the TL. All the distances are in millimeters and angles are in degrees. M1, M2, M3 and M4 indicate the positions of the microphones used to measure the sound pressure levels.

Using the plane wave tube described above, the transfer functions between the complex sound pressure at the four microphone locations M1, M2, M3 and M4 and the reference signal (signal sent to the loudspeaker) were measured. The transfer functions were used to compute the sound transmission loss using the hypothesis of anechoic tube ending (Song and Bolton, 2000; Olivieri, Bolton and Yoo, 2006). Details of the approach for TL measurement can be found in the literature (Williams *et al.*, 2007). Pressure microphones GRAS® model 40AQ have been used.

Adopting a complex exponential representation and the origin of the coordinate system on the sample surface, the sound pressure and particle velocity in frequency domain are given by:

$$\begin{aligned}
 P(x, \omega) &= \begin{cases} A(\omega)\exp(-jkx) + B(\omega)\exp(jkx) & x \leq 0 \\ C(\omega)\exp(-jkx) + D(\omega)\exp(jkx) & x \geq l \end{cases} \\
 V(x, \omega) &= \begin{cases} \frac{A(\omega)\exp(-jkx) + B(\omega)\exp(jkx)}{\rho_0 c} & x \leq 0 \\ \frac{C(\omega)\exp(-jkx) + D(\omega)\exp(jkx)}{\rho_0 c} & x \geq l \end{cases} \quad (1)
 \end{aligned}$$

where ω is the angular frequency, k is the wave number, given by $k = (\omega c) - j\alpha$ (Note that k can be a complex to add a viscoelastic and thermal dissipation to the pressure and velocity), and l is the length of the first section of the tube,

upstream from the sample. Here, we assume $\alpha=0$. A , B , C and D are complex amplitudes of the plane wave components. The coefficients A to D can be expressed in function of the measured transfer functions at the positions 1 to 4, respectively, as:

$$\begin{aligned} A &= \frac{j(H_{P_1R} \exp(jkx_2) - H_{P_2R} \exp(jkx_1))}{2\sin[k(x_1 - x_2)]} & C &= \frac{j(H_{P_3R} \exp(jkx_4) - H_{P_4R} \exp(jkx_3))}{2\sin[k(x_3 - x_4)]} \\ B &= \frac{j(H_{P_2R} \exp(-jkx_1) - H_{P_1R} \exp(-jkx_2))}{2\sin[k(x_1 - x_2)]} & D &= \frac{j(H_{P_4R} \exp(-jkx_3) - H_{P_3R} \exp(-jkx_4))}{2\sin[k(x_3 - x_4)]} \end{aligned} \quad (2)$$

where H_{P_nR} represent the complex data from the frequency response function (FRF) measured between the noise source and microphone n .

The sound TL is defined by:

$$TL = 10 \log_{10} \left(\frac{W_i}{W_t} \right) \quad (6)$$

where W_i and W_t represent the incident and transmitted sound Power respectively. For a perfect anechoic termination ($D=0$), assuming normal incident plane waves, the sound TL is given by:

$$TL = 10 \log_{10} \left(\left| \frac{A^{(anechoic)}}{C^{(anechoic)}} \right|^2 \right) \quad (7)$$

EXPERIMENTAL SETUP

In this experimental setup, the primary disturbance is generated by the plane wave tube loudspeaker fed with a signal composed by eight frequencies. These frequencies were determined by the domain frequency FX-LMS blocks and discretization, defined by the relation:

$$f_i = \frac{i}{2Ndt} \quad (8)$$

Where f_i indicates the i th frequency at which the controller will act, N varies according the buffer data block size which feeds the algorithm - in both controllers, the buffer size was 16 -, the i index varies from 1 to the block size, dt indicates the sample time of the digital signal processor (DSP) where the controllers are implemented. As long as the goal of this work is to compare the FX-LMS efficiency in the time and frequency domain, a sine sum (periodic signal) containing only the frequencies of interest was synthesized and applied to the system as a primary source disturbance. As a consequence, the sound transmission loss will be determined only at those discrete frequencies. The analyzed frequencies were 80, 100, 120, 140, 160, 180, 200, 220, and 240Hz This sum of sines was generated in a dSPACE 1104 board to reduce the dSPACE 2103 processor activity.

The measuring procedure consisted in a sum of sines applied as disturbance to be controlled, also called primary disturbance, for each one of the control strategies (time FX-LMS with microphone or particle velocity sensor as error sensor and frequency FX-LMS with microphone or particle velocity sensor as error sensor). The smart foam actuator is placed midway along the tube and a GRAS 40AQ microphone is used to measure the sound pressure at the points M1 to M4, illustrated in Figure 5, to estimate the sound transmission loss provided by the smart foam system.

The control filters adaptation was carried on until the control signal reached 70% of the maximum amplifier working tension, approximately 140Vpp, thus avoiding distortions and eventual non linearity. After reaching this limit, the adaptation was interrupted and the sound pressure measuring in the M1 and M4 points was performed. The error sensors that feed the adaptive controller filter were positioned downstream from the smart-foam actuator, 10mm from the actuator surface. To verify the influence of an external noise disturbance at the error sensors and in the controllers adaptive process, an external noise source was placed close to the plane waves tube termination (white noise, 20-500Hz) to generate a contaminating noise uncorrelated with the primary source targeted for control, but in the same frequency range of interest. In an analogous way, when the control signal reached 70% of the maximum tension of the amplifier, the adaption was interrupted as well as the external noise disturbance and the pressure was measured at the M1 and M4 points. The low-pass filters installed in both dSPACE card outputs are also known as reconstruction filters. The function of these filters is to smooth out the effects of the zero order holders existing in the digital/analog converter outputs. The low-pass filter at the input of dSPACE® 2103 DSP board, as described in the scheme, has the function of preventing "aliasing."

All sensors used in the experiment have standard ICP connections, which require the presence of a signal conditioner between the sensors (Microphone and Microflow) and the anti-aliasing filter shown in the scheme of Figure 6. As the HP 3566A spectrum analyzer already has ICP conditioners in its input channels, there was no need for coupling the conditioner to the microphones M1 to M4.

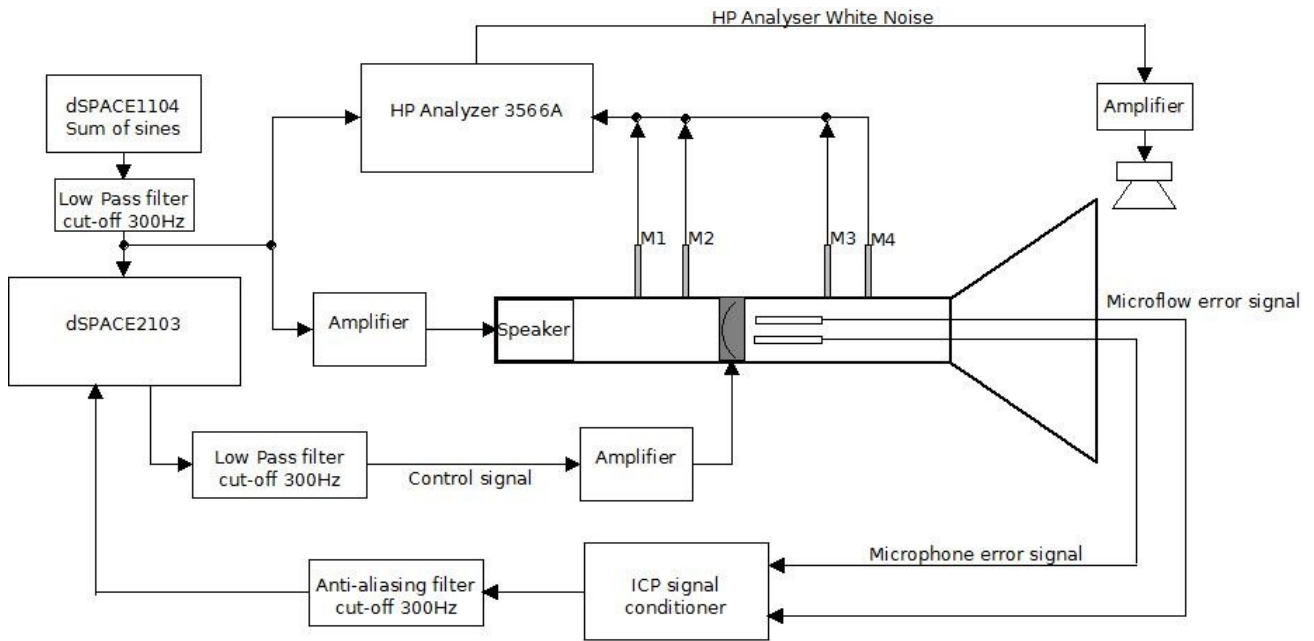


Figure 6: Experimental setup used to measure the active sample TL.

RESULTS

The results of sound transmission loss measuring taken at the 8 frequencies are presented in Figure 7.

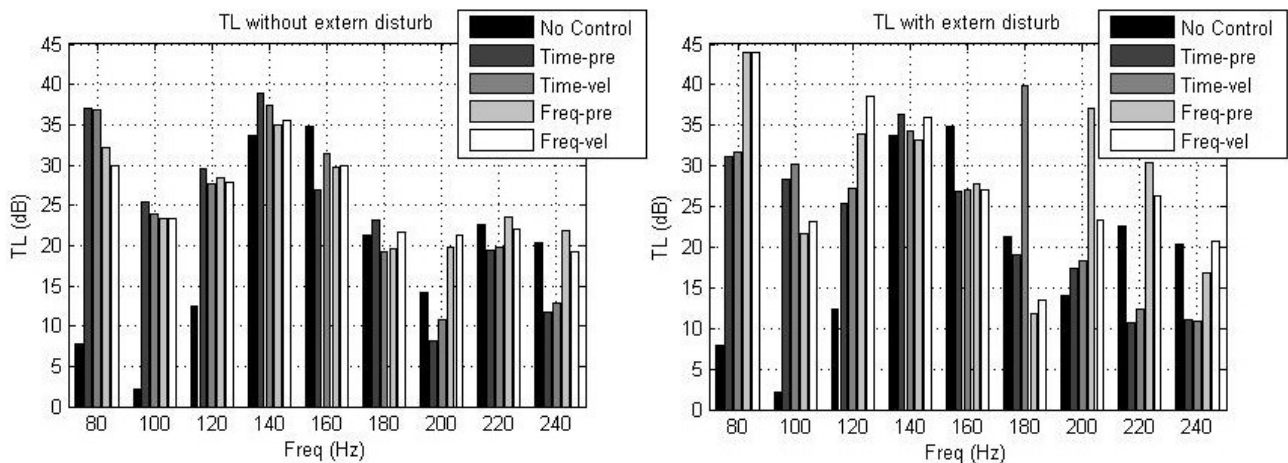


Figure 7: Sound transmission loss measured with different kinds of controller and error sensors. In the legend, *Time* means a FX-LMS time domain controller and *Freq* means FX-LMS frequency domain controller, *vel* indicates a particle velocity error sensor and *pre* indicate pressure error sensor.

As long as a well defined trend cannot be easily observed for the different sensors and control strategies, a logarithmic sum of the sound transmission losses was computed. It is shown in Figure 8, where it is possible to observe that, without external noise disturbance, the FX-LMS in the time domain using the microphone as error sensor is more effective, contradicting the expectation that the frequency domain controller would be more effective, independently of the error sensor used.

Applying the external noise disturbance during the controller adapting phase, an improvement happened on the sound transmission loss. The strategy that yielded the best result consisted of using the FX-LMS controller in the frequency domain and the particle velocity as error sensor, which was expected, since this controller in frequency does not recognize frequencies different from the harmonics given by Eq. (8), and the particle velocity sensor is less sensitive to the external noise disturbance that cause the air particle displacements to occur in different directions.

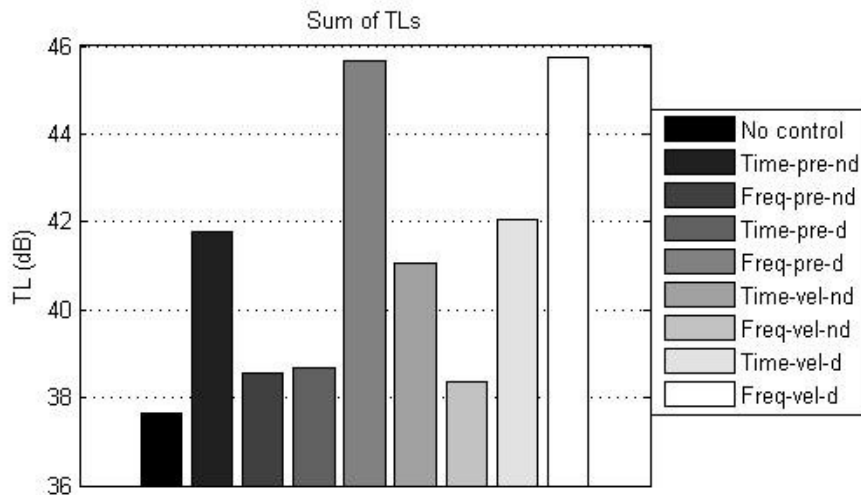


Figure 8: Logarithmic sum of TL in all the investigated frequencies. In the legend, *nd* means without external noise disturbance and *d* means with external disturbance for controllers in the time or frequency domain with particle velocity or pressure as error sensor.

It was not expected that the controller performance in the frequency domain would be poorer than the same controller in the time domain without the presence of an external noise disturbance. One possible reason is the fact that the computational cost of the FX-LMS in the time domain is much lower and this lowers the time lag between the input of the primary signal and the control signal output, which favors the adaptation. This fact is not observed when the external noise disturbance is applied, because the time controller acts in all the frequencies sensed by the error sensor. Therefore, without external noise disturbance the objective was acting on eight frequencies, while with the external noise disturbance the number of frequencies increase (as much as the secondary plant identification used on the filtering process allows), thus penalizing the convergence process and degrading the controller performance. In the frequency domain FX-LMS, although it has a higher computational cost, the acting region is limited to the discrete frequencies given by Eq. (8), independently of the external noise disturbance.

CONCLUSION

In the present work, an experimental comparison between a time domain and a frequency domain FX-LMS controller applied to a smart panel with an acoustic actuator tested in a plane wave tube with two different error sensors - a pressure sensor and a particle velocity sensor - is presented. The performance of the different controllers using different error sensors was evaluated based on the gain on the transmission loss of the active panel compared to the passive one. In the absence of external noise disturbance, the time domain controller gave good results regardless of the sensor used. In this configuration, the strategy that used the microphone as error sensor was more efficient. However, when an external noise disturbance was applied, the frequency domain controller using the particle velocity sensor was the most efficient strategy, since this controller does not act at frequencies that are different from the ones it was designed to control, and the velocity sensor does not measure particle velocity components other than the one along the direction it is positioned to measure, thus improving the controller performance compared with the same setup with a microphone as error sensor.

ACKNOWLEDGMENTS

We express our gratitude to FAPESP and CNPq for the financial support to this research.

REFERENCES

- Donadon, L. V. et al, 2006, "Comparing a filtered-x LMS and an H2 controller for the attenuation of the sound radiated by a panel", Proceedings of the International Conference on Noise and Vibration Engineering., Leuven, Belgium.
- Gentry, C. A., Guigou, C., Fuller, C. R., 1997, "Smart foam for application in passive-active noise radiation control", Journal of Acoustical Society of America, Vol. 101, No. 4, pp. 1771-1778.
- Guigou, C., Fuller, C. R., 1998, "Adaptive feedforward and feedback methods for active/passive sound radiation control using smart foam", Proceedings – National Conference on Noise Control Engineering, Vol. 2, pp 127-136.
- Juang, J., Pappa, R., 1985, "An eigensystem realization algorithm for modal parameter identification and model reduction", Journal of Guidance, Control and Dynamics, Vol. 5, No. 8, pp. 620-627.

Evaluation of feedforward control strategies with different error sensors

- Kim, S. Y., Kim, G., Roh, C. H., 2002, "Active noise control with a hybrid control algorithm using active/passive smart foam actuator", Proceedings of SPIE – The International Society for Optical Engineering, Vol. 4701, pp. 413-425.
- Kuo, S. M., Morgan, D. R., 1996, "Active Noise Control System: Algorithms and DSP implementations", John Wiley and Sons, Inc, New York, USA.
- Olivieri, O., Bolton, J. S., Yoo, T., 2006, "Measurement of transmission loss of materials using a standing wave tube", Proceedings of the 35th International Congress on Noise Control Engineering (INTER-NOISE 2006), Honolulu, USA, 2001.
- Song, B. H., Bolton, J. S., 2000, "A transfer-matrix approach for estimating the characteristic impedance and wave numbers of limp and rigid porous materials", Journal of Acoustical Society of America, Vol. 107, No. 3, pp. 1331-1152.
- Siviero, D. A. *et al*, 2010, "An experimental investigation of a hybrid active/passive panel for increased transmission loss at low frequencies", Proceedings of the International Conference on Noise and Vibration Engineering., Leuven, Belgium.
- Widrow, B., Stearns, S. D., 1985, "Adaptive Signal Processing", [S. I.]: Prentice-Hall.

Metamodelling Studies for Flutter Prediction of Wings

Paulo Roberto Caixeta Júnior¹, Flávio Donizeti Marques¹

¹ Universidade de São Paulo, Escola de Engenharia de São Carlos, Departamento de Engenharia de Materiais, Aeronáutica e Automobilística, Laboratório de Aeroelasticidade, Av. Trabalhador Sancarlene, 400, São Carlos, SP, Brasil

Abstract: This work presents a comparison of three metamodeling techniques applied to the flutter aeroelastic analysis of wings. The aim is to find out which among neural networks, radial basis function interpolation and radial basis function neural networks deals more properly with the dynamic aeroelasticity problem. Latin Hypercube Sampling is used to create a database that is afterwards evaluated by a aeroelastic solution code based on strip theory and Theodorsen unsteady aerodynamics with K-method for flutter speed determination. A Finite Element Method based code is used for structural dynamic analysis. This database containing samples features and their respective flutter critical speed is then used to implement the proposed metamodels. Results and discussion on the performance of the metamodels are addressed. This work is part of an implementation in progress of a Multidisciplinary Design Optimization (MDO) tool for the design of flexible aircraft wings.

Keywords: metamodel, aeroelasticity, flutter, MDO

NOMENCLATURE

EI_i = Bending stiffness at wing root or wing tip, $[Nm^2]$
 GJ_i = Torsion stiffness at wing root or wing tip, $[Nm^2]$
 b = Wing span, m

S = Wing area, m^2
 Λ = Wing leading edge sweep angle, $degrees$
 λ = Wing taper ratio, $[-]$
 V_{crit} = Flutter critical speed, m/s
 M = Mass, kg

Subscripts

$i = 1, 2, \dots, 8$ Wing spanwise stations

INTRODUCTION

Multidisciplinary design optimization (MDO) is a growing approach in the design of new products in the aerospace industry. It is a design tool that integrates several disciplines inside an optimization environment, allowing designers to act simultaneously on parameters that are generally treated separately, e.g., aerodynamic shape and structural strength, fluid-structure interaction analysis and mechanisms. MDO can be used in any stage of the design, although most of the available works apply the tool in preliminary or detailed designs with a few using MDO at the conceptual design stage.

Usually in an aircraft design the aeroelastic verifications occur in advanced stages (De Baets, 2004), which can be a problem when changes are needed as these may be very expensive at advanced stages, whereas in first stages changes are inexpensive. In this context, it seems reasonable to impose aeroelastic constraints to a MDO methodology, as a first step into a new optimal design environment to assist conceptual design studies.

Computational costs may be a problem in MDO schemes, which prevents proper searching on the design space and complicates the disciplines integration. An alternative to deal with the challenge of reducing computational effort during extensive design space exploration is the use of metamodeling concept (Wang & Shan, 2007). A metamodel is a model of a model, which assumes simplified mathematical forms to approximate computation-intensive functions. Metamodeling techniques are able to improve the understanding of input and output variables relationship, to provide tools for optimization and design space exploration that are faster than the conventional computer analysis, and finally they simplify the integration of computational codes (Simpson et al., 2001). Hence, a metamodel for flutter speed prediction seems very suitable for a MDO tool proposed (Caixeta Jr. & Marques, 2009a).

This work presents studies on three metamodeling techniques, including artificial neural networks, radial basis function interpolation and interpolation by radial basis function, applied to predict flutter speed of wings. The aim is to determine which one of them surrogates more satisfactorily the aeroelastic problem. The metamodel will be part of an MDO scheme under development (Caixeta Jr., 2006; Caixeta Jr. & Marques, 2009b,a, 2010). Artificial neural networks, also known as neural networks (NN), are mathematical tools that mimic the nervous systems of living beings to obtain knowledge from given data. The learning processes are also similar to nature. They are widely used in artificial intelligence systems and also as surrogate models in engineering works, where fast responses are desired. A variation of the typical NN is the radial basis function (RBF) NN, which differs from the first by using RBFs as the activation functions, instead of the sigmoidal function. The training process is also different as it does not just define the synaptic weights but the number of neurons in its layer as well (it is a simple single layer neural network). The interpolation by

radial basis function considers an approximating function that is a linear combination of radially symmetric functions, each centered on a definite point given. With this function adjusted to the solutions of the proposed problem it is possible to promptly obtain the outputs for given inputs, which makes the RBF interpolation an interesting tool for MDO studies.

The mathematical models used to create databases for metamodels are a finite element model (FE) for structural dynamics, an unsteady aerodynamic model based on strip theory and linear potential flow and a K-method for flutter prediction. The database creation is conducted applying a design-of-experiments technique called Latin Hypercube, to reach a smartly distributed sampling through the solution domain.

AEROELASTIC SOLUTION

The wing structural model has been achieved with a finite element code based on the Bernoulli-Euler beam element restricted to 3 degrees of freedom per node. The FE model element considers bending as represented by the translations in z -axis and the rotations in x -axis, while the rotations in y -axis describe beam torsion. Lumped mass and inertia moment elements may be located at the nodes to represent non-structural weight and other bodies attached to the wing. Conventional FE discretization process is considered, where Hermite polynomials are used as shape functions to calculate beam element deformation. Then, stiffness and mass element matrices can be assessed and combined to produce the global FE structural model (Craig, 1981). For flutter prediction, the structural model must be conveniently transformed to modal variable space, that is:

$$[M_{gen}] \{\ddot{\eta}(t)\} + [K_{gen}] \{\eta(t)\} = 0 \quad , \quad (1)$$

where $[M_{gen}]$ and $[K_{gen}]$ are the generalized mass and stiffness matrices, respectively, and $\{\eta(t)\}$ is the modal coordinate vector.

The FE code also provides the total mass of the structure that, together with the dynamic features, represent the complete set of structural information necessary to the aeroelastic model. The aeroelastic model to the prediction of flutter speed (Silva, 1994) has used the strip theory approach to account for the unsteady aerodynamic loading. A simple swept wing model, where the fuselage and other bodies are added as lumped masses, is adopted in this work. Figure 1 shows the aerodynamic model in terms of strips together with FE modeling nodes of the structure. The distribution must be in a way that each FE node coincides with an aerodynamic strip, so that each element contribution to the flutter prediction method may be computed. Flutter critical speed prediction is performed by means of the K -method (Silva, 1994; Hodges & Pierce, 2002), and extracted from V - g - f curves.

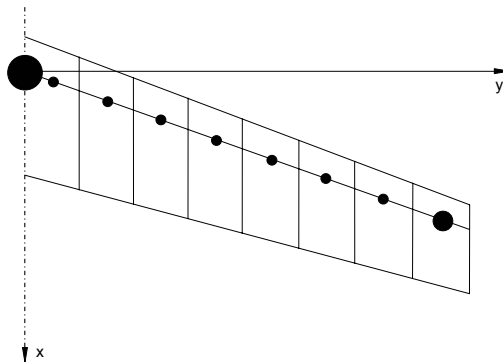


Figure 1 – Wing model schematics (aerodynamic strips and FE nodes).

NN METAMODEL

An artificial neural network (ANN) is a mathematical tool inspired by the brain of animals (Haykin, 1999). The feedforward ANN is composed of processing units called neuron, similar to the neurons of living creatures. The most usual model of neuron is the perceptron, shown in Fig. 2. In this model the input signals are multiplied by the weights (also known as synaptic weights, resembling the synapse of biological neurons) that measure the net connections importance. They are added and the result is compared to the bias (or threshold), creating the activation potential. On this an activation function is applied, after which the neuron output is reached. According to Fig. 2, the output may be mathematically described as:

$$o_j = \varphi \left(\theta_j + \sum_{i=1}^n x_i \cdot w_{ij} \right) \quad . \quad (2)$$

As activation function the sigmoidal functions, such as the hyperbolic tangent, that is,

$$\varphi(x) = \frac{2}{1 + e^{-2x}} - 1 \quad (3)$$

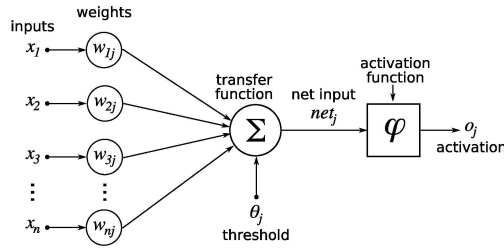


Figure 2 – Artificial neuron model - the perceptron.

Feedforward neural network architecture represents the way in which the neurons are connected. This feature makes them more complex, capable of learning more information. Training an ANN is the learning process where knowledge is given to it. In this process the synaptic weights are adjusted to accomplish the expected results from the net when given variables are inputted. There are several training algorithms known, among which the Levenberg-Marquardt back-propagation is one of the most efficient for multilayer networks.

Neural networks are suitable for the concept of metamodeling, because of their ability to work as surrogates of complex systems. Here, the NN metamodel (*cf.* Fig. 3), considers as input variables those that describe the wing bending and torsion stiffness distributions. For bending stiffness the values for EI and GJ at each semi-spanwise station describe the stiffnesses distributions of the wing span b , taper ratio (λ) and sweep speed (V_{crit}).

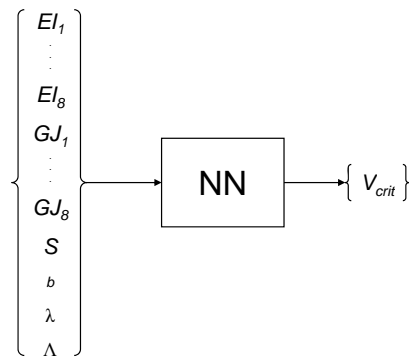


Figure 3 – NN metamodel input and output variables.

RADIAL BASIS FUNCTION INTERPOLATION METAMODEL

A real function dependent only on its argument magnitude is called radial. If $g(x) = \phi(\|x\|) = \phi(r)$, where $\phi : [0; 1] \rightarrow \mathfrak{R}$ and r is the length of the vector \mathbf{x} , then, $\phi(r)$ is called a radial basis function (RBF) (Buhmann, 2003).

$$y(\mathbf{x}) = \sum_{i=1}^N w_i \phi(\|\mathbf{x}\|), \quad (4)$$

The most common RBFs are:

- Linear:

$$\phi(r) = r \quad (5)$$

- Gaussian:

$$\phi(r) = \exp\left(-\frac{r^2}{2\beta^2}\right) \quad , \text{ for some } \beta > 0 \quad (6)$$

- Multiquadric:

$$\phi(r) = \sqrt{r^2 + \beta^2} \quad , \text{ for some } \beta > 0 \quad , \quad (7)$$

- Polyharmonic spline:

$$\phi(r) = r^k, \quad k = 1, 3, 5, \dots \quad , \quad (8)$$

$$\phi(r) = r^k \ln(r), \quad k = 2, 4, 6, \dots \quad , \quad (9)$$

$$\phi(r) = r^2 \ln(r) \quad (\text{thin plate spline}), \quad (10)$$

where $r = \|\mathbf{x} - \mathbf{x}_i\|$ for $i = 1, 2, \dots, N$ and β is a constant used to adjust the RBF shape.

The RBF interpolation considers the approximation $s(\mathbf{x})$, for a function $f(\mathbf{x})$, i.e.,

$$s(\mathbf{x}) \approx f(\mathbf{x}) \quad , \quad (11)$$

as a linear combination of N RBFs, so that:

$$s(\mathbf{x}) = \sum_{i=1}^N w_i \phi(\|\mathbf{x} - \mathbf{x}_i\|) \quad , \quad (12)$$

where w_i , for $i = 1, 2, \dots, N$, are weight factors.

The metamodel routine was based on a Matlab™ routine developed by Chirokov (2006), which is based on an interpolating function of the form,

$$s(\mathbf{x}) = a_0 + a_1 \mathbf{x} + \sum_{i=1}^N w_i \phi(\|\mathbf{x} - \mathbf{x}_i\|) \quad . \quad (13)$$

RADIAL BASIS FUNCTION NN METAMODEL

The main idea over RBF NNs is based on the RBF interpolation principles described previously. It differs from basic NN aforementioned in three aspects: the activation function is a RBF, the architecture of the feedforward network is defined by the training process (it is not predefined as the NN above) and it is a double layer network.

The training process start with few RBF neurons at the first layer and the linear system for synaptic weights and biases is solved. This step is repeated adding neurons to the first layer until the error goal or the maximum number of neurons is achieved.

LATIN HYPERCUBE

McKay et al. (1979) were the first to describe the technique of the Latin Hypercube (also known as Latin Hypercube Sampling - LHS). It is a statistical method that distributes samples through the dimensions of an array in a way not to repeat a value for each of the variables. To exemplify this concept, a square grid is a Latin Square (a 2D Latin Hypercube) if, and only if there is only one sample at each row and each column, as illustrated in Fig. 4. The Latin Hypercube is the generalization of this concept to a N-dimensional problem.

X			
	X		
			X
		X	

Figure 4 – Latin Square sampling.

RESULTS

The following sections present results from the database creation with LHS and the aeroelastic solution, as well as from the metamodels adjusted to this database.

Metamodeling Database

As described previously, the creation of the database has been made by using LHS to define the sampling. The variables used to describe each individual are the bending and torsion stiffness coefficients at 8 spanwise stations (see Fig. 1), the wing span, b , wing area, S , leading edge sweep angle, Λ , and taper ratio, λ , making a total of 20 variables. The working range for each variable has been chosen from previous evaluations to work inside a flutter critical speed range where the aeroelastic solution is considered reliable, and are shown in Tab. 1.

Table 1 – Variables working range.

Variable	Min. value	Max. value	Unit
EI_1	90,000	110,000	Nm^2
EI_8	70,000	–	Nm^2
GJ_1	90,000	110,000	Nm^2
GJ_8	70,000	–	Nm^2
b	20	21.5	m
S	21	22.5	m^2
Λ	0	3	$^\circ$
λ	0.7	1	–

The values of stiffness constants are defined respecting some imposed boundaries, in order to have coherent stiffnesses distributions, with values decreasing from root to tip. This is done by multiplying the values given by the LHS routine, which range from 0 to 1, by the range of each variable. For example, the first EI value (EI_1) is defined in the interval shown in Tab. 1. From the second to the eighth, the interval is given by the previous value (EI_1 , in the case of EI_2) and the minimum value (70,000). The same criteria is used for both variables sets EI and GJ .

To finally obtain the database, 1000 samples were created and evaluated by the aeroelastic solution code. For subsequent statistical evaluation of the adjusted metamodels, two approaches have been used. First, a different 1500 samples database was created, following the same previous procedure and considerations. Then 5 different populations of 500 samples each were also created.

NN Generalization

The NN training process has been attained via Levenberg-Marquardt backpropagation algorithm (Hagan et al., 1996) using the database described above. After tests with several different architectures, the NN metamodel architecture of 20-40-1 has been assumed and trained, revealing good generalization capability. A statistical evaluation were performed with 1500 solutions generalized and compared to the aeroelastic model results, from which were obtained for V_{crit} a mean error of 0.16 % and a standard deviation of 0.18 %. Figure 5 shows the results of the statistical evaluation of the 1500 samples database, where continuous lines are the 5% error lines and the dashed lines are 10% error lines. The second statistical analysis performed, which used 5 samples of 500 individuals each, making a total of 2500 individuals, resulted in a V_{crit} mean error of 0.15 % and again a standard deviation of 0.18 %.

RBF Interpolation

RBF Interpolation was performed using the Gaussian RBF, considering as RBF constant $\beta = 0.05$. The results of this metamodeling is shown in Fig. 6, where continuous lines are the 5% error lines and the dashed lines are 10% error lines. This metamodeling is acceptable from around 58 m/s to around 71 m/s , but outside this range the quality of results degrades. Even with this behaviour, the data from the first statistic evaluation are reasonable with the V_{crit} mean error of 1.88 % and the standard deviation of 1.69 %. The second statistical approach resulted in a V_{crit} mean error of 1.82 % and the standard deviation of 1.58 %.

RBF NN Generalization

The parameters considered for the implementation of this RBF NN include a spread of 10 for the RBF (the best adjustment from values tested) and a maximum number of neurons allowed to be added of 2000. The resulting net has 784 neurons at the RBF activation function layer and the generalization performed for the 1500 samples statistical analysis is shown in Fig. 7, where again the continuous lines are the 5% error lines and the dashed lines are 10% error lines. The performance of this metamodeling is slightly better then that of RBF Interpolation, presenting a V_{crit} mean error of 1.02 % and the standard deviation of 1.47 %, although still worse the pure NN. From the second statistical evaluation, the V_{crit} mean error was of 0.96 % and the standard deviation was of 1.18 %.

Table 2 summarizes the data obtained from both statistical analyses.

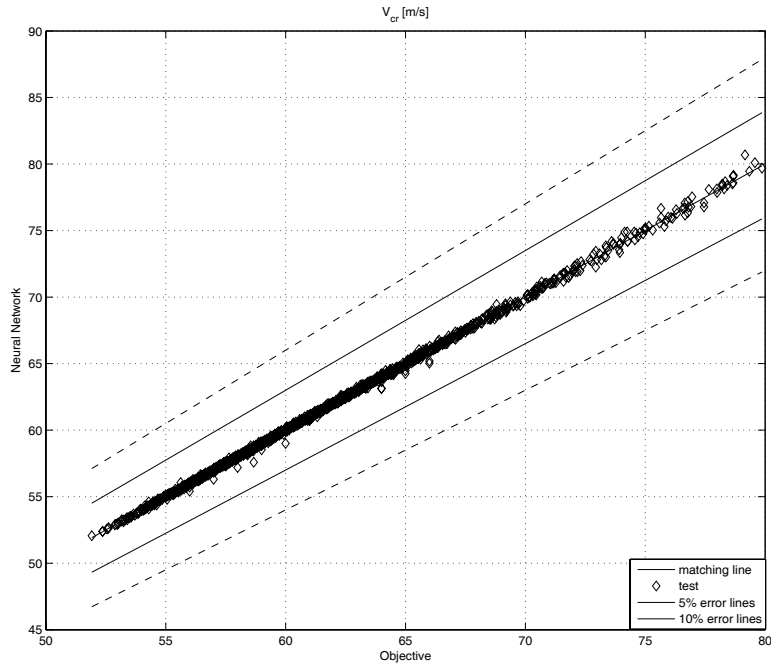


Figure 5 – NN statistical evaluation results (V_{crit} [m/s] in both axis).

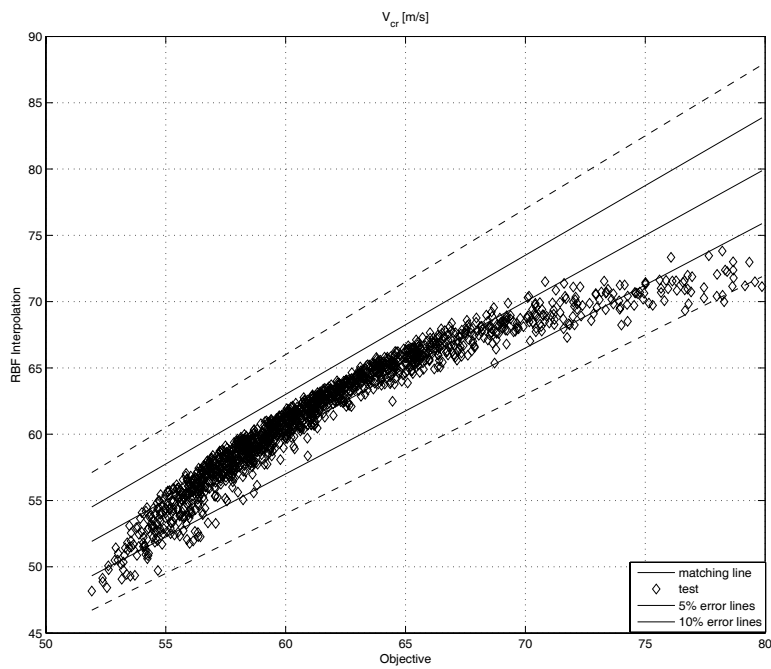


Figure 6 – RBF Interpolation statistical evaluation results (V_{crit} [m/s] in both axis).

CONCLUSIONS

The metamodelling of aeroelastic flutter solution by three techniques, NN, RBF Interpolation and RBF NN are investigated. The creation of a database for the implementation of metamodelling may be a hard task once it has to reach as much as possible the entire solution domain. Therefore, Latin Hypercube Sampling technique of design of experiments was used to create the database and presented good results. The metamodelling was verified with respect to an aeroelastic model for flutter critical speed and presented mean squared error of no more than 1.88% and standard deviation of 1.69% in the worst case among all results, for RBF Interpolation. The best metamodelling among the three, for the proposed aeroelastic problem, is the NN which presented for V_{crit} a mean error of 0.16 % and a standard deviation of 0.18 % in the first statistical analysis and a mean error of 0.16 % for V_{crit} with standard deviation of 0.18 % in the second statistical approach. The metamodelling has the advantage of easily integrating disciplines in one robust code, as shown in this work by their capability of assimilating knowledge to provide V_{crit} from structural parameters. With such tools, aircraft designers could have adequate information about the aeroelastic behavior of a wing at the conceptual design stage, and they could also

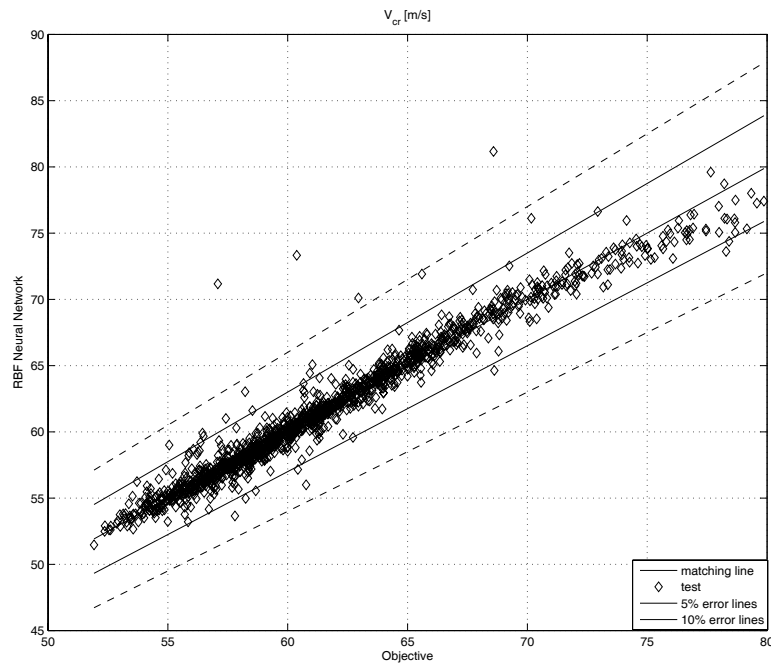


Figure 7 – RBF NN statistical evaluation results (V_{crit} [m/s] in both axis).

Table 2 – Statistical analyses of metamodels.

Metamodel	1500 samples		5×500 samples	
	Mean error [%]	Standard deviation [%]	Mean error [%]	Standard deviation [%]
NN	0.16	0.18	0.15	0.18
RBF interp.	1.88	1.69	1.82	1.58
RBF NN	1.02	1.47	0.96	1.18

explore and learn more about the design variables domain.

FUTURE STEPS

After the presented results, the NN metamodel has been chosen to be employed on a MDO tool under development, as mentioned previously. It will be expanded to generalize another important parameter of the wing that is the structural mass. These 2 outputs are conflicting features of a wing and will allow interesting multiobjective optimization studies.

ACKNOWLEDGEMENTS

The authors acknowledge the financial support of CNPq during the tenure of this research work.

REFERENCES

- Buhmann, M. D. (2003). *Radial Basis Functions: Theory and Implementations*. Cambridge University Press.
- Caixeta Jr., P. R. (2006). *Otimização Multidisciplinar em Projeto de Asas Flexíveis*. Master's thesis, Escola de Engenharia de São Carlos, Universidade de São Paulo.
URL <http://www.teses.usp.br/teses/disponiveis/18/18135/tde-22122006-111540/>
- Caixeta Jr., P. R., & Marques, F. D. (2009a). Aeroelastic wing MDO using metamodel based on neural networks. In *Proceedings of the 8th World Congress on Structural and Multidisciplinary Optimization - WCSMO8*. Lisbon, Portugal.
- Caixeta Jr., P. R., & Marques, F. D. (2009b). Dynamic aeroelasticity constraints in multidisciplinary design optimization of flexible wings. In *Proceedings of the XIII International Symposium on Dynamic Problems of Mechanics - DINAME 2009*. Angra dos Reis, Brazil.
- Caixeta Jr., P. R., & Marques, F. D. (2010). Neural network metamodel-based MDO for wing design considering aeroelastic constraints. In *Proceedings of the 6th AIAA Multidisciplinary Design Optimization Specialist Conference*. Orlando, USA.
- Chirokov, A. (2006). Scattered data interpolation and approximation using radial basis functions.
URL <http://www.mathworks.com/matlabcentral/fileexchange/10056>

Metamodelling for Flutter Prediction of Wings

- Craig, R. R. (1981). *Structural Dynamics*. Estados Unidos: John Wiley & Sons, Inc.
- De Baets, P. W. G. (2004). *A Methodology for Aeroelastic Constraint Analysis in a Conceptual Design Environment*. Ph.D. thesis, School of Aerospace Engineering, Georgia Institute of Technology.
- Hagan, M. T., Demuth, H. B., & Beale, M. H. (1996). *Neural Network Design*. Boston, MA, USA.: PWS Publishing Co.
- Haykin, S. (1999). *Neural Networks: A Comprehensive Foundation*. Upper Saddle River, NJ: Prentice-Hall, Inc.
- Hodges, D. H., & Pierce, G. A. (2002). *Introduction to Structural Dynamics and Aeroelasticity*. New York: Cambridge University Press.
- McKay, M. D., Beckman, R. J., & Conover, W. J. (1979). A comparison of three methods for selecting values of input variables in the analysis of output from a computer code. *Technometrics*, 21(2), 239–245.
URL <http://www.jstor.org/stable/1268522>
- Silva, R. G. A. (1994). *Análise Aeroelástica no Espaço de Estados Aplicada a Aeronaves de Asa Fixa*. Master's thesis, Escola de Engenharia de São Carlos, Universidade de São Paulo.
- Simpson, T. W., Peplinski, J., Koch, P. N., & Allen, J. K. (2001). Metamodels for computer-based engineering design: Survey and recommendations. *Engineering with Computers*, 17(2), 129–150.
- Wang, G. G., & Shan, S. (2007). Review of metamodeling techniques in support of engineering design optimization. *Journal of Mechanical Design*, 129(4), 370–380.

RESPONSIBILITY NOTICE

The author(s) is (are) the only responsible for the printed material included in this paper.

Experimental Study of the Nonlinear Hybrid Energy Harvesting System

Karami, M. A.¹, Varoto, P. S.², Inman, D. J.³

¹ PhD Candidate and ICTAS Doctoral Scholar, Department of Engineering Science and Mechanics, Virginia Tech, Blacksburg, VA, USA

² Full Professor on Dynamics and Vibrations, Escola de Engenharia de São Carlos – USP, São Carlos, SP, Brasil

³ George R. Goodson Professor, Center for Intelligent Material Systems and Structures, Mechanical Engineering Department, Virginia Tech, Blacksburg, VA, USA

Abstract: This paper aims to perform an experimental investigation of the proposed hybrid energy harvester. A nonlinear energy harvesting structure is proposed to convert ambient vibrations to the electrical energy using the piezoelectric and electromagnetic mechanisms. A repelling magnetic force is introduced to the system to both reduce and resonant frequency of the system and increase the frequency bandwidth by making the vibrations nonlinear. The paper is the continuation of a previous work by the authors in which the vibrations of the harvester was analytically characterized. Both mono-stable and bi-stable situations are studied. Depending on the level of excitations the bi-stable system can exhibit oscillations about each of its equilibriums, chaotic vibrations, or the limit cycle oscillations (LCO) over both of the equilibriums. The proper design of the harvester allows the system to perform Limit Cycle Oscillations in response to moderate base excitations. The paper discusses the experimental results on electromechanical vibrations and the energy generation of the nonlinear hybrid harvester at different magnetic force levels, excitation frequencies and excitation levels.

Keywords: piezoelectric energy harvesting, nonlinear vibrations, magnetic forces, limit cycle oscillations

NOMENCLATURE

A = Cross sectional area
 R = Load resistance
 e_{ij} = piezoelectric constants
 c_{ij} = stiffness coefficients
 $w(x,t)$ = Displacement function

M = Mass
 W = Energy
 L_g = Lagrangian
 T = Kinetic energy
 V = Potential energy
 G = Magnetic force
 L = length

I = Polar moment of inertia

Subscripts

p relative to piezoelectric
 s relative to substructure
 m relative to magnetic
 e relative to electric

Greek Symbols

ϕ = mode shape function
 ρ = mass density

INTRODUCTION

Energy harvesting is the process of scavenging small amounts of power from the ambient energy in the environment. This paper focuses on energy harvesting from vibrations. Such ambient energy can come from bridge vibrations, tire motion or the human heart beating. The minute energy can power up sensor nodes and therefore reduce the wiring complications or eliminate the need of changing batteries frequently. For more information on general energy harvesting the reader may refer to Anton et al. [2007].

During the past two years nonlinear energy harvesting has received substantial attention. The nonlinearity can be natural (for example the nonlinear material properties of the piezoelectric substance [Tripplet, 2009]) or can be synthetic. If in addition to the lateral direction the beam is excited longitudinally, the governing equation of the system includes some nonlinear expression in the form of parametric excitation [Daqaq, 2008]. The most common mechanism of making the beam nonlinear is by placement of permanent magnets [Stanton, 2010, Cottone, 2009, Shahrz, 2008, Erturk, 2009]. After modeling their systems and deriving the nonlinear governing equations most of these researchers have used numerical or experimental methods to solve the governing equations. Among the mentioned literature on magnetically nonlinear harvesters only Mann and Simms [2009] uses analytical perturbation methods, but they only solve the mechanical system and ignores the electromechanical coupling.

An electromechanical model was introduced by the first and third author Karami [2010] to result the governing equations and predict vibration and power harvesting behavior of the proposed nonlinear hybrid energy harvesting device. Based on the model we designed and fabricate a prototype to show nonlinear vibrations characteristics for low

frequency and low amplitude base oscillations. The current paper summarizes the results of experiments performed using the prototype. The paper follows by introducing the hybrid nonlinear harvesting device and driving the governing differential equations. Next we discuss the fabrication of the prototype and the test procedure. The experimental results are presented in three sections. The first two results sections are dedicated to mono-stable harvesting and the third section presents small vibrations, chaotic motion and limit cycle oscillations of the bi-stable harvester.

THE NONLINEAR HYBRID ENERGY HARVESTING DEVICE

The hybrid nature of the nonlinear harvesting device proposed here is illustrated in Fig. 1. We use magnetic forces in our system to reduce nonlinear behavior. The magnetic force between the tip and base magnets is repulsive and therefore counteracts the elastic behavior. The existence of nonlinear forces acting on the beam introduces nonlinear hardening terms, which are explained in section 0. The piezoelectric element bounded to the beam harvests energy from beam deflection. As a novel approach we have placed electromagnetic coils in the system. When the beam vibrates the magnetic tip mass passes by the coils and generates electricity. The system is a hybrid energy harvester in the sense that, it uses two different methods (piezoelectric and electromagnetic transduction) for power harvesting.

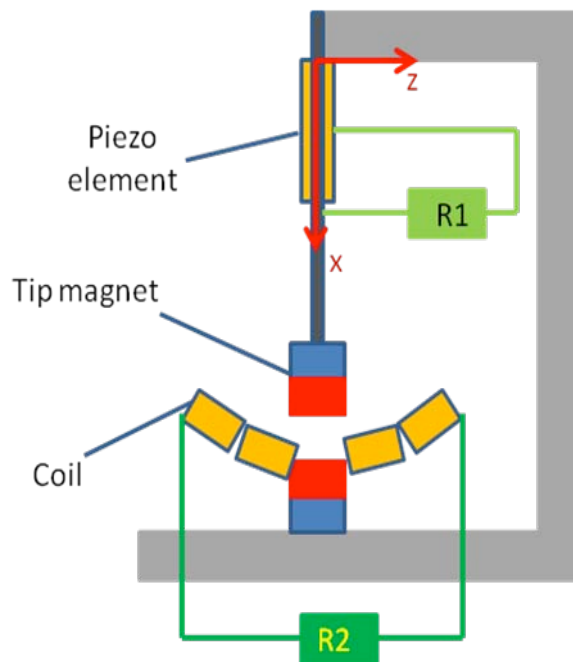


Figure 1 – Schematic view of hybrid energy harvester

GOVERNING EQUATIONS AND POSSIBLE SCENARIOS

We use the energy methods to model the dynamics of the system. The harvester is made up of three coupled systems; the cantilever beam which is characterized by the deflection of beam, the circuit connected to the piezoelectric element and the circuit connected to the coils. The electrical circuit for harvesting is simplified to be only a resistor in order to focus on the transduction. The value of the resistive load in the piezoelectric circuit is R_1 and the value of the resistive load in the electromagnetic circuit is R_2 . The energy in various components of the entire electromechanical system is: the elastic and magnetic potential energies stored in the beam and the magnetic field (V), the electrostatic energy stored in the piezoelectric patch (w_e), the kinetic energy stored in the beam and the tip mass (T), the magnetic potential energy between the tip and base magnets (G), the electromagnetic energy stored in the coils (W_m) and the energies dissipated by the resistors and damping of the beam. The displacement of the beam, the flux linkage across the piezoelectric element and the charge through the coils are the coordinates used for identifying the system. Following the guidelines in Preumont [2006], the Lagrangian of the system is:

$$L_g = T - V + W_e + W_m \quad (1)$$

The dynamic deflection of the beam is simplified by a single mode Galerkin's method. The deflection at each point and at a certain time relative to the base is $w(x, t) = \phi(x)u(t)$. The approach is a common practice in study of nonlinear vibrations of bi-stable structures [Stanton, 2010] and is justified by center manifold reduction [Moon, 1979]. The static deflection shape of the beam under a unit load applied to the tip is used as the shape function.

The following integrals are defined to facilitate abbreviation of formulas:

$$\begin{aligned} \phi_{20}^L &= \int_0^L \phi^2(x) dx & \phi_{20}^{L_l} &= \int_0^{L_l} \phi^2(x) dx \\ \phi_{22}^L &= \int_0^L (\phi''(x))^2 dx & \phi_{22}^{L_l} &= \int_0^{L_l} (\phi''(x))^2 dx \end{aligned} \quad (2a)$$

$$\begin{aligned} \phi_{10}^L &= \int_0^L \phi(x) dx & \phi_{10}^{L_l} &= \int_0^{L_l} \phi(x) dx \\ \phi_{22}^{L_l} &= \int_0^{L_l} \phi''(x) dx \end{aligned} \quad (2b)$$

Each of the terms in Lagrangian are related to the states as follows:

$$W_e - V = \iiint_{vol} \left(-\frac{1}{2} c_{ij} S_i S_j + e_{ij} E_i S_j + \frac{1}{2} \varepsilon_{ij} E_i E_j \right) - G(w_{end}(t)) \quad (3)$$

where c_{ij} are the stiffness coefficients, e_{ij} are the piezoelectric constants [Leo, 2007], E_i are the electric field components and $G(w_{end}(t))$ is the magnetic force potential. The Magnetic force is experimentally measured and is characterized as $f = -a w_{end} + b w_{end}^3$. The magnetic force potential is therefore: $G(w_{end}) = -\frac{a}{2} w_{end}^2 + \frac{b}{4} w_{end}^4$. We let Y_s denote the Young's modulus of the steel substrate, Y_p the Young's modulus of the piezoelectric patch, I_s the area moment of inertia of the steel beam about its geometric center and I_p stand for the area moment of inertial of the cross section of each piezoelectric patch about the center line of the steel substructure. Eq. (3) is simplified to:

$$\begin{aligned} W_e - V &= -\frac{b\phi(L)^4}{4} u(t)^4 - \left\{ -\frac{a\phi(L)^4}{2} + \frac{1}{2} Y_s I_s \phi_{22}^L + Y_p I_p \phi_{22}^{L_l} \right\} u(t)^2 + \\ &\frac{2A_p \bar{z}_p \phi_{22}^{L_l} \varepsilon_{13}}{h_p} \lambda_1(t) u(t) + \frac{\varepsilon_{33} A_p L_l}{h_p^2} \lambda_1(t)^2 \end{aligned} \quad (4)$$

In Eq. (4), $\lambda_1(t)$ is the flux linkage across the piezoelectric patch, A_p is the cross-sectional area and \bar{z}_p is the z -coordinate of the centroid of the patch. The z and x -coordinates have been defined in Fig. 1. The base motion, characterized by $r(t)$, should be taken into account when calculating the kinetic energy. The kinetic energy is evaluated as

$$\begin{aligned} T &= \left[\frac{1}{2} \rho_s A_s \phi_{20}^L + \frac{1}{2} \rho_p A_p \phi_{20}^{L_l} + \frac{1}{2} M_{tip} \phi(L)^2 \right] \dot{u}^2(t) + \\ &\left[\rho_s A_s \phi_{20}^L + 2\rho_p A_p \phi_{20}^{L_l} + M_{tip} \phi(L) \right] \dot{u}(t) \dot{r}(t) + \frac{1}{2} [M_{tip} + M_s + 2M_p] \dot{r}^2(t) \end{aligned} \quad (5)$$

The densities of the steel substrate and the piezoelectric patch are ρ_s and ρ_p respectively. The total mass of the substrate and each of the piezoelectric patches are M_s and M_p . The cross sectional area of the substrate is A_s and M_{tip} stands for the mass of the tip magnet. When the tip magnet passes by the coils some electromagnetic energy conversion occurs. The electromagnetic coupling can be characterized by the coupling coefficient, T_m .

When the tip magnet passes by the coils with the velocity \dot{w}_{end} , a force of magnitude $T_m \dot{w}_{end}$ impedes the motion of tip magnet. The current in the coils is i_2 . At the same time a potential difference is generated across the coil which equals $T_m \dot{w}_{end}$. The charge passing through the coils is noted by q_2 and the overall inductance of the coils is l . The following two terms in the Lagrangian represent the electromechanical energy in the coils:

$$W_m^* - V = \frac{1}{2} l \dot{q}_2^2 + T_m \dot{q}_2 \phi(L) u \quad (6)$$

The Euler-Lagrange equations for our three degrees of freedom system is:

$$\begin{aligned} \frac{d}{dt} \left(\frac{\partial L_g}{\partial \dot{u}} \right) - \frac{\partial L_g}{\partial u} &= -c_f \dot{u} \\ \frac{d}{dt} \left(\frac{\partial L_g}{\partial \dot{\lambda}_1} \right) - \frac{\partial L_g}{\partial \lambda_1} &= -\frac{\dot{\lambda}_1}{R_1} \\ \frac{d}{dt} \left(\frac{\partial L_g}{\partial \dot{q}_2} \right) - \frac{\partial L_g}{\partial q_2} &= -R_2 \dot{q}_2 \end{aligned} \quad (7)$$

The damping coefficient of the mechanical spring is denoted by c_f . Performing the derivations in Eq. (7), dividing by the modal mass and grouping the terms results:

$$\left\{ \begin{aligned} u + ku + \tilde{b}u^3 &= -d\dot{u} - \tilde{\psi}_1 V_1 + \tilde{\gamma} \dot{q}_2 - \hat{m} \ddot{r}(t) \\ \dot{V}_1 + \frac{V_1}{R_1 C_0} &= \frac{\tilde{\psi}_2}{C_0} \dot{u} \\ \frac{d i_2}{dt} + \frac{R_2}{l} i_2 &= -\tilde{\gamma} \dot{u} \end{aligned} \right. \quad (8)$$

The coefficients in Eq. (8) are given as:

$$\begin{aligned} \tilde{m} &= \rho_s A_s \phi_{20}^L + 2\rho_p A_p \phi_{20}^{L_1} + M_{tip} \phi^2(L) & \hat{m} &= \frac{\rho_s A_s \phi_{10}^L + 2\rho_p A_p \phi_{10}^{L_1} + M_{tip} \phi(L)}{\tilde{m}} \\ k &= \frac{-a\phi^2(L) + Y_s I_s \phi_{22}^L + 2Y_p I_p \phi_{22}^{L_1}}{\tilde{m}} & \tilde{\psi}_1 &= -\frac{2A_p \tau_p \phi_{12}^{L_1} \epsilon_{13}}{\tilde{m} h_p} \\ \tilde{b} &= \frac{b\phi^4(L)}{\tilde{m}} & C_0 &= \frac{2\epsilon_{33} A_p L_1}{h_p^2} \\ d &= \frac{c_f}{\tilde{m}} & \tilde{\psi}_2 &= \tilde{m} \tilde{\psi}_1 \\ \tilde{\gamma} &= T_m \phi(L) \end{aligned} \quad (9)$$

The second and third terms on the right hand side of Eq. (8-a) represent the ‘‘drag’’ terms introduced by the piezoelectric patch and the electromagnetic coils. The energy transferred to the electric circuits reduces the mechanical energy of the beam and therefore slightly suppresses its oscillations.

The sign of the linear restoring coefficient, k , can be positive or negative. The familiar positive coefficient corresponds to low magnetic forces. In this situation the zero deflection equilibrium is stable and the system is a ‘‘nonlinear mono-stable oscillator’’ coupled to the piezoelectric and electromagnetic circuits.

If the tip magnet is close to the base the repelling force between the magnets, which forces the tip away from the zero deflection, becomes significant. The $\mathbf{u} = \mathbf{0}$ equilibrium will be unstable but there will be two stable equilibriums on the left and right side of zero deflection ($\mathbf{u} = \pm \mathbf{u}^*$). In this situation the system is ‘‘nonlinear bi-stable oscillator’’ coupled to the piezoelectric and electromagnetic circuits. The nonlinear vibrations of the nonlinear bi-stable oscillator is discussed in section 0.

FABRICATION AND TESTING PROCEDURE

The beam element in the hybrid harvester is a bimorph where the substrate is a 152.4 X 25.4 X 0.635 mm spring steel beam as shown in the experimental setup of Fig. 2a. There are two QP10n Mide’ QuickPacks placed on the sides of the beam. For proper clamping of the beam part of the piezoelectric patches and the substrate are clamped. The effective length of the substrate outside the clamp is 127 mm. The first 38.1 mm of the beam is covered on both sides by the Quickpacks. The blue electromagnetic coils illustrated in Fig. 2b are modified small transformers. The ferroelectric coil of the transformer has been removed to prevent sudden interference with the motion of the tip magnet. Only one of the coils of the transformer (the top coils) are wired to the electromagnetic load. The coils are placed in carefully

machined aluminum supports. The aluminum support can be elevated and oriented using the two brass vertical screws. This allows optimal placement of the electromagnetic coils along the course of motion of the tip magnet.

The tip magnet is composed of three rare earth magnets the two 12.7 X 12.7 X 12.7 mm cubic magnets are stabilized on the sides of the ferroelectric spring steel by being placed on top of a 25.4 X 25.4 X 3.17 mm magnet. All the magnets are positioned to have their south poles pointed downwards. The base magnet is a 25.4 X 25.4 X 3.17 mm rare earth magnet with its south pole oriented upwards to repel the tip magnets. The strong magnetic force attaches the base magnet to a steel block, used to position the base magnet. A rail mechanism allows positioning of the base magnet and the two electromagnetic coils on its sides. The height of the vertical support connected to the column of the energy harvester can be adjusted. By adjusting the elevation of the beam we can vary the distance between the tip and base magnets and achieve different vibration scenarios.

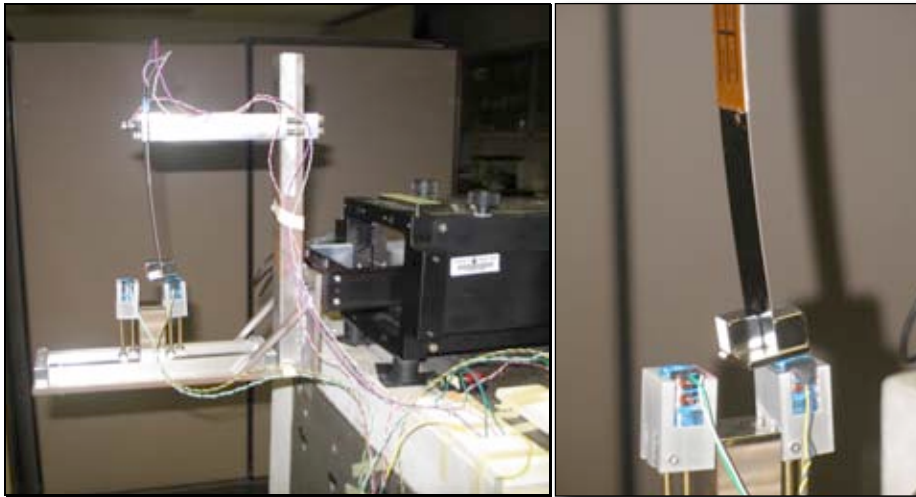


Figure 2: Experimental setup: (a) Connection of the hybrid harvester to the shaker; (b) Detail of the electromagnetic transduction element

The velocity of the tip magnet is measured using a Polytec OFV 303 laser vibrometer. The base acceleration (the acceleration of the frame of the harvester) is measured by a tear drop accelerometer. The voltage across the resistive load connected to the piezoelectric patches, and the voltage across the electromagnetic load are also measured. Siglab data acquisition interface from Spectral Dynamics is used for data collection.

MONO-STABLE PIEZOELECTRIC HARVESTER

The mono-stable nonlinear vibrations occur when the distance between the base and the tip magnets is larger than a certain threshold. In that working condition the passive magnetic forces reduce the natural frequency of the harvester and also make it nonlinear. The zero deflection equilibrium however remains stable. The following tests examine the vibration characteristics and the power harvesting trend of the hybrid energy harvester as a function of the distance between the magnets, the base excitation level, the excitation frequency and the load. The Virtual Sine Sweep (VSS) feature of Siglab has been used to collect the data presented in this section. The VSS software only records the ratio between input to its 2nd-4th channel and the voltage reading at its first channel. We therefore have measured the transfer function corresponding to tip velocity, piezoelectric voltage and the electromagnetic voltage divided by the base accelerations. As the first step we only implement the piezoelectric harvesting and do not install the electromagnetic coils.

Magnet spacing

The distance between the magnets changes the magnetic force and thus changes both the natural frequency and the nonlinearities. The smaller the distance between the magnets, the smaller the natural frequency and the more significant the nonlinear effect. It can be seen from Fig. 3 that smaller magnet gap also corresponds to larger damping. Clearly the peaks of tip velocity FRF at small magnet gaps are shorter and wider compared to the corresponding peaks when the magnets are far from each other. One reason for this phenomenon is the eddy currents generated in the steel block, which hold the base magnet in place. When the tip and base magnets are close to each other the magnetic field fluctuations due to the motion of the tip magnet are significant. This field fluctuation induces eddy currents in the structure and dissipates some energy.

The nonlinearity is hardening nonlinearity and becomes more visible when the amplitude of the tip deflection is large. For large tip deflections the peaks of FRF curve bends to the right, but at the same time shortens. This increases the bandwidth of the harvester but reduces the power generation.

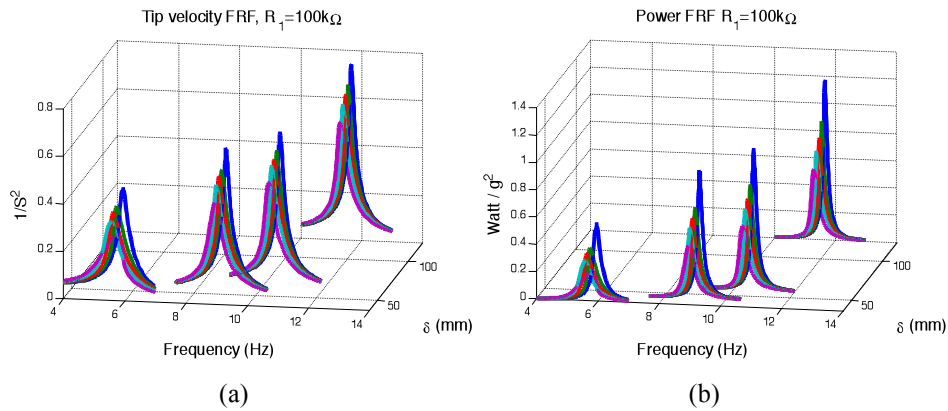


Figure 3: Relation between the magnet spacing and a) Tip velocity/base acceleration frequency response function and b) harvested power/ base acceleration² frequency response function. The colors represent different base acceleration: blue: 0.15, green 0.3, red 0.74, cyan 1.5, magenta 3 m.s⁻².

Resistive load

There is an optimal value for the resistive load in terms of the power production. At this optimal value however the velocity will be minimal. Since the nonlinearity is more significant when the amplitude of motion is large, at optimal resistance where is the amplitude of motion is minimal, the nonlinear effects become less dominant. This phenomenon is illustrated in Fig. 4.

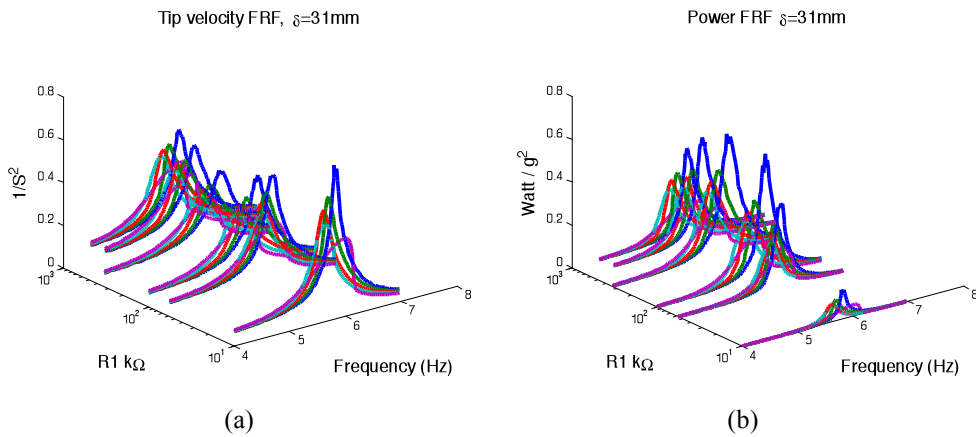


Figure 4: Relation between the resistive load across the piezoelectric patch and a) Tip velocity/base acceleration frequency response function and b) harvested power/ base acceleration² frequency response function. The colors represent different base acceleration: blue: 0.15, green 0.3, red 0.74, cyan 1.5, magenta 3 m.s⁻².

MONO-STABLE HYBRID HARVESTER

This section explores the behavior of hybrid mono-stable nonlinear harvester. The main difference between this section and previous section is the inclusion of the electromagnetic harvesting in experimental study.

Magnet Distance

Figure 5 illustrates that the natural frequency of the harvester increases with magnet distance. The hardening nonlinearity however decreases with the magnet gap. The damping in the structure decreases with the magnet distance due to presence of eddy currents. Decreasing the distance therefore increases the bandwidth at the cost of reduction in motion amplitude. The decrease in the velocity magnifies in piezoelectric and electromagnetic power curves. The electromagnetic power is more sensitive to amplitude of oscillation than the piezoelectric power. As illustrated in Fig. 2b the coils are on the sides of the tip magnet. If the range of motion of the tip mass is below a certain limit, the magnet would not pass over the coils and therefore there would be a significant loss in electromagnetic power generation.

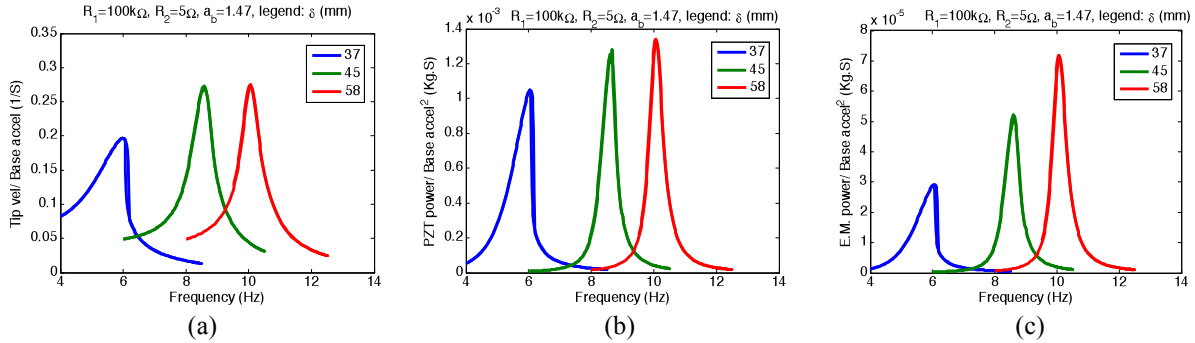


Figure 5: Relation between the magnet distance and a) tip velocity transfer function, b) piezoelectric power transfer function, c) electromagnetic power transfer function.

Base acceleration

As illustrated in Fig. 6 the nonlinear behavior intensifies with the base acceleration. Since the type of nonlinearity is hardening this results in some decrease in the amplitude of motion and correspondingly the harvested power. The power drop in electromagnetic harvesting is more visible for the reasons discussed in previous sections.

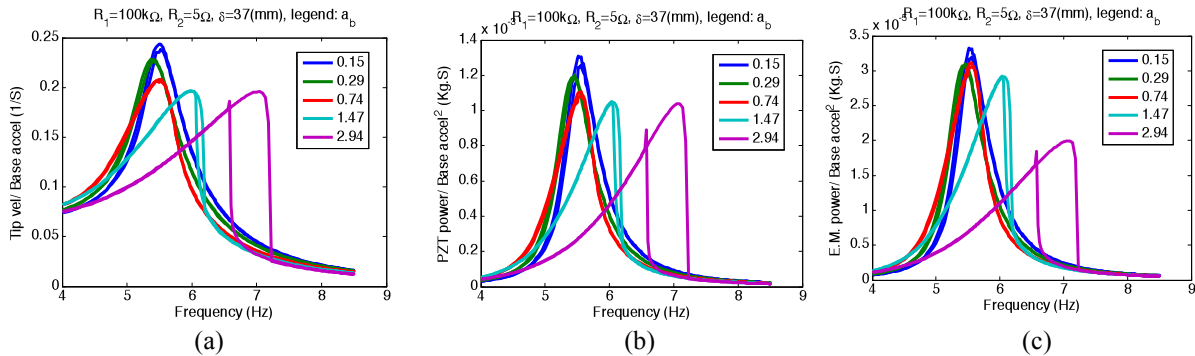


Figure 6: Relation between the base acceleration and a) tip velocity transfer function, b) piezoelectric power transfer function, c) electromagnetic power transfer function.

The piezoelectric load

The variations in the piezoelectric shunt resistance results in effects similar to changes in resonant frequency and damping. Figure 7 illustrates that the optimal resistance for Piezoelectric harvesting is 100 k Ω . The optimal piezoelectric load however results in the minimum tip velocity and correspondingly minimum electromagnetic power generation.

Experimental Study of the Nonlinear Hybrid Harvester

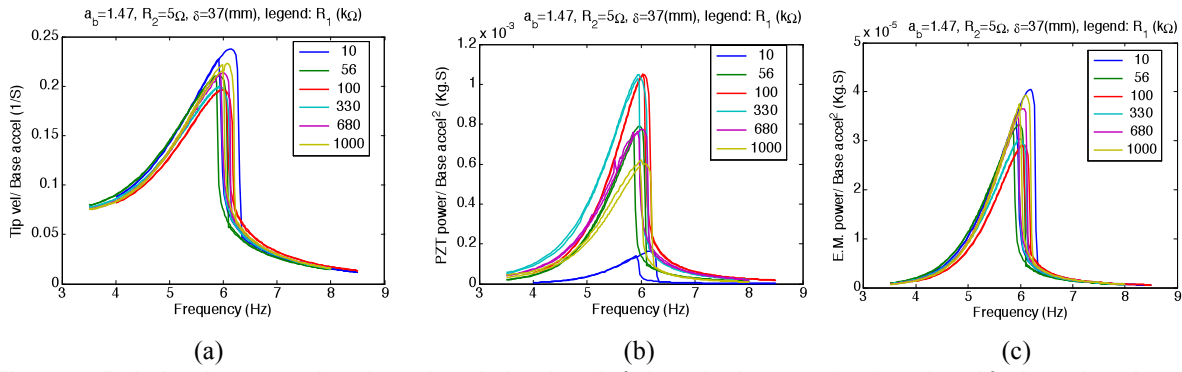


Figure 7: Relation between the piezoelectric load and a) tip velocity transfer function, b) piezoelectric power transfer function, c) electromagnetic power transfer function.

The electromagnetic load

In principle, the electromagnetic load affects the power harvesting similar to the piezoelectric load. However the optimal electromagnetic load is in order of Ohms and for the examined device is less than the resistance of the wires. As illustrated in Fig. 8, the optimal electromagnetic load is less than the smallest shunt resistance and the power decreases with the electromagnetic resistance. The tip velocity and the piezoelectric power are almost insensitive to the electromagnetic shunt resistance. The situation has been predicted by modeling performed by Karami [2010].

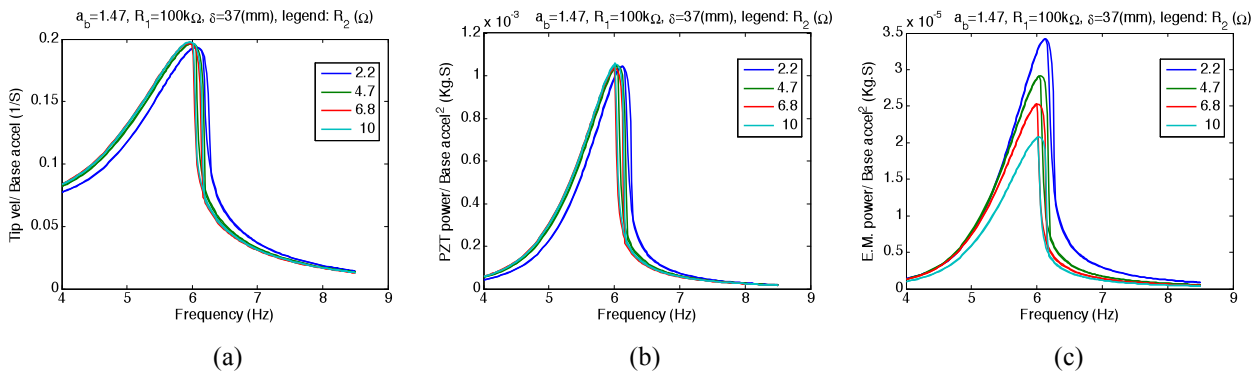


Figure 8: Relation between the electromagnetic load and a) tip velocity transfer function, b) piezoelectric power transfer function, c) electromagnetic power transfer function.

BI-STABLE HARVESTER

When the distance between the base and the tip magnets is less than 27mm the zero deflection equilibrium of the beam is not stable. There are two equilibriums on the sides which are stable. The motion of the harvester can be one of three forms: small oscillations about any of the stable equilibriums, chaotic motion, or large limit cycle oscillations circling both stable equilibriums. In the following we experimentally examine the conditions that give rise to any of the possible motion patters.

Base acceleration

The experimental results for the case where the magnet distances is 27 mm has been illustrated in Fig. 9. When the base excitations are smaller than 3 m.s^{-2} the beam oscillates about either of the stable equilibriums. The motion is referred to as small amplitude oscillations. For larger base excitations the motion can be chaotic or limit cycle oscillations. The amount of harvested power from limit cycle oscillations is an order of magnitude larger than power from chaotic motion which in turn is an order of magnitude larger than small oscillations' power.

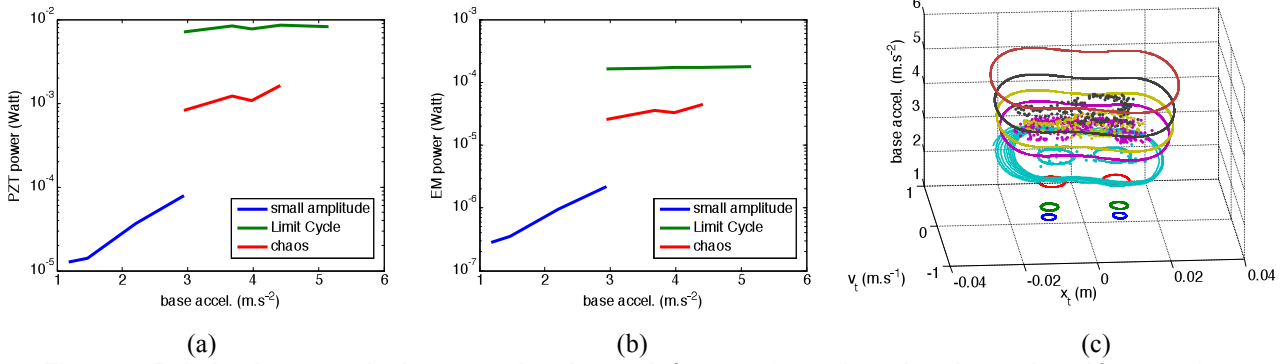


Figure 9: Relation between the base acceleration and a) power from piezoelectric patches, b) power from electromagnetic coils, c) phase portrait and Poincare map.

Excitation frequency

In the following we examine the variations of mechanical motion and harvested power with the base excitation frequency. The effects are different depending on the level of base accelerations. We therefore conduct three series of tests and illustrate the results in Figs. 10, 11 and 12.

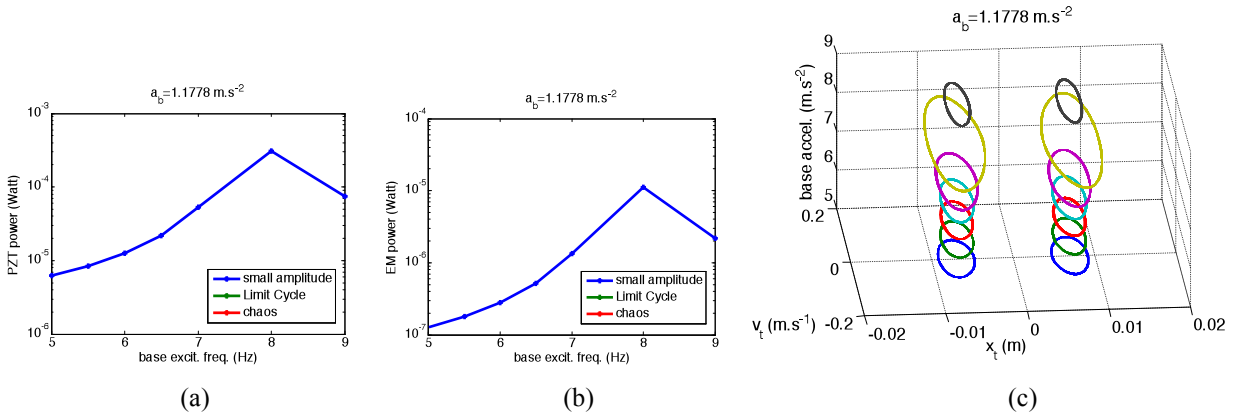


Figure 10: Relation between the frequency of the 1.18 m.s⁻² base excitation and a) power from piezoelectric patches, b) power from electromagnetic coils, c) phase portrait.

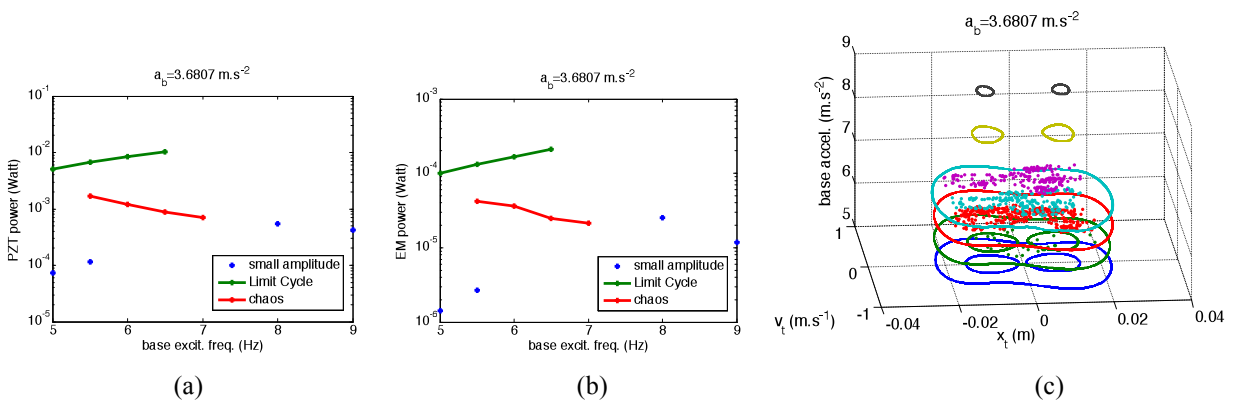


Figure 11: Relation between the frequency of the 3.68 m.s⁻² base excitation and a) power from piezoelectric patches, b) power from electromagnetic coils, c) phase portrait.

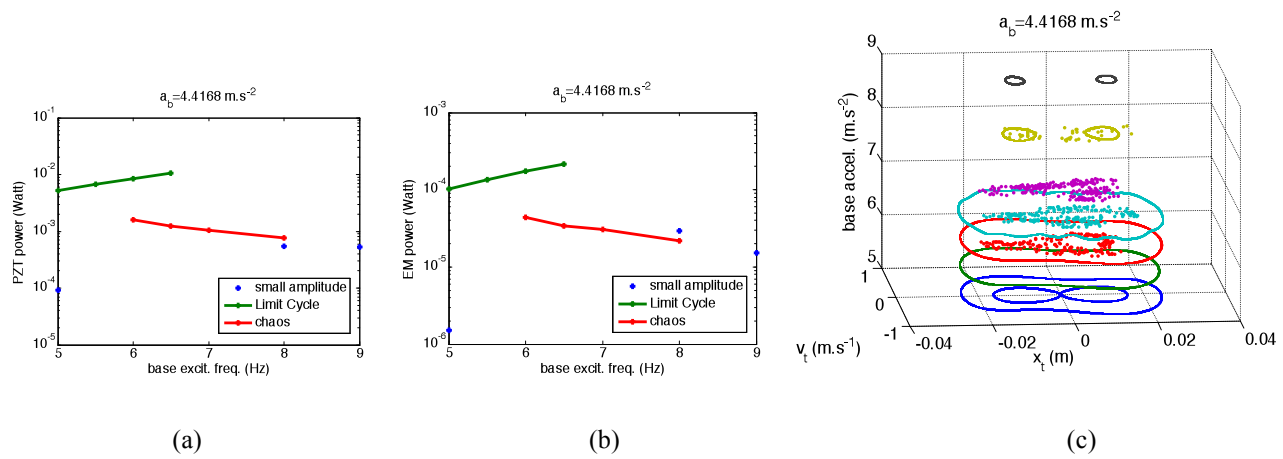


Figure 12: Relation between the frequency of the 4.42 m.s^{-2} base excitation and a) power from piezoelectric patches, b) power from electromagnetic coils, c) phase portrait.

CONCLUSIONS

A comprehensive experimental investigation was conducted on the vibrations characteristics and power generation of the novel hybrid nonlinear energy harvester. The harvester utilizes passive magnetic forces to both reduce the natural frequency and introduce useful nonlinearities to the harvesting system. The device has been modeled using energy methods. The first set of experiments is for the softly nonlinear system where only piezoelectric transduction is implemented. The second case study considers the softly nonlinear system where both piezoelectric and electromagnetic transductions harvest energy. The final set of tests is dedicated to bi-stable situation and the small amplitude oscillation, chaotic motion and limit cycle oscillations are all investigated.

ACKNOWLEDGMENTS

Mr. Karami acknowledges the support received from Virginia Tech towards the development of this work. Prof. Varoto acknowledges the opportunity to get involved in this research project as a Visiting Scholar at CIMSS and is grateful to USP and FAPESP (grant # 2009/06347-7) for the financial support.

REFERENCES

- Anton, S., Sodano, H., 2007, "A review of power harvesting using piezoelectric materials (2003-2006)," *Smart Materials and Structures*, vol. 16, p. 1.
- Arnold, D., 2007, "Review of microscale magnetic power generation," *IEEE Transactions on Magnetics*, vol. 43, pp. 3940-3951.
- Barton, D. A. W., Burrow, S. G., Clare, L. R., 2009, "Energy harvesting from vibrations with a nonlinear oscillator," in *ASME-IDETC*, San Diego CA.
- Beeby, S.P., Tudor, M. J., White, N. M., 2006, "Energy harvesting vibration sources for microsystems applications," *Measurement science and technology*, vol. 17, p. 175.
- Cook-Chennault, K., Thambi, N., Sastry, A., 2008, "Powering MEMS portable devices—a review of non-regenerative and regenerative power supply systems with special emphasis on piezoelectric energy harvesting systems," *Smart Materials and Structures*, vol. 17, p. 043001.
- Cottone, F., Vocca, H., Gammaitoni, L., 2009, "Nonlinear energy harvesting," *Physical Review Letters*, vol. 102, p. 80601.
- Daqaq, M., Stabler, C., Qaroush, Y., Seuaciuc-Osorio, T., 2009, "Investigation of Power Harvesting via Parametric Excitations," *Journal of Intelligent Material Systems and Structures*, vol. 20, p. 545.
- Erturk, A., Hoffmann, J., Inman, D. J., 2009, "A piezomagnetoelastic structure for broadband vibration energy harvesting," *Applied Physics Letters*, vol. 94, p. 254102.

- Karami, M., A., Inman, D. J., 2010, "Nonlinear Hybrid Energy Harvesting utilizing a Piezo-magneto-elastic spring," presented at the 17th SPIE Annual International Symposium on Smart Structures and Materials & Nondestructive Evaluation and Health Monitoring, San Diego, CA.
- Leo, D. J., 2007, *Engineering Analysis of Smart Material Systems*: Wiley.
- Mann, B., 2009, "Energy criterion for potential well escapes in a bistable magnetic pendulum," *Journal of Sound and Vibration*, vol. 323, pp. 864-876.
- Mann, B., Owens, B., 2009, "Investigations of a nonlinear energy harvester with a bistable potential well," *Journal of Sound and Vibration*.
- Mann, B., Sims, N., 2009, "Energy harvesting from the nonlinear oscillations of magnetic levitation," *Journal of Sound and Vibration*, vol. 319, pp. 515-530.
- Moon, F., Holmes, P., 1979, "A magnetoelastic strange attractor," *Journal of Sound Vibration*, vol. 65, pp. 275-296.
- Preumont, A., 2006, *Mechatronics: dynamics of electromechanical and piezoelectric systems*: Kluwer Academic Pub.
- Priya, S., 2007, "Advances in energy harvesting using low profile piezoelectric transducers," *Journal of Electroceramics*, vol. 19, pp. 167-184.
- Priya S., Inman, D. J., 2008, *Energy Harvesting Technologies*: Springer.
- Shahruz, S., 2008, "Increasing the Efficiency of Energy Scavengers by Magnets," *Journal of Computational and Nonlinear Dynamics*, vol. 3, p. 041001.
- Stanton, S., McGehee, C., Mann, M., 2010, "Nonlinear dynamics for broadband energy harvesting: Investigation of a bistable piezoelectric inertial generator," *Physica D: Nonlinear Phenomena*.
- Stanton, S., McGehee, C., Mann, B., 2009, "Reversible hysteresis for broadband magnetopiezoelastic energy harvesting," *Applied Physics Letters*, vol. 95, p. 174103.
- Triplett, A., Quinn, D., 2009, "The Effect of Non-linear Piezoelectric Coupling on Vibration-based Energy Harvesting," *Journal of Intelligent Material Systems and Structures*, vol. 20, p. 1959.

RESPONSIBILITY NOTICE

The authors are the only responsible for the printed material included in this paper.

Thermal and Dynamic Analysis of the Rotor/Stator Contact in Turbomachinery

André Brandão¹, Fabrice Thouverez², and Laurent Blanc²

¹ Universidade de Brasília (UnB) – Campus Universitário Darcy Ribeiro. Brasília – DF, Brazil.

² École Centrale de Lyon - 36 avenue Guy de Collongue - Ecully, France.

Abstract: This paper presents the study of the interaction between a bladed-rotor and its stator. Once the tangential velocity on the end of the blades of such a machine can reach 500m/s, this interaction can even cause the destruction of the structure, it is then very important to analyze this interaction. Besides that, a thermal analysis regarding the heat production from the friction is also developed on this work.

Keywords: dynamics, thermics, rotor/ stator interaction, contact, non-linear analysis

INTRODUCTION

Turbomachineries are usually composed by a great number of bladed wheels. These bladed rotors reassure the energy exchange between the engine and the air, what makes them key pieces on turbomachinery, ergo they must respond to high standards in terms of mechanical resistance, aerodynamic performance and temperature. In addition to that, the sources of vibration on this type of structure are many; however the vibration amplitudes must be low to reassure a satisfying lifetime for the machine. Nowadays the research for higher performance on the turbomachinery tends to designs with fewer compression stages, what makes the whole ensemble much lighter but also implies the need of much higher compression rates on each stage. This goal can be achieved by making the gap between the blades and the fixed parts smaller, almost eliminating the aerodynamic losses. This kind of designs makes the risk of contact between the parts much higher. The tangential velocity on the extremity of these kinds of turbomachineries can reach up to 500 m/s, and the contact could cause the destruction of the machine if its conditions were not controlled. Indeed, if their conditions were not controlled, these contacts can take place during the normal functioning of the machine, because of unbalanced masses on the rotor, aerodynamic charges or even manoeuvring charges.

The proposed study is focalized on the interaction phenomena between the rotor end the stator, i.e. the moving and fixed parts of the turbomachinery on relatively long time intervals were the parts touch slightly to reach a steady state movement. The interest is focused on the coupling between the vibration modes of the two parts, causing a vibrational coincidence that can be very important in terms of deformation amplitudes. Then a thermo mechanical analysis is developed to understand the heat generation due to the friction and the issues linked to dilatation. A basic model script is proposed aiming to simulate these phenomena with the best simplicity/reality rate possible.

DYNAMIC ANALYSIS WITHOUT THERMIC EFFECTS

In this chapter the aspects of the initial proposed problem, which does not involve the thermal effects caused by the friction, will be presented. The problem will be detailed as well as the resolution strategies and the obtained results.

Presenting the problem

Rotordynamics

Some relevant aspects about the study of rotordynamics must be presented before the developed model. The possible sources of excitation on this kind of systems are many. There can be unbalanced masses applying a cyclic force due to centrifugal effects, the aeromechanical coupling on these structures is also significant. These traditional sources will not be applied on our model. Further ahead the excitation strategy will be detailed.

A very important phenomenon on turbomachinery dynamics is the modal interaction, and its understanding is of high importance on our study. The modal interaction is a dynamic coupling phenomenon that takes place, under certain conditions, when the bladed rotor touches the stator. This can happen because the rotor and stator are close and because the vibration amplitudes of a structure can become very high if it is excited according to its eigen modes. The occurrence of this kind of interaction is bound to a set of conditions as follows:

- Both structures assume deformed configurations propitious to the energy exchange, i.e. they both vibrate in one or two modes of same diameter ;
- Each structure vibrates on the frequency of the considered eigen mode ;
- The propagation velocities of the modes, which are turning modes, are the same in the fixed frame of reference.

Physically, the condition for modal interaction is:

$$\omega_c = n_d \Omega - \omega_{br} \quad (1)$$

Where ω_c is the frequency of the mode considered for the carter and ω_{br} , the one of its homologue for the bladed rotor, n_d the number of diameters of the stator's deformation and Ω the rotation speed of the rotor.

The bladed disc and flexible stator model

Now, the simplified model of a bladed wheel with a flexible carter retained for this study of modal interaction is presented. It's important to notice that the stator is modeled on the fixed frame of reference and the wheel on the turning frame.

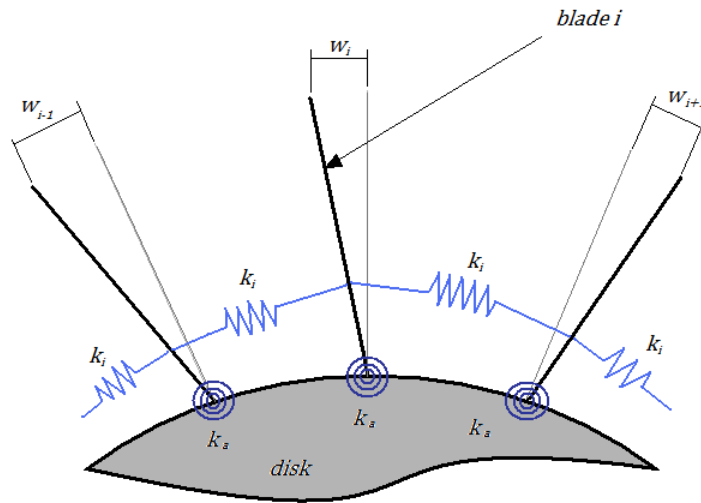


Figure 1 – Bladed wheel model (Legrand, 2005).

We have used a linear model for the bladed wheel in which the blades are rigid and connected to the central disc by torsion springs of stiffness k_a . The link between one blade and the one next to it is done by means of linear springs of stiffness k_i placed between them, Fig.1. In order to make the model as realistic as possible, we've used as the parameter b the equivalent stiffness seen from the tip of the blade of a straight elastic beam with rectangular section fixed to the disc's periphery and with flexural movement along the orthoradial direction. Its dimensions are length L_x in the radial direction, width L_y along the axis of the disc and thickness h in the orthoradial direction. It is made of steel of Young's modulus E , Poisson's modulus ν and specific mass ρ . The movement equation is as shown on the Eq. (2) for the case of 6 blades.

$$\begin{bmatrix} M_a & 0 & 0 & 0 & 0 & 0 \\ 0 & M_a & 0 & 0 & 0 & 0 \\ 0 & 0 & M_a & 0 & 0 & 0 \\ 0 & 0 & 0 & M_a & 0 & 0 \\ 0 & 0 & 0 & 0 & M_a & 0 \\ 0 & 0 & 0 & 0 & 0 & M_a \end{bmatrix} \begin{Bmatrix} \dot{w}_1 \\ \dot{w}_2 \\ \dot{w}_3 \\ \dot{w}_4 \\ \dot{w}_5 \\ \dot{w}_6 \end{Bmatrix} + \begin{bmatrix} b+c & -c & 0 & 0 & 0 & -c \\ -c & b+c & -c & 0 & 0 & 0 \\ 0 & -c & b+c & -c & 0 & 0 \\ 0 & 0 & -c & b+c & -c & 0 \\ 0 & 0 & 0 & -c & b+c & -c \\ -c & 0 & 0 & 0 & -c & b+c \end{bmatrix} \begin{Bmatrix} w_1 \\ w_2 \\ w_3 \\ w_4 \\ w_5 \\ w_6 \end{Bmatrix} = \begin{Bmatrix} 0 \\ 0 \\ 0 \\ 0 \\ 0 \\ 0 \end{Bmatrix} \quad (2)$$

Where w_i is the orthoradial displacement of the tip of the blade i and M_a is the generalized mass.

$$M_a = \frac{\rho h L_x L_y}{5} \quad (3)$$

The parameters b and M_a become then functions of the geometric and material characteristics of the blade. The expression of c is a function of the distance β between the linking spring and the disc's periphery.

$$b = \frac{k_a}{L_x^2} = \frac{E h^3 L_y}{3 L_x^3 (1 - \nu^2)} ; \quad c = k_i * \frac{\beta}{L_x} \quad (4)$$

The geometric and material parameters used for the bladed wheel on the simulations have the following values :

Table 1 - Bladed wheel geometric and material parameters.

L_x	L_y	h	ρ	E	ν	k_i	β
0.5m	0.3m	0.01m	$7.8 * 10^3 kg/m^3$	210GPa	0.3	800kN/m	2mm

We have not considered the force due to unbalance on this example.

The stator was modeled with a n_d -diameters model as an elastic ring. Only one number of diameters was used at each time. The tangential deformation of the ring at the angular position ϕ has, then, the following expression:

$$s(\phi, t) = A_{n_d}(t) \cos(n_d\phi) + B_{n_d} \sin(n_d\phi), \quad n_d \in \mathbb{N}, n_d \geq 2 \quad (5)$$

In addition to that, the ring is inextensible. This means that we can impose a relation between its tangential and radial deformations: $u_s(\phi, t) = \partial s(\phi, t) / \partial \phi$. The radial deformation of the ring at the angular position ϕ has, then, the following expression:

$$u_s(\phi, t) = -n_d A_{n_d}(t) \sin(n_d\phi) + n_d B_{n_d}(t) \cos(n_d\phi), \quad n_d \in \mathbb{N}, n_d \geq 2 \quad (6)$$

The kinetic energy T and potential energy U of the system are defined as :

$$T = \frac{1}{2} \int_0^{2\pi} \rho_{stat} S_{stat} [\dot{u}_s(\phi, t)^2 + \dot{w}(\phi, t)^2] R_{stat} d\phi \quad (7)$$

$$U = \frac{1}{2} \int_0^{2\pi} \frac{E_{stat} I_{stat}}{R_{stat}^3} \left[\frac{\partial u_s}{\partial \phi}(\phi, t) + u_s(\phi, t) \right]^2 d\phi \quad (8)$$

Where ρ_{stat} , S_{stat} , E_{stat} and I_{stat} are the density, the transversal section area, Young's modulus and the diametral inertia for the stator, then we use an energy approach to obtain the matrix equation that characterizes the dynamics of the system:

$$\begin{bmatrix} (n_d^2 + 1)M_s & 0 \\ 0 & (n_d^2 + 1)M_s \end{bmatrix} \begin{Bmatrix} \ddot{A}_{n_d} \\ \ddot{B}_{n_d} \end{Bmatrix} + \begin{bmatrix} 2n_d^2(n_d^2 + 1)K_s & 0 \\ 0 & 2n_d^2(n_d^2 + 1)K_s \end{bmatrix} \begin{Bmatrix} A_{n_d} \\ B_{n_d} \end{Bmatrix} = \begin{Bmatrix} 0 \\ 0 \end{Bmatrix} \quad (9)$$

Where $K_s = \frac{E_{stat} I_{stat}}{R_{stat}^3}$ and $M_s = 2\pi\rho R_{stat} S_{stat}$. The geometric parameters used for the stator on the simulations are the following:

Table 2 - Flexible stator geometric parameters.

S_{stat}	I_{stat}	δ	R_{stat}
$1.2 * 10^{-2} m^2$	$1.6 * 10^{-6} m^4$	0.5mm	0.5005m

Resolution Strategies

The Time Integrator

Then, the motion equations of the entire problem can be put under the classical matrix form:

$$\mathbf{M}\ddot{\mathbf{u}}(t) + \mathbf{C}\dot{\mathbf{u}}(t) + \mathbf{K}\mathbf{u}(t) = \mathbf{F}(t) \quad (10)$$

Where \mathbf{M} , \mathbf{C} and \mathbf{K} are the system's mass, damping and stiffness matrices. The \mathbf{F} vector represents the forces applied on this system. Solving this equation means to verify the relation at many consecutive time instants t_n , for which $\mathbf{u}(t_n) = \mathbf{u}_n$. The equation is discretized on the time. The time integrators, or direct integration methods, are numerical procedures used to solve such differential equations. They are largely used mainly because of the great facility presented to apply them on calculation software such as Matlab and their capacity of treating linear system as well as non-linear systems.

In our case a centered finite differences approach is used following Legrand's conclusions (Legrand, 2005). Indeed he showed that this explicit scheme gave a good balance between stability and numerical costs for rotor-stator interaction problems. We can, then, calculate the prediction $\mathbf{u}_{n+1,p}$ in function of \mathbf{u}_n and \mathbf{u}_{n-1} by:

$$\left(\frac{M}{\Delta t^2} + \frac{C}{2\Delta t}\right) \mathbf{u}_{n+1,p} = \mathbf{F}_n + \left(2\frac{M}{\Delta t^2} - \mathbf{K}\right) \mathbf{u}_n + \left(\frac{C}{2\Delta t} + \frac{M}{\Delta t^2}\right) \mathbf{u}_{n-1} \quad (11)$$

Where the index , p indicates the predicted value of the variable. What was shown is the procedure for the prediction of the degrees of freedom positions on the studied system, but without the acknowledgement of the contact between the parts. For that, on each time step we do a second procedure, which we call correction step, to test if there is contact between the parts and, if there is, correct the position of the touching parts. The procedures for this second step are described on the following paragraphs.

Modeling the Contact

The contact problems can be considered equivalent to minimization problems. On the following explanations, one of the most classical methods for the acknowledgement of the contacts on the numerical procedures will be shown, which is the Lagrange multipliers method, used on this study. They consist on regularizations of non linear laws for the contact and the friction in function only of the displacements.

If after the predicted displacements the rotor penetrates the stator, a correction is needed for the system to verify the following conditions :

$$g_{n+1} = \mathbf{u}_{relative} - \delta = 0 \quad (12)$$

$$\left(\frac{M}{\Delta t^2} + \frac{C}{2\Delta t}\right) (\mathbf{u}_{n+1,p} + \mathbf{u}_{n+1,c}) = \mathbf{F}_n + \mathbf{F}_{cont,n+1} + \left(2\frac{M}{\Delta t^2} - \mathbf{K}\right) \mathbf{u}_n + \left(\frac{C}{2\Delta t} + \frac{M}{\Delta t^2}\right) \mathbf{u}_{n-1} \quad (13)$$

Where g_{n+1} is the gap between the parts and $\mathbf{u}_{n+1,c}$ and $\mathbf{F}_{cont,n+1}$ are the corrections to consider in order to validate these two equations, knowing that $\mathbf{u}_{n+1,c} + \mathbf{u}_{n+1,p} = \mathbf{u}_{n+1}$. The Eq.(12) is a compatibility condition for the displacements : the rotor cannot penetrate the stator, i.e. g_{n+1} cannot be positive, if there is contact the gap must be exactly zero. Eq.(13) assures the force balance on the system when the contact forces $\mathbf{F}_{cont,n+1}$ are considered.

The exact equation for the gap, Eq.(12), is, on the studied cases, always non-linear. We can linearize it though, calculating approximations for small values of g_{n+1} . The expression becomes, then:

$$g_{n+1} \approx g_{n+1,p} + \mathbf{C}_{N_{n+1,p}} \cdot \mathbf{u}_{n+1,c} = 0 \quad (14)$$

Where $g_{n+1,p}$ is the predicted value for the gap before the correction, $\mathbf{C}_{N_{n+1,p}}^T$ is the linearized vector that gives us the the normal force direction on the contact, $\mathbf{C}_{T_{n+1,p}}^T$ will be its homologue for the tangential forces. Then, with a Lagrange multipliers approach we can write the contact forces as follows :

$$\mathbf{F}_{cont} = \mathbf{F}_{contN} + \mathbf{F}_{contT} = -[\mathbf{C}_N + \mathbf{C}_T] \lambda_N = -\mathbf{C}_{NT} \lambda_N \quad (15)$$

And we can define the problem with the two following equations :

$$g_{n+1} \approx g_{n+1,p} + \mathbf{C}_{N_{n+1,p}} \cdot \mathbf{u}_{n+1,c} = 0 \quad (16)$$

$$\left(\frac{M}{\Delta t^2} + \frac{C}{2\Delta t}\right) \mathbf{u}_{n+1,c} = \mathbf{F}_{cont,n+1} = -\mathbf{C}_{NT_{n+1,p}} \lambda_{N_{n+1}} \quad (17)$$

This well defined system of two equations and two unknown variables, namely $\lambda_{N_{n+1}}$ et $\mathbf{u}_{n+1,c}$ is solved.

$$\lambda_{N_{n+1}} = \left[\mathbf{C}_{N_{n+1,p}}^T \left(\frac{M}{\Delta t^2} + \frac{C}{2\Delta t}\right)^{-1} \mathbf{C}_{NT_{n+1,p}} \right]^{-1} g_{n+1,p} \quad (18)$$

$$\mathbf{u}_{n+1,c} = -\left(\frac{M}{\Delta t^2} + \frac{C}{2\Delta t}\right)^{-1} \mathbf{C}_{NT_{n+1,p}} \lambda_{N_{n+1}} \quad (19)$$

So, for each analyzed problem the expressions for $g_{n+1,p}$, $\mathbf{C}_{N_{n+1,p}}^T$ and $\mathbf{C}_{NT_{n+1,p}}$ must be developed in function of the degrees of freedom as accurately as possible for the contact to be well simulated.

It is very important to notice that on our bladed wheel and flexible carter model the unbalance forces on the rotor are not acknowledged. We must then find a way of generating the first contact that will be maintained afterwards by the modal interaction phenomenon. The strategy used here was presented on (Legrand, 2005). An initial punctual impulsions is given to the carter hard enough to cause the parts to touch.

On the simulations that were made on this study a 200 $N.s$ impulsions was applied on the exterior surface of the stator on the angular position $\phi = \pi/4$ and at $t = 20dt$, where dt is the time step which is defined on Eq. (23).

The gap

For our reference problem, the gap must be calculated separately for each one of the blades. The contact instant is illustrated on Fig. 2:

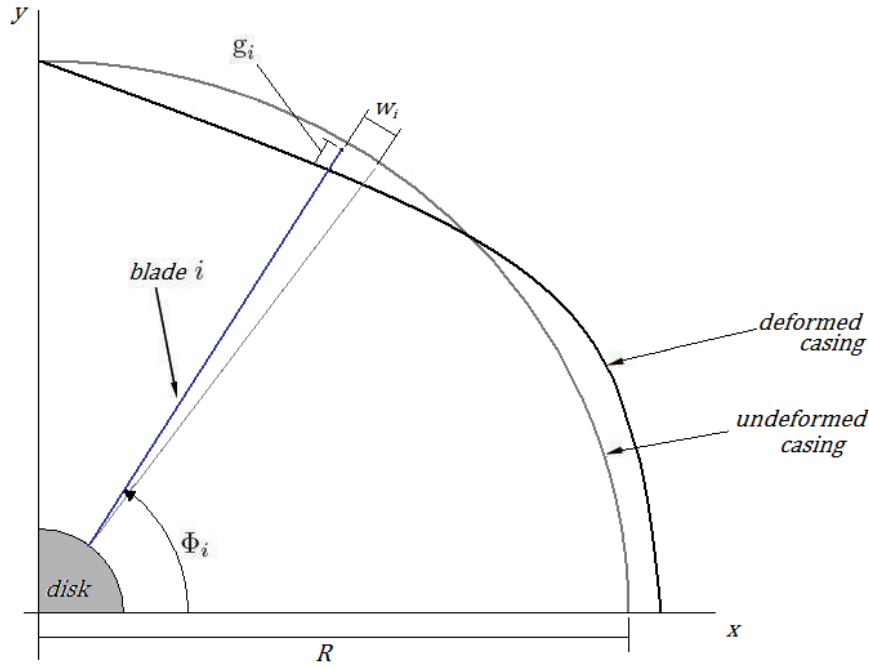


Figure 2 – Contact between blade and stator.

The gap can, then, be calculated, considering the rigid body movements of both the stator and the rotor - \mathbf{U}^r and \mathbf{U}^s -, as shown on the Eq.(20).

$$g_{n+1,p}^i = \delta + u_s(\phi_{n+1,p}^i)_{n+1,p} + U_{x_{n+1,p}}^r \cos(\phi_{n+1,p}^i) + U_{y_{n+1,p}}^r \sin(\phi_{n+1,p}^i) - U_{x_{n+1,p}}^s \cos(\phi_{n+1,p}^i) - U_{y_{n+1,p}}^s \quad (20)$$

Where ϕ^i is the angular position of the end of the blade i and are given by the following expression:

$$\phi_{n+1,p}^i = \frac{2\pi}{N_a}(i-1) + \tan^{-1}\left(\frac{w_{n+1,p}^i}{L_x}\right) + \Omega t_{n+1} \quad (21)$$

Calculating \mathbf{C}_N and \mathbf{C}_T

The vectors \mathbf{C}_N and \mathbf{C}_T are shown below. The blade that is in contact and for which we make the correction is represented by jj , N is the number of blades on the rotor and V_s is the slip velocity at the point of contact.

$$\mathbf{U} = \begin{Bmatrix} A_{n_d} \\ B_{n_d} \\ U_x^s \\ U_y^s \\ U_x^r \\ U_y^r \\ \lambda_1 \\ \vdots \\ \lambda_{jj} \\ \vdots \\ \lambda_N \end{Bmatrix}; \mathbf{C}_{N_{n+1,p}} = \begin{Bmatrix} -n_d \sin(n_d \phi_{n+1,p}^{jj}) \\ n_d \cos(n_d \phi_{n+1,p}^{jj}) \\ -\cos(\phi_{n+1,p}^{jj}) \\ -\sin(\phi_{n+1,p}^{jj}) \\ \cos(\phi_{n+1,p}^{jj}) \\ \sin(\phi_{n+1,p}^{jj}) \\ 0 \\ \vdots \\ \frac{\partial u_s(\phi_{n+1,p}^{jj})}{\partial \phi} \\ R_{stat} \\ \vdots \\ 0 \end{Bmatrix}; \mathbf{C}_{T_{n+1,p}} = \text{sign}(V_s) \mu \begin{Bmatrix} -\cos(n_d \phi_{n+1,p}^{jj}) \\ -\sin(n_d \phi_{n+1,p}^{jj}) \\ \sin(\phi_{n+1,p}^{jj}) \\ -\cos(\phi_{n+1,p}^{jj}) \\ -\sin(\phi_{n+1,p}^{jj}) \\ \cos(\phi_{n+1,p}^{jj}) \\ 0 \\ \vdots \\ 1 \\ \vdots \\ 0 \end{Bmatrix} \quad (22)$$

Because of the approximations especially on some of the expressions used on the correction step, it happens sometimes that the gap does not come to exactly zero after this step. To minimize this error and verify the relation on Eq.(12) we remake the correction step until the moment in which the gap is inside a tolerance value. The tolerance value used on our simulations was $10^{-10}m$.

The studied cases

The developed model can be analyzed by two different approaches: with or without the rigid body movement for the rotor and stator. Those two cases were simulated. The obtained results are presented on the following paragraphs.

With modal interaction without rigid body movement

The Fig.3 shows the coupled deformed states of the system while on modal interaction. On the turning frame of reference these configurations are constant and do not depend on the time, i.e. the system becomes a static problem on the turning frame of reference.

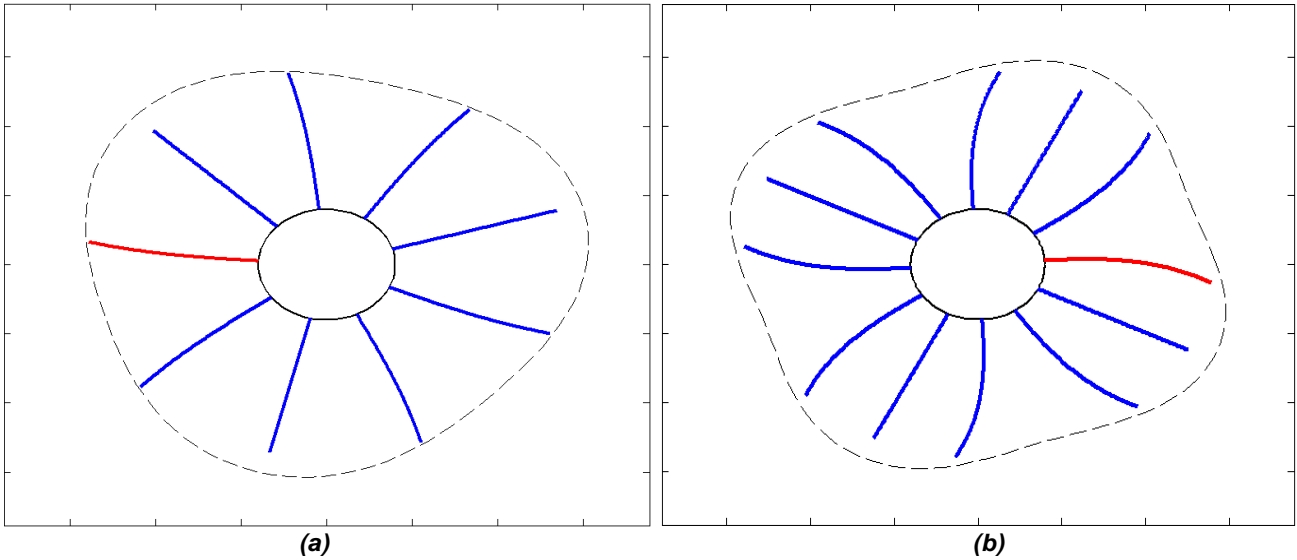


Figure 3 – Coupled deformation states for the stator modeled with 3 (a) and 4 (b) diameters (displacements magnified 50x).

We can see Fig. (3) that on this steady state there are some blades that develop a permanent contact with the stator and others that are never in contact. On Fig.4 we see the orthoradial displacement of one of the blades in permanent contact, and we can notice that its position stabilizes on a position different than zero. All the results below were obtained for a 3-diameter deformation on the stator and a rotation velocity of 4800rpm, calculated using Eq. 1.

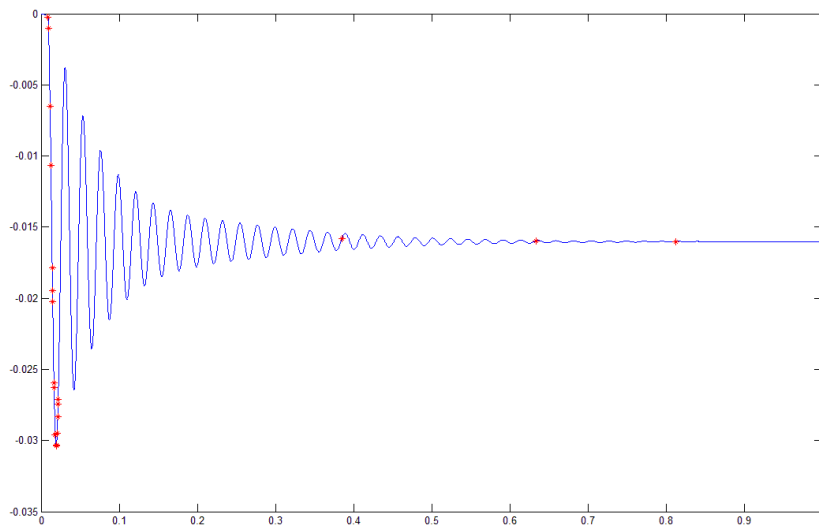


Figure 4 – Orthoradial displacement (m) in function of time (s) of a blade in permanent contact.

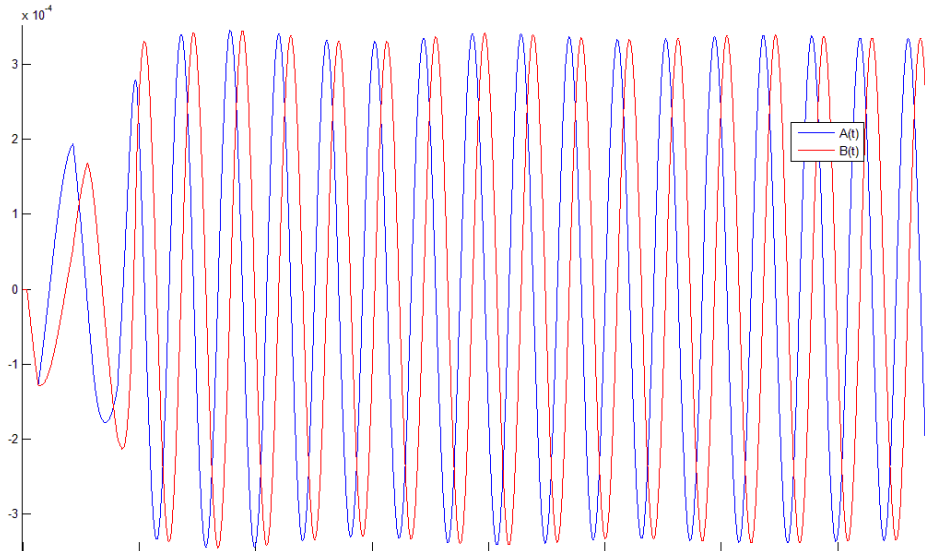


Figure 5 – Modal vibrations of the carter. A(t), in blue, and B(t) (m), in red, in function of the time (s).

It can be noticed on Fig. 5 that the modal vibrations of the carter reach a steady state with a constant phase angle after the coupling of the structures, which is established around $t = 0.01s$.

The choice of time step for this system’s calculation when it’s on modal interaction can be very delicate. The linkage between the bladed wheel and the carter after the coupling happens by means of the direct contact between the blades and the stator, what creates a non-linear interface with a high stiffness. The time step must be chosen sufficiently small for the contact to be well modeled and for the method to converge. The time step was, then, chosen in functions of the maximum resonance frequency among all the degrees of freedom and multiplied by a factor η :

$$dt = \frac{2\pi}{\eta * \max\{\omega_a, \omega_b\}} \quad (23)$$

Where ω_a is the resonance frequency of the flexible stator and ω_b is the maximum resonance frequency for the bladed wheel. The optimum value for the factor was $\eta = 2 * 10^4$.

With modal interaction and with rigid body movement

To have a closer look on the effects of the contact forces on the stator and on the rotor, a model allowing the 4 degrees of liberty of rigid body movement of these two structures is introduced. Two different behaviors are studied.

The first behavior takes place if we don’t include the friction forces in the simulation. In that case, we see that, after the coupling, the rigid body’s dof are in free vibration, without any significant excitation. After the beginning of the permanent contact, it is as if, on the turning frame of reference, those two bodies were only one rigid body vibrating in with a certain damping and consequently returning to the initial undisturbed position. We can see on Fig. 6 the horizontal rigid body movement of the stator in function of time. This analysis is, then, equivalent to the other one without the rigid body degrees of freedom, because, after the coupling, these dof are not excited.

On the other hand, when we include the friction on the calculations we can see that, even after the coupling, there is significant movement on the rigid body degrees of freedom Fig.7. We can notice that the movement is still centered on zero, but it doesn’t reach a steady state, as on the case without the friction forces. What we see is actually a chaotic behavior.

Calculation time

The developed Matlab script has as its base a big *for* type routine in which all the variables as calculated at each time step. Because of the need of a very small time step this routine is made around 280.000 times to simulate only 5 seconds of vibration and that implies in almost 9 hours of calculation.

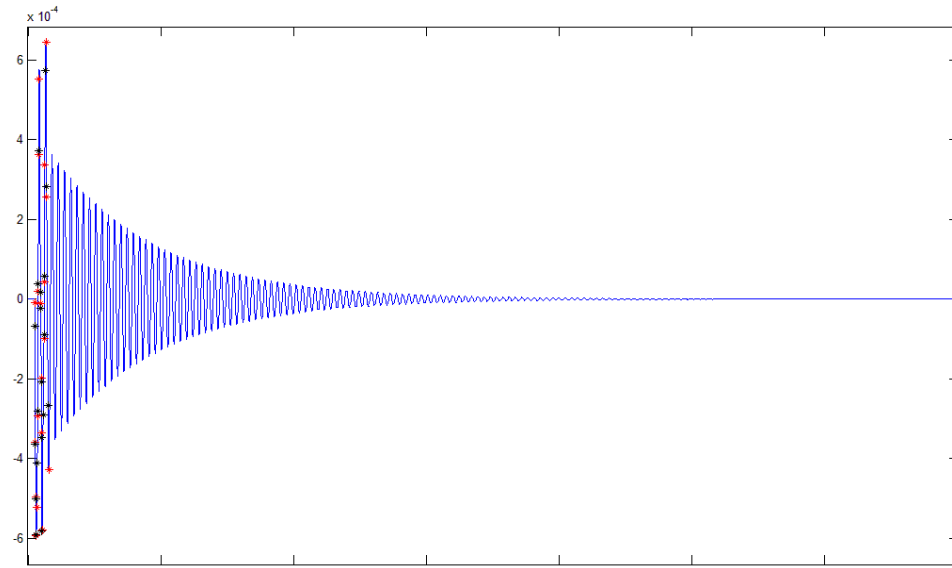


Figure 6 – Rotor horizontal rigid body movement (m) vs the time (s). Modal interaction with no friction.

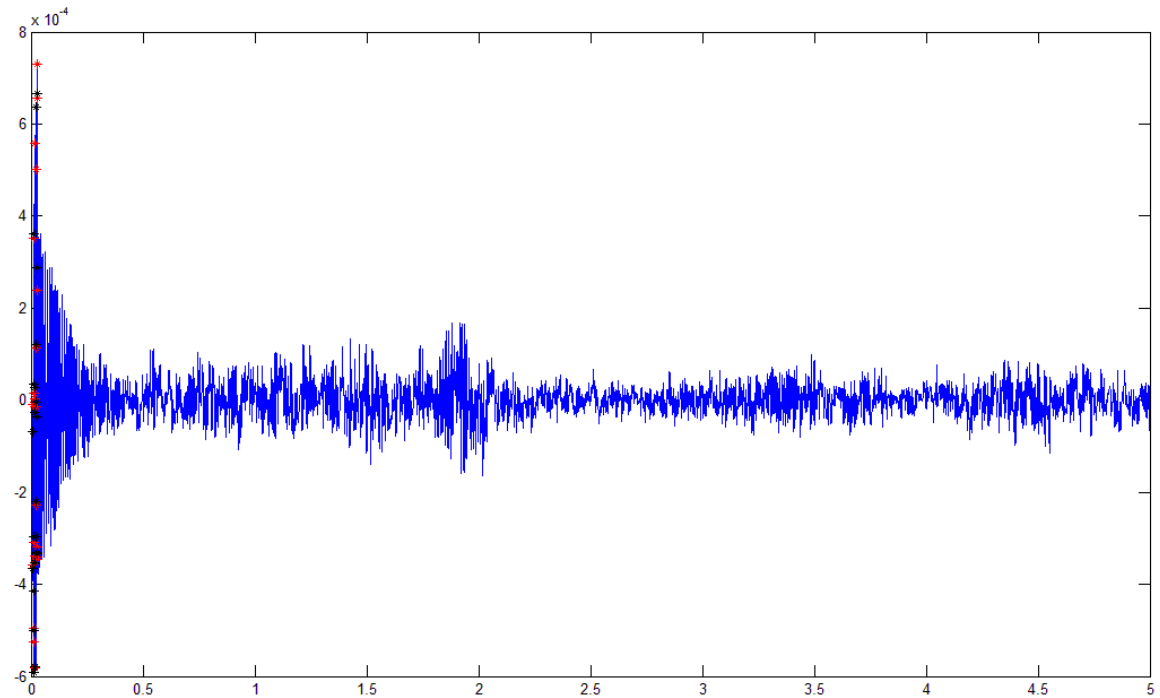


Figure 7 – Rotor horizontal rigid body movement (m) vs the time (s). Modal interaction with friction.

THERMOMECHANICAL ANALYSIS

The interaction between each blade and the stator’s internal surface can generate very high temperatures. The thermal study of this interface is therefore very interesting and important for this system’s analysis. The dilatation phenomena can modify an important way the contact between the parts. Indeed, the increase on the blade’s size due to the higher temperatures decreases the distance to the stator and, in the case of the permanent contact, increases the contact pressure. On the other hand the increase of the radius of the stator decreases that contact pressure.

In this section will be shown the model dedicated to this thermomechanical analysis as well as the results obtained on the simulations for the case with modal interaction and without the rigid body’s dof, which creates a permanent contact between the parts.

Mathematical model

A model was developed based on that presented by (Gu, Shillor, 2001), where a beam is analyzed with the heat source being the friction on one of its ends, as shown on Fig.8.

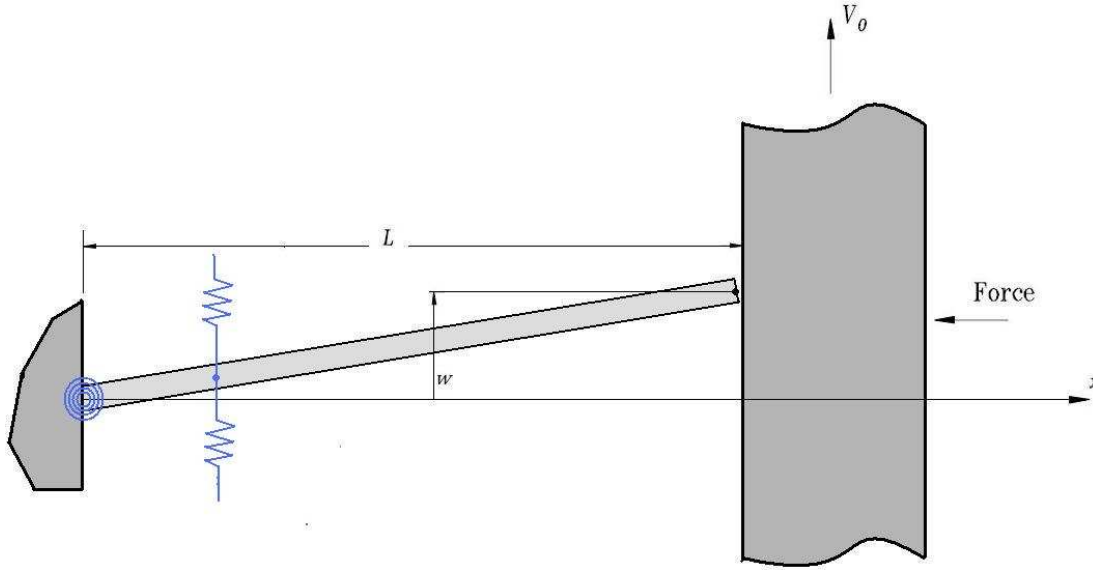


Figure 8 – Beam in friction.

The picture shown on Fig. 8 presents a beam with orthoradial deformation λ . At each moment, the contact between a blade and the stator is, then, modeled as for the beam on Fig. 8. The equations related to this model are the following:

$$KT_{,xx} - hr(T - T_a) = \rho c \dot{T}, \quad 0 < x < L, \quad t > 0, \quad (24)$$

$$T(0, t) = T_0, \quad t > 0, \quad (25)$$

$$-KT_{,x}(L, t) = -\mu p V_0 + h_s(T_L - T_s), \quad t > 0, \quad (26)$$

$$T(x, 0) = T_a, \quad 0 < x < L, \quad (27)$$

Where $T(x, t)$ is the blade temperature on the position x and time t ; K is the materials thermal conductivity ; h is the heat exchange coefficient between the pieces and the environment or convection coefficient ; r is the perimeter-area ratio of a transversal section of the blade; T_a , is the temperature of the external environment ; ρ is the density of the material ; c is the specific heat of the material ; μ is the kinetic friction coefficient ; p is the pressure between on the contact surface ; T_L is the temperature $T(L, t)$ at the end of the blade; T_s is the temperature of the stator at the contact point, which is also calculated at each time step; h_s is the heat exchange coefficient on the contact between the blade and the stator ; T_0 is the temperature of the disc to which the blades are attached and V_0 is the relative sliding velocity in the contact point. The sub index , x indicates the spatial derivative.

Discretizing the equations

A finite differences method was used to discretize Eqs. (24-27) in time and space aiming to apply them on our Matlab routine. Three different equations must be used : one for $x = L$, which acknowledges the friction heat source, a second one for $0 < x < L$, which has only diffusion and conduction terms and the last one for $x = 0$, which takes into account the heat exchange between blade and the central disc.

The procedure for the discretization of Eq.(24) is shown below :

$$K \frac{\Delta(\Delta T_x)}{dx^2} - hr(T_j - T_a) = \rho c \frac{\Delta T_t}{dt};$$

$$\frac{S dx dt}{S dx \rho c} * \left[-K \frac{(2T_j - T_{j+1} - T_{j-1})}{dx^2} - hr(T_j - T_a) \right] = \Delta T_t;$$

$$\frac{dt}{dm c} * \left[-K \frac{(2T_j - T_{j+1} - T_{j-1})}{dx} S - S dx hr(T_j - T_a) \right] = \Delta T_t. \quad (28)$$

Where T_j is the temperature of the j -th discretized part of the blade, which was divided in N parts ; ΔT_x is the temperature variation on the x direction and ΔT_t is the temperature variation in time.

The Eq. (28) is, then, valid for $0 < x < L$. If we add the energy production terms from the friction and heat conduction by contact we obtain the equation for $x = L$:

$$\frac{dt}{dm c} * \left[\mu p V_0 S - K \frac{(T_N - T_{N-1})}{dx} S - S dx hr(T_N - T_a) - Sh_s(T_N - T_s) \right] = \Delta T_t \quad (29)$$

And if we add to Eq.(28) the condition of Eq.(25) we obtain the equation valid for $x = 0$:

$$\frac{dt}{dm c} * \left[-K \frac{(2T_1 - T_0 - T_2)}{dx} S - S dx hr(T_1 - T_a) \right] = \Delta T_t \quad (30)$$

The procedures for the stator are analogous, knowing that Eq.(24) is valid for all positions and Eq.(31) is valid for the part in contact with a blade.

The thermal dilatation

To acknowledge the thermal dilatation effects on the system we must introduce the relation between temperature variation ΔT and size variation Δx :

$$\Delta x = \alpha x_0 \Delta T \quad (31)$$

We can calculate the size of the blade j at each instant k using the equation:

$$L^k = L^{k-1} + \sum_{i=1}^{i=N} \alpha dx(T_i^k - T_i^{k-1}) \quad (32)$$

The thermal dilatation of the stator can be transformed in an increase on the radial displacement u_s . The expression for that will be, then, a superposition of the inextensible elastic deformation given by Eq.(6) and deformation caused by the temperature changes which can be expressed as follows :

$$U_{th}(\phi, t) = -\alpha R(T(\phi, t) - T(\phi, 0)) \quad (33)$$

The new expression for the radial displacement $u_s(\phi, t)$ becomes, then :

$$u_s(\phi, t) = -n_d A_{n_d}(t) \sin(n_d \phi) + n_d B_{n_d}(t) \cos(n_d \phi) + U_{th}(\phi, t) \quad (34)$$

Simulation Results

The carter was discretized in 10 parts and each blade in 5 parts. We have simulated 5 seconds of vibration with a friction coefficient $\mu = 0.15$. The thermal parameters used were :

Table 3 - Thermal parameters.

c	α	T_a	T_0	h	h_s	K
$460 \frac{J}{kg \cdot ^\circ C}$	$12 \frac{\mu m}{m \cdot ^\circ C}$	$20^\circ C$	$20^\circ C$	$850 \frac{W}{m^2 \cdot ^\circ C}$	$500 \frac{W}{m^2 \cdot ^\circ C}$	$47 \frac{W}{m \cdot ^\circ C}$

Fig.19 shows the temperature distribution on the carter after those 5 simulated seconds.

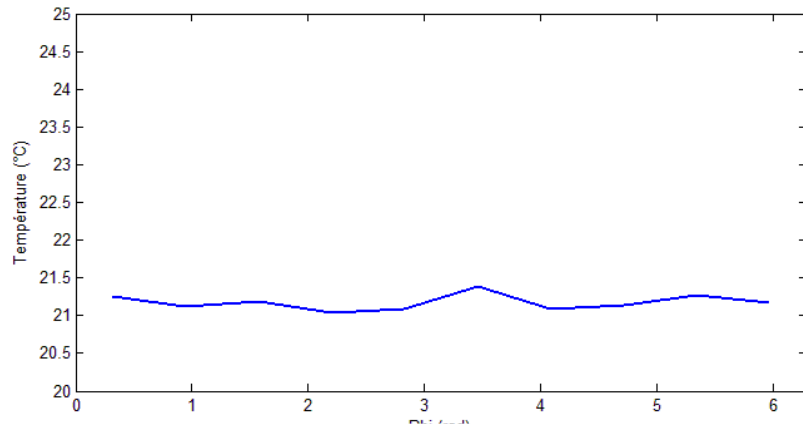


Figure 9 – Temperature distribution on the stator at $t = 5s$.

The Figs. 10 and 11 show the temperature evolution on the different parts of the stator and on the last part of each of the blades on permanent contact in function of time.

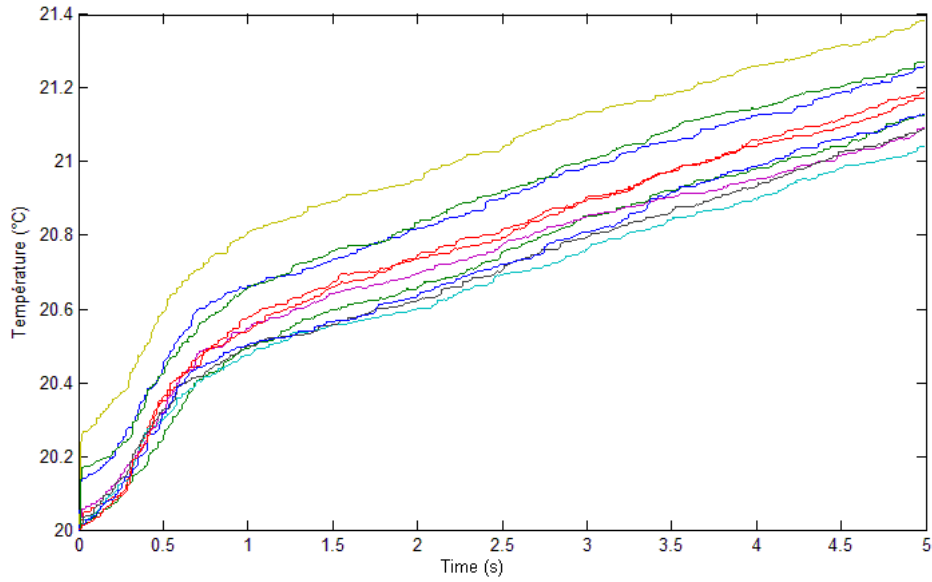


Figure 10 – Temperature evolution of the 10 discretized parts of the stator in function of time.

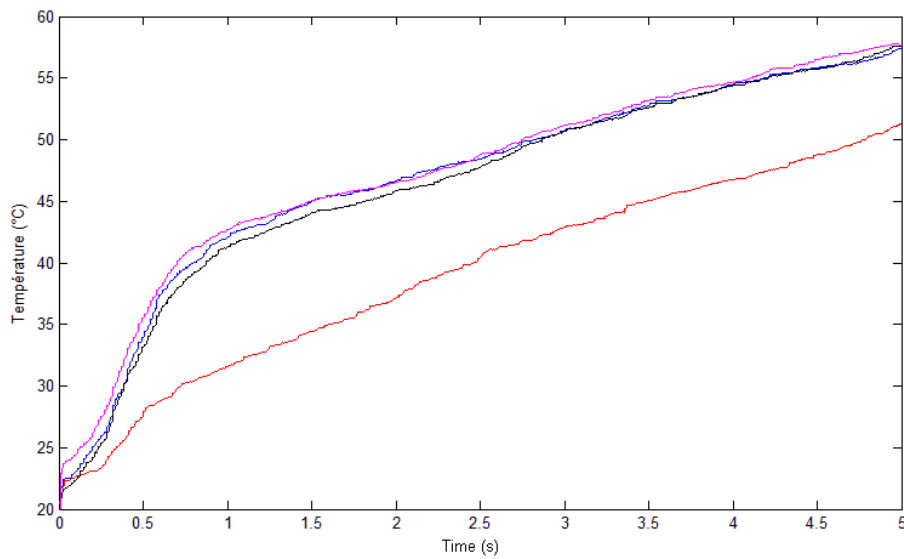


Figure 11 – temperature evolution on the blades in permanent contact in function of time.

We can observe that the system has not yet reached a thermal steady state after the 5 seconds simulated even with the high convection coefficient used. However, the temperature evolution of the parts of the system is already homogenous. The complete simulation with thermal analysis is very expansive in calculation time. The 5 simulated seconds took 16 hours of calculation on a PC equipped with an Intel Core 2 Duo 3.1GHz processor. The effect of dilatation was not very significant, the maximum dilatation on the blades being of 40 μm .

CONCLUSIONS

The analysis of the modal interaction with the rigid body dof included reveals complex behaviors especially if the friction is taken into account, indeed in this case we observe a chaotic behavior. This system could require a more delicate analysis which could be made through stochastic modeling. In future studies this should be a priority.

The thermal analysis of the system gave interesting results, but also revealed that the Matlab script should be optimized in terms of calculation time. Because of that time limitation we were not yet able to develop a further analysis on the thermal steady state, which could reveal some important results especially in terms of dilatation which could cause a significant change in the contact between the parts, but not after 400 rotations in our test case. Wear consideration should also be taken into account in the future.

REFERENCES

- Lesaffre N., Sinou J.-J., Thouverez F., *Contact analysis of a flexible bladed-rotor*, European Journal of Mechanics A/ Solids 26 (2007), p.541–557.
- Legrand M., Pierre C., Cartraud P., Lombard J.-P., *Two-dimensional modeling of an aircraft engine structural bladed disk-casing modal interaction*, Journal of Sound and Vibration 319 (2009), p.366–391.
- Lesaffre N., *Stabilité et Analyse Non-Linéaire du Contact Rotor-Stator*, Thèse de doctorat de l'École Centrale de Lyon (2007). In french.
- Legrand M., *Modèles de Prédiction de l'Interaction Rotor/Stator dans un Moteur d'Avion*, Thèse de doctorat de l'École Centrale de Nantes (2005). In french.
- Demailly D., *Étude du Comportement non-Linéaire dans le Domaine Fréquentiel*, Thèse de doctorat de l'École Centrale de Lyon (2007). In french.
- Gu R.J., Shillor M., *Thermal and Wear Analysis of an Elastic Beam in Sliding Contact*, International Journal of Solids and Structures 38 (2001), p.2323–2333.

RESPONSIBILITY NOTICE

The authors are the only responsible for the printed material included in this paper.

Development and Performance Analysis of an Autocalibration Method for Tri-axis Sensors in Attitude Estimation Systems

Osmar Tormena Junior¹, Francisco Granziera Júnior² and Marcelo Carvalho Tosin³

^{1, 2, 3} Universidade Estadual de Londrina - Centro de Tecnologia e Urbanismo - Departamento de Engenharia Elétrica,
Rod. Celso Garcia Cid PR 445 km 380, Campus Universitário, Londrina, PR - CEP 86051-980

Abstract: In this work, it is presented an useful method to autocalibrate tri-axis sensors, commonly used in systems where attitude information is needed, like robotics, vehicle control and, more recently, entertainment. The tri-axis sensor model includes its scale factor and bias in each sensing axis as well as three deviation angles from the perfect orthogonal triad. The proposed method uses a Least Squares Estimator to find linear intermediate variables from which will be solved algebraically the model parameters. The method was developed to be fully autonomous, self calibrating the sensor on the run. This leads to a reduced error in the physical measurements needed to estimate, and sometimes control, the attitude of a body, increasing the reliability and accuracy of the system as a whole. In the end, it is proposed a performance prediction and analysis methodology, an useful tool in the system design process.

Keywords: *Autocalibration, Attitude Estimation, Calibration performance analysis*

INTRODUCTION

The attitude of a body is commonly needed in applications such as robotics and vehicle control. The accuracy of this information is bounded by several parameters; one of them is the precision of some physical quantity measurement that is used as an attitude reference. An attitude system for terrestrial applications, generally uses Earth's gravitational and magnetic fields as references for attitude estimation, which means the use of three axes accelerometers and magnetometers to obtain the needed information.

The calibration procedure proposed in this paper has some improvements over traditional methods: Besides the estimation of scale factor and bias parameters of each sensing axis, it also compensates for the fact that the triad may not be perfectly aligned or orthogonal. More important, the calibration procedure is fully autonomous, without the need of any particular action that deviates from the normal operation, like have the system perform specific rotations or, assuming that the attitude is known, the system switches to a calibration mode. The only necessary condition to use this methodology is that the physical quantity being used as a reference vector must have its absolute value known.

The parameter estimation algorithm developed in this paper has its roots in the work published by Foster and Elkaim, (2008), which is an extension of the work by Gebre-Egziabher, et al. (2001). In that work, a tri-axis sensor autocalibration is done by estimating the following parameters: three scale factors and biases values, one for each sensing axis, and the orthogonality errors in the sensor triad that can be represented, without loss of generality, by three angles. This adds up to an estimation problem of nine parameters, which can be solved using at least nine linearly independent measurements cleverly applied to a Least Squares Estimator (LSE). Very often it is preferable to use more than nine measurements to minimize the effects of noise corruption over the estimated parameters.

Also used as a reference for the methodology developed here was the work of Alonso and Shuster (2002) and Lerner and Shuster (1979), which contributed to some general ideas about calibration of sensors in attitude systems.

With the addition of the orthogonality deviations, the estimation problem becomes non-linear. Non-linear estimators are very complex and computer intensive. To avoid these difficulties, the estimation problem was approached in a manner that it estimates nine linear intermediate variables. These variables are non-linear functions of the actual calibration parameters, which are solved algebraically from them. This way, the difficulties of a non-linear estimation are swapped by an easy to compute algebraic relation.

This work also points out an useful relationship between the pointing error of a sensor (i.e. the direction error between the measurement and the actual physical quantity) and the ratio between noise level and the spreading of the samples over the geometrical locus of the possible measurements, which is an ellipsoid. This relationship is of great value when one needs to define how good a specific design can be.

This spreading of the calibration samples can be understood as a way to quantify the linear independence between all the samples in the calibration data pool. This can be stated in a more formal way as the collinearity of a observation matrix, as the samples can be arranged as rows in a observation matrix from which the estimation process takes place, as will be shown in the next Section.

The methodology developed here is well suited to boost the performance of low to medium precision attitude systems, which recently found their way in a number of applications in the consumer market, especially entertainment,

like gaming console joysticks, smartphones and special devices for handicapped people. This is because the developed technique makes feasible the use of lower end and cheaper tri-axis sensors, or a mechanical design with wider tolerances, easier and cheaper to produce, without effective loss of accuracy on the system response. That is, the use of an autocalibration procedure compensates for the use of lower precision sensors, reducing the overall production costs and improving the system reliability at the same time.

METHODOLOGY

For a tri-axis sensor, integrated or assembled, the sensor model can be written as follow:

$$\begin{aligned}\hat{u}_x &= au_x + x_0 & \hat{u}_y &= b(u_y \cos(\rho) + u_x \sin(\rho)) + y_0 \\ \hat{u}_z &= c(u_z \cos(\phi) \cos(\lambda) + u_y \sin(\lambda) + u_x \sin(\phi) \cos(\lambda)) + z_0\end{aligned}\quad (1)$$

Where the subscripts x, y and z represent the sensing axes, \hat{u}_x , \hat{u}_y and \hat{u}_z are the sensor outputs and u_x , u_y and u_z are the components of the physical quantity. The values a , b and c are the sensibility of the x, y and z axes, respectively, x_0 , y_0 and z_0 represent the offset of each axis. The angle ρ represents the y'-axis misalignment, inside the xy plane, the angles ϕ and λ represent deviations of the z'-axis from the xz and yz planes, respectively. In Figure 1, x, y and z represent the proper orthogonal triad axes while x', y' and z' are the actual misaligned triad.

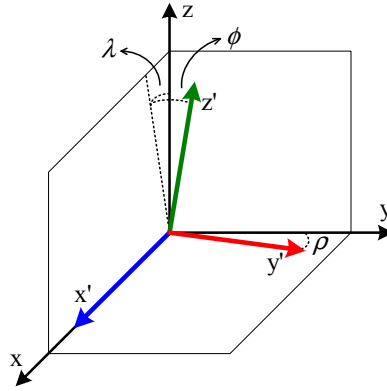


Figure 1 – Graphical illustration of the orthogonality deviation angles.

The absolute value of the physical quantity is used as a boundary condition that must be satisfied:

$$|\mathbf{u}|^2 = u_x^2 + u_y^2 + u_z^2 \quad (2)$$

Rewriting Eq. (1), solving for the physical quantity actual value:

$$\begin{aligned}u_x &= \frac{(\hat{u}_x - x_0)}{a} & u_y &= \frac{a(\hat{u}_y - y_0) - b \sin(\rho)(\hat{u}_x - x_0)}{abc \cos(\rho)} \\ u_z &= \frac{(abc \cos(\rho)(\hat{u}_z - z_0) - ac \sin(\lambda)(\hat{u}_y - y_0) + bc(\sin(\rho) \sin(\lambda) - \cos(\rho) \sin(\phi) \cos(\lambda))(\hat{u}_x - x_0))}{abc \cos(\rho) \cos(\phi) \cos(\lambda)}\end{aligned}\quad (3)$$

Substituting Eq. (3) into Eq. (2), one gets an expression in the following form:

$$A\hat{u}_x^2 + B\hat{u}_x\hat{u}_y + C\hat{u}_x\hat{u}_z + D\hat{u}_y^2 + E\hat{u}_y\hat{u}_z + F\hat{u}_z^2 + G\hat{u}_x + H\hat{u}_y + I\hat{u}_z + J = 0 \quad (4)$$

Where the intermediate variables A , B , C , D , E , F , G , H , I , and J are non-linear functions of the actual sensor parameters. This way, Eq. (4) is non-linear in terms of the sensor parameters, but it is linear in terms of the intermediate variables. Equation (4) can be written in a more convenient form as follows:

$$\frac{A\hat{u}_x^2}{F\hat{u}_z^2} + \frac{B\hat{u}_x\hat{u}_y}{F\hat{u}_z^2} + \frac{C\hat{u}_x\hat{u}_z}{F\hat{u}_z^2} + \frac{D\hat{u}_y^2}{F\hat{u}_z^2} + \frac{E\hat{u}_y\hat{u}_z}{F\hat{u}_z^2} + \frac{G\hat{u}_x}{F\hat{u}_z^2} + \frac{H\hat{u}_y}{F\hat{u}_z^2} + \frac{I\hat{u}_z}{F\hat{u}_z^2} + \frac{J}{F\hat{u}_z^2} = -1 \quad (5)$$

In matrix notation:

$$\underbrace{\begin{bmatrix} \hat{u}_{x_1}^2 / \hat{u}_{z_1}^2 & \hat{u}_{x_1} \hat{u}_{y_1} / \hat{u}_{z_1}^2 & \dots & 1 / \hat{u}_{z_1}^2 \\ \vdots & \ddots & \ddots & \vdots \\ \hat{u}_{x_n}^2 / \hat{u}_{z_n}^2 & \hat{u}_{x_n} \hat{u}_{y_n} / \hat{u}_{z_n}^2 & \dots & 1 / \hat{u}_{z_n}^2 \end{bmatrix}}_{\mathbf{X}} \underbrace{\begin{bmatrix} A/F \\ B/F \\ \vdots \\ J/F \end{bmatrix}}_{\mathbf{k}} = \underbrace{\begin{bmatrix} -1 \\ \vdots \\ -1 \end{bmatrix}}_{\mathbf{w}} \quad \text{or} \quad \mathbf{X}_{n \times 9} \mathbf{k}_{9 \times 1} = \mathbf{w}_{n \times 1} \quad (6)$$

Where n is the number of measurements used for the estimation, \mathbf{X} is the measurements, or observation, matrix, \mathbf{k} is the intermediate variables vector and \mathbf{w} is a negative ones vector. The choice of putting $F\hat{u}_z^2$ as a common factor in Eq. (5) is due to the fact that F is the simplest of the non-linear functions from A to J . This way, the algebraic work solving the sensor parameters from A/F , B/F , ..., J/F was minimized.

Solving Eq. (6) for \mathbf{k} , using the Moore-Penrose Pseudo Inverse (also called Generalized Inverse), one reaches Eq. (7), which is mathematically equivalent to a Least Squares Estimator.

$$\hat{\mathbf{k}} = (\mathbf{X}^T \mathbf{X})^{-1} \mathbf{X}^T \mathbf{w} \quad (7)$$

Where $\hat{\mathbf{k}}$ indicates the estimated intermediate variables vector. Equation (7) is a critical point in the estimation problem, this is mostly due to two factors: First, although it is possible to solve the Moore-Penrose Pseudo Inverse the way it is stated in Eq. (7), this approach lacks numerical robustness and is error prone. The best way to compute the pseudo inverse is applying Eq. (7) not directly over \mathbf{X} , but on its QR decomposition (where \mathbf{X} is factored in a orthogonal matrix \mathbf{Q} and a upper triangular matrix \mathbf{R}) or SVD (Singular Value Decomposition), where \mathbf{X} is factored in a positive diagonal matrix and two unitary matrices. Second, the product $\mathbf{X}^T \mathbf{X}$ has the characteristic of amplifying the noise present in \mathbf{X} so, in order to form a well-conditioned system, the collinearity of \mathbf{X} must be the smallest possible (i.e. the samples used in the autocalibration procedure must be well spread over the ellipsoid). A more detailed analysis of the generalized inverse can be found in Rao and Mitra (1970).

The orthogonal deviation angles are expected to be very small (less than five degrees for assembled triads and less than one degree in integrated tri-axis sensors), so the small angles approximation ($\sin \theta \approx \theta$ and $\cos \theta \approx 1$) can be used to minimize the algebraic work solving the sensor parameters in terms of the intermediate variables, without appreciable loss of precision. Applying some algebra, it is possible to reach the following solution for the sensor parameters (the ‘‘hat’’ ($\hat{\cdot}$) means estimated value):

$$\begin{aligned} \hat{x}_0 &= \frac{4\chi\delta + \chi\epsilon^2 - 2\eta\beta - \eta\gamma\epsilon - \iota\beta\epsilon + 2\iota\gamma\delta}{2\gamma^2\delta + \gamma^2\epsilon^2 - 8\alpha\delta - 2\alpha\epsilon^2 + 2\beta^2 + 2\beta\gamma\epsilon} & \hat{y}_0 &= \frac{\gamma^2\eta + \gamma^2\epsilon\iota - 4\alpha\eta - 2\alpha\epsilon\iota + 2\beta\chi + \beta\gamma\iota + \chi\gamma\epsilon}{-2\gamma^2\delta - \gamma^2\epsilon^2 + 8\alpha\delta + 2\alpha\epsilon^2 - 2\beta^2 - 2\beta\gamma\epsilon} \\ \hat{z}_0 &= \frac{2\gamma^2\delta\iota - \gamma^2\eta\epsilon - 4\alpha\delta\iota + 2\alpha\eta\epsilon + \beta^2\iota - \beta\chi\epsilon - \eta\gamma\beta + 2\chi\gamma\delta}{2\gamma^2\delta + \gamma^2\epsilon^2 - 8\alpha\delta - 2\alpha\epsilon^2 + 2\beta^2 + 2\beta\gamma\epsilon} & \hat{c} &= \frac{1}{|\mathbf{u}|} \sqrt{\kappa + \left(\frac{\gamma^2}{4} - \alpha\right) \hat{x}_0^2 - \delta \hat{y}_0^2 + \hat{z}_0^2 - \beta \hat{x}_0 \hat{y}_0 - \epsilon \hat{y}_0 \hat{z}_0 - \gamma \hat{x}_0 \hat{z}_0} \quad (8) \\ \hat{b} &= \frac{\hat{c}}{\sqrt{-\delta}} & \hat{a} &= \frac{\hat{c}}{\sqrt{\frac{\gamma^2}{4} - \alpha}} & \hat{\rho} &= \frac{\hat{a}\hat{b}\beta}{2\hat{c}^2} & \hat{\phi} &= \frac{\hat{a}\gamma}{2\hat{c}} & \hat{\lambda} &= \frac{\epsilon}{2\sqrt{-\delta}} \end{aligned}$$

Assuming:

$$\alpha = -A/F \quad \beta = -B/F \quad \gamma = -C/F \quad \delta = -D/F \quad \epsilon = -E/F \quad \chi = -G/F \quad \eta = -H/F \quad \iota = -I/F \quad \kappa = -J/F \quad (9)$$

Although finding this solution involved a long and complex algebraic work, once it was done, one can easily apply these solutions very easily, reaching the desired sensor parameters with much less computational load than a direct approach of the non-linear estimation.

RESULTS

The proposed solution was simulated in a computer, using MatLab®. Preliminary tests showed that using more than thirty samples in the autocalibration process would bring no effective gain in noise corruption over the estimated values. This way, the numerical values exposed in this Section were obtained through an autocalibration procedure using thirty samples, in order to keep the computational workload minimal. The present noise level is considered to be in the order of one thousandth of the physical quantity absolute value, which is quite true for inexpensive MEMS sensors, that are the kind of sensor which the presented methodology was developed for.

At this stage of the methodology development, it was decided to use simulated data to carry out performance analysis because of its flexibility. This way it was possible to evaluate the autocalibration quality over a wide range of noise level and typical parameters, instead of a specific characteristic of a particular sensor.

There is little to no reason to believe that the results obtained through simulation would differ appreciably from results obtained in a hardware implemented system with real data. Thus the results presented in this Section are justified by themselves and the approach used proved to be helpful in the determination of a very interesting relationship, as will be shown later.

Table 1 – Comparing the amplitude of error in typical datasheet values and the error in calibrated systems (for the Freescale accelerometer MMA7340L).

Sensor Errors	Typical Error	Calibrated Error
Sensitivity	± 6%	± 1,5%
Offset	± 6%	± 1%
Orthogonality	± 0,9°	± 0,2°

As shown in Frosio, Pedersini and Borghese (2009), the sensor pointing error can be represented by two angles in a plane orthogonal to the physical quantity used as attitude reference, as shown in Fig. 2.

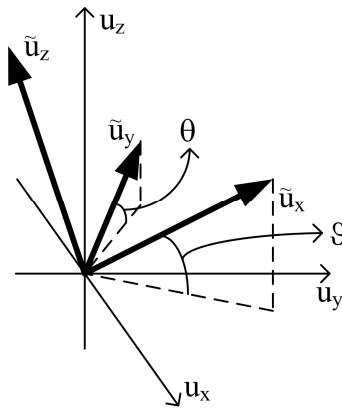


Figure 2 – Angular pointing error of a miscalibrated triad sensor.

Mathematically:

$$\vartheta = \arctan\left(\frac{a_x}{\sqrt{a_y^2 + a_z^2}}\right) \quad \theta = \arctan\left(\frac{a_y}{\sqrt{a_x^2 + a_z^2}}\right) \quad (10)$$

Where it is assumed that the z sensor axis is parallel to the reference vector, the angle ϑ defines the error of the x sensor axis from the plane orthogonal to the reference vector. The angle θ works the same way for the y sensor axis.

The results displayed in Fig. 3(a) show that the pointing accuracy in the sensor measurements is dramatically increased for a calibrated system, with a mean error much closer to zero, and with a smaller variance around its mean, which means a much better precision. These results were obtained in an autocalibration simulation with thirty samples and with corruption of Additive Gaussian White Noise (AWGN), with standard deviation of one thousandth of the physical quantity absolute value, independently over the three sensor axis.

Figure 3(b) shows the relationship between the quadratic mean of the pointing error angles and the ratio of the sensor typical noise standard deviation (σ_{Noise} - where the noise is assumed to be AWG) and a measure of how spread, or different (i.e. linearly independent), are the samples used in the calibration process (measured as the standard deviation σ_{Signal} of the samples in degrees, over the ellipsoid that is the geometrical locus of all possible measurements). This shows how much precise one can expect the calibration procedure to be, for a specific set of samples and noise condition. The relationship displayed in Fig. 3(b) is where the flexibility provided by simulated data can be appreciated because this way, one can simply evaluate the total pointing error with sample geometrical distribution over any condition of noise and *a priori* sensor miscalibration.

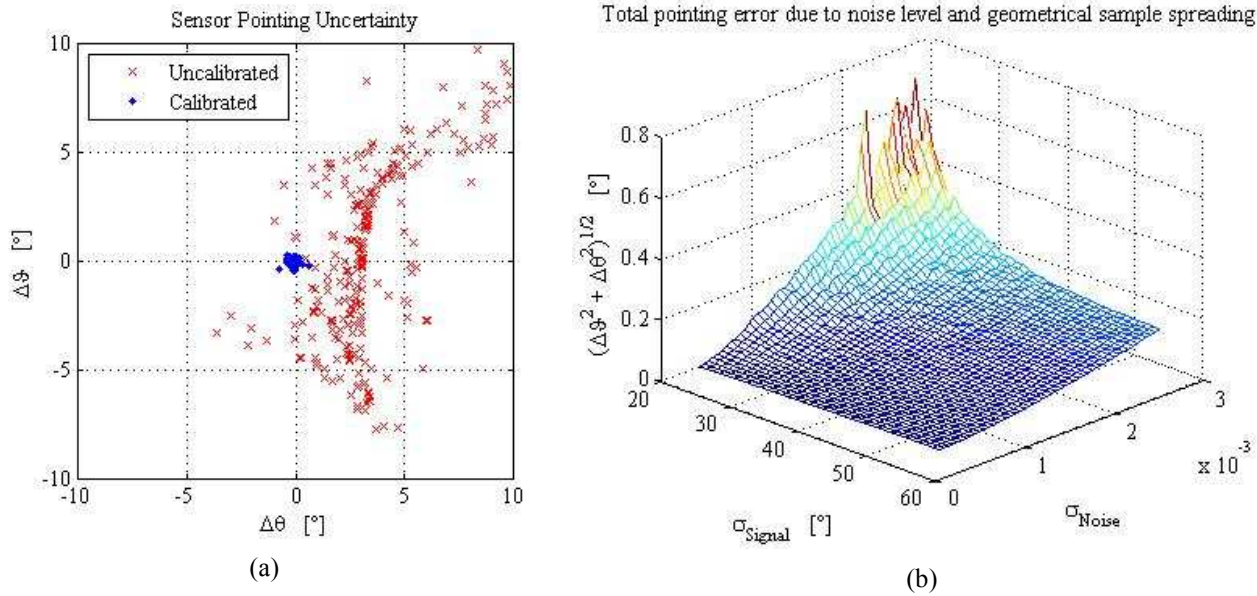


Figure 3 – (a) Comparison between calibrated and uncalibrated sensor pointing accuracy. (b) Pointing accuracy and its relation to noise and sample spreading.

CONCLUSION

As can be noted from Eq. (2), if the system is in a condition where the sensor is not only sensing the reference vector, but the resultant of it and a perturbation, then this data cannot be used in the calibration procedure. An event like this may arise if the sensor, say an accelerometer is in free fall, or in the case of a magnetometer, if it is in proximity of ferromagnetic material. To circumvent this error source, the data used by the calibration system must be filtered to eliminate samples where the measured absolute value differs over a threshold from the modeled absolute value.

From Eq. (5) it can also be noted that points with the z-component of the physical quantity null or too close to zero must be avoided by the calibration systems, as it would lead to a division by zero in the matrix computation causing numerical instability. It was also found out that every sample with its x or y component too close to zero must be avoided in the calibration procedure because, in presence of noise, it leads to an ill-conditioned system.

The Figure 3(a) shows how the pointing uncertainty and error of the measured reference vector, can be minimized. For a normalized measure, this is understood as a smaller versor variance and mean error, the first is the bounding parameter when the attitude variance is determined, the second is a systematic error and should be minimized, if not nullified for the proper operation of an attitude estimation algorithm. These facts show how much the attitude precision and accuracy will be improved in an autocalibrated system when compared to a system using typical datasheet parameters or which has become uncalibrated under use.

Figure 3(b) it is shown a characteristic that is quite unexplored in similar works, that is: in a calibration procedure with a fixed number of samples and, for specific conditions of sample "spreading" over the ellipsoid and noise level, there is a bounding value of how good the calibration can be, and as a consequence, how precisely the sensor will detect the actual direction of the physical quantity used as attitude reference. This constitutes in a valuable source of information and an important tool for designing autocalibrated attitude estimation systems, and predict more reliably an expected performance.

Finally, after all these considerations, the developed autocalibration methodology is found to be functional in its two principal aspects: reliability and accuracy. The method is reliable because its autonomous characteristic is implemented cleverly, so that it will only recalibrate the systems if the overall conditions are favorable for doing so, that is, the physical measurements are not being corrupted by external interferences, the thirty samples from the data pool need to be geometrically well spaced and with non-zero components, in order to avoid ill-conditioned systems or computational issues which make the calibration poorer, contributing to the accuracy of the method.

Thus, it can be concluded that the developed methodology of autocalibration for tri-axis sensors in attitude applications is a great boost for making attitude systems technology more robust and cheaper to implement in its most diverse fields, like aerospace, entertainment, medical, etc.

ACKNOWLEDGMENTS

The authors are grateful to the Brazilian Space Agency (AEB), which through the Uniespaço II Program sponsored this research. The authors also are thankful to Londrina State University (UEL), that provided its physical and human resources that made this research work possible.

REFERENCES

- Alonso, R. and Shuster, M. D., 2002, "TWOSTEP: A Fast Robust Algorithm for Attitude-Independent Magnetometer-Bias Determination", *The Journal of Astronautical Sciences*, Vol. 50, No. 4, pp. 433-451.
- Foster, C.C. and Elkaim, G.H., 2008, "Extension of a Two-Step Calibration Methodology to Include Nonorthogonal Sensor Axes", *IEEE Transactions on Aerospace and Electronic Systems*, Vol. 44, No. 3, pp. 1070-1078.
- Frosio, I., Pedersini, F. and Borghese, N.A., 2009, "Autocalibration of MEMS Accelerometers", *IEEE Transactions on Instrumentation and Measurement*, Vol. 58, No. 6, pp. 2034-2041.
- Gebre-Egziabher, D. et al., 2001, "A Non-Linear, Two-Step Estimation Algorithm for Calibrating Solid-State Strapdown Magnetometers", In: 8th International St. Petersburg Conference on Navigational Systems. St. Petersburg, Russia.
- Lerner, G. M. and Shuster, M. D., 1979, "Magnetometer Bias Determination and Attitude Determination for Near-Earth Spacecraft", In: AIAA Guidance and Control Conference. Boulder, Colorado, USA.
- Rao, C. R. and Mitra, S. K., 1970, "Generalized Inverse of a Matrix and its Applications", In: 6th Berkeley Symposium on Mathematical Statistics and Probability. Berkeley, California, USA.

RESPONSIBILITY NOTICE

The authors are the only responsible for the printed material included in this paper.

Bonding influence in the electromechanical (EM) admittance of piezoelectric sensors bonded to structures based on EMI technique

Hector A. Tinoco, Alberto L. Serpa

Department of Computational Mechanics, Faculty of Mechanical Engineering, University of Campinas, 13083-970
Campinas-SP, Brazil. E-mail: andrest149@gmail, serpa@fem.unicamp.br

Abstract: Electromechanical impedance technique (EMI) is employed with piezoelectric transducers which emit electrical signatures when the host structure is deformed. Piezoelectric transducers are permanently bonded by a small adhesive layer to the host structure. The adhesive bond layer certainly affects the mechanical coupling between the structure and the piezoelectric material, since the transmission of strain/force is carried out through shear stress and normal stress. In this study it will be considered shear effects. The aim of this study is to show how electromechanical (EM) admittance spectrum is modified depending on the conditions of bonding between the piezoelectric transducers and the structure, given that the mechanical impedance of the structure is coupled through the bonding layer. Therefore both the natural frequencies and EM admittance signatures are modified by the conditions of coupling. A proposed model of an adhesive coupling parameter is established in this study for determining the coupling effects induced by the adhesive layer. Therefore, this study reveals that the changes in the EM admittance spectrum can be originated by mechanical conditions of coupling or adhesive properties.

Keywords: EMI technique, piezoelectric sensor, bonding, EM admittance.

INTRODUCTION

Piezoelectric transducers have begun to increase in popularity in different areas of structural mechanics in the last years. They are used as sensors and as actuators in smart structures (Liu et al. 2006). Piezoelectric transducers are available in many ways and shapes (PI ceramics, 2009). Most extensively, piezoelectric transducers are used in the form of thin sheets which can be embedded or bonded to structures by means of an adhesive layer. They are used to measure directly the local dynamic and static response of a structure. When the structure is stressed mechanically, the piezoelectric material bonded to the structure acts to produce an electrical charge (direct effect, piezoelectric sensor). On the other hand, a mechanical strain through the piezoelectric material is produced when an electrical field is applied along the perpendicular plane which presents a dipole (indirect effect, piezoelectric actuator) (Tinoco et al. 2010). In this decade the piezoelectric transducers have been widely used in structural health monitoring (SHM) (Yu et al. 2008; Staszewski et al. 2009), nondestructive evaluation (NDE) (Tanasoiu et al. 2002), nondestructive inspection (NDI) (Diamanti et al. 2007), and applications of several types in structural engineering (Bhalla and Soh, 2004a; Liu et al. 2006).

Smart sensor technologies have provided different tools for analyzing the behavior of structures when they are submitted to random forces. NDE and SHM are areas in which many researchers are interested with aim to observe the behavior of structures to extract natural frequencies and analyzing them for detecting damage in an earliest state. This makes possible to preserve the integrity of structures. Different techniques have been developed for extracting and analyzing natural frequencies of structures. Some techniques have been proposed to locate and quantify damages in structures from natural frequencies and modal shapes measured; such as curvature mode shape method (Pandey et al. 1991), stiffness method (Zimmerman and Kaouk, 1994), flexibility method (Pandey and Biswas, 1994) and damage index method (Stubbs and Kim, 1994). Other techniques have been established for carrying out NDE and SHM with piezoelectric sensors, such as acoustic emission techniques (AE) (Kessler and Spearing, 2002), Lamb waves technique (Ng and Veidt, 2009), electromechanical impedance technique (EMI) (Liang et al. 1994; Annamdas and Soh, 2007a; Panigrahi et al. 2010) and others techniques (Tan and Tong, 2004; Kisa, 2004). However, the more used and most important techniques are EMI and Lamb waves technique, since these techniques present many advantages with respect to the others (Giurgiutiu, 2007). In this study it will be considered only the EMI technique.

EMI technique is based on the electromechanical coupling phenomena between a host structure and piezoelectric transducers. Piezoelectric transducers are adhered to a structure by means of an adhesive layer. Adhesive layer provides the necessary stiffness for coupling piezoelectric transducers mechanically to the structure, and so transmits forces across the adhesive layer. Electrical signatures applied or emitted by the piezoelectric material when the structure is stressed or deformed, are analyzed relating the voltage (electric potential applied or obtained from bottom and top electrodes) and the current that cross the piezoelectric transducer. With voltage and current signatures the electrical impedance (Park et al. 2003) of the piezoelectric transducer is determined.

Electrical impedance is the ratio between the voltage and the current (Dorf and Svoboda, 2001). EMI technique is a very sensitive method for working in a high frequency range (typically >30 kHz), as it shown by Park et al. (2003) and by Giurgiutiu (2007). Changes in the electrical impedance or admittance spectrum (inverse of the electrical impedance) of the electromechanical system are indicators of structural changes or damage (Yan et al. 2007a; Yan et al. 2007b). Detailed explanations of the EMI technique can be found in the research of Liang et al. (1996) and Giurgiutiu and Rogers (1997). The advantages of the EMI technique include fast dynamic response, long-term durability, negligible ageing, high sensitivity and immunity to ambient noise (Giurgiutiu and Rogers, 1997; Yan and Chen, 2010).

The first model that related the mechanical impedance of a piezoelectric material and a structure with electro-mechanical (EM) impedance of the piezoelectric material was proposed by Liang et al. (1994). In their research the influence of the adhesive layer was not considered. Then, the Liang et al. (1994) model was modified by Xu and Liu (2002) including adhesive coupling. The Xu and Liu (2002) model considered the adhesive interface between a piezoelectric patch and a structure. Complete mechanical system (structure / adhesive / piezoelectric) was established as a spring-mass-damper system for carrying out the EM analysis. Bhalla and Soh (2004) extended 1D electromechanical model to two-dimensional (2D) EM model. They analyzed the force transfer mechanisms through the adhesive layer at the adhered interface. Further, a parametric study was carried out using the influence of various parameters associated with the bond layer on the EM admittance response. Recently, Annamdas and Soh (2007) presented the formulation of a three-dimensional (3D) model of a piezoelectric transducer embedded to a structure, considering the mass of both the piezoelectric transducers and the adhesive layer. The model was verified experimentally and it showed that the presence of thick adhesive significantly reduces the magnitude of the EM signature.

Other studies on the effects of the adhesive layer on the functionality of the sensor have also been carried out. For instance, Han et al. (2008) show a study of the effects of adhesive layer on the dynamic response of the sensor under loading frequencies. Results indicate that the adhesive layer have significant effects on sensor response. Tinoco et al. (2010) carried out a numerical study on the effects of the bonding mechanical properties on the electrical response of piezoelectric sensors. Some parameters such as the length of the piezoelectric sensor and thickness of the adhesive layer presented influence on electrical signatures emitted by piezoelectric sensor. In their study it is shown that partial debonding of piezoelectric sensor cannot be considered as an imminent failure with respect to its functionality, however the debonding of the sensor affects the electric performance of the sensor.

This study shows how the adhesive layer, which integrates the structure with the sensors, affects the signatures of the EM admittance spectrum obtained by piezoelectric sensors. As it is shown in this study, EMI technique is based on EM coupling that exist in sensors and structure, and whose principle aim is to determine changes in the EM admittance spectrum. In EMI technique, the changes in the EM admittance spectrum or specifically changes in natural frequencies identified are considered eventually indicators of structural modification. A proposed model of an adhesive coupling parameter is established for determining coupling effects induced by the adhesive layer. Therefore, this study reveals that changes in the EM admittance spectrum can be originated by mechanical conditions of coupling or adhesive properties.

PIEZOELECTRIC TRANSDUCERS

Constitutive equations

Piezoelectric transducers acts in two forms, as sensor (direct effect) and as actuators (indirect effect). The mathematical model of mechanical-electric field coupling phenomenon in piezoelectric materials can be expressed by constitutive equations (Bhalla and Soh, 2004) in which the EM properties are represented as

$$D_i = \varepsilon_{ij}^{\sigma} E_j + d_{im}^{\sigma} \sigma_m, \quad (1)$$

$$S_k = d_{jk}^E E_j + s_{km}^E \sigma_m, \quad (2)$$

where, S_k is the strain vector (6×1) (dimensionless), D_i (coulomb/m²) is the electric displacement of size (3×1), E (volt/m) is the applied electric field vector (3×1), σ_m (N/m²) is the mechanical stress vector (6×1), $\varepsilon_{ij}^{\sigma}$ is the complex dielectric permittivity of the piezoelectric material at constant stress of size (3×3) (farad/m). d_{im}^{σ} (3×6) and d_{jk}^E (6×3) are piezoelectric strain coefficients. s_{km}^E is the complex elastic compliance at constant electric field. Superscripts σ and E indicate that the quantity has been measured at constant stress and constant electric field, respectively.

Piezoelectric sensor

Using constitutive equations (see Eq. (1) and (2)), Yang and Ngoi, (1999) established the following relation

$$D_i = d_{im} \sigma_m, \quad (3)$$

$$S_k = s_{km}^E \sigma_m. \quad (4)$$

Equations (3) and (4) represent coupled model to a piezoelectric sensor. In equations (3) and (4) can be observed that electric field does not appear, since it is not applied in the piezoelectric material. Therefore $E_k = 0$.

AXIAL DYNAMIC MODEL

Figure 1 shows a piezoelectric transducer bonded to a structure by means of an adhesive layer. Host structure is submitted to controlled or random forces which are originated in other sections of the structure. Adhesive layer permits that piezoelectric sensor can convert the deformations of the structure in electrical signatures measures. In Fig.1 $u_s(x, t)$ and $u_p(x, t)$ represent the displacements of the structure and the piezoelectric sensor.

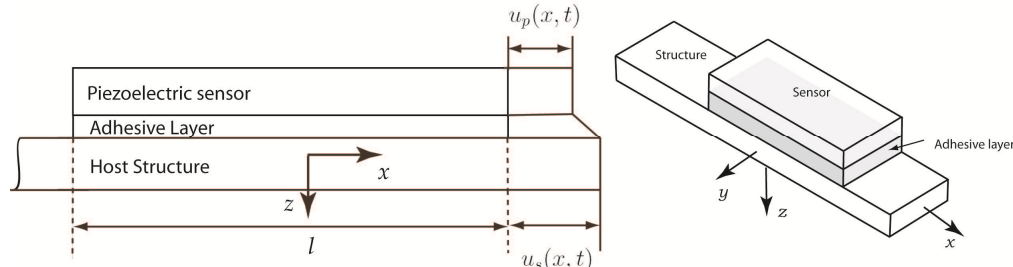


Figure 1- Patch structure-adhesive layer-PZT

Adhesive Bond mechanical influence

Adhesive layer provides mechanical coupling to transmit forces from the structure to piezoelectric sensor. When the structure begins deforming, adhesive layer begins to strain piezoelectric sensor. When forces are transmitted, two type of stresses in the adhesive interface, peel stress and shear stress appear (Luo and Tong, 2002). However, in this work it is considered shear stresses only. Adhesive layer produces shear stress which is bigger in the ends of the adhesion interfaces than in the central part of adhesion interfaces. When the structure is submitted to a known force, the non-uniform distribution of shear stress on the flanges of bonding through the interfaces of the host structure and the piezoelectric patch is called *shear lag effect*. Some works that consider the shear stress produced by bonding, are Luo and Tong (2002), Yan et al. (2007a) and Tinoco et al. (2010).

Coupled dynamic model considering adhesive bond

In Fig. 2, $\sigma_p(x, t)$ is normal stress in the piezoelectric sensor and $\sigma_s(x, t)$ is the normal stress of the host structure caused by an applied force. All materials are considered isotropic and homogenous.

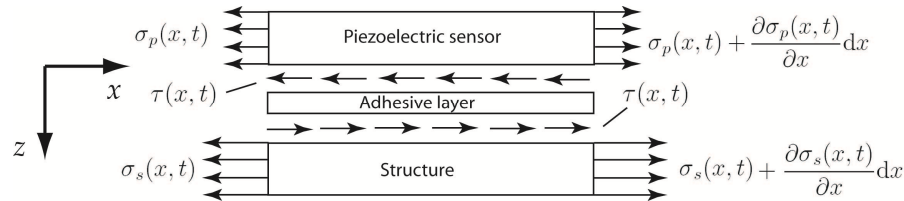


Figure 2 - Dynamic equilibrium of an infinitesimal element of the set structure-adhesive layer- piezoelectric sensor

In order to the establish dynamic mathematical model which can represent the displacements in the time of the set structure-adhesive-piezoelectric sensor, it is established from Fig. 2 the dynamic equilibrium of the sensor (see Eq. (5)) and the structure (see Eq. (7)) such that

$$\rho_p w_p h_p \frac{\partial^2 u_p(x, t)}{\partial t^2} - E_p w_p h_p \frac{\partial^2 u_p(x, t)}{\partial x^2} + \tau(x, t) = 0, \quad (5)$$

where $u_p(x, t)$ is the displacement, ρ_p is the density, h_p is the thickness (z - direction), w_p is the width (y - direction), E_p is the elasticity modulus and the subscript “p” indicates piezoelectric sensor. $\tau(x, t)$ is the shear stress along the adhesion interface. It was approximated according to Crawley and De Luis (1987) by

$$\tau(x, t) = \frac{G_a(u_s(x, t) - u_p(x, t))}{h_a}, \quad (6)$$

where $u_s(x, t)$ is the displacement of the structure, h_a is the thickness of the adhesive and G_a is the shear modulus of the

adhesive. Equilibrium equations to the displacements of the structure are determined by

$$\rho_s w_s h_s \frac{\partial^2 u_s(x, t)}{\partial t^2} - E_s w_s h_s \frac{\partial^2 u_s(x, t)}{\partial x^2} - \tau(x, t) = 0, \quad (7)$$

where $u_s(x, t)$ is the displacement, ρ_s is the density, h_s is the thickness (z - direction), w_s is the width (y - direction), E_s is the elasticity modulus and the subscript "s" indicates structure.

EMI TECHNIQUE

The basic concept of the EMI technique is to use high frequency vibrations (Park et al. 2003) to monitor a local area of the structure determining changes in the EM admittance spectrum. These changes would indicate damage or structural modification. Many experimental applications with EMI technique have been implemented (Bhalla and Soh, 2004a; Giurgiutiu, 2007; Yan and Chen, 2010). For instance, the damage detection is possible due to the fact that actuators propagate waves of high frequency on structure in order to obtain electrical signatures in an area constrained by sensors. Electrical signatures relate the electrical impedance of the piezoelectric patch with the structural mechanical impedance. EM Impedance-based model uses the dynamic of the piezoelectric patch and the structural impedance to determine natural frequencies with EM admittance spectrum obtained by means of the sensor. Both analytical and experimental investigations have shown that the EMI technique is very effective to identify local incipient damages in various structures (Park et al. 2003; Yan et al. 2007a).

EM admittance to 1D model

The electrical admittance of electric circuit is composed of a real part ($G(\omega)$ conductance) and an imaginary part ($B(\omega)$ susceptance) (Dorf and Svoboda, 2001) and it is written as

$$\bar{Y}(\omega) = \frac{I(\omega)}{V(\omega)} = G(\omega) + B(\omega)j, \quad (6)$$

where $I(\omega)$ is the electrical current and $V(\omega)$ is the voltage. From constitutive equations (1) and (2) the dynamic equilibrium of a mechanical system axial (1D) equivalent to a piezoelectric patch was calculated by Liang et al. (1994). They related EM admittance $\bar{Y}(\omega)$ with mechanical impedance of a structure by means of the following formulation

$$\bar{Y}(\omega) = 2\omega j \frac{w_p l}{h_p} \left[\bar{e}_{33}^\sigma - d_{31}^2 \bar{E}_p + \left(\frac{Z_p(\omega)}{Z_s(\omega) + Z_p(\omega)} \right) d_{31}^2 \bar{E}_p \left(\frac{\tan(k(\omega)l)}{k(\omega)l} \right) \right], \quad (7)$$

where l is the length of the PZT, d_{31} is the piezoelectric strain coefficient corresponding to 1 (x) – 3 (z) axis, $\bar{E}_p = E_p(1 + \eta i)$ is the complex Young's modulus of the piezoelectric patch and $\bar{e}_{33}^\sigma = e_{33}^\sigma(1 + \delta i)$ is the complex electric permittivity of the PZT material at constant stress σ . η and δ denote both mechanical and dielectric loss factors and k is the wave number which is given by

$$k(\omega) = \omega \sqrt{\frac{\rho_p}{E_p}}, \quad (8)$$

where ρ_p is the density of piezoelectric material, ω is the angular frequency and $Z_p(\omega)$ is the mechanical impedance of the piezoelectric patch, which can be calculated by

$$Z_p(\omega) = \frac{k(\omega)w_p h_p \bar{E}_p}{j\omega \tan(k(\omega)l)}. \quad (9)$$

$Z_s(\omega)$ represents the mechanical impedance of host structure. The mechanical impedance is given in terms of the frequency as

$$Z_s(\omega) = \frac{K_s(\omega)}{j\omega}, \quad (10)$$

where $K_s(\omega)$ is the dynamic stiffness of the structure. Mechanical impedance can be determined using the finite element method. Dynamic stiffness can be represented by

$$K_s(\omega) = \frac{F_s(\omega)}{X_s(\omega)}, \quad (11)$$

where $F_s(\omega)$ is the amplitude of applied force and $X_s(\omega)$ is the amplitude displacement of a point in the structure. In modal analysis, the mechanical impedance for a system of MDOF (Multi-degree-of-freedom) can be represented with a matrix. It is important to mention that the mechanical impedance reflects the properties of a linear system of vibration, similar to the natural frequencies and mode shapes of the system. Therefore, they do not depend on external forces. The dependency can only occur if the system dynamics has nonlinear behavior.

Modified EMI 1D model

Piezoelectric patches are available as thin sheets (PI ceramics, 2009), which can only generate longitudinal expansion and contraction. This means that the set sensor-adhesive-structure can be represented as a 1D spring-mass-damper (SMD). Liang et al. (1994) established a previous model of a one degree-of-freedom (DOF). This model did not consider the influence of the adhesive layer. Liang et al. (1994) model considered that $u_s(l, t) = u_s(l, t)$. This implies that the displacement of the structure in the driving point end (see Fig. 3) is equal to displacement of piezoelectric material in the end.

Driving point shown in Fig. 3 represents the point that is being displaced by the adhesive layer which is represented by the displacement $u_p(x, t)$. Xu and Liu (2002) presented a SMD with two DOF considering the adhesive interface as a SMD, as it is shown in Fig. 3. They considered the driving point at the adhesive interface as $u_p(x, t)$.

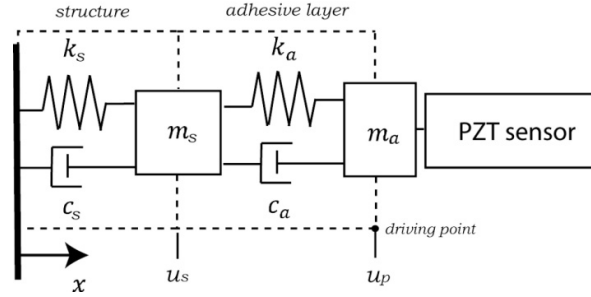


Figure 3 - Analogous mechanical system for coupling PZT-adhesive-structure, Xu and Liu (2002)

Figure 3 has two SMD systems coupled in series. Therefore, Xu and Liu (2002) assumed the relation of impedances as an equivalent mechanical impedance. Then, the equivalent coupled system of impedance was resolved as

$$Z_{se}(\omega) = \frac{Z_a(\omega)Z_s(\omega)}{Z_a(\omega) + Z_s(\omega)} = \left(\frac{K_a(\omega)}{K_a(\omega) + K_s(\omega)} \right) Z_s(\omega) = \xi Z_s(\omega), \quad (12)$$

where $Z_a(\omega)$ is the mechanical impedance of adhesive layer, $Z_s(\omega)$ is the mechanical impedance of the structure, $K_a(\omega)$ is the dynamic stiffness of adhesive layer and $K_s(\omega)$ is the dynamic stiffness of host structure. From (12) the coupling parameter ξ is given by

$$\xi = \frac{1}{1 + \frac{K_s(\omega)}{K_a(\omega)}}. \quad (13)$$

Equation (12) shows that the equivalent mechanical impedance of set structure-adhesive is coupled by means of ξ parameter. Eq. (13) shows that ξ parameter depends on dynamic stiffness of the structure and dynamic stiffness of the adhesive layer. Therefore, Xu and Liu (2002) defined a new electrical admittance which is determined by

$$\bar{Y}(\omega) = 2\omega j \frac{w_{pzt}l}{h_{pzt}} \left[\frac{e_{33}^{\sigma}}{e_{33}^{\sigma}} - d_{31}^2 y^E + \left(\frac{Z_p(\omega)}{\xi Z_s(\omega) + Z_p(\omega)} \right) d_{31}^2 y^E \left(\frac{\tan(k(\omega)l)}{k(\omega)l} \right) \right]. \quad (14)$$

Proposed model for obtaining ξ parameter

Figure 4 shows the set structure-adhesive-sensor which is submitted to a force $F(0.5l, t) = F(0.5l)e^{i\omega t}$ in $x = 0.5l$.

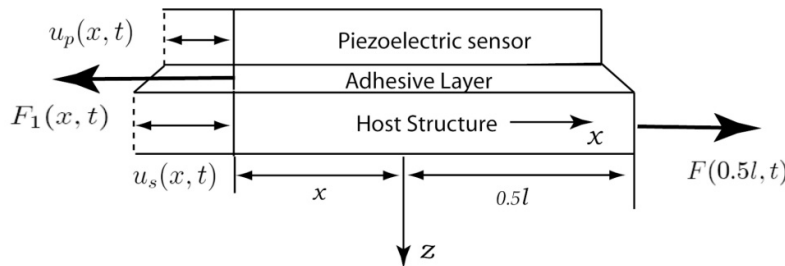


Figure 4 - Free body to the set structure-adhesive-piezoelectric sensor

From Fig. 4 we can establish the following relation

$$F_1(x, t) = \sigma_p(x, t)w_p h_p, \quad (15)$$

and also we can establish from Fig. 4 the following relation

$$F_1(x, t) = Z_s(\omega)j\omega u_s(x, t). \quad (16)$$

From (15) and (16) it is determined that

$$\sigma_p(x, t)w_p h_p = Z_s(\omega)j\omega u_s(x, t), \quad (17)$$

and organizing Eq. (17) we obtain that

$$\frac{\partial u_p(x, t)}{\partial x} = \frac{Z_s(\omega)j\omega u_s(x, t)}{w_p h_p E_p}. \quad (18)$$

Introducing Eq. (6) in (7), we have that

$$\rho_s w_s h_s \frac{\partial^2 u_s(x, t)}{\partial t^2} - E_s w_s h_s \frac{\partial^2 u_s(x, t)}{\partial x^2} - \frac{G_a (u_s(x, t) - u_p(x, t))}{h_a} = 0. \quad (19)$$

In order to solve (19), the displacement solutions of the structure and sensor are established by $u_s(x, t) = u_s(x)e^{i\omega t}$ and $u_p(x, t) = u_p(x)e^{i\omega t}$. Substituting $u_s(x, t)$ and $u_p(x, t)$ in (19) we can obtain that

$$-\rho_s w_s h_s \omega^2 u_s(x) - E_s w_s h_s \frac{\partial^2 u_s(x)}{\partial x^2} - \frac{G_a (u_s(x) - u_p(x))}{h_a} = 0. \quad (20)$$

Differentiating (20) with respect to x it is possible to obtain that

$$-\rho_s w_s h_s \omega^2 \frac{\partial u_s(x)}{\partial x} - E_s w_s h_s \frac{\partial^3 u_s(x)}{\partial x^3} - \frac{G_a \partial u_s(x)}{h_a \partial x} + \frac{G_a \partial u_p(x)}{h_a \partial x} = 0, \quad (21)$$

and introducing (18) in (21) it is determined that

$$-E_s w_s h_s \frac{\partial^3 u_s(x)}{\partial x^3} - \left(\frac{G_a}{h_a} + \rho_s w_s h_s \omega^2 \right) \frac{\partial u_s(x)}{\partial x} + \frac{G_a Z_s(\omega)j\omega}{h_a w_p h_p E_p} u_s(x, t) = 0. \quad (22)$$

Equation (22) can be solved in the following form, the solution of the displacement of the structure is established as $u_s(x) = ae^{\lambda x}$, and then, substituting $u_s(x)$ in (22), we have that

$$\lambda^3 + \left(\frac{G_a}{E_s w_s h_s h_a} + \frac{\rho_s}{E_s} \omega^2 \right) \lambda - \frac{G_a Z_s(\omega)j\omega}{h_a E_s w_s h_s w_p h_p E_p} = 0. \quad (23)$$

The roots of the cubic equation shown in (23) can be obtained with the Cardano's formula (Borwein and Erdélyi, 1995) such as

$$\lambda_1 = A + B, \lambda_{2,3} = -\frac{1}{2}(A + B) \pm \frac{i\sqrt{3}}{2}(A - B). \quad (24)$$

where $D = \left(\frac{p}{3}\right)^3 + \left(\frac{q}{2}\right)^3$, $A = \left(-\frac{q}{2} - \sqrt{D}\right)^{1/3}$, $B = -\frac{p}{3A}$, $p = \left(\frac{G_a}{E_s w_s h_s h_a} + \frac{\rho_s}{E_s} \omega^2\right)$ and $q = -\frac{G_a Z_s(\omega)j\omega}{h_a E_s w_s h_s w_p h_p E_p}$.

The solution of the displacements to the structure is determined by

$$u_s(x) = a_1 e^{\lambda_1 x} + e^{\alpha x} (a_2 \cos(\beta x) + a_3 \sin(\beta x)) \quad (25)$$

where $\alpha = -\frac{1}{2}(A + B)$ and $\beta = \frac{\sqrt{3}}{2}(A - B)$.

From (20) we can determine the displacement of the piezoelectric sensor as

$$u_p(x) = \left(1 + \frac{h_a \rho_s w_s h_s \omega^2}{G_a}\right) u_s(x) + \frac{h_a E_s w_s h_s}{G_a} \frac{\partial^2 u_s(x)}{\partial x^2}. \quad (26)$$

From (5) it is determined that

$$\rho_p w_p h_p \frac{\partial^2 u_p(x, t)}{\partial t^2} - E_p w_p h_p \frac{\partial^2 u_p(x, t)}{\partial x^2} + \frac{G_a (u_s(x, t) - u_p(x, t))}{h_a} = 0, \quad (27)$$

but $u_s(x, t) = u_s(x)e^{i\omega t}$ and $u_p(x, t) = u_p(x)e^{i\omega t}$. Then (27) remains in the following form

$$-\rho_p w_p h_p \omega^2 u_p(x) - E_p w_p h_p \frac{\partial^2 u_p(x)}{\partial x^2} + \frac{G_a}{h_a} u_s(x) - \frac{G_a}{h_a} u_p(x) = 0, \quad (28)$$

Differentiating (18) with respect to x , it is calculated that

$$\frac{\partial^2 u_p(x)}{\partial x^2} = \frac{Z_s(\omega)j\omega}{w_p h_p E_p} \frac{\partial u_s(x)}{\partial x}, \quad (29)$$

and introducing (29) in (28) and dividing the result in $u_s(x)$ we have that

$$-Z_s(\omega)j\omega \frac{\partial u_s(x)}{\partial x} \frac{1}{u_s(x)} + \frac{G_a}{h_a} = \left(\rho_p w_p h_p \omega^2 + \frac{G_a}{h_a} \right) \frac{u_p(x)}{u_s(x)}. \quad (30)$$

Organizing (30), it is determined the following relation in displacements, such that

$$u_s(x) = \gamma(x, \omega) u_p(x), \quad (31)$$

where,

$$\gamma(x, \omega) = \frac{\left(\rho_p w_p h_p \omega^2 + \frac{G_a}{h_a} \right)}{-Z_s(\omega)j\omega \frac{\partial u_s(x)}{\partial x} \frac{1}{u_s(x)} + \frac{G_a}{h_a}}. \quad (32)$$

Equation (31) shows that the displacement $u_s(x)$ is coupled by means of the mechanical parameters of the set structure-adhesive-sensor. In Eq. (16) was shown that the mechanical impedance of structure is determined with the displacement $u_s(x)$. However for determining the mechanical impedance the displacement in the interface adhesive-sensor $u_p(x)$ should be considered, as it is shown in Fig. 3. Then, replacing (31) in (16), Eq. (16) can be written as

$$F_1(x) = Z_s(\omega)j\omega \gamma(x, \omega) u_p(x). \quad (33)$$

We established equivalent mechanical impedance including adhesive coupling as

$$Z_{eq}(\omega) = \gamma(x, \omega) Z_s(\omega). \quad (34)$$

Equation (34) can be included in the electrical admittance shown in Eq. (7) and we obtain similarly Eq. (14) proposed by Xu and Liu (2002). Based on the analysis presented in this section, we can establish the following relation with Xu and Liu (2002) model, such that

$$\gamma(x, \omega) = \xi = \frac{1}{1 + \frac{K_s(\omega)}{K_a(\omega)}}. \quad (35)$$

NUMERICAL EXAMPLE

Figure 5 shows the set structure-adhesive-sensor submitted to the force $P(l/2, t) = 60e^{i\omega t}$ in the end $x = l/2$ along the axis x . Host structure is divided in two sections, section A and section B. Sections division is carried out with the aim to determine mechanical impedance of each structural section. Boundary conditions for Eq. (25) and its derivatives are $u_s(-l/2) = P(-l/2)l_A/w_s h_s$, $\frac{\partial u_s(l/2)}{\partial x} = P(l/2)/w_s h_s$ and $\frac{\partial u_p(-l/2)}{\partial x} = 0$ (applied to Eq. (18)). Physical and geometric properties of the set exposed in Fig. 5 are shown in Table 1.

Table 1 – Physical and geometric properties of Fig. 1

Item	Sensor	Structure A	Structure B	Adhesive layer
	PZT-5A	Aluminum	Aluminum	Araldite
Density ($kg \cdot m^{-3}$)	7500	2700	2700	7850
Young Modulus (Gpa)	120.34	70	70	2.84
Constant d_{31} ($C \cdot N^{-1}$)	-171×10^{-12}
Relative permittivity	1.470
Thickness (mm)	0.2667	0.25	0.25	0.3
Length (mm)	$l = 30$	$l_A = 300$	$l = 30$	$l = 30$

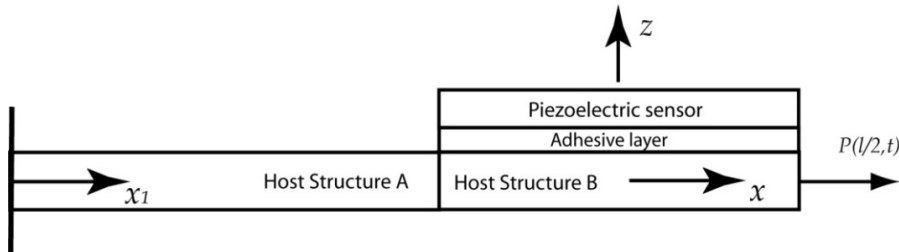


Figure 5 - Set structure-adhesive-sensor with an applied force

Results and discussion

Figure 6a shows sensor and structure (A+B) mechanical impedances. Sensor mechanical impedance was determined with Eq. (9) and host structure mechanical impedances A and B were determined by an algorithm of finite elements with truss elements implemented by Kwon (2000) and modified in MATLAB for determining impedances.

In the algorithm of finite elements rods A and B were divided in ten elements obtaining mass and stiffness matrices for determining mechanical impedances of rods. Then, it was calculated equivalent mechanical impedance of structures A and B. Structural (A+B) natural frequencies in a range of 0 to 30000 Hz can be observed in Fig. 6a. Natural frequencies of the sensor cannot be seen because they are in a major frequencies range. With mechanical impedance values (structure and sensor) determined, it is possible to obtain EM admittance spectrum related to the sensor (see Fig. 6b and Fig. 7).

Figure 6b shows EM admittance spectrum calculated with Xu and Liu (2002) variation in Liang et al. (1994) model (see Eq. (14)). In this figure it is possible to observe how coupling of ξ parameter (see Eq. (13)) modifies natural frequencies in the admittance spectrum lecture. When $\xi = 0$, the sensor is free or debonded completely, this means that structural natural frequencies do not appear in admittance spectrum. When $\xi = 1$, this means that dynamic stiffness of the adhesive layer is equal to dynamic stiffness of the structure (see Eq. (13)) in all frequency range (Liang et al. (1994) model). However, the mechanical properties and dynamic behavior of the adhesive layer and the structure are different. Therefore, ξ parameter cannot be constant in all frequency range, since it depends on $K_s(\omega)$ and $K_a(\omega)$, as it shown in Eq. (13)

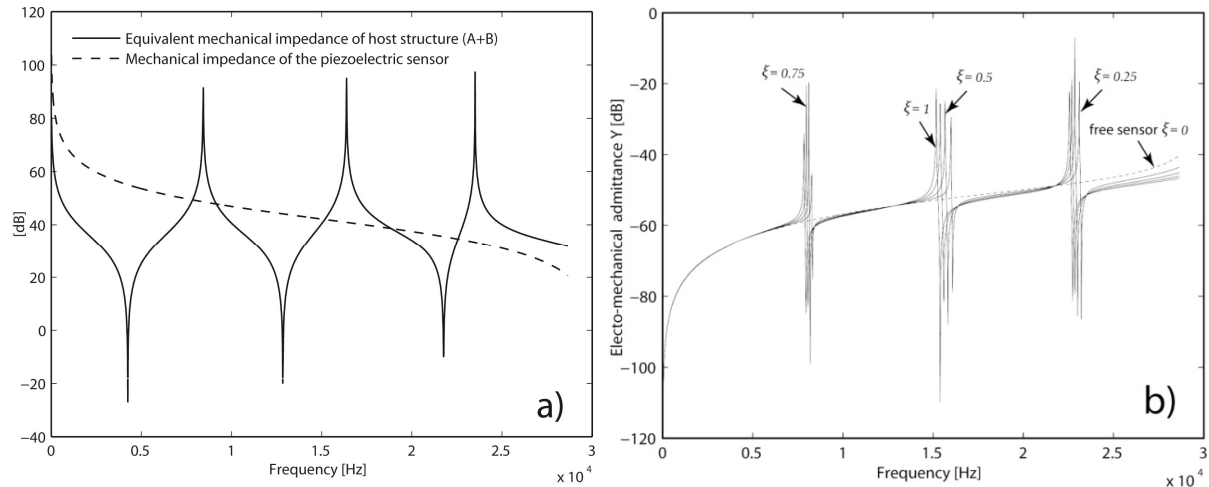


**Figure 6 - a. Mechanical impedance of the structure (A+B) and of the sensor
b. Electro-mechanical admittance obtained with Xu and Liu (2002) model**

Figure 7 shows EM admittance spectrum calculated with proposed $\gamma(l/2, \omega)$ parameter and $\omega \in (0, 30000)$. $\gamma(l/2, \omega)$ parameter includes the properties of bonding, such as G_a (shear modulus) and h_a (adhesive thickness), as also the mechanical and geometrics properties of the structure and the sensor. In Fig. 7 there is also shown a parametric analysis with EM admittance spectrum varying G_a parameter with the following values, $0.001G_a$, G_a and $1000G_a$ (G_a value is given in Table 1).

In Fig. 7 it can be observed that for $0.001G_a$ two resonant peaks appears, which perturb the lecture of the natural frequencies in the admittance spectrum. When the frequency is bigger, left resonant peak begins to be near of natural frequency obtained in the model without adhesive (Liang et al. 1994). However, the EM admittance spectrum is perturbed by right resonant peak. Therefore, it would generate confusion for identifying the natural frequencies by the noise introduced to the EM admittance spectrum. When shear modulus has the value of G_a , two resonant peaks also appear. In this case the right peak diminished its amplitude. Left resonant peak each time is most near to resonant peak obtained by model without adhesive in last natural frequency. When shear modulus take $1000G_a$ value, left resonant peak take approximately the value of the peak obtained without inclusion of the adhesive (Liang et al. 1994). However, in section A it is possible to observe a second small resonant peak. Second peak is also a perturbation of the EM admittance spectrum, but its amplitude is smaller. It is important to point out that when the G_a modulus is bigger, the model shows that displacements $u_p(x)$ and $u_s(x)$ are equal, and the proposed model has tendency to the Liang et al. (1994) model. But, the great difference of the proposed model with the model established by Xu and Liu (2002) is that our model introduces perturbations caused by adhesive properties, sensor properties and structural properties in the EM admittance spectrum.

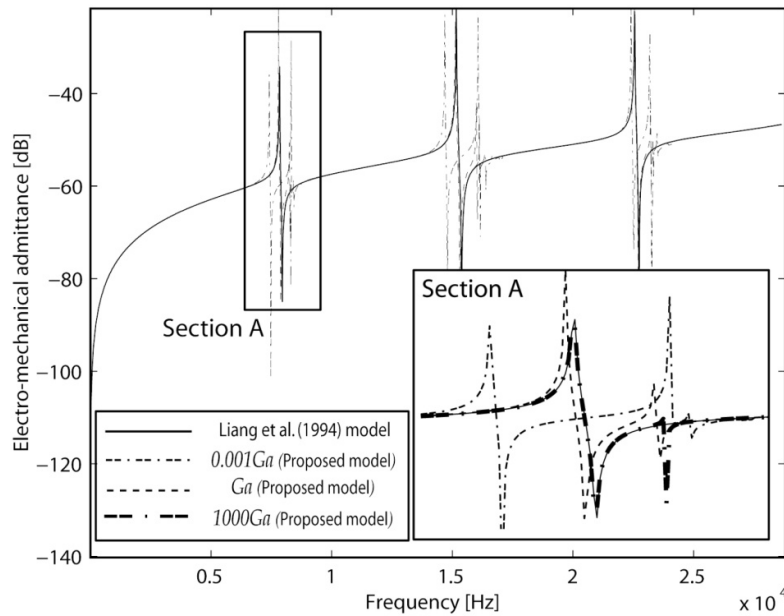


Figure 7 - EM admittance including proposed γ parameter

CONCLUSIONS

This study reveals the importance of the adhesive bonding layer in the embedding of the piezoelectric sensors in smart structures. The bond interface is an important factor in the electrical signatures emitted by the piezoelectric sensor. Since, the adhesive layer modifies the amplitude and the frequency of the EM admittance spectrum. The analysis with dynamic coupling parameter proposed showed that the adhesive properties introduce perturbations in EM admittance spectrum. Parametric results showed that when stiffness of the adhesive is bigger, the admittance spectrum obtained with the proposed parameter presents a tendency to a model that includes the adhesive layer. This demonstrated that elastic property of the adhesive introduces great error if its elastic modulus is smaller.

Therefore, it is important to point out that adhesive bonding effects are important in the failure identification. Since, in SHM the modification of the structural mechanical impedance corresponds to structural damage or modification. The knowledge of the effects caused by adhesive coupling can help to determine failures in the piezoelectric sensors.

ACKNOWLEDGMENTS

The authors are grateful to CAPES (Coordenação de Aperfeiçoamento de Pessoal de Nível Superior) for the financial support.

REFERENCES

- Annanddas, V.G.M., and Soh, C.K., 2007, "Three Dimensional Electromechanical Impedance Model II: Damage Analysis and PZT Characterization", *Journal of Aerospace Engineering*, Vol. 20, No. 1, pp. 63–71.
- Annanddas, V.G.M., and Soh, C.K., 2007a, "An Electromechanical Impedance Model of a Piezoceramic Transducer-Structure in the Presence of Thick Adhesive Bonding", *Smart Materials and Structures*, Vol. 16, pp. 673-686.
- Bhalla, S., and Soh, C. K. 2004, "Electromechanical Impedance Modeling for Adhesively Bonded Piezo-Transducers", *Journal of Intelligent Material Systems and Structures*, Vol. 15, No. 4, pp. 955-972.
- Bhalla, S., and Soh, C.K., 2004a, "Structural Health Monitoring by Piezo-Impedance Transducers: Modeling", *Journal of Aerospace Engineering, ASCE*, Vol. 17, No. 4, pp. 154–165.
- Borwein, P., and Erdélyi, T., 1995, *Cubic Equations, in Polynomials and Polynomial Inequalities*, SpringerVerlag, New York.
- Crawley, E.F., and de Luis, J., 1987, "Use of Piezoelectric Actuators as Elements of Intelligent Structures", *AIAA Journal*, Vol. 25, No. 10, pp. 1373-1385.
- Diamanti, K., Soutis C., and Hodgkinson, J.M., 2007, "Piezoelectric Transducer Arrangement for the Inspection of Large Composite Structures", *Composites Part A: Applied Science and Manufacturing*, Vol. 38, No. 4, pp. 1121-1130.
- Dorf, R.C., and Svoboda, J.A., 2001, "Introduction to Electric Circuits", 5th Edition, Wiley and Sons.

- Giurgiutiu, V., Rogers, C.A., 1997, "The Electro-Mechanical (E/M) Impedance Method for Structural Health Monitoring and Non-Destructive Evaluation", In: Workshop on Structural Health Monitoring, pp. 433-444.
- Giurgiutiu, 2007, "Structural Health Monitoring with Piezoelectric Wafer Active Sensors", Academic Press, Burlington, MA.
- Ha, S.K., Keilers, C., and Chang, F.K., 1992, "Finite Element Analysis of Composite Structures Containing Distributed Piezoelectric Sensors and Actuators", AIAA Journal, Vol. 30, No. 3, pp. 772-780.
- Kessler, S.S., and Spearing, S.M., 2002, "Design of a Piezoelectric-Based Structural Health Monitoring System for Damage Detection in Composite Materials", In: Proceedings of Smart Structures and Materials 2002: Smart Structures and Integrated Systems. pp. 86-96.
- Kisa, M., 2004, "Free Vibration Analysis of a Cantilever Composite Beam with Multiple Cracks", Composites Science and Technology, Vol. 64, No. 9, pp. 1391-1402.
- Kwon Y. W. and Bang H., 2000, "The Finite Element Method Using MATLAB", Second Edition. CRC Press.
- Liang, C., Sun, F.P., and Rogers, C.A., 1994, "Coupled Electromechanical Analysis of Adaptive Material Systems. determination of the Actuator Power Consumption and System Energy Transfer", Journal of Intelligent Material Systems and Structures, Vol. 5, No. 1, pp.12-20.
- Liang, C., Sun, F., and Rogers, C.A., 1996, "Electro-Mechanical Impedance Modeling of Active Material Systems", Smart Materials and Structures, Vol. 5, No. 2, pp. 171-186.
- Liu, S.C, Tomizuka, M., and Ulsoy, G., 2006, "Strategic Issues in Sensors and Smart Structures", Structural Control and Health Monitoring, Vol.13, No. 6, pp. 946-957.
- Luo, Q., Tong, L., 2002. "Exact static solutions to piezoelectric smart beams including peel stresses, Part II: Numerical results, comparison and discussion", International Journal of solid and Structures, Vol. 39, No. 18 , pp. 4697-4722.
- Ng, C.T., and Veidt, M., 2009, "A Lamb-Wave-Based Technique for Damage Detection in Composite Laminates", Smart Materials and Structures, Vol. 18, N. 7, pp. 1-12.
- Pandey, A.K., Biswas, M., and Samman, M.M., 1991, "Damage Detection from Changes in Curvature Mode Shapes", Journal of Sound and Vibrations, Vol. 145, No. 2, pp. 321-332.
- Pandey, A.K., and Biswas, M., 1994, "Damage Detection in Structures Using Changes in Flexibility", Journal of Sound and Vibrations, Vol. 169, No. 1, pp. 3-17.
- Panigrahi, R., Bhalla, S., and Gupta, A., 2010, "A Low-Cost Variant of Electro-Mechanical Impedance (EMI) Technique for Structural Health Monitoring", Experimental Techniques, Vol. 34, N. 2, pp. 25-29.
- Park, G., Soh, H., Farrar, C.R., and Inman D.J., 2003, "Overview of Piezoelectric Impedance Based Health Monitoring and Path Forward", Shock and Vibration Digest, Vol. 35, No. 6, pp. 451-463.
- PI Ceramic, 2009, Web site: <http://www.piceramic.de> [accessed on 20 august 2009].
- Sirohi, J., and Chopra, I., 2000, "Fundamental Understanding of Piezoelectric Strain Sensors", Journal of Intelligent Material Systems and Structures, Vol.11, No. 4, pp. 246-257.
- Staszewski, W.J., Mahzan, S., and Traynor, R., 2009, "Health Monitoring of Aerospace Composite Structures-Active and Passive Approach", Composites Science and Technology, Vol. 69, No.11, pp. 1678-1685.
- Stubbs, N., and Kim, J.T., 1994, "Field verification of a non-destructive damage localization and severity estimation algorithm", Texas A&M University Report Prepared for New Mexico State University.
- Tan, P., and Tong, L., 2004, "Identification of Delamination in a Composite Beam Using Integrated Piezoelectric Sensor/Actuator Layer", Composite Structures, Vol. 66, No. 5, pp. 391-398.
- Tanasoiu V., Miclea C., and Tanasoiu C., 2002, "Nondestructive Testing and Piezoelectric Ultrasonics Transducer for Wood and Built in Wooden Structures", Journal of Optoelectronics and Advanced Materials, Vol. 4, No. 4, pp. 949-957.
- Tinoco, H.A., Serpa, A.L., and Ramos, A.M., 2010, "Numerical Study of the Effects of Bonding Layer Properties on Electrical Signatures of Piezoelectric Sensors", Mecánica Computacional, Vol. 29, No. 86, pp. 8391-8409.
- Xu, Y.G., and Liu, G.R., 2002, "A Modified Electro-Mechanical Impedance Model of Piezoelectric Actuator-Sensors for Debonding Detection of Composite Sensors", Journal of Intelligent Material Systems and Structures. Vol. 13, No. 6, pp. 389-396.
- Yan, W., Lim, C.W., Chen, W.Q., and Cai, J.B., 2007a, "Modeling of EMI Response of Damaged Mindlin-Herrmann Rod", International Journal of Mechanical Sciences, Vol. 49, No. 12, pp. 1355- 1365.
- Yan, W., Lim, C.W., Cai, J.B., and Chen, W.Q., 2007b, "An Electromechanical Impedance Approach for Quantitative Damage Detection in Timoshenko Beams with Piezoelectric Patches," Smart Materials and Structures, Vol. 16, No. 4, pp. 1390-1400.
- Yan, W., and Chen, W.Q., 2010. "Structural health monitoring using high-frequency electromechanical impedance signatures", Advances in Civil Engineering, Vol. 2010, 429148.
- Yang, S., and Ngoi, B., 1999, "General sensor equation and actuator equation for the theory of laminated piezoelectric plates", Vol. 8, No. 3, pp. 411-415.
- Yu, L., Santoni-Bottai, G., Xu, B., Liu, W., and Giurgiutiu, V., 2008, "Piezoelectric Wafer Active Sensors for in Situ Ultrasonic Guided Wave SHM", Fatigue & Fracture of Engineering Materials & Structures, Vol. 31, No. 8, pp. 611-628.
- Zimmerman, D.C., and Kaouk, M., 1994, "Structural Damage Detection Using a Minimum Rank Update Theory", Journal of Vibration and Acoustic, Vol. 116, No. 2, pp. 222-231.

Hamiltonian Dynamics and Geometry of a Class of Mobile, Multibody Systems

Eric Conrado de Souza, eric.csouza@yahoo.com

Av. Humberto de Alencar Castelo Branco, n.3972, Depto. de Engenharia Mecânica, Centro Universitário FEI, São Bernardo do Campo, SP, 09850-901, Brasil

Newton Maruyama, maruyama@usp.br

Av. Prof. Mello Moraes n.2231, Depto. de Engenharia Mecatrônica e de Sistemas Mecânicos, Escola Politécnica, Universidade de São Paulo, São Paulo, SP, 05508-900, Brasil

Abstract. *In what follows, we present the dynamical model for a proposed class of mobile, multibody robotic systems which are able to steer themselves around on the plane. The modeling procedure is obtained through the Hamiltonian framework, for which a new phase space parametrization is obtained. Geometrical interpretation for the modeling approach is emphasized.*

Keywords: *Mobile robots, Interconnected systems, Differential geometric methods*

INTRODUCTION

The current paradigm of many areas in robotics consists in mimicking nature and relying on the various mechanisms in biology as inspirational templates for systems design with focus on enhancing the controlled dynamical performance and pushing forward the robotic systems capability for interaction with the environment.

Under this motivational setting we propose a class of planar multibody or interconnected robotic systems.

Definition 1 (Mobile Multibody System, Souza and Maruyama (2010)) *Let a dynamical system of Figure (1) be described as one formed by N articulated rigid bodies subject to external system forces f_i and torques T_i , for $i = 1, \dots, N$. The external forces can be taken as propulsion actuators, e.g. gas jets, enabling the system to be steerable on the inertial space and to freely position the system center of mass.*

The system has a broad scope in aerospace Rui *et al.* (2000), Dubowsky and Papadopoulos (1993) and in underwater Yuh and West (2001) related robotic applications.

The thruster-free, dynamical modeling, through the Hamiltonian approach, of such systems was presented in Sreenath (1987). We extend this here to include the translational actuation as defined above and rewrite the dynamics under new coordinate parametrization, see also Souza and Maruyama (2010). In depth technical treatment stemming from geometrical methods for classical mechanics, as seen in the Lagrangian approach to modeling in Cortizo (1991) and elsewhere, will be refrained from here. Instead we employ the less demanding and, otherwise, more straightforward Hamiltonian approach to system modeling. A geometrical approach to the modeling of a proposed class of multibody systems through the Lagrangian approach can be found in Souza and Maruyama (2007).

We remark, however, that the dynamic model obtained from either approach could be used for the control design presented below - of course.

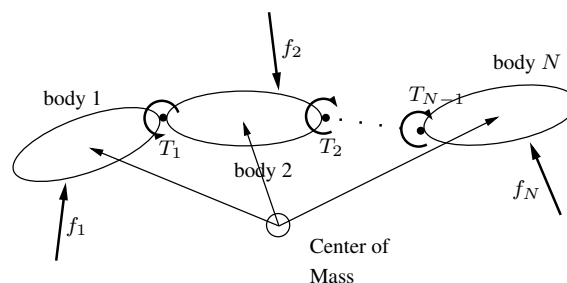


Figure 1. Mobile multibody system.

SYSTEM MODELING

The modeling of a multi-body system of the class mentioned previously will assume the neglect of potential and dissipative forces. We also adopt friction-less joint hinges. In order to simplify the expressions, the thruster forces are taken to act at the center of mass of the bodies and are not vectorized.

The System Configuration Space

The configuration space Q of a planar rigid body is the special Euclidian group in the plane denoted by $SE(2)$.¹ Because the groups $SE(2)$ and $SO(2) \times \mathbb{R}^2$ are isomorphic to each other the following mapping is naturally defined

$$SE(2) \ni \begin{bmatrix} \mathbf{R} & \mathbf{r} \\ \mathbf{0}_{1 \times 2} & 1 \end{bmatrix} \mapsto (\mathbf{R}, \mathbf{r}) \in SO(2) \times \mathbb{R}^2$$

where $\mathbf{R} \in SO(2)$ is the body rotation matrix, and \mathbf{r} the distance of its center of mass from the inertial frame origin. We will identify the elements of $SE(n)$ with the elements of $SO(n) \times \mathbb{R}^n$. Moreover, we can identify the groups $SO(2)$ and the circle \mathbb{S}^1 because we parameterize $\mathbf{R}_i = \mathbf{R}(\theta_i)$ by $\theta_i \in \mathbb{S}^1$, ($i = 1, \dots, N$), defined by the isomorphism given below:

$$SO(2) \ni \mathbf{R} \mapsto (x_1, x_2) \in \mathbb{S}^1 \subset \mathbb{R}^2, \quad \text{where} \quad \sqrt{x_1^2 + x_2^2} = 1.^2$$

For a planar multibody system composed of N **free** bodies, the configuration space is

$$Q_{free} = (\mathbb{R}^2 \times \mathbb{S}^1) \times \dots \times (\mathbb{R}^2 \times \mathbb{S}^1) \quad (N\text{-times})$$

with configuration $q \in Q_{free}$, where $q = ((\mathbf{R}_1, \mathbf{r}_1), (\mathbf{R}_2, \mathbf{r}_2), \dots, (\mathbf{R}_N, \mathbf{r}_N))$. Alternatively, in the coordinates, q also takes the form using vector notation:

$$q = \begin{bmatrix} (\mathbf{r}_1, \theta_1)^T \\ \vdots \\ (\mathbf{r}_N, \theta_N)^T \end{bmatrix} \in Q_{free}$$

From this point forward, we specialize the multibody system to the interconnected one, which is made up by bodies physically coupled in pairs to each other by hinges, Fig. 1. This coupling defines the (holonomic) *hinge constraint*, which, for a multibody system composed of rigid body with arbitrary inertial and geometric properties, becomes

$$\mathbf{r}_{j+1} = \mathbf{r}_j + \mathbf{R}(\theta_j)\mathbf{d}_{j,j+1} - \mathbf{R}(\theta_{j+1})\mathbf{d}_{j+1,j}, \quad (1 \leq j < N)$$

where Hence, the configuration space for the interconnected system $Q \subset Q_{free}$ simplifies to:

$$Q = \mathbb{R}^2 \times SO(2) \times \dots \times SO(2) \quad (N\text{-times})$$

From the above, we parameterize $\mathbf{R}_i = \mathbf{R}(\theta_i) \in SO(2)$ by $\theta_i \in \mathbb{S}^1$, and $i = 1, \dots, N$. Thus, Q may be written as:

$$Q = \mathbb{R}^2 \times \mathbb{S}^1 \times \dots \times \mathbb{S}^1 \quad (N\text{-times})$$

and consequently, choosing one system point with distance $\mathbf{r} \in \mathbb{R}^2$ to the inertial frame, system configuration is $q = (\mathbf{r}, \theta_1, \theta_2, \dots, \theta_N) = (\mathbf{r}, \boldsymbol{\theta}) \in Q$. Let $T_q Q$ be the tangent space over the configuration space Q at every $q \in Q$. The generalized velocity $\dot{q} \in T_q Q$ at q , has coordinates $(\dot{\mathbf{r}}, \dot{\boldsymbol{\theta}})$. The equations of motion for system dynamics are given on the system state-space. In the Lagrangian setting the state-space is taken to be the tangent bundle TQ . Thus, for the configuration $q = (\mathbf{r}, \boldsymbol{\theta})$, the state space TQ is given by $(\dot{\mathbf{r}}, \dot{\boldsymbol{\theta}}) \in T_q Q = T_q(\mathbb{R}^2 \times \mathbb{S}^1 \times \dots \times \mathbb{S}^1)$.

Definition 2 (Principal Bundle) Let Φ_g be a Lie group G -action on the configuration manifold Q , for $g \in G$. The space Q is locally diffeomorphic to the product of the quotient space Q/G with the group space G , i.e., $Q \simeq Q/G \times G$. The quotient space $Q/G \equiv B$ is also known as the shape space. In this product structure, an element of Q is parametrized by (b, g) , where $b \in B$. The map $\pi : Q \rightarrow B$ is a projection onto the first factor. The 4-tuple (Q, π, B, G) is a **principal bundle** or structure.

We use this structure to model the system dynamics, where the base space coordinates b will indicate joint angles ϕ at the system hinges.

System Hamiltonian and Lagrangian

The total kinetic energy K_E for the planar system, composed of N bodies, is the sum of the individual kinetic energies K_{E_k} . Thus, the system equations of motion are dictated by inertial dynamics only. For a rigid body B on the plane, any point of the body, in body coordinates, may be specified by \mathbf{X} . If the body frame distance from the inertial frame is \mathbf{r} ,

¹The $SE(n)$ group is the semi-direct product $SO(n) \ltimes \mathbb{R}^n$, for any $n \in \mathbb{N}$.

then the inertial position of any body point is $x = \mathbf{R}\mathbf{X} + \mathbf{r}$. The system Lagrangian L is solely determined by the total kinetic energy K_E of the system, given the absence of potential and dissipative forces:

$$L = \sum_{k=1}^N K_{E_k} = \sum_{k=1}^N \frac{1}{2} \int_{\mathcal{B}_k} \rho(\mathbf{X}_k) \|\dot{x}_k\|^2 d^2 \mathbf{X}_k$$

On a Riemannian context (with $\langle\langle \cdot, \cdot \rangle\rangle$ as kinetic energy metric), the Lagrangian is defined by $\langle\langle \cdot, \cdot \rangle\rangle_{\mathbb{G}}$ as:

$$L(v_q) = \sum_{k=1}^N K_{E_k} = \frac{1}{2} \langle\langle \dot{q}, \dot{q} \rangle\rangle_{\mathbb{G}} = \frac{1}{2} \dot{q}^T \mathbb{G} \dot{q} \quad (1)$$

where \mathbb{G} is the generalized system inertia matrix. Let $\mathbf{r}_{cm} \in \mathbb{R}^2$ denote the system's center of mass position, given in the inertial reference frame. An element of the tangent space $T_q Q$ is $(\dot{\mathbf{r}}_{cm}, \dot{\theta}_i)$. The corresponding element on the dual space over the system configuration $T_q^* Q$, called moment phase space, can be computed by applying Legendre's Transform $\mathbb{F}L : TQ \rightarrow T^*Q$ to (q, \dot{q}) , giving $p \in T_q^* Q$. This transform maps velocities and momentums between the tangent TQ and cotangent T^*Q bundles. Fixing configuration coordinates q , $T_q^* Q$ has the canonical coordinates (q^i, p_i) , for $i = 1, \dots, N$, where the conjugated moment $p := \partial L(q, \dot{q}) / \partial \dot{q}$ is determined by:

$$\mathbb{F}L(q, \dot{q}) = \mathbb{F}L(\dot{\mathbf{r}}_{cm}, \dot{\theta}_1, \dots, \dot{\theta}_N) \mapsto [\mathbf{p}_{cm}, \boldsymbol{\mu}] = p$$

From the tangent bundle transformation above, we specify the elements of cotangent bundle: the angular momenta $\boldsymbol{\mu} = [\mu_1, \dots, \mu_N]$ is defined by $\boldsymbol{\mu} = \mathbb{J}\boldsymbol{\omega}$ and the center of mass linear momenta $\mathbf{p}_{cm} \in \mathbb{R}^2$ is obtained by $\mathbf{p}_{cm} = m\dot{\mathbf{r}}_{cm}$, where m is the system mass. Thus, $p \in T_q^* Q$ is given by $(\mathbf{p}_{cm}, \boldsymbol{\mu}) \in \mathbb{R}^2 \times T_{\theta_1}^* \mathbb{S}^1 \times \dots \times T_{\theta_N}^* \mathbb{S}^1$, (N -times). And, finally, because the system inertia matrix \mathbb{J} is positive definite, \mathbb{J} is invertible and we find the system Hamiltonian $H(q, p) : T^*Q \rightarrow \mathbb{R}$ as

$$H(\boldsymbol{\theta}, \mathbf{p}_{cm}, \boldsymbol{\mu}) = \frac{1}{2} \boldsymbol{\mu}^T \mathbb{J}^{-1} \boldsymbol{\mu} + \frac{\|\mathbf{p}_{cm}\|^2}{m}. \quad (2)$$

It is a known fact that the planar system is characterized by having $SE(2)$ Lie group symmetry. System dynamical symmetry translates to an invariance of the associated Hamiltonian function.

SYSTEM MODEL ON THE PHASE SPACE

We now present the system dynamics and specialize the rotational dynamics to a symplectic structure by showing the Poisson bracket degeneration of the translational dynamics. The structure of the N -body system equations of motion is Poisson and the Poisson bracket lifts the configuration trajectory to the cotangent bundle T^*Q . Thus, in coordinates: $z = (q, p) = (\mathbf{r}_{cm}, \boldsymbol{\theta}, \mathbf{p}_{cm}, \boldsymbol{\mu}) \in T^*Q$ and $H(z) = H(\boldsymbol{\theta}, \mathbf{p}_{cm}, \boldsymbol{\mu})$, and the system equations of motion give:

$$\dot{z} = \{z, H\} = X_H(z) \Rightarrow \begin{cases} \dot{\mathbf{r}}_{cm} = \{\mathbf{r}_{cm}, H\} \\ \dot{\mathbf{p}}_{cm} = \{\mathbf{p}_{cm}, H\} \\ \dot{\theta}_i = \{\theta_i, H\} \\ \dot{\mu}_i = \{\mu_i, H\} \end{cases}$$

and system dynamics phase space is even dimensional, given by $n = 2N + 4$. We evaluate initially the Poisson bracket for the first equations to render the system center of mass translational dynamics:

$$\begin{cases} \dot{r}_x = \frac{\partial H}{\partial p_x}, & \dot{p}_x = -\frac{\partial H}{\partial r_x} = 0 \\ \dot{r}_y = \frac{\partial H}{\partial p_y}, & \dot{p}_y = -\frac{\partial H}{\partial r_y} = 0 \end{cases} \quad (3)$$

where $\mathbf{r}_{cm} = (r_x; r_y)$ and $\mathbf{p}_{cm} = (p_x; p_y)$. The two momentum expressions are null due to the invariance of H w.r.t the position coordinates \mathbf{r}_{cm} ; reaffirming, according to Noether, conservation of linear momentum. The system rotational dynamics follows from the expressions:

$$\dot{\theta}_i = \frac{\partial H}{\partial \mu_i} \quad \text{and} \quad \dot{\mu}_i = -\frac{\partial H}{\partial \theta_i}, \quad (i = 1, 2, \dots, N) \quad (4)$$

The above rotational dynamics further specialize to a Poisson manifold, as observed by the non-degenerate Poisson bracket³. This symplectic structure can also be observed in the submanifold of Q relative to the dynamics in the base space B .

³Bracket not identically null.

Remark 1 One can show that a Poisson manifold is given by the disjoint union of its symplectic leaves. Thus, system dynamics can be parameterized in each foliation of the principal structure. Dynamics in each leaf is invariant since, for zero-input, system momentum is conserved, as stated by Noether's Theorem. The symplectic leaf on which system dynamics evolve is specified when the values for system linear \mathbf{p}_{cm} and angular μ momenta are fixed; these correspond to the $SE(2)$ group directions. System motion on the leaf is completely specified by the reduced equations of motion. Notice that the symplectic structure of the translation motion is degenerative due to $\dot{\mathbf{p}}_{cm} = 0$ and, hence, trivial, as given in (3). For the 2-body system, the rotational dynamics in each symplectic leaf evolves in a Poisson submanifold of four dimensions, as detailed next.

Reparametrizing (4) for the joint angles $\phi_i = \theta_{i+1} - \theta_i$, one can compute the system rotational dynamics, through the Poisson bracket, to be, see Sreenath (1987):

$$\dot{\phi}_i = \frac{\partial H}{\partial \mu_{i+1}} - \frac{\partial H}{\partial \mu_i}, \quad (i = 1, \dots, N-1) \quad \text{and} \quad \dot{\mu}_i = \frac{\partial H}{\partial \phi_i} - \frac{\partial H}{\partial \phi_{i-1}}, \quad \left(\frac{\partial H}{\partial \phi_N} = \frac{\partial H}{\partial \phi_{-1}} = 0 \right). \quad (5)$$

The **reduced** equations above describe the multibody system dynamics on each symplectic leaf. One might notice the lack of attitude or orientation information, of the system as a whole, in regard to the inertial frame, besides translational dynamics. This is a consequence of system invariance w.r.t. the symmetry group $SE(2)$. Observe, also, that although the dynamics remain locally in a Poisson space, the system reduced equations no longer possess a symplectic structure in the space of variables, as seen in (4).

Equations of Motion under new parametrization

It is possible, however, to recover the lost system orientation information w.r.t. the inertial frame by simply patching to (5) some extra measure of inertial attitude. Define the orientation θ_{cm} of the mobile frame at the center of mass w.r.t. the inertial frame:

$$\theta_{cm} = \frac{1}{N} \sum_{i=1}^N \theta_i \quad (6)$$

The coordinate θ_{cm} together with joint angles ϕ can be used to define a diffeomorphism P between the different parameterizations in Q by

$$\begin{bmatrix} \theta_{cm} \\ \phi \end{bmatrix} = P(\theta) \quad \Rightarrow \quad [P] = \begin{bmatrix} 1/N & 1/N & \cdots & 1/N \\ -1 & 1 & 0 & \cdots \\ 0 & -1 & 1 & \ddots \\ \vdots & \ddots & \ddots & \ddots \\ 0 & \cdots & -1 & 1 \end{bmatrix} \quad (7)$$

Remark 2 The definition for the θ_{cm} orientation above is satisfactory because it's canonical, see Lanczos (1986) for details, and independent of shape coordinates ϕ and, thus, does not account for motion exclusively on the shape space B . The induced matrix $[P]$ of the coordinate mapping P is positive definite and invertible. Additionally, notice that because P is a linear transformation, it is, therefore, a global diffeomorphism. Observe also that $\det[P]$ is unitary, allowing for volume preservation between the coordinates of both parameterizations.

The $[P]^T$ matrix translates the cotangent lift of the mapping P as detailed in the Appendix A. We present next the system eq. of motion in the new coordinates. From the system Hamiltonian expression, we get that the system Hamiltonian can be written w.r.t. the original as with new system momenta:

$$H = \frac{1}{2} \boldsymbol{\mu}^T \mathbb{J}_{\theta}^{-1} \boldsymbol{\mu} = \frac{1}{2} ([P]^T \boldsymbol{\mu}')^T \mathbb{J}_{\theta}^{-1} ([P]^T \boldsymbol{\mu}') = \frac{1}{2} (\boldsymbol{\mu}')^T [P] \mathbb{J}_{\theta}^{-1} [P]^T \boldsymbol{\mu}' = \frac{1}{2} (\boldsymbol{\mu}')^T (\mathbb{J}_{(\theta_{cm}, \phi)})^{-1} \boldsymbol{\mu}'$$

Thus, the inertia matrix in the new parametrization \mathbb{J}' for the phase space T_q^*Q is

$$\mathbb{J}_{(\theta_{cm}, \phi)} = (P^T)^{-1} \mathbb{J}_{\theta} P^{-1}$$

In order to rewrite the system dynamics with new coordinates, we begin with time rate of the new coordinates

$$\dot{\mu}' = ([P]^T)^{-1} \dot{\mu} \quad \Rightarrow \quad \dot{\mu}' = ([P]^T)^{-1} \dot{\mu},$$

so the equations of motion are still functions of the old coordinates $\dot{\mu}' = \dot{\mu}'(\theta, \mu)$. Using the definition for the mapping P and the corresponding cotangent lift

$$\begin{bmatrix} \theta_{cm} \\ \phi \end{bmatrix} = [P]\theta \quad \text{and} \quad \mu = [P]^T \mu',$$

the new eq. of motion can be evaluated for the new coordinates, resulting in the expressions $\dot{\mu}' = \dot{\mu}'(\theta_{cm}, \phi, \mu')$. We next verify the equations of motion in the new coordinates. Dynamics on the group $SO(2)$ is obtained by

$$\dot{\theta}_{cm} = \frac{\partial H_0}{\partial p_{\theta_{cm}}} \quad \text{and} \quad \dot{p}_{\theta_{cm}} = -\frac{\partial H_0}{\partial \theta_{cm}}$$

and on the base space $Q/SO(2)$, for $(i = 1, \dots, N - 1)$:

$$\dot{\phi}_i = \frac{\partial H_0}{\partial p_{\phi_i}} \quad \text{and} \quad \dot{p}_{\phi_i} = -\frac{\partial H_0}{\partial \phi_i}.$$

Multibody System Input Modeling

Renaming the drift dynamics Hamiltonian H to H_0 , the control system Hamiltonian is

$$H(q, p, u) = H_0(q, p) - \sum_{j=1}^m H_j(q, p) u_j \quad (8)$$

where u_j are generalized function inputs and H_j are usually named *coupling* or *interaction* Hamiltonians. The multibody system is also *simple*, and, hence, $H_j(q, p) = H_j(\theta)$. The translational eq. of motion for the system center of mass are

$$\dot{r}_i = \frac{\partial H_0}{\partial p_i} - \sum_{j=1}^N \frac{\partial H_j}{\partial p_i} u_j = \frac{\partial H_0}{\partial p_i} \quad \text{and} \quad \dot{p}_i = -\frac{\partial H_0}{\partial r_i} + \sum_{j=1}^N \frac{\partial H_j}{\partial r_i} u_j = \sum_{j=1}^N \frac{\partial H_j}{\partial r_i} u_j, \quad (i = \{x, y\}) \quad (9)$$

where $[\partial H_j / \partial p_i] = \mathbf{0}_{2 \times m}$ and $[\partial H_0 / \partial r_i] = \mathbf{0}_{2 \times 1}$, for $m = N$, and where the input functions $u = [u_j] \in U \subset \mathbb{R}^m$ correspond to external forces f_j . Additionally, we can define the above input structure in terms of the generalized translational dynamics input τ_{trans} , which renders the linear momenta eq. of motion as

$$\begin{aligned} \dot{p}_i &= \sum_{j=1}^N \frac{\partial H_j}{\partial r_i} u_j \\ &= \begin{bmatrix} \frac{\partial H_1}{\partial r_x} & \dots & \frac{\partial H_N}{\partial r_x} \\ \frac{\partial H_1}{\partial r_y} & \dots & \frac{\partial H_N}{\partial r_y} \end{bmatrix} \begin{bmatrix} f_1 \\ \vdots \\ f_N \end{bmatrix} = [\tau_i] = \tau_{trans}(f_1, \dots, f_N), \quad (i = \{x, y\}) \end{aligned}$$

We resort to Newtonian mechanics for the above modeling of thruster inputs. A brief geometric interpretation is made below. For joint torques T_i and generalized torques τ_i , the input structure modifies the unreduced rotational dynamics (4) as follows:

$$\dot{\theta}_i = \frac{\partial H_0}{\partial \mu_i} \quad \text{and} \quad \dot{\mu}_i = -\frac{\partial H_0}{\partial \theta_i} + T_i + \tau_i, \quad (i = 1, 2, \dots, N). \quad (10)$$

And in like manner, the reduced, forced rotational dynamics (5) accounting for external and internal inputs is written as

$$\dot{\phi}_i = \frac{\partial H_0}{\partial \mu_{i+1}} - \frac{\partial H_0}{\partial \mu_i} \quad (i = 1, \dots, N - 1) \quad \text{and} \quad \dot{\mu}_i = \frac{\partial H_0}{\partial \phi_i} - \frac{\partial H_0}{\partial \phi_{i-1}} - T_{i+1} + T_i + \tau_i, \quad (i = 1, \dots, N). \quad (11)$$

Denoting by f the system drift vector field, the system equations of motion (10), can be recast in vector field format:

$$\dot{z} = f(z) + \sum_{j=1}^m g_j u_j = f(z) + \tau,$$

where $\tau = [\mathbf{0}_{(1 \times N+2)}, \tau_{trans}, \tau_{rot}]^T$ is the generalized input and function of the input vector fields g_j and where the vector $\tau_{rot}(T_i, \tau_i)$ drives the rotational dynamics. The input τ , which translates the newtonian forces f_i and torques T_j to equations of motion inputs, can equally be interpreted in the geometrical setting. By showing the equivalence of the system equations of motion under two sets of coordinates for Q , which are related by point transformations, one finds the input τ as an element of the cotangent bundle T^*Q since these transform as the components of a covector field on Q , Bullo and Lewis (2005).

Notice that the linear and angular momenta of the system center of mass, corresponding to the $SE(2)$ group directions of the *principal* structure, $(p_{cm}, p_{\theta_{cm}})$, are constants of motion and, thus, conserved quantities, as predicted by Noether's Theorem.

Example: The 2-Body System

Let the two bodies of a 2-interconnected-body system, be labeled as 1 and 2. These are elliptical, homogeneously distributed masses where m_i is the i -th body mass, d_i is the distance from the i -body center of mass to the hinge. The full 4-dimensional space Q equals $\mathbb{R}^2 \times \mathbb{S}^1 \times \mathbb{S}^1$. A tangent bundle TQ element is $(q, \dot{q}) = ((\mathbf{r}_1, \theta_1, \theta_2), (\dot{\mathbf{r}}_1, \dot{\theta}_1, \dot{\theta}_2))$. Using the decomposition provided by the principal bundle structure, coordinates become $q = (\phi, g)$, where $g = (\mathbf{r}_{cm}, \theta_{cm})$ is an $SE(2)$ group element, the base space Q/G coordinate $\phi = \theta_2 - \theta_1$ is the joint angle. From (7), the system inertial orientation, measured by the angle between the mobile frame at the center of mass to the inertial frame, is taken to be $\theta_{cm} = (\theta_1 + \theta_2)/2$. The reduced tangent space coordinates are $(\phi, \dot{\phi}, \xi_B) \in (TQ)/G$ where $g^{-1}\dot{g} = \xi_B \in \mathfrak{g}$ is the body frame velocity. The tangent space over Q/G has coordinates $(\phi, \dot{\phi}) \in T(Q/G) = \mathbb{S}^1 \times \mathbb{R}$.

The symmetric, invertible inertia matrix \mathbb{J} for the 2-body system is, see Sreenath (1987):

$$\mathbb{J} = \begin{bmatrix} \tilde{I}_1 & \epsilon\lambda \\ \epsilon\lambda & \tilde{I}_2 \end{bmatrix} \quad (12)$$

where, for the relative angle $\phi = \theta_2 - \theta_1$ - the sole coordinate of the base space B , the function λ is given by $\lambda(\phi) = d_1 d_2 \cos(\phi)$ and also

$$\tilde{I}_i = I_i + \epsilon d_i^2 \quad \text{and} \quad \epsilon = \frac{m_1 m_2}{m_1 + m_2}.$$

From (1), the system Lagrangian specializes to

$$L(v_q) = \frac{1}{2} \langle \langle \dot{q}, \dot{q} \rangle \rangle_G = \frac{1}{2} \boldsymbol{\omega}^T \mathbb{J} \boldsymbol{\omega} + \frac{1}{2} m \|\dot{\mathbf{r}}_{cm}\|^2$$

where \mathbb{J} is given in (12) and $m = m_1 + m_2$ is the system total mass. Using (7) to define the new momentum vector $\boldsymbol{\mu}' = [p_{\theta_{cm}}, p_\phi]^T$, the system Hamiltonian $H_0(\phi, \mathbf{p}_{cm}, \boldsymbol{\mu}')$ function is written, from (2), as

$$H_0 = \frac{1}{2} \boldsymbol{\mu}'^T ([P]\mathbb{J}(\phi)[P]^T)^{-1} \boldsymbol{\mu}' + \frac{\|\mathbf{p}_{cm}\|^2}{m}.$$

System input is made up by two thrusters (f_1, f_2) and a joint torque T . The equations of motion for the translational (trivial) dynamics are, from (9):

$$\begin{aligned} \dot{r}_x &= \frac{p_x}{m_1 + m_2} = \frac{p_x}{m} & \text{and} & \quad \dot{p}_x = \sin(\phi/2 - \theta_{cm})f_1 + \cos(\phi/2 + \theta_{cm})f_2, \\ \dot{r}_y &= \frac{p_y}{m_1 + m_2} = \frac{p_y}{m} & \text{and} & \quad \dot{p}_y = \cos(\phi/2 - \theta_{cm})f_1 - \sin(\phi/2 + \theta_{cm})f_2. \end{aligned} \quad (13)$$

which, in this case, the evaluation of the interaction Hamiltonians give

$$\begin{bmatrix} \frac{\partial H_1}{\partial r_x} & \frac{\partial H_2}{\partial r_x} \\ \frac{\partial H_1}{\partial r_y} & \frac{\partial H_2}{\partial r_y} \end{bmatrix} = \begin{bmatrix} \sin(\theta_{cm} - \phi/2) & \sin(\theta_{cm} + \phi/2) \\ \cos(\theta_{cm} - \phi/2) & \cos(\theta_{cm} + \phi/2) \end{bmatrix}.$$

The system rotational dynamics on $SE(2)$, from (11) and reparametrized with the mapping (7) and its cotangent lift, are determined by

$$\dot{\theta}_{cm} = \frac{\partial H_0}{\partial p_{\theta_{cm}}} = \frac{1}{2} \frac{p_{\theta_{cm}}}{(\tilde{I} + K \cos(\phi))} \quad \text{and} \quad \dot{p}_{\theta_{cm}} = -\frac{\partial H_0}{\partial \theta_{cm}} + \tau_p, \quad \left(\frac{\partial H_0}{\partial \theta_{cm}} = 0 \right) \quad (14)$$

where $d_i = d$, $\tilde{I}_i = \tilde{I}$, and $K = \epsilon d^2$. The external torque τ_p is function of the propulsion forces f_i and of the distances from system center of mass to the points of action of these f_i forces. Thus, from free body diagrams, we get:

$$\tau_p = (d/2)(\cos(\phi) + 1)(f_2 - f_1). \quad (15)$$

Observe that the system translational and rotational dynamics, described by the momenta of the $SE(2)$ group directions, $(\mathbf{p}_{cm}, p_{\theta_{cm}})$, is conserved. Hence, the angular momenta $p_{\theta_{cm}}$, also given by the bodies individual angular momentum $\mu_1 + \mu_2$, is constant. The reduced rotational dynamics (11), by:

$$\dot{\phi} = \frac{\partial H_0}{\partial p_\phi} = \frac{2p_\phi}{(\tilde{I} - K \cos(\phi))} \quad \text{and} \quad \dot{p}_\phi = -\frac{\partial H_0}{\partial \phi} + T = \frac{K \sin(\phi)}{4} \left(\frac{4p_\phi^2}{(\tilde{I} - K \cos(\phi))^2} - \frac{p_{\theta_{cm}}^2}{(\tilde{I} + K \cos(\phi))^2} \right) + T.$$

The torque T is realized by rotational actuator delivering torque at the joint.

The 2-body system dynamics is given by the drift vector field $f = (\dot{r}_x, \dot{r}_y, \dot{\theta}_{cm}, \dot{\phi}, \dot{p}_x, \dot{p}_y, \dot{p}_{\theta_{cm}}, \dot{p}_{\phi})^T$ and by the (f_1, f_2, T) -parameterized input vector fields

$$g_1 = \begin{bmatrix} \mathbf{0}_{(1 \times 4)} \\ \cos(\phi/2 - \theta_{cm}) \\ \sin(\phi/2 - \theta_{cm}) \\ -(d/2)(\cos(\phi) + 1) \\ 0 \end{bmatrix}, \quad g_2 = \begin{bmatrix} \mathbf{0}_{(1 \times 4)} \\ \cos(\phi/2 + \theta_{cm}) \\ -\sin(\phi/2 + \theta_{cm}) \\ (d/2)(\cos(\phi) + 1) \\ 0 \end{bmatrix}, \quad g_3 = \begin{bmatrix} \mathbf{0}_{1 \times 4} \\ 0 \\ \vdots \\ 0 \\ 1 \end{bmatrix}.$$

The two bottom lines of the drift vector field f correspond to the time-rate of the angular momenta $p_{\theta_{cm}}, p_{\phi}$. These equations of motion degenerate to the rigid body dynamics when the two bodies are at relative rest ($\dot{\phi} \equiv 0$).

Example: Phase Space parametrization for the N -Body System

We next propose a couple of examples which could encompass systems which are composed of bodies with different inertia and geometric properties. One possibility is to modify (7) to define system orientation θ_{cm} given by a weighted sum of the bodies attitudes with their corresponding inertia values

$$\theta_{cm} = \frac{I_1\theta_1 + I_2\theta_2 + \dots + I_N\theta_N}{I_1 + I_2 + \dots + I_N} = \frac{1}{\sum_{i=1}^N I_i} \sum_{i=1}^N I_i\theta_i$$

where I_i is the inertia of the i -th body. Notice that the above renders a constant point transformation P .

One could be led to conjecture whether it is possible to obtain a system phase space parametrization which decouples the system orientation θ_{cm} coordinate dynamics from those of shape space coordinates ϕ . It is easy to check that the above constant transformations for the 2-body system provide this sought for decomposition given its relatively simple dynamics. For an arbitrary N -body system this is also possible because the inertia matrix \mathbb{J} is real symmetric. In fact, by the (finite) real spectral theorem, any symmetric matrix can be diagonalized by an orthogonal matrix whose columns are the corresponding matrix eigenvectors. Hence, for the matrix V composed of the orthogonal eigenvectors of \mathbb{J} , we get

$$\mathbb{J}_d(\phi) = V^{-1}(\phi)\mathbb{J}(\phi)V(\phi) = V^T(\phi)\mathbb{J}(\phi)V(\phi),$$

where \mathbb{J}_d is the diagonal inertia matrix. However, in order to write the system Lagrangian or Hamiltonian under the new parametrization (q', p') we need \mathbb{J}_d as a function of the new rotational configuration coordinates in q' . Hence, one needs to integrate $\delta q' = V(q)\delta q$, solve for $q = q(q')$ and plug it in $\mathbb{J}_d(q)$ to get $\mathbb{J}_d(q')$. And this represents a major approach drawback given it is extremely difficult - if not impossible - to obtain the inverse coordinate transformation since V in $\delta q' = V(q)\delta q$ may be transcendental.

We propose instead to decouple the θ_{cm} dynamics from the base space (internal) dynamics, which corresponds to a block diagonal inertia matrix. This is clearly a less demanding task than the above full diagonalization of \mathbb{J} . We seek a diffeomorphism P such that θ_{cm} depends only on the conjugate momentum $p_{\theta_{cm}}$:

$$\dot{\theta}_{cm} = \frac{p_{\theta_{cm}}}{I_t(\phi)}, \quad I_t(\phi) = \mathbf{1}_N^T \mathbb{J}(\phi) \mathbf{1}_N,$$

where I_t is the locked inertia tensor. Defining the coordinate θ_{cm} by simply integrating the above expression we get

$$\theta_{cm}(\phi) := \int_0^{t^*} \frac{\mathbf{1}_N^T \mathbb{J}(\phi) \dot{\theta}}{\mathbf{1}_N^T \mathbb{J}(\phi) \mathbf{1}_N} dt = \int_{\theta^0}^{\theta^*} \frac{\mathbf{1}_N^T \mathbb{J}(\phi)}{\mathbf{1}_N^T \mathbb{J}(\phi) \mathbf{1}_N} d\theta = \int_{\theta_1^0}^{\theta_1^*} \frac{\mathbf{1}_N^T J_1(\theta)}{\mathbf{1}_N^T \mathbb{J}(\theta) \mathbf{1}_N} d\theta_1 + \dots + \int_{\theta_N^0}^{\theta_N^*} \frac{\mathbf{1}_N^T J_N(\theta)}{\mathbf{1}_N^T \mathbb{J}(\theta) \mathbf{1}_N} d\theta_N,$$

where $\mathbb{J} = [J_1 \dots J_N]$. Of course the system θ_{cm} dynamics in this case depends on the system shape given that the locked inertia tensor varies with shape space coordinates ϕ and so, therefore, $P = P(\phi)$. The corresponding diffeomorphism P between the momenta coordinates is equally derived by the cotangent lifting as described in the Appendix A.

GEOMETRIC PHASES

Generally, the system motion in the bundle T^*Q with a cyclic motion in the base space B undergoes a shift in a direction not belonging to B called a phase shift or geometric phase, for zero total momentum. The magnitude of this shift is a function of the curvature of the connection, i.e. a measure of how curved a space is, and the area enclosed by the path the system dynamics performs in B . This shift is often given by an element of a group G , such as a rotation or translation group. Hence, changes in internal shape generate a shift in the system overall orientation. As will be seen next, the phase shift is related to the changing of the locked inertial tensor since it is dependent on the shape of the system.

System angular momenta $\boldsymbol{\mu}$, given in the inertial frame, may be obtained by the following relation with the system's $N \times N$ inertia matrix \mathbb{J} and angular velocity $\boldsymbol{\omega}$:

$$\boldsymbol{\mu} = \mathbb{J}\boldsymbol{\omega} \quad (16)$$

The system total angular momentum $\bar{\boldsymbol{\mu}}$ is computed by adding all the bodies individual angular momenta

$$\bar{\boldsymbol{\mu}} = \sum_{k=1}^N \boldsymbol{\mu}_k = \mathbf{1}_N^T \mathbb{J} \boldsymbol{\omega} \quad (17)$$

where $\mathbf{1}_N$ is a column vector of one's with N entries. The system is assumed to have zero total momentum, thus we can write:

$$\mathbf{1}_N^T \mathbb{J} \boldsymbol{\omega} = \bar{\boldsymbol{\mu}} = 0, \quad \Rightarrow \quad \mathbf{1}_N^T \mathbb{J} d\boldsymbol{\theta} = 0 \quad (18)$$

where $d\boldsymbol{\theta} = [d\theta_1, \dots, d\theta_N]^T$. Expanding the vector $d\boldsymbol{\theta}$, it follows that

$$\begin{aligned} d\boldsymbol{\theta} &= \begin{bmatrix} d\theta_1 \\ d\theta_1 - (d\theta_1 - d\theta_2) \\ \vdots \\ d\theta_1 - (d\theta_1 - d\theta_2) \cdots - (d\theta_{N-1} - d\theta_N) \end{bmatrix} = \begin{bmatrix} d\theta_1 \\ d\theta_1 \\ \vdots \\ d\theta_1 \end{bmatrix} + \begin{bmatrix} 0 \\ -(d\theta_1 - d\theta_2) \\ \vdots \\ -(d\theta_1 - d\theta_2) \cdots - (d\theta_{N-1} - d\theta_N) \end{bmatrix} \\ &= \begin{bmatrix} 1 \\ 1 \\ \vdots \\ 1 \end{bmatrix} d\theta_1 + \begin{bmatrix} 0 & 0 & \cdots & 0 \\ 1 & 0 & \cdots & 0 \\ \vdots & \cdots & \cdots & \vdots \\ 1 & 1 & \cdots & 1 \end{bmatrix} \begin{bmatrix} d\phi_1 \\ d\phi_2 \\ \vdots \\ d\phi_N \end{bmatrix} \\ &= \mathbf{1}_N d\theta_1 + \mathbf{M} d\boldsymbol{\phi} \end{aligned}$$

where \mathbf{M} is a $N \times (N - 1)$ matrix. The above gives

$$\mathbf{1}_N^T \mathbb{J} d\boldsymbol{\theta} = \mathbf{1}_N^T \mathbb{J} \mathbf{1}_N d\theta_1 + \mathbf{1}_N^T \mathbb{J} \mathbf{M} d\boldsymbol{\phi},$$

and considering zero angular momentum and from Eq. (18) we have

$$\mathbf{1}_N^T \mathbb{J} \mathbf{1}_N d\theta_1 = -\mathbf{1}_N^T \mathbb{J} \mathbf{M} d\boldsymbol{\phi} \quad \Rightarrow \quad d\theta_1 = -\frac{\mathbf{1}_N^T \mathbb{J} \mathbf{M}}{\mathbf{1}_N^T \mathbb{J} \mathbf{1}_N} d\boldsymbol{\phi}$$

yielding

$$\Delta\theta_1 = -\int_{\Gamma} \frac{\mathbf{1}_N^T \mathbb{J} \mathbf{M}}{\mathbf{1}_N^T \mathbb{J} \mathbf{1}_N} d\boldsymbol{\phi} = -\int_{\Gamma} \mathcal{A}(\boldsymbol{\phi}) d\boldsymbol{\phi} \quad (19)$$

where Γ is a closed path contour in the base or shape space. The system mechanical connection \mathcal{A} is concerned with the contribution of system motion in the base space to the group directions, Souza and Maruyama (2007). The scalar $\mathbf{1}_N^T \mathbb{J} \mathbf{1}_N$ is the system's locked inertia with shape determined by $\boldsymbol{\phi}$. By Frobenius's theorem this phase shift determines a non-integrable constraint, as in general in the case of nonholonomic systems. In particular, it defines a linear constraint in the angular relative velocities⁴.

The Geometric Context

Recall that the $SE(2)$ group is not abelian which, in turn, renders a non-abelian Lie algebra $\mathfrak{se}(2)$. It can be shown that the dynamics on the $SO(2)$ abelian part decouples from the vector space \mathbb{R}^2 and non-abelian part of the group. The holonomy of the connection, that is mechanical, derives from the abelian part only of the group space $SE(2)$. Hence, for $g(0) = I_3$, the holonomy for an abelian group may be computed as a line integral Marsden *et al.* (1990):

$$g(1) = \exp\left(-\int_0^1 \mathcal{A}_{\mathfrak{g}}(\boldsymbol{\phi}) \dot{\boldsymbol{\phi}}(t) dt\right) = \exp\left(-\int_{\Gamma} \mathcal{A}_{\mathfrak{g}}(\boldsymbol{\phi}) d\boldsymbol{\phi}\right) \quad (20)$$

⁴There are also examples in which the constraint exists as a nonlinear function of the velocity

where $\mathcal{A}_{\mathfrak{g}} : TQ \rightarrow \mathfrak{g}$ is the abelian component of the connection and $\exp : \mathfrak{se}(2) \rightarrow SE(2)$ is the exponential map given by:

$$\exp(\omega, v_x, v_y) = (\theta, r_x, r_y)$$

where $(\omega, v_x, v_y) \in \mathbb{R}^3 \simeq \mathfrak{se}(2)$, where the \exp map for $SE(2)$ is detailed in the Appendix B. Notice that the expression (20) does not involve a parametrization of the closed path transversed on the shape space.

The holonomy of the non-abelian or translational component, on the other hand, does depend on the starting and finishing points of the chosen parametrization.

In the case where the symmetry group G is an abelian group, the phase shift may also be computed by the curvature \mathcal{B} of the principle connection, which, from (20) gives:

$$\text{holonomy} := \theta(1) = - \int_{\Gamma} \mathcal{A}(\phi) d\phi = - \iint_{\Omega} \mathcal{B} d\Omega \quad (21)$$

where Ω is the area enclosed within Γ and $\Gamma = \partial\Omega$. The last equality above stems from Green's Theorem. The magnitude of the phase shift depends on (is a function of) the curvature of the connection and the area enclosed by the path transversed in the base space.

Example: Geometric Phases for the 3-Body System

From (19), the geometric phase can be computed according to the following expression:

$$\begin{aligned} \Delta\theta_1 &= - \int_{\Gamma} \mathcal{A}(\phi) d\phi = - \int_{\Gamma} [f_1(\phi) d\phi_1 + f_2(\phi) d\phi_2] \\ &= - \left[\int_{(0,0)}^{(\alpha,0)} f_1(\phi) d\phi_1 + \int_{(\alpha,0)}^{(\alpha,\beta)} f_2(\phi) d\phi_2 + \int_{(\alpha,\beta)}^{(0,\beta)} f_1(\phi) d\phi_1 + \int_{(0,\beta)}^{(0,0)} f_2(\phi) d\phi_2 \right] \end{aligned}$$

where Γ is the loop in the (ϕ_1, ϕ_2) -space: $\Gamma = [(0, 0), (\alpha, 0), (\alpha, \beta), (0, \beta), (0, 0)]$. Alternatively, the curvature of the connection in this case could be computed by the two-form \mathcal{B} as

$$\mathcal{B} = d\mathcal{A} = \left(\frac{\partial f_2}{\partial \phi_1} - \frac{\partial f_1}{\partial \phi_2} \right) d\phi_1 \wedge d\phi_2 \quad (22)$$

Geometric phases could be used as an input strategy, along with the thruster inputs, to modify the system overall orientation.

CONCLUSION & FUTURE RESEARCH

In the paragraphs above, a geometric approach for the dynamical modeling in the Hamiltonian setting was reviewed with relative detail and employed to the modeling of the proposed multibody system. Emphasis was given to the geometric interpretation of the input structure for the proposed multibody system, the system geometric phase variation with internal motion only, and examples of the system phase space parametrization. Current research efforts concentrate on trajectory generation techniques for this class of systems.

ACKNOWLEDGEMENTS

The authors thank CAPES for financial support, Prof. N. E. Leonard for hosting the first author's one-year research visit to Princeton University and colleague Marko Ackermann from FEI for a fruitful discussion.

REFERENCES

- Bullo, F. and Lewis, A.D., 2005. *Geometric Control of Mechanical Systems: Modeling, Analysis, and Design for Simple Mechanical Systems*, Vol. 49 of *Texts in Applied Mathematics*. Springer.
- Cortizo, S.F., 1991. "Classical mechanics - on the deduction of lagrange's equations". *Reports on Mathematical Physics*, Vol. 29, No. 1, pp. 45-54.
- Dubowsky, S. and Papadopoulos, E., 1993. "The kinematics, dynamics, and control of free-flying and free-floating space robotic systems". *IEEE Transactions on Robotics and Automation*, Vol. 9, No. 5, pp. 531-543.
- Lanczos, C., 1986. **The Variational Principles of Mechanics**. Dover Publications, Inc., 4th edition.
- Marsden, J.E., Montgomery, R. and Ratiu, T.S., 1990. "Reduction, symmetry, and phases in mechanics". *Memoirs American Mathematical Society*, Vol. 88, No. 436.

- Rui, C., Kolmanovsky, I.V. and McClamroch, N.H., 2000. “Nonlinear attitude and shape control of spacecraft with articulated appendages and reaction wheels”. *IEEE Transactions on Automatic Control*, Vol. 45, No. 8, pp. 1455–1469.
- Souza, E.C. and Maruyama, N., 2007. “Lagrangian modeling for a class of mobile multibody systems”. *Proc. of the 3rd IFAC Symposium on Systems, Structure and Control, Foz do Iguaçu, Brazil*.
- Souza, E.C. and Maruyama, N., 2010. “Feedback linearization for stabilization of a class of mobile, multibody systems”. *Proc. of the 49th IEEE Conference on Decision and Control, Atlanta, USA*.
- Sreenath, N., 1987. *Modeling and Control of Multibody Systems*. Ph.d. thesis report, University of Maryland.
- Yuh, J. and West, M., 2001. “Underwater robotics”. *Advanced Robotics*, Vol. 15, No. 5, pp. 609–639. Review paper.

APPENDIX A: COTANGENT LIFT OF A MAPPING

The cotangent lift T^*f of a diffeomorphism f is computed by the pairing

$$\langle T^*f(\mu'), \omega \rangle = \langle \mu, Tf(\omega) \rangle$$

The above is none other than a restatement of Hamilton’s principle with the Legendre transformed Lagrangian and which remains invariant under point transformations, Lanczos (1986). Evaluating the above pairing for the diffeomorphism $f = P$, when P is realized by the matrix $[P]$, gives

$$\begin{aligned} \langle \mu, Tf(\omega) \rangle &= tr((\mu')^T [P] \omega) \\ &= tr(\omega^T [P]^T \mu') \\ &= \langle \omega, [P]^T \mu' \rangle \end{aligned}$$

Therefore, $\mu = T^*f(\mu') = [P]^T \mu'$ and the old and new momenta coordinates are related by

$$\mu = [P]^T \mu' \quad \Leftrightarrow \quad \mu' = ([P]^T)^{-1} \mu$$

APPENDIX B: EXPONENTIAL MAPPING

The exponential map $\exp : \mathfrak{se}(2) \rightarrow SE(2)$ is defined by

$$\exp(\xi) = \gamma_\xi(1), \quad \xi \in \mathfrak{se}(2)$$

where γ is an integral curve which is tangent to the group identity element I_3 at time 0, i.e., $\gamma_\xi(0) = I_3$. For a given algebra element $t\xi = t(\omega, \mathbf{v}) \in \mathfrak{se}(2)$ we get, for $t\omega \neq 0$

$$\exp(t\xi) = \begin{bmatrix} \mathbf{R}(t\omega) & \mathbf{p}(t) \\ \mathbf{0} & 1 \end{bmatrix} \in SE(2) \quad (23)$$

where

$$\mathbf{p}(t) = \frac{1}{t\omega} \begin{bmatrix} \sin(t\omega) & -(1 - \cos(t\omega)) \\ 1 - \cos(t\omega) & \sin(t\omega) \end{bmatrix} \begin{bmatrix} tv_x \\ tv_y \end{bmatrix}$$

When $t\omega = 0$, it follows from l’Hospital rule that $\exp(t\xi)$ is simply $t\xi$.

RESPONSIBILITY NOTICE

The authors are the only responsible for the printed material included in this paper.

A BAYESIAN INFERENCE APPROACH TO ESTIMATE ELASTIC AND DAMPING PARAMETERS OF A STRUCTURE SUBJECTED TO VIBRATION TESTS

Carlos F. Matt¹ and Daniel A. Castello²

¹ Department of Lines and Substations, Electric Power Research Center (CEPEL), Avenida Horácio Macedo 354, Ilha do Fundão, Rio de Janeiro, Brazil, P.O. Box 68007, Zip Code 21941-590

² Department of Mechanical Engineering, Federal University of Rio de Janeiro (Poli/COPPE), Avenida Um sem número, Ilha do Fundão, Rio de Janeiro, Brazil, P.O. Box 68005, Zip Code 21945-970

Abstract. *In the present work, deterministic and statistical inversion approaches are employed to estimate one spring stiffness and one viscous damping coefficient of a two degree-of-freedom spring-mass-damper system. Simulated measurements derived from the solution of the corresponding forward problem corrupted with noise are used for the estimation process of the target parameters. Three inverse problem formulations are investigated. In the first one, the variance of the error is assumed to be known and the sought-after parameters are estimated from the minimization of the ordinary least-squares norm. Two different scenarios, in which multiple experimental data are available independently or simultaneously for the inverse analysis, are investigated. In the second one, the variance of the error is known and from the Bayesian statistical inversion approach, one derives both point estimates and probability distributions for the unknown parameters. Finally, in the third one, the variance of the error is unknown and also becomes a sought-after parameter. Again, with the Bayesian statistical inversion approach, one derives both point estimates and probability distributions for the unknown parameters. Markov Chain Monte Carlo sampling methods with the Metropolis-Hastings algorithm are employed in order to draw samples from the posterior distribution and then to compute statistics for the unknown parameters of interest.*

Keywords: *inverse problems; Bayesian inference; parameter estimation; structural dynamics; uncorrelated errors*

INTRODUCTION

In the last decades one has faced an increasing level of complexity associated with engineering design, particularly due to the use of advanced materials. This trend naturally leads to an ever increasing need for robust and accurate characterization methods. Inverse problems have played an essential role in this scenario and received much attention in diverse engineering branches, e.g., heat conduction [9, 10, 11, 13], geophysics [8], solid mechanics, structural vibrations [15], to name just a few. Inverse problems seek to infer parameters characterizing a physical system of interest from indirect measurements of some of its features. Suitable methods for reliable inferences should take into account the maximum of information and data available from both theoretical and practical knowledge. Inverse problems are also particularly attractive in situations where the direct measurement of a target feature for the system under analysis is unfeasible, which is quite usual in many industry environments. On the other hand, inverse problems are often ill-posed in the sense that the solution may not exist and be unique and, more importantly, it does not depend continuously on the data such that a small perturbation in the data may cause large deviations in the solution [1]. Regularization methods try to alleviate this shortcoming by modifying the original ill-posed problem to an approximate biased well-posed problem; the most widely used are Tikhonov's regularization procedure and Beck's function approach [5].

In practical applications, data are always noisy and uncertain due to inherent variability in the measurement process. Furthermore, the forward model may be imperfect and imprecise due to unavoidable simplifications made when one constructs a mathematical model for a physical system of interest; hence, predictive quantities are also uncertain. Several methods have been proposed in order to address inverse problems under uncertainties, e.g., sensitivity analysis [8], the extended maximum likelihood method [4], the spectral stochastic method [3] and the Bayesian inference approach [5, 6].

Bayesian inference approach offers a rigorous framework for inverse problems with noisy data and uncertain forward models. It yields an ensemble of inverse solutions consistent with the given data in the form of a probability distribution, namely, the posterior probability density function, which encapsulates all available information about the inverse problem. Once the posterior probability distribution becomes available, various summarizing statistics such as expected values, modes, marginal distributions and credible intervals may be computed in order to quantify the uncertainty associated with a specific inverse solution. Bayesian inference approach contrasts with most deterministic inverse techniques, which give only a single estimate of the inverse solution without assessing its uncertainty. In most deterministic inverse techniques, neither errors in the measured data nor uncertainties in model predictions are rigorously accounted for. At best, the error covariances are incorporated into a weighted least-squares norm to be minimized. Another interesting feature of Bayesian inference approach, not explored in this work, is that it also provides a flexible regularization to the inverse solution since the non-trivial problem of selecting an appropriate regularization parameter may be resolved through hierarchical models;

see References [6, 1] for further details.

In the present work, both deterministic and Bayesian inference approaches are employed to estimate one spring stiffness and one viscous damping coefficient of a two degree-of-freedom spring-mass-damper system. Simulated measurements derived from the solution of the corresponding forward problem corrupted with noise are used for the estimation process of the target parameters. Three inverse problem formulations are investigated. In the first inverse problem formulation, the variance of the error is assumed to be known and the unknown parameters are estimated from the minimization of the ordinary least-squares norm. Two different scenarios, in which multiple experimental data are available independently or simultaneously for the inverse analysis, are investigated. In the second inverse problem formulation, the variance of the error is assumed to be known and from the Bayesian inference approach, one derives both point estimates and posterior probability distributions for the unknown parameters. Finally, in the third inverse problem formulation, the variance of the error is unknown and also becomes a sought-after parameter. With the Bayesian inference approach, one derives point estimates and posterior probability distributions for the unknown parameters, including the error variance. Markov Chain Monte Carlo sampling methods with the Metropolis-Hastings algorithm [6, 16] are employed in order to draw samples from the posterior distribution and then to compute statistics such as means, variances and covariances.

The paper is organized as follows. In section 2 one describes both deterministic and statistical inverse problem solutions. In section 3, one describes the physical system under investigation, the forward model, the strategy to generate the simulated experimental data and the estimates for the unknown parameters obtained with a deterministic and Bayesian inference approaches described on section 2. Finally, section 4 provides the main conclusions and final remarks.

INVERSE PROBLEM

Given a parameter vector $\boldsymbol{\theta} \in \mathcal{D}$, where \mathcal{D} denotes the parameter space, the forward problem comprises the solution of the governing equations that describe mathematically the physical system of interest in order to determine the state \mathbf{U} ; this mathematical relationship may be written in a general form as

$$\mathcal{M}(\mathbf{U}, \boldsymbol{\theta}) = 0 \quad (1)$$

where \mathcal{M} denotes a mathematical operator (possibly nonlinear) that maps the parameter vector $\boldsymbol{\theta} \in \mathbb{R}^{N_\theta}$ into the state vector $\mathbf{U} \in \mathbb{R}^{N_U}$, with N_θ and N_U being, respectively, the number of model parameters and the number of states that completely describes the physical system under investigation. Outputs of interest, $\bar{\mathbf{y}} \in \mathbb{R}^{N_y}$, may also be expressed in terms of the state \mathbf{U} and the parameter vector $\boldsymbol{\theta}$ through the following general relationship

$$\mathcal{C}(\mathbf{U}(\boldsymbol{\theta}), \bar{\mathbf{y}}) = 0 \quad (2)$$

where the mathematical operator \mathcal{C} maps the state \mathbf{U} to the outputs of interest $\bar{\mathbf{y}}$ and N_y denotes the total number of observed data. Depending on the system investigated, the outputs of interest may coincide with the state \mathbf{U} itself. For simplicity of notation, the outputs from the forward model, $\bar{\mathbf{y}}$, may also be shortly written as $\bar{\mathbf{y}}(\boldsymbol{\theta})$. The associated inverse problem involves determining an unknown parameter vector $\boldsymbol{\theta}$ given a set of measurements of the outputs $\mathbf{y} \in \mathbb{R}^{N_y}$.

Deterministic approach

Given a set of measurements of the outputs $\mathbf{y} \in \mathbb{R}^{N_y}$, the deterministic approach comprises the estimation of the unknown parameters $\boldsymbol{\theta}$ by writing the inverse problem as an optimization problem of the kind

$$\min_{\boldsymbol{\theta}} \|\mathbf{y} - \bar{\mathbf{y}}(\boldsymbol{\theta})\|_{L_2}^2 \quad (3)$$

subjected to the following restrictions

$$\mathcal{M}(\mathbf{U}, \boldsymbol{\theta}) = 0 \quad (4)$$

$$\mathcal{C}(\mathbf{U}(\boldsymbol{\theta}), \bar{\mathbf{y}}) = 0 \quad (5)$$

and $\boldsymbol{\theta} \in \mathcal{D}$. Many optimization algorithms may be employed to solve the above inverse problem; in this work, it is solved through the classical Levenberg-Marquardt iterative procedure [12].

Bayesian inference approach

Bayesian inference approach reformulates the inverse problem as a statistical inference problem. Now, the solution of the inverse problem takes a form of a posterior probability distribution $p(\boldsymbol{\theta}|\mathbf{y})$ which is the conditional probability distribution of the unknown parameters given a set of measurements of outputs or observed data \mathbf{y} . Within the Bayesian framework, both predicted and observed quantities are regarded as random variables. The randomness is directly connected to the concept of uncertainty. Hence, the central characteristic of Bayesian inference approach is an explicit use of

probabilities for quantifying uncertainties. Using Bayes' theorem for conditional probabilities, the posterior probability distribution can be written as

$$p(\boldsymbol{\theta}|\mathbf{y}) = \frac{p(\mathbf{y}|\boldsymbol{\theta})p(\boldsymbol{\theta})}{p(\mathbf{y})} \quad (6)$$

where $p(\boldsymbol{\theta})$ denotes the prior probability distribution, $p(\mathbf{y})$ denotes the marginal probability distribution of the observed data and $p(\mathbf{y}|\boldsymbol{\theta})$ denotes the likelihood function, which corresponds to the conditional probability of the observed data given a set of input parameters. The prior probability distribution contains all available information on the distribution of $\boldsymbol{\theta}$ before any measurements have been incorporated into the inference. The likelihood function represents the probability distribution of the errors between output model predictions, $\bar{\mathbf{y}}(\boldsymbol{\theta})$, and actual observed data, \mathbf{y} . For a fixed set of observed data \mathbf{y} , $p(\mathbf{y})$ is independent of $\boldsymbol{\theta}$; hence, it may be regarded as a normalization constant and given by

$$p(\mathbf{y}) = \int_{\mathcal{D}} p(\mathbf{y}|\boldsymbol{\theta})p(\boldsymbol{\theta}) d\boldsymbol{\theta} \quad (7)$$

such that Eq. (6) may be rewritten as follows

$$p(\boldsymbol{\theta}|\mathbf{y}) \propto p(\mathbf{y}|\boldsymbol{\theta})p(\boldsymbol{\theta}) \quad (8)$$

henceforth designated as the unnormalized posterior probability distribution. The posterior probability distribution (possibly unnormalized) is thus the final goal of a Bayesian inference approach. Note that the normalizing constant $p(\mathbf{y})$ involves multidimensional integrals, which may be hard to compute for high-dimensional parameter space \mathcal{D} .

In a general case, no information is assumed about the unknown parameters $\boldsymbol{\theta}$, except that it must rely on the parameter domain \mathcal{D} [18]. Thus, non-informative prior distributions, such as a uniform distribution over $\boldsymbol{\theta} \in \mathcal{D}$, are commonly enforced. However, if additional information about the distribution of $\boldsymbol{\theta}$ is available, it would be incorporated into the prior distribution. Another interesting feature of a Bayesian inference approach is its capability to make posterior predictions for unobservable quantities of interest, once $p(\boldsymbol{\theta}|\mathbf{y})$ becomes available. Denoting by $\tilde{\mathbf{y}}$ an unobservable quantity of interest different from the outputs $\bar{\mathbf{y}}$, its posterior probability distribution may be computed as follows

$$p(\tilde{\mathbf{y}}|\mathbf{y}) = \int_{\mathcal{D}} p(\tilde{\mathbf{y}}|\boldsymbol{\theta})p(\boldsymbol{\theta}|\mathbf{y}) d\boldsymbol{\theta} \quad (9)$$

where the probability distribution $p(\tilde{\mathbf{y}}|\boldsymbol{\theta})$ may be obtained from uncertainty propagation through the general predictive model $\mathcal{H}(\boldsymbol{\theta}, \tilde{\mathbf{y}}) = 0$.

Markov chain Monte Carlo (MCMC) sampling

To sum up, the end result of modelling in the Bayesian formalism is the posterior distribution $p(\boldsymbol{\theta}|\mathbf{y})$. In many cases of interest, the full posterior probability distribution is analytically intractable, since the number of components in $\boldsymbol{\theta}$ may be very large and the prior probability distribution $p(\boldsymbol{\theta})$ may be nonstandard or may involve information which is difficult to express in analytical terms. In these situations, inference about the unknown parameters may be treated by simulation: it is enough that the plausibility of any particular guess at $\boldsymbol{\theta}$ be tested by simulating the physical process leading from $\boldsymbol{\theta}$ to $\bar{\mathbf{y}}$. Samples from a set $\Theta \subset \mathcal{D}$ are drawn, each sample drawn with the posterior probability $p(\boldsymbol{\theta}|\mathbf{y})$. In this way, one gets the set $\Theta = \{\boldsymbol{\theta}^{(1)}, \boldsymbol{\theta}^{(2)}, \dots, \boldsymbol{\theta}^{(N_s)}\}$ of samples distributed like the posterior distribution; hence, inference on the posterior state space becomes inference on the set Θ . For instance, the posterior mean, $\boldsymbol{\mu}_{\boldsymbol{\theta}|\mathbf{y}}$, defined as

$$\boldsymbol{\mu}_{\boldsymbol{\theta}|\mathbf{y}} \equiv E[\boldsymbol{\theta}|\mathbf{y}] = \int_{\mathcal{D}} \boldsymbol{\theta} p(\boldsymbol{\theta}|\mathbf{y}) d\boldsymbol{\theta} \quad (10)$$

may be computed as

$$\boldsymbol{\mu}_{\boldsymbol{\theta}|\mathbf{y}} \approx \frac{1}{N_s} \sum_{k=1}^{N_s} \boldsymbol{\theta}^{(k)} \quad (11)$$

for independent samples $\boldsymbol{\theta}^{(k)}$, $k = 1, 2, \dots, N_s$, drawn from the posterior distribution $p(\boldsymbol{\theta}|\mathbf{y})$. Likewise, the posterior covariance matrix, $\boldsymbol{\Sigma}_{\boldsymbol{\theta}|\mathbf{y}}$, and the posterior mode or the maximum a posteriori estimate, $\hat{\boldsymbol{\theta}}_{\text{MAP}}$, defined as

$$\boldsymbol{\Sigma}_{\boldsymbol{\theta}|\mathbf{y}} \equiv E[(\boldsymbol{\theta} - \boldsymbol{\mu}_{\boldsymbol{\theta}})(\boldsymbol{\theta} - \boldsymbol{\mu}_{\boldsymbol{\theta}})^T] = \int_{\mathcal{D}} (\boldsymbol{\theta} - \boldsymbol{\mu}_{\boldsymbol{\theta}})(\boldsymbol{\theta} - \boldsymbol{\mu}_{\boldsymbol{\theta}})^T p(\boldsymbol{\theta}|\mathbf{y}) d\boldsymbol{\theta} \quad (12)$$

and

$$\hat{\boldsymbol{\theta}}_{\text{MAP}} = \operatorname{argmax} p(\boldsymbol{\theta}|\mathbf{y}) \quad (13)$$

may be computed as follows:

$$[\Sigma_{\theta|\mathbf{y}}]_{ij} \approx \frac{1}{N_s - 1} \sum_{k=1}^{N_s} (\theta_i^{(k)} - \mu_{\theta,i}) (\theta_j^{(k)} - \mu_{\theta,j}) \quad (14)$$

and

$$\hat{\theta}_{\text{MAP}} \approx \operatorname{argmax} \{p(\theta^{(k)}|\mathbf{y}), k = 1, 2, \dots, N_s\}. \quad (15)$$

In other words, the sample mean, the sample variance and the sample mode computed from the samples in the set Θ^N provide estimates for the posterior mean, posterior covariance matrix and posterior mode. Sampling-based methods are called Monte-Carlo methods. However, standard sampling methods are useless when the posterior probability distribution involves many variables and is otherwise intractable. In particular, one generally needs to have a closed form for the normalizing constant $p(\mathbf{y})$. On the other hand, Markov chain sampling methods are a powerful tool to simulate multivariate and nonstandard distributions and do not require the knowledge of the normalizing constant. Two widely used Markov Chain sampling methods are the Metropolis-Hastings and the Gibbs sampling algorithms [6, 16]. In the current work, the Metropolis-Hastings algorithm with a multivariate uniform proposal distribution is employed to explore the posterior state-space. The Metropolis-Hastings algorithm implemented in the current work comprises the following steps.

- Step 1. Set $k = 0$ and choose an initial value, $\theta^{(0)}$, for the the vector of unknown parameters: $\theta^{(k)} = \theta^{(0)}$.
- Step 2. While $k \leq N_s - 1$, do the following
 - Step 2.1 Generate a candidate θ^* from the proposal distribution $g(\theta^*|\theta^{(k)})$.
 - Step 2.2 Generate a random number u from the uniform distribution $U(0, 1)$.
 - Step 2.3 If $u \leq \alpha(\theta^*, \theta^{(k)})$ then $\theta^{(k+1)} = \theta^*$; otherwise, $\theta^{(k+1)} = \theta^{(k)}$.
 - Step 2.4 Set $k = k + 1$ and go to Step 2.1.

In Metropolis-Hastings algorithm above described, one adopts a symmetrical proposal distribution such that $\theta^* = \theta^{(k)} + \boldsymbol{\eta}$, where $\boldsymbol{\eta} \sim U[(-\delta_1, \delta_1) \otimes (-\delta_2, \delta_2) \otimes \dots \otimes (-\delta_{N_\theta}, \delta_{N_\theta})]$; that is, a Metropolis random walk [17]. The symbols $\delta_1, \delta_2, \dots, \delta_{N_\theta}$ are prescribed parameters that control the spread over the posterior state-space and the mixing behavior of the chain. Large values for $\delta_i, i = 1, 2, \dots, N_\theta$, imply too much rejection of the proposed candidates θ^* requiring thus a large number number of samples N_s in order to efficiently explore the posterior state-space. Meanwhile, quite small values for them imply too much acceptance of the proposed candidates θ^* in a narrow region of the posterior state-space such that a large number of samples N_s is also required to efficiently explore it.

The acceptance probability ratio, $\alpha(\theta^*, \theta^{(k)})$, is defined as

$$\alpha(\theta^*, \theta^{(k)}) = \min \left\{ 1, \frac{p(\theta^*|\mathbf{y}) g(\theta^{(k)}|\theta^*)}{p(\theta^{(k)}|\mathbf{y}) g(\theta^*|\theta^{(k)})} \right\} = \min \left\{ 1, \frac{p(\theta^*|\mathbf{y})}{p(\theta^{(k)}|\mathbf{y})} \right\} \quad (16)$$

where the last equality in Eq. (16) arises because the proposal distribution $g(\theta^*|\theta^{(k)})$ is symmetrical. A good choice for the initial state of the Markov chain, $\theta^{(0)}$, which is adopted in the current work, is the maximum a posteriori estimate, $\hat{\theta}_{\text{MAP}}$. It may be computed using well-known optimization (minimization/maximization) algorithms. In the next sections, one describes the physical system under investigation, the forward model, the strategy to numerically generate the simulated experimental data and the estimates obtained for the unknown parameters using the deterministic and the statistical approaches previously described.

RESULTS AND CONCLUSIONS

Physical system investigated

The mechanical system under investigation comprises a damped spring-mass with two degrees-of-freedom and lumped parameters as depicted in Figure 1. The (true) values of the physical parameters are $m_1 = 1 \text{ kg}$, $m_2 = 2 \text{ kg}$, $c_1 = 0.2 \text{ Nsm}^{-1}$, $c_2 = 0.4 \text{ Nsm}^{-1}$, $k_1 = 500 \text{ Nm}^{-1}$ and $k_2 = 300 \text{ Nm}^{-1}$. The unknown model parameters of interest to be estimated are k_1 and c_1 , parameterized as $k_1 = \theta_1 \times 10^2$ and $c_1 = \theta_2 \times 10^{-1}$ such that $\theta = [\theta_1 \ \theta_2]^T$.

Forward model

The forward model for the spring-mass-damper system shown in Figure 1 comprises the following coupled system of second-order ordinary differential equations, written in matrix form as

$$\begin{bmatrix} m_1 & 0 \\ 0 & m_2 \end{bmatrix} \begin{Bmatrix} \ddot{u}_1(t) \\ \ddot{u}_2(t) \end{Bmatrix} + \begin{bmatrix} c_1 + c_2 & -c_2 \\ -c_2 & c_2 \end{bmatrix} \begin{Bmatrix} \dot{u}_1(t) \\ \dot{u}_2(t) \end{Bmatrix} + \begin{bmatrix} k_1 + k_2 & -k_2 \\ -k_2 & k_2 \end{bmatrix} \begin{Bmatrix} u_1(t) \\ u_2(t) \end{Bmatrix} = \begin{Bmatrix} 0 \\ f_2(t) \end{Bmatrix} \quad (17)$$

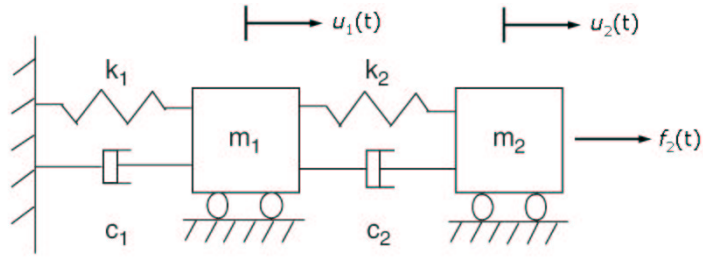


Figure 1. Two degree-of-freedom spring-mass-damper system.

and subjected to zero initial conditions, where $u_i(t)$, $i = 1, 2$, denotes the displacement of the i -th block, a dot above a variable denotes its time derivative and $f_2(t)$ denotes the excitation force applied at block 2. Defining $v_1(t)$ and $v_2(t)$ as $\dot{u}_1(t)$ and $\dot{u}_2(t)$, respectively, one may rewrite the above system of coupled second-ordinary differential equations as follows

$$\dot{\mathbf{U}} = \begin{Bmatrix} \dot{u}_1(t) \\ \dot{u}_2(t) \\ \dot{v}_1(t) \\ \dot{v}_2(t) \end{Bmatrix} = \begin{Bmatrix} v_1(t) \\ v_2(t) \\ \frac{1}{m_1} [-(c_1 + c_2)v_1(t) + c_2 v_2(t) - (k_1 + k_2)u_1(t) + k_2 u_2(t)] \\ \frac{1}{m_2} [f_2(t) + c_2 v_1(t) - c_2 v_2(t) + k_2 u_1(t) - k_2 u_2(t)] \end{Bmatrix} \quad (18)$$

or, shortly, as $\dot{\mathbf{U}}(t) = \mathbf{G}(\boldsymbol{\theta}, \mathbf{U}(t))$ with $\mathbf{U}(0) = \mathbf{0}$, which may be further recast as Eq. (1). The first two natural frequencies of the system under investigation correspond to 1.484 Hz and 4.676 Hz, respectively. These natural frequencies are the eigenvalues of the homogeneous system associated with Eq. (17) (i.e., by setting $f_2(t) = 0$). The simulated experimental data are generated assuming the displacement $u_1(t)$, at discrete time instants t_i , $i = 1, 2, \dots, N_y$, as the observed variables; in other words, $\bar{\mathbf{y}} = [u_1(t_1) \ u_1(t_2) \ \dots \ u_1(t_{N_y})]^T$. In the next subsection one describes the numerical procedure to generate the simulated experimental data.

Simulated experimental data

Figure 2 illustrates the procedure to numerically obtain the simulated experimental data, assuming that the errors ν_i , $i = 1, 2, \dots, N_y$, are additive, with zero mean and with an $N_y \times N_y$ covariance matrix $\boldsymbol{\Sigma}_e$. Hence, the components of the observed data vector, y_i , $i = 1, 2, \dots, N_y$, are generated with the aid of the following expression

$$y_i = u_1(t_i) + \nu_i \quad (19)$$

or, equivalently,

$$y_i = \bar{y}_i + \nu_i. \quad (20)$$

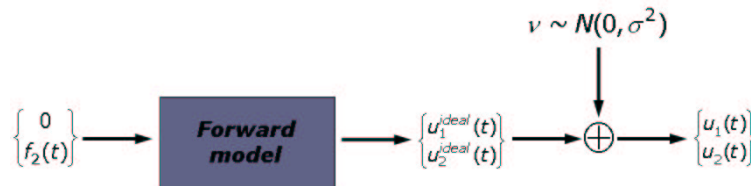


Figure 2. Procedure to numerically generate the simulated observed data for the estimation processes.

The additive errors ν_i , $i = 1, 2, \dots, N_y$ may encompass both measurement and modelling errors. Only uncorrelated errors with Gaussian distribution are investigated in the current work. Uncorrelated errors satisfy the following identity: $\text{cov}[\nu_i, \nu_j] = 0$, for $i \neq j$, $i, j \in \{1, 2, \dots, N_y\}$. By further assuming that the errors ν_i possess a constant variance σ^2 , the covariance matrix is simplified to $\boldsymbol{\Sigma}_e = \sigma^2 \mathbf{I}$, where \mathbf{I} denotes the $N_y \times N_y$ identity matrix. Hence, for these uncorrelated errors, the likelihood function becomes

$$p(\mathbf{y}|\boldsymbol{\theta}) \propto \frac{1}{(\sigma^2)^{N_y/2}} \exp \left\{ -\frac{1}{2\sigma^2} [\mathbf{y} - \bar{\mathbf{y}}(\boldsymbol{\theta})]^T [\mathbf{y} - \bar{\mathbf{y}}(\boldsymbol{\theta})] \right\}. \quad (21)$$

In order to generate the simulated observed data, the variance σ^2 needs to be computed. It is evaluated for a prescribed signal-to-noise ratio (SNR), defined as follows

$$\text{SNR} \equiv 20 \log_{10} \left(\frac{\sigma_{\bar{\mathbf{y}}}}{\sigma} \right) \quad (22)$$

where $\sigma_{\bar{y}}$ denotes the variance of the output data \bar{y} , given by

$$\sigma_{\bar{y}} = \frac{1}{N_y - 1} \sum_{i=1}^{N_y} (\bar{y}_i - \mu_{\bar{y}})^2 \quad \text{with} \quad \mu_{\bar{y}} = \frac{1}{N_y} \sum_{i=1}^{N_y} \bar{y}_i. \quad (23)$$

The observed data illustrated in Figure 3 comprise 2048 data points recorded with a sampling frequency of 409.6 Hz; hence, $t_i = (i - 1) \times (1/409.6)$, $i = 1, 2, \dots, 2048$. These data are obtained from the output of the forward model, \bar{y}_i , $i = 1, 2, \dots, 2048$, which, in turn, are computed for a sine sweep excitation $f_2(t)$ of the following kind

$$f_2(t) = 100 \cos(\Omega(t)t) \quad (24)$$

where the time-dependent excitation frequency $\Omega(t)$ grows linearly from Ω_{\min} to Ω_{\max} set, respectively, to 0 Hz and 10 Hz. Figure 4 shows the sine sweep excitation used to generate the simulated observed data indicated in Figure 3. The simulated data shown in Figure 3 are generated for an uncorrelated noise with SNR = 10 dB. Note that the lower the numerical value of the signal-to-noise ratio (in dB) the higher is the noise content in the observed data. Although the simulated data comprise 2048 data points, only the first 128 are effectively used for the inverse problem solutions, i.e., $N_y = 128$.

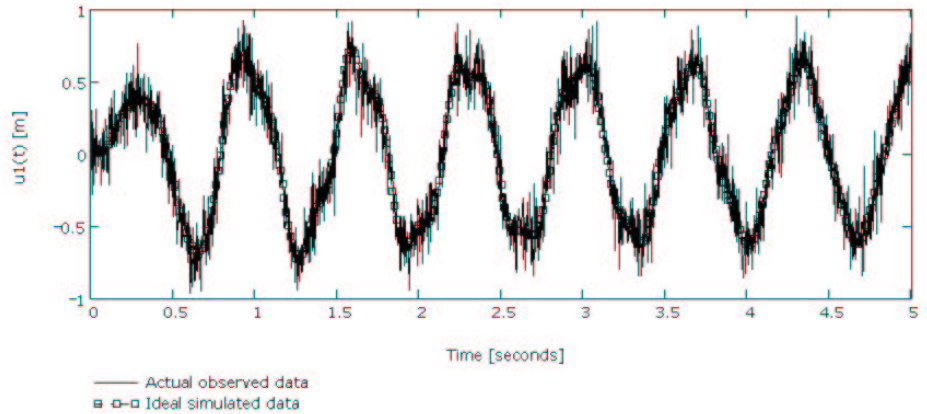


Figure 3. Simulated observed data generated with uncorrelated noise and SNR = 10 dB.

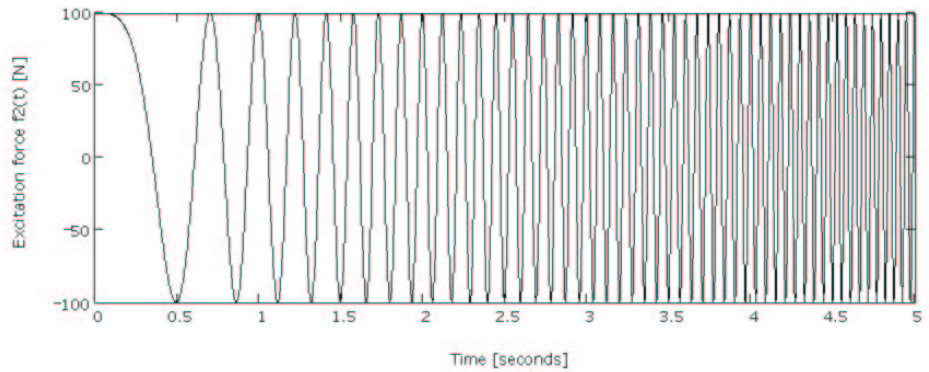


Figure 4. Sine sweep excitation $f_2(t)$ used to generate the simulated observed data.

Three inverse problem formulations are investigated, henceforth designated as IP1, IP2 and IP3. In IP1, the unknown parameters to be estimated are θ_1 and θ_2 and they are estimated from the minimization of the ordinary least-squares norm. Two different scenarios, in which multiple experimental data are available independently or simultaneously for the inverse analysis, are investigated. In IP2, one assumes that the errors are additive, uncorrelated and Gaussian distributed with known constant variance σ^2 . With the Bayesian inference approach, one derives point estimates and the joint and marginal posterior probability distributions for θ_1 and θ_2 , for Gaussian prior distributions for both θ_1 and θ_2 . IP3 is a slight modification of IP2, in which the variance σ^2 is assumed to be unknown and also becomes a parameter to be estimated from observed data. The following parameterization is adopted for σ : $\sigma = \gamma \times 10^{-1}$. Using the Bayesian inference approach, one derives an expression for the unnormalized (joint) posterior probability distribution $p(\theta, \gamma|\mathbf{y})$, from which both point estimates and marginal posterior probability distributions, $p(\theta_i|\mathbf{y})$ and $p(\gamma|\mathbf{y})$, $i \in \{1, 2\}$, are derived, for Gaussian prior distribution for θ_1 and θ_2 and for a scale invariant prior distribution for σ .

IP1: deterministic inverse solution

For IP1, the unknown parameters to be estimated are the stiffness k_1 and the viscous damping coefficient c_1 . The *deterministic* inverse solution relies on the minimization of the ordinary least-squares norm, $S_{LS}(\boldsymbol{\theta})$, given by

$$S_{LS}(\boldsymbol{\theta}) = \|\mathbf{y} - \bar{\mathbf{y}}(\boldsymbol{\theta})\|_{L_2}^2 = [\mathbf{y} - \bar{\mathbf{y}}(\boldsymbol{\theta})]^T [\mathbf{y} - \bar{\mathbf{y}}(\boldsymbol{\theta})]. \quad (25)$$

The estimated displacements \bar{y}_i , $i = 1, 2, \dots, N_y$, are computed from the solution of the forward model given by Eq. (17) for the sine sweep excitation mathematically described by Eq. (24). The vector of unknown parameters $\boldsymbol{\theta} = [\theta_1 \ \theta_2]^T$ is estimated through the classical Levenberg-Marquardt iterative procedure [12]. At the end of the Levenberg-Marquardt iterative procedure, one may compute an approximation for the covariance matrix of the unknown parameters, $\boldsymbol{\Sigma}_\theta$, through the following expression [14]

$$\boldsymbol{\Sigma}_\theta = (\mathbf{J}^T \mathbf{J})^{-1} \sigma^2 \quad (26)$$

where $J_{pq} \equiv \partial \bar{y}_p(\boldsymbol{\theta}) / \partial \theta_q$, $p, q = 1, 2, \dots, N_\theta$, denotes the components of the sensitivity matrix evaluated at the least-squares estimator, $\hat{\boldsymbol{\theta}}_{LS} \equiv \text{argmin} S_{LS}(\boldsymbol{\theta})$. The least-squares estimate is $\hat{\boldsymbol{\theta}}_{LS} = [4.013 \ 155.67]^T$ and the computed covariance matrix is

$$\boldsymbol{\Sigma}_\theta = \begin{bmatrix} 1.023 & -96.77 \\ -96.77 & 1.09 \times 10^4 \end{bmatrix}. \quad (27)$$

Note that the point estimates obtained for both k_1 and c_1 possess large discrepancies with respect to their corresponding true values, as the simulated experimental data has been corrupted by a significant noise content (SNR = 10 dB). Note also that the variance for θ_2 is about four orders of magnitude higher than the variance for θ_1 . Such behavior may be attributed to the fact that the time-domain displacement of block 1 (the observed variable) is much more sensitive to θ_1 than to θ_2 , as can be seen from the plot of the normalized sensitivity coefficients, $\theta_1 \partial \bar{y}_i / \partial \theta_1$ and $\theta_2 \partial \bar{y}_i / \partial \theta_2$, $i = 1, 2, \dots, N_y$, illustrated in Figure 5.

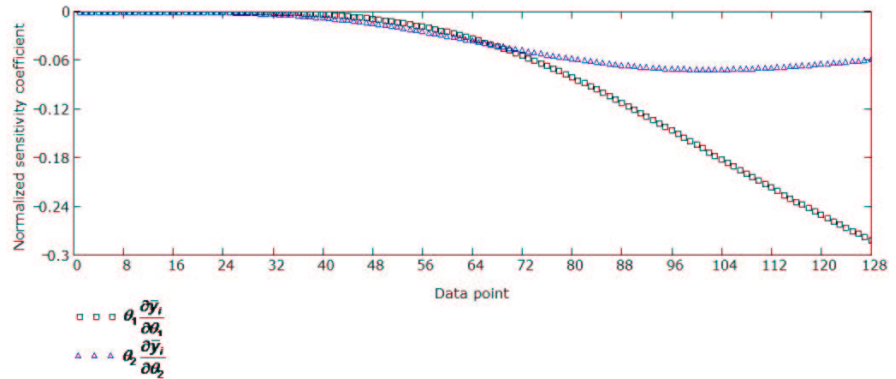


Figure 5. Normalized sensitivity coefficients evaluated at the least-squares estimate $\hat{\boldsymbol{\theta}}_{LS}$.

Once estimates are available for the unknown parameters, one may compute an estimate for the known variance of the experimental data σ^2 . For independent and identically distributed noise samples, the variance σ^2 may be evaluated from the following relationship [14]

$$\hat{\sigma}^2 = \frac{S_{LS}(\hat{\boldsymbol{\theta}}_{LS})}{N_y - N_\theta}. \quad (28)$$

Table 1. Estimation of the variance of observed data for three independent realizations. True value: $\sigma^2 = 1.877 \times 10^{-2}$

Realization	$\hat{\theta}_{LS,1}$	$\hat{\theta}_{LS,2}$	$\hat{\sigma}^2$
1	4.013	1.557×10^2	1.794×10^{-2}
2	5.157	2.661	1.789×10^{-2}
3	5.214	2.308×10^1	1.641×10^{-2}

The variance of the error, $\hat{\sigma}^2$, computed from Eq. (28) may be compared with the known true value of σ^2 , prescribed during the generation of the observed data. Table 1 shows the results obtained for the variance $\hat{\sigma}^2$, computed from Eq.

(28), for three independent realizations of simulated experimental data with SNR = 10 dB. For the three realizations performed, the variance computed from Eq. (28) agrees very well with the corresponding true value.

If multiple experimental data are available to the analyst, two different kinds of parameter estimation may be performed. In the first one, it is assumed that each realization of an experiment is independent from the others (they might be obtained by different researchers, with different experimental apparatus and test methods, for example). Hence, for each independent realization, an inverse problem of parameter estimation is solved in order to provide the unknown parameters (here, θ_1 and θ_2). The next step is thus to compute the expected value and the variance of the unknown parameters by taking the sample mean and the sample variance as approximations to the aforementioned statistics. Table 2 shows the sample mean and the sample variance for θ_1 and θ_2 , computed from the estimates $\boldsymbol{\theta}^{(j)} = [\theta_1^{(j)} \theta_2^{(j)}]^T$, $j = 1, 2, \dots, N_s$. Each estimate $\boldsymbol{\theta}^{(j)}$, $j = 1, 2, \dots, N_s$, derives from the minimization of the ordinary least-squares norm for an independent realization of \mathbf{y} . Five independent realizations of \mathbf{y} with different signal-to-noise ratios are generated for the deterministic inverse problem solution, i.e., $N_s = 5$. The chosen signal-to-noise ratios are 15, 20, 25, 30 and 35 dB. Based on the re-

Table 2. Sample mean and sample variance of the unknown parameters θ_1 and θ_2 for five independent realizations of \mathbf{y} .

Realization	SNR [dB]	θ_1	θ_2
1	15	5.049	2.691×10^1
2	20	5.047	-1.000×10^1
3	25	5.005	4.634
4	30	5.002	-8.454×10^{-3}
5	35	5.043	-3.480
Sample mean		5.029	3.611
Sample variance		5.56×10^{-4}	1.98×10^2

sults indicated in Table 2 one may verify that the sample mean for θ_1 agrees quite well with the corresponding true value; contrarily, the sample mean for θ_2 largely deviates from its corresponding true value. It is interesting to note the large sample variance computed for θ_2 . The simple exercise performed here clearly indicates that the ordinary least-squares estimate of a low-sensitivity parameter (with respect to the chosen observed variables) may be quite inaccurate, even for a low noisy data.

In the second scenario, it is assumed that all realizations of an experiment for the physical system under investigation are available simultaneously to the analyst; they are generally obtained by repeating the test without changing the experimental set-up. In such situations, the unknown parameters are estimated through the minimization of the weighted least-squares norm, $S_{\text{WLS}}(\boldsymbol{\theta})$

$$S_{\text{WLS}}(\boldsymbol{\theta}) = [\mathbf{y} - \bar{\mathbf{y}}(\boldsymbol{\theta})]^T \boldsymbol{\Sigma}_e^{-1} [\mathbf{y} - \bar{\mathbf{y}}(\boldsymbol{\theta})] \quad (29)$$

where now the components of \mathbf{y} on Eq. (29) are the expected values of y_i , $i = 1, 2, \dots, N_y$, denoted by $E[y_i]$ and computed as follows

$$E[y_i] \approx \frac{1}{N_s} \sum_{k=1}^{N_s} y_i^{(k)}. \quad (30)$$

The symbol $y_i^{(k)}$ appearing on Eq. (30) stands for the i -th component of the vector \mathbf{y} for the k -th sample. The components of the covariance matrix of the error, $\boldsymbol{\Sigma}_e$, are given by $[\boldsymbol{\Sigma}_e]_{ij} = 0$, if $i \neq j$ and $[\boldsymbol{\Sigma}_e]_{ij} = \sigma_i^2$, if $i = j$, $i, j \in \{1, 2, \dots, N_y\}$, with σ_i^2 given by

$$\sigma_i^2 = E[(y_i - E[y_i])^2] \approx \frac{1}{N_s - 1} \sum_{k=1}^{N_s} (y_i^{(k)} - E[y_i])^2. \quad (31)$$

The estimates for the unknown parameters θ_1 and θ_2 are obtained from the minimization of the weighted least-squares norm through the classical Levenberg-Marquardt iterative procedure. The expression for an estimate of the covariance matrix of the unknown parameters, $\boldsymbol{\Sigma}_\theta$, becomes [14]

$$\boldsymbol{\Sigma}_\theta = (\mathbf{J}^T \boldsymbol{\Sigma}_e^{-1} \mathbf{J})^{-1}. \quad (32)$$

The estimates obtained for θ_1 and θ_2 for five simultaneous realizations of \mathbf{y} with SNR = 10 dB (i.e., for $N_s = 5$) are, respectively, 4.988 Nm^{-1} and $5.851 \times 10^1 \text{ Nsm}^{-1}$. The computed variances for θ_1 and θ_2 are, respectively, 0.254 and 3.000×10^3 . Based on the results indicated in Table 2, one verifies a slight discrepancy between the sample mean and the weighted least-squares estimate for θ_1 and a higher discrepancy between the sample mean and the weighted least-squares estimate for θ_2 . Note that, for the two scenarios investigated, the estimates obtained for θ_2 are quite inaccurate;

furthermore, the variance for θ_2 is more than three orders of magnitude higher than that for θ_1 . Hence, point estimates for damping coefficients based on measured time-domain responses and least-squares minimization may be quite inaccurate depending on the noise content in the observed data and sensitivity to the observed response. A natural question to ask is how to better quantify these uncertainties. Bayesian inverse solution provides not only point and crude variance estimates but rather complete quantitative descriptions for the uncertainties associated with the unknown parameters in terms of their (joint and marginal) probability distributions.

IP2: Bayesian inverse solution

For the Bayesian inverse solution of IP2, one assumes that the errors are additive, uncorrelated and Gaussian distributed with zero mean and constant (known) variance σ^2 . Hence, one has the following expression for the unnormalized posterior probability distribution:

$$p(\boldsymbol{\theta}|\mathbf{y}) \propto \exp \left\{ -\frac{1}{2\sigma^2}(\mathbf{y} - \bar{\mathbf{y}}(\boldsymbol{\theta}))^T (\mathbf{y} - \bar{\mathbf{y}}(\boldsymbol{\theta})) \right\} p(\boldsymbol{\theta}). \tag{33}$$

Three different prior probability distributions $p(\boldsymbol{\theta})$ are investigated: (i) a uniform prior distribution; (ii) a bivariate Gaussian distribution with mean $\boldsymbol{\mu}_\theta$ and covariance matrix $\boldsymbol{\Sigma}_\theta$; and (iii) independent two-parameter Weibull distributions for θ_1 and θ_2 , i.e., $p(\boldsymbol{\theta}) = p(\theta_1)p(\theta_2)$, with

$$p(\theta_1) \propto \left(\frac{\theta_1}{\lambda_1}\right)^{r_1-1} \exp \left\{ -\left(\frac{\theta_1}{\lambda_1}\right)^{r_1} \right\} \text{ and } p(\theta_2) \propto \left(\frac{\theta_2}{\lambda_2}\right)^{r_2-1} \exp \left\{ -\left(\frac{\theta_2}{\lambda_2}\right)^{r_2} \right\} \tag{34}$$

where $\lambda_1, r_1, \lambda_2, r_2$ are prescribed (known) scale and shape parameters. These scale and shape parameters could also be regarded as unknown parameters and thus incorporated into the inverse problem formulation to be estimated from observed data. This hierarchical modelling is another advantage of Bayesian inference approach. Parameters from prior distributions when incorporated into the inverse problem formulation are commonly referred to as hyperparameters [6]. The unnormalized posterior probability distributions are thus given as follows:

(i) uniform prior distribution

$$p(\boldsymbol{\theta}|\mathbf{y}) \propto \exp \left\{ -\frac{1}{2\sigma^2}(\mathbf{y} - \bar{\mathbf{y}}(\boldsymbol{\theta}))^T (\mathbf{y} - \bar{\mathbf{y}}(\boldsymbol{\theta})) \right\}; \tag{35}$$

(ii) bivariate Gaussian prior distribution

$$p(\boldsymbol{\theta}|\mathbf{y}) \propto \exp \left\{ -\frac{1}{2} \left[(\mathbf{y} - \bar{\mathbf{y}}(\boldsymbol{\theta}))^T \sigma^{-2} (\mathbf{y} - \bar{\mathbf{y}}(\boldsymbol{\theta})) + (\boldsymbol{\theta} - \boldsymbol{\mu}_\theta)^T \boldsymbol{\Sigma}_\theta^{-1} (\boldsymbol{\theta} - \boldsymbol{\mu}_\theta) \right] \right\}; \tag{36}$$

(iii) independent two-parameter Weibull prior distributions

$$p(\boldsymbol{\theta}|\mathbf{y}) \propto \left(\frac{\theta_1}{\lambda_1}\right)^{r_1-1} \left(\frac{\theta_2}{\lambda_2}\right)^{r_2-1} \exp \left\{ -\frac{1}{2} \left[(\mathbf{y} - \bar{\mathbf{y}}(\boldsymbol{\theta}))^T \sigma^{-2} (\mathbf{y} - \bar{\mathbf{y}}(\boldsymbol{\theta})) + 2 \left(\left(\frac{\theta_1}{\lambda_1}\right)^{r_1} + \left(\frac{\theta_2}{\lambda_2}\right)^{r_2} \right) \right] \right\}. \tag{37}$$

Two important remarks may be drawn from the above expressions for the posterior probability distribution. Firstly, for uniform prior probability distribution, the maximum a posteriori, $\hat{\boldsymbol{\theta}}_{\text{MAP}}$, and the maximum likelihood, $\hat{\boldsymbol{\theta}}_{\text{ML}}$, estimates are equivalent, i.e., $\hat{\boldsymbol{\theta}}_{\text{MAP}} = \hat{\boldsymbol{\theta}}_{\text{ML}}$. Secondly, for Gaussian prior probability, the maximum a posteriori estimate is the solution of the following minimization problem:

$$\hat{\boldsymbol{\theta}}_{\text{MAP}} = \underset{\boldsymbol{\theta} \in \mathcal{D}}{\text{argmin}} (\mathbf{y} - \bar{\mathbf{y}}(\boldsymbol{\theta}))^T \sigma^{-2} (\mathbf{y} - \bar{\mathbf{y}}(\boldsymbol{\theta})) + (\boldsymbol{\theta} - \boldsymbol{\mu}_\theta)^T \boldsymbol{\Sigma}_\theta^{-1} (\boldsymbol{\theta} - \boldsymbol{\mu}_\theta) \tag{38}$$

from which one can see a compromise between the data misfit (first term), weighted by the error variance, and prior knowledge about the unknown parameters $\boldsymbol{\theta}$ (second term), weighted by its covariance matrix $\boldsymbol{\Sigma}_\theta$. Hence, Bayesian inference approach also provides point estimates for the unknown parameters; furthermore, it recovers standard estimators such as the maximum likelihood and the maximum a posteriori.

Figure 6 plots the histograms corresponding to the posterior marginal probability distributions for θ_1 and θ_2 , for a uniform prior probability distribution. Figure 7 illustrates the Markov chain samples drawn from the posterior probability distribution with the aid of the Metropolis-Hastings algorithm, for the uniform prior probability. From the samples obtained, one evaluates the posterior mean, the maximum a posteriori and the posterior covariance matrix, yielding $\boldsymbol{\mu}_{\boldsymbol{\theta}|\mathbf{y}} = [5.296 \quad -2.479]^T$, $\hat{\boldsymbol{\theta}}_{\text{MAP}} = [4.016 \quad 155.28]^T$ and

$$\boldsymbol{\Sigma}_{\boldsymbol{\theta}|\mathbf{y}} = \begin{bmatrix} 0.123 & -0.203 \\ -0.203 & 29.91 \end{bmatrix}. \tag{39}$$

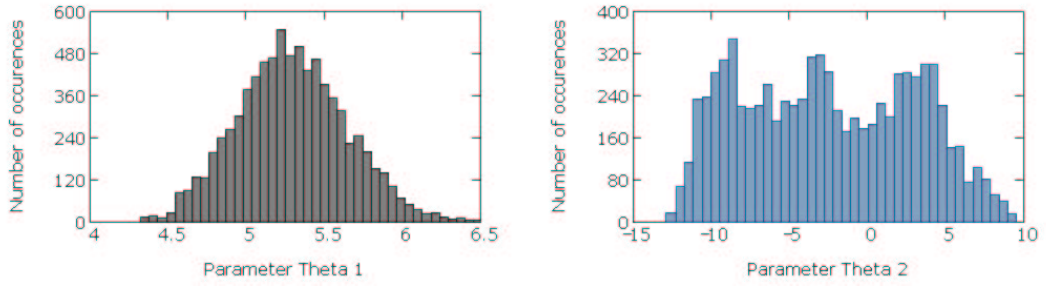


Figure 6. Marginal posterior histograms for θ_1 and θ_2 , for IP2 with uniform prior probability distribution.

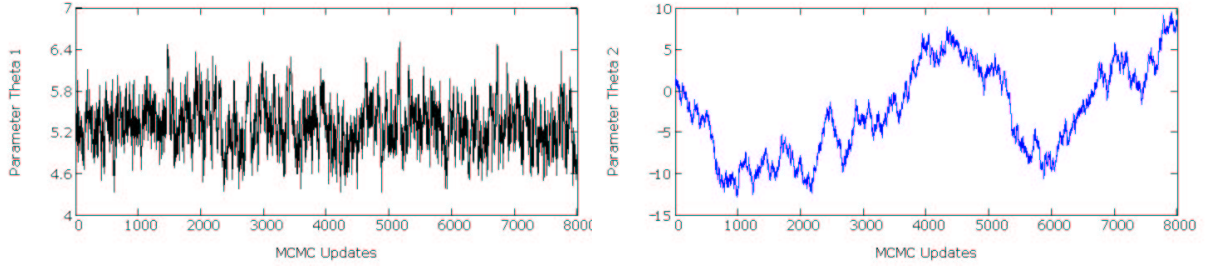


Figure 7. Markov chain samples drawn from the posterior probability distribution, for IP2 with uniform prior probability distribution.

Figure 8 plots the histograms corresponding to the posterior marginal probability distributions for θ_1 and θ_2 , for a Gaussian prior probability distribution with

$$\boldsymbol{\mu}_\theta = [5 \ 2]^T \text{ and } \boldsymbol{\Sigma}_\theta = \begin{bmatrix} 0.20 & 0.08 \\ 0.08 & 0.20 \end{bmatrix}. \quad (40)$$

Samples from the posterior probability distribution $p(\boldsymbol{\theta}|\mathbf{y})$ given by Eq. (36) are drawn with the aid of the Metropolis-Hastings algorithm. Figure 9 illustrates the Markov chain samples drawn from the posterior probability distribution, for the Gaussian prior probability. From the samples obtained, one evaluates the posterior mean, the maximum a posteriori and the posterior covariance matrix, yielding

$$\boldsymbol{\mu}_{\theta|\mathbf{y}} = [5.143 \ 2.067]^T, \hat{\boldsymbol{\theta}}_{\text{MAP}} = [5.135 \ 2.061]^T \text{ and } \boldsymbol{\Sigma}_{\theta|\mathbf{y}} = \begin{bmatrix} 0.070 & 0.020 \\ 0.020 & 0.157 \end{bmatrix} \quad (41)$$

from which one concludes that the prior and posterior correlation coefficients between θ_1 and θ_2 are, respectively, 0.4 and 0.189.

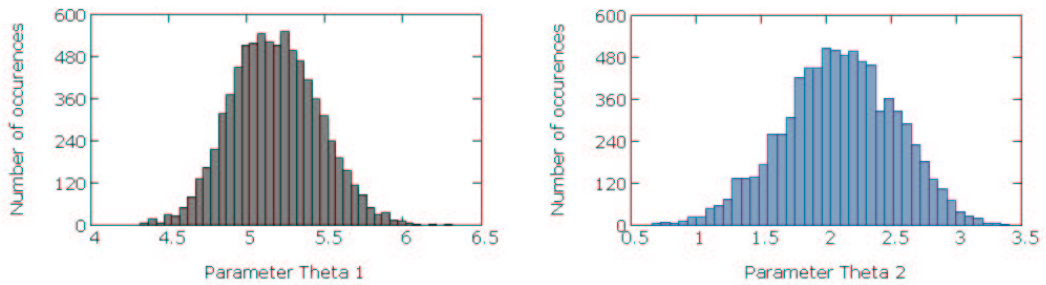


Figure 8. Marginal posterior histograms for θ_1 and θ_2 , for IP2 with Gaussian prior probability distribution.

Figure 10 plots the histograms corresponding to the posterior marginal probability distributions for θ_1 and θ_2 , for independent two-parameter Weibull prior probability distributions with $\lambda_1 = 5.479$, $\lambda_2 = 2.107$, $r_1 = 4.5$ and $r_2 = 9.5$. Figure 11 illustrates the Markov chain samples drawn from $p(\boldsymbol{\theta}|\mathbf{y})$ given by Eq. (37), for the independent two-parameter Weibull prior distributions. The posterior mean, the maximum a posteriori and the posterior covariance matrix are $\boldsymbol{\mu}_{\theta|\mathbf{y}} = [5.238 \ 2.012]^T$, $\hat{\boldsymbol{\theta}}_{\text{MAP}} = [5.210 \ 2.084]^T$ and

$$\boldsymbol{\Sigma}_{\theta|\mathbf{y}} = \begin{bmatrix} 0.122 & -1.935 \times 10^{-3} \\ -1.935 \times 10^{-3} & 0.066 \end{bmatrix} \quad (42)$$

from which one concludes that the posterior correlation coefficient between θ_1 and θ_2 is -0.021 .

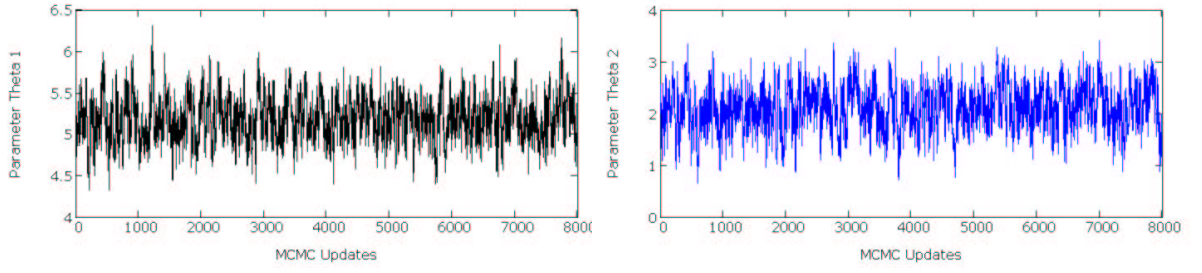


Figure 9. Markov chain drawn from the posterior probability distribution, for IP2 with Gaussian prior probability distribution.

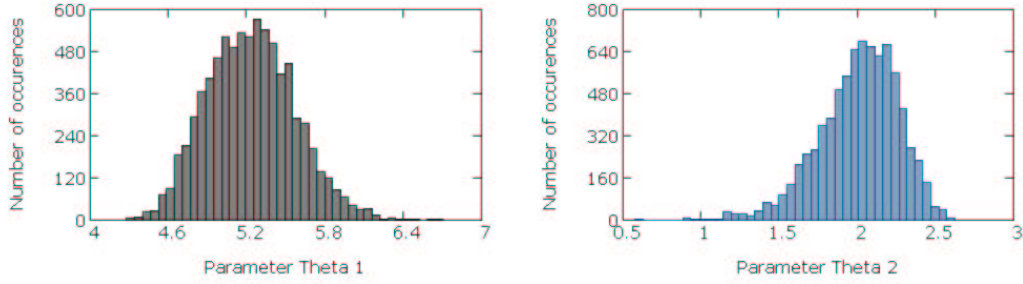


Figure 10. Marginal posterior histograms for θ_1 and θ_2 , for IP2 with independent two-parameter Weibull prior probability distribution.

IP3: Bayesian inverse solution

For the Bayesian inverse solution of IP3, one assumes that the errors are additive, uncorrelated and Gaussian distributed with zero mean and **unknown** constant variance σ^2 , parameterized as $\sigma = \gamma \times 10^{-1}$. Now, the parameter γ becomes also an unknown parameter to be estimated from observed data; therefore, the expression for the posterior probability distribution must be slightly changed. From Bayes' rule for conditional probability, one has

$$p(\boldsymbol{\theta}, \gamma | \mathbf{y}) \propto p(\mathbf{y} | \boldsymbol{\theta}, \gamma) p(\boldsymbol{\theta}, \gamma). \quad (43)$$

Substituting the expression for the likelihood function yields

$$p(\boldsymbol{\theta}, \gamma | \mathbf{y}) \propto \frac{1}{\gamma^{N_y}} \exp \left\{ -\frac{1}{2\gamma^2 \times 10^{-2}} [\mathbf{y} - \bar{\mathbf{y}}(\boldsymbol{\theta})]^T [\mathbf{y} - \bar{\mathbf{y}}(\boldsymbol{\theta})] \right\} p(\boldsymbol{\theta}, \gamma). \quad (44)$$

By assuming that the unknown parameters $\boldsymbol{\theta}$ and the error variance σ^2 are independent random variables, one may rewrite Eq. (44) as follows:

$$p(\boldsymbol{\theta}, \gamma | \mathbf{y}) \propto \frac{1}{\gamma^{N_y}} \exp \left\{ -\frac{1}{2\gamma^2 \times 10^{-2}} [\mathbf{y} - \bar{\mathbf{y}}(\boldsymbol{\theta})]^T [\mathbf{y} - \bar{\mathbf{y}}(\boldsymbol{\theta})] \right\} p(\boldsymbol{\theta}) p(\gamma). \quad (45)$$

Since σ measures the width of a probability distribution, it must be a non-negative number. For scale invariant prior distribution for σ one must have an uniform probability density as a function of $\log(\sigma)$ or, equivalently, $p(\sigma) \propto 1/\sigma$ [19]. Hence, $p(\gamma) \propto 1/\gamma$ and the posterior probability distribution becomes

$$p(\boldsymbol{\theta}, \gamma | \mathbf{y}) \propto \frac{1}{\gamma^{N_y+1}} \exp \left\{ -\frac{1}{2\gamma^2 \times 10^{-2}} [\mathbf{y} - \bar{\mathbf{y}}(\boldsymbol{\theta})]^T [\mathbf{y} - \bar{\mathbf{y}}(\boldsymbol{\theta})] \right\} p(\boldsymbol{\theta}). \quad (46)$$

The numerical results reported for IP3 are computed for the independent two-parameter Weibull prior probability distribution with $\lambda_1 = 5.479$, $\lambda_2 = 2.107$, $r_1 = 4.5$ and $r_2 = 9.5$, as indicated in Table 3. The posterior correlation coefficients among the three unknown parameters are $\rho_{\theta_1\theta_2} = 0.011$, $\rho_{\theta_1\gamma} = -0.033$ and $\rho_{\theta_2\gamma} = -0.01$.

FINAL REMARKS

In the present work, deterministic and statistical inversion approaches were employed to estimate stiffness and damping parameters of a two degree-of-freedom spring-mass-damper system. Simulated measurements derived from the solution of the corresponding forward problem corrupted with uncorrelated Gaussian-distributed additive noise were used for the estimation process. Three inverse problem formulations were investigated. In the first one, the variance of the error

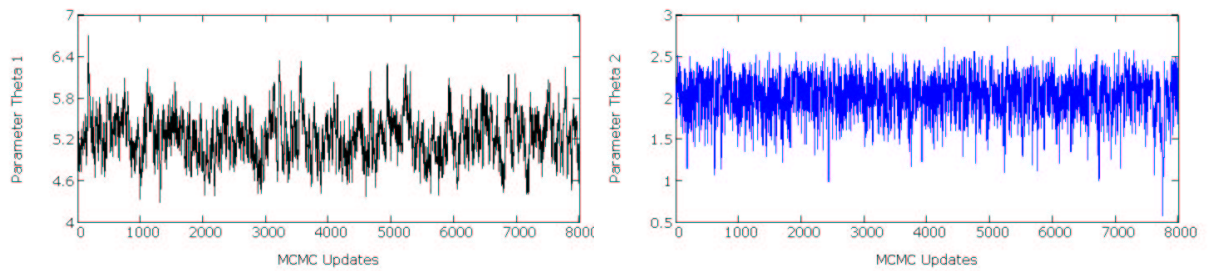


Figure 11. Markov chain samples drawn from the posterior probability distribution, for IP2 with independent two-parameter Weibull prior probability distribution.

Table 3. Mean value, mode and variance for the unknown parameters θ and γ , for independent two-parameter Weibull prior distribution for θ and for a non-informative scale invariant prior distribution for γ . True value for γ is 1.37.

Parameter	Mean value	Mode	Variance
θ_1	5.222	5.202	1.00×10^{-1}
θ_2	2.008	2.076	6.35×10^{-2}
γ	1.359	1.345	7.00×10^{-3}

was assumed to be known and the unknown parameters were estimated from the minimization of the least-squares norm. Two different scenarios, in which multiple experimental data were available independently or simultaneously for the inverse analysis, were investigated. Quite inaccurate estimates as well as large variances were obtained for the damping parameter, due to the low sensitivity of the chosen observed data with respect to that parameter. In the second one, the variance of the error was assumed to be known and from the Bayesian statistical inversion approach, one derived both point estimates and probability distributions for the unknown parameters, for both non-informative and highly informative prior distributions. Finally, in the third one, the variance of the error was assumed to be unknown and became a sought-after parameter along with the stiffness and damping parameters. With the Bayesian statistical inversion approach, one derived point estimates, joint and marginal probability distributions for the unknown parameters. The exercises performed here clearly demonstrated that Bayesian inference approach indeed offers a rigorous framework to treat inverse problems with noisy data, uncertain forward models and low-sensitivity model parameters.

REFERENCES

- B. Jin, *Fast Bayesian approach for parameter estimation*, International Journal for Numerical Methods in Engineering 76 (2008), pp. 230–252.
- Y. M. Marzouk, H. N. Najm and L. A. Rahn, *Stochastic spectral methods for efficient Bayesian solution of inverse problems*, Journal of Computational Physics 224 (2007), pp. 560–586.
- V. A. B. Narayanan and N. Zabarar, *Stochastic inverse heat conduction using a spectral approach*, International Journal for Numerical Methods in Engineering 60 (2004), pp. 1–24.
- T. D. Fadale, A. V. Nenarokomov and A. F. Emery, *Uncertainties in parameter estimation: the inverse problem*, International Journal of Heat and Mass Transfer 38 (1995), pp. 511–518.
- J. Kaipio and E. Somersalo, *Statistical and computational inverse problems*, Springer, New York, 2005.
- A. Gelman, J. B. Carlin, H. S. Stern and D. B. Rubin, *Bayesian data analysis*, 2nd edition, Chapman & Hall, Boca Raton, 2003.
- B. Jin and J. Zou, *A Bayesian inference approach to the ill-posed Cauchy problem steady-state heat conduction*, International Journal for Numerical Methods in Engineering 76 (2008), pp. 521–544.
- N. Z. Sun and W. G. Yeh, *A stochastic inverse solution for transient groundwater flow: parameter identification and reliability analysis*, Water Resources Research 28 (1992), pp. 3269–3280.
- J. Wang and N. Zabarar, *A Bayesian inference approach to the inverse heat conduction problem*, International Journal of Heat and Mass Transfer 47 (2004), pp. 3927–3941.
- J. Wang and N. Zabarar, *Hierarchical Bayesian models for inverse problems in heat conduction*, Inverse Problems 21 (2005), pp. 183–206.
- J. Wang and N. Zabarar, *Using Bayesian statistics in the estimation of heat source in radiation*, International Journal of Heat and Mass Transfer 48 (2005), pp. 15–29.
- M. N. Özisik and H. R. B. Orlande, *Inverse Heat Transfer: Fundamentals and Applications*, Taylor & Francis, New York, 2000.

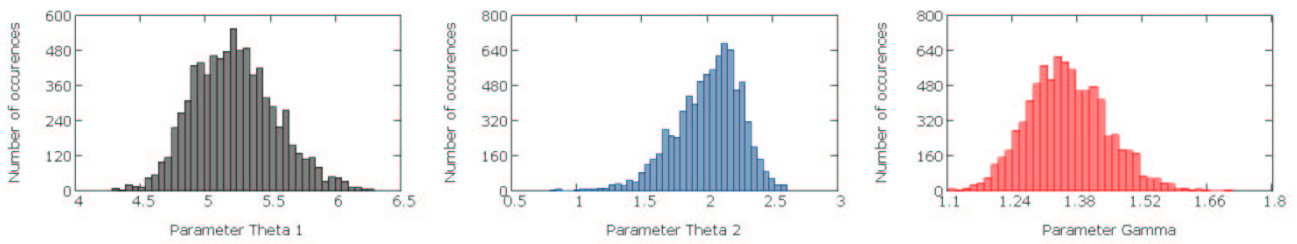


Figure 12. Marginal posterior histograms for θ_1 , θ_2 and γ , for IP3 with independent two-parameter Weibull prior probability distribution for θ and non-informative scale invariant prior distribution for γ .

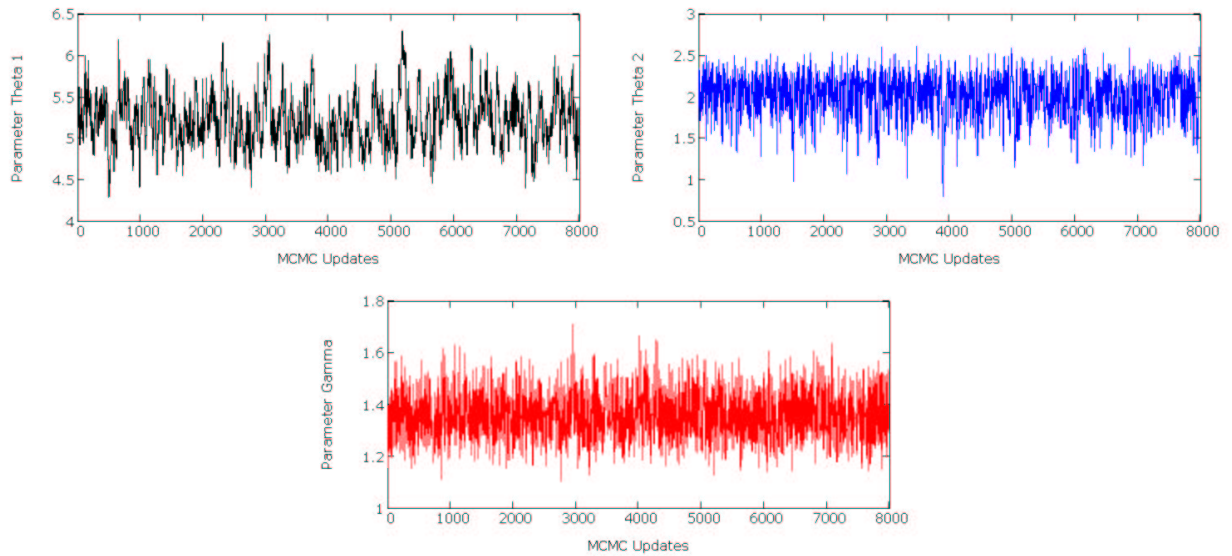


Figure 13. Markov chain samples drawn from the posterior probability distribution, for IP3 with independent two-parameter Weibull prior probability distribution for θ and non-informative scale invariant prior distribution for γ .

A. F. Emery, *Estimating deterministic parameters by Bayesian inference with emphasis on estimating the uncertainty of the parameters*, Inverse problems in Science and Engineering 17 (2009), pp. 263–274.
 J. V. Beck and K. J. Arnold, *Parameter Estimation in Engineering and Science*, John Wiley & Sons, 1977.
 M. Muto and J. L. Beck, *Bayesian updating and model class selection for hysteretic structural models using stochastic simulation*, Journal of Vibration and Control 14 (2008), pp. 7–34.
 W. R. Gilks, S. Richardson and D. J. Spiegelhalter (eds.), *Markov Chain Monte Carlo in Practice*, Chapman & Hall, London, 1996.
 J. E. Gentle, *Random Number Generation and Monte Carlo Methods*, 2nd edition, Springer, New York, 2003.
 D. Galbally, K. Fidkowski, K. Willcox and O. Ghattas, *Non-linear model reduction for uncertainty quantification in large-scale inverse problems*, International Journal for Numerical Methods in Engineering 81 (2010), pp. 1581–1608.
 G. K. Nicholls, S. M. Tan and C. Fox, *PHYSICS 707 Inverse Problems*, The University of Auckland (2010), Chapter 8, pages 8-8, 8-9.

RESPONSIBILITY NOTICE

The author(s) is (are) the only responsible for the printed material included in this paper

Development Environment for Optimized Locomotion System of Planetary Rovers

Bernd Schäfer¹, Alexandre Carvalho Leite², and Bernhard Rebele¹

¹ German Aerospace Center (DLR), Institute of Robotics and Mechatronics, Münchner Str. 20, D-82234 Wessling, Germany

² Currently at DLR, Germany, as Guest Scientist from Instituto Nacional de Pesquisas Espaciais (INPE), São José dos Campos, SP, Brazil

Abstract: This paper addresses the first steps that have been undergone to set up the development environment w.r.t. optimization and to modelling and simulation of the overall dynamics of the rover driving behaviour under all critical surface terrains, like soft and hard soils, slippage, bulldozing effect and digging in soft soil. Optimization is based on MOPS (Multi-Objective Parameter Synthesis), that is capable of handling several objective functions such as mass reduction, motor power reduction, increase of traction forces, rover stability guarantee, and more. The tool interferes with Matlab/Simulink and with Modelica/Dymola for dynamics model implementation. For modelling and simulation of the overall rover dynamics and terramechanical behaviour in all kind of soils we apply a Matlab based tool that takes advantage of the multibody dynamics tool Simpack. First results of very promising rover optimizations 6 wheels are presented that improve ExoMars rover type wheel suspension systems. Performance of driveability behaviour in different soils is presented as well. The next steps are discussed in order to achieve the planned overall development environment.

Keywords: *multibody dynamics, planetary rovers, optimization, terramechanics, simulation*

NOMENCLATURE

J_{mass} = overall mass of a vehicle, kg

m_{parts} = mass of a mechanical part, kg

$J_{avpower}$ = average consumed power, W

Greek Symbols

Δt = simulation time, s

τ = torque provided by powered wheel, Nm

ω = wheel's angular velocity, rad/s.

Subscripts

$parts$ index of a mechanical part

$wheels$ index of a powered wheel

INTRODUCTION AND MOTIVATION

Mobile systems for planetary surface exploration of Moon, Mars and other celestial bodies are attracting more and more importance for the scientific community. Also, for the exploration of geologically interesting areas this holds true in preparation for future missions with much larger extent such as an envisaged sample return mission to Mars, or even for a manned mission. First un-manned wheeled rovers have been sent to Moon very early already, the two Lunochod rovers in 1970 and 1972, but with remote operations from Earth. In recent years, rovers have been sent to Mars (NASA Mars Pathfinder Sojourner with launch in 1996, and the twin rovers MER Opportunity und Spirit with launch in 2003) that operated with some kind of increased autonomy very successfully. Next, two rovers will be sent to Mars again, the NASA Mars Science Laboratory MSL to be launched in 2011, and ESA's ExoMars rover with expected launch date in 2018 (Fig. 1). All these Mars rovers have in common that they were operating or will be operating in a more or less moderate surface terrain, in equatorial regions, i.e. close to lower latitudes. In all these Mars missions 6-wheeled rovers have been employed.

The Mars missions were very successful and MER rover Opportunity still is exploring Mars terrain. Although the two show-pieces, the MER twin rovers, have been roving and exploring the surface for incredible 6 years now, the exploration area and their driven path lengths are relatively small compared to the long operations time of several years. For Spirit this yielded 7.7 km (dated from spring 2009 when the rover got stuck, until now), and for Opportunity 20.6 km (dated from 12 May 2010). Although craters with soft inclination were visited by the twin rovers as well, the rovers have been designed to operate in a more or less moderately structured surface terrain. Moreover, due to the limited rover intelligence on-board, daily driving and operations is strongly constrained to low speed and to small driven distance. In the mean, a distance of 100 m per Mars day has been reached.

The exploration of much larger surface areas at comparatively similar mission times is one of the major impacts to come up with an essentially increased scientific output compared to present rover missions. Moreover, the very high development and mission costs are justified much easier by exceeding the mission operations time and the planetary surface area to be explored, remarkably. Figure 2, however, gives an impression where scientists might want to go but engineers may get nightmares with wheeled rover technologies. To reach, at least, several of the goals mentioned before,

novel approaches for mobile systems development together with their intelligent and autonomous motion guidance and control have to be followed and realized. Our main objectives are to increase rover driving speed, to increase the wheel-soil interacting forces which are transmitted from drive motors to the ground, and to add more autonomy while driving through larger planetary surface regions. All this includes increase of motor performance by using new light-weight motor technology, novel actuator design concepts for both driving and steering capabilities, reduction of the entire rover chassis and locomotion mass, advanced wheel suspension systems to distribute the wheel forces almost uniformly to all wheels, and to guarantee for rover stability in all envisaged critical driving states ranging from smoothly inclined planes to steep slopes and even crevasses to be negotiated. Moreover, advanced controller algorithms are required that take care of slippage between the wheels and soft and hard soils, and to reduce slip to a certain minimum.



Figure 1 – ESA's ExoMars rover to be launched to Mars in 2018.

The expertise and achieved developments of the institute with respect to the goals stated above will be integrated into an overall development and design tool that optimizes a next generation planetary rover and which is used for design support. Expertise is available in rover kinematics/dynamics optimization, in multibody dynamics and terramechanics, in energy management and minimization, and in design of advanced controller approaches. The overall goal then will be the realization of a demonstrator rover that features new characteristics such as high mobility, energy efficiency, increased autonomy and long range driving capabilities at given total mass. In parallel, the development environment at its final stage will act as a design tool, and will very rapidly assist in optimized rover designs that fit to any type of terrain topology, to given total mass, available energy resources, desired rover speeds and driving ranges.





Good Compromise

Figure 2 – Planetary surface topologies: (top) scientist’s dream site, a nightmare for rover design engineers; (bottom) a good compromise.

This paper will address the first steps that have been undergone to set up the development environment w.r.t. optimization and to modelling and simulation of the overall dynamics of the rover driving behaviour under all critical surface terrains, like soft and hard soils, slippage, bulldozing effect and digging in soft soil. Optimization is based on MOPS (Multi-Objective Parameter Synthesis), that is capable of handling several objective functions such as mass reduction, motor power reduction, increase of traction forces, rover stability guarantee, and more. The tool interfaces with Matlab/Simulink and with Modelica/Dymola for dynamics model implementation. For modelling and simulation of the overall rover dynamics and terramechanical behaviour in all kind of soils we apply a Matlab based tool that takes advantage of the multibody dynamics tool Simpack. First results of very promising rover optimizations for 4 and 6 wheels are presented that improve ExoMars rover type wheel suspension systems. Performance of driveability behaviour in different soils is presented as well and compared to certain test results obtained in a lab environment. The next steps are discussed in order to achieve the planned overall development environment.

DESIGN AND BOUNDARY CONDITIONS FOR OPTIMAL ROVER DESIGN

Several major constraints have to be considered that drive the design and development for optimal rovers. They arise from two main sets of requirements, i.e. mission and system requirements. For mission requirements, we mainly have to consider items like

- Target planet or moon: gravity, solar constant, radiation, temperature range
- Mission duration
- Surface topology, i.e. terrain: flat, soft/hard, sandy, gravel, rocky, cliffy, steep slopes, crater
- Latitude: equatorial, temperate zone, polar
- Payload: what size, power and mass

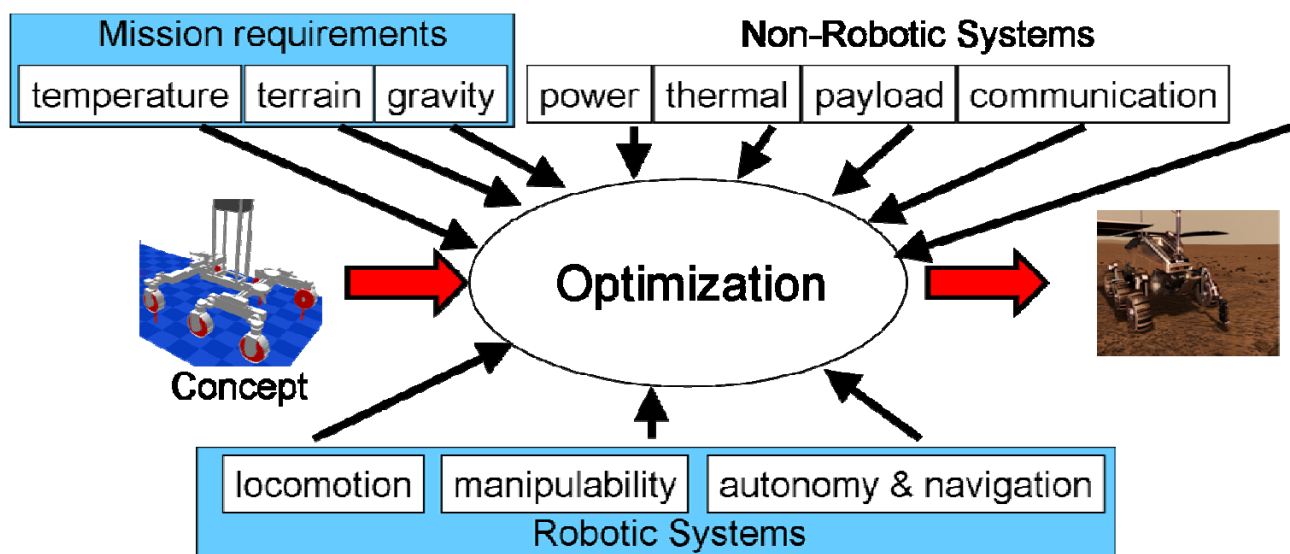


Figure 3 – Mission and system requirements that drive the optimal design of a wheeled rover.

For system requirements, the main items to regard are

- Mass and power limits
- Subsystems like
 - power (solar, battery, RTG Radio-isotopic generators)
 - thermal control (passive, active, RHU Radio-isotopic heating unit)
 - communication (with lander, orbiter, earth)
 - autonomy (rover-based cameras for navigation, orbiter-based cameras)
- Accomodation of payload on the rover
- Sample collection (from ground, subsurface, by drilling)
- Transport to lander
- Manipulability: robotic arm on rover, for grasping specific devices, various tools for sample acquisition and instrument deployment on planetary surface
- Locomotion concept: how many wheels, suspension kinematics, which wheels shall be actuated for driving and steering
- Technological Readiness (TR): what is the level of TR (the so-called TRL) for the various subsystems and components?

All these components and items have influence on rover sizing w.r.t. mass, power, and actuator dimensioning for driving and steering. They all impact on each other mutually. Figure 3 gives an overview how these components are expected to react with each other. Hence, it is very important to integrate all these mutual influences within a unique software environment that serves as the basis for a global design and development tool, and that covers modelling, optimization and simulation in one tool. Figure 4 addresses the complete development cycle for all the phases starting from conceptual work, going to first designs, performing validation between simulation and breadboard development by correlating testing with simulation results, and finally reaching the desired flight version.

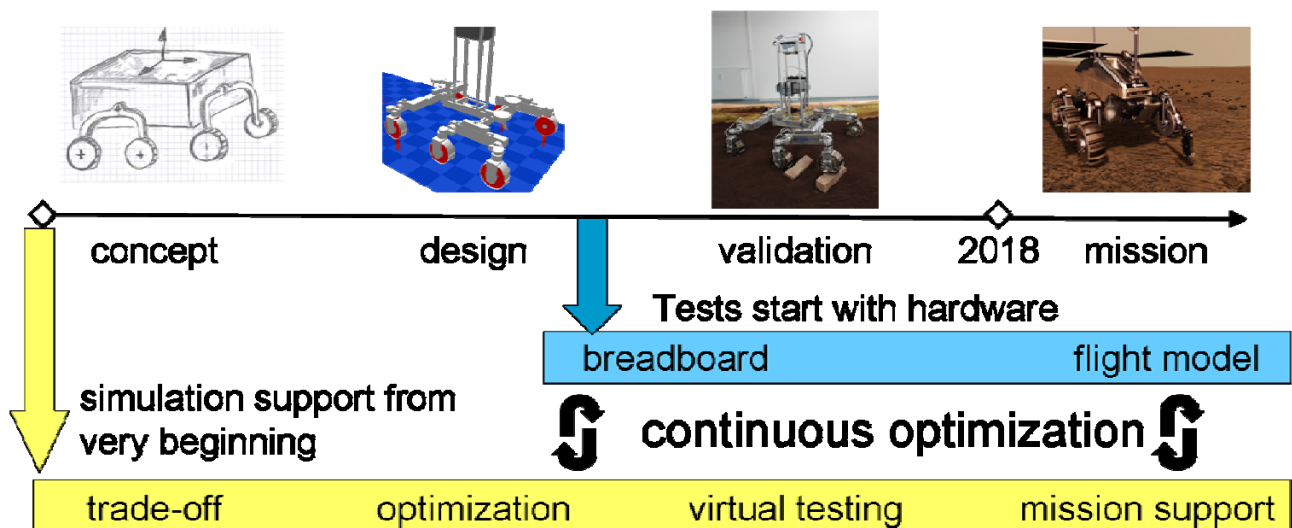


Figure 4 – Four steps of rover design, from conceptual work to flight version; to achieve confidence by combination of testing and simulation.

CONCEPTUAL ROVER DESIGN: MULTIBODY SYSTEM AND TERRAMECHANICS MODELING AND SIMULATION

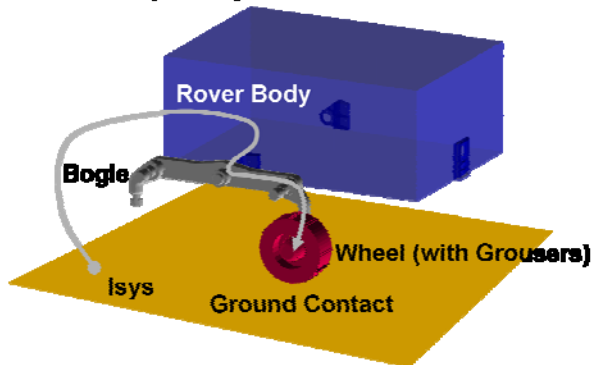
To support the design optimization and to demonstrate the rover performance on both hard and soft soil terrain, we have set up a modeling and simulation tool that makes use of a multibody system (MBS) approach for the rover dynamics, SIMPACK software tool, and which interacts with very detailed and complex terramechanics models for the wheel-soil interaction (Krenn et al., 2008), being part of the MBS environment (Fig. 5). This methodology is used to rapidly set up a design concept on best engineering knowledge and experience gathered by past rover designs. Mobility performance simulations on various terrains then are obtained (Schäfer et al., 2010), and can give a first indication of how to drive the subsequent optimization process w.r.t. the proper selection of objective functions and to rover parameters to be chosen for optimization (Fig. 6).

Moreover, at the end, when the optimization process has been accomplished successfully, this MBS tool is used to demonstrate again the, hopefully, better performance of the optimized rover design compared to the conceptual, first approach. Although we also need MBS and terramechanics models within the optimization phase, those models have to be taken in a constraint or reduced manner in order not to oversize the overall optimization problem. In the optimization phase, we rather want to focus on the features that drive the optimization process, i.e. proper objective function selection, choice of the demanding rover design parameters, regarding the impacts from mission and system

requirements. However, this all requires precise modeling as well, but on a lower level compared to the conceptual rover modeling and simulation phase. In the end, having different modeling and simulation approaches at hand, this very nice feature is expected to increase reliability and efficiency of the simulation runs, before going for manufacturing, breadboarding and testing of the rover hardware.

MBS Topology / Kinematic Chain :

Isys → Rover Body → Bogie → Wheel → Ground Contact



MBS Topology / Kinematic Chain: Details

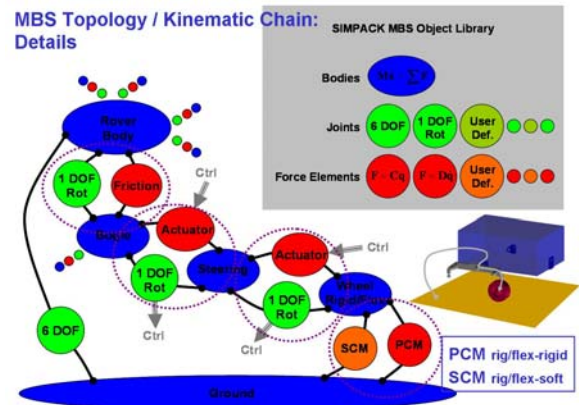


Figure 5 – Typical MBS topology approach: kinematic chain from inertial reference system to rover body, rover bogie (suspension), wheel and wheel-soil interaction. Various user defined force elements are to be applied for passive (spring, damper) and active (motorized, control) actuation between the elements. PCM (rigid soil) and SCM (soft soil) represent force elements that model the wheel-soil interaction.

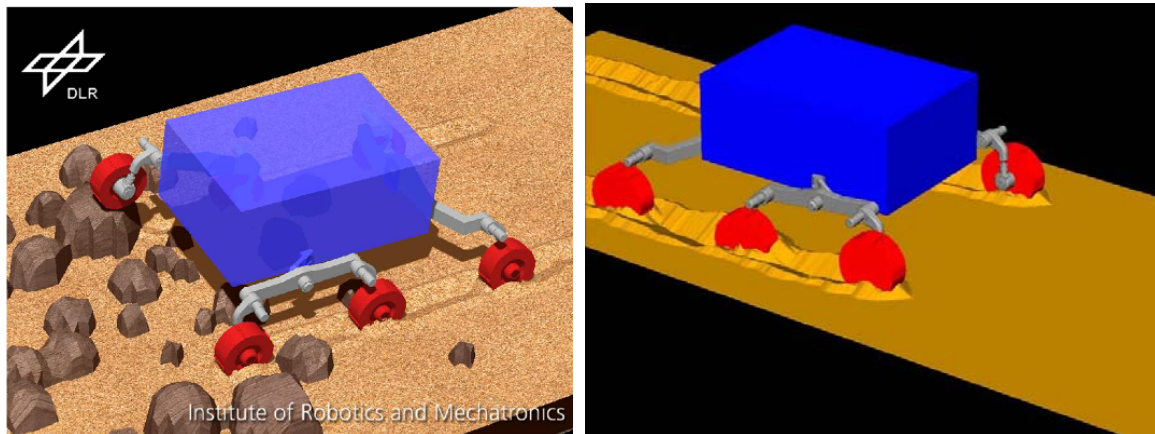


Figure 6 – Simulation results for a 6-wheeled planetary rover driving on soft soil (right) and mixed soil (left).

DESIGN OPTIMIZATION

Our design optimization methodology is separated in four different phases. First, a standard simulation model is set up with specific contact models for various terrain topologies. Then, objective functions and feasible regions are determined and selected properly. What follows, is a multi-case optimization and robust solution assessment. And finally the optimization tool is described and applied.

MBS model and wheel-soil contact models

To constrain the optimization problem we use a MBS approach with specific contact models. The kinematic structure is modeled with standard components (joints and rigid bodies) of MBS software (in this case Dymola®/Modelica), as shown in Fig. 7 (top). The contact model between each wheel and soil/obstacles deals with arbitrarily deformed terrains, rigid surfaces, soft surfaces and complex shaped rocks (Fig. 7, bottom).

Most of our modeling effort is in contact modeling, since this is very specific for all-terrain vehicles. The main idea of our contact model is to apply terramechanics theory (Fig. 7, bottom, (a)) on a laterally discretized wheel (Fig. 7, bottom, (b)) to compute some of the traction and resistance forces. Contact between the models and rocks is computed with the well-known Coulomb friction model, but the contact must be detected. For that purpose we use the collision detection techniques implemented in the SOLID® library (Fig. 7, bottom, (c)). Forces acting on the lateral of the wheel are highly dependant on the lateral shape of the wheel, the computation of these forces is based on vector calculus over a surface represented as a triangle soup (Fig. 7, bottom, (d)).

Note, that a multi-wheeled vehicle generates tracks which affect the sinkage of the following wheels. To compute this effect properly, the terrain is deformed for each contact patch on a simulation integration step (Fig. 7, bottom, (e)). A highly subdivided triangle-faceted mesh represents the deformed terrain.

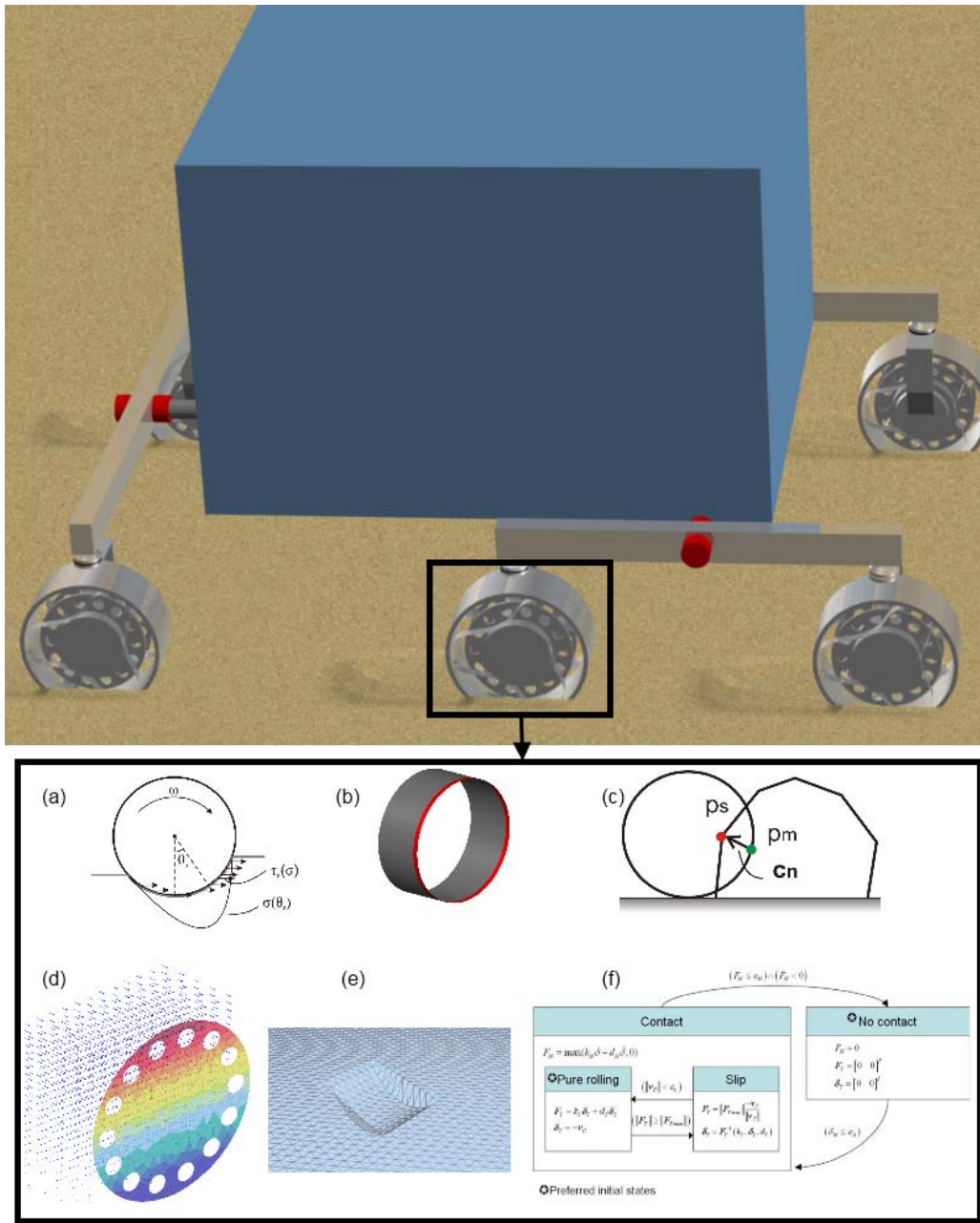


Figure 7 – Overview of multibody simulation model (top) and contact models (bottom): a) normal and tangential pressure distributed on a slice; b) clear-cut of a discrete slice; c) wheel-stone contact detection; d) pressure field acting on the bump-stop; e) deformed surface; f) states diagram of the contact model.

Moreover, the wheels are allowed to loose contact with the surface or with the rocks. Furthermore, rigid surfaces contacts are constrained to keep tangential forces inside the friction cone. This constraint embodies the transition between pure rolling and slipping behavior. To represent all these state transitions, there is a state machine which implements the state transitions and assures the proper change of the structure of the system of Differential Algebraic Equations in the simulation model (Fig. 7, bottom, (f)).

Objective functions and feasible region mapping

There are some characteristics of planetary exploration rovers which are well suited to achieve desired performance indices of trafficability, maneuverability, terrainability, automobility and mission requirements (Apostolopoulos, 2001) for conceptual definitions. Some of those characteristics are: slippery behavior, sinkage behavior, consumed power, weight and dynamic stability. They can be stated as metrics to achieve better performance in soft soil with irregular

distribution of rocks. As an example, three objective functions, J , are being used in this work to quantify the performance of rovers. They are: overall mass,

$$J_{mass} = \sum_{parts} m_{parts} \tag{1}$$

average consumed power,

$$J_{avpower} = \sum_{wheels} \frac{1}{\Delta t} \int_0^{\Delta t} |\tau \cdot \omega|_{wheel} dt \tag{2}$$

and dynamic/static stability. The static stability margin is computed as the worst case stability margin between longitudinal and lateral static stability margins. The dynamic stability margin is very useful when the wheels are in contact with the uneven terrain, which is computed as in Papadopoulos and Rey (1996). Static stability measures are useful in soft terrain traveling, and the vehicle length and track are the most impacting design parameters. Dynamic stability is appropriate in rough terrain navigation; this is highly affected by vehicle suspension design parameters. Overall mass can be computed without the need of simulation, since it is a static objective function but with direct impact in all dynamic objective functions. Average consumed power is explicitly integrated in the simulation time domain and highly sensitive to terrain variations, control laws of the motion controllers, geometry and inertia parameters.

The design parameters are limited due to manufacturing constraints and system requirements; this defines the feasible parameter region. Figure 8 shows the mapping of the feasible parameter region into the feasible objective function region of a single wheel driving straight ahead on rigid or soft surface. The figure shows individual mapping of the ExoMars-type wheel on a range of radius/width configurations into its corresponding mass/power performance. Note that the intermediate parameter choices are mapped exactly in the intermediate feasible objective function region and that the contour of the feasible parameter region embodies exactly the feasible objective function region. In this case, the multi-objective optimization problem is a trade-off solution without the need of optimization algorithms, because it is not numerically intensive.

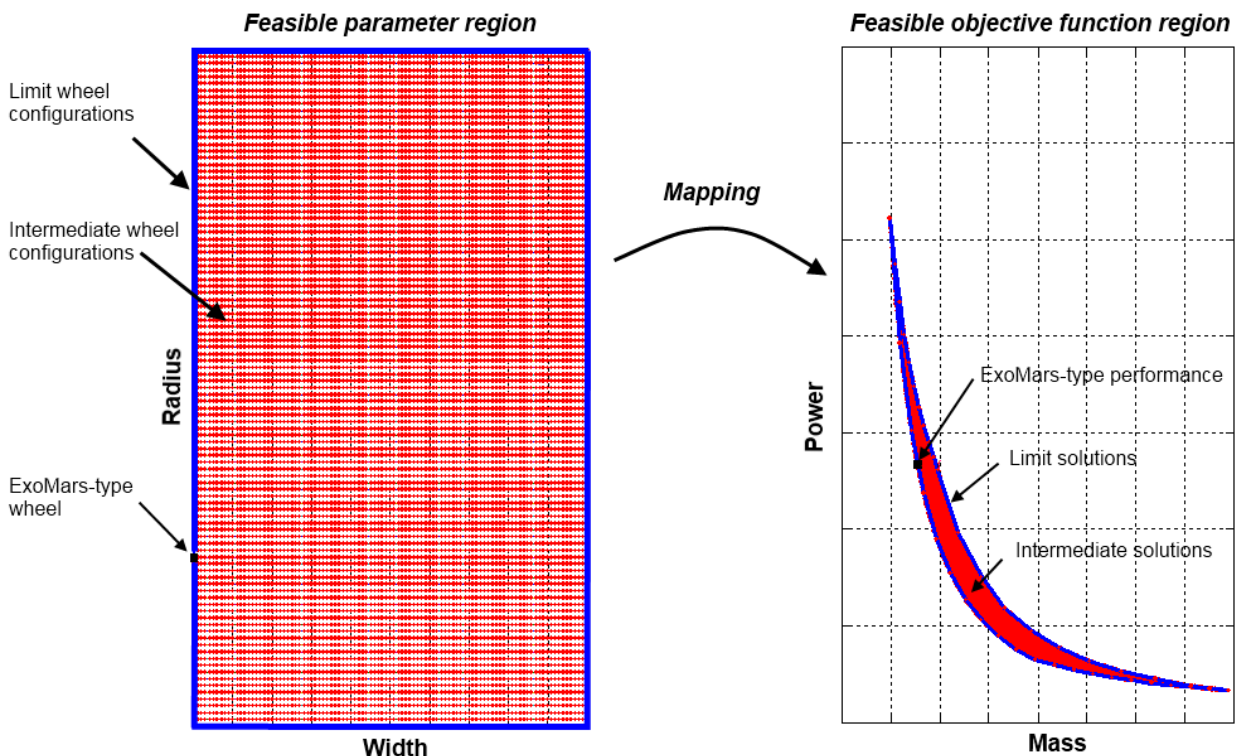


Figure 8 – Mapping of the feasible parameter region (here, wheel radius and wheel width) into the feasible objective function region for a single wheel.

It is interesting to use this insight to search optimal solutions for general multi-wheeled all-terrain vehicles. We applied the same mapping procedure on a two-wheeled bogie in the same simulation conditions. The results are that of Fig. 9.

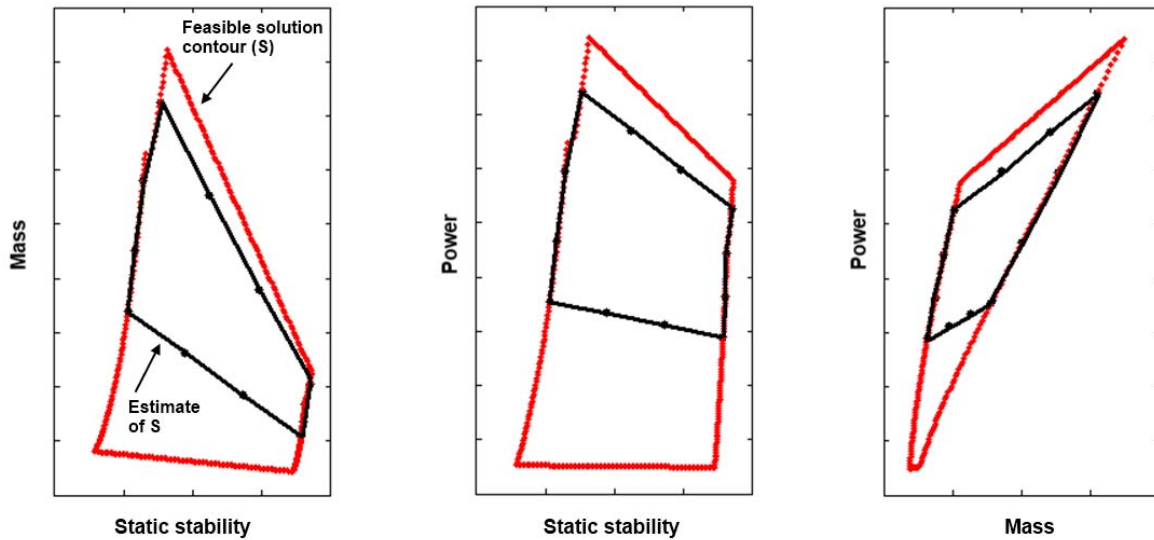


Figure 9 – Mapping of the feasible parameter region into the feasible objective function region for a two-wheeled bogie.

This new case introduces a new insight which can be extended (it was verified) for four and six wheels. The feasible objective region mapped from intermediate design parameters generates the feasible solution contour S . The contour S embodies the contour generated from the hypercubic feasible parameter region (no more a rectangle like in Fig. 9) of the bogie design parameters (length, surface area, distance between bogie and wheels, wheel radius and wheel width). This result can be directly applied to an optimization procedure, because the embodied contour is a reasonable estimate for the contour S , to which the optimal solutions belong. It was applied in the optimization process of a six-wheeled ExoMars-type rover, the convergence was improved and became four times faster than without previous knowledge of the estimate of S .

Multi-case optimization and robust solution

A planetary rover can achieve high performance indexes for some scenario (e.g. driving straight ahead on a rigid surface), but it can be quite unsatisfactory for other most representative scenarios (Fig. 10) with pure undulating terrain (dunes) or sandy environment with randomly spaced rocks. This is the main reason to adopt the multi-case optimization approach, where the optimal solution is found in order to agree with several simulation scenarios. It can be seen as an additional constraint to the optimization problem, because the terrain is one of the inputs of the MBS model.

Multiple cases approach allows the search of a robust solution. In other words, a robust vehicle with high capability of driving with improved performance in worst case scenarios and mission specific scenarios. Some of these cases are illustrated in Fig. 11. The four cases illustrated there are intended to provide suitable simulation inputs to the MBS model in order to find a robust optimal rover design. The assumption behind this approach is that the synthesized rover will achieve optimal performance in most of the real situations during its mission on another planet or asteroid. Additional parameter changes can generate other instances of scenarios. A specific scenario can be instantiated into several others with different terramechanics properties, friction coefficients, gravity, rock distributions, slope angle of the terrain, shapes of the rocks, etc. The more scenarios are available, the more constrained is the problem and more robust is the solution.

Sensitivity analysis can also be performed with respect to scenario parameters or design parameters, because the objective functions are functions of both sets of parameters. The multi-case optimization approach has two drawbacks. The first is that it requires more computation time, since one dynamic simulation of a specific planetary rover is required for each scenario. The second drawback is that unpredictable numerical instability is more likely to occur among several rover configurations and scenarios. When this situation takes place it ruins the optimization iteration, because there will be a wrong evaluation of the objective functions. To cope with the two drawbacks, a modeling effort is required, because the simulation must be numerically stable and computed fast by the numerical integrators. This is a challenge with the nonlinear/variable-structure simulation model used in this work. Some equations of the contact model are coupled with computational algorithms which cannot be reduced algebraically. These algorithms were implemented using the BLAS (Basic Linear Algebra Subprograms) to vector/matrix operations and take advantage of the specific characteristics of the application. For instance, mesh updates and subdivisions can take advantage of the fact that it represents a surface and not a general hull, memory and processing can be saved. Intersection area computation in collision detection was partially solved analytically which also reduces computational cost. Although

future implementations using GPUs (Graphics Processing Unit) are planned to further reduce computation optimization time.

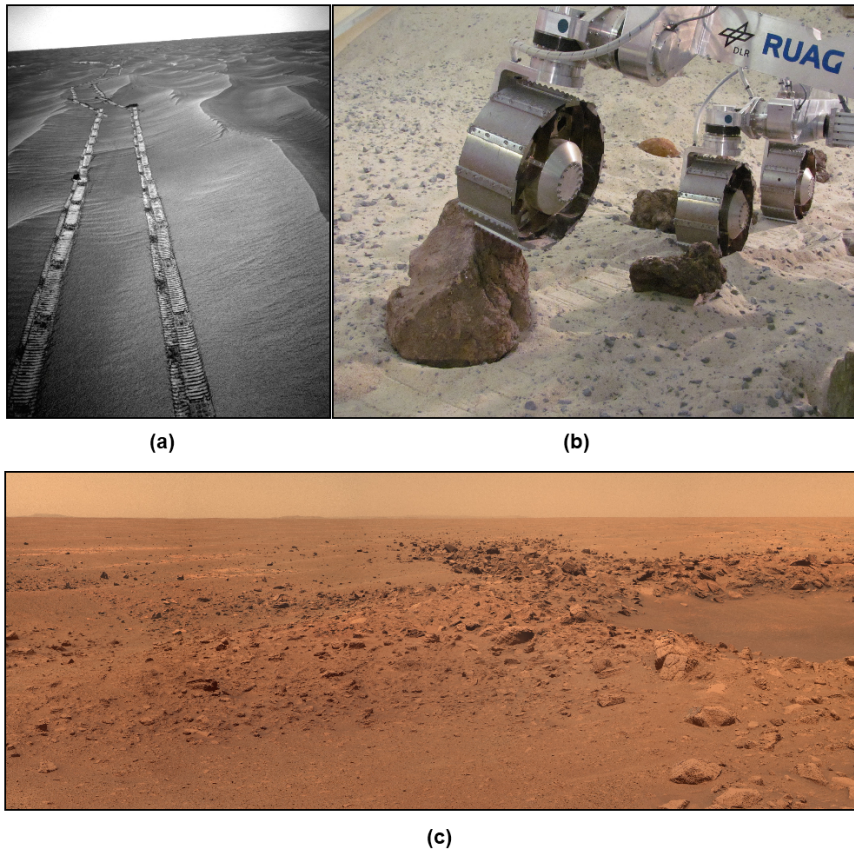


Figure 10 – Real scenarios: a) and c) MER rovers (NASA, 2010), b) ExoMars testbed (DLR, 2010).

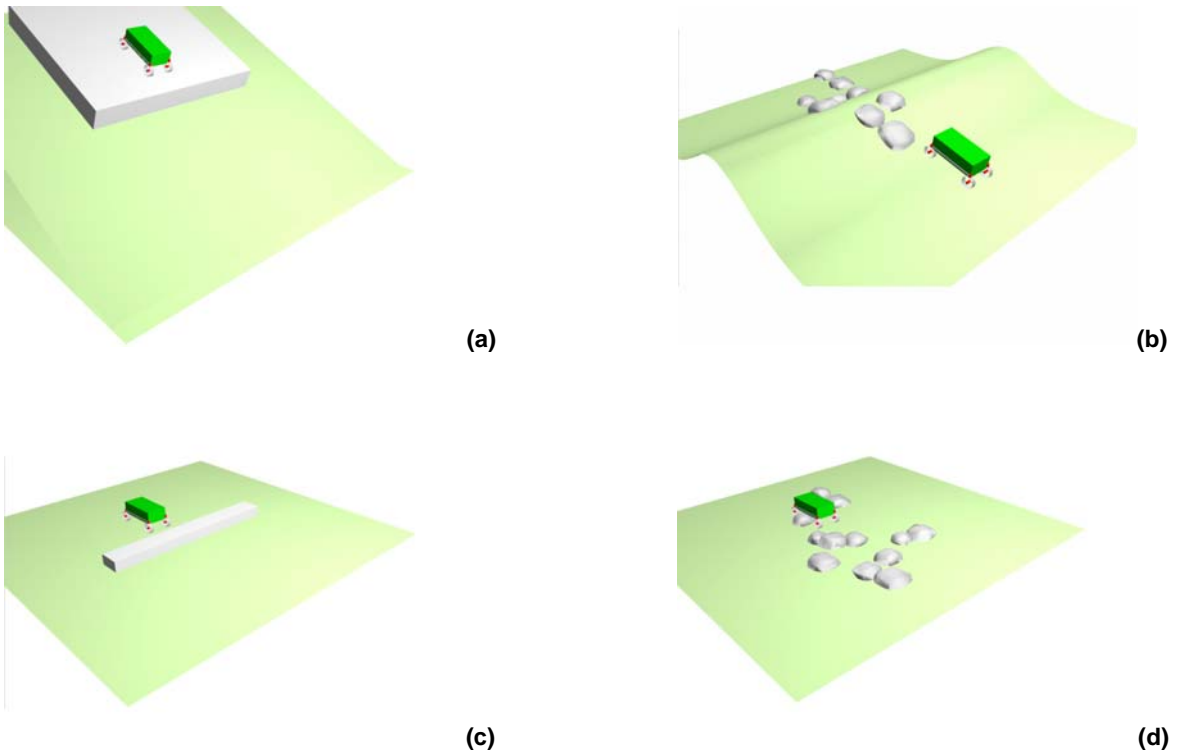


Figure 11 – Multi-cases: a) step-down/downhill; b) Gaussian terrain with stones; c) plane with step; d) plane with stones.

Optimization tool

The contact models, MBS models, optimization strategies and objective functions are components of an optimization tool under development. This tool can be used to synthesize optimal planetary exploration rovers regarding multiple objective functions. Figure 12 shows the sequential steps performed in our optimization tool.

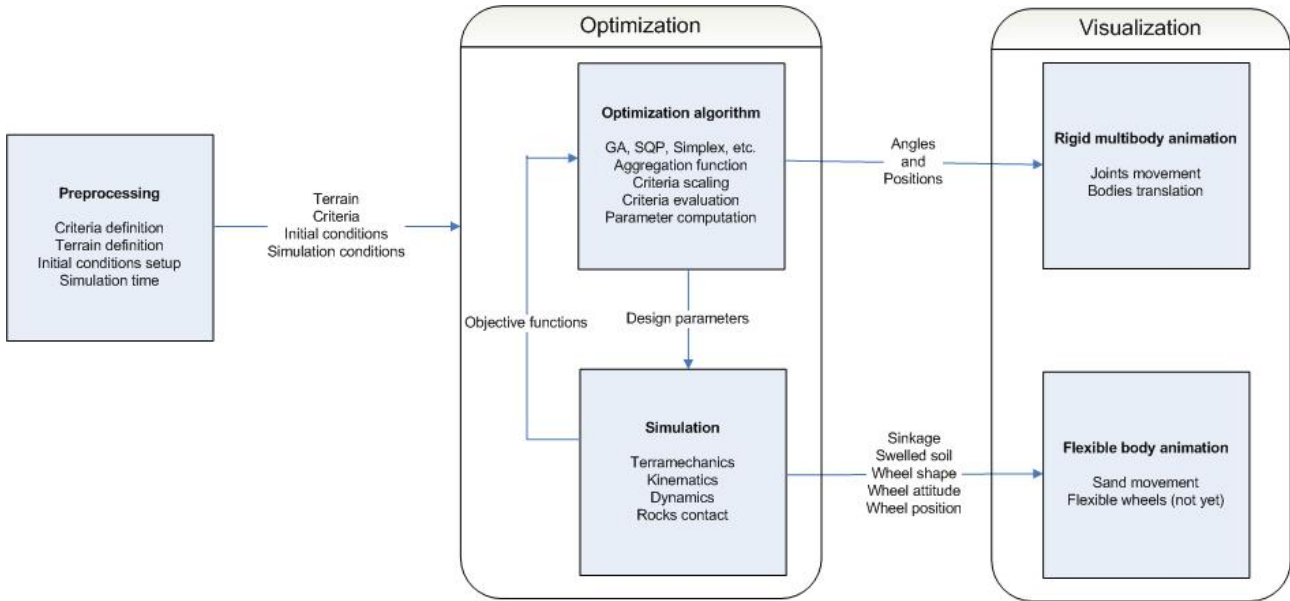


Figure 12 – Steps inside the optimization tool.

Initially, the scenarios (terrain definition, vehicle initial location, and suspension/wheels states and simulation time) and the objective functions are defined in the preprocessing phase. The next step is the optimization loop, one of the several optimization methods available in MOPS can be chosen. The optimizer changes the design parameters and runs each scenario simulation to evaluate numerically the objective functions. At the end of the optimization, the results can be not only plotted, but also shown as animations of the optimized planetary rover driving on several scenarios and compared with some predetermined configuration to depict improvements.

The softwares used to implement the whole tool and the dataflow between them is shown in Fig. 13. Note, that the tool can also be used as a modeling tool (through contact models available in Dymola environment). One can understand Dymola as the modeling and simulation environment, MATLAB/MOPS as the preprocessing, optimization and interface environment, and Blender as the rendering environment.

The inputs to the whole process are three:

1. A MBS model
2. Simulation scenarios
3. Desired objective functions to be optimized

The outputs of the whole process are:

1. A robust optimal planetary exploration rover
2. Graphs showing its performance (parallel coordinates, bar plots and time plots)
3. Animations showing performance and comparison with other designs

CONCLUSIONS AND FUTURE WORK

This work has focused on first steps optimize conceptual planetary rover designs w.r.t certain objective functions. Optimization is based on a Multi-Objective Parameter Synthesis approach, that is capable of handling several objective functions such as mass reduction, motor power reduction, increase of traction forces, rover stability guarantee, and more. The optimization tool is still in development and the first version is not yet fully available. However, further improvement in the optimization capabilities, of the simulation models and new visualization options are well defined for future implementations. Further assets will also deal with various kinematics of the suspension system to find optimal solutions.

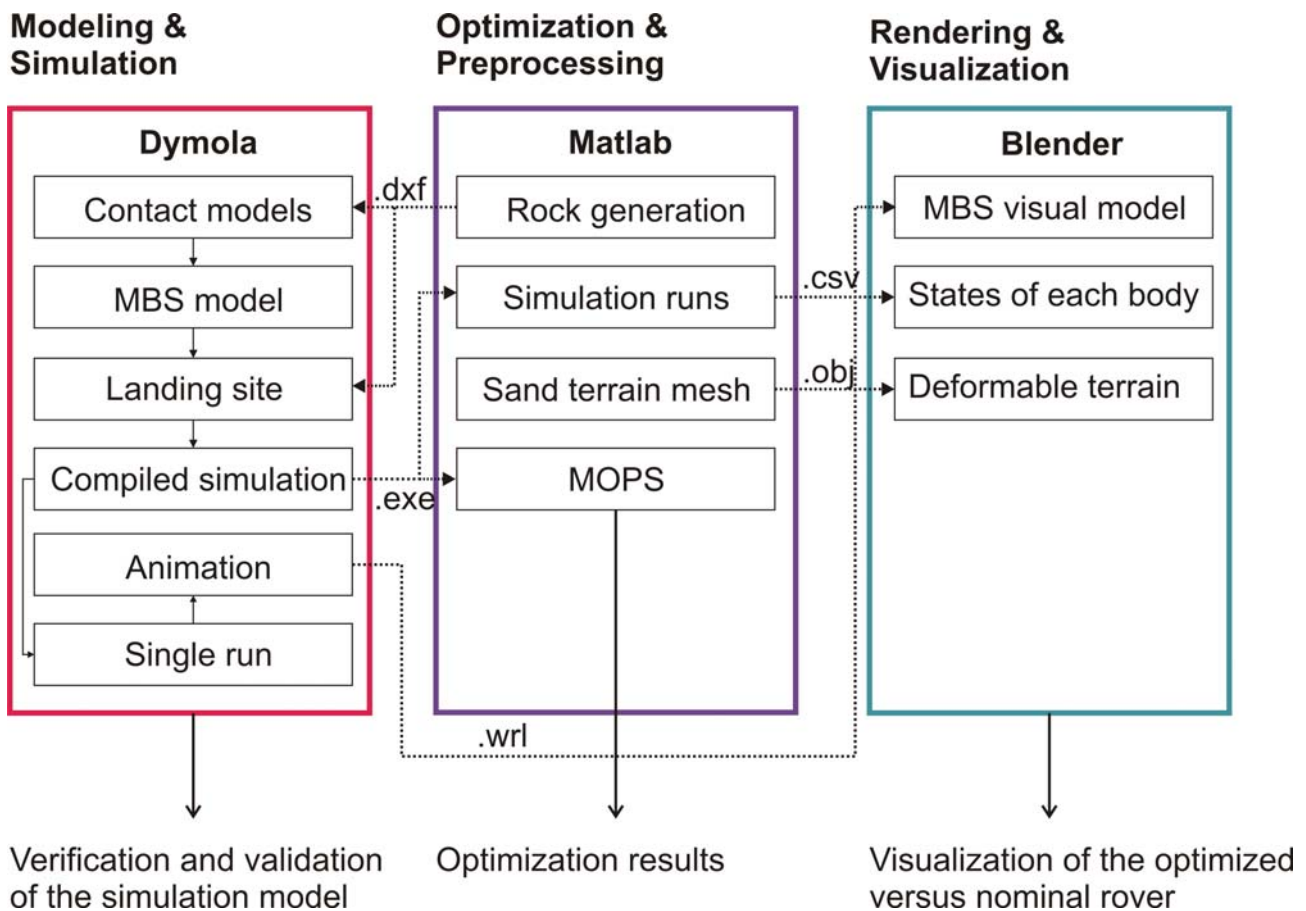


Figure 13 – Dataflow in the optimization tool.

ACKNOWLEDGMENTS

The authors wish to gratefully acknowledge the support by DAAD, the German Academic Exchange Service (Deutscher Akademischer Austauschdienst), to financially grant the stay of guest scientist Alexandre Carvalho Leite at the DLR Institute of Robotics and Mechatronics.

REFERENCES

- Apostolopoulos, D. M., 2001, "Analytical Configuration of Wheeled Robotic Locomotion", PhD Thesis, Carnegie Mellon University, Pennsylvania, USA.
- DLR, 2010, "Mars-Rover im Prüfungsstress", http://www.dlr.de/desktopdefault.aspx/tabid-6221/10233_read-27122/.
- Krenn, R., Gibbesch, A. and Hirzinger, G., 2008, "Contact Dynamics Simulation of Rover Locomotion", Proc. i-Sairas, 9th International Symposium on Artificial Intelligence, Robotics and Automation in Space, Los Angeles, CA, USA.
- NASA, 2010, "National Space Science Data Center", <http://nssdc.gsfc.nasa.gov/>.
- Papadopoulos, E. G. and Rey, D. A., 1996, "A New Measure of Tipover Stability Margin for Mobile Manipulators", In IEEE International Conference on Robotics and Automation (ICRA'96), Minneapolis, USA.
- Schäfer, B., Gibbesch, A., Krenn, R. and Rebele B., 2010, "Planetary Rover Mobility Simulation on Soft and Uneven Terrain", J. Vehicle System Dynamics, Special Issue, Vol. 48, pp. 149-169.

RESPONSIBILITY NOTICE

The authors are the only responsible for the printed material included in this paper.

Testbed for Inertial PIG Sensors Calibration

Winderson E. dos Santos¹, Carlo A. Zanetti Pece¹, Walter A. Kapp² and Gustavo Emmendoerfer²

¹ UTFPR – Universidade Tecnológica Federal do Paraná

Av. Sete de Setembro 3165 – Curitiba – PR – 80.230-901 – Brazil

² EngeMOVI – Engenharia de Automação e Projetos Mecânicos Ltda.

Rua Algacyr Munhoz Mader 3775 sala 11 – Curitiba – PR – 81350-910 – Brazil

Keywords: *testbed, gyroscope, calibration*

NOMENCLATURE

T1 = input mechanical torque	K = harmonic-drive rigidity constant	T = motor output torque
T2 = output mechanical torque	K12 = toothed belt rigidity constant	Tm = unloaded motor torque
θ_1 = input angular position	V _{ar} = reference armature voltage	Tr = load torque
θ_2 = output angular position	Ci = controller's integral gain	Jm = motor rotor inertia
n = harmonic-drive transmission ratio	Gv = controller's proportional gain	Fm = motor axis friction forces
J = harmonic-drive inertia	V _a = armature voltage	ω = motor velocity
J1 = input driving pulley inertia	V _g = motor back fem voltage	θ = motor axis angle
J2 = output pulley inertia	R _a = motor armature resistance	s = frequency plane complex variable
J12 = toothed belt inertia	I _a = motor armature current	
N1 = teeth number in the input pulley	K _t = torque constant	
N2 = teeth number in the output pulley	K _v = velocity constant	

INTRODUCTION

In any measurement system, there will be always the need to know accurately the corresponding calibration parameters. A gyroscope is a classical example of these systems, and includes as parameters the scale factor, bias, noise and stability.

Gyroscopes used in applications (e.g. inertial PIG) demand periodical calibration. The sensors used in inertial systems are modeled in such a way that the resulting calibration equations allow for the best possible precision (Leite Filho, 2007). It has been shown by (Gonzales and De Souza, 2007) and by (Carrara and Milani, 2007) that testbeds make it possible to simulate and control attitude. This paper discusses the main aspects of the development of a testbed for inertial PIG sensors calibration (Kapp, 2007), (Emmendoerfer, 2008).

Gyroscopes and odometers are possibly the main pieces of equipment in an inertial PIG, particularly when a three-dimensional trajectory is being considered. Therefore, the main objective of a testbed would be the identification of the gyroscopes parameters, within an acceptable uncertainty. These parameters include: scale factor, drift, asymmetry, dead zone, thermal influence, noise, and other non-linearities. Moreover, should be also considered the misalignment errors when the sensors are strapdown, and lastly the simulation of movements expected in real PIG missions.

This testbed is supposed to provide data for not only practical simulations of the Inertial PIG, but also other more academic objectives, such as the possibility to foster empirical research on software simulators, signal processing methods, and other uncertainties in inertial navigation systems, as shown in (Carrara and Milani, 2007), (Carvalho, Theil and Kuga, 2007), (Kuga, Milani and Einwoegerer, 2007) and (Silva, 2007). Furthermore, it can also be used in the identification of the rigid body inertial parameters (Schedlinski, 2001), and also in the implementation of nonlinear filters.

The design, manufacturing and integration of all mechatronic elements has been a joint enterprise between UTFPR and an engineering company called EngeMovi (Curitiba-PR), and was supported by Sebrae/Finep (MPE 10-2005). The testbed's installation happened simultaneously to the writing of this paper. A photo of the testbed properly installed at UTFPR is shown in Fig. 1. The next sections of this article describe the electronic and mechanism details that make this testbed capable of not only statically orienting a body with a resolution of 0.18 arc-sec, but also achieving velocities of 450°/s and accelerations of 1125°/s².

MECHANICAL PROJECT

The first phase on the testbed's mechanical project considered (a) the mobile three axis unit kinematic structure, and (b) the components layout (Kapp, 2008). Next, it was modeled the mechanism dynamic behavior in order to obtain data

to specify the drivers; transmissions, servomotors, and corresponding electrical power. Having defined all components, it was then possible to build a detailed three-dimensional CAD model, which employed concepts from precision mechanics, avoiding altogether metrological problems.

Objectives and specifications

The initial objective in this project was the development of a rotational three axis calibration testbed characterized by a spherical robotic joint. It was supposed to have one axis with which one could explore the dynamics of the gyroscopes used in the Inertial PIG project. The other two axis were supposed to be capable of reproducing any trajectory executable by the Inertial PIG (Janschek, 2007).

The testbed was also supposed to have a resolution equal or better than 5 times gyroscope's resolution, and an angular positioning uncertainty of at least 5 times the gyroscope's bias stability added by its angle random walk. The gyroscope specifications are (Honeywell, 2007): 450°/s maximum angular velocity; 0,04°/h random walk; resolution of 1164352 pulses/revolution; and 454g total mass. Other important characteristic are: cylindrical geometry, strapdown housing unit, 3.25kg of total mass, 149 mm of diameter, and 150mm of length.

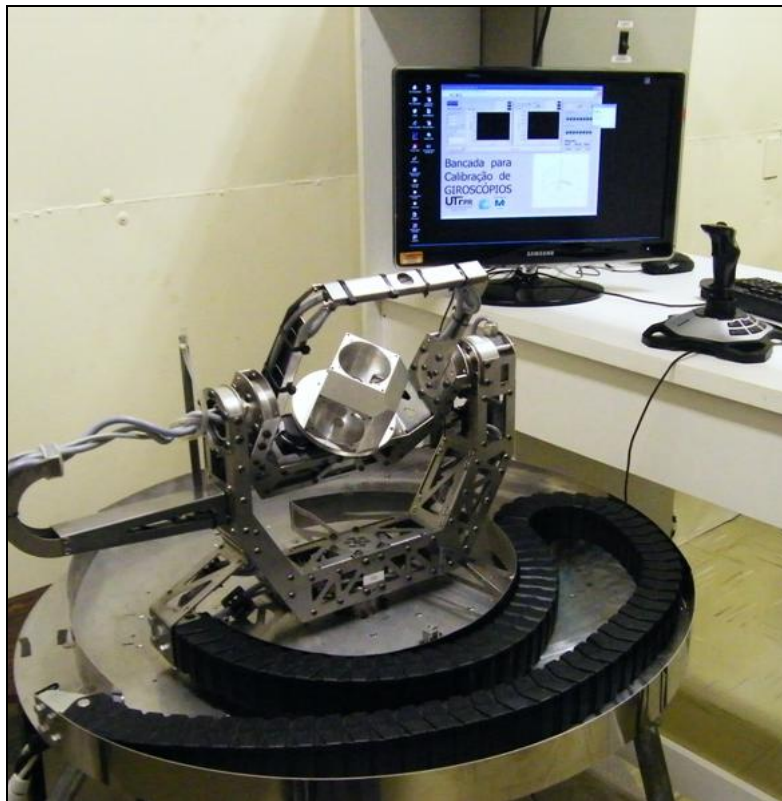


Figure 1 - Photo of testbed installed at the UTFPR laboratory.

Mechanical modelling

The testbed final design, showed in Fig 2, has the following structural elements: a stabilizing base, six legs, a stationary table, the mobile three axis unit, and the power unit.

The stabilizing base is a reinforced 440 kg concrete block, which “floats” over a thick sand layer. It works as a filter to the low ground frequencies, and as a dissipator to the vibrations generated by the testbed itself. The diameter of the circumscribed circle is 1,4m.

The testbed's legs are configured such as in a Stewart platform. Such platform has six adjustable legs, making it possible the complete testbed positioning. The Stewart platform is a rigid structure that provides a “mechanical ground” from stationary table to stabilizing base.

The stabilizing table is a circular steel plane which fixes and orients the first moving axis. During its installation, a spirit level was used in order to guarantee a true vertical orientation to this first moving axis (axis 3). The testbed's circular shape was also useful when installing the power-guide chain. The circular shape allowed a 540° free rotational moving range.

The power unit is composed of amplifiers and electrical sources, which power the servomotors and electronics of the testbed driving system.

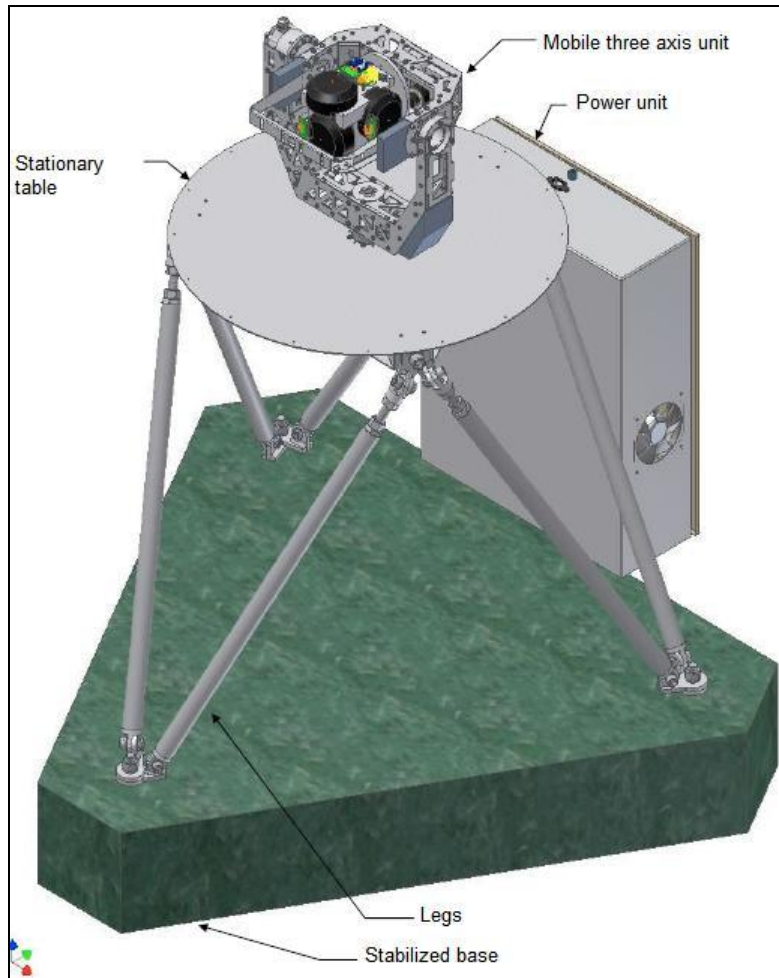


Figure 2 - Testbed layout.

Mobile three axis unit

Figure 3 shows the mobile three axis unit, which is compounded by elements: rotational table, motor 1 axis, link12, counterweight ballast of axis 2, motor 2 axis, auxiliary bearing, electric roof gutter, link23, motor 3 axis and counterweight ballast of axis 3. All elements are following commented.

Rotational table is fitting to insert the Pig Inertial strapdown unit base, which centralize and line up to the testbed axis 1. Besides it references to testbed zero angle marker.

The motor of axis 1 has larger dynamic capability in order to provide a gyroscope calibration. In this axis was used a 150W servomotor coupled by a amplifier transmission (with HTD belts) just to provide a better mechanical impedance compatibility.

The link12 is a cradle structure, constructed by stainless steel plate cuted by laser process, and with milled aluminum cubes. Such structure was optimized to guarantee high rigidity with low weight.

There was necessary uses two counterweight ballast, with 850g each one, in order to balance gravitational effects in the axis 2 feed driver system.

The feed driver system of axis 2 was dimensioned for a dynamic to Inertial Pig trajectory simulation, requiring a 60W power servomotor. Coupling between motor and transmission input axis has made, like in the two others drive systems, by HTD belts. This contributes both for a friction torque reduction and to a better mechanical impedance compatibility.

In relation to auxiliary bearing, it's important to comment that weight of total load in axis 2 (sum of strapdown unit, rotational table, motor 1 axis and link12) is too high to be dynamically supported only by axis 2 bearing. So, it was used an auxiliary bearing, made by a narrow roller, allowing to pass a special alignment tool in their center, and after to pass electrical cables between link12 and link23.

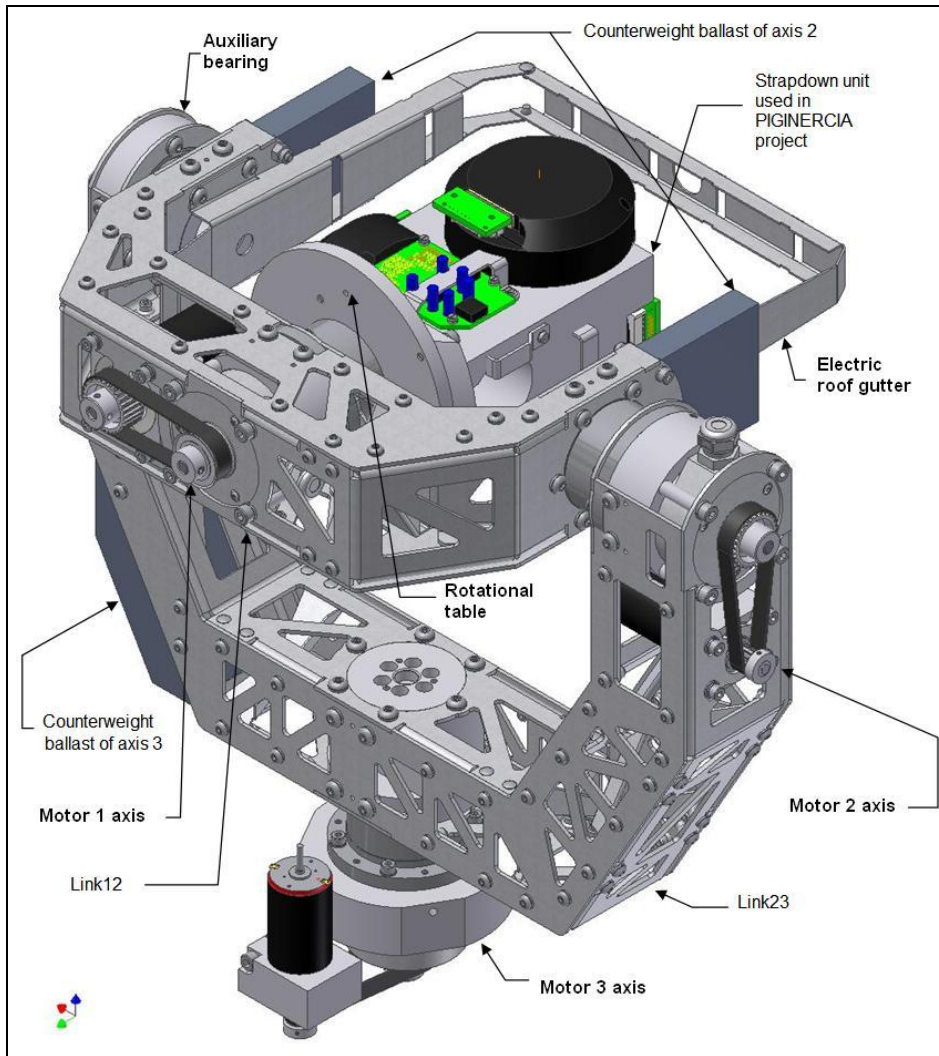


Figure 3- Testbed mobile unit.

Electric roof gutter is a structure that provides a way to conduct electric cables to the instruments to be calibrated over rotational table, in a concentric alignment with axis 1. Such roof also restricts the volume over rotational tables in a 200/200mm diameter/height, avoiding collisions when all axes will be moving.

Link23 is used to join axes 2 and 3. It is, like previously saw link12, a cradle type structure, constructed from stainless steel plates and with milled aluminum cubes.

The feed system to axis3 is identical of axis2 elements. Due to their axis verticality, the static load in such feed driver system is equal to zero, cancelling all gravitational effects. On the other hand, because this axis transport all other move loads, their dynamical demand is greater. Then, because the transmission system is equal to the used in axis 2, the final mechanical impedance compatibility was poor than last one, although the coupling factor is in an acceptable range. This fact occurred because wasn't possible to change the transmission ratio (a limitation imposed by maximum velocity reached if motor uses the same electrical voltage level that other axes).

In order to balance the axis3 dynamic load, there was necessary use 1,87kg counterweight ballast in the link23. The main reason in guarantee such equilibrium is the fact that axis2 feed driver system reflects as a load in axis3.

Motoring system

The concept used in the design of the driving system is unusual. As shown in Figure 4, feedback from encoder is taken in an indirect way, as mean as just after belt-pulley transmission and before harmonic-driver. In most applications encoders are placed together motor axis (indirect feedback) or together load axis (direct feedback).

Due both, as this encoder model has rigid bearing, and there is an Oldham couple in the harmonic-driver, it is possible to transfer torque only by encoder installed in a original bearing situated in harmonic-driver output. At encoder external extremity of such axis was placed the pulley of a teeth-belt reduction, which serves as couple with motor, and permits to adjust motor torque and inertial compatibility. This configuration also results in a compact and elegant layout putting motor parallel to other devices.

At the joint 1 was used a 150W power motor, and coupling transmission is in fact a light amplifier. In the others two joints was used 60W power motors with a 2,0308 coupling transmission ratio.

In joint 1 case happen a rotational speed of 7500RPM in the harmonic-driver axis, which is a value above maximum recommended velocity using original grease lubrication. So, lubrication system needed be change by oil. For this harmonic-drover housing was hind provided in order to retain lubricant. Supplementary, encoder also has a hinder so that it completes housing box.

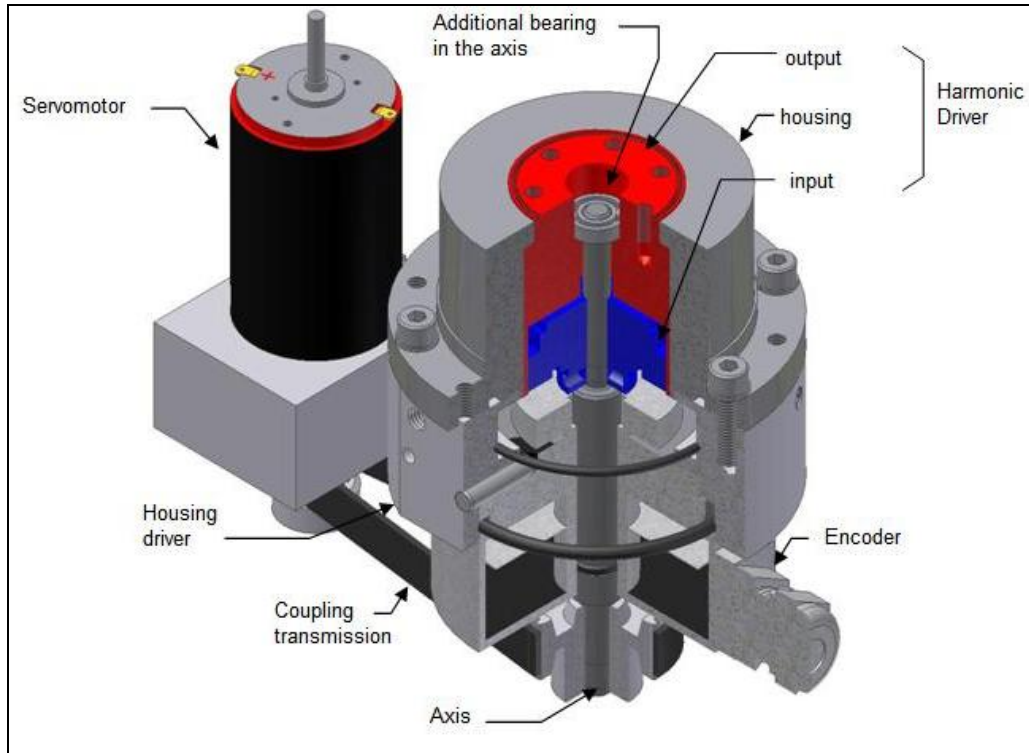


Figure 4 - Mechanical driver configuration per axis.

The testbed has been designed to achieve the following performance:

Table 1 – Designed testbed motion performance

Maximum load capability		6 kg
Maximum load volume:	Diameter	200 mm
	Height	200 mm
Motion ranges:	Joint1	free
	Joint2	$\pm 2\pi$ rad ($\pm 360^\circ$)
	Joint3	$\pm 3\pi/2$ rad ($\pm 270^\circ$)
Spherical dynamic (in any axis):	Maximum velocity	3,34 rad/s (190 °/s)
	Maximum acceleration	4,53 rad/s ² (260 °/s ²)
	Acceleration angle	1,23 rad (70,4 °)
	Acceleration period	0,74
Calibration dynamic (only in the axis1):	Maximum velocity	7,85 rad/s (450 °/s)
	Maximum acceleration	19,6 rad/s ² (1125 °/s ²)
	Acceleration angle	$\pi/2$ rad (90 °)
	Acceleration period	0,4 s

TRANSMISSIONS ELEMENTS

The mechanical elements used to transmit motion/torque are basically harmonic-drives and pulley/belt sets. These elements have their schematic representations shown in figure 5.

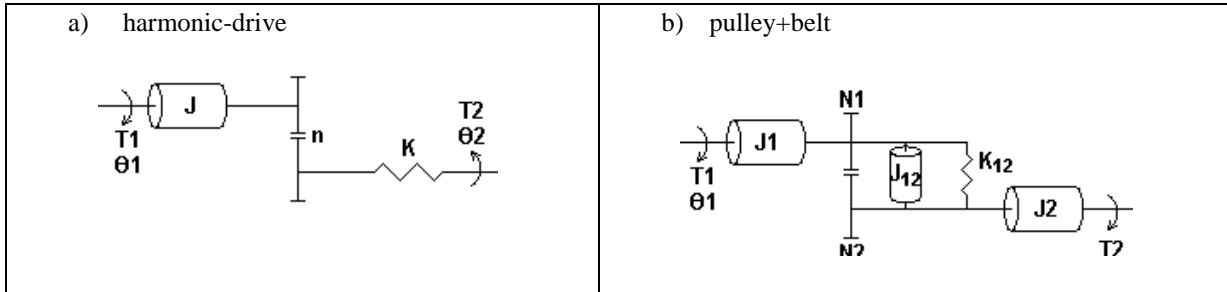


Figure 5 - Schematic representation: a) harmonic-drive, b) pulley+belt.

The in/out torque relationship is given by:

$$T2 = \eta \cdot N \cdot T1, \quad (1)$$

$$N = \begin{cases} n & \text{(harmonic drive)} \\ \frac{N2}{N1} & \text{(pulley + belt)} \end{cases}. \quad (2)$$

The harmonic-drive efficiency is given by $N_{HD} \approx 0,76$ and the pulley/belt efficiency by $N_{BP} \approx 0,95$.

The mechanical driving model for each of the testbed's joints is depicted in figure 6, where M is the motor, Jm and Je are the inertias for the axes and encoders respectively, and Fm the corresponding friction.

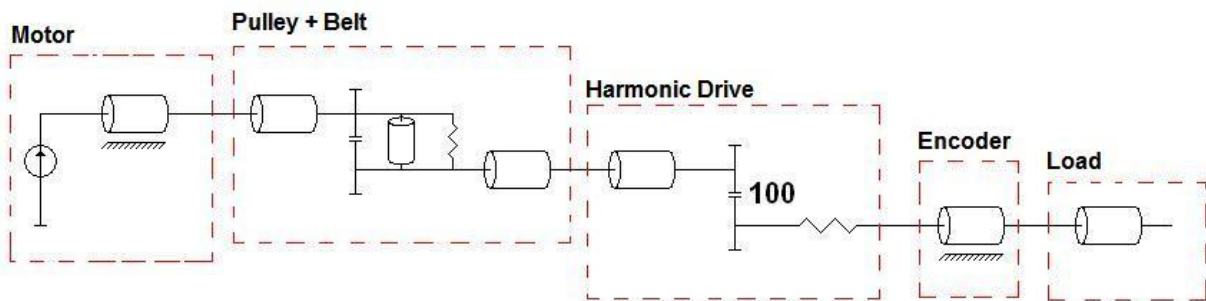


Figure 6 - Schematic diagram of transmissions elements

SERVOMOTOR

The driving system for each of the joints is composed of a brushless CC servomotor whose power is 60 W for the base joints, and 150 W for the calibration joint. These motors were chosen given the fact that they can operate with high torques/velocities when driving low frictional high inertia loads, which is exactly the case of the testbed's joints.

The power unit has been designed to power all testbed's circuits, to make the interface between the testbed and the computer, and to amplify the motion control signal for the servomotors. It is basically composed of servo-amplifiers (Maxon Motor ADS_50/5), the control interface (National Instruments UMI 7764), and power fonts of 5 and 49 V. The other unit components are: on/off signalized switch, 5A fuse for protection, input power connector, auxiliary outlet, toroidal transformer, emergency stop button, forced ventilation fans, and a connector to the main umbilical cable, which connects the power unit and the testbed.

The testbed's driving mechanism can be thought of as composed of torque/motion motors and transmissions. These elements have been specified in such way that they could be easily found (commercially available), and yet satisfying the design requirements. In this fashion, the chosen motors are CC servomotors from Maxon RE series, whose catalogue data are next presented:

Table 2 – Motors technical characteristics

PARAMETER X MOTOR MODEL (manufacturer code)	310009	148877
Power [W]	60	150
Nominal voltage [V]	48	48
No load speed [rpm]	8490	7580
Stall torque [mNm]	1020	2500
Speed/torque gradient [rpm/mNm]	8.33	3.04
No load current [mA]	78.5	68.6
Starting current [A]	19.0	41.4
Terminal resistance [Ω]	2.52	1.16
Max. speed [rpm]	12000	8200
Max. continuous current [A]	1.72	3.3
Max. continuous torque [mNm]	88.2	201.0
Max. Efficiency [%]	88.0	91.8
Torque constant [mNm/A]	53.8	60.3
Velocity Constant [rpm/V]	178	158
Mechanical time Constant [ms]	3.01	4.26
Rotor inertia [J_m] [gcm^2]	34.5	134.0
Terminal inductance [mH]	0.513	0.330
Thermal-resistance housing-ambient [K/W]	6.00	4.65
Thermal-resistance winding-housing [K/W]	1.70	1.93
Mass [g]	238	480

These motors, identified as 60W and as 150W, are fed by electric drivers from the same maker. The operating voltage for the motor power circuit is 49Vcc. The electric motor drivers have been set to operate in torque mode, which supplies a controlled current that ranges from -5A to +5A, accordingly to the controller reference signal (-+/10V). The drivers are switched by 50kHz pulse width modulation (PWM). The drivers have also been gain adjusted for velocity and current, besides having received limiters to constant and peak currents.

In order to obtain a position feedback signal, all motors have an incremental 18,000 tracks encoder. So, when set to the quadrature mode, it is possible to obtain a final resolution of 72,000 increments per complete cycle. Additionally, when this value is multiplied by the harmonic-driver ratio, a final axes resolution of 7,200,000 increments is achieved.

A block diagram for each set motor/amplifier is show in Figure 7.

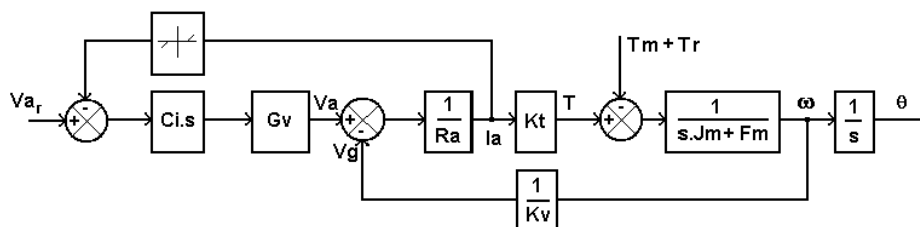


Figure 7 - Motor plus driver model diagram.

It should be noted that the testbed is an open automated system. This fact associated with the powerful motion control platform features allows one to perform a myriad of experiments and tests. This is an important advantage when considering the conventional black box like configuration of the proprietary rotational simulators.

KINEMATIC FORMULATION

Testbed kinematic equations follow to a spherical joint pattern, similar to others found in robot wrists or mechanisms. Such kinematic configuration would be better depicted by the chain representation showed in Figure 8.

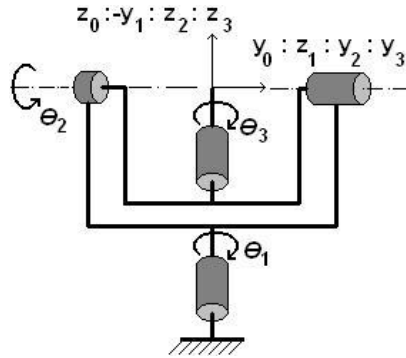


Figure 8 - Testbed kinematic chain representation

It is important to observe that the axes nomenclature is inverted in relation to the project one, that is, joint 1 corresponds to axis 3 and joint 3 correspond to axis 1. This peculiarity occurs because the kinematic analysis starts from the base axes, while the mechanism design starts from the output axes.

The testbed’s direct kinematics can be formalized via the well know Denavit-Hartenberg methodology (Kapp, 2007). The resulting transformation (pure rotation) matrix is next shown:

$$R = \begin{pmatrix} C_1 C_2 C_3 - S_1 S_3 & -C_1 C_2 S_3 - S_1 C_3 & C_1 S_2 \\ S_1 C_2 C_3 + C_1 S_3 & -S_1 C_2 S_3 + C_1 C_3 & S_1 S_2 \\ -S_2 C_3 & S_2 S_3 & C_2 \end{pmatrix} \quad (3)$$

where $C_i = \cos(\theta_i)$, and $S_i = \sin(\theta_i)$. Then, from expression (3) the following equations can be extracted:

$$\theta_1 = ATAN2(R23/ R13), \quad (4)$$

$$\theta_2 = ACOS(R33), \text{ para: } -90 < \theta_2 < 90 \text{ } \} \text{ and} \quad (5)$$

$$\theta_3 = ATAN2(R32/ R31). \quad (6)$$

These results express the testbed’s inverse kinematic relationships.

PRELIMINARY RESULTS

The testbed is operational since mid 2010. Some preliminary dynamical aspects may now be analyzed. One important question is: how was the control system behavior? For answer this question it is possible to use software MAX (Measurement and Automation Explorer) from National Instruments. Follow it is presented how the axis have been behaved after a suitable tune in the PID motion control gains.

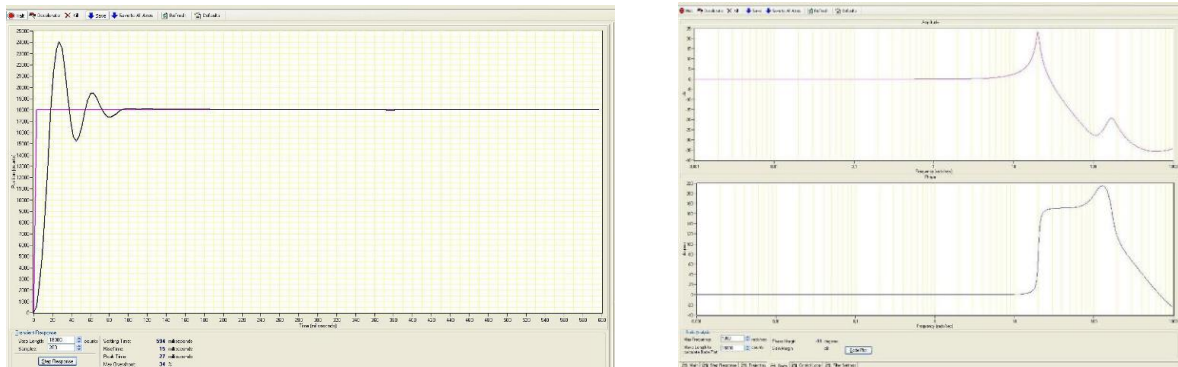


Figure 9 – Control behavior of axis 1: step response (left), frequency response (right).

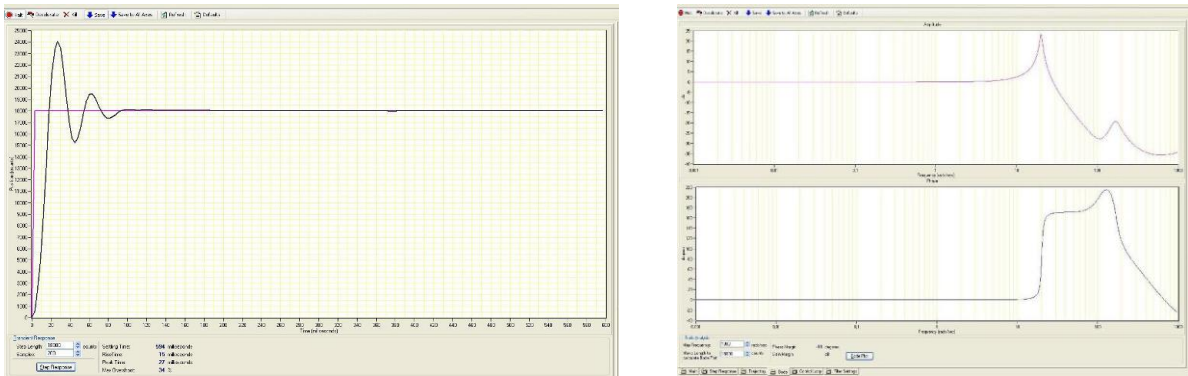


Figure 10 – Control behavior of axis 2: step response (left), frequency response (right).

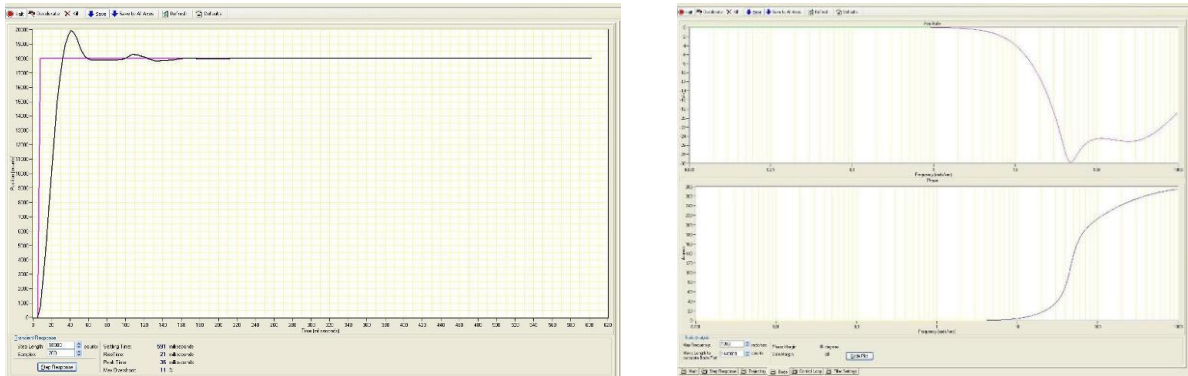


Figure 11 – Control behavior of axis 3: step response (left), frequency response (right).

As is possible to see in Figures 9 and 10, axis 1 and 2 presented similarity in control behavior. This was expected for those this axes because they have small friction load torque. Then resonance frequency of 13Hz and 20Hz was measured as at axes 1 and 2 respectively. PID gains was choose using an auto-tuning function as a start values and then a manual fine-tuning tracking smallest both settling time and overshoot, but without regimen error.

About axis 3, there no occurs resonance because high load friction torque presented. This is imposed by power-guide chain when moving over stabilized table. This axis was tuning following same objectives of other two axes.

A final measurement test was proceed applying a constant rotation of 0,05°/s in the calibration axis (axis 1) and, using gyroscope, taking measure as show in Figure 12. There is important point out that the axis, in this experiment, was oriented perpendicular to Earth axis rotation, in order to minimize planet move into the measure.

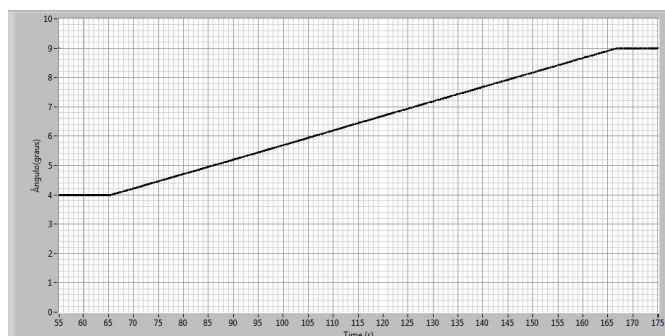


Figure 12 – Gyroscope measure.

CONCLUSIONS

The UTFPR has developed a testbed for the calibration of gyroscopes, particularly those supposed to be used in the Inertial PIG Project (Kapp, 2007), (Emmendoerfer, 2009). The mechanical design has been optimized both technically and economically. The structural components were manufactured from high tensile steel plates via laser cutting. The method proved to be low cost and the final product presented high rigidity and low weight.

The supporting Stewart platform is adjustable allowing for the necessary leveling. The platform has been installed over a seismic concrete/sand base which filters mechanical vibrations.

The servomotor design is in some way innovative. The semi-direct feedback is obtained through the installation of the encoder before the harmonic-drive. This configuration allows a 100 times amplification in the resolution of the orientation positioning.

It should be reminded that the open structure of the testbed is an important advantage when compared with other commercial rotational simulators. The access to the project data allows one to perform tests which would be otherwise difficult or even impossible.

The testbed is nowadays operational, making it possible the duplication of the tests mentioned in (Sciavicco and Siciliano, 2005), (Roquete, 2007) and (Dos Santos, Gavloski and De Vecchi, 2008). Furthermore, it can also be used in third party requests.

In a near future, the testbed uncertainties and imprecisions are supposed to be addressed as proposed by (Leite Filho and Carrijo, 2007), and (Brito, Barbosa and Da Silva, 2007). The results and conclusions should then support deeper analysis on this strategic theme for anyone looking for the benefits of inertial navigation systems.

REFERENCES

- Brito, A. G.; Barbosa, E. G. *et* Da Silva, C. H. – Identificação de mesa rotativa para ensaios de sensores inerciais. V SBEIN. RJ, 2007, Brasil.
- Carrara, V *et* Milani, P. G. – Controle de uma Mesa de Mancal a Ar de um Eixo Equipada com Giroscópio e Roda de Reação. V SBEIN. RJ, 2007, Brasil.
- Carvalho, G. B.; Theil, S. *et* Kuga, H. K. – IMU: Generic Model Development Approach. V Simpósio Brasileiro de Engenharia Inercial. Rio de Janeiro, 2007, Brasil.
- Dos Santos, W. E., Gavloski, P. C. *et* De Vecchi, R. – Avaliação de uma Bancada para Calibração de Giroscópios. Seminário de avaliação de trabalhos de conclusão de curso do DAELT/UTFPR. Curitiba, Brasil, 2008.
- Emmendoerfer, G. - Desenvolvimento e Implementação de um Sistema Inercial de Trajetórias de Dutos. Dissertação de Mestrado apresentado à UTFPR. Curitiba, PR, Brasil, 2008.
- Emmendoerfer, G. *et alli* - Pipelines Inspection Gauge with Inertial Measurement System. Proceedings of the XIII International Symposium on Dynamic Problems of Mechanics (DINAME 2009), Brazil, 2009.
- Gonzales, R. G. *et* De Souza, L. C. G. – Kakman Filter Performance Evaluation for Attitude Estimation and Control of a Satellite Simulator. V Simpósio Brasileiro de Engenharia Inercial. Rio de Janeiro, 2007, Brasil.
- Honeywell. - Manual do Giroscópio HONEYWELL GG1320AN01. 2007.
- Janschek, K. - Pig Report. Projeto de pesquisa PIG Inércia. UTFPR, Curitiba, PR, Brasil, 2007.
- Kapp, W. A. - Projeto Mecânico da Bancada de Calibração. Projeto de pesquisa PIG Inércia. Universidade Tecnológica Federal do Paraná, Curitiba, PR, Brasil, 2008.
- Kapp, W. A. - Projeto mecânico do PIG inercial. Projeto de pesquisa PIG Inércia. Universidade Tecnológica Federal do Paraná, Curitiba, PR, Brasil, 2007.
- Kuga, H. K.; Milani, P. G. *et* Einwoegerer, W. – Experimentos de alinhamento de unidade de medida inercial baseada em MEMS (Micro Electro-Mechanical Systems). V SBEIN. RJ, 2007, Brasil.
- Leite Filho, W. de C – Panorama de Algoritmos de Navegação Inercial “Strapdown”. V SBEIN. RJ, 2007, Brasil.
- Leite Filho, W. de C. *et* Carrijo, D. S. – Ensaios para Identificação da Banda Passante de Sensores Inerciais. V SBEIN. RJ, 2007, Brasil.
- Pece, C. A. Z. e Almeida, S. F. M. Z. Atingindo Linearidade em Cinemática de Atitude para Ângulos Moderados de Rotação. In: V Simpósio Brasileiro de Engenharia Inercial, Rio de Janeiro, RJ, CD-ROM, 2007.
- Roquete, P. – Metodologia para Avaliação da Confiabilidade Metrológica de Sistemas Inerciais Puros. V SBEIN. RJ, 2007, Brasil.
- Schedlinski, C *et* Link, M - A Survey of Current Inertia Parameter Identification Methods. Mechanical Systems and Signal Processing. Disponível on-line em <http://www.ideallibrary.com>. Academic Press, 2001.
- Sciavicco, L. *et* Siciliano, B. – Modelling and Control of Robot Manipulators. Springer-Verlag London. RU, 2005.
- Silva, C. A. *et alli* – Software Simulador de um Determinador de Atitude. V SBEIN. RJ, 2007, Brasil.

RESPONSIBILITY NOTICE

The authors are the only responsible for the printed material included in this paper.

HARDWARE-IN-THE-LOOP SIMULATION OF AN H_∞ CONTROLLER ON THE STABILIZATION OF A 2-DOF QUADROTOR

Ricardo Breganon¹, Rafael C. B. Sampaio², Mateus Moreira de Souza¹, Fabio Toledo Bonemer De Salvi¹,
Eduardo M. Belo¹, Marcelo Becker²

¹ University of São Paulo, EESC/LADinC

² University of São Paulo, EESC/LabRoM

Abstract: Unmanned aerial vehicles, such as helicopters, quadrotors or planes are of a great importance when it comes to working in environment that is inaccessible or when terrain is exposed to hazards such as natural disasters and wars. Nowadays, UAVs have been used in civil and military industry. This paper presents the design and implementation of a robust H_∞ controller, applied in an experimental plant of a quadrotor, fixed in workbench. This system is connected in a fixed base, just allowing the roll and pitch motions, therefore with only two degrees of freedom. The position of the system is corrected through the response of the sensor, which act on control action of the rotors. A quadrotor is a flying object having two pairs of rotors rotating in opposite directions, minimizing the gyroscopic effect. A mathematical model of the quadrotor will also be presented in this paper. Physical systems are subject the perturbation of different types. Uncertainty in the mathematical model of the system is, in general, modeled as a perturbation to the nominal model. The uncertainties have several origins, can be highlighted: the existence of errors in the values of model parameters or parameters values are unknown; the parameters in the linear model can vary due to non linearities or variation of the operation point; the errors associated with instruments measurement and the structure of the model at high frequencies are not known, so that the uncertainties can cross the actual gain of the plants. To perform the experiment, we used a computer with operating system Windows XP, a controller card to control of fast prototyping dSPACE 1103, which has good processing power, vital to many applications involving sensors and actuators. The dSPACE also works with a real time interface, where the controller is fully programmable in blocks diagrams in SIMULINK®. Simulations will be accomplished to verify the response of the system through the mathematical simulation environment Matlab/SIMULINK are adjusted where the weighting functions of H_∞ controller to obtain the performance characteristics, accuracy and stability desired for the quadrotor. The understanding of the effects of the weighting functions on the control system is crucial for modeling the desired specifications. The standard problem of H_∞ control is formulated in terms of finding a controller K, which will be implemented in the control system. In this work the results obtained after adjustment of the weighting functions of the controller through simulations with the linear model will be compared with the results of the controller applied to the experimental model through the technique "hardware-in-the-loop." The results will show the performance and the efficiency of the applied methodology.

Keywords: quadrotor, robust controller, H_∞ , MAVs, UAVs

INTRODUCTION

Unmanned aerial vehicles (UAVs) are crafts capable of flying without an onboard pilot, with own power supply. They can be controlled remotely by an operator, or can be controlled autonomously via preprogrammed flight paths. A quadrotor helicopter is an aircraft whose lift is generated by four rotors, with two pairs of counter-rotating, fixed-pitch blades located at the four corners of the aircraft. The control of such a craft is accomplished by varying the speeds of the four motors relative to each other (NWE et al., 2008). More importantly, an UAV can maintain the flight beyond the limits of an human pilot (EFE, 2007). However, the quadrotor is a dynamically unstable nonlinear system which requires a suitable vehicle control system. One drawback of small UAVs in nearly all types of application is the reduced payload and the limited amount of batteries that can be carried (Voos, 2009).

The development of aerial robots that are able to fly autonomously is one of the greatest challenges of robotics and aerospace engineering in the very beginning of 21th Century. After the development of microelectronics and then the miniaturization of components, mini aerial vehicles (VAVs) have gained ground. The field of research involving those devices offers a great variety of possibilities to be explored (BOUABDALLAH et al., 2007), highlighting, i.e., embedded systems for robust control and stabilization of aerial machines. Mini aerial vehicles (MAVs) can be extremely useful in aerial surveillance to fire combat, localization and rescue of people and animals in places of difficult access, i.e., in mountains, for border patrol and gathering of samples over the atmosphere. Likewise, they can be very effective in the inspection and surveillance of indoor environment. In agriculture, they can be widely employed on detection of diseases by aerial capturing of images (KIM et al., 2010) (TISDALE, et al., 2006). Indeed, to exemplify how useful MAVs can be in many aspects of daily-basis, a research was run after Katrina's hurricane in New Orleans in 2005, aiming to establish some rules to determine the correct operations with MAVs (PRATT, et al., 2009).

Affected by aerodynamic forces, the quadrotor dynamics is nonlinear, multivariable, and is subject to parameter uncertainties and external disturbances. The control of a quadrotor must: to meet the stability, robustness and desired dynamic properties; to be able to handle nonlinearity; and to be adaptive to changing parameters and environmental disturbances.

Main difficulties concerns to parametric uncertainties, non-modeled dynamics, and external disturbances, which result in the raising of complexity of design of. Many of advanced control methods, such as feedback linearization, have been developed to meet the demands on performance (BENALLEGUE, 2007).

We focus our work on the synthesis and the analysis of a robust H_∞ controller (DOYLE, et al., 1989) (ZHOU, 1997) so that we can understand the behavior of the quadrotor in MAV configuration, which when it is subject to external perturbations. Thus, as our aim was, *a priori*, to analyze the controller, we attached the aircraft to a test bench in our laboratory, in order to ease the access to the quadrotor. The model is obtained through the virtual prototyping ADAMS® environment system, using modeling techniques of multi-body systems to get the dynamic equations of motion.

QUADROTOR STABILIZATION PROBLEM FORMULATION

Platform & Problem Statement

The platform comprehends an X-shaped 2-DoF structure built from carbon fiber, as one may see in Fig. 1 (a). We used four aeronautic brushless DC Motors to compose the power plant of the aircraft, which are attached to a half distance between the tip of each arm and the center of gravity of the quadrotor. The CG of the equipment is fixed to a vertical articulation that is connected to a metallic bar which, in turn, is linked to a steel stand. We consider the entire structure as a rigid body. The whole platform, including the quadrotor itself and the PC plus cabling communication interface can be seen in Fig. 1 (b).

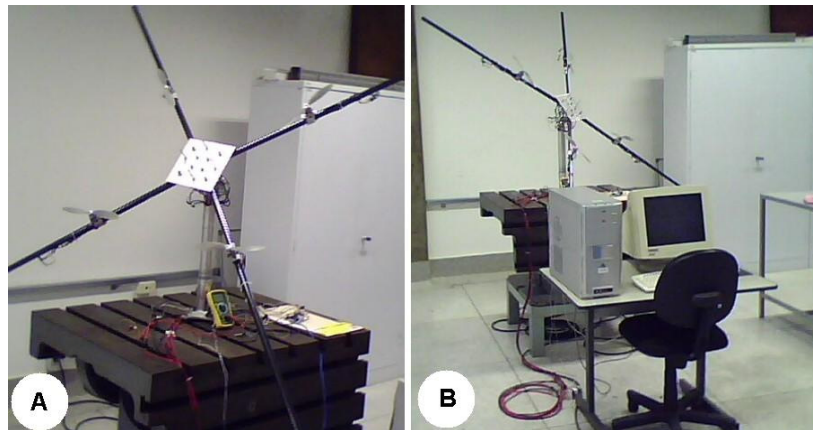


Fig. 1 - The quadrotor structure mounted over the steel stand (a) and the dSpace™ communication interface (b).

The problem of control of the stability of the quadrotor lies in the correct application of electric current to the each one of the four motors individually. Each motor runs after the application of PWM whose duty cycle range starts from 1ms (minimum rotation) and operates until 2ms (maximum rotation). The high level of nonlinearities associated to the quadrotor makes the whole process of design of the controller highly dependent of contour conditions. For example, it was necessary to add a minimum constant pulse to act over the motors to guarantee that they never turn off due to the moment of inertia of the shaft. If it happens when the aircraft is running, the control process turns uncontrollable.

Besides, the variable “time” is a very important point to be considered in such experiment. Thus, the success of a real time HiL (Hardware-in-the-Loop) application experiment depends of a high performance communication interface. In our case, we used the dSpace™ 1103 interface board to acquire/send signals from/to the quadrotor. A Simulink™ toolbox was employed to allow the sketch of the control block diagram. The communication speed chosen to control the quadrotor was fixed around 1kHz. We also used saturators to protect motors from overcurrent hazard. Likewise, the control signal was normalized to accomplish to the appropriated signals that the motor speed drivers demands.

The power plant of the quadrotor is composed by two pairs of counter-rotating propellers (1,3) and (2,4) as one may see in Fig. 2. Figure 2-A shows that the rotation of each pair occurs in opposite directions. This is a very well-known intentional resource to cancel the torques, which allows us to neglect Coriolis effect.

Therefore, roll and pitch rotations are achieved by varying the speed of rotation of each one of the electric motors. The pitch rolling moment is obtained by maintaining the rotation speeds of motors 2 and 4 constant, and varying the speed of motors 1 and 3. However, the speed of motors 1 and 3 must vary in a symmetrically opposite way. It means that as the speed of the propeller of motor 1 raises, the speed of rotation of the propeller of motor 3 must decrease, as it can be seen in Fig. 2-B. The same happens to the roll axis. Motors 1 and 3 keep rotating at the same speed. As there is an increase in the rotation of the propellers of motor 2, motor 4 relaxes in the same proportion, as it can be seen from Fig. 2-C.

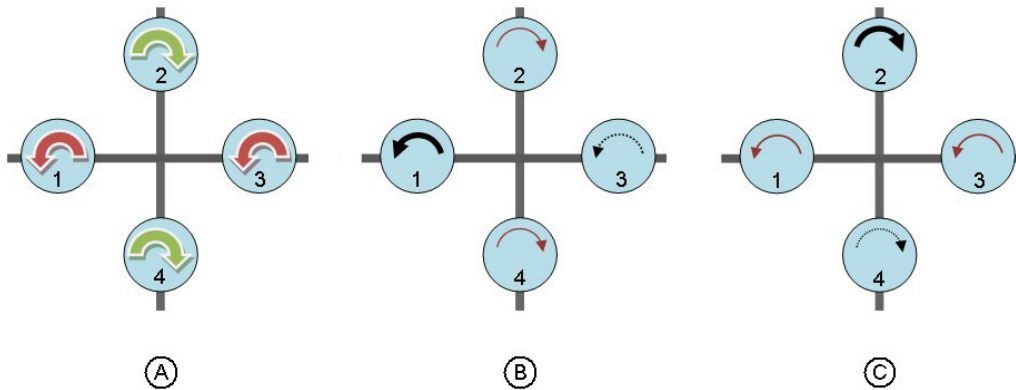


Fig. 2 - Direction of rotation of the motors (A) and variations in the speed of the propellers to generate pitch (B) and roll (C) moments.

DYNAMICAL MODELING OF THE QUADROTOR

As our purpose is to control the quadrotor aircraft through the use of a H_∞ robust controller, it is mandatory that we have the dynamical model of the system. That is one of the requirements of H_∞ synthesis. Likewise, instead of manually sketching the mathematical model to obtain the so-called space state equations of the system, we used ADAMS®, a powerful computational mathematical tool for design and analysis of multi-body dynamical systems, such as the quadrotor.

The whole process consists in providing ADAMS® with some basic information concerning the quadrotor, such as the material of which the aircraft is made, the precise positions and the information about all components of the equipment, such as the position and orientation of the motors and their weights, the exact degrees of freedom of the dynamical system, among many others. The resulting sketch of the quadrotor can be seen in Fig. 3. At the end of the process of design, one can simulate the then-sketched system from ADAMS® simulation environment. However, our interest lies in the matrices that compose the state space equations of the quadrotor. Based on the physical and structural description of the system, the software provides one with the above mentioned matrices.

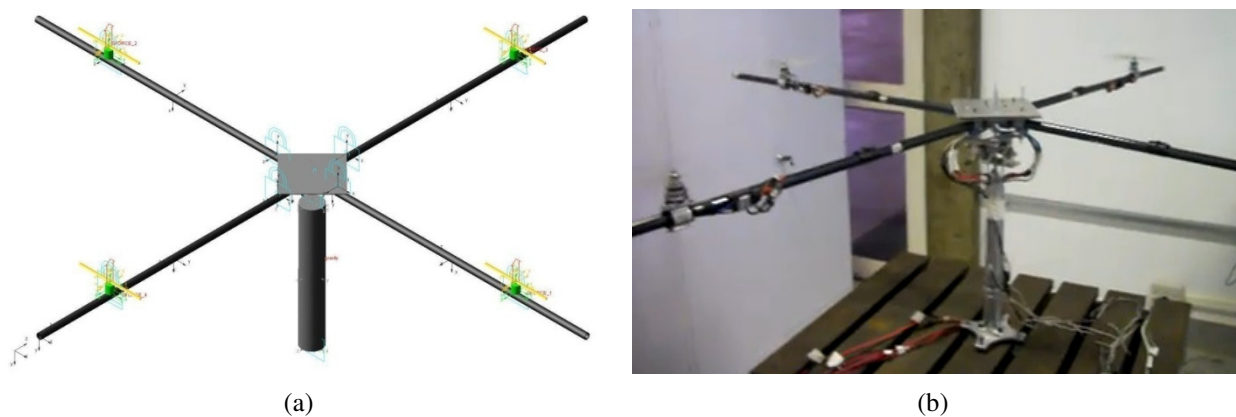


Fig 3 – Computational representation of the quadrotor in ADAMS® (a) and the quadrotor itself (b).

Aiming to treat the quadrotor mathematically, we can represent the dynamical model of it in the state-space form as follows:

$$\dot{x} = Ax + Bu \tag{1}$$

$$y = Cx + Du$$

Where x is the state vector, y is the output vector and u is the control vector. Thus, after solving the state equations of quadrotor, ADAMS® provides us with the matrices A, B, C and D that composes the state-space representation of our quadrotor, as follows:

$$A = \begin{bmatrix} 0 & 4.1397 & 0 & 0 \\ 1 & 0 & 0 & 0 \\ 0 & 0 & 0 & 4.1449 \\ 0 & 0 & 1 & 0 \end{bmatrix} ; B = 1.0 \cdot 10^3 \cdot \begin{bmatrix} 0 & -1.2052 & 0 & 1.2052 \\ 1 & 0 & 0 & 0 \\ 1.2067 & 0 & -1.2067 & 0 \\ 0 & 0 & 0 & 0 \end{bmatrix} \tag{2}$$

$$C = \begin{bmatrix} 0 & 0 & 0 & -0.0012 \\ 0 & -0.0012 & 0 & 0 \end{bmatrix} ; D = \begin{bmatrix} 0 & 0 & 0 & 0 \\ 0 & 0 & 0 & 0 \end{bmatrix}$$

THE H_∞ CONTROLLER SYNTHESIS PROCESS

The H_∞ controller designed was based on the work of (DOYLE, et al., 1989) and (ZHOU, 1997). The process to be controlled is a feedback MIMO system, where the plant G is now represented by its augmented plant G_{ap} . The general structure of the augmented plant used to design the controller may be observed in Fig. 4., where w is the input and Z_1 and Z_2 are the outputs. Our goal is to find a controller K whose closed-loop transfer matrix norm, between T_{zw} and $Z_{1...2}$, can be given by:

$$T_{wz} = \left\| \begin{bmatrix} W_1 S \\ W_2 K S \end{bmatrix} \right\|_\infty = \left\| \begin{bmatrix} W_1 S \\ W_2 R \end{bmatrix} \right\| < 1 \tag{3}$$

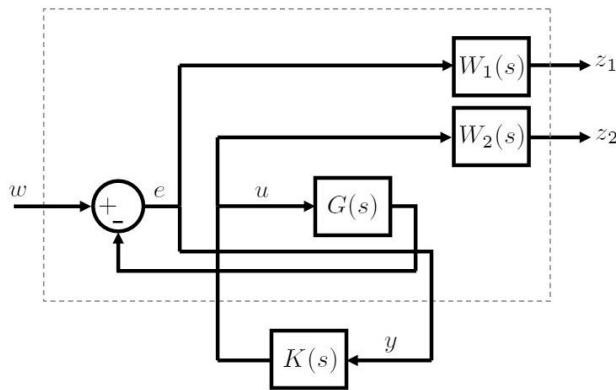


Fig. 4 – General representation of the augmented plant G_{ap} .

Where $W_{1,2}$ represent the controller weighting functions. Mixed sensitivity problem was considered, which is one of the goals of the H_∞ controller. In this context, S is the sensitivity function while R is the input sensitivity function, given by:

$$S = (I + L)^{-1} \tag{4}$$

$$R = K(I + L)^{-1} \tag{5}$$

Where L is the system open-loop transfer function written as:

$$L = GK \tag{6}$$

Both sensitivity and input sensitivity functions denote the system robustness relative to disturbances rejection. It is necessary that the gains of R are low at high frequencies so that noises/disturbances rejection can be guaranteed. On the other hand, S gains must be low at low frequencies to achieve the same rejection. Singular values analysis also are a good indicative of the robustness of the system against noises and disturbances in general. It is essential to select the weight matrices properly for W_i , so that Eq. (3) can provide the system with robust control actions, satisfying the project demands concerning the stabilization of the quadrotor, which are: 1) *stability against model parametric variations*, 2) *stationary error ≈ 0* , 3) *robustness even with open-loop uncertainties and variations*, 4) *robustness against noises which are inserted into the plant*. The H_∞ controller weighting functions estimation is a quite complex process that often demands iterative algorithms and does not exist a direct and specific formulation to achieve this goal. From the classic control theory, speed response is proportional to natural frequency ω_n and overshoot is determined by damping ratio ζ . As the desired performance is directly related to the sensitivity function, we consider ω_n and ζ . directly related to sensitivity functions (ZHOU, 1997), given by:

$$S = \frac{s(s + 2\zeta\omega_n)}{s^2 + 2\zeta\omega_n s + \omega_n^2} \tag{7}$$

Although it is possible, from time domain, to calculate their corresponding parameters in frequency domain in terms of band ω_n and peak sensibility M_s , we analyze only the steady-state error with respect to a step input signal whose value is given by ϵ and that allows the choice of W_e function which satisfies the condition $|W_e(0)| \geq 1/\epsilon(0)$, so that $\|W_e S\|_\infty$. Maximum gain M_u of KS can assume high values while high frequencies gain is limited by bandwidth ω_b and sensor frequencies, for instance. In order to attenuate those frequencies, it is desired to reach values beyond the desired control band. In other words, it is necessary to find the singular values of $|S(j\omega)|(W_e)$ and $|KS(j\omega)|(W_u)$ functions for the H_∞ controller. Both weighting functions obtained are given by Eqs. (8) and (9) as follows:

$$W_e(s) = \frac{0.2s + 1 \cdot 10^{-5}}{3.162 s + 3.162 \cdot 10^{-5}} \tag{8}$$

$$W_u(s) = \frac{100s + 10000}{10s + 100000} \tag{9}$$

The controller K can be represented in its compact form (ZHOU, 1997), as follows:

$$K = \left[\begin{array}{c|c} A & B \\ \hline C & D \end{array} \right] \tag{10}$$

From the obtained Eqs. (8) and (9) and all the procedures previously presented, the controller K , in its space-state compact form, is finally achieved:

$$K = \left[\begin{array}{cccccccccccc|cc} -4,2644 & -13,4992 & 8,61E-07 & 2,53E-06 & -0,00364 & -36336,3 & 0,004875 & 36336,32 & 7,71E-06 & -26,8027 & -0,00031 & 2496,579 \\ 1 & -4,18654 & 0 & 1,69E-07 & 0 & 0 & 0 & 0 & 0 & 0 & -0,0001 & 1192,67 \\ 8,60E-07 & 2,52E-06 & -4,2779 & -13,5387 & 36376,94 & 0,000482 & -36376,9 & -0,00333 & -26,9045 & 5,97E-06 & 2499,713 & -0,00015 \\ 0 & 1,69E-07 & 1 & -4,18917 & 0 & 0 & 0 & 0 & 0 & 7,83E-24 & 1193,418 & -2,48E-05 \\ 6,87E-08 & 1,90E-07 & -0,55772 & -1,1615 & -307,434 & -2,99E-05 & 207,434 & 4,61E-05 & -3,50761 & 5,05E-07 & 0 & 0 \\ 0,55666 & 1,158557 & -2,03E-08 & -8,91E-08 & -2,99E-05 & -306,782 & 3,69E-05 & 206,7819 & -4,27E-07 & 3,498737 & 0 & 0 \\ -8,76E-08 & -2,29E-07 & 0,557722 & 1,161496 & 207,434 & 3,69E-05 & -307,434 & -5,32E-05 & 3,507612 & -6,23E-07 & 0 & 0 \\ -0,55666 & -1,15856 & 6,40E-08 & 1,80E-07 & 4,62E-05 & 206,7819 & -5,32E-05 & -306,782 & 7,02E-07 & -3,49874 & 0 & 0 \\ 0 & 6,31E-30 & 0 & 0 & 0 & 0 & 0 & 0 & -1,00E-05 & -4,46E-32 & 0,000548 & -3,40E-27 \\ 0 & 0 & 0 & 0 & 0 & 0 & 0 & 0 & 9,43E-31 & -1,00E-05 & 1,29E-29 & 0,000548 \\ \hline 6,34E-10 & 1,75E-09 & -0,00515 & -0,01072 & 89,47958 & -2,76E-07 & 1,914984 & 4,26E-07 & -0,03238 & 4,66E-09 & 0 & 0 \\ 0,005139 & 0,010696 & -1,88E-10 & -8,23E-10 & -2,76E-07 & 89,4856 & 3,41E-07 & 1,908964 & -3,94E-09 & 0,0323 & 0 & 0 \\ -8,09E-10 & -2,12E-09 & 0,005149 & 0,010723 & 1,914984 & 3,41E-07 & 89,47958 & -4,91E-07 & 0,032381 & -5,76E-09 & 0 & 0 \\ -0,00514 & -0,0107 & 5,91E-10 & 1,66E-09 & 4,26E-07 & 1,908964 & -4,91E-07 & 89,4856 & 6,48E-09 & -0,0323 & 0 & 0 \end{array} \right] \tag{11}$$

EXPERIMENTAL RESULTS

Figure 5 shows a sequence of images that illustrates the process of stabilization of the quadrotor. A disturbance was manually simultaneously inserted at the two axes, in order to simulate a change in the angle of stability. The normal operation set point can be seen in Fig 5-a. Note that all four motors are running and they perfectly aligns the aircraft axes to the horizon. Fig. 5-b shows the exact moment when external forces disturb the equilibrium point in both axes. It is expected that the controller is able to compensate it with the combination of torques at the four motors simultaneously. One may see that the controller imposes the necessary counter-torque to bring the axis to the equilibrium point. An overshoot is perceived in attempting to stabilize the aircraft, which may be seen in Figs. 5-c and 5-d. However, Figs. 5-e and 5-f show that, in the next step of the stabilization process, the quadrotor smoothly returns to the stability set point.

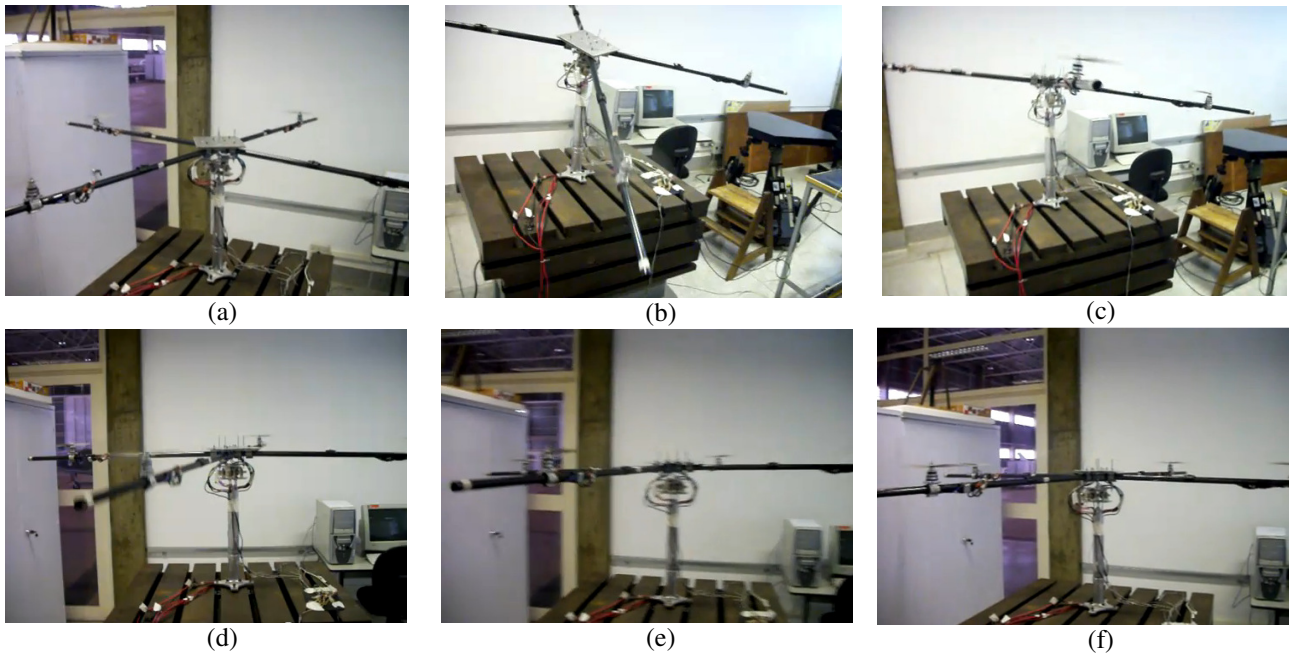


Fig. 5 – Sequence of shots of the stabilization process of the quadrotor against an external force disturbing both roll and pitch axes.

Figure 6 shows the response of the four motors in attempt to stabilize the quadrotor. The plots make it easy to note the counter-torque strategy.

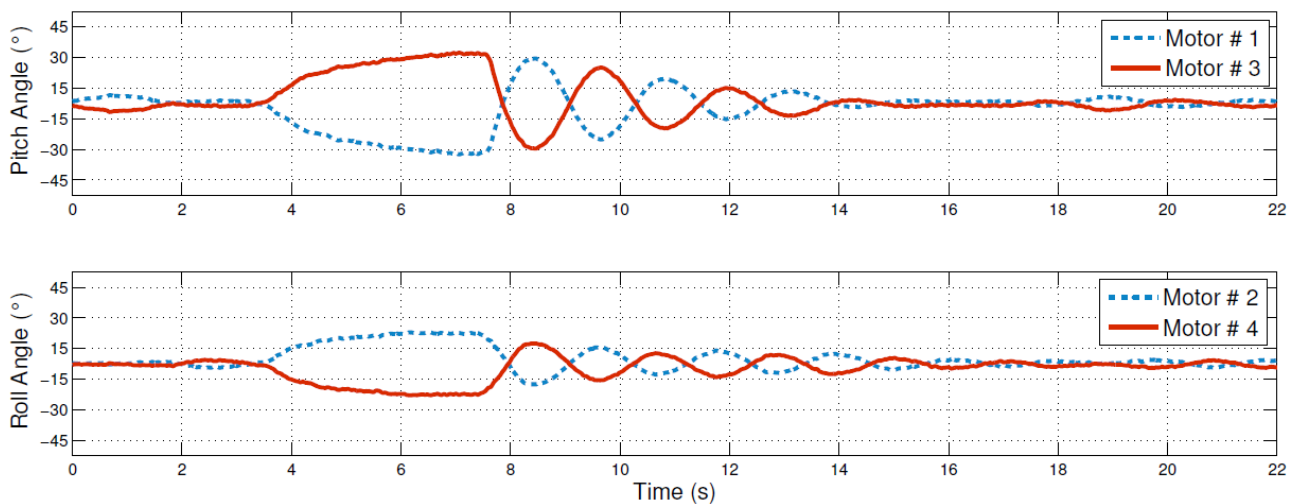


Fig. 6 – Plot of the control action to compensate the external disturbances over both axes.

The sequence of images in Fig. 6 shows another essay where, this time, the pitch axis suffers the influence of an external force, moving it away from its equilibrium point (Fig. 7-a). Figures 7-b and 7-c show the effort of the controller, in attempt to bring the axis to the set point. One may clearly observe the effect of the coupling of the two axes in Figs. 7-d and 7-e. Whereas that there is a natural coupling relation between both axis, which is inherent to the dynamical model of the quadrotor, the disturbance over pitch axis is propagated over roll axis. Thus, the equilibrium point of roll axis was also disturbed. However, the H_∞ controller minimizes the coupling effect, as one may see in Fig 7-f. In other circumstances, that effect would be more observable.

In terms of curves, Fig. 8 shows the responses of the controller to the referred external force at the instant 7s. Physically, it may represent a wind shear condition over a specific motor or axis, which is a very common situation in flight. One may see that, as it is expected, motors 1 and 3 promptly act over the disturbance. It is important to note that the control actions are symmetric for each pair of motors. Thus, as motor 3 tries to impose a torque to bring the axis back to its original position, motor 1 relaxes at the same proportion, in order to minimize the current consumption and to ease the effort of motor 3.

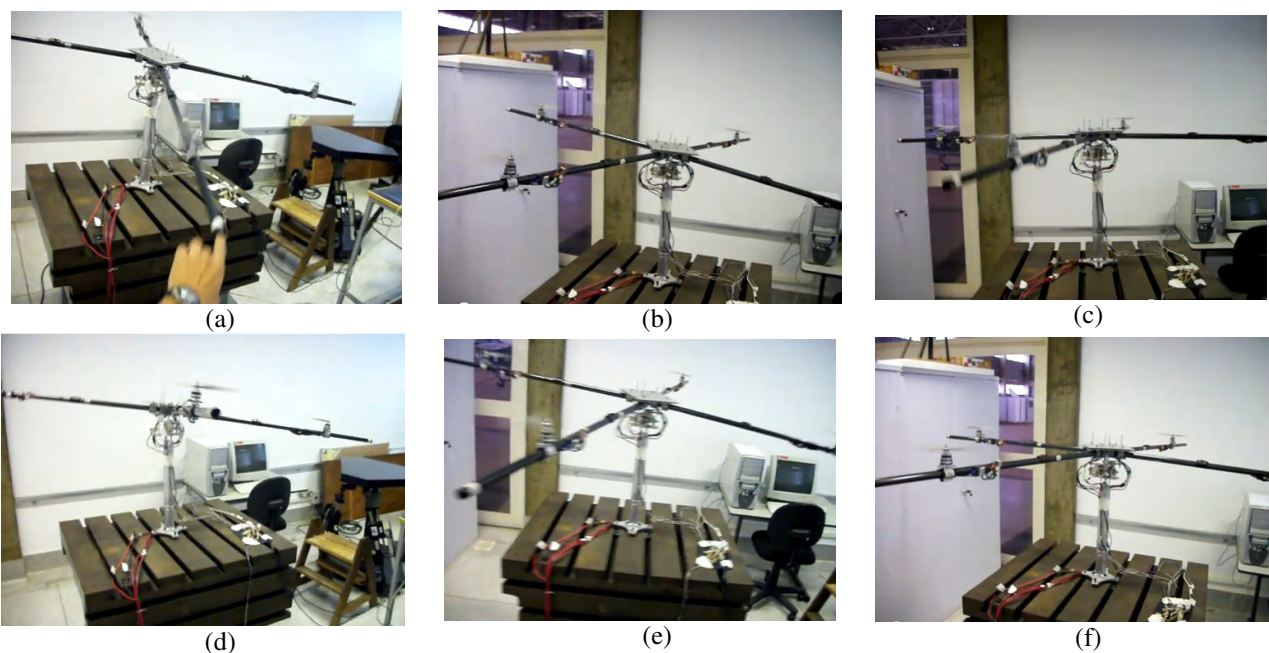


Fig. 7 - Sequence shot of the stabilization process of the quadrotor against an external force disturbing both roll and pitch axes.

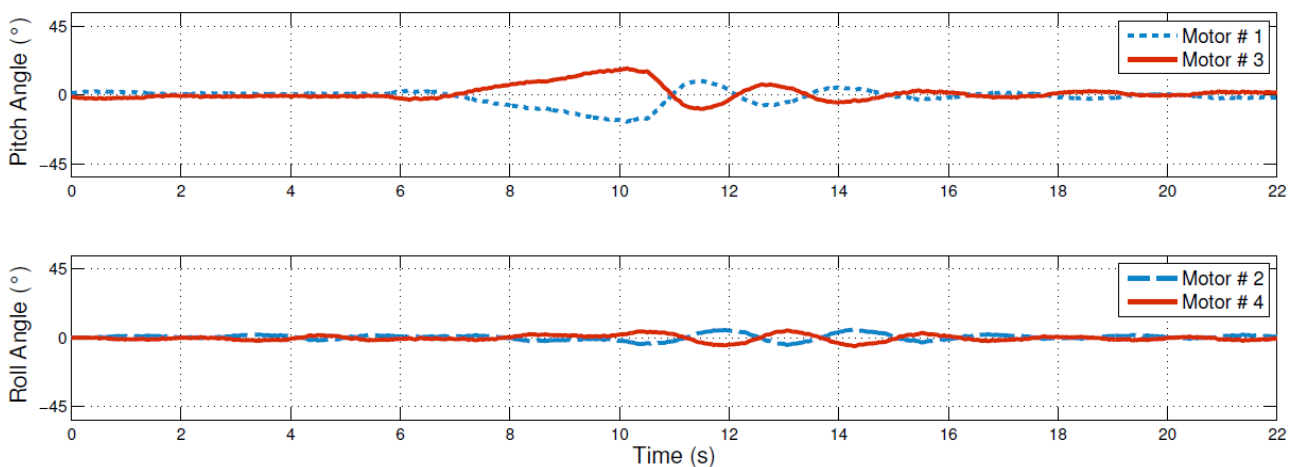


Fig. 8 – Plot of the control action to compensate the external disturbances over the pitch axis.

The same experiment was run under the same circumstances. This time, a disturbance was inserted over the roll axis. Fig. 9 shows the effort of motor 4 to bring the axis back to the equilibrium point while motor 2 relaxes. In fact, an interchange of torques happens between motors 2 and 4, which always occurs symmetrically. Again, the coupling effect is visible. However, the H_∞ controller minimizes this effect without implicating in the destabilizing the aircraft.

The sequence of shots shows the process of stabilization. One may see in Fig. 9-a that the roll axis is shifted from the equilibrium point to a certain arbitrary angle. The controller then raises rotation over the propeller of motor 2 to bring the axis back to its position. It can be noted, from Figs. 9-b, 9-c and 9-d that an overshoot is present. Especially in Fig. 9-e, one may clearly note the coupling effect actuating over the pitch axis, which causes a slight imbalance over it. Figure 9-f shows the moment when the aircraft is fully stabilized.

Figure 10 shows the exact moment (7s) when the external disturbance moves the axis off of its set point. Promptly, the control first raises the rotation on the motor 2 propeller and relaxes the rotation in motor 4, which brings the axis again to the equilibrium point. This process is extended, by alternating the forces of the two motors until the whole aircraft is completely aligned to the horizon.

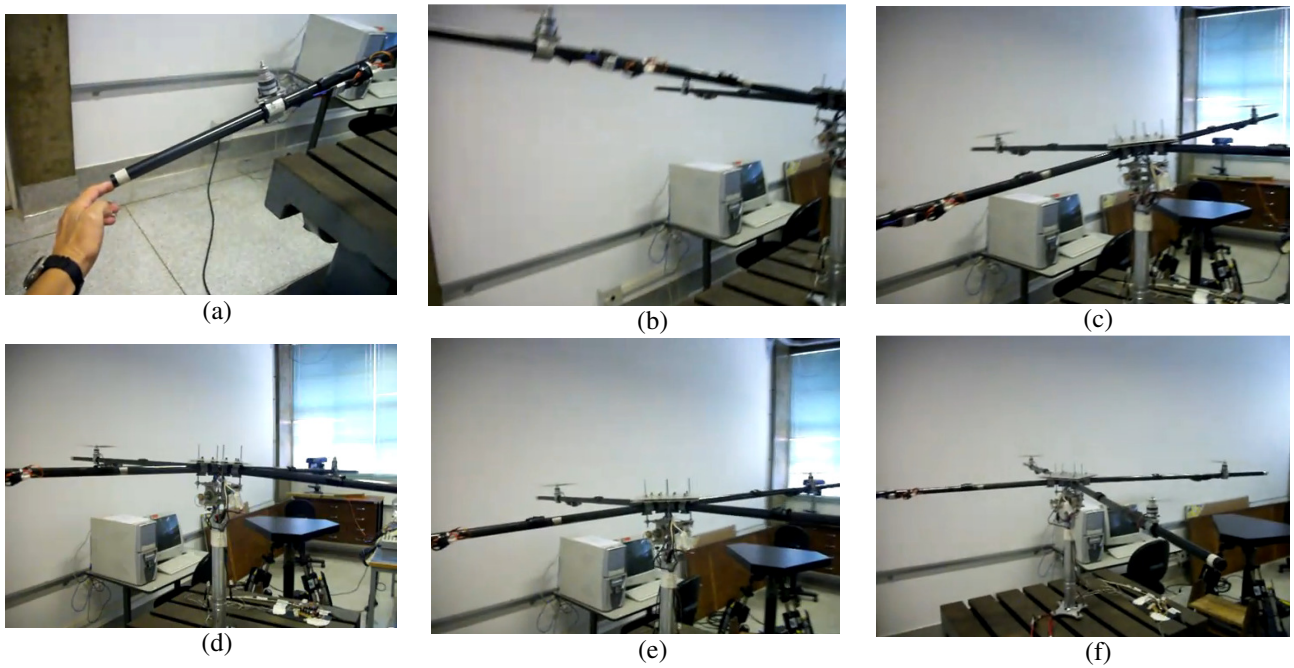


Fig. 9 - Sequence shot of the stabilization process of the quadrotor against an external force disturbing both roll and roll axis.

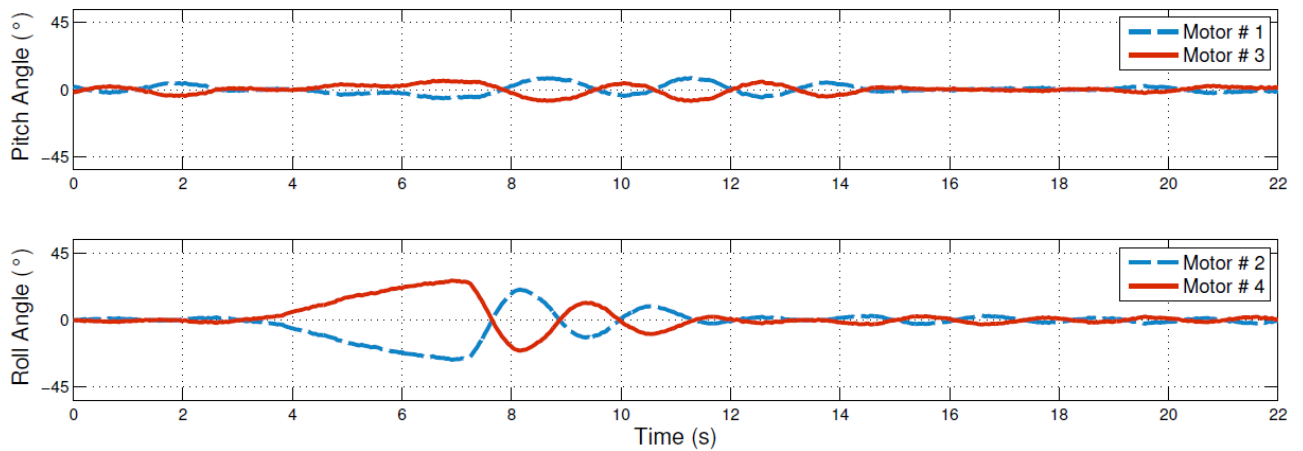


Fig. 10 – Plot of the control action to compensate the external disturbances over the roll axis.

CONCLUSIONS AND FUTURE WORKS

The success of the synthesis of a robust H_∞ controller lies in the correct determination of the state space equations of the dynamical system to be controlled. Otherwise, the inaccuracy of the mathematical model of the plant can severely implicate in an inefficient control system.

Our results prove that both our control synthesis and our methodology to determine the state-space equations of the aircraft through the use of ADAMS converge to the appropriated control of the quadrotor in many of the possible circumstances in which the aircraft can considerably be taken of its equilibrium point. Despite of the natural coupling relation between rolling and pitch axes, the H_∞ controller was capable of minimizing the influence of this effect, in all cases, bringing the quadrotor to its equilibrium point. Moreover, we conclude that, due to its huge capability to reject noises, H_∞ controller allows cheap sensors sets, as it the case of simple potentiometers, to be used to detect the error of stability. In addition to cheapen the cost of the experiment, it considerably eases the assembly of the sensing stage.

Next step consists in adding a 3rd DoF to the quadrotor, which refers to the z axis and, thus, to the yaw moment.

ACKNOWLEDGEMENT

Authors would like to thank Prof. Adriano A. G. Siqueira for his valuable contribution. Authors also would like to thank CNPq (Conselho Nacional de Pesquisa) for supporting this research.

REFERENCES

- BOUABDALLAH, S.; BECKER, M.; AND SIEGWART, R. (2007). Autonomous miniature flying robots: coming soon! - Research, Development, and Results. IEEE Robotics and Automation Society Magazine, Vol. 14, No. 3, pp. 88-98.
- KIM, J, KANG, M., PARK, S. (2010). Accurate Modeling and Robust Hovering Control for a Quad-rotor VTOL Aircraft. Journal of Intelligent and Robotic Systems, Volume 57, Issue 1-4 (January 2010), Pages: 9 - 26
- TISDALE, J.; RYAN, A.; ZENNARO, M.; XIAO XIAO; CAVENEY, D.; RATHINAM, S.; HEDRICK, J.K.; SENGUPTA, R.; , "The software architecture of the Berkeley UAV Platform," Computer Aided Control System Design, 2006 IEEE International Conference on Control Applications, 2006 IEEE International Symposium on Intelligent Control, 2006 IEEE , vol., no., pp.1420-1425, 4-6 Oct. 2006
- PRATT, K. S., MURPHY, R., STOVER, S., AND GRIFFIN, C. 2009. CONOPS and autonomy recommendations for VTOL small unmanned aerial system based on Hurricane Katrina operations. J. Field Robot. 26, 8 (Aug. 2009), 636-650
- DOYLE, J. C., K. GLOVER, P. P. K. AND FRANCIS, B. A, State-space Solutions to Standard H2 and H_∞ Control Problems, Vol. 34, 1989
- ZHOU, K., Essentials of Robust Control, Prentice Hall, 1997
- NWE, TIN THET, HTIKE THAN, MON KHINE MYINT, NAING ZAW MIN AND MYINT, YIN MON Application of an Inertial Navigation System to the Quad-rotor UAV using MEMS Sensors World Academy of Science, Engineering and Technology 42 2008.
- EFE, MEHMET ONDER Robust Low Altitude Behavior Control of a Quadrotor Rotorcraft Through Sliding Modes Proceedings of the 15th Mediterranean Conference on Control & Automation, 2007, Athens – Greece.
- VOOS H: Nonlinear Control of a Quadrotor Micro-UAV using Feedback- Linearization. IEEE Int Conf on Mechatronics, M_alaga, Spain, 2009.
- BENALLEGUE A., MOKHTARI A. and FRIDMAN L. High-order sliding-mode observer for a quadrotor UAV, International Journal Of Robust And Nonlinear Control, 2007.

RESPONSIBILITY NOTICE (HEADING 1, HELVETICA 11PT BOLD ALL CAPS)

The author(s) is (are) the only responsible for the printed material included in this paper.

Sliding Mode Control with Adaptive Fuzzy Dead-Zone Compensation for Uncertain Nonlinear Systems

Wallace Moreira Bessa¹, Aline Souza de Paula², and Marcelo Amorim Savi³

¹ Universidade Federal do Rio Grande do Norte, Centro de Tecnologia, Departamento de Engenharia Mecânica, Campus Universitário Lagoa Nova, CEP 59072-970, Natal, RN, Brazil
E-mail: wmbessa@ufrnet.br

² Universidade de Brasília, Departamento de Engenharia Mecânica, CEP 70910-900, Brasília, DF, Brazil
E-mail: alinedepaula@unb.br

³ Universidade Federal do Rio de Janeiro, Centro de Tecnologia, Departamento de Engenharia Mecânica, Bloco G, Sala 204, CEP 21945-970, Cidade Universitária, RJ, Brazil
E-mail: savi@mecanica.ufrj.br

Abstract: The dead-zone nonlinearity is frequently encountered in many industrial automation equipments and its presence can severely compromise control system performance. In this work, an adaptive variable structure controller is proposed to deal with a class of uncertain nonlinear systems subject to an unknown dead-zone input. The adopted approach is primarily based on the sliding mode control methodology but enhanced by an adaptive fuzzy algorithm to compensate the dead-zone. Using Lyapunov stability theory and Barbalat's lemma, the convergence properties of the closed-loop system are analytically proven. In order to illustrate the controller design methodology, an application of the proposed scheme to a chaotic pendulum is introduced.

Keywords: Adaptive algorithms, Chaos control, Dead-zone, Fuzzy logic, Sliding modes.

INTRODUCTION

Dead-zone is a hard nonlinearity that can be commonly found in many industrial actuators, especially those containing hydraulic valves and electric motors. Dead-zone characteristics are often unknown and, as previously reported in the research literature, its presence can drastically reduce control system performance and lead to limit cycles in the closed-loop system.

The growing number of papers involving systems with dead-zone input confirms the importance of taking such a non-smooth nonlinearity into account during the control system design process. The most common approaches are adaptive schemes (Hua *et al.*, 2008; Ibrir *et al.*, 2007; Tao and Kokotović, 1994; Wang *et al.*, 2004; Yoo *et al.*, 2009; Zhou, 2008; Zhou and Shen, 2007; Zhou *et al.*, 2006), fuzzy systems (Kim *et al.*, 1994; Lewis *et al.*, 1999; Oh and Park, 1998; Bessa *et al.*, 2010a), neural networks (Šelmić and Lewis, 2000; Tsai and Chuang, 2004; Zhang and Ge, 2007, 2009) and variable structure methods (Corradini and Orlando, 2002; Shyu *et al.*, 2005). Many of these works (Kim *et al.*, 1994; Oh and Park, 1998; Šelmić and Lewis, 2000; Tao and Kokotović, 1994; Tsai and Chuang, 2004) use an inverse dead-zone to compensate the negative effects of the dead-zone nonlinearity even though this approach leads to a discontinuous control law and requires instantaneous switching, which in practice can not be accomplished with mechanical actuators. To overcome this limitation, smooth inverses were adopted in (Zhou, 2008; Zhou and Shen, 2007; Zhou *et al.*, 2006). An alternative scheme, without using the dead-zone inverse, was originally proposed by Lewis *et al.* (1999) and also adopted by Wang *et al.* (2004). In both works, the dead-zone is treated as a combination of a linear and a saturation function. This approach was further extended by Ibrir *et al.* (2007) and by Zhang and Ge (2007), in order to accommodate non-symmetric and unknown dead-zones, respectively. Non-symmetric dead-zones based on (Ibrir *et al.*, 2007) were treated in (Hua *et al.*, 2008; Yoo *et al.*, 2009) using adaptive methods and the dead-zone model proposed in (Zhang and Ge, 2007) were also adopted in (Zhang and Ge, 2008, 2009). Considering the dead-zone model presented in (Lewis *et al.*, 1999), Bessa *et al.* (2010a) proposed an adaptive fuzzy compensation scheme to cope with the resulting unknown saturation function.

Sliding mode control is an appealing control technique because of its robustness against both structured and unstructured uncertainties as well as external disturbances. Nevertheless, the discontinuities in the control law must be smoothed out to avoid the undesirable chattering effects. The adoption of properly designed boundary layers have proven effective in completely eliminating chattering, however, leading to an inferior tracking performance. In order to enhance the tracking performance, some adaptive strategy should be used for uncertainty/disturbance compensation. As demonstrated by (Bessa and Barrêto, 2010), adaptive fuzzy algorithms can be properly embedded in smooth sliding mode controllers to compensate for modeling inaccuracies, in order to improve the trajectory tracking of uncertain nonlinear systems. It has also been shown that adaptive fuzzy sliding mode controllers are suitable for a variety of applications ranging from underwater robotic vehicles (Bessa *et al.*, 2008, 2010b) to the chaos control in a nonlinear pendulum (Bessa *et al.*, 2009). On this

basis, a robust and very attractive approach was proposed by Bessa *et al.* (2010c) for the control of an electro-hydraulic system subject to an unknown dead-zone. The adopted scheme is primarily based on a smooth sliding mode controller, but an adaptive fuzzy inference system was embedded within the boundary layer to compensate for dead-zone effects.

In this paper, a generalization of the control scheme presented by Bessa *et al.* (2010c) is proposed for a class of n^{th} -order uncertain nonlinear systems subject to unknown dead-zone input. Rigorous proofs of the boundedness and convergence properties of the closed-loop signals by means of Lyapunov stability theory and Barbalat's lemma are presented. As an application of the general procedure, the chaos control of a nonlinear pendulum that has a rich response, presenting chaos and transient chaos (De Paula *et al.*, 2006), is treated. Numerical simulations are carried out illustrating the stabilization of some UPOs of the chaotic attractor showing an effective response. Unstructured uncertainties related to unmodeled dynamics and structured uncertainties associated with parametric variations are both considered in the robustness analysis. A comparison between the stabilization of a general orbit and unstable periodic orbits embedded in chaotic attractor is performed showing the less energy consumption related to UPOs.

PROBLEM STATEMENT

Consider a class of n^{th} -order nonlinear systems:

$$x^{(n)} = f(\mathbf{x}) + h(\mathbf{x})v \quad (1)$$

where the scalar variable $x \in \mathbb{R}$ is the output of interest, $x^{(n)} \in \mathbb{R}$ is the n^{th} derivative of x with respect to time $t \in [0, +\infty)$, $\mathbf{x} = [x, \dot{x}, \dots, x^{(n-1)}] \in \mathbb{R}^n$ is the system state vector, $f, h : \mathbb{R}^n \rightarrow \mathbb{R}$ are both nonlinear functions and $v \in \mathbb{R}$ represents the output of a dead-zone function $\Upsilon : \mathbb{R} \rightarrow \mathbb{R}$, as shown in Fig. 1, with $u \in \mathbb{R}$ stating for the controller output variable.

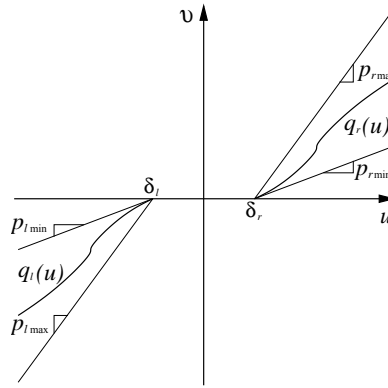


Figure 1 – Dead-zone nonlinearity.

The adopted dead-zone model is a slightly modified version of that proposed by Zhang and Ge (2007), which can be mathematically described by

$$v = \Upsilon(u) = \begin{cases} q_l(u) & \text{if } u \leq \delta_l \\ 0 & \text{if } \delta_l < u < \delta_r \\ q_r(u) & \text{if } u \geq \delta_r \end{cases} \quad (2)$$

In respect of the dead-zone model presented in Eq. (2), the following assumptions can be made:

Assumption 1 The dead-zone output v is not available to be measured.

Assumption 2 The dead-band parameters δ_l and δ_r are unknown but bounded and with known signs, i.e., $\delta_{l \min} \leq \delta_l \leq \delta_{l \max} < 0$ and $0 < \delta_{r \min} \leq \delta_r \leq \delta_{r \max}$.

Assumption 3 The functions $q_l : (-\infty, \delta_l]$ and $q_r : [\delta_r, +\infty)$ are C^1 and with bounded positive-valued derivatives, i.e.,

$$\begin{aligned} 0 < p_{l \min} \leq q'_l(u) \leq p_{l \max}, \quad \forall u \in (-\infty, \delta_l], \\ 0 < p_{r \min} \leq q'_r(u) \leq p_{r \max}, \quad \forall u \in [\delta_r, +\infty), \end{aligned}$$

where $q'_l(u) = dq_l(z)/dz|_{z=u}$ and $q'_r(u) = dq_r(z)/dz|_{z=u}$.

Remark 1 Assumption 3 means that both q_l and q_r are Lipschitz functions.

From the mean value theorem and noting that $q_l(\delta_l) = q_r(\delta_r) = 0$, it follows that there exist $\xi_l : \mathbb{R} \rightarrow (-\infty, \delta_l)$ and $\xi_r : \mathbb{R} \rightarrow (\delta_r, +\infty)$ such that

$$\begin{aligned} q_l(u) &= q'_l(\xi_l(u))[u - \delta_l] \\ q_r(u) &= q'_r(\xi_r(u))[u - \delta_r] \end{aligned}$$

In this way, Eq. (2) can be rewritten as follows:

$$v = \Upsilon(u) = \begin{cases} q'_l(\xi_l(u))[u - \delta_l] & \text{if } u \leq \delta_l \\ 0 & \text{if } \delta_l < u < \delta_r \\ q'_r(\xi_r(u))[u - \delta_r] & \text{if } u \geq \delta_r \end{cases} \quad (3)$$

or in a more appropriate form:

$$v = \Upsilon(u) = p(u)[u - d(u)] \quad (4)$$

where

$$p(u) = \begin{cases} q'_l(\xi_l(u)) & \text{if } u \leq 0 \\ q'_r(\xi_r(u)) & \text{if } u > 0 \end{cases} \quad (5)$$

and

$$d(u) = \begin{cases} \delta_l & \text{if } u \leq \delta_l \\ u & \text{if } \delta_l < u < \delta_r \\ \delta_r & \text{if } u \geq \delta_r \end{cases} \quad (6)$$

Remark 2 Considering Assumption 2 and Eq. (6), it can be easily verified that $d(u)$ is bounded: $|d(u)| \leq \delta$, where $\delta = \max\{-\delta_{l \min}, \delta_{r \max}\}$.

In respect of the dynamic system presented in Eq. (1), the following assumptions will also be made:

Assumption 4 The function f is unknown but bounded by a known function of \mathbf{x} , i.e., $|\hat{f}(\mathbf{x}) - f(\mathbf{x})| \leq \mathcal{F}(\mathbf{x})$ where \hat{f} is an estimate of f .

Assumption 5 The input gain $h(\mathbf{x})$ is unknown but positive and bounded, i.e., $0 < h_{\min} \leq h(\mathbf{x}) \leq h_{\max}$.

CONTROLLER DESIGN

The proposed control problem is to ensure that, even in the presence of parametric uncertainties, unmodeled dynamics and an unknown dead-zone input, the state vector \mathbf{x} will follow a desired trajectory $\mathbf{x}_d = [x_d, \dot{x}_d, \dots, x_d^{(n-1)}]$ in the state space.

Regarding the development of the control law, the following assumptions should also be made:

Assumption 6 The state vector \mathbf{x} is available.

Assumption 7 The desired trajectory \mathbf{x}_d is once differentiable in time. Furthermore, every element of vector \mathbf{x}_d , as well as $x_d^{(n)}$, is available and with known bounds.

Now, let $\tilde{x} = x - x_d$ be defined as the tracking error in the variable x , and

$$\tilde{\mathbf{x}} = \mathbf{x} - \mathbf{x}_d = [\tilde{x}, \dot{\tilde{x}}, \dots, \tilde{x}^{(n-1)}]$$

as the tracking error vector.

Consider a sliding surface S defined in the state space by the equation $s(\tilde{\mathbf{x}}) = 0$, with the function $s : \mathbb{R}^n \rightarrow \mathbb{R}$ satisfying

$$s(\tilde{\mathbf{x}}) = \left(\frac{d}{dt} + \lambda \right)^{n-1} \tilde{x}$$

or conveniently rewritten as

$$s(\tilde{\mathbf{x}}) = \mathbf{c}^T \tilde{\mathbf{x}} \quad (7)$$

where $\mathbf{c} = [c_{n-1}\lambda^{n-1}, \dots, c_1\lambda, c_0]$ and c_i states for binomial coefficients, i.e.,

$$c_i = \binom{n-1}{i} = \frac{(n-1)!}{(n-i-1)!i!}, \quad i = 0, 1, \dots, n-1 \quad (8)$$

which makes $c_{n-1}\lambda^{n-1} + \dots + c_1\lambda + c_0$ a Hurwitz polynomial.

From Eq. (8), it can be easily verified that $c_0 = 1$, for $\forall n \geq 1$. Thus, for notational convenience, the time derivative of s will be written in the following form:

$$\dot{s} = \mathbf{c}^T \dot{\tilde{\mathbf{x}}} = \tilde{x}^{(n)} + \bar{\mathbf{c}}^T \tilde{\mathbf{x}} \quad (9)$$

where $\bar{\mathbf{c}} = [0, c_{n-1}\lambda^{n-1}, \dots, c_1\lambda]$.

Now, let the problem of controlling the uncertain nonlinear system (1) be treated in a Filippov's way (Filippov, 1988), defining a control law composed by an equivalent control $\hat{u} = \widehat{hp}^{-1}(-\hat{f} + x_d^{(n)} - \bar{\mathbf{c}}^T \tilde{\mathbf{x}})$, an estimate $\hat{d}(\hat{u})$ and a discontinuous term $-K \operatorname{sgn}(s)$:

$$u = \widehat{hp}^{-1}(-\hat{f} + x_d^{(n)} - \bar{\mathbf{c}}^T \tilde{\mathbf{x}}) + \hat{d}(\hat{u}) - K \operatorname{sgn}(s) \quad (10)$$

where $\widehat{hp} = \sqrt{h_{\max} p_{\max} h_{\min} p_{\min}}$ with $p_{\max} = \max\{p_{l \max}, p_{r \max}\}$ and $p_{\min} = \min\{p_{l \min}, p_{r \min}\}$, K is a positive gain and $\operatorname{sgn}(\cdot)$ is defined as

$$\operatorname{sgn}(s) = \begin{cases} -1 & \text{if } s < 0 \\ 0 & \text{if } s = 0 \\ 1 & \text{if } s > 0 \end{cases}$$

Based on Assumptions 2–5 and considering that $\mathcal{H}^{-1} \leq \widehat{hp}/(hp) \leq \mathcal{H}$, where $\mathcal{H} = \sqrt{(h_{\max} p_{\max})/(h_{\min} p_{\min})}$, the gain K should be chosen according to

$$K \geq \mathcal{H}[\widehat{hp}^{-1}(\eta + \mathcal{F}) + \mathcal{H}(\delta + |\hat{d}|) + (\mathcal{H} - 1)|\hat{u}|] \quad (11)$$

where η is a strictly positive constant related to the reaching time.

Therefore, it can be easily verified that (10) is sufficient to impose the sliding condition

$$\frac{1}{2} \frac{d}{dt} s^2 \leq -\eta |s|$$

which, in fact, ensures the finite-time convergence of the tracking error vector to the sliding surface S and, consequently, its exponential stability.

In order to obtain a good approximation to $d(u)$, the estimate $\hat{d}(\hat{u})$ will be computed directly by an adaptive fuzzy algorithm.

The adopted fuzzy inference system was the zero order TSK (Takagi–Sugeno–Kang), whose rules can be stated in a linguistic manner as follows:

$$\text{If } \hat{u} \text{ is } \hat{U}_i \text{ then } \hat{d}_i = \hat{D}_i, \quad i = 1, 2, \dots, N$$

where \hat{U}_i are fuzzy sets, whose membership functions could be properly chosen, and \hat{D}_i is the output value of each one of the N fuzzy rules.

Considering that each rule defines a numerical value as output \hat{D}_i , the final output \hat{d} can be computed by a weighted average:

$$\hat{d}(\hat{u}) = \frac{\sum_{i=1}^N w_i \cdot \hat{d}_i}{\sum_{i=1}^N w_i} \quad (12)$$

or, similarly,

$$\hat{d}(\hat{u}) = \hat{\mathbf{D}}^T \Psi(\hat{u}) \quad (13)$$

where, $\hat{\mathbf{D}} = [\hat{D}_1, \hat{D}_2, \dots, \hat{D}_N]$ is the vector containing the attributed values \hat{D}_i to each rule i , $\Psi(\hat{u}) = [\psi_1(\hat{u}), \psi_2(\hat{u}), \dots, \psi_N(\hat{u})]$ is a vector with components $\psi_i(\hat{u}) = w_i / \sum_{i=1}^N w_i$ and w_i is the firing strength of each rule.

In order to ensure the best possible estimate $\hat{d}(\hat{u})$, the vector of adjustable parameters can be automatically updated by the following adaptation law:

$$\dot{\hat{\mathbf{D}}} = -\gamma s \Psi(\hat{u}) \quad (14)$$

where γ is a strictly positive constant related to the adaptation rate.

It's important to emphasize that the chosen adaptation law, Eq. (14), must not only provide a good approximation to $d(u)$ but also not compromise the attractiveness of the sliding surface, as will be proven in the following theorem.

Theorem 1 Consider the uncertain nonlinear system (1) subject to the dead-zone (4) and Assumptions 1–7. Then, the controller defined by (10), (11), (13) and (14) ensures the convergence of the tracking error vector to the sliding surface S .

Proof: Let a positive-definite function V_1 be defined as

$$V_1(t) = \frac{1}{2}s^2 + \frac{\mathcal{H}\widehat{hp}}{2\gamma} \Delta^T \Delta$$

where $\Delta = \hat{\mathbf{D}} - \hat{\mathbf{D}}^*$ and $\hat{\mathbf{D}}^*$ is the optimal parameter vector, associated to the optimal estimate $\hat{d}^*(\hat{u})$. Thus, the time derivative of V_1 is

$$\begin{aligned} \dot{V}_1(t) &= s\dot{s} + \mathcal{H}\widehat{hp}\gamma^{-1} \Delta^T \dot{\Delta} \\ &= (\tilde{x}^{(n)} + \bar{\mathbf{c}}^T \tilde{\mathbf{x}})s + \mathcal{H}\widehat{hp}\gamma^{-1} \Delta^T \dot{\Delta} \\ &= (x^{(n)} - x_d^{(n)} + \bar{\mathbf{c}}^T \tilde{\mathbf{x}})s + \mathcal{H}\widehat{hp}\gamma^{-1} \Delta^T \dot{\Delta} \\ &= (f + hp\dot{u} - hp\dot{d} - x_d^{(n)} + \bar{\mathbf{c}}^T \tilde{\mathbf{x}})s + \mathcal{H}\widehat{hp}\gamma^{-1} \Delta^T \dot{\Delta} \\ &= [f + hp\widehat{hp}^{-1}(-\hat{f} + x_d^{(n)} - \bar{\mathbf{c}}^T \tilde{\mathbf{x}}) + hp\hat{d} - hpK \operatorname{sgn}(s) - hp\dot{d} - (x_d^{(n)} - \bar{\mathbf{c}}^T \tilde{\mathbf{x}})]s + \mathcal{H}\widehat{hp}\gamma^{-1} \Delta^T \dot{\Delta} \end{aligned}$$

Defining the minimum approximation error as $\varepsilon = \hat{d}^* - d$, recalling that $\hat{u} = \widehat{hp}^{-1}(-\hat{f} + x_d^{(n)} - \bar{\mathbf{c}}^T \tilde{\mathbf{x}})$, and noting that $\dot{\Delta} = \dot{\hat{\mathbf{D}}}$ and $f = \hat{f} - (\hat{f} - f)$, \dot{V}_1 becomes:

$$\begin{aligned} \dot{V}_1(t) &= -[(\hat{f} - f) - hp\varepsilon - hp(\hat{d} - \hat{d}^*) + \widehat{hp}\hat{u} - hp\hat{u} + hpK \operatorname{sgn}(s)]s + \mathcal{H}\widehat{hp}\gamma^{-1} \Delta^T \dot{\hat{\mathbf{D}}} \\ &= -[(\hat{f} - f) - hp\varepsilon - hp(\hat{\mathbf{D}} - \hat{\mathbf{D}}^*)\Psi(\hat{u}) + \widehat{hp}\hat{u} - hp\hat{u} + hpK \operatorname{sgn}(s)]s + \mathcal{H}\widehat{hp}\gamma^{-1} \Delta^T \dot{\hat{\mathbf{D}}} \\ &= -[(\hat{f} - f) - hp\varepsilon - hp\Delta^T \Psi(\hat{u}) + \widehat{hp}\hat{u} - hp\hat{u} + hpK \operatorname{sgn}(s)]s + \mathcal{H}\widehat{hp}\gamma^{-1} \Delta^T \dot{\hat{\mathbf{D}}} \end{aligned}$$

Since $\mathcal{H}^{-1} \leq \widehat{hp}/(hp) \leq \mathcal{H}$, it follows that

$$\dot{V}_1(t) \leq -[(\hat{f} - f) - \mathcal{H}\widehat{hp}\varepsilon + \widehat{hp}\hat{u} - \mathcal{H}\widehat{hp}\hat{u} + \mathcal{H}^{-1}\widehat{hp}K \operatorname{sgn}(s)]s + \mathcal{H}\widehat{hp}\gamma^{-1}\Delta^T[\dot{\mathbf{D}} + \gamma s\Psi(\hat{u})]$$

Thus, by applying the adaptation law (14) to $\dot{\mathbf{D}}$:

$$\dot{V}_1(t) \leq -[(\hat{f} - f) - \mathcal{H}\widehat{hp}\varepsilon + \widehat{hp}\hat{u} - \mathcal{H}\widehat{hp}\hat{u} + \mathcal{H}^{-1}\widehat{hp}K \operatorname{sgn}(s)]s$$

Furthermore, considering Assumptions 2–5, defining K according to (11) and verifying that $|\varepsilon| = |\hat{d}^* - d| \leq |\hat{d} - d| \leq |\hat{d}| + \delta$, one has:

$$\dot{V}_1(t) \leq -\eta|s| \quad (15)$$

which implies $V_1(t) \leq V_1(0)$ and that s and Δ are bounded. Considering that $s(\tilde{\mathbf{x}}) = \mathbf{c}^T\tilde{\mathbf{x}}$, it can be verified that $\tilde{\mathbf{x}}$ is also bounded. Hence, equation (9) and Assumption 7 implies that \dot{s} is also bounded.

Integrating both sides of (15) shows that

$$\lim_{t \rightarrow \infty} \int_0^t \eta|s| d\tau \leq \lim_{t \rightarrow \infty} [V_1(0) - V_1(t)] \leq V_1(0) < \infty$$

Since the absolute value function is uniformly continuous, it follows from Barbalat's lemma (Khalil, 2001) that $s \rightarrow 0$ as $t \rightarrow \infty$, which ensures the convergence of the tracking error vector to the sliding surface S and completes the proof. \square

However, the presence of a discontinuous term in the control law leads to the well known chattering phenomenon. To overcome the undesirable chattering effects, Slotine (1984) proposed the adoption of a thin boundary layer, S_ϕ , in the neighborhood of the switching surface:

$$S_\phi = \{\tilde{\mathbf{x}} \in \mathbb{R}^n \mid |s(\tilde{\mathbf{x}})| \leq \phi\} \quad (16)$$

where ϕ is a strictly positive constant that represents the boundary layer thickness.

The boundary layer is achieved by replacing the sign function by a continuous interpolation inside S_ϕ . It should be noted that this smooth approximation, which will be called here $\varphi(s, \phi)$, must behave exactly like the sign function outside the boundary layer. There are several options to smooth out the ideal relay but the most common choices are the saturation function:

$$\operatorname{sat}(s/\phi) = \begin{cases} \operatorname{sgn}(s) & \text{if } |s/\phi| \geq 1 \\ s/\phi & \text{if } |s/\phi| < 1 \end{cases} \quad (17)$$

and the hyperbolic tangent function $\tanh(s/\phi)$.

In this way, to avoid chattering, a smooth version of Eq. (10) can be adopted:

$$u = \widehat{hp}^{-1}(-\hat{f} + x_d^{(n)} - \bar{\mathbf{c}}^T\tilde{\mathbf{x}}) + \hat{d}(\hat{u}) - K\varphi(s, \phi) \quad (18)$$

Nevertheless, it should be emphasized that the substitution of the discontinuous term by a smooth approximation inside the boundary layer turns the perfect tracking into a tracking with guaranteed precision problem, which actually means that a steady-state error will always remain. According to (Bessa, 2009) and considering a second order system with a smooth sliding mode controller, the tracking error vector will exponentially converge to a closed region $\Phi = \{\tilde{\mathbf{x}} \in \mathbb{R}^n \mid |s(\tilde{\mathbf{x}})| \leq \phi \text{ and } |\tilde{x}^{(i)}| \leq \sigma_i \lambda^{i-n+1} \phi, i = 0, 1, \dots, n-1\}$, with σ_i defined as

$$\sigma_i = \begin{cases} 1 & \text{for } i = 0 \\ 1 + \sum_{j=0}^{i-1} \binom{i}{j} \sigma_j & \text{for } i = 1, 2, \dots, n-1. \end{cases} \quad (19)$$

NONLINEAR PENDULUM

As an application of the control procedure, a nonlinear pendulum is investigated. This pendulum is based on an experimental set up, previously analyzed by Franca and Savi (2001) and Pereira-Pinto *et al.* (2004). De Paula *et al.* (2006)

presented a mathematical model to describe the dynamical behavior of the pendulum and the corresponding experimentally obtained parameters.

The schematic picture of the considered nonlinear pendulum is shown in Fig. 2. Basically, the pendulum consists of an aluminum disc (1) with a lumped mass (2) that is connected to a rotary motion sensor (4). This assembly is driven by a string-spring device (6) that is attached to an electric motor (7) and also provides torsional stiffness to the system. A magnetic device (3) provides an adjustable dissipation of energy. An actuator (5) provides the necessary perturbations to stabilize this system by properly changing the string length.

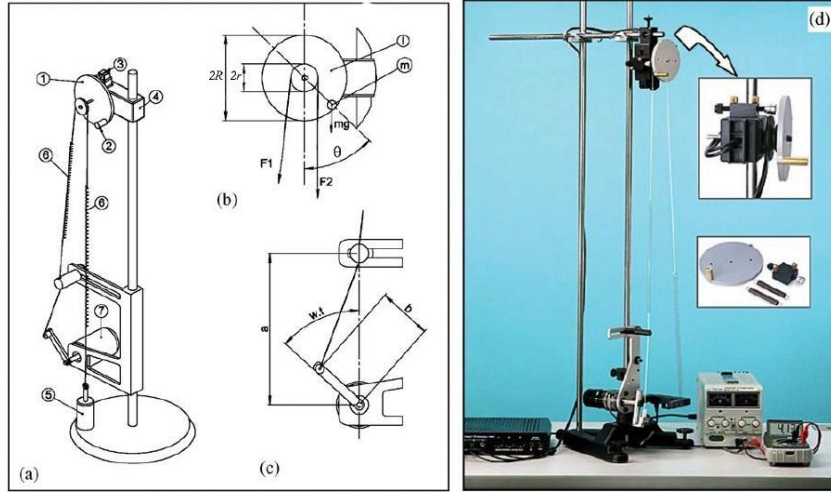


Figure 2 – (a) Nonlinear pendulum – (1) metallic disc; (2) lumped mass; (3) magnetic damping device; (4) rotary motion sensor (PASCO CI-6538); (5) anchor mass; (6) string-spring device; (7) electric motor (PASCO ME-8750). (b) Parameters and forces on metallic disc. (c) Parameters from driving device. (d) Experimental apparatus.

In order to obtain the equations of motion of the experimental nonlinear pendulum it is assumed that system dissipation may be expressed by a combination of a linear viscous dissipation together with dry friction. Therefore, denoting the angular position as θ , the following equation is obtained (De Paula *et al.*, 2006):

$$I\ddot{\theta} + \zeta\dot{\theta} + \mu \operatorname{sgn}(\dot{\theta}) + k2r^2\theta + mgR\sin(\theta) = kr[\sqrt{a^2 + b^2 - 2ab\cos(\omega t)} - (a - b) - \Delta l] \quad (20)$$

where ω is the forcing frequency related to the motor rotation, a defines the position of the guide of the string with respect to the motor, b is the length of the excitation crank of the motor, R is the radius of the metallic disc and r is the radius of the driving pulley, m is the lumped mass, ζ represents the linear viscous damping coefficient, while μ is the dry friction coefficient; g is the gravity acceleration, I is the inertia of the disk-lumped mass, k is the string stiffness and Δl is the length variation in the spring provided by the linear actuator (5).

De Paula *et al.* (2006) show that this mathematical model presents results that are in close agreement with experimental data. The pendulum equation can be expressed in terms of Eq. (1) by assuming that $\mathbf{x} = [\theta, \dot{\theta}]$, $h = kr/I$ and $v = -\Delta l$. The function f can be obtained from Eq. (1) and Eq. (20).

CONTROLLING THE NONLINEAR PENDULUM

In order to illustrate the controller design method and to demonstrate its performance, consider the nonlinear pendulum, mathematically described by Eq.(20), with a dead-zone input defined by

$$v = \begin{cases} 0.9(u + 0.003) & \text{if } u \leq \delta_l \\ 0 & \text{if } \delta_l < u < \delta_r \\ 1.0(u - 0.002) & \text{if } u \geq \delta_r \end{cases} \quad (21)$$

where $\delta_l = -0.003$ and $\delta_r = 0.002$.

On this basis, according to the previously described control scheme and considering $s = \dot{e} + \lambda e$, with $e = \theta - \theta_d$ as the tracking error, \dot{e} as the first time derivative of e and θ_d as the desired trajectory, a smooth control law can be defined as follows

$$u = \widehat{h}p^{-1}(-\widehat{f} + \ddot{\theta}_d - \lambda\dot{e}) + \widehat{d}(\widehat{u}) - K \operatorname{sat}(s/\phi)$$

The controller capability is now investigated by considering numerical simulations. The fourth order Runge-Kutta method is employed and sampling rates of 107 Hz for control system and 214 Hz for dynamical model are assumed. The model parameters are chosen according to (De Paula *et al.*, 2006): $I = 1.738 \times 10^{-4} \text{ kg m}^2$; $m = 1.47 \times 10^{-2} \text{ kg}$; $k = 2.47 \text{ N/m}$; $\zeta = 2.368 \times 10^{-5} \text{ kg m}^2/\text{s}$; $\mu = 1.272 \times 10^{-4} \text{ N m}$; $a = 1.6 \times 10^{-1} \text{ m}$; $b = 6.0 \times 10^{-2} \text{ m}$; $r = 2.4 \times 10^{-2} \text{ m}$; $R = 4.75 \times 10^{-2} \text{ m}$ and $\omega = 5.61 \text{ rad/s}$.

For tracking purposes, different UPOs are identified using the close return method (Pereira-Pinto *et al.*, 2004) and two of these are chosen as desired trajectories in the numerical studies that follows.

Regarding controller parameters, the following values were chosen: $\mathcal{F} = 1.2$; $\mathcal{H} = 1.1$; $\delta = 0.003$, $\phi = 1.0$; $\lambda = 0.8$; $\eta = 0.05$ and $\gamma = 0.6$. Concerning the fuzzy system, triangular and trapezoidal membership functions are adopted for U_i , with the central values defined $C = \{-1.0; -0.5; -0.1; 0.0; 0.1; 0.5; 1.0\} \times 10^{-2}$. It is also important to emphasize, that the vector of adjustable parameters was initialized with zero values, $\hat{\mathbf{D}} = \mathbf{0}$, and updated at each iteration step according to the adaptation law presented in Eq. (14).

In order to evaluate the control system performance, a period-1 UPO was identified using the close return method De Paula *et al.* (2006) and chosen to be stabilized. The obtained results are presented in Fig. 3.

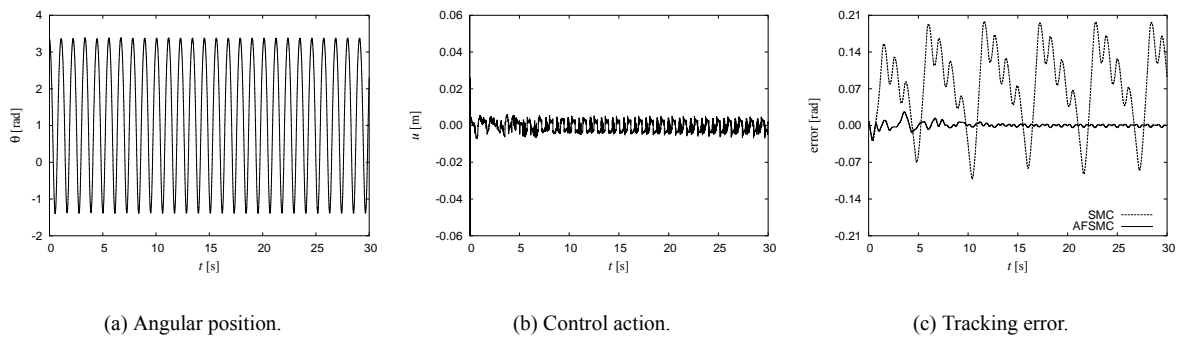


Figure 3 – Tracking of period-1 UPO.

As observed in Fig. 3, even in the presence of a dead-zone input, the adaptive fuzzy sliding mode controller (AFSMC) is capable to provide the trajectory tracking with a small associated error. It should be emphasized that the control action u represents the length variation in the string and only tiny variations are required to provide such different dynamic behaviors, which actually allows a great flexibility for the controlled nonlinear system.

It can be also verified that the proposed control law provides a smaller tracking error when compared with the conventional sliding mode controller (SMC), Fig. 3(c). By considering simulation purposes, the AFSMC can be easily converted to the classical SMC by setting the adaptation rate to zero, $\gamma = 0$.

The idea of the UPO control is interesting since these orbits are embedded in the chaotic attractor and, therefore are natural orbits related to the system dynamics. Hence, it is an important task to evaluate a comparison of the control action required to stabilize some UPOs and a general orbit (artificial or non-natural). Basically, three different situations are treated. In the first case, Fig. 4(a) and Fig. 4(d), a general artificial orbit $[\theta_d, \dot{\theta}_d] = [1.0 + 2.35 \sin(2\pi t), 4.70\pi \cos(2\pi t)]$ is considered. A second case, on the other hand, stabilizes a period-1 UPO, Fig. 4(b) and Fig. 4(e). Although both orbits are similar, it should be highlighted that the controller requires less effort to stabilize the UPO. Even with more complicated orbits, as is the case of the period-4 UPO shown in Fig. 4(c), the amplitude of the control action, Fig. 4(f), is significantly smaller when compared with the control effort required to stabilize the general orbit. The control of unstable periodic orbits is the essential aspect to be explored in chaos control that can confer flexibility to the system with low energy consumption.

CONCLUSIONS

The present work addresses the problem of controlling uncertain nonlinear systems subject to an unknown dead-zone input. An adaptive fuzzy sliding mode controller is proposed to deal with the trajectory tracking problem. The convergence properties of the closed-loop system are analytically proven using Lyapunov stability theory and Barbalat's lemma. To illustrate the controller design method and to evaluate its performance, the proposed scheme is applied to a chaotic pendulum. The control system performance is investigated showing the tracking of a generic orbit as well as for UPO stabilization. The improved performance over the conventional sliding mode controller is demonstrated. It is also shown that the controller needs less effort to stabilize an UPO when compared with a general non-natural orbit. This is an essential point related to chaos control that can confer flexibility to the system dynamics changing response with low power consumption.

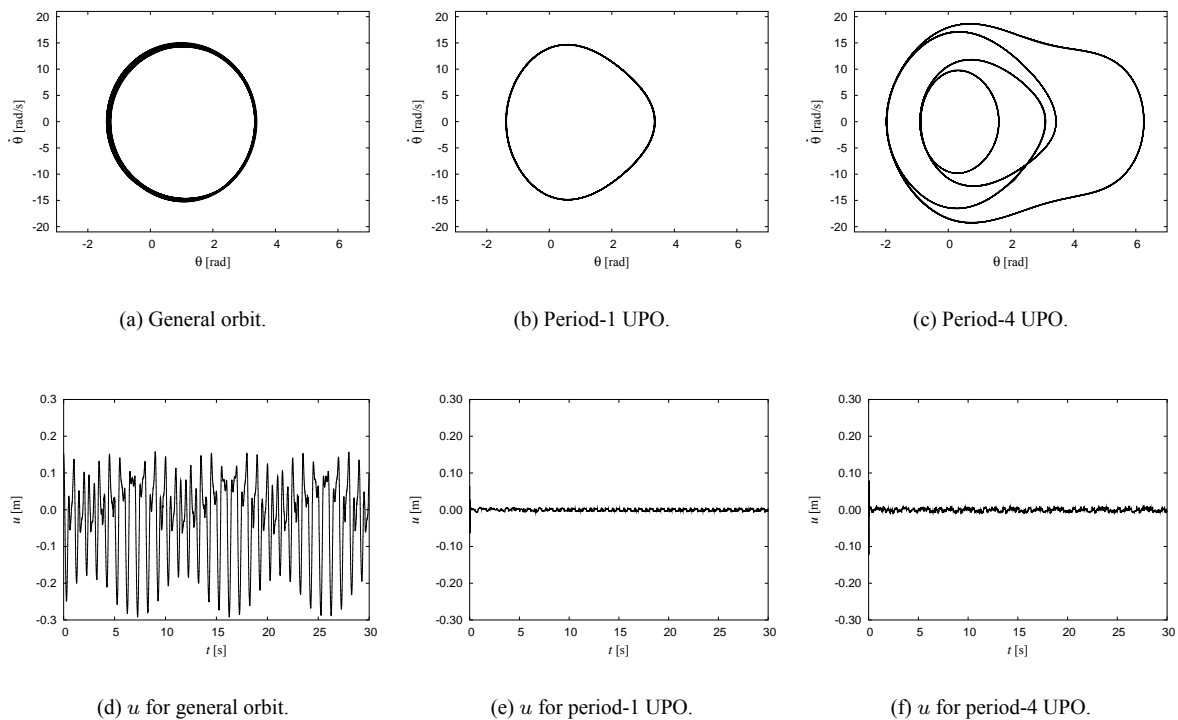


Figure 4 – Control action required to stabilize a general orbit and 2 different UPOs.

ACKNOWLEDGEMENTS

The authors would like to acknowledge the support of the Brazilian Research Agencies CNPq and FAPERJ, and through the INCT-EIE (National Institute of Science and Technology - Smart Structures in Engineering) the CNPq and FAPEMIG. The Air Force Office of Scientific Research (AFOSR) is also acknowledged.

REFERENCES

- Bessa, W.M., 2009. "Some remarks on the boundedness and convergence properties of smooth sliding mode controllers". *International Journal of Automation and Computing*, Vol. 6, No. 2, pp. 154–158.
- Bessa, W.M. and Barrêto, R.S.S., 2010. "Adaptive fuzzy sliding mode control of uncertain nonlinear systems". *Controle & Automação*, Vol. 21, No. 2, pp. 117–126.
- Bessa, W.M., De Paula, A.S. and Savi, M.A., 2009. "Chaos control using an adaptive fuzzy sliding mode controller with application to a nonlinear pendulum". *Chaos, Solitons & Fractals*, Vol. 42, No. 2, pp. 784–791.
- Bessa, W.M., Dutra, M.S. and Kreuzer, E., 2008. "Depth control of remotely operated underwater vehicles using an adaptive fuzzy sliding mode controller". *Robotics and Autonomous Systems*, Vol. 56, No. 8, pp. 670–677.
- Bessa, W.M., Dutra, M.S. and Kreuzer, E., 2010a. "An adaptive fuzzy dead-zone compensation scheme and its application to electro-hydraulic systems". *Journal of the Brazilian Society of Mechanical Sciences and Engineering*, Vol. 32, No. 1, pp. 1–7.
- Bessa, W.M., Dutra, M.S. and Kreuzer, E., 2010b. "An adaptive fuzzy sliding mode controller for remotely operated underwater vehicles". *Robotics and Autonomous Systems*, Vol. 58, No. 1, pp. 16–26.
- Bessa, W.M., Dutra, M.S. and Kreuzer, E., 2010c. "Sliding mode control with adaptive fuzzy dead-zone compensation of an electro-hydraulic servo-system". *Journal of Intelligent and Robotic Systems*, Vol. 58, No. 1, pp. 3–16.
- Corradini, M.L. and Orlando, G., 2002. "Robust stabilization of nonlinear uncertain plants with backlash or dead zone in the actuator". *IEEE Transactions on Control Systems Technology*, Vol. 10, No. 1, pp. 158–166.
- De Paula, A.S., Savi, M.A. and Pereira-Pinto, F.H.I., 2006. "Chaos and transient chaos in an experimental nonlinear pendulum". *Journal of Sound and Vibration*, Vol. 294, pp. 585–595.
- Filippov, A.F., 1988. *Differential Equations with Discontinuous Right-hand Sides*. Kluwer, Dordrecht.

- Franca, L.F.P. and Savi, M.A., 2001. "Distinguishing periodic and chaotic time series obtained from an experimental pendulum". *Nonlinear Dynamics*, Vol. 26, pp. 253–271.
- Hua, C.C., Wang, Q.G. and Guan, X.P., 2008. "Adaptive tracking controller design of nonlinear systems with time delays and unknown dead-zone input". *IEEE Transactions on Automatic Control*, Vol. 53, No. 7, pp. 1753–1759.
- Ibrir, S., Xie, W.F. and Su, C.Y., 2007. "Adaptive tracking of nonlinear systems with non-symmetric dead-zone input". *Automatica*, Vol. 43, pp. 522–530.
- Khalil, H.K., 2001. *Nonlinear Systems*. Prentice Hall, New Jersey, 3rd edition.
- Kim, J.H., Park, J.H., Lee, S.W. and Chong, E.K.P., 1994. "A two-layered fuzzy logic controller for systems with deadzones". *IEEE Transactions on Industrial Electronics*, Vol. 41, No. 2, pp. 155–162.
- Lewis, F.L., Tim, W.K., Wang, L.Z. and Li, Z.X., 1999. "Deadzone compensation in motion control systems using adaptive fuzzy logic control". *IEEE Transactions on Control Systems Technology*, Vol. 7, No. 6, pp. 731–742.
- Oh, S.Y. and Park, D.J., 1998. "Design of new adaptive fuzzy logic controller for nonlinear plants with unknown or time-varying dead zones". *IEEE Transactions on Fuzzy Systems*, Vol. 6, No. 4, pp. 482–491.
- Pereira-Pinto, F.H.I., Ferreira, A.M. and Savi, M.A., 2004. "Chaos control in a nonlinear pendulum using a semi-continuous method". *Chaos, Solitons and Fractals*, Vol. 22, No. 3, pp. 653–668.
- Šelmić, R.R. and Lewis, F.L., 2000. "Deadzone compensation in motion control systems using neural networks". *IEEE Transactions on Automatic Control*, Vol. 45, No. 4, pp. 602–613.
- Shyu, K.K., Liu, W.J. and Hsu, K.C., 2005. "Design of large-scale time-delayed systems with dead-zone input via variable structure control". *Automatica*, Vol. 41, pp. 1239–1246.
- Slotine, J.J.E., 1984. "Sliding controller design for nonlinear systems". *International Journal of Control*, Vol. 40, No. 2, pp. 421–434.
- Tao, G. and Kokotović, P.V., 1994. "Adaptive control of plants with unknown dead-zones". *IEEE Transactions on Automatic Control*, Vol. 39, No. 1, pp. 59–68.
- Tsai, C.H. and Chuang, H.T., 2004. "Deadzone compensation based on constrained RBF neural network". *Journal of The Franklin Institute*, Vol. 341, pp. 361–374.
- Wang, X.S., Su, C.Y. and Hong, H., 2004. "Robust adaptive control of a class of nonlinear systems with unknown dead-zone". *Automatica*, Vol. 40, pp. 407–413.
- Yoo, S.J., Park, J.B. and Choi, Y.H., 2009. "Decentralized adaptive stabilization of interconnected nonlinear systems with unknown non-symmetric dead-zone inputs". *Automatica*, Vol. 45, pp. 436–443.
- Zhang, T.P. and Ge, S.S., 2007. "Adaptive neural control of MIMO nonlinear state time-varying delay systems with unknown dead-zones and gain signs". *Automatica*, Vol. 43, pp. 1021–1033.
- Zhang, T.P. and Ge, S.S., 2008. "Adaptive dynamic surface control of nonlinear systems with unknown dead zone in pure feedback form". *Automatica*, Vol. 44, pp. 1895–1903.
- Zhang, T.P. and Ge, S.S., 2009. "Adaptive neural network tracking control of MIMO nonlinear systems with unknown dead zones and control directions". *IEEE Transactions on Neural Networks*, Vol. 20, No. 3, pp. 483–497.
- Zhou, J., 2008. "Decentralized adaptive control for large-scale time-delay systems with dead-zone input". *Automatica*, Vol. 44, pp. 1790–1799.
- Zhou, J. and Shen, X.Z., 2007. "Robust adaptive control of nonlinear uncertain plants with unknown dead-zone". *IET Control Theory & Applications*, Vol. 1, No. 1, pp. 25–32.
- Zhou, J., Wen, C. and Zhang, Y., 2006. "Adaptive output control of nonlinear systems with uncertain dead-zone nonlinearity". *IEEE Transactions on Automatic Control*, Vol. 51, No. 3, pp. 504–511.

RESPONSIBILITY NOTICE

The authors are the only responsible for the printed material included in this paper.

Analysis of the Hearing Temporary Threshold Shift (TTS) of Subjects Exposed to Whole Body Vibration (WBV) Alone

Dornela, J.G.^{1,2,a}, Duarte, M.L.M.^{1,2,b}, Almeida, L.V.M.², Donadon, L.V.^{1,2}, Batista Filho, M.C.³, Moreira, M.R.R.O.², Ferreira, C.H.², Dantas, B.L.C.⁴, Santos, M.A.R.⁵

^a julianadornela@yahoo.com.br, ^b mlduarte@dedalus.lcc.ufmg.br

¹ GRAV_{HB}: Group of Acoustics and Vibration in Human Beings; DEMEC: Mechanical Engineering Department, Universidade Federal de Minas Gerais, Av. Antônio Carlos, 6627 – Pampulha, Belo Horizonte/MG, Brazil, 31270-901.

² PPGMEC/UFMG: Post-Graduation Program in Mechanical Engineering; Universidade Federal de Minas Gerais (UFMG)

³ Control Engineering and Automation; Universidade Federal de Minas Gerais (UFMG)

⁴ FALE/UFMG: Faculty of Arts, Universidade Federal de Minas Gerais (UFMG)

⁴ HC/UFMG: Hospital das Clínicas, Universidade Federal de Minas Gerais, Av. Alfredo Balena, 110, Belo Horizonte/MG, Brazil, 30130-100

*Abstract: This work evaluates the Temporary Threshold Shift (TTS) of healthy volunteers when exposed only to whole-body vibration (WBV). Such physical agent is common in working environments, or even in leisure ones, although its association with other physical agents is more frequent. Nevertheless, as a public health measure, it is important to understand the relationship of this physical agent alone on hearing, before investigating such effect when it is associated with other agents. The results were evaluated using the Distortion Product Otoacoustic Emission (DPOAE) exam. The analysis was performed statistically using the parametric Student *t* test. Two vertical (*z*-axis) WBV exposures at 5Hz, 2.12 m/s² amplitude during 18 min, with a 10-12 minutes average interval between the exposures, were used. These parameters were chosen to be within the health safety levels set by the European Directive (2002). The evaluation was performed after each individual exposure so to investigate the cumulative influence. However, for the frequency, amplitude and duration used in this study no influence between the isolated exposure to WBV and TTS was found. A total of 19 volunteers took part in the study and the analysis was performed considering both ears. The literature is very controversial about the influence of WBV on hearing, in other words, there are studies that found hearing loss due to WBV exposure and studies that found no change. The current study also found no relationship between the isolated exposure to WBV and hearing loss on humans. Therefore, to verify why some studies arrived to different conclusion, an investigation about the influence of the sample size used should be performed, as well as a study using other exposure levels and types of excitations.*

Keywords: Whole-Body Vibration (WBV), Temporary Threshold Shift (TTS), Distortion Product Otoacoustic Emission (DPOEA)

INTRODUCTION

Whole-body vibration (WBV) is a physical stimuli that, besides being frequently present in many workplaces, such as industries, transport, construction, railway, mining, agricultural machinery, are also found in the daily lives of people. There are a lot of studies investigating the influence of whole-body vibration (WBV) on human beings. The majority of the studies investigating the influence of WBV in humans, however, do so evaluating their effects on the human spine (Bovenzi and Hulshof, 1999; Lings and Lebouef-Yde, 2000; Gallais and Griffin, 2006). It is clear that an association exists between WBV and spinal system disorders (Wilder, 2007) and others disorders such as neck-shoulder problems, circulatory, reproductive, digestive, genital/urinary and auditory effects (Vinet Report, 2001; ISO2631-1, 1997; Seidel and Heide, 1986). As mentioned by Griffin (1996), the increase of hearing loss among subjects exposed to vibration might be attributed to the transmission of the vibration to the inner ear. That might either directly affect hearing or increase the susceptibility of the subject to NIHL (Noise Induced Hearing Loss).

In general, laboratory studies measure the hearing thresholds before and after the exposures, looking for changes between the tests. The shifts are known as the Temporary Threshold Shifts (TTS). The TTS allows verifying immediate damage on hearing. They are temporary because the hearing thresholds come back to normal after a resting period, generally set as 14h (NIOSH, 1996). According to Pekkarinen (1995) the temporary threshold shifts (TTS) found in the laboratory studies may give indirect evidence of the permanent threshold shift (PTS) due to long-term exposures at workplaces.

There are very few articles in the literature investigating the isolated effects of whole-body vibration (WBV) on human hearing and these studies are normally quite old and unclear (Okada *et al.*, 1972, Yokoyama, Osako and Yamamoto, 1974; Manninen, 1984a, 1985; Seidel *et al.* 1992; Izumi, 2006). From this list of studies, three found auditory deficits (TTS) after exposure to WBV (Okada *et al.*, 1972; Manninen, 1984a; Manninen, 1985), whereas four

studies found no harmful effects of such exposure on human hearing (Yokoyama, Osako and Yamamoto, 1974; Manninen, 1984a; Seidel *et al.* 1992; Izumi, 2006). It can be observed that the methodology within the studies vary and that may explain some of the findings; although even within the same author and the same methodology, some controversies can be noted, as it will be mentioned later (Manninen, 1984a; Manninen, 1985).

Regarding the studies that found TTS after exposure to WBV, Okada *et al.* (1972) found significant TTS only when the exposure was at 5 Hz with 500 cm/s² amplitude or 10 and 20 Hz with 1000 cm/s² amplitude. In exposures with lower amplitudes (100 cm/s²) no significant effect on hearing was found. The exposure was applied during 60 min in their study. Manninen (1985) also found significant TTS after WBV, however, considering three consecutive exposures of 2.12 m/s² during 16 minutes each at 5 Hz. In his previous study (Manninen, 1984a), when using also three consecutive exposures at 2.44 m/s² during 16 minutes, he also found a slightly change in TTS.

However, on the same study (Manninen, 1984a), when using the same methodology as the one used in 1985, therefore, considering smaller amplitude (2.12 m/s²) but with the same duration, repetition and frequency, he did not found any TTS.

Analyzing the studies where no TTS was found, it can be observed that, although Izumi's methodology (Izumi, 2006) was based on Manninen studies, since she used only one exposure, her total WBV was smaller. She used a 6 Hz, 2.45 m/s² during 18 min to be within the European Directive (2002) EAV health levels. Yokoyama, Osako and Yamamoto (1974) also used vibration values (5 Hz, 6 mm, during 20 minutes) similar to those of Izumi (2006) and Manninen (1984a, 1985). Seidel *et al.* (1992) used vibration values (two consecutive z-axis exposure during 11 minutes each at 2.01 Hz, 2 m/s²), differing mainly from the studies of Manninen who performed a greater number of exposures.

None of the found studies, however, have monitored the quantity of the whole-body vibration that really reaches the inner ear. Therefore, that was not the case in the present study also.

According to the European Directive (2002), there are two distinct values to be observed in order to monitor health problems related to WBV or HAV exposure, to know: the Exposure Action Value (EAV) and the Exposure Limit Value (ELV). The EAV is the value for an 8h daily exposure when employers should take preventive measures and improvement actions to reduce vibration levels. For WBV exposures, the EAV is 0.5 m/s² for an 8-hour journey (what corresponds to a Vibration Dose Value – VDV of 9.1 m/s^{1.75}). The ELV is the value that no exposure should exceed. Its value for WBV is 1.15 m/s² (or a VDV of 21 m/s^{1.75}). However, the European Directive 2002 does not say much about the individual health effects caused by WBV, only provides guidelines for safety. So, many authors investigate these effects, as it is the current case, since the human beings are frequently part of industrial processes involving some kind of vibration.

The values of vibration used in this work tried to simulate real working conditions, taking into consideration the safety aspects of the European Directive (2002). This study sought to investigate what are the effects of the isolated WBV on human hearing. A higher total exposure level of WBV than the one used at Izumi's study was used here, in order to understand if the negative influence of WBV on hearing there was due to the level used, since some of the other mentioned studies found a positive correlation between this physical stimulus and the hearing loss.

METHODOLOGY

Volunteer Selection

The data collection was made at the Audiology Sector of the Clinics' Hospital of the Universidade Federal de Minas Gerais at the city of Belo Horizonte, Brazil. The ethics committee for human research of the University (COEP/UFMG) approved the study previously, as recommended by Griffin (1996).

The population chosen as volunteers was composed by young adults, with normal hearing and without history of occupational exposure to noise or vibration. There were a total of 19 subjects (10 men and 9 women).

All the selected volunteers were submitted to a battery of hearing tests that aimed to check their good auditory condition. The hearing tests performed were: a) Othoscopy, for checking possible obstructions in the external ear and b) Distortion Product Otoacoustic Emission (DPOAE) test, to investigate answers of the cells of the inner ear in the frequency band from 750 Hz to 8 kHz. Volunteers with any alteration in the auditory tests should be excluded, as this could mask or even prevent the accomplishment of the DPOAE tests and the detection of a possible TTS. Nevertheless, for the present sample, that was not the case. The examinations were performed in a soundproof booth properly calibrated and the equipment properly calibrated AUDX - Bio-logic® was used to measure and register the DPOAE of the inner ear. Two values were obtained for the DPOAE tests performed before any exposure to WBV and the average value was used as reference for the comparison with the results obtained after the exposure, so to verify its influence.

Testing Parameters

The level of WBV used in this work regarding both the frequency and amplitude values was based on everyday occupational situations and similar researches to this work (Manninen 1986, 1985, 1984a, 1984b, 1983a and 1983b; Seidel *et al.* 1992; Soliman *et al.* 2003; Izumi, 2006) that served as the basis for the methodology used. For the

frequency selection, the majority of the studies used values below 8 Hz. Balbinot (2001) and Rehn et al. (2005) showed that most vehicles in real situations have the maximum peak occurring around or below 6 Hz. Also, within the 4-8 Hz interval the weighting curve of the ISO2631-1 (1997) standard has unit value, showing that this is most important range also.

To determine the testing time to be used based on a pre-defined amplitude of vibration (to be within either the EAV or the ELV set by European Directive (2002)), a *Whole body vibration calculator* (HSE, 2006) was used. This consists of a spreadsheet based on the ISO2631-1 (1997) standard where it is possible to determine the magnitude or duration of vibration used (fixing the other) to be equivalent to an eight hours working journey. So, the pre-defined amplitude was chosen to be the one used by Manninen (1985), however, considering more exposures than at Izumi's work (2006), so to result in a higher total exposure level than at the latter, but smaller than at the former.

Therefore respecting the ELV safety levels set by the European Directive (2002) but going higher than the EAV level, it was proposed 2 sinusoidal excitation exposures at 5 Hz frequency in the Z direction, with average amplitude of 2.12 m/s^2 rms during 18 minutes each. Between the first and second exposure there was an average interval of 10-12 minutes, which was the necessary time to perform all the necessary hearing evaluations.

Experimental Setup

Figure 1 shows the vibratory system used during the tests. A detail of the vibration platform can be seen in the photograph presented at Fig. 2.

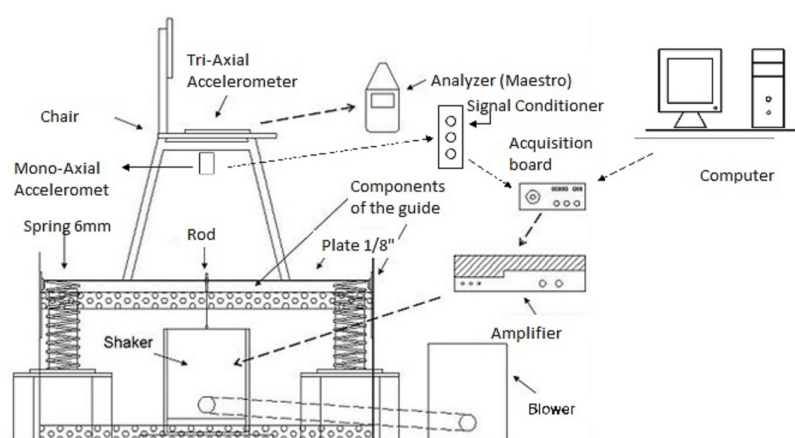


Figure 1 - Scheme vibratory system used in tests



Figure 2 - Photo vibrating platform

The subjects sat in a wooden chair having metallic feet, with backrest but no cushion. It was positioned over a metallic plate (750 x 1000 x 3 mm) with reinforced edges. The position of the chair was such that the center of gravity of the setup (chair + subject) was coincident with the geometry center of the plate, in order to avoid undesirable rotational movements that could damage the shaker. The plate was supported by four compression steel springs with 76 mm external diameter, 350 mm height, wire diameter of 6 mm and 9 spirals. The excitation was provided by a Dynamic Solution® shaker model VTS150, positioned under the platform. A steel pushrod with 3.0 mm diameter and approximately 107 mm variable length with screws of 5 mm welded in each end was used to transmit the excitation to the platform. The 5 Hz sinusoidal frequency used was generated by a Photon II acquisition board from LDS and

amplified by two amplifiers (a Crown Amplifier® CE2000 and a B&K 4810 amplifier). An APTechnologies® AP5213 tri-axial accelerometer was positioned on the chair seat, using a standard seat pad, Griffin (1996). That signal was sent to a portable analyzer model Maestro from 01-dB. A control system was developed using a National Instrument acquisition board model NI Speed 33 to maintain the excitation at the desirable level (Batista Filho *et al*, 2010). For that a standard ICP control accelerometer model 352A from PCB Piezotronics was used.

RESULTS AND DISCUSSION

In order to compare the influence of the WBV on hearing of the volunteers, a comparison of the OEA results obtained before and after the exposure to WBV was performed. Such comparison was performed statistically using the parametric Student t-test. The null hypothesis (H_0) was considered as the absence of differences between the tests before and after the exposure to WBV, and the alternative hypothesis (H_1) as being when this difference is present and statistically significant. The confidence level (α) used was set as 5%. For the OEA exams, H_1 checked if the results after the WBV exposure presented smaller results than the reference results (obtained before the WBV exposure), since it is aimed a decrease on the response amplitude after exposure (that is, post-WBV < reference).

Table 1 presents the OEA analysis results on dB scale for left and right ears respectively for the first and the second WBV exposure in that order. For the confidence level used, it is possible to see that for the WBV exposure there was no significant difference between the results obtained before and after any of the two exposures.

Table 1 – Student T-Test results for the OEA exams – dB scale

<i>Exposure</i>	$\alpha = 0,05$	750 Hz	984 Hz	1500 Hz	2016 Hz	3000 Hz	3984 Hz	6000 Hz	7969 Hz
1 st WBV (Left ear)	Reject H_0 ? H_1 : WBV < Ref.	No	No	No	No	No	No	No	No
1 st WBV (right ear)	Reject H_0 ? H_1 : WBV < Ref.	No	No	No	No	No	No	No	No
2nd WBV (Left ear)	Reject H_0 ? H_1 : WBV < Ref.	No	No	No	No	No	No	No	No
2nd WBV (right ear)	Reject H_0 ? H_1 : WBV < ref.	No	No	No	No	No	No	No	No

So, by the results of the statistical analysis, it is observed that the levels of WBV used in this study did not cause TTS. That agrees with the findings of most studies in the literature that evaluated the human hearing after exposure to WBV alone and found no effect of WBV on TTS (Yokoyama, Osako and Yamamoto, 1974; Manninen, 1984a; Seidel *et al.* 1992 and Izumi, 2006).

Analyzing the two studies that found TTS after the WBV exposure, it should be noted that Okada *et al.* (1972), despite having used similar WBV frequency to the studies that found no effect on hearing, used higher exposure levels when compared to other studies that found no effects. Manninen (1985) also used frequency values similar to studies that found no effect on hearing, but the total exposure value used by Manninen (1985) was also greater than that used by those studies.

CONCLUSION

The objective of this study was to check the influence of WBV on the hearing of healthy subjects, aiming to understand this very common occupational risk problem in the health of workers.

Despite the increase on the WBV exposure level used in the present work compared with Izumi (2006) study, no influence of the WBV on hearing was still obtained. It is believed that the levels used in this study are still not sufficient to cause a temporary change of human hearing. Nevertheless, they are within the safety limits set by the European Directive (2002).

Since the three studies that found TTS after WBV (Okada *et al.* 1972, Manninen, 1984a and Manninen, 1985) used amplitude levels higher than those studies that found no such effect, it is believed that higher amplitude values of WBV that caused TTS.

However, for the level and frequency used here, that is, 2.12 m/s² at 5 Hz, even for two simultaneous exposures, it was concluded that there was no significant interaction between the WBV exposure and hearing, evaluated using the TTS (Temporary Threshold Shift). Although it is presumed that in a noise environment the WBV could provoke increased hearing loss, from the tests performed here, nothing can be aid in that respect. However, that hypothesis should be tested in conjunction.

Further research with larger samples should also be conducted to clarify from what level WBV alone can be damaging to human hearing, although the most difficult point is to establish the safety parameters for hearing, since the European Limits are general.

ACKNOWLEDGMENTS

The authors would like to thank the Clinic Hospital of Minas Gerais (HC/UFGM) for the cooperation program to develop this research, especially Dr. Celso Becker and his secretary Elisa Maria Oliveira Santos for all the help. Also, to thank the volunteers who took part in the experiments. The research was performed using FAPEMIG grant TEC951-09. The first author would like also to acknowledge the scholarship from CNPq.

REFERENCES

Balbinot, A., 2001, "Caracterização dos níveis de vibração em motoristas de ônibus: um enfoque no conforto e na saúde". *Tese* Doutorado em Engenharia Mecânica pela Universidade Federal do Rio Grande do Sul . Porto Alegre, Brasil.

Batista Filho, M., Donadon, L., Duarte, M., Galvez, J., 2010, "Implementation of a Control System in a Platform for Whole-Body Vibration (WBV) Tests." Congresso Brasileiro de Automática, Brazil .

Bovenzi, M., 1996, "Low back pain disorders and exposure to whole body vibration in the workplace." *Seminars in Perinatology* , pp. 38-53.

Bovenzi, M., Hulshof, C., 1999, "An update review of epidemiologic studies on the relationship between exposure to whole body vibration and low back pain." *Int. Arch. Environment Health* , pp. 351-365.

European Directive 2002/44/EC., 2002, On the Minimum Health and Safety Requirements Regarding the Exposure of workers to the risks Arising From Physical Agents (vibration). European Parliament and of the Council .

Gallais, L., Griffin, M., 2006, "Low back pain in car drivers: A review of studies published 1975 to 2005." *Journal of Sound and Vibration* , pp. 499-513.

Griffin, M., 1996, *Handbook of Human Vibration*. London: Academic Press.

Hamernik, R. P., Ahroon, W. A., Davi, R. I., & Axelsson, A. (1989). Noise and vibration interactions: Effects on hearing. *J. Acoust Soc Am* , pp. 2129-2137.

HSE., 2006, "Health and Safety Executive Whole-body Vibration calculator." Acesso em 2010, disponível em <http://www.hse.gov.uk/vibration/wbv/wholebodycalc.htm>.

ISO 2631/1., 1997, International Organization for Standardization – Mechanical Vibration and Shock – Evaluation of Human Exposure to Whole-Body Vibration – Part1:General Requirements. International Organization for Standardization .

Izumi, R., 2006, "Efeitos de vibrações e níveis de pressão sonora elevados na mudança temporária de limiar auditivo." *Dissertação* defendida pela Universidade Federal de Minas Gerais . Belo Horizonte, Minas Gerais, Brasil.

Lings, S., Lebouef Yde, C., 2000, "Whole body vibration and low back pain: a systematic, critical review of the epidemiological literature 1992-1999". *Int Arch Occup Environment Health* , pp. 290-297.

Manninen, O., 1986, "Bioresponses in men after repeated exposures to single and simultaneous sinusoidal or stochastic whole body vibrations of varying bandwidths and noise." *Int Arch Occup Environ Health* , pp. 267-295.

Manninen, O., 1985, "Cardiovascular changes and hearing threshold shifts in men under complex exposures to noise, whole body vibrations, temperatures and competition type psychic load." *Int Arch Occup Environ Health* , pp. 251-274.

Manninen, O., 1984b, "Hearing threshold and heart in men after repeated exposure to dynamic muscle work, sinusoidalvs stochastic whole body vibration and stable broadband noise". *Int Arch Occup Environ Health* , pp. 19-32.

Manninen, O., 1983a, "Studies of combined effects of sinusoidal whole body vibrations and noise of varying bandwidths and intensities on TTS2 in men." *Int Arch Occup Environ Health* , pp. 273-288.

Manninen, O., Ekblom, A., 1984a, "Single and joint actions of noise and sinusoidal whole body vibration on TTS2 values and low frequency upright posture sway in men." *Int Arch Occup Environ Health* , pp. 1-17.

Manninen, O., 1983b, "Simultaneous effects of sinusoidal whole body vibration and broadband noise on TTS2's and R wave amplitudes in men at two different dry bulb temperatures." *Int Arch Occup Environ Health* , pp. 289-297.

NIOSH, N. I., 1996, *Preventing Occupational Hearing Loss. A Practical guide*. U. S. Department of Health and Human Services.

Okada, A., Miyake, H., Yamamura, K., Minami, M., 1972, "Temporary Hearing Loss Induced by Noise and Vibration". *Journal of the acoustical Society of America* , pp. 1240-1248.

Pekkarinen, J., 1995, "Noise, Impulse noise and other physical factors: combined effects on hearing." *Occupational Medicine* , pp. 545-559.

Rehn, B., Nilsson, T., Olofsson, B., Lundstrom, R., 2005, "Whole-body vibration exposure and non-neutral neck postures during occupational use of all-terrain vehicles." *Ann. Occup. Hyg.* , pp. 267-275.

Seidel, H., Heide, R., 1986, "Long-terms Effects of Whole Body Vibration: a Critical Survey of the Literature." *Int Arch Occup Environ Health* , pp. 1-26.

Seidel, H., Bluthner, R., Martin, J., Menzel, G., Panuska, R., Ullsperger, P., 1992, "Effects of isolated and combined exposures to whole-body vibration and noise on auditory-event related brain potentials and psychophysical assessment." *European Journal of Applied Physiology* , pp. 376-382.

Soliman, S., El-atreby, M., Tawfik, S., Holail, E., Iskandar, N., Abou-setta, A., 2003, "The interaction of whole-body vibration and noise on the cochlea". *International Congress Series* , pp. 209-216.

Vinet Report., 2001, "Research Network on detection and prevention of Injuries due to Occupational Vibration Exposures (Vibration Injury network - VINET). Final report Appendix W1A, Guidelines and questionnaires for whole body vibration health surveillance .

Wilder, D., 2007, "The biomechanics of vibration and low back pain". *American Journal of Industrial Medicine* , pp. 577-588.

Yokoyama, T., Osako, S., Yamamoto, K., 1974, "Temporary Threshold Shifts Produced by Exposure to Vibration, Noise and Vibration-plus-Noise". *Acta Otolaryng* , pp. 207-212.

RESPONSIBILITY NOTICE

The author(s) is (are) the only responsible for the printed material included in this paper.

Modeling the response in vehicular vibroacoustic systems

Walter Jesus Paucar Casas¹, Vinícius Ribeiro da Silva¹, and Régis Eduardo Antich¹

¹ Universidade Federal do Rio Grande do Sul, Departamento de Engenharia Mecânica, Rua Sarmento Leite 425, Bairro Cidade Baixa, Porto Alegre - RS, CEP 90050-170, Brazil

Abstract: Currently, consumers are more exigent about dynamic comfort issues when using a machine, product or equipment, particularly with regard to noise and vibration. It is common to find in these cases that two or more physical domains interact, constituting a coupled system. In many of these situations it is not more realistic the independent modeling of only one domain, without the simultaneous participation of the remaining domains. The objective of this research involves dealing with simplified vibroacoustic systems for evaluating its response, aiming the vibroacoustic optimization. With this purpose, we develop tools through the finite element method, on the modeling and simulation of the frequency response in vehicular applications. To achieve these goals, we reviewed some models of coupled systems based on the formulation of the structure displacement u and pressure p of the acoustic field. The modal frequency response on vibroacoustic systems was implemented in a commercial program. We study a vehicular vibroacoustic cabin with dimensions proportionately reduced and analyze the frequency response in various situations. For the analyzed conditions, the frequency response decreases considerably in the range of 20 to 200 Hz for the fluid pressure of some predefined node, allowing us to have a tool to control the response of a given region, according to certain requirements.

Keywords: fluid-structure interaction, frequency response analysis, finite element method

INTRODUCTION

A typical case of a coupled system is one that presents dynamic fluid-structure interaction, where the fluid and structural domains can not be solved independently, because of interface forces, which can significantly alter the behavior of the system as a whole, (Msc.Software, 1996).

In this work we study the problem of dynamic fluid-structure interaction, considering small amplitude oscillations, *i.e.* problems where the fluid displacement is small; however the influence of the interaction is important. Several systems are modeled taking into account the fluid-structure coupling. Some examples involve aerospace applications, underwater acoustics, fuel tanks, electrical transformers, pipelines, pressure vessels, vehicle cabins (De Mello, 2003), among others.

The vibroacoustic system can experiment some level of resonance due to the effect of certain requests. It is better to avoid such a situation that can modify the properties of sound transmission, or also cause fracture by breaking the structure. Nowadays, for some products, the prediction of the vibroacoustic behavior is a design prerequisite.

This work involves the treatment of problems with focus on vibroacoustic comfort, and then some tools are developed using the finite element method, concerning to the modeling and optimization of the vibroacoustic response in vehicular applications.

FLUID-STRUCTURE COUPLED SYSTEM

When solving coupled fluid-structure systems under dynamic excitation, the fluid domain influences the behavior of the structure and vice versa, *i.e.*, the vibration of the structure is influenced by the fluid pressure variation and the acoustic waves are sensitive to the variation of the structural displacement. In the context of free vibration, the natural frequencies and modes of the coupled system are different from those presented by the uncoupled sub-systems.

The energy of a coupled mode is divided between the structure and the fluid. Usually the largest amount of energy remains in the fluid or in the structure, from which the coupled system is classified as dominated by the fluid or by the structure (De Mello, 2003).

Usually a mode dominated by the structure is originated by a structural uncoupled mode inducing an acoustic mode in the fluid. Also, a mode dominated by the fluid is an acoustic mode inducing a mode in the structure. The way the fluid influences the movement of the structure is the pressure at the interface surface, as well as the movement of the surface interface modifies the acoustic field.

The compact matrix form of Eq. (1) gives the coupled formulation $u-p$ in displacement of the structure and pressure of the fluid:

$$\begin{bmatrix} \mathbf{M}_{ss} & \mathbf{0} \\ \mathbf{M}_{fs} & \mathbf{M}_{ff} \end{bmatrix} \begin{Bmatrix} \ddot{\mathbf{u}} \\ \ddot{\mathbf{p}} \end{Bmatrix} + \begin{bmatrix} \mathbf{K}_{ss} & \mathbf{K}_{sf} \\ \mathbf{0} & \mathbf{K}_{ff} \end{bmatrix} \begin{Bmatrix} \mathbf{u} \\ \mathbf{p} \end{Bmatrix} = \begin{Bmatrix} \mathbf{f}_s \\ \mathbf{f}_f \end{Bmatrix} \quad (1)$$

For the case of free vibration, the second term of Eq. (1) is zero. The non symmetrical presentation of this formulation is its main disadvantage because of it is not possible to use several efficient algorithms developed for symmetric matrices. The main advantage of this formulation is its small number of degrees of freedom for modeling the fluid domain, especially when compared with models based on vectorial variables for the fluid.

MODAL FREQUENCY RESPONSE OF THE COUPLED FLUID-STRUCTURE SYSTEM

It is assumed that the modes of the coupled system can be obtained using the conventional techniques for calculating λ eigenvalues, and right and left eigenvectors, ϕ and $\bar{\phi}$ respectively. Then, these variables can be used for evaluating the Modal Frequency Response (MFR), according to the superposition given by Eqs. (2) and (3):

$$\mathbf{U} = \sum_{i=1}^n \phi_i Q_i = \sum_{i=1}^n \phi_i \left(\frac{1}{\lambda_i - \omega^2} \right) \bar{\phi}_i^T \mathbf{F}, \quad (2)$$

$$Q_i = \left(\frac{1}{\lambda_i - \omega^2} \right) \bar{\phi}_i^T \mathbf{F}. \quad (3)$$

One obvious advantage of the superposition technique of coupled modes is the possibility of including only a limited number of modes in the analysis, lower than the total number of degrees of freedom of the system.

RESULTS

A simplified model of a vehicle cabin is studied with the objective of quantifying the structural-acoustic coupling through analysis of modes and natural frequencies, in order to evaluate and optimize its frequency response for a specific range of frequencies. The original model to be studied is presented in Fig. 1.

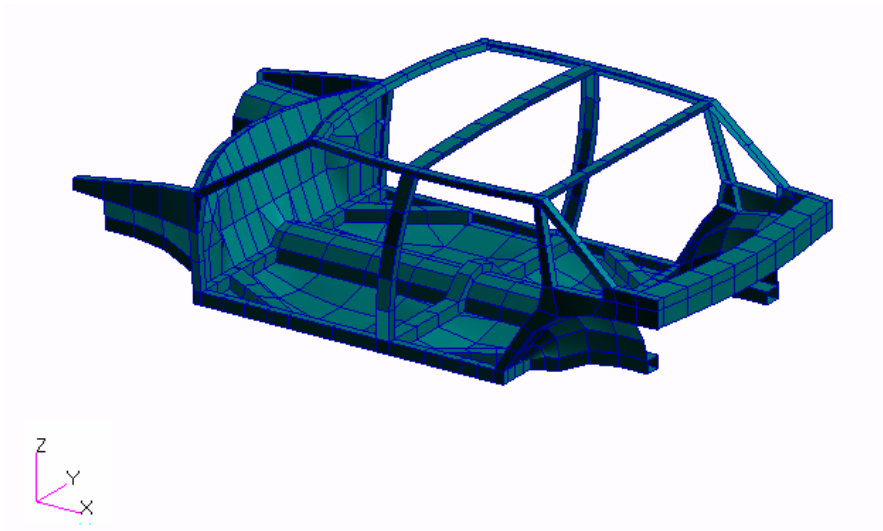


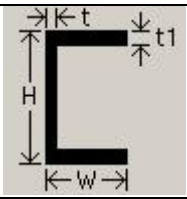
Figure 1 - Source model of the vehicle cabin

Chassis structure formed by beams

The chassis is modeled by C-section beams with dimensions shown in Tab. 1. The material used is steel with properties of the elastic modulus $E=2.07 \times 10^{11}$ N/m², density $\rho=7800$ kg/m³ and Poisson's ratio $\mu=0.292$. The chassis is supported on four vertices, represented by the boundary conditions $u_z=r_z=0$.

Table 1 - Cross sections of the chassis beams

Variable	Dimension
W (m)	0.002
H (m)	0.002
t (m)	0.002499999
t_1 (m)	0.002499999



Body structure formed by plates

The plates used in the model of the body are composed by different materials. To overcome the effects of different types of materials that are used in the manufacturing of the body and especially on the doors of the vehicle, we explore the idea of an equivalent material with customized elastic modulus, density and Poisson's ratio, as can be shown in Tab. 2.

Table 2 - Material properties of the different parts of the vehicle cabin

Property	Rear	Floor	Cabin ceiling, ceiling rear trunk	Front	Doors	Windows (glass)
<i>Number of plates</i>	1	1	1	1	2	1
Plate thickness h (mm)	5	7	4	6	8	5
Gap h_{livre} (mm)	4	4	4	4	4	---
Total thickness h_t (mm)	9	11	8	10	12	5
E_{steel} (N/m ²) *	2.07E11	2.07E11	2.07E11	2.07E11	2.07E11	4.60E10
E_{eq} (N/m ²)	6.39E10	8.38E10	5.18E10	7.45E10	1.84E11	4.60E10
Mass (<i>Number of plates</i>)	1	1	1	1	2	1
Apparent volume $\left[\frac{(Number\ of\ plates)\ h + h_{free}}{h} \right]$	1.8	1.57	2	1.67	2.5	1.0
ρ_{steel} (kg/m ³) *	7800	7800	7800	7800	7800	2600
ρ_{eq} (kg/m ³)	4340	4970	3900	4680	6240	2600
Poisson's ratio ν	0.235	0.235	0.235	0.235	0.235	0.245
E_{eq}/ρ_{eq}	1.47E7	1.69E7	1.33E7	1.60E7	2.95E7	1.77E7

* Except the glass windows

For evaluating the equivalent elastic modulus E_{eq} we start by considering the hypothesis of stiffness as given for the natural frequency in plates (Blevins, 1995), according to Eq. (4):

$$\omega = \sqrt{\frac{k}{m}} = \sqrt{\frac{\frac{E h^3}{48(1-\nu^2)ab} [f(\nu, a, b)]}{\frac{\rho hab}{6300} [f(a, b)]}} = \sqrt{\frac{E h^2}{\rho} [f(\nu, a, b)]}. \tag{4}$$

It is observed from this expression that the stiffness k depends on the product $E \cdot h^2$, while the mass m depends exclusively on the density ρ . The equivalent stiffness k_{eq} of plates in parallel results:

$$k_{eq} = \sum_{i=1}^{N^\circ\ plates} k_i = \sum_{i=1}^{N^\circ\ plates} E_i h_i^2. \tag{5}$$

For the case of plates of the same thickness h and material with elastic modulus E ,

$$k_{eq} = N^\circ\ plates \cdot E \cdot h^2. \tag{6}$$

The equivalent stiffness for the total thickness h_t , where the free thickness is added to the thickness h of the plates, can be expressed as:

$$k_{eq} = E_{eq} h_t^2. \quad (7)$$

Equating the last two expressions,

$$E_{eq} = \frac{(N^\circ \text{ plates}) h^2}{h_t^2} E. \quad (8)$$

The density ρ of a plate with mass m , volume V , surface area A and constant thickness h , can be expressed as:

$$\rho = \frac{m}{V} = \frac{m}{A h} \quad (9)$$

The equivalent density ρ_{eq} of a plate composed of several plates of different materials is calculated taking into account two hypotheses, the first is concerned to the thickness of the gap h_{ivre} or lighter materials that are considered to obtain the total V_t , while the second establishes that the total mass m_t is essentially equal to the sum of the plates masses,

$$\rho_{eq} = \frac{m_t}{V_t} = \frac{(N^\circ \text{ plates}) m}{A [(N^\circ \text{ plates}) h + h_{free}]} = \left(\frac{m}{A h} \right) \left[\frac{(N^\circ \text{ plates})}{(N^\circ \text{ plates}) h + h_{free}} \right], \quad (10)$$

$$\rho_{eq} = \rho \left[\frac{(N^\circ \text{ plates})}{(N^\circ \text{ plates}) h + h_{free}} \right]. \quad (11)$$

The body is supported on four vertices, represented by the boundary conditions $u_z=r_z=0$.

Structural cabin formed by beams and plates

In this case the structure of the cabin is formed by the chassis and the body, modeled by beams and plates respectively. The chassis is modeled with beams of cross sections and materials specified in Tab. 1, while the body with plates of dimensions and materials specified in Tab. 2.

The structure is supported on four vertices, represented by the boundary conditions $u_z=r_z=0$.

Acoustic cabin

The cabin is modeled with fluid elements, air density $\rho=1.204 \text{ kg/m}^3$ and speed of sound in air $c=347 \text{ m/s}$.

Structural-acoustic cabin

The structure of the cabin formed by the chassis and the body is modeled with beams (586 CBAR) and plates (4504 CQUAD4) elements, respectively, while the acoustic cabin is modeled with fluid elements (22048 CHEXA). The chassis is modeled with beams of dimensions specified in Tab. 1, the body is modeled with plates of dimensions and materials specified in Tab. 2, and the cabin is modeled with hexahedral solids.

The structure of the cabin is supported on four vertices, represented by the boundary conditions $u_z = r_z = 0$, as shown in Fig. 2.

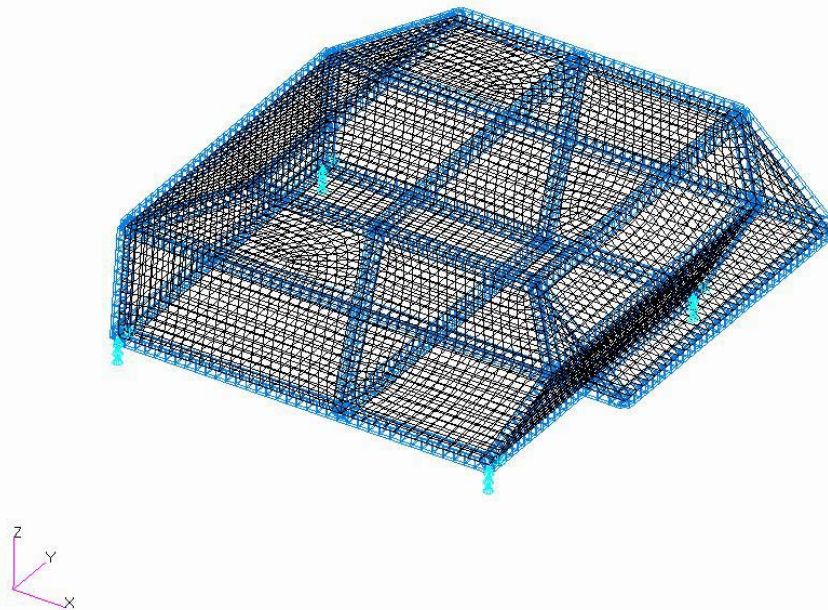


Figure 2 - Structural-acoustic model of the vehicle cabin

We can see in Fig. 3 some coupled modes with the corresponding natural frequencies values, where the fluid fringes match the structural displacements.

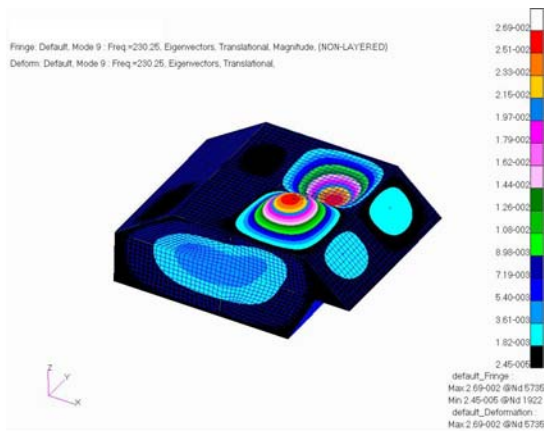
MINIMIZATION OF THE FREQUENCY RESPONSE

In this case, the objective function for response optimization is written as the minimization of the mean square fluid pressure p at node 10436 of the fluid medium, in Pa, for a given range of frequencies i between 20 and 200 Hz, without change appreciably the weight of the system, according to Eq. (12).

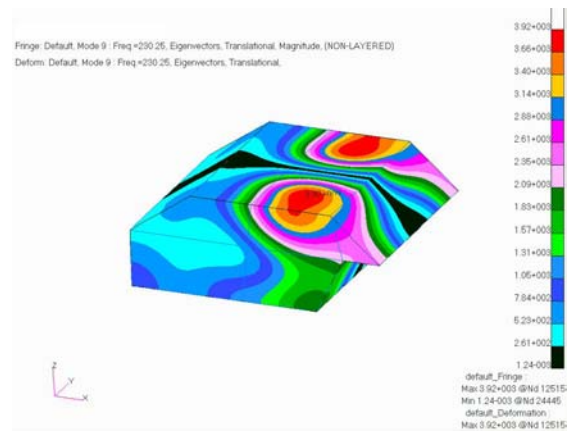
$$\text{Min } f = \sum_{i=20}^{100} (p_{10436}^i)^2 + 2 \sum_{i=51}^{100} (p_{10436}^{2i})^2 \quad (12)$$

Table 3 shows the thicknesses values of the plates before and after the minimization of the response, where the variables of the system are the thicknesses of the plates as indicated. The constraints are concerned to the minimum and maximum thickness, while maintaining constant the structural volume.

Response in vehicular vibroacoustic systems

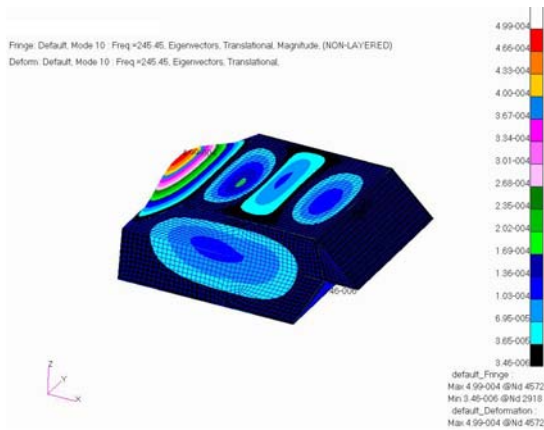


a) Structural displacement

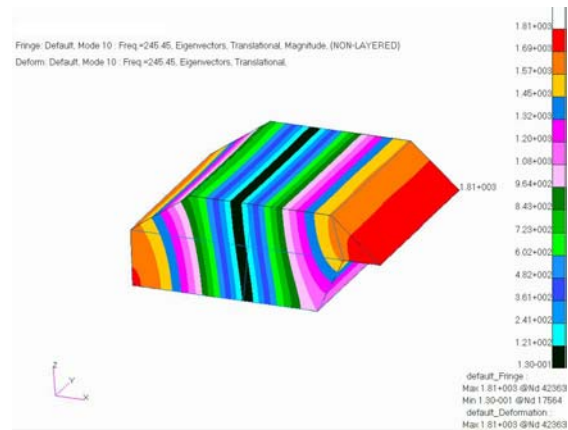


b) Fringes of fluid pressure

Mode 9: natural frequency 230.25 Hz

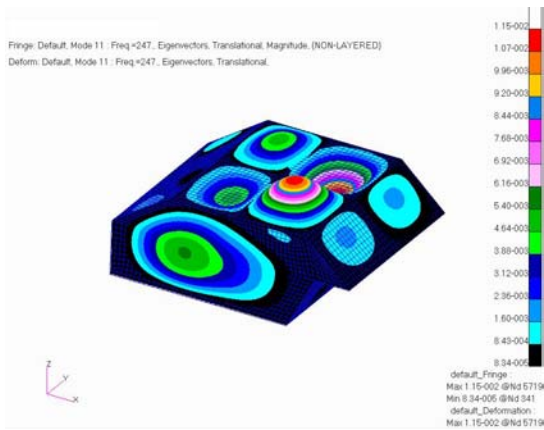


a) Structural displacement

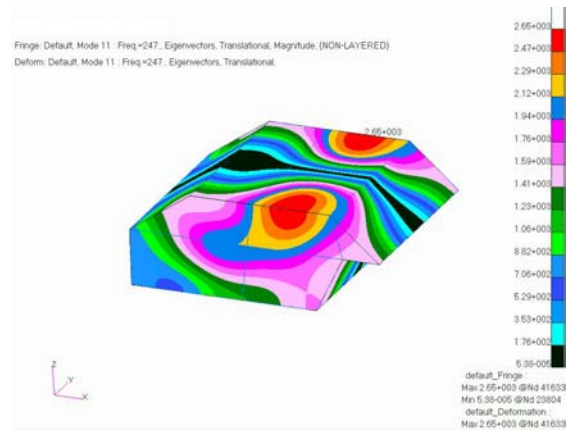


b) Fringes of fluid pressure

Mode 10: natural frequency 245.45 Hz



a) Structural displacement



b) Fringes of fluid pressure

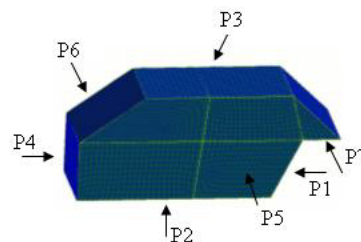
Mode 11: natural frequency 247 Hz

Figure 3 - Coupled modes of the cabin model before the optimization

Table 3 - Variables resulting from optimization of the response

Variável	Initial thickness (m)	Boundaries (m)		Optimized thickness (m)
P1	0,005	0.0040	0.016	0,00466
P2	0,007	0.0035	0.014	0,00732
P3	0,004	0.0025	0.010	0,0027
P4	0,006	0.0030	0.012	0,00691
P5	0,008	0.0020	0.008	0,00728
P6	0,005	0.0020	0.008	0,006028
P7	0,004	0.0025	0.010	0,00312

Variable	Rear P1	Floor P2	Cabin ceiling P3	Front P4	Doors P5	Windows (glass) P6	Ceiling rear trunk P7
----------	---------	----------	------------------	----------	----------	--------------------	-----------------------



The red curve of the non optimized frequency response has appreciably higher values between 20 and 200 Hz, as shown in Fig. 4, for the fluid pressure p of node 10436, allowing us to have a tool to control the response of a given region, according to needs.

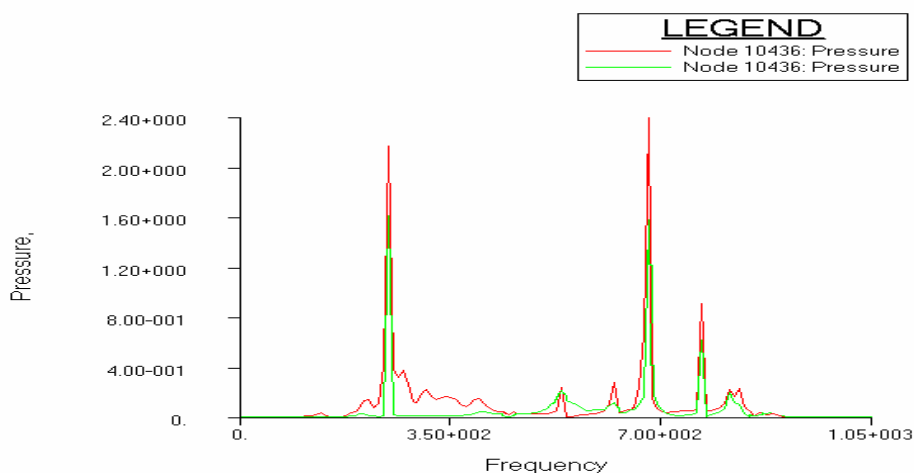


Figure 4 – Frequency response function before and after optimization

CONCLUSIONS

In general, the pressure fringes in the fluid follow the shape of the structural displacements or vice versa. With this observation and considering the values of the uncoupled and coupled frequencies we can define if the fluid or the structure predominates in the coupled mode.

For the case of the vibroacoustic reduced vehicle cabin, and for the analyzed conditions, the frequency response decreases considerably in the range of 20 to 200 Hz for the fluid pressure of the node 10436.

REFERENCES

Blevins, R.D., 1995, “Formulas for Natural Frequency and Mode Shape”, Krieger Publishing Company.
 De Mello, R., 2003, “Análise da Sensibilidade do Campo Acústico Veicular à Excitação do Sistema de Transmissão”, Dissertação de Mestrado em Engenharia Mecânica, Universidade Federal de Santa Catarina, Florianópolis – SC, Brasil, 245 p.
 Msc.Software, 1996, “NAS115 Fluid-Structure Analysis Using MSC.Nastran. Course Notes”, The MacNeal-Schwendler Corporation.

RESPONSIBILITY NOTICE

The authors are the only responsible for the printed material included in this paper.

Vehicle Dynamics for Response Modeling in Freight Cars

Walter Jesus Paucar Casas¹, and Carlos Henke Viganico²

¹ Universidade Federal do Rio Grande do Sul, Departamento de Engenharia Mecânica, Rua Sarmento Leite 425, Bairro Cidade Baixa, Porto Alegre - RS, CEP 90050-170, Brazil

² Randon Implementos, Av. Abramo Randon 770, Bairro Interlagos, Caxias do Sul - RS, CEP 95055-010, Brazil

Abstract: The dynamics of freight vehicles involves basically two types: the longitudinal impacts and the vibrations originated by the trail. Severe vibrations can shake or move the load from its initial position, increasing the damage because of the contact wheel-rail and originating instability in the forces relations between the wheel and the rail, which can cause unbalance of the vehicle as well as its derailment. To evaluate the dynamics of freight vehicles, a multibody model of a box-type vehicle is developed. The equations of motion were derived using Lagrange's equations and exposed in the form of state equations. Some coupled accelerations are resolved through Gauss-Jordan's method. All of the accelerations are then integrated numerically with the technique of Runge-Kutta to obtain new speeds and displacements, which are used for evaluating the accelerations for the next time. This process is repeated for each time step and new values are calculated using the previous ones. The proposed Program for Dynamic Analysis of Freight Vehicles is compared and validated with another program of the literature in the mode of Pitch and Bounce, showing a good agreement of results.

Keywords: *multibody dynamics, freight car, railway dynamics, response analysis*

INTRODUCTION

Accidents, load loss and damages to the environment in the rail transport have been a serious problem along the years. In Brazil, considering the ANTT (2010) data, the number of accidents for millions of trains by kilometer (train-kilometer - measure unit that represents the movement of a train, through one kilometer) has been decreasing. However when we compared these data with other countries, such as the United States that it shows similar territorial extension with Brazil, we observed that the index of accidents is still very large.

More and more the attempts to identify the reasons and to solve the problems of accidents have been goals of research. The dynamics of the vehicle and its load contributed significantly for railway accidents.

The multibody system dynamics can be used for the development and solution of the nonlinear equations that govern the complex movement of the components of freight vehicles, which can suffer displacements and rotations.

The wheel-rail interaction is an important element in freight vehicles, described in terms of contact forces as well as other kinematic and dynamic variables, associated with the hunting phenomena, which is the origin for the lateral oscillation and yaw angles that contribute to the instability of the vehicle, particularly in certain operation speeds. The algorithms of multibody systems can also be used for studies of derailment sceneries and development of derailment criterions (Shabana et al., 2007).

The objective of this work is to develop a multibody model of a freight vehicle for realizing dynamic simulations in any box vehicle. The specific objectives of the work are:

- To compare the developed mathematical model with the IIT one, which was previously validated with some test data.
- To analyze the vehicle behavior through the performance criteria evaluation using the most important dynamic cases of operation described in the norm of the AAR (Association of American Railroads), with emphasis in the regimes of hunting, twist and roll, pitch and bounce, yaw and sway.

Among the main works used in this case we highlight the study of Wiebe (1974) for the characterization of the damping of the trucks and the development of the dynamic model. Another essential study was the model of Willis and Shum (1977), which served as basis for the modeling and for the evaluation of several operation situations.

The studies of nonlinear friction in rail trucks developed by Harder (2000) were used to define the model of friction in the trucks of this work.

The theory of Nadal (1908), used to foresee the derailment phenomenon, is an important parameter of performance evaluation used massively in the rail literature and also in this work.

The derailment ways, which were characterized in a simple form by Ehrenbeck and Polcari (1984), allow to understand the nature and conditions for dangerous situations, which were appraised in this work.

As reference for studies of performance evaluation, the AAR (2007) supplies a complete sequence of conditions and parameters for simulations that represent real operation conditions, which will be adopted for performance evaluation of the developed model.

VEHICLE CHARACTERIZATION

The model will be based on the type of vehicle and trucks more used in the Brazilian railroads. Most of the products transported in the railroads are made inside of closed vehicles, (ANTT, 2010). Based on these observations, a boxcar vehicle with a truck of three pieces is chosen for the base of the model. The dynamic environment of these vehicles can be considered as representative of the operations found in the rail transport.

After the selection of the vehicle and truck, the other components of the system should be identified and their characteristics determined. Initially the vehicle is considered as a system with five masses, linear springs and dampers, and nonlinear effects associated with the solid length of the springs, gaps, among others. The developed program receives the name of PADVF (Program for Dynamic Analysis of Freight Vehicles), to simplify its meaning and usage in this work.

For mathematical modeling of the vehicle, a nonlinear model with 24 degrees of freedom was developed. It simulates a boxcar vehicle of 70 ton with five connected masses by springs and dampers. The five masses represent: the vehicle body, the front and rear bolsters, and the front and rear trucks (both sideframes and wheels). The degrees of freedom modeled for the different masses are defined in Table 1.

Table 1 – Degrees of freedom of the model

Mass	Degree of freedom translational			Degree of freedom rotational		
	Vertical	Lateral	Longitudinal	Sway	Pitch	Roll
Vehicle (m_1)	z_1	x_1	y_1	α_1	ϕ_1	ψ_1
Bolster (m_2)	z_2			α_2	ϕ_2	ψ_2
Bolster (m_3)	z_3			α_3	ϕ_3	ψ_3
Truck (m_4)	z_4	x_4		α_4	ϕ_4	ψ_4
Truck (m_5)	z_5	x_5		α_5	ϕ_5	ψ_5

Figure 1 shows the configuration of springs and dampers of the freight vehicle model in study.

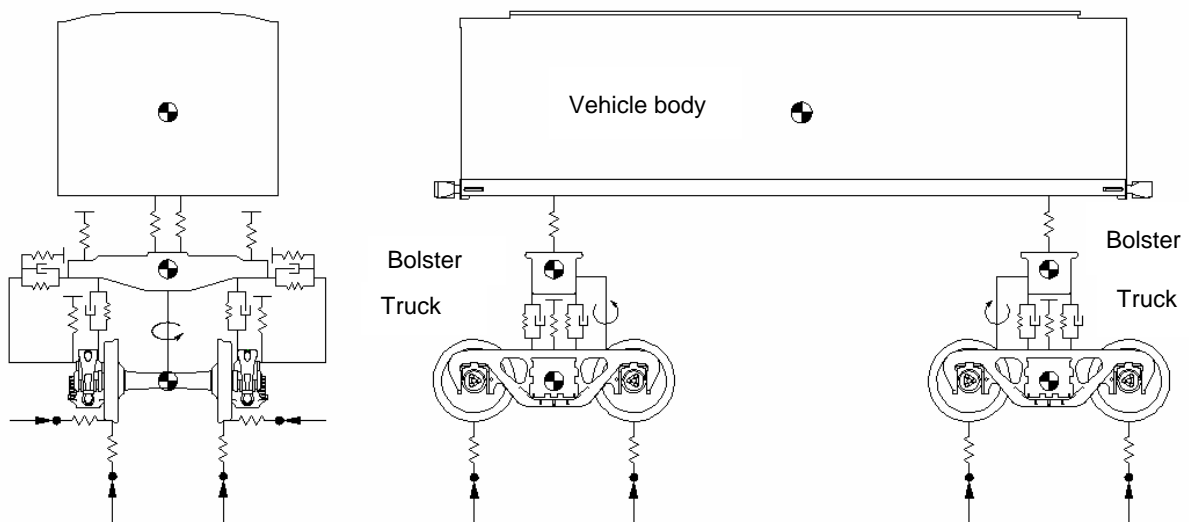


Figure 1 - Model of a freight vehicle

Figure 2 shows the characteristics and dimensions for freight vehicles of 70 and 100 t and their corresponding mechanical components. The mass values, moment of inertia and dimensions of the vehicles in study are presented in Table 2 and Table 3, where the stiffness characteristics are supplied for the elements used in the modeling of the truck.

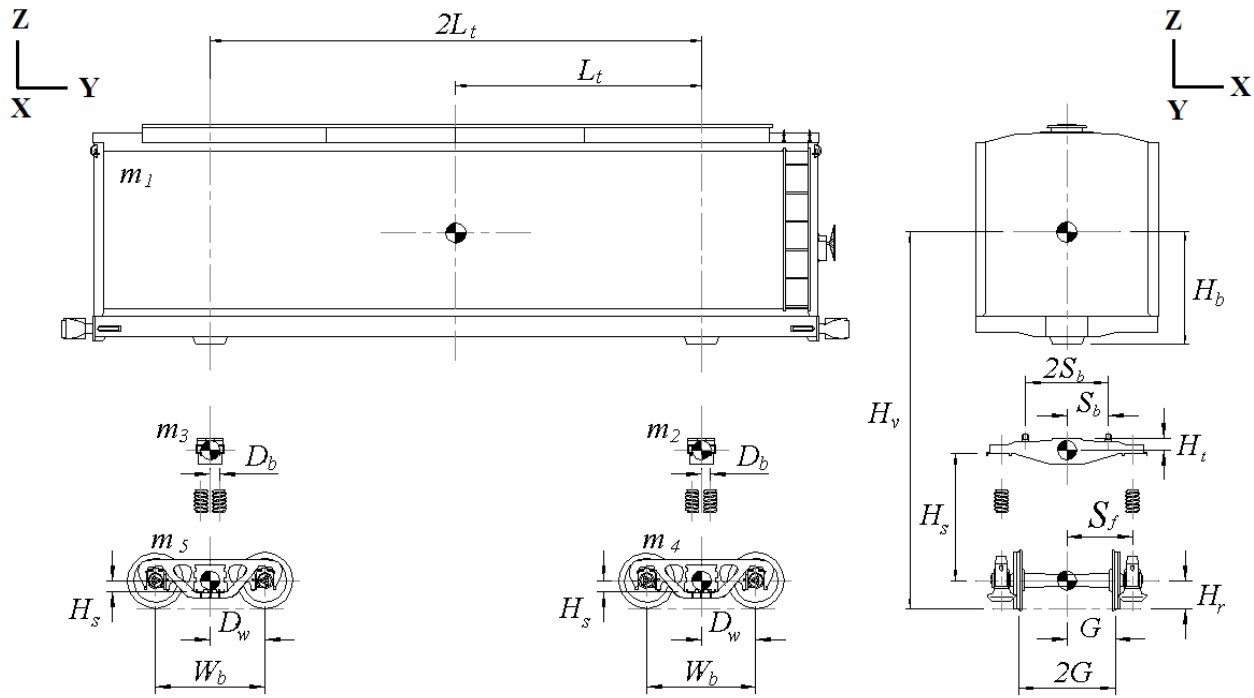


Figure 2 – Characteristics and dimensions of a freight vehicle type *Boxcar*

Table 2 – Input data: mass and mass moment of inertia

Description	Symbol	<i>Boxcar</i> 70 t		<i>Boxcar</i> 100 t	
		Empty	Loaded	Empty	Loaded
Total vehicle mass	m_t	21466 kg (47323 lb)	101106 kg (222900 lb)	29000 kg (63934 lb)	137806 kg (303810 lb)
Body vehicle mass	m_1	13800 kg (30423 lbs)	93440 kg (206000 lbs)	18200 kg (40124 lbs)	127006 kg (280000 lbs)
Longitudinal inertia of the body vehicle	I_{y1}	2.162E4 N m s ² (1.91E5 lbf in s ²)	1.456E5 N m s ² (1.29E6 lbf in s ²)	3.120E4 N m s ² (2.760E5 lbf in s ²)	2.485E5 N m s ² (2.20E6 lbf in s ²)
Lateral inertia of the body vehicle	I_{x1}	2.721E5 N m s ² (2.41E6 lbf in s ²)	1.881E6 N m s ² (1.66E7 lbf in s ²)	2.910E5 N m s ² (2.580E6 lbf in s ²)	3.254E6 N m s ² (2.88E7 lbf in s ²)
Vertical inertia of the body vehicle	I_{z1}	2.746E5 N m s ² (2.43E6 lbf in s ²)	1.855E6 N m s ² (1.64E7 lbf in s ²)	2.840E5 N m s ² (2.52E6 lbf in s ²)	3.175E6 N m s ² (2.81E7 lbf in s ²)
Truck bolster mass	m_2, m_3	522 kg (1150 lbs)		690 kg (1520 lbs)	
Longitudinal inertia of the bolster	$I_{y2,3}$	1.356E3 N m s ² (1.20E4 lbf in s ²)		1.491E3 N m s ² (1.320E4 lbf in s ²)	
Lateral inertia of the bolster	$I_{x2,3}$	298 N m s ² (2640 lbf in s ²)		316 N m s ² (2800 lbf in s ²)	
Vertical inertia of the bolster	$I_{z2,3}$	1.356E3 N m s ² (1.20E4 lbf in s ²)		1.491E3 N m s ² (1.320E4 lbf in s ²)	
Sideframe and wheels masses	m_4, m_5	3311 kg (7300 lbs)		4710 kg (10385 lbs)	
Longitudinal inertia of the truck	$I_{y4,5}$	2169 N m s ² (1.92E4 lbf in s ²)		2.603E3 N m s ² (2.304E4 lbf in s ²)	
Lateral inertia of the truck	$I_{x4,5}$	1.356E6 N m s ² (1.20E5 lbf in s ²)		1.627E4 N m s ² (1.440E5 lbf in s ²)	
Vertical inertia of the truck	$I_{z4,5}$	1.356E6 N m s ² (1.20E5 lbf in s ²)		1.627E4 N m s ² (1.440E5 lbf in s ²)	

Table 3 – Input data: springs stiffness

Description	Variable	Boxcar 70 t	Boxcar 100 t
Stiffness of the front center plate	K_1, K_2	1.166E8 N/m (6.66E5 lbf/in)	1.166E8 N/m (6.66E5 lbf/in)
Stiffness of the rear center plate	K_7, K_8	1.166E8 N/m (6.66E5 lbf/in)	1.166E8 N/m (6.66E5 lbf/in)
Stiffness of the front side bearing	K_5, K_6	1.166E8 N/m (6.66E5 lbf/in)	1.166E8 N/m (6.66E5 lbf/in)
Stiffness of the rear side bearing	K_{11}, K_{12}	1.166E8 N/m (6.66E5 lbf/in)	1.166E8 N/m (6.66E5 lbf/in)
Stiffness of the vertical springs of the front truck	K_{13}, K_{14} K_{15}, K_{16}	1.824E6 N/m (1.042E4 lbf/in)	2.31E6 N/m (13194 lbf/in)
Stiffness of the vertical springs of the rear truck	K_{17}, K_{18} K_{19}, K_{20}	1.824E6 N/m (1.042E4 lbf/in)	2.31E6 N/m (13194 lbf/in)
Stiffness of the lateral springs of the front truck	K_{13L}, K_{14L} K_{15L}, K_{16L}	7.75E5 N/m (4425 lbf/in)	9.04E5 N/m (5161 lbf/in)
Stiffness of the lateral springs of the rear truck	K_{17L}, K_{18L} K_{19L}, K_{20L}	7.75E5 N/m (4425 lbf/in)	9.04E5 N/m (5161 lbf/in)
Vertical stiffness of the rail – front truck	K_{21}, K_{22} K_{23}, K_{24}	1.84E6 N/m (1.05E5 lbf/in)	1.84E6 N/m (1.05E5 lbf/in)
Vertical stiffness of the rail – rear truck	K_{25}, K_{26} K_{27}, K_{28}	1.84E6 N/m (1.05E5 lbf/in)	1.84E6 N/m (1.05E5 lbf/in)
Lateral stiffness of the rail – front truck	K_{21L}, K_{22L} K_{23L}, K_{24L}	1.226E7 N/m (7.00E4 lbf/in)	1.226E7 N/m (7.00E4 lbf/in)
Lateral stiffness of the rail – rear truck	K_{25L}, K_{26L} K_{27L}, K_{28L}	1.226E7 N/m (7.00E4 lbf/in)	1.226E7 N/m (7.00E4 lbf/in)
Stiffness of solid length of the group of springs	K_{BOM}	1.166E8 N/m (6.66E5 lbf/in)	1.166E8 N/m (6.66E5 lbf/in)
Contact stiffness between bolster and truck sideframe	K_{GIB}	1.166E8 N/m (6.66E5 lbf/in)	1.166E8 N/m (6.66E5 lbf/in)
Solid length of the spring	T_L	9.37E-2 m (3.69 in)	1.016E-1 m (4.0 in)
Torsional stiffness between bolster and truck	K_{T24}, K_{T35}	2.993E7 N/rad (6.73E6 lbf/rad)	4.294E7 N/rad (9.654E6 lbf/rad)
Pitch stiffness between bolster and truck	K_{P24}, K_{P35}	1.868E7 N/rad (4.20E6 lbf/rad)	2.680E7 N/rad (6.03E6 lbf/rad)

COMPUTATIONAL MODELING

For dynamic simulation of the model, an iterative methodology was developed. The variations of the surface of the rails are the source of excitation. An excitement is applied to the model and the resultant accelerations are computed. Some coupled accelerations are resolved with a subroutine that calculates them through Gauss-Jordan's method. All of the accelerations are then integrated numerically with the technique of Runge-Kutta in the form of state equations to obtain speeds and displacements in the center of gravity of the different masses of the model. These new speeds and displacements are used for evaluating the accelerations of the next time. This process is repeated for each time step and new values are calculated using the previous ones.

The computational model developed to solve the equations and to simulate the dynamic responses of the system consists of a main program and eleven subroutines, as shown in Figure 3.

The program MAIN works as a coordinator of subroutines. It calls the subroutines ACEL and RK to obtain values of acceleration, speeds and displacements in the center of gravity of the different masses of the model.

The subroutine ACEL evaluates some coupled accelerations that appear in the state equations and they will be considered as constants for each time step. The subroutines YEXCIT and ZEXCIT supply the rails input. Sixteen variables of coupled acceleration (originated from the rotational coordinates) are grouped in five matrices, which are resolved with the method of Gauss-Jordan and then these accelerations are returned to the program MAIN.

The subroutine RK is a program developed in accordance with the requirements of numerical integration of the model. This work uses the function ode45, available in MATLAB, based in the Runge-Kutta method of fourth order.

The subroutine GAPCAL calculates the vertical reaction in the side bearings of the bolster. The subroutine WHEELCAL calculates the load on the wheels and the lateral reaction of the truck bolster. The subroutine PLATECAL calculates the vertical reactions of the rear and front center plates. The subroutine GROUPCAL calculates the compression force and displacement of the group of springs of the truck.

The subroutine SPRINGCAL provides important information concerning to the load and displacements in all spring elements. This subroutine is used to determine the L/V value of the wheels, essential for predicting the phenomenon of rising of the wheels, which under severe conditions can cause derailment.

The subroutine MILATCAL is used to calculate the lateral acceleration of the vehicle body. The subroutine MIVERTCAL is used to calculate the vertical acceleration of the vehicle body.

The subroutine YEXCIT is used to calculate the rail input for a variation in alignment. This subroutine is used mainly to evaluate the mode of *yaw* and *sway*. The subroutine ZEXCIT is used to calculate the rail input for a variation of cross-level (vertical). This subroutine is used mainly to evaluate the modes of *twist* and *roll* and *pitch* and *bounce*.

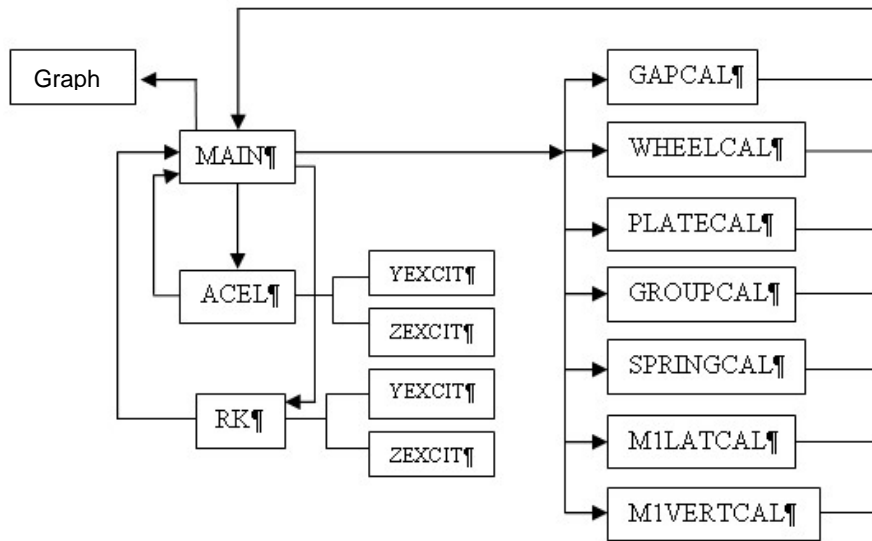


Figure 3 – Flowchart of the program PADVF

The step size for integration is evaluated with a technique based on the natural frequency of the lowest-mass of the system, in this case the bolster of the truck (Shabana et al., 2007). The natural frequency can be determined using the total stiffness of the springs group of the truck K_{RT} , and the mass of the bolster M_T ,

$$K_{RT} = 4 (7.75E5 + 1.166E8) \text{ N/m} = 4,695E8 \text{ N/m} \quad (1)$$

$$M_T = 522 \text{ kg} \quad (2)$$

and the natural frequency results:

$$f_n = \sqrt{\frac{K_{RT}}{M_T}} = 9.50 \text{ Hz} \quad (3)$$

The time period is given by:

$$\tau = \frac{1}{f_n} = 0.0015 \text{ s} \quad (4)$$

Using a practical method, it is considered that 8 iterations per response cycle is the minimum using the *Runge-Kutta*. Thus, the step size is determined as:

$$h = \frac{\tau}{8} = \frac{0.00105}{8} = 0.00013 \text{ s} \quad (5)$$

PERIODIC IRREGULARITIES

The periodic components observed in the measure of the vertical spectra are originated by the joints of the rails, which are subjected to batters at rail ends. The ends of each rail segment are hit and driven down by the impact forces that occur at the joints. For staggered joints as shown in Figure 4, the form of each rail can be approximate by a rectified sinusoidal wave (RSW):

$$z_d = S|\text{sen}(u)| \tag{6}$$

$$z_e = S\left|\text{sen}\left(u - \frac{\pi}{2}\right)\right| \tag{7}$$

$$u = \Omega x / 2 \tag{8}$$

$$\Omega = 2\pi / L_R \tag{9}$$

where:

S : amplitude of RSW, m;

L_R : length of the rails, m;

x : distance along the track, m;

Ω : wave number, rad/m;

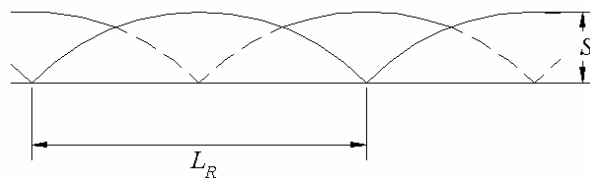


Figure 4 – Vertical periodic irregularities of the right and left rails

MODEL VALIDATION

In this work, the mathematical model of the freight vehicle (PADVF) will be validated following two developed models, tested experimentally and already used. The first model is of the Stucki Company (Wiebe, 1974), which was developed to study the requirements of damping for the control of vertical movements and the *roll angle* of freight cars.

The second model was developed by Willis and Shum (1977). It consists of a nonlinear mathematical model which includes coupling load elements, the vehicle body, truck movements and characteristics of the track. This model, known as model IIT, was correlated with test data from AAR.

The comparison between the validated models and the proposed one (PADVF) is characterized by the presentation of the basic characteristics, similarities and differences among the models, according to Table 4.

Table 4 Models comparison

Parameter	Model Stucki	Model IIT	Model PADVF
Degrees of free	20	27	24
Objective	Vehicle's <i>Roll</i> and <i>Bounce</i>	Dynamics of the load element	Dynamics of the vehicle and trucks
Vehicle body	1 mass	1 mass	1 mass
Damping model	Friction and viscous	Friction and viscous	Equivalent viscous
Allowed track input	Vertical	Vertical, Lateral	Vertical, Lateral
Vehicle type	<i>Hopper</i> – 100 ton	<i>Boxcar</i> – 70 ton	<i>Boxcar</i> – 70 ton / 100 ton
Distance between center of trucks	13.7 m (45 ft)	11.9 m (39 ft)	12.04 m (39.5 ft) / 14.02 m (46.0 ft)
Critical velocity <i>Twist</i>	24.1 km/h (15 mph)	28.1 km/h (17.5 mph)	28.0 km/h (17.4 mph) / 23.0 km/h (14.3 mph)

The models Stucki and IIT were developed in the USA, and they are based in the English system of units, then the graphs of this validation remain with these units in their ordinates. The track gauge considered in the simulations is the American standard of 1.435 m (56.5 in). The graphs in the model PADVF follow these references.

Validation for *Pitch and Bounce* – Model IIT x Model PADVF

The comparison considers both vehicles of the type Boxcar with 70 ton and other characteristics shown in Table 4. The simulations are performed considering the rail joints in phase and with the vehicle riding on two *Bumps* (protrusions) with amplitude of 38.1 mm (1.5 in) and continuing on a flat track, as shown in Figure 5. The vehicle speed for the simulation is 96.4 km/h (60 mph).

The items evaluated in the comparison of models for the regime of *Pitch* and *Bounce* are:

- (a) Vertical reaction at the front center plate – Figure 6.
- (b) Compression of the group of springs in the front truck, right side – Figure 7.
- (c) Vertical reaction at the rear center plate – Figure 8.
- (d) Compression of the group of springs in the rear truck, right side – Figure 9.

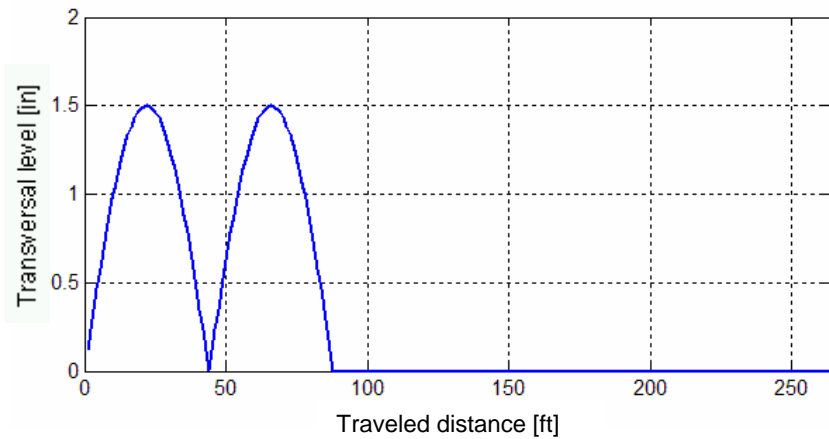


Figure 5 – Variation of transversal level of the track for *Pitch* and *Bounce*

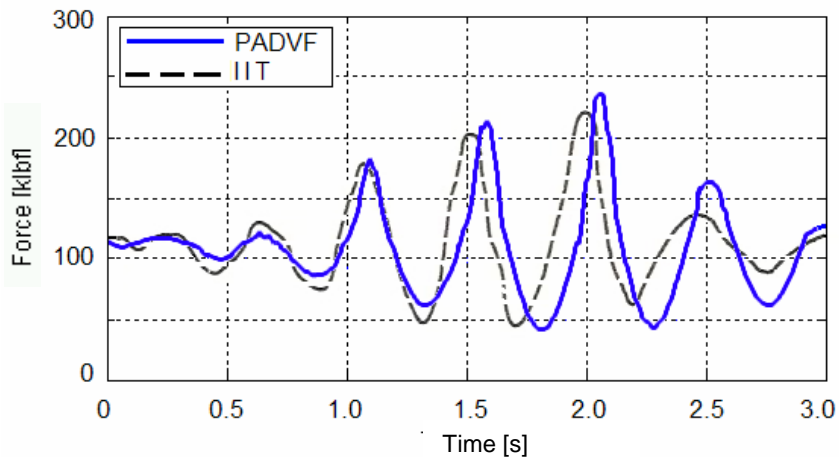


Figure 6 – Vertical reaction at the front center plate: Model IIT x Model PADVF

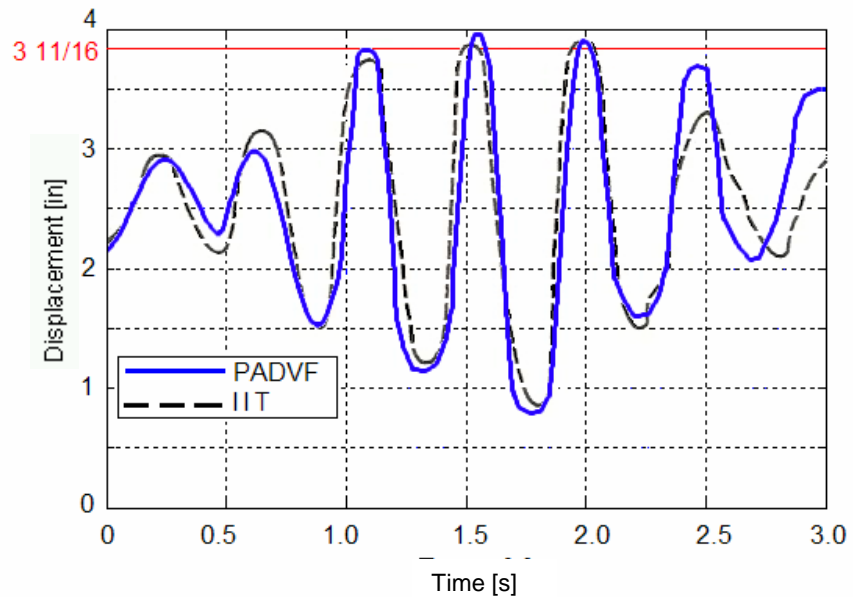


Figure 7 - Compression of the group of springs in the front truck , right side: Model IIT x Model PADVF

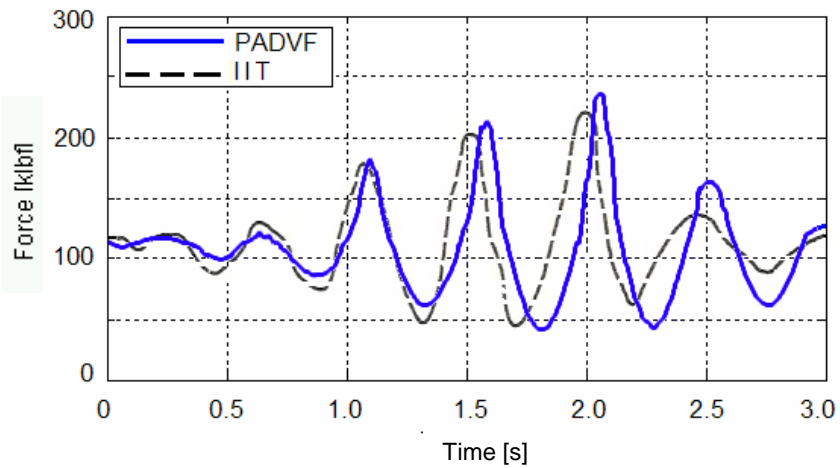


Figure 8 - Vertical reaction at the rear center plate: Model IIT x Model PADVF

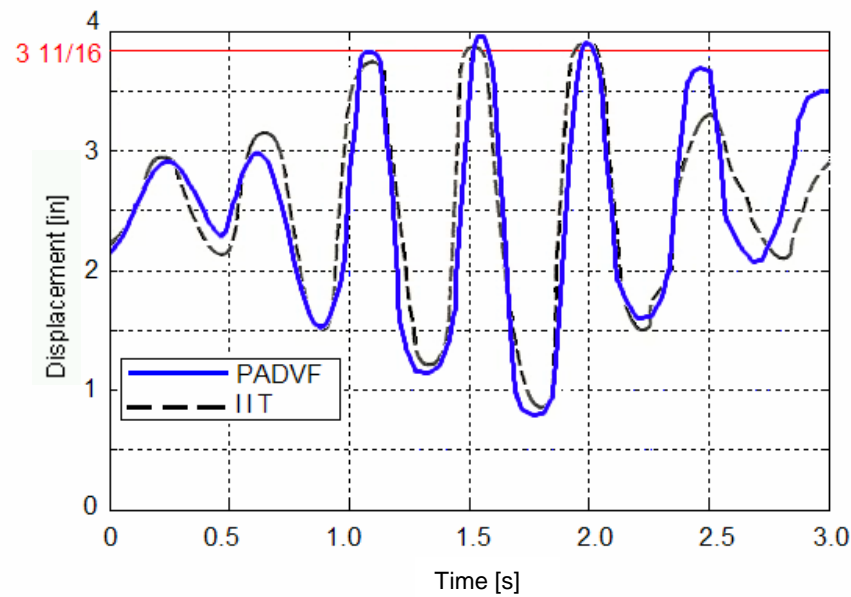


Figure 9 - Compression of the group of springs in the rear truck, right side: Model IIT x Model PADVF

The most important results of the simulations represented above are summarized and presented in Table 5.

Table 5 – Comparison between models IIT and PADVF for *Pitch* and *Bounce*

Parameter	Model IIT	Model PADVF	Diference
Maximum load at the front center plate	217 klbf	229.4 klbf	5.7 %
Maximum load at the rear center plate	205 klbf	204 klbf	0.5 %
Number of cycles of simulation	6	6	0 %
Number of compressions at springs of the front truck	2	2	0 %
Number of compressions at springs of the rear truck	2	2	0 %
Interval between compression of springs – front truck	0.47 s	0.45 s	4.3 %
Interval between compression of springs – rear truck	0.47 s	0.45 s	4.3 %

CONCLUSIONS

The comparison between the models of freight cars IIT and PADVF was carried out with vehicles of similar characteristics and showed good agreement. Both vehicles are of the type *Boxcar* of 70 t and the distance between centers of trucks is close to the rail length, i.e., close to the wavelength of the track.

The simulation for *Pitch* and *Bounce* due to the trail input showed load results amplified at the center plate (1020.4 kN - 229.4 klbf at the front center plate), corresponding to a difference between models equal to 5.7%.

The displacement of the springs group reached the solid length of the springs (93 6 mm - 3 11/16 in) in both models, a phenomenon that occurs in situations of *Bounce*.

REFERENCES

- AAR, 2007, “Chapter XI Section C Part II”, Washington D.C, USA.
- ANTT, 2010, “Evolução do transporte ferroviário”, Available in: www.antt.gov.br/concessaofer/EvolucaoFerroviaria.pdf. Access in 07/20/2010.
- Ehrenbeck, R., and Polcari, S., 1984, “Vehicle/Track Interaction Assessment Techniques”, U.S. Department of Transportation, Report N° DOT/FRA/ORD-84/01.2.
- Harder, R. F., 2000, “Dynamic Modeling and Simulation of Three-Piece North American Freight Vehicle Suspension with Non-Linear Frictional Behaviour Using ADAMS/Rail”, 5th ADAMS/Rail User’s Conference, Harlem, USA.
- Nadal, M. J., 1908, “Locomotives a Vapeur”, in Collection Encyclopédie Scientifique, Bibliothèque de Mécanique Appliquée et Génie, Vol.186, Paris, France.

Shabana, A. A., Zaazaa, K. E., Sugiyama, H., 2007, "Railroad Vehicle Dynamics – A Computational Approach", CRC Press, Boca Raton, Florida, USA, 360 p.

Wiebe, D., 1974, "Damping Requirements to Control Vertical and Roll Motion of Freight Cars", Rail Transportation Division, ASME Winter Annual Meeting.

RESPONSIBILITY NOTICE

The authors are the only responsible for the printed material included in this paper.

Active Control of Sound Transmission with Arrays of Smart Panels using Decentralized Velocity Feedback Control

Andre Lucchino Goldstein

Universidade Estadual de Campinas, Faculdade de Engenharia Mecânica, DMC, Rua Mendeleev, 200, Campinas, SP, Brazil

Abstract: This paper presents a theoretical investigation of the active control of sound transmission through a double panel partition consisting of a base plate (source panel) that is covered by multiple stiff panels, or tiles, which are connected to the base structure through active-passive mounts. Each active-passive mount is represented by a soft spring in parallel with an actuator that generates a control force reacting off the panels, and that is driven to cancel the velocity of the tile at a point sensor location. Assuming each tile behaves rigidly in the control bandwidth, controlling the velocity at the sensor location results in reducing the tile local volume velocity. The mathematical model of structural acoustic system is developed using a mobility matrix approach. In this work the implementation of a decentralized feedback control system to control the sound transmission through the double panel partition with multiple active-passive tiles is investigated. Each smart panel actuator/sensor pair is considered as an independent control channel implementing direct velocity feedback control. The stability of the decentralized control system is investigated using Nyquist general stability criteria for multi-channel control systems. The system is shown to be unconditionally stable for the case of ideal skyhook force actuators and collocated sensor/actuator pairs. In the case of more practical reactive force actuator, since the active mount applies forces at the tile and source panel, the sensor/actuator pair is not collocated and the control system is only conditionally stable. The performance of the control system is evaluated computing the sound radiated power by the tiles for the passive and active cases, when the source panel is excited by an acoustic plane wave. In addition, the maximum stable gain of the control system is d for different air cavity depth values and for the presence of porous acoustic absorbing material in the cavity. Simulation results indicate that it is possible to achieve significant attenuation of the sound transmission through the double panel partition with the decentralized velocity feedback active-tile system.

Keywords: active control, decentralized feedback, sound transmission

INTRODUCTION

Nowadays, numerous applications require lightweight partitions with high transmission loss over a broad frequency range. A common solution consists of double panel partitions that are often used in the aeronautical and aerospace industry for controlling the transmission of sound when high transmission loss is required with a relatively lightweight structure, such as aircraft fuselage walls. However, the transmission loss performance of the double panel degrades at low frequencies due to the coupling between the partition panels, around the mass-air-mass resonance of the partition, and where the sound absorption material placed in the cavity between the panels is ineffective and can even be lower than that of a single panel (Fahy and Gardonio, 2006). The poor low frequency transmission loss of double panel partitions has motivated the use of active control methods (Nelson and Elliott, 1992 and Fuller, Elliott and Nelson, 1996) aiming at increasing the low frequency transmission loss.

The active control of sound transmission through double panel partitions has attracted a lot of research. In Sas et al. (1995) acoustic actuators and microphone error sensors were placed in the air gap to cancel sound pressure. Carneal and Fuller (2004) demonstrated the use of active structural acoustic control to reduce the sound transmission through double-panels applied to noise reduction in aircraft interiors. Piezoelectric actuators were used to apply control forces to the structure and a feedforward controller minimized the radiated power sensed by microphones located in the acoustic far field. In Gardonio and Elliott (1999) the active control of sound transmission through double panels was investigated analytically considering the simultaneous use of acoustic actuators in the air gap and active vibration isolators connecting the panels.

Decentralized active control strategies have received a lot of attention in response to the scalability problems associated with centralized control strategies. Decentralized control means that inputs and outputs can be paired together such that the plant is divided into multiple independent loops that can be controlled independently. A theoretical analysis of a smart panel for the control of sound transmission was presented by Elliott et al. (2002), where a thin rectangular aluminum panel simply supported along its edges was considered with sixteen decentralized velocity feedback loops with ideal point force actuators with collocated ideal velocity sensors. Significant reductions in both the spatially averaged kinetic energy of the panel and its radiated sound power was obtained for an optimal value of feedback gain. The feedback controller in that case was unconditionally stable, allowing the implementation of

desired feedback gains. In Alujević et al. (2008,2008a) a double panel system with decentralized active damping units for the control of sound transmission was considered, where the aim was to generate active damping across the two panels so that the low frequency resonant sound transmission is reduced. It was shown that when reactive actuators are used, performance and stability of the system is limited by a feed-through effect via the mounting system or the air in the cavity.

In this work a theoretical investigation is presented on the control of sound transmission through a structure covered with lightweight stiff panels, or tiles, attached to the base structure through active-passive soft mounts, which could be implemented in practical applications using for example piezoelectric based Thunder actuators (Goldstein and Fuller, 2002). A coupled structural-acoustic model of the double panel partition based on a mobility matrix approach was used to investigate the potential performance of active-passive tile approach in the active control of sound transmission. The feasibility of using a decentralized velocity feedback control with independent single channel controllers for each tile is investigated including the sound transmission performance and stability analysis of the control system. A decentralized system would facilitate the practical implementation of a multiple tile system in a large scale application.

DOUBLE PANEL SYSTEM WITH ARRAY OF SMART PANELS

The double panel structure investigated in this work is represented in Figure 1. The base, or source, panel consists of an 800x600x2.5mm aluminum plate with Young modulus $E = 70\text{GPa}$ and density $\rho = 2700\text{kg/m}^3$, with simply supported boundary conditions. The radiating surface consists of sixteen radiating panels assumed to have free-free boundary conditions and that are not structurally coupled to each other at the panel boundaries. Each smart panel is a 200x150x3mm honeycomb plate with Young modulus $E = 15\text{GPa}$ and density $\rho = 380\text{kg/m}^3$. The base panel and the 16 radiating panels are acoustically coupled through a 120mm deep air cavity and coupled structurally through the massless elastic mounts with stiffness $k = 8000\text{N/m}$. Each radiating panel is assumed to have an ideal point velocity sensor located at its center at the same location where the elastic mount is attached. Any gaps between the panels are assumed to be sealed with a compliant gasket that does not affect the panel vibrations. The base plate is acoustically excited by a plane wave incident at elevation angle of 45° and azimuth angle of 45° and the radiating panels are assumed to be in an infinite baffle radiating into free space.

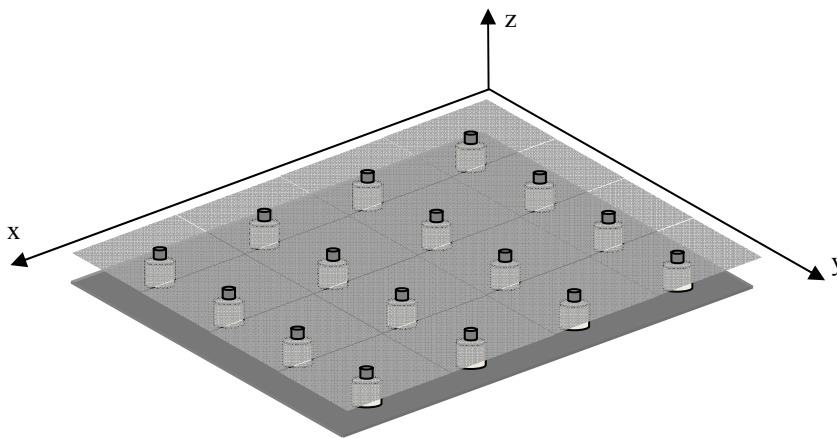


Figure 1 - Double panel system with array of 16 smart panels

Mathematical Model

The mathematical model presented next is based on a mobility matrix approach detailed for example in Fahy and Gardonio (2006). The model schematic is shown in Figure 2 where it is assumed that the system is divided into individual components, which are the source panel (base rectangular plate), the transmitting system (airborne and structural borne transmitting paths), and the radiating panels (tiles). The transmitting system consists of an airborne path, which is the air confined between the base plate and the tile, and a structural borne path, which consists of the elastic mounts connecting the base plate and the tile. The dynamics of each of these components is modeled using point and transfer mobilities or impedances.

The structural transmitting path consists of n mounts connecting the base plate and the receiving tile at a finite number of junctions. The forces and velocities transmitted at each junction are restricted in this model to the components of force and motion that are perpendicular to the surface of the system. Thus, at each element, for each frequency of excitation, the motion and forces transmitted by the structural path are given by a single complex parameter:

$$v_{mi} = \dot{u}_i \quad (1)$$

$$f_{mi} = F_{zi} \quad (2)$$

The airborne transmitting path, which is the acoustic transmission through the air confined between the base plate and the receiving tiles, is taken into account by dividing the boundary surface of the cavity with the base plate and tiles in k small elements much smaller than the acoustic wavelength. Each of these elements in the boundary surface is connected to either the base plate or to a receiving tile at the geometrical center of the element. In addition, each element is assumed to vibrate only in the direction perpendicular to the surface. Thus, at each element, the motion and forces transmitted by the acoustic path are given, for each frequency, by a single complex parameter written as:

$$v_{ai} = \dot{w}_i \quad (3)$$

$$f_{ai} = F_{zi} \quad (4)$$

The velocity and force components at the isolator mounts and at the acoustic boundary elements junctions are grouped together to form three pair of vectors: the base velocity vector and the base force vector, the transmitting system velocity vector and force vector, and the receiver velocity vector and force vector. The base velocity vector and force vector are given as:

$$v_b \equiv \begin{Bmatrix} v_{bm} \\ v_{ba} \end{Bmatrix} \quad (5)$$

$$f_b \equiv \begin{Bmatrix} f_{bm} \\ f_{ba} \end{Bmatrix} \quad (6)$$

where v_{bm}, f_{bm} are the velocities and forces at the junctions between the base plate and the elastic mounts, and f_{ba}, v_{ba} are the velocities and forces at the junctions between the base plate and the acoustic elements.

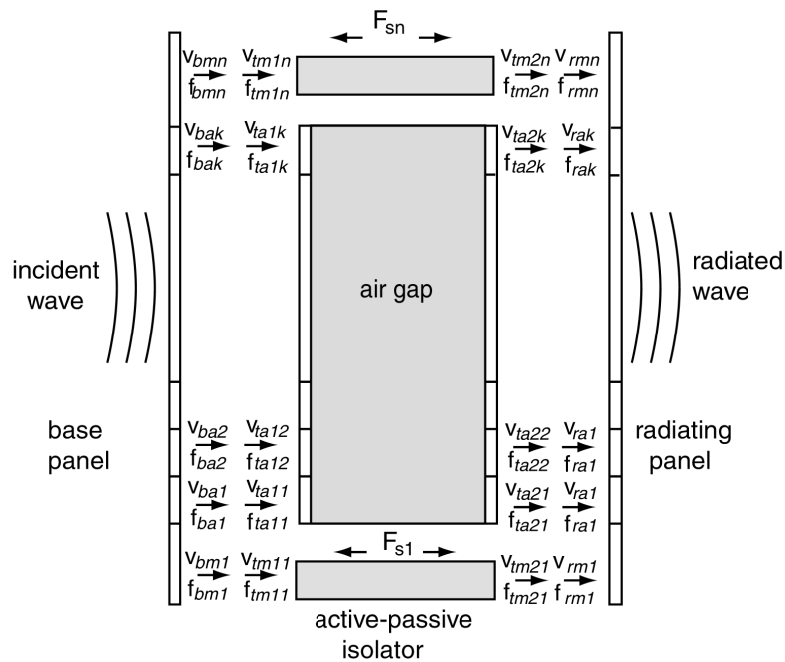


Figure 2 – Schematic of structural-acoustic model using the impedance-mobility method

The receiver velocity and force vectors are given as:

$$v_r \equiv \begin{Bmatrix} v_{rm} \\ v_{ra} \end{Bmatrix} \quad (7)$$

$$f_r \equiv \begin{Bmatrix} f_{rm} \\ f_{ra} \end{Bmatrix} \quad (8)$$

where v_{rm} and f_{rm} are the velocities and forces at the junctions between the receiver plate and the elastic mount, and v_{ra} and f_{ra} are the velocities and forces at the junctions between the receiver plate and the acoustic elements.

Finally, the transmitting system velocity and force vectors are given as:

$$v_t \equiv \begin{Bmatrix} v_{tm1} \\ v_{ta1} \\ v_{tm2} \\ v_{ta2} \end{Bmatrix} \quad (9)$$

where v_{tm1} , f_{tm1} are the velocities and forces at the junctions between the base plate and the elastic mounts, and v_{ta1} , f_{ta1} are the velocities and forces at the junctions between the base plate and the acoustic elements, v_{tm2} , f_{tm2} are the velocities and forces at the junctions between the receiver plate and the elastic mounts, and v_{ta2} , f_{ta2} are the velocities and forces at the junctions between the receiver plate and the acoustic elements.

The vector of elemental base velocities and the vector of elemental receiver velocities can be written in function of the base point and transfer mobilities and forces respectively as:

$$v_b = M_{b1}f_b + M_{b2}q_p \quad (10)$$

$$v_r = M_{r1}f_r + M_{r2}q_f \quad (11)$$

where M_{b1} and M_{b2} are mobility matrices of the base panel, M_{r1} and M_{r2} are a mobility matrices of the receiver panels, q_p is the primary excitation vector, and q_f is a flanking excitation vector.

The force vector is given by the transmitting path impedance matrix containing point and transfer for each element of the acoustic and mechanical transmission paths:

$$f_r = Z_{t1}v_t + Z_{t2}q_s \quad (12)$$

To solve for the displacement of the source and receiver plates for a given configuration of force disturbances, it is necessary to compute the mobility matrices describing the dynamics of the source and receiver plates, and the impedance matrices of the mounts and acoustic cavity. The expressions for the mobilities of the base and receiver panels and the assembly of the mobility matrices can be found in Goldstein (2006).

In addition, the mounting system dynamics is given by mount mechanical impedance. Assuming the mounts to be simple spring-dampers, the mount mechanical impedance is:

$$Z_m = c_m + k_m / i\omega \quad (13)$$

The dynamics of the acoustic cavity is described by an impedance matrix formed by point and transfer impedances between each of the finite number of elements in the base and receiver plates. These impedance functions can be derived using a modal formulation as presented in Nelson and Elliott, (1992).

The base and receiver displacement vectors can be grouped as in a single expression as:

$$v_{br} = M_{br1}f_{br} + M_{br2}Q_{pf} \quad (14)$$

Where: $M_{br1} = \begin{bmatrix} M_{b1} & 0 \\ 0 & M_{r1} \end{bmatrix}$, $M_{br2} = \begin{bmatrix} M_{b2} & 0 \\ 0 & M_{r2} \end{bmatrix}$ and $q_{pf} = \begin{bmatrix} q_p \\ q_f \end{bmatrix}$

The velocity continuity and force equilibrium conditions are given by $v_t = v_{br}$ and $f_t = -f_{br}$.

Now, using the velocity continuity and force equilibrium conditions the equation for the base and receiver velocities can be written in function of the primary disturbance and control forces as:

$$v_{br} = Q_{pv}q_{pf} + Q_{sv}q_s \quad (15)$$

Where

$$Q_{pv} = (I + M_{br1}Z_{t1})^{-1}M_{br2} \quad (16)$$

$$Q_{sv} = -(I + M_{br1}Z_{t1})^{-1} M_{br1}Z_{t2} \quad (17)$$

The total sound power radiated by the receiving panel is evaluated using the receiving panel elemental velocities multiplied by the radiation resistance matrix:

$$\Pi_r = v_r^H R v_r \quad (19)$$

Finally, if a harmonic incident plane acoustic wave is assumed to excite the base panel, the primary excitation source becomes a vector of point forces acting on the center of each acoustic element of the base panel. The force at each element due to the pressure field on the plate is given in Wang, Fuller and Dimitriadis (1991).

Decentralized Feedback Control

In the case of negative velocity feedback control, with control gain g , with control gain g , the control force is:

$$q_s = -g v_{rm} = -g S_{vm} v_{br} \quad (20)$$

Equation (6) can be rewritten as:

$$v_{br} = Q_{pv} q_{pf} + Q_{sv} (-g S_{vm} v_{br}) = (I + g S_{vm} Q_{sv})^{-1} Q_{pv} q_{pf} \quad (21)$$

The block diagram representing a decentralized feedback control system is presented in Figure 3. The $m \times m$ square plant $G(s)$ with elements g_{ij} is to be controlled using a diagonal controller $H(s)$. The plant open loop transfer functions are given by:

$$G(s)H(s) = \begin{bmatrix} g_{11}(s)h & 0 & 0 & 0 \\ 0 & g_{22}(s)h & \cdots & \vdots \\ \vdots & \vdots & \ddots & \vdots \\ 0 & 0 & \cdots & g_{mm}(s)h \end{bmatrix} \quad (22)$$

where g_{ii} are the diagonal elements of $G(s)$ and h is the feedback gain. The feedback control loop transfer function for the channel i is denoted as $L_i = g_{ii}h$ which is the i th diagonal element of the matrix $G(s)H(s)$.

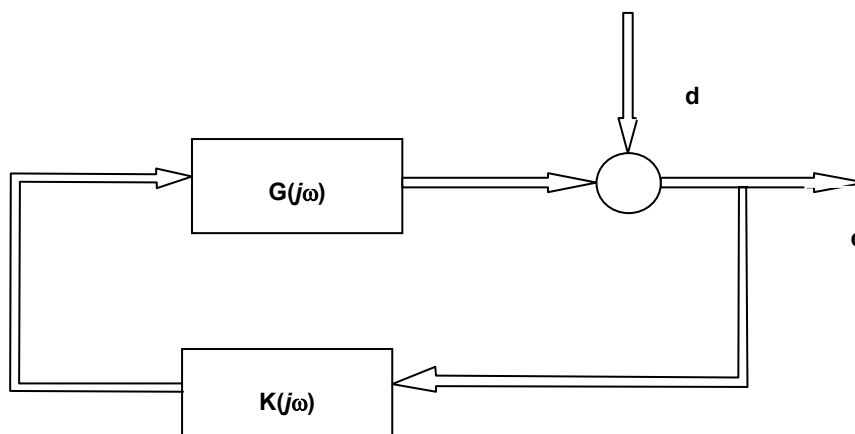


Figure 3 - Multichannel control system implementing direct velocity feedback, with plant $G(s)$ and controller $H(s)$

SIMULATION RESULTS FOR MULTIPLE SMART PANELS

The mathematical model outlined above was used to compute the plant transfer functions required to assess the stability characteristics of the control system and to evaluate the sound transmission through the double panel system in the passive and active cases. Figure 4 shows the velocity of the base panel and of the radiating panel at locations corresponding to one of the mounts, where it is possible to note a mass-air-mass resonance around 57Hz. The base panel and the radiating panels are strongly coupled until about 200Hz where it is observed that passive vibration isolation effects start to occur. Figure 5 shows the vibrating shapes of the base and radiating panels at two different frequencies.

Stability and control performance

The total response of the system to the primary and secondary (control) forces can be computed based on the plant responses and actuator signals. In the case of a single-input single-output control system, the stability of the system can be determined by Nyquist criteria plotting the frequency response function of the open loop system $G(s)H(s)$ in the complex plane. The system will be unstable for a gain that causes locus of open loop to enclose the $(-1,0)$ point. In the case of a multi-input multi-output system, the coupling between the actuators implies that it is not enough to look at the stability of each control channel. The stability of the multichannel decentralized feedback control system must be assessed using the Nyquist generalized stability criteria to plot the Nyquist loops for each of the independent control loops (Skogestad and Postlethwaite, 1996). The approach consists on performing an eigenvalue analysis of the open loop system matrix, using for example MATLAB eigenvalue analysis functions. The eigenvalues must then be sorted according to the ordering of the eigenvectors. The stability margin and maximum stable gain of the system are determined so that the locus of the largest eigenvalue does not encircle the $(-1,0)$ point. After the stability of the multi channel feedback control system is ascertained, the closed loop response at the sensor output is predicted by:

$$H(j\omega) = h\mathbf{I} \tag{23}$$

$$v_r = [\mathbf{I} + \mathbf{G}(j\omega)\mathbf{H}(j\omega)]^{-1} \mathbf{d} \tag{24}$$

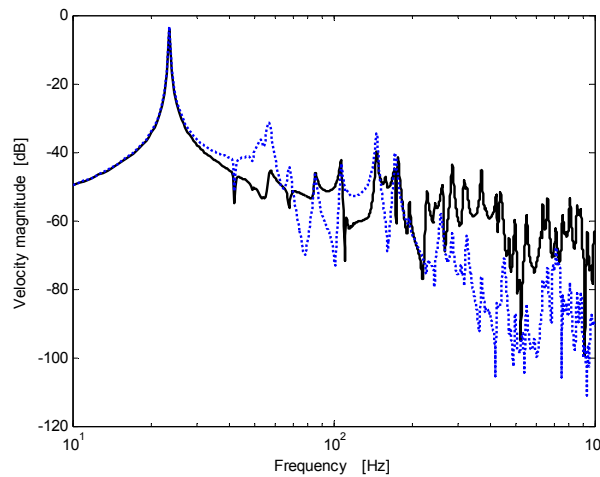


Figure 4 - Velocities of base panel and radiating panels at the mount location

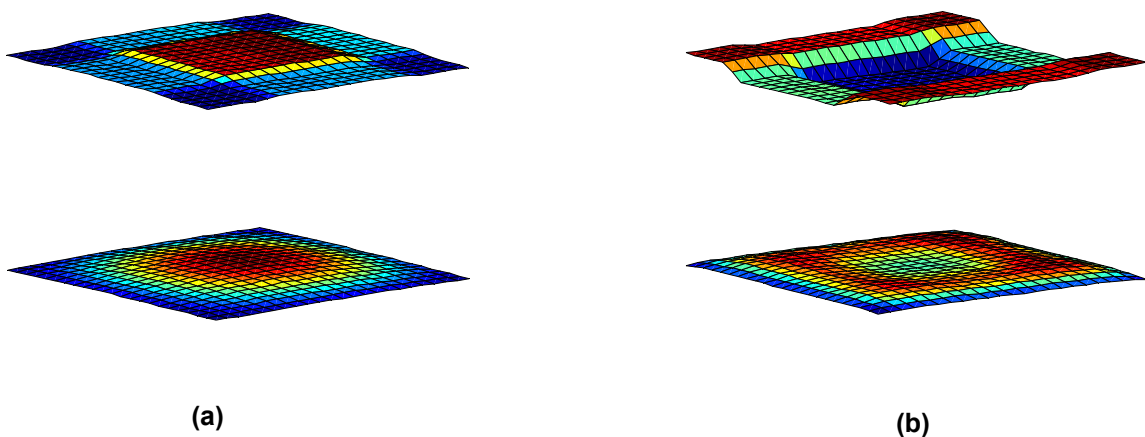


Figure 5 - Vibration shapes of the base panel and array of 16 tiles without control at (a) 25 Hz and (b) 57Hz

Sound transmission results with skyhook actuators

In this section, the performance of a 16 channels decentralized velocity feedback control system is considered assuming ideal skyhook force actuators that act only on the radiating panel. In this case the velocity sensors and force actuators are collocated and the unconditional stability of the feedback system is guaranteed (Jayachandran and Sun, 1997 and Elliott et al., 2004). The Nyquist plot of one of the eigenvalues of the open loop transfer function matrix is

shown in Figure 6 where it is observed that the loci of the plot response is never crosses the negative real axis as expected for a stable system.

The mathematical model is used to compute the sound power radiated by the tiles in the passive and active cases for increasing gain values. The simulation results for increasing values of feedback gains are shown in Figure 7. The curves show that as the increase in control gains are followed by increased active damping with decreasing response of the radiating panel at resonance frequencies. As very large gain values are reached, there is a ‘pinning’ effect at the sensor/actuator positions (Elliott et al., 2002) with large attenuations. At these gains values the radiating panel operates with new resonance frequencies and additional reductions in sound power cannot be achieved.

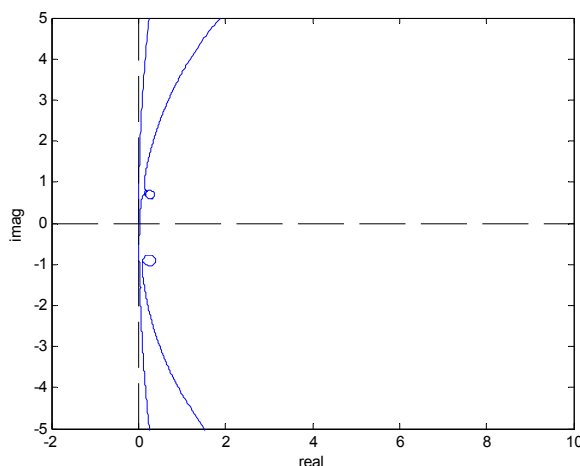


Figure 6–Nyquist plot of largest magnitude eigenvalue of 16 channel decentralized system with skyhook actuators, gain = 100

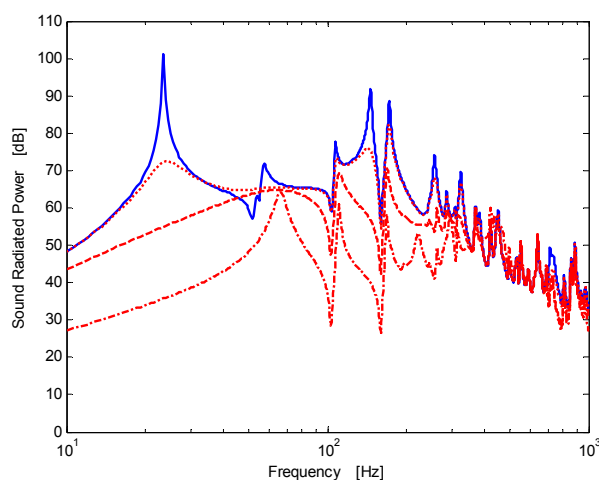


Figure 7 – Sound power of radiating tiles for 16 channel decentralized feedback control system with “skyhook” actuators– blue thick solid line: no control; red dotted line: gain=10; red dashed line: gain=100; red dashed-dotted line: gain=1000

Sound transmission results with reactive actuators

Next, the active control of sound transmission through a double panel system with 16 tiles and “reactive” force actuators is investigated. Now it is assumed that the actuators react off the base plate. In this case the velocity of each tile is a result of the collocated actuator force and a component caused by the reaction force applied to the base panel. The reaction force causes base vibrations that transmit back to the tiles structurally through the mounts and acoustically via the air cavity. In this case, the sensor and actuator are no longer collocated and the control system is no longer unconditionally stable. In order to compute the performance of the decentralized control system, the maximum stable gain has to be determined using the generalized Nyquist criteria.

The Nyquist plot of the largest magnitude eigenvalue of the open loop response matrix using forces reacting off the panels is shown in Figure 8. Note that for the system of Figure 6 with skyhook actuators the eigenvalue loci is restricted to the right side of the complex plane, while for the case of a reactive force actuator, the eigenvalue loci crosses the negative real axis limiting the maximum gain that can be applied. The maximum stable gain in this case can be

determined by observing the eigenvalue loci of the plant responses for different gain values and taking note of where it crosses the negative real axis and the distance to the (-1,0) point. Following this procedure the maximum stable gain is determined to be around $g = 150$. The sound radiated power for the double panel system with multiple tiles for different values of feedback control gain is shown in Figure 9 showing significant attenuation in the low frequency range, above the first resonance of the base panel around 25Hz and up to about 400 Hz.

It is interesting to compare the maximum stable gain for a double panel partition that has a single larger radiating panel with the same properties of tiles, to the maximum stable gain of the multiple tile system. The Nyquist plot of the largest eigenvalue of the matrix of open loop transfer functions for the case of a single large radiating panel is shown in Figure 10 for a gain of 100. When compared to Figure 8 we note that the system is unstable for the single panel case for the same gain value applied to the tiles system. This indicates that for the system studied the use of multiple tiles helps in decoupling of the control channels, which favorably improves the maximum stable gain that can be applied in the decentralized feedback control system.

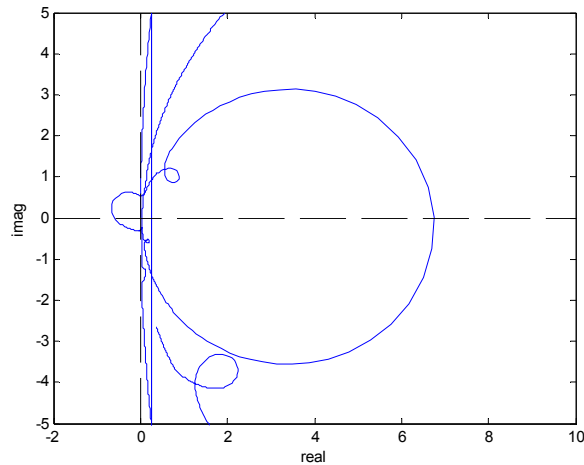


Figure 8 – Nyquist plot of the largest eigenvalue of open loop responses of a 16 channel decentralized velocity feedback control system with reactive actuators, gain = 100.

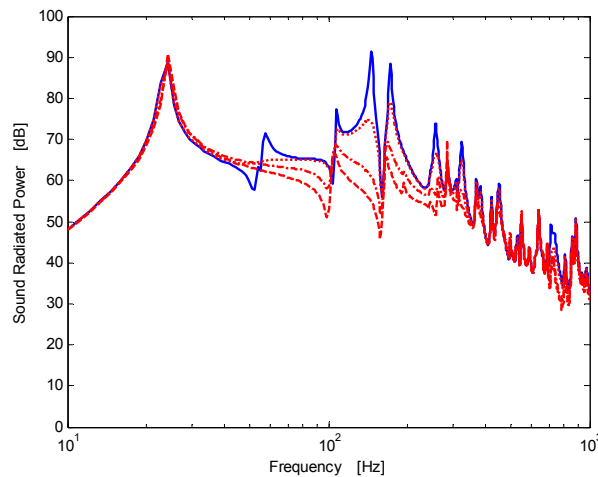


Figure 9– Sound power radiated by the 16 tiles for a 16 channels decentralized feedback control system with “reactive” force actuators– blue thick solid line: no control; red dotted line: gain=10; red dashed line: feedback gain=50; red dash-dotted line: gain=100.

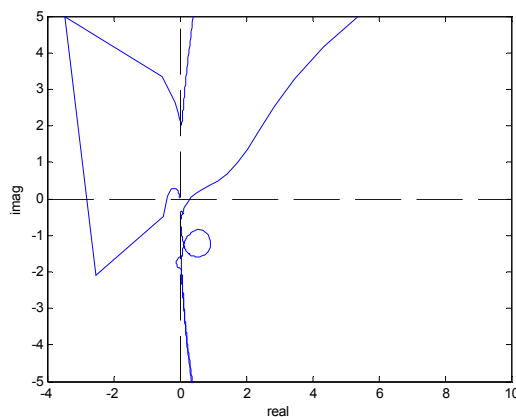


Figure 10 – Nyquist plot for double panel with a single large radiating plate and 16 channel decentralized control system with reactive force actuators and gain = 100;

Effect of the inter panel distance and damping on stability

The control channels are coupled through the off-diagonal terms of the plant matrix $G(s)$ that represent the structural acoustic coupling that occurs by the control force excitation of the source panel and air cavity. In this section the generalized Nyquist criteria is used to determine the effect on the stability margins for different air cavity configurations. First, the effect the air gap depth between the panels is investigated by computing the plant responses for different panel distances. Then it is assumed that the air cavity is filled with damping material to assess the effect of adding damping to the air cavity on the stability margins compared to the undamped case.

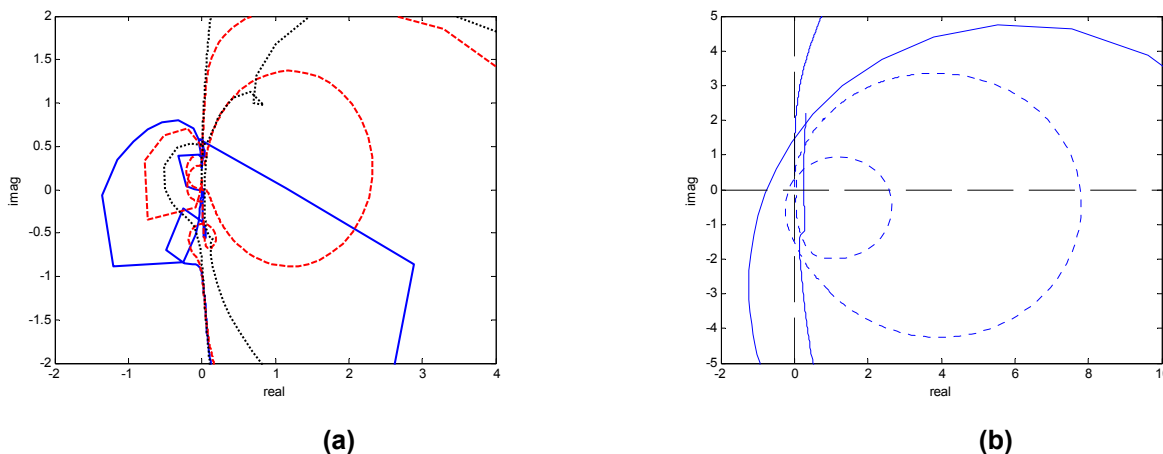


Figure 11– Nyquist plot of largest eigenvalue for different air cavity configurations - (a) different inter-panel distances, gap = 40mm (solid blue line), 80mm (red dashed line) and 120mm (black dotted line), gain = 100; (b) air cavity with damping material for gain = 100 (dashed) and gain = 500 (solid trace)

The Nyquist plot of the eigenvalues of the open loop transfer function matrix with gain of 100 and for panel distances of 40mm, 80mm and 120mm is shown in Figure 11(a). Note that the distance of the point where the eigenvalue loci crosses the negative real axis to the $(-1,0)$ point increases for larger air gap depths.

In practical applications of double panel structures the air cavity is usually filled with sound absorbing material, which can be included in the mathematical model of the system by using an equivalent fluid model that have a complex wave number and complex specific impedance (Allard and Atalla, 2009) with the expressions below. This formulation assumes that the absorption material frame remains motionless and has porosity close to 1.

$$Z^{ac}(\omega) = \rho c [1 + 0.0571X^{-0.754} - i0.087X^{-0.732}] \quad \text{and} \quad k^{ac} = \frac{\omega}{c} [1 + 0.0978X^{-0.700} - i0.189X^{-0.595}]$$

where $X = \rho f / \sigma$, ρ is the air density and σ is the material flow resistivity. Substituting the parameters of the fluid with the complex parameters above, the Nyquist plot of the plant response matrix for a 16 tiles system has been computed for a system with the cavity completely filled with porous material as shown in Figure 11 (b) for two different gain values. The results indicate that the system with acoustic damping material in the air cavity allows for higher maximum stable gains than maximum gains obtained in the undamped air cavity case with a Nyquist plot shown in Figure 8.

Conclusion

In this work the control of sound transmission through a double panel system using an array of active tiles with independent velocity feedback control loops was investigated. A mathematical model based on a mobility matrix approach was presented and used to simulate the structural-acoustic response of an acoustically excited double panel system with a simply supported source panel and 16 tiles connected to the source panel with elastic mounts. The model was used to compute the sensor/actuator pair transfer-functions, the actuator control signals and the total system response to both the control and disturbance excitations. The control system performance was assessed by comparing the sound power radiated by the tiles in the passive and active cases, for different gain values. It was seen that for the case that assumes ideal skyhook forces and collocated sensor actuator pairs, the system is unconditionally stable and the sound power radiated showed large reductions in sound transmission. In the case of more practical control actuator implementation that generates forces reacting off the panels, the sensor-actuator is no longer collocated and the system was shown to be conditionally stable. The stability margins and maximum stable gains were determined using the generalized Nyquist criteria based on the loci of the eigenvalues of the open loop response matrix. The sound radiated power was computed up to the maximum stable gain value showing that significant attenuation can be obtained in the low frequency range. Additional simulations showed the effect of different the air cavity configurations on the stability margin of the system. The stability margin of the system was shown to increase for larger plate separation distance and simulation results indicated that the use of acoustic absorption porous material in the gap helps to reduce the coupling of control channels through the air cavity, improving the stability margins and allowing for higher control gain.

ACKNOWLEDGMENTS

The authors are grateful to the government funding agency Fundação de Amparo à Pesquisa de São Paulo, FAPESP.

REFERENCES

- Allard, J.F. and Atalla, N., 2009, "Propagation of Sound in Porous Media", John Willey & Sons.
- Alujević, N., Gardonio P., Frampton K.D, 1998, "Smart Double Panel with Decentralized Active Damping Units for the Control of Sound Transmission", *The American Institute of Aeronautics and Astronautics Journal*. 46(6), 1463-1475
- Alujević, N., Frampton K.D., Gardonio P., 2008a, "Stability and Performance of a Smart Double Panel with Decentralized Active Dampers", *The American Institute of Aeronautics and Astronautics Journal*. 46(7), 1747-1756.
- Carneal, J.P. and Fuller, C.R., 2004, "An Analytical and Experimental Investigation of Active Structural Acoustic Control of Noise Transmission through Double Panel Systems", *Journal of Sound and Vibration*, 272, 749–771.
- Elliott, S.J. Gardonio P., Sors, T.C and Brennan, M.J., 2002, "Active Vibroacoustic Control with Multiple Local Feedback Loops", *The Journal of Acoustical Society of America* 111(2), 908-915.
- Elliott, S.J., Benassi, L., Brennan, M.J., Gardonio, P. and Huang, X., 2004, "Mobility Analysis of Active Isolation Systems", *Journal of sound and Vibration*, 271, pp. 297-321.
- Fahy, F.J. and Gardonio, P., 2006, *Sound and Structural Vibration*, Elsevier, London.
- Fuller, C.R, Elliott, S.J. and Nelson, P.A, 1996, *Active Control of Vibration*, Academic Press. London.
- Gardonio, P. and Elliott, S.J, 1999, "Active Control of Structure-Borne and Airborne Sound Transmission through Double Panel". *Journal of Aircraft*, 36 (6), 1023–1032.
- Goldstein, A.L., "Control of Sound Transmission with Active-Passive Tiles", 2006, Ph.D. Dissertation, Virginia Polytechnic Institute and State University, Blacksburg, VA, USA.
- Goldstein, A.L, Fuller, C.R, 2002, "Control of Sound Transmission with Active-Passive Tiles", *Proceedings of ACTIVE*, Southampton, United Kingdom
- Jayachandran, V. and Sun, J.Q, 1997, "Unconditional Stability Domains of Structural Control Systems Using Dual Actuator-Sensor Pairs", *Journal of Sound and Vibration*, 208, 159-166.
- Nelson P.A. and Elliott S.J., 1992, *Active Control of Sound*, Academic Press. London.
- Sas, P., Bao, C., Augusztinovicz, F. and Desmet, W., 1995, "Active Control of Sound Transmission Through a Double Panel Partition," *J. of Sound and Vibration*, 180 (4), 609-625.
- Skogestad, S. and Postlethwaite, I., 1996, "Multivariable Feedback Control", Wiley, New York.
- Wang, B.T., Fuller, C.R, Dimitriadis, E.K., 1991, "Active Control of Noise Transmission Through Rectangular Plates Using Multiple Piezoelectric or Multiple Point Force Actuators", *J. Acoustical Society of America*, 90, 2830-2830.

RESPONSIBILITY NOTICE

The author is the only responsible for the printed material included in this paper.

Non linear dynamics of a structure supported by rubber mounts

Benjamin Thomas¹, Lionel Manin², Régis Dufour² and Philippe Goge¹

¹ Valeo Engine Cooling, Branch Simulation Department, La Verrière, France

² Université de Lyon, CNRS, INSA-Lyon, LaMCoS UMR5259, F69621, Villeurbanne, France

Abstract: The hysteretic behavior of mechanical components permits efficient passive control of mechanical system vibrations but makes response prediction delicate due to their high non linearity. In this work, the generalized Dahl model is applied to rubber mounts used to support automotive engine cooling module. The general idea is to define an analytical model for the rubber mount, and to implement it into a global finite element model of the engine cooling module. The work presented illustrates the method on a simplified system. The rubber mounts exhibit a non-linear behavior which depends on preload and frequency. Analytical restoring force models are well adapted to simulate their behavior. An experimental investigation was conducted in order to identify the model parameters. The model considers: two envelop curves (upper and lower) which can be modeled by polynomial functions, a parameter beta that governs the transition between the compression and extension phases of the rubber mount. Based on the load-deflection hysteretic loops measured, an automated procedure was realized to extract the polynomial coefficients of the envelop curves and beta. The calculated coefficients are function of the preload and the excitation frequency. Hence, the behavior of the rubber mounts can predicted versus time. In a second time, the model identified is implemented in a finite element model of a cantilever beam supported by a rubber mount at its free end. The dynamic transient response to a forced excitation is predicted and compared to experimental results.

Keywords: Non linear dynamics, restoring force, hysteresis, rubber mount, parameter identification

INTRODUCTION

The qualification of on-board manufactured components pushes the automotive suppliers to subject their products to vibration tests defined by standards that are more and more drastic for fitting the complex car environment solicitations. On-board automotive equipments are subjected to base or active excitations which can be time varying, combined and superposed, see Fig. 1&2.

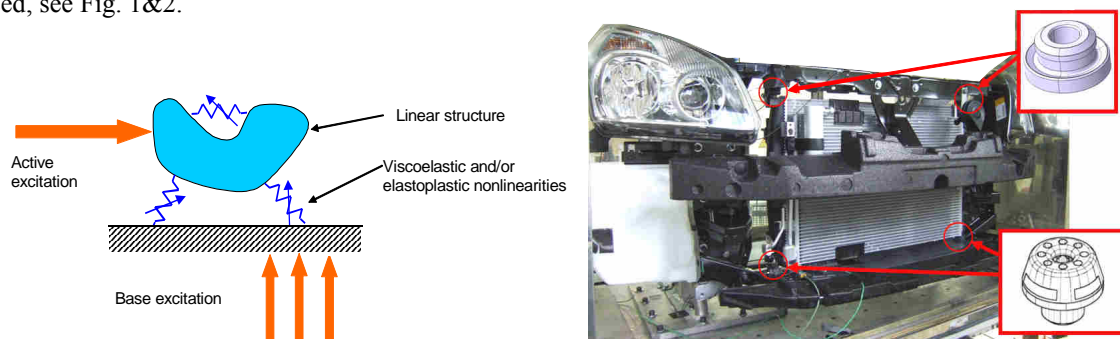


Figure 1 – Linear on-board equipment with nonlinear suspension (Automotive front end with cooling module), upper and lower rubber mounts.

Amongst all the different types of suspension, see the review of Ibrahim (2008), the passive suspension made of elastomer mounts remains the best choice regarding the economical-performance compromise. For reducing the numbers of tests, it takes advantages to develop a FE model involving the nonlinearities and dissipation brought mainly by the rubber mounts. The dynamic condensation technique associated with the FE method is usually used because it is well-adapted for modeling the linear behavior of structures, Craig and Bampton (1968). The physical degrees of freedom (DOF) kept in the reduced basis permit connecting the nonlinear mechanical component, Gjika et al. (1996). To sum-up modelling rubber mounts requires to take into account a multi-parameter dependence because, pre-load, type of excitation, forcing frequency, frequency and amplitude deflection, warm-up and ambient temperature have different effects on the nonlinear behaviour (Nashif et al., 1985, Petit et al. and Braquins, 2008).

The non linear behavior of mechanical components can be modeled either by parametric models or non-parametric models (Vestroni and Noori, 2002). The former provide stiffness and damping parameters (such as Kelvin Voigt, Maxwell or Masing models) that are introduced in the first member of the equation of motion while the latter give a restoring force (such as the Dahl model) introduced in the second member. Al Majid and Dufour (2002, 2004) proposed a generalized Dahl model for force-deflection loop. It can model different behaviors such as softening, hardening or a combination of both and has been used for predicting the time response of a beam with an all-metal mount, subjected to

shocks, and to harmonic force. This model has been applied to a belt tensioner (Michon et al., 2005), and a passive actuator for the autonomous deployment of a hexapod (Aridon et al., 2009).

The rubber mounts considered for this study are used to support the cooling module of an automotive engine as shown in figures 1 and 2. Their modeling requires extending the generalized Dahl model to take into account their visco-elastic behavior. The objective is to demonstrate that this restoring force model is efficient and easy to use and can advantageously replace rheological models. It is described by a first order differential equation which can be coupled with equations of motion of the equipment, forcing the non linear response prediction to be integrated in the time domain. The experimental identification of the model parameters is presented. It is the purpose of the first section.

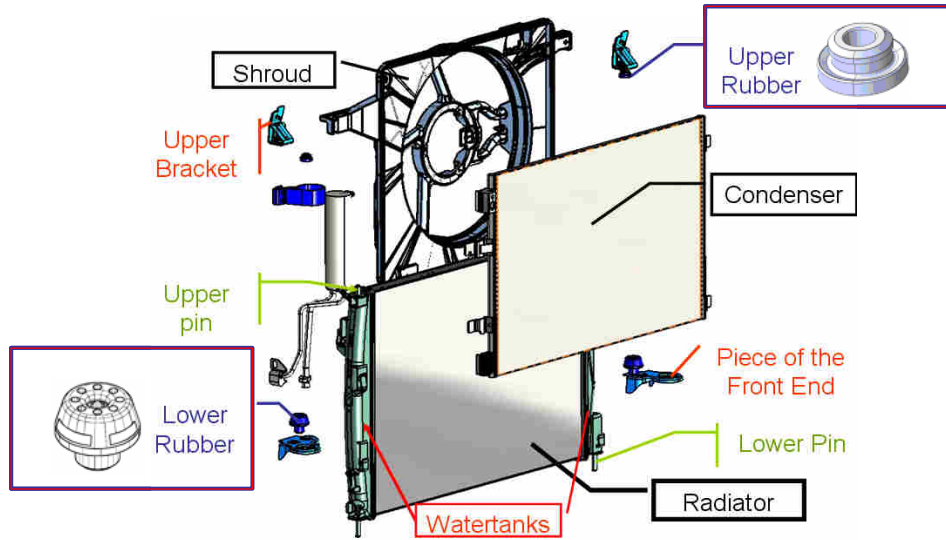


Figure 2 – exploded view of the cooling module.

In the second section, the implementation of the generalized Dahl model extended to the rubber mount is implemented in a FE code. First the identified model is validated. Then, a cantilever beam supported at its free end by a rubber mount is considered to couple a finite element model with the restoring force model developed. The computed and measured behavior are compared.

A RESTORING FORCE MODEL FOR RUBBER MOUNT

The investigated rubber mounts are made of pure elastomer, exhibiting a visco-elastic behavior. Moreover, the equipment-mount interface and the end-stop phenomena add also deflection nonlinearities. Therefore establishing a finite element model considering all these phenomena is not easy for such a component and it appears logical to extract the required parameters from measured force-deflection loops. Such a non linear behavior makes the prediction of the global assembly delicate, Lacarbonara and Vestroni (2003). In order to obtain the most general and easily formulated model, the aim is to model the force deflection loop based on boundary curves, which can be temperature, frequency and amplitude dependent.

The generalized Dahl's model (GDM)

Let u and R be the deflection and the restoring force respectively. The model is expressed with equation [1]:

$$\frac{dR}{dt} = \beta \frac{du}{dt} * (h - \text{sgn}(\frac{du}{dt}) * R) \quad (1)$$

where the envelope curve h is given by:

$$h = 0.5 * ((h_u - h_l) * \text{sgn}(\frac{du}{dt}) + (h_u + h_l)) \quad (2)$$

with β a parameter that has a stiffness dimension and h_u, h_l the upper and lower boundary curves approximated by a polynomial expansion which depend on deflection, rate of deflection, temperature and forcing frequency. Hence, this model is able to take into account a combination of phenomena such as dry friction at the interface of parts, visco-elastic behavior, mechanical gaps or end-stops. Consequently, it requires an experimental identification of its parameters.

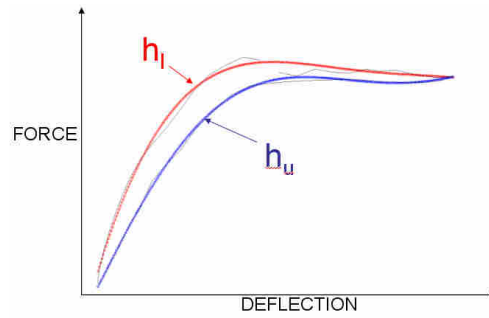


Figure 3 – Example of upper (h_u) and lower (h_l) boundary curves

Experimental parameter identification of the rubber mount model

Two testing apparatus have been designed to characterize the rubber mounts for axial-compression and shear loading (see Fig. 4). The shear test shown in figure 4b is done with two symmetric rubber mounts in order to avoid the bending moment. The boundary conditions of the rubber mount are the same as in operating conditions, i.e. pieces of the plastic and metallic interfaces have been used (Fig. 6). For the lower rubber mount, the pin of the watertank is used as the exciter connection and a piece of the front end as the casing. It permits to reproduce the conditions of use.

A shaker subjected the item to a sinusoidal deflection of amplitude u_l and forcing frequency Ω . A bias u_0 permits to impose a preload. The deflection imposed to the rubber is measured by an eddy current sensor, and the transmitted force by a piezo-electric load cell. The forcing frequency and deflection amplitude ranges have been chosen accordingly to the real power spectral density (PSD) tests performed on the automotive engine cooling module. The maximum frequency is chosen as twice the frequency range (usual criteria for mode extraction in PSD numerical simulation). Only results obtain on the lower rubber mount are presented in this paper, similar testing and model parameter identification were done on the upper rubber mount.

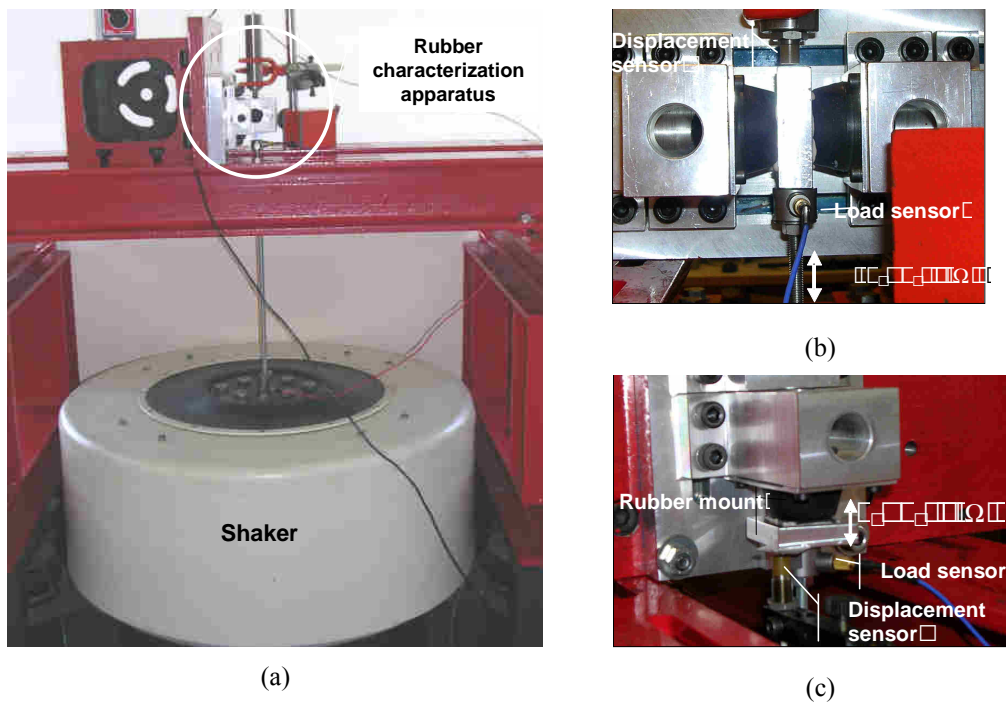


Figure 4: Testing devices (a), shear (b) and axial (c) tests applied on the lower rubber mount.

The lower rubber mount was subjected to the deflection amplitudes u_l [0.1 , 0.25 , 0.5 , 0.75, 1, 1.2] mm in the axial direction, with the excitation frequencies Ω [5.6, 10, 18, 32, 56, 75, 100, 130] Hz, hence 48 force-deflection loops were measured.

The force and deflection loops plotted in figure 5b highlight the nonlinear behavior of the lower rubber mount: indeed, designed to support half of the cooling module weight, it has the degree of freedom to translate along the pin of the watertank (Fig. 6). In the case of large deflection amplitudes, during a part of time the rubber mount is no more compressed, and the force reaches a threshold corresponding to the friction force between the pin and the rubber, see figure 6.

Non linear dynamics of a structure supported by rubber mounts

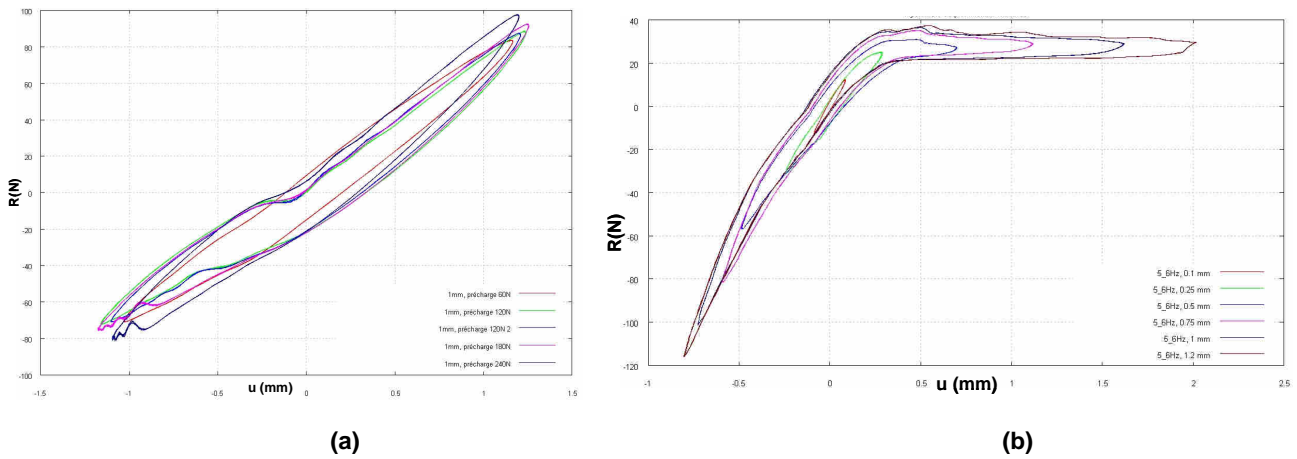


Figure 5: Examples of measured force-deflection loops: (a) 24Hz, shear loading, +/- 1mm, several pre-loads (b) 5.6Hz, compression loading for several deflection amplitudes

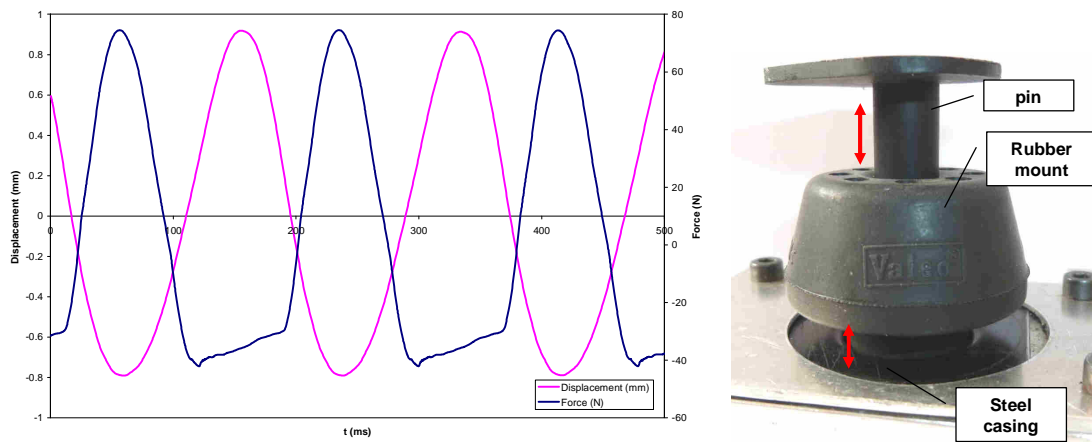


Figure 6: Example of time recording for the measured force and deflection, 5.6Hz compression loading

For the post processing of the measured force-deflection loops, an automated data processing has been programmed for identifying the GDM parameters. It permits the determination of the polynomial coefficients used to model the boundary curves of the hysteresis loop, and also the parameter β .

Average cycle extraction

The first step of the parameter identification process is to correct the raw experimental data to make their processing easier and run faster. Hence an average hysteresis loop is calculated for each of the loops recorded. To achieve this, a spatial averaging of the values is performed (Fig. 7). The working plane that contains the cycle is divided in small rectangles. A sweep is made on all the rectangles to define if points of the curves are inside or not. For a not empty rectangle, an average point is created as the barycentre of the inside points.

Determination of the envelop curves

After determining the average cycle, the identification of the GDM parameters requires a sorting of the points. We have to define for each point if it belongs to the upper or the lower curves of the cycle. The sorting of the points is automated by comparing the coordinates of the points to the ones of the cycle skeleton curve (Fig. 8). The points of the skeleton curve must be first created. The range of the deflection is divided in equal stripes. For each an average point is calculated, and then a curve fitting between the average points is used to obtain the skeleton curve.

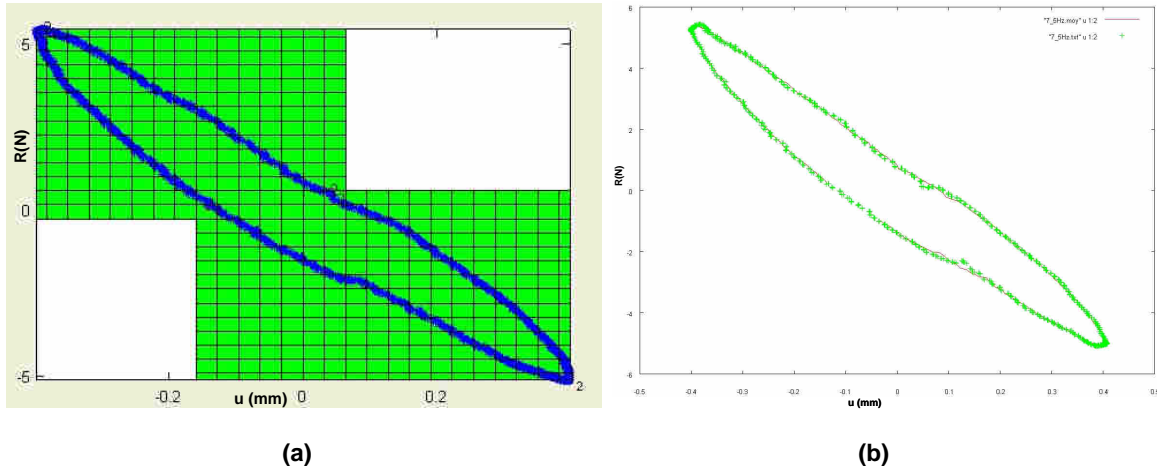


Figure 7: (a) Spatial averaging process, (b) example of resulting average cycle (red), on original points (green)

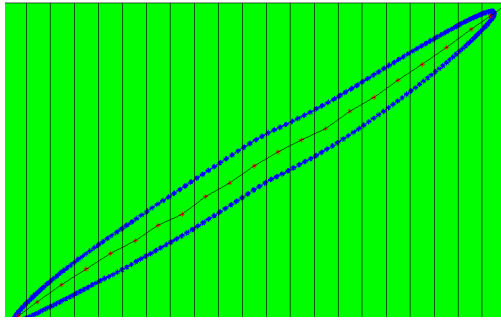


Figure 8: Cycle with its skeleton curve

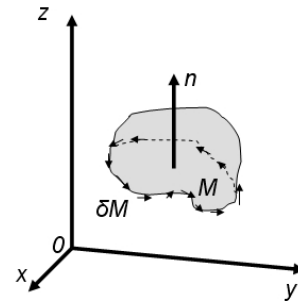


Figure 9: illustration of Stokes' theorem

In this work, the two envelop curves h_u and h_l are approximated using polynomial interpolation. Several tests have shown that the measured force-deflection cycles can be approximated satisfactorily with 3rd order polynomial forms of the deflection u such as:

$$R = a_0 + a_1u + a_2u^2 + a_3u^3 \quad (3)$$

Where the a_n coefficients depend on the excitation parameter. The reconstruction of the restoring force model is based on the incremental calculation of the restoring force thanks to its derivative.

$$R_{t+dt} = R_t + \frac{dR_t}{dt} \cdot dt \quad \text{where } \frac{dR_t}{dt} \text{ is given by (1).} \quad (4)$$

One has also to consider that the imposed deflection during the test may not correspond exactly to what was defined in the control software of the shaker. Therefore, it is necessary to evaluate what are the real values from the measurements. Since the excitation is harmonic we have to evaluate its related parameters U_0 and U_1 as:

$$U = U_0 + U_1 \sin(2\pi\Omega t) \quad (5)$$

These parameters are obtained by calculating the intersection points of the two polynomial envelop curves. These points correspond to the roots of the function defined by:

$$Q(u) = P_u(u) - P_l(u) \quad (6)$$

where P_u and P_l are the polynomial functions corresponding to the upper and lower envelops. Actually, the intersection points satisfy the relation:

$$P_u(u) = P_l(u) \quad (7)$$

In our case study, the polynoms order is larger than 2. Therefore, there can be more than 2 real roots for the function Q , it implies to manually eliminate complex roots and non physical values given the range of deflection.

Determination of β

The parameter β is related to the area of the hysteretic loop. An automated procedure to evaluate the value of this parameter is based on the minimization of the difference between the computed areas of the experimental and the interpolated cycles. The area of any surface can be approached thanks to differential geometry. Stokes' theorem (Macdonald, 2004), which is a central result on differential form integration, enables to obtain the formula for switching from perimeter to area. Let M be an oriented smooth manifold of dimension n and let w be an $n-1$ differential form that is compactly supported on M . One can write:

$$\int_M dw = \int_{\partial M} w \tag{8}$$

where d denotes the exterior derivative, ∂M the boundary of M . Another version of this theorem known as the Green Riemann theorem gives a differential form on \mathbb{R}^2 (Marsden, 2006):

$$\int_{\partial M} [f \cdot dx + g \cdot dy] = \iint_M \left[\frac{\partial g}{\partial x} - \frac{\partial f}{\partial y} \right] dx dy \tag{9}$$

To obtain immediately an area definition, the best way is to define the differential form as:

$$\left(\frac{\partial g}{\partial x} - \frac{\partial f}{\partial y} \right) = 2 \quad \text{where } g=x \text{ and } f=-y \tag{10}$$

With the previous equation one gets:

$$\int_{\partial M} [-y \cdot dx + x \cdot dy] = 2 \iint_M dx dy \tag{11}$$

$$0.5 * \int_{\partial M} [-y \cdot dx + x \cdot dy] = \iint_M dx dy = S \tag{12}$$

where S is the inner area of the closed curve. Finally, the discrete formulation is given by:

$$0.5 * \sum_i^n (-y_i \cdot dx_i + x_i \cdot dy_i) = S \tag{13}$$

where dx_i et dy_i are calculated as :

$$\begin{aligned} dx_i &= (x_{i+1} - x_{i-1}) / 2 \\ dy_i &= (y_{i+1} - y_{i-1}) / 2 \end{aligned} \tag{14}$$

The parameter β can then be evaluated by comparison between the experimental area and the model area.

Iterative reconstruction of the restoring force model

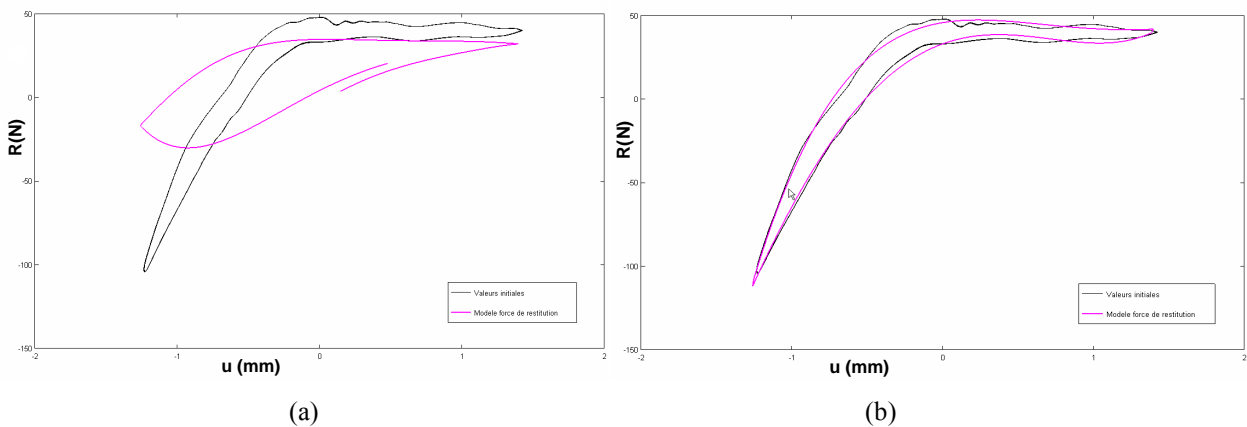


Figure 10: Calculated cycles obtained with 3rd order polynomials, for $\beta = 1$ (a), $\beta = 262$ (b)

The automated data processing was developed in the OCTAVE environment, a GNU-licensed MATLAB-like application. Its interface enables to perform the post processing of tests data with modifiable parameters such as the degree of the polynomial interpolation, the range of force and deflection, the frequency (Fig. 11). After uploading a measurement results file, a first processing is performed with a chosen order for polynomial form. The user can then modify parameters to better fit the experimental cycle.

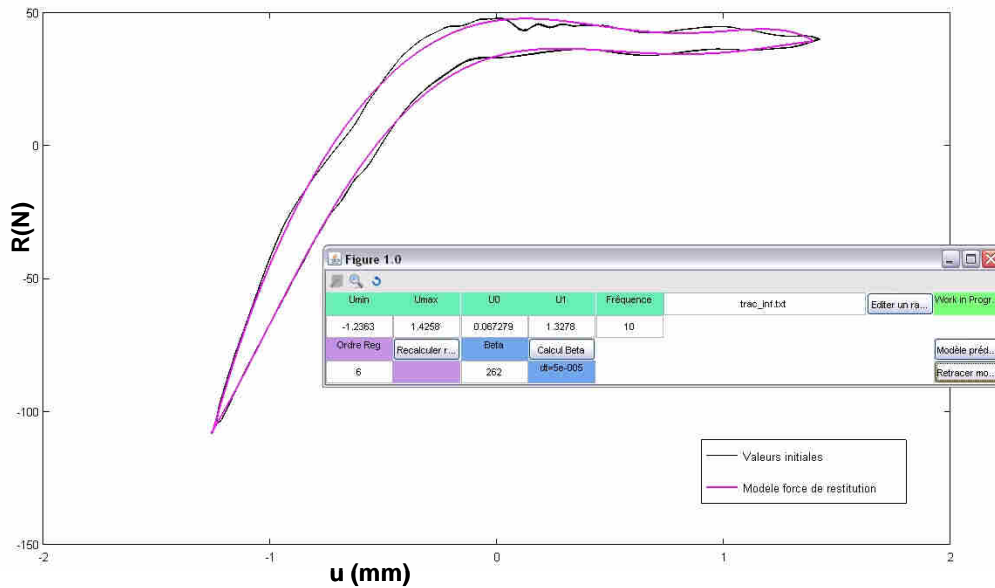


Figure 11: Example of the program interface for test data post-processing

The identification tests carried permit obtaining a database of model parameters (i.e. polynomial coefficients for upper and lower envelop curves, β) for all the couples ($u1, \Omega$). These parameters are used to predict the restoring force produced by the rubber mount subjected to a given deflection at a given frequency. In practice, the parameters are stored in matrices, so that knowing the deflection amplitude and the sollicitation frequency they are selected.

SIMULATIONS

Automotive suppliers perform random vibration tests on their components within the car manufacturer environment. In the case of engine cooling module, it requires validating the structure with its non linear supporting mounts. Actually, such rubber components are not taken into account in all numerical simulations whereas they can have a big impact on the structure dynamic behavior. Indeed, it is observed that the lower rubber mounts amplify the excitation imposed to the whole automotive front end during qualification tests. That is why a numerical model of rubber mounts, fully integrated to an industrial finite element analysis solver, is required.

Results and solver integration

The developed software for the model parameter identification enables to quickly characterize the rubber among a wide range of excitations. A program to generate the interpolated hysteresis cycles has also been realized, it permits simulating the measured cycles (Fig. 12).

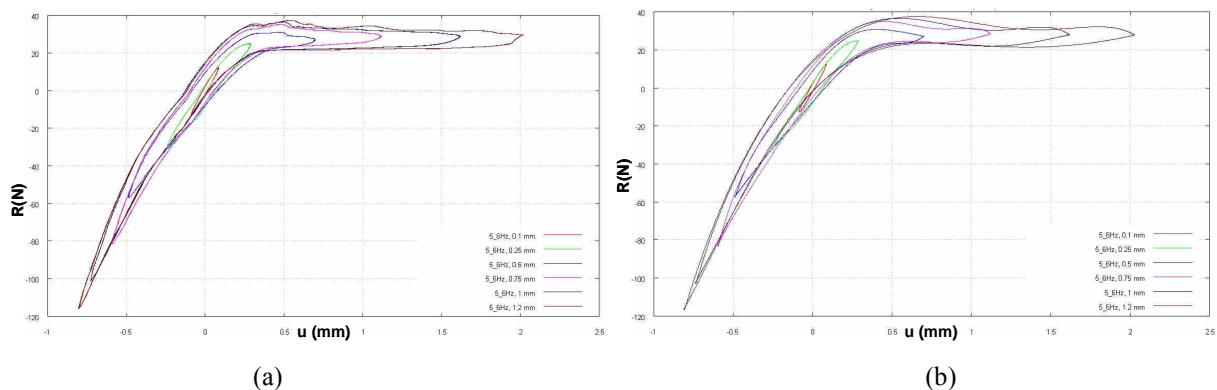


Figure 12: Comparison between measured (a) and simulated (b) cycles

Integration to Abaqus

The model and the algorithms developed have been integrated to Abaqus 6.9 thanks to user subroutines. In particular, the routine UAMP enables to define an amplitude value with commands defined by the user. Our amplitude is obtained thanks to previously defined algorithm and interpolation with frequency and displacement obtained from the Finite Element simulation. This amplitude modulates a force imposed at a node representing the upper bound of the rubber. Abaqus Viewer enables to post process history outputs to draw the hysteretic cycles (Fig. 13).

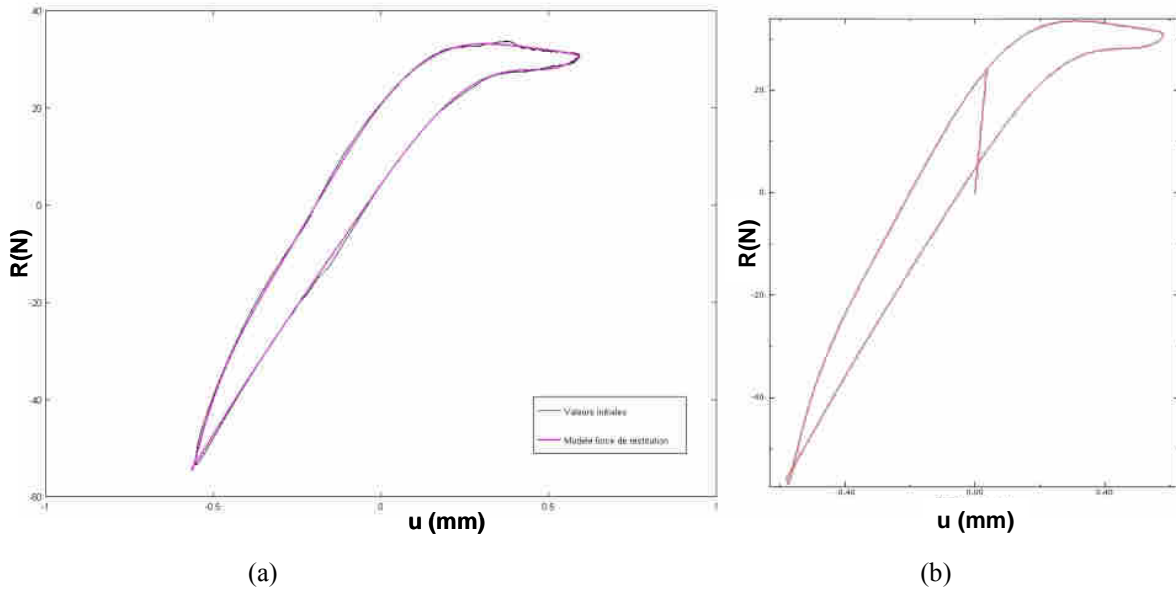


Figure 13: Experimental cycle (a) and the restoring force model implemented in Abaqus (b)

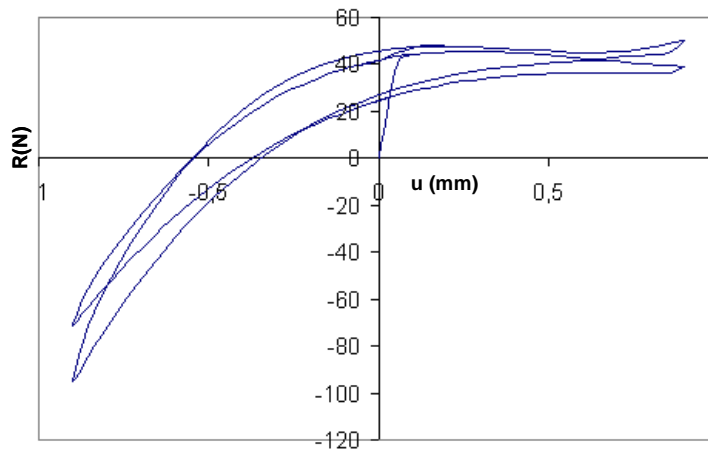


Figure 14: simulated force-deflection cycles for an imposed deflection with frequency change

In order to test the robustness of the model for switching from one frequency of excitation to another one, it is subjected to the following deflection:

$$u = u_1 \cdot \sin(2\pi \cdot \Omega \cdot t) \quad \text{where, } \Omega = 10\text{hz for } t \in [0, 0.2\text{s}] \text{ and } \Omega = 20\text{Hz for } t \in]0.2, 0.6] \quad (15)$$

Application on a simple structure

The aim is to connect the analytical model of the rubber suspension to the finite element model of a structure. A simple structure is considered here (Fig. 15), it is a cantilever beam supported at its free end by a rubber mount. The beam is subjected to harmonic or random excitation by mean of a rod connected to a shaker

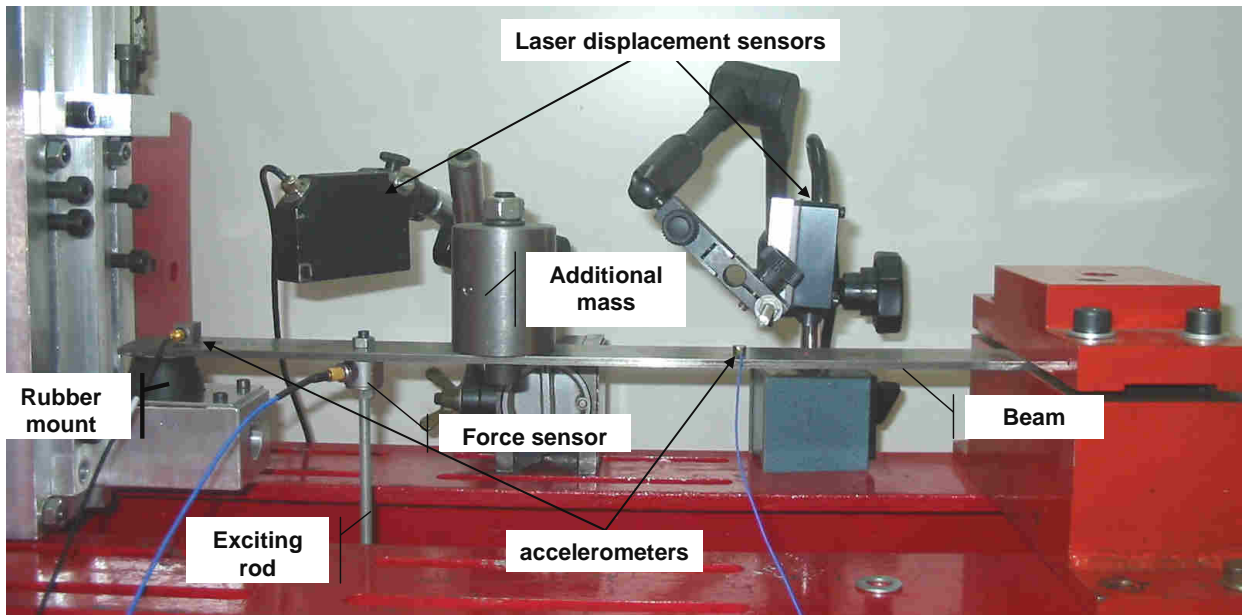


Figure 15: experimental device used for the validation.

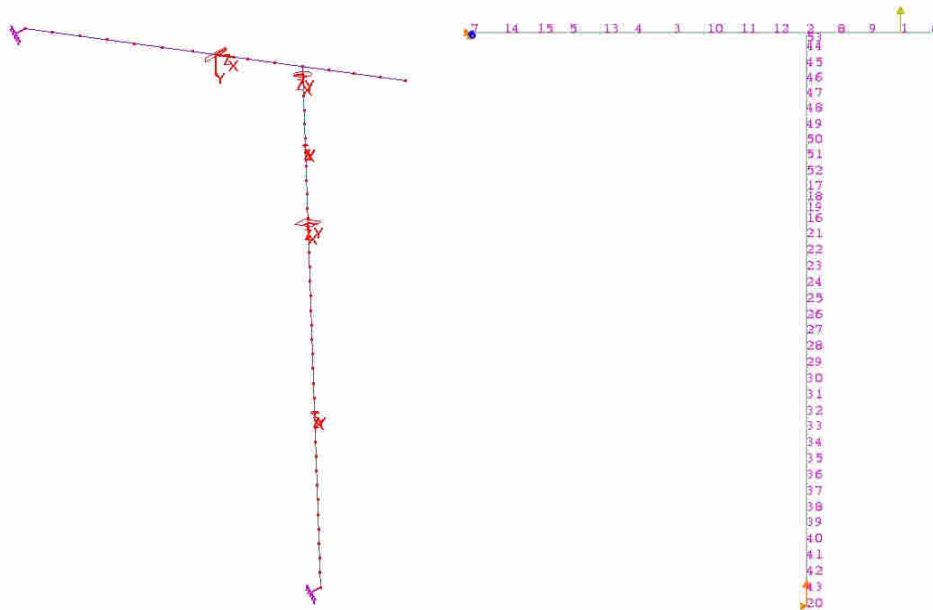


Figure 16: FEM of the structure.

The structure is modeled with 2D beam elements with 3 dof per node. The mesh contains around fifty elements. The rubber mount when considered is introduced by a force at node 1, see figure 16. Several first simulations are performed without the rubber mount in order to tune the Rayleigh damping coefficients α and β (Eq. 16). These coefficients are determined from the comparison of the computed and measured FRF for the two first modes, one obtains $\alpha=5.43$ and $\beta=2.42e-6$ (Fig. 17a).

$$[C] = \alpha[M] + \beta[K] \quad (16)$$

The first simulation results are presented here. The simulation process and particularly the communication between the FE model and the restoring-force model implemented is still under development. Figure 17b shows a comparison of the computed and mesured displacement at node 9 (Laser sensor) when the rubber mount is considered and for a single harmonic imposed deflection.

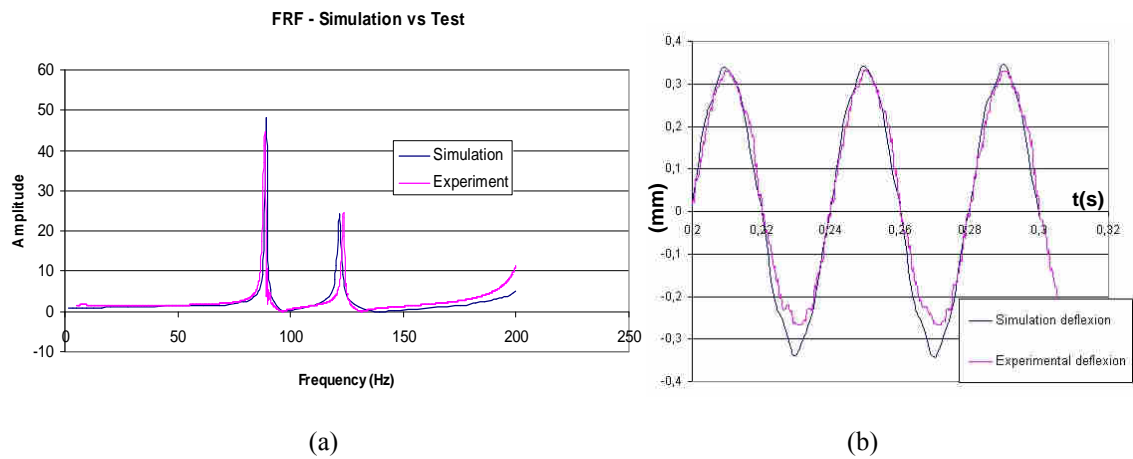


Figure 17: (a) computed and measured FRF at node 8, (b) computed and measured displacement vs. time at node 9.

CONCLUSION

The work presented is part of a project that aim at simulating the dynamic behavior of an automotive engine cooling module within its environment and integrating the non linear behavior of its rubber mount suspensions. The study has presented the characterization apparatus used to identify the rubber mounts behavior for several loading cases. An efficient method has been defined to automatically extract from experimentations the parameters of the generalized Dahl's model for rubber mount suspensions. The model permits to simulate the restoring force generated by the rubber mount when subjected to an imposed deflection with varying amplitude and frequency, in the range of the characterization tests performed. Implemented in the industrial solver Abaqus to simulate the hysteresis behavior of the rubber mounts, the model has been coupled with the FE model of a simple structure. First simulation results and comparisons with experimentation permit to validate the method.

REFERENCES

- Al Majid, A., Dufour, R., Formulation of a hysteretic restoring force model. Application to vibration isolation, *Nonlinear Dynamics*, Vol. 27, Springer Netherlands, (2002), pp. 69-85.
- Al Majid, A., Dufour, R., Harmonic response of a structure mounted on an isolator modelled with a hysteretic operator: experiments and prediction, *Journal of Sound and Vibration*, Vol. 277 (1-2), Academic Press, (2004), pp. 391-403.
- Aridon, G., Remond, D., Morestin, F., Blanchard, L., Dufour, R., Self-deployment of a tape-spring hexapode: experimental numerical investigation, *Journal of Mechanical Design*, ASME, (2009), Vol. 131, Iss. 2, 021003, 8p., doi:10.1115/1.3042148.
- Craig, R.R., Bampton, M.C.C, Coupling of substructures for dynamic analysis, *AIAA Journal*, Vol.6(7), (1968).
- Gjika, K., Dufour, R., Ferraris, G., Transient response of structures on viscoelastic or elastoplastic mounts: prediction and experiment, *Journal of Sound and Vibration*, Vol. 198(3) (1996), Academic Press pp. 361-378.
- Ibrahim, R.A., Review: recent advances in nonlinear passive vibration isolators, *Journal of Sound and Vibration*, Vol. 314, Academic Press (2008), pp. 371-452.
- Lacarbonara, W., Vestroni, F., Nonclassical responses of oscillators with hysteresis, *Nonlinear Dynamics*, Vol.32, Springer Netherlands (2003), pp. 235-258.
- Macdonald, A., Stokes' Theorem, Department of Mathematics, Luther College, Decorah U.S.A,(2004).
- Marsden, J.E., Differential Forms and Stokes' Theorem, Control and Dynamical Systems, Caltech (2006).
- Michon, G., Manin, L., and Dufour, R., Hysteretic behaviour of a belt tensioner: modelling and experimental investigation, *Journal of Vibration and Control*, Vol. 11 (9), Academic Press, (2005), pp. 1147-1158.
- Nashif, D., Jones, D.I.G., Henderson, J.P., *Vibration damping*, Wiley, (1985).
- Petitot, G., Barquins, M., Matériaux caoutchouteux- Morphologies, Formulations, Adhérence, Glissance et Usure, Presses Polytechniques Romandes, (2008).
- Vestroni, F., Noori, M., Hysteresis in mechanical systems - modelling and dynamic response, *International Journal of Non-Linear Mechanics*, Vol. 37, Elsevier Science, (2002), pp. 1261-1262.

Structural Modeling of Orthotropic Thin Plates by the Spectral Element Method

Nivaldo B. F. Campos¹

¹ Department of Exact and Earth Sciences, UNIFESP, Rua Prof. Artur Riedel, 275, 09972-270, Diadema, SP, Brazil

Abstract: Nowadays, the most commonly used methods for dynamic simulations of mechanical structures are the finite element method (FEM), and the boundary element method (BEM). Both are based on the discretization of the structure into small elements, in which the dynamic field variables are expressed in terms of approximated shape functions. As a consequence of this characteristic, the modeling for medium and high frequencies using these techniques will require that the size of the elements becomes smaller as the frequency increases, while its number needs to be increased. For structures that are usual in some areas, this will be possible only with an unreasonable computational effort, which is responsible for restricting the use of these methods practically to low-frequency applications. Wave methods such as the spectral element method (SEM) do not need mesh refinement at medium and high frequencies, and can model a continuous domain with just one element because it is based on a matrix formulation of the general solution for the partial differential equation of the problem. Until recently, its application to structural dynamics was limited to model beams and Levy type plates, but in a previous work the author has succeeded in applying SEM to model isotropic rectangular thin plates with arbitrary boundary conditions. This paper extends this work to allow the modeling of orthotropic thin plates by obtaining its dynamic stiffness matrix. The problem was solved both for the homogeneous and forced cases and numerical examples were developed to demonstrate the accuracy of the method by comparing it to FEM. The results obtained has proved to be appealing and its accuracy and computational cost make it a potential tool for structural analysis of thin plates in mid and high frequency ranges.

Keywords: Energy Spectral Element Method, Energy Finite Element Method, Spectral Element Method, Power Flow, High Frequency, Plates.

NOMENCLATURE

a = plate dimension on x direction
 b = plate dimension on y direction
 c = vector of constants
d, $\tilde{\mathbf{d}}$ = vector of energy density at the boundary
D, $\tilde{\mathbf{D}}$ = matrix of energy density
f, $\tilde{\mathbf{f}}$ = vector of power flow at the boundary
F, $\tilde{\mathbf{F}}$ = matrix of power flow
 h = plate thickness
 i = imaginary number

k_x = wave number in x direction
 k_y = wave number in y direction
 m = bending moment
 P = transverse dynamic load
S = dynamic stiffness matrix
 t = time
T = diagonal matrix of trigonometric terms of Fourier series
 v = shear force
 w = plate out of plane displacement

ρ = density
 ν = Poisson coefficient
 ∇^4 = biharmonic operator
 Ψ = vector of basis functions
 η = structural loss factor
 ϕ = plate slope

Subscripts

m, n = number of a Fourier series coefficient

Greek Symbols

ω = circular frequency

INTRODUCTION

Nowadays, the most commonly used methods for dynamic simulations of mechanical structures are the Finite Element Method (FEM) (Zienkiewicz and Taylor, 2000) and the Boundary Element Method (BEM) (Banerjee and Butterfield, 1981), which are deterministic methods. Both are based on the discretization of the structure into small elements, in which the dynamic field variables are expressed in terms of approximated shape functions. As a consequence of this characteristic, the modeling for medium and high frequencies using these techniques will require that the size of the elements becomes smaller as the frequency increases, while its number needs to be increased. For structures that are usual in some areas, like the aerospace industry, this will be possible only with an unreasonable computational effort, which is responsible for restricting the use of these methods practically to low-frequency applications.

For high-frequency modeling, probabilistic techniques such as the Statistical Energy Analysis (SEA) (Lyon and DeJong, 1995) have been developed. In this technique, the model is divided in a number of subdomains, for which only averaged energy levels are predicted. Therefore, it is unable to give results at discrete points of the problem domain. As any other method, its accuracy depends on the validity of the assumptions that were made, and in the case of SEA, these assumptions are high modal density and light coupling between subsystems in the frequency range of interest. Often,

they are not valid in the middle frequency range or in structures with stiff members connected to thin shells, which limits the use of the method to the high-frequency range.

For applications at mid-frequency range, adequate prediction techniques are still not available. In this frequency range, the computational efforts of conventional element based techniques become already prohibitively large, while the basic assumptions of the probabilistic techniques are not yet valid.

In an attempt to overcome these difficulties, it have recently been developed many attractive methodologies based on an indirect Trefftz approach (Jin et al., 1993, Desmet et al., 2001), which can be classified as wave based methods. These methods do not require mesh discretization to model a domain with constant geometric and physical properties, since the pressure or displacement fields are described by wave functions that exactly satisfy the differential equation of the problem. The solutions, obtained as an infinite series truncated accordingly to the desired precision, are able to describe an infinite number of modes and are obtained by determining the unknown contribution of the wave factors, what is done by introducing the boundary conditions of the problem. The matrices produced are smaller than the ones from FEM and BEM, and in spite of the fact that they are fully populated and frequency dependent, it has proven that the methods are computationally more efficient for the analysis of steady-state vibroacoustic problems.

A comprehensive overview of the methodologies used in the wave based methods is presented by Desmet (2002). Among them, in the area of structural dynamics, it should be mentioned the superposition method, developed by Gorman (1999), and applied mainly to model free-free plates. The image method, first used in modeling acoustic problems, was extended by Gunda et al. (1995) to treat beams and plates. Kulla (1997) presented a high precision finite element method, which was able to model beams and plates with arbitrary boundary conditions. The same approach was used by Kevorkian and Pascal (2001) and Casemir et al. (2005) on the continuous element method. Lee and Lee (1999) applied the spectral element method to model Levy type plates and Doyle (1997) gave a Fourier approach to it. Arruda et al. (2004) extended the work of Lee and Doyle, developing a spectral element for reinforced panels extended the work of Lee and Doyle, developing a spectral element for reinforced Levy type plates and Campos and Arruda (2008) presented a spectral element capable to model thin plates with and without reinforcing beams and arbitrary boundary conditions.

In this paper, the spectral element method is extended to treat orthotropic thin plates with any boundary conditions. The dynamic stiffness matrix for a spectral orthotropic plate element is developed and the problem is solved both for the homogeneous and forced cases. Numerical examples were developed to demonstrate the accuracy of the method and the results were compared with those obtained with FEM.

THE ORTHOTROPIC THIN PLATE DIFFERENTIAL EQUATION

Solution for the thin plate differential equation

In this section, a Fourier series solution for the differential equation of an orthotropic thin plate is used to obtain the matrices of displacements and forces, dependents on x , y and the circular frequency ω , at the boundaries of the plate. From these rectangular matrices it is possible, by a new series expansion, to obtain square matrices dependents only on ω , which combined will result in the dynamic stiffness matrix of the problem.

Starting from the governing equation in the frequency domain of an anisotropic thin plate obtained from the work of Lekhnitskii (1968), the lateral mid-surface deflection w satisfies the differential equation

$$D_{11} \frac{\partial^4 w}{\partial x^4} + 4D_{16} \frac{\partial^4 w}{\partial x^3 \partial y} + 2(D_{12} + 2D_{66}) \frac{\partial^4 w}{\partial x^2 \partial y^2} + 4D_{26} \frac{\partial^4 w}{\partial x \partial y^3} + D_{22} \frac{\partial^4 w}{\partial y^4} - D_{11} k^4 w = P(x, y) \quad (1)$$

where

$$k = \sqrt[4]{\omega^2 \rho h} \quad (2)$$

with h been the plate thickness and ρ the material density.

Let's now consider an orthotropic rectangular thin plate. The differential equation for this kind of structure can be derived from Equation (1) as

$$D_{11} \frac{\partial^4 w}{\partial x^4} + 2(D_{12} + 2D_{66}) \frac{\partial^4 w}{\partial x^2 \partial y^2} + D_{22} \frac{\partial^4 w}{\partial y^4} - D_{11} k^4 w = P(x, y) \quad (3)$$

assuming that

$$D_{16} = D_{26} = 0 \quad (4)$$

and

$$\mathbf{D} = \begin{bmatrix} D_{11} & D_{12} & 0 \\ D_{12} & D_{22} & 0 \\ 0 & 0 & D_{66} \end{bmatrix} = \frac{1}{\det(\mathbf{S})} \frac{h^3}{12} \begin{bmatrix} S_{22}S_{33} - (S_{23})^2 & S_{13}S_{23} - S_{12}S_{33} & 0 \\ S_{13}S_{23} - S_{12}S_{33} & S_{11}S_{33} - (S_{13})^2 & S_{12}S_{13} - S_{11}S_{23} \\ 0 & 0 & S_{11}S_{22} - (S_{12})^2 \end{bmatrix}, \quad (5)$$

$$\mathbf{S} = \begin{bmatrix} \frac{1}{E_x} & -\frac{\nu}{E_x} & 0 \\ -\frac{\nu}{E_x} & \frac{1}{E_y} & 0 \\ 0 & 0 & \frac{1}{G} \end{bmatrix}, \quad (6)$$

with E_x and E_y been the Young Modulus in the x and y direction respectively and G the shear modulus.

In order to solve Equation (3), in its homogenous form

$$D_{11} \frac{\partial^4 w}{\partial x^4} + 2(D_{12} + 2D_{66}) \frac{\partial^4 w}{\partial x^2 \partial y^2} + D_{22} \frac{\partial^4 w}{\partial y^4} - D_{11} k^4 w = 0 \quad (7)$$

it will be assumed a solution of the form

$$w(x, y; \omega) = C e^{p x} e^{q y} \quad (8)$$

Introducing Equation (8) into Equation (7), it will be obtained the characteristic equation for the homogeneous differential equation as

$$D_{11} p^4 + 2(D_{12} + 2D_{66}) p^2 q^2 + D_{22} q^4 - k^4 = 0 \quad (9)$$

There are infinite values of p and q that satisfy Equation (9). Let's assume that the solution in the x direction can be expanded as an exponential Fourier series. A general term of this series for a rectangular plate with dimensions $L_x = 2a$ and $L_y = 2b$. and for a given $m \in \mathbb{N}$, will be expressed as

$$p_m = \pm \frac{i m \pi}{a} = \pm i k_{xm} \quad \text{with} \quad k_{xm} = \frac{m \pi}{a}, \quad m = 0, 1, 2, \dots \quad (10)$$

Introducing the expression for p_m into Equation (9), it will define four values for q_m as

$$q_{1m} = \pm i k_{1ym}; \quad k_{1ym} = \sqrt{\frac{\left(D_{22} k^4 + \left((D_{12} + 2D_{66})^2 - D_{11} D_{22} \right) k_{xm}^4 \right)^{1/2} - (D_{12} + 2D_{66}) k_{xm}^2}{D_{22}}} \quad (11)$$

$$q_{2m} = \pm k_{2ym}; \quad k_{2ym} = \sqrt{\frac{\left(D_{22} k^4 + \left((D_{12} + 2D_{66})^2 - D_{11} D_{22} \right) k_{xm}^4 \right)^{1/2} + (D_{12} + 2D_{66}) k_{xm}^2}{D_{22}}} \quad (12)$$

and, therefore, a given m will yield eight basis solutions for Equation (7), which grouped in a set can be expressed as

$$w_{1m} = \left(C'_{1m} e^{i k_{1ym} y} + C'_{2m} e^{-i k_{1ym} y} + C'_{3m} e^{k_{2ym} y} + C'_{4m} e^{-k_{2ym} y} \right) e^{i k_{xm} x} + \left(C'_{5m} e^{i k_{1ym} y} + C'_{6m} e^{-i k_{1ym} y} + C'_{7m} e^{k_{2ym} y} + C'_{8m} e^{-k_{2ym} y} \right) e^{-i k_{xm} x} \quad (13)$$

where the terms $C'_{1m}, C'_{2m}, \dots, C'_{8m}$, are unknown constants to be determined.

Applying the same approach to the solution in the y direction, it will be obtained another set of equations as

$$w_{2n} = \left(C'_{9n} e^{ik_{1xm}x} + C'_{10n} e^{-ik_{1xn}x} + C'_{11n} e^{k_{2xn}x} + C'_{12n} e^{-k_{2xn}x} \right) e^{ik_{yn}y} + \left(C'_{13n} e^{ik_{1xn}x} + C'_{14n} e^{-ik_{1xn}x} + C'_{15n} e^{k_{2xn}x} + C'_{16n} e^{-k_{2xn}x} \right) e^{-ik_{yn}y} \quad (14)$$

with

$$k_{1xn} = \sqrt{\frac{\left(D_{11}k^4 + \left((D_{12} + 2D_{66})^2 - D_{11}D_{22} \right) k_{yn}^4 + \right)^{1/2} - (D_{12} + 2D_{66})k_{yn}^2}{D_{11}}} \quad (15)$$

$$k_{2xn} = \sqrt{\frac{\left(D_{11}k^4 + \left((D_{12} + 2D_{66})^2 - D_{11}D_{22} \right) k_{yn}^4 + \right)^{1/2} + (D_{12} + 2D_{66})k_{yn}^2}{D_{11}}} \quad (16) \quad 2$$

The solution for the homogenous differential Equation (7) will be therefore

$$w(x, y; \omega) = \sum_{m=0}^{\infty} w_{1m} + \sum_{n=0}^{\infty} w_{2n} = \sum_{n=0}^{\infty} (w_{1n} + w_{2n}) \quad (17)$$

whose explicit expression for a given $n \geq 1$, with the Fourier series in trigonometric form and with new constants C_{1m} , C_{2m} , ..., C_{16m} in which are contained the constants presented in Equations (13) and (14) and the imaginary number i that multiplies the sine functions, is

$$w(x, y; \omega)_n = \cos(k_{xn}^c x) \left(C_{1n} e^{ik_{1yn}y} + C_{2n} e^{-ik_{1yn}y} + C_{3n} e^{k_{2yn}y} + C_{4n} e^{-k_{2yn}y} \right) + \cos(k_{yn}^c y) \left(C_{5n} e^{ik_{1xm}x} + C_{6n} e^{-ik_{1xn}x} + C_{7n} e^{k_{2xn}x} + C_{8n} e^{-k_{2xn}x} \right) + \sin(k_{xn}^s x) \left(C_{9n} e^{ik_{1yn}y} + C_{10n} e^{-ik_{1yn}y} + C_{11n} e^{k_{2yn}y} + C_{12n} e^{-k_{2yn}y} \right) + \sin(k_{yn}^s y) \left(C_{13n} e^{ik_{1xn}x} + C_{14n} e^{-ik_{1xn}x} + C_{15n} e^{k_{2xn}x} + C_{16n} e^{-k_{2xn}x} \right) \quad (18)$$

where, for sine functions,

$$k_{xn}^s = \frac{(2n-1)\pi}{2a}, \quad k_{yn}^s = \frac{(2n-1)\pi}{2b} \quad n = 1, 2, 3, \dots \quad (19)$$

and, for cosine functions,

$$k_{xn}^c = \frac{n\pi}{a}, \quad k_{yn}^c = \frac{n\pi}{b} \quad n = 1, 2, 3, \dots \quad (20)$$

Defining

$$\Psi_n = \left\{ \cos(k_{xn}^c x) e^{ik_{1yn}y} \quad \cos(k_{xn}^c x) e^{-ik_{1yn}y} \quad \dots \quad \sin(k_{yn}^s y) e^{k_{2xn}x} \quad \sin(k_{yn}^s y) e^{-k_{2xn}x} \right\}^T \quad (21)$$

and

$$\mathbf{c}_n = \{ C_{1n} \quad C_{2n} \quad \dots \quad C_{15n} \quad C_{16n} \}^T \quad (22)$$

Equation (18) becomes

$$w(x, y; \omega)_n = \Psi_n^T \cdot \mathbf{c}_n \quad (23)$$

For $n = 0$,

$$w(x, y; \omega)_0 = \begin{aligned} & C_{10}e^{iky} + C_{20}e^{-iky} + C_{30}e^{ikx} + C_{40}e^{-ikx} + \\ & C_{50}e^{ikx} + C_{60}e^{-ikx} + C_{70}e^{ikx} + C_{80}e^{-ikx} \end{aligned} \quad (24)$$

and

$$\Psi_0 = \left\{ e^{iky} \quad e^{-iky} \quad e^{ky} \quad e^{-ky} \quad e^{ikx} \quad e^{-ikx} \quad e^{kx} \quad e^{-kx} \right\}^T \quad (25)$$

$$\mathbf{c}_0 = \left\{ C_{10} \quad C_{20} \quad C_{30} \quad C_{40} \quad C_{50} \quad C_{60} \quad C_{70} \quad C_{80} \right\}^T \quad (26)$$

Therefore

$$w(x, y; \omega)_0 = \Psi_0^T \cdot \mathbf{c}_0 \quad (27)$$

Assuming now $n=0, 1, 2, \dots$, it can be defined

$$\Psi = \left\{ \begin{array}{c} \Psi_0 \\ \Psi_1 \\ \vdots \\ \Psi_n \end{array} \right\} \quad \text{and} \quad \mathbf{c} = \left\{ \begin{array}{c} \mathbf{c}_0 \\ \mathbf{c}_1 \\ \vdots \\ \mathbf{c}_n \end{array} \right\} \quad (28)$$

and a general expression for the displacements, in vector form, will be given by

$$w(x, y; \omega) = \Psi^T \cdot \mathbf{c} \quad (29)$$

Spectral dynamic stiffness matrix

The orthotropic thin plate spectral dynamic stiffness matrix can be obtained by writing the shear forces and the moments as a function of the displacements and slopes at the boundaries along the x and y directions. These terms are defined by the well known relations

$$\phi_x(x, y; \omega) = -\frac{\partial w(x, y; \omega)}{\partial x} \quad (30)$$

$$\phi_y(x, y; \omega) = -\frac{\partial w(x, y; \omega)}{\partial y} \quad (31)$$

$$m_x(x, y; \omega) = -\left(D_{11} \frac{\partial^2 w(x, y; \omega)}{\partial x^2} + D_{12} \frac{\partial^2 w(x, y; \omega)}{\partial y^2} \right) \quad (32)$$

$$m_y(x, y; \omega) = -\left(D_{12} \frac{\partial^2 w(x, y; \omega)}{\partial x^2} + D_{22} \frac{\partial^2 w(x, y; \omega)}{\partial y^2} \right) \quad (33)$$

$$v_x(x, y; \omega) = -\left(D_{11} \frac{\partial^3 w(x, y; \omega)}{\partial x^3} + (D_{12} + 4D_{66}) \frac{\partial^3 w(x, y; \omega)}{\partial x \partial y^2} \right) \quad (34)$$

$$v_y(x, y; \omega) = -\left(D_{22} \frac{\partial^3 w(x, y; \omega)}{\partial y^3} + (D_{12} + 4D_{66}) \frac{\partial^3 w(x, y; \omega)}{\partial x \partial y^2} \right) \quad (35)$$

Evaluating Equations (17), (30) and (31) at the boundaries and assembling the results, a vector $\tilde{\mathbf{d}}$ of displacements on the boundaries, is obtained

$$\tilde{\mathbf{d}} = \tilde{\mathbf{D}} \cdot \mathbf{c} \quad (36)$$

where

$$\tilde{\mathbf{d}}(x, y) = \{w(-a, y) \quad w(a, y) \quad w(x, -b) \quad w(x, b) \quad \phi_x(-a, y) \quad \phi_x(a, y) \quad \phi_y(x, b) \quad \phi_y(x, b)\}^T \quad (37)$$

$$\tilde{\mathbf{D}}(x, y) = \begin{bmatrix} d_{1,0}^1 & \cdots & d_{8,0}^1 & d_{1,1}^1 & \cdots & d_{16,1}^1 & \cdots & d_{1,n}^1 & \cdots & d_{16,n}^1 \\ d_{1,0}^2 & \cdots & d_{8,0}^2 & d_{1,1}^2 & \cdots & d_{16,1}^2 & \cdots & d_{1,n}^2 & \cdots & d_{16,n}^2 \\ \vdots & \vdots & \vdots & \vdots & \vdots & \vdots & \vdots & \vdots & \vdots & \vdots \\ d_{1,0}^8 & \cdots & d_{8,0}^8 & d_{1,1}^8 & \cdots & d_{16,1}^8 & \cdots & d_{1,n}^8 & \cdots & d_{16,n}^8 \end{bmatrix} \quad (38)$$

$$\mathbf{c} = \{C_{1,0} \quad \cdots \quad C_{8,0} \quad C_{1,1} \quad \cdots \quad C_{16,1} \quad \cdots \quad C_{1,n} \quad \cdots \quad C_{16,n}\}^T \quad (39)$$

Proceeding in the same way in relation to the forces at the boundaries, it will be obtained

$$\tilde{\mathbf{f}} = \tilde{\mathbf{F}} \cdot \mathbf{c} \quad (40)$$

where

$$\tilde{\mathbf{f}} = \{-v(-a, y) \quad v(a, y) \quad -v(x, -b) \quad v(x, b) \quad -m_x(-a, y) \quad m_x(a, y) \quad -m_y(x, -b) \quad m_y(x, b)\}^T \quad (41)$$

$$\tilde{\mathbf{F}} = \begin{bmatrix} f_{1,0}^1 & \cdots & f_{8,0}^1 & f_{1,1}^1 & \cdots & f_{16,1}^1 & \cdots & f_{1,n}^1 & \cdots & f_{16,n}^1 \\ f_{1,0}^2 & \cdots & f_{8,0}^2 & f_{1,1}^2 & \cdots & f_{16,1}^2 & \cdots & f_{1,n}^2 & \cdots & f_{16,n}^2 \\ \vdots & \vdots & \vdots & \vdots & \vdots & \vdots & \vdots & \vdots & \vdots & \vdots \\ f_{1,0}^8 & \cdots & f_{8,0}^8 & f_{1,1}^8 & \cdots & f_{16,1}^8 & \cdots & f_{1,n}^8 & \cdots & f_{16,n}^8 \end{bmatrix} \quad (42)$$

In order to eliminate the dependence on x and y of $\tilde{\mathbf{d}}, \tilde{\mathbf{D}}, \tilde{\mathbf{f}}$ and $\tilde{\mathbf{F}}$, they will be expanded in a trigonometric Fourier series and the coefficients of the sine and cosine terms will be placed in two different lines. Truncating this series at an adequate number of terms m , the resulting constant matrices will be square. In this way, we will have

$$\tilde{\mathbf{f}} = \tilde{\mathbf{F}} \cdot \mathbf{c} \Rightarrow \mathbf{T} \cdot \mathbf{f} = \mathbf{T} \cdot \tilde{\mathbf{F}} \cdot \mathbf{c} \Rightarrow \mathbf{f} = \mathbf{F} \cdot \mathbf{c} \Rightarrow \mathbf{c} = \mathbf{F}^{-1} \cdot \mathbf{f} \quad (43)$$

$$\tilde{\mathbf{d}} = \tilde{\mathbf{D}} \cdot \mathbf{c} \Rightarrow \mathbf{T} \cdot \mathbf{d} = \mathbf{T} \cdot \tilde{\mathbf{D}} \cdot \mathbf{c} \Rightarrow \mathbf{d} = \mathbf{D} \cdot \mathbf{c} \Rightarrow \mathbf{c} = \mathbf{D}^{-1} \cdot \mathbf{d} \quad (44)$$

where

$$\mathbf{T} = \begin{bmatrix} \mathbf{T}_0 & & & & \\ & \mathbf{T}_1 & & & \\ & & \mathbf{T}_2 & & \\ & & & \ddots & \\ & & & & \mathbf{T}_n \end{bmatrix} \quad (45)$$

with \mathbf{T}_0 an 8×8 identity matrix and

$$\mathbf{T}_n = \begin{bmatrix} \mathbf{T}_{yn} & & & & \\ & \mathbf{T}_{xn} & & & \\ & & \mathbf{T}_{yn} & & \\ & & & \ddots & \\ & & & & \mathbf{T}_{xn} \end{bmatrix} \quad (46)$$

where

$$\mathbf{T}_{xn} = \begin{bmatrix} \cos \frac{n\pi}{a} x & & & & & \\ & \sin \frac{(2n-1)\pi}{2a} x & & & & \\ & & \cos \frac{n\pi}{a} x & & & \\ & & & \sin \frac{(2n-1)\pi}{2a} x & & \\ & & & & \cos \frac{n\pi}{a} x & \\ & & & & & \sin \frac{(2n-1)\pi}{2a} x \end{bmatrix} \quad (47)$$

$$\mathbf{T}_{yn} = \begin{bmatrix} \cos \frac{n\pi}{b} y & & & & & \\ & \sin \frac{(2n-1)\pi}{2b} y & & & & \\ & & \cos \frac{n\pi}{2b} y & & & \\ & & & \sin \frac{(2n-1)\pi}{2b} y & & \\ & & & & \cos \frac{n\pi}{2b} y & \\ & & & & & \sin \frac{(2n-1)\pi}{2b} y \end{bmatrix} \quad (48)$$

Eliminating \mathbf{c} from Equations (43) and (44), it yields

$$\mathbf{S} \cdot \mathbf{d} = \mathbf{f} \quad (49)$$

where

$$\mathbf{S} = \mathbf{F} \cdot \mathbf{D}^{-1} \quad (50)$$

with \mathbf{S} been the dynamic spectral stiffness matrix.

For plates with free-free or clamped-clamped boundary conditions, its natural frequencies and modes can be obtained by setting respectively the vectors \mathbf{f} or \mathbf{d} equal to zero on Equation (49) and solving the resulting eigenproblem. The vector of coefficients \mathbf{c} can be obtained by solving Equation (44) or (43) respectively. For mixed boundary conditions, the non nulls terms of vectors \mathbf{f} and \mathbf{d} should be merged in a new vector and the corresponding terms of matrices \mathbf{F} and \mathbf{D} in a new matrix, allowing the vector \mathbf{c} to be determined in a similar way as in Equation (43) or (44).

Case of inhomogeneous boundary conditions

If forces or displacements are imposed to the plate at the boundaries, the displacement field can still be obtained with the homogeneous formulation by introducing the boundary displacements and forces in vectors \mathbf{d} and \mathbf{f} , respectively. The boundary conditions can be imposed by expanding them in the same Fourier series used in obtaining the dynamic stiffness matrix and inserting the coefficients obtained in the corresponding positions of vectors \mathbf{d} or \mathbf{f} . For the particular case of a punctual unitary force – considered as a boundary condition - applied to an edge along the y direction and at an arbitrary position $y=y_0$, which can be expressed as $P = P_0 \delta(y-y_0)$, the expansion in a Fourier series will produce coefficients given by

$$fc_0 = \frac{1}{2b} \int_{-b}^b P_0 \delta(y-y_0) dy, \quad fc_n = \frac{1}{b} \int_{-b}^b P_0 \delta(y-y_0) \cos \frac{n\pi y_0}{b} dy, \quad (51)$$

$$fs_0 = \frac{1}{2b} \int_{-b}^b P_0 \delta(y-y_0) dy, \quad fs_n = \frac{1}{b} \int_{-b}^b P_0 \delta(y-y_0) \cos \frac{n\pi y_0}{b} dy, \quad (52)$$

which, after integrating and introducing $P_0=1$, results in

$$fc_0 = \frac{1}{2b}, \quad fc_n = \frac{1}{b} \cos \frac{n\pi y_0}{b}, \quad fs_0 = 0, \quad fs_n = \frac{1}{b} \sin \frac{(2n-1)\pi y_0}{2b} \quad (53)$$

Introducing these coefficients in \mathbf{f} and imposing the boundary conditions on Equation (49), in the same way as it is done in the finite element method, the value of \mathbf{d} can be obtained which, introduced in Equation (54), will completely determine the displacement field as

$$w(x, y; \omega) = \boldsymbol{\psi}^T \cdot \mathbf{D}^{-1} \cdot \mathbf{d} \tag{54}$$

NUMERICAL VALIDATION

In this section it is presented numerical implementations of SEM to validate its formulation for orthotropic thin plates.

Low frequency verification

In order to verify the orthotropic formulation for SEM developed in this work, it was applied to perform a dynamic analysis of a free-free plate used by Grédiac and Paris (1996)0 in obtaining the elastic constants of composite materials. The plate has the following physical and geometric properties: $E_x = 120$ MPa, $E_y = 10$ MPa, $G = 4.9$ MPa, $\rho = 1510$ Kg/m³, $\nu = 0.3$, $h = 0.001$ m, $L_x = L_y = 0.20$ m and is submitted to a unitary harmonic load applied at point $(-0,059, -0.1)$, as showed in Figure 1.

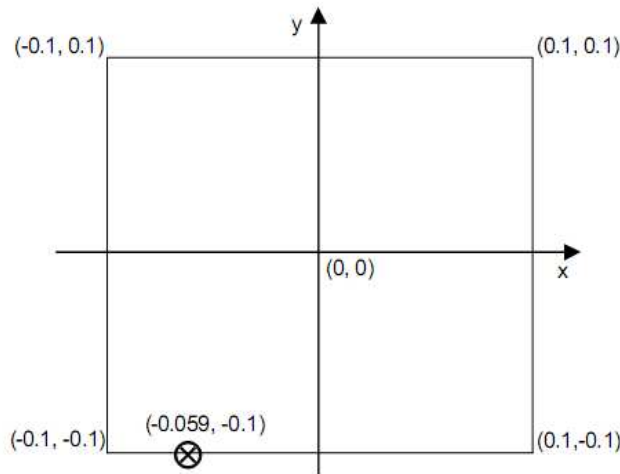


Figure 1: Free-Free plate under unitary harmonic load

The frequency response function (FRF) of the plate at the loading point was obtained using just one SEM element with 15 terms of the Fourier series expansion, and the result is showed in Figure 2.

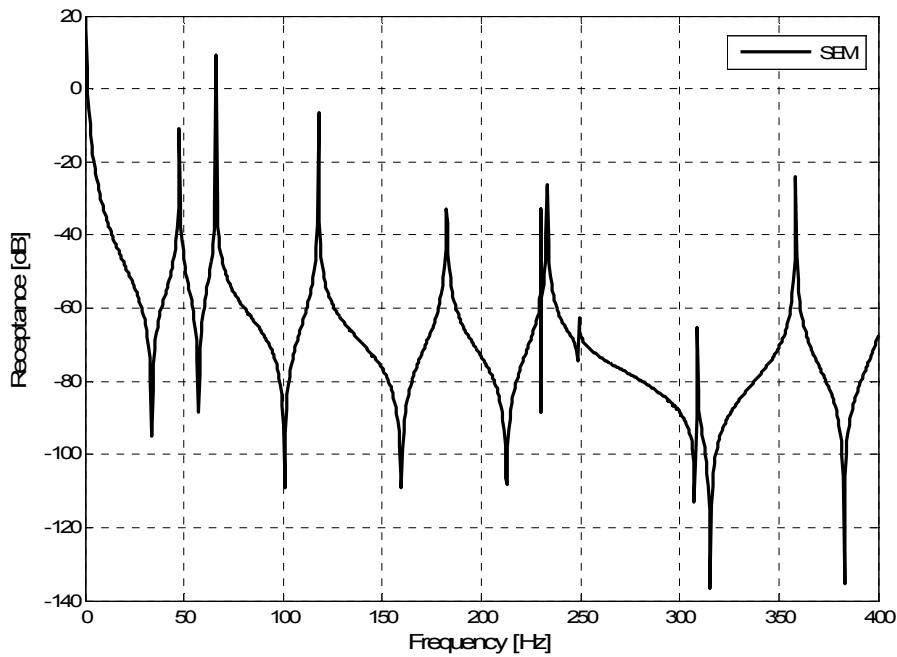


Figure 2: Frequency response function for a low frequency range

The plate first nine natural frequencies were extracted from the FRF and compared with that obtained by Gréniac. Both results are in good agreement as shown in Table 1.

Natural Frequencies									
Gréniac	47,5	65,7	117,4	180,4	227,9	232,6	247,1	306,3	354,9
SEM	47,6	66,1	117,7	182,5	229,7	233,3	249,1	309,0	358,5
Variation (%)	0,21	0,61	0,26	1,16	0,79	0,30	0,81	0,88	1,01

Table1: Comparison of natural frequencies obtained by Gréniac e by SEM

High frequency verification

To verify the accuracy of the method at high frequencies, the FRFs for the same plate, but loaded at point (0.0, -0.1), was obtained for a frequency range of 7.0 - 7.3 KHz. The FRF was obtained by SEM and compared with those from a commercial FEM software. The FEM FRFs were obtained for models with an increasing number of elements. Figure 3 shows that as the number of elements increase, the FRFs obtained from FEM converge to the spectral result obtained with just one spectral element, the same used in the previous example. In all cases, the SEM computational time cost was much lower than those required by FEM.

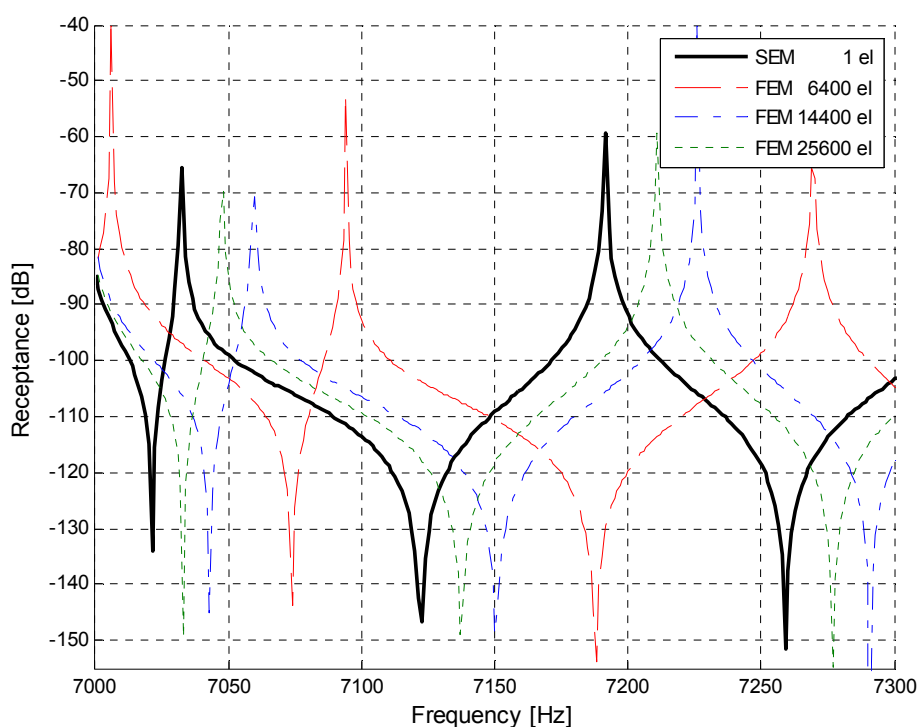


Figure 2: Frequency response function for a high frequency range

CONCLUSIONS

It was developed a spectral element that can be used to model orthotropic thin plates with arbitrary boundary conditions and a detailed description on how to obtain all the terms needed to implement it was presented. The results obtained using SEM proved to be appealing and its accuracy (comparable to the accuracy obtained with FEM) and computational cost make it a potential tool for structural analysis of thin plates in mid and high frequency ranges. Further development to allow the application of any kind of loads, domains with polygonal shapes and structures made of anisotropic materials are been carrying out in order to make it possible to apply the method to a larger number of structures.

REFERENCES

- Arruda, J.R.F., Donadon, L.V., Nunes, R.F. and Albuquerque, E.L., 2004, "On the Modelling of Reinforced Plates in the mid-frequency range", INTERNOISE 2004 - The 13th International Congress and Exposition on Noise Control Engineering, Prague, Czech Republic, August 22-25.
- Banerjee, P.K. and Butterfield, R., 1981, "Boundary Element Methods in Engineering Science", McGraw-Hill Book Company, UK.

- Campos, N.B.F., Arruda, J.R.F., "On The Modeling of Beam Reinforced Thin Plates Using the Spectral Element Method", In: Shock and Vibration: Special issue of ICED 2007, Volume 15, no 3-4, 2008.
- Casimir, J.B., Kevorkian, S. and Vinh, T., 2005, "The dynamic stiffness matrix of two-dimensional elements: application to Kirchhoff's plate continuous elements", *Journal of Sound and Vibration* 287, pp. 571-589
- Desmet, W., Sas, P. and Vandepitte, D., 2001, "An indirect Trefftz-method for the steady-state dynamic analysis of coupled vibro-acoustic systems", *Computer Assisted Mechanics and Engineering Sciences*, 8, 271-288.
- Desmet, W., 2002, "Mid-frequency vibro-acoustic modelling: challenges and potential solutions", in *Proceedings of ISMA2002 - Volume II*, Leuven, Belgium, pp. 835-862.
- Doyle, J.F., 1997, "Wave propagation in structures: spectral analysis using fast discrete Fourier transforms", 2nd ed., Springer-Verlag.
- Gorman, D. J., 1999, "Vibration Analysis of Plates by the Superposition Method" (Series on Stability, Vibration and Control of Systems Series a, Volume 3), World Scientific Publishing Company, 270 p.
- Gunda, R., Vijayakar, S.M. and Singh, R., 1995, "Method of images for the harmonic response of beams and rectangular plates", *Journal of Sound and Vibration* 185(5), pp. 791-808.
- Grédiac, M., Paris, P.A., 1996, "Direct Identification Of Elastic Constants Of Anisotropic Plates By Modal Analysis: Theoretical And Numerical Aspects", *Journal of Sound and Vibration*, 195(3), 401-415.
- Jin, W.G., Cheung, Y.K. and Zienkiewicz, O.C., 1993, "Trefftz method for Kirchhoff plate bending problems", *International Journal for Numerical Methods in Engineering* 36, 765-781.
- Kevorkian, S. and Pascal, M., 2001, "An accurate method for free vibration analysis of structures with application to plates", *Journal of Sound and Vibration* 246 (5), pp. 795-814.
- Kulla, P.H., 1997, "High precision finite elements", *Finite Elements in Analysis and Design* 26, pp. 97-114.
- Lee, U. and Lee, J., 1999, "Spectral-element method of Levy-type plates subjected to dynamic loads", *Journal of Engineering Mechanics*, February, pp. 243-247.
- Lyon, R.H. and DeJong, R.G., 1995, "Theory and Application of Statistical Energy Analysis", Butterworth-Heinemann, Boston.
- Lekhnitskii, S.G. , 1968, "Anisotropic Plates", Gordon and Breach, New York.
- Przemieniecki, J.S., 1985, "Theory of matrix structural analysis", Dover, New York.
- Ungar, E.E., 1961, "Transmission of plate flexural waves through reinforcing beams; dynamic stress concentrations", *Journal of the Acoustical Society of America*, Vol. 33, pp. 633
- Zienkiewicz, O.C. and Taylor, R.L., 2000, "The Finite Element Method – Volume 1: the basis", Fifth Edition, Butterworth-Heinemann, Boston.

RESPONSABILITY NOTICE

The author is the only responsible for the printed material included in this paper.

Self-Heating Effects in Viscoelastic Dampers – Modeling and Experimental Assessment

Jean de Cazenove¹, Antonio Marcos Gonçalves de Lima¹, and Domingos Alves Rade¹

¹ Federal University of Uberlândia-School of Mechanical Engineering, Campus Santa Mônica – P.O.Box 593, CEP 38400-902, Uberlândia-MG, Brazil

Abstract: In this paper a hybrid numerical-experimental investigation on the self-heating phenomenon in viscoelastic materials subjected to cyclic loadings is reported. The main goal is the development of a finite-element-based methodology intended to perform the thermoviscoelastic analysis of viscoelastic dampers accounting for the self-heating effects. Since direct coupling between thermal and structural fields would result in prohibitive computational costs, the problem is solved by assuming weak coupling and the nonlinear coupled thermal and structural analyses are performed in a sequential iterative scheme, implemented in ANSYSTM finite element code. In order to evaluate the accuracy of the modeling procedure, the numerical results obtained in terms of temperature evolutions are compared with those generated by experiments carried-out in laboratory. In the numerical and experimental studies it is considered the influence of various factors on self-heating, such as excitation frequency and excitation amplitude. It is shown, both numerically and experimentally, that the temperature rises can be significant enough to jeopardize the effectiveness of viscoelastic dampers. Also, the numerical procedure suggested has shown to be adequate for predicting the self-heating effects in complex viscoelastic devices of practical interest.

Keywords: viscoelastic damping, thermoviscoelasticity, self-heating, finite elements

INTRODUCTION

In the context of passive control of vibrations, viscoelastic materials have been intensively investigated lately, since they present great efficiency in mitigating vibrations at moderate application and maintenance costs. However, when these materials are subjected to cyclic loadings, especially in applications where they are applied as discrete devices, such as translational or rotational mounts, a significant amount of energy is transformed into heat within the material volume (Cazenove et al., 2009; Gopalakrishna and Lai, 1998). This phenomenon, known as *self-heating*, causes local temperature increase, and may affect significantly the damping capability of damping devices, since the mechanical properties of viscoelastic materials are highly dependent on temperature (Nashif et al., 1985; Christensen, 1982). According to Gopalakrishna and Lai (1998), the local temperature values inside the viscoelastic materials used in tall buildings can increase by 10°C in a few seconds when a storm occurs. Also, as recalled by Lesieutre and Govindswamy (1995), self-heating may result in two distinct situations, namely: (i) thermal equilibrium, which occurs after a large number of cycles if the influence of the temperature on the mechanical properties is small enough; (ii) uncontrolled temperature rise inside the viscoelastic media, known as *thermal runaway*, if the temperature related to the glass transition region is reached (Lesieutre and Godwinswamy, 1995).

The determination of the temperature distribution within viscoelastic materials subjected to cyclic loadings is an interesting nonlinear multiphysical problem, which involves the resolution of a coupled structural-thermal problem to determine strain rates and temperature evolution. Gopalakrishna and Lai (1998) have proposed an iterative methodology to determine the equilibrium temperature distribution inside viscoelastic materials applied as translational mounts. Rittel (1999) and Rittel and Rubin (2000) have defined a thermal conversion parameter as a fraction of the mechanical power dissipated by the viscoelastic effects. Those authors have shown that this parameter is strongly dependent on the strain rate and amplitude of the cyclic loading. Moreover, as it is very difficult to estimate, its value has been assumed rather arbitrarily in the range [0.1 – 1.0].

Due to the fact that the finite element (FE) method has become the most used method for the analysis and design of complex engineering problems, the prediction of the temperature distribution in a viscoelastic material due to self-heating is based on such models. Since direct coupling between thermal and structural fields would result in prohibitive computational costs, the main goal is the development of a sequential iterative scheme based on finite element method intended to perform the thermoviscoelastic analysis of discrete viscoelastic dampers accounting for the self-heating phenomenon. This iterative solution procedure was implemented in ANSYSTM finite element software by using ANSYS Parametric Design Language (APDL).

In the remainder, after the presentation of the main theoretical aspects, the description of a hybrid numerical-experimental investigation on the self-heating phenomenon in a two-dimensional viscoelastic mount subjected to cyclic loadings is reported. In the numerical and experimental studies it was considered the influence of various factors on self-heating, such as excitation frequency, excitation amplitude, and thermal conversion ratio. Also, given the difficulty

in estimating thermophysical parameters involved in the numerical model, an identification procedure based on numerical optimization was implemented in order to find the optimal values of those parameters by minimizing a cost function representing the differences between measured and model-predicted temperatures. Based on the obtained results, it is possible to conclude about the effectiveness of the numerical methodology proposed in order to determine the temperature evolution in viscoelastic materials generated by the self-heating phenomenon. Also, it is demonstrated that the self-heating phenomenon is of primary importance for the design of viscoelastic dampers in practical applications.

FINITE ELEMENT MODELING OF VISCOELASTIC SYSTEMS

By neglecting other forms of damping, the global FE equations of motion in the frequency domain of a viscoelastic structure, can be expressed as follows (de Lima et al., 2010):

$$\mathbf{Z}(\omega, T)\mathbf{Q}(\omega, T) = \mathbf{F}(\omega) \quad (1)$$

where $\mathbf{Z}(\omega, T) = [\mathbf{K}_e + G(\omega, T)\bar{\mathbf{K}}_v - \omega^2\mathbf{M}]$ is the so-named dynamic stiffness matrix, $\mathbf{M} \in R^{N \times N}$ is the mass matrix, $\mathbf{K}_e \in R^{N \times N}$ is the stiffness matrix corresponding to the purely elastic parts, and $G(\omega, T)\bar{\mathbf{K}}_v \in C^{N \times N}$ is the frequency- and temperature-dependent viscoelastic stiffness matrix. N is the number of degrees-of-freedom (DOF's), and $\mathbf{Q}(\omega, T) \in R^N$ and $\mathbf{F}(\omega) \in R^N$ are, respectively, the vectors of the amplitudes of the harmonic generalized displacements and external loads. The complex modulus function of the viscoelastic material can be decomposed into real and imaginary parts, according to $G(\omega, T) = G'(\omega, T) + iG''(\omega, T)$ as storage, where $G'(\omega, T)$ and $G''(\omega, T)$ are the storage and loss *moduli*, respectively. Hence, the dynamic stiffness matrix can be cast in the following form:

$$\mathbf{Z}(\omega, T) = [\mathbf{K}^*(\omega, T) + i\omega\mathbf{C}_{eq}(\omega, T) - \omega^2\mathbf{M}] \quad (2)$$

where $\mathbf{K}^*(\omega, T) = \mathbf{K}_e + G'(\omega, T)\bar{\mathbf{K}}_v$, $\eta(\omega, T) = G''(\omega, T)/G'(\omega, T)$ is the so-named loss factor of the viscoelastic material, and $\mathbf{C}_{eq}(\omega, T) = \frac{\eta(\omega, T)G'(\omega, T)}{\omega}\bar{\mathbf{K}}_v$ is the equivalent viscous damping matrix.

Equation (2) shows that the introduction of the viscoelastic effect into the finite element model gives rise to a system of equations of motion in the frequency domain of the same form as those based on the assumption viscous damping matrix proportional to the stiffness matrix, with a frequency- and temperature-dependent proportionality coefficient given by $\alpha(\omega, T) = \eta(\omega, T)/\omega$. This fact can be explored for the computation of the dynamic responses of viscoelastically damped components using commercial available FE codes, for which the option for proportional damping is usually available. Such possibility is considered in this paper. Also, it must be emphasize that in the formulation of Eq. (1), it was assumed the widely accepted hypothesis of a constant (frequency-independent) Poisson ratio for the viscoelastic material. As a result, the longitudinal modulus $E(\omega, T)$ has been assumed to be proportional to the shear modulus $G(\omega, T)$ by the relation $G(\omega, T) = E(\omega, T)/2(1 + \nu)$. It should be mentioned that this assumption has been argued in some studies, based on experimental evidences (Moreau, 2007). Consequently, one of the two *moduli* can be factored-out of the viscoelastic stiffness matrix, according to $\mathbf{K}_v(\omega, T) = G(\omega, T)\bar{\mathbf{K}}_v$ in the present case. Also, it should be noted that any pair formed from the parameters $G'(\omega, T)$, $G''(\omega, T)$ and $\eta(\omega)$ completely characterizes the dynamic behavior of viscoelastic materials in the frequency domain. This model is adopted in this study since it enables the use of the data commonly provided by the manufacturers of viscoelastic materials in terms of storage *modulus* and loss *modulus* versus frequency, or storage modulus and loss factor versus frequency, without any need of performing curve-fitting.

THERMOVISCOELASTIC FORMULATION

Consider the following transient heat equation that expresses the relationship between the heat generation rate and the spatial and temporal variations of the temperature, in which thermo-elastic effects are neglected (Rittel, 1999):

$$q_g + k\nabla^2 T(t, x, y, z) = \rho c_p \dot{T}(t, x, y, z) \quad (3.a)$$

with the following thermal boundary conditions:

$$\begin{cases} T = T_0 & \text{in } \partial\Omega_D \\ q = q_0 & \text{in } \partial\Omega_N \\ q = h(T - T_\infty) & \text{in } \partial\Omega_C \end{cases} \quad (3.b)$$

where k , ρ and c_p represent, respectively, the heat conductance, the mass density and the specific heat coefficient of the material. The term $k\nabla^2 T(t, x, y, z)$ represents the heat conduction that is obtained by applying the Fourier's law to an infinitesimal material volume (Lienhard and Lienhard, 2004), while $\rho c_p \dot{T}(t, x, y, z)$ is the heat stored within the material. Equation (3.b) shows the thermal boundary conditions applied on the boundary of the domain, $\partial\Omega$, in which, $T_0(t, x, y, z)$, $q_0(t, x, y, z)$, $h(x, y, z)$ and $T_\infty(t, x, y, z)$ represent, respectively, the imposed temperatures (Dirichlet conditions on $\partial\Omega_D$), the heat flow (Neumann conditions on $\partial\Omega_N$), the natural convection coefficient, and the ambient temperature.

The heat generation rate q_g is related to the dissipated mechanical power, \dot{w}_m , by the following expression:

$$q_g = \beta \dot{w}_m \quad (4)$$

where β represents the thermal conversion ratio defined as a fraction of the mechanical power dissipated by the viscoelastic effects. For most viscoelastic polymers, this parameter is strongly dependent on the strain rate and the amplitude of the cyclic loading. The complementary part of the dissipated power, $(1-\beta)\dot{w}_m$, is stored within the material through microstructural changes (Rittel and Rubin, 2000).

For a linear viscoelastic material subjected to sinusoidal stresses, $\boldsymbol{\sigma}(t) = \boldsymbol{\sigma}_0 \sin(\omega t)$, the strain response is $\boldsymbol{\varepsilon}(t, \omega, T) = \boldsymbol{\varepsilon}_0(\omega, T) \sin(\omega t + \delta)$ where ω is the frequency, and δ is the phase angle. Thus, the dissipated mechanical power can be expressed as the product of the components of the stress vector and strain rate vector as follows:

$$\dot{w}_m(t, \omega, T) = \boldsymbol{\sigma}(t)^T \dot{\boldsymbol{\varepsilon}}(t, \omega, T) = G(\omega, T) \boldsymbol{\varepsilon}^T(t, \omega, T) \bar{\mathbf{C}} \dot{\boldsymbol{\varepsilon}}(t, \omega, T) \quad (5)$$

where $\mathbf{C}(\omega, T) = G(\omega, T) \bar{\mathbf{C}}$ is the matrix of frequency- and temperature-dependent material properties, defined in such a way that $\boldsymbol{\varepsilon}(t, \omega, T) = \mathbf{C}^{-1}(\omega, T) \boldsymbol{\sigma}(t)$. Upon introduction of the complex modulus function $G(\omega, T) = G'(\omega, T) + iG''(\omega, T)$ into Eq. (5), it is possible to show that the contribution of the imaginary part to the dissipated energy associated to the purely elastic power stored in the viscoelastic material vanishes over a cycle of vibration. On the other hand, the real part corresponds to the viscous power, which is given by:

$$\dot{w}_m(t, \omega, T) = -\omega G''(\omega, T) \boldsymbol{\varepsilon}_0^T(\omega, T) \bar{\mathbf{C}} \boldsymbol{\varepsilon}_0(\omega, T) \sin^2(\omega t + \delta) \quad (6)$$

As recalled by Gopalakrishna and Lai (1998), the direct application of Eq. (6) in order to compute the heat generation rate for a coupled thermo-mechanical analysis would result in prohibitive computational costs. Thus, the term $\sin^2(\omega t + \delta)$ is substituted by its average value, resulting in the following expression for the heat generation rate:

$$q_g(\omega, T) = |\beta \dot{w}_m(t, \omega, T)| = \frac{1}{2} \beta \omega G''(\omega, T) \boldsymbol{\varepsilon}_0^T(\omega, T) \bar{\mathbf{C}} \boldsymbol{\varepsilon}_0(\omega, T) \quad (7)$$

Associating equations (3) and (7) one writes:

$$\frac{1}{2} \beta \omega G''(\omega, T) \boldsymbol{\varepsilon}_0^T(\omega, T) \bar{\mathbf{C}} \boldsymbol{\varepsilon}_0(\omega, T) + k\nabla^2 T(t, x, y, z) = \rho c_p \dot{T}(t, x, y, z) \quad (8)$$

Equation (8) represents the thermoviscoelastic problem to be solved in order to predict the temperature rise when the viscoelastic material is submitted to harmonic cyclic loading. The following features of this mathematical model must be pointed-out: (i) it is, in general, a nonlinear system of equations as the loss modulus is most frequently a nonlinear function of the temperature to be determined. Thus, exact solutions cannot be easily obtained and numerical resolution schemes must be used; (ii) the computation of the complex modulus as a function of the temperature in the context of the resolution scheme can be made either by considering the nomogram data of the viscoelastic provided by the manufactures or by using the reduce frequency and shift factor concepts (Drake and Soovere, 1984); (iii) it enables to account for general strain states (two- or three-dimensional) by the proper inclusion of the strain components into the strain vector; (iv) it is a coupled thermal-mechanical problem, as strains and temperature are interrelated.

In order to solve the coupled problem (8) by using FE modeling procedures, the heat generation rate must be calculated for each viscoelastic element from displacement amplitudes obtained from the harmonic analyses. This can be done by integrating the first term appearing in Eq. (8) over the volume of each viscoelastic element, as follows:

$$q_g^{(e)}(\omega, T) = \frac{\beta \omega \eta(\omega, T)}{2V_{(e)}} \mathbf{u}_{(e)}^T \mathbf{K}'_v(\omega, T)_{(e)} \mathbf{u}_{(e)} \quad (9)$$

where $\mathbf{K}'_v(\omega, T)_{(e)}$ is the real part of the viscoelastic stiffness matrix and superscript (e) indicates quantities defined at element level.

ITERATIVE RESOLUTION PROCEDURE

Based on the previously mentioned features regarding the coupled problem to be solved, in this paper, the main goal is the development of a FE-based methodology intended to perform the thermoviscoelastic analysis accounting for the self-heating phenomenon. Since direct coupling between thermal and structural fields would result in prohibitive computational costs, the problem was solved by assuming weak coupling between thermal and mechanical fields (Schapery, 1964) and the nonlinear coupled problem was solved by using the sequential iterative scheme shown in Fig. 1.

The iterative solution procedure was implemented in ANSYS™ finite element software by using the ANSYS Parametric Design Language (APDL), which offers the possibility of defining the whole FE model consisting in two distinct solution environments, namely the transient thermal and harmonic structural fields, considering the same discretization mesh. The main steps of the iterative procedure can be summarized as follows: (i) at the beginning of the process, the viscoelastic stiffness and equivalent damping matrices for an excitation frequency ω_0 and for an initial temperature value T_0 are computed, taking into account the mechanical boundary conditions; (ii) next, the strain rates for each viscoelastic element are computed by performing harmonic structural analyses. This enables to compute the heat generation rate according to Eq. (8); (iii) next, a new set of temperature values are generated by performing a transient thermal analysis, taking into account the thermal boundary conditions. A new iteration is initiated and the structural and thermal analyses are performed based on the latest set of temperature values generated, taking into account updated viscoelastic materials properties. The iterative process is stopped when a convergence criterion based on temperature variations between two consecutive iterations is satisfied within a specified tolerance.

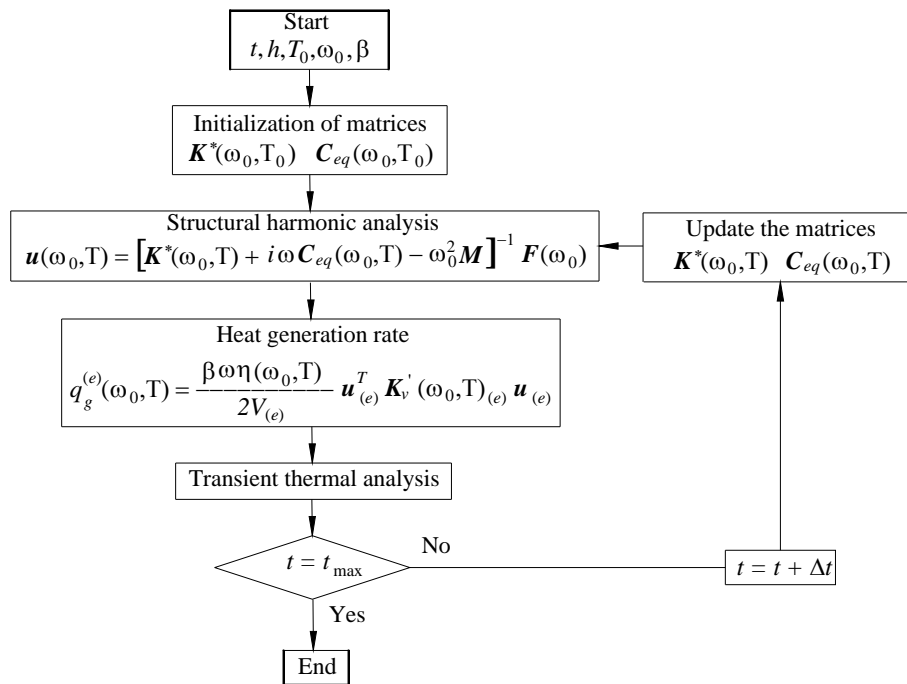


Figure 1 – Flow chart of the iterative procedure implemented in ANSYS™ code to solve the coupled thermomechanical problem

NUMERICAL SIMULATION

In this section, numerical simulations are presented in order to illustrate the main features and capabilities of the thermomechanical modeling methodology. In the simulations that follow it is considered the commercially available viscoelastic material VHB 9469™ manufactured by 3M™, presented in the form of adhesive tape. Also, a tabular representation of the mechanical properties of such material in terms of the storage and loss moduli measured at different temperatures for an excitation frequency was generated from the reduced frequency nomogram provided by the manufacturer.

Numerical simulations were performed with the translational viscoelastic mount consisting of two viscoelastic layers inserted between three steel plates, with the intermediate plate subjected to a cyclic loading, $F(t) = F_0 \sin(2\pi f_0 t)$, as depicted in Fig. 2, with the indicated geometrical dimensions and the mechanical boundary conditions. The main interest is to investigate the influence of the excitation frequency, f_0 , and amplitude of the excitation, F_0 , on the

temperature rise in the viscoelastic media due to the self-heating phenomenon. Also, Fig. 2 shows its associated finite element mesh, in which, the analysis is two-dimensional and symmetric according to the plane of symmetry *a-a*. Table 1 provides the values of the physical properties used to perform the thermal analysis.

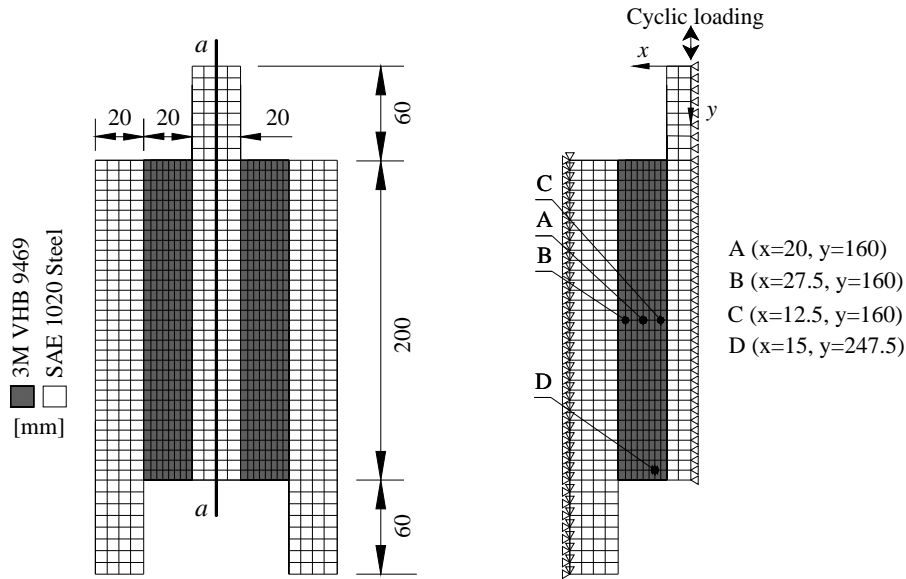


Figure 2 – Geometric dimensions of the translational damper and its FE mesh with the applied mechanical boundary conditions.

Table 1 – Thermal properties for the SAE 1020 steel and VHB 9469 material

Material	ρ [kg/m ³]	c_p [J/(kg.K)]	k [W/(m.K)]	β
VHB 9469	1100	2000	0.16 ⁽¹⁾	0.8
SAE 1020	7850	476	35	0

⁽¹⁾ From 3M™ technical report

In the thermomechanical simulations, the discretization was done using two-dimensional coupled field elements, in which, for the structural analysis, the 2D plane stress element *PLANE42* was used, having eight nodes and three DOF's per node (displacements in *x*, *y* and *z* directions). For the thermal analysis, the corresponding 2D element *PLANE55* was chosen, having the same number of nodes and one DOF per node (temperature). The total number of mechanical and thermal DOF's are 1677 and 559, respectively. As thermal boundary conditions, it is assumed heat transfer by natural convection between the surfaces of the outer-steel plates and the surrounding air, with $h = 15 \text{ W}/(\text{m}^2\text{K})$, and an ambient temperature value of $T_\infty = 25^\circ\text{C}$. This value is assumed as uniform initial temperature in the damper at the beginning of the simulation. The computations performed according to the iterative procedure presented in the flow-chart of Fig. 1, consist in obtaining the temperature values at node A located on the middle-plane of the viscoelastic layer, as indicated in Fig. 2.

Figure 3 shows the temperature evolutions for three different situations as depicted on the same figure. From Figs. 3(a) and 3(c) it is interesting to note that, as the excitation frequency and the amplitude of the excitation increase, the self-heating effects become more pronounced, resulting in a significant augmentation of the temperature values in the viscoelastic material. Temperature increases are found to be as high as 10.4°C. It will be shown later on that such temperature variation can cause strong influence on the stiffness and damping properties of the viscoelastic material. Also, one can identify a progressive stabilization of the temperatures in the loading phase (from $t = 0\text{s}$ to $t = 12000\text{s}$), and a strong and immediate decrease of the temperature values after the removal of the loading.

Figure 4 enables to verify the influence of the self-heating on the viscoelastic material properties for the translational mount for $\beta = 0.8$, $f_0 = 10\text{Hz}$ and $F_0 = 600\text{N}$. It is observed that the temperature rise due to the self-heating in the viscoelastic material leads to maximum decreases of the storage modulus and loss factor of 26% and 63%, respectively. Clearly, variations of such magnitudes can lead to significant decrease of the damping performance of viscoelastic dampers in practical engineering applications.

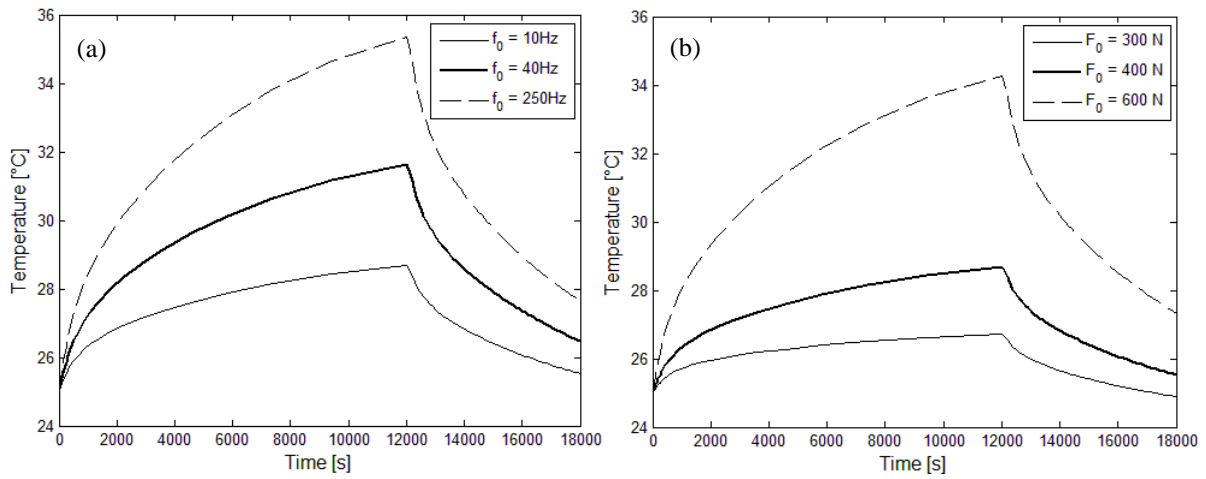


Figure 3 – Temperature evolution at point A: (a) $F_0 = 400N$, $\beta = 0.8$; (b) $\beta = 0.8$, $f_0 = 10Hz$.

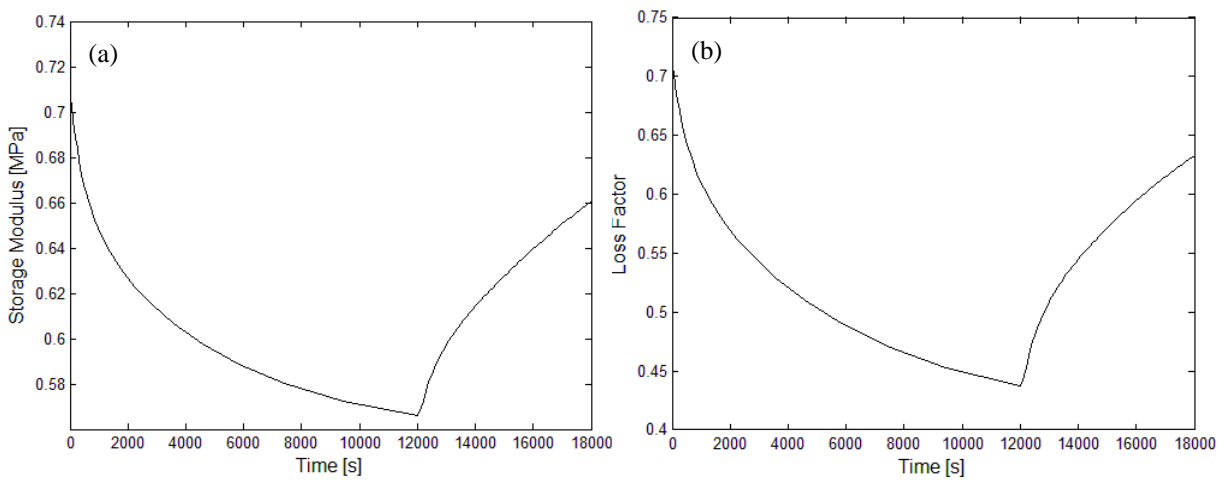


Figure 4 – Storage modulus (a) and loss factor (b) at point A as a function of the time generated by the self-heating.

EXPERIMENTAL STUDY

This section is dedicated to the experimental validation of the numerical methodology proposed to solve the thermomechanical problem. Within this context, a curve-fitting procedure has been implemented in order to identify the thermal parameters for the viscoelastic material based on an optimization procedure. Figure 5(b) shows the translational mount constructed by inserting two 5mm thick layers of 3M™ VHB 9469 rubber-like material between three rigid steel blocks attached to a rigid frame, which is mounted in a universal test machine, as shown in Fig. 5(a). The thermal properties assumed for the steel and the viscoelastic material, are given in Tab. 1. Temperature measurements were performed on six points of the specimen, corresponding to the locations of the thermocouples, as indicated in Fig. 5(c).

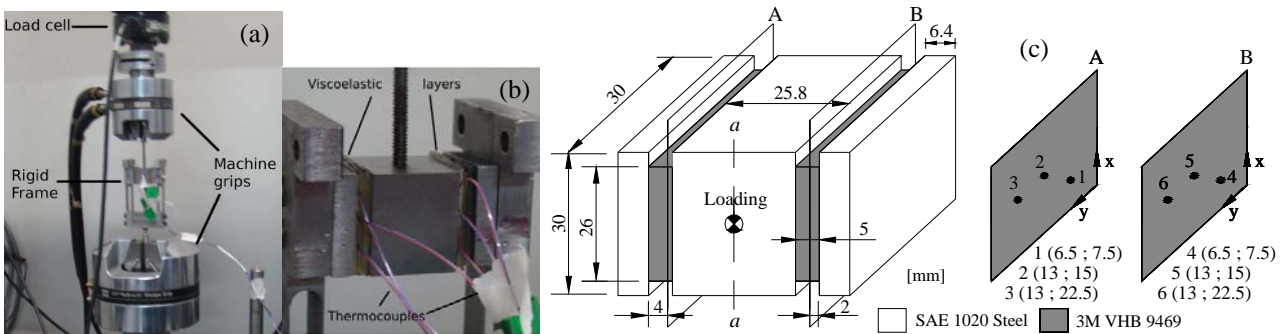


Figure 5 – (a) translational damper mounted in a universal test machine; (b) detail of the viscoelastic damper; (c) geometric dimensions of the damper and illustration of the planes used to fix the thermocouples 1 to 6.

The temperatures at the measurement locations for the six test scenarios described in Tab. 2 were acquired by using a signal analyzer Agilent™ 34970. Also, for all tests, a vertical displacement $u(t) = u_0 \sin(2\pi f_0 t)$ has been imposed on the translational damper during 3360 seconds.

Table 2 – Definition of the parameters used in the experimental tests.

Loading parameters	Test scenario			
	(a)	(b)	(c)	(d)
f_0 [Hz]	10		15	
u_0 [mm]	1	1.5	1	1.5

Among the measurement points, those identified by numbers 2 and 5 have been chosen for the presentation of the results shown in Fig. 6, which confirm the influence of the displacement amplitude and frequency on the self-heating phenomenon in the viscoelastic media. Also, it is apparent that the displacement excitation amplitude has a more significant influence than the excitation frequency on the temperature evolutions. This can be understood by examining Eq. 9, which shows that the generated heat depends linearly on the excitation frequency and on the square of the displacement amplitude. Also, it can be perceived a progressive stabilization of the temperatures during the loading phase, and a strong and immediate decreasing of the temperatures after the removal of the cyclic loading. Furthermore, it is interesting to note, for all tests, the presence of a first phase in the beginning of the loading process during, approximately, 120 seconds, characterized by a fast increase in the temperature values at both measurement points. The second phase is characterized by the stabilization of the temperatures, and after the removal of the loading, a steep decrease in the temperature values is observed. These experimental observations are in agreement with the results obtained from numerical simulations.

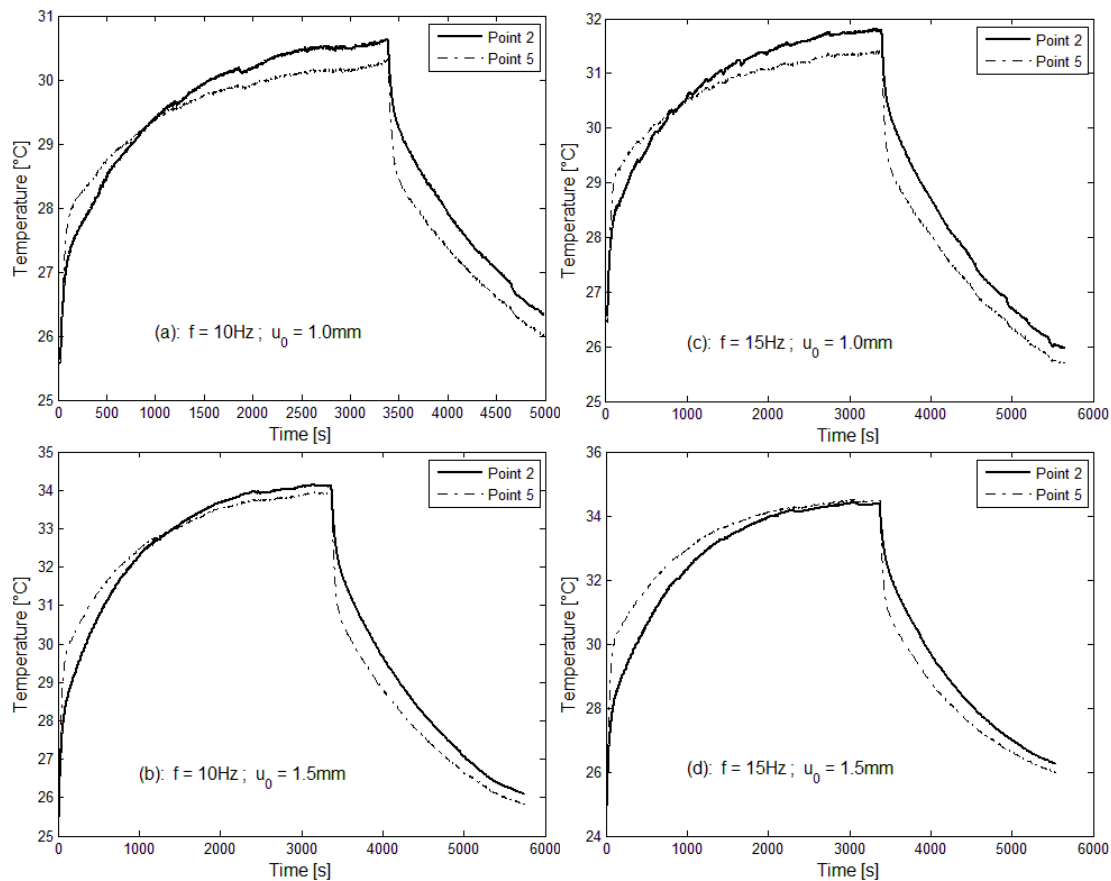


Figure 6 – Experimental temperature values for all tests for points 2 and 5.

Curve-fitting procedure

In the previously section, the obtained experimental temperature values for the translational mount subjected to a cyclic loading due to the self-heating phenomenon have been shown. However, the direct comparison between these results with those obtained from the numerical simulations would not possible since, for this later, the values of the thermal conversion ratio, β , and the natural convection coefficient, h , have been assumed arbitrarily, based on values proposed in the literature. It is widely known that these two parameters have a range of values depending upon several conditions such as the shape and the characteristics of the viscoelastic surface, and the operational conditions such as

the strain amplitudes. Thus, having a numerical model at disposal, it was found to be interesting to develop a curve-fitting procedure experimental data in order to identify these parameters.

The experimental tests described in Tab. 2 have been performed in similar environmental conditions, in such a way that the natural convection coefficient can be assumed to be the same for all the tests. However, the thermal conversion ratio is strongly dependent on the loading conditions. Thus, the following optimization strategy to fit this parameter has been proposed: (i) first, the parameters β and h are identified by using Genetic Algorithms (Vanderplaats, 2005) to minimize the objective function $F_{obj} = \sum_{i=1}^n (T_{exp}^i - T_{sim}^i)^2$ where T_{sim}^i and T_{exp}^i are the numerical and the experimental temperature values, respectively, and n is the number of points considered in the experimental results of test scenario (a), chosen as reference. The optimal parameter, h_{opt} , obtained is used in the next identification processes and the interest in the next step is to identify the optimal values of the thermal conversion ratio for the tests (b), (c) and (d), by using the golden section algorithm (Vanderplaats, 2005).

Figure 7(a) compares the typical temperature evolution predicted by the adjusted FE model using the optimal values, $\beta_{opt} = 0.1755$ and $h_{opt} = 13.016 \text{ W.m}^{-2}.\text{K}^{-1}$, with the experimental counterparts obtained at point 2 for test scenario (a). It can be noted that the experimental temperature evolution is approximated quite well by the numerical predictions, demonstrating that the numerical-computational procedure suggested is adequate for predicting the self-heating effects in discrete viscoelastic damping devices. For the other experimental tests the same curve-fitting procedure has been applied, in which the interest is to optimize the parameter β by considering the $h_{opt} = 13.016 \text{ W.m}^{-2}.\text{K}^{-1}$ obtained previously. The optimal thermal conversion ratios obtained were $\beta_{opt} = 0.15$ for test (b), $\beta_{opt} = 0.108$ for test (c) and

$\beta_{opt} = 0.0178$ for test (c). It can be seen that as the strain amplitude increases, the thermal conversion ratio decreases. This phenomenon is due to the fact that a complementary part of the dissipated power is stored in the viscoelastic material through microstructural changes. As a result, as the strain amplitudes increase, the microstructural modifications become more pronounced, and a lower fraction of the dissipated energy is converted into heat.

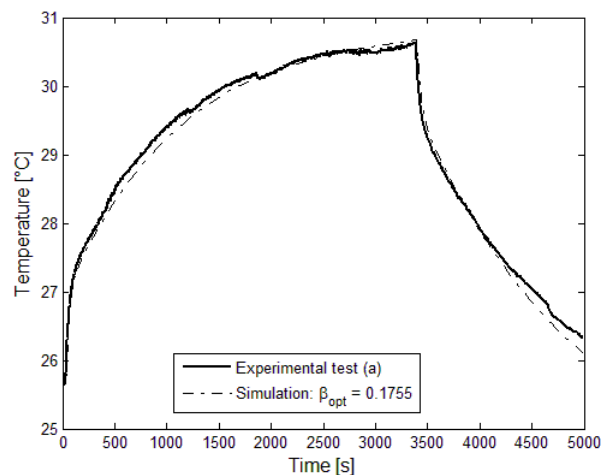


Figure 7 – Comparison between typical experimental and optimal numerical temperature evolutions in the translational damper at point 2 for test (a).

CONCLUDING REMARKS

A FE-based methodology for analysing the self-heating phenomenon in discrete viscoelastic damping devices has been suggested and evaluated by means of numerical simulations and experimental tests. The main feature of the modelling strategy is the use of a sequential iterative scheme by assuming a weak coupling between the thermal and structural fields, which has been implemented in ANSYS™ code by using the ANSYS Parametric Design Language (APDL). Also, one advantage of the proposed methodology is its ability to incorporate the viscoelastic behaviour in commercial FE codes based on the concept of equivalent damping matrix and the complex modulus function, in which, the values of the storage modulus and loss factor provided by the material manufacturers, accounting for the dependency of the viscoelastic properties on frequency and temperature, are used. Another aspect that must be pointed out in the thermal analysis of viscoelastic materials is the difficulty in estimating their thermal properties. To cope with this problem, a curve fitting procedure based on the formulation of an optimization problem has been suggested and implemented.

The numerical and experimental results show that the frequency and the amplitude of the cyclic loading can affect significantly the temperature evolution generated by the self-heating phenomenon. As a result, one can observe an immediate strong variation in the storage modulus and loss factor of the viscoelastic material, affecting its damping capability. Hence, one conclude that the estimation of the temperature distribution in viscoelastic materials subjected to

cyclic loading generated by the self-heating phenomenon is of primary importance for the design of viscoelastic damping devices in practical engineering applications.

ACKNOWLEDGMENTS

The authors are grateful to the Brazilian Research Council – CNPq for the continued support to their research work, especially through research projects 480785/2008-2 (A.M.G. de Lima) and 306822/2009-1 and 482963/2009-3 (D.A. Rade), and to Minas Gerais State Agency FAPEMIG for the financial support to their research activities.

REFERENCES

- Cazenove, J., de Lima, A.M.G., Rade, D.A., “Numerical of Self-heating Effects in Viscoelastic Dampers”, Proceedings of the 20th International Congress of Mechanical Engineering (COBEM), Gramado, RS, Brazil, 2009.
- Christensen, R.M., 1985, “Theory of viscoelasticity: An introduction”, Academic Press Inc., New York, 2nd edition.
- de Lima, A.M.G., Rade, D.A. and Léopore-Neto, F.P., 2009, “An efficient modeling methodology of structural systems containing viscoelastic dampers based on frequency response function substructuring”, *Mechanical System and Signal Processing*; Vol. 23, No. 4, pp. 1272-1281.
- Drake, M.L. and Soovere, J., 1984, “A design guide for damping of aerospace structures, in: AFWAL Vibration Damping Workshop Proceedings, Vol. 3, Atlantic City, USA.
- Gopalakrishna, H.S. and Lai, M.L., 1998. “Finite Element Heat Transfer Analysis of Viscoelastic Damper for Wind Applications”, *Journal of Wind Engineering and Industrial Aerodynamics*, Vol. 77, pp. 283–295.
- Lesieutre, G.A. and Govindswamy, K., 1995. “Finite element modeling of frequency-dependent dynamic behavior of viscoelastic materials in simple shear,”. *International Journal of Solids and Structures*, Vol. 33, pp. 419–432.
- Lienhard, J.H.I. and Lienhard, J.H.V., 2004, “A Heat Transfer Textbook”, Third edition, Phlogiston Press, Cambridge.
- Moreau, A., “Identification de propriétés viscoélastiques des matériaux polymères par mesures de réponses en fréquences de structures », Doctorate thesis, INSA, Rouen, France, 2007.
- Nashif, A. D., Jones, D. I. G. and Henderson, J. P., 1985, “Vibration damping”, John Wiley & Sons, New York.
- Rittel, D., 1999, “On the Conversion of Plastic Work to Heat during High Strain Rate Deformation of Glassy Polymers”, *Mechanics of Materials*, Vol. 31, pp. 131-139.
- Rittel, D. and Rubin, Y., 2000, “An Investigation of the Heat Generated during Cyclic Loading of Two Glassy Polymers. Part II: Thermal Analysis”, *Mechanics of Materials*, Vol. 32, pp. 149-159.
- Schapery, R.A., 1964, “Effect of cyclic loading on the temperature in viscoelastic media with variable properties”, *AIAA Journal*, Vol. 2, No. 5, pp: 827-835.
- Vanderplaats, G.N., 2005, “Numerical Optimization Techniques for Engineering Design”, Fourth Edition Vanderplaats Research and Development, Inc. Colorado Springs, USA.

RESPONSIBILITY NOTICE

The authors are the only responsible for the printed material included in this paper.

Application of a Computer Vision Method and a Kalman Filter to Identify the Kinematics and the Dynamics of a Scaled-Model Riser

Martins, F.P.R.¹, Trigo, F.C.², Silva Jr., H.C.³, Fleury, A.T.⁴

¹ Escola Politécnica da Universidade de São Paulo, Av. Prof. Mello Moraes, 2231, S. Paulo, flavius.martins@poli.usp.br

² Escola Politécnica da Universidade de São Paulo, Av. Prof. Mello Moraes, 2231, S. Paulo, flavio.trigo@poli.usp.br

³ Instituto de Pesquisas Tecnológicas do Estado de S. Paulo, Av. Prof. Almeida Prado, 532, S. Paulo, helio.jr@ipt.br

⁴ Centro Universitário da FEI, Av. Humberto de Alencar Castelo Branco, 3972, S.B. do Campo, ag.fleury@fei.edu.br

Abstract: Aiming at overcoming the difficulties derived from the traditional camera calibration methods to record the underwater environment of a towing tank where experiments of scaled-model risers were carried on, a computer vision method, combining traditional image processing algorithms and a self-calibration technique was implemented. This method was used to identify the coordinates of control-points viewed on a scaled-model riser submitted to a periodic force applied to its fairlead attachment point. To study the observed motion, the riser was represented as a pseudo rigid body model (PRBM) and the hypotheses of compliant mechanisms theory were assumed in order to cope with its elastic behaviour. The derived Lagrangian equations of motion were linearized and expressed as a state-space model in which the state variables include the generalized coordinates and the unknown generalized forces. The state-vector thus assembled is estimated through a Kalman Filter. The estimation procedure allows the determination of both the generalized forces and the tension along the cable, with statistically proven convergence.

Keywords: Dynamics, Kalman filter, compliant mechanisms, computer vision, motion analysis

NOMENCLATURE

θ_i = PRBM's angular displacements

$\dot{\theta}_i$ = PRBM's angular velocities

$\ddot{\theta}_i$ = PRBM's angular accelerations

K_i = PRBM's spring coefficients

K_θ = PRBM's standard spring coefficients

L = PRBM's bar lengths

γ = PRBM's largest bar length to actual bar length ratio

m = PRBM's bar mass

p = weight per length ratio

p_s = underwater weight per length ratio

E = material modulus of elasticity

I = PRBM's bar section area inertia moment

T = kinetic energy

V = potencial energy

L = Lagrangian

F_{θ_i} = generalized force at node i

F = traction force

INTRODUCTION

The non-intrusive characteristics of the image-based instrumentation necessary to implement motion analysis is an important advantage of this approach compared to the classical measurement methods based on the use of accelerometers and load cells. Successive advances in the area of computer vision, concerning video segmentation, object tracking and camera calibration, have also contributed to the application of image-based methods to the analysis of kinematics phenomena that are difficult to measure, like the human motion (Moeslund *et al.*, 2006), or that occur in regions of difficult access, as the underwater environments (Shortis *et al.*, 2009).

Recently, this technique has been included in the palette of experimental methods of the Oceanic and Naval Engineering Center of IPT, in order to improve the quality of the measurements required by the hydrodynamics tests in a towing tank with scaled-models of ships and oceanic structures like platforms and risers. Although these measurements have been successfully accomplished with the aid of a commercial motion analysis tool, the camera calibration algorithms (Schalkoff, 1989) adopted by this software assume the use of calibration objects to previously measure the three-dimensional space according to a metrological procedure difficult to be done in an underwater environment.

To cope with the various constraints imposed by the measurement environment, several camera self-calibration methods have been proposed in the literature (Hartley, 1997; Valdés and Ronda, 2005; Habed and Boufama, 2006; Menuet *et al.*, 2007). Since these methods are based on invariant geometrical properties of the projective space (Veblen and Young, 1938; Ayres Jr., 1967), they do not depend on the use of calibration artifacts and, consequently, give rise to a calibrated space that is not limited by the volume of those objects. Such characteristics are specially helpful in the approach of underwater experiments with scaled-model risers (long flexible ducts used by the petroleum industry to pump oil and natural gas to the platforms).

Although the dynamics of cables has been longly approached in the early literature of theoretical mechanics (Beghin, 1952; Pérès, 1962), the recent technological advances observed in the petroleum industry concerning subsea fields extraction has fostered the research of this subject. Pesce (1997) performed a thorough investigation about the static and dynamic behaviours of risers under two-dimensional configurations. Using the theory of thin rods, it was shown that the effect of flexural rigidity is restricted to the regions close to the extremities of the riser; the dynamic model, on the other hand, was formulated as the solution of a perturbation problem around the equilibrium configuration. Both models – the static and the dynamic – were validated against experimental results. Using the finite element program ANSYS, Campos (1997) developed a computational non-linear model for a catenary riser, whose responses, concerning the dynamic bending moments near the touchdown point, are close to the ones derived from the application of previously proposed analytical models. Takafuji (2010), likewise, generated dynamical models through the finite element method, representing the catenary riser by beam elements. Firstly, a complete non-linear dynamical model was analysed using a time-domain technique. Then, the non-linearities of the original model were removed and a frequency-domain technique was applied, giving rise to results that compared well with the previous ones.

Considering that computer vision methods are not yet extensively adopted by the naval laboratories as a measurement tool, not so many works have been reported concerning application of those techniques to identify riser motions. Menezes (2008), aided by an image processing and computer graphics tool, constructed a computer vision procedure whose temporal estimates of the scaled model riser configuration were very close to the ones generated by a set of accelerometers fixed to the model. Using classical image segmentation algorithms, Amarante (2010) implemented a computer vision procedure to identify the temporal geometrical variations of a catenary riser near the touchdown point; in his work, the direct linear transformation was applied to map the Euclidean three-dimensional space to the projective two-dimensional spaces of the cameras.

In this article we explore the combination of a computer vision technique to measure the state variables that characterize the temporal configurations of a scaled-model riser and a Kalman filter that, using these measurements, estimates the state variables as well the generalized forces acting along the riser.

MATERIALS AND METHODS

A scaled-model riser, whose geometrical and physical characteristics are shown in Table 1, was submitted to a series of tests in a towing tank, where the flexible line assumed a typical catenary configuration, with its lower end anchored at the towing tank floor and its fairlead attachment point hinged to a harmonic oscillator assembled on a platform over the water line (Fig. 1). The riser motion is known from the time evolution of the locations of 200mm equally spaced small circular markers attached to the line, and is recorded by a high resolution video camera (JAI CV-A1) coupled to a varifocal lens (6mm-12mm). Connected to an asynchronous frame grabber (Coreco-Imaging PC2-Vision) and inserted on a water-proof canister installed inside the tank, the image acquisition system was set up to record up to 4MB monochromatic images of the region near the touchdown zone at the frequency of 100MB/s.

Table 1. Scaled-model riser: Geometrical properties, structural properties and distributed applied forces.

Length	8.190 m	Linear density	0.2190 kg/m
Diameter	0.254 m	Submerged linear density	0.1001 kg/m
Rigidity modulus	$1.337 \times 10^{-6} \text{ kg.m}^2$		

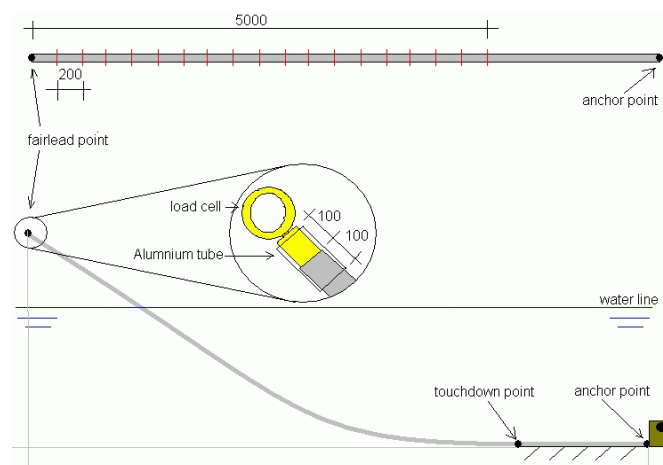


Figure 1 - Experimental setup.

Using the above referred image acquisition system, a series of images describing the planar motion of the scaled model riser were collected. As can be seen in Fig. 2a, the images generated by the experimental setup easily permit to estimate the inclination angle α between the image horizontal axis and the image towing bottom line. Furthermore, the measurement of distances between successive markers in the rotated image of Fig. 2b along its horizontal axis indicate that the horizontal scale does not change with position, i.e., that:

$$d_{1,2} = d_{2,3} = \dots d_{n-1,n} = d \tag{1}$$

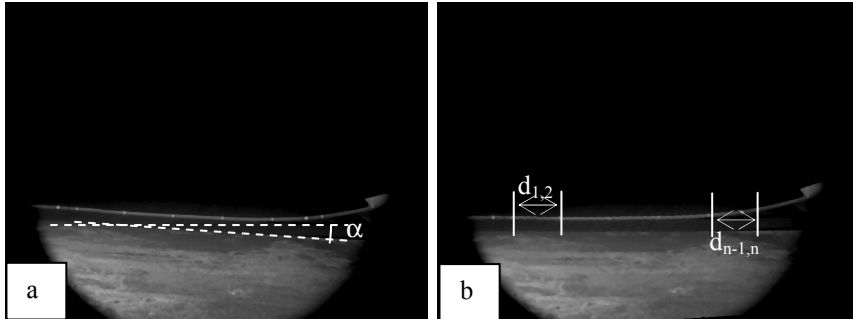


Figure 2. (a) Original image. (b) Image (a) rotated to align the towing bottom line with the horizontal axis.

The above results permit to assume that the projective transformation applied by the camera can be approximated by an affinity (see Fig. 3) with uniform horizontal and vertical scales estimated, respectively, by:

$$s_x = \frac{\ell}{d} \tag{2}$$

$$s_y = \frac{(s_\theta s_x \sin \theta)^2}{s_x^2 - s_\theta^2 \cos^2 \theta} \tag{3}$$

where ℓ , the distance between markers, is a priori known (200mm), θ is the angle between the segment AB and the horizontal line and s_θ is the scale measured along the segment AB.

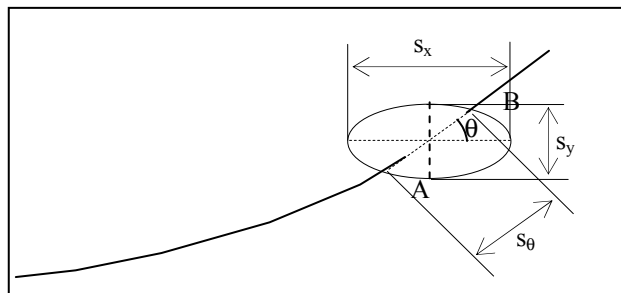


Figure 3. Measurement of the scale factors along a generic direction of the image plane.

After applying to the rotated images a segmentation process featured to isolate the image centroids (x_{im_i}, y_{im_i}) of the markers (see Fig. 4), their motion plane coordinates (x_i, y_i) were obtained by a simple scaling operation. So, observations of the scaled model riser kinematics could be properly described along the time.



Figure 4. Identified markers of a segmented image.

Using the theory of compliant mechanisms (Howell, 2001), the scaled-model riser was represented as a pseudo rigid body model (PRBM) composed of segments of rigid bars linked by torsional springs (see Fig. 5) with constants that depend on the respective boundary conditions. As illustrated in Fig. 5, the number of degrees of freedom of the generated model is compatible with the observed kinematics data and the PRBM's equivalent compliant properties of the mechanism are calculated according to the expressions suggested by Weight (2001) concerning flexible beams submitted to some previously established load and boundary conditions.

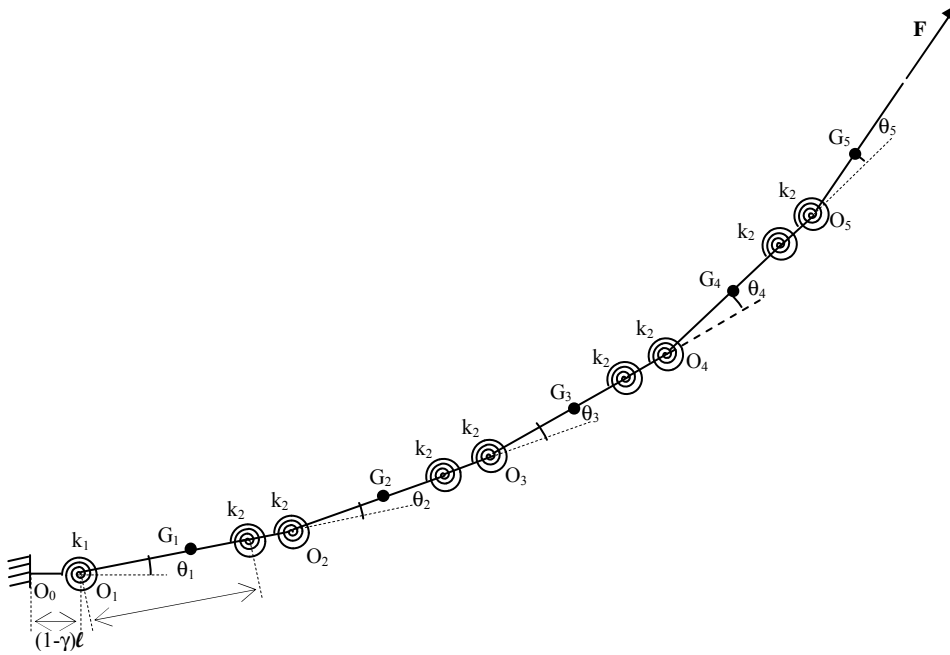


Figure 5. PRBM for the scaled model riser.

For the fixed-fixed beam boundary condition, the spring constant is:

$$K = \frac{2\gamma K_{\theta} EI}{\ell} \quad (4)$$

where, according to Howell (2001), $\gamma=0.85$ and $K_{\theta}=2.6$.

Considering that all the springs or pairs of springs correspond to the same fixed-fixed beam boundary conditions, then:

$$k_1 = k_2 = K = \frac{2\gamma K_{\theta} EI}{\ell} \quad (5)$$

Moreover, the serial pairs of springs can be substituted by an equivalent spring with constant given by

$$k'_2 = \frac{k_2}{2} = \frac{\gamma K_{\theta} EI}{\ell} \quad (6)$$

In order to write the Lagrangian equations for the compliant mechanism of Fig. 5, the expressions for the kinetic energy, the potential energy and the generalized forces were properly developed.

The kinetic energy is given by:

$$T = \frac{1}{2} \sum m_i v_{G_i}^2 + \frac{1}{2} \sum J_{G_i} \dot{\theta}_i^2 \quad (7)$$

where

$$\vec{v}_{G_i} = \vec{v}_{O_i} + \dot{\theta}_i \vec{k} \wedge (G_i - O_i) \quad (8)$$

and J_{G_i} is the moment of inertia of the segment $O_{i-1}O_i$.

After substituting (8) in (7), the following expression for the kinetic energy results:

$$\begin{aligned}
T = & \frac{m\ell^2}{2} \left[\left(\frac{\gamma^2}{4} + 4 \right) \dot{\theta}_1^2 + \left(\frac{\gamma^2}{4} + 3 \right) \dot{\theta}_2^2 + \left(\frac{\gamma^2}{4} + 2 \right) \dot{\theta}_3^2 + \left(\frac{\gamma^2}{4} + 1 \right) \dot{\theta}_4^2 + \frac{\gamma^2}{4} \dot{\theta}_5^2 \right] + \\
& \frac{m\ell^2}{2} \left[(6 + \gamma) \dot{\theta}_1 \dot{\theta}_2 \cos \theta_2 + (4 + \gamma) \dot{\theta}_1 \dot{\theta}_3 \cos(\theta_2 + \theta_3) + (2 + \gamma) \dot{\theta}_1 \dot{\theta}_4 \cos(\theta_2 + \theta_3 + \theta_4) \right] + \\
& \frac{m\ell^2}{2} \left[\gamma \dot{\theta}_1 \dot{\theta}_5 \cos(\theta_2 + \theta_3 + \theta_4 + \theta_5) \right] + \\
& \frac{m\ell^2}{2} \left[(4 + \gamma) \dot{\theta}_2 \dot{\theta}_3 \cos \theta_3 + (2 + \gamma) \dot{\theta}_2 \dot{\theta}_4 \cos(\theta_3 + \theta_4) + \gamma \dot{\theta}_2 \dot{\theta}_5 \cos(\theta_3 + \theta_4 + \theta_5) \right] + \\
& \frac{m\ell^2}{2} \left[(2 + \gamma) \dot{\theta}_3 \dot{\theta}_4 \cos \theta_4 + \gamma \dot{\theta}_3 \dot{\theta}_5 \cos(\theta_4 + \theta_5) + \gamma \dot{\theta}_4 \dot{\theta}_5 \cos \theta_5 \right] + \\
& \frac{J}{2} \left[\dot{\theta}_1^2 + (\dot{\theta}_1 + \dot{\theta}_2)^2 + (\dot{\theta}_1 + \dot{\theta}_2 + \dot{\theta}_3)^2 + (\dot{\theta}_1 + \dot{\theta}_2 + \dot{\theta}_3 + \dot{\theta}_4)^2 + (\dot{\theta}_1 + \dot{\theta}_2 + \dot{\theta}_3 + \dot{\theta}_4 + \dot{\theta}_5)^2 \right]
\end{aligned} \tag{9}$$

The potential energy of the scaled-model riser encompasses the energy stored in the springs and the potential of the gravitational and hydrostatic forces. So, it is described by:

$$\begin{aligned}
V = & \frac{1}{2} (k_1 \theta_1^2 + k_2 \theta_2^2 + k_2 \theta_3^2 + k_2 \theta_4^2 + k_2 \theta_5^2) + \\
& p_s \ell^2 \left[\left(4 + \frac{\gamma}{2} \right) \sin \theta_1 + \left(3 + \frac{\gamma}{2} \right) \sin(\theta_1 + \theta_2) + \left(2 + \frac{\gamma}{2} \right) \sin(\theta_1 + \theta_2 + \theta_3) \right] + \\
& p_s \ell^2 \left[\left(1 + \frac{\gamma}{2} \right) \sin(\theta_1 + \theta_2 + \theta_3 + \theta_4) + \left(1 + \frac{\gamma}{2} \right) \sin(\theta_1 + \theta_2 + \theta_3 + \theta_4 + \theta_5) \right]
\end{aligned} \tag{10}$$

where p_s is the underwater weight per length ratio.

The generalized force F_{α} applied at the node O_s , is:

$$F_{\alpha} = F_x \frac{\partial x_5}{\partial \theta_i} + F_y \frac{\partial y_5}{\partial \theta_i} \tag{11}$$

Adopting $L=T-V$ and applying to Eq. (9) to (11) above the Lagrangian equations, given by:

$$\frac{d}{dt} \left(\frac{\partial L}{\partial \dot{\theta}_i} \right) + \left(\frac{\partial L}{\partial \theta_i} \right) = F_{\alpha} \tag{12}$$

we obtain the following equations:

$$\begin{aligned}
\frac{d}{dt} \left(\frac{\partial L}{\partial \dot{\theta}_1} \right) + \left(\frac{\partial L}{\partial \theta_1} \right) = F_{\theta_1} \Rightarrow \\
\left[m\ell^2 \left(\frac{\gamma^2}{4} + 4 \right) + 5J \right] \ddot{\theta}_1 + \left[\frac{m\ell^2}{2} (6 + \gamma) \cos \theta_2 + 4J \right] \ddot{\theta}_2 + \left[\frac{m\ell^2}{2} (4 + \gamma) \cos(\theta_2 + \theta_3) + 3J \right] \ddot{\theta}_3 + \\
\left[\frac{m\ell^2}{2} (2 + \gamma) \cos(\theta_2 + \theta_3 + \theta_4) + 2J \right] \ddot{\theta}_4 + \left[\frac{m\ell^2}{2} \gamma \cos(\theta_2 + \theta_3 + \theta_4 + \theta_5) + 3J \right] \ddot{\theta}_5 - \\
\frac{m\ell^2}{2} \left[(6 + \gamma) \sin \theta_2 \dot{\theta}_2^2 + (4 + \gamma) \sin(\theta_2 + \theta_3) \dot{\theta}_2 \dot{\theta}_3 + (2 + \gamma) \sin(\theta_2 + \theta_3 + \theta_4) \dot{\theta}_2 \dot{\theta}_4 + \gamma \sin(\theta_2 + \theta_3 + \theta_4 + \theta_5) \dot{\theta}_2 \dot{\theta}_5 \right] - \\
\frac{m\ell^2}{2} \left[(4 + \gamma) \sin(\theta_2 + \theta_3) \dot{\theta}_3^2 + (2 + \gamma) \sin(\theta_2 + \theta_3 + \theta_4) \dot{\theta}_3 \dot{\theta}_4 + \gamma \sin(\theta_2 + \theta_3 + \theta_4 + \theta_5) \dot{\theta}_3 \dot{\theta}_5 \right] - \\
\frac{m\ell^2}{2} \left[(2 + \gamma) \sin(\theta_2 + \theta_3 + \theta_4) \dot{\theta}_4^2 + \gamma \sin(\theta_2 + \theta_3 + \theta_4 + \theta_5) \dot{\theta}_4 \dot{\theta}_5 \right] - \frac{m\ell^2}{2} \left[\gamma \sin(\theta_2 + \theta_3 + \theta_4 + \theta_5) \dot{\theta}_5^2 \right] + k_1 \theta_1 + \\
p_s \ell^2 \left[\left(\frac{\gamma}{2} + 4 \right) \cos \theta_1 + \left(\frac{\gamma}{2} + 3 \right) \cos(\theta_1 + \theta_2) + \left(\frac{\gamma}{2} + 2 \right) \cos(\theta_1 + \theta_2 + \theta_3) + \left(\frac{\gamma}{2} + 1 \right) \cos(\theta_1 + \theta_2 + \theta_3 + \theta_4) \right] + \\
p_s \ell^2 \left[\frac{\gamma}{2} \cos(\theta_1 + \theta_2 + \theta_3 + \theta_4 + \theta_5) \right] = -F\ell \left[\sin \theta_1 + \sin(\theta_1 + \theta_2) + \sin(\theta_1 + \theta_2 + \theta_3) \right] \cos(\theta_1 + \theta_2 + \theta_3 + \theta_4 + \theta_5) - \\
F\ell \left[\sin(\theta_1 + \theta_2 + \theta_3 + \theta_4) + \sin(\theta_1 + \theta_2 + \theta_3 + \theta_4 + \theta_5) \right] \cos(\theta_1 + \theta_2 + \theta_3 + \theta_4 + \theta_5) + \\
F\ell \left[\cos \theta_1 + \cos(\theta_1 + \theta_2) + \cos(\theta_1 + \theta_2 + \theta_3) \right] \sin(\theta_1 + \theta_2 + \theta_3 + \theta_4 + \theta_5) + \\
F\ell \left[\cos(\theta_1 + \theta_2 + \theta_3 + \theta_4) + \cos(\theta_1 + \theta_2 + \theta_3 + \theta_4 + \theta_5) \right] \sin(\theta_1 + \theta_2 + \theta_3 + \theta_4 + \theta_5)
\end{aligned} \tag{13}$$

$$\begin{aligned}
 & \frac{d}{dt} \left(\frac{\partial L}{\partial \dot{\theta}_2} \right) - \frac{\partial L}{\partial \theta_2} = F_{\theta_2} \Rightarrow \\
 & \left[\frac{m\ell^2}{2} (6 + \gamma) \cos \theta_2 + 4J \right] \ddot{\theta}_1 + \left[\frac{m\ell^2}{2} \left(\frac{\gamma^2}{2} + 6 \right) + 4J \right] \ddot{\theta}_2 + \left[\frac{m\ell^2}{2} (4 + \gamma) \cos \theta_3 + 3J \right] \ddot{\theta}_3 + \\
 & \left[\frac{m\ell^2}{2} (2 + \gamma) \cos(\theta_3 + \theta_4) + 2J \right] \ddot{\theta}_4 + \left[\frac{m\ell^2}{2} \gamma \cos(\theta_3 + \theta_4 + \theta_5) + J \right] \ddot{\theta}_5 - \\
 & \frac{m\ell^2}{2} \left[(6 + \gamma) \sin \theta_2 \dot{\theta}_1 \dot{\theta}_2 + (4 + \gamma) \sin \theta_3 \dot{\theta}_3^2 + (2 + \gamma) \sin(\theta_3 + \theta_4) \dot{\theta}_3 \dot{\theta}_4 + \gamma \sin(\theta_3 + \theta_4 + \theta_5) \dot{\theta}_3 \dot{\theta}_5 \right] + \\
 & \frac{m\ell^2}{2} \left[(2 + \gamma) \sin(\theta_3 + \theta_4) \dot{\theta}_4^2 + \gamma \sin(\theta_3 + \theta_4 + \theta_5) \dot{\theta}_5^2 \right] + \\
 & \frac{m\ell^2}{2} \left[(6 + \gamma) \sin \theta_2 \dot{\theta}_1 \dot{\theta}_2 + (4 + \gamma) \sin(\theta_2 + \theta_3) \dot{\theta}_1 \dot{\theta}_3 + (2 + \gamma) \sin(\theta_2 + \theta_3 + \theta_4) \dot{\theta}_1 \dot{\theta}_4 + \gamma \sin(\theta_2 + \theta_3 + \theta_4 + \theta_5) \dot{\theta}_1 \dot{\theta}_5 \right] + \\
 & k_2 \theta_2 + p_s \ell^2 \left[\left(\frac{\gamma}{2} + 3 \right) \cos(\theta_1 + \theta_2) + \left(\frac{\gamma}{2} + 2 \right) \cos(\theta_1 + \theta_2 + \theta_3) + \left(\frac{\gamma}{2} + 1 \right) \cos(\theta_1 + \theta_2 + \theta_3 + \theta_4) \right] + \\
 & p_s \ell^2 \left[\frac{\gamma}{2} \cos(\theta_1 + \theta_2 + \theta_3 + \theta_4 + \theta_5) \right] = \\
 & -F\ell \left[\sin(\theta_1 + \theta_2) + \sin(\theta_1 + \theta_2 + \theta_3) + \sin(\theta_1 + \theta_2 + \theta_3 + \theta_4) + \sin(\theta_1 + \theta_2 + \theta_3 + \theta_4 + \theta_5) \right] \cos(\theta_1 + \theta_2 + \theta_3 + \theta_4 + \theta_5) + \\
 & F\ell \left[\cos(\theta_1 + \theta_2) + \cos(\theta_1 + \theta_2 + \theta_3) + \cos(\theta_1 + \theta_2 + \theta_3 + \theta_4) + \cos(\theta_1 + \theta_2 + \theta_3 + \theta_4 + \theta_5) \right] \sin(\theta_1 + \theta_2 + \theta_3 + \theta_4 + \theta_5)
 \end{aligned} \tag{14}$$

$$\begin{aligned}
 & \frac{d}{dt} \left(\frac{\partial L}{\partial \dot{\theta}_3} \right) - \frac{\partial L}{\partial \theta_3} = F_{\theta_3} \Rightarrow \\
 & \left[\frac{m\ell^2}{2} (4 + \gamma) \cos(\theta_2 + \theta_3) + 3J \right] \ddot{\theta}_1 + \left[\frac{m\ell^2}{2} (4 + \gamma) \cos \theta_3 + 3J \right] \ddot{\theta}_2 + \left[\frac{m\ell^2}{2} \left(\frac{\gamma^2}{2} + 4 \right) + 3J \right] \ddot{\theta}_3 + \\
 & \left[\frac{m\ell^2}{2} (2 + \gamma) \cos \theta_4 + 2J \right] \ddot{\theta}_4 + \left[\frac{m\ell^2}{2} \gamma \cos(\theta_4 + \theta_5) + J \right] \ddot{\theta}_5 - \\
 & \frac{m\ell^2}{2} \left[(4 + \gamma) \sin(\theta_2 + \theta_3) \dot{\theta}_1 \dot{\theta}_2 + (4 + \gamma) \sin(\theta_2 + \theta_3) \dot{\theta}_1 \dot{\theta}_3 + (4 + \gamma) \sin \theta_3 \dot{\theta}_2 \dot{\theta}_3 + (2 + \gamma) \sin \theta_4 \dot{\theta}_4^2 \right] + \\
 & \frac{m\ell^2}{2} \left[\gamma \sin(\theta_4 + \theta_5) \dot{\theta}_4 \dot{\theta}_5 + \gamma \sin(\theta_4 + \theta_5) \dot{\theta}_5^2 \right] + k_2 \theta_3 + \\
 & p_s \ell^2 \left[\left(\frac{\gamma}{2} + 2 \right) \cos(\theta_1 + \theta_2 + \theta_3) + \left(\frac{\gamma}{2} + 1 \right) \cos(\theta_1 + \theta_2 + \theta_3 + \theta_4) + \frac{\gamma}{2} \cos(\theta_1 + \theta_2 + \theta_3 + \theta_4 + \theta_5) \right] = \\
 & -F\ell \left[\sin(\theta_1 + \theta_2 + \theta_3) + \sin(\theta_1 + \theta_2 + \theta_3 + \theta_4) + \sin(\theta_1 + \theta_2 + \theta_3 + \theta_4 + \theta_5) \right] \cos(\theta_1 + \theta_2 + \theta_3 + \theta_4 + \theta_5) + \\
 & F\ell \left[\cos(\theta_1 + \theta_2 + \theta_3) + \cos(\theta_1 + \theta_2 + \theta_3 + \theta_4) + \cos(\theta_1 + \theta_2 + \theta_3 + \theta_4 + \theta_5) \right] \sin(\theta_1 + \theta_2 + \theta_3 + \theta_4 + \theta_5)
 \end{aligned} \tag{15}$$

$$\begin{aligned}
 & \frac{d}{dt} \left(\frac{\partial L}{\partial \dot{\theta}_4} \right) - \frac{\partial L}{\partial \theta_4} = F_{\theta_4} \Rightarrow \\
 & \left[\frac{m\ell^2}{2} (2 + \gamma) \cos(\theta_2 + \theta_3 + \theta_4) + 2J \right] \ddot{\theta}_1 + \left[\frac{m\ell^2}{2} (2 + \gamma) \cos(\theta_3 + \theta_4) + 2J \right] \ddot{\theta}_2 + \left[\frac{m\ell^2}{2} (2 + \gamma) \cos \theta_4 + 2J \right] \ddot{\theta}_3 + \\
 & \left[\frac{m\ell^2}{2} \left(\frac{\gamma^2}{2} + 2 \right) + 2J \right] \ddot{\theta}_4 + \left[\frac{m\ell^2}{2} \gamma \cos \theta_5 + J \right] \ddot{\theta}_5 - \\
 & \frac{m\ell^2}{2} \left[(2 + \gamma) \sin(\theta_2 + \theta_3 + \theta_4) \dot{\theta}_1 \dot{\theta}_2 + (2 + \gamma) \sin(\theta_2 + \theta_3 + \theta_4) \dot{\theta}_1 \dot{\theta}_3 + (2 + \gamma) \sin(\theta_2 + \theta_3 + \theta_4) \dot{\theta}_1 \dot{\theta}_4 + (2 + \gamma) \sin(\theta_3 + \theta_4) \dot{\theta}_2 \dot{\theta}_3 \right] + \\
 & \frac{m\ell^2}{2} \left[(2 + \gamma) \sin(\theta_3 + \theta_4) \dot{\theta}_2 \dot{\theta}_4 + (2 + \gamma) \sin(\theta_3 + \theta_4) \dot{\theta}_2 \dot{\theta}_4 \gamma \sin \theta_4 \dot{\theta}_3 \dot{\theta}_4 + \gamma \sin \theta_5 \dot{\theta}_5^2 \right] + k_2 \theta_4 + \\
 & p_s \ell^2 \left[\left(\frac{\gamma}{2} + 1 \right) \cos(\theta_1 + \theta_2 + \theta_3 + \theta_4) + \frac{\gamma}{2} \cos(\theta_1 + \theta_2 + \theta_3 + \theta_4 + \theta_5) \right] = \\
 & -F\ell \left[\sin(\theta_1 + \theta_2 + \theta_3 + \theta_4) + \sin(\theta_1 + \theta_2 + \theta_3 + \theta_4 + \theta_5) \right] \cos(\theta_1 + \theta_2 + \theta_3 + \theta_4 + \theta_5) + \\
 & F\ell \left[\cos(\theta_1 + \theta_2 + \theta_3 + \theta_4) + \cos(\theta_1 + \theta_2 + \theta_3 + \theta_4 + \theta_5) \right] \sin(\theta_1 + \theta_2 + \theta_3 + \theta_4 + \theta_5)
 \end{aligned} \tag{16}$$

$$\begin{aligned}
\frac{d}{dt} \left(\frac{\partial L}{\partial \dot{\theta}_5} \right) - \frac{\partial L}{\partial \theta_5} = F_{\theta_5} \Rightarrow \\
\left[\frac{m\ell^2}{2} \gamma \cos(\theta_2 + \theta_3 + \theta_4 + \theta_5) + J \right] \ddot{\theta}_1 + \left[\frac{m\ell^2}{2} \gamma \cos(\theta_3 + \theta_4 + \theta_5) + J \right] \ddot{\theta}_2 + \left[\frac{m\ell^2}{2} \gamma \cos(\theta_4 + \theta_5) + J \right] \ddot{\theta}_3 + \\
\left[\frac{m\ell^2}{2} \gamma \cos(\theta_4 + \theta_5) + J \right] \ddot{\theta}_4 + \left[\frac{m\ell^2}{2} \frac{\gamma}{2} + J \right] \ddot{\theta}_5 - \\
\frac{m\ell^2}{2} \left[\gamma \sin(\theta_2 + \theta_3 + \theta_4 + \theta_5) (\dot{\theta}_1 \dot{\theta}_2 + \dot{\theta}_1 \dot{\theta}_3 + \dot{\theta}_1 \dot{\theta}_4 + \dot{\theta}_1 \dot{\theta}_5) + \gamma \sin(\theta_3 + \theta_4 + \theta_5) (\dot{\theta}_2 \dot{\theta}_3 + \dot{\theta}_2 \dot{\theta}_4 + \dot{\theta}_2 \dot{\theta}_5) \right] + \\
\frac{m\ell^2}{2} \left[\gamma \sin(\theta_4 + \theta_5) (\dot{\theta}_3 \dot{\theta}_4 + \dot{\theta}_3 \dot{\theta}_5) + \gamma \sin \theta_5 \dot{\theta}_4 \right] + \\
\frac{m\ell^2}{2} \left[\gamma \sin(\theta_2 + \theta_3 + \theta_4 + \theta_5) \dot{\theta}_1 \dot{\theta}_5 + \gamma \sin(\theta_3 + \theta_4 + \theta_5) \dot{\theta}_2 \dot{\theta}_5 + \gamma \sin(\theta_4 + \theta_5) \dot{\theta}_3 \dot{\theta}_5 + \gamma \sin \theta_5 \dot{\theta}_4 \dot{\theta}_5 \right] + k_2 \theta_5 + \\
p_s \ell^2 \left[\frac{\gamma}{2} \cos(\theta_1 + \theta_2 + \theta_3 + \theta_4 + \theta_5) \right] = 0
\end{aligned} \tag{17}$$

After linearizing the Eq. (13) to (17) above, we obtain:

$$\begin{aligned}
\left[\frac{m\ell^2}{2} \left(\frac{\gamma^2}{2} + 2 \right) + 5J \right] \ddot{\theta}_1 + \left[\frac{m\ell^2}{2} (6 + \gamma) + 4J \right] \ddot{\theta}_2 + \left[\frac{m\ell^2}{2} (4 + \gamma) + 3J \right] \ddot{\theta}_3 + \left[\frac{m\ell^2}{2} (2 + \gamma) + 2J \right] \ddot{\theta}_4 + \left[\frac{m\ell^2}{2} \gamma + J \right] \ddot{\theta}_5 + \\
k_1 \theta_1 + p_s \ell^2 \left(10 + \frac{5}{2} \gamma \right) = F \ell (\theta_2 + 2\theta_3 + 3\theta_4 + 4\theta_5)
\end{aligned} \tag{18}$$

$$\begin{aligned}
\left[\frac{m\ell^2}{2} (6 + \gamma) + 4J \right] \ddot{\theta}_1 + \left[m\ell^2 \left(\frac{\gamma^2}{4} + 3 \right) + 4J \right] \ddot{\theta}_2 + \left[\frac{m\ell^2}{2} (4 + \gamma) + 3J \right] \ddot{\theta}_3 + \left[\frac{m\ell^2}{2} (2 + \gamma) + 2J \right] \ddot{\theta}_4 + \left[\frac{m\ell^2}{2} \gamma + J \right] \ddot{\theta}_5 + \\
k_2 \theta_2 + p_s \ell^2 (6 + 2\gamma) = F \ell (\theta_3 + 2\theta_4 + 3\theta_5)
\end{aligned} \tag{19}$$

$$\begin{aligned}
\left[\frac{m\ell^2}{2} (4 + \gamma) + 3J \right] \ddot{\theta}_1 + \left[\frac{m\ell^2}{2} (4 + \gamma) + 3J \right] \ddot{\theta}_2 + \left[m\ell^2 \left(\frac{\gamma^2}{4} + 2 \right) + 3J \right] \ddot{\theta}_3 + \left[\frac{m\ell^2}{2} (2 + \gamma) + 2J \right] \ddot{\theta}_4 + \left[\frac{m\ell^2}{2} \gamma + J \right] \ddot{\theta}_5 + \\
k_2 \theta_3 + p_s \ell^2 \left(3 + \frac{3}{2} \gamma \right) = F \ell (\theta_4 + 2\theta_5)
\end{aligned} \tag{20}$$

$$\begin{aligned}
\left[\frac{m\ell^2}{2} (2 + \gamma) + 2J \right] \ddot{\theta}_1 + \left[\frac{m\ell^2}{2} (2 + \gamma) + 2J \right] \ddot{\theta}_2 + \left[\frac{m\ell^2}{2} (2 + \gamma) + 2J \right] \ddot{\theta}_3 + \left[m\ell^2 \left(\frac{\gamma^2}{4} + 1 \right) + 2J \right] \ddot{\theta}_4 + \left[\frac{m\ell^2}{2} \gamma + J \right] \ddot{\theta}_5 + \\
k_2 \theta_4 + p_s \ell^2 (1 + \gamma) = F \ell \theta_5
\end{aligned} \tag{21}$$

$$\left[\frac{m\ell^2}{2} \gamma + J \right] \ddot{\theta}_1 + \left[\frac{m\ell^2}{2} \gamma + J \right] \ddot{\theta}_2 + \left[\frac{m\ell^2}{2} \gamma + J \right] \ddot{\theta}_3 + \left[\frac{m\ell^2}{2} \gamma + J \right] \ddot{\theta}_4 + \left[\frac{m\ell^2}{2} \frac{\gamma^2}{2} + J \right] \ddot{\theta}_5 + k_2 \theta_5 + p_s \ell^2 \frac{\gamma}{2} = 0 \tag{22}$$

The set of linearized differential Eq. 18-22 in the generalized coordinates must now be solved for those coordinates and for the unknown cable tension F , a forcing term that occurs at the right side of Eq. (18) to (21) and contribute to the bending moment at the end of each but the outermost right segment of the compliant mechanism model. In order to solve the stated problem, we formulate it as a state-space problem and use a Kalman filter to estimate the state, a vector containing the generalized coordinates and its derivatives plus the unknown forcing terms. The approach we used to obtain the state-space model is described next.

Equations (18) to (22) are a space discretized and time continuous representation of the compliant mechanism approach to the suspended cable problem; accordingly, they can be written as

$$[M] \ddot{\theta}(t) + [K] \theta(t) = \Psi(t), \tag{23}$$

in which $[M]$, $[K] \in R^{5 \times 5}$ are respectively the inertia and stiffness matrices, $\theta(t) \in R^{5 \times 1}$ is a vector of generalized coordinates and $\Psi(t) \in R^{5 \times 1}$ accounts for all terms that do not contain the generalized coordinates and their derivatives. As it is noticeable from Eq. (18) to (22), the continuous-time model thus assembled is coupled in the second

derivatives, i. e., matrix $[M]$ is not diagonal; however, since it is real and simetric, it is possible to write a linear map $L : \underline{\theta} \rightarrow \underline{\eta}$ such that

$$\underline{\theta}(t) = [L]\underline{\eta}(t), \quad (24)$$

$[L]$ being a square non-singular constant matrix of order 5. As a consequence of substitution of Eq. (24) into Eq. (23) and multiplying both sides by $[L]^T$, one obtains

$$[L]^T [M [L]\underline{\ddot{\eta}}(t) + [L]^T [K [L]\underline{\eta}(t) = [L]^T \underline{\Psi}(t), \quad (25)$$

or, in shorter form,

$$[M_d]\underline{\ddot{\eta}}(t) + [K_s]\underline{\eta}(t) = \underline{\Omega}(t), \quad (26)$$

with $[M_d]$ a diagonal matrix and $[K_s]$ a simetric matrix, thus decoupling the system in the second derivatives of the generalized coordinates and allowing its description in a canonical state-space framework. In this work, we employed an appropriate built-in **Octave** function to obtain the transformation matrix $[L]$. The components of the state-vector are, then, $x_i(t)$, $i = 1 : 10$ with

$$\begin{aligned} \eta_1 &= x_1 & \eta_2 &= x_3 & \dots & \eta_5 &= x_9 \\ \dot{\eta}_1 &= x_2 = \dot{x}_1 & \dot{\eta}_2 &= x_4 = \dot{x}_3 & \dots & \dot{\eta}_5 &= x_{10} = \dot{x}_9 \end{aligned} \quad (27)$$

For the ordinary case in which the forcing vector of the right-hand side of Eq. 26 is known, $\underline{x}(t) \in R^{10}$ would be the state-vector of the Kalman filter process model, represented in matrix form as

$$\dot{\underline{x}} = F_p \underline{x} + G_p \underline{\Omega}, \quad F_p \in R^{10 \times 10}, G_p \in R^{10 \times 5} \quad (28)$$

Nevertheless, since our interest is to estimate not only the generalized coordinates but also the forcing vector, we include those terms in the estimation problem by augmenting the ordinary state-vector. Firstly, we consider the forcing vector as the output of a linear filter driven by zero-mean Gaussian white noise:

$$\begin{aligned} \dot{\underline{x}}_f &= F_f \underline{x}_f + G_f \underline{w}_f, \quad \underline{x}_f, \underline{w}_f \in R^5, \quad \underline{w}_f \sim N(0, Q) \\ \underline{y}_f &= H_f \underline{x}_f \end{aligned} \quad (29)$$

Equations (29), in which F_f , G_f and H_f are identity matrices of order 5, exhibit respectively the state-space process and observation models for the unknown forcing vector $\underline{\Omega}(t) = \underline{x}_f(t)$. Next, those equations are used to augment the system and observation state-space models for the original generalized coordinates according to Eq. (30),

$$\begin{Bmatrix} \dot{\underline{x}} \\ \dot{\underline{x}}_f \end{Bmatrix} = \begin{bmatrix} F_p & G_p H_f \\ \mathbf{0}_{5 \times 10} & F_f \end{bmatrix} \begin{Bmatrix} \underline{x} \\ \underline{x}_f \end{Bmatrix} + \begin{bmatrix} \mathbf{0}_{10 \times 5} \\ G_f \end{bmatrix} \underline{w}_f \quad \Rightarrow \dot{\underline{X}} = A \underline{X} + B \underline{w}_f, \quad A \in R^{15 \times 15}, B \in R^{15 \times 5}, \quad (30)$$

that provide the process state-space model in which both the generalized coordinates and the forcing terms constitute the state variables to be estimated. In view of Eq. (28) and (29), it should be emphasized that process uncertainties, expressed by the random vector \underline{w}_f are implicitly assumed to be restricted to the unknown forcing terms. This is a feasible assumption, since the simplification introduced by modeling the actual experimental riser as two-bar compliant mechanism according to Howell (2008) is capable of reproducing large displacements of an actual continuous beam, whose elastic curve results from the solution of an elliptical differential equation.

The observation equation for the augmented model will be assembled taking into account that the only measurements available are angular displacements of the bars, obtained from images grabbed by a video camera. Those images, through a segmentation procedure, provide Cartesian coordinates of a set of markers that are used to generate the correspondent angles. Inherent errors in the image segmentation procedure are modeled as zero-mean Gaussian noise with covariance matrix R , allowing for the observation equation to be written as

$$\underline{Y} = [H_p \quad \mathbf{0}_{5 \times 5}] \underline{X} + \underline{v} \quad \Rightarrow \underline{Y} = H \underline{X} + \underline{v}, \quad H_p \in R^{5 \times 10}, \underline{v} \in R^5, \underline{v} \sim N(0, R), \quad (31)$$

The state-space representation of the riser dynamical model according to Eq. (30) and (31) is hybrid (continuous-discrete), since the state evolves continuously, whereas measurements are available at specific sample times. For computational purposes, in this work the continuous process model was discretized (with the aid of a built-in function in

Octave) using the same time step-size as that of the measurements, i.e, each k^{th} iteration of the filter corresponds to a new measurement available. The obtained discrete-time process model is, then,

$$\underline{X}(t_k) = \Phi(t_k, t_{k-1})\underline{X}(t_{k-1}) + B_d(t_k)\underline{w}_f(t_k), \quad (32)$$

in which $\underline{X}(t_k)$ is the state vector k^{th} time step $k\Delta t$, $\Phi(t_k, t_{k-1})$ is the discrete-time transition matrix, and $B_d(t_k)\underline{w}_f(t_k)$ is the discrete-time forcing vector. Accordingly, the discrete-time observation equation is

$$\underline{Y}(t_k) = H\underline{X}(t_k) + \underline{v}(t_k). \quad (33)$$

Regarding the estimation procedure, it suffices to mention that recursive estimation theory based on Kalman filtering is extensively discussed in the literature, see for instance Jazwinski (1970); thus, for the moment, we only state the hypotheses used and provide a brief explanation of the algorithm through its equations. As already mentioned, white noise sequences \underline{w}_f and \underline{v} are assumed zero-mean Gaussian with associated covariance matrices; in addition, those sequences are considered mutually independent and, as a consequence of being Gaussian, they are also uncorrelated. Covariance matrices Q and R are admitted constant and diagonal, whose elements are the variances of each state-variable.

For the model given by Eq. (32) and (33), there is a forecast stage that seeks to produce the best estimates (in a stochastic least-squares sense) by propagating the previous estimated state based on the process model and its known (or admitted) statistics before new information is available. This way, Eq. (34)

$$\underline{X}^f(t_k) = \Phi\underline{X}^u(t_{k-1}) \quad (34)$$

provides the state estimation forecast and eq. (35)

$$P^f(t_k) = P^u(t_{k-1}) + Q(t_{k-1}) \quad (35)$$

gives the estimation error covariance matrix forecast. When new data is available, an update stage provides proper correction to the forecasted estimates of the state and error covariance according to Eq. (36) and (37),

$$\underline{X}^u(t_k) = \underline{X}^f(t_k) + K(t_k)\{\underline{y}(t_k) - H\underline{X}^f(t_k)\} \quad (36)$$

$$P^u(t_k) = (I - K(t_k)H)P^f(t_k). \quad (37)$$

It must be pointed out that in Eq. (36), $\underline{y}(t_k)$ is employed to represent the measurement vector, distinct from $\underline{Y}(t_k)$, measurement model.

The correction is provided by the Kalman gain matrix, computed according to Eq. (38)

$$K(t_k) = P^f(t_k)H\{HP^f(t_k)H^T + R(t_k)\}^{-1}, \quad (38)$$

thus completing the prediction-correction steps necessary for the next iteration of the filter.

RESULTS AND DISCUSSION

The previously described experimental setup grabbed images at a rate of 28 frames/s, thus providing observations of the position of each one of the five markers attached to the suspended cable at every 0.036 seconds. Computed Cartesian coordinates of the markers were used to get the effective angular observations for the Kalman filter estimation procedure. The covariance matrices were $\mathbf{Q}=\mathbf{0.9 I}_{15}$ (process model noise covariance matrix, assumed constant), $\mathbf{R}=\mathbf{0.01 I}_5$ (measurement model noise covariance matrix, assumed constant) and $\mathbf{P}_0=\mathbf{0.5 I}_{15}$ (state-estimation error covariance matrix); the initial state-vector was

$$[-0.0183; 0.0276; 0.0085; 0.0262; 0.0633; 0.253; -0.5087; 0.011; 0.245; -0.189; 0.0376; 0.025; 0.0153; 0.0063; 0.0]^T,$$

obtained as the mean value of measurements from the three first frames grabbed. The last 5 state-variables correspond to bending moments computed using a static estimate of the traction force on the cable, $F=0.5$ N.

Estimates for the state-variables angular displacement and rotation are shown in Figs. 6 and 7. Those ten variables are the ones of the “original” dynamical system, i.e., without the augmentation that included forcing terms as state variables to be estimated. From Fig. 6, one realizes that the results are coherent since angular displacements have higher amplitudes for those nodes close to the left-side of the cable; in addition, angular velocities behave accordingly, see Fig. 7.

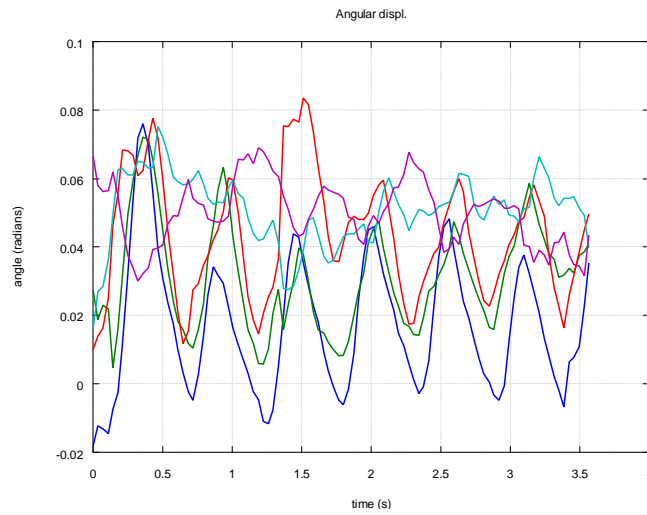


Figure 6: Angular displacements of the model bars at the rotational springs.

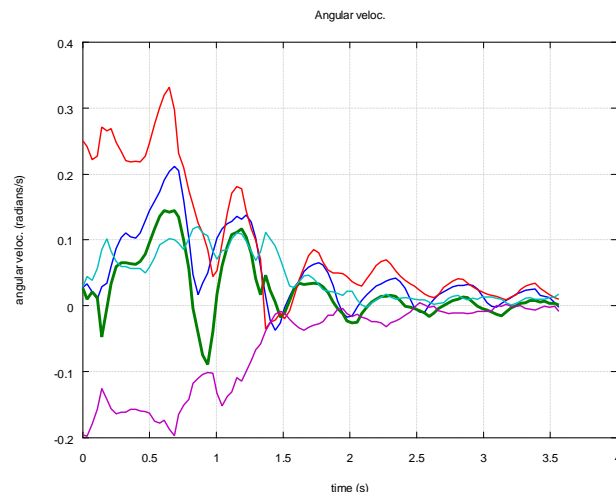


Figure 7: Angular velocity of the model bars attached to rotational springs.

Results of generalized forces depicted on Fig. 8 also corroborate the previous assertions, for moments (in this case, generalized forces are bending moments at the edge of each pair of bars setting) at the left-side of the cable present higher amplitudes, that decrease in the direction of the right-side. Particularly interesting is that, for the generalized force corresponding to state-variable number 15, the bending moment at the free-end of the cable, as shown by the purple curve, has mean value around zero from 2.5 seconds onward (the actual mean value in this range is -0.0058 N.m), complying with what was theoretically expected.

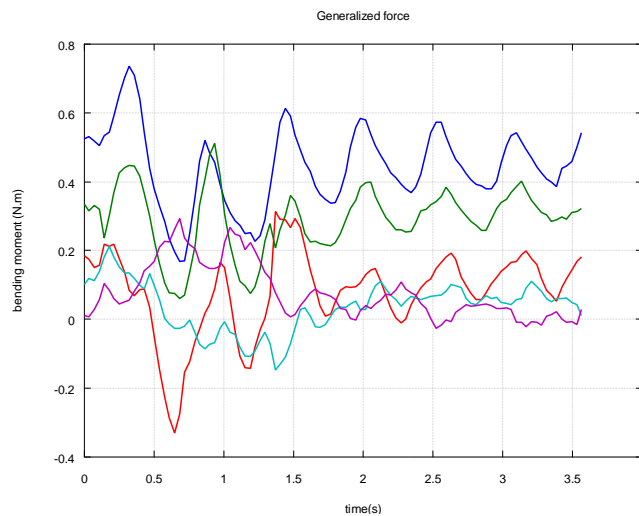


Figure 8: Estimates of generalized forces.

When the generalized forces, the 11th to 15th state-variables of the augmented state-space model are used to compute tension values on the string, its mean value is 10.9 N for the values calculated from curves representing state-variables 11 to 14, as seen of Fig. 9; regarding the 15th state-variable, its mean value is zero, for the same reasons stated above. It is as well worthwhile to mention that curves representing state-variables 11 to 14 present peaks whose amplitudes is decreasing, therefore suggesting that, if more observations were available, the estimates would converge to the above-mentioned mean value.

In order to support the assertions of the last paragraph, two evidences of the convergence of the estimation procedure are provided by the behaviour of the error covariance matrix and the normalized residual. The Euclidean norm of the estimation error covariance matrix $P^u(t_k)$ during the estimation process is depicted in Fig. 10, from which it is possible to realize that, after great amplitudes at the beginning of the process, once more observations are available, the error decreases and reaches a steady-state value, which indicates that the procedure has converged. This condition is, however, not enough to guarantee the actual convergence. As stated by Jazwinski (1970), actual convergence of the estimation process must be asserted by the inspection of the observation the difference between the effective measurement and its value as calculated by the filter using the last available state estimate. An estimation process is considered convergent once the normalized observation residuals is zero-mean Gaussian with standard deviation between $-3\sigma_v$ and $3\sigma_v$, given by Eq. (39)

$$r_v = \frac{1}{\ell \sigma_v} \sum_{j=1}^{\ell} (\underline{Y}_j(t_k) - \underline{X}_j^f(t_k)) , \quad (39)$$

where ℓ represents measurement vector dimension, in our case, $\ell = 5$. In Fig. 11, it is shown that those requirements are fulfilled, because $E[r_v] = 0.012$ and $E[r_v^2] = 0.17$; therefore, one concludes that the procedure actually converges.

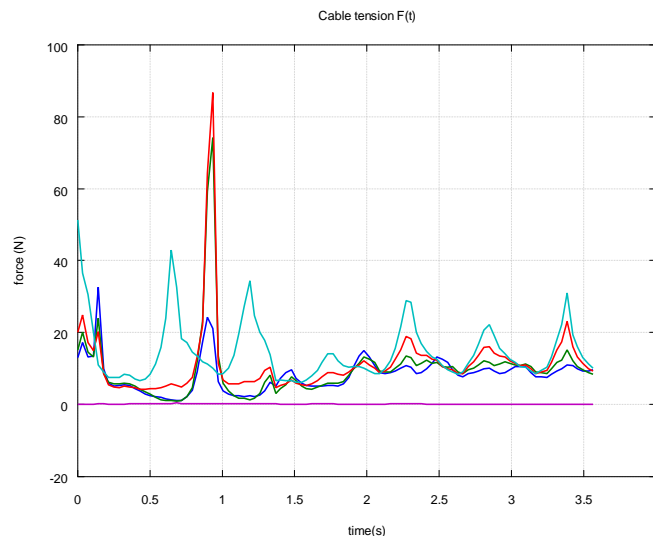


Figure 9: Estimates of cable tension.

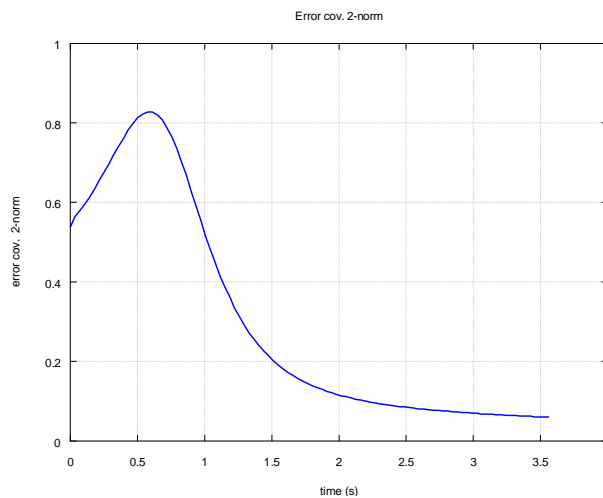


Figure 10: Error covariance matrix Euclidean norm.

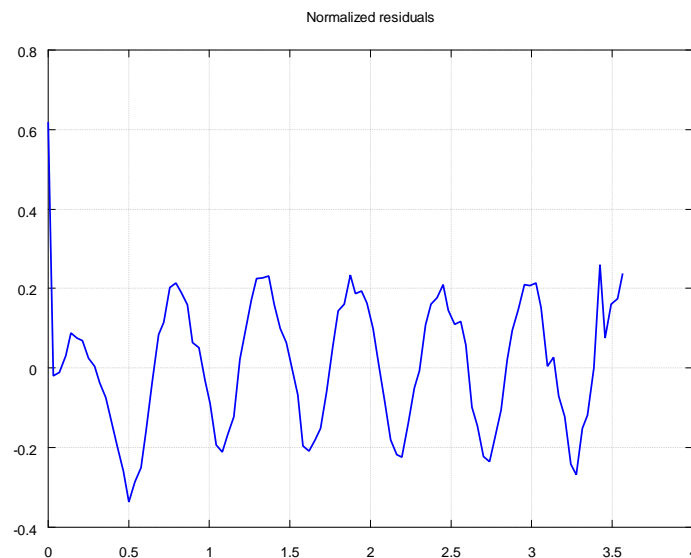


Figure 11: Normalized observation residuals.

CONCLUSIONS

This work investigated the use of a new approach to analyse the dynamics of an underwater suspended cable through image-based instrumentation associated to parameter estimation techniques. A scaled-model riser has undertaken several tests in a controlled environment. Simple self calibration procedures applied to images grabbed by a video camera provided observations used in a state-space model of the system dynamics obtained from the application of compliant mechanisms theory to spatially discretize the riser specimen. The system dynamical model was simulated through a linear Kalman filter in which the state-variables of the augmented state-space vector included the unknown generalized forces at the end of each discretized segment of the cable. Results from the simulations suggest that it is possible to use the described approach to estimate both the bending moments along the cable and the tension force at its free extremity. This assertion is corroborated by statistical evidence of the convergence of the filtering process, namely, decreasing error covariance matrix Euclidean norm and consistency of the normalized observation residuals.

ACKNOWLEDGMENTS

This work was supported by CNPq as part of the project 471880/2006-0 – “Identificação da Cinemática de Embarcações e Estruturas Oceânicas Utilizando Visão Computacional”. Fourth author also gratefully acknowledges CNPq for financial support.

REFERENCES

- Amarante, R.M., 2010, “Estudo da estatística e dinâmica de linhas, sob configuração de catenária, através da identificação geométrica, processamento e análise de imagens digitais”. Dissertação de mestrado, Escola Politécnica, Universidade de São Paulo.
- Ayres Jr, F., 1967, “Theory and Problems of Projective Geometry”. Schaum Publishing Co.
- Beghin, H., 1952, “Mécanique Théorique et Appliquée”, Tome 1. Gauthier-Villars, 551p.
- Campos, L.A., 1997, “Análise de esforços dinâmicos na região do ‘touchdown point’ de um riser rígido em catenária”. Dissertação de mestrado, Escola Politécnica, Universidade de São Paulo.
- Gonzalez, R., Woods, R.E., 2002, “Digital Image Processing”. Prentice-Hall, 2nd edition, 793p.
- Habed, A., Boufama, B., 2006, “Camera Self-Calibration from Bivariate Polynomial Equations and Coplanarity Constraints”. *Image and Vision Computing*, 24, pp.498-514.
- Hartley, R.I., 1997, “Self-Calibration of Stationary Cameras”. *International Journal of Computer Vision*, 22(1), pp. 5-23.
- Jazwinski, A.H., 1970, “Stochastic Processes and Filtering Theory”, Academic Press, New York, USA, 376 p.
- Menezes Jr., L.F., 2008, “Processamento de imagens na análise dinâmica de risers de produção de petróleo com modelo de escala reduzida em ambiente de laboratório”. Tese de doutorado, Faculdade de Engenharia Mecânica, Unicamp.
- Menudet, J.F., Becker, J.M., Fournel, T., Menessier, C., 2007, “Plane-Based Camera Self-Calibration by Metric Rectification of Images”. *Image and Vision Computing*, pp.1-22.

- Moeslund, T.B., Hilton, A., Krüger, V., 2006, "A Survey of Advances on Vision-Based Human Motion Capture and Analysis", *Computer Vision and Image Understanding*, 104, pp. 90-96.
- Pèrès, J., 1962, "Mécanique Générale". Masson & Cie, 407p.
- Pesce, C.P., 1997, "Mecânica de cabos e tubos submersos lançados em 'catenária': uma abordagem analítica e experimental". Tese de livre-docência, Escola Politécnica, Universidade de São Paulo.
- Shortis, M., Harvey, E., Abdo, D., 2009, "A Review of Underwater Stereo Image Measurement for Marine Biology and Ecology Applications", *Oceanographic and Marine Biology: An Annual Review*, 47, pp. 257-292.
- Schalkoff, R.J., 1989, "Digital Image Processing and Computer Vision". John Wiley and Sons.
- Takafuji, F.C.M., 2010, "Dinâmica tridimensional de risers". Tese de doutorado, Escola Politécnica, Universidade de São Paulo.
- Valdés, A., Ronda, J.I., 2005, "Camera Autocalibration and the Calibration Pencil". *Journal of Mathematical Imaging and Vision*, Vol.23, pp. 167-174.
- Veblen, O., Young, J.W., 1938, "Projective Geometry", vol. 1, 2. The Athenaeum Press.
- Weight, B.L., 2001, "Development and design of constant-force mechanisms". Thesis. Brigham Young University, Department of Mechanical Engineering.

RESPONSIBILITY NOTICE

The authors are the only responsible for the printed material included in this paper.

Application of the Generalized Programmed Motion Equations to Kinematic and Dynamic Task Planning for Constrained Mechanical Systems

Elżbieta Jarzębowska

Warsaw University of Technology, Institute of Aeronautics and Applied Mechanics, 00-665 Warsaw, Nowowiejska 24, Poland

Abstract: In the paper an application of the generalized programmed motion equations to kinematic and dynamic task planning for constrained, specifically nonholonomic, mechanical systems is presented. The target application of task planning is tracking control. It is presented how to merge all tasks requested for the controlled system into one kinematic or dynamic reference model provided a task may be specified by an algebraic or differential equation. Also, it is demonstrated that the kinematic or dynamic reference model plays a role of a task planner and outcomes of the task planner are inputs to a tracking control strategy. The pre-planned tasks may be executed using the model reference tracking control strategy for programmed motion. Its architecture enables an application of existing tracking algorithms even these dedicated to holonomic systems.

Keywords: task planning, tracking control, constrained systems, dynamic control model

NOMENCLATURE

<p>B = $(k \times n)$-dimensional matrix of constraint equations, C = $(n-k)$-dimensional vector of centrifugal and Coriolis forces, D = $(n-k)$-dimensional vector of gravity forces, $2b$ = distance between mobile platform wheels, d = distance along x between the robot mass center and the midpoint between the wheels, I = moment of inertia, k = number of constraint equations, l_1, l_2 = manipulator link lengths, m = mass,</p>	<p>M = $(n-k) \times n$ inertia matrix, n = state space dimension, p = programmed constraint order, q = generalized coordinates vector, r = wheel radius, Q = $(n-k)$-dimensional vector of external forces, T = kinetic energy, V = $(n-k)$-dimensional velocity dependent vector, x_c, y_c = mobile platform mass center coordinates,</p> <p>Greek Symbols</p> <p>τ = control input vector,</p>	<p>φ = unicycle and mobile platform orientation angle, φ_r, φ_1 = roll angles of mobile platform wheels, θ = unicycle roll angle, θ_1, θ_2 = manipulator joint angles,</p> <p>Subscripts</p> <p>1 refers to the vector of independent coordinates, 2 refers to the vector of dependent coordinates</p>
---	--	--

INTRODUCTION

In nonlinear control motion planning for constrained, specifically nonholonomic, systems is usually understood as providing collision-free admissible paths in their configuration space. Motion planners compute paths, which have to be transformed into trajectories. Motion planning in the sense of path planning arises two problems: the existence of a collision-free path and the computation of such a path. As discussed in Laumond et al. (1998), for symmetric small-time controllable systems the existence of admissible collision-free path between two given configurations is equivalent to the existence of any collision-free path between these configurations. Methods used in path planning are purely geometric control methods; see e.g. (Laumond et al., 1998, Murray et al., 1996, Tilbury et al., 1995). Algorithms that solve path planning problems are referred to as steering methods, e.g. steering using sinusoids, the goursat normal forms approach; some of them are reported in (Murray et al., 1996, Tilbury et al., 1995). The transformation of an admissible path into an admissible trajectory is a classical problem which has been solved in a numerous ways (Laumond et al., 1998). Trajectories planned are then executed mostly by control algorithms at the system kinematic model level.

In work (Tan and Xi, 2002) a kind of an integrated approach to task planning is presented. The integration relies upon the coordination of a mobile manipulator and a nonholonomic cart motions and the task is the cart pushing with no violation of the nonholonomic constraints. It illustrates a typical case when different path planning algorithms are developed to different tasks. These tasks differ based on a required work and systems that do the work but all considered motions are along specified trajectories.

Another approach is used to complex systems, e.g. mobile manipulators where the task is attributed to a manipulator end effector, however, the platform has also to move some pre-specified trajectory (Papadopoulos and Poulakakis, 2000). There, the nonholonomic constraints for the mobile base are combined with the velocity of the manipulator end effector. The final kinematic equations assume that the mobile platform velocity and its trajectory are known. Also, the desired end effector trajectory is delivered and time to accomplish the task is specified. The trajectory planning part of

the control problem is achieved by solving the kinematic equations. The desired trajectories produced at the kinematic level are inputs to a control algorithm at the dynamic level. A dynamic control model is developed using the Lagrange's equations with multipliers. They have to be decoupled from the multipliers to yield a dynamic control model.

The examples above demonstrate that a trajectory to follow, which is executed by a control algorithm at the kinematic or dynamic level is generated by a trajectory planner or delivered by other means; more details can be found in (Van Nieuwstadt, 1997). Also, the tracking control problem is sometimes understood as two-stage control where a trajectory is generated first and then it is tracked. An *a priori* specification of a trajectory is usually based upon the knowledge of a task nature, like in (Papadopoulos and Poulakakis, 2000) where the task is a crack sealing in a pavement and the crack shape is obviously known.

When a task is different than a trajectory to track, the usual approach in nonlinear control is to handle each task separately. There were neither task planners nor general methods or procedures. There are numerous examples of tasks different than a trajectory to track, e.g. for underactuated systems a second order nonholonomic non-material constraint originates from control or design requirements (Nakamura et al., 1997). In navigation of wheeled mobile robots, to avoid wheel slippage and mechanical shock during motion, a dynamic constraint put on the acceleration has to be taken into account (Koh and Cho, 1999). In path planning problems, for car-like robots, to secure motion smoothness two additional constraints are put upon trajectory curvature and its time derivative (Koh and Cho, 1999, Oriolo et al., 2002, Scheuer and Laugier, 1998, Shekl and Lumelsky, 1998). A special interest and challenge in control design is attributed to the curvature of a desired trajectory. It is obvious that a wheeled vehicle is capable of following a trajectory of some limited curvature. The limits depend upon the vehicle design. Usually, the constraint on the trajectory curvature is specified as an extra demand, which is not treated as another control goal. Many works in this spirit report controller designs with the limits on the trajectory curvature taken into account; e.g (Ballucchi et al., 1996, Kim et al., 2009). The tasks as described above may be specified by constraint equations of the second and third orders, respectively. Driving and task constraints are examples of non-material constraints (de Jalon and Bayo, 1994). Non-material constraints on a space vehicle velocity are reported in (Vafa, 1991). A trajectory to track may be viewed as a task. Only the trajectory is formulated in the equation form and merged systematically into a control design process.

In the paper an application of the generalized programmed motion equations to kinematic and dynamic task planning for constrained mechanical systems is presented. The target application of task planning is tracking control. The main contribution of the paper is twofold. First, we present how to merge all tasks requested for the controlled system into one kinematic or dynamic reference model provided that a task may be specified by an algebraic or differential equation. Secondly, we demonstrate that the kinematic or dynamic reference model plays a role of a task planner and its outcomes are inputs to a tracking control algorithm.

The main motivations for this work origin from two sources. First one is related to mechanics and modeling of constrained systems. Modeling methods have to manage demands of the growing complexity of systems and further applications including control in the first place. The second comes from a process of designing nonlinear controllers that takes advantage of available modeling methods which analytical mechanics offers. For years, there were routine methods of dynamic modeling, i.e. based upon the Lagrange approach and routine methods for planning motions which were limited to planning trajectories. The complexity of system designs, control requirements and constraints were moved to stages of a controller design and its implementation. We demonstrate that the complexity associated with the constraints on systems may be handled by appropriate modeling.

SPECIFICATION OF CONTROL ORIENTED TASKS

A concept of constraints in classical mechanics is based on the assumption that constraints are given *a priori* and they are put upon a mechanical system through other bodies or physical systems, i.e. when bodies are in contact with each other and roll without slipping. They are position and kinematic constraints, they are "known" and "given" by Nature (Murray et al., 1996, de Jalon and Bayo, 1994), and usually they are referred to as material constraints.

Material constraints are a significant class of motion limitations in engineering practice but there are many problems for which constraints are of a different nature. For example, in design or operation problems constraints are formulated before a system is designed. Tasks are excellent examples of such constraints. They are specified first and then we develop dynamic or control models of a system that performs work. Generally, sources of these constraints are not in other bodies. They are referred to as non-material and may arise as performance, design, operation, control or safety requirements. They can be formulated by algebraic or differential equations, or inequalities. The non-material constraints are referred to as programmed (Jarzębowska, 2002, 2007).

Definition 1: A programmed constraint is any requirement put on a physical system motion specified by an equation.

Definition 2: A programmed motion is a system motion that satisfies a programmed constraint.

A system may be subjected to both material and programmed constraints.

Based on definitions 1 and 2 we may introduce the following classification of programmed constraints:

1. Position programmed constraints:

$$f_{\alpha}(t, q_1, \dots, q_n) = 0, \quad \alpha = 1, \dots, a, a < n \quad (1)$$

which may be written as $A_1(t,q)=0$, where A_1 is an a -dimensional vector. The programmed constraints (1) also restrict allowable velocities and accelerations.

2. Kinematic programmed constraints:

$$f_\beta(t, q_1, \dots, q_n, \dot{q}_1, \dots, \dot{q}_n) = 0, \quad \beta = 1, \dots, k, k < n \quad (2)$$

which we write as $B_1(t, q, \dot{q})=0$, where B_1 is a k -dimensional vector. The constraints (2) restrict accelerations allowable by the program and if they are nonholonomic, they do not restrict positions.

3. High order programmed constraints:

$$B_\beta(t, q\dot{q}, \dots, q^{(p)}) = 0, \quad (3)$$

where p is a constraint order and B_β is a k -dimensional vector. Equations (3) can be nonlinear in $q^{(p)}$. Differentiation of (3) with respect to time, until the highest derivative of a coordinate is linear, results in equations linear with respect to this highest coordinate derivative. Without loss of generality, we assume that " p " stands for the highest order derivative of a coordinate which appears linearly in a constraint equation and the constraints are linear in all p -th order derivatives. It let us write the constraints in the form

$$B(t, q\dot{q}, \dots, q^{(p-1)})q^{(p)} + s(t, q\dot{q}, \dots, q^{(p-1)}) = 0, \quad (4)$$

where B is a $(k \times n)$ -dimensional matrix with $n > k$, and it is assumed to have full rank, and s is a $(k \times 1)$ -vector.

According to definitions 1 and 2, and (1), (2) and (4), driving and task constraints, performance goals or other requirements on a system motion to obtain its specified performance may be included into the "programmed constraints" class. They play the same role - they program the motion. The constraints (4) are referred to as the unified constraint formulation. For the constraints (4) we formulate the following definition.

Definition 3: The constraint equations (4) are completely nonholonomic if they cannot be integrated with respect to time, i.e. we cannot obtain constraint equations of a lower order. If we can integrate (4) $(p-1)$ or less times, i.e. we can obtain nonholonomic constraints of first orders or orders lower than p , we say that (4) are partially integrable. If (4) can be integrated completely, i.e. we obtain constraints of the form $A_\beta(t, q)=0$, they are holonomic.

From the control theory perspective, nonholonomic constraints and their sources are viewed in a different way than in analytical mechanics. There are three situations when nonholonomic constraints may arise:

1. Explicit kinematic constraints are put upon systems.
2. Conservation laws, which are preserved by Lagrange's or Hamilton's equations.
3. Underactuated systems, which are usually treated separately and classified as systems with constraints on controls.

Some conclusions may be drawn based on this classification. Firstly, excluding underactuated systems, nonholonomic constraints that are incorporated into kinematic or dynamic control models are material first order or they specify conservation laws. Secondly, Lagrange's methods and their modifications are applied for the generation of equations of motion of systems subjected to these constraints. Thirdly, the constraints of the form (4) are not merged into any control model.

The programmed constraints are proper to describe tasks. In this approach, mobile manipulators or other vehicles are viewed as constrained systems and constraints may originate from different sources like (Jarzębowska, 2007):

1. Material constraints, which are position or kinematic. They can be holonomic or nonholonomic specified by (1), (2), and conservation laws, also specified by (2).
2. Programmed constraints (4), which are non-material and put on systems in order to specify their desired motions.
3. Constraints that may come from dynamic, design, control or operation specifications including underactuated systems – if possible specified by (4).
4. Constraints that may specify obstacles in a robot or manipulator workspace – some may be specified by (4).

Material constraints, especially nonholonomic, are well known in dynamics and control, and appropriate tools are developed to study systems with such constraints, e.g. (Murray, Li and Sastry, 1996, Oriolo, De Luca and Vendittelli, 2002). Dynamic models for constrained systems are developed based on classical mechanics methods, mostly on Lagrange's equations with multipliers or Kane's approach. It means that only first order constraints are merged into these models. Programmed constraints and constraints from groups 3 and 4 are taken into account when control strategies are to be designed to obtain motions that satisfy these constraints. The above modeling procedure and control design are typical ways in which tasks are executed within nonlinear control theory framework. Exceptions are a position constraint for a trajectory to track that has the form (1) and the so-called driving coordinate, which has the form (2). They are the only constraints specified as control oriented tasks.

Since now on, we let constraints be holonomic or nonholonomic, material or programmed.

Proposition 1

The equations of constraints in the form (4) can specify both material and programmed constraints.

They are referred to as a unified constraint formulation.

Proof: The proof is based upon reasoning that the type of constraint equations does not influence generation of equations of motion of a system subjected to these constraints. The only concern is the constraint order and if the constraints are ideal. By "type of constraint equations" we mean whether constraints are material or non-material. Indeed, when $p=0$ we get a constraint in the form (1), i.e. a position constraint which may be a material constraint that describes, for example, a constant distance between link ends, or be a programmed constraint that specifies a desired trajectory for the end-effector. When $p=1$, a constraint equation is in the form (2) and it can be a material constraint that describes the condition of rolling without slipping. However, it can be a programmed constraint that specifies, for example, the end-effector motion with some desired velocity. For both examples of constraint types for $p=1$ equations of motion are generated in the same way provided that constraints are ideal. Material constraints are of orders equal to zero or one and can be presented by (1) or (2). Constraint equations for $p>1$ are of the non-material type. When needed, two or more such constraint equations, each of a different type, may be listed in (4). The constraint formulation (4) can be used then to specify constraint equations of any order and type. *q.e.d.*

It has to be noted that constraint equations which were investigated so far resulted in the so-called Chaplygin forms of control models, mostly driftless and differentially flat, and could be transformed into the power or chained forms or to their extensions. A tracking control design for such systems can be considered a solved problem, at least theoretically (Kolmanovsky and McClamroch, 1995). However, systems with both material and programmed constraints may result in non-Chaplygin control models (Jarzębowska, 2007) and may not be transformable into any special control form.

KINEMATIC BASED TASK PLANNING

Kinematic task planning refers to planning a task based upon a fully specified program, i.e. the number of the material and programmed constraints is equal to the number of a system degrees of freedom. Such situation may occur when several motion requirements are specified. For example, for a manipulator end-effector one may want to specify both trajectory and velocity changes. The velocity control can be significant if motion termination is needed when the program is accomplished. The kinematic model becomes a reference model for control design.

Definition 4: The kinematic model of a system that consists of material and programmed constraint equations and the program is fully specified, is referred to as a kinematic reference model.

The kinematic reference model is in the form (4) but now B is a $(n \times n)$ matrix, with n being the number of all constraint equations equal to the number of the configuration space.

Corollary 1: The high order constraint equations (4) can be transformed into the state space control form

$$\dot{x} = f(x) + g(x)u(t). \quad (4a)$$

Proof: Introduce a new p -vector $x = (x_1, \dots, x_p)$ such that $x_1 = q, \dot{x}_1 = x_2, \dots, \dot{x}_{p-1} = x_p$. If time t is present explicitly in (4), we may reorder coordinates and then $x_0 = t$. With the new vector x eq. (4) can be written as

$$\begin{aligned} \dot{x}_1 &= x_2, \\ \dot{x}_2 &= x_3, \\ &\vdots \\ \dot{x}_{p-1} &= x_p, \\ B(x_1, \dots, x_p) \dot{x}_p &= -s(x_1, \dots, x_p) \end{aligned} \quad (5)$$

or

$$C_p(x) \dot{x} = b(x), \quad (5a)$$

where C_p is a $(p-1+k) \times p$ matrix and b is a $(p-1+k)$ - dimensional vector. Let $f(x)$ be a particular solution of (5a) so $C_p(x)f(x) = b(x)$. Let $g(x)$ be a $p \times (n-k)$ full rank matrix whose column space is in the null space of $C_p(x)$, i.e. $C_p(x)g(x) = 0$. Then, the solution of (5) is given by (4a) for any smooth vector $u(t)$.

The problem with the constraints (5a) is converted into a control problem for a system with high order constraints. In general, a drift term is present in (4a) or the constraints may be non-Chaplygin. Since (4a) is a state space control form of the unified constraint formulation (4), we refer to it as a unified state space control form. The kinematic control model (4a) is only formally equivalent to the one usually used in nonlinear control, since in (4a) $u_i, i=1, \dots, m$, may not have a physical interpretation of velocities. They may be accelerations or their time derivatives.

The kinematic reference model is a motion planner and its outputs are inputs to a controller which is to be designed.

DYNAMIC BASED TASK PLANNING

Dynamic task planning refers to planning a task based upon a partially specified program, i.e. the number of the material and programmed constraints is less than the number of a system degrees of freedom. It requires solutions to the constrained dynamics of a system, when the constraints are of the form (4). It requires then a theoretical framework for

the generation of equations of motion of a system subjected to high order constraints (4). The framework is based upon the analytical mechanics method that yields the generalized programmed motion equations - GPME (Jarzębowska, 2002, 2006, 2008).

The GPME for a system subjected to constraints (4) are $(n-k)$ second order differential equations, which together with k constraint equations (4), form the set of equations of motion in the form

$$\begin{aligned} M(q)\ddot{q} + V(q,\dot{q}) + D(q) &= Q(t, q, \dot{q}), \\ B(t, q, \dot{q}, \dots, q^{(p-1)})q^{(p)} + s(t, q, \dot{q}, \dots, q^{(p-1)}) &= 0, \end{aligned} \quad (6)$$

where M is a $(n-k) \times n$ inertia matrix, V is a $(n-k)$ -dimensional velocity dependent vector, D is a $(n-k)$ -dimensional vector of gravity forces, and Q is a $(n-k)$ -dimensional vector of external forces.

Equations (6) are free of the constraint reaction forces, which are eliminated during the derivation process. They are in the reduced state form, which is ready for the development of a dynamic control model.

Definition 5: The constrained dynamic model of a system (6) is referred to as a dynamic reference model.

The dynamic reference model is a motion planner now and its outputs are inputs to the dynamic control model, which is also based upon the GPME as demonstrated in next sections. Since the programmed constraint may be specified for a system before it is designed or put into operation, it has to be verified whether it is feasible for the system equipped with given power sources. The verification has to be done by inspections of solutions of (6).

To derive the GPME (6) for a system subjected to p -th order constraints the following algorithm, which enables automation of the equations generation, is developed (Jarzębowska, 2007).

Algorithm

Assume that the constraints (4) can be solved at least locally with respect to $q_\beta^{(p)}$, i.e.

$$q_\beta^{(p)} = g_\beta^{(p)}(t, q_1, \dots, q_n, \dot{q}_1, \dots, \dot{q}_n, \dots, q_{k+1}^{(p)}, \dots, q_n^{(p)}). \quad \beta=1, \dots, k \quad (1a)$$

1. Construct a function P_p such that

$$P_p = \frac{1}{p} [T^{(p)} - (p+1)T_0^{(p)}] \quad \text{and} \quad T_0^{(p)} = \sum_{\sigma=1}^n \frac{\partial T}{\partial q_\sigma} q_\sigma^{(p)} \quad (2a)$$

2. Construct a function R_p such that

$$R_p = P_p - \sum_{\sigma=1}^n q_\sigma^{(p)} Q_\sigma = R_p(t, q_\sigma, \dot{q}_\sigma, \dots, q_\mu^{(p)}, q_\beta^{(p)}, q_\sigma^{(p+1)}). \quad (3a)$$

3. Construct a function R_p^* , in which $q_\beta^{(p)}$ from (3a) are replaced with (1a)

$$R_p^* = R_p^*(t, q_\sigma, \dot{q}_\sigma, \dots, q_\mu^{(p)}, g_\beta^{(p)}(t, q_\sigma, \dots, q_\mu^{(p)}), q_\sigma^{(p+1)}) = R_p^*(t, q_\sigma, \dot{q}_\sigma, \dots, q_\mu^{(p)}, q_\sigma^{(p+1)}). \quad (4a)$$

4. Assuming that $\partial Q_\sigma / \partial q_\sigma^{(p)} = 0$, the desired GPME for a system with p -th order constraints (1a) have the form

$$\frac{\partial R_p^*}{\partial q_\mu^{(p)}} = \frac{\partial R_p}{\partial q_\mu^{(p)}} + \sum_{\beta=1}^k \frac{\partial R_p}{\partial q_\beta^{(p)}} \frac{\partial g_\beta^{(p)}}{\partial q_\mu^{(p)}} = 0. \quad \mu = k+1, \dots, n \quad (5a)$$

It can be proved that Eq. (5a) are $(n-k)$ second order equations of motion and together with (1a) are equivalent to (6).

The most important property of (5a) is that they are free of constraint reaction forces. They are the smallest set of motion equations. It makes them suitable for control applications. Equations (5a) are referred to as a unified dynamic model for a constrained system. Dynamic models presented in, for example (Yun and Sarkar, 1998, You and Chen, 1993), are peculiar cases of (5a) for $p=1$.

GENERATION OF REFERENCE MOTIONS - EXAMPLES

Examples that follow present the way in which tasks may be specified by the programmed constraints.

Two-link planar manipulator model

Consider the two-link planar manipulator model with two degrees of freedom described by Θ_1, Θ_2 . Its geometry and inertia properties, in SI units, are: $l_1=1, l_2=0.6, I_{z1}=0.12, I_{z2}=0.25, r_1=l_1/2, r_2=l_2/2$ and $m_1=1, m_2=2$. We formulate a requirement that the manipulator end-effector is to track a trajectory whose curvature changes in a specified way, i.e. $\Phi^* = \frac{d\Phi(t)}{dt}$. This task yields the programmed constraint, which specified in joint coordinates, has the form

$$\ddot{\Theta}_2 = F_1 - F_2 \ddot{\Theta}_1, \quad (7)$$

$$\text{where } F_1 = \frac{A_\phi - A_1 - A_2 a_o}{a_2 + a_4 a_o}, \quad F_2 = \frac{a_1 + a_2 + a_o(a_3 + a_4)}{a_2 + a_4 a_o}, \quad A_\phi = \frac{-\Phi(a_5^2 + a_6^2) [\dot{\Phi}(a_5^2 + a_6^2) + 3\Phi(a_5 a_7 + a_6 a_8)]}{a_6(a_5 a_8 - a_7 a_6)}, \quad a_o = a_5 / a_6.$$

$$A_1 = 3a_3\dot{\Theta}_1\ddot{\Theta}_1 + 3a_4(\ddot{\Theta}_1 + \ddot{\Theta}_2)(\dot{\Theta}_1 + \dot{\Theta}_2) - a_1\dot{\Theta}_1^3 - a_2(\dot{\Theta}_1 + \dot{\Theta}_2)^3,$$

$$A_2 = 3a_3\dot{\Theta}_1\ddot{\Theta}_1 + 3a_2(\ddot{\Theta}_1 + \ddot{\Theta}_2)(\dot{\Theta}_1 + \dot{\Theta}_2) + a_3\dot{\Theta}_1^3 + a_4(\dot{\Theta}_1 + \dot{\Theta}_2)^3,$$

$$a_1 = -l_1 \sin\Theta_1, a_2 = -l_2 \sin(\Theta_1 + \Theta_2), a_3 = -l_1 \cos\Theta_1, a_4 = -l_2 \cos(\Theta_1 + \Theta_2), a_5 = a_1\dot{\Theta}_1 + a_2(\dot{\Theta}_1 + \dot{\Theta}_2), a_6 = -a_3\dot{\Theta}_1 - a_4(\dot{\Theta}_1 + \dot{\Theta}_2),$$

$$a_7 = a_1\dot{\Theta}_1 + a_3\dot{\Theta}_1^2 + a_2(\ddot{\Theta}_1 + \ddot{\Theta}_2) + a_4(\dot{\Theta}_1 + \dot{\Theta}_2)^2, a_8 = -a_3\ddot{\Theta}_1 + a_1\dot{\Theta}_1^2 - a_4(\ddot{\Theta}_1 + \ddot{\Theta}_2) + a_2(\dot{\Theta}_1 + \dot{\Theta}_2)^2.$$

The second requirement is that the end-effector has a specified velocity, i.e. $\sqrt{\dot{x}^2 + \dot{y}^2} - v_p = 0 = B_1$. For these two constraint equations the kinematic reference model is

$$\begin{bmatrix} F_2 & 1 \\ (a_9 - a_{10})F_2 & 0 \end{bmatrix} \begin{bmatrix} \ddot{\Theta}_1 \\ \ddot{\Theta}_2 \end{bmatrix} = \begin{bmatrix} F_1 \\ \dot{v}_p^2 + v_p\ddot{v}_p - a_{10}F_1 - A_3 - S \end{bmatrix}, \quad (8)$$

where the programmed velocity is $v_p = l$, and the trajectory curvature $\Phi(t)$ is assumed to be constant. Other quantities in (8) are $A_3 = a_7^2 + a_8^2 + a_5A_1 + a_6A_2$, $a_9 = a_5(a_1 + a_2) - a_6(a_3 + a_4)$, $a_{10} = a_5a_2 - a_6a_4$.

The function S consists of stabilizing terms, i.e. $S = \alpha\dot{B}_1 + \beta B_1$, where α, β are rates of convergence of the differentiated constraint to the original and are selected to be $\alpha = 20$, $\beta = 3$. In our example S has the form

$$S = \alpha(a_5a_7 + a_6a_8 - v_p\dot{v}_p) + \beta(\sqrt{a_5^2 + a_6^2} - v_p). \quad (9)$$

The reference motion according to (8) and its tracking by the PD controller are presented in Fig. 1 and 2. Figure 3 presents accelerations of both joints as time functions, and figure 4 - time histories of position tracking errors.

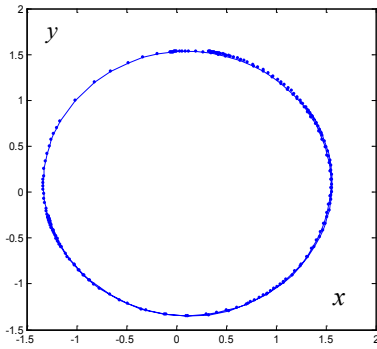


Figure 1 - Reference (—) and controlled (ooo) motions of the end-effector

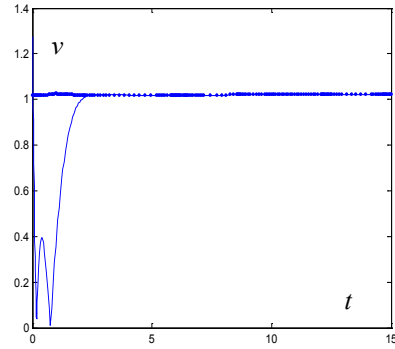


Figure 2 - Tracking of the end-effector velocity vs. time

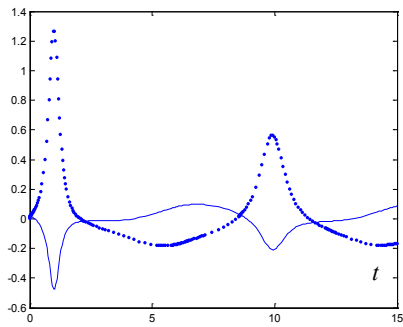


Figure 3 - Joint accelerations $\ddot{\theta}_1$ (ooo), $\ddot{\theta}_2$ (—) vs. time

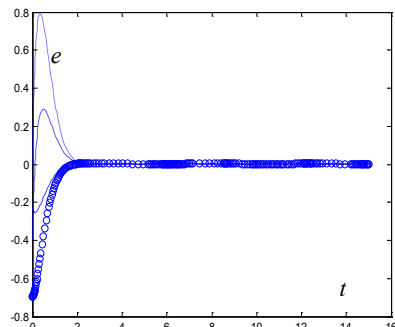


Figure 4 - Tracking errors: e_{θ_1} (ooo), e_{θ_2} (—), $e_{\dot{\theta}_1}$ (...), $e_{\dot{\theta}_2}$ (---) vs. time

Unicycle model

Consider a mobile platform whose kinematics is equivalent to that of a unicycle. The task for the platform is to track a desired trajectory to a rest position. To this end, supplement the equation of the material constraints

$$\dot{x} = r\dot{\theta}\cos\varphi, \dot{y} = r\dot{\theta}\sin\varphi, \quad (10)$$

by a programmed constraint, i.e. a desired trajectory

$$\dot{\varphi} = \sin(0.5\pi - t), \quad (11)$$

and by one more equation that specifies termination of motion after a predefined time. Select an initial velocity, say $v=10$ m/s, and terminate motion after 20 seconds, i.e. $v=f(t)$. The kinematic reference model is

$$\begin{bmatrix} 1 & 0 & 0 & 0 \\ 0 & 1 & 0 & 0 \\ 0 & 0 & 1 & 0 \\ 0 & 0 & 0 & 1 \end{bmatrix} \begin{bmatrix} \dot{x} \\ \dot{y} \\ \dot{\varphi} \\ \dot{\varphi} \end{bmatrix} - \begin{bmatrix} f(t)\cos\varphi \\ f(t)\sin\varphi \\ f(t)/r \\ \sin(0.5\pi - t) \end{bmatrix} = 0. \quad (12)$$

Figures 5 and 6 present tracking of the programmed motion specified by (12) using the Wen-Bayard controller.

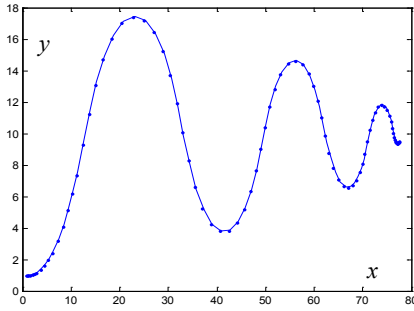


Figure 5 – Programmed motion tracking by the Wen-Bayard controller (●●)

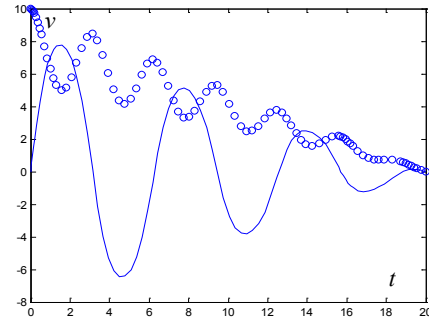


Figure 6 - Unicycle velocity components v_x (—), v_y (ooo) vs. time

Two wheeled mobile robot model

Consider a mobile robot that consists of a platform and two actuated wheels (Jarzębowska, 2007). The task for the robot is to track a reference trajectory

$$B_1 = x_C^2 + y_C^2 - R^2(t) = 0, \quad R(t) = 0.2 + 0.01t. \quad (13)$$

The robot is subjected to the material constraint equations

$$\begin{aligned} \dot{y}_C \cos\varphi - \dot{x}_C \sin\varphi - \dot{\varphi}d &= 0, \\ \dot{x}_C \cos\varphi + \dot{y}_C \sin\varphi + \dot{\varphi}b &= \dot{\varphi}_r r, \\ \dot{x}_C \cos\varphi + \dot{y}_C \sin\varphi - b\dot{\varphi} &= r\dot{\varphi}_l. \end{aligned} \quad (14)$$

The reference dynamics is developed for $n=5, k=4, p=1$, using the Algorithm. It is of the form

$$\begin{aligned} \tilde{m}_{11}\ddot{\varphi}_r + \tilde{m}_{12}\ddot{\varphi}_l + \tilde{m}_{13}\ddot{x}_C + \tilde{m}_{14}\ddot{y}_C + \tilde{m}_{15}\ddot{\varphi} + v_1 &= 0, \\ \dot{y}_C \cos\varphi - \dot{x}_C \sin\varphi - d\dot{\varphi} &= 0, \\ \dot{x}_C \cos\varphi + \dot{y}_C \sin\varphi + b\dot{\varphi} &= r\dot{\varphi}_r, \\ \dot{x}_C \cos\varphi + \dot{y}_C \sin\varphi - b\dot{\varphi} &= r\dot{\varphi}_l, \\ x_C^2 + y_C^2 - (0.2 + 0.01t)^2 &= 0, \end{aligned} \quad (15)$$

where $\tilde{m}_{11} = 2I_w \left(\frac{dv}{rw} + s \right)$, $\tilde{m}_{12} = 2I_w \left(\frac{dv}{rw} - s \right)$, $\tilde{m}_{13} = \left[2m_w d \sin\varphi - (m + 2m_w) \frac{dy_C}{w} \right]$, $\tilde{m}_{14} = \left[(m + 2m_w) \frac{dx_C}{w} - 2m_w d \cos\varphi \right]$,

$\tilde{m}_{15} = I_c + 2I_m + 2m_w b^2$, $v_1 = \frac{4m_w d \sigma^*}{w} \dot{\varphi} - \frac{6m_w d^2}{w} \dot{\varphi}^2$, $w = x_C \cos\varphi + y_C \sin\varphi$, $v = x_C \sin\varphi - y_C \cos\varphi$, $s = b/r$,

$\sigma^* = \sigma_1 B_1 - \dot{R}(t)/2$. The term σ^* is introduced to stabilize the numerical solution to the programmed constraint.

Physical parameters of the robot, in SI units, are: $m_c = 0.55$, $m_w = 0.05$, $d = 0.05$, $r = 0.026$, $b = 0.075$, $I_m = 0.23 \cdot 10^{-6}$, $I_c = 0.0182$, $I_w = 0.17 \cdot 10^{-4}$. To track the programmed motion we use the Wen-Bayard controller.

Tracking of the programmed motion (13) is presented in Fig. 7. Control torques as time functions applied to the wheels are shown in Fig. 8.

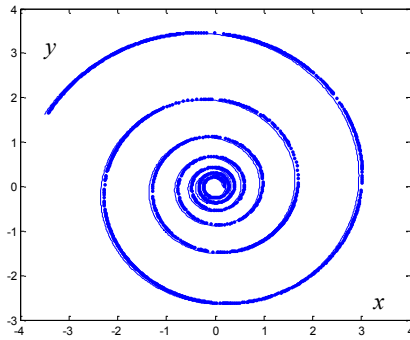


Figure 7 - Reference (—) and controlled (●●●) robot motions within 6 minutes

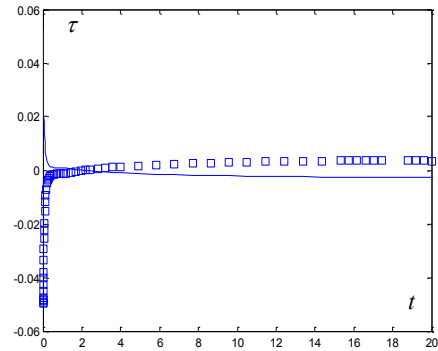


Figure 8 - Torques of the Wen-Bayard controller: (□□) - right wheel, (—) - left wheel

TRACKING A REFERENCE MOTION – CONTROL STRATEGY

We employ the reference dynamic model (6) and the reference kinematic model (4) to design a control strategy for tracking programmed motions. The control objective of programmed motion tracking is formulated as follows: **Given a programmed motion specified either by the reference kinematics (4) or by the reference dynamics (6), design a feedback controller that can track the desired programmed motion.**

In our setting the objective of control design is to make system positions $q_i, i=1, \dots, n$, and their time derivatives follow programmed positions $q_{ip}(t)$ and their time derivatives.

To achieve the control objective we design a tracking strategy whose architecture is presented in Fig. 9. It is based on two models: the reference kinematic (4) or reference dynamic (6) models and the unified dynamic control model

$$\begin{aligned} M(q)\ddot{q} + C(q,\dot{q})\dot{q} + D(q) &= E(q)\tau, \\ B_1(q)\dot{q} &= 0. \end{aligned} \quad (16)$$

The control model (16) is developed using Algorithm for $p=1$. Only the material constraints $B_1(q)\dot{q}=0$ are merged into it. The motivation to design such a tracking strategy is that a variety of programmed constraint equations disable the design of a general scheme of a tracking controller. Instead, in our tracking strategy we separate programmed constraints from material constraints. All constraint equations on a system are merged into the reference dynamics (6) or kinematics (4). The material constraints are merged into the unified dynamic control model (16). This separation of constraint types between the two reference models has tremendous implications. Firstly, (16) is equivalent to the dynamic control model that nonlinear control uses and secondly, the control law block may consist of both controllers that are designed for holonomic systems and model-based controllers for nonholonomic systems. Also, this control architecture is suitable for underactuated systems. Outputs of (4) or (6) are inputs to a tracking controller in (16).

From the point of view of control, the model reference tracking strategy for programmed motion may be compared with two-degree of freedom design (Van Nieuwstadt, 1997). First, we generate motion that takes the system to the goal configuration and it is consistent with material constraints. Then, we design a controller that tracks this motion.

Advantages of the programmed motion tracking strategy can be summarized as follows:

- The reference models (4) and (6) can include arbitrary order nonholonomic constraints. In this way any programmed motion can be planned.
- The tracking strategy separates material constraints from programmed. Then, the dynamic control model (16) is equivalent to models nonlinear control theory uses, i.e. models based upon Lagrange's approach.
- The equivalence of (16) and models based on Lagrange's approach promotes the adoption of existing control algorithms even these dedicated to holonomic systems.
- The equivalence of (16) and models based on Lagrange's approach enables the use of controllers which were verified through laboratory tests and proved their good performance.
- The dynamic control model (16) enables selecting states which are to be controlled.
- The tracking strategy takes advantage of one dynamic control model (16) for both holonomic and nonholonomic systems.
- The tracking strategy enables designing tracking controllers for both motion and a force applied on the environment since the reference dynamics can be derived in the joint or task spaces (Jarzębowska, 2007).
- The tracking strategy extends "trajectory tracking" to "programmed motion tracking".
- The tracking strategy can be applied to systems whose dynamics are completely known and to systems with parametric or structural uncertainties (Jarzębowska, 2008).
- The tracking strategy can be applied to underactuated systems (Jarzębowska, 2007).

- The reference models can be generated off-line and stored in a computer. A library of reference models that plan different tasks can be created. All they can be applied to one dynamic control model of a specific system.

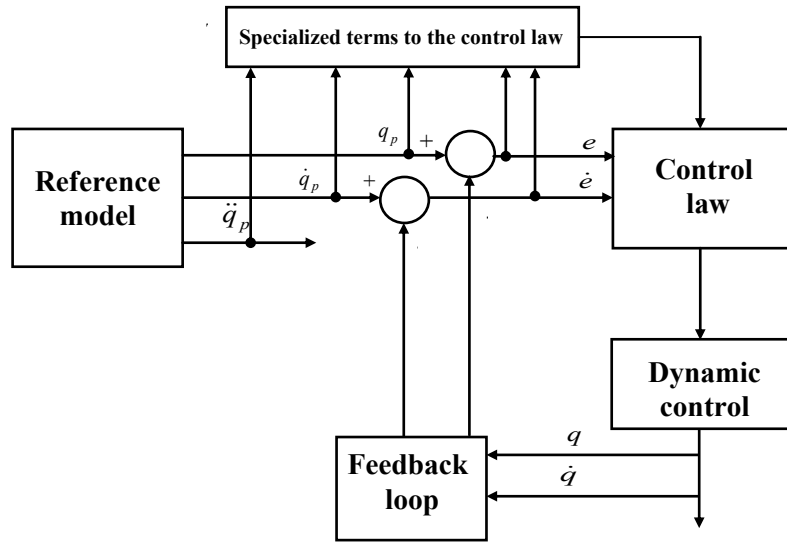


Figure 9 - Architecture of the model reference tracking control for programmed motion

Tracking a reference motion by the two wheeled mobile robot model

The control dynamics for the robot is

$$\begin{aligned} M\ddot{q}_1 + C(\dot{q}_2)\dot{q}_1 + D\dot{q}_1 &= \tau, \\ \dot{q}_2 &= B(q_2)\dot{q}_1, \end{aligned} \quad (17)$$

where: - partition of $q \in R^5$ is $q = (q_1, q_2)$, $q_1 \in R^2$, $q_2 \in R^3$, and $q_1 = (\varphi_r, \varphi_l)$, $q_2 = (x_c, y_c, \varphi)$.

- the inertia matrix is $M = \begin{bmatrix} m_{11} & m_{12} \\ m_{21} & m_{22} \end{bmatrix}$ and $m_{11} = \frac{r^2}{4b^2}(mb^2 + I) + I_w$, $m_{12} = \frac{r^2}{4b^2}(mb^2 - I)$, $m_{21} = m_{12}$, $m_{22} = m_{11}$,
- the total mass consists of mass of the platform m_c and of two wheels $2m_w$, i.e. $m = m_c + 2m_w$,
- moments of inertia are: I_c, I_w, I_m – through the robot mass center, of the wheel about its axis, and about its diameter, and $I = m_c d^2 + 2m_w b^2 + I_c + 2I_m$,
- the velocity dependent matrix is $C = \begin{bmatrix} 0 & c_{12} \\ -c_{12} & 0 \end{bmatrix}$ and $c_{12} = \frac{r^2 d}{2b} m_c \dot{\varphi}$,
- the matrix B in the constraint equation is $B = \begin{bmatrix} 0.5r \cos \varphi & 0.5r \cos \varphi \\ 0.5r \sin \varphi & 0.5r \sin \varphi \\ 0.5r/b & -0.5r/b \end{bmatrix}$,
- the matrix of damping coefficients is $D = \text{diag}(d_{11}, d_{22})$,
- control torque vector is $\tau \in R^2$, $\tau = (\tau_r, \tau_l)$. These are real torques applied to the wheels.

Tracking the programmed motion is presented in figures 7 and 8.

Based on the above example, it can be seen that due to the separation of programmed and material constraints between two models, we can use controllers that are dedicated to holonomic systems.

CONCLUSIONS

In the paper we develop both kinematic and dynamic reference models for task planning. The tasks are motions preplanned for a system to follow. Tasks that may be specified by algebraic or differential equations may be merged into the reference models to provide a control engineer desired motion patterns. The reference models are developed based on the GPME. From the point of view of control design outputs from the reference models are inputs to tracking controllers. We design a tracking control strategy to execute tasks planned for mechanical systems. We demonstrate that one strategy serves both reference motion planners. It can be then a unified procedure for motion planning with trajectory planning as a peculiar case.

REFERENCES

- Balucchi, A., Bicci, A., Balestino, A. and Casalino, G., 1996, "Path Tracking Control for Dubin's Car", Proc. IEEE Int. Conf. Robot. Automat., Minneapolis, MN, USA, Vol. 4, pp. 3123-3128.
- de Jalon, J.G., Bayo, E., 1994, "Kinematic and Dynamic Simulation of Multibody Systems", Mech. Eng. Series, Berlin: Springer-Verlag.
- Jarzębowska, E., 2002, "On Derivation of Motion Equations for Systems with Nonholonomic High-Order Program Constraints," Multibody System Dynamics, Vol. 7(3), pp. 307-329.
- Jarzębowska, E., 2006, "Control Oriented Dynamic Formulation of Robotic Systems with Program Constraints," Robotica, Vol. 24(1), pp. 61-73.
- Jarzębowska, E., 2007, "Model-Based Tracking Control Strategies for Constrained Mechanical Systems", International SAR, Palermo, Italy.
- Jarzębowska E., 2008, "Advanced Programmed Motion Tracking Control of Nonholonomic Mechanical Systems", IEEE Transactions on Robotics, Vol. 24, No 6, pp.1315-1328.
- Kim, J., Zhang, F. and Egerstedt, M., 2009, "Curve Tracking Control for Autonomous Vehicles with Rigidly Mounted Range Sensors", J. Intell. Robot. Syst., Vol. 56, pp. 177-197.
- Koh, K.C., Cho, H.S., 1999, "A Smooth Path Tracking Algorithm for Wheeled Mobile Robots with Dynamic Constraints," J. Intell. Robot. Syst., Vol. 24, pp. 367-385.
- Kolmanovsky, I., McClamroch, H., 1995, "Developments in Nonholonomic Control Problems", Systems and Control Letters, pp. 20-36.
- Laumond, J.P., Sekhavat, S. and Lamineux, F., 1998, "Guidelines in Nonholonomic Motion Planning for Mobile Robots", LAAS report no 9748, France.
- Murray, R.M., Li, Z. and Sastry, S.S., 1996, "A Mathematical Introduction to Robotic Manipulation", CRC Press, Boca Raton.
- Nakamura, Y., Suzuki, T. and Koinuma, M., 1997, "Nonlinear Behavior and Control of a Nonholonomic Free-Joint Manipulator", IEEE Trans. Robot. Automat., Vol. 13(6), pp. 853-862.
- Van Nieuwstadt, M.J., 1997, "Trajectory Generation for Nonlinear Control Systems", Techn. Report CDS-96-011, Dept. Mech. Eng. CalTech.
- Oriolo, G., De Luca, A. and Vendittelli, M., 2002, "WMR Control via Dynamic Feedback Linearization: Design, Implementation, and Experimental Validation," IEEE Trans. Contr. Systems Techn., Vol. 10(6), pp. 835-852.
- Papadopoulos, E., Poulakakis, J., 2000, "Trajectory Planning and Control for Mobile Manipulator Systems", Proc. 8th IEEE Mediterranean Conf. Control and Automation, Patras, Greece.
- Scheuer, A., Laugier, Ch., 1998, "Planning Sub-Optimal and Continuous-Curvature Paths for Car-Like Robots," in Proc. IEEE/RSJ Int. Conf. Intell. Robot. Syst., pp. 25-31.
- Shekl, A.M., Lumelsky, V.L., 1998, "Motion Planning for Nonholonomic Robots in a Limited Workspace," in Proc. IEEE/RSJ Int. Conf. Intell. Robot. Syst., pp. 1473-1478.
- Tan, J., Xi, N., 2002, "Integrating Task Planning and Control for Mobile Manipulators", Proc. 2002 IEEE Int. Conf. Robotics and Automation, Washington, DC, pp. 382-387.
- Tilbury, D., Murray, R.M. and Sastry, S.S., 1995, "Trajectory Generation for the N-Trailer Problem Using Goursat Normal Forms", IEEE Trans. Automat. Contr., 40(5), pp. 802-819.
- Yun, X., Sarkar, N., 1998, "Unified Formulation of Robotic Systems with Holonomic and Nonholonomic Constraints," IEEE Trans. Robot. Automat., vol. 14(4), pp. 640-650.
- You, L-S., Chen, B-S., 1993, "Tracking Control Designs for Both Holonomic and Nonholonomic Constrained Mechanical Systems: A Unified Viewpoint," Int. J. Control., vol. 58(3), pp. 587-612.
- Vafa, Z., 1991, "Space Manipulator Motion with No Satellite Attitude Disturbances," in Proc. IEEE Int. Conf. On Robot. Automat., pp. 1770-1775.

THE ANGULAR KURTOSIS AND POWER: NEW FEATURES FOR MACHINING MONITORING

M. Lamraoui^{1,2}, M. Thomas¹, M. El Badaoui², I. Zaghbani¹ and V. songméné¹

¹École de Technologie Supérieure, 1100 Notre Dame Ouest, Montréal, H1C 1K3 Québec, Canada

² Université de Lyon, F-42023, Saint Etienne, LASPI, F-42334, IUT de Roanne, France

marc.thomas@etsmtl.ca

ABSTRACT: It is now accepted that the vibration signals from rotating machinery are very often cyclostationary (random phenomena repeating at each cycle). The statistical properties of these signals are periodic with respect to the machine cycle. This periodicity is induced by the cyclic operation of the machine. Previous studies have highlighted the cyclostationarity of internal combustion engines' signal, bearings, and gears. Unfortunately, the studies on signal processing in high speed milling have not been exploited by this concept in the literature. The synchronous analysis allows for fully exploiting this property of cyclostationarity and providing new tools consistent with physics. A new indicator for monitoring, called the angular Kurtosis, is developed in this study. This new indicator allows for detecting the instant where the Kurtosis takes high or low values, and thus identifying the source of defects. The angular power and kurtosis are estimated from the angular analysis. The analysis consists in re-sampling the signal angularly acquired in time domain and then cut the signal in consecutive blocks of length equal to the period of the cycle and calculate the angular 's statistics. Finally this statistics are analyzed in angular or frequency domain.

We present in this study a new application for monitoring cyclostationarity signals by using the Angular Kurtosis. It can detect the angle position where physical phenomena happen. The results have shown that, by machining in the unstable region, chatter is produced that results in flat angle kurtosis, such as pseudo (white) random signal with flat spectrum. On the other hand, a study on tool wear conducted in the stable region has shown an increase of power spikes corresponding at locations of contact between the tool and workpiece with clear periodic spectrum while the angular Kurtosis became flat with a random spectrum. Consequently, this study has opened new avenues for the use of cyclostationary signal characteristics in the diagnosis and monitoring of high-speed machining (HSM).

Keywords: *Vibration, cutting tools, High Speed Machining, angular kurtosis, angular power, chatter, wear, monitoring*

Nomenclature

t = time, s

T = period, time s

$x(t)$ = stochastic process

E = operator

M_x = mean

V_x = variance

P_x = power

Kur_x = Kurtosis

K = number of blocks

D = tool diameter, mm

H = overhang length, mm

L = tool length, mm

Z = number of teeth

θ = angle, °

Θ = blocks's length

$\wp\{\cdot\}$ = operator of cyclic averaging

α = cyclic frequency, Hz

α_r = orthogonal rake angle, °

γ_r = tool orthogonal clearance, °

β = tool cutting edge, °

A_p = maximum depth of cut, mm

INTRODUCTION

The optimization of the systems of production is a permanent concern of the industrialists mainly in the sector of the manufacturing where the economic stakes are important. Consequently, the diagnosis of the cutting tool health becomes so essential. In the machining domain, global indicators and spectrum analysis are often used to extract the information about the wear of the cutting tools. However these methods suppose that the signals stemming from the machine are stationary. By definition, the stationary signals are presenting physical phenomena which maintain a constant statistical behavior in time. However, the rotating machinery cannot undergo stationary operations, so even under conditions of constant operations (velocity, couple, and temperature). Successions of the phenomena take place in the cycle of the machine and so release energies, such as shocks due to the work of metals by the cutting tool in manufacturing. It is recognized actually that the majority of the mechanical signals are intrinsically non-stationary because of the evolutionary phenomena which generate them and that main of the defects can be detected in this non-stationary part of signal. Consequently, even if it simplifies the treatments, the hypothesis of the stationarity is not able to reveal the required information. The cyclostationarity analysis allows for showing this information for cyclic and repetitive phenomena which are particular cases of no stationarity. It will then be possible in this context, to add to the classic indicators, an additional dimension which translates its cyclic evolution.

The first studies on the cyclostationarity date back to 1950s with the works of Bennett (1958) and Gladyshev (1961, 1963). Recently, the domain knew an increasing interest, mainly because of its applications in telecommunication. The cyclostationarity allowed for improving the precision and the reliability of algorithms existing in noisy environment. It also opened the way to new perspectives concerning problems previously treated (Garder et al, 1989-1993) and allowed to obtain interesting results in blind separation “(Antoni et al, 2005), (Sghir et al, 2009a), (Sghir et al, 2009b)” and identification in experimental modal analysis (Antoni et al, 2004).

The objective of this article is to present a new method for the monitoring of the cutting tool health in the operation of high speed milling. This method combines the cyclostationary aspect, which characterizes the signals of milling, and the angular kurtosis and power. By detecting the angle where the kurtosis takes high or low values, as for example in the passage of teeth, it allows for detecting the source of the impact. In this paper, after having presented the notion of cyclostationarity, its physical origins and its mathematical properties, the cyclostationarity of the vibratory processes stemming from rotating machines is discussed and we present the angular analysis, in particular the angular kurtosis and power and its algorithm of estimation. We present then the experimental part of its application on signals stemming from an operation of high speed milling.

CYCLOSTATIONARITY OF VIBRATIONS OF ROTATING MACHINES

The rotating machines are governed by mechanisms which evolve cyclically. Consequently, for stable functioning (speed, pressure, temperature, driving cycle, period of the reducer), the physical parameters which describe the generation of the vibrations undergo periodic behavior, such as the strengths of excitations distributed periodically or the strengths of excitation led by repetitive impacts.

This part discussed on the vibratory behavior of machines subjected to cyclostationary. Studies have already put in evidence the cyclostationarity of the signals of combustion engines (Antoni et al., 2002a-2002b), bearings (Randall and Antoni, 2002) and gears (Antoni et al, 2004). The recognition of the cyclostationarity of the signals of rotating machines allows for taking into account their natural unstationary behavior by designing new features of treatment, more effective and more precise than those traditionally based on the hypothesis of stationarity. The innovation lies on an additional dimension related to angular variables which describe the evolution of the machine behavior. We show in the following section, the theoretical aspects of cyclic energy and spectral indicators.

CYCLOSTATIONARITY

Time properties

Suppose that $\{x(t)\}_{t \in \mathbb{R}}$, $x \in \mathbb{C}$, the stochastic process which describes the vibrations of a location of a mechanical structure, according to time t .

i) The process $x(t)$ is cyclostationary in the strict sense with regard to period T if its conjoint density of joint probability $p_x(x(t_1), \dots, x(t_n); t_1 \dots t_n)$ is periodic of period T :

$$p_x(x(t_1), \dots, x(t_n); t_1 \dots t_n) = p_x(x(t_1 + T), \dots, x(t_n + T); t_1 + T \dots t_n + T) \quad (1)$$

ii) The process $x(t)$ is said cyclostationary at order 1 (CS1) with regard to period T if its moment of order 1, $m_x(t)$ exists and is periodic of period T :

$$m_x(t) \triangleq E\{x(t)\} = m_x(t + T) \quad (2)$$

iii) The process $x(t)$ is said cyclostationary at order 2 (CS2) with regard to the period T if its moments of order 2 exist and are periodic. In particular, his function of auto-covariance $K_{xx}(t_1, t_2)$ is a periodic function of period T :

$$E\{[x(t_1) - m_x(t_1)][x^*(t_2) - m_x^*(t_2)]\} \triangleq K_{xx}(t_1, t_2) \triangleq K_{xx}(t_1 + T, t_2 + T) \quad (3)$$

iv) The process $x(t)$ is said cyclostationary at order 3 (CS3) with regard to period T if its moments of order 3 exist and are periodic. In particular, his function of bi-correlation $K_{3x}(t_1, t_2, t_3)$ is a periodic function of period T :

$$E\{[x(t_1) - m_x(t_1)][x^*(t_2) - m_x^*(t_2)][x^*(t_3) - m_x^*(t_3)]\} \triangleq K_{3x}(t_1, t_2, t_3) \triangleq K_{3x}(t_1 + T, t_2 + T, t_3 + T) \quad (4)$$

v) The process $x(t)$ is said cyclostationary at order 4 (CS4) with regard to period T if its moments of order 4 exist and are periodic. In particular, his function of tri-correlation $K_{4x}(t_1, t_2, t_3, t_4)$ is a periodic function of period T :

$$E\{[x(t_1) - m_x(t_1)][x^*(t_2) - m_x^*(t_2)][x^*(t_3) - m_x^*(t_3)][x^*(t_4) - m_x^*(t_4)]\} \triangleq K_{4x}(t_1, t_2, t_3, t_4) \triangleq K_{4x}(t_1 + T, t_2 + T, t_3 + T, t_4 + T) \quad (5)$$

A process which verifies “Eq. 2” and “Eq. 3” is said cyclostationary in the large sense (CSSL). In our study, we are almost exclusively interested in the cyclostationary processes in the broad sense which represent the most common case, the cases of cyclostationarity in the superior orders being not very probable in vibratory mechanics.

Notion of cycloergodism

In the stationary and ergodic case, the averages of set of all the realizations and the temporal averages of a realization are equal. In other words, the statistical parameters of the random process $x(t)$ can be estimated by making temporal averages on some particular realizations. These two hypotheses have a big practical importance because generally, we have only a realization of the random process which is a signal measurement. Thus, it is possible to characterize our signals from a single realization by spreading the notion of ergodicity to the cyclostationary processes. We speak then of cycloergodicity. As the notion of ergodism appeals to the notion of kurtosis, the notion of cycloergodism will appeal to the notion of angular kurtosis. The objective of the next section is to introduce the notion of angular analysis; in particular the angular kurtosis.

ANGULAR ANALYSIS AND ESTIMATION OF THE ANGULAR KURTOSIS

The acquisition in angular sampling is particularly suitable for realizing statistics on the cycles of the vibratory signals, by synchronizing them over the period of the basic cycle (Bonnardot et al, 2004). Another procedure requires to re-sampling the signal in batch mode, based on techniques more or less elaborated according to the order of interpolation required on the signal of an encoder acquired together with the temporal signal. Techniques of real-time re-sampling were also proposed (Bonnardot, 2004).

In this paper, we are going to use another method detailed in the experimental part because we do not possess the information of optical encoder to make the angular re-sampling. The angle of rotation θ of the cycling machine is considered as a generic variable, because $\{x(\theta)\}_{\theta \in \mathbb{Z}}$ is a stochastic process containing an important number of cycles and $x(\theta)$ is a particular realization w .

The signal is cut in K consecutive blocks of length Θ , after that the mean, the variance, the power and the angular kurtosis are calculated by (“Eq. 6”, “Eq.7”, “Eq.8” and “Eq.9”) respectively:

$$m_x(\theta)]_{\Theta}^K = \frac{1}{K} \sum_{k=0}^{K-1} x[\text{mod}(\theta + k\Theta, K\Theta)] \quad (6)$$

$$V_x(\theta)]_{\Theta}^K = \frac{1}{K} \sum_{k=0}^{K-1} (x[\text{mod}(\theta + k\Theta, K\Theta)] - m_x(\theta)]_{\Theta}^K)^2 \quad (7)$$

$$P_x(\theta)]_{\Theta}^K = \frac{1}{K} \sum_{k=0}^{K-1} (x[\text{mod}(\theta + k\Theta, K\Theta)])^2 \quad (8)$$

$$Kur_x(\theta)]_{\Theta}^K = \frac{1}{K} \sum_{k=0}^{K-1} \{(x[\text{mod}(\theta + k\Theta, K\Theta)] - m_x(\theta)]_{\Theta}^K\}^4 / (V_x(\theta)]_{\Theta}^K)^2 \quad (9)$$

where $\text{mod}(a, b)$ is the rest of the whole division of a by b . The function mod allows for defining the angular average for each θ . This operation is schematized on “Fig. 1”.

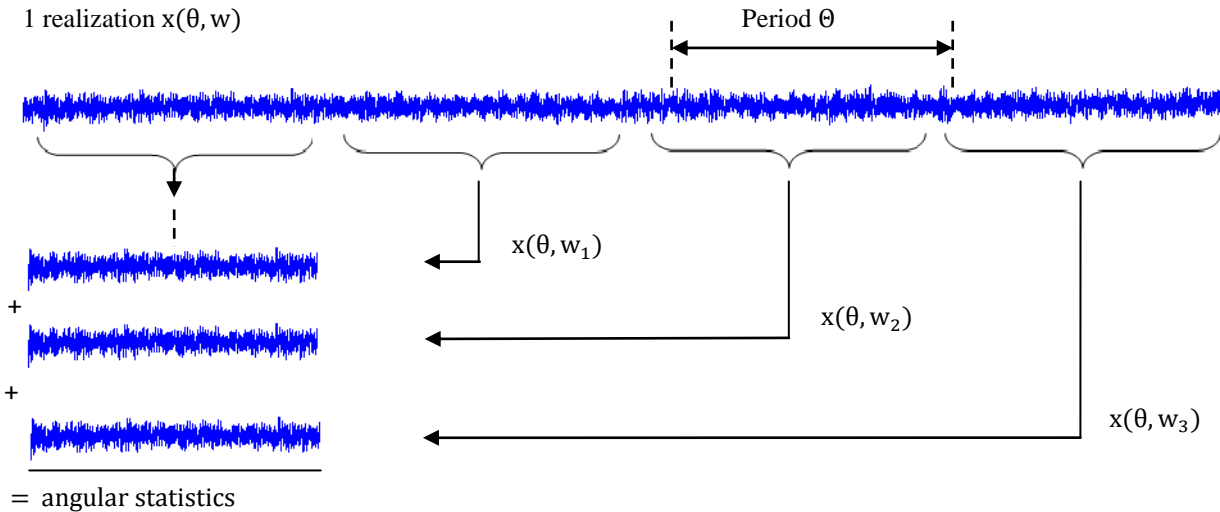


Figure 1 - Calculation of the angular mean.

Because the angular mean defined by “Eq. 6” was extracted from a periodic component which admits series of Fourier, it can also be written when the number of blocks is infinite:

$$m_x(\theta)]_{\Theta}^K = \wp\{x(u)\} = \sum_{k=-\infty}^{+\infty} P_{\Theta}\{x(u)\} e^{2\pi jk\theta/\Theta} \quad (10)$$

with $P_{\Theta}\{x(u)\} = \left\{ \lim_{W \rightarrow \infty} \frac{1}{W} \int_{-W/2}^{W/2} x(u) e^{-2\pi jku/\Theta} du \right\}$, the Fourier coefficients at the cyclic frequency and $\alpha = 1/\Theta$ and $\wp\{\cdot\}$, an operator of cyclic averaging.

The periodic constituent is then generated by the series of Fourier. The immediate mean thus appears as a filter selecting only the frequency $1/\Theta$ and its harmonics. The cyclic mean of the immediate power $\wp\{|x(\theta)|^2\}$ represents periodic fluctuations in the energy. It is represented itself by its coefficients of Fourier which translates the intensity of the periodic components of the energy with the cyclic frequencies. It is thus interesting to decompose these quantities also into frequency, by means of the spectral correlation SC_x^α . It is a frequency function with two variables: the frequency f and the cyclic frequency α . The angular kurtosis, defined by "Eq.9", supplies coefficients at each angle θ . They are normalized with regard to the cyclic energy of signal. This tool is going to allow for detecting the angular positions where the kurtosis takes high or low values, and thus to detect the source of impacts. If the angular kurtosis is periodic, we say that $x(\theta)$ represented by the coefficients of Fourier is cyclo-stationary at the order 4, and thus is possible. This tool may thus be used for the monitoring of the cutting tool wear in high speed milling (Lamraoui et al, 2010).

EXPERIMENTATION

EXPERIMENTAL SET UP

The vibratory signals and forces from a 3axes milling machine (Nexus 410) have been recorded during an operation of milling (50% radial immersion). The characteristics of the milling machine are illustrated in "Tab. 1".

Table 1 - Characteristics of the milling machine.

Machine type	3 Axes Nexus 410 with digital controls
Controller	Mazatrol 640M
Maximum speed of rotation(rpm)	12000
Displacement (mm)	560*409*510
Maximum feed rate (m/min)	36 m/min

Two accelerometers have been placed on a static part of the spindle, the first one is fixed in the feed direction and the second in the orthogonal direction (#1, #2 in "Fig. 2-a"). The time signals were acquired via a system of acquisition LMS SCADAS III with a sampling frequency of 48 KHz. A table dynamometer (Kistler 9255-B) was used for measuring the cutting forces (#5 in fig. 2).

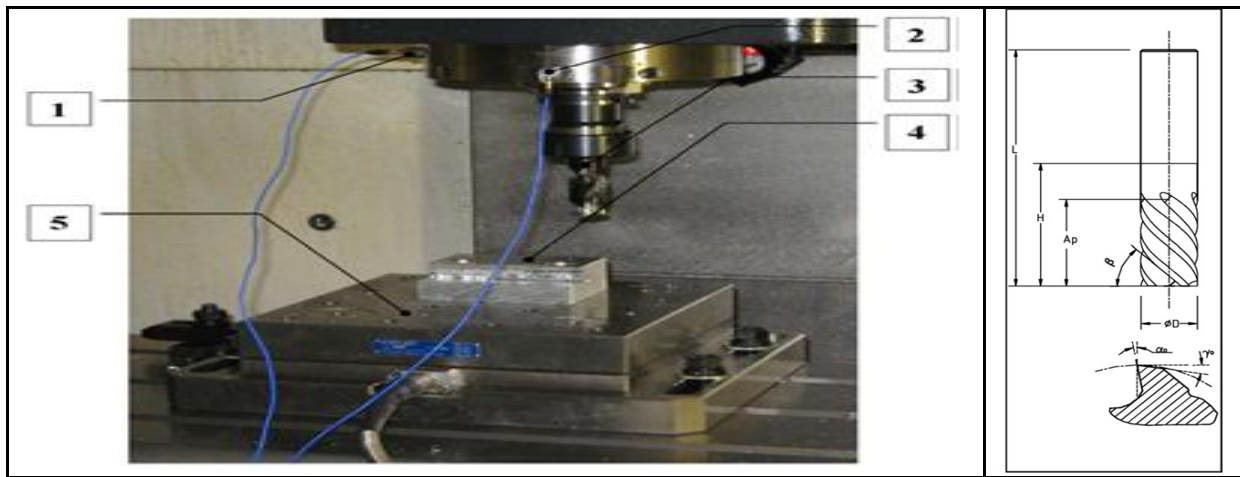


Figure 2 - (a) Experimental measurement of vibrations: #1 accelerometer in the feed direction , #2 accelerometer in the orthogonal direction, #3 cutting tool with 4 teeth, #4 machined piece, #5 dynamometer (Kistler 9255-B), (b) geometrical description of the tool (to the right).

The parameters of machining are presented in “Tab. 2”. We effected four different tests; the first corresponds to a machining operation in stable conditions of cutting (Spindle speed = 3761 rev/min, Axial depth = 5.08). We change the spindle speed in the second test and we effected the milling operation in a chatter’s area. For the third test we took a spindle speed close to the resonance. Finally, we took the same conditions of the first test, and we did a fourth test with a tool that has advanced wear. “Tableau 3” shows the characteristics of the cutting tool.

Table 2 - Parameters of machining

Test#	Spindle speed [rev/min]	Cutting speed [m/min]	Axial depth [mm]	Radial depth [mm]	feed by tooth [mm/tooth]
1,4	3761 (62.7 Hz)	300	5.08	12.7	0.203
2	7523 (125.4 Hz)	600	5.08	12.7	0.203
3	11284 (188 Hz)	900	5.08	12.7	0.203

Table 3 - Geometry of the tool (ISO3002-1)

Symbol	Terminology	Geometry and tolerance
α_r (°)	Orthogonal rake angle	12 ±3
γ_r (°)	Tool orthogonal clearance	8 ±3
B (°)	Tool cutting edge	30±2
A_p (mm)	Maximum depth of cut	25.4
D (mm)	Tool diameter	25.4
H (mm)	Overhang length	76.2
L (mm)	Tool length	101.6
Z	Number of teeth	4

METHODOLOGY AND DISCUSSIONS

CLASSICAL ANALYSIS

“Figure 3” shows the acceleration and force signals in the feed direction for a spindle speed of 62.47 Hz. We can distinguish three zones in the acceleration signal: the spindle rotations without cutting, the spindle rotation without cutting, and the cutting part. In this paper, only the cutting part has been analyzed. Force and acceleration signals reflect a cyclic and repetitive phenomenon which occurs during the operation of machining. “Figure 4” represents the acceleration signals used for estimating the angular kurtosis, at each spindle speeds.

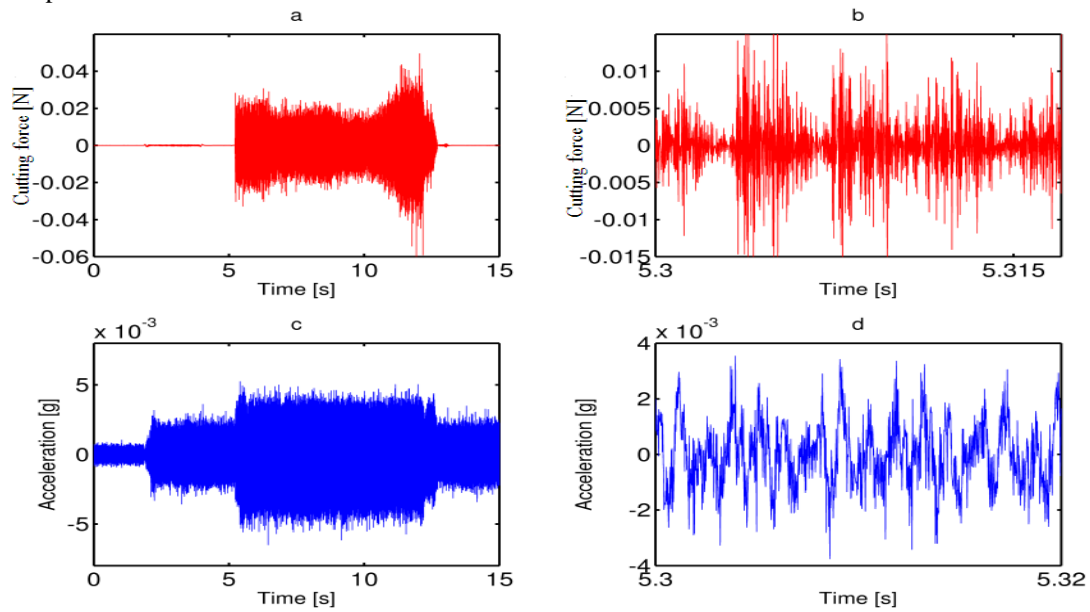


Figure 3 - Acceleration and force signals for the cutting test 1, (a) complete signal of force, (b) zoom shows the force signal, (c) complete signal of acceleration, (d) zoom of the acceleration signal.

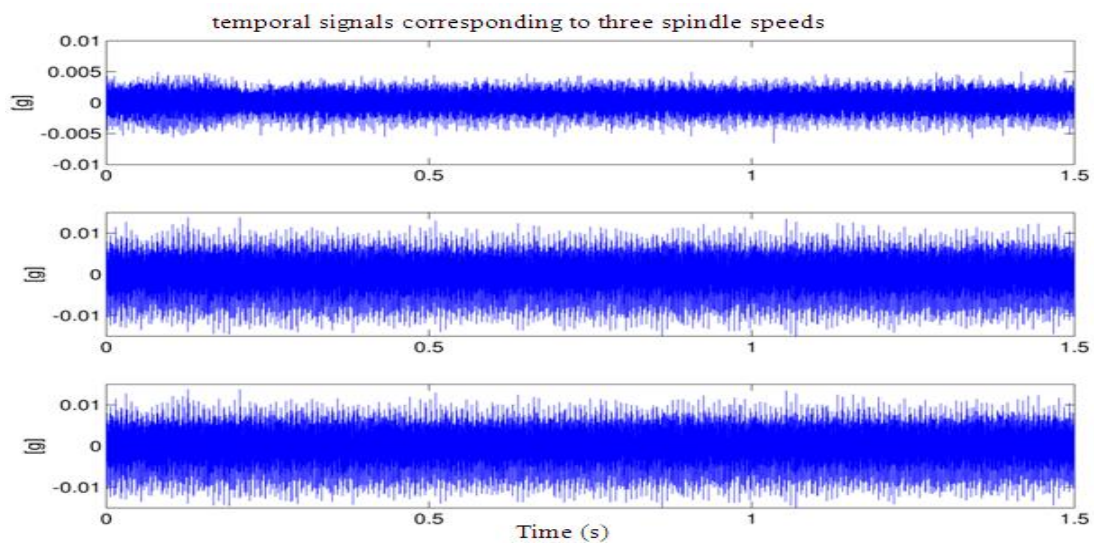


Figure 4 - Time signals corresponding to three spindle speeds.

“Figure 5” shows the spectrum of these three signals. We easily noticed the frequency of rotation of the spindle and its harmonics (since we have a comb excitation). The amplitude of the fourth harmonic is higher than the others, since it corresponds to the number of teeth. With the rotation speed of 188 Hz (test 3), the 4th harmonic (752 Hz) is close of a resonance frequency. This explains why the amplitude is very high and why the frequency is large band as it is usual at the natural frequency.

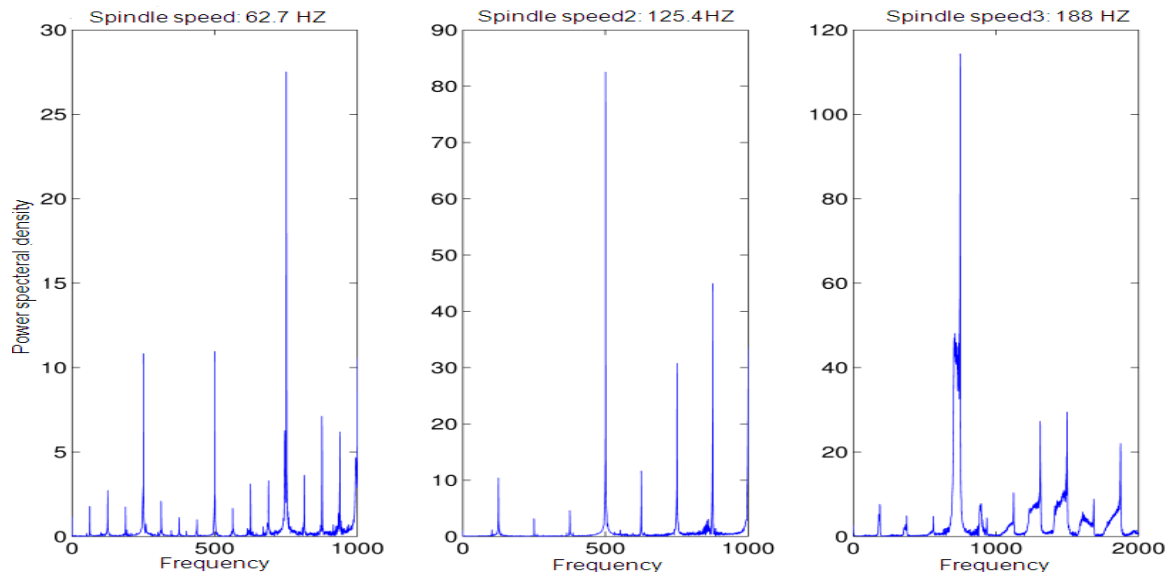


Figure 5 - vibratory Spectrum at each spindle speed.

In order to estimate the instantaneous speed, the signal is first pass-band filtered around the teeth frequency. The choice of the filter width is delicate. To do this, it would be necessary to know the speed variations to choose correctly the width of this filter, and a bad choice of this parameter would conduct to bad estimation of the instantaneous speed. Instead, we have preferred to estimate the instantaneous phase of the signal calculated from the analytical signal and derive the phase with regard to time to obtain the instantaneous frequency.

ANGULAR ANALYSIS

The angular analysis consists in calculating the evolution of statistical parameters during a cycle according to the angle θ , instead of time t . For that purpose, the signal is cut in consecutive blocks of length equal to the period of the cycle. The cyclic period has to be exactly known to be able to cut the signal in cycles. Usually, the kinematics of the machine is known and the knowledge of this period doesn't create a real problem. However, the unavoidable fluctuations of the rotational speed involve variations of this period and the number of samples by cycle may vary from a cycle to the other one. So, to estimate correctly the angular statistics, it is imperative to compensate for these variations by synchronizing the cycles between them. To do this, the method of synchronization of maximization of the cross-correlation has been used. This method requires the presence of a recurring pattern from a cycle to the other one. It consists in measuring the delay of this pattern for every cycle with regard to a cycle taken as reference from the maximum of the function of cross-correlation.

This delay is then compensated in the frequency domain by applying to the cycle a phase shifter. This last filter presents a constant gain of 0 dB and a linear phase. It allows for applying a delay of group to the input signal. “Figures 6” and “Fig. 8” represent the results before and after synchronization of signal in the case of test1 (rotation speed 63Hz); the number of points by period of rotation of the spindle is 765 points,

every block contains 10 cycles of rotation of the spindle. The delays of the cycle blocks with regard to a reference block for three velocities are caught up via the method of maximization of the cross-correlation. Figure 7 represents these delays.

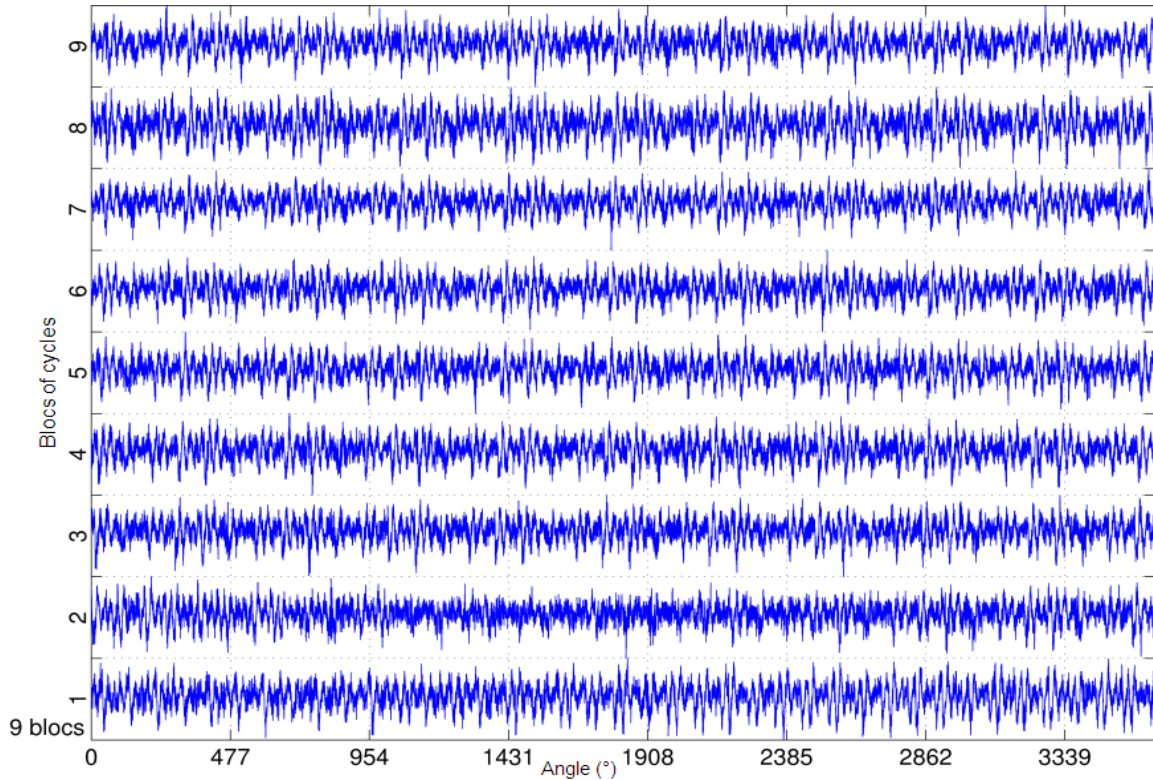


Figure 6 -Blocks of the cycles of tes1 before synchronization, (10 cycles by block).

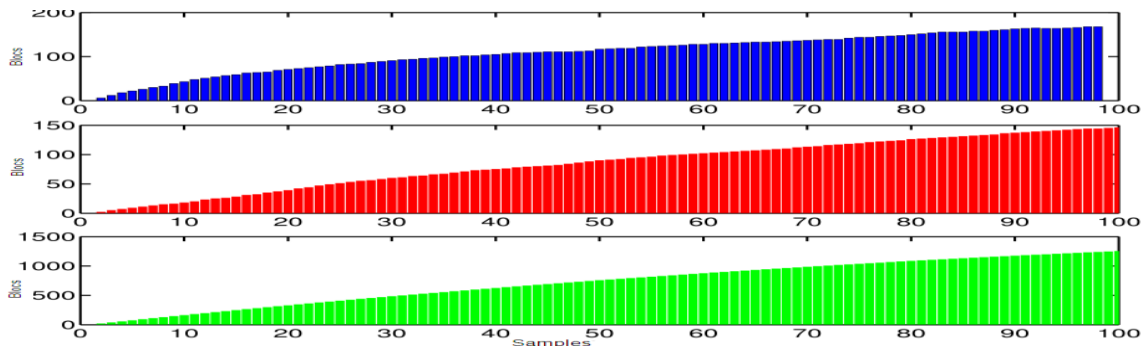


Figure 7 - Delays of blocks with regard to a reference block, estimated for three tests, at the top (test1), in the middle (test2) and below (test3).

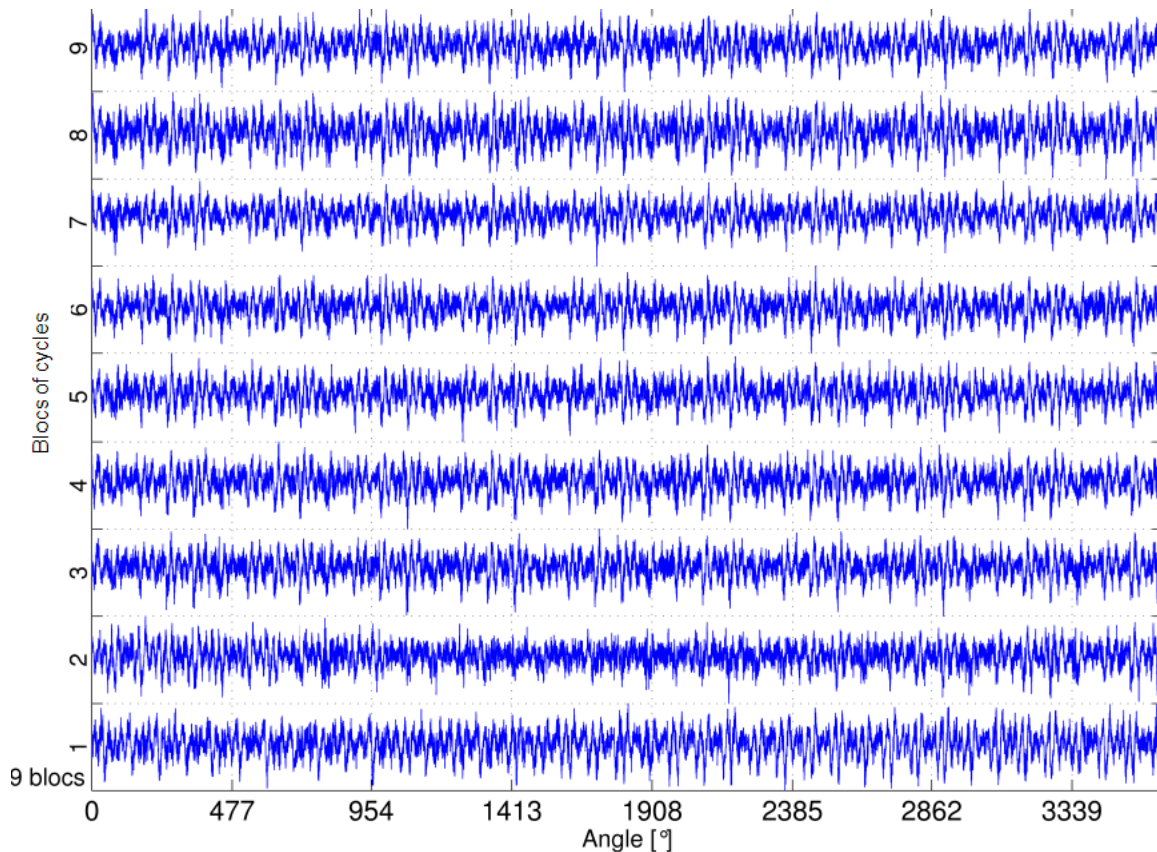


Figure 8 - Cycle blocks of test 1 after synchronization, (10 cycles by block).

Having synchronized these blocks between them, the average, the variance, the power and the angular kurtosis defined by formulae (“Eq.6”, “Eq.7”, “Eq.8” and “Eq.9”) can be calculated. “Figure 9” represents the signal of test 1, with its average and its angular variance. The angular average presents the periodic contribution of the vibratory signal. In that case, we can say that the average signal is cyclostationary at order 1. This type of cyclostationarity arises from a macroscopic phenomenon of determinist nature (for exemple: the passage of teeth on the workpiece), whereas the angular variance reports periodic fluctuations in the energy, in that case the signal is cyclostationary at order 2. This variance informs us about the energy produced by a tooth into the workpiece. “Figure 10” represents the spectrum of mean for the three tests (1, 2, and 3). On the other hand, tool wear (or breakage) will generate a strong shock and thus a strong power. By using a representation angle–frequency of signals after subtraction of the angular average (residual signal), we can follow the evolution of this energy (see “Fig. 11”).

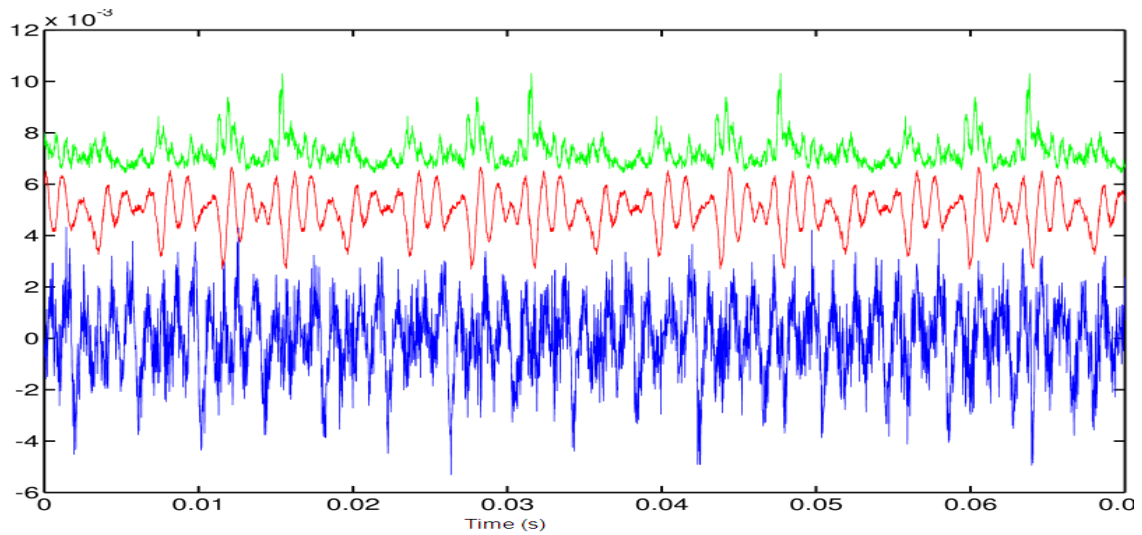


Figure 9 - Signal (blue:down) with its mean (red: in the middle) and angular variance (green:top).

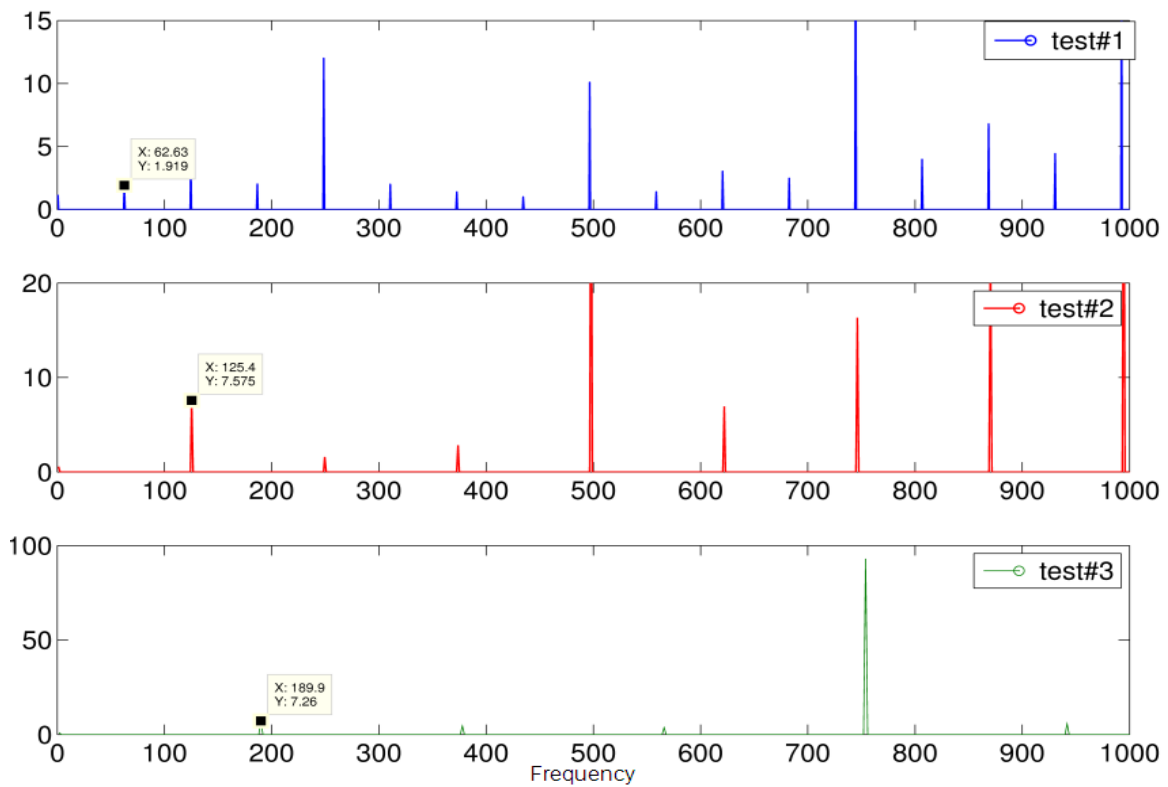


Figure10 - Spectrum of the mean for the three tests (the mentioned frequencies is corresponding to the rotational frequencies).

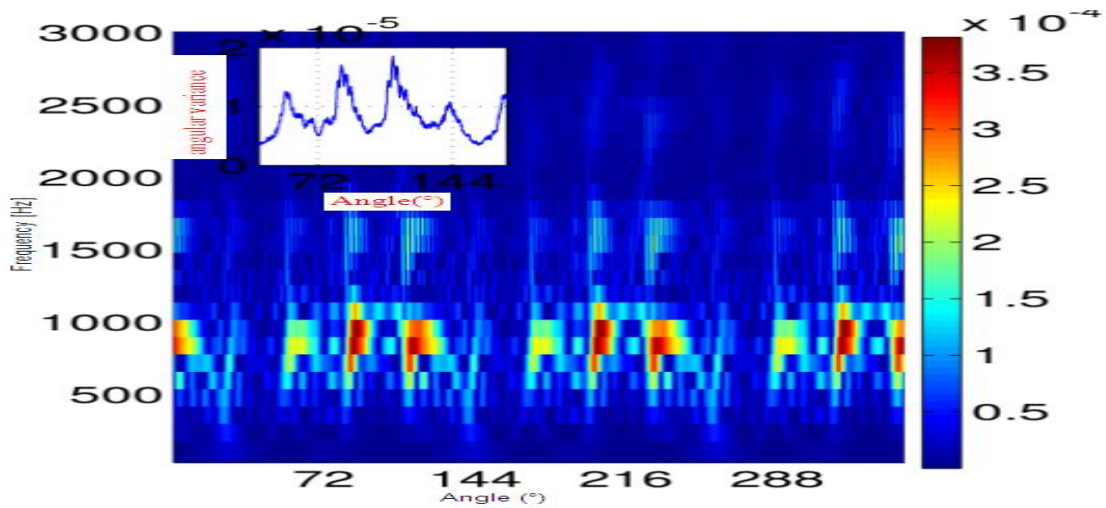


Figure 11 - Representation angle-frequency of three cycle's residual signal with a zoom of the angular variance (test 1).

DETECTION OF CHATTER

The angular kurtosis is very sensitive to shocks, and allows for finding the angular position at which an event can occur. “Figure 12” represents this measurement for the three different cases (test1, test2, test3). Large shocks are corresponding to the passage of teeth on the workpiece. The angular kurtosis for the second case (test 2) does not present a characteristic pattern of shocks, but has rather a pseudo-random shape. In fact, as revealed by the diagram of stability lobes (Zaghbani and Songméné, 2009), generated for various parameters of cutting, which allows for identifying the zones of stability according to the cutting speeds and the depth of cutting , the parameters considered for the test 2 were conducted to chatter (see Fig. 13).

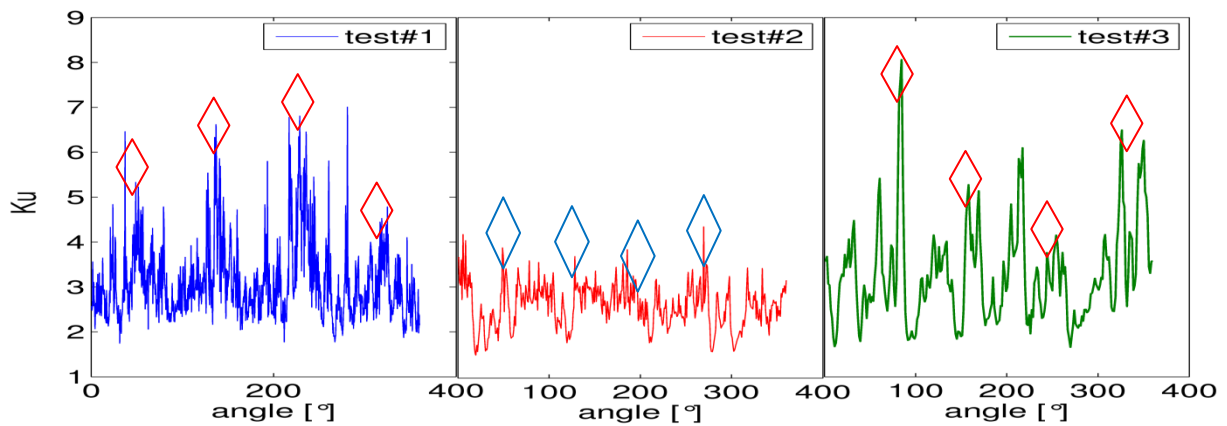


Figure 12 - Angular Kurtosis for test#1, #2, #3.

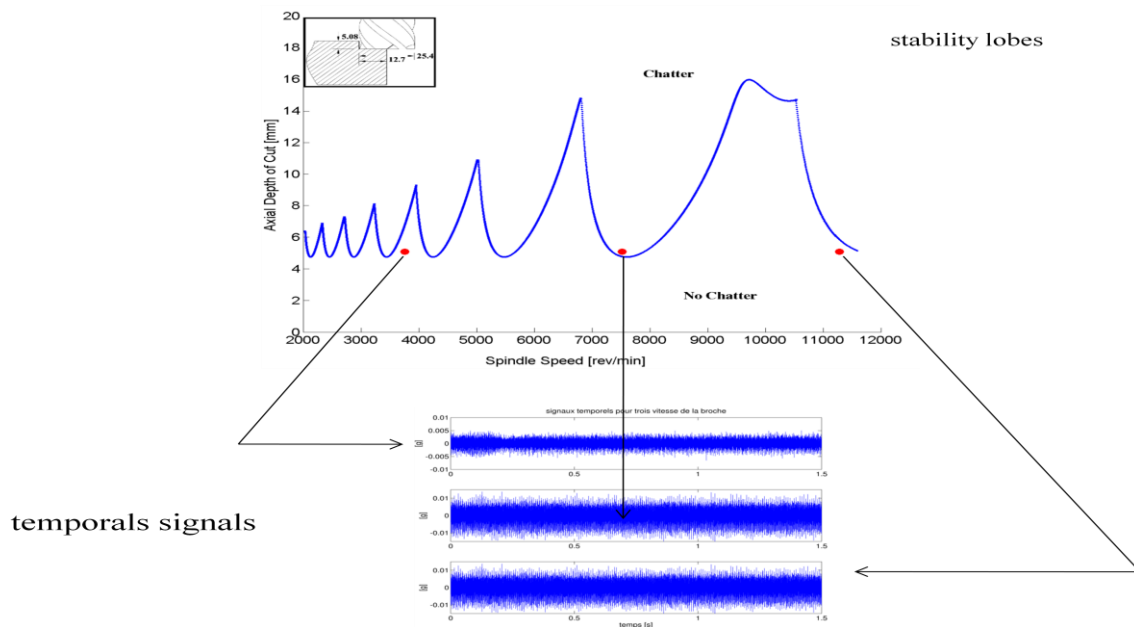


Figure 13 - Diagram of stability lobes (the three signals are corresponding to test#1, test#2 and test#3).

DETECTION OF TOOL WEAR

The angular power characterizes the phenomena of impulsive shocks produced by the passages of teeth into the workpiece and gives high values if a wear takes place. To realize the test of teeth wear, we realized the three tests #1, #2, #3, by carrying out diverse tasks of machining even after a machining into the unstable zone (chatter). Finally, we realized the machining again with the parameters of test #1 for comparison with the first test #1. Figure 14 represents the angular power. We can notice 4 peaks that are corresponding to the passage of every tooth. For an important wear (Fig. 14-b), a strong increase of all these peaks is detected. This results from mechanical and thermal requests engendered by the relative motions between the plate and the tool. This wear involves an increase of energy. The angular monitoring of these peaks represents a new tool of diagnosing tool wear.

Furthermore, we can notice around the passage of a single tooth, three small angular peaks, corresponding to the three contact points between a single tooth and a surface to be machined (see arrows on “Fig. 14.a”). From the angular power, we can thus predict the number of contact points (if we don’t have too much important wear) and even we can monitoring the variation of the rake angle from its reference value (see “Tab. 3”), by following the difference between the both angles of contact identified by green rhombuses on Figure 15-a. The calculated experimental value $\tilde{\alpha}_r = 12.23^\circ$ (see “Fig. 15-a”) can be compared with the theoretical value $\alpha_r = 12 \mp 3^\circ$. According to the figure 15-b, we can also estimate if there is a variation of the contact between teeth by comparing the angular position with the theoretical value of 90 degrees (4 teeth).

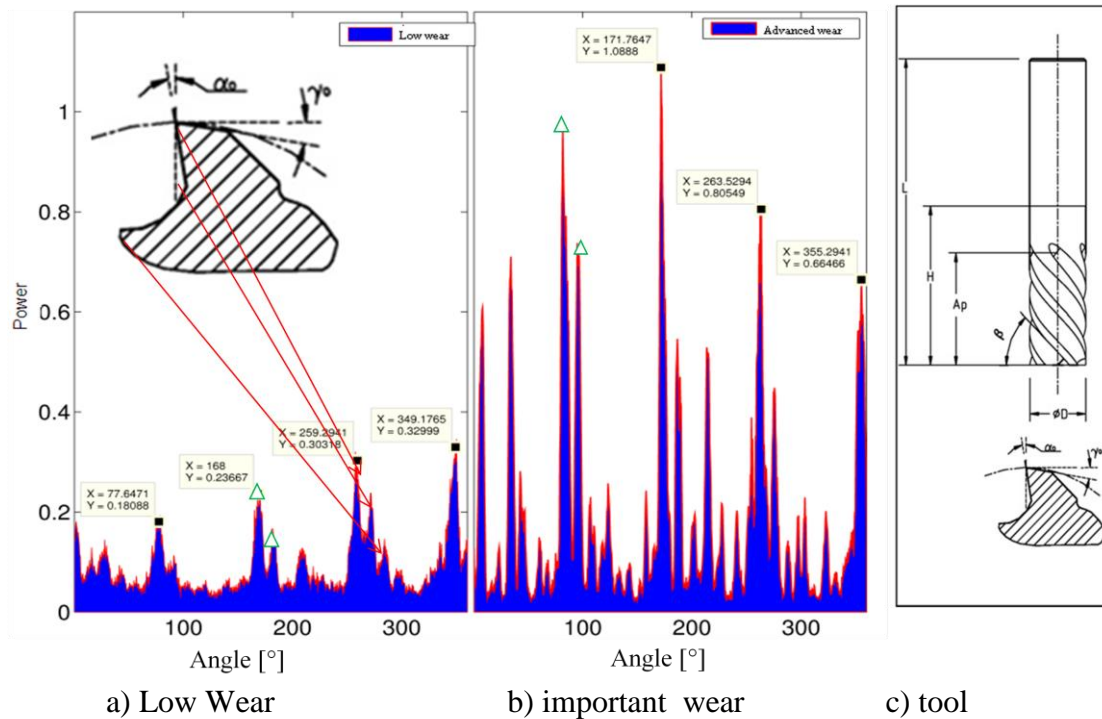


Figure14 - Angular Power in two cases, a) initial wear and b) high wear (the mentioned values are corresponding to the angles of contact: 3 contact points generate the three high values of power), (c) geometrical description of tool.

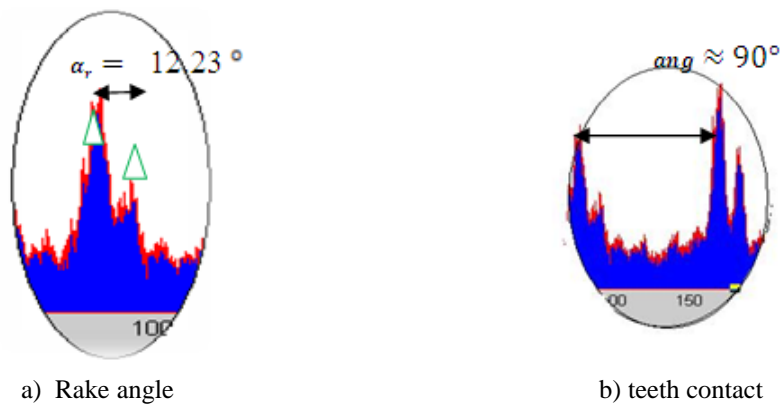


Figure15 - a) Calculation of the angle α_r . b) ang corresponds to the angle between 2 successive teeth

It's then possible to study the passage of four teeth into the material at each revolution. The existence of tooth wear or failure between two teeth means that each tooth does not have the same amount of material so that the power produced at each crossing tooth is not the same (see the amplitude of the main peaks, "Fig. 16").

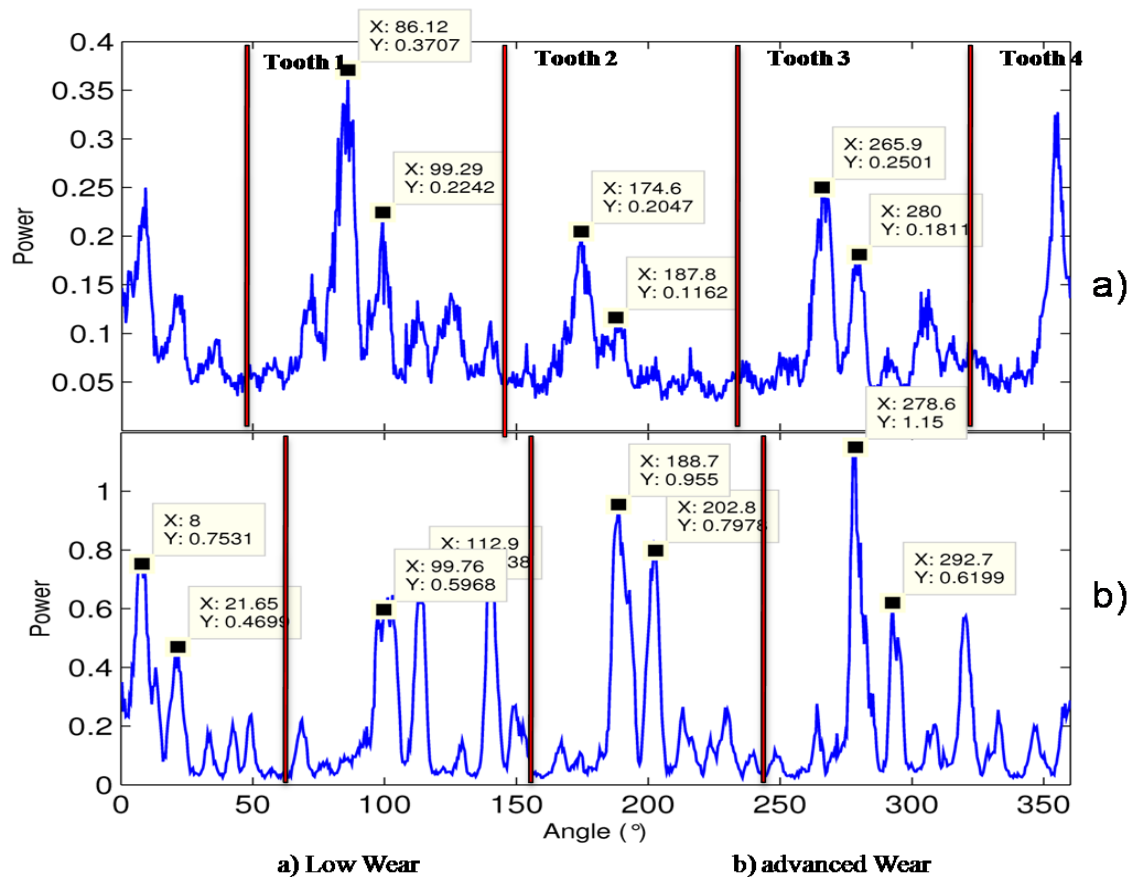


Figure 16 - Angular Power in two cases, a) initial wear and b) important wear.

In “Fig. 16”, we calculated the contact angle for each teeth pass. The amplitude of the main peaks is corresponding to the passage of the teeth. The results are summarized in “Tab. 4”.

Table 4 – Values of the angles and amplitudes

	Tooth1	Tooth2	Tooth3	Tooth4
Angle α_r low wear °	13.17	13.2	14.1	14.1
Angle α_r advanced wear	13.14	14.1	14.1	13.65
Amplitude low wear	0.37	0.20	0.25	0.32
Amplitude advanced wear	0.59	0.79	0.61	0.75

We can notice that there is not a great difference between the angles of contact for both initial and advanced wear, except for the tooth 2. On the other hand, significant increases in amplitude of power at the tooth passage and its rake angle can be easily detected and the greatest amplification (important wear divided by low wear =3.9) is detected on tooth #2 (“Fig. 17”). The increase of angular power may be considered as a wear criterion and its amplification allows for detecting which tooth is more affected. The variation of rake angle and power amplitude allow for confirming this diagnosis when the wear is very important.

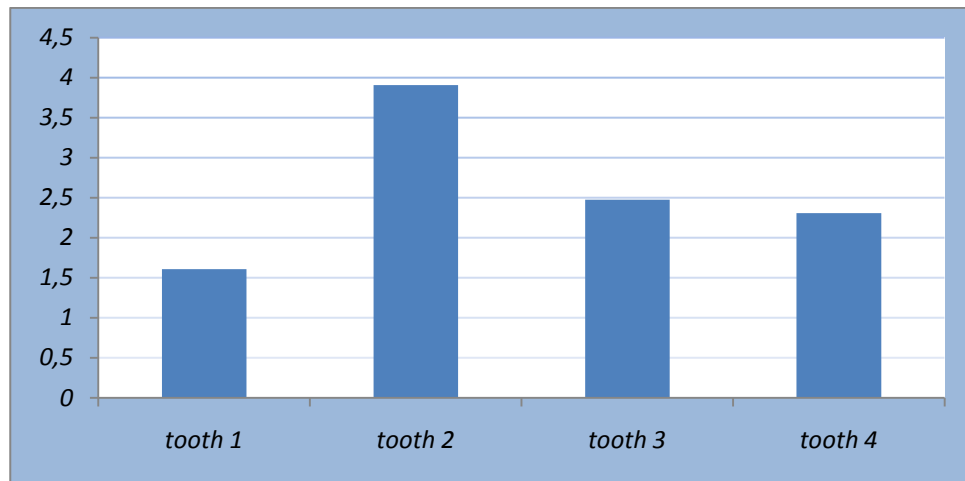


Figure 17- Amplification of angular power by teeth.

“Figure 18” illustrates an angle-frequency analysis with the residual signals (subtraction of the angular mean) for both cases of wear. We can distinguish very well the frequencies and the spikes of the angular Kurtosis (in zoom) when there is no wear (“Fig. 18-a”). The peaks corresponding to the four teeth are very well defined when there is no wear. When the wear becomes important, the spikes of the angular Kurtosis disappeared and it is less easy to distinguish the frequencies of the residual signal. This is due to the lack of shocks due to the tool wear, which produces a pseudo random signal (see “Fig. 19”). The wear involves a decrease of impulses, and thus a flattening of angular Kurtosis.

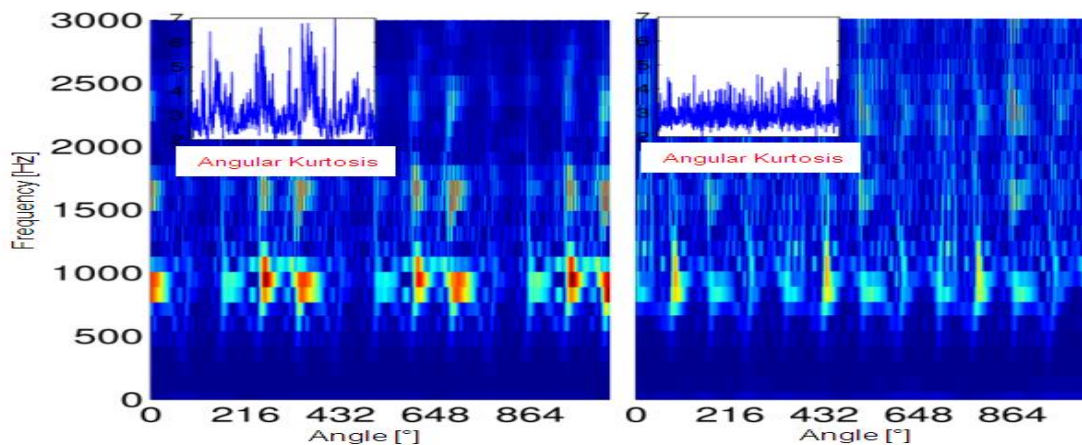


Figure 18 - Representation angle-frequency, (to the right) an advanced wear, (to the left) an initial wear.

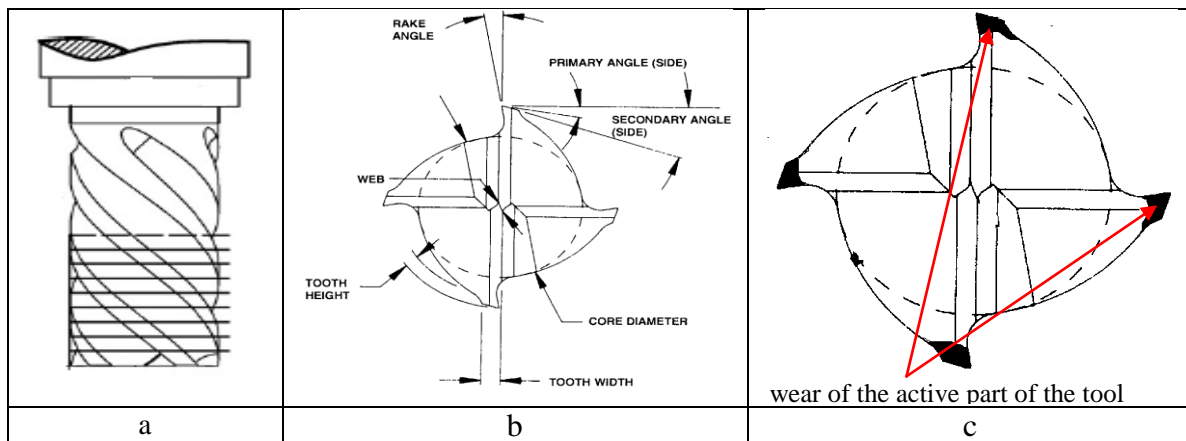


Figure 19 - (a) Simplification of the tool, (b) tool without wear, (c) tool with wear.

CONCLUSIONS

This study showed the advantage to use cyclostationarity analysis of vibratory signals in machining monitoring. Four cases of machining have been investigated, one with low wear, one in the unstable zone in order to produce chatter, one at high speed close to the resonances and finally, and one with damaged tools by wear. The use of angular power, angular kurtosis and residual signals has shown their efficiency to detect tool wear and chatter and may be considered as new tools for the diagnosis of defects. In fact, when the teeth are damaged, the impact is less sensitive, but the energy increases. Consequently, the diagnosis is revealed by an increase of the angular power and a decrease of the angular Kurtosis. Furthermore, the angle-frequency of the residual signal revealed that the tooth frequencies are less significant when the teeth are damaged. When the wear is important, we can notice a variation of the rake angle and an increase of its corresponding power. These studies are still preliminary and the research will continue to improve this technique.

ACKNOWLEDGMENTS

The authors would like to thank the CRSNG-RDC program of the Council of Research in Natural Sciences and Engineering of Canada, CRIAQ, Aeronautic Bombardier and Pratt and Whitney Canada Inc. for their financial support in this research.

REFERENCES

- Antoni J. and P. W. Ha. 2004. A Consistent Estimator for Frequency Response Functions with Input and Output Noise, *IEEE Instrumentation and Measurement*, 53 (2): 457-465.
- Antoni J. et al, 2002a. Effective vibration analysis of IC Engines using Cyclostationarity. Part I: A methodology for Condition Monitoring, *Journal of Sound and Vibration*, 257 (5): 815-837.
- Antoni J. et al, 2002b. Effective vibration analysis of IC Engines using Cyclostationarity. Part II: New Results on the Reconstruction of the Cylinder Pressure, *Journal of Sound and Vibration*, 257 (5): 839-856.
- Antoni J., Bonnardot F., Raad A. and El Badaoui M., 2004. Cyclostationary modeling of rotating machine vibration signals. *Mechanical Systems and Signal Processing* **18**, 1285-1314.
- Antoni J. and F. Guillet, 2005. Blind separation of convolved cyclostationary processes, *Signal Processing*, 85: 51-66.
- Bennett W., 1958. Statistics of regenerative digital transmission, *Bell Systems Technical Journal*, 37: 1501-1542.
- Bonnardot F. et al, 2004. Unsupervised Angular Resampling and Noise Cancellation for Planetary Bearing Fault Diagnosis, *International Journal of Acoustics and Vibrations*.
- Bonnardot F., 2004. Comparaison entre les analyses angulaires et temporelles des signaux vibratoires de machines tournantes. Etude du concept de cyclostationnarité floue, *Thèse, Institut National Polytechnique de Grenoble*.
- Gladyshev E., 1961. Periodically correlated random sequences, *Soviet Mathematics Doklady*, 2: 385-388.
- Gladyshev E., 1963. Periodically and almost-periodically correlated random processes with continuous time parameter, *Theory of Probability and Its Applications*, 8: 173-177.
- Gardner W. A. et al, 1989. Frequency-Shift Filtering Theory for Adaptive Co-Channel Interference Removal, *23rd Asimolar Conference on Signals, Systems and Computers*. 562-567.
- Gardner W. A. and Archer T.L., 1993. Exploitation of Cyclostationarity for Identifying the Volterra Kernels of Nonlinear Systems, *IEEE Transactions on Information Theory*; 39 (2): 535-542.
- Lamraoui M., Thomas M., El Badaoui M. et Zaghbani I., Juin 2010. Le kurtosis angulaire comme outil de diagnostic du broutage et d'usure des outils de coupe. *Proceedings of Vibration, Choc et bruit (VCB2010)*, Lyon, France, paper AC-29, 21 p.
- Sghir K.A., M. El Badaoui, M. Thomas, I. Zaghbani, V. Songméné, A. Lakis, N. Mureithi, Mai 2009. Identification aveugle paramétrique de la fonction de réponse impulsionnelle basée sur la cyclostationnarité de second ordre à partir des réponses seulement, *Proceedings of Industrial Risk Assesment (CIRI)*, Reims, 16 p.
- Sghir K. A., M. El Badaoui, M. Thomas, F. Guillet, M. Bakrim and D. Aboutajdine, July 2009. Parametric blind identification of the transfer function from vibration measurements based on second order cyclostationarity. *Proceedings of 16th Int. congress on Sound and Vibration*, Krakow (Poland), 8 p.
- Zaghbani I. and V. Songméné, 2009. Estimation of machine-tool dynamic parameters during machining operation through operational modal analysis, *International Journal of Machine Tools and Manufacture*, 49(12-13): 947-957.

New USP Wave Basin - Mechatronic and Hydrodynamic Design Aspects

Mario L. Carneiro¹, Pedro C. de Mello¹, Julio C. Adamowski¹, Kazuo Nishimoto² and Eduardo A. Tannuri¹

¹ Department of Mechatronics Engineering, Escola Politécnica, University of São Paulo

² Department of Naval Arch. and Ocean Engineering, Escola Politécnica, University of São Paulo

Abstract: Since 2006, a new active absorption wave basin is being developed at the University of São Paulo. The tank is able to generate and absorb waves from 0.5Hz to 2.0Hz, by means of 148 active flap-type wave makers distributed along the four faces of a square with 14m x 14m. An independent mechanical system drives each flap, by means of a 1HP servo-motor and a ball-screw based transmission system. This paper presents aspects related with the design of the mechanical, electrical, control, automation and measurement systems. A detailed description of the control algorithm used for both generating and absorbing the waves is presented, based on the linear wave theory. After the complete installation and commissioning of the devices, several experiments were conducted in order to define and calibrate the algorithms. Preliminary experimental validation is also presented.

Keywords: wave maker, wave basin, wave Absorption, wave generation.

NOMENCLATURE

A = Wave amplitude, m.

c = unidirectional generation transfer function

e = directional generation transfer function

D(θ_m) = spatial spread function with constant energy in each frequency.

f = wave frequency, Hz.

h = still water level height, m.

h₁ = distance between flap pivot point to tank bottom, m.

h₂ = distance between flap pivot point to driver arm, m.

k = wave number, m⁻¹.

l = flap breadth, m.

L = wave length, m.

H = wave height, m.

S = flap stroke, m.

p = pressure, N/m².

S(ω_n) = wave power spectrum, m².s.

t = time, s.

x = horizontal coordinate, m.

X = flap position, m.

z = vertical coordinate, m.

bsr = ball screw reduction, m/rev.

F = load force, N.

M = momentum, N*m.

T = torque, N*m.

s = flap area, m².

J = moment of inertia, kg*m².

a_r = radial acceleration of the ball screw, rad/s².

g = gravity acceleration, m/s².

C_R = reflection coefficient, %.

x_{cg} = x position of the mass centre of the flap., m.

x_{cg0} = x coordinate distance between the flap mass centre and pivot point at vertical position, m.

h_{cg} = distance of the flap mass centre and the pivot point, m.

Greek Symbols

θ = wave direction.

ϵ_{nm} = random phase, [0...2 π].

ϕ = velocity potential.

ρ = water density, kg/m³.

ω = angular velocity, rad/s

Superscripts

~ = relative to experimental values.

Subscriptions

N number of frequency components.

M number of directional components.

I number of flaps.

p relative to progressive wave.

j relative to evanescent waves.

0 relative to flap position (x=0).

i relative to incident wave.

r relative to reflected wave.

INTRODUCTION

The design of offshore and naval structures or vehicles strongly depends on reduced-scale experiments conducted on tanks. Initially, resistance tests were executed on towing tanks, without waves. The main purpose was to obtain hulls with minimum resistance and maximum advance velocity. With increasing demand for understanding the performance of ships in waves, tanks were gradually equipped with a wave generator. Seakeeping tests, for example, are extremely important for the design of moored platforms used in offshore oil exploration industry. However, there is the problem associated with the reflected waves on the wall of the tank. This phenomenon degrades the quality of the wave field in the tank, and the actual ocean wave is not well represented.

To avoid this problem, very large ocean wave tanks have been constructed (typically tanks with 30m x 40m), equipped with wave generators in one or two sides of the tank, and with passive absorbers (beach) on the other sides. The main drawbacks associated with those tanks are the high construction costs and the low-quality of the absorption of waves with high periods. Recent developments in control and automation allowed the construction of the active wave generator, a device that can generate and absorb waves simultaneously. They are installed around the complete perimeter of the tank, eliminating reflections that cause interference in the wave field. No more passive beaches are required, and the dimensions of the tank may be very small compared with the traditional tank. However, complex automation systems and control algorithms are required. Following this concept, the USP new wave basin was conceived for testing offshore structures and providing calibration and validation results for the numerical models

implemented in the Numerical Offshore Tank (TPN) time-domain simulator. A view of the new wave basin is presented in Fig. 1.

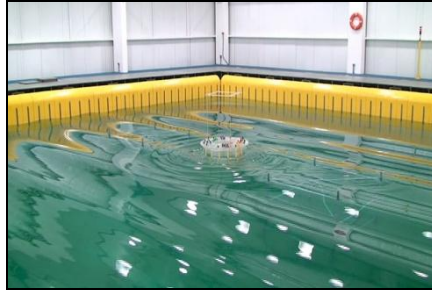


Figure 1 – A view of the wave basin during an experiment with a model of mono column platform.

The USP tank is composed by 148 active flap-type wavemakers, in a square configuration (14mx14m). It will be able to generate and absorb multi-directional unimodal and multi-modal wave spectrum, with or without directional spreading. Because of those features, it is a useful laboratory for the study of the two critical Brazilian coast weather phenomena. More than 40% of the Campos and Santos Basin wave state are typically bimodal, containing a local sea and a swell, coming from the middle Atlantic. Another important phenomenon happens when cold masses arrive from Southwest, generating sudden changes in wind/wave direction, from NE to SW. This occurrence is more likely to happen in autumn (March to May) and spring (September to November), and may be extremely fast (1 to 3 hours). Such characteristics impose several constraints in the design of offshore platforms and operations, and can be extensively evaluated in the new tank.

There are two similar active absorption tanks located in Japan. The Amoeba (Advanced Multiple Organized Experimental Basin) wave tank in Osaka University is a prototype small tank of variable geometry Naito, et al. (1996) and Naito (2006). Wave making is based on a system of plungers and the wave absorption control is performed by monitoring the vertical velocity and the force exerted on each wave maker. A larger facility was opened in 2002 in the National Maritime Research Institute (NMRI) in Tokyo. The Deep-sea basin, Maeda (2004), consists of a circular wave tank with a diameter of 14m, equipped with a set of 128 flap-type wave makers along its circumference. The methodology for absorption control is different from the one employed at the Amoeba basin: wave-probes mounted on each flap measure the wave elevation continuously and, by comparing it with predicted values, provide the data necessary to correct the input signal for flap motion in order to absorb the reflected waves.

This paper presents the relevant aspects related with the mechanical design of the USP wave generator, which is based on linear wave generation theory. Mechatronics and hydrodynamics aspects of the design of the tank, including the dimensioning of the driving system, wave generation limits, automation architecture, are presented. The automation and control architecture implemented in the USP tank is also discussed.

The wave generation and absorption control algorithms used in the tank are detailed, and some results are presented. Experimental tests have been used to verify the theoretical formulation used. These algorithms calculate the motion of the wave makers both to generate and absorb the required wave field by taking into account the layout of the flaps and the limits of wave generation. The experimental transfer function that relates the flap motion to the generated wave is used for the calculation of the motion of each flap. The time series for generation waves have been calculated for all of the 148 wave makers. In that way it is possible to generate regular waves at any direction and frequency. Expanding the directions and frequencies, like the work of Nohara et al. (1996), it is possible to generate multi-directional and multi-modal wave spectrum, with or without directional spreading.

Absorption tests were conducted with regular waves. The time domain algorithm proposed by Schaffer (2001) was implemented. It is based on a digital filter and uses the position of the motor as the commanded variable. The algorithm has hydrodynamic feedback based on the measurement of surface elevation at each flap. The algorithm presented absorption results with reflection coefficient smaller than 11% for regular waves in the frequency range of 0.4 to 1.1 Hz.

HYDRODYNAMICS BASIC ASPECTS – WAVEMAKER TRANSFER FUNCTION

Considering linear wave theory, the wave generated by the sinusoidal motion of the wave generator can be described by its velocity potential function, given by:

$$\phi = A_p \cosh[k_p(h+z)] \sin(k_p x - \omega t) + \sum_{j=1}^{\infty} C_j e^{-k_j x} \cos[k_j(h+z)] \cos(\omega t) \quad (1)$$

The first term of Eq. (1) is the progressive wave. The second term is related to the evanescent modes, composed by a series of stationary waves. The height of evanescent waves exponentially decays with distance from generator, and they can be neglected for distances larger than three times the wave length. The wave number k_p is related with the

progressive wave and its frequency dependency is given by the dispersion relation Eq. (2), while the wave number k_j is related with the evanescent wave modes and have infinity solutions Eq. (3).

$$\omega^2 = gk_p \tanh(k_p h) \quad (2)$$

$$\omega^2 = gk_j \tan(k_j h) \quad (3)$$

The parameters A_p and C_j for a flap type wave generator is given by:

$$A_p = \frac{S\omega}{2k_p^2} \frac{\sinh(k_p h) + \frac{\cosh(k_p h_1) - \cosh(k_p h)}{k_p (h - h_1)}}{\frac{\sinh(2k_p h)}{4k_p} + \frac{h}{2}} \quad (4)$$

$$C_j = \frac{S\omega}{2k_j^2} \frac{\sin(k_j h) + \frac{\cos(k_j h) - \cos(k_p h_1)}{k_j (h - h_1)}}{\frac{\sin(2k_j h)}{4k_j} + \frac{h}{2}} \quad (5)$$

The generation transfer function relates the progressive wave amplitude measured in the tank (A_i) with the flaps sinusoidal movement amplitude (X_i) for different wave frequencies. It has been studied by several authors, such as Dean and Dalrymple (1984) and Schäffer (1996), and can be obtained directly from Eq. (1). If the waves are taken far from the wave generator, the transfer function can be written for oblique waves as:

$$\frac{A_i}{X_0} = ie_0 = \frac{i}{\cos \theta} c_0 \quad (6)$$

Where i is the imaginary number and represents the 90° phase shift between the wave and the flap movement, θ is the wave propagation direction. The generation transfer function with perpendicular propagation direction c_0 , for a flap type wave generator can be written as:

$$c_0 = \left(\frac{4 \sinh(k_p h)}{k_p h_2} \right) \left(\frac{k_p (h - h_1) \sinh(k_p h) - \cosh(k_p h) + \cosh(k_p h_1)}{\sinh(2k_p h) + 2k_p h} \right) \quad (7)$$

Near to the wave generator, the evanescent wave modes should be observed:

$$\frac{A_0}{X_0} = i \left(e_0 + \sum_{j=1}^{\infty} e_j \right) \quad (8)$$

Where A_0 is the complex amplitude of the wave level measured in front of the flap and e_j is the transfer function of the j -th evanescent wave mode, for a flap type wave generator it is given by:

$$e_j = \frac{k_j}{k_{xj}} c_j = \frac{k_j}{k_{xj}} \left(\frac{-4 \sin(k_j h)}{k_j h_2} \right) \left(\frac{k_j (h_1 - h) \sin(k_j h) - \cos(k_j h) + \cos(k_j h_1)}{\sin(2k_j h) + 2k_j h} \right) \quad (9)$$

In which k_j is the wave number of the evanescent mode j and k_{xj} is its x-component. An example of the progressive transfer function and the full transfer function considering perpendicular propagation direction are shown in Fig 2.

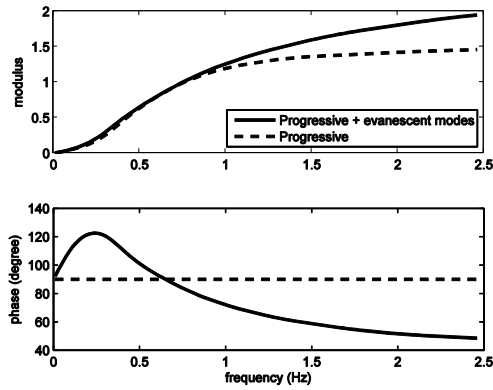


Figure 2 – Generation transfer functions.

MECHANICAL DESIGN

Each wave generator is driven by one servo-motor and transmission is based on a ball-screw system. Each flap is 1.62m high with underwater height of 1.2m, and breadth of 0.36m. The still water level is 4.1m. Active wave absorption requires a hydrodynamic feedback, for this purpose each flap is equipped with an ultrasonic waveprobe integrated on its front. A schematic view of the flap system is presented in Fig. 3.

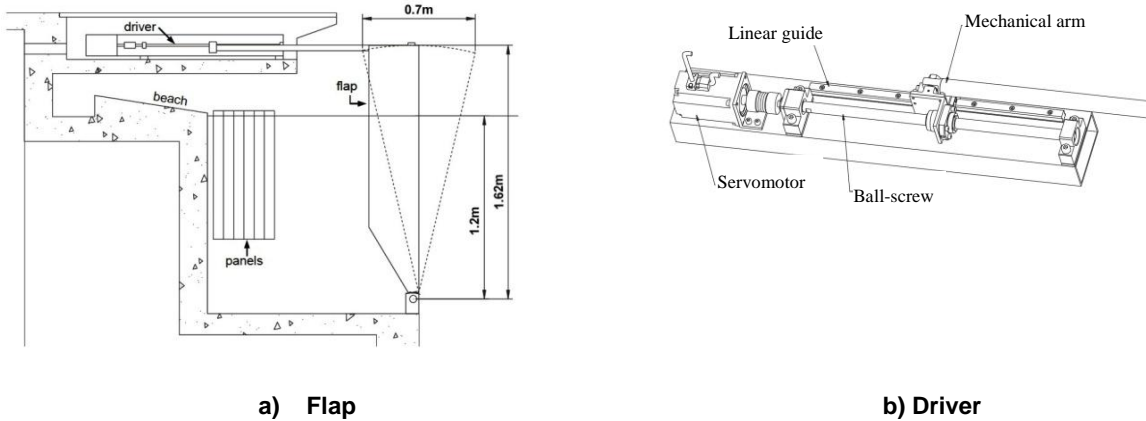


Figure 3 – Schematic representation of the flap system.

The system was designed to generate waves in a frequency ranging from 0.4 to 2.0 Hz and a maximum wave height of 0.40m, considering the limits of the mechanical system and the theoretical wave breaking limit of 14% steepness (L/H). Wave generation limits can be visualized in Fig. 4 as the intersection of the areas below limiting factors (wave steepness, maximum design wave, flap stroke and screw velocity).

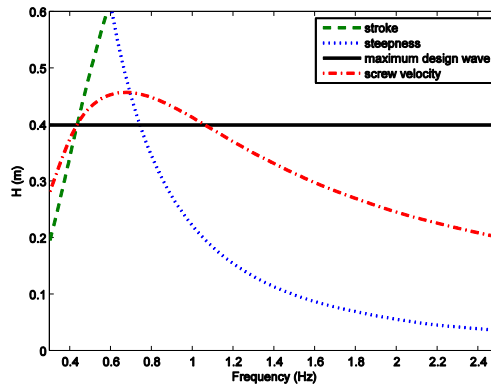


Figure 4 – Wave height generation limits x frequency.

The load force is composed by the hydrodynamic and inertial reaction, as well as the force due to flap weight (Souza and Morishita, 2003). The force components as calculated through a momentum applied on the pivot point:

$$F = \frac{M}{h_2} = \frac{M_h + M_i + M_g}{h_2} \quad (10)$$

The moment related to the pivot point, due to the hydrodynamic forces, is given by the pressure integration in both sides of the flap:

$$M_h = \int_s (h - h_1 + z) p ds = 2l \int_{-h+h_1}^0 (h - h_1 + z) \rho \left[\frac{\partial \phi}{\partial t} \right]_{x=0} dz \quad (11)$$

where, s is flap area and l is its breadth. Solving the integral in Eq. (11) yields:

$$\begin{aligned} M_h &= a_1 \cos(\omega t) + a_2 \sin(\omega t) \\ a_1 &= \frac{-2\omega l \rho A_p}{k_p^2} [k_p h \sinh(k_p h) - k_p h_1 \sinh(k_p h) - \cosh(k_p h) + \cosh(k_p h_1)] \\ a_2 &= -2\omega l \rho \sum_{j=1}^{\infty} \frac{C_j}{k_j^2} [k_j h \sin(k_j h) - k_j h_1 \sin(k_j h) + \cos(k_j h) - \cos(k_j h_1)] \end{aligned} \quad (12)$$

The momentum due to flap inertia is given by:

$$M_i = J \omega^2 \tan^{-1} \left(\frac{S}{2(h - h_1)} \right) \sin(\omega t) \quad (13)$$

The third term related with flap weight is calculated by:

$$M_g = mg x_{cg} = mg \left[x_{cg0} + h_{cg} \tan^{-1} \left(\frac{S}{2(h - h_1)} \right) \sin(\omega t) \right] \quad (14)$$

The necessary motor torque is calculated using Eq. (10) added to the forces due to screw and motor inertia:

$$T = \frac{bsr}{2\pi} F + (J_f + J_m) \alpha_r \quad (15)$$

Figure 4a shows the 3 force components and Fig. 4b shows the calculated torque. While in Tab. 1 is presented the parameters calculated for specifying the motor taking into account the maximum wave height (Fig. 4).

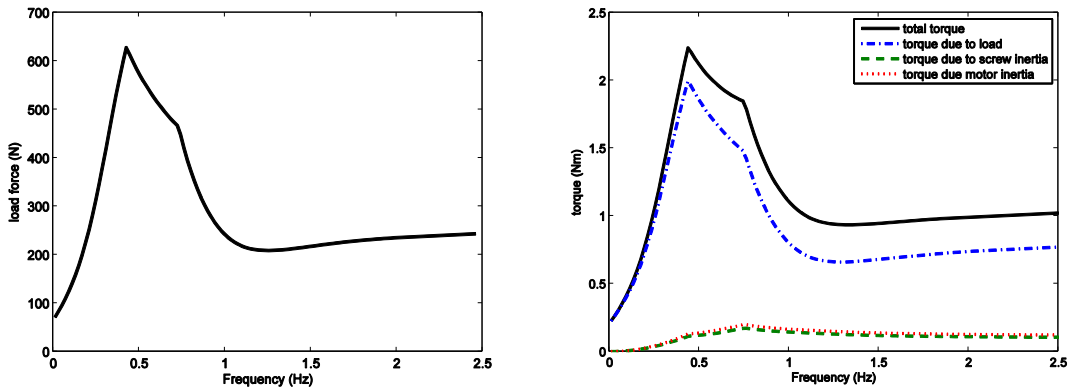


Figure 5 – Load force and motor torque.

Table 1 – Parameters used for specifying mechanical components.

Properties	Values
Linear velocity at ballscrew nut (m/s)	1.068
Linear acceleration at ballscrew nut (m/s ²)	4.418
Force at ballscrew nut (N)	620
Motor velocity (RPM)	3204
Motor acceleration (rad/s ²)	1388
Motor torque (N/m)	2.215
Motor power (W)	742

CONTROL ARCHITECTURE

The control architecture implemented in the TPN active absorption wave tank is based on standard industrial equipment. Nowadays, new generations of industrial automation equipments are strongly improved in terms of capacity, scalability, modularity and flexibility, in order to comply with the present industrial demand. Furthermore, personal computers performance is enhanced, mainly using parallel processing in multi-core machines. Therefore, while in the past it would be necessary to have a specifically designed hardware to run a wave generator, now it can be done using carefully specified modern standard equipments.

The control and automation system architecture is designed to do the following tasks during one scan cycle:

- Send position and velocity command signals for each one of the 148 servo-drives,
- Read the 148 encoders (real position of each servo-motor)
- Read the acquired signals from the 152 wave sensors mounted in the flaps
- Communicate with a supervisory/control system implemented in a personal computer (PC), sending the signals of the encoders and wave sensors and receiving the positions and velocity commands

In addition, a high level user interface was implemented, in order to obtain an easy and remote data manipulation, tests and adjustment procedure. All development can be done directly from the personal computer, minimizing efforts and time. Control algorithms are implemented using Matlab/Simulink computer language.

Aiming to achieve such functional targets, a model based on communication networks was adopted. The model consists of two distinct optical communication networks: one linking the industrial execution PLCs (programmable logic computer) to the control PC; and another to link the servo-motion commanding CPUs, which drive the motors. It was used three industrial execution PLCs: two for flap driving, and the third one for the wave sensor acquisition control. Figure 6 illustrates the wave generator control architecture.

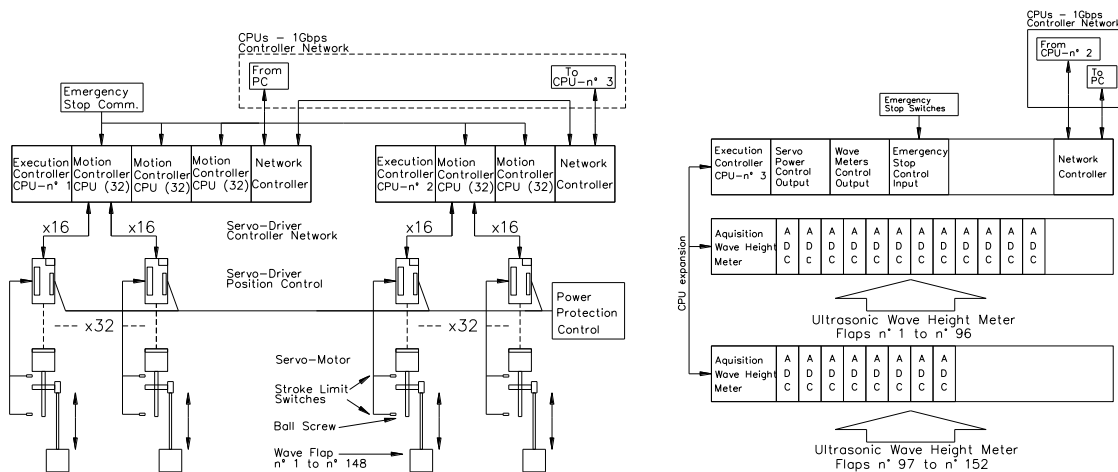


Figure 6 – Wave generator control architecture.

WAVE GENERATION ALGORITHMS

The wave generation theory using flap-type wave makers is well addressed in the specialized literature. In the linear theory context, multi-directional waves can be generated by the summation of many wave components with different frequencies and directions, as described by Nohara et al. (1996). The summation in frequency can be made according to a prescribed power spectrum ($S(\omega)$), while the summation in direction follows a energy spreading function ($D(\theta)$). The final result is a short-crested wave field, as indicated in Eq. 16 and 17. When the summation is made only in frequency, the result is a long-crested sea. The term $D(\theta)$ is zero for every direction other than the prescribed wave direction. Regular waves are obtained by considering only one amplitude and one frequency.

$$X_I(t) = \sum_{n=1}^N \sum_{m=1}^M \frac{a_{nm}}{c_0} \cdot \cos(2\pi \cdot f_n \cdot t - ik_{pn} l \sin \theta_m + \varepsilon_{nm}) \cdot \cos \theta_m \quad (16)$$

where a_{nm} is the wave amplitude of the component of frequency n , and direction m , given by:

$$a_{nm} = (2 \cdot S(\omega_n) \cdot D(\theta_m) \cdot \Delta\omega \cdot \Delta\theta)^{1/2} \quad (17)$$

The wave generation algorithm was implemented using MATLAB®, by means of a pre-processing offline algorithm. The expansion for regular waves takes short time to be executed (approximately 3s processing time), the long-crested wave expansion has an intermediate computational cost (70s), and the short-crested wave expansion is very demanding (600s). The implementation was divided in three parts because, due to the great number of components to be summed, the processing time could be extremely long. The spectrum may be defined by a parametric JONSWAP, Pierson-Moskowitz or Bretschneider formulation (Chakrabarti, 1987). For the directional spreading, different kinds of parametric models can be adopted, as detailed in the work of Mitsuyasu, et al., (1975) and Hasselmann, et al., (1980).

WAVE ABSORPTION ALGORITHM

The absorption algorithm is based on Schäffer (2001), which uses the elevation of the waves in front of each wave generator as hydrodynamic feedback and flap position reference as control signal. The frequency domain expression for the flap position X_0 can be formulated as:

$$X_0 = (2A_I - A_0)F \quad (18)$$

$$F = \frac{-i}{e_0 - \sum_{j=1}^{\infty} e_j} \quad (19)$$

where, A_I is the complex amplitude of incident desired wave, A_0 is the complex amplitude of the measured wave at wave maker ($x = 0$) and F_0 is a complex transfer function related to the inverse of the flap generation transfer function (A_0/X_0) and its implementation in time domain is made by a recursive digital filter:

$$\tilde{F} = \frac{\sum_{l=-M_2}^{M_2} \sum_{k=0}^{M_1} a_{k,l} z_1^{-k} z_2^{-l}}{1 - \sum_{l=-N_2}^{N_2} \sum_{k=1}^{N_1} b_{k,l} z_1^{-k} z_2^{-l}} ; \quad z_1 = e^{i\omega\Delta t} ; \quad z_2 = e^{i\omega\Delta y} \quad (20)$$

The coefficients $a_{k,l}$ and $b_{k,l}$ can be obtained by optimization to match \tilde{F} and F_0 . Remembering that the poles of the digital filter must be within the unit circle in z -plane to certify stability constrains. The optimization method used in this work was the Large Scale Nonlinear Least Squares of MATLAB®. In this work was studied only the unidirectional case, with $M_2=N_2=0$.

During the optimization, high frequency responses should also be reduced to avoid instability, as shown for example in Fig. 7. The higher the order of the filter more response peaks occurs at high frequency, therefore the order of the filter should be small as possible.

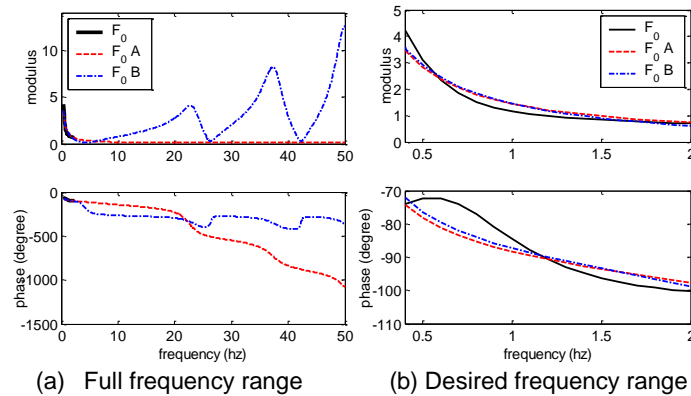


Figure 7 - Example of filter optimization, where F_0 is the target filter, F_0A was optimized considering high frequency response and F_0B was optimized using only desired frequency range.

During preliminary experimental tests high-frequency oscillations of the flaps were observed. In order to avoid these oscillations, a reduction gain K_p was introduced, that way Eq. 18 is substituted by Eq. 21. A compensation for the motor response M and the communication delay D was added in Eq. 19, also a second order Butterworth low pass filter BW was added to help decrease high frequency response, and this is done by optimizing F_M instead F (Eq. 22). Figure 8 shows the modified absorption control block diagram.

$$X_0 = K_p(2A_I - A_0)F_M \quad (21)$$

$$F_M = \frac{F}{M.D.BW} \quad (22)$$

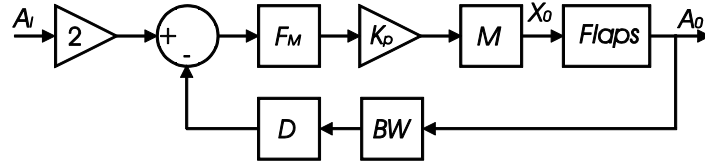


Figure 8 – Absorption control block diagram.

The system performance is measured by the reflection coefficient C_R , defined as:

$$C_R = 1 - \lambda = \frac{\tilde{A}_I - A_I}{\tilde{A}_R - A_I} \quad (23)$$

As proposed by Schaffer (2001), the reflection coefficient can be predicted theoretically or obtained experimentally by the following expressions, which already include the modifications implemented on this work:

$$\lambda = \frac{2e_0}{\frac{-i}{\tilde{F}_M \cdot M \cdot D \cdot BW \cdot K_p} + e_0 + \sum_{j=1}^{\infty} e_j} \quad (24)$$

$$\tilde{\lambda} = \frac{2e_0 \tilde{X}_0}{-i(2A_I - \tilde{A}_0) + \tilde{X}_0 \left(e_0 + \sum_{j=1}^{\infty} e_j \right)} \quad (25)$$

EXPERIMENTAL RESULTS

Wave generation in Wave Basin

Initial wave generation tests were executed in the wave tank, following Eq. (16). Those experiments were conducted as part of the calibration and initial tests. For example, Fig. 9 shows a regular wave and an irregular wave, with and without directional spreading. The visual analysis of the wave front confirms the qualitative performance of the generation algorithm.

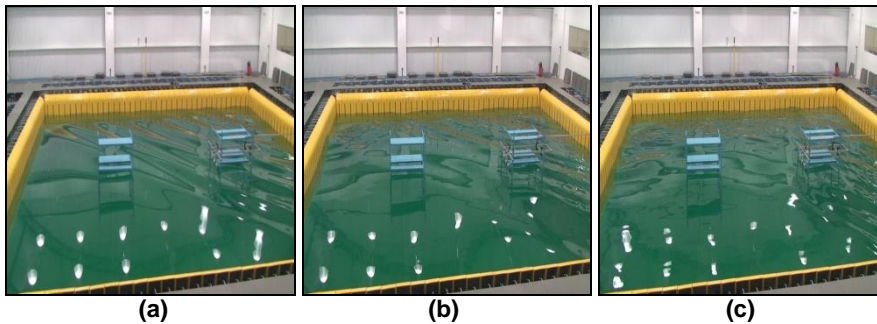


Figure 9 – Wave generation examples: (a) regular wave, (b) Irregular Jonswap long-crested wave with $T_p=1.4$ seg, $H_s=8$ cm and $\gamma=1.4$, with no directional spreading, (c) same irregular wave with spreading.

Wave Absorption results

The experiments consisted on the generation of regular waves with different amplitudes and frequencies by the original wave making system. After some time, the waves reach the flaps which should then actuate to absorb them. The reflection coefficient C_R is estimated by the method proposed by Schaffer (2001) and also by the method proposed by Mansard & Funke, showing in Isaacson (1991), using the signals from 3 wave probes installed in the center of the wave basin.

Table 2 shows a summary of the generated waves. Figure 10 shows the absorption results, comparing the theoretical expected reflection coefficient (Eq. 24) and the experimental values obtained by the method proposed by Schaffer (2001) (Eq. 25) and method proposed by Mansard & Funke. For these experiments K_p was fixed equal to 0.97 and the 2nd order Butterworth filter (BW) with cutoff frequency equal to 8Hz.

Table 2 – Summary of the generated waves.

Frequency (Hz)	A_f (mm)	L (mm)	Steepness H/L (%)
0.50	31.2	6235.7	1.0
0.75	13.9	2772.8	1.0
1.00	15.6	1559.7	2.0
1.25	10.0	998.2	2.0
1.50	6.9	693.2	2.0
1.75	5.1	509.3	2.0
2.00	3.9	389.9	2.0

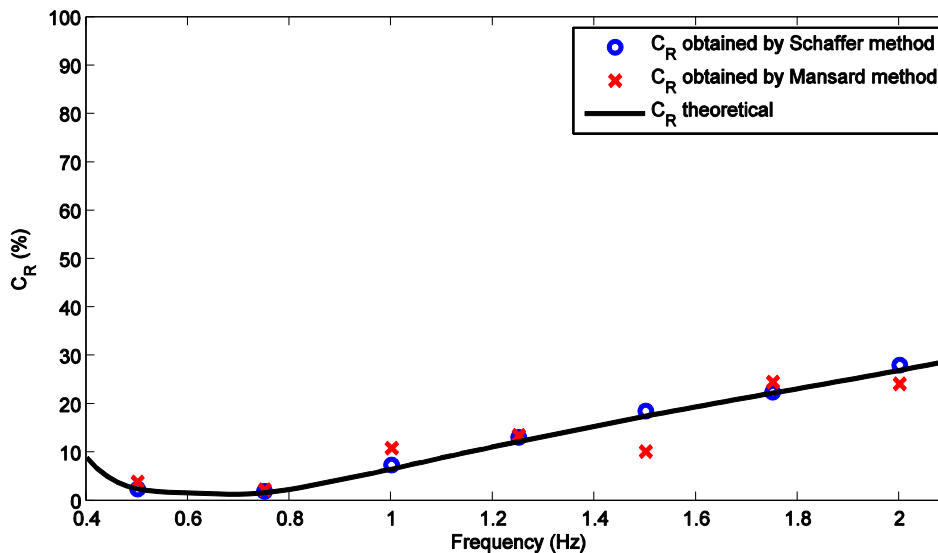


Figure 10 – Reflection coefficient.

CONCLUSIONS

This work presented the theoretical and experimental background that was applied in the development of the new wave basin constructed in the University of São Paulo, in the Numerical Offshore Tank (TPN) Laboratory. All technological challenges during the design, commissioning and initial operations were discussed. A reliable and safe automation system has been developed, as well as simple and robust control software architecture. The mechanical development and construction of the flaps were also detailed. A discussion about the generation and active absorption algorithms used in the TPN wave tank is also presented.

Generation is based on the time realization of the frequency domain transfer functions of each flap, considering the linear superposition of them. Both regular and irregular waves can be generated, with or without directional spreading.

The absorption algorithms were tested. It is implemented in the time domain space proposed by Schäffer, 2001. The original theory was modified to include a compensation for the mechanical dynamics response and the delay of the control system loop. The algorithm presented accepted performance, with a reflection coefficient up to 11% for wave frequency between 0.4Hz and 1.1Hz. The wave reflection for frequencies higher than 1.1Hz is too big and the author

intend to test another optimization algorithm to achieve a better match with theoretical filter. Experiments with irregular and multidirectional waves will be presented in a future work.

ACKNOWLEDGMENTS

The authors acknowledge Petrobras for the financial support and for the motivation of this work. The first author acknowledges the São Paulo State Research Foundation (FAPESP Proc. No. 2008/06428-4). The third, fourth and fifth authors acknowledge the National Council for Scientific and Technological Development (CNPq) for the research grants.

REFERENCES

- Chakrabarti, S. K., 1987, "Hydrodynamics of Offshore Structures", WIT press, USA.
- Dean R.G. and Dalrymple R.A., 1984, "Water wave mechanics for engineers and scientists.", Prentice-Hall Inc., Englewood Cliffs, New Jersey, USA.
- Hasselmann D. E., Dunckel M. and Ewing J. A., 1980, "Directional Wave Spectra Observed during JONSWAP 1973.", *Journal of Physical Oceanography*, August, Vol. 10. pp. 1264-1280.
- Isaacson M., 1991 "Measurement of Regular Wave Reflection.", *Journal of Waterway, Port, Coastal, and Ocean Engineering* Nov/Dec, Issue. 6, Vol. 117, pp. 553-569.
- Maeda K., Hosotani, N., Tamura, K., and Ando, H., 2004, "Wave Making Properties of Circular Basin.", *International Symposium on Underwater Technology.*, pp. 349-354.
- Mitsuyasu H. [et al.], 1975, "Observations of the Directional Spectrum of Ocean Waves Using a Cloverleaf Buoy.", *Journal of Physical Oceanography.*, October, Vol. 5, pp. 750-760.
- Naito S. [et al.], 1996, "A new configuration of wave basin and a control of wave generation and absorption - the case when an advancing ship comes across the given waves.", *Proceedings of the 4th Pacific/Asia Offshore Mechanics Symposium.*, Pusan, Korea, Vol. 226, pp. 207-212.
- Naito S., 2006, "Wave generation and absorption in wave basins: theory and application.", *Proceedings of the 16th International Offshore and Polar Engineering Conference.*, San Francisco, California, USA.
- Nohara B. T., Yamamoto I. e Matsuura M., 1996, "The organized motion control of multi-directional wave maker.", *Proceedings of the 4th International Workshop on Advanced Motion Control.*, Vol. 2, pp. 470-475.
- Schäffer H. A., 1996, "Second-order wavemaker theory for irregular waves.", *Ocean Engineering.*, Vol. 23, pp. 47-88.
- Schäffer H.A., 2001, "Active Wave Absorption in Flumes and 3D Basins", *Proceedings of 4th Int. Symp. on Ocean Wave Measurement and Analysis*, San Francisco, USA, ASCE, pp. 1200-1208.
- Souza, C.A.G.F. and Morishita, H.M., 2003, "Evaluation of a flap type wave generator", *17th International Congress of Mechanical Engineering COBEM'03*, Brazil.

RESPONSIBILITY NOTICE

The author(s) is (are) the only responsible for the printed material included in this paper.

Control Tuning Methods applied to Dynamic Positioning Systems

Eduardo A. Tannuri¹, Helio M. Morishita², Rafael R. Marangoni¹, Fernando T. Mazzilli³

¹ Department of Mechatronics Engineering, Escola Politécnica, University of São Paulo

² Department of Naval Arch. and Ocean Engineering, Escola Politécnica, University of São Paulo

³ Department of Mechanics Engineering, Escola Politécnica, University of São Paulo

The present paper discusses two methods for adjusting control gains for a Dynamic Positioning System. The first method is based on a simplified model of the floating vessel, and the gains are obtained by a pole-placement technique. The second method is based on optimization using genetic algorithm, and a detailed dynamic model of the vessel is required. Both simulation and experimental results are used to validate and to compare the methods.

Keywords: PID control, Dynamic Positioning System, pole-placement, genetic algorithm

NOMENCLATURE

a_i = weighting factors.
A, B = matrixes of weighting factors.
 b_i = weighting factors.
 B = vessel beam, m.
 D = individual.
 d_i = elements of the individuals.
 D_i = Derivative gain, N.s/m or N.m.s/rad.
 e_i = position or heading error, m or rad.
 F_T = Actuators total force or moment, N or N.m.
 F_E = Environmental total force or moment, N or N.m.
 I_i = Integral gain, N/m.s or N.m/rad.s.
 I_Z = moment of inertia about Z, kg.m².
 L = vessel length, m.
 M = vessel mass, kg.
M = mass matrix.

M_{ij} = added mass, kg or kg.m².
 P_i = Proportional gain, N/m or N.m/rad.
 S = Objective or fitness function.
 p = probability.
 N = number of individuals.
 t = generation.
 T = vessel draft, m.
 u, v, r = vessel velocities, m/s and rad/s.
 u_c, v_c, r_c = vessel velocities (current related), m/s.
 Z = set of random numbers
 x, y = vessel position, m.
 x_G = position of the center of mass, m
 z_i = random numbers

β = definition of non dominant pole.
 δ = modification in the individual.
 γ = parameter of genetic algorithm.
 ψ = heading angle, rad
 ζ = damping factor.
 ω_n = natural frequency, rad/s
v = vector of vessel velocities

Superscriptions
 ' = relative to new generation.

Subscriptions
 c related to crossover.
 m related to mutation.

Greek Symbols
 α = parameter of genetic algorithm

INTRODUCTION

Dynamic Positioning (DP) Systems are defined as a set of components used to keep a floating vessel on a specific position or pre-defined path through the action of propellers. DPS include position and heading measurement systems, a set of control algorithms and propellers. Several offshore operations are carried out using DPS, such as drilling, pipe-laying, offloading and diving support. DPS relies on control of the motion of the vessel in the horizontal plane, namely, surge, sway and yaw by counteracting forces and moments due to current, wind and waves. In terms of control it can be understood as a multivariable, non-linear, overactuated and stochastic system. In light of this complexity the performance of the DPS is carefully checked by dynamic simulation and experimental tests. In Brazil, Petrobras has supported research to elaborate digital simulator and develop laboratory facilities to perform tests with scale model in tank as well. (Tannuri and Morishita, 2006; Morishita et al., 2009).

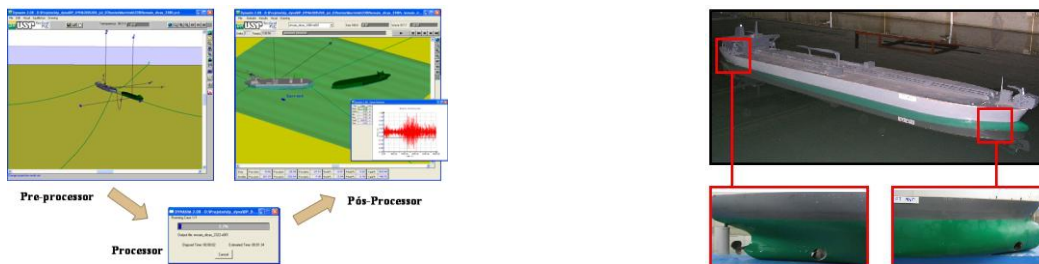


Figure 1 – (left) Numerical time-domain simulator ; (right) Small scale experimental DP vessel

All those numerical and experimental tools have allowed to execute several analysis, involving studies of new layouts for DP vessels, definition of the viability of offshore operations with DP vessels, power dimensioning, calculation of operational availability and capability analysis.

However, a ship equipped with DP system requires proper tuning of the gains of the control system. This process, in real vessels, is carried out by executing several preliminary simulations and then performing some tests at sea during the commissioning of the DP System. In the case of the numerical and experimental analysis previously mentioned, it is important to define a simple and expedite way to tune the control parameters. Those analyses normally comprehend several DP layouts and vessel's configurations, and the tuning of each controller must be easily done.

This paper presents two systematic techniques for adjusting of the control gains. The first technique is based on closed loop pole placement. The adjustment of control gains becomes a fairly simple process, requiring the designer only to estimate the characteristic frequency and damping of the closed loop system. The second one is based on an optimization method using the genetic algorithm proposed by Herrera and Lozano (2000). In this case, a function to be minimized is defined, containing an estimate of the total power consumption and positioning error, for each set of control gains. A simulation tool is used to evaluate this function for each set of control gains defined by the evolution of the genetic algorithm. The performance of the DP vessels with the gains obtained from both approach are evaluated numerically and experimentally with scale models in mild conditions.

MATHEMATICAL MODEL

The modeling of dynamics of a vessel in the horizontal plane is formulated considering an earth-fixed frame $Ox_Ey_Ez_E$ and a vessel fixed reference frame $GXYZ$, as indicated in Figure 2. The origin of the vessel fixed frame is located in the centerline, in a distance x_g from the center of gravity. The axes of each body-fixed co-ordinate system coincide with the principal axes of inertia of the vessel. To represent the intricate motion of a vessel at sea the mathematical model is usually split in two terms namely the low frequency motion caused by wind, current and second-order wave forces, and the high frequency motions caused by the first order wave forces. The former results by applying the Newton law and the latter are time series generated from a spectrum of the motion for each degree of freedom.

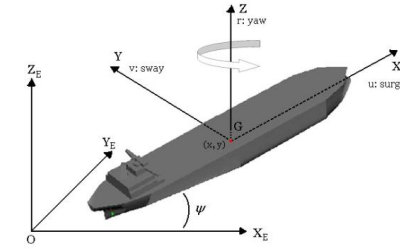


Figure 2 – Earth fixed and vessel fixed references frames

The equations for low frequency motions, related to the body fixed reference frame, and considering added mass forces, are given by:

$$\mathbf{M} \dot{\mathbf{v}} + \mathbf{C}(\mathbf{v})\mathbf{v} = \mathbf{F}_E + \mathbf{F}_T \quad (1)$$

where:

$$\mathbf{v} = [u \ v \ r]^T, \quad \mathbf{M} = \begin{bmatrix} M + M_{11} & 0 & 0 \\ 0 & M + M_{22} & Mx_g + M_{26} \\ 0 & Mx_g + M_{26} & I_z + M_{66} \end{bmatrix}, \quad \mathbf{C}(\mathbf{v}) = \begin{bmatrix} 0 & 0 & -(M + M_{22})v + (Mx_g + M_{26})r - (M_{11} - M_{12})v_c \\ 0 & 0 & -(M + M_{11})u - (M_{11} - M_{12})u_c \\ 0 & 0 & (Mx_g + M_{26})u \end{bmatrix},$$

M is the mass of the vessel, M_{ij} , $i, j = 1, 2, 6$ are the added mass coefficients in surge, sway and yaw, respectively; u and v are the surge and sway velocities, respectively; u_c and v_c are current speeds related to the body fixed frames, respectively; r is the yaw rate; I_z is the moment of inertia about vertical axis; \mathbf{F}_E and \mathbf{F}_T represent the total external and acutators forces and moment in surge, sway and yaw directions, respectively; dot means time derivative of the variable. The position and heading of the vessel related to the earth-fixed coordinate system are obtained from the following equation

$$\dot{\mathbf{x}} = \mathbf{J}(\mathbf{x})\mathbf{v} \quad (2)$$

where $\mathbf{x} = [x \ y \ \psi]^T$, $\mathbf{J}(\mathbf{x}) = \begin{bmatrix} \cos\psi & -\sin\psi & 0 \\ \sin\psi & \cos\psi & 0 \\ 0 & 0 & 1 \end{bmatrix}$, x , y and ψ are the coordinates and heading of the vessel in the earth fixed frame respectively.

SYSTEM DESCRIPTION

In the present paper a DP barge and two different DP Shuttle Tankers (ST) will be considered. In the latter case both tankers have the same main particulars but they differ in the actuator configurations. The main particulars and the actuators configurations of the vessels are presented in Table 1

Table 1 – Vessels main data

	Barge (1:48)	Full loaded ST A (1:125)	Ballasted ST A (1:125)	Full loaded ST B (1:70)	Ballasted ST B (1:70)
Length (L)	121.9 m	2182mm		3841mm	
Beam (B)	30.48 m	368mm		655mm	
Draft (T)	5.18 m	130mm	64mm	225mm	114mm
Mass (m)	17177 ton	89 kg	40 kg	500 kg	227 ton
Propellers	6 azimuth	1 main propeller+rudder 1 bow + 1 stem tunnel thruster		1 main propeller+rudder 1 bow + 1 stem tunnel thruster 1 bow + 1 stem azimuth thruster	

Pictures of small scale models of all vessels are presented in Figure 3 below.

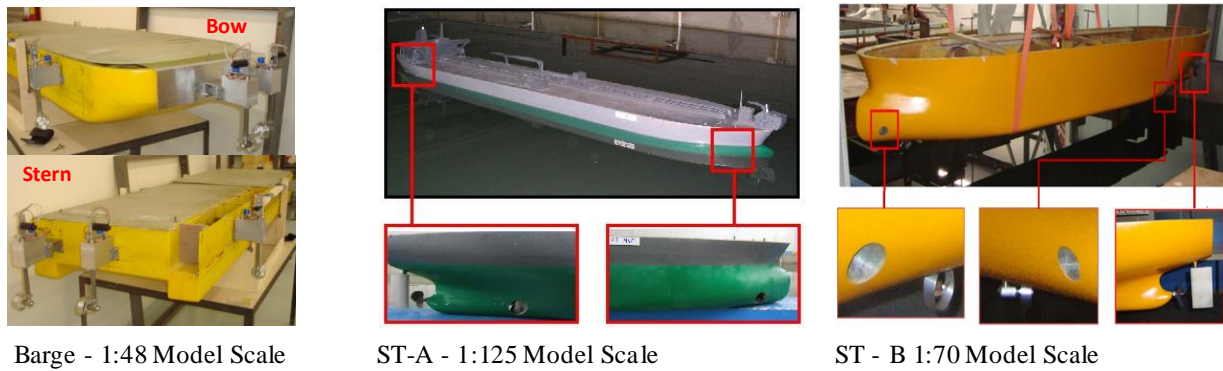


Figure 3 – Small Scale models of the vessels used in the present paper

DP CONTROL

A typical block diagram of a DP System is presented in Figure 4. A linear controller is used to calculate the required total control forces (surge, sway forces and yaw moment). LQG control or PID control are normally used, and in the present paper the later will be considered. Furthermore, DP system requires a special feature that is the filtering of the high frequency motions due to the waves. In fact the environmental disturbances acting on a ship induce at least two distinct motions. The first-order wave forces induce high-frequency motions while winds, currents and second-order wave forces induce low-frequency oscillations and steady motions. DP system must suppress the low-frequency motion, keeping the vessel mean position as close as possible to the desired position. In general, the counteraction of the first-order wave induced motions is avoided since it would require a huge power, leading to extra fuel consumption and propulsion system degradation. A notch filter is normally used for this purpose. Since the system is normally over-actuated, a thrust allocation algorithm is also necessary to distribute the forces among the propellers. Finally, a wind feed-forward action is normally used, since wind measurement is available.

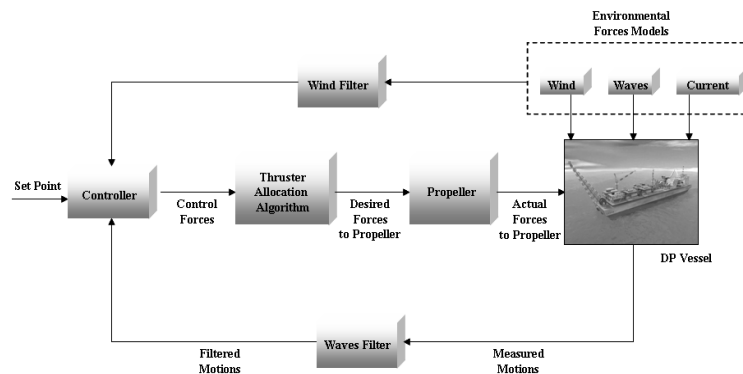


Figure 4 – DP system block diagram

The tuning of PID parameters is quite difficult, due to the large inertia of the system, coupling between the motions (mainly between sway and yaw) and some delay introduced by the wave-filter. Before presenting the tuning methods proposed in the paper, a qualitative analysis of the influence of the PD terms will be exposed. The following PID structure is considered:

$$F_{iT} = P_i \cdot e_i(t) + D_i \cdot \frac{de_i(t)}{dt} + I_i \cdot \int e_i(\tau) d\tau$$

The subscript i stands for the motion being considered ($i=1$ for surge; 2 for sway and 6 for yaw), and e is the error. Figure 5 shows color plots of the three important performance parameters, considering several PD gains for surge motion control. The ST-A is considered, in a 1:150 reduced scale and a step set-point change of 0.2m. The set of gains obtained by the Method 2 (Genetic Algorithm) is also indicated by a black dot, and three different sets are also indicated for a later investigation. The performance parameters are obtained for a control loop with or without the wave notch filter, in order to emphasize the influence of that filter in the closed loop dynamics.

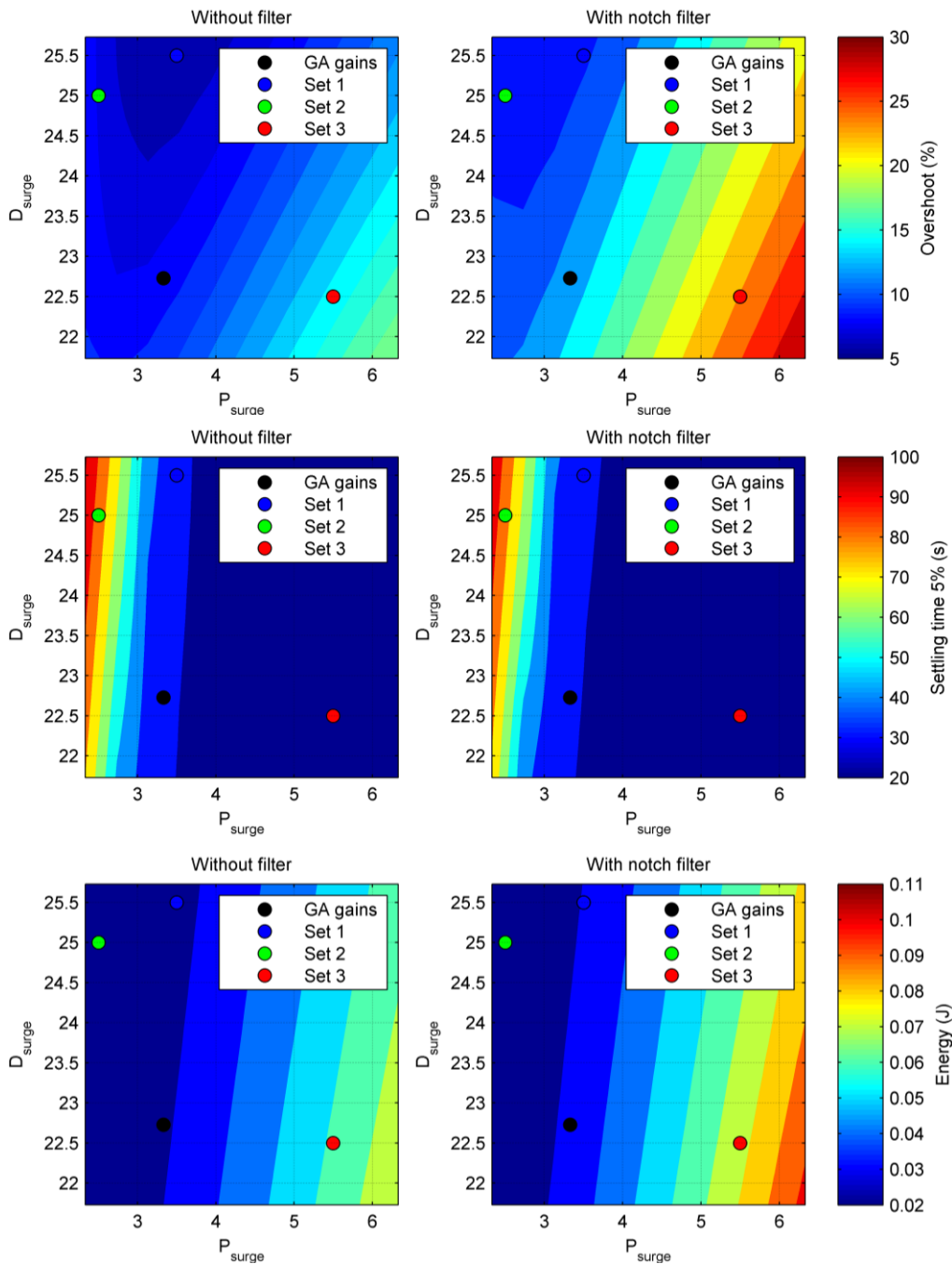


Figure 5 – Overshoot of surge motion

As expected, a higher Proportional (P) gain takes to a larger overshoot, a smaller settling time (the system gets faster) and larger energy consumption. A higher Derivative (D) gain causes a reduction in the overshoot, and a less sensitive reduction in the energy. Also, a slightly increase in the settling time is also observed. Considering all parameters, the introduction of the notch filter degrades the performance, if compared to the case without the filter. The time series for the four sets of gains are presented in Figure 6. This analysis demonstrates that the proper tuning must consider the tradeoff between closed loop velocity and energy consumption.

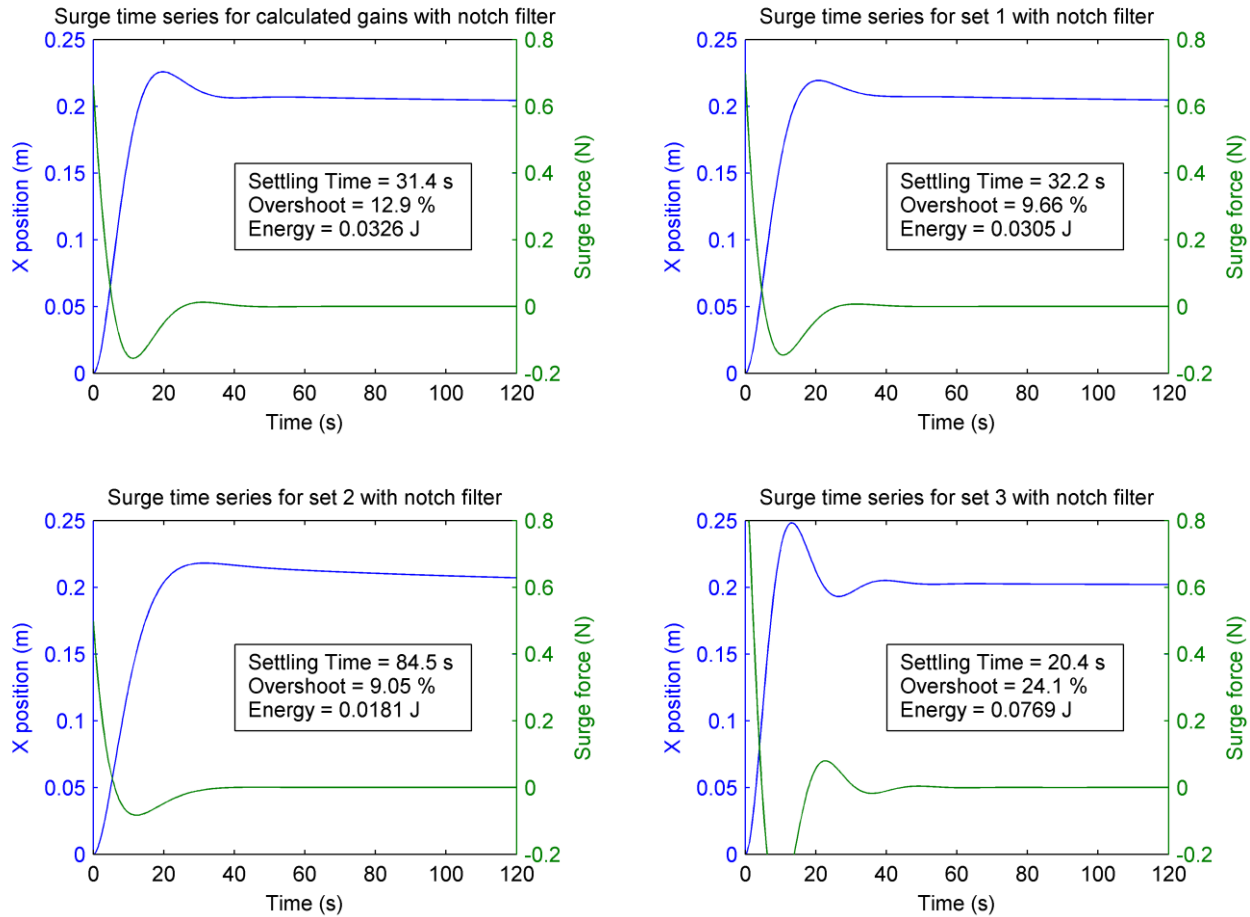


Figure 6 – Time series for the four sets of gains

METHOD 1 – POLE PLACEMENT TECHNIQUE

The DP system is composed by three uncoupled PID controllers associated with wave notch filters, as formulated in Tannuri;Morishita (2006). The pole-placement technique is based on the simplified dynamical model for each (uncoupled) horizontal motion of the vessel. The procedure will be detailed for the surge (longitudinal) motion, and is also applied for sway and yaw motions.

The low-frequency dynamics of one of the vessel's motion, disregarding damping and nonlinear components, coupling and the wave filter, can be written as:

$$(M + M_{ii})\ddot{x}_i = F_{iT} + F_{iE} \quad (3)$$

where M is the mass, M_{ii} is the added mass for the motion i , \ddot{x}_i is the vessel acceleration in direction i , F_{iT} is the total thrusters surge force and F_{iE} is the total surge environmental forces.

Disregarding the environmental forces (disturbances), the simplified control loop considering a PID control, for surge motion, is given by:

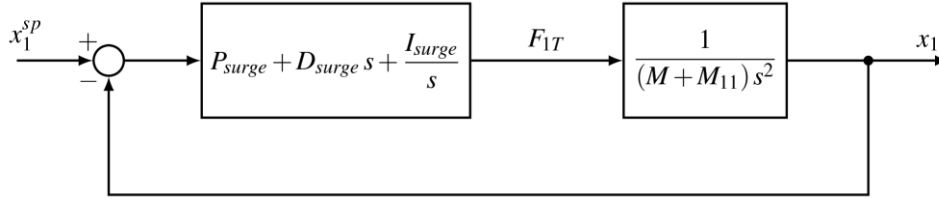


Figure 7 – Closed loop control block diagram.

Using block diagram algebraic calculation, the 3rd order closed-loop transfer function is obtained:

$$\frac{D_{surge}s^2 + P_{surge}s + I_{surge}}{(M + M_{11})s^3 + D_{surge}s^2 + P_{surge}s + I_{surge}} \quad (4)$$

and the two dominant poles are set as $-\omega_n\zeta \pm \omega_n j$. The non-dominant pole is set as $-\beta\omega_n$, with $\beta = 10$. The parameters ω_n and ζ are the closed-loop natural frequency and damping factor of the corresponding motion. PID gains are then evaluated:

$$\begin{aligned} P_i &= (M + M_{ii})(1 + 2\beta\zeta^2)\omega_n^2 \\ D_i &= (M + M_{ii})(2 + \beta)\zeta\omega_n \\ I_i &= (M + M_{ii})\beta\zeta\omega_n^2 \end{aligned} \quad (5)$$

The parameters ω_n and ζ may be obtained by the desired motion specification of the closed-loop system (specification of settling time and overshoot for example).

METHOD 2 – OPTIMIZATION USING GENETIC ALGORITHM

The key idea of Genetic Algorithms (GAs) is to define a searching process based on principles of natural evolution, i.e., by changing chromosomes based on crossover and mutation taking into account the selection process. In practical terms the set of the chromosomes, called as the population, means a set of the possible solutions, and crossover and mutation are related to the process of the generation of the new possible solutions. This procedure is based on probabilistic methods that try to simulate the natural evolution.

In this work the Genetic Algorithm was applied in order to find the minimum value of the following objective function (fitness function):

$$S = \int_0^t [\mathbf{F}_T(\lambda) \mathbf{A} \mathbf{F}_T^T(\lambda) + \boldsymbol{\varepsilon}(\lambda) \mathbf{B} \boldsymbol{\varepsilon}^T(\lambda)] d\lambda \quad (6)$$

where

$$\begin{aligned} \mathbf{F}_T &= [F_{1T} \quad F_{2T} \quad F_{3T}] \\ \boldsymbol{\varepsilon} &= [e_1 \quad e_2 \quad e_3] \\ \mathbf{A} &= \text{diag}[a_1 \quad a_2 \quad a_3] \\ \mathbf{B} &= \text{diag}[b_1 \quad b_2 \quad b_3] \end{aligned}$$

In which $F_{iT}(t)$ and $e(t)$ are, respectively, the control forces and error in each direction, with $i = 1, 2$ and 3 corresponding to surge, sway and yaw degrees of freedom and a_i and b_i are weighting factors. The evaluation of S function is done by mean of the numerical simulation of the system. One should notice that both the control forces and error depend on the gain of the controller.

The genetic algorithm used in the present paper for the minimization of the function S is based on the work of Herrera and Lozano (2000). It is a Gradual Distributed Real Coded Genetic Algorithm (GD-RCGA) with BLX- α crossover operator, non-uniform mutation and roulette selection. As in every gradual distributed GA, the population was divided into several subpopulations and genetic algorithms with different configurations were applied to each one. The difference among these subpopulations is the exploratory degree, what provides a better algorithm behavior with the migration scheme adopted for trading chromosomes between them. Particular routines of the GA are described below.

Selection

The selection mechanism chooses the elements randomly based on its fitness value. In a subpopulation with N individuals and each one with fitness S , the probability p_i of the element i be selected is (Goldberg, 1989):

$$p_i = \frac{s_i^{-1}}{\sum_{j=1}^N s_j^{-1}} \quad (7)$$

Crossover

Crossover is a way of generating two new individuals, based on two selected chromosomes, with a probability p_c . The BLX- α operator is adopted as the crossover routine and it consists in generating two new chromosomes randomly over an interval created with the two individuals selected for crossover. In addition, this operator has a α parameter, which is different for each subpopulation and defines the balance between exploration and exploitation.

More detailed, BLX- α creates an offspring $Z = (z_1 \dots z_9)$ where z_i is a number chosen randomly from the interval $[\min_i - I * \alpha, \max_i + I * \alpha]$, where $\min_i = \min \{x_i, y_i\}$, $\max_i = \max \{x_i, y_i\}$ and $I = \max_i - \min_i$ (Herrera and Lozano, 2000).

The α parameter defines the balance between exploration and exploitation, what means respectively searching for new solution in different function domain regions and refining actual chromosomes. For $\alpha < 0.5$, the subpopulation has a more exploiting behavior, for $\alpha > 0.5$ the exploration performance is more apparent and for $\alpha = 0.5$ an equilibrium between exploration and exploitation is achieved. As presented in Table 2, for each subpopulation a different value of α is defined.

Table 2 – α parameter to each subpopulation (Herrera and Lozano, 2000)

Subpopulations							
Exploitation				Exploration			
e_4	e_3	e_2	e_1	E_1	E_2	E_3	E_4
0,1	0,2	0,3	0,4	0,5	0,6	0,7	0,8

Mutation

The mutation technique is used to avoid the algorithm to fall into a local minimum. The non-uniform mutation was applied in order to change randomly a chromosome selected with a probability p_m .

In case of an individual $D = [d_1 \dots d_9]$ be selected for mutation, the new chromosome $D' = [d'_1 \dots d'_9]$ is obtained through:

$$d'_i = d_i + \delta_i, \text{ with } i = 1, \dots, 9 \quad (8)$$

Using the random variable:

$$\delta_i = \begin{cases} (d_{i,\max} - d_i) \cdot (1 - [z_i]^{r(t)}) \\ \text{with probability } q_i = \frac{1}{2} \\ (d_{i,\min} - d_i) \cdot (1 - [z_i]^{r(t)}) \\ \text{with probability } 1 - q_i = \frac{1}{2} \end{cases}$$

Where z_i is a random number uniformly distributed in the interval $[1,0]$, $d_{i,\max}$ and $d_{i,\min}$ are the maximum and minimum values (on actual generation) of the gain K corresponded by i , and

$$\gamma(t) = \left(1 - \frac{t}{t_{\max}}\right)^\beta \quad (9)$$

On actual generation t , with exogenous strategy parameter $\beta = 1$ and the maximum number of generations $t_{\max} = 80$ (Neubauer, 1997).

Migration

Migration is a method that consists in moving the best individual of each subpopulation to another, following a variable scheme. The migration occurs in every five generations, and its scheme changes successively between the three types represented in the Figure 1 (Herrera and Lozano, 2000). Refinement migrations contribute to exploitation, refinement/exploratory migrations contribute to both exploitation and exploration, and exploration migrations contribute to exploration.

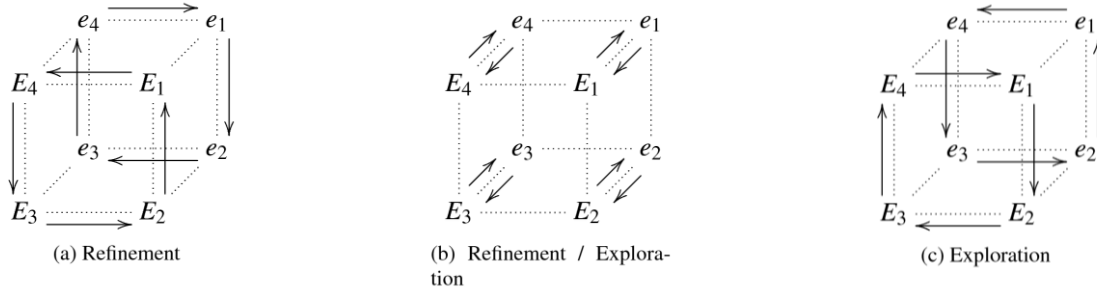


Figure 1 – Types of migration (Herrera and Lozano, 2000)

Remark 1: The definition of the search domain is crucial to the GA’s performance. If the region of search is too large, the algorithm possibly will take a long time to find the optimum value. On the other hand, if the domain is relatively short, it may not contain the global minimum of the fitness function. For GA applications, in order to define a suitable explore region, it’s generally necessary a good knowledge about the function to be optimized.

Based on the experience acquired with preliminary experiments, the probability of the crossover and mutation were assumed respectively as $p_c = 70\%$ and $p_m = 5\%$. The number of subpopulations was 8 with 20 chromosomes each.

RESULTS – METHOD 1

The parameters ω_n e ζ of each motion must be properly selected, in order to define the trade-off between positioning (small error) and thrust (small control action). General specification for second order system transient response may be used for selecting adequate values for ω_n e ζ (Ogata, 2010). General rules for the 2% settling time and overshoot (M_p) are:

$$t_{\text{settling}}^{2\%} = \frac{4}{\zeta\omega_n} ; M_p (\%) = \exp\left(-\pi\zeta/\sqrt{1-\zeta^2}\right) \quad (10)$$

The time series of the motions for the ballasted ST-A, considering step-changes in the set-points, are given below. These figures contain numerical simulations and experimental results in 1:150 reduced scale. The tuning parameters adopted for this vessel are $\omega_n = 0.08\text{rad/s}$ (0.0065rad/s in real scale) and $\zeta = 0.7$ for all motions. Very good agreement between numerical and experimental results was obtained. The expected 2% settling time ($4/\zeta\omega_n$) is 72s, coherent with the obtained results. However, the actual overshoot is larger than the expected value (<5% for $\zeta = 0.7$), for the three motions. Effects not considered in the dynamics (1), such as propeller dynamics and delays, may explain such difference.

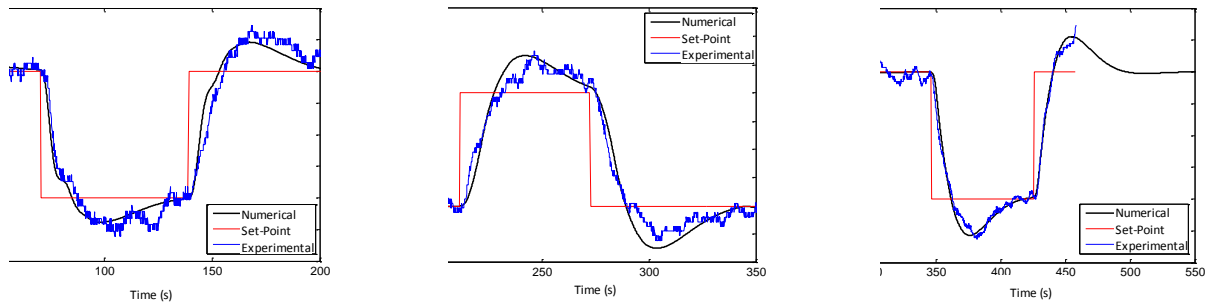


Figure 8 – Time series of ballasted DP ST-A– Method 1.

A similar test was conducted with the ballasted ST-B. These figures contain numerical simulations and experimental results in 1:70 reduced scale. The tuning parameters for surge, sway and yaw motions are 0.04rad/s ; 0.06 rad/s and 0.08rad/s respectively and $\zeta = 1.0$. A good trade-off between settling time and overshoot is obtained. Some discrepancies between numerical and experimental results are due to the propeller dynamics not considered in the numerical model. The gains here obtained by the Method 1 were used in the first tests of Petrobras using a DP model scale shuttle tanker, conducted at Labocean, RJ (Tannuri et al., 2010).

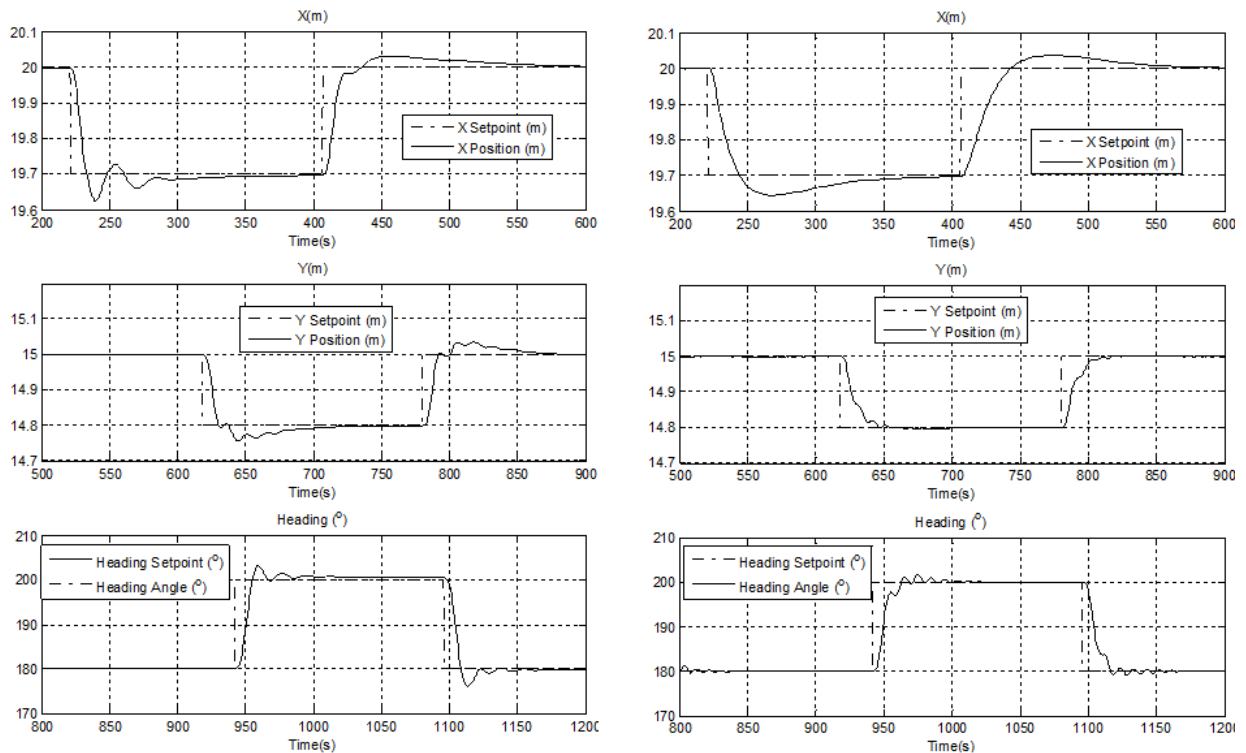


Figure 9 – Time series of ballasted DP ST-B– Method 1 (left - simulation ; right - experiments)

By the analyses of the previous results, it can be concluded that Method 1 may be used as a first estimate of control gains for both simulation or experimental analysis.

RESULTS – METHOD 2

The method 2 (genetic algorithm) was applied to the ballasted ST-A, and very good results were obtained. Figure 10 shows the time series of the motions considering step-changes in the set-points.

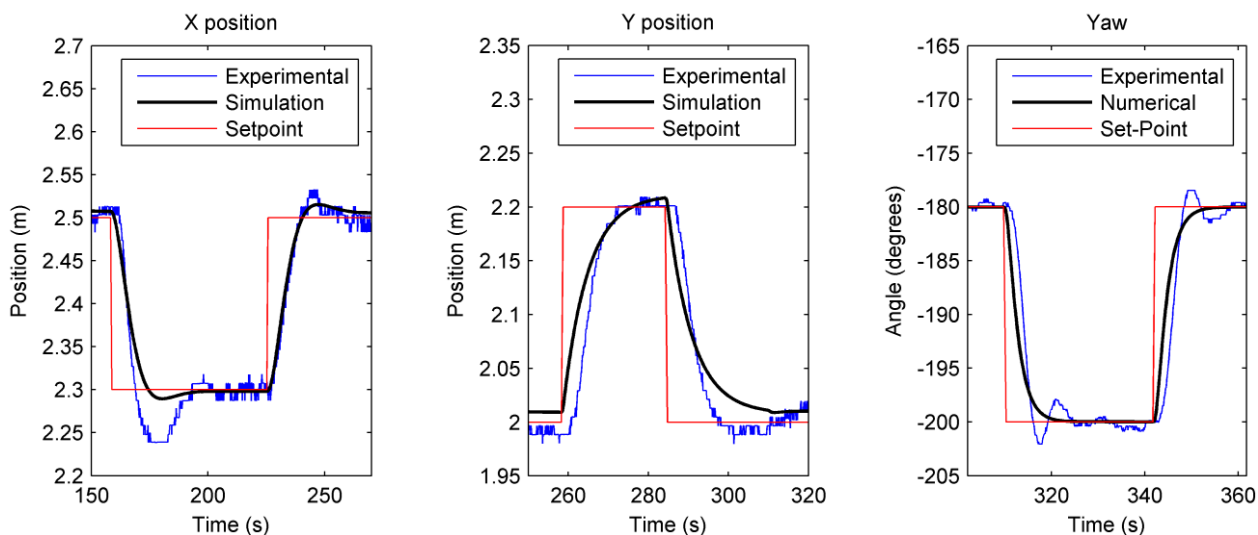


Figure 10 – Time series of DP ballasted shuttle tanker – Method 2.

Comparing to the results of Method 1, it can be seen that surge motion performance are quite similar, but sway and yaw motions present a much smaller settling time and overshoot, compared to Method 1.

GENERAL COMMENTS AND CONCLUSIONS

The Method 1 (pole placement) has the advantage of a straightforward application, and does not require previous simulations. The parameters ω_n e ζ may be obtained by the specification of closed loop response. Some discrepancies were observed between the specified closed loop response and the response obtained in the numerical and simulation results, due to the simplicity of the dynamics used for the pole-placement technique.

Method 2 (genetic algorithm) requires an accurate numerical model of the system and several time domain simulations, in order to minimize the cost function. If the numerical model is accurate, a very good performance may be achieved, as shown in the paper. However, if a poor model is used, the results may be quite unsatisfactory.

The Method 1 was chosen to be implemented in the simulation and experimental tools for evaluating DP System, that are being developed by Petrobras in cooperation with USP and other Brazilian universities.

ACKNOWLEDGMENTS

The authors acknowledge Petrobras for the financial support and for the motivation of this work. The first and fourth authors acknowledge the National Council for Scientific and Technological Development (CNPq) for the research grants.

REFERENCES

- Herrera F. and Lozano M., 2000, "Gradual distributed real-coded genetic algorithms". *Evolutionary Computation, IEEE Transactions on*, 4(1):43–63, Apr.
- Goldberg, D. E., 1989, *Genetic Algorithms in Search, Optimization, and Machine Learning*, Addison-Wesley.
- Ogata, K., 2010, *Modern Control Engineering*, 5th Edition, Prentice Hall.
- Morishita, H.M. ; Tannuri, E. A. ; Saad, A. C. ; Sphaier, S. H. ; Lago, G.A. ; Moratelli Jr., L. 2009, *Laboratory Facilities for Dynamic Positioning System. Proceedings of 8th Conference on Manoeuvring and Control of Marine Craft (MCMC'2009)*, Guarujá, Brazil.
- Neubauer, A., 1997, "Adaptive Non-uniform Mutation for Genetic Algorithms". *Proceedings of the International Conference on Computational Intelligence, Theory and Applications*. Pages 24-34.
- Tannuri, E.A. and Morishita, H.M., 2006, "Experimental and Numerical Evaluation of a Typical Dynamic Positioning System". *Applied Ocean Research*, v. 28, p. 133-146.
- Tannuri, E. A. ; Morishita, H.M. ; Vilaça, R. M. ; Saad, A. C., 2010, "Numerical and experimental analysis of a typical DP shuttle tanker operating in Brazilian waters". In: *8th IFAC Conference on Control Applications in Marine Systems, CAMS 2010, Rostock-Warnemünde, Germany*.

RESPONSIBILITY NOTICE

The author(s) is (are) the only responsible for the printed material included in this paper.

Luni-solar and geopotential perturbations on a close satellite

Giorgio E. O. Giacaglia¹, Bob E. Schutz²

¹ University of Taubaté, Dept. of Mechanical Engineering, Rua Daniel Danelli s/n, Taubaté, SP, Brazil, 12060-440

² University of Texas at Austin, Center for Space Research, R1000, Austin, Texas, USA, 78759-5321

Abstract: Equations for long period perturbations due to the Moon and Sun are developed and applied to equations expressing their influence on the secular rates due to the Earth potential field. Analytical results represent with good approximation observed values for the amplitude and periods of the perturbed elements of a satellite. As an example, we have computed these values for a particular GPS satellite

Keywords: Luni-solar perturbations, Long period, Secular rates

NOMENCLATURE

G = gravitational constant
 m = mass
 n = mean motion
 a = semi-major axis
 C₂₀ = second harmonic coefficient of the Earth
 e = eccentricity
 PRN03 = GPS satellite
 RAAN = right ascension of ascending node
 GPS = Global Positioning System

M = mean anomaly
 f = frequency
 ℓ, m, p, q = integers
 N = gravitational factor

Greek Symbols

β = defined by Eq. 3
 ω̃ = longitude of perigee
 Ω = longitude of ascending node
 λ = mean longitude
 δ = perturbation in satellite variables.

Subscripts

M relative to Moon
 ☐ relative to Sun
 ⊕ relative to Earth
 2 second order perturbation
 sec = secular rate

INTRODUCTION

Several works have been published dealing with third body perturbations on a satellite of the Earth and other celestial bodies. A complete review was published in 2003 (Giacaglia and Prado, 2003). We have recently developed theories dealing with satellites orbits of small eccentricity and small inclination (Giacaglia, 1975; Prado, 2003; Solórzano and Prado, 2004, Giacaglia and Schutz, 2008 a, 2008b, 2009). Some results obtained in the above papers and in Van de Graff (1977) have been used. In this work the use of classical Keplerian elements show no singularities in the equations of motion. We initially evaluate long period luni-solar perturbations and apply the results to the secular rates in longitude of perigee, longitude of ascending node and mean longitude produced by the Earth major oblateness. The results are in agreement with observations over a long period of time (Schutz and Giacaglia, 2009)

The Basic Problem

Long Period and Secular Perturbations due to the Geopotential and the Lunar Gravitational Field on a an artificial satellite of the Earth, using ecliptic coordinates for the Moon and equatorial coordinates for the satellite, are developed. For solar perturbations the theory is applicable with obvious adaptations. It is shown that Lagrange Differential Equations, for a special set of coordinates, are non singular for small eccentricity and inclination (except retrograde equatorial orbits), even when developing the disturbing function in terms of classical Keplerian Elements. Equations for long period and secular perturbations due to the Moon and due to the Earth potential field are derived. We give the equations expressing the influence of the third body long period and secular perturbations on the secular rates due to the Earth potential field. Preliminary results show good agreement with observed values (Schutz and Giacaglia, 2009).

The question arising from the use of the longitude of the perigee and the longitude of the ascending node should take into account the D'Alembert Characteristics. If the derivative of the disturbing function with respect to the longitude of the perigee is not zero, it must be factored by at least the first power of the eccentricity. Similarly, if the derivative of the disturbing function with respect to the longitude of ascending node is not zero, then it is factored by at least the first power of sine of half the inclination.

Because of these considerations, no singularities will be present in the right hand members of Lagrange Equations. Singularities in the derivatives with respect to the eccentricity and the inclination are only apparent due, again, to D'Alembert Characteristics.

In case of no resonances between the motion of the satellite and that of the Moon, the elimination of short period terms (depending on the mean anomaly *M* of the satellite) reduce to the evaluation of definite integrals, that can be expressed all in closed form, both in the eccentricity and inclination.

The Mathematical Approach

The averaged long period and secular disturbing function does not depend on the mean longitude and it is an explicit function of time only through the coordinates of the Moon and Sun, considering the inclination of the Moon with respect to the ecliptic and de obliquity of the ecliptic to be constant, which is a good approximation.

The integration of the pertinent equations can be performed numerically by using as input lunar ecliptic coordinates – or, for that matter, equatorial coordinates, in which case the theory is greatly simplified – stored in memory. This will produce precise evaluation of the true lunar motion. However, such a method can be very expensive in time.

A good approximation can be obtained by considering the inclination, eccentricity and semi-major axis and the obliquity of the ecliptic to be constant and the angular coordinates of the Moon with respect to the ecliptic to be linear functions of time. Also, an expansion in power series of the eccentricity of the Moon orbit will converge rapidly owing to the small value of this eccentricity, about 0.05.

The disturbing function of the Moon in a primitive form is transformed into orbital elements and rotation of the lunar coordinates to an ecliptic frame of reference, improving the results obtained by Kaula (1961).

The differential equations of motion for the satellite contains the frequencies which are integer multiples of the mean motion of the perigee of the satellite and the Moon and Sun, longitude of the ascending node of the satellite and the Moon and the ecliptic mean longitude of the Moon and Sun. These frequencies give an indication of possible resonances.

We should remember that one of the results of Kolmogorov (1953) celebrated work on quasi periodic motions, is that for large enough integers the denominator above can become smaller than any given quantity, which the basis for showing that perturbations techniques based on successive approximations, as for instance, Canonical Methods or Lie Series Methods, cannot converge to the true solution. In this respect, we must rely on Poincaré (1989) statement about asymptotic series “stop the series at a low degree of approximation”.

Approximate values for the Moon and Sun angular variables are used to estimate the secular rates of the satellite perigee and ascending node. For a satellite with eccentricity 0.007, inclination 60° and semi-major axis of 26.750 km we have the secular motion in longitude of perigee is approximately 24.85×10^{-3} degree/day and in longitude of the ascending node is approximately 33.26×10^{-3} degree/day, both negative, so we can estimate the amplitude associated to any given set of the 8 integers entering the frequencies of the solution. Exact evaluation of the integral leading to the mean eccentricity and mean inclination should be from an initial time of observation up to any given successive time, and this requires a transformation from osculating to mean elements, a task to be developed in a future work.

By considering lunar and solar perturbations, in the absence of resonances, secular perturbations due to the Moon are obtained by eliminating all angular variables in the disturbing function. The equations of motion are greatly simplified, even because the angular variables appearing explicitly in the equations are considered to be affected only by secular variations.

Simple equations are found for the secular rates in longitude of perigee, ascending node and mean longitude of the satellite

For a real analysis of perturbations of an artificial satellite we consider perturbations due to the Earth gravity field, noting that up to geosynchronous heights the dominant term is due the Earth oblateness. Secular perturbations in eccentricity and inclination are zero, only being affected by short period and long period terms. As a first approximation, the secular rates may be computed by a simple quadrature, by keeping constant the right-hand members of the pertinent differential equations. Direct additions of secular rates due to the Moon (and / or Sun) and the geopotential are obtained.

When no resonances occur, the long period perturbations are defined by simply eliminate the dependence of the Disturbing Function from the mean longitude. The period of rotation of the Earth, about 24 hours, is considered a long period.

The final task has been to take into consideration the influence of the third body on the secular rates resulting from the Earth potential field. This is done by developing variational equations for the secular rates of the satellite angular variables, where the eccentricity and inclination are affected by long period perturbations due to the Moon and Sun. The corresponding equations are easily constructed and, since there is no secular change in semi-major axis, the secular part of the mean motion in longitude is constant.

Perturbations Evaluation

It is noted that Moon perturbations are factored by

$$Gm_M = \frac{m_M n_M^2 a_M^3}{m_M + m_\oplus} = N_M^2 a_M^3 = (1.59 \times 10^{-5} \text{ rev}^2 \text{ day}^{-2}) a_M^3 \quad (1)$$

This energy when compared with the central Newtonian attraction of the Earth gives a ratio of 1.2×10^{-7} for low satellites and 3.18×10^{-5} for geosynchronous satellites. For the Sun it is found that

$$Gm_\square = \frac{m_\square n_\square^2 a_\square^3}{m_\square + m_\oplus} = N_\square^2 a_\square^3 = (0.75 \times 10^{-5} \text{ rev}^2 \text{ day}^{-2}) a_\square^3 \quad (2)$$

The satellite Keplerian negative energy is

$$F_0 = n^2 a^2 / 2 \quad (3)$$

The relative size of the perturbing force function wrt the main Keplerian central attraction is given by

$$v = R'/F_0 = 2N_M^2/n^2 \quad (4)$$

$$\text{For low satellites (T} \cong 90 \text{ min), } v \cong 1.2 \times 10^{-7}. \quad (5)$$

$$\text{For high satellites (T} \cong 24 \text{ h), } v \cong 3.18 \times 10^{-5}. \quad (6)$$

It is seen that perturbations from the Moon and the Sun in a low satellite are comparable in magnitude. In the above range of periods, with low values of the eccentricity, the dominant part of the disturbing function of a satellite is due to the Earth oblateness (C_{20}) and lunar (and solar) perturbations are about second order with respect to this. In cases of higher satellites, depending on the values of semi-major axis and eccentricity, the situation might even be reverted, so that for a full evaluation of the lunar perturbations, truncation of the corresponding disturbing function may not be advisable.

Long Period Perturbations

The integration of the pertinent equations can be performed numerically by using as input lunar and solar ecliptic coordinates or equatorial coordinates stored in memory, in which case the theory is greatly simplified. This will produce precise evaluation of the true lunar motion. However, such a method can be very expensive in time. Using the ecliptic as a reference, a good approximation can be obtained by considering the inclination, eccentricity and semi-major axis of the Moon and Sun and the obliquity of the ecliptic ε fixed values and the corresponding angular values to be linear functions of time, neglecting accelerations of these elements. Also, an expansion in power series of the eccentricity of the Moon and Sun will converge rapidly owing to the small value of the eccentricity of the Moon orbit.

Taking into account only the major flattening of the Earth Potential Field, for a GPS satellite with eccentricity 0.006, inclination 54° and semi-major axis of 26.560 km we obtain the following secular rates

$$\dot{\omega}_{\text{sec}} = -2.766 \times 10^{-4} \text{ degree/day} \quad (7)$$

$$\dot{\Omega}_{\text{sec}} = -1.212 \times 10^{-3} \text{ degree/day} \quad (8)$$

Approximate values for the Moon and Sun are

$$\begin{aligned} \dot{M}_M &= 13.126 \text{ degree/day} \\ \dot{\omega}_M &= 0.113 \text{ degree/day} \\ \dot{\Omega}_M &= -0.053 \text{ degree/day} \\ \dot{M}_\square &= 0.985609 \text{ degree/day} \\ \dot{\omega}_\square &= 0.985609 \times 10^{-6} \text{ degree/day} \end{aligned} \quad (9)$$

Taking into account the lowest degree in the harmonics ($\ell = 2$) the frequencies involved are

$$\begin{aligned} f_{2mpp'm'q'}^\pm &= (2-2p)\dot{\omega}_{\text{sec}} + (m-2+2p)\dot{\Omega}_{\text{sec}} \pm \\ &\pm (2-2p')\dot{\omega}_M \pm (2-2p'+q')\dot{M}_M \pm m'\dot{\Omega}_M \\ &\pm (2-2p'')\dot{\omega}_\square \pm (2-2p''+q'')\dot{M}_\square \end{aligned} \quad (10)$$

for $m = 0, 1, 2$; $m' = 0, 1, 2$; $p, p', p'' = 0, 1, 2$; $q', q'' = \dots, -2, -1, 0, 1, 2, \dots$ and we can estimate the periods associated to any given set of integers $p, m, p', m', q', p'', q''$.

Secular Perturbations

For a real analysis of perturbations of an artificial satellite we must consider perturbations due to the Earth gravity field, noting that up to geosynchronous heights the dominant term is due the Earth oblateness.

As a first approximation, the secular rates may be computed by a simple quadrature, by keeping constant the right-hand members of the pertinent differential equations. These secular rates are affected by short and long period perturbations, through a, e and I , a task to be undertaken in a future work. In order to simplify matters and give a preliminary example, we shall consider the Moon to move on the ecliptic and, therefore neglect the longitude of the

ascending node of the lunar orbit, keeping only the argument of perigee. Under these hypotheses a direct addition of secular rates due to the Moon, Sun and the geopotential gives

$$\begin{aligned} \dot{\omega}_{\text{sec}} = & \frac{3nC_{20}b^2}{4\gamma^4a^2}(1 + 2\cos I - 5\cos^2 I) + \\ & + \frac{3(\mu_M n_M^2 + \mu_{\square} n_{\square}^2)}{8n\gamma} [5\cos^2 I - (3e^2 + 2)\cos I - (1 - e^2)] \end{aligned} \quad (11)$$

$$\dot{\Omega}_{\text{sec}} = \frac{3nC_{20}b^2}{2\gamma^4a^2} \cos I - \frac{3(\mu_M n_M^2 + \mu_{\square} n_{\square}^2) \cos I}{8n\gamma} (3e^2 + 2) \quad (12)$$

$$\begin{aligned} \dot{\lambda}_{\text{sec}} = & n + \frac{3nC_{20}b^2}{4\gamma^4a^2} [-(3\gamma - 5)\cos^2 I + 2\cos I + (1 + \gamma)] + \frac{\mu_M n_M^2 + \mu_{\square} n_{\square}^2}{16n\gamma} \times \\ & \times [3(10 - \gamma e^2 - 9\gamma^2)\cos^2 I - 6(3e^2 + 2)\cos I - \gamma(6\gamma + 9e^2 + 1)] \end{aligned} \quad (13)$$

where

$$\mu_M = Gm_M / (m_M + m_{\oplus}) \text{ and } \mu_{\square} = Gm_{\square} / (m_{\square} + m_{\oplus}) \quad (14)$$

We have evaluated the secular rates (Table 1) assuming the values (Schutz, 2009)

$$\begin{aligned} T &= 0.498634 \text{ day}, n = 12.5944 \text{ rd / day}, a = 26560 \text{ km} \\ b &= 6378 \text{ km}, e = 0.006, I = 54^\circ, C_{20} = -1.083 \times 10^{-3} \end{aligned}$$

Table 1 – Secular Rates due to Earth (C₂₀), Moon and Sun

Element	Rates (rd)
Longitude of perigee	-2.766 x 10 ⁻⁴
Longitude of ascending node	-1.212 x 10 ⁻³
Mean longitude	n + 1.898 x 10 ⁻³

The resulting period in all variables, corresponding to either $\cos 2\tilde{\omega}$ or $\sin 2\tilde{\omega}$ is given by $T_{2\tilde{\omega}} = 11\,352 \text{ days}$ which agrees closely with the observed values as shown in Fig. 1 through Fig. 4.

The long period perturbations due to the Moon and Sun are given by

$$\dot{e}_{lp} = \frac{15(\mu_M n_M^2 + \mu_{\square} n_{\square}^2)\gamma e}{8n} \sin^2 I \sin 2\tilde{\omega} \quad (16)$$

$$\dot{I}_{lp} = -\frac{15(\mu_M n_M^2 + \mu_{\square} n_{\square}^2)e^2}{16n\gamma} \sin 2I \sin 2\tilde{\omega} \quad (17)$$

$$\dot{\tilde{\omega}}_{lp} = \frac{15(\mu_M n_M^2 + \mu_{\square} n_{\square}^2)}{8n\gamma} (1 - e^2 + e^2 \cos I - \cos^2 I) \cos 2\tilde{\omega} \quad (18)$$

$$\dot{\Omega}_{lp} = \frac{15(\mu_M n_M^2 + \mu_{\square} n_{\square}^2)e^2 \cos I}{8n\gamma} \cos 2\tilde{\omega} \quad (19)$$

$$\dot{\lambda}_{lp} = \frac{15(\mu_M n_M^2 + \mu_{\square} n_{\square}^2)}{16n\gamma} [2\gamma^2 + 2e^2 \cos I - 2\cos^2 I - (1 + e^2)\gamma \sin^2 I] \cos 2\tilde{\omega} \quad (20)$$

Integration , keeping constant the metric variables on the right hand side, yields

$$\delta_1 e_p = -\frac{15(\mu_M n_M^2 + \mu_\square n_\square^2) e \gamma}{16 n \dot{\omega}_{\text{sec}}} \sin^2 I \cos 2\tilde{\omega} \quad (21)$$

$$\delta_1 I_p = -\frac{15(\mu_M n_M^2 + \mu_\square n_\square^2) e^2}{32 n \dot{\omega}_{\text{sec}} \gamma} \sin 2I \cos 2\tilde{\omega} \quad (22)$$

$$\delta_1 \tilde{\omega}_p = \frac{15(\mu_M n_M^2 + \mu_\square n_\square^2)}{16 n \dot{\omega}_{\text{sec}} \gamma} (1 - e^2 + e^2 \cos I - \cos^2 I) \sin 2\tilde{\omega} \quad (23)$$

$$\delta_1 \Omega_p = \frac{15(\mu_M n_M^2 + \mu_\square n_\square^2) e^2 \cos I}{16 n \dot{\omega}_{\text{sec}} \gamma} \sin 2\tilde{\omega} \quad (24)$$

$$\delta_1 \lambda_p = \frac{15(\mu_M n_M^2 + \mu_\square n_\square^2)}{32 n \dot{\omega}_{\text{sec}} \gamma} [2\gamma^2 + 2e^2 \cos I - 2\cos^2 I - (1 + e^2)\gamma \sin^2 I] \sin 2\tilde{\omega} \quad (25)$$

The numerator in these perturbations is of the order of 10^{-5} and will overcome the value of the denominator. The resulting amplitudes of long period perturbations due to the Moon and Sun are given in Table 2.

Table 2 – Amplitudes and Period of Luni-Solar Long Period PO perturbations

Element	Amplitude (rd)	Period (days)
Eccentricity	4.40×10^{-4}	11 352
Inclination	1.90×10^{-6}	11 352
Longitude of perigee	7.38×10^{-2}	11 352
Longitude of ascending node	2.12×10^{-4}	11 352
Mean longitude	3.69×10^{-2}	11 352

Influence of Luni-Solar Perturbations on Secular Rates due to the Earth Gravity Field

The task is to take into consideration the influence of the third body on the secular rates resulting from the Earth potential field. Taking into account variational equations, the second order perturbations in secular rates are obtained from

$$\frac{d}{dt}(\delta_2 \tilde{\omega}_{\text{sec}}) = \frac{\partial \dot{\tilde{\omega}}_{\text{sec}}}{\partial e} \delta_1 e_{\ell p} + \frac{\partial \dot{\tilde{\omega}}_{\text{sec}}}{\partial I} \delta_1 I_{\ell p} \quad (26)$$

$$\frac{d}{dt}(\delta_2 \Omega_{\text{sec}}) = \frac{\partial \dot{\Omega}_{\text{sec}}}{\partial e} \delta_1 e_{\ell p} + \frac{\partial \dot{\Omega}_{\text{sec}}}{\partial I} \delta_1 I_{\ell p} \quad (27)$$

$$\frac{d}{dt}(\delta_2 \lambda_{\text{sec}}) = \frac{\partial \dot{\lambda}_{\text{sec}}}{\partial e} \delta_1 e_{\ell p} + \frac{\partial \dot{\lambda}_{\text{sec}}}{\partial I} \delta_1 I_{\ell p} \quad (28)$$

where $\delta_1 e_{\ell p}$, $\delta_1 I_{\ell p}$ are perturbations due to a third body while $\delta_2 \tilde{\omega}_{\text{sec}}$, $\delta_2 \Omega_{\text{sec}}$, $\delta_2 \lambda_{\text{sec}}$ are clearly second order perturbations on secular motions induced by the geopotential. We initially consider just third body long period perturbations. In order to do this we consider the above variational equations where the secular variations on the right hand side are given by Eqs. (11), (12) and (13)

By considering the major terms already computed for the above quantities, we find from Eqs. 86 to 88 the following partials

$$\begin{aligned} \frac{\partial}{\partial e} \dot{\omega}_{\text{sec}} &= \frac{3nC_{20}b^2e}{\gamma^6 a^2} (1 + 2\cos I - 5\cos^2 I) + \\ &+ \frac{3e(\mu_M n_M^2 + \mu_{\square} n_{\square}^2)}{8n\gamma^3} [5\cos^2 I + (3e^2 - 8)\cos I + \gamma^2] \end{aligned} \quad (29)$$

$$\begin{aligned} \frac{\partial}{\partial I} \dot{\omega}_{\text{sec}} &= \frac{3nC_{20}b^2}{4\gamma^4 a^2} (2\sin I + 5\sin 2I) + \\ &+ \frac{3(\mu_M n_M^2 + \mu_{\square} n_{\square}^2)}{8n\gamma} [-5\sin 2I + (3e^2 + 2)\sin I] \end{aligned} \quad (30)$$

$$\frac{\partial}{\partial e} \dot{\Omega}_{\text{sec}} = \frac{6nC_{20}b^2e}{\gamma^6 a^2} \cos I - \frac{3(\mu_M n_M^2 + \mu_{\square} n_{\square}^2)e \cos I}{8n\gamma^3} (9e^2 - 4) \quad (31)$$

$$\frac{\partial}{\partial I} \dot{\Omega}_{\text{sec}} = -\frac{3nC_{20}b^2}{2\gamma^4 a^2} \sin I + \frac{3(\mu_M n_M^2 + \mu_{\square} n_{\square}^2) \sin I}{8n\gamma} (3e^2 + 2) \quad (32)$$

$$\begin{aligned} \frac{\partial \dot{\lambda}_{\text{sec}}}{\partial I} &= \frac{3nC_{20}b^2}{4\gamma^4 a^2} [(3\gamma - 5)\sin 2I - 2\sin I] + \\ &+ \frac{\mu_M n_M^2 + \mu_{\square} n_{\square}^2}{16n\gamma} \times [33(10 - \gamma e^2 - 9\gamma^2)\sin 2I + 6(3e^2 + 2)\sin I] \end{aligned} \quad (33)$$

$$\begin{aligned} \frac{\partial \dot{\lambda}_{\text{sec}}}{\partial e} &= \frac{3nC_{20}b^2e}{4\gamma^6 a^2} [(-9\gamma + 20)\cos^2 I + 8\cos I - (4 + 5\gamma)] + \frac{(\mu_M n_M^2 + \mu_{\square} n_{\square}^2)e}{16n\gamma^3} \times \\ &\times [3(10 + 8\gamma^2 - e\gamma^2 + e^2\gamma)\cos^2 I - 6(3e^2 + 6\gamma^2 + 2)\cos I + 6\gamma^2(1 - 3\gamma)] \end{aligned} \quad (34)$$

The amplitudes of these differentials are given in Table 3.

Table 3 – Amplitude (rd/day) of Coefficients for Variational Equations 26 through 28

Coefficients	$\dot{\omega}_{\text{sec}}$	$\dot{\Omega}_{\text{sec}}$	$\dot{\lambda}_{\text{sec}}$
$\partial/\partial e$	-6.67×10^{-6}	-1.63×10^{-5}	5.71×10^{-7}
$\partial/\partial I$	-3.85×10^{-3}	-9.10×10^{-4}	4.00×10^{-3}

Recalling Equations (26), (27) and (28), we find the influence of long period perturbations due to the Moon and Sun on the secular rates due to the Earth gravity field

$$\begin{aligned} \frac{d}{dt} (\delta_2 \dot{\omega}_{\text{sec}}) &= -\frac{15(\mu_M n_M^2 + \mu_{\square} n_{\square}^2)e \sin I}{16n\gamma \dot{\omega}_{\text{sec}}} \times \\ &\times \left\{ \frac{\partial \dot{\omega}_{\text{sec}}}{\partial e} (1 - e^2) \sin I + \frac{\partial \dot{\omega}_{\text{sec}}}{\partial I} e \cos I \right\} \cos 2\tilde{\omega} \end{aligned} \quad (35)$$

$$\begin{aligned} \frac{d}{dt} (\delta_2 \dot{\Omega}_{\text{sec}}) &= -\frac{15(\mu_M n_M^2 + \mu_{\square} n_{\square}^2)e}{16n\gamma \dot{\omega}_{\text{sec}}} \times \\ &\times \left\{ \frac{\partial \dot{\Omega}_{\text{sec}}}{\partial e} (1 - e^2) \sin I + \frac{\partial \dot{\Omega}_{\text{sec}}}{\partial I} e \cos I \right\} \cos 2\tilde{\omega} \end{aligned} \quad (36)$$

$$\frac{d}{dt}(\delta_2 \dot{\lambda}_{\text{sec}}) = \frac{15(\mu_M n_M^2 + \mu_{\square} n_{\square}^2) e \sin I}{16n \dot{\omega}_{\text{sec}}} \left\{ -\frac{\partial \dot{\lambda}_{\text{sec}}}{\partial e} \gamma \sin I - \frac{\partial \dot{\lambda}_{\text{sec}}}{\partial I} e \cos I \right\} \cos 2\tilde{\omega} \quad (37)$$

Integration of these equations may be performed by keeping constant all metric elements since they are not affected by secular perturbations. The result is given as follows:

$$\delta_2 \dot{\omega}_{\text{sec}} = -\frac{15(\mu_M n_M^2 + \mu_{\square} n_{\square}^2) e \sin I}{32n\gamma \dot{\omega}_{\text{sec}}^2} \left\{ \frac{\partial \dot{\omega}_{\text{sec}}}{\partial e} (1-e^2) \sin I + \frac{\partial \dot{\omega}_{\text{sec}}}{\partial I} e \cos I \right\} \sin 2\tilde{\omega} \quad (38)$$

$$\delta_2 \dot{\Omega}_{\text{sec}} = -\frac{15(\mu_M n_M^2 + \mu_{\square} n_{\square}^2)}{32n\gamma \dot{\omega}_{\text{sec}}^2} \left\{ \frac{\partial \dot{\Omega}_{\text{sec}}}{\partial e} (1-e^2) \sin I + \frac{\partial \dot{\Omega}_{\text{sec}}}{\partial I} e \cos I \right\} \sin 2\tilde{\omega} \quad (39)$$

$$\delta_2 \dot{\lambda}_{\text{sec}} = -\frac{15(\mu_M n_M^2 + \mu_{\square} n_{\square}^2) \sin I}{32n \dot{\omega}_{\text{sec}}^2} \left\{ \frac{\partial \dot{\lambda}_{\text{sec}}}{\partial e} \gamma \sin I + \frac{\partial \dot{\lambda}_{\text{sec}}}{\partial I} e \cos I \right\} \sin 2\tilde{\omega} \quad (40)$$

Equations (38), (39), (40) give the major coupling between the secular rates due to the Earth flattening and the long term influence of the Moon and Sun.

Perturbations of secular rates due to luni-solar long period perturbations are given in Table 4.

Table 4 – Luni-Solar Long Period Perturbations on Secular Rates due to Earth (C₂₀)

Secular rate	Amplitude (rd/day)	Period (days)	Amplitude over the period (degrees)
$\delta_2 \dot{\omega}_{\text{sec}}$	1.99×10^{-8}	11 352	1.29×10^{-2}
$\delta_2 \dot{\Omega}_{\text{sec}}$	4.07×10^{-7}	11 352	2.65×10^{-1}
$\delta_2 \dot{\lambda}_{\text{sec}}$	-2.90×10^{-6}	11 352	-1.66×10^{-4}

Equations (38), (39), (40) give the major coupling between the secular rates due to the Earth flattening and the long term influence of the Moon and Sun. The period of these perturbations relates to the secular rate of the longitude of perigee, given by

$$\begin{aligned} \dot{\omega}_{\text{sec}} = & \frac{3nC_{20}b^2}{4\gamma^4 a^2} (1 + 2\cos I - 5\cos^2 I) + \\ & + \frac{3(\mu_M n_M^2 + \mu_{\square} n_{\square}^2)}{8n\gamma} [5\cos^2 I - (3e^2 + 2)\cos I - (1 - e^2)] \end{aligned} \quad (41)$$

We may consider a good approximation to set the eccentricity equal to zero, so that

$$\dot{\omega}_{\text{sec}} = \frac{3nC_{20}b^2}{4a^2} (1 + 2\cos I - 5\cos^2 I) + \frac{3(\mu_M n_M^2 + \mu_{\square} n_{\square}^2)}{8n} (5\cos^2 I - 2\cos I - 1) \quad (42)$$

For the Moon and Sun we have used the values given by Eqs. (1) and (2).

$$\begin{aligned} \mu_M n_M^2 &= 1.59 \times 10^{-5} \text{ rev}^2 \text{ day}^{-2} = 6.2707 \times 10^{-4} \text{ rd}^2 \text{ day}^{-2} \\ \mu_{\square} n_{\square}^2 &= 0.75 \times 15^{-5} \text{ rev}^2 \text{ day}^{-2} = 2.9579 \times 10^{-4} \text{ rd}^2 \text{ day}^{-2} \end{aligned} \quad (43)$$

Discussion

As given by Schutz and Giacaglia (2009) the evolution of the longitude of the perigee and of the longitude of the ascending node, over a decade, of a selected GP satellite are shown in the Fig. 1 and Fig. 2, respectively, while long terms variations in eccentricity and inclination are given in Fig. 3 and Fig.4.

PRN03: 1996 - June 2008

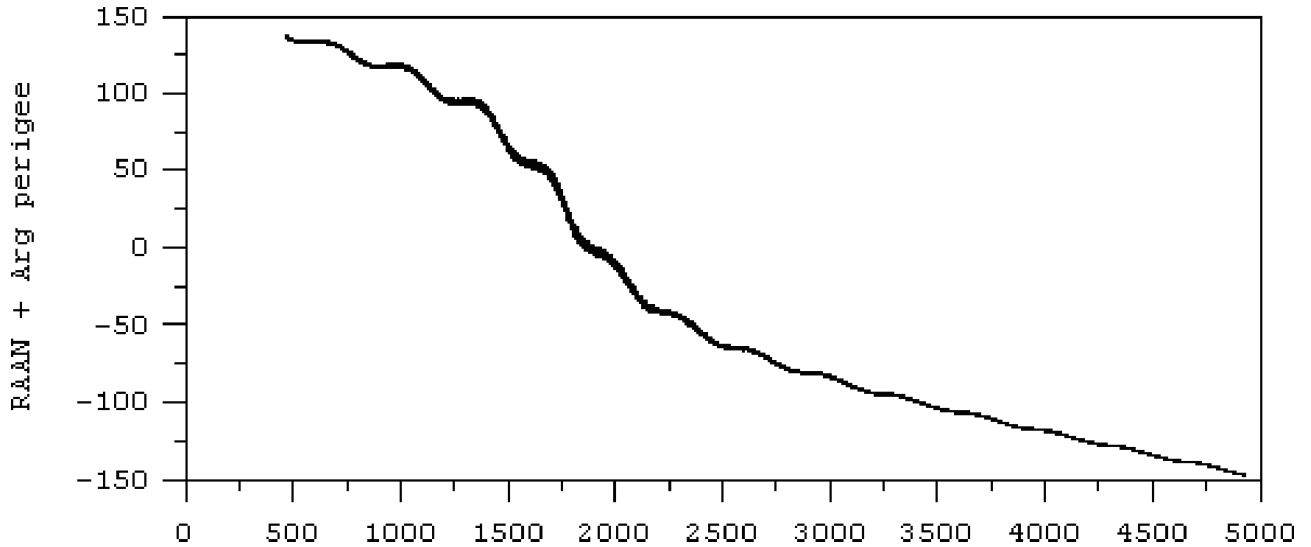


Figure 1 – Long Term Evolution of Longitude of Perigee (Schutz and Giacaglia, 2009)

We can observe three basic periods in the eccentricity (a period of about 365 days or 0.986 degree/day, a period of 27 days or 13.3 degree per day and a very long period) and three basic periods in the inclination (a periods of about 180 days or 2.0 degree/day, a period of 14 days or 25.7 degree/day and a very long period). The long periods are not well defined but, in any event, they are at least 10,000 days. This periods agree very closely with the periods obtained from observations, as seen in Fig. 1 through Fig. 4.

PRN03: 1996 - June 2008

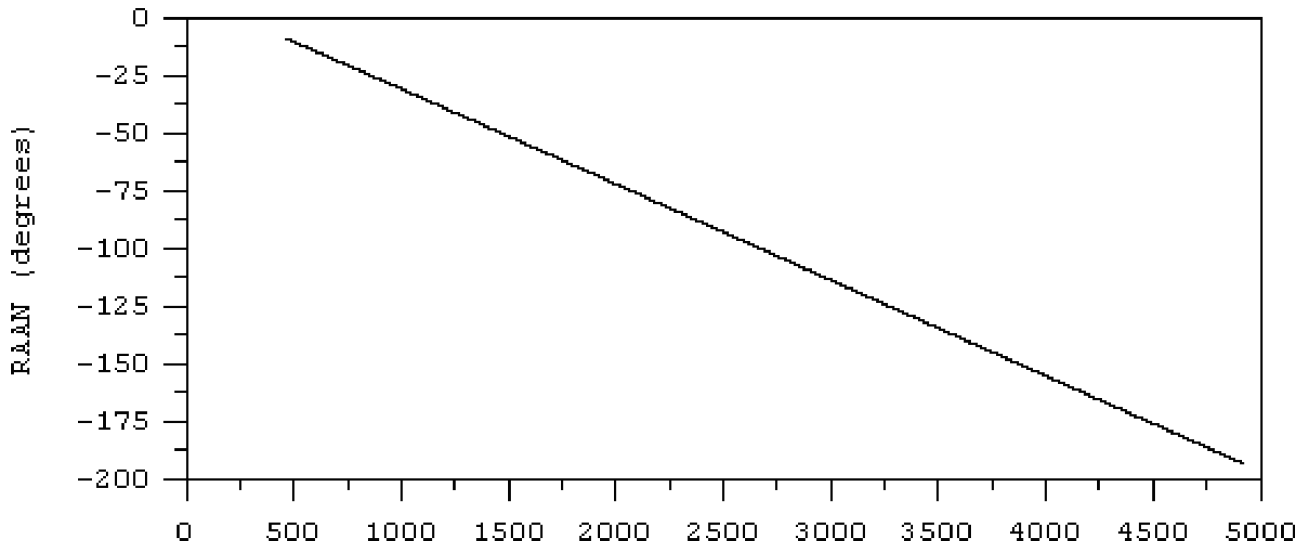


Figure 2 – Long Term Evolution of Longitude of Ascending Node (Schutz and Giacaglia, 2009)

The possible frequencies due to earth oblateness, lunar and solar perturbations, setting $\ell = 2$, are given by Eq. (41)

$$f_{\ell m p p' m' q' p'' q''}^{\pm} = (\ell - 2p) \dot{\omega}_{\text{sec}} + (m - \ell + 2p) \dot{\Omega}_{\text{sec}} \pm (\ell - 2p') \dot{\omega}_M \pm (\ell - 2p' + q') \dot{M}_M \pm m' \dot{\Omega}_M \pm (\ell - 2p'') \dot{\omega}_{\square} \pm (\ell - 2p'' + q'') \dot{M}_{\square} \quad (41)$$

Analytical results obtained in previous sections show that the dominant terms in long period perturbations are due to the longitude of perigee, corresponding to $\ell = 2, p = 0$, all other integers considered equal to zero.

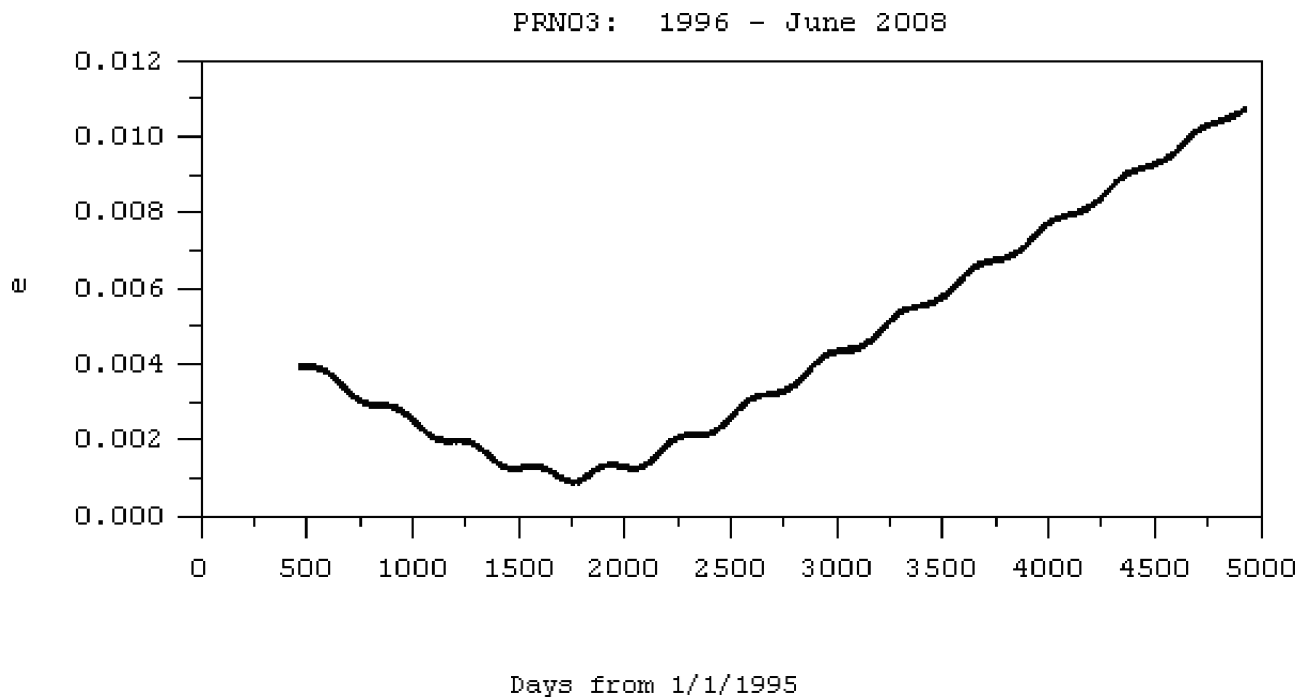


Figure 3 – Long Term Evolution of Eccentricity (Schutz and Giacaglia, 2009)

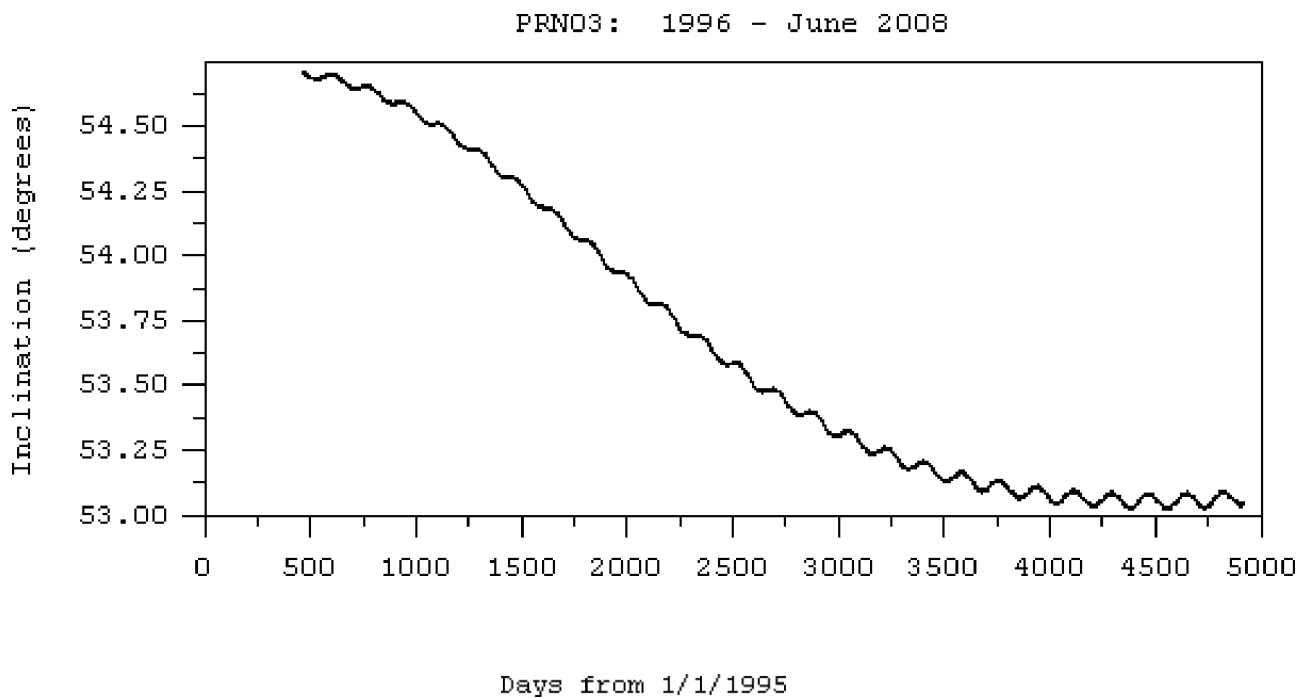


Figure 4 – Long Term Evolution of Inclination (Schutz and Giacaglia, 2009)

Conclusions

Despite the fact that no resonances have been assumed in the development of the theory, the periods for the evolution of the satellite elements are in good agreement with the observed behavior in the motion of satellites with small eccentricity, which is the case of GPS satellites

ACKNOWLEDGMENTS

The first author is grateful to FAPESP, The Sao Paulo Research Foundation, for providing a visiting researcher scholarship at the National Institute for Space Research – INPE, during the year of 2009 and to CNPq, The Brazilian

National Council for Research, for providing a Visiting Specialist Scholarship at INPE during the first quarter of 2010. Continuous support from the University of Taubaté is gratefully acknowledged.

REFERENCES

Giacaglia, G. E. O. and Prado, A. F. B. A. (2003) "Third Body Perturbations on Satellites", INPE, São José dos Campos, SP, Brazil, ISBN85-17-00010-2

Giacaglia, G. E.O. (1975). The Equations of motion of an Artificial Satellite in Non Singular Variables. AMRL Report Number 1072, UT Austin

Giacaglia, G. E.O. and Schutz, B. E. (2008 b). Third body perturbations on satellite orbits with small eccentricity, Symposium Honoring Byron Tapley's 50 Years of Contributions to Aerospace Education, Research and Service, Austin, Texas, February 2008

Giacaglia, G.E.O. and Schutz, B. E. (2008 a). Small eccentricity satellite orbits: Linear perturbations, Advances in the Astronautical Sciences, Vol. 130, pp. 1557-1569, Univelt Publishing, San Diego.

Giacaglia, G.E.O. and Schutz, B. E. (2009). A non singular approach in Satellite Theory, Advances in the Astronautical Sciences, Vol. 134, pp. 585-600, Univelt Publishing, San Diego.

Kaula, W. M. (1961). Development of the lunar and solar disturbing functions for a close satellite. Astron. Journ., vol. 67, p. 300.

Kolmogorov, A. N. (1953) "On the Conservation of Quasiperiodic Motions for a Small Change in the Hamiltonian Function", Dokl. Akad. Nauk USSR, 98, 527-530.

Poincaré, H. (1898) "Les Méthodes Nouvelles de la Mécanique Céleste" (vol. 2) Gauthier-Villars, Paris (Dover Reprint, New York, 1957).

Prado, A. F. B. A. (2003) Third-Body Perturbation in Orbits around natural satellites, J. Guidance, Control and Dynamics, V. 25, N. 1

Schutz, B. and Giacaglia, G.E.O. (2009). Decade-Scale GPS Orbit Evolution and Third Body Perturbations. Paper 092407, AIAA/AAS Astrodynamics Specialist Conference, Honolulu.

Solórzano, C.R.H., Prado, A. F. B. A. (2004) Third-Body Perturbation using a Single Averaged Model, Advances In Space Dynamics 4: Celestial Mechanics and Astronautics, H. K. Kuga, Editor, Instituto Nacional de Pesquisas Espaciais – INPE, São José dos Campos, SP, Brazil.

Van de Graff, R. C. (1977), A semi-analytic Method for computing Third-body effects on Earth's and Lunar Satellite orbits. Delft Univ. of Technology, Dept. of Aerospace Eng., Report LR-231

RESPONSIBILITY NOTICE

The authors are the only responsible for the printed material included in this paper.

Modeling and Experiments of a Two-link Flexible Manipulator

Jorge A. B. Gripp¹, Fábio L. M. Santos¹, Clayton Rodrigues Bernardo¹, and Luiz Carlos S. Góes¹

¹ ITA - Instituto Tecnológico de Aeronáutica, Divisão de Engenharia Mecânica-Aeronáutica.
Praça Mal. Eduardo Gomes, n. 50, Vila das Acácias. 122280-900 – São José dos Campos, SP, Brasil

Abstract: Flexible manipulator systems exhibit many advantages over their traditional (rigid arm) counterparts. However, they have not been favored in production industries due to the obvious disadvantages in modeling and controlling the manipulator. This paper presents theoretical modeling and experiments of a two-link flexible manipulator driven by two brushless DC motors. The joint motion between the two links is separated into two inertias, each of them clamped in one link, in contrast to the conventional modeling that considers only one inertia fixed in the previous link. A finite dimensional model is derived using assumed modes method. It is considered the first and second vibration modes of each flexible link. Explicit equations of motion are derived using the Lagrangian approach. Effectors and sensors are also modeled. Afterwards experimental data is obtained through a setup with a dSPACE Hardware and Software, together with MATLAB - Simulink. Non-parametric system identification is performed by plotting frequency response functions using the experimental data.

Keywords: modeling, identification, flexible robots

INTRODUCTION

The standard assumption that robotic manipulators consist only of rigid bodies is valid only for slow motion and small interacting forces. If flexibility is not taken into account, a degradation of the overall expected performance of the robot typically occurs. Flexibility manifests itself as mechanical oscillations and static deflections, greatly complicating the motion control of a mechanical arm. If the time to settle the oscillations is significant relative to the cycle time of the overall task, flexibility will be a major consideration in the arm design (De Luca and Book, 2008).

In this paper, theoretical modeling and experiments of a two-link flexible manipulator system are presented. Experimental data is collected in order to identify a non-parametric model of the system.

The experimental apparatus is a two-link flexible manipulator driven by two brushless DC motors and monitored by tachometers, potentiometers, strain gages, and accelerometers. A pneumatic system provides a frictionless cushion of air below the manipulator that moves in the horizontal plane. Both motors are excited with chirp signals and the experimental data is obtained through a setup with dSPACE hardware and software, together with MATLAB and Simulink.

From the modeling point of view the joint motion between the two links is separated into two inertias, each of them clamped in one link, in contrast to the conventional modeling that considers only one inertia fixed in the previous link as in De Luca and Siciliano (1991) and in Lee and Lee (2002).

The assumed modes method is adopted in order to obtain a finite-dimensional model that includes additional generalized coordinates that describe the elastic deflections. The Lagrangian approach is used to derive the dynamic model of the robotic structure. Explicit equations of motion are detailed assuming two modes of vibration for each link. The effectors and sensors are also modeled in order to derive a complete and explicit model of the whole system.

Furthermore, non-parametric system identification is performed by plotting frequency response functions using the experimental data collected.

KINEMATIC MODELING

Consider a two-link flexible manipulator with rotary joints subject to bending deformation that moves on a planar surface as showed in Fig. 1. Each link is denoted by an index i , where $i = 1, 2$. Three coordinate systems are established: the inertial system (X, Y) and two moving systems (X_i, Y_i) associated to each link i . The rigid motion is described by the joint angles θ_i , while $y_i(x_i)$ denotes the transversal deflection of link i at abscissa x_i , $0 < x_i < l_i$, where l_i is the link length. The angle between the coordinates (X_2, Y_2) and (X, Y) is $\alpha_2 = \theta_1 + \theta_2 + y'_{ie}$, where $y'_{ie} = (\partial y_i / \partial x_i)|_{x_i=l_i}$ and we consider the approximation $\arctan y'_{ie} = y'_{ie}$.

Vector $\mathbf{p}_i = [x \quad y]^T$ is the absolute position of a point along the link i with respect to coordinates (X, Y) , ${}^i\mathbf{p}_i = [x_i \quad y_i]^T$ represents a point with respect to coordinates (X_i, Y_i) , $\mathbf{p}_{ie} = [l_i \quad y_{ie}]^T$ represents the position of the end of link i with respect to coordinates (X, Y) .

The position of a point on link 1 is denoted in Eq. (1) and the position of a point on link 2 is denoted in Eq. (2).

$$\mathbf{p}_1 = \mathbf{R}_1^1 \mathbf{p}_1 \quad (1)$$

$$\mathbf{p}_2 = \mathbf{p}_{1e} + \mathbf{R}_2^2 \mathbf{p}_2 \quad (2)$$

$$\mathbf{R}_i = \begin{bmatrix} c_i & -s_i \\ s_i & c_i \end{bmatrix} \quad (3)$$

Where $y_{ie} = y_i(l_i)$, $y_i = y_i(x_i)$, $s_1 = \sin \theta_1$, $s_2 = \sin \alpha_2$, $c_1 = \cos \theta_1$, and $c_2 = \cos \alpha_2$.

From Eq. (1)-(3) is possible to derive the square of velocities denoted in Eq. (4)-(7). It was considered the approximations $x_i \gg y_i$ and $l_i \gg y_{ie}$ in Eq. (4)-(7) because the bending deformations are much smaller than the link length, i.e. second-order terms involving products of deformations were neglected.

$$\dot{\mathbf{p}}_1^T \dot{\mathbf{p}}_1 = (x_1 \dot{\theta}_1 + \dot{y}_1)^2 \quad (4)$$

$$\dot{\mathbf{p}}_{1e}^T \dot{\mathbf{p}}_{1e} = (l_1 \dot{\theta}_1 + \dot{y}_{1e})^2 \quad (5)$$

$$\dot{\mathbf{p}}_2^T \dot{\mathbf{p}}_2 = (l_1 \dot{\theta}_1 + \dot{y}_{1e})^2 + (x_2 \dot{\alpha}_2 + \dot{y}_2)^2 + 2[(l_1 \dot{\theta}_1 + \dot{y}_{1e})(x_2 \dot{\alpha}_2 + \dot{y}_2) \cos(\theta_1 - \alpha_2)] \quad (6)$$

$$\dot{\mathbf{p}}_{2e}^T \dot{\mathbf{p}}_{2e} = \{(l_1 \dot{\theta}_1 + \dot{y}_{1e})^2 + (l_2 \dot{\alpha}_2 + \dot{y}_{2e})^2 + 2[(l_1 \dot{\theta}_1 + \dot{y}_{1e})(l_2 \dot{\alpha}_2 + \dot{y}_{2e}) \cos(\theta_1 - \alpha_2)]\} \quad (7)$$

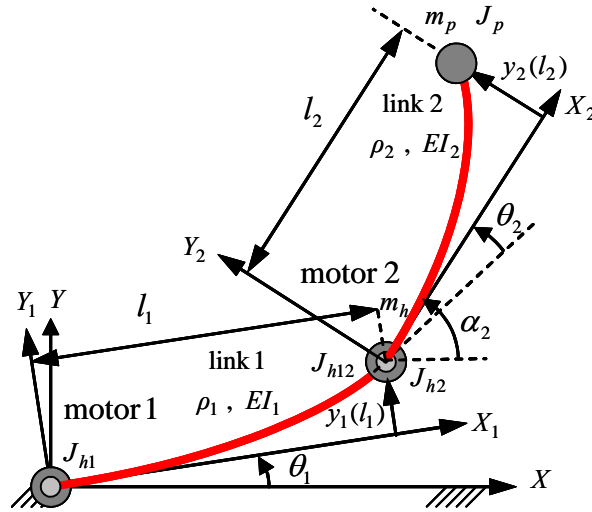


Figure 1 – Diagram the two-link flexible manipulator

LAGRANGIAN MODELING

Lagrangian mechanics is a re-formulation of classical mechanics that uses conservation of energy. In Lagrangian mechanics, the equations of motion of a system of particles are derived by solving the Lagrange equations. The kinetic energy T and potential energy U are computed to calculate the Lagrangian $L = T - U$.

The kinetic energy of the two-link flexible manipulator in Fig. 1 the sum of the following contributions:

$$T = T_b + T_h + T_p + \sum_{i=1}^2 T_i \quad (8)$$

The kinetic rotational energy of the rigid body of moment of inertia J_{h1} located at the basis is:

$$T_b = \frac{1}{2} J_{h1} \dot{\theta}_1^2 \quad (9)$$

The kinetic energy of the rigid bodies located between the links in Eq. (10) depends on the moment of inertia of the body clamped at the first link J_{h12} , the body clamped at the second link J_{h2} and the sum of the bodies mass m_h .

$$T_h = \frac{1}{2} m_h (\dot{\mathbf{p}}_{1e}^T \dot{\mathbf{p}}_{1e}) + \frac{1}{2} J_{h12} (\dot{\theta}_1 + \dot{y}'_{1e})^2 + \frac{1}{2} J_{h2} \dot{\alpha}_2^2 \quad (10)$$

Where $\dot{y}'_{ie} = \frac{d}{dt} \left(\left(\partial y_i / \partial x_i \right) \Big|_{x_i=l_i} \right)$. The kinetic energy of the payload m_p at the tip of second link is:

$$T_p = \frac{1}{2} m_p (\dot{\mathbf{p}}_{2e}^T \dot{\mathbf{p}}_{2e}) + \frac{1}{2} J_p (\dot{\alpha}_2 + \dot{y}'_{2e})^2 \quad (11)$$

The kinetic energy of the flexible link i with linear density ρ_i is:

$$T_i = \frac{1}{2} \int_0^{l_i} \rho_i (\dot{\mathbf{p}}_i^T \dot{\mathbf{p}}_i) dx_i \quad (12)$$

The potential energy of the system is due to the elastic potential of each flexible link i with elastic modulus E and second moment of area density I_i . No gravitational potential energy is considered because the system moves on the horizontal plane.

$$V = \sum_{i=1}^2 \frac{1}{2} \int_0^{l_i} EI_i \left(\frac{\partial^2 y_i(x_i, t)}{\partial x_i^2} \right)^2 dx_i \quad (13)$$

The assumed modes method is adopted in order to obtain a finite-dimensional model that includes additional generalized coordinates that describe the elastic deflections $y_i(x_i, t)$. The deflection is separate in time and space in Eq. (14).

$$y_i(x_i, t) = \sum_{j=1}^n \phi_{ij}(x_i) \delta_{ij}(t) \quad (14)$$

In this paper we consider the first two modes, i.e. $n=2$. Defining $\mathbf{\Phi}_1 = [\phi_{11}, \phi_{12}]^T$, $\mathbf{\Phi}_2 = [\phi_{21}, \phi_{22}]^T$, $\mathbf{g}_1 = [\delta_{11}, \delta_{12}]^T$, and $\mathbf{g}_2 = [\delta_{21}, \delta_{22}]^T$, Eq. (14) becomes Eq. (15). The shape equations ϕ_{11} , ϕ_{12} , ϕ_{21} , and ϕ_{22} are calculated in Appendix.

$$y_i(x_i, t) = \mathbf{\Phi}_i^T(x_i) \mathbf{g}_i(t) \quad (15)$$

The Lagrangian in Eq. (16) is derived from Eq. (4)-(13) and (15).

$$\begin{aligned} L = & \frac{1}{2} m_h (l_1 \dot{\theta}_1 + \mathbf{\Phi}_{1e}^T \dot{\mathbf{g}}_1)^2 + \frac{1}{2} m_p \left[(l_2 \dot{\theta}_1 + \mathbf{\Phi}_{1e}^T \dot{\mathbf{g}}_1)^2 + (l_2 \dot{\alpha}_2 + \mathbf{\Phi}_2^T \dot{\mathbf{g}}_2)^2 \right] \\ & + m_p (l_1 \dot{\theta}_1 + \mathbf{\Phi}_{1e}^T \dot{\mathbf{g}}_1) (l_2 \dot{\alpha}_2 + \mathbf{\Phi}_2^T \dot{\mathbf{g}}_2) \cos(\theta_1 - \alpha_2) + \frac{1}{2} J_{h1} \dot{\theta}_1^2 + \frac{1}{2} J_{h12} (\dot{\theta}_1 + \mathbf{\Phi}_{1e}^T \dot{\mathbf{g}}_1)^2 \\ & + \frac{1}{2} J_{h2} \dot{\alpha}_2^2 + \frac{1}{2} J_p (\dot{\alpha}_2 + \mathbf{\Phi}_2^T \dot{\mathbf{g}}_2)^2 + \frac{1}{2} \int_0^{l_1} \rho_1 (x_1 \dot{\theta}_1 + \mathbf{\Phi}_1^T \dot{\mathbf{g}}_1)^2 dx_1 + \frac{m_2}{2} (l_1 \dot{\theta}_1 + \mathbf{\Phi}_{1e}^T \dot{\mathbf{g}}_1)^2 \\ & + \frac{1}{2} \int_0^{l_2} \rho_2 (x_2 \dot{\alpha}_2 + \mathbf{\Phi}_2^T \dot{\mathbf{g}}_2)^2 dx_2 + (l_1 \dot{\theta}_1 + \mathbf{\Phi}_{1e}^T \dot{\mathbf{g}}_1) \cos(\theta_1 - \alpha_2) \int_0^{l_2} \rho_2 (x_2 \dot{\alpha}_2 + \mathbf{\Phi}_2^T \dot{\mathbf{g}}_2) dx_2 \\ & - \frac{1}{2} \int_0^{l_1} EI_1 \left(\frac{\partial^2 \mathbf{\Phi}_1^T}{\partial x_1^2} \mathbf{g}_1 \right)^2 dx_1 - \frac{1}{2} \int_0^{l_2} EI_2 \left(\frac{\partial^2 \mathbf{\Phi}_2^T}{\partial x_2^2} \mathbf{g}_2 \right)^2 dx_2 \end{aligned} \quad (16)$$

Where $m_2 = \int_0^{l_2} \rho_2 dx_2$, $\mathbf{\Phi}_i = \mathbf{\Phi}_i(x_1)$, $\mathbf{\Phi}_{ie} = \mathbf{\Phi}_i(l_1)$, $\mathbf{\Phi}'_{ie} = \frac{d}{dt} \left(\left(\partial \mathbf{\Phi}_i / \partial x_i \right) \Big|_{x_i=l_i} \right)$.

Equation (18) is the Lagrange equation or Euler-Lagrange equation, where the Lagrangian L is a function of a vector of generalized coordinates $\mathbf{q} = [\theta_1 \ \theta_2 \ \mathbf{g}_1^T \ \mathbf{g}_2^T]^T = [\theta_1 \ \theta_2 \ \delta_{11} \ \delta_{12} \ \delta_{21} \ \delta_{22}]^T$.

$$\frac{d}{dt} \left(\frac{\partial L}{\partial \dot{\mathbf{q}}} \right)^T - \left(\frac{\partial L}{\partial \mathbf{q}} \right)^T = \mathbf{f} \quad (17)$$

Where $\mathbf{f} = [\tau_1 \ \tau_2 \ 0 \ 0 \ 0 \ 0]^T$ is the vector of generalized forces on the system.

As result of the Lagrangian approach, Eq. (16)-(17) derives the equations of motion:

$$\mathbf{M}(\mathbf{q})\ddot{\mathbf{q}} + \mathbf{h}(\mathbf{q}, \dot{\mathbf{q}}) + \mathbf{K}\mathbf{q} = \mathbf{f} \quad (18)$$

Where \mathbf{M} is the inertia matrix, \mathbf{h} is the Coriolis vector and centrifugal forces and \mathbf{K} is the stiffness matrix.

EFFECTORS AND SENSORS MODELING

The generalized forces vector \mathbf{f} presented at Eq. (17) is a function of the actuator torque in the joint of the basis τ_1 and in the joint between the two links τ_2 . Each effector is a DC electric motor as showed in Fig. 2. Sensor modeling intends to present \mathbf{f} as a function the input vector $\mathbf{u} = [e_1 \ e_2]^T$.

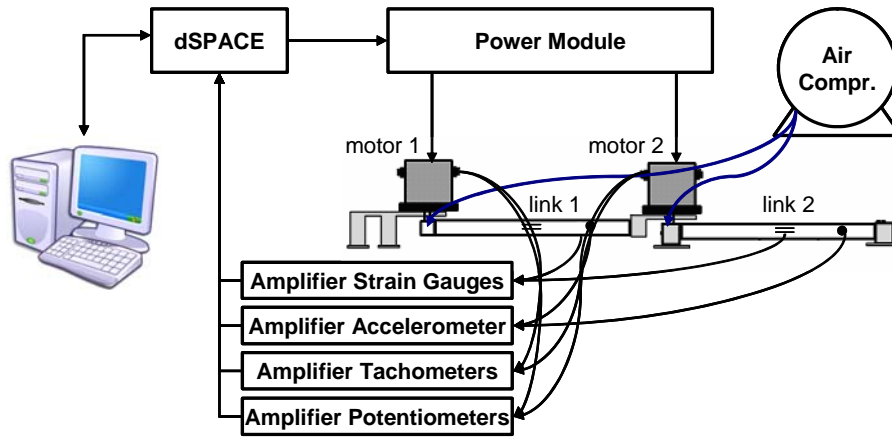


Figure 2 – Experimental Setup

The modeling of a DC motor is given by Eq. (19), where e_i is the armature voltage, i_{ai} is the armature current, R_a is the armature resistance, L_a is the armature inductance, k_b is the counter-electromotive force constant, $\dot{\theta}_i$ is the motor angular velocity. The part regarding the inductance L_a in Eq. (22) is not taken into account because is much smaller than R_a portion:

$$e_a = R_a i_{ai} + L_a \frac{di_{ai}}{dt} + k_b \dot{\theta}_i \quad (19)$$

The torque generated by the DC motor τ_m is proportional to i_{ai} , where k_t is the motor torque constant:

$$\tau_m = k_t i_{ai} \quad (20)$$

The resulting torque τ_i is computed excluding part of τ_m dispelled by friction, where c_v is the friction constant:

$$\tau_i = \tau_m - c_v \dot{\theta}_m \quad (21)$$

From Eq. (19)-(21) it is possible to define τ_i as function of e_i and $\dot{\theta}_i$, where $i = 1, 2$.

$$\tau_i = (k_t / R_a) e_i - (k_t k_b / R_a + c_v) \dot{\theta}_i \quad (22)$$

Using Eq. (22) it is possible to define \mathbf{f} as function of \mathbf{u} . Equation (18) can be rewritten as:

$$\mathbf{M}(\mathbf{q})\ddot{\mathbf{q}} + \mathbf{D}\dot{\mathbf{q}} + \mathbf{K}\mathbf{q} + \mathbf{h}(\mathbf{q}, \dot{\mathbf{q}}) = \mathbf{Q}\mathbf{u} \quad (23)$$

$$\mathbf{Q} = \frac{k_t}{R_a} \begin{bmatrix} 1 & 0 \\ 0 & 1 \\ 0 & 0 \\ 0 & 0 \\ 0 & 0 \\ 0 & 0 \end{bmatrix}, \mathbf{D} = \left(\frac{k_t k_b}{R_a} + c_v \right) \begin{bmatrix} 1 & 0 & 0 & 0 \\ 0 & 1 & 0 & 0 \\ 0 & 0 & 0 & 0 \\ 0 & 0 & 0 & 0 \\ 0 & 0 & 0 & 0 \\ 0 & 0 & 0 & 0 \end{bmatrix} \quad (24)$$

We define the state vector \mathbf{x} as in Eq. (25) and the output vector \mathbf{y} as in Eq. (26). Figure 3 shows the input vector \mathbf{u} produced by two chirp signals and the output vector \mathbf{y} .

$$\mathbf{x} = \begin{bmatrix} \mathbf{q} \\ \dot{\mathbf{q}} \end{bmatrix} = [\theta_1 \quad \theta_2 \quad \delta_{11} \quad \delta_{12} \quad \delta_{21} \quad \delta_{22} \quad \dot{\theta}_1 \quad \dot{\theta}_2 \quad \dot{\delta}_{11} \quad \dot{\delta}_{12} \quad \dot{\delta}_{22} \quad \dot{\delta}_{21}]^T \quad (25)$$

$$\mathbf{y} = [e_{ac1} \quad e_{ac2} \quad e_{sg1} \quad e_{sg2} \quad e_{tac1} \quad e_{tac2} \quad e_{pot1} \quad e_{pot2}]^T \quad (26)$$

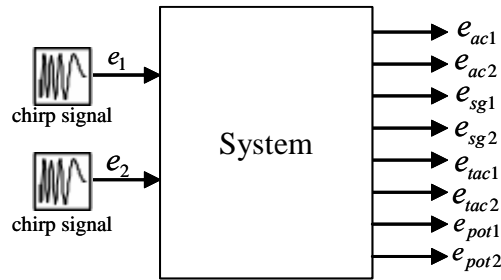


Figure 3 – Diagram representing inputs and outputs of the system

Equations (27)-(28) are the state-space representation, where \mathbf{A} is the state matrix, \mathbf{B} is the input matrix, and \mathbf{C} is the output matrix. Linearization of Eq. (23) around $\mathbf{x} = \mathbf{0}$ leads to numeric values of matrices \mathbf{A} and \mathbf{B} .

$$\dot{\mathbf{x}} = \mathbf{A}\mathbf{x} + \mathbf{B}\mathbf{u} \quad (27)$$

$$\mathbf{y} = \mathbf{C}\mathbf{x} \quad (28)$$

Output matrix \mathbf{C} is showed in Eq. (34), considering e_{aci} is the integral of the accelerometer output over time, e_{sgi} is the strain gage output, and e_{taci} is the tachometer output as in Eq. (29)-(32).

$$e_{aci} = G_{aci} (x_i \dot{\theta}_i + \dot{y}_i) \Big|_{x_i=l_{aci}} \quad (29)$$

$$e_{sgi} = G_{sgi} \left(\partial^2 y_i / \partial x_i^2 \right) \Big|_{x_i=l_{sgi}} \quad (30)$$

$$e_{taci} = G_{taci} \dot{\theta}_i \quad (31)$$

$$e_{poti} = G_{poti} \theta_i \quad (32)$$

Equations (27)-(28) derives frequency response functions $\mathbf{H}(s)$, where $s = j2\pi f$ is the complex angular frequency:

$$\mathbf{H}(s) = \mathbf{C}(s\mathbf{I} - \mathbf{A})^{-1} \mathbf{B} \quad (33)$$

Theoretical model frequency response functions $\mathbf{H}(s)$ of sensors of accelerometers, strain gages, and tachometers are presented in Fig. 4.

$$\mathbf{C}^T = \begin{bmatrix}
0 & 0 & 0 & 0 & 0 & 0 & 0 & G_{pot1} & 0 \\
0 & 0 & 0 & 0 & 0 & 0 & 0 & 0 & G_{pot2} \\
0 & 0 & G_{sg1} \left(\frac{\partial^2 \phi_{11}}{\partial x_1^2} \right) \Big|_{x_1=l_{sg1}} & 0 & 0 & 0 & 0 & 0 & 0 \\
0 & 0 & G_{sg1} \left(\frac{\partial^2 \phi_{12}}{\partial x_1^2} \right) \Big|_{x_1=l_{sg1}} & 0 & 0 & 0 & 0 & 0 & 0 \\
0 & 0 & 0 & G_{sg2} \left(\frac{\partial^2 \phi_{21}}{\partial x_2^2} \right) \Big|_{x_2=l_{sg2}} & 0 & 0 & 0 & 0 & 0 \\
0 & 0 & 0 & G_{sg2} \left(\frac{\partial^2 \phi_{22}}{\partial x_2^2} \right) \Big|_{x_2=l_{sg2}} & 0 & 0 & 0 & 0 & 0 \\
G_{ac1} l_{ac1} & 0 & 0 & 0 & 0 & G_{tac1} & 0 & 0 & 0 \\
0 & G_{ac2} l_{ac2} & 0 & 0 & 0 & 0 & G_{tac2} & 0 & 0 \\
G_{ac1} \phi_{11} \Big|_{l_{ac1}} & 0 & 0 & 0 & 0 & 0 & 0 & 0 & 0 \\
G_{ac1} \phi_{12} \Big|_{l_{ac1}} & 0 & 0 & 0 & 0 & 0 & 0 & 0 & 0 \\
0 & G_{ac2} \phi_{21} \Big|_{l_{ac2}} & 0 & 0 & 0 & 0 & 0 & 0 & 0 \\
0 & G_{ac2} \phi_{22} \Big|_{l_{ac2}} & 0 & 0 & 0 & 0 & 0 & 0 & 0
\end{bmatrix} \quad (34)$$

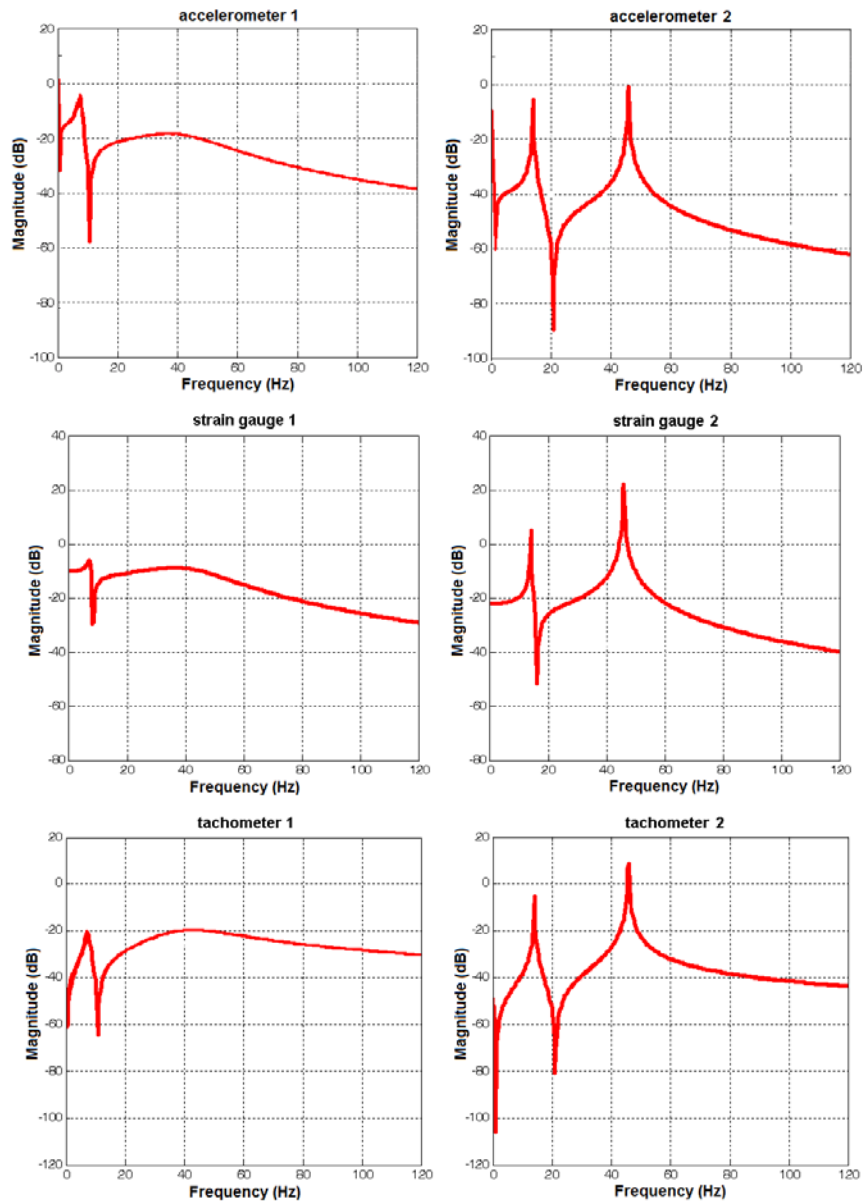


Figure 4 – Theoretical model frequency response functions of sensors

EXPERIMENTAL RESULTS

The experimental apparatus is shown in Fig. 2. The frequency range desired was 0 to 120 Hz, enough to identify the two first vibration modes. A chirp (sweep signal) from 0 to 120 Hz is applied to the motors and data is collected at 250 samples per second through a setup with dSPACE hardware and software, together with MATLAB and Simulink.

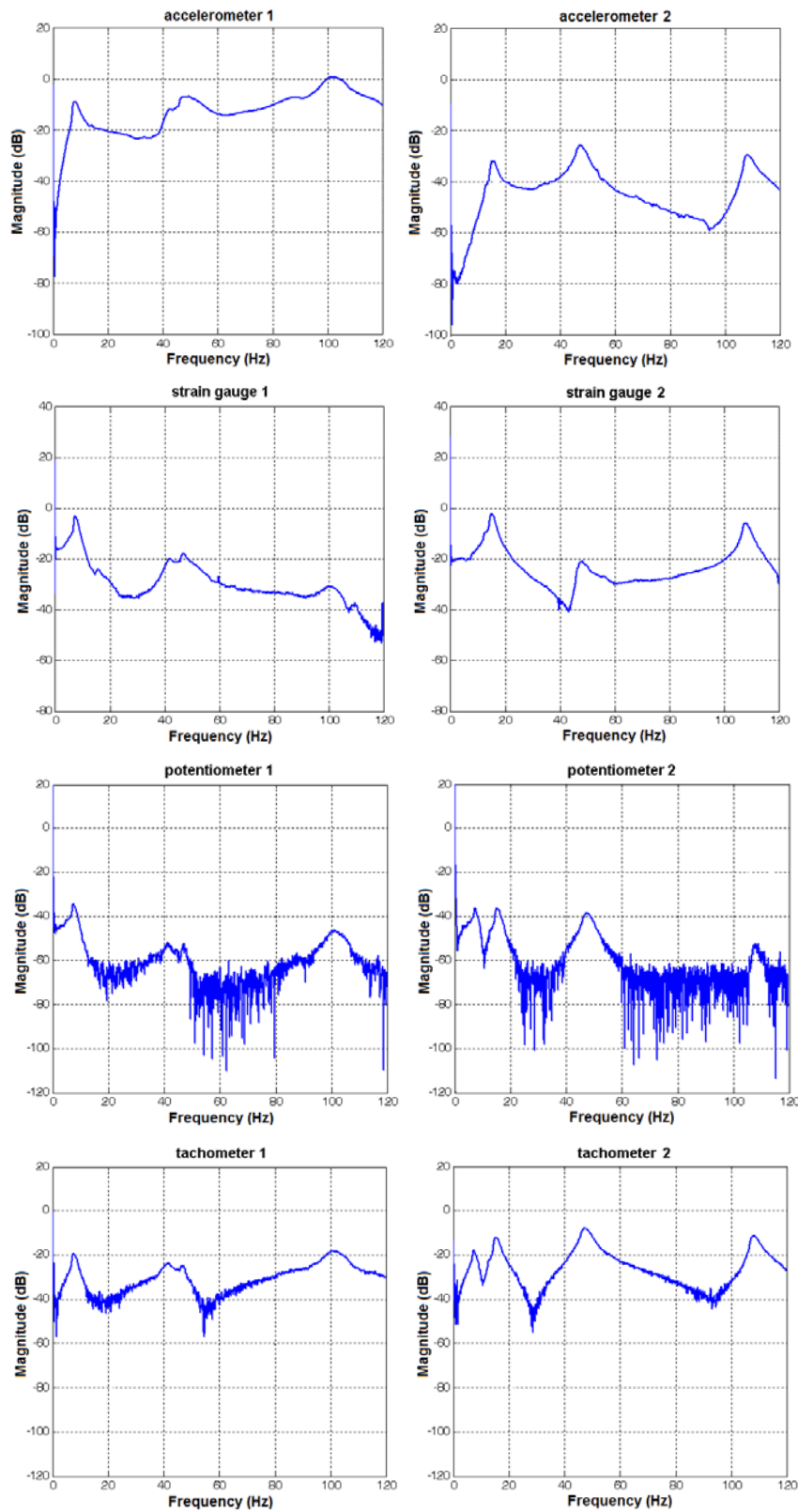


Figure 5 – Experimental frequency response functions of sensors

Welch Method is used to estimate the power spectral density as in Ljung and Glad (1994). Each collected signal was divided in 40 segments with 50% overlap to smooth the curve and a Hamming window was used. This procedure is

contained at MATLAB function “tfestimate”. Experimental frequency response functions of sensors of accelerometers, strain gages, tachometers, and potentiometers are presented in Fig. 5.

Comparing the first and second natural frequencies in Fig. 4 with those in Fig.5 shows the difference between theoretical and experimental natural frequencies is less than 10%. The measured frequency range is enough to show a third natural frequency in Fig. 5. A third natural frequency is not present at Fig. 4 because only first two modes were modeled.

CONCLUSION

This paper presented modeling and nonparametric identification of a two-link manipulator with two flexible links. Dynamic model was derived based on Lagrangian approach assuming two modes of vibration for each link. Sensors and actuator were also modeled, deriving a complete set of dynamic equations.

The rigid joint motion between the two links was separated into two inertias, in contrast to the conventional modeling that considers only one inertia fixed in the previous link.

The theoretical model and experimental results were generated. As expected, only first two natural frequencies are described by the theoretical model, i.e. the third natural frequency of the experimental curve unsurprisingly is not present at theoretical curve.

Theoretical curves successfully describe the first and second natural frequencies of the system with less than 10% of error.

Future research efforts will be devoted for parametric identification of the two-link manipulator.

ACKNOWLEDGMENTS

The authors thank CNPq (Conselho Nacional de Desenvolvimento Científico e Tecnológico) and CAPES (Coordenadoria de Aperfeiçoamento de Pessoal de Nível Superior) for promoting and supporting this research.

REFERENCES

- De Luca, A. and Book, W., 2008, “Robots with Flexible Elements”, In: Siciliano, B. and Khatib, O., “Springer Handbook of Robotics”, Springer, pp. 287-319.
- De Luca, A. and Siciliano, B., 1991, “Closed-Form Dynamic Model of Planar Multilink Lightweight Robots”, IEEE Transactions on Systems, Man and Cybernetics, v. 21, n. 4, p. 826-839.
- Junkins, J. L. and Kim, Y., 1993, “Introduction to dynamics and control of flexible structures”, AIAA, Washington, DC, 452p.
- Lee, S. and Lee, C., 2002, “Hybrid Control Scheme for Robust Tracking of Two-Link Flexible Manipulator”, Journal of Intelligent and Robotic Systems, v. 34, n. 4, p. 431-452.
- Lemos, N. A., 2004, “Mecânica Analítica”, 1. ed. São Paulo: Editora Livraria da Física. v. 1. 386 p.
- Ljung, L. and Glad, T., 1994, “Modeling Of Dynamic Systems”, Part III – Identification, Prentice Hall, c8, pp. 191-226.
- Ogata, K., 2003, “Engenharia de controle moderno”, 4 ed., S.Paulo, Pearson Prentice Hall, 788p.
- Sen, P.C, 1997, “Principles of Electric Machines and Power Electronics”, John Wiley and Sons, 2nd Edition, 640 p.

RESPONSIBILITY NOTICE

The authors are the only responsible for the printed material included in this paper.

APPENDIX

Shape equations ϕ_{ij}

The deflection is separate in time and space in Eq. (14). Each flexible link may be modeled as Euler-Bernoulli beam satisfying the equation:

$$EI_i \frac{\partial^4 y_i(x_i, t)}{\partial x_i^4} + \rho_i \frac{\partial^2 y_i(x_i, t)}{\partial t^2} = 0 \quad (\text{A.1})$$

Proper boundary conditions are imposed at the base and end of each link. The link inertia is much smaller than lumped bodies inertias, so it is reasonable to assume each link constrained at the base (De Luca and Siciliano, 1991).

$$y_i(0, t) = 0 \quad (\text{A.2})$$

$$y'_i(0, t) = 0 \quad (\text{A.3})$$

Boundary conditions at end of each link consider the balance of bending moment and shear force:

$$EI_i \frac{\partial^2 y_i(x_i, t)}{\partial x_i^2} \Big|_{x_i=l_i} = -J_{Li} \frac{d^2}{dt^2} \left(\frac{\partial y_i(x_i, t)}{\partial x_i} \Big|_{x_i=l_i} \right) - (MD)_i \frac{d^2}{dt^2} \left(y_i(x_i, t) \Big|_{x_i=l_i} \right) \quad (\text{A.4})$$

$$EI_i \frac{\partial^3 y_i(x_i, t)}{\partial x_i^3} \Big|_{x_i=l_i} = M_{Li} \frac{d^2}{dt^2} \left(y_i(x_i, t) \Big|_{x_i=l_i} \right) + (MD)_i \frac{d^2}{dt^2} \left(\frac{\partial y_i(x_i, t)}{\partial x_i} \Big|_{x_i=l_i} \right) \quad (\text{A.5})$$

Where $M_{L1} = m_2 + m_h + m_p$, $M_{L2} = m_p$, $J_{L1} = \frac{1}{3} m_2 l_2^2 + J_{h12} + J_{h2} + J_p + m_p l_2^2$, $J_{L2} = J_p$, $(MD)_2 = 0$, and $(MD)_1 = \left(\frac{1}{2} m_2 l_2 + m_p l_2 \right) \cos \theta_2 - \left[\left(\int_0^{l_2} \rho_2 \phi_{21} dx_2 + m_p \phi_{21,e} \right) \delta_{21} + \left(\int_0^{l_2} \rho_2 \phi_{22} dx_2 + m_p \phi_{22,e} \right) \delta_{21} \right] \sin \theta_2$.

Generalized coordinates $\delta_{ij}(t)$ can be redefined as:

$$\delta_{ij}(t) = \exp(j\omega_{ij}t) \quad (\text{A.6})$$

Solutions for shape equations $\phi_{ij}(x_i)$ are derived from the Euler-Bernoulli beam equation (A.1) and from (14) and (A.6):

$$\phi_{ij}(x_i) = C_{1,ij} \sin(\beta_{ij} x_i) + C_{2,ij} \cos(\beta_{ij} x_i) + C_{3,ij} \sinh(\beta_{ij} x_i) + C_{4,ij} \cosh(\beta_{ij} x_i) \quad (\text{A.7})$$

Where $\beta_{ij}^4 = \omega_{ij}^2 \rho_i / EI_i$. Applying boundary conditions eq. (A.2)-(A.3) to (A.7) leads to:

$$C_{3,ij} = -C_{1,ij} \quad (\text{A.8})$$

$$C_{4,ij} = -C_{2,ij} \quad (\text{A.9})$$

Mass boundary conditions (A.4)-(A.5) applied to (A.7) lead to an equation system (A.10).

$$\left[\mathbf{F}(\beta_{ij}) \right] \begin{bmatrix} C_{1,ij} \\ C_{2,ij} \end{bmatrix} = 0 \quad (\text{A.10})$$

Non-null solutions for $C_{1,ij}$, $C_{2,ij}$ are only possible if determinant of (2x2) matrix $\mathbf{F}(\beta_{ij})$ is null, leading to frequency equation (A.11). There are considered the first two solutions for β_{ij} .

$$\begin{aligned} & \left(1 + \cos(\beta_{ij} l_i) \cosh(\beta_{ij} l_i) \right) - \frac{M_{Li} \beta_{ij}}{\rho_i} \left(\sin(\beta_{ij} l_i) \cosh(\beta_{ij} l_i) - \cos(\beta_{ij} l_i) \sinh(\beta_{ij} l_i) \right) \\ & - \frac{J_{Li} \beta_{ij}^3}{\rho_i} \left(\sin(\beta_{ij} l_i) \cosh(\beta_{ij} l_i) + \cos(\beta_{ij} l_i) \sinh(\beta_{ij} l_i) \right) + \frac{M_{Li} J_{Li} \beta_{ij}^4}{\rho_i^2} \left(1 - \cos(\beta_{ij} l_i) \cosh(\beta_{ij} l_i) \right) = 0 \end{aligned} \quad (\text{A.11})$$

Remaining constants $C_{1,ij}$, $C_{2,ij}$ are found using Eq. (A.10) depending on a scale factor. This scale factor is chosen using a suitable normalization as in Eq. (A.12).

$$\int_0^{l_i} \rho_i \phi_{ij}^2 dx_i = m_i \quad (\text{A.12})$$

Intelligent mode shapes recognition using Fourier descriptors with application in SHM

Joseph Morlier¹, Mauricio Bergh¹, Pierre Selva² and Laurent Mevel³

¹ Université de Toulouse, ICA, ISAE DMSM, 10 avenue edouard Belin 31005 Toulouse cedex 4, France

² Medsys Air et Espace, Toulouse, France

³ INRIA, I4S, IRISA Campus de Beaulieu Rennes, France

Keywords: *vibration, modeshapes, feature recognition, classification*

INTRODUCTION

The main objective of this study is to develop an alternative criterion for modeshape classification, as the currently available one, MAC (Modal Assurance Criteria), is only a vector correlation representing modeshape similarities. This new method is developed to provide a set of features (Fourier Descriptors) for comparing modeshapes with “local” similarities of higher interest than “global” similarities. This new method uses Image Processing and Pattern Recognition tools and is validated on a simple plate under vibration. A procedure for damage detection comparing two successive states (undamaged-damaged) is also proposed.

Theoretical background

Modal analysis and MAC

Modal analysis is a process whereby one can describe a structure in terms of its natural characteristics, which are the frequency, damping and mode shapes – its dynamic properties [Ewins].

MAC provides a measure of consistency (degree of linearity) between estimates of a modal vector. This provides an additional confidence factor in the evaluation of a modal vector from different excitation (reference) locations or different modal parameter estimation algorithms. The modal assurance criterion's values go from zero, representing no consistent correspondence, to one, representing a consistent correspondence. In this manner, if the modal vectors under consideration truly exhibit a consistent, linear relationship, the modal assurance criterion should approach unity and the value of the modal scale factor can be considered reasonable. Note that, unlike the orthogonality calculations, the MAC is normalized by the magnitude of the vectors and, thus, is bounded between zero and one.

But the MAC can only indicate consistency, not validity or orthogonality. If the same errors, random or bias, exist in all modal vector estimates, this is not detected by the modal assurance criterion [Allemang].

MAC can be interpreted as the cosine of the angle between the numerical and measured eigenvectors. However, MAC index carries no explicit information on shape features. A new technique, based on the well-developed paradigms of Image Processing (IP) and Pattern Recognition (PR) are considered in this paper.

From image processing to feature extraction

IP is a set of computational techniques for analyzing, enhancing and reconstructing images. A typical PR approach involves the estimation of a series of shape attributes or features with good discriminative capability. The mapping from the space of shapes to the space of shape descriptors should determine the distance between descriptors of two models as a meaningful measure of the underlying similarity of their shapes [Nixon].

Fourier Descriptors (FD) describe a family of related image features. Generally, it refers to the use of a Fourier Transform to analyze a closed planar curve. FDs were originally proposed in 1960 by Cosgriff [Cosgriff], and thereafter became popular among the pattern recognition community through publications like Zahn [Zahn], Persoon and Fu [Pearson] and are among the most popular shape representation methods for vision and pattern recognition applications. The basic idea underlying this approach consists in representing the shape of interest in terms of a 1D, 2D or even 3D signal. Many studies have been lead on the use of the Fourier Descriptors as a mechanism for shape identification [Lin et al, Zahn and Roskies]. Some work has also been done using Fourier descriptors to assist in Optical Character recognition (OCR) [Grandlund, Trier et al]. In the context of OCR, the planar curve is generally derived from a

character boundary. Since each character's boundary is a closed curve, the sequence of (x, y) coordinates that specifies the curve is periodic. This makes it ideal for analysis with a Discrete Fourier Transform (DFT).

There are several variations of Fourier Descriptor features and of their use in shape recognition. For example, the formulation used by [Zahn and Roskies] applies the Fourier Transform to the sequence of angular differences between line segments in the curve, while the method used by [Granlund] is to apply the transform to the sequence of complex numbers formed by $x + iy$, where the point on the curve is (x, y) . The method used in this project is most similar to the Elliptic Fourier Descriptors [Kuhl and Giardina]. This method involves applying separate Fourier transforms to the sequence of x components and the sequence of y components of each curve. This allows the curve to be reconstructed exactly from the feature data, provided that all components of the frequency spectrum are saved. It is not typically necessary to do this, however, as most of the information about the curve is contained in the low frequency components of its transform.

Elliptic Fourier descriptors

Shape Descriptors (SD)

The SD of an image (modeshape) may be considered as a point in the shape-feature vector space. 2D mode shapes are considered in this paper. Thus, the general form of SD can be expressed as :

$$D = f[I(x,y)] \quad (1)$$

where $I(x,y)$ denotes the displacement modeshape function and $f[*]$ is the transformation extracting the shape features.

More specifically, we can project the image onto the kernel function $R(x,y)$ as :

$$D = \int_{\Omega} R(x,y)I(x,y)dxdy \quad (2)$$

where Ω is the domain of definition.

Shape descriptors are so dependant on the kernel function. Fourier, Wavelets and Zernike moments have been successfully used [Wang et al 2009] for mode-shape recognition and finite element model updating. Here we choose to study modeshapes using the Elliptic Fourier Descriptor.

Some properties of the FDs directly follow from the underlying theory of the Fourier transforms and series, for instance, the invariance to geometric transformations.

The FD is based on the frequency components from Fourier Transform (FT) of the images. According to the well-known theory of the FT, the kernel function of the SD is the complex valued sinusoid,

$$D_f(u,v) = \int_{-\infty}^{+\infty} \int_{-\infty}^{+\infty} e^{-i2\pi(ux+vy)} I(x,y)dxdy \quad (3)$$

$D_f(u,v)$ is a continuous function having the same cardinality as $I(x,y)$, and for real applications, this needs to be reduced whilst retaining as much information as possible. Generally the low frequency and higher energy components are sufficient to describe the shape.

Elliptic Fourier Descriptors (EFD)

The cumulative angular function transforms the two-dimensional (2D) description of a curve into a one-dimensional periodic function suitable for Fourier analysis. In contrast, *EFD* maintain the description of the curve in a 2D space (Granlund, 1972). This is achieved by considering that the image space defines the complex plane. That is, each pixel is represented by a complex number. The first coordinate represents the real part, while the second coordinate represents the imaginary part. Thus, a curve is defined as

$$c(t) = x(t) + jy(t) \quad (4)$$

Here, we consider that the parameter t is given by the arc-length parameterization. Figure 1 shows an example of the complex representation of a curve. This example illustrates two periods of each component of the curve. In general, $T = 2\pi$, thus the fundamental frequency is $\omega = 1$. It is important to notice that this representation can be used to describe open curves. In this case, the curve is traced twice in opposite directions (Figure 1).

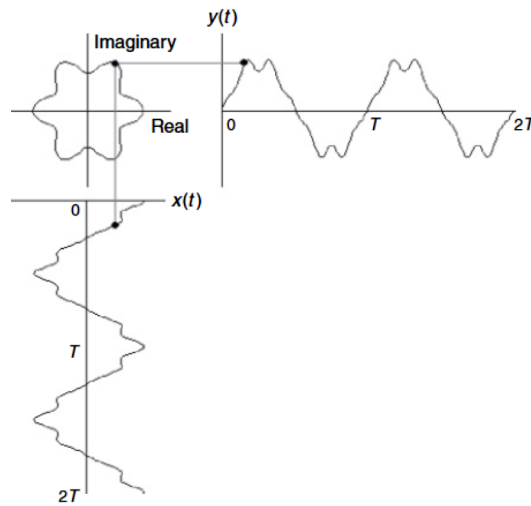


Figure 1 – Example of complex curve representation [Nixon et al]

To obtain the elliptic Fourier descriptors of a curve, we need to obtain the Fourier expansion of the curve. The Fourier expansion can be performed by using the complex or trigonometric form.

In general, the equation linking curve and Fourier expansion terms is expressed in matrix form as

$$\begin{bmatrix} x(t) \\ y(t) \end{bmatrix} = 0.5 \begin{bmatrix} a_{x0} \\ a_{y0} \end{bmatrix} + \sum_{k=1}^{\infty} \begin{bmatrix} a_{xk} & b_{xk} \\ a_{yk} & b_{yk} \end{bmatrix} \begin{bmatrix} \cos(k\omega t) \\ \sin(k\omega t) \end{bmatrix} \quad (5)$$

Each term in this equation has an interesting geometric interpretation as an elliptic phasor (a rotating vector). That is, for a fixed value of k, the trigonometric summation defines the locus of an ellipse in the complex plane. We can imagine that as we change the parameter t the point traces ellipses moving at a speed proportional to the harmonic number k [Nixon et al].

Plate example

We compute the dynamic behavior of a Cantilever Free Cantilever Free (CFCF) plate on ABAQUS. The modeshapes (eigen vectors) are obtained using a standard eigenvalue solver. The figure 2 plots the 6 first mode shapes.

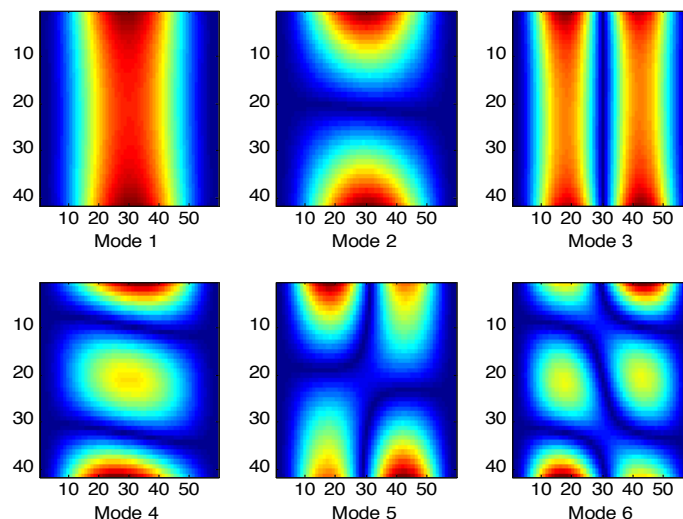


Figure 2 – 6 first modeshapes of CFCF plate

The nodal lines are obtained by thresholding (displacement close to zero). For each modeshapes we can save nodal lines in a bitmap file (image) for further analysis with image processing tools.

Using a classical EFD algorithm (Figure 3), contour are extracted from the nodal lines data using IP thresholding. From the complex curve, we compute Normalized Fourier Transform, then Fourier Descriptors and finally we are able to reconstruct each mode shape. One drawback of the method is that the image resolution should be enhanced (from 40 by 50 pixels to 200 by 250 pixels, so the resolution is increased by a factor 5 by splines interpolation). Retrieval of the original modeshape can accurately be obtained by the inverse Fourier transform (Figure 3b).

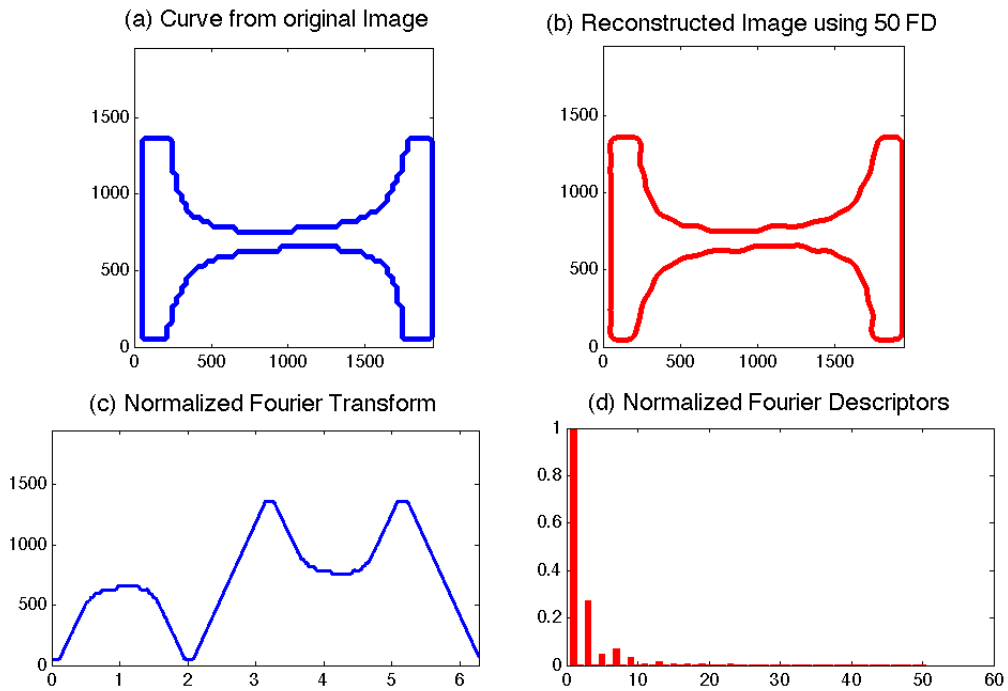


Figure 3 – Elliptic Fourier descriptor are used to reconstruct mode 2 (a) based on 50 fourier descriptors (d).

Good approximation may reasonably be achieved by retaining only a small number of high energy terms (50 terms). We can see clearly the approximation is enhanced with number of Fourier Descriptors (Figure 4).

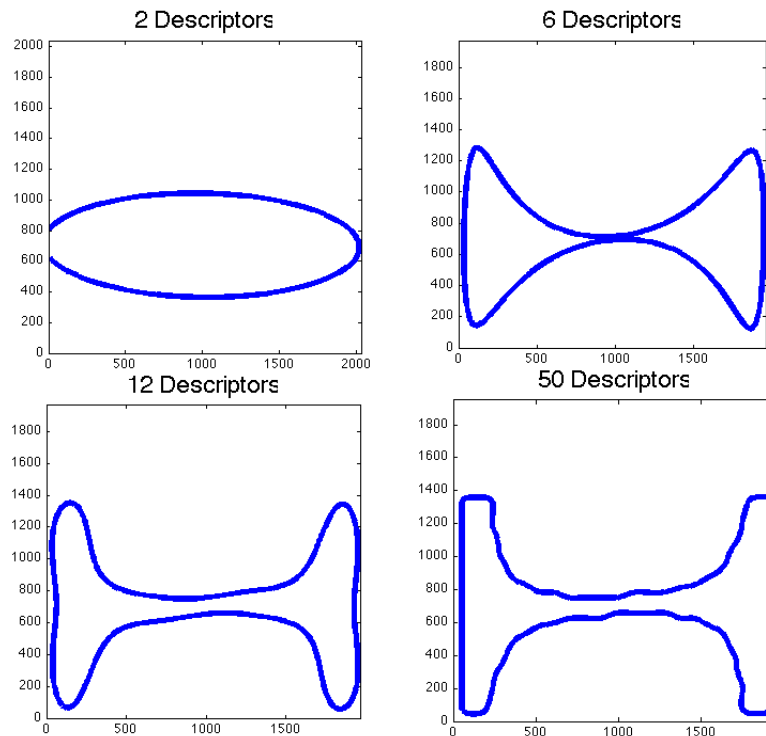


Figure 4 – A schematic contour gradual reconstruction of mode 2, using, respectively, 2, 6, 12 and 50 descriptors

Comparison with MAC: results and discussion

The MAC is used to analyse the correlation between the undamaged plate mode shapes with each other, the following results are obtained (Figure 5).

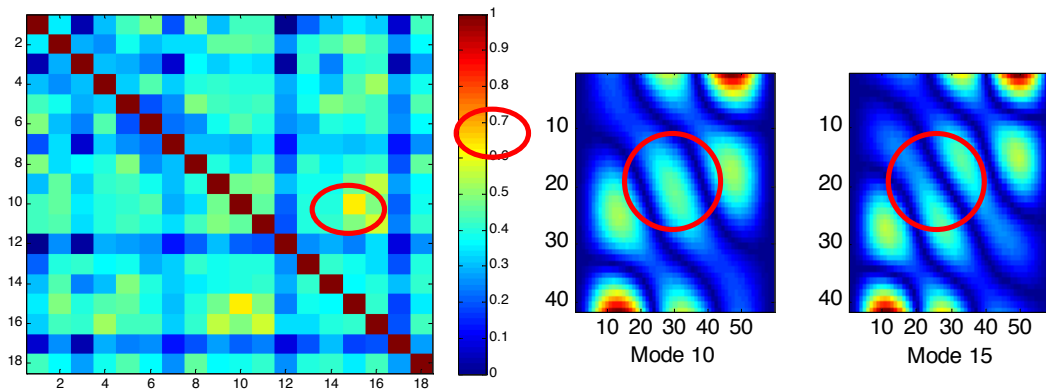


Figure 5 – MAC exhibits high similarities (>0.7) between mode 10 and 15 (red circle), but comparing mode 10 and 15 we can easily see the difference in the center of the plate

From the MAC results on a simple plate we can observe high similarities between mode 10 and 15 for example (so a coefficient close to 0.7 in the MAC matrix). But just comparing FD of these two modes (Figure 6), we can see that important dissimilarities exist. We can also conclude that reconstruction from FD can help to have “local” information of dissimilarities.

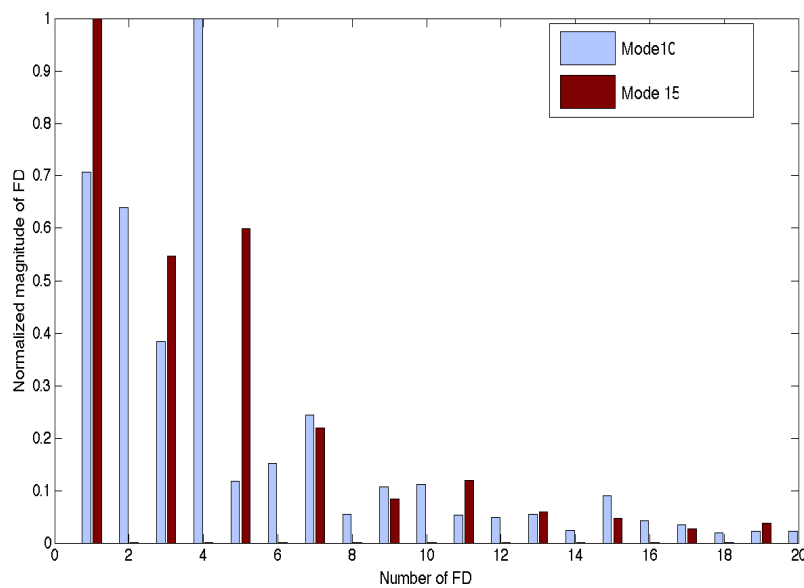


Figure 6 – Dissimilarities can be seen between mode 10 and 15 comparing relative amplitude of Fourier Descriptors

An advanced criteria “correlation of Fourier Descriptor” adapted from correlation of Zernike moment [Wang] should be developed to distinguish close modes using the advantage of comparing at different levels of approximation (From Fourier to Wavelets Descriptors).

Application in Damage detection

Changes in modal parameters (frequency, damping, mode shapes) are commonly used in SHM to detect, localize and identify damages in structures. FRF updating process can help to localize damages [Shahdin] but modeshapes are often difficult to use as a tool for localization of damages. In fact, direct comparison of modeshapes of damaged and undamaged plate gives no reliable information about the damage location because many false damages can appear in the map of absolute value of difference of 2 states of modeshapes (damaged, undamaged).

This method will help us to select “interesting modes” in all the modal basis. How do we classify them? Just in selecting modes with the lowest correlation using a mixed indicator. This indicator is just the combination of coefficient

of correlation (R) and slope of the polynomial regression (order 1) between two sets of FD (state 1, undamaged, state 2, damaged) with equal weights).

For Finite Element Analysis with ABAQUS we use following dimension and properties:

Plate dimension are 236 x 291 mm, and material properties are close to T700/M21 (laminate composites): density =1550kg/m³, E1=110.3GPa, E2=E3=7.69GPa, G12=G13=4.75GPa, G23=2.746GPa.

Figure 7 shows the FE model with delamination in the right down part of the plate, and eigenvalues (modal frequencies) in the [0-2030Hz] frequency bandwidth (15 modes with higher energy).

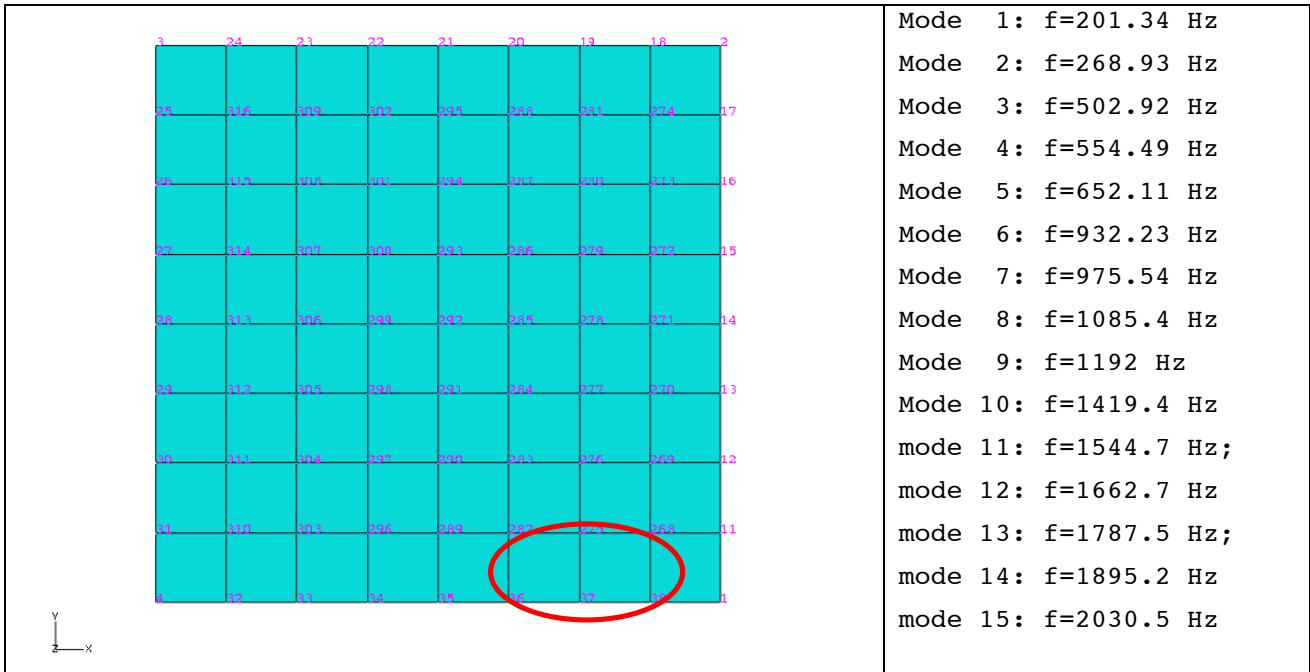


Figure 7 – Finite element model (Abaqus) of a CFCF plate with delamination (red circle) and natural frequencies of pristine plate

In a first approach we only compute the MAC between state 1 and 2 (Figure 8). We can not conclude about the damage existence and location only using this result (very close from the MAC using only undammaged case on Figure 5).

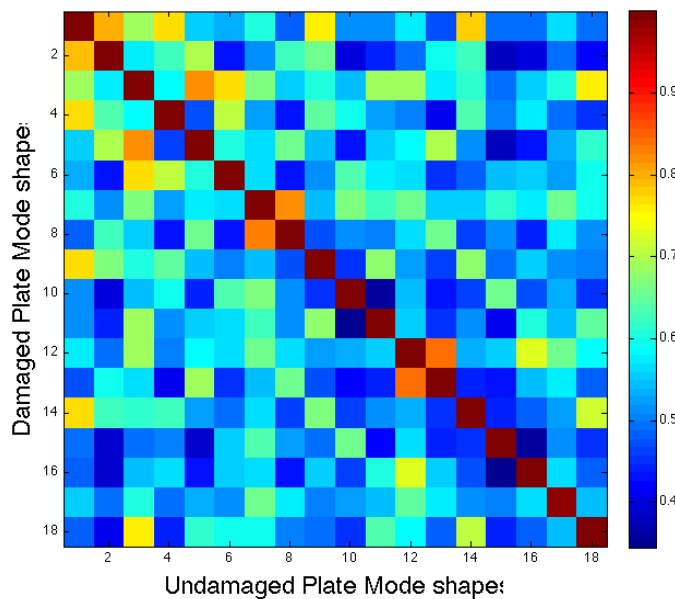


Figure 8 – Modal Assurance Criteria (MAC) of modeshapes of undamaged plate Vs damaged plate gives no information about the damage location

In a second approach we compare FD of the 15 modeshapes between the 2 states (undamaged, damaged). It also seems to have high correlation between the 2 cases (Figure 9).

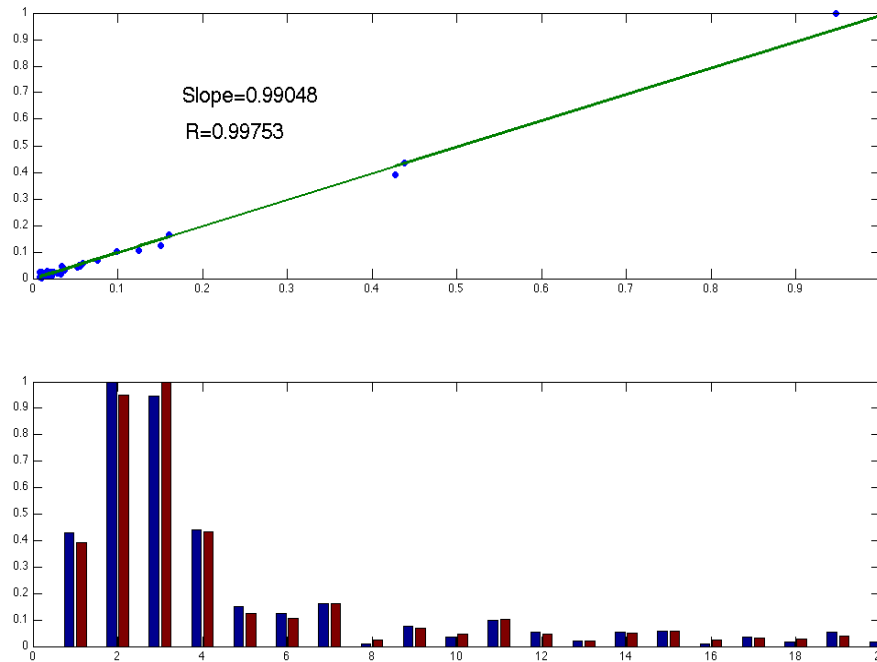


Figure 9 – Comparison of Fourier Descriptors of mode 9 for undamaged and damaged cases : on top regression which allows to establish indicators to classify interesting mode shapes

It is interesting to note that the results obtained from classification from R and slope are slightly different (Mode 9 is always the most dissimilar), so we decide to average the influence of these two indicators by creating the mixed indicators which is just the average of R and slope (Figure 10). It aims at quantifying the “local dissimilarities” of the modeshapes.

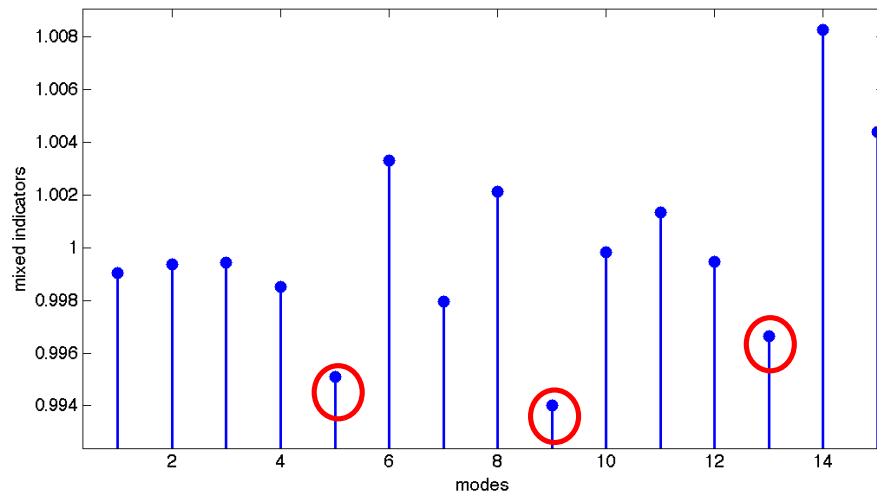


Figure 10 – Mixed indicators vs modes, high changes of this indicator permits to see the influence of damage on the nodal line changes. In red extracted mode shapes for damage localization

The mapping of a potential damage zone (MD) is then created by a weighted indicator based on the absolute difference between selected modeshapes $U_{state}^{mode}(x,y)$ (step 2 is damaged case, step 1 is undamaged case) taking into account only dissimilar modes in the modal basis.

In fact even if each difference localizes the damage by a peak, it exists in every difference false damages (with lower values). So MD has been developed to intersect the location where changes are high and then, the more modes have this change, the more MD is high (Figure 11).

$$MD(x,y) = abs(U^9_2(x,y) - U^9_1(x,y)) \cap abs(U^5_2(x,y) - U^5_1(x,y)) \cap abs(U^{13}_2(x,y) - U^{13}_1(x,y))$$

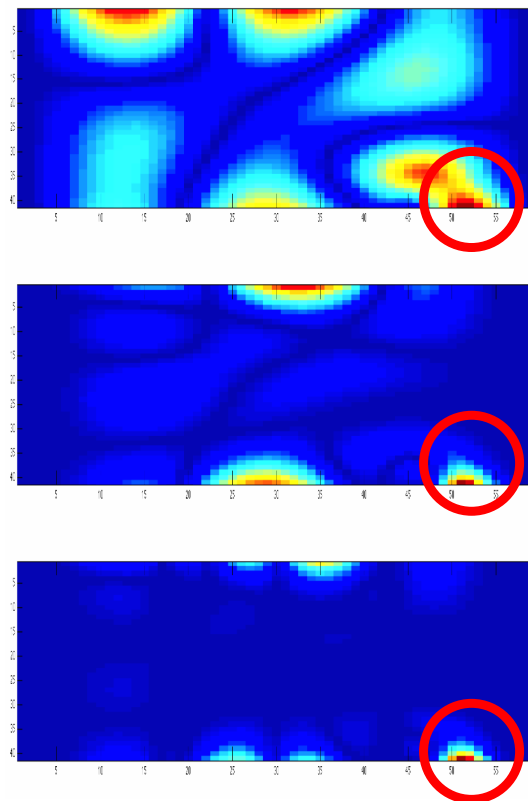


Figure 11 –Difference between selected modeshapes (5,9,13). Top mode 9 only, middle combination of mode 5,9, down combination of mode 5,9,13. Taking into account several interesting modes permits to reduce influence of false damages.

CONCLUSION

Shape Descriptors show the desirable properties of computational efficiency and ease of image reconstruction using a small number of SD terms. The Elliptic Fourier Descriptors are more general and very effective at extracting mode-shape features by virtue of their sinusoidal patterns. Nodal lines are able to characterize mode shapes very easily. We can wonder if experimentally, is it more convenient (or reliable) to measure displacement or to measure nodal line (null displacement)? Finally, we also validated our method on a CFCF plate demonstrating the quality of advanced for both modeshapes tracking and damage localisation. Futur works will focus on wavelets decomposition as enhanced feature descriptors.

ACKNOWLEDGMENTS

This research was fund by EPICEA project (SAPES composites)

REFERENCES

- Allemang, Randall J., The Modal Assurance Criterion – Twenty Years of Use and Abuse, University of Cincinnati, Cincinnati, Ohio
- R. L. Cosgriff, "Identification of Shape," Report No 820-11 of the Ohio State University Research Foundation 1960.
- D. J. Ewins: Modal Testing: Theory, Practice and Application
- G. H. Granlund, *Fourier preprocessing for hand print character recognition* IEEE Trans. Comput., vol. C-21, 195--201, 1972.
- F.P. Kuhl and Ch.R. Giardina, *Elliptic Fourier Features of a Closed Contour*, CGIP 18, 236-258 (1982)
- C.-S. Lin and C.-L. Hwang. *New Forms of Shape Invariants from Elliptic Fourier Descriptors*. Pattern Recognition, 20(5):535--545, 1987.

- Mark S. Nixon, Alberto S. Aguado "Feature Extraction and Image Processing Second edition" Copyright © 2008 Elsevier
- E. Persoon and K.-S. Fu, "Shape discrimination Using Fourier Descriptors," *IEEE Transactions on Systems Man and Cybernetics*, vol. SMC-7, pp. 170-179, 1977.
- O. Trier and A. Jain and T. Taxt, *Feature extraction methods for character recognition - A survey*. Pattern Recognition 29, pp. 641-662, 1996.
- A. Shahdin, J. Morlier, H. Niemann, and Y. Gourinat, Correlating low energy impact damage with changes in modal parameters: diagnosis tools and FE validation, *Structural Health Monitoring* 9(6), 2010.
- Weizhuo Wang, John E. Mottershead, Cristinel Mares, Mode-shape recognition and finite element model updating using the Zernike moment descriptor, *Mechanical Systems and Signal Processing*, Volume 23, Issue 7, October 2009, Pages 2088-2112
- Weizhuo Wang, John E Mottershead, Cristinel Mares, Vibration mode shape recognition using image processing, *Journal of Sound and Vibration*, Volume 326, Issues 3-5, 9 October 2009, Pages 909-938
- Weizhuo Wang, John E Mottershead, and Cristinel Mares, "Shape descriptors for mode-shape recognition and model updating" *Journal of Physics: Conference Series*, Volume 181, Number 1,2009
- C. T. Zahn and R. Z. Roskies. *Fourier descriptors for plane closed curves*. IEEE Transactions on Computers, 1972.

RESPONSIBILITY NOTICE

The author(s) is (are) the only responsible for the printed material included in this paper.

Concomitant Vortex Induced Vibration Experiments: a Cantilevered Flexible Cylinder and a Rigid Cylinder Mounted on a Leaf-spring Apparatus

Guilherme R. Franzini^{1*}, Celso P. Pesce¹, Rodolfo T. Gonçalves², André L.C. Fuarra^{1,2} and

Adriano A. P. Pereira³

Escola Politécnica – University of São Paulo, Brazil

¹ *Fluid-Structure Interaction and Offshore Mechanics Laboratory – LIFE&MO*

² *Numerical Offshore Tank – TPN*

IPT – Technological Research Institute, São Paulo, Brazil

³ *Naval and Ocean Engineering Center*

* Corresponding author: gfranzini@usp.br

ABSTRACT

This paper presents experimental results of Vortex Induced Vibrations (VIV), concomitantly carried out in water with a flexible cylinder, rigidly fixed, and with a ‘rigid’ cylinder, mounted on an elastic apparatus. The experiment was run at IPT¹ Towing Tank facility, in a side by side arrangement. The flexible cylinder is simply fixed at the upper end. For the flexible cylinder, two degrees of freedom (2DOF) are implied for each vibration mode: crosswise and aligned with respect to the incident flow. The elastic support to which the ‘rigid’ cylinder is mounted is made of two vertical leaf springs, fixed to two thick horizontal plates, conferring to the cylinder a single degree of freedom (SDOF) to oscillate transversally with respect to the incident flow. The mass ratios of the cylinders are almost the same, around 1.2 and 1.4 respectively, very low values, typical of long ocean pipe structures, as risers and pipelines. The structural damping ratio is also typically low and such as to guarantee high amplitude responses. Besides usual spectral and statistical analysis the Hilbert-Huang spectral analysis technique is applied, as, strictly, VIV is a non-stationary oscillation emerged from a nonlinear dynamic system. A discussion is made on the distinct VIV behaviors of the SDOF and the 2DOF systems.

Keywords: VIV, rigid cylinder, flexible cylinder, concomitant measures, Hilbert-Huang Technique, leaf-spring apparatus.

INTRODUCTION

In the marine riser scenario, a very rich dynamic behavior can be observed in different time-scales. Some aspects of this dynamics are multi-modal excitation, natural frequency modulations, parametric and internal resonances, mode switching and jumps. Such nonlinear responses usually arise from the fluid-structure dynamic interaction or from nonlinear boundary conditions or even from large structural displacements.

A particular fluid-structure problem which has been the focus of investigation during the last decades is the Vortex-Induced Vibrations (VIV). VIV is a self-excited and self-limited nonlinear resonant phenomenon in which the amplitude of oscillation of the structure reaches values with order of one to two structural diameters. Despite the amplitude being relatively small if compared to the length of the modes typically excited, such a phenomenon is generally significant if mechanical fatigue assessments are concerned.

The nonlinear resonance occurs through a lock-in phenomenon, the frequency of the shed vortex being controlled by the frequency of oscillation of the structure. Such a synchronism is regulated by some parameters. The most important one is the Strouhal number that relates the shedding vortex frequency to the velocity of the flow and to the diameter of the cylinder. Another important parameter is the mass ratio, that relates the vibrating mass to the displaced mass in the fluid. A third one is the structural damping coefficient. The fourth one is the Reynolds number and the fifth one is the

¹ IPT – Technological research Institute of São Paulo State, Brazil.

added mass coefficient. All these parameters regulate the amplitude and frequency responses of the system. The lock-in phenomenon starts at relatively small crosswise oscillations of the cylinder, at small reduced velocities (or normalized frequencies) and ends up at high reduced velocities, after peaking in the intermediate range.

During lock-in, a variety of shedding modes may occur, depending on the mass ratio, on the mass-damping parameter and on the Reynolds number. Some fundamental papers concerning VIV and shedding modes are the ones by Bearman (1984), Khalak and Williamson (1999), Govardhan and Williamson (2000), Williamson and Govardhan (2006), Jauvtis and Williamson (2006). The variety of the modes comprise, among others: (i) the so called 2S mode, characterized by the shedding of single counter rotating vortices, at each cycle of crosswise oscillation of the cylinder; the 2P mode, when two pairs of counter-rotating vortex are shed, at each cycle; (iii) the 3-T mode, when two triplets of vortices are shed, at each cycle. All those may be called symmetrical shedding modes. The first one is related to the 'initial branch' of the amplitude response, at the beginning of the lock-in. The second one is related to the 'upper' and the 'lower branches', all along the lock-in. The change of vortex modes, from 2S to 2P, characterizes the change from the initial to the upper branch. The distinction between the upper and the lower branch depends strongly on the mass ratio and the mass-damping parameters and, consequently, on the magnitude of the amplitude response. The amplitude response is of order 1.0 diameter in the upper mode and half this value along the flat region that characterizes the lower branch. The 3T mode may exist at low mass ratios if two degrees of freedom are allowed, crosswise and aligned with the flow. This mode characterizes highly nonlinear couplings between the inline and the crosswise vibrations, and may occur for rigid cylinders mounted on 2DOF elastic apparatuses as well as for flexible cylinders; see Pesce and Fujarra (2000), Jauvtis and Williamson (2004), Pesce and Fujarra (2005) and Stappenbelt and Lalji (2008). The amplitude response linked to this shedding mode was called by Jauvtis and Williamson the 'super-upper branch', as is related to very large crosswise amplitudes, of order of 1.2 to 1.6 diameters. Within that context, the study of the nonlinear interactions between the wake dynamics and the slender structure is obviously of great importance.

One example of nonlinear interactions effects is related to vortex-induced vibrations jumps; see Pesce and Fujarra (2000, 2005). Or to mode-switching; see Fujarra et al (2001), Pesce et al (2006b). Other nonlinear behaviors are related to the frequency and the amplitude modulation effects on the VIV response, leading to internal resonance and to hysteresis. The papers by Franzini et al (2008, 2010) focus on such effects studying the dynamics of a rigid cylinder mounted on a special elastic apparatus. This apparatus is exactly the same used in the present analysis and consists of a leaf-spring elastic base with a variable leaf-spring span which may be controlled by a conventional electric system (step-motor driven) assembled to a central, long and very small pitch screw; see Fig. 1.

Having all these nonlinear interaction effects in mind, the objective of the present paper is to carry out some comparative fundamental investigation on the dynamics of two similar structures. The first one consists of a long flexible cylinder, rigidly fixed at one end and free at the other extremity. The second structure is a 'rigid' cylinder fixed at one end at an elastic apparatus. The dynamic response similarity existent between these two types of elastic structures is very well known and documented. However, to the authors' knowledge, a single experiment with concomitant measures, during unique runs, i.e., at the same time and therefore at exactly the same Reynolds number and same reduced velocities, the same level of pre-existent turbulence and the same mass-ratio, has not yet been report.

The experiment was run at IPT Towing Tank facility, in a side by side arrangement; Fig. 3. Both experimental setups were mounted on a towing tank carriage, having the cylinders piercing the free surface vertically. The setups were designed as to present the same mass ratio parameters and equal (first) natural frequencies corresponding to crosswise oscillation. Free-oscillations decaying experiments preceded the VIV experiments, from which important dynamic parameters were obtained. The runs covered the whole range of reduced velocity corresponding to the excitation of the rigid body mode of the 'rigid' cylinder and to the first elastic mode of the flexible cylinder. As, strictly, VIV is a non-stationary oscillation emerged from a nonlinear dynamic system, besides usual spectral and statistical analysis the Hilbert-Huang spectral analysis technique; Huang et al (1998) is applied, following the works by Pesce et al (2006a), Franzini et al (2008) and Gonçalves et al (2010, 2011a).

Section 2 brings some details on the experimental apparatuses and arrangements, along with the results of experimental evaluation of dynamic parameters. Section 3 presents results of the experiments and brings the comparative analysis by comparing and discussing the corresponding amplitude and frequency response curves. Section 4 concludes the paper.

EXPERIMENTAL SETUPS AND ARRANGEMENTS

The leaf-spring apparatus and the mounted 'rigid' cylinder

The leaf-spring apparatus is shown in Fig. 1. A detailed description of this elastic support can be viewed in Franzini et al (2008). The text below is essentially extracted from the cited reference. The experimental apparatus is a variable-span leaf-spring system that can deal with elastic mounted cantilevered cylinders, either rigid or flexible ones. The device allows crosswise vibrations only and was designed, considering the IPT towing tank and the NDF² re-circulating

² Nucleous of Dynamics and Fluids, Department of Mechanical Engineering, Escola Politécnica, USP.

water channel characteristics, to cover a particular range of reduced velocities and frequency modulations. FEA and genetic algorithm techniques guided the design towards an improved performance.

A conventional electric system (step-motor driven) controls the vertical position of the clamp, through a central, long and very small pitch screw. This makes the spring-leaves rigidity to vary according the clamp position, enabling to modulate the first natural frequency of the system in crosswise direction.

The present apparatus can be instrumented in various ways. Strain-gages may be placed on the spring-leaves, enabling to identify their vibration; see Fajarra and Pesce (2002). Accelerometers may be fixed to the lower rigid plate or inside the cylinder. The motion of the lower plate may be tracked optically. For the ‘rigid’ cylinder assembling, a single transversal accelerometer may be used to measure the crosswise oscillation.

Table 1 shows the main geometric parameters of the device, in this case assembled to a ‘rigid’ cylinder. The aspect ratio of the ‘rigid’ cylinder is 35.5 (immersed part). Table 2 shows the inertial parameters of this particular ‘rigid’ cylinder assembling. The mass ratio parameter is defined as $m^* = 4m/(\rho\pi D^2L)$, where m is the inertial mass, ρ is the density of the water, D is the external diameter and L is the immersed length. Notice that the inertial mass includes all vibrating masses.



Figure 1 – The leaf-spring apparatus.

Table 1. Geometric parameters; Franzini et al (2008).

Rigid Cylinder	
Material	Al alloy
External diameter (mm)	25.4
Internal diameter (mm)	23.4
Total length (mm)	1000
Immersed length (mm)	900
Leaf-Springs	
Material	Al alloy
Maximum length (mm)	800
Minimum length (mm)	200
Width (mm)	100
Thickness (mm)	0.8
Lower rigid plate	
Material	Al alloy
Width (mm)	100
Length (mm)	100
Thickness (mm)	4

Table 2. Parameters for a typical FEA analysis; Franzini et al (2008).

Lower rigid plate mass (kg)	0.417
Rigid cylinder mass (kg)	0.227
Total moving structural mass (kg)	0.644
Leaf-spring span length (mm)	479
Mass ratio, m^*	1.41

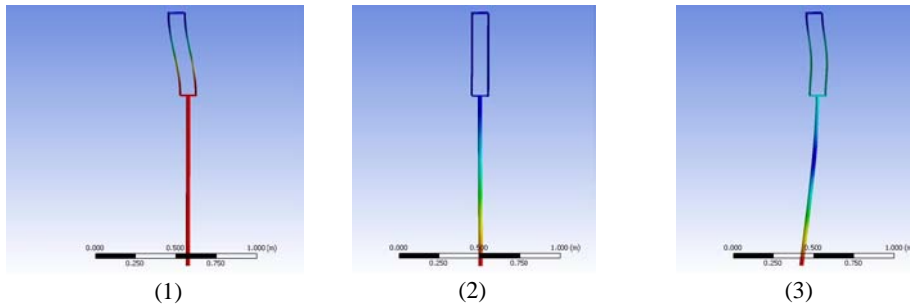


Figure 2. ‘Rigid’ cylinder mounted on the spring-leaves apparatus. The three first eigenmodes: 1.26, 10.01, 14.29Hz. Spring-leaves span: 485mm. FEM analysis; Franzini et al (2008).

Figure 2 illustrates the results of a numerical modal analysis in still water obtained with usual FEA, extracted from Franzini et al (2008). In that analysis, the added mass coefficient has been set to 1.12, which was determined after comparing results of experimental decaying tests in air and water. In that case the leaf-springs span length is 479mm. As can be seen, the first vibration mode is a ‘rigid body’ one, with a 1.26Hz eigenfrequency. The second eigenfrequency corresponds to the first pure bending mode of the ‘rigid’ cylinder (bending is minimal) and the third one shows simultaneous bending of the spring-leaves and the ‘rigid’ cylinder. The values of the second and third eigenfrequencies are high if compared to the first one and do not affect the dynamic phenomena at low towing speeds, at least not substantially. Table 3 shows the first natural frequency as a function of the span length L_s of the leaf-springs, measured from the clamp to the lower rigid plate where the cylinder is fixed. The experimental values are compared to those from FEA.

Table 3. Eigenfrequencies (Hz) in water. ‘Rigid’ cylinder mounted on the leaf-spring apparatus.

Span length (mm)	Experimental (Hz)	FEA (Hz)
264	3.01	3.21
300	2.50	2.45
370	1.81	1.92
428	1.46	1.53
485	1.19	1.26
770	0.66	0.68
780	0.63	0.63
790	0.61	0.59

(*) added-mass coefficient: 1.12; (**); Franzini et al (2008).

The apparatus is low structural damped. In fact, the structural damping coefficient is very low. Typically, the structural damping coefficient is of order $\zeta \cong 0.1\%$ in air, at amplitude values of circa $A^* = A_y/D \cong 0.7$, leading to a mass-damping parameter $\alpha = (m^* + C_a)\zeta$ lower than 0.025, where $C_a = 4m_a/(\rho\pi D^2L)$ is the added mass coefficient; see Franzini et al (2008).

The rigidly fixed flexible cylinder

The flexible cylinder is made of a PVC inner circular rod covered by an elastomeric pipe which was molded over the core. The 15mm diameter PVC core is responsible for the bending stiffness of the model while the elastomeric covering provides the 25.4mm hydrodynamic external diameter. Table 4 shows the main geometric characteristics of

the flexible cylinder, compared to those of the rigid one. The flexible cylinder is rigidly fixed to the towing carriage and has the other extremity free to vibrate. The structural damping coefficient in air is very low, below 0.5%.

Table 4. Geometric and dynamic characteristics

	D [mm]	L/D	m^*	f_1 [Hz]	EI [Nm ²]
Rigid model	25.4	35.5	1.4	1.19	'rigid'
Flexible model	25.4	35.5	1.2	1.17	5.20

The side by side arrangement

Figure 3 shows the side by side arrangement in the towing tank. The experimental setup is mounted on the carriage with the cylinders piercing the free surface vertically. A very small portion of the cylinders is left above water. No endplate is used in either cylinder. A recent study on the effect of end plates or free ends in the VIV response may be found in Morse et al (2008). We choose to run the experiments with a leaf-spring span length of 485mm, corresponding to a rigid body oscillation eigenfrequency in water of 1.19Hz; see Table 3. The length of the cantilevered flexible cylinder has been adjusted such that the first bending eigenfrequency in water resulted in 1.17Hz, a value almost identical to the previous one. The IPT towing tank carriage may operate accurately and safely, both from the point of view of the system and of the structural integrity of the apparatuses, in the velocity range $0.1m/s \leq U \leq 4.5m/s$. This range covers the whole resonant response of both cylinders, considering the rigid body mode of the 'rigid' cylinder and the first bending mode of the flexible one. The reduced velocity $V_r = U/f_1D$ lies, then, in the interval $3.0 < V_r < 15.0$ and the corresponding Reynolds number in the interval $2.5 \times 10^3 < Re < 1.14 \times 10^4$.

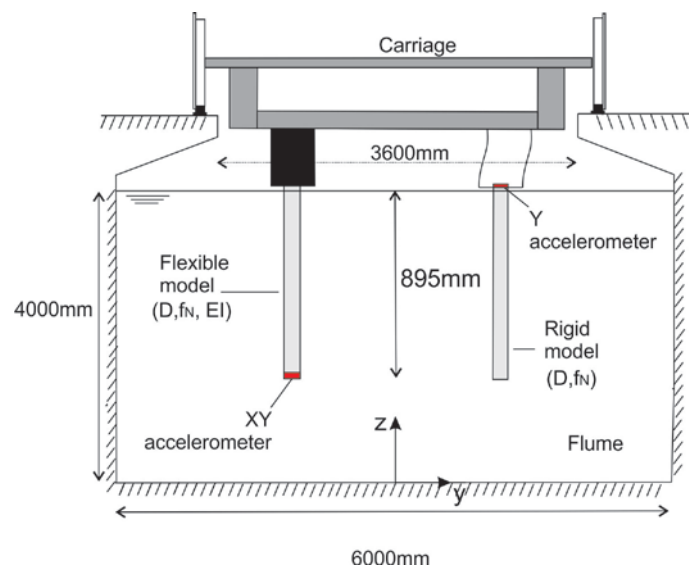


Figure 3 – Side by side arrangement in IPT towing tank.

Accelerometers were attached to the experimental apparatuses. A SDOF accelerometer was positioned over the lower horizontal plate of the leaf-spring apparatus aligned with the y axis, i.e., crosswise to the incoming flow. A 2DOF accelerometer was installed at the lower extremity of the flexible cylinder, with axes aligned with the incoming flow (x) and crosswise to it (y). Figure 3 gives a sketch of the arrangement, where the cylinders dimensions are out of scale. Note that the distance between cylinders is much larger than their respective diameters as well are the distances between the cylinders and the walls.

ANALYSIS OF THE CONCOMITANT VIV EXPERIMENTS

Analysis methodology

Besides standard linear spectral analysis methods, the post-processing of the numerical and experimental signals included the use of the Hilbert-Huang Transform (HHT) technique, what enables a clearer spectral (time-frequency-amplitude) picture of the nonlinear system response; see Huang et al (1998). This is a consequence of the intrinsic non-stationary nature of the VIV, making the HHT to appear as an adequate choice, as it has been developed for treating non

stationary signals emerged from nonlinear systems. The application of such a technique to VIV was pioneered by Pesce et al (2006a) and followed by a series of publications of this research group, as those by Silveira et al (2007), Franzini et al (2008³, 2010), Gonçalves et al (2010, 2011a).

The standard analysis and the HHT technique were applied to the VIV displacements of both cylinders. Such displacements were obtained by numerically integrating the signals of the accelerometers twice. The double integration was carried out in the frequency domain by using a common FFT algorithm, forward and backward. An ideal rectangular band pass filter, with cut-off frequencies 0.50 and 12.0Hz, was applied to the calculated displacement Fourier spectrum in order to get rid of the expected non-zero mean and integration drifting. It is worth mentioning that the non-zero mean and the integration drifting would constitute what is called ‘trend’ in the HHT technique and could be treated a posteriori. The choice of filtering low frequency components a priori makes the analysis easier. The responses of displacement amplitude and dominant frequency are calculated at each reduced velocity.

Three types of main results are shown in graphic form. The first type gives the amplitude and the dominant frequency response as function of the reduced velocity. The second one shows, for selected runs, typical displacements signals and their respective HHT spectra: the Hilbert-Huang amplitude spectrum (HHS), the ‘marginal spectrum’ (MS) and the ‘instantaneous energy level’ (IE); see Huang et al (1998) and for the specific application in VIV, Pesce et al (2006a) and Gonçalves et al (2011a). The third type of results are Lissajou figures, showing xy trajectories of the flexible cylinder free tip.

The MS is the time integral of the HHS and offers a measure of total amplitude (or energy) contribution from each frequency value. In the Fourier representation, the existence of energy at a frequency ω means a component of a sine or a cosine wave persisted through the time span of the data. In the HHT, the existence of energy at the frequency ω only means that there is a higher probability for such a wave to appear locally. The IE is the frequency integral of the square of the HHS, i.e. of energy, calculated over the whole significant domain of frequency and can be used to observe the energy fluctuation over time, i.e. the energy modulation.

It is worth noticing that the HHT determines the relevant statistical parameters from the Intrinsic Mode Functions (IMF), corresponding to each frequency component present in the Hilbert Huang spectrum. The characteristic displacement amplitude, as proposed by Gonçalves et al (2011a), is evaluated by calculating the average value among the 10% largest amplitudes which are obtainable from the HH spectrum, $H(\omega, t)$. On the other hand, the characteristic frequency is defined as the average frequency related to the 10% largest amplitudes. As the whole signal is considered, a better statistic analysis is achieved.

Experimental results and discussion

Figures 4 and 5 show amplitude and frequency responses of displacements as function of the reduced velocity. The responses of the flexible and the ‘rigid’ cylinders, compared in the graphs, were determined by the two alternative techniques: the ‘traditional analysis’ and the ‘HHT’. The reduced velocity is defined as $V_r = U/f_0 D$, where U is the carriage speed, D is the diameter of the cylinder and f_0 is the corresponding natural frequency measured from decaying experiments in still water. In the present experiments, $f_0=1.19\text{Hz}$ for the rigid cylinder and $f_0=1.17\text{Hz}$, for the flexible cylinder, vibrating in its first eigenmode. The amplitude responses are shown normalized by the diameter and by the corresponding modal factor, γ , that is equal to 1, for a rigid body translation, which is the case of the elastically ‘rigid’ cylinder and is equal to 1.305 for a cantilevered flexible cylinder vibrating in its first bending mode; see, e.g., Blevins (1990).

For the flexible cylinder inline and crosswise amplitude responses are shown. Only the crosswise (or transversal) amplitude response is presented for the rigid cylinder, as it is fixed to a SDOF elastic apparatus. The mass ratio parameter m^* is 1.2 for the rigid cylinder and 1.4 for the flexible one, typical low values. Dominant frequency responses f_y of crosswise oscillations are shown normalized with respect to f_0 . On the other hand, dominant frequency responses f_x of inline oscillations of the flexible cylinder are shown as a ratio with respect to f_y .

Regarding SDOF VIV, recall that based on experimental observations of distinct vortex modes formations Govardhan and Williamson (2000) divided the response branches in ‘initial’, ‘upper’ and ‘lower’. Observing the transversal displacement responses of the rigid cylinder, typical curves are found. In fact, the rigid cylinder exhibits the classic initial, upper and lower branches of responses. The upper branch has a peak of circa 0.9 at a reduced velocity of 0.6. This is typical of SDOF experiments in this range of Reynolds numbers; see Govardhan and Williamson (2006). The lower branch, a flat region, extends from $V_r \sim 9.0$ to $V_r \sim 12.0$. Typical dominant frequency responses were also found. Notice that the dominant frequency trace increases almost linearly with the reduced velocity up to the ending of the upper branch, presenting an almost invariant pattern within the lower branch and jumping up at its end, the end of the major VIV synchronization. Recall that the effective natural frequency of oscillation actually increases with the reduced velocity as the added mass decreases; see, e.g., Fujarra and Pesce (2002).

³ By using the same spring-leaf apparatus, this technique was explored in Franzini et al (2008) and shown to be particularly useful in obtaining the whole VIV response (amplitude and frequency curves) from a single run, under a single towing velocity, therefore at a constant Reynolds number. This was possible since the natural frequency was modulated in time, making the reduced velocity to vary during that particular constant velocity run. In the present paper this technique is used to analyze single VIV runs, each at a single reduced velocity, with no modulation of the natural frequency.

Focusing on the comparison between the results obtained with the two alternative methods of analysis it can be said that both give essentially the same results. Differences are very small. This can be attributed to the quite regular and almost monochromatic character of these SDOF oscillations, all along the range of strong synchronization. In fact, the amplitude spectrum is usually narrow within the resonance range. The marginal spectrum shown in Figure 6c, at the reduced velocity corresponding to the response peak, illustrates this fact clearly.

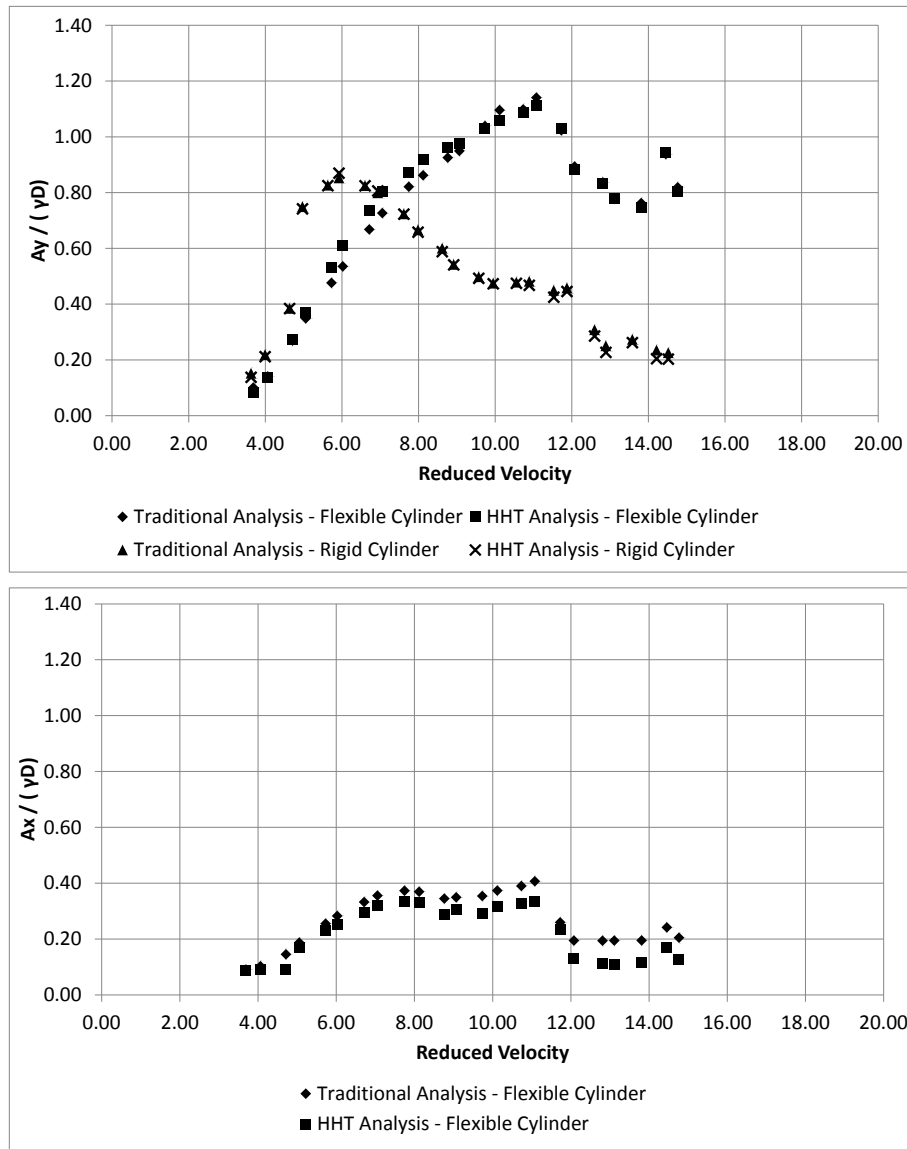


Figure 4. VIV amplitude responses as function of the reduced velocity. Flexible ($m^*=1.2$) and elastically mounted rigid cylinder ($m^*=1.4$). Comparing Hilbert-Huang spectral analysis and traditional statistics techniques.

On the other hand, 2DOF experiments may present amplitude responses with wider spectra. In fact, coupling between inline and crosswise oscillations are prone to occur and many times has been shown in the technical literature. As observed in the introduction, at low mass ratio parameters ($m^* = 2.4$), with a rigid cylinder mounted on a 2DOF pendular apparatus, Jauvtis and Williamson (2004) showed that also exists a narrow ‘super upper branch’, with response amplitudes reaching values of circa 1.3 - 1.5, similar results can also be found in Stappenbelt and Lalji (2008) and Blevins and Coughran (2009). Such a ‘super upper branch’ response was related to the so called 3T vortex shedding mode. A very large crosswise oscillation at high reduced velocity, presenting a branch discontinuity with a jump, had been observed before by Pesce and Fujarra (2000) from experiments with a cantilevered flexible cylinder, with the same mass ratio ($m^* = 2.4$). The recognition of the existence of the ‘super upper branch’ in that previous flexible cylinder experiment was made in Pesce and Fujarra (2005), after comparing, with a remarkable agreement, the results of Jauvtis and Williamson (2004). As a matter of fact the large crosswise amplitude response of 2DOF VIV depends on low values of mass ratios and damping coefficients. For a recent and comprehensive comparative analysis at low mass ratios,

see Gonçalves et al (2011b). In this last work, a close similarity is shown between flexible and rigid cylinders, being those mounted on pendulum bases or pivoted at one end.

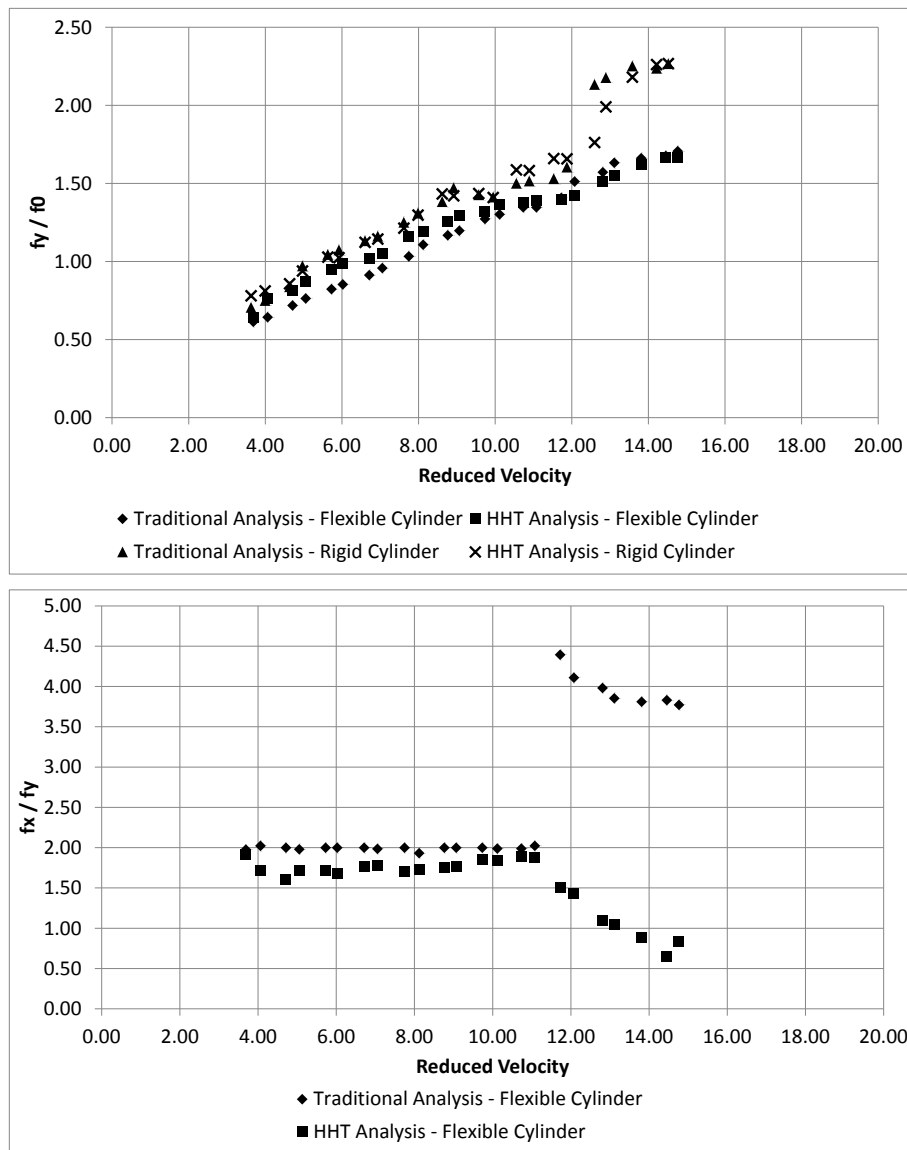


Figure 5. VIV dominant frequency responses as functions of the reduced velocity. Flexible ($m^*=1.2$) and elastically mounted rigid cylinder ($m^*=1.4$). Comparing Hilbert-Huang spectral analysis and traditional statistics techniques.

Figure 6a and 6b illustrate some of these points, showing a wide spectrum for the crosswise vibration and a multichromatic spectrum for the inline vibration. As a matter of fact, the inline oscillations usually present a much richer frequency composition. Symmetry requires a double frequency response with respect to the crosswise oscillation, as clearly shown in Figures 5b and 6b. This is also clearly depicted in the Lissajou trajectories shown in Figure 8. Also clear in Figure 5b is the presence of frequency components four times larger, in a typical subharmonic response in even higher reduced velocities.

Observing in Figure 4 the amplitude response of the flexible cylinder a typical behavior is also obtained. The inline oscillations bend the crosswise amplitude response curve to the right. A larger peak of about 1.15 is achieved, at $V_r \sim 11.1$ ($Re \sim 8.5 \times 10^3$), probably the end of a ‘super upper branch’. This increase in the peak of the crosswise oscillation amplitude is mainly provoked by a positive transfer of kinetic energy from the vortex shedding and from the cylinder inline vibration, which presents a relatively large response of circa 0.35-0.40, in the interval $7.0 < V_r < 11.1$. The inline amplitude peaks at $V_r \sim 8.0$, decreases a small amount and starts increasing again at $V_r \sim 9.0$, presenting a maximum at $V_r \sim 11.1$.

Notice, however, that within the interval $3.0 < V_r < 7.0$, the crosswise oscillations of the flexible cylinder are smaller than that of the SDOF rigid cylinder. In this interval, the inline oscillations are essentially driven by the 2S and 2P

vortex shedding modes and by the crosswise oscillations. Following the nomenclature by Govardhan and Williamson, this range can be divided into two: the ‘initial branch’, $3.0 < V_r < 5.0$, and the range $5.0 < V_r < 7.0$, from which the upper branch starts developing. In the ‘initial branch’ ($3.0 < V_r < 5.0$) the flexible cylinder crosswise response follows closely below that of the rigid cylinder. Then after an inflection, at $V_r \sim 5.0$, a small decrease in the slope may be perceived and the flexible cylinder response detaches even more from the rigid cylinder one. This slope is almost invariant, up to $V_r \sim 7.0$, point at which the inline amplitude response reaches its flat branch.

From another point of view, following the Lissajou trajectories in Figure 8, it can be observed large eight-shaped pictures, that denote a strong x - y synchronization, start at $V_r \sim 7.0$, becoming more and more defined and clear as the reduced velocity increases. The most clear eight-shaped trajectory happens at $V_r \sim 9.0$. From this point on, up to $V_r \sim 11.1$, the eight-shaped trajectories become less defined, evidencing other frequency components and a much less regular pattern. Nevertheless, the crosswise oscillations at $V_r \sim 11.1$ are circa 15% larger than at $V_r \sim 9.0$. There is, therefore, strong evidences that the ‘upper branch’ extends in the interval $7.0 < V_r < 9.0$ and that is in the range, $9.0 < V_r < 11.1$, that the ‘super upper branch’ appears in the present experiment.

Notice also that, after the ‘super upper branch’, both, the crosswise and the inline amplitude decreases and the eight-shaped Lissajou trajectories gradually disappear. A much more random behavior is depicted, despite the crosswise oscillation amplitude remains relatively high, about 0.8. In this range of high reduced velocities ($12.0 < V_r < 15.0$), the Reynolds number is in the range $8.5 \times 10^3 < Re < 1.15 \times 10^4$, i.e., far enough from the beginning of the so-called ‘drag crisis’. Moreover, a considerable amount of energy was also observed in the inline oscillations around the frequency 7.3Hz, which corresponds to the natural frequency of the second bending moment of the flexible cylinder. In other words, a first inline resonance appeared. In fact, if the reduced velocity is re-normalized with respect to the second natural frequency, it takes the value 2.4 and, as well known, the first inline resonance usually appears around that reduced velocity⁴. Summarizing, the inline excitation of the second bending moment is now concomitant with the VIV oscillations corresponding to the first mode, in a rather and much more complex behavior.

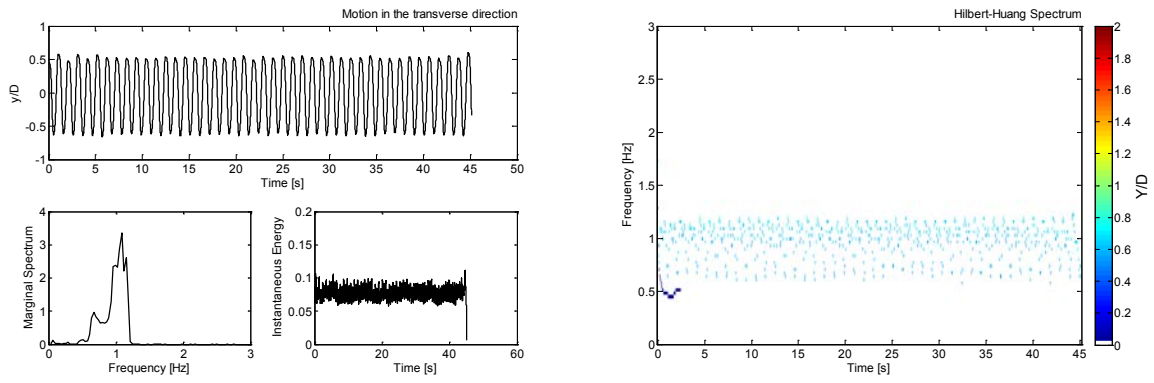
Many other points and comments could be made, by particularly observing the results of two illustrative HHT analyses. For instance, Figure 6 shows results for both cylinders at $V_r \sim 6.0$, that corresponds to the amplitude response peak of the SDOF rigid cylinder. Observing Figure 6c, for the rigid cylinder, notice the clear and well defined dominant frequency time trace that is slightly modulated about 1.2Hz. On the other hand, observing the inline response HH spectrum of the flexible cylinder, three modulated frequencies clearly appear. The dominant one at about 2Hz; coherently the dominant one for the crosswise oscillation is close to 1Hz.

Figure 7 shows the HHT analyses at $V_r \sim 11.1$, point that corresponds to the end of the ‘super upper branch’ of the flexible cylinder. All the features discussed above on the flexible cylinder behavior are evident. In fact, the marginal spectra are much wider than the corresponding ones at $V_r \sim 6.0$. Moreover, looking at the crosswise oscillations in Figure 7a, not only the dominant frequency about 1.5Hz is now heavily modulated but a lower frequency, modulated around 0.5Hz, appears, denoting the existence of a super harmonic of order 3. Inspecting the frequency structure of the inline oscillations by looking at Figure 7b, a much more scattered picture is obtained. However, by looking simultaneously to the marginal spectrum and to the frequency time traces, the dominant frequency about 1.5Hz still appears, together with the modulated third order super harmonic about 0.5Hz and a second order sub harmonic about 3Hz. Figure 7 also shows the HHT analysis for the rigid cylinder, at $V_r \sim 11.1$. This point is at the end of the respective lower branch, where synchronization starts diminishing. Coherently, the crosswise oscillation is highly modulated and the marginal spectrum wide. Two main highly modulated dominant frequencies appear scattered in the frequency time trace.

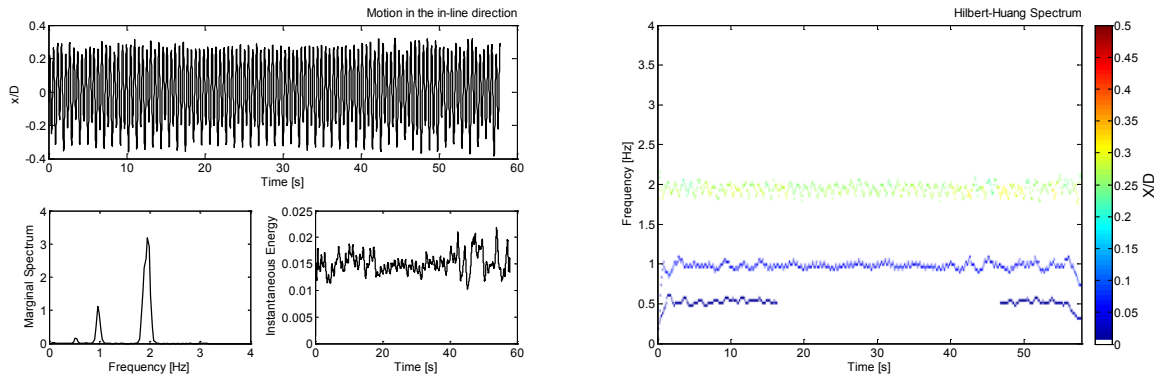
CONCLUSIONS

This paper presented an experimental analysis of VIV experiments carried out concomitantly with a rigid cylinder fixed at a SDOF spring-leaf elastic apparatus and with a clamped flexible cylinder. The cylinders have the same diameter and length. The set ups are both very low damped and present, practically, the same low mass ratio parameter, 1.4 and 1.2. From single accelerometer measurements the displacements were obtained through a direct integration in the frequency domain, by using a FFT algorithm back and forward. Two distinct analysis methods were applied. The first one is a standard statistic method. The second one is based on the Hilbert-Huang spectral analysis technique (HHT). The results are remarkably consistent with previous one published in the technical literature. The SDOF rigid cylinder exhibited the classical initial, upper and lower branches of amplitude responses. The flexible cylinder, for its turn, exhibited the behavior of previous 2DOF experiments, with a strong evidence of the appearance of a ‘super upper branch’, in the manner defined by Jauvtis and Williamson (2004), addressed by Pesce and Fujarra (2005) and, recently, by Stappenbelt and Lalji (2008). As previously shown in Pesce et al (2006), Franzini et al (2008) and Gonçalves et al (2010, 2011a), the HHT enabled to better explore the rich dynamic scenario that is characteristic of the VIV phenomenon, particularly present whenever 2DOF systems are involved.

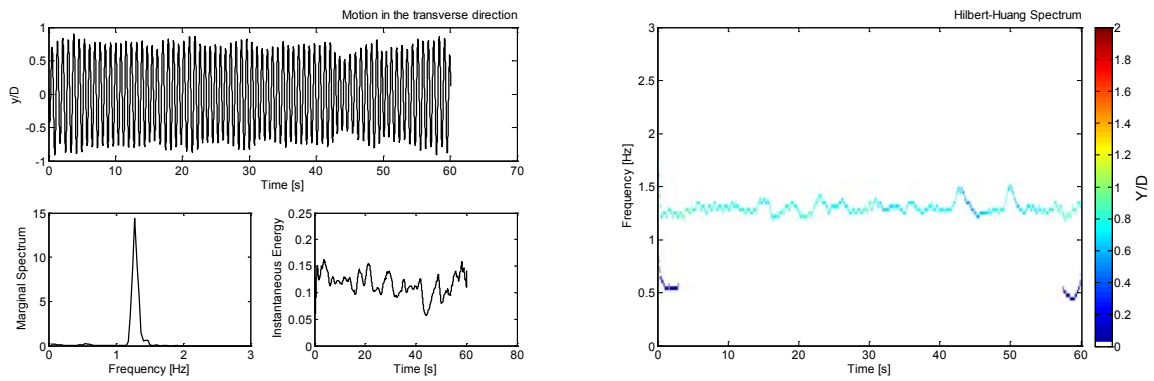
⁴ The inline resonance corresponding to the first bending mode did not appear due to the cut off frequency used in the filtering of accelerometer signal



(a) Crosswise VIV – Flexible Cylinder. $V_r = 6.03$

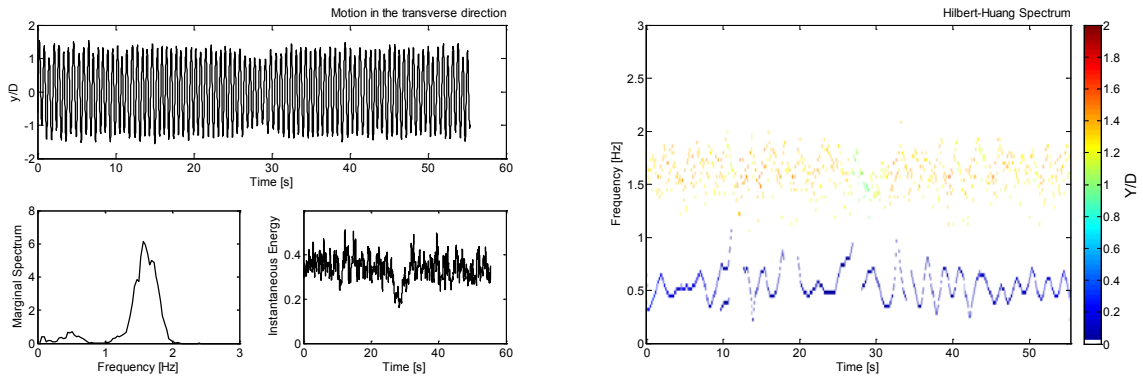


(b) Inline VIV – Flexible Cylinder. $V_r = 6.03$

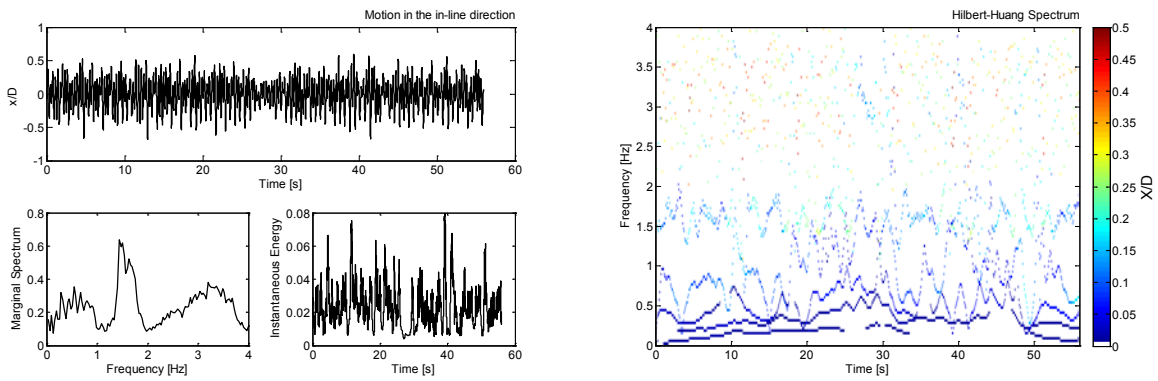


(c) Crosswise VIV – Rigid Cylinder. $V_r = 5.92$

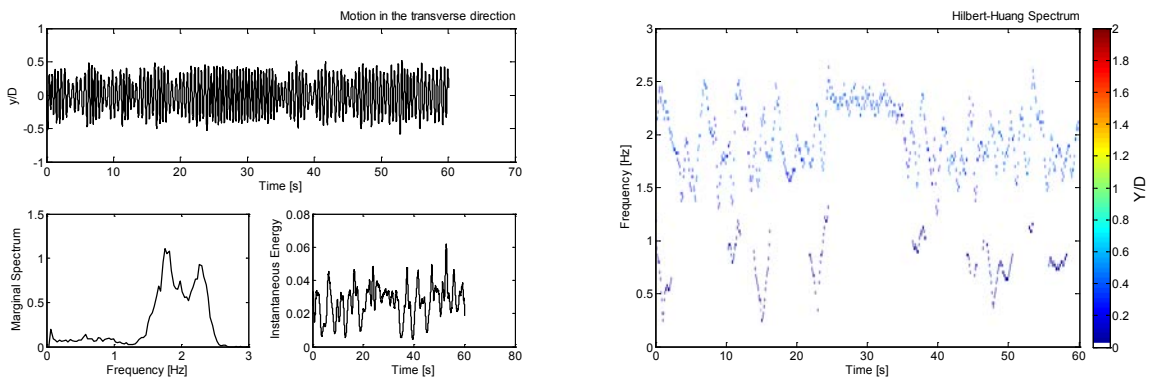
Figure 6. Left: displacement time series, Marginal Spectrum and Instantaneous Energy Level. Right: Hilbert-Huang Amplitude Spectrum. Flexible cylinder ($m^*=1.2$) and elastically mounted rigid cylinder ($m^*=1.4$).



(a) Crosswise VIV – Flexible Cylinder. $V_r = 11.08$



(b) Inline VIV – Flexible Cylinder. $V_r = 11.08$



(c) Crosswise VIV – Rigid Cylinder. $V_r = 10.89$

Figure 7. Left: displacement time series, Marginal Spectrum and Instantaneous Energy Level. Right: Hilbert-Huang Amplitude Spectrum. Flexible cylinder ($m^*=1.2$) and elastically mounted rigid cylinder ($m^*=1.4$).

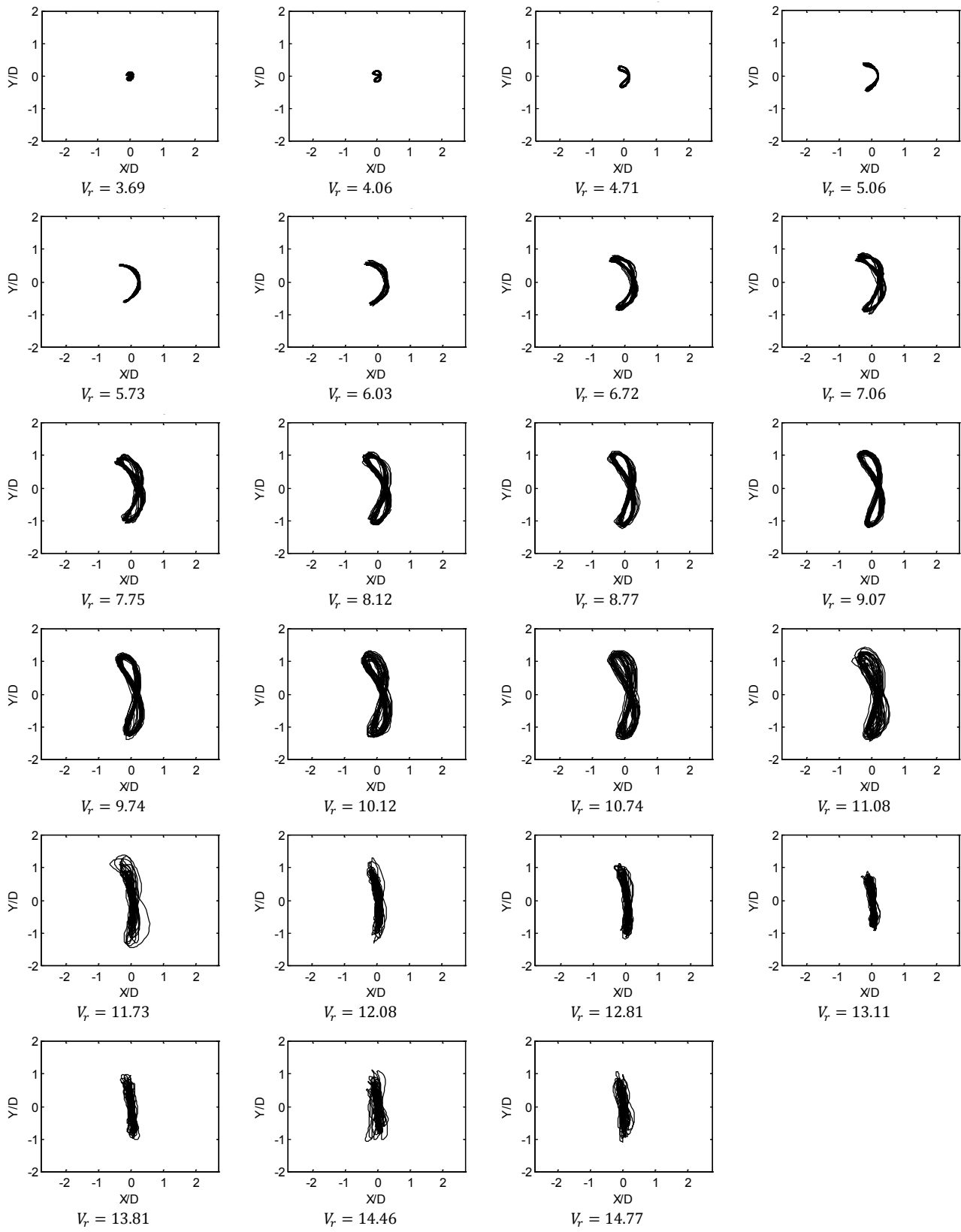


Figure 8. Lissajou figures showing the x - y trajectories of the flexible cylinder free tip at various reduced velocities.

ACKNOWLEDGMENTS

The authors acknowledge CNPq, FAPESP and FINEP for sponsoring the research activities on VIV and riser dynamics. The authors thank the Technological Research Institute of São Paulo State (IPT) for making possible the use of its towing tank.

REFERENCES

- Bearman, P.W., 1984, "Vortex Shedding from Oscillating Bluff Bodies", *Annual Review of Fluids Mechanics*, Vol. 16, 195-222.
- Blevins, R. D., 1990. *Flow-Induced Vibration*. Ed. Krieger, Malabar, FL.
- Blevins, R. D., & Coughran, C. S., 2009. "Experimental Investigation of Vortex-Induced Vibration in One and Two Dimensions With Variable Mass, Damping, and Reynolds Number". *Journal of Fluids Engineering*, Vol. 131.
- Franzini, G.R., Pereira, A.A.P, Fajarra, A.L.C. and Pesce, C.P., 2008, "Experiments of VIV under frequency modulation and at Constant Reynolds Number", Proceedings OMAE08, 27th International Conference on Offshore Mechanics and Arctic Engineering, Lisbon, Portugal.
- Franzini, G.R., Pesce, C.P., Gonçalves, R.T., Fajarra A.L.C. and Meneghini, J.R., 2010, "An experimental investigation on frequency modulated VIV in a water channel", BBVIV6 - Proceedings of the 6th Bluff Bodies Wakes and Vortex-Induced Vibrations Conference.
- Fajarra, A.L.C., Pesce, C.P., 2002, "Added Mass of an Elastically Mounted Rigid Cylinder in Water Subjected To Vortex-Induced Vibrations", 21st International Conference on Offshore Mechanics and Arctic Engineering, Oslo, Norway, 23-28 June.
- Fajarra, A.L.C, Pesce, C.P., Flemming, F. and Williamson, C.H.K., 2001 "Vortex-Induced Vibrations of a Flexible Cantilever", *J Fluids and Structures*, Vol. 15 (3-4), 651-658.
- Gonçalves, R.T., Rosetti, G.F, Franzini, G.R., Fajarra, A.L.C. and Nishimoto, K., 2010 "Case Study of Vortex-induced Motions (VIM) on a Monocolumn Platform Applying the Hilbert-Huang Transform Method", 20th International Offshore (Ocean) and Polar Engineering Conference, Beijing, China.
- Gonçalves, R.T., Franzini, G.R., Rosetti, G.F, Fajarra, A.L.C. and Nishimoto, K., 2011a "Analysis Methodology for Vortex-Induced Motions (VIM) of a Monocolumn Platform Applying the Hilbert-Huang Transform Method", *J. Offshore Mechanics and Arctic Engineering*, Vol. 133 (in press).
- Gonçalves, R.T., Freire, C.M., Rosetti, G.F., Franzini, G.R., Fajarra, A.L.C. and Meneghini, J.R., 2011b, "Experimental Comparisons to Assure the Similarity Between VIM (Vortex-induced Motions) and VIV (Vortex-induced Vibration) Phenomena", to appear in the 30th International Conference on Ocean, Offshore and Arctic Engineering, Rotterdam, The Netherlands.
- Govardhan, R. and Williamson, C.H.K., 2000, "Modes of Vortex Formation and Frequency Response of a Freely Vibrating Cylinder", *J Fluid Mechanics*, Vol. 420, 85-130.
- Govardhan, R.N., Williamson, C.H.K., 2006, "Defining the 'Modified Griffin Plot' in Vortex-Induced Vibration: Revealing the Effect of Reynolds Number Using Controlled Damping", *J Fluid Mechanics*, Vol. 561, 147-180.
- Huang, N. E., Shen, Z., Long, S.R., Wu, M.C., Shih, H.H., Zheng, Q., Yen, N., Tung, C.C. and Liu, H.H., 1998, "The empirical mode decomposition and the Hilbert spectrum for nonlinear and non-stationary time series analysis", *Proc. R. Soc. A*, Vol. 454, 903-955.
- Jauvtis, N. and Williamson, C.H.K., 2004, "The Effect of Two Degrees of Freedom on Vortex-Induced Vibration at Low Mass and Damping", *J Fluid Mechanics*, Vol. 509, 23-62
- Khalak, A. & Williamson, C. H. K., 1999, "Motions, forces and modes transitions in Vortex-Induced Vibration at low Reynolds Number", *Journal of Fluids and Structures*, Vol. 13, 813-851.
- Morse, T.L., Govardhan, R.N., Williamson, C.H.K., 2008, "The Effect of End Conditions on the Vortex-Induced Vibration of Cylinders", *J Fluids and Structures*, Vol. 24, 1227-1239.
- Pesce, C.P. and Fajarra, A.L.C., 2000, "Vortex-Induced Vibrations and Jump Phenomenon: experiments with a clamped flexible cylinder in water", *Int. J of Offshore and Polar Engineering*, Vol. 10, 26-33.
- Pesce, C. P. and Fajarra, A. L. C., 2005, "The 'super-upper branch' VIV response of flexible cylinders", BBVIV4, June 2005, Santorini, Greece.
- Pesce, C.P., Fajarra, A.L.C, Kubota, L.K., 2006a, "The Hilbert-Huang Spectral Analysis Method Applied to VIV". Proceedings OMAE06, 25th Int. Conference on Offshore Mechanics and Arctic Engineering, Hamburg, Germany.
- Pesce, C.P., Martins, C.A. and Silveira, L.M.Y., 2006b, "Riser-Soil Interaction: Local Dynamics at TDP and a Discussion on the Eigenvalue and the VIV Problems", *J Offshore Mechanics and Arctic Engineering*, Vol. 128, 39-55.

Rilling, G., Flandrin P., Gonçalves, P., 2003, "On Empirical Mode Decomposition and its algorithms" *EEE-EURASIP Workshop on Nonlinear Signal and Image Processing*. NSIP-03, Grado (I).

Stappenbelt, B., and Lalji, F., 2008, "Vortex-induced Vibration Super-Upper Response Branch Boundaries". *Int Journal of Offshore and Polar Engineering*, Vol. 18, 99-105.

Silveira, L.M.Y, Martins, C.A., Cunha, L.D, Pesce, C.P., 2007, "An Investigation on the Effect of Tension Variation on VIV of Risers", *Proceedings of OMAE'07, 26th International Conference on Offshore Mechanics and Arctic Engineering*, June 10-15, San Diego, USA.

Williamson, C. H. K. & Govardhan, R. N., 2004, "Vortex Induced Vibrations", *Annual Review of Fluids Mechanics*, Vol. 36, 43-455.

RESPONSIBILITY NOTICE

The authors are the only responsible for the printed material included in this paper.

Motorcycle cornering behavior modeling.

Rafael Donadio¹

Roberto Bortolussi¹

¹ Centro Universitário da FEI

Abstract: The market for motorcycles has been showing a continuous increase in sales in last years. This result is driven by the change of perception by the consumers not to despise the two-wheeled vehicle as a transport. Fuel economy, parking easiness and speed of locomotion confirm the absorption of this product on the market. But the growth of scientific research in motorcycles dynamics do not grow in the same market rate, making it an issue to be exploited to improve the safety of the rider or assist in new projects development. This work uses a multi body motorcycle model containing 4 rigid bodies connected by revolution joints parameterized by 7 degrees of freedom. The model includes the major geometric and inertial characteristics of the motorcycle. It was used in the mathematical model nonlinear algebraic equations. The model is subjected to curvilinear trajectory with constant radius and speed, allowing to know the behavior of the motorcycle on a steady state maneuver, using two input parameters imposed by the pilot: angle of steering and roll angle. The simulation results are discussed and presented in graphical form. Aiming to validate the mathematical model, using an instrumented motorcycle with data acquisition equipment and comparing the actual values with those obtained in the mathematical model.

Keywords: Motorcycle lateral dynamics. Multi body system. Steady state cornering. Data acquisition

NOMENCLATURE

reference coordinates systems:

(X, Y, Z) = ground coordinate system

(X_I, Y_I, Z_I) = rotating coordinate system (I)

(x_d, y_d, z_d) = front reference coordinate system

(x_r, y_r, z_r) = rear reference coordinate system

a = mechanical trail

A = origin of coordinate system (t)

a_g = centre of mass acceleration

a_n = front wheel normal trail

a_t = tire trail

b_t = longitudinal position of rear centre of mass

C = turning centre point

d = coordinate system (d)

d_p = forward displacement of the tire contact point

e_d = eccentricity of front centre of mass

E_d = front tire longitudinal force

E_r = rear tire longitudinal force

F = lateral force

F_A = aerodynamic force on the rear frame

F_D = aerodynamic drag force

F_d = lateral front tire force

F_{Gd} = gravity forces on the front frame

F_{Gr} = gravity forces on the rear frame

F_L = aerodynamic lift force

F_{Pd} = road reaction, front

F_{Pr} = road reaction, rear

F_S = aerodynamic side force

F_t = lateral rear tire force

g = acceleration due to gravity

G_d = front center of mass

G_r = rear center of mass

h_t = height of rear centre of mass

I_{CXZd}, I_{CYZd} = components of inertia tensor of front frame with respect to (X_I, Y_I, Z_I)

I_{CXZr}, I_{CYZr} = components of inertia tensor of rear frame with respect to (X_I, Y_I, Z_I)

I_{wd} = front wheel inertia

I_{wr} = rear wheel inertia

I_{xd}, I_{yd}, I_{zd} = components of inertia tensor of front frame with respect to (x_f, y_f, z_f)

I_{xr}, I_{yr}, I_{zr} = components of inertia tensor of rear frame with respect to (x_r, y_r, z_r)

K_d = angular momentum of the front frame

K_r = angular momentum of the rear frame

K_{Wd} = angular moment of the front wheels

K_{Wr} = angular moment of the rear wheels

l_z = z_d position of front centre of mass

m = total motorcycle mass

M_A = torque of aerodynamic forces

M_{Ax}, M_{Ay}, M_{Az} = components of aerodynamic torque

m_d = front mass

M_{Gd} = torques of gravity forces, front frame

M_{Gr} = torques of gravity forces, rear frame

M_{Rd} = torques of reaction forces, front

M_{Rr} = torques of reaction forces, rear

m_r = rear mass

M_{Tz} = twisting torque

M_x = overturning torque

M_{xd}, M_{yd}, M_{zd} = torques on front wheel

M_{xr}, M_{yr}, M_{zr} = torques on rear wheel

M_y = rolling resistance torque

M_z = yaw torque

N = vertical force

N_d = front wheel load

N_r = rear wheel load

p = wheelbase

P_d = front tire contact point

P_r = rear tire contact point

Q = point on steering axis

R = circle radius

R_d = front wheel radii

R_{Gd} = path radius of front centre of mass with respect to (X_I, Y_I, Z_I)

R_{Gr} = path radius of rear centre of mass with respect to (X_I, Y_I, Z_I)

R_r = rear wheel radii

S = longitudinal force

S_d = longitudinal front tire force

s_p = lateral deformation

S_r = longitudinal rear tire force

t = coordinate system (t)

t_d = front tire head radii

t_r = rear tire head radii

V = forward speed

X_{Gd}, Y_{Gd}, Z_{Gd} = coordinates of centre of mass of front frame in (X_I, Y_I, Z_I)

X_{Gr}, Y_{Gr}, Z_{Gr} = coordinates of centre of mass of rear frame in (X_I, Y_I, Z_I)

X_{P_d} = coordinates of P_d in (X_I, Y_I, Z_I)
 X_{P_f} = coordinates of P_f in (X_I, Y_I, Z_I)
 Y_{P_d} = coordinates of P_d in (X_I, Y_I, Z_I)
 Y_{P_f} = coordinates of P_f in (X_I, Y_I, Z_I)
 Δ = effective steering angle
 δ = steering angle

ε = caster angle
 λ_d = front tire side slip angle
 λ_r = rear tire side slip angle
 ρ_d = front tire centre-line radius
 ρ_r = rear tire centre-line radius
 φ = roll angle

Ψ = yaw angle
 μ = pitch angle
 μ_f = rolling friction coefficient
 ω_d = front wheel spin rate
 ω_r = rear wheel spin rate

INTRODUCTION

The technical description for one vehicle "single track", as the motorcycle is called in the literature, it is tied to single impression it leaves behind as it passes over the sand, for example. This peculiarity is the source of everything that makes the study of the vehicle undeniably complex, and yet at the same time so fascinating.

Another factor is that the means of transport commonly used in day-to-day is so familiar that they are driven with ease which can essentially be reduced to two vehicle categories, two and four wheels. The first category is the bicycles and the motorcycles, which are equivalent in cinematic terms and the second the cars, which certainly is the most studied vehicle today, with extensive bibliography.

A crucial consideration on these vehicles is that when a car is at rest, with or without passengers aboard, it remains in stable equilibrium. However, a motorcycle upright tends to fall, unless a suitable support or supported by the rider.

A little observation brings to light some fundamental differences in the comparison of the two vehicles in motion:

An inexperienced person driving a motor vehicle, intuitively and quickly realized that when the steering wheel is turned one direction, the vehicle is oriented in the same direction, so they can drive the car precisely in the direction they want to go.

However, even an adult inevitably involves potential embarrassment and difficulty associated with attempting to ride a bike for the first time - beginners are forced to put their feet on the ground, trying to maintain balance while trying to keep the bike in the right direction. Initially, the bike is ridden supporting themselves with their feet, avoiding a fall, but after some training, it appears that the faster the bike is conducted, the easier it is to keep it balanced.

Controlling a two-wheeled vehicle is, in fact, nothing simple and intuitive, but there is no doubt that the motorcycle is a functional means of transport and it is also an exciting source of entertainment.

In the past, some studies were developed using single-track vehicles. Whipple (1899) studied the stability of motion assuming bicycle with rigid tires. Sharp (1971) was among the first to investigate the stability of the motorcycle using the tire properties. In 1980, Koenen published a stability study that caters to large lateral accelerations involving large rolling angles. As the vehicle models became more complex with the interaction between the tire and the ground it was necessary to develop more detailed tire models. Iffelsberger (1991), Wisselman et al. (1993), Breur (1998), Sharp et al. (2001) and Berrita et al. (2000) produced works in this direction. In 1999 Cossalter published a work developing nonlinear dynamic equations in steady state cornering.

Meijaard (2006) presented a single track model with a linear model of four rigid bodies, very close to the model studied in this work, but the author decided that the tires have ideal contact with the ground (sharp edge). This model was discarded since it does not slip angles.

The model developed in this paper was presented by Cossalter (1999). In it the motorcycle is modeled with the nonlinear algebraic equations, considering the lateral and longitudinal slip of the driven wheel. The model presented is valid for large values of motorcycle roll angle.

Motorcycle inertial and geometric properties, slip curves of the front and rear tire, the kinematic equations and nonlinear algebraic equations were programmed using the Matlab. Like a motorcycle, the system input is the roll angle and steering angle. The capacity of acceleration and braking of the motorcycle were discarded because the maneuver is performed under steady state. The simulation results are represented by graphs where there are the values of angle of cinematic steering, vertical and lateral force and lateral tire slip angle.

Model description

The motorcycle comprises a system of four rigid bodies: rear structure (including chassis, engine, the fuel tank and rider), front structure (handlebars and fork) and front and rear wheel, as previously mentioned. The front and rear structures are connected by a revolution joint. The front and rear wheels are connected respectively to the rear frame and fork for revolution joints. The effect of front and rear suspension is not taken into account, since in a steady curve the suspension deflection does not change. The rider is considered a rigid body securely attached to the rear structure. The aerodynamic force distribution on the motorcycle is: drag, lift, lateral forces (acting at the center of mass of the rear structure) and three torques.

The contact between the tire and the track is described by means of linking. If the wheel slips both in longitudinal and in lateral, the restrains allow five degrees of freedom (two translational and three rotational). The lateral forces exerted on the tires around the track are very important in the dynamic and steady state and they are related to slip angle and roll angle. The front and rear tire side slip are described by λ_d and λ_t respectively. In relation to the longitudinal slip, the front wheel does not slip, not producing longitudinal tire force as the rolling resistance effect was neglected, in contrast with the rear wheel produces longitudinal tire force causing longitudinal slip (COSSALTER, 2006).

Three coordinate systems are introduced to describe the dynamic properties and kinematics of the vehicle. Coordinate system t (x_t, y_t, z_t) as in Figure 1 is fixed to the structure and the rear plane x_t, z_t is the symmetry plane of rear structure. When the vehicle is upright and the steering angle is zero, axis x_t and y_t are on plan horizontally and x_t points straight ahead, z_t axis is vertical and points downward, the origin and the point P_t contact the rear wheel overlap.

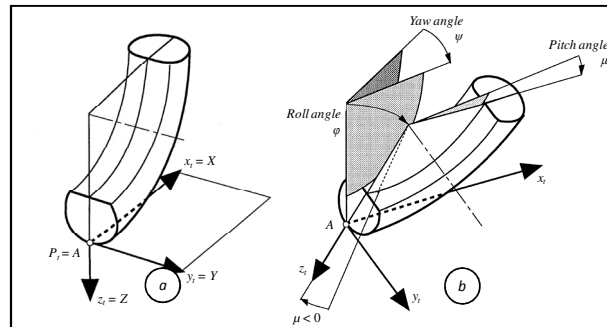


Figure 1: Motorcycle t coordinate system, in upright position (a) and any position (b).

The coordinate system d (x_d, y_d, z_d), as shown in Figure 2 is fixed on to front structure and it is described as follows: the source is located at point Q , which is the point of intersection between the axis of rotation of the steering system and the plane perpendicular to the axis of rotation direction, which passes through the center of the rear wheel axle z_d and it is aligned with the axis of rotation direction pointing downward; y_d axis is parallel to the axis of rotation of the front wheel; axis x_d is in the plane of symmetry of the front structure.

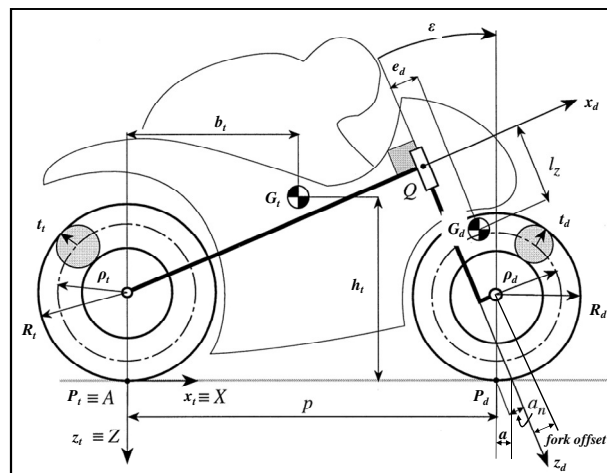


Figure 2: Motorcycle geometry and d coordinate system.

Another coordinate system, according Figure 3, which is useful in the development of dynamic equations in steady state is a rotating coordinate system l (X_l, Y_l, Z_l). The source is located in the center of rotation of the motorcycle (C). The Z_l axis is vertical and points downward (Z axis is parallel to the ground). The axis X_l is in the XY plane and parallel to symmetry plane of rear structure. The Y_l -axis completes the coordinate system.

$$I_{CYZt} = m_t Y_{Gt} Z_{Gt} + \cos \varphi \sin \varphi (I_{zt} \cos^2 \mu + 2I_{xzt} \cos \mu \sin \mu) + \cos \varphi \sin \varphi (I_{xt} \sin^2 \mu - I_{yt}) \quad (11)$$

$$\begin{aligned} I_{CYZd} = & m_d Y_{Gd} Z_{Gd} + \cos \varphi \sin \varphi (\mu + \varepsilon) (I_{xd} - I_{yd}) (\cos^2 \varphi - \sin^2 \varphi) \\ & + \cos \varphi \sin \varphi \{ I_{xd} [\cos^2 \delta \sin^2 (\mu + \varepsilon) - \sin^2 \delta] \\ & + I_{yd} [\sin^2 \delta \sin^2 (\mu + \varepsilon) - \cos^2 \delta] + I_{zd} \cos^2 (\mu + \varepsilon) \} \end{aligned} \quad (12)$$

Tire modeling

The forces and moments produced by the tire as Cossalter (2006) are illustrated in the following figures: Figure 4a forces acting on the intersection point between the plane of symmetry and the track in Figure 4b forces acting on the point of tire contact Figure 4c and production of the moment M_x , M_y , M_z .

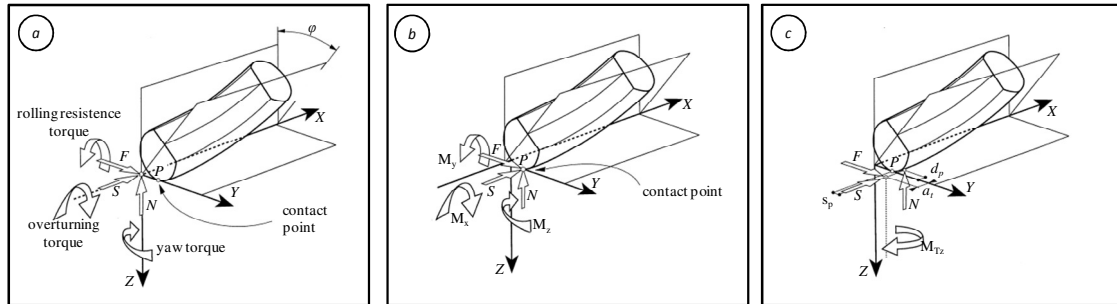


Figure 4: (a) Forces at the contact point, and the main moments. (b) Forces acting on intersection point between the plane of symmetry and the track. (c) Tire contact point details.

Longitudinal front wheel slip is zero because the wheel is not driving. The longitudinal force is related to rolling friction only, the longitudinal force on front tire is determined by:

$$S = -\mu_f N \quad (13)$$

The moment of rolling resistance is calculated by:

$$M_y = d_p N \quad (14)$$

The torque M_x (overturning torque) is caused by lateral deformation of the tire s_p .

$$M_x = -s_p N \quad (15)$$

As Cossalter (1999) s_p displacement is usually small due to high lateral stiffness of the tire, so the moment M_x is zero. Torque M_z is produced by the lateral force F , longitudinal force ($S > 0$ propulsion, $S < 0$ braking) and M_{Tz} (twisting torque):

$$M_z = -a_t(\lambda)F - s_p S + M_{Tz}(\varphi) \quad (16)$$

The first term due to lateral force tends to align the wheel in the direction of movement of the motorcycle. The offset $t(\lambda)$, whose distribution depends on the distribution of lateral force is called the tire trail (Figure 1). It is calculated as the ratio between the torque M_z and lateral force and longitudinal force when the roll angle is zero, a good approximation according to the experimental results (COSSALTER, 1999):

$$a_t = -t_0 \left(1 - \left| \frac{\lambda}{\lambda_{max}} \right| \right) \quad (17)$$

The second term of equation 16, because the longitudinal force, just tends to align the wheel if the longitudinal force is tractive. As the displacement s_p is usually very small, this term can be considered zero (COSSALTER, 1999). The third term is the twisting torque, which arises due to the roll angle and tends to align the wheel. As Cossalter (1999) assume a linear function based on experimental results, where M_j is 0.024 to front tire and 0.028 to rear tire.

$$M_{Tz} = M_1 \varphi \tag{18}$$

Equation solving

The equations are nonlinear (due to the formulas of the tires and kinematic equations) and are solved numerically for specific values assigned to roll angle and steering angle. First, the tire slips were set equal to zero and the equations become a linear system of six equations with six unknowns: $N_t, N_d, F_t, F_d, S_t, \psi^2$.

After the first calculation, ignoring the side slip, values of normal and lateral forces are obtained and used for the side slip angles of front and rear tire. With the slip obtained, the calculation is done again obtaining a new set of lateral forces, vertical, propulsive force and angular velocity.

The equations were organized to solve the system of the form $A.X = B$ each calculation step is defined by the range of values attributed to steering and rolling and the value of the six unknowns was obtained.

$$\begin{bmatrix} a_{11} & a_{12} & a_{13} & a_{14} & a_{15} & a_{16} \\ b_{11} & b_{12} & b_{13} & b_{14} & b_{15} & b_{16} \\ c_{11} & c_{12} & c_{13} & c_{14} & c_{15} & c_{16} \\ d_{11} & d_{12} & d_{13} & d_{14} & d_{15} & d_{16} \\ e_{11} & e_{12} & e_{13} & e_{14} & e_{15} & e_{16} \\ f_{11} & f_{12} & f_{13} & f_{14} & f_{15} & f_{16} \end{bmatrix} \begin{bmatrix} \Psi \\ S_t \\ N_d \\ F_d \\ F_t \\ N_t \end{bmatrix} = \begin{bmatrix} gg \\ hh \\ ii \\ jj \\ kk \\ ll \end{bmatrix} \tag{19}$$

Due to lack of data related to the tires (the parameters are normally confidential and not published by manufacturers), the values for forces and side slips were obtained directly from the curve of the tire thus decreasing the error in the calculation of the forces produced by the tire. Using the Pacejka Magic Formula (2002) these curves were obtained in tire test equipment and the result is found in Cossalter (2008). The test result allows composing curves as a function of lateral slip, normalized lateral force (lateral force / vertical force on the tire) and camber angle. These curves have been programmed along with the other equations. The curves related to the front and rear tire are shown in Figure 5.

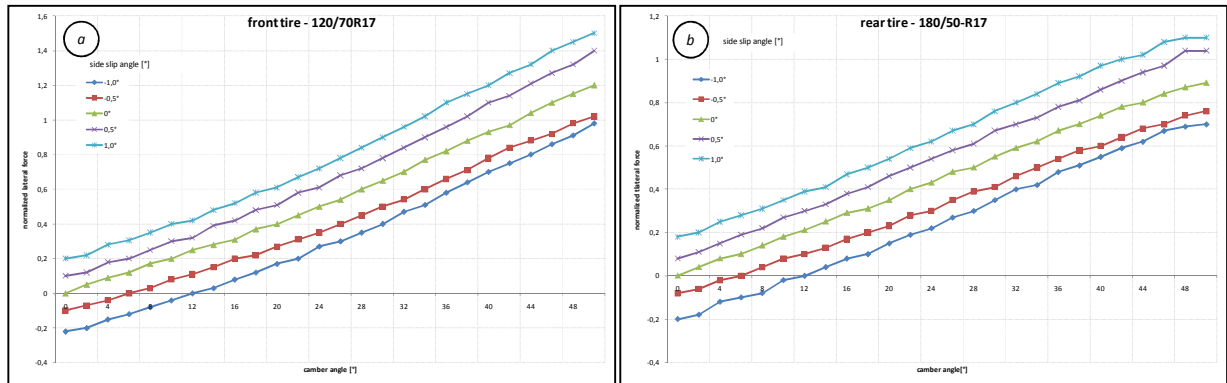


Figure 5: (a) front tire side slip curve, (b) rear tire side slip curve

MATERIALS AND METHODS

Aiming to validate the mathematical model used in this study, tests were done using a Suzuki Bandit N650 motorcycle in stock configuration. These validations enabled also to check whether the simplifications of the mathematical model used are satisfactory.

The center of mass of the motorcycle was obtained using a load cell on each wheel and a signal conditioner (Figure 6a). The methodology used was proposed by Milliken and Milliken (1995, p. 669) to get the height and longitudinal position of center of mass motorcycle. The motorcycle was leaned over load cells with an angle of 27.3°. This angle serves the recommendation of Reimpell, Stoll and Betzler (2001, p.390) reducing the calculation error. The inertia moments used were not measured due to the difficulty in disassembling the motorcycle. The values were obtained from Cossalter (1999), because, the motorcycle has similar mass and inertia characteristics.

For the motorcycle speed, an inductive sensor from AIM in each motorcycle wheel was used. This sensor captures the transition metal in the face of the sensor without contact (Figure 6a and b).

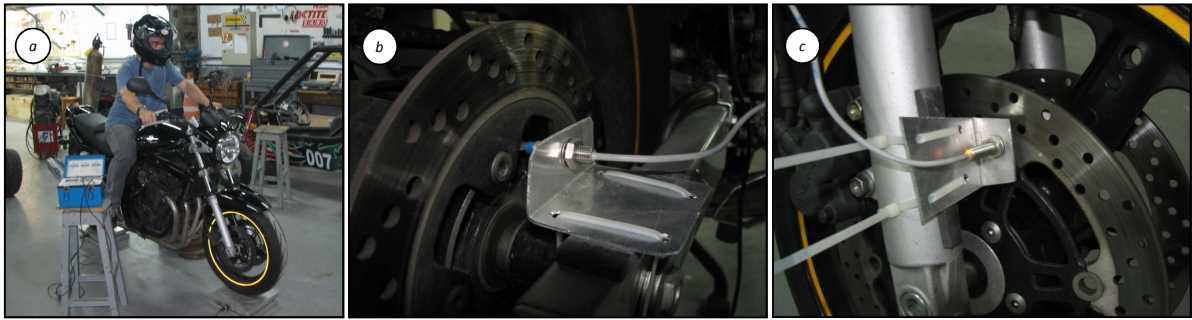


Figure 6: (a) center of mass, (b) rear wheel speed sensor, (c) front wheel speed sensor

The steering angle was measured using a potentiometer installed between the front structure and the steering system and interconnected with pulleys and belt (Figure 7a). With an objective to verify the motorcycle trajectory and use the *AIM* feature for calculating the radius of curvature (feature already implemented in the *AIM*) it was necessary to install the module and GPS antenna on the motorcycle fuel tank (figure 7b). To control all the experiment a point of opening and closing the lap was defined. An infrared sensor was installed on the motorcycle which receives the signal from the transmitter installed on the test track (figure 7c).

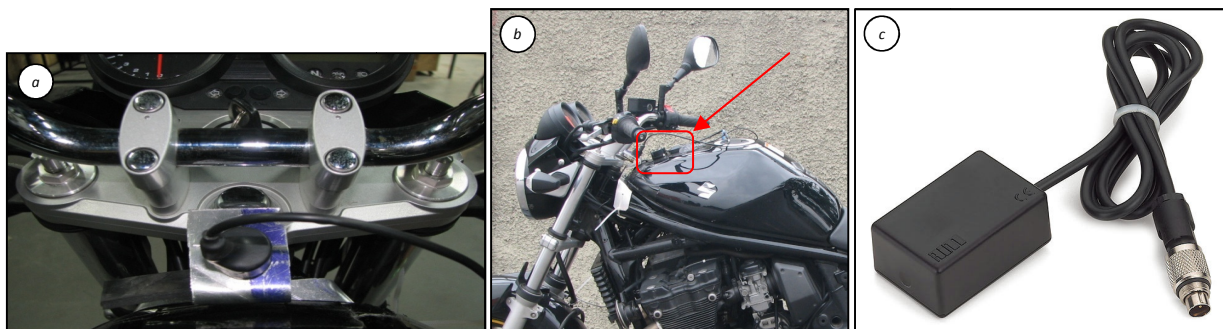


Figure 7: (left) steering angle installed, (center) GPS antenna, (right) lap sensor.

The signal acquisition system chosen was the *AIM Evo3 Lane* of Italian manufacturing and used in professional motorsport. This system was chosen because it has good performance, expandability; possess all the functions of a signal conditioner and its own software for analysis and storage of data with graphical interface. The *AIM* module was installed in the center of mass of the motorcycle (Figure 8) with the goal of using inertial accelerometers built into equipment to obtain longitudinal and lateral acceleration for further studies. The equipment normally operates at a temperature zone which was installed as in the installation manual.

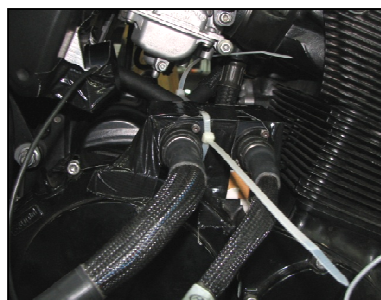


Figure 8: AIM installed in motorcycle center of mass.

To measure the motorcycle roll angle was used an articulated arm (figure 9a) fixed to the motorcycle structure with ball joints. At the other end of the articulated arm there is a tire with directional system of its own (commercially called caster), ensuring contact between the tire and the ground during the circular path. There is a LVDT (linear variable displacement transducer) in the arm that provides the location of the bar against the motorcycle, thus determining the roll angle of the motorcycle.

Detailed roll angle meter device (Figure 9b):

- 1) ϕ 150 mm caster, with self directional system;
- 2) 2x M8 screw;
- 3) 20x20 mm steel bar with 2 mm thickness;
- 4) Linking bracket
- 5) LVDT, Penny and Giles, MLS 130/150/R/N.

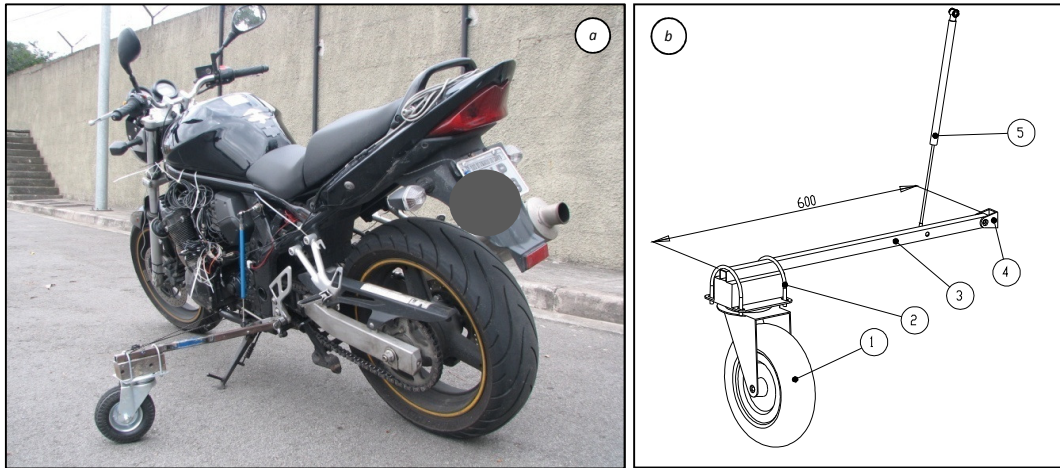


Figure 9: (a) motorcycle fully instrumented with roll meter bar, (b) roll meter device detailed.

The system was calibrated with the aid of a digital angle meter fixed to the front frame of the motorcycle, determining each sign for each roll angle of the motorcycle. The calibration curve is shown in Figure 10:

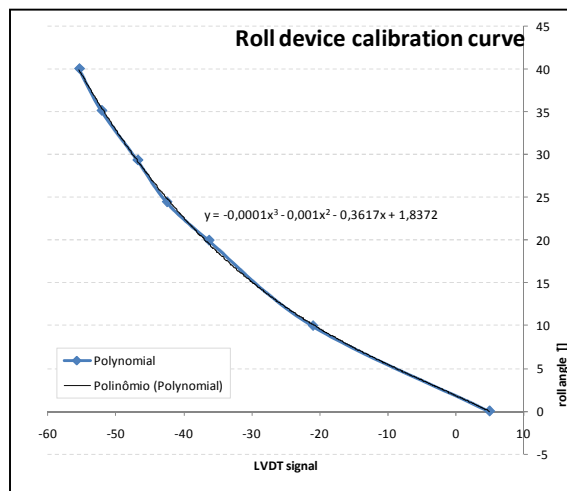


Figure 10: LVDT Calibration curve.

A table was created with the roll angle values by the input signal in signal conditioner (AIM). This curve was approximated by a polynomial of third degree, and used the function obtained in the visualization software of acquired data.

The entire test was performed at FEI University campus. Cones were used for marking the track trajectory. The rider was instructed not to move the body during the motorcycle rolling, thereby ensuring the initial condition of the model proposed (rider fixed to motorcycle rear structure). For space limitation reasons, the curvature radius of 20 m were used and varied the speed until the limit which was necessary to ensure the motorcycle balance.



Figure 11: Test performing at FEI campus.

The test was performed on two different days, the first with 14 laps and second with 10 laps. The first day was vital for the decision to create the acquisition arm for roll angle measurement. It was discovered that the accelerometers and gyroscopic inside the signal acquisition module were not efficient to manage the values tested (40°). The second day of testing was characterized by the arm implementation and partial tests to check whether the system was safe for the rider and whether the arm had sufficient bending stiffness to avoid damage to the LVDT and ensure results accuracy.

RESULTS

Simulation results

The simulation results are presented in graphs where the x-axis represents the motorcycle roll angle and y-axis represents the steering angle. The curves in full lines represent speed curves of the motorcycle and the dotted line represents the radius of curvature. The graph colors represent a simulated variable (effective steering angle, pitch angle, vertical force on the front and rear tire, lateral force on the front and rear tire, slip angle of the front and rear tire) and the results are provided by the variation of colors and with the descriptions given by the top bar or side bar of the chart.

As shown in Figure 12, it appears that even for small values of steering angle δ there is the front tire slip represented by the color gradient and scale at the top of the chart, thus producing lateral force needed to keep the motorcycle in circular path. With constant motorcycle speed by 40 km/h, there is between point K and L a variation of the radius of curvature of the motorcycle 20-70 m. In point L, it has a 30° roll angle, 3.4° of steering angle and a side slip angle of 0.7° . Point K, it has a 9° roll angle, 1.2° of steering angle and a slip angle of tire sidewall of 0.25° . It appears that at the point K, due to the large radius of curvature the motorcycle tire rolling is roughly as cinematic, causing a smaller slip angle side compared with that determined in point L.

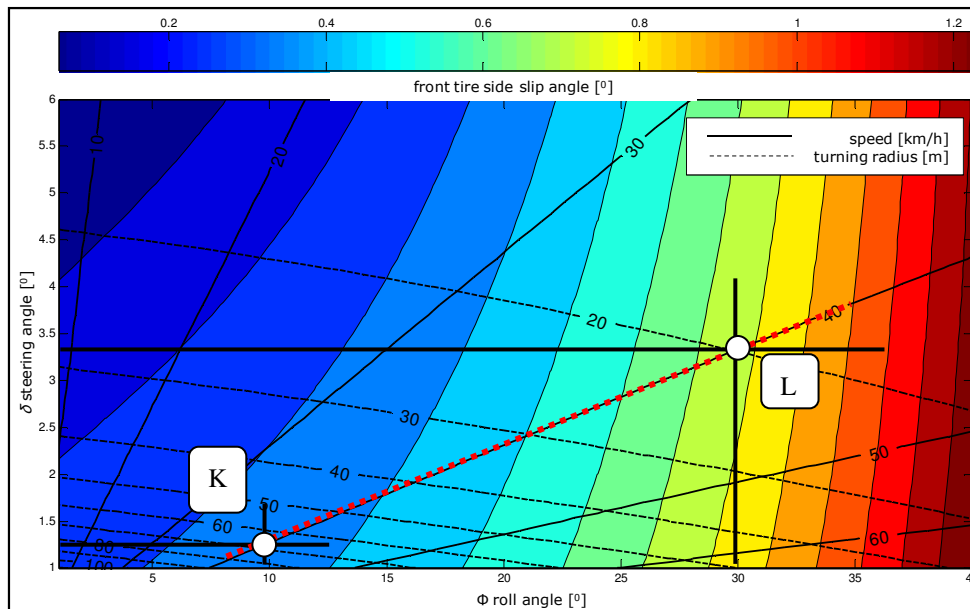


Figure 12: Front tire side slip angle variation.

Experimental results

Initially the accuracy of data collected in the test was confirmed. With the aid of GPS, the circular path of the motorcycle was found. Two tools were used to do the verification: the first was overlapping the coordinates exporting the GPS data and importing it into Google Earth (Figure 13a) and checking even the circular path than maneuvers diameter (40 m).;s

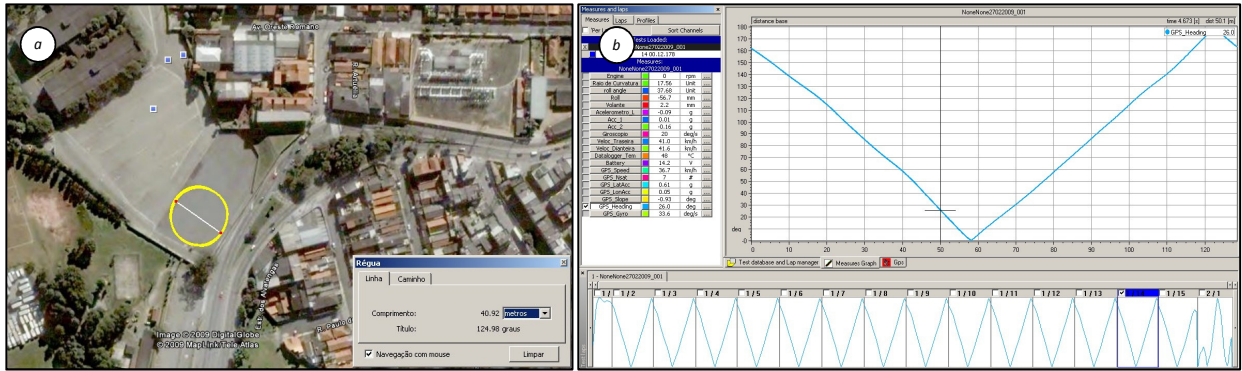


Figure 13: (a) Trajectory verification using the GPS output, (b) satellite orientation.

Another tool used was the motorcycle satellite orientation (figure 13b). There are variations between 0 and 180° linear, confirming the quality of the circular path.

The test results on the 14th lap are shown at figure 14. The horizontal axis of the graph represents the extension of the lap (about 130 m). The vertical axes represents from left to right: speed, steering angle and roll angle. The vertical bar identifies the time when the data was chosen. The red line represents the steering angle in degrees (3.02°), the blue line represents the motorcycle roll angle (34.36°) and green to the front wheel speed (42.5 km/h).

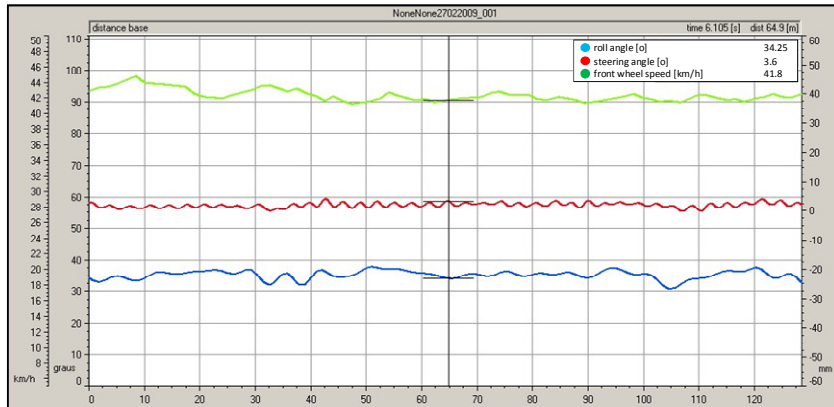


Figure 14: Experimental test results.

The figures represented above were overlaid with the graphs presented in the result simulation graphs and shown in Figure 15. First crossed 3° steering angle with 35° of roll angle on the graph in Figure 15. This overlap allows two important parameters, the speed of the motorcycle and the radius of curvature. Observe that the intersection radius of curvature is equal to 20 m theoretical and speed 45 km/h. There was a small deviation in the value of speed obtained in the practical test (42.5 km/h). This deviation was considered acceptable for low speed involved in the test.

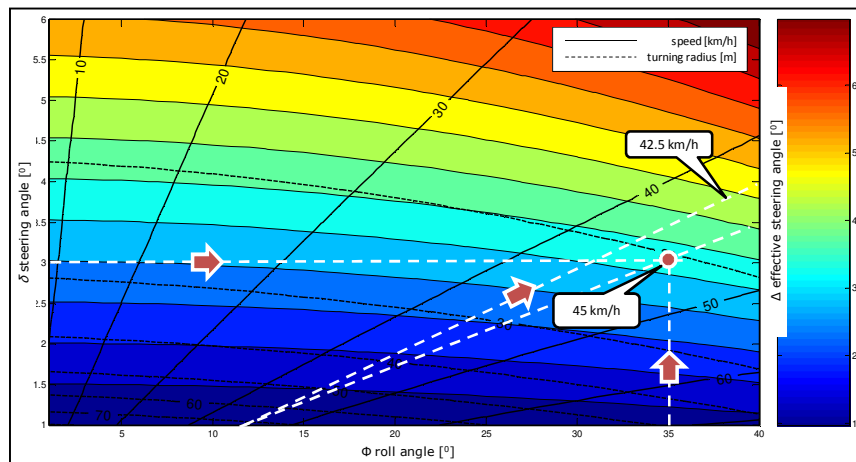


Figure 15: Experimental results overlay.

Model modification

A constant need for vehicle designers is to understand the behavior of the vehicle during the design phase, avoiding undesirable reactions or functions. This prior knowledge is only possible using computer simulations, or prototype construction, the latter usually very expensive and time consuming.

Another major function of the mathematical models is to obtain improvements of the system to certain reactions. In the specific case of this work was chosen to alter the tires characteristics and check the consequences of this in the motorcycle directional behavior. This parameter was chosen because, among the possible parameters to change in a motorcycle the tire is the simplest parameter to be changed (from the manufacturer, for example). The other parameters (geometric, for example) require changes in the mechanical characteristics of the motorcycle.

The first change was to increase by 10% the camber stiffness coefficient of the front tire, impacting on adherence of the tire to the ground; the second change was to reduce by 10% the camber stiffness coefficient of the front tire. The camber stiffness coefficient directly influences the lateral force produced by the tire.

In Figure 16, at point A on a curve with a speed of 40 km/h and curvature radius of 30 m the motorcycle must be with a steering angle of 2.5° and 22.0° roll angle. Also to do a curve with a speed of 60 km/h and radius of curvature of 40 m (B) requires a steering angle of 1.5° and roll angle of 34.0°. The speed and roll angle will be presented as a reference for future analysis. The motorcycle is equipped with tires in the "standard" configuration. The difference between the side slip of the tires provides the directional behavior of the motorcycle. It is also observed that the motorcycle has under steer behavior in under roll angles below 7° as indicated in the chart (red triangular area on the bottom left graph) and over steer above this value, characterizing the motorcycle as over steer most use.

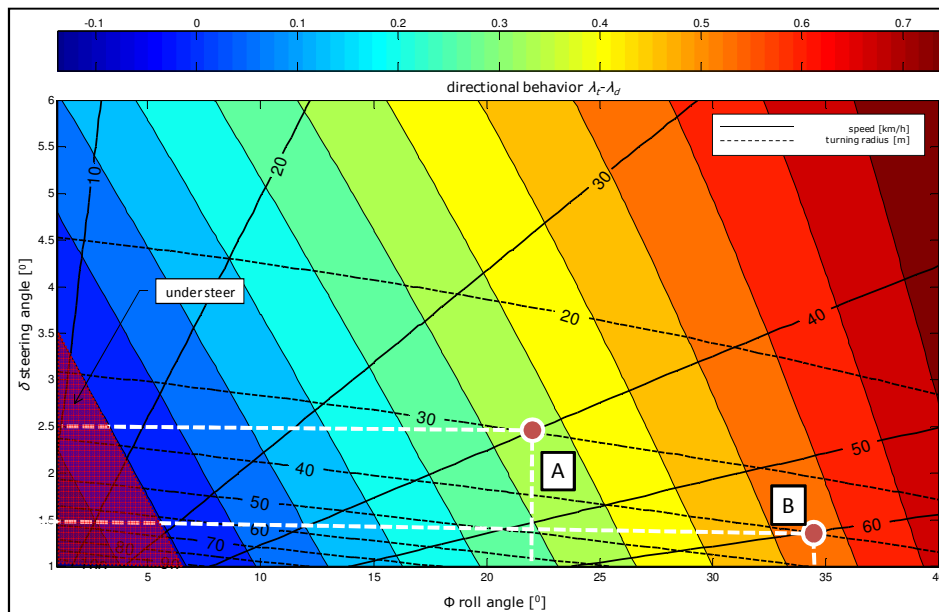


Figure 16: Variation of the difference between the front and rear tire side slip (front and rear tire "standard").

In Figure 17, the motorcycle front tire with camber stiffness coefficient increased by 10% and keeping the rear tire in the configuration standard and using the speed and radius of curvature as previously proposed (40 km/h ; 30 m 60 km/h ; 40 m) the motorcycle meets the condition of equilibrium with a steering angle of 2.3° and roll angle 22° to the first condition (A) and 1.2° of steering angle with 34° roll angle. Note a reduction in the steering angle required to meet the speed and maneuvering within the radius of curvature proposed, because the increase of camber stiffness coefficient, the tire provides greater lateral force compared with the tire in "standard" configuration.

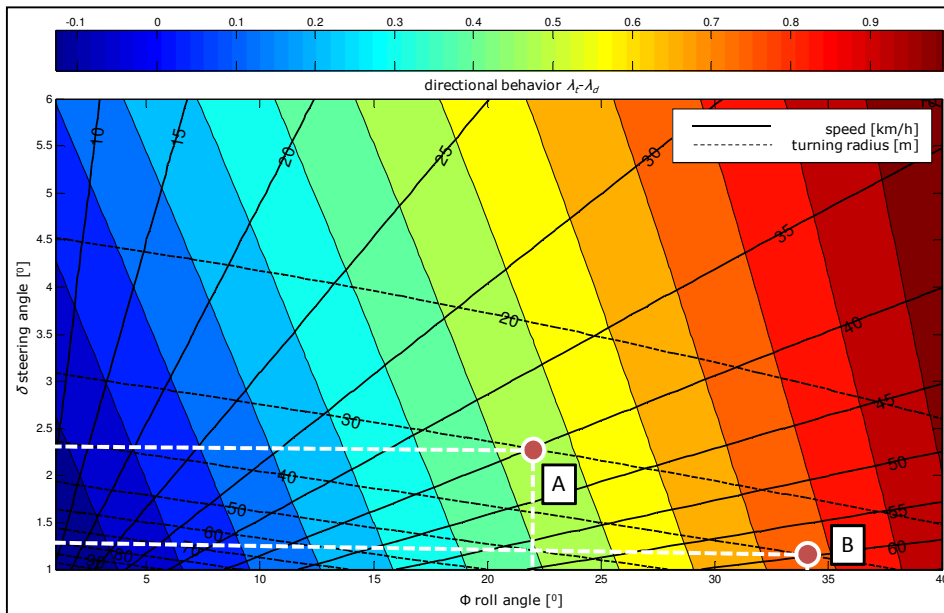


Figure 17: Variation of the difference between the front and rear tire side slip (front tire with the camber stiffness coefficient increased by 10% and rear standard).

In Figure 18, used the velocity and radius of curvature (40 km/h ; 30 m and 60 km/h ; 40 m), but the front tire had a camber stiffness coefficient reduced by 10% in the front tire and remained the rear tire to the standard configuration, the motorcycle meets the condition of equilibrium with a steering angle 2.7° and 22° of roll angle for the first hypothesis (A) and 1.7° angle of steering with 34° roll angle for the second hypothesis (B). In this configuration, the steering angle are greater in both situations, because the configuration of the tire provides less lateral force than the configuration used in "standard", requiring a steering angle increase.

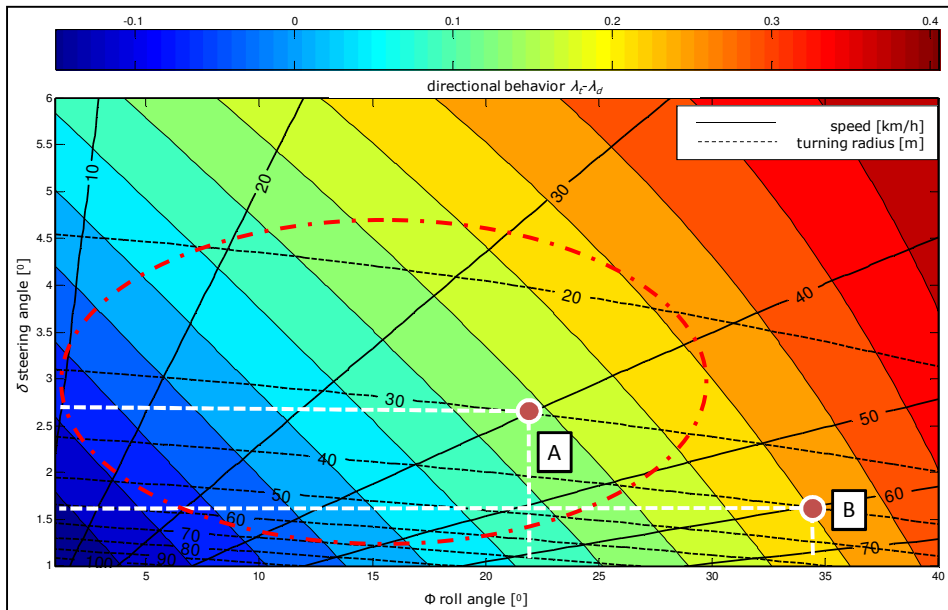


Figure 18: Variation of the difference between the front and rear tire side slip (front tire with the camber stiffness coefficient decreased by 10% and rear standard).

As result of the simulation there is a large zone that the motorcycle have neutral directional behavior ($\lambda_r - \lambda_d = 0$), featuring a motorcycle with directional behavior safer in steady state cornering. This zone can be observed in the area outlined in red dashed line in Figure 18, this area includes the regime of common use of motorcycles.

CONCLUSION

This work allowed interacting directly with a multibody model of a motorcycle in a steady state curve. This model is useful in the development phase of a motorcycle anticipating directional characteristics and behaviors reducing development time and prototype test vehicles, which are usually expensive and require long construction time.

The graphical results allowed a unified view of the simulated variation parameters versus the input parameters (steering angle and roll angle) and speed of the motorcycle and radius of curvature.

The mathematical model has consistent appropriate results for the proposed changes, as theory suggested by the references used in this work.

There was also a need to adapt the automotive dedicated data acquisition equipment to use on motorcycles, because the high angles of roll (about 40°) present a problem for conventional signal acquisition "hardware" used in automotive applications, where angles are no bigger than 7° . The construction of a specific device for reading the roll angle of the motorcycle was of vital importance to the experiment and made the data acquisition system more flexible as to the applicability. Even the system added to a point of contact between the motorcycle and to the ground due to contact of rotation on the ground which did not influence the lateral dynamics of the motorcycle and so little on results.

The results of the mathematical model are compatible with the experimental results, for the range of speeds and radii of curvature.

The study confirmed the different directional motorcycle behavior to vary the camber stiffness coefficient to the front tire. The directional behavior is an important feature in the development of a motorcycle making it safer and easier the riding.

ACKNOWLEDGMENTS

To my beloved parents, my wife and Dr. Agenor de Toledo Fleury.

REFERENCES

- Breur, T; Pruckner, A. (1998): "Advanced dynamics motorbike analysis and driver simularion". In: 13th European ADAMS User Conference, Paris, 1998.
- Berrita, R.; Biral, F.; Garbin,S. (2000): "Evaluation of motorcycle handling and multibody modeling and simulation". In: Proceedings of 6th int. conference on high tech engines and cars, Modena, 2000.
- Cossalter, V. "Motorcycle Dynamics", 2008, Second Edition.
- Cossalter, V. "Gli pneumatici della motocicletta": 2008. Disponível em: <http://www.dinamoto.it/DINAMOTO/online%20papers/Pneumatici_file/Pneumatici.htm> Acesso em: 13 out. 2008.
- Cossalter, V., Da Lio Mauro, Lot Roberto. "Steady Turning of Two-Wheeled Vehicles". Vehicle System Dynamics, EUA, v. 31, n. 2, p. 157-181, fev. 1999.
- Iffelsberger, L. (1991): "Application of vehycle dynamics simulation in motorcycle development". Safety enviroment future. Forschungsefte Zweiradsicherheit, 7, 1991.
- Koenen, C.."Vibrational modes of motorcycle in curves." In: Proceedings of the int. motorcycle safety conference, Wash. D.C., Motorcycle safety foundation, Vol. II, 1980.
- Meijaard J. P., Papadopoulos J. M., Ruina A. and Schwab4 A. L.: "Linearized dynamics equations for the balance and steer of a bicycle: a benchmark and review", 2006.
- MILLIKEN, W.F.; MILLIKEN, D.L. Race car vehicle dynamics. SAE International, Warrendale, 1995.
- Pacejka, H.B. "Tire and vehicle dynamics". 2002. Society of Automotive Engineers, Inc.
- REIMPELL, J.; STOLL, H.; BETZLER J. The automotive chassis: Engineering principles. Butterworth Heinemann, 2001.
- Sharp, R.S. "Stability, control and steering responses of motorcycles". Vehicle system dynamics, 35, 4-5, 2001.
- Sharp, R.S. "The stability and control of motorcycles". Journal of mechanical engineering science, 13, 5, I.Mech. E., 1971.
- Wisselman, D.; Iffelsberger, D.; Brandlhuber, B. (1993): "Einsatz eines Fahrdynamik-simulationsmodells in der motorradentwicklung bei BMW". ATZ, 95, 2, 1993.
- Whipple, F.J.W. The Stability of the motion of a bicycle. Quart. J. of purê and applied mathematics, 30, 1899.

RESPONSIBILITY NOTICE

The author(s) is (are) the only responsible for the printed material included in this paper.

On the Active and Semi-Active controls of the Helicopter Blade-Sailing Phenomenon in Unsteady Flow

Kleber A. L. Castão¹, Vinicius Piccirillo¹, Luiz C. S. Góes¹, Roberto L. C. B. Ramos²

¹ Instituto Tecnológico de Aeronáutica - Praça Marechal Eduardo Gomes, 50 - Vila das Acácias - CEP 12.228-900, SP, Brasil, pcmec@ita.br, kcastao@ita.br, goes@ita.br.

² Universidade Federal do ABC - Rua Oratório, 305 - Bangu - CEP 09280-550, SP, Brasil, rlcbamos@gmail.com

Abstract: In this paper is presented a mathematical modeling of a very important phenomenon that occurs in helicopters and the application of some techniques of active and semi-active control to eliminate the occurrence of this one. Is also done in this paper the analysis of the unsteady flow response of a helicopter Blade-Sailing using two different smart-materials and the predictive control strategies trying to avoid this phenomenon. The semi-active control strategy is carried out involving a Magnetorheological damper (MRD) and the predictive control is done using the MPC technique. The aeroelastic analysis focuses on the performance of a proposed semi-active and active controllers with respect to the reduction of blade flapping vibrations in articulated rotors during engagement shipboard operations.

Keywords: Blade Sailing Phenomenon, Magnetorheological Damper, Predictive Control, Unsteady Flow.

INTRODUCTION

Flow-induced unsteady loads are often related to large vibrations and damage in flexible structures. Shipboard helicopters, operating in the hostile maritime environment from frigate-like platforms, are especially susceptible to these effects during rotor engagement/disengagement operations under high wind-over-deck (WOD) conditions. These dangerous conditions are amplified by the ship structure, which generates flow velocity gradients and vortices over the flight deck. Therefore, shipboard helicopter operations are among the most hazardous military operations and the shipboard environment imposes severe restrictions on the missions and determines stringent requirements for the design of aerial vehicles.

The problem of flight in the vicinity of ships is usually called Dynamic Interface (DI) problem (Rhodes and Healey, 1992). Among the dynamic phenomena in the DI that must be analyzed and controlled, one is especially important for rotary-wing aircraft: *blade sailing*.

Blade sailing is an aeroelastic transient phenomenon characterized by the occurrence of large flapping vibrations, possibly associated with tunnel/tail-boom strikes, due to fluid-structure interactions during engagement or disengagement operations of helicopter rotors under high wind conditions (Newman, 1995). The blade-sailing control problem has a theoretical importance, due to the nonlinear time-varying characteristics of the associated blade flapping oscillator, which is also subjected to large disturbances. Considering the ubiquitous use of the shipboard helicopter in critical defense missions, the problem has a practical relevance as well, as shown by a recent NATO symposium about the study of flow-induced unsteady loads and the impact on military applications (Wall et al., 2005).

In order to avoid this aeroelastic phenomenon in the helicopter rotor, we have used a new smart material, the Magnetorheological Damper (MRD). The MRD is a device which have a type of smart fluid inside, when this fluid is subjected to a magnetic field, it greatly increases its apparent viscosity, to the point of becoming a visco-elastic solid. The yield stress of the fluid when in its active state can be controlled very accurately by varying the magnetic field intensity. With the same objective, we have developed a predictive controller, using MPC technique, obtaining very good results.

AEROELASTIC MODELING AND NUMERICAL RESULTS TO THE MRD APLICATION

The blade-sailing aeroelastic model to response problems can be greatly simplified by considering the forces and moments actuating only in the flapping plane, as shows Fig. 1. The forces at the blade element for the simplified blade-sailing planar model, according to a frame rotating with the blade.

The simplified diagram of forces at a planar blade element, see Newman (1995), illustrates the main factors that govern the blade-sailing behavior. The resulting moments about the flapping hinge in conjunction with the droop/flap stop effects, modeled as a nonlinear rotational spring (representing the stiffness), determine the blade tip deflections related to the angle β . Ship motion effects are not included.

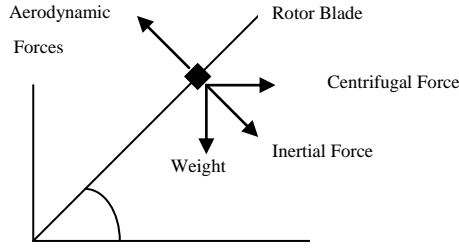


Figure 1: Forces at a flapping planar blade element for the proposed blade-sailing model (rotating frame)

Fig. 2 shows the flow velocity components in the plane of the rotor for the proposed blade-sailing model, considering the WOD conditions. V_{WOD} and Ψ_{WOD} are, the magnitude and direction, respectively, of the incoming wind velocity with respect to the ship centerline

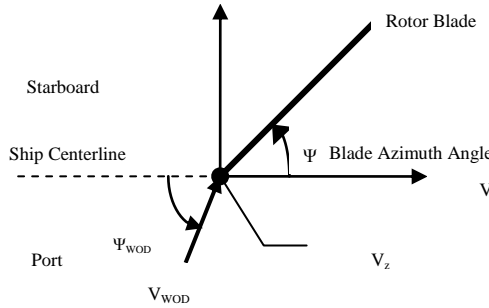


Figure 2: Flow velocity components for the WOD conditions

The blade-sailing modeling is based on a proposed rotary-wing aeroelastic scheme applied to articulated shipboard rotor blades, according to the Figs. 1 and 2, taking into account some simplifying assumptions (Ramos, 2007; Ramos et al, 2009a; Ramos et al, 2009b). The flapping motions of the blade with the effect of MRD, are represented by the following equations:

$$I_B \ddot{\beta} + I_B \Omega^2 \beta + I_B \sigma(\beta) + F_d(\dot{\beta}, i) = -I_B \frac{3}{2R} g + M_{as} + M_u \quad (1)$$

where term M_{as} is the moment due to the aerodynamic forces related to the ship airwake, collective/cyclic commands and rotor blade motions, $F_d(\dot{\beta}, i)$ is the force generated by the MRD and the M_u is related to the control inputs .

The three-dimensional ship airwake pattern can be modeled according to the mean $(\overline{V}_x, \overline{V}_y, \overline{V}_z)$ and fluctuating (V'_x, V'_y, V'_z) flow velocity WOD components, as follows (Keller, 2001):

$$\mathbf{V}_x = \overline{\mathbf{V}}_x + \mathbf{V}_x, \quad \mathbf{V}_y = \overline{\mathbf{V}}_y + \mathbf{V}_y, \quad \mathbf{V}_z = \overline{\mathbf{V}}_z + \mathbf{V}_z \quad (2)$$

The flow field that affects the rotor behavior is non-uniform and unsteady, thus, the three velocity components vary with space and time. Mean flow velocity gradients arise due to the ship geometry and the fluctuating flow velocity components arise due to the ship geometry and also to the meteorological effects, like turbulence from storms.

To simplify the aeroelastic analysis, only the lateral (90° or 270°) wind condition is considered, focusing the ship air wake modeling on the effects of the horizontal and vertical velocity components related to this worst-case blade-sailing condition (Newman 1990). The WOD velocity component V_x is neglected. For a typical frigate-like configuration with only one flight deck, as considered in this work, the WOD horizontal velocity V_y for the lateral condition can be considered uniform along the shipboard rotor.

The mean flow vertical velocity related to the interaction between the lateral undisturbed wind flow and a typical frigate-like structure can be approximated by a linear distribution along the flight deck and the helicopter rotor (Newman, 1990; Geyer et al, 1998; Keller, 2001). Therefore, for a rotor blade element at radial station r and azimuth Ψ , and constant WOD horizontal velocity component V_y , the WOD mean vertical velocity, according to the linear distribution approximation (“linear gust model”), is given by:

$$\overline{V}_z = K_v V_y \frac{r}{R} \sin \Psi \quad (3)$$

Unsteady flow effects can be modeled by considering a sinusoidal gust across the rotor disk for the WOD fluctuating vertical velocity component, representing the effects of the dominant frequency ω_f of the ship air wake on the helicopter rotor, as follows:

$$V'_z = K_f V_y \sin \omega_f t \quad (4)$$

The gust amplitude parameters K_v and K_f , and the sinusoidal gust frequency ω_f govern the flow-induced unsteady loads associated with the WOD vertical velocity component, which characterizes a flow field over the flight deck that varies with space and time according to Eqs. 3 and 4.

The aerodynamic components affecting a shipboard rotor blade can be calculated according to the blade-element theory, as follows (Keller, 2001):

$$\begin{aligned} V_x &= V_{WOD} \cos \Psi_{WOD}, & V_y &= V_{WOD} \sin \Psi_{WOD}, \\ U_T &= \Omega r - V_y \cos \Psi + V_x \sin \Psi, \\ U_P &= r\dot{\beta} + (V_y \sin \Psi + V_x \cos \Psi)\beta - V_z \end{aligned} \quad (5)$$

In particular, Ψ_{WOD} is equal to 90° for lateral port side winds and to 270° for lateral starboard side winds. U_P and U_T are, respectively, the normal and tangential flow velocity components at the blade element at radial station r , azimuth Ψ and flapping angle β . These flow velocity components are illustrated in Fig. 3, according to the blade-element theory (Dowell, 1995). $V_z(r, \Psi)$ is the WOD vertical velocity at a blade element and $\Omega(t)$ is the time-varying rotational speed during shipboard engagement or disengagement operations.

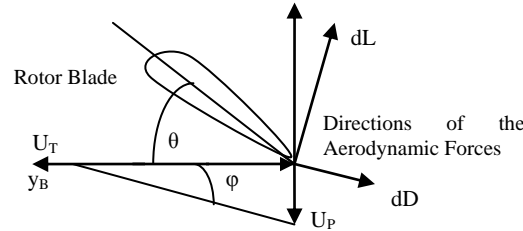


Figure 3: Aerodynamic forces and flow velocities at a blade element.

The lift force dL and the aerodynamic moment dM_{as} for a blade element can be obtained from the following equations:

$$\begin{aligned} \theta_0 &= \theta_{.75} - (3/4)\theta_{tw} \\ \theta &= \theta_0 + \theta_{1s} \sin \Psi + \theta_{1c} \cos \Psi + \theta_{tw}(r/R) \\ \alpha &= \theta - (U_P / U_T) \\ dL &= (1/2)\rho U_T^2 ca \alpha dr \\ dM_{as} &= r dL \end{aligned} \quad (6)$$

Eq. 6 yields the following aerodynamic moment at a blade element on the radial position r :

$$dM_{as} = \frac{1}{2} \rho U_T^2 ca \left(\theta - \frac{U_P}{U_T} \right) r dr = \frac{1}{2} \rho ac (\theta U_T^2 - U_P U_T) r dr \quad (7)$$

Substituting the expressions for the blade-element flow velocities given by Eq. 5 into Eq. 7 and integrating along the blade, yields:

$$M_{as} = \frac{1}{2} \rho a c \int_0^R \left\{ \begin{aligned} &\theta (\Omega r - V_y \cos \Psi + V_x \sin \Psi)^2 - \\ &-(\Omega r - V_y \cos \Psi + V_x \sin \Psi) \left[r \dot{\beta} + (V_y \sin \Psi + V_x \cos \Psi) \beta - V_z \right] \end{aligned} \right\} r dr \quad (8)$$

Considering that:

$$I_B = \frac{\mu R^3}{3}; \quad \gamma \equiv \frac{3 \rho a c R}{\mu}; \quad \mu_x \equiv \frac{V_x}{\Omega R}; \quad \mu_y \equiv \frac{V_y}{\Omega R} \quad (9)$$

where γ is the Lock number and μ_x, μ_y are advance ratio parameters, Eq. 8 yields for the blade aerodynamic moment:

$$M_{as} = M_{ai} + M_{atw} + M_{a\dot{\beta}} + M_{a\beta} + M_{az} \quad (10)$$

where:

$$\begin{aligned} M_{ai} &= I_B \frac{\gamma \Omega^2}{8} \left[1 + \frac{8}{3} (\mu_x \sin \Psi - \mu_y \cos \Psi) + 2 (\mu_x \sin \Psi - \mu_y \cos \Psi)^2 \right] \theta_i \\ M_{atw} &= I_B \frac{\gamma \Omega^2}{2} \left[\frac{1}{5} + \frac{1}{2} (\mu_x \sin \Psi - \mu_y \cos \Psi) + \frac{1}{3} (\mu_x \sin \Psi - \mu_y \cos \Psi)^2 \right] \theta_{tw} \\ M_{a\dot{\beta}} &= I_B \frac{\gamma \Omega}{8} \left[-1 - \frac{4}{3} (\mu_x \sin \Psi - \mu_y \cos \Psi) \right] \dot{\beta} \\ M_{a\beta} &= I_B \frac{\gamma \Omega^2}{8} \left[-\frac{4}{3} (\mu_x \cos \Psi + \mu_y \sin \Psi) + (\mu_y^2 - \mu_x^2) \sin 2\Psi + 2\mu_x \mu_y \cos 2\Psi \right] \beta \\ M_{az} &= I_B \frac{\gamma \Omega}{8R} \left\{ \left[1 + \frac{4}{3} (\mu_x \sin \Psi - \mu_y \cos \Psi) \right] V_{zg} + \left[\frac{4}{3} + 2 (\mu_x \sin \Psi - \mu_y \cos \Psi) \right] V_{zu} \right\} \end{aligned} \quad (11)$$

and

$$\begin{aligned} \theta_i &= \theta_0 + \theta_{1s} \sin \Psi + \theta_{1c} \cos \Psi \\ V_{zg} &= K_v V_y \sin \Psi \\ V_{zu} &= K_f V_y \sin \omega_f t \end{aligned} \quad (12)$$

In Eq. 11, $M_{ai}, M_{atw}, M_{a\dot{\beta}}, M_{a\beta}, M_{az}$ are, respectively, the aerodynamic moments due to the blade pitch input, to the blade built-in twist, to the blade flapping rate, to the blade flapping angle, and to the WOD vertical velocity. The WOD vertical velocity factor related to the flow velocity gradients V_{zg} in Eq. 12 is valid, in particular, for lateral wind conditions ($V_x = 0$, $\Psi_{WOD} = 90^\circ$ or 270°), according to the linear distribution approximation for the ship airwake given by Eq. 3. For more details, see (Ramos, 2007; Ramos et al, 2009a; Ramos et al, 2009b)..

Then, the equations obtained to represent this problem and with the MRD effect are

$$\begin{aligned} &\ddot{\beta} + \frac{\gamma \Omega}{8} \left[1 + \frac{4}{3} (\mu_x \sin \Psi - \mu_y \cos \Psi) \right] \dot{\beta} \\ &+ \Omega^2 \left\{ 1 + \frac{\gamma}{8} \left[\frac{4}{3} (\mu_x \cos \Psi + \mu_y \sin \Psi) - (\mu_y^2 - \mu_x^2) \sin 2\Psi - 2\mu_x \mu_y \cos 2\Psi \right] \right\} \beta + \\ &\sigma(\beta) + F_d(\dot{\beta}, i) = + \frac{\gamma \Omega^2}{8} \left[1 + \frac{8}{3} (\mu_x \sin \Psi - \mu_y \cos \Psi) + 2 (\mu_x \sin \Psi - \mu_y \cos \Psi)^2 \right] \theta_i \\ &+ \frac{\gamma \Omega^2}{2} \left[\frac{1}{5} + \frac{1}{2} (\mu_x \sin \Psi - \mu_y \cos \Psi) + \frac{1}{3} (\mu_x \sin \Psi - \mu_y \cos \Psi)^2 \right] \theta_{tw} - \frac{3}{2R} g \\ &+ \frac{\gamma \Omega}{8R} \left\{ \left[1 + \frac{4}{3} (\mu_x \sin \Psi - \mu_y \cos \Psi) \right] V_{zg} + \left[\frac{4}{3} + 2 (\mu_x \sin \Psi - \mu_y \cos \Psi) \right] V_{zu} \right\} \end{aligned} \quad (15a)$$

The term in red represents the effect of MRD in the equation. Put this equation in state variable form, becomes possible to obtain the behavior of our system under MRD effects and in Unsteady flow effects.

And to the active control simulations, we have:

$$\begin{aligned}
 & \ddot{\beta} + \frac{\gamma\Omega}{8} \left[1 + \frac{4}{3} (\mu_x \sin \Psi - \mu_y \cos \Psi) \right] \dot{\beta} + \Omega^2 \left\{ 1 + \frac{\gamma}{8} \left[\frac{4}{3} (\mu_x \cos \Psi + \mu_y \sin \Psi) - \right. \right. \\
 & \left. \left. - (\mu_y^2 - \mu_x^2) \sin 2\Psi - 2\mu_x \mu_y \cos 2\Psi \right] \right\} \beta + \sigma(\beta) = \\
 & \frac{\gamma\Omega^2}{8} \left[1 + \frac{8}{3} (\mu_x \sin \Psi - \mu_y \cos \Psi) + 2 (\mu_x \sin \Psi - \mu_y \cos \Psi)^2 \right] \theta_u \\
 & + \frac{\gamma\Omega^2}{8} \left[1 + \frac{8}{3} (\mu_x \sin \Psi - \mu_y \cos \Psi) + 2 (\mu_x \sin \Psi - \mu_y \cos \Psi)^2 \right] \theta_i + \\
 & \frac{\gamma\Omega^2}{2} \left[\frac{1}{5} + \frac{1}{2} (\mu_x \sin \Psi - \mu_y \cos \Psi) + \frac{1}{3} (\mu_x \sin \Psi - \mu_y \cos \Psi)^2 \right] \theta_{tw} \\
 & + \frac{\gamma\Omega}{8R} \left\{ \left[1 + \frac{4}{3} (\mu_x \sin \Psi - \mu_y \cos \Psi) \right] V_{zg} + \left[\frac{4}{3} + 2 (\mu_x \sin \Psi - \mu_y \cos \Psi) \right] V_{zu} \right\} - \frac{3}{2R} g
 \end{aligned} \tag{15b}$$

Therefore, according Eq. 15b, the single-degree-of-freedom blade-sailing behavior is governed by a nonlinear ordinary differential equation (ODE) with time-varying coefficients. To carry out the parametric and control analysis, the nonlinear aeroelastic blade-sailing Eq. 15b can be rewrite as following;

$$\ddot{\beta} + c_{\dot{\beta}}(t)\dot{\beta} + c_{\beta}(t)\beta + \sigma(\beta) = u(t) + x_0(t) \tag{15c}$$

where $c_{\dot{\beta}}(t)$, $c_{\beta}(t)$ are the damping and stiffness time varying coefficients, respectively, $\sigma(\beta)$ is the nonlinear stiffness function related to the droop/flap stop effects, $u(t)$ represent the active control input and $x_0(t)$ is the sum of the effects due to the exogenous inputs at the right side of Eq. (4).

Considering $x = \begin{bmatrix} \beta & \dot{\beta} \end{bmatrix}^T = \begin{bmatrix} x_1 & x_2 \end{bmatrix}^T$, a state-space model can be obtained from Eq. (5) as follows:

$$\begin{aligned}
 \dot{x}_1 &= x_2 \\
 \dot{x}_2 &= -c_{\dot{\beta}}(t)x_2 - c_{\beta}(t)x_1 - \sigma(x_1) + u(t) + x_0(t)
 \end{aligned} \tag{15d}$$

MRD Theoretical Model

It is well known that the Magnetorheological Fluid (MRF) consists of a mineral oil based fluid (or silicone, water, etc.) with micron magnetic particles in suspension, which line up in parallel to a applied magnetic field, forming a species of chain. When the structure is submitted to a vibration, these chains break, wasting energy and, the magnetic field cause the reconstruction of them. The continuous breaking and reconstitution of these chains allow the fluid to waste energy of the system (Liu, 2000), by responding in this way, the damping presents a hysteretic behavior.

The hysteretic model of MRD used in this paper was presented Pierrick Jean in his PhD thesis (Pierrick, 2006). This model considers several properties of the damper in each region of the operation, pre-yield and pos-yield, for example.

Below, are presented the equations that represent the hysteretic model:

$$\begin{aligned}
 F_d &= k_{pre}(i_c)(x_2 - x_1) + c_{pre}(\dot{x}_2 - \dot{x}_1) \\
 m_1 \ddot{x}_1 &= k_{pre}(i_c)(x_2 - x_1) + c_{pre}(i_c)(\dot{x}_2 - \dot{x}_1) - \chi(\dot{x}_1, i_c) \\
 \chi(\dot{x}_1, i_c) &= F_y(i_c) \tanh(\alpha \dot{x}_1) + c_{post}(i_c) \dot{x}_1 \\
 k_{pre}(i_c) &= a_{pr} + b_{pr} \tanh(c_{pr} i_c) \\
 c_{pre} &= cte, \alpha = cte \\
 F_y(i_c) &= a_y + b_y \left(1 + \frac{c_y}{d_y - c_y} e^{-i_c/c_y} + \frac{d_y}{c_y - d_y} e^{-i_c/d_y} \right) \\
 c_{post}(i_c) &= a_{po} + b_{po} \tanh(c_{po} i_c)
 \end{aligned} \tag{16}$$

where F_d is the force generated by the damper and $k_{pre}, c_{pre}, \chi(\dot{x}_1, i_c), F_y, c_{post}, \alpha$ are values that control the hysteresis loop of the model and are related to the characteristics of the fluid and to the characteristics of the device. Note that the parameters k_{pre}, F_y and c_{post} are dependent of the applied current in the damper. Below Fig.4a shows the hysteresis loops obtained by simulations of the model.

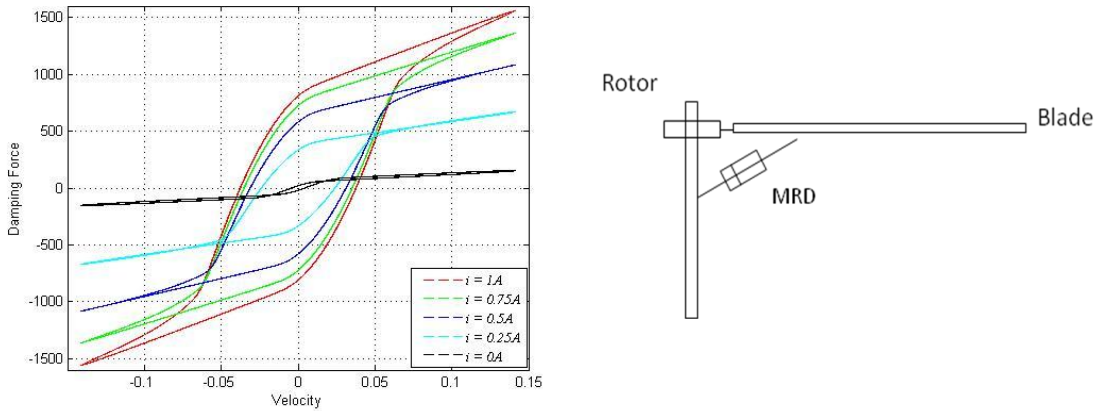


Fig. 4. Hysteresis loops of the MRD model.

To summarize, we have a model of the MR damper that enables one to predict the damper force as a function of piston displacement and velocity (relative to the damper body displacement and velocity) and of the current in the damper coil.

The proposed application of the MRD in this problem, was presented in Fig. 4b, Thus, we have:

$$M_{Fd} = r_{MR} F_d(i, \dot{\beta}) \quad (16)$$

where r_{MR} is the point where the MRD is fixed in the blade.

Numerical simulations

In the numerical simulations, are presented four conditions, obtained by the combinations of the parameters of horizontal WOD velocities and linear WOD gust to obtain situations where the blade sailing phenomenon is worst, that is, the blade reaches the tail of the helicopter. The current applied to the MRD is increased to obtain a lot of results in order to show the effect of this device, searching a good suppression of the blade sailing phenomenon.

The combinations used in the simulations are:

1. A starboard side uniform WOD horizontal velocity of 42.5 kt with a WOD linear gust parameter Kv equal to 0.1;
2. A starboard side uniform WOD horizontal velocity of 45 kt with a WOD linear gust parameter Kv equal to 0.1;
3. A starboard side uniform WOD horizontal velocity of 42.5 kt with a WOD linear gust parameter Kv equal to 0.25;

The parameters used in these simulations are the same used in Ramos et al (2009a) and Geyer et al (1998) and are based on the H-46 Sea Knight shipboard helicopter, which has a history of several tunnel-strike occurrences during engagement and disengagement operations in the DI.

Now, we show the results of the simulated conditions.

Is possible to observe that, in the first condition (Fig. 5a), the simulation of blade sailing phenomenon without the MRD effect show that the blade reaches the tail boom of the helicopter. But, with the inclusion of the MRD in the rotor and increasing the current applied to the damper, we get a good attenuation of the blade amplitude, showing an alternative to suppression of the phenomenon, with a little applied current in the damper, using little energy.

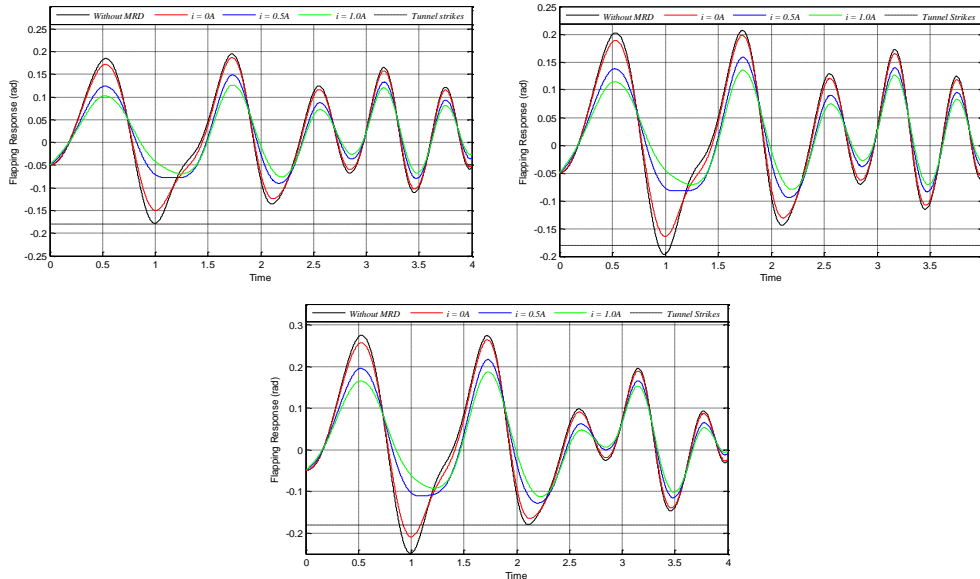


Figure 5: Flapping response to the three situations

In the second simulation, see Fig. 5b, is showed a condition where the blade exceeds the amplitude that occurs the tunnel strikes. This condition is very dangerous. Hence, we show the MRD effect in this situation, this is, we can see a great blade motion reduction, effectively reducing the phenomenon studied.

The MRD also remove the blade sailing phenomenon in the third condition (Fig. 5c). Note that, in first and second conditions with $I = 0A$, the tunnel strikes is removed, but in this condition with $I = 0A$, the phenomenon is not removed. With the increase of the current, the objective is reached.

AEROELASTIC MODELING AND NUMERICAL RESULTS TO THE PREDICTIVE CONTROL STRATEGY

Fig. 6 presents the main elements of the discrete-time predictive control formulation adopted in this work. The process model is employed to calculate output predictions up to N steps in the future, where N is termed “Prediction Horizon”. Such predictions are determined on the basis of all information available up to the present time (k^{th} sampling instant), and are also dependent on the control sequence that will be applied. The optimization algorithm is aimed at determining the sequence $\{u[k-1+i], i = 1, \dots, M\}$ that minimizes the cost function specified for the problem, subject to constraints on the input and output of the plant. The value of M (“Control Horizon”) is smaller than N , and the optimization assumes that $u[k-1+i] = u[k+M-1]$ for $M < i \leq N$. The control is implemented in a receding horizon manner, that is, only the first element of the optimized control sequence is applied to the plant and the optimization is repeated at the next sampling instant, on the basis of fresh state measurements.

The plant input, the output of interest and the reference signal are denoted by $u \in \mathbb{R}^2$, $y \in \mathbb{R}$, and $r \in \mathbb{R}$, respectively. In addition, $\hat{y}[k+i|k]$ denotes the prediction of the output at instant $k+i$ on the basis of the measured state $x[k] \in \mathbb{R}^2$. The optimal control at instant k is denoted by $u^*[k]$.

The task of designing a predictive control law can be divided into two phases. The first concerns the identification of a mathematical model capable of representing the behavior of the real process. The second is linked to implementation of a predictive control algorithm appropriate. This determines the control actions based on the minimization of a cost function considering future responses predicted in the model of the process.

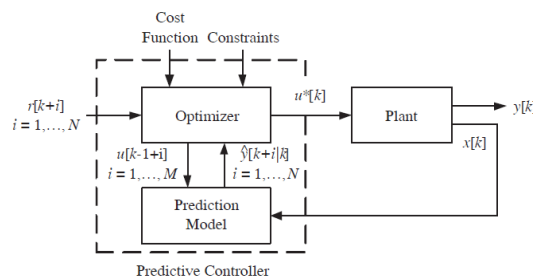


Figure 6: Predictive control loop employing state feedback.

Assuming the linear model for the plant dynamics, the state equations and output can be discretized in the form below:

$$\begin{aligned} x(k+1) &= Ax(k) + Bu(k) \\ y(k) &= Cx(k) \end{aligned} \quad (17)$$

It can then be shown in Maciejowski (2002), that the output predictions can be related to the future control variations as $\hat{Y} = G\Delta\hat{U} + \hat{F}$, where

$$G = HT_N, \quad \hat{F} = H1_N u(k-1) + \Phi x(k)$$

and

$$\hat{Y} = \begin{bmatrix} \hat{y}[k+1] \\ \hat{y}[k+2] \\ \vdots \\ \hat{y}[k+N] \end{bmatrix}, H = \begin{bmatrix} CB & 0 & \dots & 0 \\ CAB & CB & \dots & 0 \\ \vdots & \vdots & \ddots & \vdots \\ CA^{N-1}B & CA^{N-2}B & \dots & CB \end{bmatrix}, \Phi = \begin{bmatrix} CA \\ CA^2 \\ \vdots \\ CA^N \end{bmatrix}$$

where T_N is a lower triangular matrix of ones ($T_N(i, j) = 1$ for $i \geq j$ and zero otherwise). Thus, the quadratic cost function that penalizes both tracking errors and control variations can be written in matrix form as;

$$J(\Delta\hat{U}) = (Y - R)^T (Y - R) + \rho \Delta\hat{U}^T \Delta\hat{U} \quad (18)$$

where

$$\begin{aligned} R &= [r[k+1], r[k+2], \dots, r[k+N]]^T \\ \Delta u[k] &= u[k] - u[k-1] \\ \Delta U &= [\Delta u[k], \Delta u[k+1], \dots, \Delta u[k+M-1]]^T \end{aligned}$$

are the vectors of optimization variables. It can thus be seen that the cost is a quadratic function of the optimization variables. The design parameter $\rho > 0$ may be adjusted to achieve a compromise between minimizing the output tracking error and minimizing variations on the control signal. Decreasing ρ tends to increase the speed of the closed-loop response at the cost of a larger control effort and a greater sensitivity to measurement noise.

In the absence of constraints, the control sequence ΔU^* that minimizes the cost function is given by $\Delta U^* = (G^T G + \rho I_M)^{-1} G^T (R - \hat{F})$, where I_M is an $M \times M$ identity matrix.

If restrictions on the manipulated and controlled variables of the form $\Delta u_{\min} \leq \Delta u[k-1+i] \leq \Delta u_{\max}$, $i = 1, \dots, M$, $u_{\min} \leq u[k-1+i] \leq u_{\max}$, $i = 1, \dots, M$, $y_{\min} \leq \hat{y}[k+1|k] \leq y_{\max}$, $i = 1, \dots, N$ are to be satisfied, the minimization of the cost is subject to the following linear constraints on ΔU :

$$\begin{bmatrix} I_M \\ -I_M \\ T_M \\ -T_M \\ G \\ -G \end{bmatrix} \Delta\hat{U} \leq \begin{bmatrix} \Gamma_M \Delta u_{\max} \\ -\Gamma_M \Delta u_{\max} \\ \Gamma_M [u_{\max} - u(k-1)] \\ \Gamma_M [u(k-1) - u_{\max}] \\ \Gamma_M y_{\max} - \hat{F} \\ \hat{F} - \Gamma_M y_{\max} \end{bmatrix} \quad (19)$$

where T_M is a lower triangular matrix of one's ($T_M(i, j) = 1$ for $i \geq j$ and zero otherwise) and Γ_M , Γ_N are $M \times 1$ and $N \times 1$ column vectors of ones, respectively (Qin and Badgwell, 2003). In this case, the unconstrained solution may not be a feasible point. The optimization problem then becomes one of Quadratic Programming (Maciejowski, 2002).

In this study, the nonlinear equation of blade sailing, presented in the previously, Eq 15d, will be used in the simulations of the model. First, the model predicted was linearized around an equilibrium position. The system below represents the linearized equations of the model in question:

$$\dot{x} = \begin{bmatrix} 0 & 1 \\ -\Omega^2 \left(1 + \frac{\omega_{nr}^2}{\Omega^2} \right) & -\frac{\gamma\Omega}{8} \end{bmatrix} x + \begin{bmatrix} 0 \\ \frac{\gamma\Omega^2}{8} \end{bmatrix} u(t) \quad (20)$$

Assuming that a zero-order-hold will keep the control signal constant between sampling instants, the model matrices resulting after linearization and discretization are as follows:

$$A_d = \begin{bmatrix} 1 & 0.001 \\ -0.0634 & 0.9948 \end{bmatrix}, B_d = \begin{bmatrix} 0 \\ 0.0274 \end{bmatrix}, C_d = [1 \ 0] \quad (21)$$

All simulations were carried out by using the Matlab software in the Simulink environment. A specific Matlab S-function was written to implement the predictive control law. The Quadratic Programming problem was solved by using the quadprog function of the Matlab Optimization Toolbox. For this study, the blade pitch control inputs from the actuators are limited to $\pm 6^\circ$ (Haber et al 2002).

In order to investigate the effect of varying the prediction horizon N , the cost parameter was fixed at $\rho = 0.00001$, the control horizon was fixed at $M = 5$ and four values of N were tested ($N = 5, 10, 30$). Fig. 7a presents the resulting responses for linear helicopter blade sailing system. On the basis of the results presented in Fig. 7a, it was deemed that $N = 10$ provides a good compromise between speed of response and damping. Therefore, such a value was adopted for the prediction horizon.

As mentioned, weu 2 superimpose the blade collective and cyclic commands, according to the IBRC scheme. Therefore, Fig. 7b shows the simulation results considering the system with and without the action of the predictive controller. Note, that when considering the control system response has a smaller overshoot, while improving the settling time of response, thus the system shows a less oscillatory. In this case we used as parameters, $\rho = 0.00001$, $N = 10$ and $M = 5$.

Now, that was designed a predictive controller that improves the response of the linearized system, we apply the same controller in the complete blade sailing nonlinear system. Fig. 8a illustrates the flap response of the system when using the predictive controller with the same design parameters of the linear system. Fig. 8 show the blade pitch control input. Simulation results show that the proposed MPC, which was designed for a nominal steady flow tunnel-strike condition, has a good performance under typical unsteady flow conditions as well, avoiding tunnel-strike occurrences and yielding significant reduction in upward flapping deflections without actuator saturation.

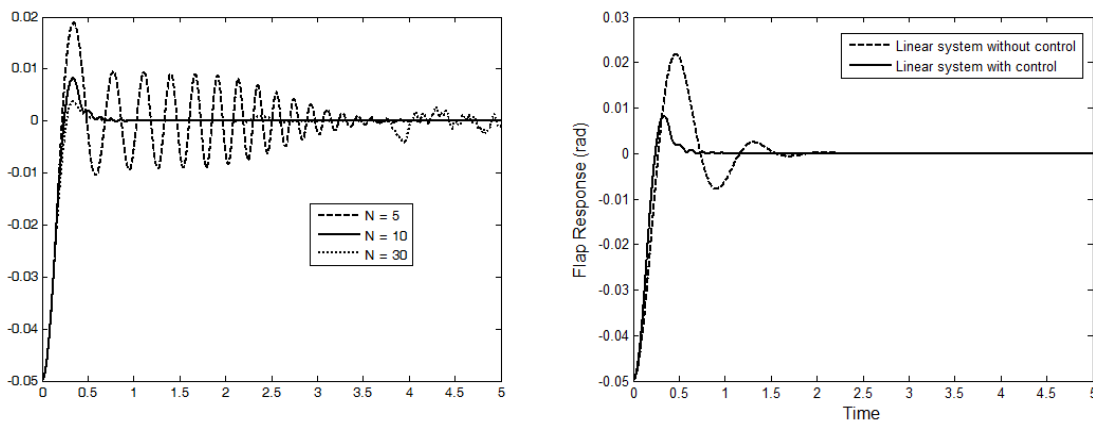


Figure 7: a) Effect of varying the prediction horizon N for a fixed control horizon ($M = 5$), b) Comparison between the linear system with and without predictive control action

Now, the next simulations illustrates the case when occur the fluctuation flow condition in relation to nominal value of V_{WOD} . Figs. 9 and 10 shows the fluctuation flow corresponds to 5% and 15% respectively of the nominal value. Note that in all situation the system present a blade sailing phenomena but when is introduced the MPC a significant reduction of flapping vibration is observed in all cases.

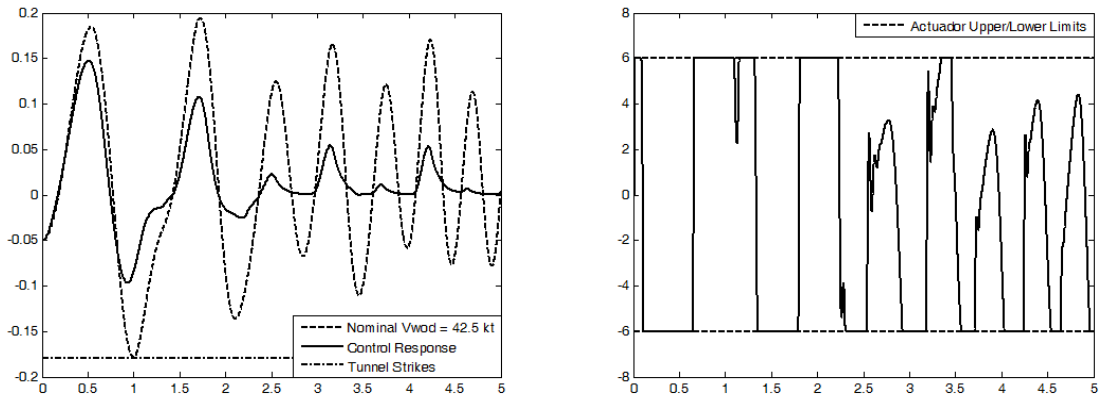


Figure 8: a) Control response for $K_f = 0.1$ and $\omega_f = 5$ rad/s, and b) Blade Pitch control input

Simulation results show that the proposed MPC IBRC-based controller, which was designed for a nominal steady flow tunnel-strike condition, has a good performance under typical unsteady flow conditions as well, avoiding tunnel-strike occurrences and yielding significant reduction in upward flapping deflections without actuator saturation.

CONCLUSION

This work was presented the formulation of the phenomenon of helicopter blade sailing, when considering the Unsteady flow. It was considered in this formulation, the addition of an MRD on the root of the blade, trying to increase the structural damping of the rotor, more precisely in the flapping motion, because in this degree of freedom is that occurs the studied phenomenon

It was shown that with this addition, it is possible to reduce the amplitude of the blade sailing phenomenon in approximately 30%, depending on the current applied to the buffer, in other words, the simulation results showed that a MRD device can significantly reduce the blade-sailing vibrations, avoiding tunnel-strike occurrences at severe unsteady flow conditions.

The results obtained in this case study suggest that MPC methodologies may be a promising alternative to the control of helicopter blade sailing system. As regards the real-time deployment of the MPC controller, the use of a linear prediction model, as the one adopted in this work, may be advisable. In fact, the quadratic programming problem stemming from the combination of a linear model, a quadratic cost function, and linear constraints, can be solved by very efficient numerical algorithms (Maciejowski, 2002).

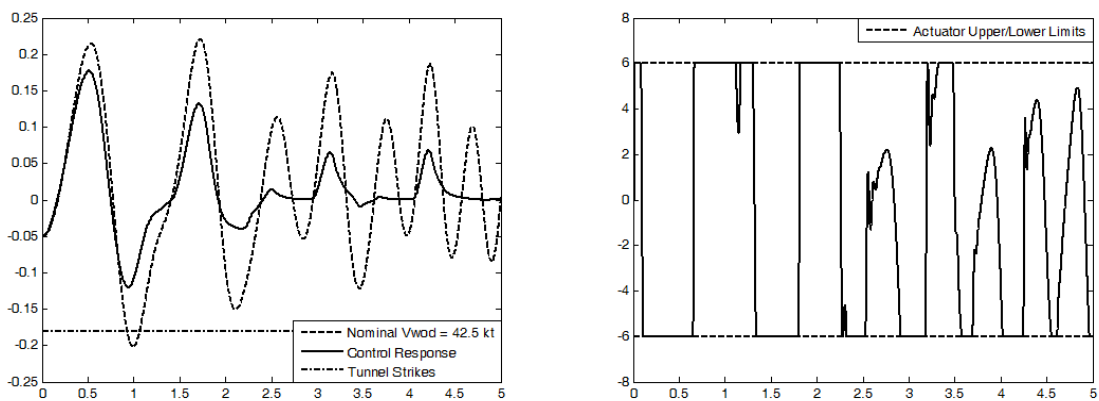


Figure 9: a) Control response: $K_f = 0.1$, $\omega_f = 5$ rad/s, and fluctuation flow of 5% ; b) Blade Pitch control input.

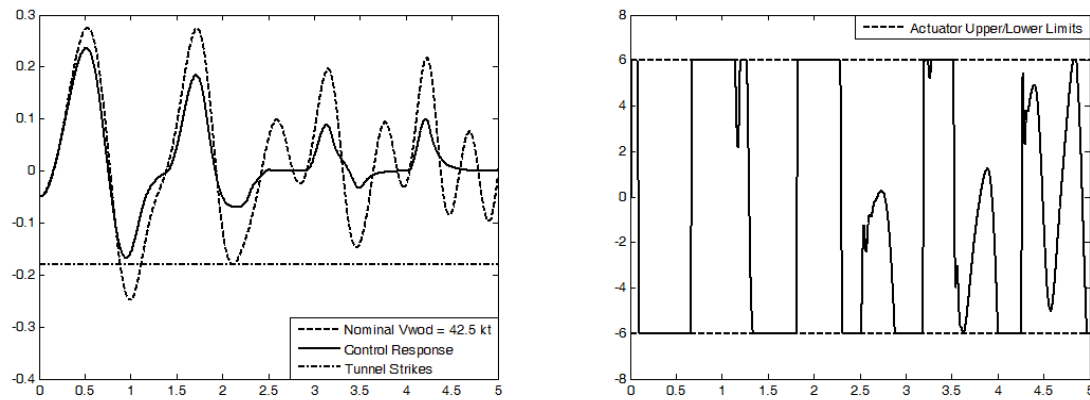


Figure 10: a) Control response: $K_f = 0.1$, $\omega_f = 5$ rad/s, and fluctuation flow of 15% b) Blade Pitch control input

The proposed MPC-IBRC scheme yields tunnel strike suppression and significant blade-sailing reduction in upward blade tip deflections without actuator saturation (limits of $\pm 6^\circ$).

REFERENCES

- Rhoades, M.M.; Healey, J.V., 1992 "Flight deck aerodynamics of a nonaviation ship". *Journal of Aircraft*, v. 29, n. 4, p. 619-626, Jul.-Aug.
- Newman, S.J., 1995, "The Verification of a Theoretical Helicopter Rotor Blade Sailing Method by Means of Windtunnel Testing", *The Aeronautical Journal of the Royal Aeronautical Society*, Vol. 99, No. 982, pp. 41-51
- Wall, A.S., Zan, S.J., Langlois, R.G. and Afagh F.F., 2005, "A Numerical Model for Studying Helicopter Blade Sailing in an Unsteady Airwake", *Flow-Induced Unsteady Loads and the Impact on Military Applications – NATO Symposium, Proceedings*.
- Johnson, W., 1994, *Helicopter Theory*. [S.l.]: Dover, p. 1-767.
- Ramos, R. L. C. B., 2007, "Aeroservoelastic Analysis of the Blade-Sailing Phenomenon in the Helicopter-Ship Dynamic Interface". Thesis (D.Sc.) – Technological Institute of Aeronautics, Brazil.
- Ramos, R.L.C.B., de Andrade, D., Goes, L.C.S., 2009a, "Individual Blade Root Control of Helicopter Blade Sailing for Articulated Shipboard Rotors", 65th American Helicopter Society Annual Forum.
- Ramos, R.L.C.B., de Andrade, D., Goes, L.C.S., 2009b, *Aeroservoelastic Analysis of a Proposed Helicopter Blade-Sailing Feedback Control System in Unsteady Flow*, 8th Brazilian Conference on Dynamics, Control and Applications, Bauru, May 18-22.
- Newman, S.J., 1990, "A Theoretical Model for Predicting the Blade Sailing Behaviour of a Semi-Rigid Rotor Helicopter". *Vertica*, 14, (4), p. 531-544.
- Geyer JR., W.P., Smith, E.C., Keller, J.A., 1998, "Aeroelastic Analysis of Transient Blade Dynamics During Shipboard Engage/Disengage Operations". *Journal of Aircraft*, v. 35, n. 3, p. 445-453.
- Keller, J.A., 2001, "Analysis and control of the transient aeroelastic response of rotors during shipboard engagement and disengagement operations". Thesis (PhD) - The Pennsylvania State University.
- Dowell, E.H. et al. (ed.). *A Modern Course in Aeroelasticity*. Kluwer Academic, 1995. Chapter 7. p. 370-437.
- Liu Y., Gordaninejad F. ; Evrensel C. A. ; Wang X., Hitchcock A, 2000, *Semi active Control of A Bridge Using Controllable Magneto-Rheological Dampers*, Proceedings of SPIE Conference on Smart Materials and Structures, Newport Beach, California.
- Pierrick, J., 2006, "Isolation vibratoire par contrôle semi-actif d'amortisseurs magnéto-rhéologiques pour l'interface lanceur/charge utile" PhD. Thesis, Conservatoire National des Arts et Métiers, ONERA, French.
- Qin, S. J., Badgwell, T. A., 2003, "A survey of industrial model predictive control technology", *Control Engineering Practice* vol.11, p.733-764.
- Maciejowski, J.M. 2002, "Predictive Control with Constraints", Prentice Hall, Harlow, England.
- Haber, A.; Jacklin, S.A.; DeSimone, G., 2002, "Development, Manufacturing, and Component Testing of An Individual Blade Control System For a UH-60 Helicopter Rotor." In: *American Helicopter Society Aerodynamics, Acoustics, and Test and Evaluation Technical Specialists Meeting*, San Francisco, CA.

RESPONSIBILITY NOTICE

The authors are the only responsible for the printed material included in this paper

A Semi-Active Flutter Control Using Smart Material

Vinícius Piccirillo¹, Kleber A. L. Castão², Luiz C. S. Góes³ and José M. Balthazar³

^{1,2,3} ITA – Technological Institute of Aeronautics, Department of Engineering Aeronautical and Mechanical, 12228-900, Sao Jose dos Campos, SP, Brazil, E-mails: pcmec@ita.br, kcastao@ita.br, goes@ita.br

⁴ UNESP – Sao Paulo State University, Department of Statistic, Applied Mathematical and Computation, CP 178, 13500 – 230, Rio Claro, SP, Brazil, E-mails: jmbaltha@rc.unesp.br,

Abstract: *In this paper, a theoretical simulation study of the response of a two degree of freedom typical airfoil section is presented. The main objective of this work is to present one solution for the flutter phenomena. The expressions of the unsteady aerodynamic lift and moment in the time domain are given in terms of the Wagner's function. Through of the numerical simulations, is presented the behavior of the aeroelastic system for the initial application of Shape Memory Alloys.*

Keywords: *Shape memory alloy, Flutter phenomenon,*

INTRODUCTION

Aeroelasticity is the dynamic interaction of structural, inertial, and aerodynamic forces. Conventional methods of examining aeroelastic behavior have relied on a linear approximation of the governing equations which describe both the flow field and the structure. Classical bending-torsion flutter can be described as the coalescing of two or more vibration modes and is the type of flutter studied herein. A wing will vibrate with flexural (bending) and torsional (pitching) components.

Flutter is the most dangerous dynamic instability that occurs when wing mode oscillations extract energy from the flow and this leads to the catastrophic failure of the structure. Divergence is a static instability that occurs when excessive aerodynamic forces due to static elastic deformation lead to structural failure. The interaction between the elastic deformations of the structure and the distribution of steady and unsteady aerodynamic forces can also lead to unacceptable vibration, self-induced oscillation, ride-quality deterioration, and fatigue failure (Bisplinghoff, R. L. et. al, 1996).

One should remark that the search for the dynamic aeroelastic instability of lifting surfaces encompasses two basic problems. One of these, based on the linearized aeroelastic equations, allows determination of the flutter boundary (Marzocca et. al., 2002). The other one, based on the nonlinear approach to the aeroelastic problem, allows determination of the character of the flutter boundary. In this sense, the flutter boundary can feature either benign or catastrophic behavior

In recent years, a semi-active control technique has been proposed, in which active and passive control principles are combined, that may find applications in flutter control. In this paper, a theoretical simulation study of the nonlinear response of a two degree of freedom typical airfoil section using a Shape Memory Alloy (SMA) is presented. The model is integrated into a numerical solution of the aeroelastic nonlinear dynamic system that results from the inclusion of Smart materials components in a dynamic structural system. The objective of the present work is to suppress the flutter phenomena of a two degree of freedom airfoil subjected to two-dimensional incompressible flow, where the simulations are investigated employing a numerically refined approach.

The application of Smart materials in this type of problem can mean a great incentive to study the applications of intelligent materials with respect to the elimination and control of aeroelastic phenomena, in helicopters and on aircraft. These studies may also signify a great advance in the study of these materials, because its application in helicopters and aircraft require the development of these devices and materials quickly and results effectively important.

SMA CONSTITUTIVE MODELING

Models with assumed phase transformation kinetics consider, besides strain (ε) and temperature (T), an internal variable (ζ), used to represent the martensitic volumetric fraction involved. The constitutive relation between stress and state variables, for SMA modeling, is considered in the rate form as follows:

$$\dot{\sigma} = D \dot{\varepsilon} + \Theta \dot{T} + \Omega \dot{\zeta} \quad (1)$$

where D represents the elastic tensor, Θ corresponds to the phase transformation tensor, and Ω is associated with the thermoelastic tensor. Due to martensitic transformation nondiffusive nature, the martensitic volumetric fraction can be expressed as function of current values of stress and temperature $\zeta = \zeta(\sigma, T)$. Several authors propose different functions to describe the volumetric fraction evolution. Some of them will be discussed from here on.

In torsional deflections of rods or tubes, the structural elements oriented in the axial direction are in pure shear. However, this is equivalent to assuming that the structural elements experience purely axial tension and transverse compression stresses in the direction that is orientated 45° from the axis of the rod. Assuming that the tensile component causes yielding and the transformation takes place along this direction, Brinson's equation can be rewritten by replacing linear stresses by shear stresses.

For a given angular deflection, the shear strains vary linearly with the radial location. The shear strain γ is expressed as a function of the angular deflection θ and the radial location r , as

$$\gamma(r) = \frac{\theta r}{l} \quad (2)$$

where l is the length of the uniform rod (or tube). From classical one-dimensional torsion theory, the shear strains and linear strains ε can be related as

$$\varepsilon(r) = \frac{\gamma(r)}{2} \quad (3)$$

The strains therefore vary linearly across the cross section of the tube, with the outer regions experiencing the highest shear (and linear) strains. For every angular displacement, the equivalent linear strains are calculated for each radial location. The resulting linear stresses σ are then calculated from the linear strains using uniaxial (in this case, Brinson) model.

$$\sigma(r) = \sigma(\varepsilon, T, r) \quad (4)$$

where T is the temperature of the specimen and r is the radial location.

In order to relate the axial stresses at each radial station thus obtained to the equivalent shear stresses, consider an element that undergoes pure shear at a particular radial location. As mentioned previously, the shear stress can be converted to a tensile force and a compressive force, both acting 45° relative to the axis of the rod. Considering Poisson's effect, the equivalent shear stresses can be related to the axial stresses by

$$\tau_r(r) = \frac{\sigma(r)}{1 + \nu} \quad (5)$$

where ν is the Poisson's ratio for the material.

The torque for a desired angle is then found by integration of the shear stresses over the radial locations as

$$T_{or} = \int_{r_1}^{r_2} (2\tau_r(r) \pi r^2) dr \quad (6)$$

where $\tau_r(r)$ is the shear stresses at a particular radial station and T_{or} is the total torque that is applied to cause the angular deflection of θ .

The shear stress–shear strain relation is expressed by the following equation:

$$\tau' = G\gamma' + \Theta T' + \Omega \zeta' \quad (7)$$

where G is the shear modulus

The martensitic transformation evolution is expressed by

$$\zeta_{S_\tau} = \frac{1 - \zeta_{S_{0\tau}}}{2} \cos \left\{ \frac{\pi}{\tau_{R_s}^{\text{crit}} - \tau_{R_f}^{\text{crit}}} \left[(1 + \nu) \tau_R - \tau_{R_f}^{\text{crit}} - C_M (T - M_s) \right] \right\} + \frac{1 - \zeta_{S_{0\tau}}}{2}$$

$$\zeta_{T_\tau} = \zeta_{T_{0\tau}} - \frac{\zeta_{T_{0\tau}}}{1 - \zeta_{S_{0\tau}}} (\zeta_{S_\tau} - \zeta_{S_{0\tau}}) \quad (8)$$

both (8) hold for $\tau_{R_s}^{\text{crit}} + C_M (T - M_s) < (1 + \nu) \tau_R < \tau_{R_f}^{\text{crit}} + C_M (T - M_s)$ and $T > M_s$.

For $T < M_s$ and $\tau_{R_s}^{\text{crit}} < (1 + \nu) \tau < \tau_{R_f}^{\text{crit}}$ the martensitic transformation is given by

$$\zeta_{S_\tau} = \frac{1 - \zeta_{S_{0\tau}}}{2} \cos \left[\frac{\pi}{\tau_{R_s}^{\text{crit}} - \tau_{R_f}^{\text{crit}}} \left((1 + \nu) \tau_R - \tau_{R_f}^{\text{crit}} \right) \right] + \frac{1 - \zeta_{S_{0\tau}}}{2}$$

$$\zeta_{T_\tau} = \zeta_{T_{0\tau}} - \frac{\zeta_{T_{0\tau}}}{1 - \zeta_{S_{0\tau}}} (\zeta_{S_\tau} - \zeta_{S_{0\tau}}) + \Delta_T \quad (9)$$

$$\text{where, } \Delta_T = \begin{cases} \frac{1 - \zeta_{T_{0\tau}}}{2} \left\{ \cos \left[a_M (T - M_f) \right] + 1 \right\} & \text{se } M_f < T < M_s, T < T_0 \\ \text{então} & 0 \end{cases}$$

The reverse transformation holds for $C_A (T - A_f) < (1 + \nu) \tau_R < C_A (T - A_s)$ and $T > A_s$ and is defined as

$$\zeta_{S_\tau} = \frac{\zeta_{S_{0\tau}}}{2} \left\{ \cos \left[a_A \left(T - A_s - \frac{(1 + \nu) \tau_R}{C_A} \right) \right] + 1 \right\}$$

$$\zeta_{T_\tau} = \zeta_{T_{0\tau}} \left\{ \cos \left[a_A \left(T - A_s - \frac{(1 + \nu) \tau_R}{C_A} \right) \right] + 1 \right\} \quad (10)$$

SMART MATERIAL APPLICATION

Figure 1 shows a sketch of a two-degree-of-freedom (2-dof) airfoil motion in plunge and pitch. The plunge deflection is denoted by h , positive in the downward direction, and α is the pitch angle about the elastic axis, positive nose up. The elastic axis is located at a distance $a_h b$ from the mid-chord, while the mass centre is located at a distance $x_c b$ from the elastic axis, where b is the airfoil semi-chord. Both distances are positive when measured towards the trailing edge of the airfoil.

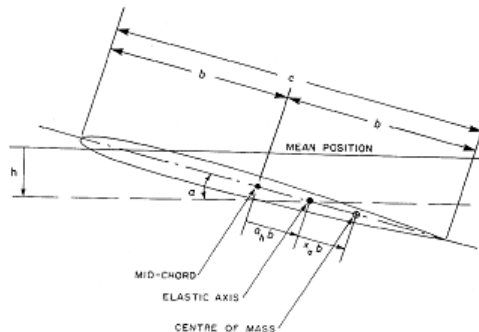


Figure 1: Schematic of airfoil with 2 d.o.f motion

The aeroelastic equations of motion for linear springs have been derived by Fung (1969). In the first case we introduce a SMA torsional tube in wing with the intention to increase the structural stiffness in aeroelastic system. For nonlinear SMA restoring forces with subsonic aerodynamics, the coupled bending-torsion equations for the airfoil can be written as follows:

$$mh'' + S_\alpha \alpha'' + K_h h = -C_L \quad (11)$$

$$S_\alpha h'' + I_\alpha \alpha'' + K_\alpha \alpha + K_{SMA_\alpha}(\alpha, T) = C_M \quad (12)$$

where the symbols m , S_α and I_α are the airfoil mass, airfoil static moment about the elastic axis, wing mass moment of inertia about elastic axis, respectively. K_h and K_α are the linear plunge and pitch stiffness terms, $K_{SMA_\alpha}(\alpha, T)$ correspond the SMA nonlinear spring stiffness in torsion, C_L and C_M are the forces and moments acting on the airfoil, respectively.

Defining

$$\tau = \frac{Ut}{b}, \quad \xi = \frac{h}{b}, \quad x_\alpha = \frac{S_\alpha}{bm}, \quad \omega_\alpha^2 = \frac{K_\alpha}{I_\alpha}, \quad \omega_\xi^2 = \frac{K_h}{I_\alpha}, \quad r_\alpha^2 = \frac{I_\alpha}{mb^2}, \quad \mu = \frac{m}{\rho b^2 \pi}, \quad \psi = \frac{\tau_R J}{I r m b^2}, \quad \bar{\psi} = \frac{\psi}{U^2 \omega_\alpha^2 r_\alpha^2}$$

the equations (11) and (12) can be written in nondimensional form as follow

$$\ddot{\xi} + x_\alpha \ddot{\alpha} + \left(\frac{\Omega}{U}\right)^2 \xi = P_1(\tau) \quad (13)$$

$$\frac{x_\alpha}{r_\alpha^2} \ddot{\xi} + \ddot{\alpha} + \frac{1}{U^2} \alpha + \bar{\psi} = Q_1(\tau) \quad (14)$$

$$\dot{\tau}_R = G(\zeta) \frac{r}{I} (\dot{\alpha} + \varepsilon_L \dot{\zeta}) \quad (15)$$

When SMA is outside the phase transformation region, the equation (18) can be simplified as

$$\dot{\tau} = G(\zeta) \frac{r}{I} \dot{\alpha} \quad (16)$$

During the phase transformation from Austenite to Martensite,

$$\dot{\tau}_R = \frac{G(\zeta) \frac{r}{I} \dot{\alpha}}{\left(1 - G(\zeta) \varepsilon_L \frac{\pi(1 - \zeta_{S_{0\tau}})}{2(\tau_s^{cr} - \tau_f^{cr})} \times (1 + \nu) \times \sin\left(\frac{\pi}{(\tau_{R_s}^{cr} - \tau_{R_f}^{cr})} \left[(1 + \nu)\tau_R - \tau_{R_f}^{cr} - C_M(T - M_s)\right]\right)\right)} \quad (17)$$

and during the phase transformation from Martensite to Austenite,

$$\dot{\tau}_R = \frac{G(\zeta) \frac{r}{I} \dot{\alpha}}{\left(1 + G(\zeta) \varepsilon_L \frac{a_A \zeta_{S_{0\tau}}}{2C_A} \times (1 + \nu) \times \sin\left(a_A \left(T - A_s - \frac{(1 + \nu)\tau_R}{C_A}\right)\right)\right)} \quad (18)$$

In equations (13) and (14), V is a nondimensional velocity defined as $V = \frac{U}{b\omega_\alpha}$ and $\Omega = \frac{\omega_\xi}{\omega_\alpha}$ where ω_ξ and ω_α are the uncoupled plunging and pitching mode natural frequencies, respectively, U is the free-stream velocity, and the dot denotes differentiation with respect to the non-dimensional time τ defined as $\tau = \frac{Ut}{b}$, where

$$P_1(\tau) = \frac{1}{m\mu} C_L(\tau) \tag{19}$$

$$Q_1(\tau) = \frac{2}{\pi\mu\alpha^2} C_M(\tau) \tag{20}$$

and $\mu = \frac{m}{\rho b^2 \pi}$ is the airfoil/air mass ratio For incompressible flow, Fung (1969) gives the following expressions for $C_L(\tau)$ and $C_M(\tau)$.

$$C_L(\tau) = \pi \left(\ddot{\xi} + a_h \ddot{\alpha} + \dot{\alpha} \right) + 2\pi \left\{ \alpha(0) + \dot{\xi}(0) + \left(\frac{1}{2} - a_h \right) \dot{\alpha}(0) \right\} \varphi(\tau) + 2\pi \int_0^\tau \varphi(\tau - \sigma) \left(\dot{\alpha}(\sigma) + \ddot{\xi}(\sigma) + \left(\frac{1}{2} - a_h \right) \ddot{\alpha}(\sigma) \right) d\sigma \tag{21}$$

$$C_M(\tau) = \pi \left(\frac{1}{2} - a_h \right) \left\{ \alpha(0) + \dot{\xi}(0) + \left(\frac{1}{2} - a_h \right) \dot{\alpha}(0) \right\} \varphi(\tau) + \pi \left(\frac{1}{2} - a_h \right) \int_0^\tau \varphi(\tau - \sigma) \left(\dot{\alpha}(\sigma) + \ddot{\xi}(\sigma) + \left(\frac{1}{2} - a_h \right) \ddot{\alpha}(\sigma) \right) d\sigma + \frac{\pi}{2} a_h \left(\ddot{\xi} - a_h \ddot{\alpha} \right) - \left(\frac{1}{2} - a_h \right) \frac{\pi}{2} \dot{\alpha} - \frac{\pi}{16} \ddot{\alpha} \tag{22}$$

where the Wagner function $\varphi(\tau)$ is given by

$$\varphi(\tau) = 1 - \psi_1 e^{-\varepsilon_1 \tau} - \psi_2 e^{-\varepsilon_2 \tau} \tag{23}$$

and the constants $\psi_1 = 0.165$, $\psi_2 = 0.335$, $\varepsilon_1 = 0.0455$ and $\varepsilon_2 = 0.3$ are obtained from Jones (1940).

Due to the presence of the integral terms in the integro-differential equations (21) and (22), it is cumbersome to integrate them numerically. A set of simpler equations was derived by Lee et. al. (1999), and they introduced four new variables

$$w_1 = \int_0^\tau e^{-\varepsilon_1(\tau-\sigma)} \alpha(\sigma) d\sigma \quad ; \quad w_2 = \int_0^\tau e^{-\varepsilon_2(\tau-\sigma)} \alpha(\sigma) d\sigma \tag{24}$$

$$w_3 = \int_0^\tau e^{-\varepsilon_1(\tau-\sigma)} \xi(\sigma) d\sigma \quad ; \quad w_4 = \int_0^\tau e^{-\varepsilon_2(\tau-\sigma)} \xi(\sigma) d\sigma$$

equations (13) and (14) can be written as

$$c_0 \ddot{\xi} + c_1 \ddot{\alpha} + c_2 \dot{\xi} + c_3 \dot{\alpha} + c_4 \xi + c_5 \alpha + c_6 w_1 + c_7 w_2 + c_8 w_3 + c_9 w_4 = P_1(\tau) \tag{25}$$

$$d_0\ddot{\xi} + d_1\ddot{\alpha} + d_2\dot{\alpha} + d_3\alpha + d_4\alpha^3 + d_5\alpha^5 + d_6\dot{\xi} + d_7\xi + d_8w_1 + d_9w_2 + d_{10}w_3 + d_{11}w_4 = Q_1(\tau) \quad (26)$$

where $P_1(\tau)$ and $Q_1(\tau)$ are functions depending on initial conditions, Wagner's function and the forcing terms, namely,

$$P_1(\tau) = \frac{2}{\mu} \left((0.5 - a_h) \alpha(0) + \xi(0) \right) \left(\psi_1 \varepsilon_1 e^{-\varepsilon_1 \tau} + \psi_2 \varepsilon_2 e^{-\varepsilon_2 \tau} \right) \quad (27)$$

$$Q_1(\tau) = -\frac{(1 + 2a_h) P_1(\tau)}{2\tau_\alpha^2} \quad (28)$$

The resulting set of nine first-order ordinary differential equations by a suitable transformation is given a

$$\frac{dX}{d\tau} = f(X, \tau) \quad (29)$$

where

$$X = \{x_1, x_2, \dots, x_9\} = \{\alpha, \dot{\alpha}, \xi, \dot{\xi}, w_1, w_2, w_3, w_4, \tau\}. \quad (30)$$

When SMA is outside the phase transformation region nine first-order ordinary differential equations by a suitable transformation is given a

$$\begin{aligned} \dot{x}_1 &= x_2 \\ \dot{x}_2 &= \frac{1}{c_1 d_0 - c_0 d_1} (c_0 E - d_0 F) \\ \dot{x}_3 &= x_4 \\ \dot{x}_4 &= \frac{1}{c_1 d_0 - c_0 d_1} (-c_1 E + d_1 F) \\ \dot{x}_5 &= x_1 - \varepsilon_1 x_5 \\ \dot{x}_6 &= x_1 - \varepsilon_2 x_6 \\ \dot{x}_7 &= x_3 - \varepsilon_1 x_7 \\ \dot{x}_8 &= x_3 - \varepsilon_2 x_8 \\ \dot{x}_9 &= G(\zeta) \frac{r}{1} x_2 \end{aligned} \quad (31)$$

During the phase transformation from Austenite to Martensite, last ordinary differential equations into eq. (31) is given by

$$\begin{aligned} \dot{x}_9 &= \frac{G(\zeta) \frac{r}{1} x_2}{A} \\ A &= \left(1 - G(\zeta) \varepsilon_L \frac{\pi(1 - \zeta S_{0\tau})}{2(\tau_{R_s}^{cr} - \tau_{R_f}^{cr})} \times (1 + \nu) \times \sin \left(\frac{\pi}{(\tau_{R_s}^{cr} - \tau_{R_f}^{cr})} \left[(1 + \nu) x_9 - \tau_{R_f}^{cr} - C_M (T - M_s) \right] \right) \right) \end{aligned} \quad (32)$$

During the phase transformation from Martensite to Austenite, last ordinary differential equations into eq. (31) becomes

$$\dot{x}_9 = \frac{G(\zeta) \frac{r}{l} x_2}{B} \quad (33)$$

$$B = \left(1 + G(\zeta) \varepsilon_L \frac{a_A \zeta_{S_{0\varepsilon}}}{2C_A} \times (1 + \nu) \times \sin \left(a_A \left(T - A_s - \frac{(1 + \nu)x_9}{C_A} \right) \right) \right)$$

where, in both cases

$$E = d_2 x_2 + d_3 x_1 + d_4 x_4 + d_5 x_3 + d_6 x_5 + d_7 x_6 + d_8 x_7 + d_9 x_8 + \frac{1}{U^2} x_1 + \bar{\psi} - Q_1(\tau) \quad (34)$$

$$F = c_2 x_4 + c_3 x_2 + c_4 x_3 + c_5 x_1 + c_6 x_5 + c_7 x_6 + c_8 x_7 + c_9 x_8 + \left(\frac{\Omega}{U} \right)^2 x_3 - P_1(\tau) \quad (35)$$

and

$$c_0 = 1 + \frac{1}{\mu}, c_1 = x_\alpha - \frac{a_h}{\mu}, c_2 = \frac{2}{\mu}(1 - \psi_1 - \psi_2), c_3 = \frac{1 + 2(0.5 - a_h)(1 - \psi_1 - \psi_2)}{\mu}, c_4 = \frac{2}{\mu}(\psi_1 \varepsilon_1 + \psi_2 \varepsilon_2),$$

$$c_5 = \frac{2}{\mu} \left\{ (1 - \psi_1 - \psi_2) + (0.5 - a_h)(\psi_1 \varepsilon_1 + \psi_2 \varepsilon_2) \right\}, c_6 = \frac{2}{\mu} \psi_1 \varepsilon_1 \left\{ 1 - (0.5 - a_h) \varepsilon_1 \right\}, c_7 = \frac{2}{\mu} \psi_2 \varepsilon_2 \left\{ 1 - (0.5 - a_h) \varepsilon_2 \right\},$$

$$c_8 = -\frac{2}{\mu} \psi_1 \varepsilon_1^2, \quad c_9 = -\frac{2}{\mu} \psi_2 \varepsilon_2^2$$

$$d_0 = \frac{x_\alpha}{r_\alpha^2} - \frac{a_h}{\mu r_\alpha^2}, d_1 = 1 + \frac{1 + 8a_h^2}{8\mu r_\alpha^2}, d_2 = \frac{1 - 2a_h}{2\mu r_\alpha^2} - \frac{(1 + 2a_h)(1 - 2a_h)(1 - \psi_1 - \psi_2)}{2\mu r_\alpha^2},$$

$$d_3 = -\frac{(1 + 2a_h)(1 - \psi_1 - \psi_2)}{\mu r_\alpha^2} - \frac{(1 + 2a_h)(1 - 2a_h)(\psi_1 \varepsilon_1 + \psi_2 \varepsilon_2)}{2\mu r_\alpha^2}, d_4 = -\frac{(1 + 2a_h)(1 - \psi_1 - \psi_2)}{\mu r_\alpha^2},$$

$$d_5 = -\frac{(1 + 2a_h)(\psi_1 \varepsilon_1 + \psi_2 \varepsilon_2)}{\mu r_\alpha^2}, d_6 = -\frac{(1 + 2a_h) \psi_1 \varepsilon_1 \left[1 - (0.5 - a_h) \varepsilon_1 \right]}{\mu r_\alpha^2}, d_7 = -\frac{(1 + 2a_h) \psi_2 \varepsilon_2 \left[1 - (0.5 - a_h) \varepsilon_2 \right]}{\mu r_\alpha^2},$$

$$d_8 = \frac{(1 + 2a_h) \psi_1 \varepsilon_1^2}{\mu r_\alpha^2}, d_9 = \frac{(1 + 2a_h) \psi_2 \varepsilon_2^2}{\mu r_\alpha^2}$$

NUMERICAL SIMULATION

The verification of the flutter velocity is obtained using the V-g-f method and for analysis the results of eqs. (13-15) we used a fourth-fifth order Runge-Kutta numerical simulation. Table 1 show the parameter values for the simulations, which are based on the typical section characteristics Tang et. al. (2004).

Table 1. Parameter of typical section.

Parameter	Description	Unit	Value
l	Span	m	0.52
b	Semi-chord	m	0.127
a	Elastic axis	m	-0.0625

m_w	Mass of wing	kg	0.713
I_α	Wing moment of inertia	kg m	0.0185
S_α	Airfoil static moment	kg	0.0726
K_α	Plunge linear stiffness	kg m/s ²	42.8
K_h	Pitch linear stiffness	kg m / s ²	2755.4

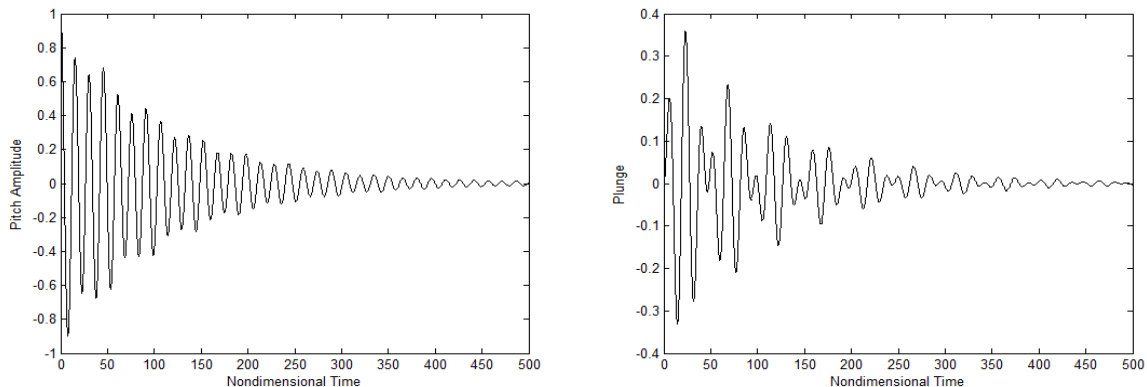
In all simulations, in order to analyze the behavior of the aeroelastic dynamical system, the spring is assumed to be made of a Ni-Ti alloy and the properties are presented in Table 2 (Elahinia and Ahmadian, 2005). In this case, we used a temperature of the alloy around $T = 80^\circ\text{C}$.

The dynamic response of the nonlinear system shown in Fig. 1 is analyzed by the Runge-Kutta integration method. Fig. 2(a) and (b) show the displacement time histories for pitch and plunge d.o.f., respectively. The displacement time history has an initial transient stage followed by a steady-state. Fig. 2(c) and (d) show the time history of torsional stress in the SMA element and the hysteric curve, respectively. The initial stress of the SMA element is equal to 300 MPa. In simulations we consider the flow velocity $V = 15 \text{ m/s}$.

Table 2. Material constants for a Ni-Ti alloy

Parameter	Description	Unit	Value
m_{SMA}	SMA mass per unit length	m	1.14×10^{-4}
T_∞	Ambient temperature	°C	20
D_A	Young modulus (austenite)	GPa	75
D_M	Young modulus (martensite)	GPa	28
Θ	Phase transformation factor	MPa°C ⁻¹	0.55
A_S	Austenite start temperature.	°C	68
A_f	Austenite final temperature	°C	78
M_S	Martensite start temperature	°C	52
M_f	Martensite final temperature	°C	42

A linear flutter analysis has been performed prior to a nonlinear analysis to determine the aeroelastic characteristics of the linear mode. Considering the linear case the critical flutter velocity is $V = 20 \text{ m/s}$. We introduce in torsional degree of freedom the SMA actuator. Figure 3 highlights the performance of SMA actuator on the time history of the airfoil subjected to a aerodynamics forces. The results reveal that in the absence of the SMA actuator, the amplitudes of the response increasing with the time, implying that the system is in close proximity to the flutter instability. However, in the presence of the SMA actuator the amplitudes decay rapidly as time unfolds. The results reveal that a combined typical section-SMA actuator can be effective than suppress the utter phenomena.



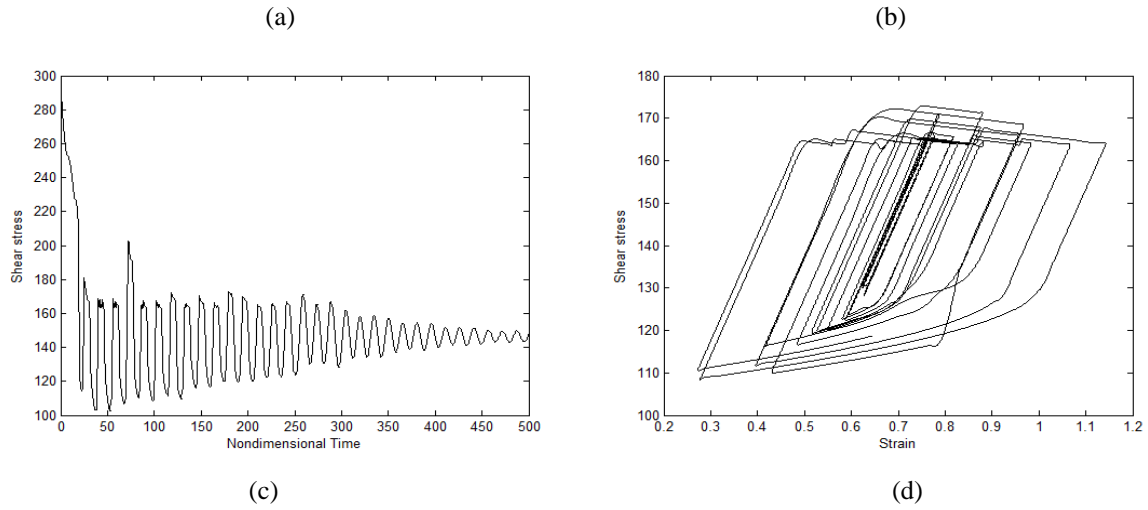


Figure 2: Behavior of typical section–SMA actuator: Time series: a) Pitch, b) Plunge, c) Shear and d) Hysteretic curve for $V = 15 \text{ m/s}$.

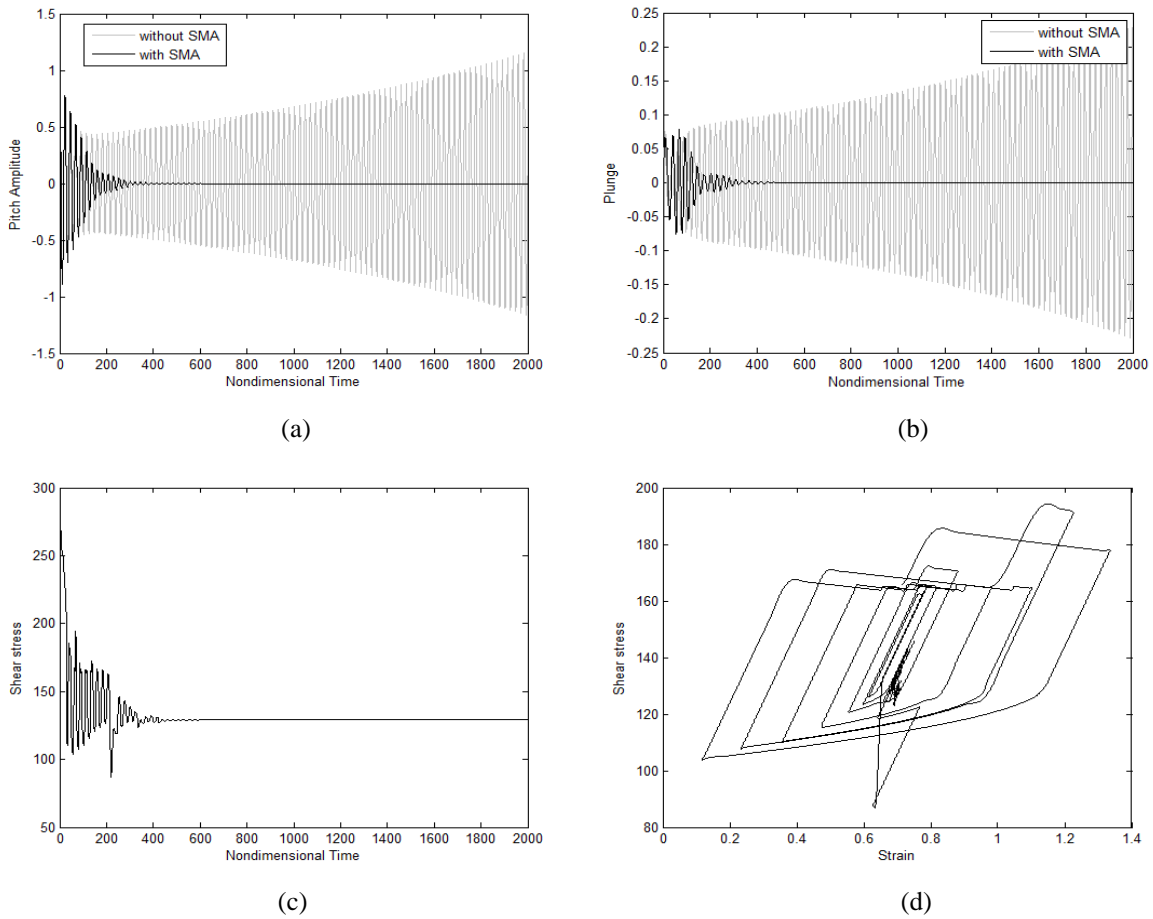


Figure 3: Behavior of typical section–SMA actuator: Time series: a) Pitch, b) Plunge, c) Shear and d) Hysteretic curve for $V = 20 \text{ m/s}$ (flutter velocity) .

CONCLUSION

A hypothesis is proposed to include the SMA material in a typical section for Flutter suppression. A numerical simulation of SMA element is based on the Brinson model. The dynamic response of a typical section with 2 DOF system with an SMA element is studied. It is found that the Runge Kutta method yields accurate and stable numerical results for 2 DOF systems with SMA elements. The response of a typical section of 2 DOF system with a SMA element shows desirable features that could facilitate the use of SMA in passive vibration control of structures. This work shows that the device is sufficiently efficient in the solution of this kind of problem.

ACKNOWLEDGEMENTS

The authors thank the support of the Brazilian government Agency CNPq.

REFERENCES

- Bisplinghoff, R. L., Ashley H., Halfman, R. L, 1996, "Aeroelasticity". New York: Dover.
- Brinson, L. C., 1993, "One-Dimensional Constitutive Behavior of Shape Memory Alloys: Thermo mechanical Derivation with Non-Constant Material Functions and Refined Martensite Internal Variable", *Journal of Intelligent Material Systems and Structures*, Vol. 4, pp. 229-242.
- Elahinia, M.H.; Ahmadian, M, 2005, "An enhanced SMA phenomenological model: II. The experimental study", *Smart materials and structures*, Vol. 14, pp. 1309-1319.
- Fung, Y.C., 1969, "An Introduction to the Theory of Aeroelasticity", Dover, New York, pp.498.
- Lee, B.H.K., Price, S.J., Wong, Y.S., 1999, "Nonlinear Aeroelastic Analysis of Airfoil: Bifurcations and Chaos", *Progress in Aerospace Science*, Vol. 35, pp. 205 – 334.
- Marzocca, P., Librescu, L., Silva, W. A., 2002, "Flutter, post-flutter and control of a supersonic 2-D lifting surface". *Journal of Guidance, Control and Dynamic*, Vol. 25, pp. 962–970.
- Tang, D.; Henri, P.G.; Dowell, E.H., 2004, "Study of Airfoil Gust Response Alleviation Using an Electro-Magnetic Dry Friction Damper. Part 1: Theory", *Journal of Sound and Vibration*, Vol. 269, pp. 853 – 874.

Multibody System Model of a Stumble in Human Gait

Marko Ackermann¹, Arturo Forner-Cordero²

¹ Department of Mechanical Engineering, Centro Universitário da FEI, São Paulo, Brazil

² Biomechatronics Lab. Mechatronics and Mechanical Systems Department. Escola Politécnica, University of São Paulo, São Paulo, Brazil

Abstract: Falls often result from perturbations during gait such as a trip or a slip, frequently after an unsuccessful recovery attempt, and can lead to severe injury, particularly in the elderly population. A biomechanical model of the body response to the perturbation during gait might uncover the mechanisms underlying the different recovery strategies and ultimately lead to a better understanding of the unsuccessful recovery process leading to a fall. This paper introduces a model of stumble in the multibody system framework. Normal gait patterns for a biomechanical model of the musculoskeletal systems are first obtained through the solution of an optimal control problem. This reference gait is then perturbed by a trip formulated as an instantaneous collision of the foot with an obstacle. The influence of the collision timing, the location of impact in the foot, as well as of the coefficient of restitution is investigated. The results show that the “uncontrolled” motion of the body just after the collision, before muscles start influencing the motion as a response to the perturbation stimulus, might be the determinant factor in the selection of the recovery strategy.

Keywords: gait simulation, stumble, recovery strategies.

INTRODUCTION

Falls are responsible for a large number of serious injuries such as hip fracture, in particular in the elderly population (Hayes et al., 1996). Falls often result from an unsuccessful recovery attempt after perturbations to the gait such as a trip, a slip or a step down (Smeeters, Hayes and McMahon, 2001). In the case of a trip due to the collision of the foot with an obstacle, two basic recovery strategies are reported in the literature, the lowering strategy and the elevating strategy (Forner Cordero, Koopman and van der Helm, 2003). The lowering strategy consists of quickly lowering the perturbed foot after the trip and is often immediately followed by a step of the contralateral leg. This strategy is observed when the trip occurs in mid or late swing. The elevating strategy is characterized by an elevation of the swing leg after the trip and is usually observed for perturbations occurring in early swing.

The success of the recovery strategy appears to be largely dictated by the ability of the body to counteract the forward inclination of the trunk (van den Bogert, Pavol and Grabiner, 2002; Forner Cordero, Koopman and van der Helm, 2004). A successful recovery strategy avoids a critical inclination with a subsequent fall by quick application of an external counteracting moment. Because in gait an external counteracting moment is due exclusively to foot-ground contact forces, the time and position of the next foot contact after the trip influence to a great extent the outcome of the recovery attempt.

In this paper we propose a model of stumble capable of predicting the response of the body, including time and position of the next foot contact, in the first hundreds of milliseconds after a simulated trip. A detailed model of the musculoskeletal system is used and the stumble simulations arise from a three-step procedure: 1) Normal, periodic gait patterns are reproduced by solving an optimal neuromuscular control problem that minimizes an appropriate cost function (Ackermann and van den Bogert, 2010); 2) The reference normal gait obtained in the previous step is perturbed by a trip modeled as an instantaneous collision of the foot with an obstacle, resulting in an instantaneous jump in the generalized velocities of the model; and 3) The dynamic response of the model after the trip is predicted by forward integration starting from the new state of the model (new generalized velocities) just after the impact, and utilizing the original muscle excitations (controls) predicted by the optimization procedure in the first step. The use of the unchanged, previously computed neural excitations in the simulation following the trip is acceptable during the first few hundreds of milliseconds after the perturbation, because of the delays in the muscle response to the perturbation. The long-latency responses are variable and start after 110 ms (Schillings, Mulder and Duysens, 2005). These delays can be modified with learning (Forner-Cordero, 2007).

The proposed model of stumble is used to investigate the influence of the time of collision in the swing phase as well as of the nature of the collision (toes or ankle collision, and coefficient of restitution) on the time and position of the next foot placement after the trip. We hypothesize that the recovery strategy, lowering or elevating, is largely determined by the “uncontrolled” dynamics of the body in the first few hundreds of milliseconds after the perturbation.

METHODS

Musculoskeletal Model

A planar musculoskeletal model (Gerritsen et al., 1998) consisting of seven rigid body segments (trunk, thighs, shanks and feet) and $f = 9$ degrees of freedom is adopted, resulting in the following equations of motion

$$\mathbf{M}(\mathbf{y})\ddot{\mathbf{y}} + \mathbf{k}(\mathbf{y}, \dot{\mathbf{y}}, t) = \mathbf{q}(\mathbf{y}, \dot{\mathbf{y}}, t), \quad (1)$$

where $\mathbf{y}(t)$ is the vector of generalized coordinates with dimension f , \mathbf{M} is the mass matrix, \mathbf{k} is the vector of Coriolis and gyroscopic forces and \mathbf{q} is the vector of generalized applied forces including muscle forces. Eight muscle groups are included in each lower limb: *Iliopsoas*, *Glutei*, *Hamstrings*, *Rectus Femoris*, *Vasti*, *Gastrocnemius*, *Soleus*, and *Tibialis Anterior*. Each muscle is represented by a three-element Hill-type muscle model and includes the first order activation dynamics and the first order contraction dynamics (McLean, Su and van den Bogert, 2003) with muscle properties extracted from Gerritsen et al. (1998). The complete musculoskeletal model has a total of 50 states in \mathbf{x} : 9 generalized coordinates in \mathbf{y} , 9 generalized velocities in $\dot{\mathbf{y}}$, 16 muscle contractile element lengths in \mathbf{l}_{ce} , and 16 muscle activations in \mathbf{a} . The dynamics of the musculoskeletal system reads as

$$\dot{\mathbf{x}}(t) = \mathbf{f}(\mathbf{x}, \mathbf{u}), \quad (2)$$

where \mathbf{u} are neural excitations to the muscles. The interaction between feet and ground is modeled by means of 10 nonlinear spring-damper elements uniformly distributed along each foot sole (Ackermann and van den Bogert, 2010). The vertical contact definition is consistent with dynamic force deformation tests from Aerts and de Clercq (1993). The horizontal contact force was modeled by a continuous approximation of Coulomb friction with $\mu=1.0$ (Ackermann and van den Bogert, 2010).

Reference Gait

The reference normal gait patterns for the model, Fig. 1, were obtained by solving an optimal neuromuscular control problem (Ackermann and van den Bogert, 2010). This problem consists of searching for time histories of controls $\mathbf{u}(t)$ and states $\mathbf{x}(t)$ that minimize a cost function J , and satisfy the musculoskeletal dynamics Eq. (2) and constraints that guarantee periodicity of gait and physiological muscle forces ($0 < \mathbf{u} < 1$). The cost function utilized was composed by two terms, one quantifying the deviation of model kinematics and ground contact forces from experimental data available in Winter (1991), and the other penalizing muscle activations squared. The average walking speed was prescribed as 1.1 m/s. The resulting optimal control problem was transformed into a large-scale Nonlinear Programming problem using direct collocation (Betts, 2001; Ackermann and van den Bogert, 2010) and solved using the SNOPT package, a large-scale, sequential quadratic programming optimization code for Matlab (Tomlab Optimization Inc., Pullman, WA). Figure 1 shows stick figures illustrating one cycle of the reference gait. The arrows indicate the orientation and amplitude of the contact force along the gait cycle.

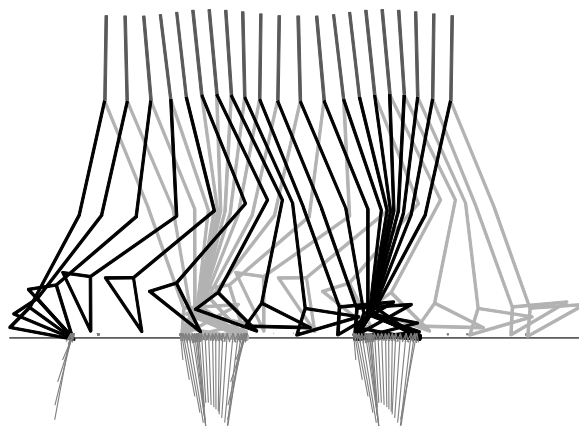


Figure 1 – Stick figure of reference gait pattern obtained by solving optimal tracking problem.

Trip as an Instantaneous Collision

The trip was modeled as an instantaneous, frictionless collision (Pfeiffer and Glocker, 2001; Schiehlen, Seifried and Eberhard, 2006) which results in a discontinuity in the generalized coordinates when the normal relative velocity of the contacting points is different than zero. In this case, according to Schiehlen, Seifried and Eberhard (2006), the normal impact force F can be added to Eq. (1) as

$$\mathbf{M}\ddot{\mathbf{y}} + \mathbf{k} = \mathbf{q} + \mathbf{w}_N F, \quad (3)$$

where \mathbf{w}_N projects the generalized velocities on the normal direction of impact. The impact causes a jump in the velocities while the position remains unchanged

$$\lim_{t \rightarrow t_s} \int_s^e (\mathbf{M}\ddot{\mathbf{y}} + \mathbf{k} - \mathbf{q} - \mathbf{w}_N F) dt = \mathbf{M}(\dot{\mathbf{y}}_e - \dot{\mathbf{y}}_s) - \mathbf{w}_N \Delta P = 0, \quad (4)$$

where the indices s and e refer, respectively, to the start and the end of the impact, and ΔP is a finite force impulse as

$$\Delta P = \lim_{t \rightarrow t_s} \int_s^e (F) dt. \quad (5)$$

Because duration of impact is infinitesimal, \mathbf{M} and \mathbf{w}_N are constant in Eq. (4) and all the other generalized forces vanish when compared to the magnitude of the impact force F . Equation (4) can be used directly to compute the generalized coordinates just after the impact when an approximation of ΔP is available from the time course of the impact force. This is the case, for instance, in the experiments described by Forner-Cordero, Koopman and van der Helm (2003).

When ΔP is unknown or not readily available, an alternative is using the kinetic coefficient of restitution e (Pfeiffer and Glocker, 1996), which is defined as the ratio of the impulses in the compression and in the restitution phases of the impact (Schiehlen, Seifried and Eberhard, 2006). An impact with $e=1$ indicates no energy loss and is called elastic, whereas an impact with $e=0$ indicates maximal energy loss and is called inelastic. For a skleronomic multibody system, from Eq. (4) and the definition of the kinetic coefficient of restitution e , the generalized velocities at the end of the impact can be computed with the following expression, see (Schiehlen, Seifried and Eberhard, 2006) for details:

$$\dot{\mathbf{y}}_e = \dot{\mathbf{y}}_s - \mathbf{M}^{-1} \left[\frac{\mathbf{w}_N (1+e) \mathbf{w}_N^T}{\mathbf{w}_N^T \mathbf{M}^{-1} \mathbf{w}_N} \right] \dot{\mathbf{y}}_s. \quad (6)$$

Simulations

A series of trips were simulated at instants corresponding to multiples of 10% from 10% to 90% of the swing phase of the reference normal gait in Fig. 1, where the swing phase is the period between toe off (0%) and the next heel contact (100%). In order to investigate the influence of the collision nature on the results, collisions were simulated at the ankle joint and at the toes, with the coefficient of restitution assuming the boundary values $e=0$ (inelastic) or $e=1$ (elastic). For each one of these conditions, trip was modeled as a frictionless, instantaneous collision against a fixed obstacle, with generalized velocities just after the collision computed with Eq. (6). Body motion after the collision was predicted by applying the unchanged, optimal neural excitations (controls) computed for the reference gait pattern.

In a further study, the measured horizontal force applied to the ankle joint of a subject to simulate a trip is applied to the model, Fig. 2. The experimental setup (Forner-Cordero, Koopman and van den Helm, 2003) consisted of a subject walking on a treadmill at 1.1 m/s. A rope attached at one end to the subject's ankle and at the other end to a locking mechanism and a load cell was responsible for applying a perturbation force to the ankle of the subject for approximately 200 ms. The force data set selected for this study corresponded to a subject whose anthropometric characteristics are similar to those of the model utilized in the simulations. The results are then compared to other two simulation results using different contact formulations: 1) impulse with same magnitude as integral of applied force over time acting at the instant of initial perturbation; 2) collision at the same instant modeled as inelastic with coefficient of restitution $e=0$.

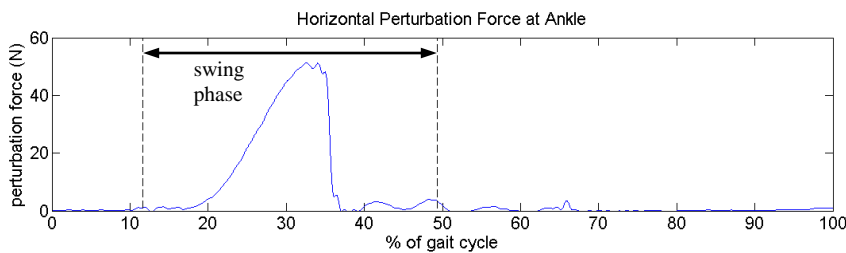


Figure 2 – Experimental horizontal perturbation force applied at the ankle joint.

RESULTS

For each simulation, the position and instant of the next foot contact following the trip was computed. Figure 3 shows snapshots of the simulated trip at three different instants for an inelastic collision ($e=0$) at the ankle. The dashed stick figures illustrate the unperturbed reference gait pattern. Figure 4 shows the predicted time between the trip and the next ipsilateral foot contact. Notice that the instant of contact after a trip is anterior to the next heel strike in normal gait (dashed line) for all simulated conditions. In the middle of the cycle (50%) the swing foot is at the lowest vertical positions, therefore, when there is a collision at the foot, it is brought to the ground, virtually bounced in the case of the elastic collisions at 40, 50 and 60% of the swing. Figure 5 shows the predicted distance between the CM and the front foot tip at the instant of foot-ground contact after the trip.

Figure 6 shows the results for the comparison of different contact formulations: a) normal unperturbed gait; b) trip with applied perturbation force $F(t)$ measured experimentally as shown in Fig. 2, (Forner-Cordero, Koopman and van den Helm, 2003); c) trip with perturbation modeled as an instantaneous impulse computed as in Eq. (5); d) trip with perturbation modeled as an instantaneous, inelastic, frictionless collision with coefficient of restitution ($e=0$).

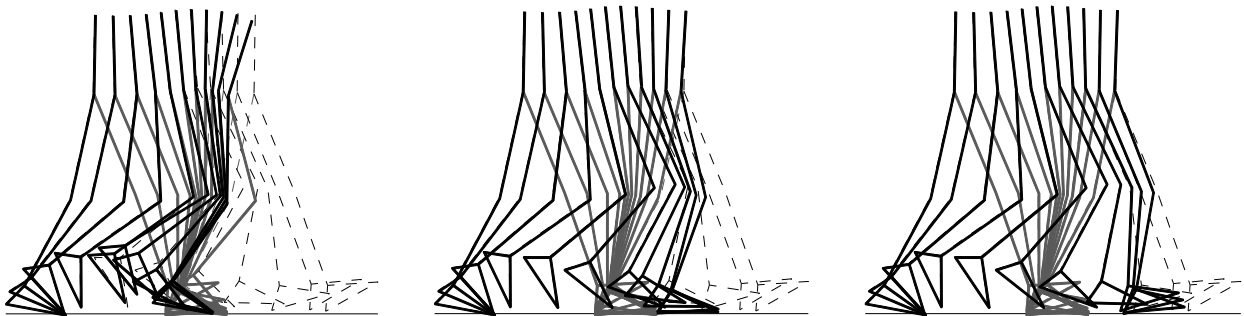


Figure 3 – Snapshots illustrating response to a trip (inelastic collision at the ankle) at 20% (0.233 s, left), 50% (0.370 s, mid), and 70% (0.462 s, right) of the swing phase.

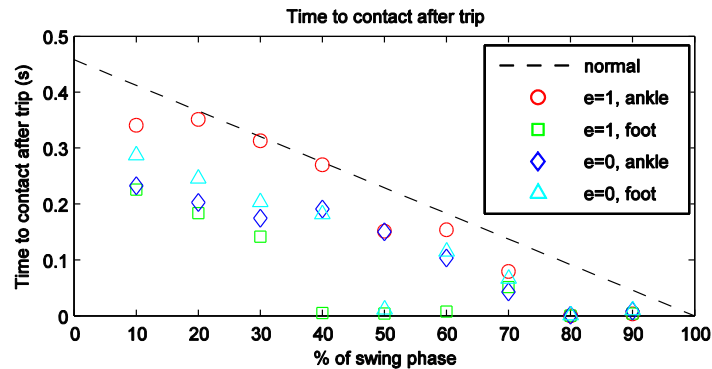


Figure 4 – Predicted time to foot-ground contact after trip.

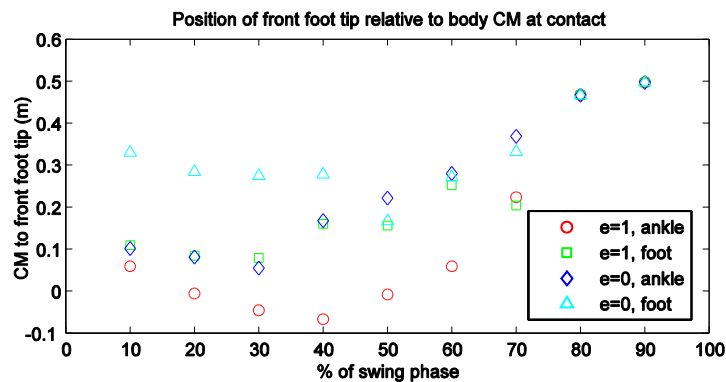


Figure 5 – Predicted distance between CM and front foot tip at foot-ground contact instant.

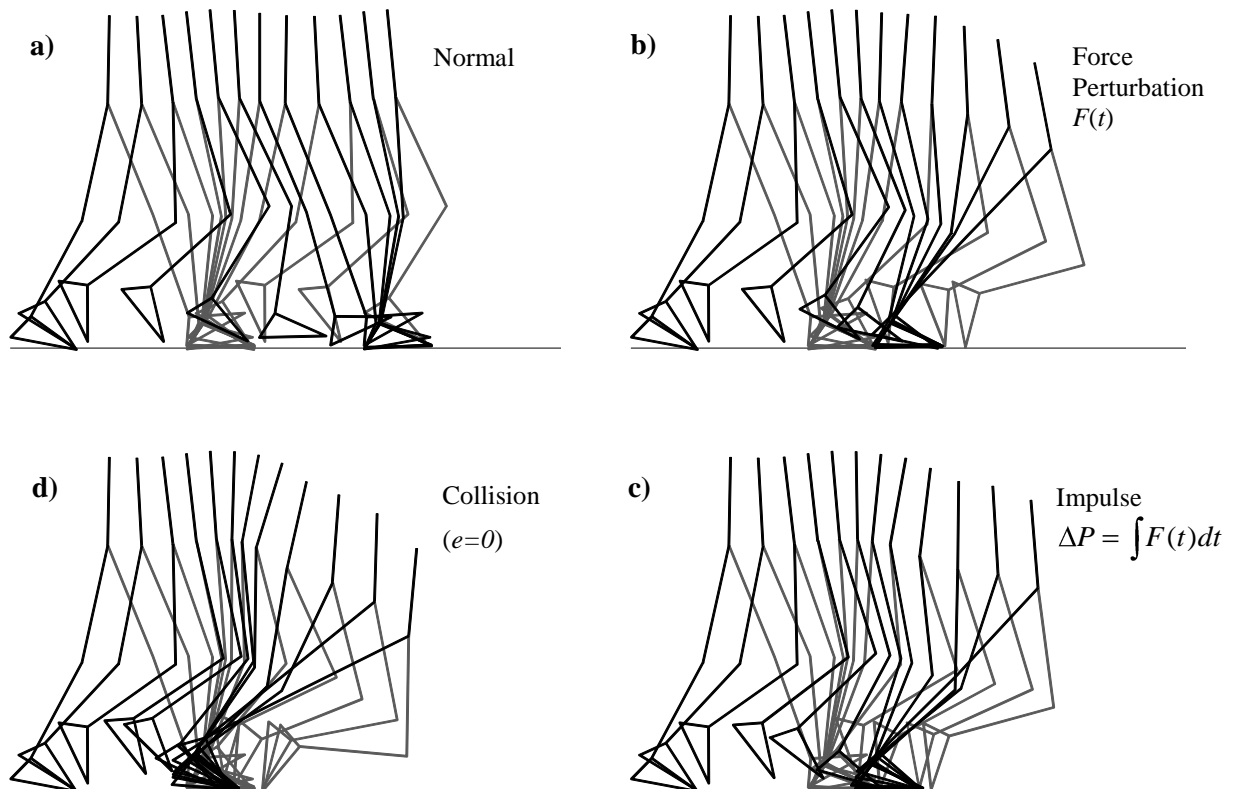


Figure 6 – Stick figures of simulations with different contact formulations: a) normal, unperturbed gait; b) experimentally measured force perturbation $F(t)$ applied to the ankle joint, Fig. 2; c) horizontal impulse applied to the ankle joint; d) inelastic frictionless collision ($e=0$) at the ankle joint.

DISCUSSION

The results are consistent with experimental data by Forner-Cordero, Koopman and van der Helm (2003), who observed subjects tend to respond with elevating strategies at early swing trips and lowering strategies at mid and late swing trips. Indeed, compared to the reference motion (dashed stick-figures), Fig. 2 shows an elevating movement of the foot just after a trip at 20% of swing, and lowering motions at 50% and 70% of swing. Interestingly, this post-trip behavior is a result of the “uncontrolled” behavior of the body after the trip, rather than an orchestrated response to the perturbation. Furthermore, according to Fig. 3, time between trip and foot-ground contact is, in particular for mid and late swing trips, within the latency period, i.e. in the first hundreds of milliseconds after a perturbation, a period in which the ongoing neuromuscular processes triggered by the perturbation have not yet altered muscle activation. These results suggest that the recovery strategy is determined to a great extent by the passive dynamics and feedforward control to the muscles.

In early trips, foot-ground contact is predicted to occur after the latency period, giving the person time to guide the limb to a more favorable position after the latency period and before the foot contacts the ground. On the contrary, in late swing trips, foot usually collides with the ground in the latency period and there is little opportunity for correction, with compensatory actions left for the following step. On the other hand, late swing trips, while offering less opportunity for correction in a first moment, lead to a favorable limb position after contact as contact occurs when leading foot is advanced with respect to the body CM. This increases the ability to counteract the forward inclination of the body, as suggested previously (Forner-Cordero, Koopman and van der Helm, 2004). Further investigation is necessary to predict the response after the latency period, which might include multiple steps and including a more complete muscular dynamics comprising reflexes and different activation patterns in order to simulate the behavior of elderly people or different pathological conditions.

The results in Fig. 6 show the importance of careful modeling of perturbations, in particular, when the perturbation is of short duration as typical in stumbling situations. In these cases, it is often convenient to formulate contact as an instantaneous event with force perturbation characterized by an equivalent impulse. Figure 6b and 6c show that, although the horizontal impulse has the same magnitude as the integral of applied force $F(t)$ over time, the results are notably different. The discrepancy can be partially explained by noting that a 200ms-perturbation is far from

instantaneous in this application and its modeling as an instantaneous event constitutes a strong simplification. In the absence of accurate measurements of perturbation force, the modeling of contact as an instantaneous collision characterized by a coefficient of restitution becomes attractive. However, selecting an appropriate coefficient of restitution is not a trivial task and the results, as illustrated in Figs. 4 and 5, are sensitive to the adopted value. Furthermore, a classical formulation of collision (with $0 < e < 1$) does not encompass all general force perturbations. In fact, the impulse applied in Fig. 6c is not sufficient to bring the ankle joint to rest and, therefore, there is no restitution phase. Consequently, there is no positive value of e equivalent to the applied impulse.

As a final consideration, it is important to mention that during impact events significant soft tissue motion occurs around the bones and the rigid body assumption loses strength. A way to consider tissue motion phenomena in a rigid body framework would be to utilize wobbling masses (Gruber et al., 1998; Pain and Challis, 2006). Gruber et al. (1998) show that, although the addition of wobbling masses to the model changes dramatically the internal forces during the first tens of ms after the beginning of impact, it has a rather limited influence on the kinematics of the model, which is perhaps the most important aspect in the study of fall mechanisms. This observation partially justifies the use of a rigid multibody model (without wobbling masses) for the study of recovery strategies after a stumble.

REFERENCES

- Ackermann, M., van den Bogert, A.J., 2010, "Optimality principles for model-based prediction of human gait", *Journal of Biomechanics*, Vol. 43, pp. 1055-1060.
- Aerts, P., de Clercq, D., 1993, "Deformation characteristics of the heel region of the shod foot during a simulated heel strike: The effect of varying midsole hardness", *Journal of Sports Sciences*, Vol. 11, pp. 449-461.
- Betts, J.T., 2001, "Practical Methods for Optimal Control using Nonlinear Programming", Philadelphia, USA: SIAM.
- Forner Cordero, A., Koopman, H.F.J.M., van der Helm, F.C.T., 2003, "Multiple-step strategies to recover from stumbling perturbations", *Gait and Posture*, Vol. 18, pp. 47-59.
- Forner Cordero, A.; Koopman H.F.J.M ; van der Helm F.C.T., 2004, "Mechanical model of the recovery from stumbling", *Biological Cybernetics*, Vol. 91, pp. 212-222.
- Forner Cordero, A., 2007, "Reduction in the reflex latencies of the Rectus Femoris during gait perturbation experiments", *Motor Control*, Vol. 11(S), pp. S178.
- Gerritsen, K.G.M., van den Bogert, A.J., Hullinger, M., Zernicke, 1998, "Intrinsic muscle properties facilitate locomotor control – a computer simulation study", *Motor Control*, Vol. 2, pp. 206-220.
- Gruber, K., Ruder, H., Denoth, J., Schneider, K., 1998, "A comparative study of impact dynamics: wobbling mass model versus rigid body models", *Journal of Biomechanics*, Vol. 31, pp. 439-444.
- Hayes, W.C., Myers, E.R., Robinovitch, S.N., van den Kroonenberg, A., Courtney, A.C., McMahon, T.A., 1996, "Etiology and prevention of age-related hip fracture", *Bone*, Vol. 18, pp. 77-86.
- Pain, M.T.G., Challis, J.H., 2006, "The Influence of soft tissue movement on ground reaction forces, joint torques and joint reaction forces in drop landings", *Journal of Biomechanics*, vol. 39, pp. 119-124.
- Pfeiffer, F., Glocker, C., 1996, "Multibody dynamics with Unilateral Contacts", Wiley, New York.
- Schiehlen, W., Seifried, R., Eberhard, P., 2006, "Elastoplastic phenomena in multibody impact dynamics", *Computer Methods in Applied Mechanics and Engineering*, Vol. 195, pp. 6874-6890.
- Smeeters, C., Hayes, W.C., McMahon, T.A., 2001, "Disturbance type and gait speed affect fall direction and impact location", *Journal of Biomechanics*, Vol. 34, pp. 309-317.
- A. M. Schillings, Th. Mulder and J. Duysens, 2005, "Stumbling Over Obstacles in Older Adults Compared to Young Adults", *J Neurophysiol*, Vol. 94, pp. 1158-1168.
- van den Bogert, A.J., Pavol, M.J., Grabiner, M.D., 2002, "Response time is more important than walking speed for the ability of older adults to avoid a fall after a trip", *Journal of Biomechanics*, Vol. 35, pp. 199-205.
- Winter, D.A., 1991, "The biomechanics and motor control of human gait: normal, elderly and pathological", 2nd ed., Waterloo: University of Waterloo Press.

RESPONSIBILITY NOTICE

The authors are the only responsible for the printed material included in this paper.

Fault Detection and Diagnosis in Sensors and Actuators of the Multi-Mission Platform in its Nominal Mode

Alexandre Carvalho Leite¹, Marcelo Lopes de Oliveira e Souza¹

¹ National Institute for Space Research – INPE, Av. Dos Astronautas, 1758-12227-010, S. J. Campos, SP, Brasil

Abstract: Fault detection and diagnosis have become an important issue in complex engineering systems, providing the essential requirements for fault tolerance, reliability and safety. An excellent example of such a system is the Multi-Mission Platform – MMP, a multipurpose satellite currently being designed by INPE. So, the objective of this paper is to discuss fault detection and diagnosis in sensors and actuators of the Multi-Mission Platform - MMP in its Nominal Mode. The methodology of fault detection and diagnosis can be used in any of the three classical approaches to deal with faults: the first, called fault avoidance, tries to avoid faults by using quality assurance, derating, screening of parts, careful assembly and soft handling during operation time or flight time; the second, called fault tolerance, considers that despite the first approach, faults still happen and must be tolerated during operation time or flight time; the third, called fault correction, considers that despite the first and second approaches, faults may need to be corrected during operation time or flight time. We employed the third approach in this work describing our assumptions, fault models, fault modes, fault detection and diagnosis schemes and an application example of the MMP including Hardware-in-the-Loop simulation results. Finally, we give some outlook about our intended implementations of supervisory control systems and conclusions and comments regarding robustness, promptness of detection and correction of diagnosis deduction sets.

Keywords: *Fault Detection, Fault Diagnosis, Fault Tolerance, Hypothesis Testing, Adaptive Threshold*

INTRODUCTION

Fault tolerance has always been known by good engineering practices like hardware redundancy. In the current complex engineering systems, there are several redundancy levels and several additional redundancy domains: software redundancy, information redundancy and time redundancy. Nowadays we have theoretic tools which allow the management of some aspects of each redundancy domain. Textbooks like Blanke et al. (2010), Gertler (1998), Isermann (2005), Korbicz et al. (2004) and Vachtsevanos et al. (2006) cover fault detection, fault diagnosis, reconfiguration and fault accommodation according with: 1) continuous approaches based on state space equations and 2) hybrid approaches leading with state space equations with varying structure.

The aerospace industry brought fault tolerance capabilities into civil and military airplanes, autonomous spacecrafts and launchers in NASA (2010a), NASA (2010b) and Boegh et al. (1997) and many other examples. Although, the faults are still happening (Funch, 2010), (Lann, 1996) and the new engineering methods must be able to cope with a broader range of fault scenarios, either by knowledge or handling of the possible faulty modes. These are the two building blocks of a fault tolerant system: knowledge gaining and fault handling actions. The next subsection will give an insight about our assumptions to build a fault tolerant system based on those building blocks.

Assumptions

There are three assumptions adopted in this work to develop a fault tolerant system:

1. There will always be intractable or inevitable fault situations during the life time of an Engineering System.
2. A valid effort is an attempt to accommodate, recover or delay some of the most probable fault modes.
3. Faults are always handled by a two layered procedure: gathering knowledge about the system's health and safety action.

The first assumption comes from an application of the *Russel's paradox*, noted by Souza (2006) and we call *Supervisor's Paradox*. The paradox is stated as follows:

There is a dynamic system automated by several Hybrid Subsystems (y). Every y of that dynamic system is kept fault-tolerant through Safety Actions ($sa(\cdot)$) performed by another Hybrid Subsystem, called x . The Hybrid Subsystem x performs $sa(\cdot)$ (i.e. acts as supervisor) in all and only those y which are not able to perform $sa(\cdot)$ themselves.

We describe the previous statement using first-order logic.

$$(\exists x)(supervisor(x) \wedge (\forall y)(\neg sa(y, y) \Leftrightarrow sa(x, y))) \quad (1)$$

If x is assigned to y (because it is also a Hybrid Subsystem), the following contradiction occurs $\neg sa(x, x) \Leftrightarrow sa(x, x)$. To avoid the tension behind the statement we made the first assumption.

Note that the context of the first assumption entitles the whole set of probable fault modes. The range of our work is still restricted by the consideration of a reduced subset of the probable fault modes.

The faults are not always present on a dynamic system; they can happen and vanish unexpectedly. Safety actions are intended to keep the dynamic system working within an acceptable or inexistent deviation of its primary objectives. These actions can be performed only after sufficient knowledge about the fault mode(s) is gained. Knowledge gathering followed by safety action is the cascaded procedure assumed as the reasonable attempt to give fault tolerant characteristic to a dynamic engineering system.

FAULT TOLERANT SUPERVISORY CONTROL (FAULT GNOSIS AND FAULT REACTOR APPROACH)

The basic idea behind the proposed procedure is a generalization of well-known FDIR (Fault Diagnosis, Isolation and Reconfiguration) systems. In our procedure, knowledge gained before the occurrence of a fault is also used to perform safety actions to delay the occurrence of a fault.

Fault Gnosis

In our approach Fault Detection, Diagnosis and Prognosis are *propositional sub theories* of a Fault Gnosis *propositional theory*, called Fault Gnosis theory for brevity. The propositional *sub theories* are defined as follows:

Fault Detection propositional theory, $\langle L_{\text{det}}, S_{\text{det}} \rangle$

$$L_{\text{det}} = \{ \text{detector, threshold, fault detection, fault occurrence, unknown} \}$$

$$S_{\text{det}} = \left\{ \begin{array}{l} \text{detector} > \text{threshold} = \text{fault detection,} \\ \text{fault detection} \supset \text{fault occurrence, } \neg \text{fault detection} \supset \text{unknown} \end{array} \right\}$$

Note that the absence of detection does not imply in a fault free case. The pair $\langle L_{\text{det}}, S_{\text{det}} \rangle$ is composed of only two axioms for a specific single fault detector.

Fault Diagnosis propositional theory, $\langle L_{\text{dia}}, S_{\text{dia}} \rangle$

$$L_{\text{dia}} = \left\{ \begin{array}{l} \text{fault occurrence, detector}_1, \dots, \text{detector}_n, \text{Symptom}_1, \dots, \text{Symptom}_m, \\ \text{fault modes, Fault set}_1, \dots, \text{Fault set}_m \end{array} \right\}$$

$$S_{\text{dia}} = \left\{ \begin{array}{l} \text{fault occurrence} \wedge \text{detector}_1 \in \text{Symptom}_1 \supset \text{fault modes} \in \text{Fault set}_1 \wedge 1 \in J, \\ \vdots \\ \text{fault occurrence} \wedge \text{detector}_1 \in \text{Symptom}_m \supset \text{fault modes} \in \text{Fault set}_m \wedge m \in J, \\ \vdots \\ \text{fault occurrence} \wedge \text{detector}_2 \in \text{Symptom}_1 \supset \text{fault modes} \in \text{Fault set}_1 \wedge 1 \in J, \\ \vdots \\ \text{fault occurrence} \wedge \text{detector}_2 \in \text{Symptom}_m \supset \text{fault modes} \in \text{Fault set}_m \wedge m \in J, \\ \text{fault modes} \in \bigcup_{i \in J} \text{Fault set}_i \end{array} \right\}$$

The diagnosis procedure instantiates several detectors and incorporates previous knowledge from m distinct *Symptom* sets. The pair $\langle L_{\text{dia}}, S_{\text{dia}} \rangle$ is composed of $n \times m + 1$ axioms, because it is dependent on the instantiation of fault detectors and size of the knowledge base; the aggregation formula is always the last axiom to give the verdict about the current faulty state.

Fault Prognostics propositional theory, $\langle L_{\text{pro}}, S_{\text{pro}} \rangle$

$$L_{\text{pro}} = \{ \text{unknown, RUL}_{\text{computation}}, \text{MCM}_{\text{computation}}, \text{MTTF}_{\text{computation}} \}$$

$$S_{\text{pro}} = \{ \text{unknown} \supset \text{MTTF}_{\text{computation}}, \text{fault occurrence} \supset \text{RUL}_{\text{computation}} \wedge \text{MCM}_{\text{computation}} \}$$

MCM means in the last propositional *sub theory* means Mission Criticality Measure, RUL means Remaining Useful Life and MTTF stands for Mean Time to Fault. We distinguish between Fault and Failure concepts; this is the reason to use Mean Time to Fault nomenclature instead of Mean Time to Failure. An interesting point in prognostics is that the

fault avoidance background is useful to define reliability measures and incorporate knowledge from the detectors. In other words, there is a blend between fault tolerance and fault avoidance worlds.

Finally we define Fault Gnosis theory as $T_G = \langle L_{det} \cup L_{dia} \cup L_{pro}, S_{det} \cup S_{dia} \cup S_{pro} \rangle$. It permits a broad range of fault knowledge acquisition. The simplest Fault Gnosis structure would be composed of one Fault Detector, one Symptom set and a MTTF estimator. One can see that the proposed Fault Gnosis theory encloses a large spectrum of fault knowledge acquisition schemes.

Fault Reactor

A Fault Reactor uses the information from the Fault Gnosis system to smoothly keep a safe trajectory of the dynamic engineering system. Control system standard specifications, MTTF and ROL must remain inside an acceptable region. The control system standard specifications envelope (e.g. overshoot and steady state error margins) is allowed to be relaxed to prioritize safety actions in case of a high (bad) MCM.

Several safety actions are possible in the case of this Meta Controller (Fault Reactor): control signal changing, actuator’s switching, fault masking, sensor signal’s weighting, controller parameter’s change, estimator parameter’s change. To draw an analogy between a Fault Reactor and a normal controller, a safety action is a kind of “control signal” of a Fault Reactor. Mathematically it can be expressed as follows.

$$safety\ action = f(MTTF, RUL, Fault\ Mode, MCM, system\ dynamics) \tag{2}$$

However the Fault Reactor is sensitive to the Fault Gnosis system, we do not design the two things together. The impact of this decision can be studied, but we are primarily concerned with the development of a Supervisory Control System (Fault Gnosis + Fault Reactor).

FAULT MODELS AND FAULT MODES

Our application example is the Multi-Mission Platform satellite (Lopes et al., 2001), gyroscopes and reaction wheels are the focused components. Four fault modes for the sensors (gyros) and additionally four fault modes for the actuators (reaction wheels) are considered. Figure 1 shows a holistic view for modeling of sensors and actuators in normal and fault modes.

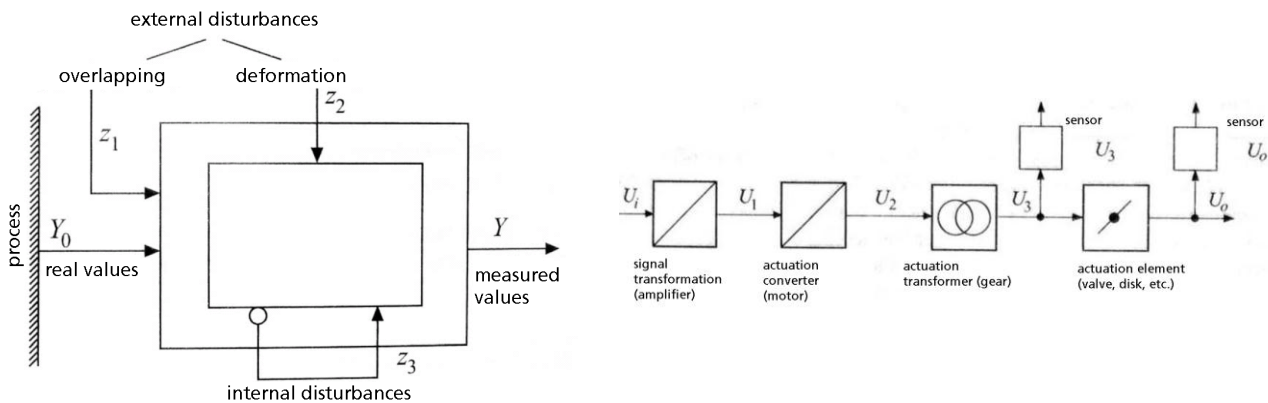


Figure 1 – General sensor (left) and actuator (right) models

The measured data acquired from the sensor is corrupted with dynamic effects of the transducer, its signal conditioning electronics and environmental factors represented as disturbances. The control action provided by the actuator comes from a series of power/signal conversions and sometimes depends on an additional simple control loop (as in the case of reaction wheels). These information and energy paths can either be sources of faults or even sources of unwanted information to confuse the fault detectors.

Figure 2 shows an example of sinusoidal sensor signals when corrupted with the four sensor fault modes: F1 – constant random value; F2 – last value; F3 – offset drift; F4 – scale factor drift. For details on the mathematical models, we refer the interested reader to Leite (2007). The mathematical models are basically mathematical functions inserted additively or multiplicatively in the noise (zero-mean Gaussian) corrupted attitude angles.

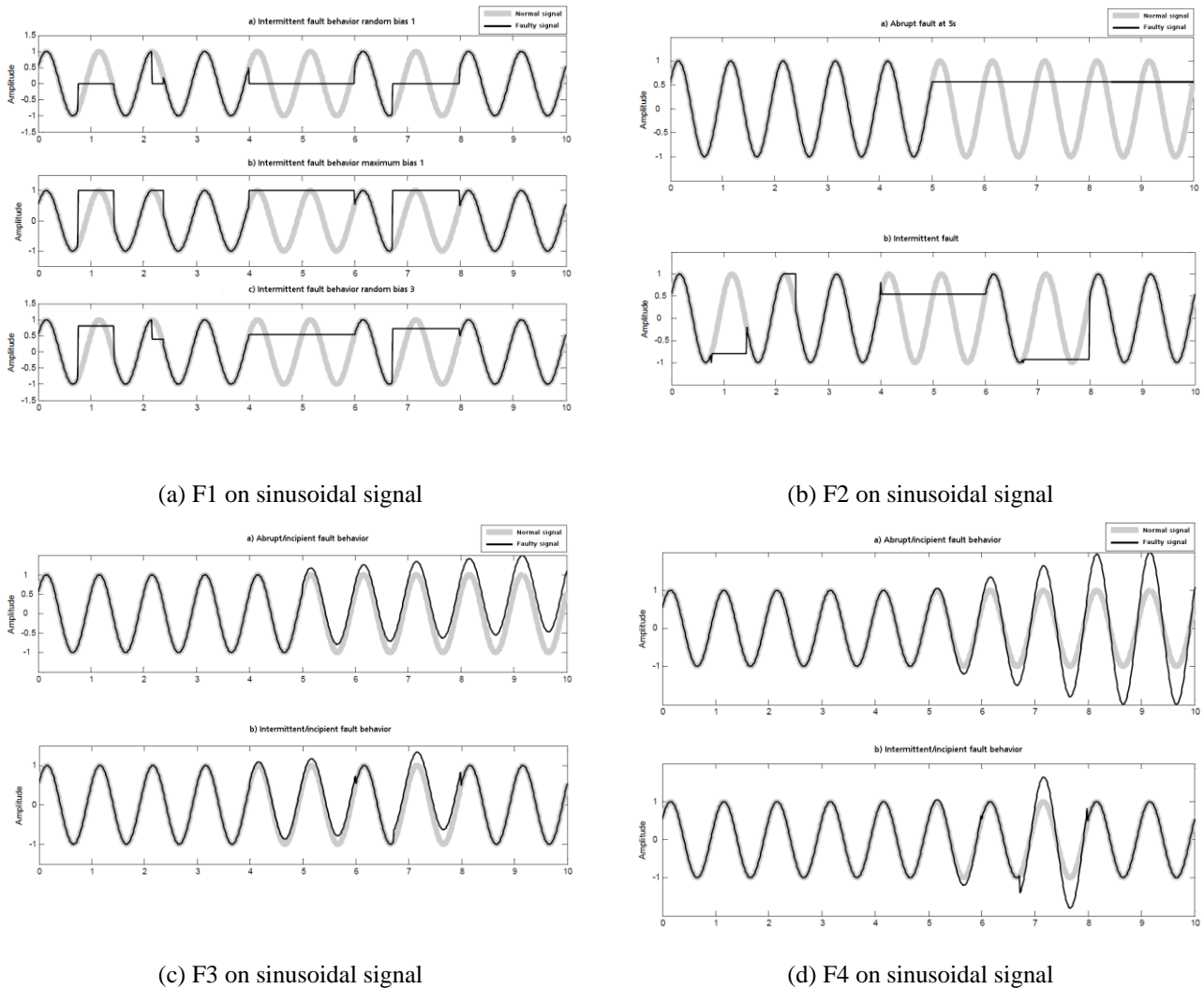


Figure 2 – Faulty signals (black) compared with a sinusoidal fault free (light gray) sensor signal.

Other four faults were adopted for the attitude actuators (reaction wheels): F5 – angular velocity above the limit; F6 – angular velocity close to zero for a long period of time; F7 – high armature current in steady state behavior; F8 – angular velocity increasing without command. The mathematical models of the actuators’ fault modes were defined on the frequency domain (Leite, 2007).

FAULT DETECTION AND DIAGNOSIS

Fault detection is performed by means of decision functions as a signal processing stage taking the measured data from the AOCS (Attitude and Orbit Control System). Figure 3 shows the overview of this Detection/Diagnosis scheme, note that the signal processing is different for sensor faults and actuator faults. Although, the processed measurements are scaled in the third stage according with adaptive thresholds, which are linear modular functions of the control actions’ amplitudes. The fourth and last stage of the Detection/Diagnosis procedure is the comparison of the thresholds under the knowledge embodied in a decision structure (a speculative truth table, see Nyberg (1999)), this is the Structured Hypothesis Test. The output of the whole signal processing task is the declaration of a set of most probable fault modes. Results can include normal mode as probable fault mode, it introduces some robustness to the diagnosis task. In the case of disturbances and faults on the same range, a probable fault mode is the fault-free state.

Our knowledge-based approach uses model knowledge in the decoupling of the signal components and filtering in the first signal processing stage; scaling with adaptive thresholds uses the knowledge about the environmental conditions like disturbance behavior and ranges; and the decision structure is designed according with the knowledge about the coupling between component-level faults and its effect on system behavior. The next sections will provide additional detail about this design procedure.

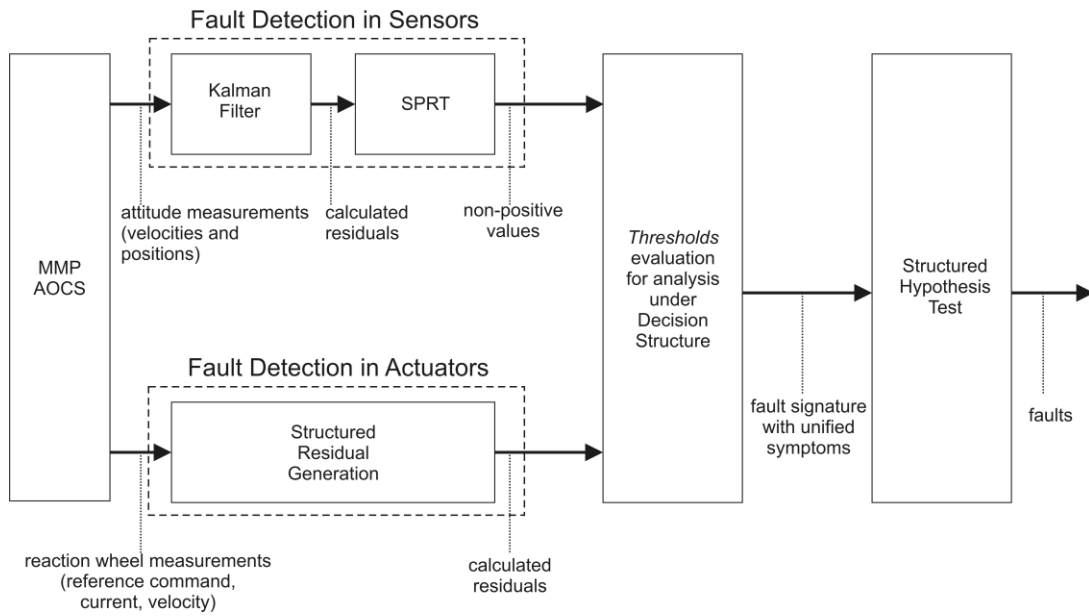


Figure 3 – Fault detection and diagnosis scheme.

Fault Detection

As commented in the previous section, the decision functions are designed according with component-level models, system behavior and environmental conditions. To design suitable decision functions sensitive to the predefined fault modes, we injected faults on our AOCS simulation model (including environment, attitude dynamics, instrumentation dynamics and signals) and investigated the effects. Table 1 summarizes the sensitivity of the Kalman filter innovations of the attitude gyroscopes as response to the faults injected on the pitch gyro in four distinct simulations.

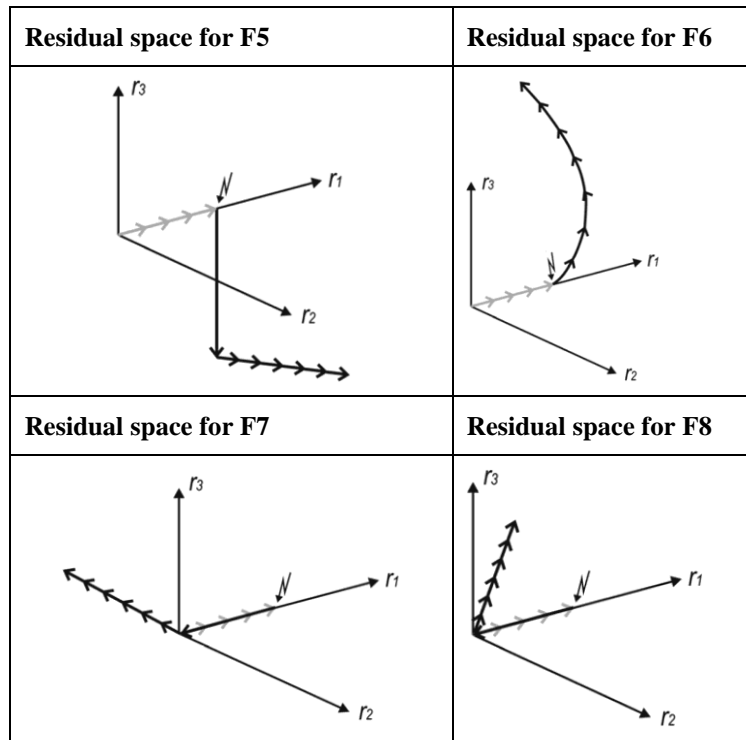
Table 1 – Sensitivity of the decision functions for the faulty sensors.

Fault mode in the pitch gyro	Roll gyro innovation	Pitch gyro innovation	Yaw gyro innovation
F1			
F2			
F3			
F4			

Observing the results of table 1, we note that the innovations of the faulty sensor are most sensitive to the injected fault. However, the behavior is not the same for other faults injected on the same sensor. There are direction change of the residuals, which is a good characteristic and valuable information used to build the decision structure.

Each reaction wheel has three structured residuals to decouple faults related with mechanical and electrical parts. Table 2 shows the trajectory of the structured residuals in the structured residual space. The direction change and increase in the amplitude of the residuals can be unstable (because the fault can make the whole AOCS unstable) or achieve quickly the steady state. The pattern provided by table 2 is appended into the decision structure to perform hypothesis testing on the diagnostics phase.

Table 2 – Structured residual space trajectory for a faulty reaction wheels.



Fault Diagnosis

After gaining knowledge about the response of the designed decision functions (innovations and structured residuals) to the component faults, it is possible to construct the decision structure like that of figure 4.

	F_1	\dots	F_q
s_1	κ_{11}	\dots	κ_{1q}
\vdots	\vdots	\ddots	\vdots
s_p	κ_{p1}	\dots	κ_{pq}

Figure 4 – Decision structure.

Each element κ of this table can assume three values: 0, 1 or \times . The semantics of these values is:

- If the current fault $F_a = F_j, \forall j \in \{1, \dots, q\}$ and the symptom (decision function compared with threshold) $s_k = 0, \forall k \in \{1, \dots, p\}$, then $\kappa_{kj} = 0$.
- If the current fault $F_a = F_j$ and the symptom (decision function compared with threshold) $s_k = 1$, then $\kappa_{kj} = 1$.

- If the symptom $s_k = 1$ or $s_k = 0$ are not sufficient information to decide about the fault characteristic, then $\kappa_{kj} = \times$.

For our application example, the Multi-Mission Platform, we used a 15×25 decision structure. This means 15 symptoms for 25 fault modes including the normal mode. Each diagnosis task is executed and several symptoms' sets are returned as a result, intersections are performed to achieve a reduced set capable of deducing the actual fault present in the system.

APPLICATION EXAMPLE: MULTI-MISSION PLATFORM IN ITS NOMINAL MODE

A satellite has several operating modes, in this work we dealt only with the nominal mode of the Multi-Mission Platform. The fault modes could occur in other stages of the satellite's life or in other operating modes, but this is not the case here. Several simulations were performance to characterize in some way the FDD (Fault Detection and Diagnosis) system. Figure 5 shows the risk measure (lose alarm rate) as a function of the amplitude of the fault F1 and the amplitude of the chosen threshold.

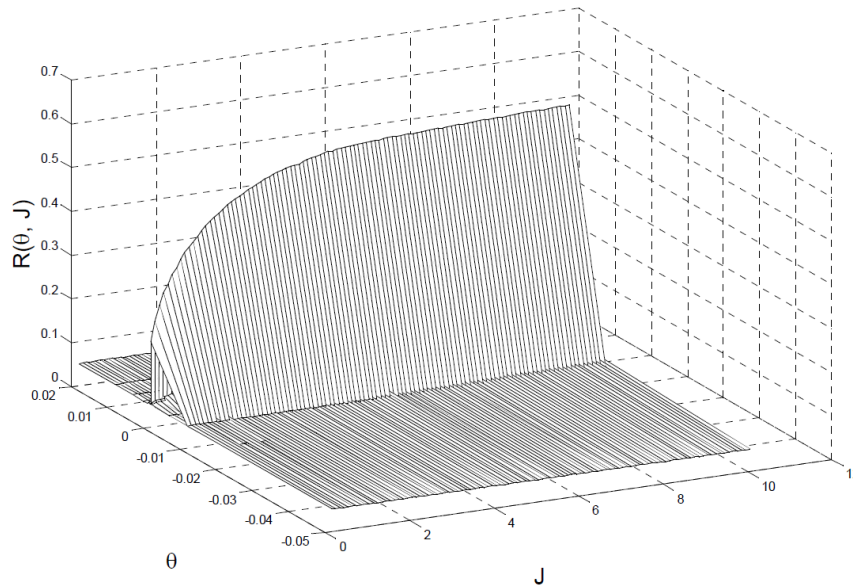


Figure 5 – Lose alarm rate R as a function of fault F1 amplitude θ and the related threshold J.

Intermittent faults may force an undesired behavior of the FDD, a delay in the declaration of the fault-free mode after a fault has vanished. It is interesting in the case of reconfiguration of the control system. See figure 6 and note that there is an exponential property in the designed FDD system when comparing alarm loss rate and fault-free declaration delay.

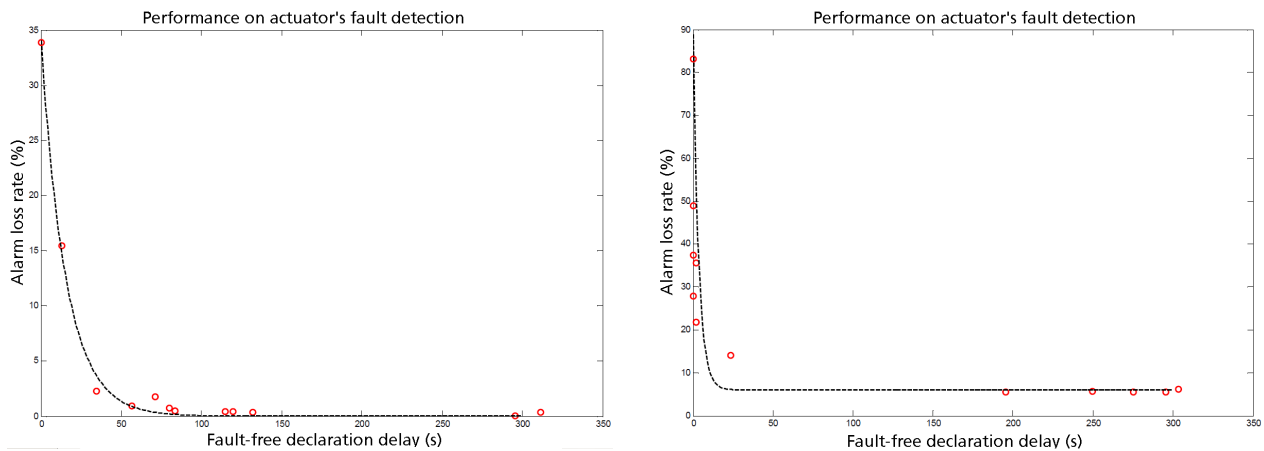


Figure 6 – Fault free delay and alarm loss rate relationship.

It shows the well known contradiction present in the design of FDD systems. But note that it can be used as a design metric to find a compromise of such performance measures and synthesize a suitable FDD system. A kind of Pareto frontier could be a reasonable trade-off solution in future designs.

The same design procedure, simulation and simulation model were used to implement a Hardware-in-the-Loop (HiL) simulation including a real DC motor in the control loop. This DC motor emulated the behavior of a reaction wheel by means of a Model Reference Adaptive Controller designed specifically to this purpose so that real failures could be applied to test the performance of our approach.

The real faults injected on the motor were: F1 – loss of stop signal of the AD converter; F2 – loss of a bit of the DA converter. Table 3 summarizes the results of the FDD system.

Table 3 – Summarized results of the HiL simulation.

Fault	Fault injected	Return to fault-free	Fault detection	Last fault declaration	Diagnostic instructions containing F1	Diagnostic instructions containing F2
F1	240s	243s	240.5s	243.9s	33	33
F2	240s	243s	240.4s	243.9s	3	36

OUTLOOK

The logical structure of Fault Diagnosis is dependant on Fault Detection. We propose one specific implementation of a Fault Gnosis structure to future works, where:

1. The design of detectors takes performance measures of the diagnosis system (false diagnostic rate and inconclusive diagnostic rate) into account. The intended approach is standard detection filters with new diagnosis specifications incorporated.
2. The adaptive thresholds are computed in order to find a compromise among the performance measures of the Detection/Diagnosis system (promptness of detection, false alarm, false diagnostic and inconclusive diagnostic). The intended approach is differential game theory and adaptive filtering.
3. The MTTF is estimated before the detection of a fault, and after that the ROL and MCM measures are estimated. The intended approach is based on reliability analysis with dynamic aspects incorporated through acquired knowledge from the detectors (residual generators).

The proposed implementation of a Fault Gnosis structure is able to provide sufficient information to synthesize a Fault Reactor. The outlook for a new Fault Tolerant Supervisory Control would include a Fault Reactor consisting in four parts:

1. Control allocation before the detection of a fault. A multi-actuated system can allocate the control signals in order to increase the MTTF of the entire system. A single-actuated system can smooth the control signal to reduce wear and contribute to the increase of the MTTF.
2. Inside a given time span of detection/diagnosis, switching control system and control reconfiguration are applied to smoothly switch between distinct fault operating modes. Fault accommodation and reconfiguration techniques are intended to be used.
3. After the defined time span, ROL assumes the role of MTTF, but in a post fault case. And performs the first part again to maintain ROL as high as possible.
4. In case of increase of MCM, the standard specifications of the control systems are relaxed and the controllers are re-synthesized to further increase ROL.

Obviously the dynamic engineering system is close to the end of its life in the case of the fourth step, but it expresses the attempt of the system to avoid and tolerate the presence of faults until the end of its useful life.

CONCLUSION AND COMMENTS

The simulation results gave us a lot of insights about improvements which can be achieved and new development directions to be followed. Promptness of detection can be achieved but at a certain cost of false alarm rate, any improvement on the promptness of detection can degrade robustness to external disturbances. Diagnosis is based on knowledge from simulation or experimentation results, and the ability to deduce a reasonable set of possible faults is constrained to this amount of knowledge. It means the fault modeling effort is always valid because experimentation can be prohibitive in several cases.

An important issue in detection is the adaptability of the thresholds; they are supposed to distinguish between disturbances and fault effects either in the absolute range or in the rate of change of the decision functions. There are lots of methods to design decision functions (residual generators), filtering techniques and observer schemes are still successfully used in fault detection context. Linear transformations to form a base of structured residuals are also modified to get highly fault-sensitive decision functions. Adaptive thresholds are our strategic choice to design robust fault detectors, and some bargaining approach should be applied in order to have a fair diagnosis deduction set.

REFERENCES

- Blanke, M., Kinnaert, M., Lunze, J., Staroswiecki, M. and Schröder, J., 2010, "Diagnosis and Fault-Tolerant Control". Ed. Springer, 2nd edition.
- Boegh, S. A., Wisniewski, R. and Bak, T., 1997, "Autonomous Attitude Control System for the Ørsted Satellite", IFAC Workshop on Control of Small Spacecraft, Breckenridge, USA.
- Funch, J., 2010, "Toyota Sudden Acceleration: A case study of the national highway traffic safety administration recalls for change", Loyola Consumer Law Review.
- Gertler, J. J., 1998, "Fault Detection and Diagnosis in Engineering Systems", Ed. CRC Press.
- Isermann, R., 2005, "Fault-Diagnosis Systems: An Introduction from Fault Detection to Fault Tolerance", Ed. Springer.
- Korbicz, J., Koscielny, J. M., Kowalczyk, Z. and Cholewa, W., 2004, "Fault Diagnosis: Models, Artificial Intelligence, Applications", Ed. Springer.
- Lann, G., 1996, "The Ariane 5 Flight 501 Failure - A Case Study in System Engineering for Computing Systems", Research report n°3079, Institut national de recherche en informatique et en automatique.
- Leite, A. C., 2007, "Detecção e diagnóstico de falhas em sensores e atuadores da plataforma multi-missão", Tese de Mestrado, Instituto Nacional de Pesquisas Espaciais – INPE, S. J. Campos, Brazil.
- Lopes, R. V. F., Silva, A. R., Saturno, M. E., Santos, W. A. and Pessota, F., 2001, "Multi-Mission Platform Attitude Control and Data Handling (ACDH) Subsystem Specification", Relatório Interno, INPE.
- NASA, 2010a, "NASA – Propulsion Controlled Aircraft", <http://www.nasa.gov/centers/dryden/history/pastprojects/PCA/index.html>.
- NASA, 2010b, "Voyager - Did you know?", <http://voyager.jpl.nasa.gov/mission/didyouknow.html>
- Nyberg, M., 1999, "Model Based Fault Diagnosis: Methods, Theory and Automotive Engine Applications", Electrical Engineering PhD. Thesis, Linköping University, Linköping – Sweden.
- Souza, M. L. O., 2006, (personal communication), August, S. J. Campos, SP, Brazil.
- Vachtsevanos, G., Lewis, F. K., Roemer, M., Hess, A. and Wu, B., 2006, "Intelligent Fault Diagnosis and Prognosis for Engineering Systems", Ed. Wiley.

RESPONSIBILITY NOTICE

The authors are the only responsible for the printed material included in this paper.

Numerical model for modal analysis of structures subjected to post-buckling

Mariano Andrés Arbelo¹, Sérgio Frascino Müller de Almeida¹, and Sandro Rondon Rett¹

¹ Instituto Tecnológico de Aeronáutica – ITA, CTA-ITA-IEM, Pça Mal. Eduardo Gomes nº 50, 12.228-900, São José dos Campos - SP, Brazil

Abstract: The aim of this paper is to present a new methodology that is able to characterize the natural frequencies of vibration of a panel subjected to compression loading in the post-buckling regime. The methodology is based on the calculation of a reduced flexibility matrix in the deformed state, considering the nonlinear behavior of the structure when loaded in the post-buckling regime. Moreover, a reduced mass matrix is calculated using a Guyan reduction. The results of the proposed methodology are compared to the classical linear frequency analysis and discussed.

Keywords: Post-buckling, Guyan reduction, Nonlinear behavior.

INTRODUCTION

The use of finite elements models for the analyses of aeronautical structures is increasing due to the potential reduction in both manufacturing and operational costs of aircraft. For example, a cost reduction is achieved by partially replacing large scale testing of substructures by their equivalent numerical models.

The first finite element models employed were able to represent adequately the behavior of aeronautical structures because classic design methodologies are based on linear analyses. In this design approaches typically limit and ultimate loads are far below the load which would cause non-linear behavior.

Consistently, the models employed for aircraft design aim at determining the linearized buckling loads and natural frequencies of a sub-structure. These models are only suitable to verify whether the buckling loads are above the operation loads and to identify the values of resonant frequencies, avoiding possible coupling of vibration modes. With this concept, the linear finite element models used to characterize the buckling loads and frequency response of structures loaded in the linear regime are adequate for the classic design of aircraft structures.

New possibilities are currently being explored due to the advances in metallic materials and the development of new high-performance composites for aeronautical industry. As a result, new design procedures need to be developed to account for buckling of the structure, keeping in mind that buckling can be an acceptable phenomenon in some regions of the flight envelope. Thus, it is necessary to predict the eventual changes in natural frequencies of those non-linearly loaded structures. Linear models are clearly unsuitable for this new design concept.

This paper aims at presenting the effects on the dynamic behavior of a structure loaded in the post buckling regime characterizing the variation of natural frequencies and mode shapes.

OBJECTIVES

The main contribution of this work is to present a numerical methodology able to characterize the modal dynamic behavior of an aeronautical structure loaded in the post buckling regime in terms of its natural frequencies and mode shapes. The methodology proposed herein can be applied to study the variations of natural frequencies of vibration and modes of any structure subjected to post buckling. Geometric and material nonlinearities, initial geometric imperfection as well failure and degradation models can also be included in the finite element model. The validation of the finite element model proposed in this work will be performed by a series of experimental tests on a flat aluminum plate with geometric imperfection, subject to uni-axially applied compressive in-plane load.

This work will present and discuss a new design methodology to obtain the natural frequencies of vibration of a structure subjected to loads in the post-buckling regime. The nonlinear effects are considered by calculating a reduced flexibility matrix of the structure in the deformed state. Additionally, a reduced mass matrix is calculated using Irons-Guyan condensation (Guyan, 1965 and Irons, 1965), in order to compute the natural frequencies of the substructure with a reduced number of degrees of freedom of the system (Craig, 2006).

REVIEW OF PREVIOUS WORK

The first works focused on the dynamic study of structures loaded in the post-buckling regime developed several analytical models which tried to characterize their free vibration behavior. However, their applicability to the aeronautical industry was limited due to the idealizations considered and to the inherent limitations of the analytical

models. Some of the earliest works of relevance were presented by Ilanko and Dickinson (1987). The authors published a series of papers detailing theoretical and experimental studies on the behavior of a simply-supported plate subjected to uni-axially, in-plane, compressive load in the post-buckling regime, measuring the changes in the fundamental frequencies of the plate. From the theoretical point of view, the authors used a Rayleigh-Ritz approximation, with a deflection function formulation for both the in- and out-of-plane behavior of the plates, which allowed for the convenient modeling of various types of in-plane boundary conditions, including those used in the experimental study. The model also considered the effects of initial geometric imperfection. Theoretical results were presented showing the influence of boundary conditions adopted and the different degrees of geometric imperfection proposed.

More details of similar works can be found in Moussaoui (2002), who presented a detailed literature review focused on research topics related to the study of nonlinear vibration in structures such as plates and shells. Among the topics mentioned in Moussaoui's paper are several references to studies of the dynamic behavior of structures subjected to loads in the post-buckling regime such as Chia (1987), Fu (1989 and 1993) and Iu (1988).

With the development of finite element models, new studies started comparing the responses of numerical and analytical models for basic structures. Cheng and Yu (2006) compared the results of the study of post-buckling behavior of laminated composite panels subjected to biaxial loads, including mode jumping, using a finite element approach and an analytical model. The results of the analytical model showed how the fundamental frequency drops to zero when the structure undergoes a bifurcation point and how it is greatly increased in the post-buckling region.

In recent years, the characterization of the vibration and stability of structures in composite laminates subjected to thermomechanical loading is been studied by many researchers due to the increased use of such materials in structural components in aerospace industry, the defense sector and other high performance systems. Girish and Ramachandra (2005) studied the variations in natural frequencies of symmetric laminated plates made of composite materials, subjected to uniform temperature loads in thickness, in the post-buckling regime. The structural model is based on a higher-order shear deformation theory incorporating the Von Kármán nonlinear relationships of displacement-strain and initial geometric imperfection. The numerical results show a decrease in natural frequencies in the pre-buckling regime. After buckling, the frequencies increase again with increasing temperature due to increased non-linear stiffness of the panel. It is also noted that the presence of small values of initial geometric imperfection in the panel significantly affects the behavior of vibration frequencies. Without geometric imperfection in the panel, the natural frequency drops to zero at critical temperature load, where buckling of the structure occurs. Moreover, with small values of initial geometric imperfection, the fundamental frequency reaches a non-zero minimum in the region of buckling load.

Other numerical works published by Singha et al (2006) and Chen & Virgin (2006) should also be mentioned. These studies were focused on investigating the dynamic behavior and the mode jumping phenomenon in the post-buckling regime of thin panels with thermomechanical loads.

Currently, some experimental work are being developed at the Instituto Tecnológico de Aeronáutica – ITA – in order to characterize the dynamic behavior of structures subjected to loads in the post-buckling regime. As an example, Almeida and Vasconcelos (2009) characterized the dynamic behavior of a reinforced panel laminated in composite materials subjected to in-plane shear loads in the pre and post-buckling regime. The results showed a significant variation if the natural frequencies and modes of vibration as a function of the applied load, as well as a loss of effectiveness of the stiffeners bonded to the panel at high frequency.

EXPERIMENTAL MODAL ANALYSIS

Materials and test device

To validate the numerical method for dynamic analysis of structures subjected to loads in the post-buckling regime, we used an aluminum plate of 2 mm thick, with initial geometric imperfection, loaded in uniaxial compression. The geometry of the plate is shown in Fig. 1.

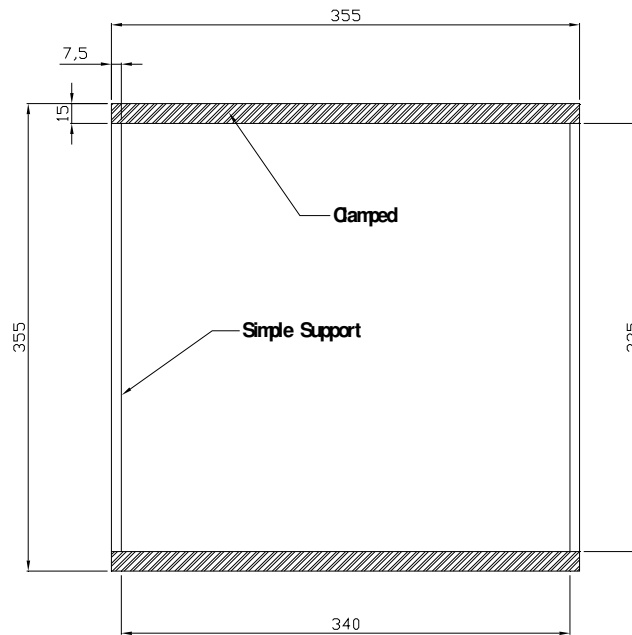


Figure 1 – Geometry of specimen (dimensions in millimeters).

The plate was mounted in a load frame with boundary conditions shown in Fig. 1. The top and bottom edges are clamped and subjected to compressive loads. The side edges are simply supported. Figure 2 depicts the panel mounted in the test device.



Figure 2 – Panel mounted in the test device.

Test methodology

For the test, the compression load was applied at a displacement rate of 0.1 mm/min using a universal INSTRON model 5500R testing machine with a 30 kN load cell and integrated displacement and load real-time recorder. An electrodynamic shaker was used to inject a random input signal perpendicular to the loaded panel. Figure 3 depicts the test setup.

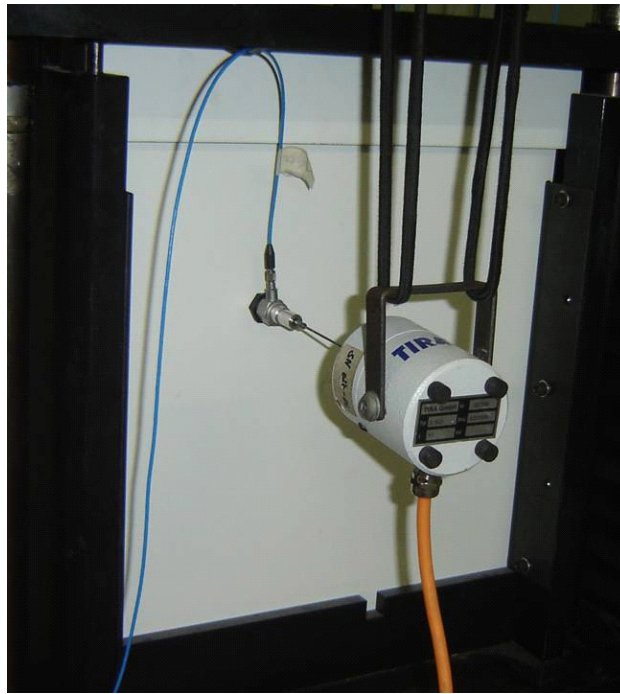


Figure 3 – Shaker mounted in the test device.

Load cells and accelerometers employed were ICP® transducers from PCB® Piezotronics. The acquisition was made using a SCADAS III of LMS International. The software for modal analysis and validation used in this work was the Test.Lab rev 10A, also from LMS.

A grid with 17 control points in the panel was used in order to adequately represent the vibration modes of the structure. Figure 4 depicts the points defined for measuring the output signals. The input signal provided by the shaker was measured at point 35. Figure 5 depicts the accelerometers placed on the panel for the test runs.

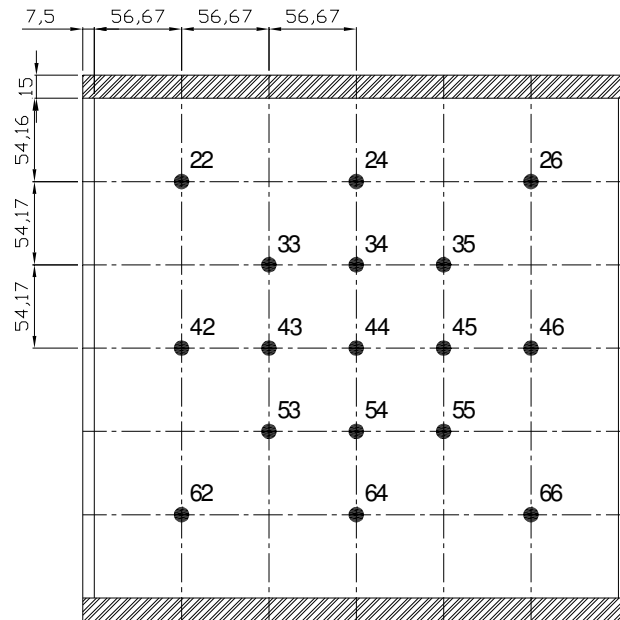


Figure 4 – Proposed setup for data acquisition.

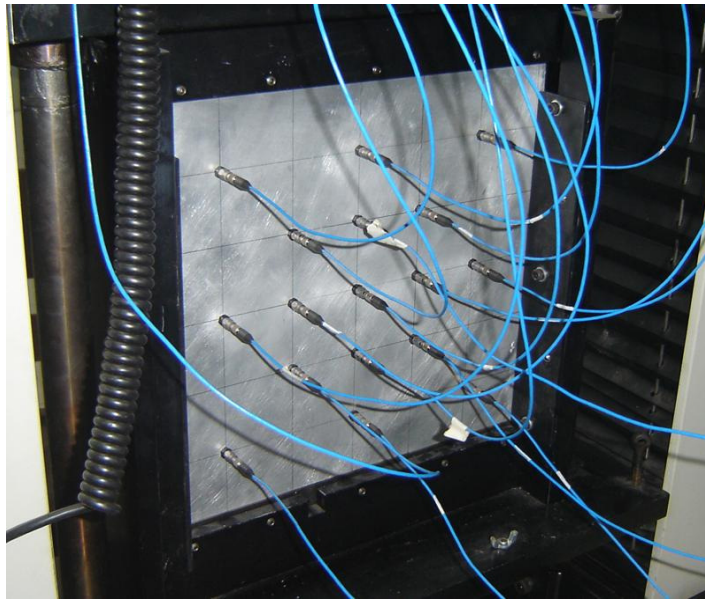


Figure 5 – Accelerometers mounted on the test panel.

The acquisition bandwidth was set from 0Hz to 640Hz, with 4096 spectral lines and a resolution of 0.15625 Hz. The acquisition time for each measurement was 6.4 s. Each *FRF* was obtained by averaging five measurements in order to reduce the presence of noise. A *Hanning* window was used for both excitation and response signals.

Results

Figure 6 depicts the experimental results corresponding to the first four vibration modes of the unloaded panel. The curves presented in Fig. 7 describe the evolution of the natural frequency of each mode of vibration obtained experimentally as a function of the applied compressive load.

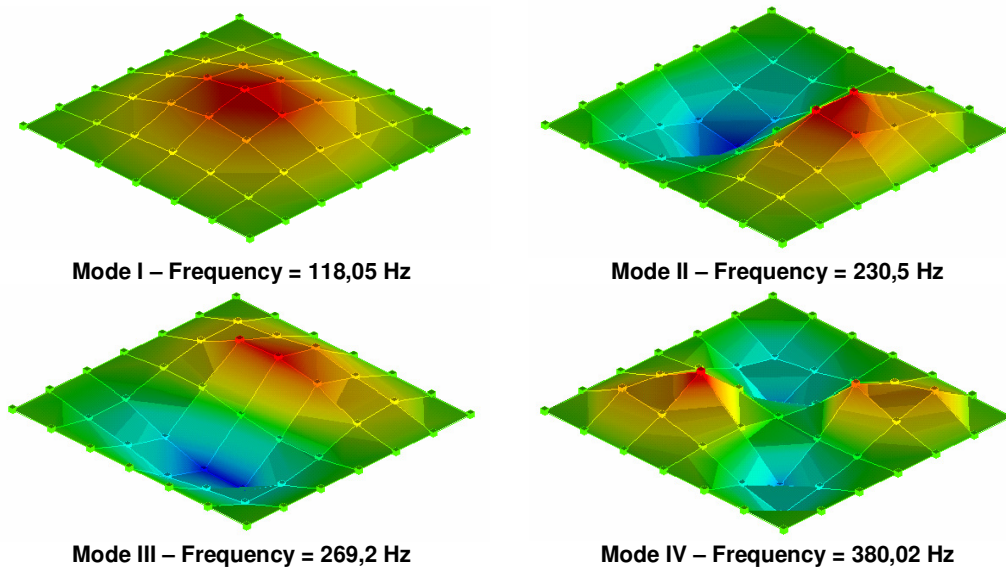


Figure 6 – Vibration modes of the panel without applied load.

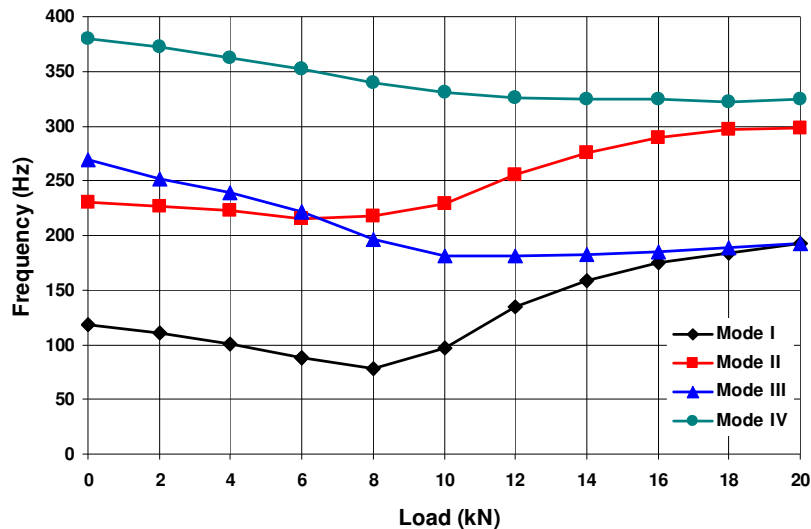


Figure 7 – Frequency vs. applied load for each vibration mode.

Some conclusions from the behavior of the panel subjected to compression load in the post buckling regime can be drawn by observing Fig 7:

- The first natural frequency of vibration of the panel decreases with increasing load in the pre-buckling regime and increases again in the post-buckling regime.
- We can observe the phenomenon of “mode jumping” between the second and third modes of vibration in the pre-buckling regime.
- The frequency values of the third and fourth vibration modes stabilize in the post-buckling regime.
- The natural frequencies corresponding to the first and second modes increase and tend to converge to the frequency values of the third and fourth modes of vibration, respectively, in the post buckling regime.

NUMERICAL MODAL ANALYSIS

In this work a finite element model was developed to characterize the behavior of an aluminum panel subjected to compression load in the pre- and post-buckling regime. The panel studied was 2 mm thick, 340 mm wide and 325 mm in length. The unloaded edges were considered simply supported. The top and bottom (loaded) edges were restrained by elastic springs which properly represent the real supporting condition of the test device. Additional boundary conditions were also considered in order to avoid rigid body motions of the panel during the analysis. The compression load was applied at the top edge of the panel. The mechanical properties used in the finite element model are listed in Tab. 1. All models were created using commercial software ABAQUS. A preliminary analysis was performed to study the convergence of the model, leading to a finite element model with 1080 S4R shell elements (ABAQUS, 2005).

Table 1 – Mechanical properties used in finite element model.

E (GPa)	ν	$\bar{\rho}$ (kg/m ³)
70	0.33	2780

Classical frequency analysis

The methodology employed in this model had two steps. Initially, a loading step using “static, general” procedure was defined and a Newton-Raphson iteration was used to solve the equilibrium equations. After loading the panel at the desired value, a “linear perturbation, frequency” step is performed using Subspace Iteration or Lanczos to compute the vibration frequencies and mode shapes of the loaded structure (ABAQUS, 2005). This type of methodology for finite element analysis has low computational cost and is widely used to characterize the behavior of aircraft structures in cases where a fast analysis is required. The model thus defined does not take into account neither the phenomena of damage and material degradation or geometric and material nonlinearities. Additionally, a linear buckling analysis was performed to compute the buckling loads and associated buckling modes. The values of buckling loads are shown in Tab. 2.

Table 2 – Numerical results of linear buckling analysis.

Buckling Mode	Load (kN)
Mode I	9.51
Mode II	15.50
Mode III	25.13
Mode IV	28.52

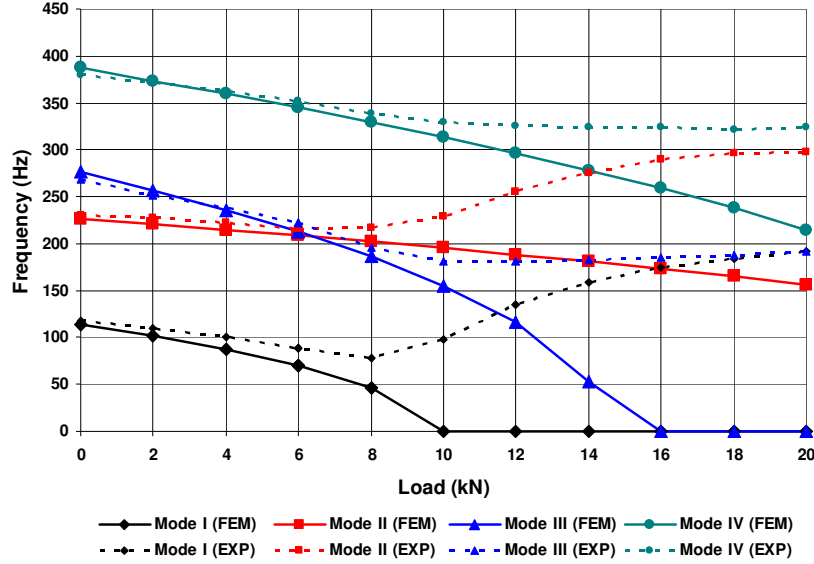


Figure 8 - Evolution of the frequencies of vibration in classical modeling. Numerical results (FEM) compared to experimental (EXP) data.

Figure 8 depicts the results for the first four vibration frequencies (FEM) compared to the experimental results (EXP). By interpreting the frequency curves of the finite element model, it is possible to observe a good correlation in the pre-buckling regime up to a load of approximately 6 kN, where mode jumping between modes 2 and 3 happens. For higher values of load the frequencies continue to decrease. The frequency value of the first vibration mode drops to zero when the model is loaded with the critical buckling load. The same phenomenon can be observed with the third vibration mode when the second buckling load is reached. This is due to the fact that the numerical flexural stiffness of the system decreases to zero as the system passes through the buckling loads. Thus, the proposed model can be used only in cases where the maximum load is far below the critical buckling load of the structure.

Proposed frequency analysis

Considering the whole model “panel + testing device” as a reduced system of N degrees of freedom contained in a set of control points, we can define a mass matrix $[M]$ invariant with the applied load and a tangent stiffness matrix $[K]$ which is the sum of the structural and tensional stiffness matrices of the reduced system. The tangent stiffness matrix can be computed using the flexibility matrix $[S]$ in the deformed state as:

$$[K] = [S]^{-1} \tag{1}$$

Thus, excluding the effects of damping of the plate, the dynamic behavior of the discrete system for the analysis of frequencies and vibration modes can be represented by:

$$[M]\{\ddot{x}\} + [K]\{x\} = \{0\} \tag{2}$$

The natural frequencies of vibration and the associated modes can be calculated by:

$$[[D] - \lambda[I]] = \{0\} \tag{3}$$

where $[D] = [M]^{-1}[K]$ and $\lambda = \omega^2$. Finally, the natural frequencies of the system will be:

$$f = \frac{\sqrt{\lambda}}{2\pi} \tag{4}$$

The flexibility matrix is characterized by the out of plane displacements presented in each control point when the structure is loaded with a known force normal to the plane of the panel. In general, each component of the flexibility matrix is calculated as:

$$S_{ij} = \frac{\delta_i}{P_j} \quad (5)$$

The ij component of the flexibility matrix is calculated as the out of plane displacement measured at control point i due to normal load applied at control point j . In addition, considering de reciprocity theorem, the components ij and ji of the flexibility matrix are the same. The reduced flexibility matrix was calculated via ABAQUS.

The proposed model employed a quasi-static load step procedure based on a dynamic relaxation method, which is adequate for the study of models with serious problems of convergence, also accounting for the effects of damage and material degradation. To characterize the post-buckling behavior of the panel in compression, an initial geometric imperfection was included in the finite element model. The model also considered geometric nonlinearities. More detailed studies were presented by Arbelo (2008). A prescribed displacement at the top loaded edge of the panel was used for the initial load in compression, in order to simulate the real load applied during testing.

A second step based on Newton-Raphson iteration was used to characterize the flexibility matrix. A known load was applied at every control point and the out of plane displacements were measured at all control points and stored. A Fortran routine was performed to automatically modify the control point to be loaded.

The reduced mass matrix was also obtained via ABAQUS. The program already incorporates the methodology of Guyan-Irons reduction in the dynamic sub-structuring package analysis. Figure 9 depicts the finite element model of the panel and the control points used in this work.

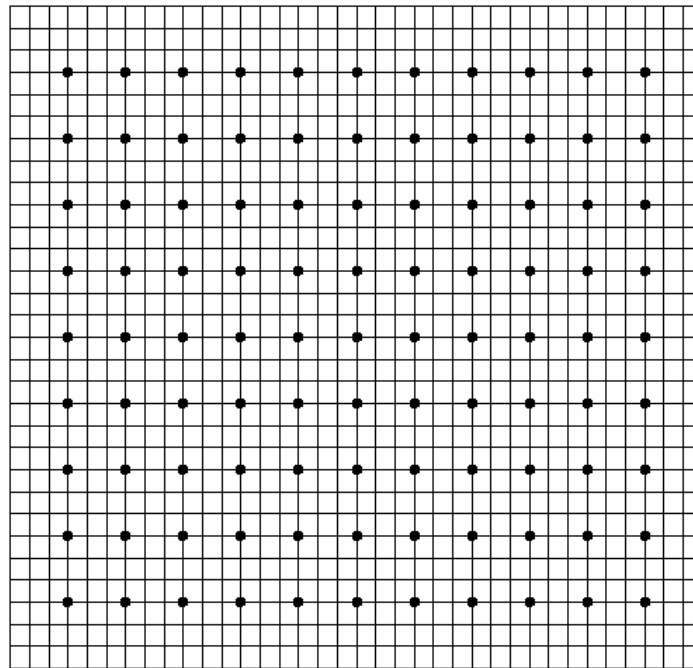


Figure 9 – Finite element model and control points.

Figure 10 shows the evolution of the natural frequencies of the first 4 modes of the panel loaded in compression. It is noticeable that in the linear regime, for load values below the first buckling load, the behavior of the natural frequencies is equal to that obtained using the classical approach. Moreover, in the post-buckling regime, the natural frequencies increase due to the nonlinear behavior of the panel. A mode jumping between the first and third modes occurs when the load applied reaches 17 kN. Similarly, when the applied load reaches 19 kN, a switch between the third and fourth mode of vibration is observed, which was not predicted by experimental modal analysis. A very good correlation is observed between the experimental modal analysis and the numerical simulation.

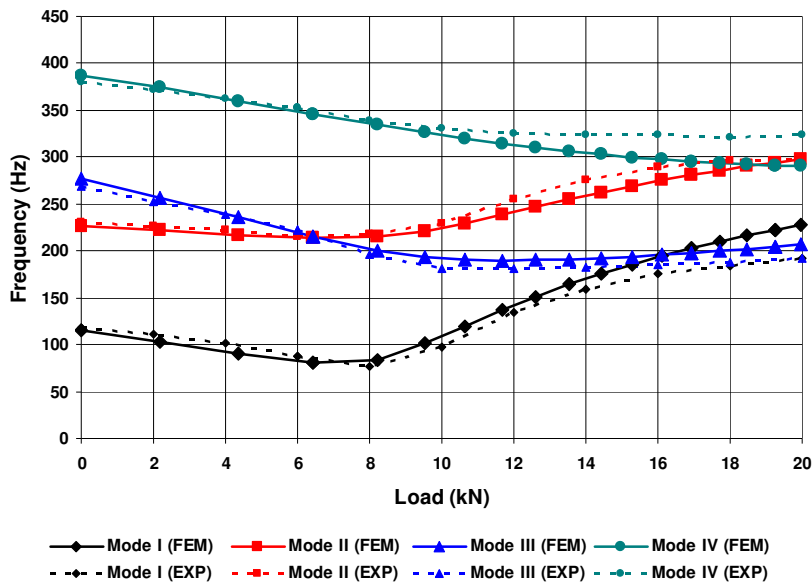


Figure 10 – Evolution of the frequencies of vibration in the proposed modeling.

CONCLUDING REMARKS

This paper presented a detailed numerical and experimental investigation on the post-buckling behavior of panels subjected to compression loads. An experimental apparatus and test setup was developed to experimentally characterize the nonlinear behavior of natural frequencies of panels in the post-buckling regime. A classical numerical approach and a new methodology for finite element analysis of the behavior of natural frequencies were also presented. The proposed methodology takes into account geometric imperfections and geometric non-linearity effects. Some conclusions of the present work are that for the cases where the applied loads are much smaller than the critical buckling load, a low-cost numerical model can be used for a quick initial analysis with satisfactory results. However, for the study of structures subjected to loads in the post buckling regime, the nonlinear analyses are more realistic and should be used in practical aeronautical structural design.

ACKNOWLEDGMENTS

The authors would like to thank the “Fundação de Amparo à Pesquisa do Estado de São Paulo (FAPESP)”, grant number 2008/05345-8 and CNPq, Grant number 305601/2007-5 for the financial support.

REFERENCES

- Arbelo, M. A., 2008, Structural Behavior of Composite Laminated Panels Subjected to In-Plane Shear Loads, Master’s Thesis, Instituto Tecnológico de Aeronáutica (in Portuguese).
- ABAQUS USER Manual v.6.5-1, 2005.
- Chen, H. and Yu, W., 2006, Postbuckling and mode jumping analysis of composite laminates using an asymptotically correct, geometrically non-linear theory, *International journal of non-linear mechanics*, v 41, 1143 – 1160.
- Chen, H. and Virgin, L. N., 2006, Finite element analysis of post-buckling dynamics in plates. Part II: A non-stationary analysis, *International journal of solid and structures*, v 43, 4008-4027.
- Chia, C. Y., 1987, Non-linear vibration and post-buckling of unsymmetrically laminated imperfect shallow cylindrical panels with mixed boundary conditions resting on elastic foundation, *International Journal of Engineering Science*, 25, 427-441.
- Craig, R. R. and Kurdila, A. J., 2006, “Fundamentals of Structural Dynamics”, Second edition, Editorial John Wiley & Sons, Inc., Hoboken, New Jersey.
- Fu, Y. M. and Chia, C. Y., 1989, Multi-mode non-linear vibration and post-buckling of anti-symmetric imperfect angle-ply cylindrical thick panels, *International Journal of Non-linear Mechanics*, v 24, 365-381.
- Fu, Y. M. and Chia, C. Y., 1993, Non-linear vibration and post-buckling of generally laminated circular cylindrical thick shells with non-uniform boundary conditions. *International Journal of Non-linear Mechanics*, v 28, 313-327.
- Girish, J. and Ramachandra, L. S., 2005, Thermal postbuckled vibrations of symmetrically laminated composite plates with initial geometric imperfections, *Journal of sound and vibration*, v 282, 1137-1153.
- Guyan, R. J., 1965, Reduction of stiffness and mass matrices. *AIAA J.*, v 3, 380.

- Ilanco, S. and Dickinson, S., M., 1987, The vibration and post-buckling of geometrically imperfect, simply supported, rectangular plates under uni-axial loading, part I: Theoretical Approach, *Journal of sound and vibration*, v 118(2), 313-336.
- Ilanco, S. and Dickinson, S., M., 1987, The vibration and post-buckling of geometrically imperfect, simply supported, rectangular plates under uni-axial loading, part II: Experimental Investigation, *Journal of sound and vibration*, v 118(2), 317-351.
- Irons, B. M., 1965, Structural eigenvalue problem: elimination of unwanted variables, *AIAA J.*, v 3, 961-962
- Iu, P. and Chia, C. Y., 1988, Non-linear vibration and postbuckling of unsymmetric cross-ply circular cylindrical shells *International, Journal of Solids and Structures*, v 24, 195-210.
- Moussaoui, F., 2002, Non-linear vibrations of Shell-type structures: A review with bibliography, *Journal of sound and vibration*, v 255(1), 161-184.
- Singha, M., K., Ramachandra, L., S. and Bandyopadhyay, J., N., 2006, Vibration behavior of thermally stressed composite skew plate, *Journal of sound and vibration*, v 296, 1093-1102.
- Vasconcelos, A. M. and de Almeida, S. F. M., 2009, Análise modal de um painel de carbono/epoxi sujeito a cargas de cisalhamento, *Proceedings: Brazilian Symposium on Aerospace Eng. & Application*, 2009.

RESPONSIBILITY NOTICE

The authors are the only responsible for the printed material included in this paper.

Robust Control of a Large Radar Antenna under Structured Uncertainties

Agenor de Toledo Fleury^{1,2}, Fabrizio Leonardi¹, Fabiano Armellini³

¹ Centro Universitário da FEI
 Av. Humberto A. Castelo Branco, 3972, CEP 09850-901, São Bernardo do Campo – SP

² Escola Politécnica da Universidade de São Paulo
 Av. Professor Mello Moraes, 2253, CEP 05508-900, São Paulo – SP

³ Allagi Engenharia Ltda
 Av. Brigadeiro faria Lima, 1461 Cj 124, CEP 1452-002, São Paulo – SP

Abstract: A radar antenna is basically composed of a primary source mounted at the focal point of a parabolic reflector. The radar illumination rule is established so that the desired beam shape is attained as precisely as possible. The mechanical movement of the set reflector-pedestal must be designed to fit the desired volume of radar exploitation. This work deals mainly with the control design of a rotating radar antenna prototype that is already operating on Mogi das Cruzes, SP, under the supervision of the Brazilian Omnisys/Atech joint venture. Since all parameters related to the dynamic model are poorly known, a robust controller has been designed to deal with the uncertainties by means of the Quantitative Feedback Theory. The controller has been designed in order to tolerate a simultaneous variation of 50% in inertia, stiffness or damping parameters of each radar subsystem. The QFT controller has been used to design a fixed PID structure and the results are compared to a previous design using the Kalman Identity and LQ controller mapped to the PID structure. The result proved that QFT leads to a more suitable controller.

Keywords: radar design; robust control; structural dynamics; finite element models; QFT

NOMENCLATURE

J_a = antenna moment of inertia, kg.m²
 K_a = antenna stiffness, N.m/rad
 B_a = antenna damping, N.m.sec/rad
 J_g = gimble moment of inertia, kg.m²
 K_g = gimble stiffness, N.m/rad
 B_g = gimble damping, N.m.sec/rad
 J_m = motor moment of inertia, kg.m²
 K_m = Motor stiffness, N.m/rad
 B_m = Motor damping, N.m.sec/rad
 K_M = Motor constant of torque, N.m/A

K_E = Motor emf constant, V.sec/rad
 R_a = Motor resistance, Ω
 L_a = motor Inductance, H
 N = mechanical reduction

Greek Symbols

θ_m = drive position, rad
 θ_1 = gear box input position, rad
 θ_2 = gear box output position, rad
 θ_g = gimble position, rad

θ_a = antenna position, rad

Subscripts

a relative to antenna
 m relative to motor
 g relative to gimble
 1 relative to gear box input
 2 relative to gear box output

INTRODUCTION

Radars are electronic sensors that use electromagnetic waves to detect objects and measure relative positions in space. Object positioning is accomplished by determining distance and attitude in relation to the radar equipment, which requires three measures: azimuth (around the vertical axis), elevation (around the horizontal axis) and the straight distance from the pointing equipment. This distance-azimuth-elevation set of measurements constitutes a spherical coordinate system with the radar antenna focal point in the origin.

Distance between target and radar is determined using the Pulse-Echo Principle in which a high power electromagnetic pulse is sent in a given direction and target distance is calculated by the signal delay (echo) from the target. The other coordinates, azimuth and elevation, are given by the angular position of the antenna-radar set relative to a fixed reference

This work deals with the position control of a large radar antenna using a two-axes gimbal of the type elevation over azimuth. Each axis performs independent motion driven by a DC brushless motor. Both are digitally controlled by a central processing system. The antenna-radar set described here is the mechatronic part of a large project that qualified Atmos (the spinoff of the Atech-Omnisys joint venture) to design and build weather radars to Brazilian authorities. The paper is based on the MSc work by Armellini (2006) where a detailed description can be found.

The work of Fleury, Leonardi and Armellini (2010), discusses the design of a robust LQ controller. However, the modeling errors due to parameters model uncertainties were treated as unstructured uncertainties, thus resulting in a conservative design. More important the tuning of the PID controller has been achieved by indirectly mapping the

control law, a fact that does not guarantee the mapped properties of the original LQ controller. This work is an improvement of the previous one. It considers the same uncertainties as structured to obtain a less conservative robust controller. To do so Quantitative Feedback Theory has been used. QFT is a frequency domain procedure that uses Nichols chart as a basic tool and allows the use of the PID structure since the beginning of the design.

Radar Design

The quality of information received by an antenna depends on its angular velocity, pointing accuracy, radar pulse parameters and electronic gain, angular aperture, antenna lobes and beam shape features. These electronic parameters and the antenna polarization define the radar structural properties: reflector shape (parabolic or semi-parabolic, for example), geometry (diameter and curvature of the dish) and primary source location over the reflector (focal distance, vertical or horizontal or circular polarization). One of the major difficulties in nowadays development projects is to combine mechanical and electrical designs to guarantee information accuracy with increasing antenna gains. Gain increase leads to larger reflectors and, consequently, to mechanical structures of complex dynamic behaviors which present several complex flexibility and vibration issues to be dealt with (Armellini, 2006). It is a task of the control system to attenuate them.

In this project, a standard two-axis elevation-over-azimuth (EL/AZ) positioner was adopted. For radars in general, positioned motion and velocity control represents a crucial feature since the radar must sweep all the aerial space around itself with a very narrow illuminating beam. For weather radars, in particular, trajectories must be prescribed and accurately tracked for cloud and other meteorological phenomena real detection.

Antenna Positioning

Radar design has evolved in parallel to control systems. In a modern radar configuration, each axis usually has a DC brushless motor, optical sensors and electromechanical transformers controlled by a central system in two independent loops. For the tasks of control, azimuth and elevation loops are somewhat identical. They differ on the mechanical parameters like inertias and stiffness, displacement bumps or controller gains.

On the other side, as antennas grow larger, the importance of system flexibilities grows in parallel. These flexibilities are due to dishes, gimbals, support structures, axles and cannot be neglected for a good design. Baek (2006) reinforces this statement when modeling an azimuth driving servo system carrying a flexible antenna. Major part of the elastic Degrees of Freedom (DOF) are assigned inside the gimbals (axles and gears) and a simple beam model is adopted for the antenna when trying to match model responses to experimental modal analysis results. Gawronski (2006) proposes that the most important measure of control performance is the error while tracking under wind gusts and compares parameter sensitivities for a rigid antenna under a PI controller and a large flexible dish using a LQG strategy to conclude that the first approach gives better simulated results. This is not surprising since flexible modes require much more accurate controllers. The question is how to design a large mechanical system that can be considered rigid in all circumstances.

In this work, the weather radar is modeled as a flexible low order system and unknown parameters are adjusted to cope with the structural analysis results. Based on this model, a robust PID controller for the azimuth axis is designed using QFT and its performance compared to a robust LQ designed by means of the Kalman Identity (Fleury, Leonardi and Armellini; 2010).

Structural Analysis

The prototype weather radar antenna is a 4.2m diameter parabolic dish built of aluminum alloy. All other parts are made in steel, including counterweights. The radar set is installed at the top of a 12m-high steel tower (See Fig 1).



Figure 1 – Test site in Mogi das Cruzes, SP (Armellini, 2006)

A Finite Element model of gimbals and dish, not including tower, has been implemented on an ANSYS 8.1 package. The resulting model has somewhat 45,000 nodes and 246,000 DOF's (Armellini, 2006) and the main frequencies and modes between 0 and 50 Hz were achieved. Numerical analysis showed 13 frequencies below 20 Hz, the first on 5.4 Hz, corresponding to elevation axis torsion mode and the second on 9.6 Hz relative to the azimuth axis torsion mode (see Fig. 2).

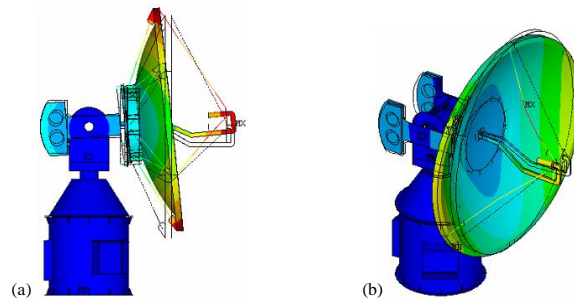


Figure 2 – First 2 antenna natural modes: (a) elevation torsion ; (b) azimuth torsion.

The Experimental Modal Analysis was performed with the radar set installed at the tower. First mode has been confirmed at 5.5 Hz but surprisingly the apparatus has shown 2 modes around 1.2 Hz in the azimuth direction and in the North (azimuth and elevation) direction. This fact seems to be associated to the tower resonance frequencies, but a deeper investigation still remains to be performed.

Control System Overview

In what follows, azimuth and elevation dynamics are assumed independent, which allows one to treat the system as two uncoupled problems. In this scenario, interactions between the two axes are modeled as disturbances. This work deals only with the azimuth angle control since this is considered the critical axis (Baek, 2006). The dynamic model includes some uncertain parameters; therefore the controller must be robust to these modeling errors. In fact, 9 mechanical parameters (inertia, stiffness and damping) are not well known to an estimated uncertainty of 50% below or above the nominal value. QFT controller is one recommended compensator for cases like this (Houpis, 1999; Yaniv, 1999). As a constraint to the problem, the compensator must have a specific structure since the real system is equipped with a PID controller. Note that this is not a problem when you use the QFT procedure since it does not require a fixed structure controller and any control law is a candidate for the design.

To investigate a system, it is mandatory to build a complete and rigorous model. However, the model normally can be less detailed for control purpose if the controller is robust in presence of modeling uncertainties. Based on this assumption, one adopts a linear model to represent all antenna dynamics. In order to represent the antenna flexibility, spring and damper elements have been associated to every degree of freedom.

The modeling errors are taken as uncertainties in transfer function of the plant, but margins of stability alone are unable to reveal the degree of robustness of a system, because even systems with favorable margins as $[90^\circ, \infty \text{ dB}]$, may have its corresponding Nyquist diagram close to $-1+0j$, and therefore, are not robust (Da Cruz, 1996). Model uncertainties can be classified as structured and unstructured. Unstructured uncertainties are usually associated to unmodeled parts of the plant that are frequency dependent such as the unknown dynamics of the actuator. The structured uncertainties are associated with parametric uncertainties such as the ones of the model in this work.

Control System Design using QFT

As a performance specification, it is desired that the control system output (antenna position) tracks a reference signal with a minimum error up to 10 rad/s and additionally rejects constant load disturbances (wind bursts) asymptotically with a setting time lower than 1 s. The maximum control effort for a 20V disturbance should not exceed 30V and all these specifications should be kept even in the presence of modeling errors of 50% in the 9 mechanical parameters (inertia, stiffness and damping).

Following Craig (1993), the first step of design procedure is the determination of templates generated by the parameters uncertainties. A template is defined as the collection of uncertain plant frequency response functions at a given frequency. For design, only the bounds of those templates are important. Performance specification imposes barriers to the loop gain in the Nichols chart, and these templates should be above barriers in the specified frequency range. Margins of stability and/or robustness associated to the maximum resonance peak of the closed loop, imposes barriers around $(0, -180^\circ)$ in the Nichols chart. The region around this point must be reshaped so that the boundary of all the templates does not violate this region. Design starts by selecting a point on the border of the template as the nominal plant and then, based on this point, the curve around $(0, -180^\circ)$ should be reshaped so that, when the nominal point does not violate the new curve, all points of the template are outside the original curve. Then, the problem of finding a controller that meets the requirements of robust performance and stability should be done, for example, by trial and error, adding poles and zeros to the controller transfer function. In this case, since the controller has a fixed structure, the design is done by manually tuning the gains. Based on the plant frequency response with nominal parameters (see

Figure 3), the system responds to approximately 100 rad/sec, but below 1 rad/s there is almost no gain variation. Then, 1, 10, 30 and 100 rad/s have been chosen as the work frequencies for the QFT design.

In the sequence, a number of 20000 plants have been chosen by the simultaneous and random variation of 9 parameters within the range of 50% above and below to nominal values in order to achieve template contours with reasonable accuracy. Figure 4 shows the templates generated for each frequency design.

The gain and phase margins or the maximum resonance peak of a closed loop system gives extra robustness in relation to parametric uncertainties already considered for stability. This is important because of the unavoidable disregarded uncertainties. However, if all uncertainties have already been considered, it is not necessary to include this extra margin. Moreover, this gap does limit the resonance peak for all real plants considered. That is, the worst case will have a limited resonance peak. This is important depending on the project and on the type of plant. Typically for mechanical plants, as is the case of this project, it is highly desirable to avoid sharp resonances. Choosing $20\log(4)$ dB as acceptable level for the closed loop resonance peak, one gets around 15° of phase margin and 2 dB of gain margin as extra robustness added to the one already considered by the parameters variation. In the design, no templates may violate the region around the point $(-180^\circ, 0 \text{ dB})$ in the Nichols chart. This is equivalent to distort this region through each template and say that the nominal plant with the controller must not violate these new regions (bounds).

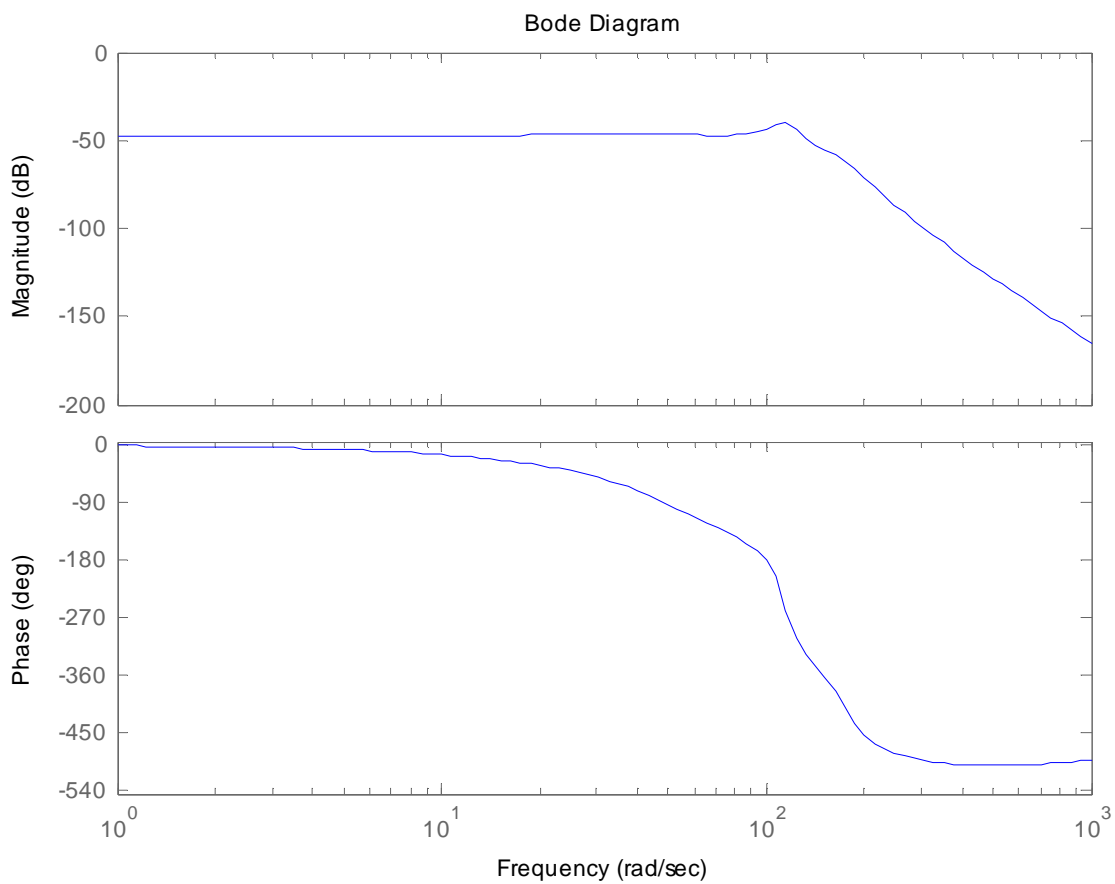


Figure 3 – Plant Frequency Response.

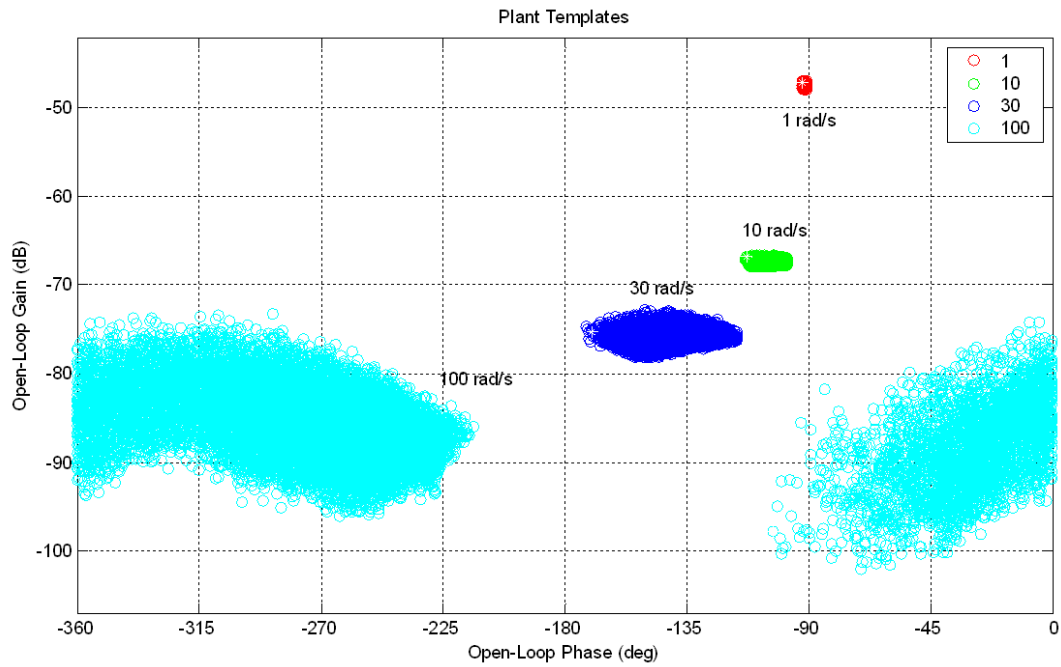


Figure 4 – Templates for each work frequency design.

Figure 5 shows the region associated to resonance peak which is a measure of the system degree of robustness. It already includes the shape adjusts due to each template at each working frequency.

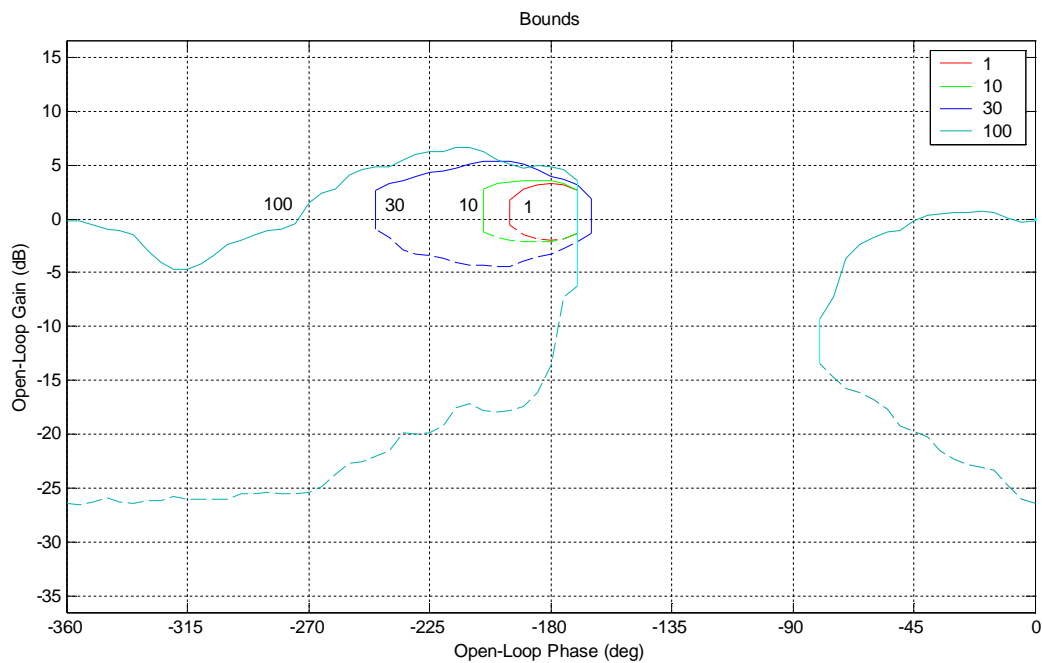


Figure 5 – Degree of robustness as bounds.

Initially, the PID controller designed in the work of Fleury, Leonardi and Armellini (2010) has been used for comparison with the QFT one. Notice that the nominal plant with the new controller does not violate any condition of robustness (bounds) (see Fig. 6). This means that the system is stable for the 20.000 plants considered and, furthermore, there are still about 15° of phase margin and 2 dB of gain margin as tolerance for any other uncertainty.

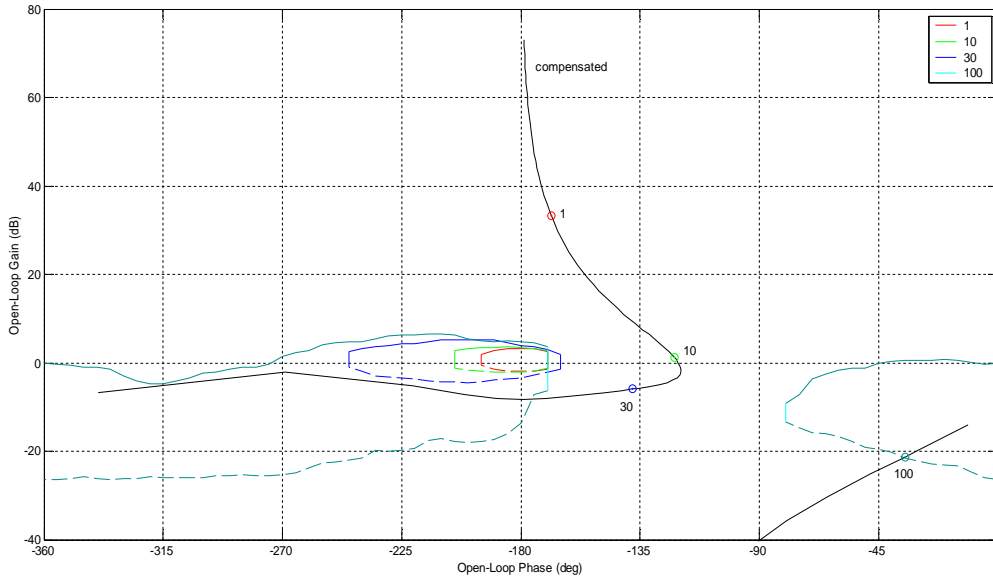


Figure 6 – Loop shaping.

However another enhancement should be made with this controller to improve system robustness. It is shown in Figure 7 the loop shaping achieved with the addition of a pole at $-80+0j$. In this new situation, the point of frequency corresponding to 100 rad/sec is more distant from the respective bound (light-blue line). This can be done with no consequences for the remaining frequencies in relation to their bounds. In the design with unstructured uncertainties shown in Fleury, Leonardi and Armellini (2010), the benefits of adding this real pole are evident only by the fact that it reduces the gain at high frequencies and thus the sensitivity in the region of frequencies where there are unavoidable uncertainties and sensor noises. Another difficulty with that previous design is the lack of guarantee of system stability, since it is not known a priori whether this addition will ensure that the new nominal plant/controller will be stable. In the QFT procedure this is inherent to the technique.

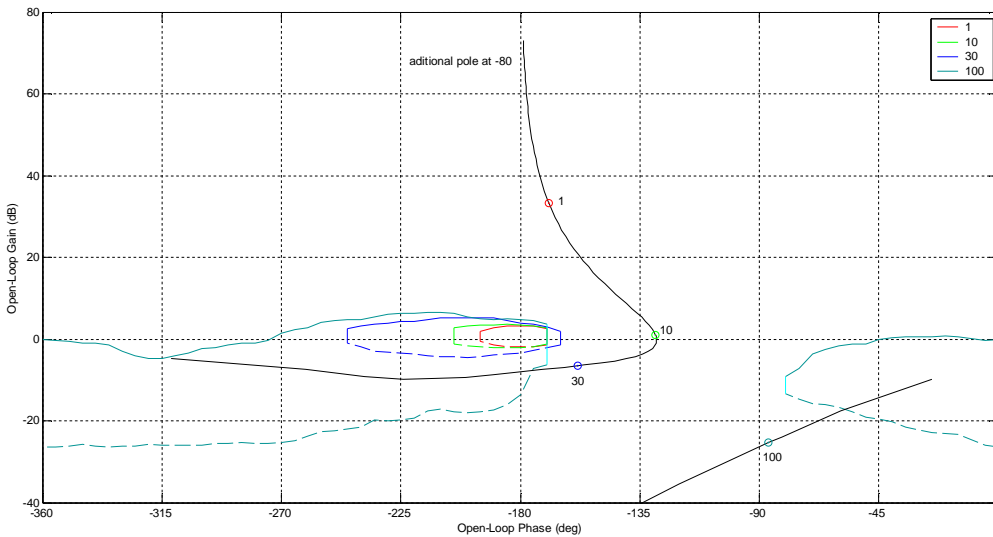


Figure 7 – Adding a pole at $-80+0j$ to the controller.

As mentioned, the inclusion of a new pole at $-80+0j$ has allowed the improvement of the controller gain, which can be increased until the limit given by the control efforts since there is no violation of bounds. As a consequence the accuracy in following the reference signal is also improved, and this is highly desirable. The loop shaping (continuous line) in Figure 8 illustrates this new situation where the gain has been doubled when compared to that one proposed in Fleury, Leonardi and Armellini (2010).

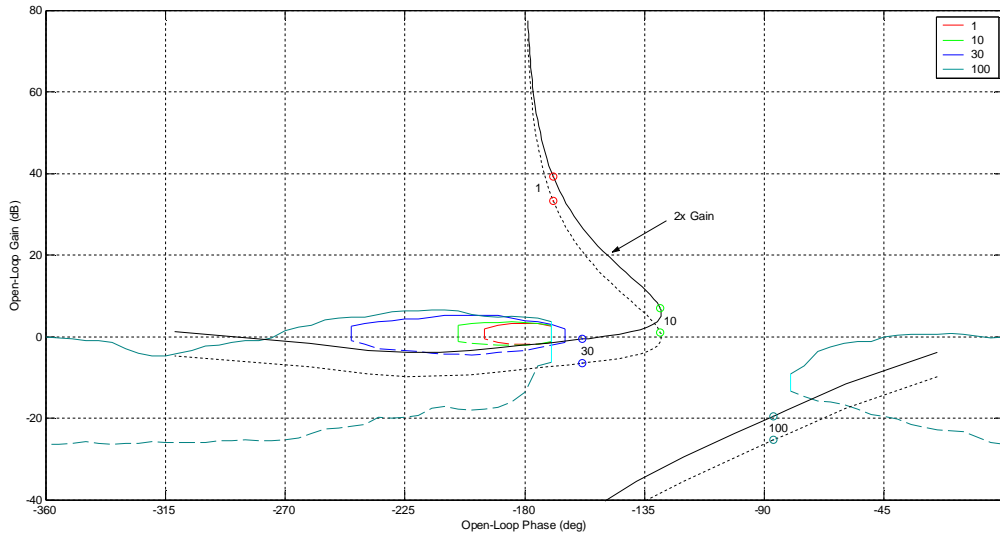


Figure 8 – Increasing the controller gain .

Figure 9 illustrates the time domain performance of the controller achieved by the addition of a pole at $-80+0j$ and the increased gain (red curve) compared with the PID controller performance proposed by Fleury, Leonardi and Armellini (2010) (orange curve). Just as in that paper, a reference signal has been filtered by the function $F(s)$ and used to reduce overshooting whenever the reference is suddenly changed

$$F(s) = \frac{1}{(0.35s + 1)^2} \quad (1)$$

One step change of 0.1 rad in the reference was applied at the beginning of the simulation and a constant disturbance of 20V was added to the control signal after 5 seconds, to represent a wind burst that causes a constant torque. Due to the filtering in the reference signal, the performance of two controllers is similar after a set point change, but the disturbance rejection became faster with the proposed controller.

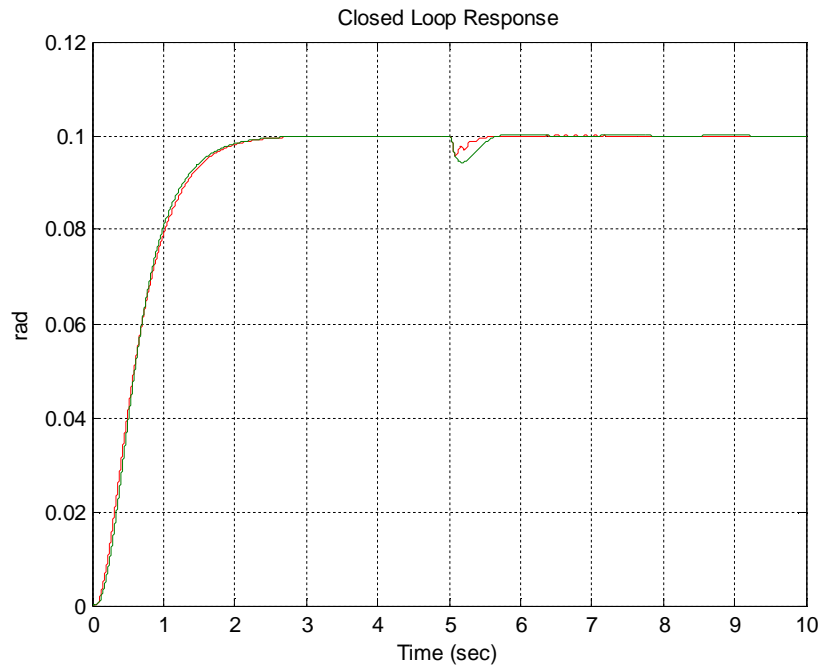


Figure 9 – Step response comparison.

Figure 10 shows the control efforts for the same test. As expected, the consequence of a high controller gain is a bigger control effort what is perceived during the disturbance rejection.

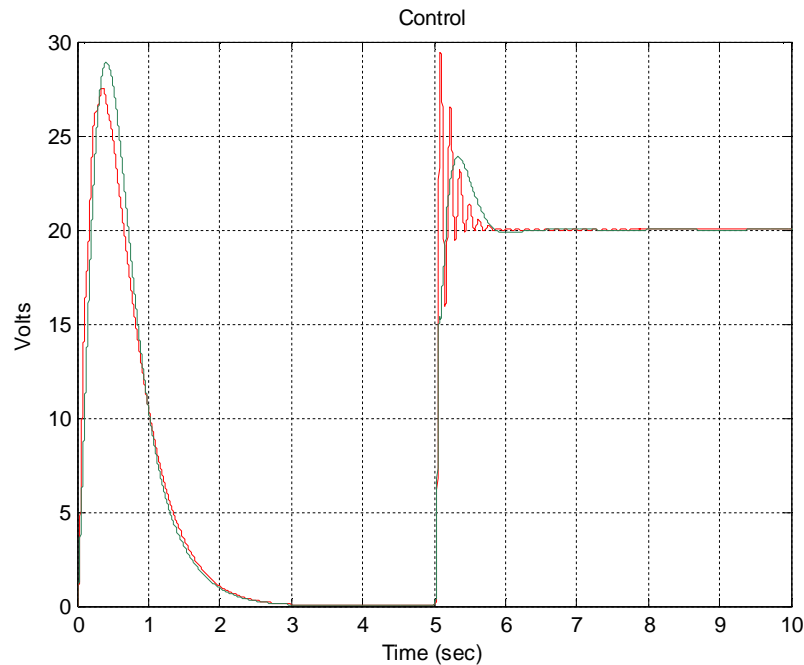


Figure 10 – Control efforts during the test.

Conclusion

QFT has permitted the achievement of very good performance even in the presence of high modeling errors associated to several model parameters. It has made possible the use of a predefined structure of the controller for the project in a quite straight manner.

This work has shown also some relevant aspects of the mechatronics design of a large radar-antenna set for weather applications. Although the control system seems to be the core of the radar design, control design is but one of the main concerns related to a consistent project (Armellini, 2006).

The prototype is operating at the test site but many things remain to be proceeded as the structural analysis and the field control experiments. Field data acquired after installation of the weather radar on the tower is strongly disturbed by tower harmonics, which turns the carrying on of experiments no elementary task.

ACKNOWLEDGMENTS

First author gratefully acknowledges CNPq for financial support. The authors also thank FAPESP for the financial support of the design of the prototype which is the object of the paper, by the PIPE program.

REFERENCES

- Armellini, F. (2006). Projeto e Implementação do Controle de Posição de uma Antena de Radar Meteorológico através de Servomecanismos. M.Sc. Dissertation (In Portuguese), Departamento de Engenharia Mecânica, Escola Politécnica da USP, 123p.
- Baek, J. H. (2006). Modeling on a Gimbal with an Antenna and Investigation on the Influence of Backlash, JSME Int Journal, Series C, Vol. 49, No.3, p804-813
- Craig, B.; Chait, Y.; Yaniv, O. (1993). “The QFT Frequency Domain Control Design Toolbox – User’s Guide”, Terasoft, Inc..
- Cruz, J. J. (1996). “Controle Robusto Multivariável”, Ed. USP, 163p.
- Fleury, A. T.; Leonardi, F.; Armellini, F. (2010). Controle Robusto da Antena de um Radar Meteorológico (In Portuguese). Anais do XVIII Congresso Brasileiro de Automática - CBA 2010, Bonito - MS.
- Houpis, C. S.; Rasmussen, S. J. (1999). “Quantitative feedback theory”, Dekker Ed.
- Gawronski, W. (2006). Servo Performance Parameters of the Deep Space Network Antennas, IPN Progress Report 42-167.
- Yaniv, O. (1999). “Quantitative Feedback Design of Linear and Nonlinear Control Systems”, Kluwer Academic Publishers.

RESPONSIBILITY NOTICE

The authors are the only responsible for the printed material included in this paper.

Influence of Cable Mass on Tendon Based Parallel Manipulator

Jorge Audrin Morgado de Gois ¹, Alexandre Back e Travi ¹, and Cícero dos Santos Mendes Lima ¹

¹ Mechanical Engineering Department, Instituto Militar de Engenharia

Abstract: Classical parallel manipulators present small workspaces, resulting from the use of rigid actuators. In order to overcome such problem, cables are used as actuation element, in an implementation called Tendon Based Parallel Manipulator – TBPM. The possibility of obtaining large or even huge workspaces combined to a fast dynamics application, like a helicopter simulator, makes a feed-forward control desirable, what makes necessary to model the whole system, including the effect caused by of long cables. This work aims to model and simulate the dynamics of a TBPM used as helicopter flight simulator. A large workspace is considered together to the combination of light platform and massive heavy cables. The simulations are analyzed to quantify the error induced by this configuration on the platform position, what will be verified in a future experiment.

Keywords: Parallel Manipulator, Tendon Based, Massive cables

NOMENCLATURE

f_p = applied force
 f_i = actuation forces
 u = cable unit vector

m = number of cables
 τ_p = applied torque
 α = catenary plane orientation

Subscripts
i relative to order of cable

INTRODUCTION

Classical parallel manipulators have their mechanical structure based on rigid actuators, i.e., hydraulic cylinders or electrical linear actuators. The rigid actuators are connected to form closed loops, so that the dimensions of the system's workspace are limited to fractions of the workspace of each actuator. As a natural consequence, those manipulators present small workspaces if compared to serial manipulators. In order to overcome such problem, instead of rigid actuators, with their inherent limited length, in early 80's (Bostelmann, Albus, Dagalakis, Jacoff, 1994) the use of cables as actuation elements was proposed. This implementation was called later Tendon Based Parallel Manipulator – TBPM (Verhoeven, 2004), where the useful length of the cables may be subjected to large variations as they are rolled in a reel. If the cables are long enough and the reels big enough too, the workspace can be largely expanded, since requirements of platform controllability are observed.



Figure 1 – Radio-Telescope controlled by a TBPM

The possibility of obtaining large or even huge workspaces makes possible TBPM applications as the antenna positioning for radio-telescopes (Fig. 1). On the other hand, most of commercial flight simulators are mounted on Stewart Platforms, what constrains the movement realized by the pilot to angular accelerations and pulses of translational acceleration. With TBPM it would be possible to subject the pilot to intervals of acceleration and still apply rotational movement. However, the radio-telescope application is quasi-static and uses a feedback control to accomplish the task. In a problem like a flight simulator, the implementation of sensors to close the loop of a feedback control is much more complicated because of its faster dynamics. Then, a feed-forward control would be desirable in such application, what makes necessary to model the whole system, including the effect caused by long cables.

This work aims to model and simulate the dynamics of a TBPM used as helicopter flight simulator. The chosen airship was a helicopter EC-120B Helibrás Colibri, because of the interest of Brazilian Army in the development of a highly realistic simulator for this airship. A workspace large enough to achieve the necessary accelerations was considered together to the combination of light platform and massive heavy cables, what means, steel cables with large diameter, strong enough for the application. The simulations are analyzed to quantify the error induced by this configuration on the platform position, what will be verified in a future experiment.

Mathematical model

The analysis of a TBPM involves the determination of the workspace, what take as parameters: base and platform geometry, maximal and minimal force on the cables, and applied forces. In this work, the base represents the structure to what the pulleys, which deliver the cables, are fixed. Actually, the geometry of the structure doesn't matter, but the positioning of the anchorage points relative to each other is important to define the workspace. The platform is the manipulated object, where once again, the anchorage points are what really matters.

If there is at least one solution for each desired position and orientation, it is sad that this configuration belongs to the Controllable Workspace. In Fig. 2 it is shown a general TBPM, with $m = 8$ cables, where applied forces and torques are f_p and τ_p , respectively.

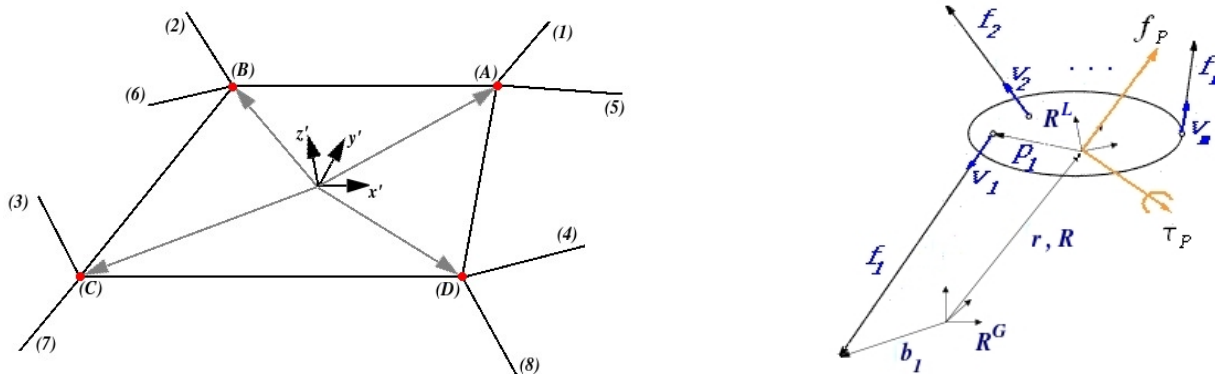


Figure 2 – General TBPM (left) and its representation (right)

Vectors f_1, \dots, f_m represent the actuation forces given by the cables. They have to be always positive in order to assure a correct actuation, otherwise the cables may become loose and no actuation occurs. Actually, in a real implementation, those forces have to lie between an upper and a lower bound, because mass and rigidity of cables may modify the actuation force. Besides, if the cables are too tight, they may simply break. In (FANG, 2005) an algorithm for the solution of the system is presented, where to solve the workspace problem, actuation forces are first calculated. Then, the used model of dynamics is (BRUCKMAN ET AL, 2008 e MIKELSON ET AL, 2008):

$$A^T f + w = 0 \tag{1}$$

Where A is the structure matrix of the problem, that is, the matrix which describes the relation between the forces applied by the cables and all other forces of the problem as weight and inertia forces, represented by w . This equation is obtained by manipulating the equilibrium equations.

From Fig. 2 we see that v_i is the unitary vector connecting the anchorage points of the cable i , while p_i is the position of the anchorage point on the platform, relative to its local system. So, considering f_i as the tension in that cable, the applied force is given as $f_i = f_i \cdot v_i$, what leads to:

$$\tag{2}$$

TBPM MODEL WITH MASSIVE CABLES

From Eq. 2, it is clear that given a state (position, orientation and velocity), one may determine the actuation forces, since the system geometry is known. A simple way to solve the workspace problem is to verify all the states (and not only position) whose solution of Eq. 1 relies in the admissible interval. With massive cables, many approaches were already suggested, but here, a simple one will be employed, adopting the following assumptions:

- Cables are considered to generate catenaries;
- The catenaries remain on vertical planes for each platform posture (position and orientation);
- Cable delivering joints are considered as punctual.

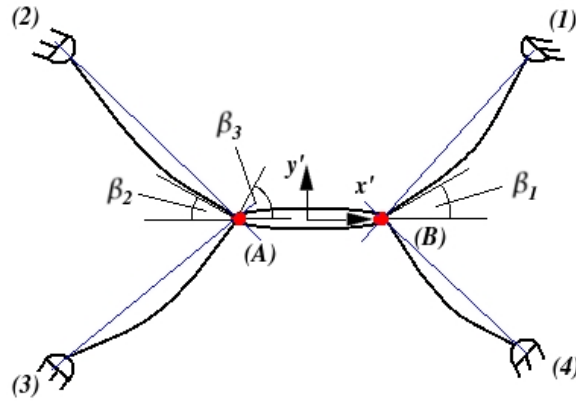


Figure 3 – Detail of TBPM with catenaries

An example of the general case, with $m = 4$ cables and 6 D.O.F. is represented in Fig. 3, where β_i is the angle between the cable catenary and the straight line connecting the anchorage points on the platform and on the base. The stress equation for cables undergoing catenaries is applied to Eq. 1, generating the model of dynamics of the TBPM with massive cables. Then, the obtained expressions for the actuation forces are:

$$\left\{ \begin{array}{l} f_1(h) = \sum_{i=1}^m u_{x,i} h_i + w_x = 0 \\ f_2(h) = \sum_{i=1}^m u_{y,i} h_i + w_y = 0 \\ f_3(h) = \sum_{i=1}^m tg(\beta_i) h_i + w_z = 0 \\ f_4(h) = \left(\sum_{j=A \dots D}^m (p_j \times [u_{x,i}; u_{y,i}; tg(\beta_i)]) \cdot h_i \right) + \tau_{ext} = \mathbf{0}_{[3 \times 1]} \end{array} \right. \quad (3)$$

where:

$$\alpha_i = \left| \arctg\left(\frac{v_{y,i}}{v_{x,i}}\right) \right|; \quad u_{x,i} = \frac{v_{x,i}}{|v_{x,i}|} \cdot \cos(\alpha_i); \quad u_{y,i} = \frac{v_{y,i}}{|v_{y,i}|} \cdot \sin(\alpha_i); \quad u_{z,i} = \frac{v_{z,i}}{|v_{z,i}|} \quad (4)$$

As we see from Eqs. 3 and 4, given the posture, it is possible to find the tension in the cables. So, in principle, it becomes possible to develop an open-loop controller to bring the platform to the desired position, since force limits are respected.

SIMULATION AND RESULTS

For the simulation the cable used presents the following characteristics: 16 mm diameter, $E=2500 \text{ N/mm}^2$, 100 kN for yielding stress and reference cross section of 123 mm^2 . The simulated platform was the cabin of the helicopter EC-120B Helibrás Colibri, with an estimated mass of 400 kg. In Fig. 4 the main measures of the airship are shown, what makes possible to estimate its inertia characteristics in order to develop the platform model.

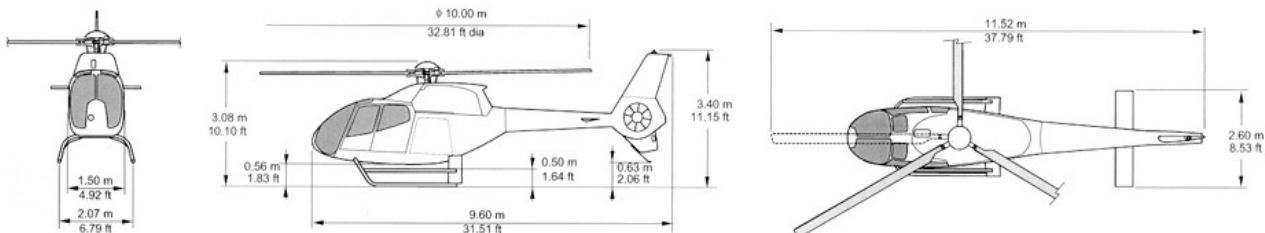


Figure 4 – Simulated helicopter (left) and base workspace (right)

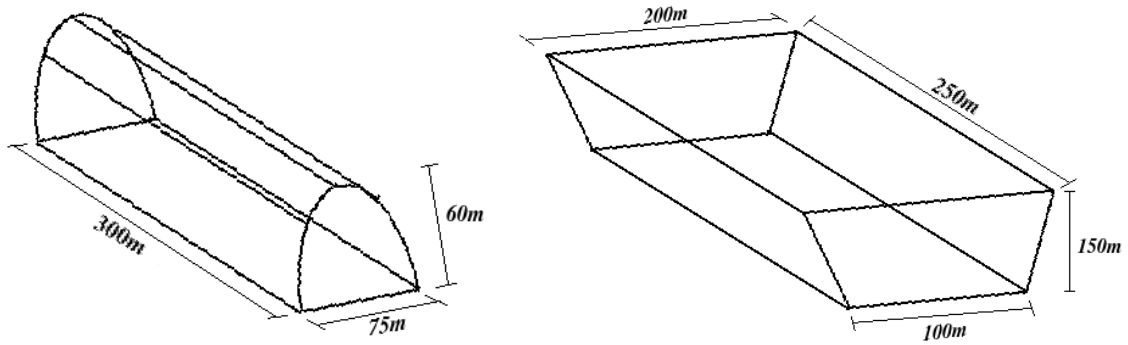


Figure 5 – Base workspace: hangar (left) and small valley (right)

In Fig. 5 it is shown the base for the workspace. One possibility is the use of a hangar, where anchorage points would be easily available. The second one would be a small valley, as available in Brazilian Army facilities in Resende – RJ, Brazil. From the base workspace, a controllable workspace as shown in Fig. 6 is generated for the prismatic base (valley).

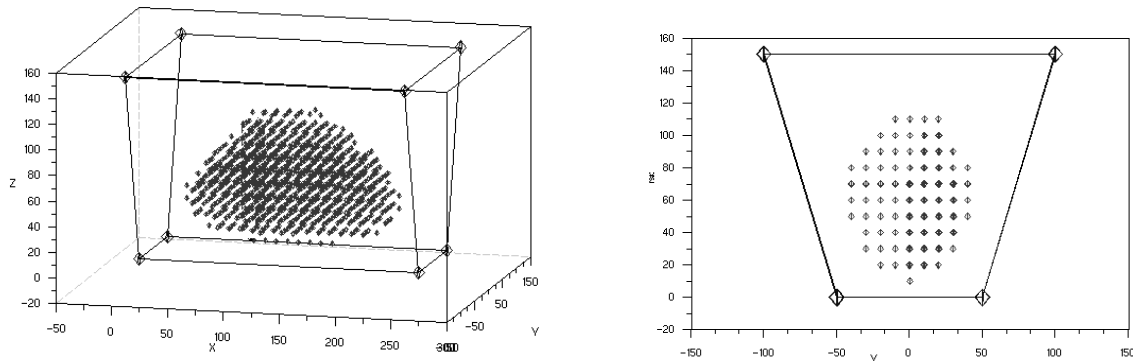


Figure 6 – Controllable Workspace isometric view (left) and frontal view (right) – (units in meters)

A test is run with a spiral trajectory, presented in Fig. 6, which is representative from the point of view of accelerations and velocities.

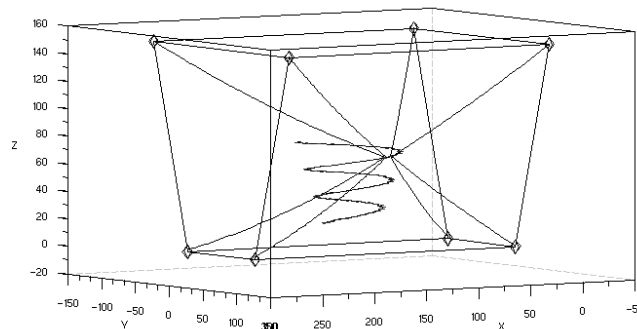


Figure 7 – Test trajectory in spiral form – (units in meters)

The model composed of Eqs. 1, 2, 3 and 4 is applied to the trajectory of Fig. 7, and the obtained results for cable length are compared to the results obtained from a model with massless cables. In Fig. 7 are shown the difference in the upper cables, which are responsible for most of the traction on the platform.

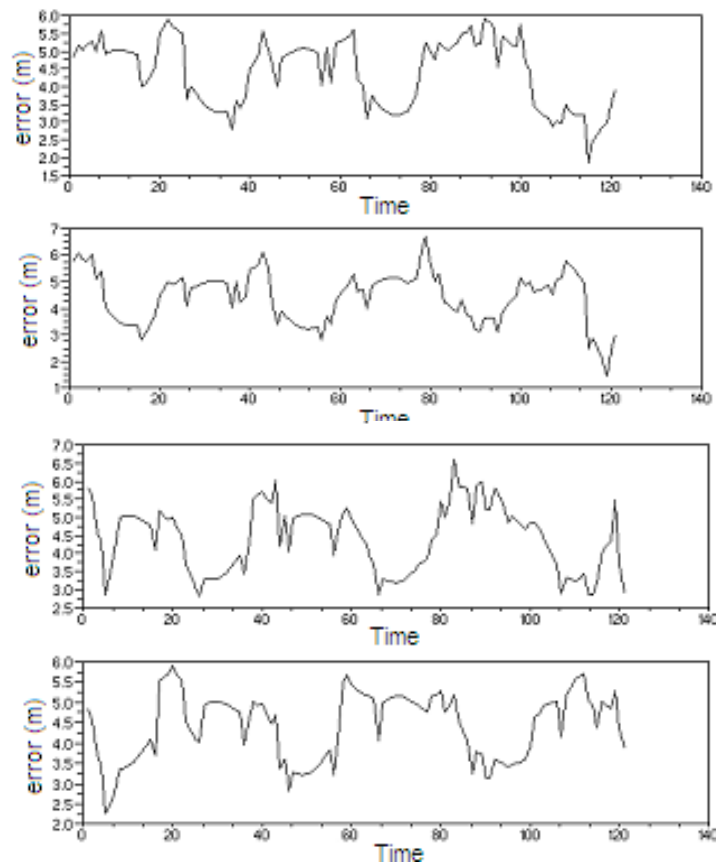


Figure 7 – Difference in trajectory caused by considerations of catenaries

From Fig. 7 it is possible to see that the error in position is about 5%. Here is considered only the deviation due to the mass of the cable.

CONCLUSION

An error of about 5% appears if the mass of bulk cables is not considered. It means that, for the project of a feed-forward control system the model here proposed may bring reasonable improvement. There are still other possible sources of error to be investigated, like elasticity of the cables. With respect to the calculated tractions for a general case, on points near to the bounds of the workspace, high acceleration are a problem, because the upper bound of traction on cables may be exceeded.

A model-based feed-forward control can be implemented from the model here presented may solve the problem of implementing a flight simulator, where the necessary accuracy is relatively low.

REFERENCES

- BOSTELMANN, R. ALBUS, J., DAGALAKIS, N., JACOFF, A. (1994) Applications of The Nist Robocrane , National Institute of Standards and Technology, Gaithersburg, University of Maryland
- BRUCKMANN, T., MIKELSONS, L., BRANDT, T., HILLER, M., and SCHRAMM, D. (2008b). Wire Robots Part II - Dynamics, Control & Application. In Lazinica, A., editor, Parallel Manipulators, ARS Robotic Books. I-Tech Education and Publishing, Vienna, Austria. ISBN 978-3-902613-20-2.
- BRUCKMANN, T.; MIKELSONS, L.; POTT, A.; ABDEL-MAKSOU, M; BRANDT, T.; SCHRAMM, D. (2009). A Novel Tensed Mechanism for Simulation of Maneuvers in Wind Tunnels. In: Proceedings of the 33rd ASME Mechanisms and Robotics Conference (MECH 2009), San Diego, California, USA, 2009.
- FANG, S. (2005). Design, Modeling and Motion Control of Tendon-based Parallel Manipulators. Ph. D. dissertation, Gerhard-Mercator-University, Duisburg, Germany. Fortschritt - Berichte VDI, Reihe 8, Nr. 1076, Düsseldorf.
- MIKELSONS, L., BRUCKMANN, T., HILLER, M., and SCHRAMM, D. (2008). A Real-Time Capable Force Calculation Algorithm for Redundant Tendon-Based Parallel Manipulators. appears in Proceedings on IEEE International Conference on Robotics and Automation.
- STURM, C.; SCHRAMM, D. (2010). On The Control of Tendon Based Parallel Manipulators. Robotics 2010, Cluj-Napoca/ Rumänien, 23.-25. September 2010.

- TRAVI, A. B. Plataforma de Stewart Acionada por Cabos, 2009, 114p, Dissertação (Mestrado em Engenharia Mecânica), Instituto Militar de Engenharia, 2010.
- VERHOEVEN, R. (2004). Analysis of the Workspace of Tendon-based Stewart Platforms. PhD thesis, University of Duisburg-Essen.

RESPONSIBILITY NOTICE

The author(s) is (are) the only responsible for the printed material included in this paper.

Nonlinear Study of Industrial Arc Spring Dampers

Said Lahri^{1,2} , Ilmar F. Santos¹ and Henning Hartmann²

¹Department of Mechanical Engineering, Technical University of Denmark,
 Nils Koppels Alle Bygning 403, DK-2800, Kgs. Lyngby, Denmark
 slah@mek.dtu.dk
 ifs@mek.dtu.dk

² Lloyds Register ODS, Titangade 15, DK-2200, Denmark,
 Henning.Hartmann@lr-ods.com
 said.lahri@lr-ods.com

Abstract: The objective of this paper is to present a numerical approach for analyzing parameter excited vibrations on a gas compressor, induced by the nonlinear characteristic of the arc spring feature of certain designs of squeeze film dampers, SFDs. The behavior of the journal is studied in preparation for varying the damping characteristics of the SFD as well as the dynamic forces acting on the SFD. Phase plane orbits together with Poincaré maps are given for different arc spring damping and static and dynamic load cases. Besides, bifurcation diagrams as a function of the arc spring damping and forces acting on the SFD are presented. It is worth mentioning, that the maps and diagrams can be used as design guidance. Finally, a comparison between the numerical results and experimental result is facilitated in form of waterfall diagrams. For this, a full scale model of the arc-spring damper was designed and build.

Keywords: nonlinear dynamics, phase plane orbits, Poincaré maps, bifurcation diagrams, chaos

NOMENCLATURE

D_1 = Damping characteristics at bearing 1 , [Ns/m]	L = Length of the compressor , [m]	y_1 = Horizontal position of the journal at bearing 1 , [m]
D_2 = Damping characteristics at bearing 2 , [Ns/m]	L_1 = Length from Cg to bearing 1 , [m]	y_2 = Horizontal position of the journal at bearing 2 , [m]
F_x = Static and dynamic forces acting in the vertical direction , [N]	L_2 = Length from Cg to bearing 2 , [m]	Greek Symbols
F_y = Static and dynamic forces acting in the horizontal direction , [N]	M_t = Mass of the compressor , [kg]	θ_x = Angular position of the compressor at Cg measured in the x-direction , [rad]
f_{dyn1} = Aerodynamic force acting on bearing 1 in the vertical direction , [N]	M_x = Bending moment acting around the vertical direction , [Nm]	θ_y = Angular position of the compressor at Cg measured in the y-direction , [rad]
I_p = Polar mass moment of inertia of the journal , [kgm ²]	M_y = Bending moment acting around the horizontal direction , [Nm]	Ω = Angular velocity of the compressor , [Hz]
I_t = Transverse mass moment of inertia of the journal , [kgm ²]	T = Time , [s]	Subscripts
K_1 = Stiffness characteristics at bearing 1 , [N/m]	x_1 = Vertical position of the journal at bearing 1 , [m]	Cg Center of gravity of the compressor
K_2 = Stiffness characteristics at bearing 2 , [N/m]	x_2 = Vertical position of the journal at bearing 2 , [m]	d_G Correlation dimension

INTRODUCTION

Squeeze film damper bearings are widely used in modern turbo machinery of high power density. Pietra and Adiletta [1] give a comprehensive review of the development of the SFD. The SFDs generate their force capability in reaction to dynamic journal motions, squeezing a thin film where the dominant mechanism is damping from shear dissipation due to the surface squeeze. The hydrodynamic reaction forces are conventionally linearized as equivalent stiffness, damping, and inertia. Diaz and San Andrés [2] provide a comprehensive review of the state of the art in prediction and experimental identification of these linear dynamic coefficients for SFD bearings. San Andrés and Santiago [3] experimentally identified damping force coefficients, for large orbital motion, which agreed well with the prediction based on the short length bearing model only if an effective damper length is used. Furthermore, their measurements of film pressures revealed an early onset of air ingestion. A lot of the theoretical attention has been paid to the centered synchronous, circular rotor motion which only exists when the damper is statically centered. However, preloaded and eccentric damper operation where the journal is statically misaligned from the bearing housing aggravates non-linear effects. These effects result in non-circular orbits, jump-phenomena and increase the likelihood of non-synchronous vibrations. Nikolajsen and Holmes [4] reported observations of non-synchronous vibrations in a test rig consisting of a flexible symmetric rotor supported by journal bearings in series with SFDs with retainer springs. The non-synchronous vibrations occurred at

speeds between two and three times the first critical speed. Zhao et al. [5] showed that jump phenomena, subharmonic and quasi-periodic motion are possible in concentric damper motions. They utilized a numerical integration scheme to predict the trajectories, calculate the Poincaré map and power spectra. Different techniques and analyses tools have successfully been employed in the non-linear analyses. Zhao et al. [6] studied how the unbalanced response of a rigid rotor, supported on an eccentric squeeze film damper, was approximated by a harmonic series whose coefficients were determined by the collocation method. Their study revealed that for large values of the unbalance and static misalignment the subharmonic and quasi-periodic motions at above twice the critical speed were bifurcated from the unstable harmonic solution. Furthermore, Sundararajan and Noah [7] exemplify how the shooting and arc-length continuation method can be utilized to locate the periodic responses, determining their stability and describing the bifurcations as a parameter is varied in the SFD system. P. Bonello et al. [8] propose a receptance harmonic balance technique for the determination of the steady state periodic response. This technique showed to be versatile and tractable for large order systems. Inayat Hussain [9] numerically investigates the effects on the bifurcations of a flexible rotor in squeeze film dampers with retainer springs, by varying gravity parameter, mass ratio, and stiffness ratio. One particular design used in large centrifugal compressors comprises a flexible curved beam supporting the journal of the SFD. While this curved beam in itself will behave as a linear spring with constant stiffness, various clearances and allowances in the assembly will cause the support conditions of the beam to change as function of deflection. As a result of this behavior the arc spring force becomes piecewise linear and the stiffness changes as a function of the displacement of the journal. This system is classified as strongly nonlinear. The present paper deals with the nonlinear analyses of the motion of a journal supported by this type of arc spring. In order to verify the damper bearing performance in preparation to the behavior of the stiffness, a full scale model of the arc-spring damper is designed and build.

SFD BEARING DESIGN, TEST AND DATA

Fig. 1(a) depicts a sketch of the considered SFD bearing design. The oil for the SFD bearing is supplied through a central circumferential groove in the outer cage. The SFD bearing is fitted with two O-rings to prevent side leakage of the oil. This type of SFD bearings designs have been used successfully in series with conventional tilting pad bearings on centrifugal compressors in the oil and gas industry. The O-rings are in radial contact between inner cage and outer

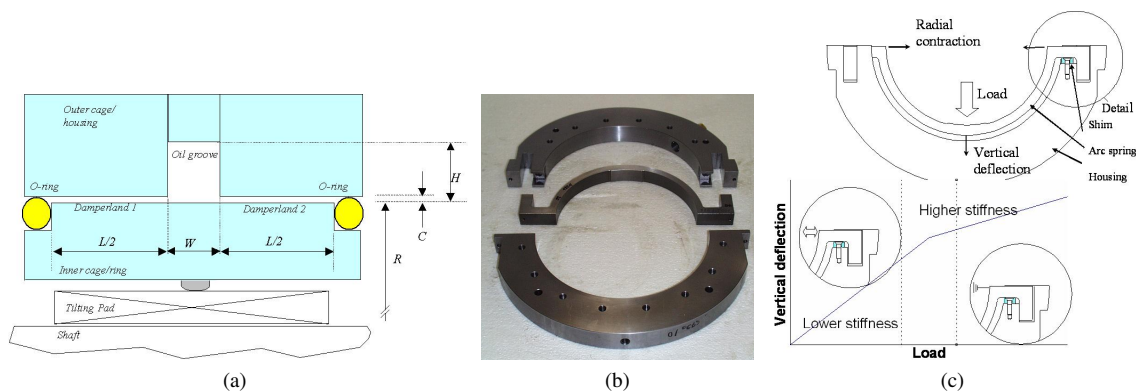


Figure 1: (a) Cross-section of the SFD bearing , (b) Arc spring beam, (c) Illustration of the stiffness behavior

housing, and therefore also contribute significantly to the impedance of the SFD bearing. The characteristic of the O-rings was studied by Smalley [10] which revealed that the O-rings contribute with dynamic stiffness K_{OR} and damping B_{OR} . These are functions of material, vibration frequency and amplitude, temperature, initial squeeze, stretch and cross-section diameter relative to O-ring groove cross section. Consequently, the impedance of the O-rings may differ in vertical and horizontal direction. For heavy rotors a mechanical spring K_{CS} is sometimes used to center the damper ring in the damper housing. In this study, the inner cage is centered inside the outer housing by means of an arc-spring. The arc-spring is a π -arc beam supported by "hooks" at both ends, see Fig. 1(b). This arc spring contributes with vertical stiffness. General knowledge about the arc spring behavior and the static push test conducted in this study revealed that the arc-spring has a non-linear behavior. Fig. 1(c) depicts an illustration of the behavior of the arc-spring. For modest loading and thereby modest vertical deflection the arc-spring is not exploited to the full, thus the stiffness tends to be lower and originates both from the bending stiffness of the arc-spring and the squeeze of the O-rings. However, as the loading is increased the radial contraction increases until the hooks encounter the supports and cause the stiffness to increase. Hence, the behavior of the stiffness in this present paper is considered as piecewise linear.

A test rig is constructed in order to measure both the static and dynamic coefficients of the industrial SFD bearings, see Fig. 2. Utilizing this test rig the stiffness of the arc-spring is investigated as a function of eccentricity, the static load level, various O-ring material, etc. This test rig was also employed in the work of Lund et al. [11].

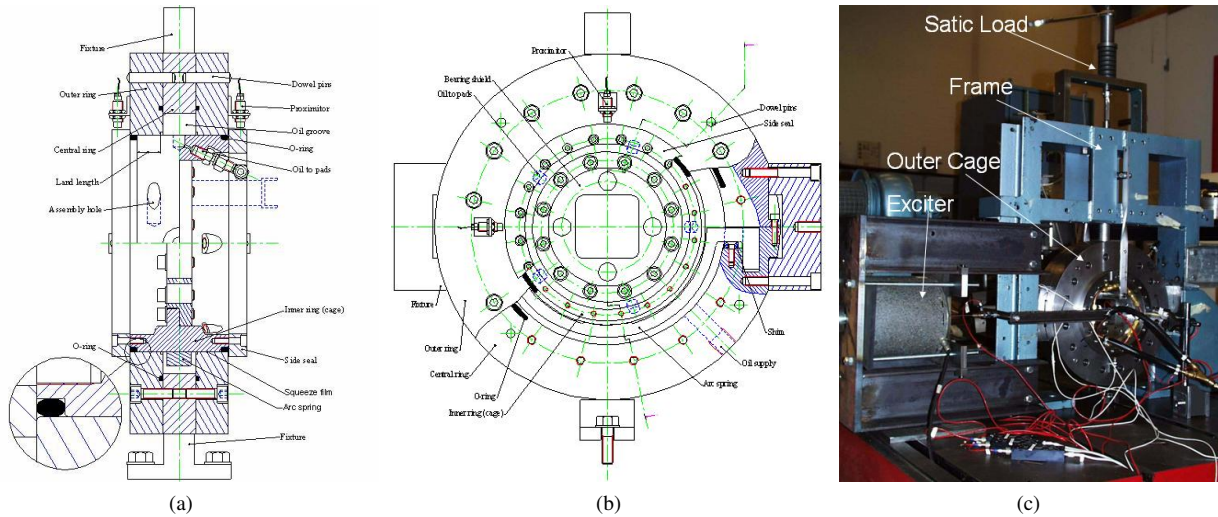


Figure 2: (a) Cross-section of test damper bearing, (b) Front view of test damper bearing, (c) SFD test rig

Arc-Spring Stiffness Coefficients-Fem Model and Push Test

The whole raison d'être for the arc spring is to counteract the static weight of the rotating assembly in order to ensure that the SFD is centered during operation of the machine. In the laboratory, the static load is simulated by means of a yoke from the inner cage to the supporting structure. This loading arrangement will in effect act in parallel with the arc spring, so in order to minimize the influence the load is applied via a stack of disc springs. The applied static load is measured by means of a (strain gauge based) load cell and the deflection by means of proximity probes measuring the relative deflection between outer housing and inner cage. The tests are conducted by static loading a 33 MN/m rated arc-spring mounted together with two Shore 75 O-rings. The configuration for the bearing housing is given in Table 1.

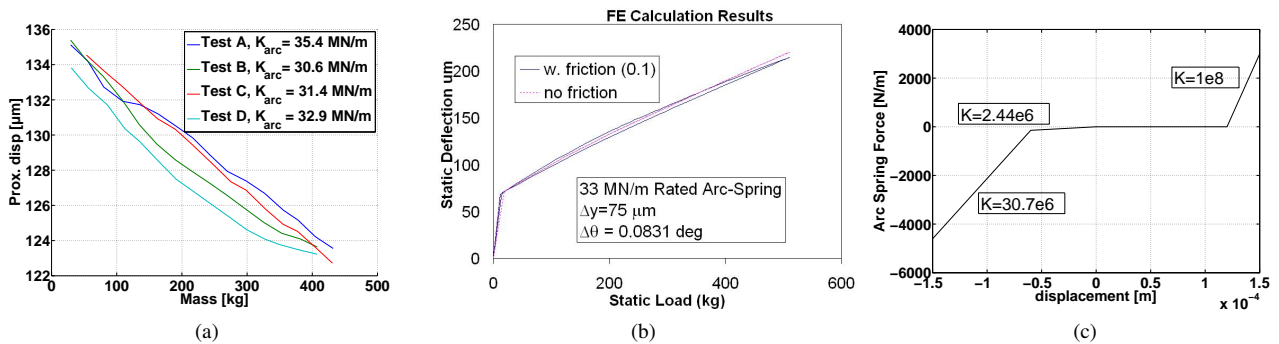


Figure 3: (a) Static load vs displacement curves obtained experimentally, (b) Deflection vs static load obtained by the FEM model, (c) Piecewise linear stiffness curve

Fig. 3(a) shows the results of the damper bearing vertical displacement of the static push tests. Given that the bearing is preloaded it is not possible to identify the stiffness changes since the hooks of the arc-spring are encountering the support and causing the arc spring to operate with “maximum” stiffness. For this reason, the radial clearance of approximately 100 µm is inadequate to unload the hooks at the support and thereby reduce the stiffness as the bearing is unloaded. Therefore, it is not possible to identify the drastical change of the stiffness (the fold of the stiffness curve) and capture the nonlinear behavior. An FEM model is conducted in order to identify the nonlinear behavior of the stiffness, investigate the stiffness changes and validate the model.

An FEM model comprising arc spring and housing is set up and takes various clearances into account by means of simple node to node contact elements. Fig. 3(b) depicts the results from the FEM analysis. In this approach it is possible to identify the changes in the stiffness curve as a function of deflection. Furthermore, good agreement between the experimental results and the FEM model is obtained.

Table 2 shows the findings of the vertical static stiffness of the arc-spring together with the O-rings.

Description	[mm]
Diameter of bearing housing	216.16
Diameter of inner cage	215.91
Radial bearing clearance	0.127
Axial length of damper land	23.495
O-ring hardness	Shore 75
Oil groove, housing (width × depth)	28.7 × 15.3
Oil groove, inner ring (width × depth)	19.85 × 12.7

Table 1: Measured test damper dimensions.

Element	Mean static stiffness [N/M]
33MN/m rated arc-spring	30.7
Shore 75 O-ring at 22 C (stiffness per O-ring)	1.2

Table 2: Mean static stiffness for load range 100 kg to 500 kg.

It is noted that the contribution to the static stiffness from the O-rings is considerable. Utilizing the findings of the stiffness behavior a non-linear stiffness characteristic in the range of the operational clearance of the bearing housing is given in Fig. 3(c). The static force acting on the bearing due to gravity will force the journal to operate at an equilibrium position where the arc-spring beam is exploited to the full. In case of exiting an aerodynamic force acting on the bearing the equilibrium point could be change leading to a change in the stiffness. A further increase of the aerodynamic force will cause the rotor to operate connected to the pedestal, where the stiffness changes drastically from 0 to approximately $1 \cdot 10^8 \text{ N/m}$.

RIGID ROTOR ON TPJB & ARC-SPRING DAMPERS-GLOBAL MODEL

A rigid rotor, representing a gas compressor, supported by SFD's at each end is considered, see Fig. 4. The rigid rotor is mounted on two identical journal bearings supported on squeeze film dampers which are supported by arc-springs. The governing equation of motion of the journal related to the the bearings is written as;

$$\mathbf{T}^{-1}\mathbf{M}\mathbf{T}\ddot{\mathbf{q}}_{cg} + \mathbf{T}^{-1}\mathbf{G}\mathbf{T}\dot{\mathbf{q}}_{cg} + \mathbf{T}^{-1}\mathbf{D}\mathbf{T}\dot{\mathbf{q}}_{cg} + \mathbf{T}^{-1}\mathbf{K}\mathbf{T}\mathbf{q}_{cg} = \mathbf{T}^{-1}\mathbf{F} \quad (1)$$

or written as,

$$\mathbf{M}_b\ddot{\mathbf{q}}_b + \mathbf{G}_b\dot{\mathbf{q}}_b + \mathbf{D}_b\dot{\mathbf{q}}_b + \mathbf{K}_b\mathbf{q}_b = \mathbf{F}_b \quad (2)$$

where,

$$\mathbf{M} = \begin{bmatrix} M & 0 & 0 & 0 \\ 0 & M & 0 & 0 \\ 0 & 0 & I_t & 0 \\ 0 & 0 & 0 & I_t \end{bmatrix}, \quad \mathbf{G} = \begin{bmatrix} 0 & 0 & 0 & 0 \\ 0 & 0 & 0 & 0 \\ 0 & 0 & 0 & -I_p\Omega \\ 0 & 0 & I_p\Omega & 0 \end{bmatrix}, \quad \mathbf{T} = \begin{bmatrix} \frac{L_2}{L} & \frac{L_1}{L} & 0 & 0 \\ 0 & 0 & \frac{L_2}{L} & \frac{L_1}{L} \\ -\frac{1}{L} & \frac{1}{L} & 0 & 0 \\ 0 & 0 & -\frac{1}{L} & \frac{1}{L} \end{bmatrix}$$

$$\mathbf{D} = \begin{bmatrix} D_1 + D_2 & 0 & D_1L_1 - D_2L_2 & 0 \\ 0 & D_1 + D_2 & 0 & D_1L_1 - D_2L_2 \\ D_1L_1 - D_2L_2 & 0 & D_1L_1^2 + D_2L_2^2 & 0 \\ 0 & D_1L_1 - D_2L_2 & 0 & D_1L_1^2 + D_2L_2^2 \end{bmatrix}$$

$$\mathbf{K} = \begin{bmatrix} K_1 + K_2 & 0 & K_1L_1 - K_2L_2 & 0 \\ 0 & K_1 + K_2 & 0 & K_1L_1 - K_2L_2 \\ K_1L_1 - K_2L_2 & 0 & K_1L_1^2 + K_2L_2^2 & 0 \\ 0 & K_1L_1 - K_2L_2 & 0 & K_1L_1^2 + K_2L_2^2 \end{bmatrix}$$

$$\mathbf{F} = \begin{Bmatrix} F_x \\ F_y \\ M_x \\ M_y \end{Bmatrix}, \quad \mathbf{q}_{cg} = \begin{Bmatrix} x \\ y \\ \theta_x \\ \theta_y \end{Bmatrix}, \quad \mathbf{q}_b = \begin{Bmatrix} x_1 \\ x_2 \\ y_1 \\ y_2 \end{Bmatrix} \quad (3)$$

The forces at the left hand side represent both the static forces due to gravity and the harmonic exciting aerodynamic forces. The vertical stiffness at the support is piecewise linear whereas it is linear in the horizontal direction. In the further

analysis and study of the system Eq (2) is written in the state space form in order to ease the numerical integration and computing the eigenvalues.

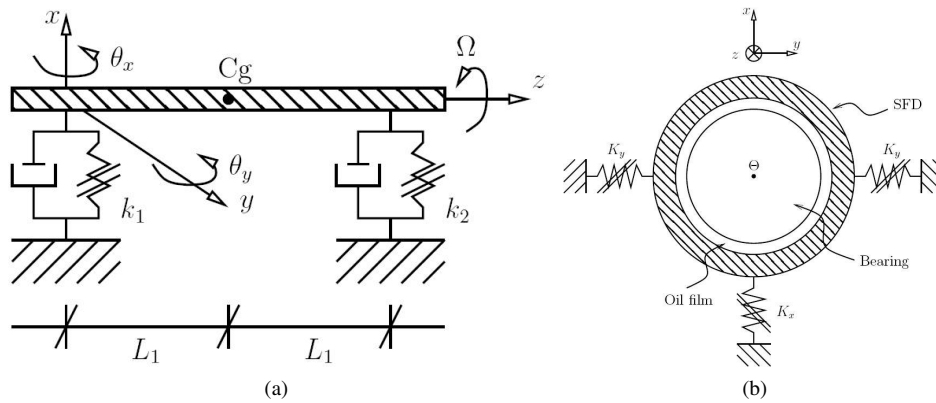


Figure 4: (a) Mechanical model, (b) Cross section at the support

NUMERICAL ANALYSES AND PRELIMINARY EXPERIMENTAL RESULTS

A numerical stitching method is employed in the nonlinear analyses of the system where the stiffness matrix changes as a function of the displacements. The numerical integration is based on the one step explicit Runge-Kutta (4,5) formula, the Dormand-Prince pair, in MATLAB. Utilizing this solver, an event function has been implemented in order to switch between the different stiffness cases. The results of the numerical analyses are illustrated in the following plots,

1. Bifurcation diagram depicting the response in the vertical direction, x_1 of the journal plotted against the speed of the rotor Ω .
2. Phase plane portraits showing the orbits in the $x_1 \times \dot{x}_1$ plane.
3. Trajectory of the journal showing the $x_1 \times y_1$ motion of the journal.
4. Poincaré map, obtained by sampling the trajectory in phase plane at a constant interval of the forcing period of $T = \frac{1}{\Omega}$ and projecting the outcome on the $x_1(nT) \times \dot{x}_1(nT)$ plane.
5. Fourier spectrum of the response

These plots are in general adequate to provide the necessary behavior and information about the dynamics of the system. However, for a system that demonstrates chaotic nature of motion these plots such as the Poincaré maps and Fourier spectra should be strengthened by either evaluating the largest Lyapunov exponents or the fractal dimension of the attractor in order to pronounce a system chaotic or strange. In this study the fractal dimension of the attractor is calculated to determine whether the journal undergoes a chaotic state of motion. The measure of the fractal has successfully been used among experimentalist. Grassberger and Procaccia [12] proposed an efficient approach for determining the correlation dimension d_G . In this approach one discretizes the points $\{\mathbf{x}_i, i = 1, \dots, n\}$ by letting the system evolve for a long time and calculating the distances between pairs of points $s_{ij} = |\mathbf{x}_i - \mathbf{x}_j|$ on the attractor. Another approach is to discretize the orbit in a pseudo space where the dimension of the attractor is embedded in an m -dimensional Euclidean space from a sample of N points where the orbit is constructed by the lagged variables. Upon choosing the time lag τ and the dimension of the space m the coordinates of the pseudo space is taking as $x(i), x(i + \tau), i = 1, 2, \dots, N - (m - 1)\tau$. Here, the value of the time lag is determined by finding the first zero of the auto-correlation function of the time series $x(i)$, i.e., letting $R(\tau) = 0$, where $R(\tau)$ is the auto-correlation function of the time series $x(i)$. In this study both of the methods are employed for determining the chaotic nature of motion of the journal. A correlation function is then calculated by constructing a sphere of radius r at each point \mathbf{x}_i and counting the number of points in each sphere, that is,

$$C(r) = \lim_{n \rightarrow \infty} \frac{1}{N^2} \sum_i^N \sum_j^N H(r - |\mathbf{x}_i - \mathbf{x}_j|) \tag{4}$$

where $H(s)$ is the Heaviside function i.e.,

$$H(s) = \left\{ \begin{array}{l} 1, \text{ if } s \geq 0, \\ 0, \text{ if } s \leq 0 \end{array} \right\} \tag{5}$$

For attractors this function has been found to exhibit a power law dependence on r as r becomes smaller and smaller as pointed by Grassberger and Procaccia [12], that is,

$$\lim_{r \rightarrow 0} C(r) = ar^{d_G} \tag{6}$$

In this way the fractal or correlation dimension is found by taking the slope of the $\ln C$ versus $\ln r$ curve. Besides providing methods for pronouncing system chaotic, the bifurcation scenarios and transition into chaos should also be considered. For non-smooth problems the transition into chaos demonstrate a much broader class of bifurcation phenomena such as *border-collision bifurcations* than for smooth systems.

Parameters	Values	Units
M_t	504	$[kg.m^2]$
I_p	5.37	$[kg.m^2]$
I_t	221.64	$[kg.m^2]$
L	2.44	$[m]$
L_1	1.30	$[m]$
L_2	1.14	$[m]$
$D_{1ver} + D_{1hor}$	10×10^3	$[Ns/m]$
$D_{2ver} + D_{2hor}$	10×10^3	$[Ns/m]$
K_{2ver}	30.7×10^6	$[N/m]$
K_{2hor}	3.07×10^6	$[N/m]$

Table 3: Parameters used to simulate the gas compressor dynamics

The parameters listed in Table 3 are employed throughout the different study cases of the motion of the journal. The stiffness in the horizontal direction is assumed to comprise 10% of the stiffness in the vertical direction at both bearings. With the object of investigating the bifurcations and the dynamic motions of the system, the journal on *bearing 1* is excited in the vertical direction by a harmonic driven aerodynamic force with the magnitude of $f_{1dyn} = 2880N$. The frequency of excitation is identical to the speed of the rotor. Furthermore, the arc spring supports the journal at a static equilibrium position of approximately $x_1 = -21.15\mu m$. The following sections process the different study cases.

Constant magnitude of the aerodynamic force and constant damping

Fig. 5(a) depicts the co-dimension one bifurcation diagram which is described on a one dimension manifold; here, it takes only the single parameter Ω to unfold them. For this figure, the transient is cut off and the motion x_1 on *bearing 1* in the vertical direction is plotted against the driving frequency Ω . The frequency range is chosen to represent a operational speed range of the compressor. The bifurcation diagram presented in Fig. 5(a) is determined by gradually increasing Ω from 70 Hz (4200 rpm) to 180 Hz (10800 rpm). In order to capture the different types of cycles within the plane the initial conditions are modified during the simulations. Therefore, after identifying the local attractors within the plane the final position and velocity (post behavior) of the journal of a previous simulation are used as the new set of initial conditions. In that way the journal remains at the attractor. However, at the bifurcation point (D) in Fig. 5(a) the journal is forced back to the center of the damper in order to capture the dynamics from point (D) to point (F). Furthermore, the system demonstrates that different types of cycles with different dynamic characteristics coexist for the wide range of Ω . Fig. 5(c) depicts the band of frequencies that the journal undergoes as the speed of the compressor is gradually increased. The waterfall diagram is computed by forcing the journal back to the static equilibrium position after each simulation and therefore depicting the power spectrum of the lower attractor. Considering the bifurcation diagram depicted in Fig. 5(a) it is seen that at the frequency range of 70 Hz (4200 rpm) to 91 Hz (5460 rpm), at point (A) to point (B), two stable attractors exist. The upper branch (C) depicts the stable *1-period* limit cycle, whereas the lower branches, from (A) to (B), depict a quasiperiodic attractor. Fig. 6(a) to Fig. 6(c) depict the dynamics of the *period-1* motion. Fig. 6(d) to Fig. 6(f) depict the dynamics of the quasiperiodic attractor. Considering the quasiperiodic attractor it is seen that the phase plane has a non-smooth and discontinuous behavior which is a result of the drastical changes in the stiffness as the journal undergoes the different stiffness zones as illustrated in Fig. 3(c). Regarding Fig. 6(e) it is clearly seen that the Poincaré return map fills up a close curve which is typical for quasiperiodic attractors. However, if the journal is attracted to the *period-1* stable limit cycle, point (C), it will operate connected to the pedestal as the location of the limit cycle exceeds the bearing clearance, whereas the quasiperiodic attractor will force the journal to operate within the bearing clearance but with super synchronous responses. Fig. 7(a) shows phase plane portrait together with local trajectories near the two attractors at the same plane, and Fig. 7(b) shows the post transient time series. A disturbance in the system can cause the trajectory to start intersecting one of the so-called sewing surfaces, i.e., surfaces that divide the phase space into domains

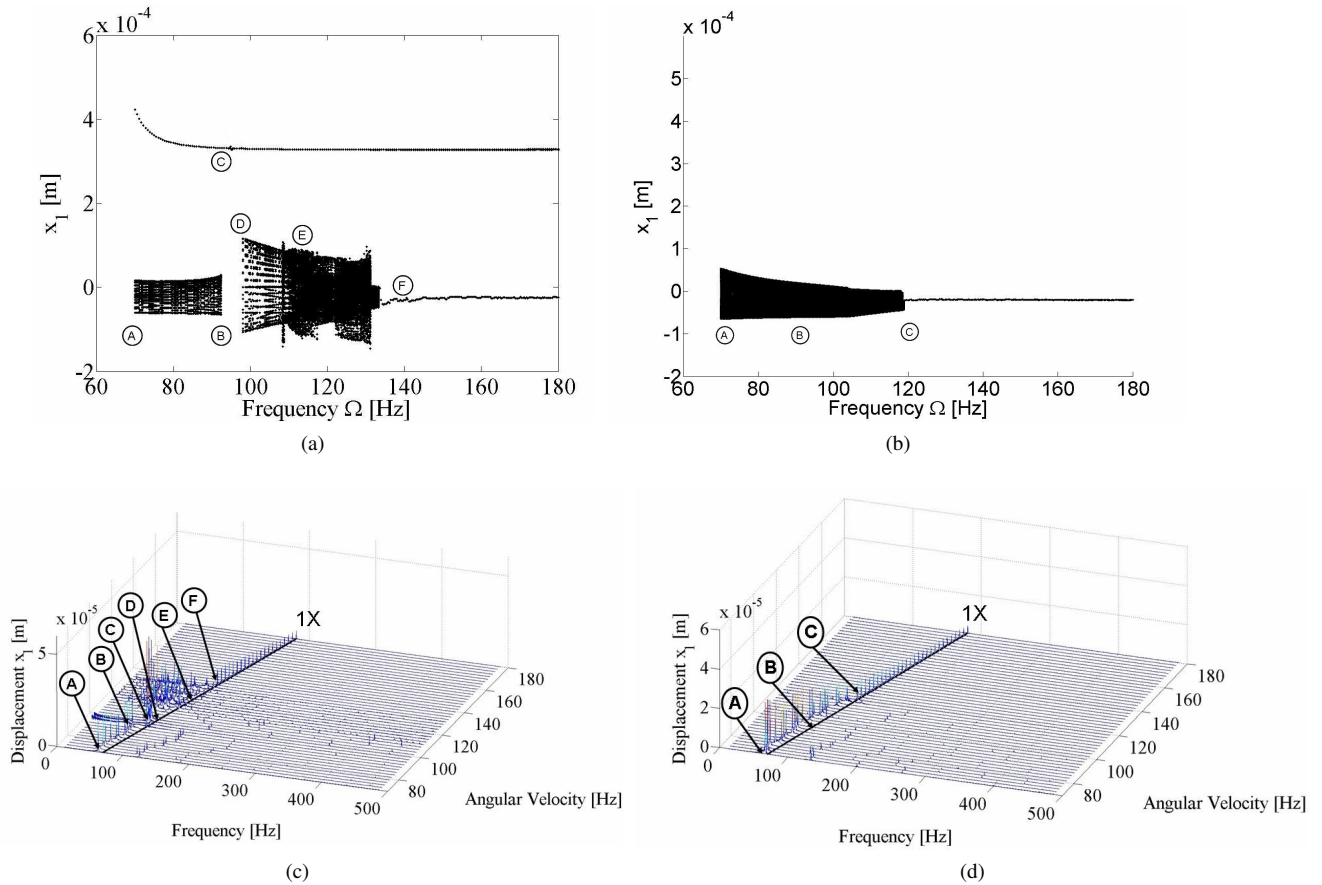


Figure 5: (a) **One dimensional Bifurcation Diagram**, (b) **One dimensional Bifurcation Diagram, increased damping**, (c) **Waterfall diagram**, (d) **Waterfall diagram, increased damping**

of different dynamics. This is referred to as *border-collision bifurcations*. Within each such domain the system is smooth, but the equation of motion changes abruptly from one domain to the next.

At approximately $\Omega = 92.7\text{Hz}$ (5562 rpm), point (B) in Fig. 5(a), a bifurcation takes place. The quasiperiodic attractor loses its stability in what seems to be in a saddle bifurcation of cycles (*blue sky bifurcation*). This is depicted in Fig. 8. Shortly after the quasi periodic attractor loses its stability there is a saddle-node remnant or ghost leading to a slow passage at the location where the quasiperiodic attractor existed and the trajectory is attracted through a collision of the so called sewing surface to the stable limit cycle. During the dangerous bifurcation the current attractor suddenly disappears and the state jumps to a remote disconnected attractor, from point (A) to point (B) in Fig. 8. Just before the bifurcation the journal undergoes super synchronous oscillations, after the bifurcation the journal undergoes synchronous motion, see the power spectrum depicted in Fig. 5(c). The bifurcation is always discontinuous. Such non-smooth changes in behavior may represent dangers to the life of the system. Reversing the change in control parameters, the state may remain on the remote attractor well below the critical value, thus giving rise to hysteresis. This bifurcation is considered critical for the system and should by different means be avoided

At the angular velocity of $\Omega = 96\text{Hz}$ (5760 rpm), point (D) in Fig. 5(a), the quasiperiodic attractor appears “*out of the clear blue sky*”, where upon it undergoes a quasiperiodic route to chaos. This route involves a transition into chaos through an interval of quasiperiodic motion, *Hopf* bifurcations, and into the transition via different forms of torus destruction (Ruelle-Takens-Newhouse scenario). Fig. 9 depicts the dynamics of the chaotic motion at the angular velocity of $\Omega = 115\text{Hz}$ (6900 rpm), point (E) in Fig. 5(a), with large amplitude orbits filling the phase plane and a broad-banded frequency spectrum. The corresponding Poincaré section and the correlation dimension given in Fig. 10 and Fig. 11 evaluated by means of the two methods, confirm that the response is chaotic. The correlation dimension is evaluated by using 15,000 points in the two approaches. The correlation dimension given in Fig. 10 is found by employing different embedded dimensions. As the embedding dimension is increased, the linear part of the slope approaches a constant value. The correlation dimension given in Fig. 11 is found by evaluating the correlation integral by employing the point on the strange attractor. The approximated correlation dimension is found to $d_G \cong 0.9890$ and $d_G \cong 0.9710$, respectively. A non-integer fractal dimension of this order indicates that the dynamics of the journal excites on a finite low dimensional

Arc spring damper features

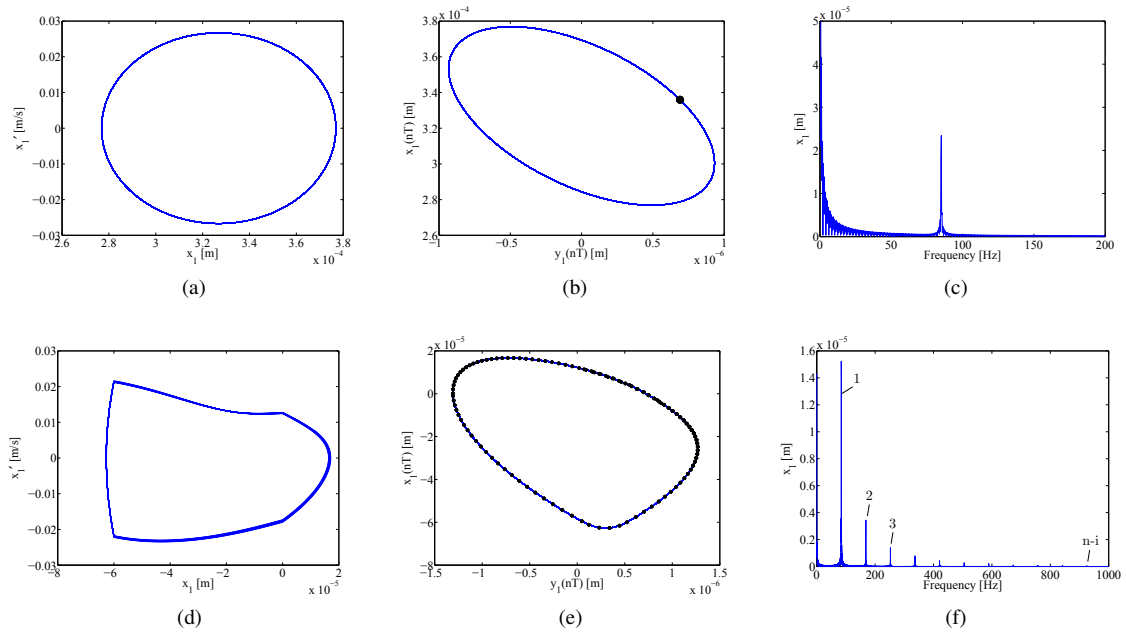


Figure 6: Dynamics of the system. Post-transient phase plane (left), Trajectory of rotor together with Poincaré section (middle) and power spectra (right)

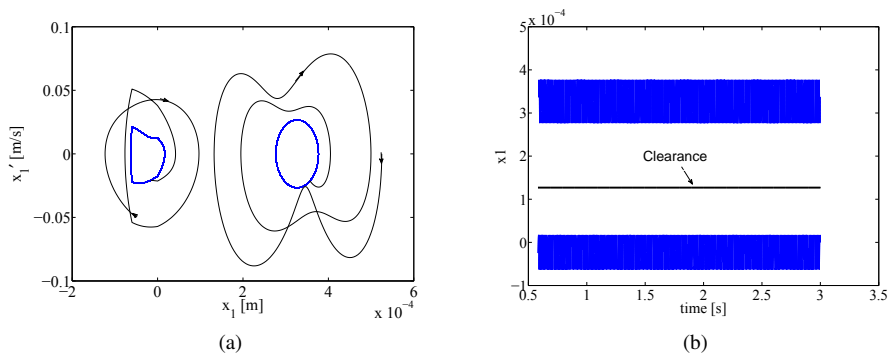


Figure 7: (a) Phase plane orbits with local trajectories, (b) Time series of the two post transient responses

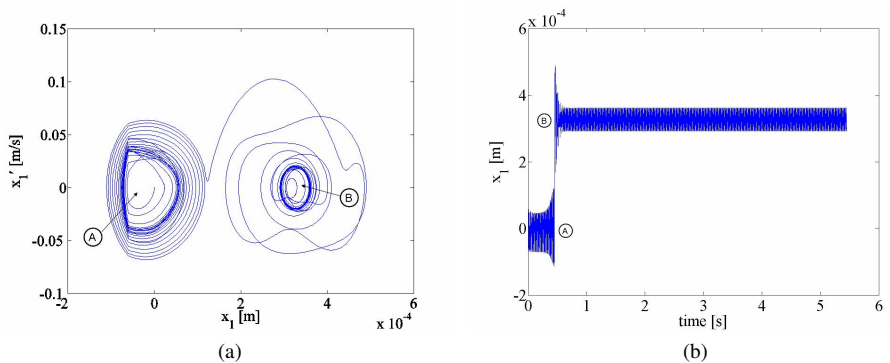


Figure 8: (a) Phase plane portrait at the bifurcation, $\Omega = 92.7Hz$ (5562 rpm), including transient behavior (b) Time series including the transient behavior

attractor.

As the angular velocity is increased the journal undergoes a quasiperiodic motion that leads to a stable *period-1* state of motion, point (F) in Fig. 5(a).

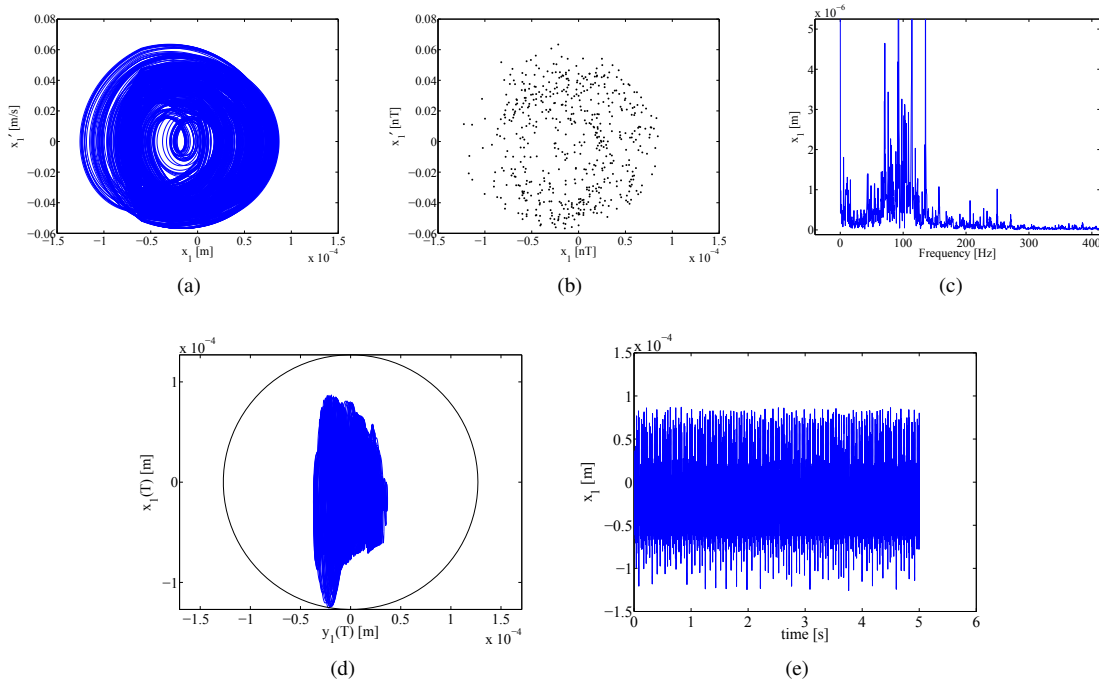


Figure 9: (a) Phase plane, (b) Poincaré section, (c) Displacement power spectrum, (d) Trajectory of rotor within the bearing clearance, (e) Time series

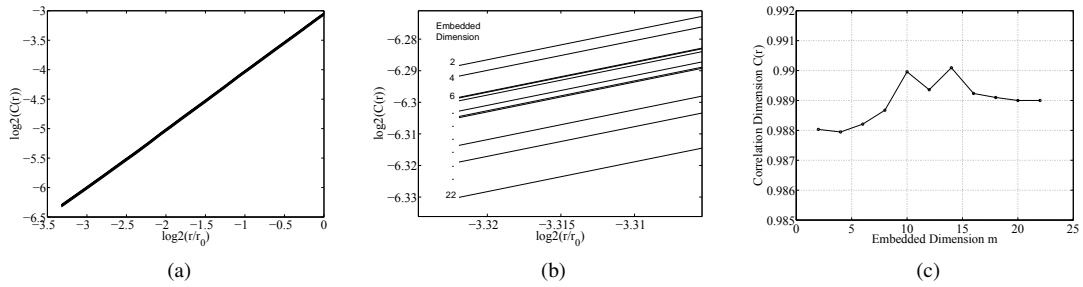


Figure 10: (a) Variation of $C(r)$ with embedded dimension m , (b) Zoom of (a) to illustrate the variation in m , (c) Variation of correlation dimension with embedding dimension m

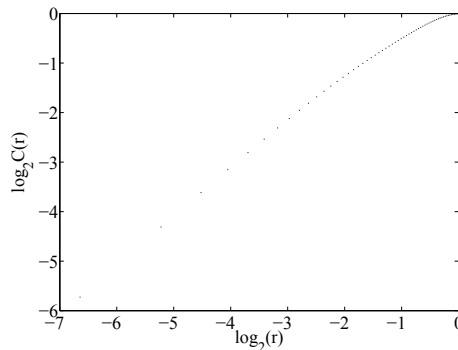


Figure 11: Correlation integral evaluated by sampling on the strange attractor

Studying the effects of the direct damping D_1 in the x_1 direction

It is shown in Fig. 5(a) that a critical bifurcation occurs at the angular velocity of $\Omega = 92.7Hz$ (5562 rpm). This bifurcation should by all means be avoided since it is crucial to the system. One approach towards avoiding the critical

bifurcation is to increase the damping D_1 . Fig. 5(b) depicts the bifurcation diagram for the case where D_1 is increased by a factor of 10 i.e., from $10000Ns/m$ to $100000Ns/m$. It is clearly seen in the bifurcation diagram that the journal stays within the bearing clearance, from point (A) to Point (C). The bifurcation diagram is computed by using the final state of motion of the journal as the new set of initial condition at each simulation. The transition into chaos is also prevented in this case. From point (A) to point (C) the journal undergoes quasiperiodic motion where upon the motion becomes *period-1*, synchronous oscillation. Fig. 5(d) depicts the band of frequencies the journal undergoes as the speed of the compressor is gradually increased. It is clearly seen that synchronous response in this case occurs at the speed of $\Omega = 120Hz$ (7200 rpm). The additional damping is generated by the squeeze effect of the SFD. Changes in geometry of the SFD can lead to an increase in the damping. Such changes involve increasing the active axial damper length and oil viscosity and reducing the radial clearance.

Comparison between experimental and numerical result

The dynamic force utilized to shake the test rig is delivered by means of a system of adjustable unbalances. These unbalances are attached to a rotor which rests in a ball bearing inside the bearing cage. Besides the proximity probes, two accelerometers are used to measure the absolute acceleration of the inner cage in vertical and horizontal direction, and a key phasor giving a common reference for the phase measurements. The damper bearing cage is centered before the test is conducted. The experimental results presented in his paper is obtained by setting the driving frequency to the constant value of $\Omega = 90Hz$ (5400 rpm). Fig. 12 depicts a comparison between the experimental and numerical results. The numerical results are in good agreement with the experimental result. It is clearly seen that the damper bearing cage undergoes super synchronous oscillations. This is caused by the fact that the journal operates close to the bend of the stiffness curve.

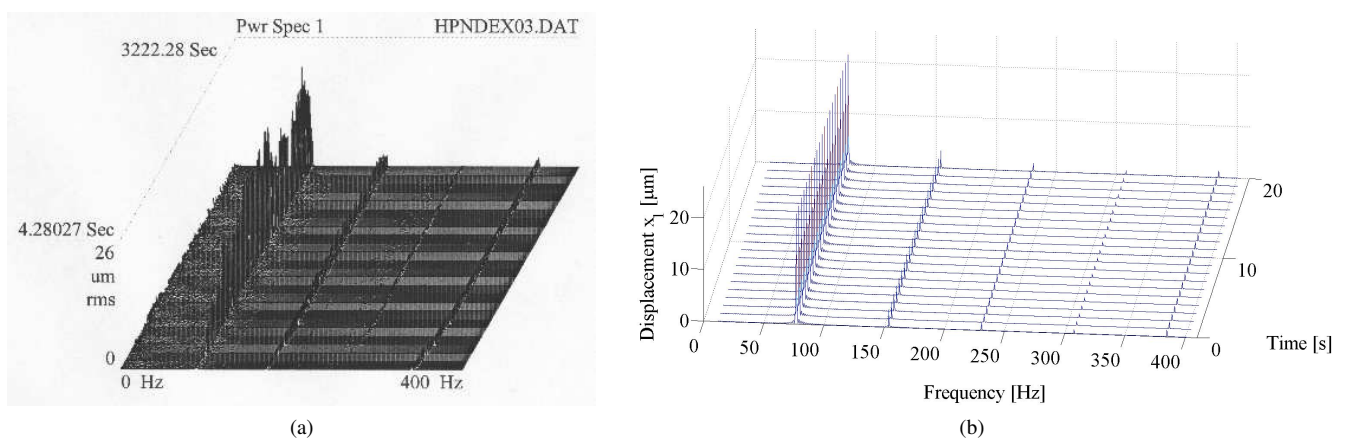


Figure 12: (a) Waterfall, experimental, (b) Waterfall, numerical $D_1 = 10000Ns/m$

CONCLUSION

The nonlinear analyses in this study revealed that the system undergoes an unfavorable bifurcation which is crucial to the system. An approach towards mitigating this effect is to increase the damping. Consequently, this is obtained by centering the journal within the SFD. A further improvement is to preload the arc spring and assure that it operates within a linear range of the stiffness curve, hence avoiding the bend in the stiffness curve. Good agreement between experimental and numerical result was obtained. Furthermore, the study revealed that for a certain frequency range the damper bearing cage undergoes super synchronous vibrations, caused by the stiffness feature of the arc spring. An increase in angular velocity leads to synchronous response as the arc spring becomes unloaded.

ACKNOWLEDGMENTS

The authors would sincerely thank Henning Hartmann and Claus Myllerup, Lloyd's Register ODS, for their effort of making the test rig and conducting the experiments.

REFERENCES

- [1] L. Della Pietra, G. Adiletta. The Squeeze Film Damper over Four Decades of Investigations. Part I: Characteristics and Operating Features. The Shock and Vibration Digest, Vol. 34, No. 1 January 2002 3-26.

- [2] Diaz .S, San Andrés .L. Orbit-based Identification of Damping Coefficients for a Rotor Mounted in Off-Centered Squeeze Film Dampers and Including Support Flexibility. ASME Paper 2000-GT-394.
- [3] San Andrés .L, De Santiago .O. Forced Response of a Squeeze Film Damper and Identification of Force Coefficients From Large Orbital Motions. ASME 2004 Vol. 126, April
- [4] Nikolajsen .J .S, Holmes .R. Investigation of Squeeze-Film Isolators for the Vibration Control of a Flexible Rotor. J Mech Eng Sci 1979 22:247-252
- [5] Zhao .J .Y, Linnet .I .W. Stability and Bifurcation of Unbalanced Response of a Squeeze Film Damped Flexible Rotor. Journal of Tribology April 1994, Vol. 116 pp 361-368
- [6] Zhao .J .Y, Linnet .I .W, McLean .L .J. Subharmonic and Quasi-Periodic Motions of an Eccentric Squeeze Film Damper-Mounted Rigid Rotor. Journal of Vibration and Acoustics July 1994, Vol. 116 pp 357-363
- [7] Sundararajan .P, Noah .S .T. Dynamics of Forced Nonlinear Systems Using Shooting/Arc-Length Continuation Methods-Application to Rotor Systems. Journal of Vibration and Acoustics January 1997, Vol. 119 pp 9-20
- [8] Bonello .P, Brennan .M .J, Holmes .R. Non-Linear Modelling of Rotor Dynamic Systems with Squeeze Film Dampers-an Efficient Integrated Approach. Journal of Sound and Vibration 2002 249(4) pp 743-773
- [9] Inayat-Hussain .J .I. Bifurcations in the response of a flexible rotor in squeeze-film dampers with retainer springs. Chaos, Solitons & Fractals 39 (2009) pp 519-532.
- [10] Smalley .A .J, Darlow .M .S, Mehta .R .K. Dynamic Characteristics of O-Rings. Asme J Mech 1978 vol. 110 pp 123-138.
- [11] Lund .J .W, Myllerup .C .M, Hartmann .H. Inertia Effects in Squeeze-Film Damper Bearings Generated by Circumferential Oil Supply Groove. Journal of Vibration and Acoustics October 2003 Vol. 125 pp 495-499
- [12] Grassberger .P, Procaccia .I. Measuring the Strangeness of Strange Attractors. Physica 9D (1983) pp 189-208.

RESPONSIBILITY NOTICE

The authors are the only responsible for the printed material included in this paper.

Robust Modelling Using Bi-Lateral Delay Lines for High Speed Simulation of Complex Systems

Petter Krus

Division of Fluid and Mechatronic Systems, Linköping University, SE-581 83 Linköping, Sweden

Abstract: A very effective method for modelling and simulation of large complex dynamic systems is represented by distributed modelling using transmission line elements (or bi-lateral delay lines). This method evolves naturally for calculation of pressures when hydraulic pipelines are modelled with distributed parameters, and it can be used to effectively partition the model to use local solvers for the differential equations in each component or subsystem. It is also applicable to other physical systems, such as mechanical, electrical, gas etc.

One interesting application for distributed solvers using bi-lateral delay lines is in real time simulation, since they are very robust and usually quite large simulation times steps can be used. Modelling for real-time applications puts special requirements on robustness in the numerical methods used. In real-time applications there is no room for decreasing time step in numerically critical stages. Furthermore, if a system is relying on a real-time simulation for its functionality, failure in the numerical properties is unacceptable. It is also in many applications possible to simulate the system faster than real time, which means that high fidelity system simulation can be used to plan ahead in control applications, and for simulation based optimisation.

Since solvers can be embedded in components or subsystems, it is very straightforward to implement parallel processing using the multi-core processors which now is the standard for desk top computers. There is also an increasing need in many situations to resolve the time scale to finer details, where the effect of wave propagation needs to be modelled.

Keywords: System simulation, transmission lines

INTRODUCTION

The interest in real-time simulation (RTS) has increased in recent years. There are several reasons for this; more functionality in products is realized through embedded software, and real-time simulation is needed in hardware-in-the-loop simulation (HWIL), which is a key technology for validation of such control systems. Also, real-time simulation is needed in human in the loop simulation (HIL), which is used both in product design and in training simulators. There are also application in the operation phase of a product, e.g. model based diagnostic systems and in model-predictive control systems. Currently, specialized, highly simplified, and often linear models are used for real-time simulation.

As a result there is increasing demands for real-time in a range of industrial applications. However, since commercial platforms for multi-domain system simulation, use architectures that are designed for off-line simulation, it is difficult if not impossible, to use anything but, highly simplified, often linear models, for real-time simulation. With the rapid development in hardware performance, real-time simulation, should no longer be a problem, but methods and tools for generating real-time simulation of high-fidelity, fully non-linear multi-domain system, is lacking. The large application for off-line simulation models in today's product development has promoted the application of central numerical solution methods. With the advent of real-time simulation models it becomes increasingly obvious that these models will differ greatly from off-line simulation models. Still, it is desirable to keep the two sets of models as close as possible.

In many real-time applications it is an advantage if the system model can be composed by distributed simulations of subsystems on different processors. Analyzing systems of components originating from different vendors may even make distributed simulations an absolute necessity, in order to limit disclosure of information. Partitioning of simulation models for parallel simulation is also useful in order to take advantage of multi-core processor architectures rapidly becoming the norm for desk top computing. High speed simulation also enables, faster than real-time simulation (FRTS), which can be used in e.g. control systems based on prediction of future responses to alternative actions (Anagnostopoulos et.al 2003). Furthermore, it also enables the use of simulation based optimisation also for larger systems.

In the recent decade, system simulation has had something of a breakthrough, where large systems can be modelled with a high degree of fidelity, i.e. Lantto et al.. However, the technologies used in commercial software are decidedly off-line technologies that do not allow for real time simulation, this includes centralized solver as the normal approach to simulation. Although great advances have been made in the development of algorithms and software, this approach suffers from inherently poor scaling. I.e. execution time grows more than linear with system size.

In contrast, distributed modelling, where solvers are embedded in subsystem, and even component models, has almost linear scaling properties. Special considerations are needed, however, to connect the subsystems to each other in a way that maintains stability properties, and do not introduce unwanted numerical effects. Technologies based on

bilateral delay lines, see Auslander 1968, (or transmission line modelling, TLM) have been developed and used for a long time at Linköping University, and has successfully been implemented in the HOPSAN simulation package, which at time of writing is the only simulation package that utilise the technology, within mechanical engineering, and fluid power. It has also been demonstrated for parallel simulation in Krus et al 1990 and subsequently by Burton et al 1994. Although the method has its roots already in the sixties, it has never been widely adopted, probably because its advantages are not evident for small systems, and that wave-propagation is regarded as a marginal phenomena in most areas, and thus not generally well understood.

Simulation using bilateral delay lines is also highly suited to simulate systems where wave propagation is an issue. One particular area is in rock drill equipment, where a high fidelity representation of wave propagation phenomena in both mechanical, and hydraulic parts, is fundamental for describing the functionality of the system.

Using distributed solvers with bi-lateral delay lines as connection elements, gives a physically motivated partitioning of the system. In this way component models can be numerically insulated from each other, which provide highly robust numerical properties. This technique is also useful for high speed simulation of systems, and has been used successfully for simulation based optimization, where the system is simulated a large number of times with different parameter sets. The use of transmission line elements for partitioning of systems is a non-exclusive approach. Conventional simulation techniques can still be used within the subsystems. This means that transmission line elements can be used to connect simulation models developed in different simulation packages. Using distributed solvers also has the advantage that it allows a model to be assembled from precompiled modules. This can be highly valuable in collaborative system design, since it does not require disclosure of the source code, when providing a module to partners.

Differential Algebraic Systems

A general approach to represent a system is to represent it as a differential algebraic system. This also allows for algebraic loops. The simulation language Modelica [6] is a language that is based on this form.

$$F(x, \dot{x}, u, t) = 0 \quad (1)$$

where x is the variable vector, u is an input vector, and t is time.

However, Eq. (1) implies that the system essentially has to be written in state space form, something that may be considered as too limited. Many relationships are usually given in transfer function form, which makes it more natural to allow for higher derivatives. The system can then instead be expressed as

$$F\left(y, \frac{dy}{dt}, \frac{d^2y}{dt^2}, \dots, \frac{d^2y}{dt^2}, t\right) = 0 \quad (2)$$

This also has the advantage that the variable vector is reduced, since y is shorter than x , y contains a subset of the states in x . It should, however, be pointed out that it is only possible to impose strong non-linearities (such as limitations on the state variables) represented in the y vector. Also all variables that are of any interest must be included in the y vector otherwise they will not be computed explicitly. Finally high order differentials should be avoided since the equations becomes numerically ill conditioned if the word length is limited.

In order to solve the dynamic part of the system in a numerically stable way, the trapezoidal rule can be used. Using the trapezoidal rule the time differential is solved as:

$$x(t+h) = x(t) + \frac{1}{2}h(x(t) + x(t+h)) \quad (3)$$

A more effective way of using the trapezoidal rule is to reformulate it in the form known as the bilinear transform.

$$\frac{d}{dt} = \frac{2(1-q^{-1})}{h(1+q^{-1})} \quad (4)$$

where q in this context represents the time displacement operator such that:

$$qy = y(t+h) \quad (5)$$

Using the bilinear transform in Eq. (4) means that it can be rewritten as a function G of y and old states.

$$G(y(t), y(t-h), \dots, y(t-nh), u(t), u(t-h), \dots, u(t-nh), t) = 0 \quad (6)$$

When solving the system all the old values $y(t-h)\dots y(t-nh)$ can be regarded as constants since they have already been established in previous time steps. Likewise the input vector is also known. Equation (6) is therefore rewritten as:

$$G(y(t), t) = 0 \tag{7}$$

In order to solve this system of equations in a numerically stable way, the Jacobian matrix is needed, which is defined as:

$$J_{ijk} = \frac{\partial G_i(y_k(t))}{\partial y_j} \tag{8}$$

The equation can then be solved numerically using Newton-Raphson iteration.

$$y_{k+1} = y_k(t) - J_k(t)^{-1} G(y_k(t)) \tag{9}$$

Since an iterative procedure is used, there is a potential for performance loss due to the number of iterations needed to solve the system. However, the values from the previous time step can be used as start values.

$$\begin{aligned} y_0(t) &= y(t-h) \\ J_0(t) &= J(t-h) \end{aligned} \tag{10}$$

If the system is linear, the system can be solved in only one iteration, and it is usually sufficient with only one iteration even for non-linear systems, especially if a small time step is used. There are, however, situations when input signals changes suddenly, e.g. a valve is changed step wise during one time step, that requires more than one iteration. In practice, however, it has been found that two iterations increase the tolerance against non-linearities dramatically, while a further increase to three iteration gives only minor improvement. Two iterations have therefore been found to be something near to an optimum for almost all situations. For implementation it is better to use LU-decomposition rather than using the matrix inverse of the Jacobian.

Provided the system is reasonably linear (slow variation of J, Eq. (9) is an A-stable method. However, in reality, rather large variations of J can be tolerated. Even pure discontinuities can also be handled satisfactory using the above approach, when fixed-time step is used (as in real-time simulation).

Eq. (9) also illustrates a dilemma associated with all numerically stable methods. They need knowledge of the Jacobian, and if the system is stiff and highly non-linear this must be updated very often. We also realize that the computational burden is much more than linearly dependent on the size of the system. This makes these methods unsuitable for large problems. Eq. (9) is, however, very effective for solving small systems which makes it very suitable for solving subsystems in a distributed modelling context.

Example

As an example the modelling of a simple hydrostatic transmission consisting of a pump and motor with an inertia load is considered.

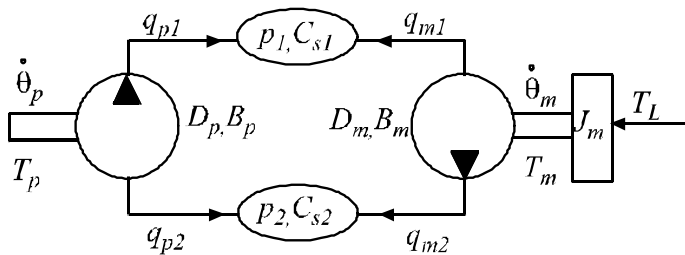


Figure 1. Hydraulic pump-motor example.

The vector F for the system equations becomes

$$F(y, \dot{y}, u, t) = \begin{pmatrix} \dot{\theta}_p B_p + \frac{P_a - P_b}{D_p} - T_p \\ -\dot{\theta}_p D_p + q_{p1} \\ \dot{\theta}_p D_p + q_{p2} \\ \dot{p}_1 - \frac{q_{m1} + q_{p1}}{C_{s1}} \\ \dot{p}_2 - \frac{q_{m2} + q_{p2}}{C_{s2}} \\ -\dot{\theta}_m D_m + q_{m1} \\ \dot{\theta}_m D_m + q_{m2} \\ -\dot{\theta}_m B_m + \frac{P_a - P_b}{D_m} - T_m \\ \ddot{\theta}_m + \frac{B_m}{J_m} \dot{\theta}_m - \frac{P_a - P_b}{J_m D_m} + \frac{T_L}{J_m} \end{pmatrix} \quad (11)$$

The variable vector y is

$$y = \begin{pmatrix} T_p \\ q_{p1} \\ q_{p2} \\ p_1 \\ p_2 \\ q_{m1} \\ q_{m2} \\ T_m \\ \theta_m \end{pmatrix} \quad (12)$$

The variable vector u is

$$u = \begin{pmatrix} \dot{\theta}_p \\ T_L \end{pmatrix} \quad (13)$$

Using bilinear transform to convert the time continuous differential algebraic system into a discrete time system yields $G(y, t) =$

$$\begin{pmatrix} DS[1, -h p_a + h p_b + D_p (h T_p + 2 B_p \theta_p)] - h p_a + h p_b + h D_p T_p - 2 B_p D_p \theta_p \\ DS[1, h q_{p1} + 2 D_p \theta_p] + h q_{p1} - 2 D_p \theta_p \\ DS[1, h q_{p2} - 2 D_p \theta_p] + h q_{p2} + 2 D_p \theta_p \\ DS[1, -2 C_{s1} p_a - h (q_{m1} + q_{p1})] + 2 C_{s1} p_a - h (q_{m1} + q_{p1}) \\ DS[1, -2 C_{s2} p_b + h (q_{m2} + q_{p2})] + 2 C_{s2} p_b + h (q_{m2} + q_{p2}) \\ DS[1, h q_{m1} - 2 D_m \theta_m] + h q_{m1} + 2 D_m \theta_m \\ DS[1, h q_{m2} + 2 D_m \theta_m] + h q_{m2} - 2 D_m \theta_m \\ DS[1, -h p_a + h p_b + D_m (h T_m - 2 B_m \theta_m)] - h p_a + h p_b + h D_m T_m + 2 B_m D_m \theta_m \\ DS[1, 2(-h^2 p_a + h^2 p_b + D_m (h^2 T_L - 4 J_m \theta_m))] + DS[2, -h^2 p_a + h^2 p_b + D_m (h^2 T_L - \\ 2 h B_m \theta_m + 4 J_m \theta_m)] - h^2 p_a + h^2 p_b + h^2 D_m T_L + 2 h B_m D_m \theta_m + 4 D_m J_m \theta_m \end{pmatrix} \quad (14)$$

where DS is the delay step function defined as

$$DS(n, x(t)) = x(t - nh) \quad (15)$$

The Jacobian of this system is:

$$J = \begin{pmatrix} h D_p & 0 & 0 & -h & h & 0 & 0 & 0 & 0 \\ 0 & h & 0 & 0 & 0 & 0 & 0 & 0 & 0 \\ 0 & 0 & h & 0 & 0 & 0 & 0 & 0 & 0 \\ 0 & -h & 0 & 2 C_{s1} & 0 & -h & 0 & 0 & 0 \\ 0 & 0 & h & 0 & 2 C_{s2} & 0 & h & 0 & 0 \\ 0 & 0 & 0 & 0 & 0 & h & 0 & 0 & 2 D_m \\ 0 & 0 & 0 & 0 & 0 & 0 & h & 0 & -2 D_m \\ 0 & 0 & 0 & -h & h & 0 & 0 & h D_m & 2 B_m D_m \\ 0 & 0 & 0 & -h^2 & h^2 & 0 & 0 & 0 & 2 h B_m D_m + 4 D_m J_m \end{pmatrix} \quad (16)$$

Eq. (9) can then be used to solve this system in each time step. Although it is possible to use Eq. (9) directly it is wise to replace the inverse of the Jacobian by using LU-decomposition instead, there are also a few other actions that can be done in order to further enhance the efficiency of the solver. In general, however, the effort to solve the system increases more than linear with the system size.

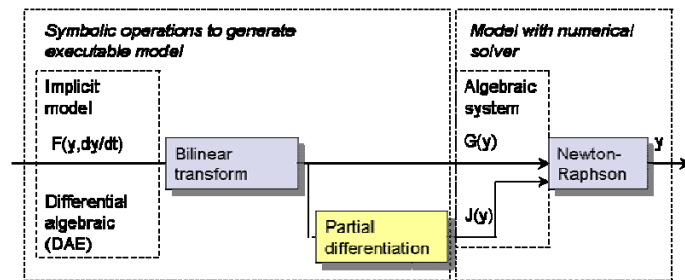


Figure 2. Scheme of transformations

Figure 2. shows a scheme of the transformations involved. The differential algebraic system DAE is transformed into time discrete form using bilinear transform. In Elmqvist et al 1995 the concept of *inline integration* is introduced, where extra equations are introduced to perform the integration. The scheme here is related but would be more appropriately called *inline transformation*, and *inline integration* can be viewed as a special case of that. The Jacobian J is obtained by symbolic partial differentiation of the time discrete system G . G and the Jacobian J are used to solve the system in each time step using the Newton-Raphson method for solving the system in each time step.

Distributed Modelling For Simulation of Fluid Power Components and Systems

Distributed parameters

Simulation of fluid power systems are characterized by difficulties such as very strong nonlinearities, stiff differential equations and a high degree of complexity. Using conventional integration techniques it is often necessary to use very small time steps in order to be able to deal with numerically stiff problems, and strong nonlinearities.

If the state variables in the system are to be unique for each subsystem and not shared by other subsystems, distributed parameters (variables) must be introduced. This can be accomplished if the propagation of waves in connecting components, such pipes, in the system is considered.

A very suitable method for modelling and simulation of large complex dynamic systems is represented by distributed modelling using transmission line elements. The origin of this concept goes back at least to Auslander 1968 [1] who first introduced transmission lines (or bi-lateral delay lines). This method evolves naturally for calculation of pressures when pipelines are modelled with distributed parameters. This approach was adopted for simulation of fluid power systems with long lines in the HYTRAN program already in the seventies.

A related method is the transmission line modelling method (TLM) presented by Johns and O'Brien (Ref. [2]) for simulation of electrical networks.

Johns and O'Brien pointed out that an important aspect of modelling using transmission line elements is that most of the numerical errors introduced by an ordinary solver are avoided. The errors made due to the introduction of transmission line elements, are better described as modelling errors.

An attractive feature with this is that laws of conservation of mass and energy still hold for the solution, since there always exist a plausible physical system for the model, although the line lengths may vary compared to the original system. This also implies that the user may tolerate a larger numerical error since, generally, quite large modelling errors are present anyway (errors of the order of 10% are generally considered acceptable from an engineering point of view).

The Unit Transmission Line Element

In transmission line modelling the basic dynamic element is the unit transmission line. In the HOPSAN package this is used to connect different components to each other. In the general case it can be used to model both capacitances and inductances. In the HOPSAN-package, however, it is used primarily to represent capacitances (oil volumes and mechanical springs).

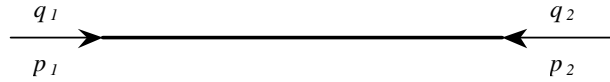


Figure 3. Transmission line

The complete set of equation that describes a lossless transmission line are:

$$\begin{aligned} p_1(t) &= p_2(t-T) + Z_c(q_1(t) + q_2(t-T)) \\ p_2(t) &= p_1(t-T) + Z_c(q_2(t) + q_1(t-T)) \end{aligned} \tag{17}$$

Here Z_c is the characteristic impedance of the line, p and q are pressures and flows respectively. T is the time delay in the line. Note that the main property of these equations is the time delay they introduce in the communication between the ends. Introducing

$$\begin{aligned} c_1(t) &= p_2(t-T) + Z_c q_2(t-T) \\ c_2(t) &= p_1(t-T) + Z_c q_1(t-T) \end{aligned} \tag{18}$$

Here c is the wave variables that represent information that has been transmitted from the other side of the transmission line. With these, the following set of equations is obtained.

$$\begin{aligned} p_1(t) &= c_1(t) + Z_c q_1(t) \\ p_2(t) &= c_2(t) + Z_c q_2(t) \end{aligned} \tag{19}$$

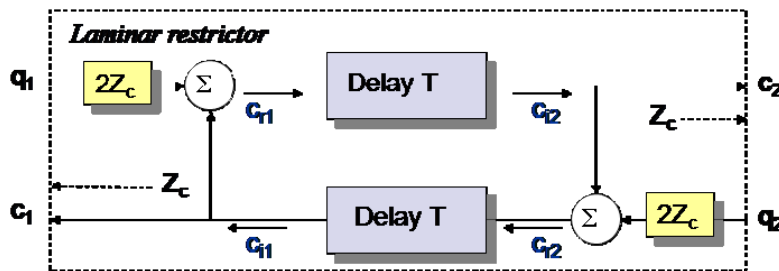


Figure 4. Block diagram of transmission line.

An interesting observation is found if c_2 in Eq. (18) is substituted with Eq. (19) and the outlet at 2 is blocked.

$$p_1(t) = p_1(t-2T) + Z_c(q_1(t-2T) + q_1(t)) \tag{20}$$

Compared to the trapezoidal method for integration

$$y(t+h) = y(t) + \frac{h}{2}(\dot{y}(t) + \dot{y}(t+h)) \tag{21}$$

Where h is the simulation time step. These equations are the same if $T=h/2$!

The relationship between flow entering a volume and the pressure can be written as:

$$\dot{p} = \frac{q}{C} \tag{22}$$

where C is the capacitance. Identification yields

$$Z_c = \frac{h}{C} \tag{23}$$

The implication of this is that the trapezoidal method is used to integrate pressure in a volume (capacitance) between two components; this corresponds to introducing a short pipe instead of a pure capacitance.

The introduction of a transmission line element in place of a capacitance can therefore be viewed as a kind of integration method. In general it can be written such that the integration of an equation as (24) is performed by splitting the variable y into the two variables y_1 and y_2 .

$$\dot{y} = f(x_1 + x_2) \tag{24}$$

These values are the same in steady state, and the difference between them can be regarded (and a measure of) a numerical error. They are calculated using the following equations.

$$\begin{aligned} y_1(t) &= y_2(t-h) = hf(x_1(t) + x_2(t-h)) \\ y_2(t) &= y_1(t-h) = hf(x_2(t) + x_1(t-h)) \end{aligned} \tag{25}$$

y_1 is then of course used at the equations associated with x_1 and y_2 with x_2 .

It should be noted that in order to further improve the numerical properties of the transmission line element damping can be introduced as in ref. [3]. This greatly improves the behaviour with no significant side effects. Since a transmission line also has inductance, an unwanted parasitic inductance will result from using a transmission line to represent a capacitance. The inductance L can be calculated as:

$$L = hZ_c = \frac{h^2}{C} \tag{26}$$

As can be seen it rapidly diminishes with step size. It also means that a transmission line can be used to replace an inductance with a resulting parasitic capacitance as a side effect.

System simulation using transmission line elements

Using this substitution for the pressures p_1 and p_2 in the hydraulic transmission example yields the new system (instead of Eq. (11)) of equations as:

$$F = \begin{pmatrix} \frac{-\dot{\theta}_p B_p D_p - p_a + p_b}{D_p} + T_p \\ q_{p1} - \dot{\theta}_p D_p \\ \dot{\theta}_p D_p + q_{p2} \\ -DS(1, p_{a2}) + p_{a1} - (q_{p1} - DS(1, q_{m1})) Z_c \\ -DS(1, p_{b2}) + p_{b1} - (q_{p2} - DS(1, q_{m2})) Z_c \\ -DS(1, p_{a1}) + p_{a2} - (q_{m1} - DS(1, q_{p1})) Z_c \\ -DS(1, p_{b1}) + p_{b2} - (q_{m2} - DS(1, q_{p2})) Z_c \\ \dot{\theta}_m D_m + q_{m1} \\ q_{m2} - \dot{\theta}_m D_m \\ \frac{\dot{\theta}_m B_m D_m - p_a + p_b}{D_m} + T_m \\ \dot{\theta}_m + \frac{\dot{\theta}_m B_m D_m + T_L D_m - p_a + p_b}{D_m J_m} \end{pmatrix} \tag{27}$$

Here the variable p_1 has been split into the variables p_{1a} and p_{1b} across the transmission line, and the same with p_2 . The variable vector becomes

$$y = \begin{pmatrix} T_p \\ q_{p1} \\ q_{p2} \\ P_{1a} \\ P_{1b} \\ P_{2a} \\ P_{2b} \\ q_{m1} \\ q_{m2} \\ T_m \\ \theta_m \end{pmatrix} \quad (28)$$

After bilinear transformation the system becomes

$$G(y, t) = \begin{pmatrix} DS[1, -h p_a + h p_b + D_p (h T_p + 2 B_p \theta_p)] - h p_a + h p_b + h D_p T_p - 2 B_p D_p \theta_p \\ DS[1, h q_{p1} + 2 D_p \theta_p] + h q_{p1} - 2 D_p \theta_p \\ DS[1, h q_{p2} - 2 D_p \theta_p] + h q_{p2} + 2 D_p \theta_p \\ -DS[1, p_{a2}] + P_{a1} + (DS[1, q_{m1}] - q_{p1}) Z_c \\ -DS[1, p_{b2}] + P_{b1} + (DS[1, q_{m2}] - q_{p2}) Z_c \\ -DS[1, p_{a1}] + P_{a2} + (DS[1, q_{p1}] - q_{m1}) Z_c \\ -DS[1, p_{b1}] + P_{b2} + (DS[1, q_{p2}] - q_{m2}) Z_c \\ DS[1, h q_{m1} - 2 D_m \theta_m] + h q_{m1} + 2 D_m \theta_m \\ DS[1, h q_{m2} + 2 D_m \theta_m] + h q_{m2} - 2 D_m \theta_m \\ DS[1, -h p_a + h p_b + D_m (h T_m - 2 B_m \theta_m)] - h p_a + h p_b + h D_m T_m + 2 B_m D_m \theta_m \\ DS[1, 2(-h^2 p_a + h^2 p_b + D_m (h^2 T_L - 4 J_m \theta_m))] + DS[2, -h^2 p_a + h^2 p_b + \\ D_m (h^2 T_L - 2 h B_m \theta_m + 4 J_m \theta_m)] - h^2 p_a + h^2 p_b + h^2 D_m T_L + \\ 2 h B_m D_m \theta_m + 4 D_m J_m \theta_m \end{pmatrix} \quad (29)$$

The corresponding Jacobian then becomes:

$$J = \begin{pmatrix} h D_p & 0 & 0 & 0 & 0 & 0 & 0 & 0 & 0 & 0 & 0 \\ 0 & h & 0 & 0 & 0 & 0 & 0 & 0 & 0 & 0 & 0 \\ 0 & 0 & h & 0 & 0 & 0 & 0 & 0 & 0 & 0 & 0 \\ 0 & -Z_c & 0 & 1 & 0 & 0 & 0 & 0 & 0 & 0 & 0 \\ 0 & 0 & -Z_c & 0 & 1 & 0 & 0 & 0 & 0 & 0 & 0 \\ 0 & 0 & 0 & 0 & 0 & 1 & 0 & -Z_c & 0 & 0 & 0 \\ 0 & 0 & 0 & 0 & 0 & 0 & 1 & 0 & -Z_c & 0 & 0 \\ 0 & 0 & 0 & 0 & 0 & 0 & 0 & h & 0 & 0 & 2 D_m \\ 0 & 0 & 0 & 0 & 0 & 0 & 0 & h & 0 & 0 & -2 D_m \\ 0 & 0 & 0 & 0 & 0 & 0 & 0 & 0 & h D_m & 0 & 2 B_m D_m \\ 0 & 0 & 0 & 0 & 0 & 0 & 0 & 0 & 0 & 2 h B_m D_m + 4 J_m D_m & 0 \end{pmatrix} \quad (30)$$

Note that this system can be partitioned into two uncoupled systems that consequently can be solved independently from each other in each time step. This means that the system can be solved using two instances of Newton-Raphson, equation (9), that are numerically insulated from each other. The price for this is that the Jacobian has become slightly larger with the introduction of two variables for p_a and p_b respectively.

Modelling of Components

In order to demonstrate the principle of component modelling the very simple laminar orifice with the resistance R_v is shown.

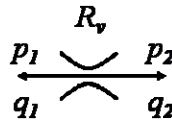


Figure 5. Laminar restrictor

The pressure-flow relationship is:

$$q_2 = \frac{p_1 - p_2}{R_v} \tag{31}$$

The following equations are solved at the component (connected to lines)

$$\begin{aligned} q_2 &= \frac{p_1 - p_2}{R_v} \\ q_1 &= -q_2 \\ p_1 &= c_1 + q_1 Z_{c1} \\ p_2 &= c_2 + q_2 Z_{c2} \end{aligned} \tag{32}$$

Here R_v is the resistance of the orifice, Z_{c1} and Z_{c2} are the characteristic impedances of the lines connected to the orifice. Being a non-dynamic linear system, these equations can be solved algebraically for q_1 and q_2 .

The equations used in the executable component model will thus be :

$$\begin{aligned} q_2 &= \frac{c_1 + c_2}{R_v + Z_{c1} + Z_{c2}} \\ q_1 &= -q_2 \\ p_1 &= c_1 + q_1 Z_{c1} \\ p_2 &= c_2 + q_2 Z_{c2} \end{aligned} \tag{33}$$

A comparison with Eq.(32) and Eq.(36) shows that the adoption to transmission lines has the same effect on the equations as adding restrictors with the resistance Z_c . As a consequence, it is rather uncomplicated to modify any component or simulator to adapt to transmission lines. The same principle is valid also for mechanical nodes. However, since a resistor is a non-dynamic component, one algebraic state is usually introduced for each connector.

The figure below shows the block diagram of the restrictor

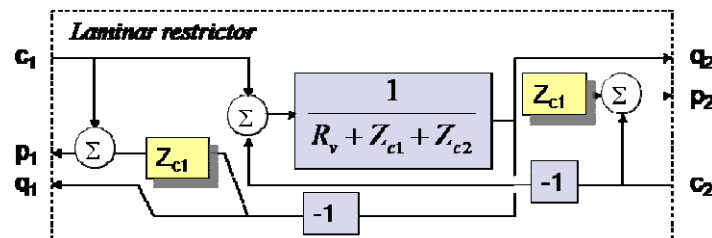


Figure 6. Block diagram of restrictor.

The laminar resistor is a simple linear model that can be derived analytically. The more general approach is using Newton-Raphson Eq.(9).

Modelling of Systems

These components can be connected for system simulation. Here also a pressure source at the right end has been added. Modelling of mechanical springs is performed in exactly the same way as the volume, since they also represent pure capacitances. The only difference is that it handles speed, instead of flow, and force, instead of pressure. The modelling of two dimensional mechanical systems is presented in detail in Krus 1995 [8].

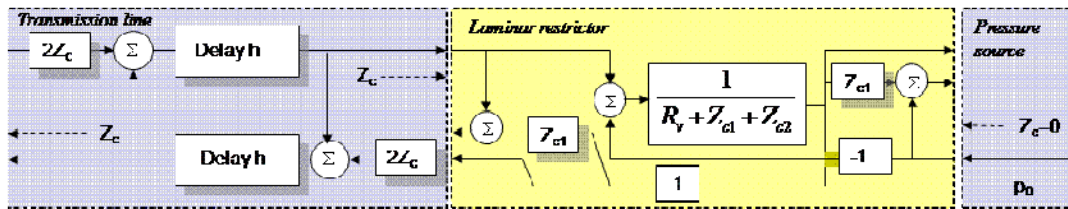


Figure 7. Assembled block diagram, showing transmission line – laminar restrictor – pressure boundary condition.

Test Example

As a test a simple spring mass system is simulated.



Figure 8. Mass spring test system.

The spring is modelled as a bi-directional delay line and is connected to a fixed point to the left and to a pure inertia load to the right. The mass is integrated using bilinear transform (equivalent to the trapezoidal rule). As can be seen the time step can be increased to 0.1 seconds and the system still shows benign behaviour, only the frequency is shifted slightly. If the time step is increased to one second the response is distorted, and much slower than the exact solution due to the influence of parasitic inductance from equation (26), but the system is still stable. If this had been a very fast component in a system, and had not been of prime interest, this behaviour could still be tolerated.

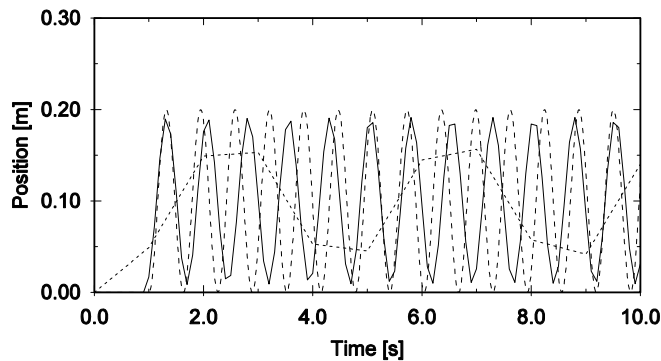


Figure 9. Simulated result of spring mass system with spring represented by transmission line. Dashed line is $h=0.01$ sec, filled is $h=0.1$ sec and dotted line is $h=1$ sec.

As a reference the spring is modelled to simply yield a force to corresponding to the compression of the spring. For slow variations, or very small time step, this should give the same result. However, since the spring is modelled as a separate component there is a time delay of one time step from the force calculated in the spring is affecting the mass, and an updated position of the mass is sent back to the spring. As a result, even with the smallest time step of one millisecond, the system show considerable divergence, and is completely unstable for a time step of 10 milliseconds. To be able to use larger time steps, it would be necessary to use one solver for the whole model.

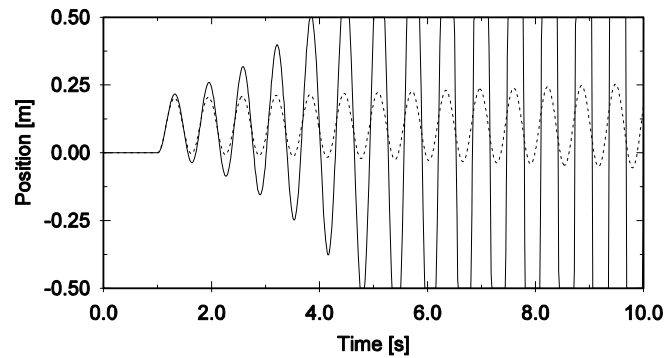


Figure 10. Simulation result of mass spring system with spring force calculated as a function of compression. Time step $h = 0.001$ seconds is dotted. $h = 0.01$ seconds is filled.

Event Free Modelling

In real time simulation it is not practical to handle events by finding zero-crossings and restart solvers when e.g. limitations in variables are hit. Therefore other mechanisms need to be used. Using the approach with differential algebraic equations that are solved through bilinear transformation and Newton-Raphson using an analytical Jacobian, it might seem that the Jacobian would be extremely difficult to derive, since most manually written models involve a great deal of conditions and jumps as they are written in a procedural style. The introduction of an automated approach means that a functional programming style is imposed (the derivative of a function can always be defined, except in singular points). Therefore all conditions have to be represented by functions. The algorithm

```
if(cond)then
```

```
  a = a1
```

```
  b = b1
```

```
  c = c1
```

```
else
```

```
  a = a2
```

```
  b = b2
```

```
  c = c2
```

```
end if
```

can be transformed into

```
a=If(cond,a1,a2)
```

```
b=If(cond,b1,b2)
```

```
c=If(cond,c1,c2)
```

Since the If function is a piecewise continuous function the differential is defined and can be used in the Jacobian. An advantage with this style of programming is that the variables a, b, and c in the example are forced to be defined for both cases, and cannot be forgotten as in normal procedural programming. This approach does not remove the events as such but there is no notion of events in the code since everything is hidden in the functions.

Application

The technique described here can be used to connect large systems for high-speed simulation. One example is given by the aircraft system model shown in the figure below. This particular model has been used to demonstrate optimization of flight control system including actuator system [12].

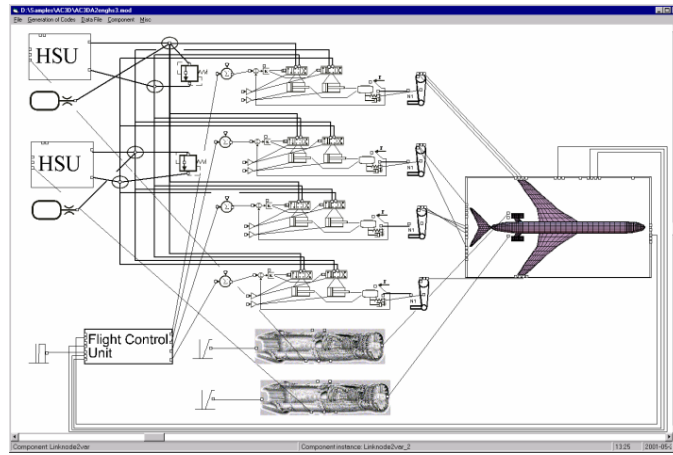


Figure 11. Aircraft simulation model

Another application is to use transmission line elements for connecting different solvers to each other in co-simulation. An example of simulation of a complete wheel loader can be found in [3] and [9].

The HOPSAN simulation package has been developed at the division since the late 1970s, and has played an important role in research projects over time. It has also been used widely in the industry. In recent years commercial software has become increasingly available, and those have also been used at the division. In 2009 the development of a new simulation platform, HOPSAN NG, was initiated. This is an object-oriented C++ application with focus on multi-core support and compatibility.

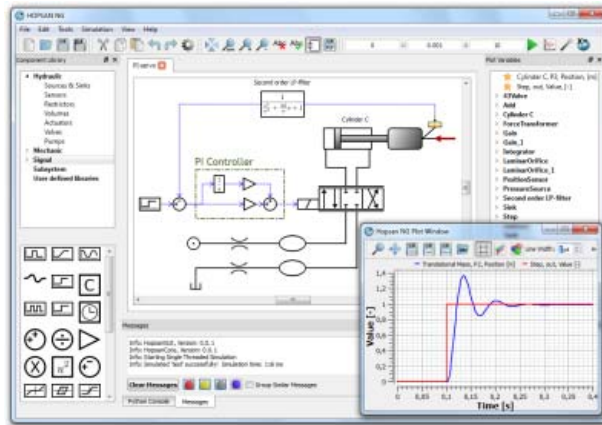


Figure 12. The HOPSAN-NG simulation package

In this paper the method of using transmission lines for partitioning complex system models has been described. Using such elements it is possible to use highly robust distributed solvers on small subsystems, which are then connected to each other using the transmission lines, for system simulation. As a result highly robust models are achieved that can be used also for real time simulation. Using transmission lines to numerically partition a system is a non-exclusive approach that can be used together with conventional solvers. In this way it is possible to obtain a very robust system modelling concept that that has been described here, which is also very useful also for real time simulation. It is also a very useful technique for connecting different simulation software in co-simulation. The transmission line modelling is implemented successfully in the HOPSAN-NG simulation software.

CONCLUSIONS

In this paper the method of using transmission lines for partitioning complex system models has been described. Using such elements it is possible to use highly robust distributed solvers on small subsystems, which are then connected to each other using the transmission lines, for system simulation. As a result highly robust models are achieved that can be used also for real time simulation. Using transmission lines to numerically partition a system is a non-exclusive approach that can be used together with conventional solvers. In this way it is possible to obtain a very robust system modelling concept that that has been described here, which is also very useful also for real time simulation. It is also a very useful technique for connecting different simulation software in co-simulation. The transmission line modelling is implemented successfully in the HOPSAN-NG simulation software.

REFERENCES

- [1] Auslander D. M., 'Distributed System Simulation with Bilateral Delay-Line Models' *Journal of Basic Engineering*, Trans. ASME p195-p200, June 1968.
- [2] Johns P. B. and M.O'Brien. 'Use of the transmission line modelling (t.l.m) method to solve nonlinear lumped networks.' *The Radio Electron and Engineer*. 1980.
- [3] Krus P., A. Jansson, J-O. Palmberg, K. Weddfeldt. "Distributed Simulation of Hydromechanical Systems". Third Bath International Fluid Power Workshop, Bath, UK 1990.
- [4] Burton, J. D., Edge, K. A., Burrows, C. R., 1993. Partitioned simulation of hydraulic systems using transmission-line modelling. In: ASME WAM, New Orleans, LA, USA. Publ by ASME, New York, NY, USA. (Using Transputer technology)
- [5] Anagnostopoulou D. and M. Nikolaidou. Timing issues and experiment scheduling in faster-than-real-time simulation. *SIMULATION*, 79(11):613–625, November 2003.
- [6] Fritzson P. "Principles of Object Oriented modelling and Simulation with Modelica 2.1", Wiley-IEEE Press. 2003.
- [7] Elmqvist H., M. Otter, F. E. Cellier. "Inline Integration: a New Mixed Symbolic/Numerical Approach for Solving Differential Algebraic Equation Systems". European Simulation Multiconference, Prague, Czech Republic, 1995.
- [8] Krus P., "An Automated Approach for Creating Components and Subsystems for Simulation of Distributed Systems", Ninth Bath International Fluid Power Workshop, Bath, UK 1996.
- [9] Krus P, K Weddfelt, J-O Palmberg,"Fast Pipeline Models for Simulation of Hydraulic Systems". *Journal of Dynamic Systems, Measurement and Control*, Trans. ASME, March 1994.
- [10] Larsson J., Interoperability in Modelling and Simulation. Linköping Studies in Science and Technology Dissertation 2003.
- [11] Lantto B., H. Ellström, Hampus Gavel, M. Jarelande, Sören Steinkellner, A. Järlestål and M. Landberg, "Modeling and Simulation of Gripen's Fluid Power Systems", Proceedings of "Recent advances in aerospace actuation systems and components", Toulouse, France, 2004.
- [12] Krus P. "Simulation Based Optimisation for Aircraft Systems", SAE 2003 Transactions Journal of Aerospace.

RESPONSIBILITY NOTICE

The author is the only responsible for the printed material included in this paper.

On a simple model for the dynamics of the vertical collapse of buildings

Celso P. Pesce and Leonardo Casetta

Escola Politécnica – University of São Paulo

Department of Mechanical Engineering

Offshore Mechanics Laboratory – LMO

* Corresponding author: ceppesce@usp.br

EXTENDED ABSTRACT

This extended abstract brings a summary of a recently submitted full paper, Pesce et al (2011). Its purpose is here restricted to highlight the discussion about a still open subject on a simple *single degree of freedom model* (SDOF), firstly proposed by Bažant and Verdure (2007) and addressed by Seffen (2008). Such model is able to describe the evolution of the avalanche front of vertically collapsing towers. However, if deduced from the usual Lagrange equation formalism, the equation of motion differs from that derived from Newton's law, written in the form of Mechersky, for a variable mass particle.

Such kind of 'apparent paradox' is commonly found in problems involving varying mass, particularly if the material system under study has the mass given as an explicit function of position or generalized coordinates. A classic example on this is the 'falling chain' problem of von Buquoy, Hopkins, Tait, Steele and Cayley. The two controversial forms of the equation of motion modeling the falling chain problem have been discussed for more than a century; see, e.g., Šima and Podolsky (2005), Wong and Yasoui (2006) and Wong, Youn and Yasui (2007). As a matter of fact, Cayley's ingenious and correct interpretation of time derivative, Cayley (1857), has been often misinterpreted as a form only fitted to that particular chain problem; see a thorough discussion in Casetta (2008). As a recent example, after theoretically contradicting Cayley's derivation, with the same kind of theoretical misinterpretation (see Wong and Yasoui (2006)), Wong and his collaborators (see Wong, Youn and Yasui (2007)), in a commendable scientific attitude, ended to experimentally confirm the classic Cayley's results.

On the other hand, Cveticanin (1993), from conservation laws and, independently, Pesce (2003), from variational principles, showed that this kind of non conservative systems are described by an extended form of the Lagrange equation. Such an extended equation carries an extra term. This term, of the form $\frac{1}{2}m'(x)\dot{x}^2$, i.e., linearly dependent on the derivative of mass with respect to position and dependent on the velocity squared, appears whenever the mass is explicitly dependent on position. The general form¹ for a system of varying mass particles, of mass m_i and position P_i is; see Pesce (2003),

$$\frac{d}{dt} \left(\frac{\partial T}{\partial \dot{q}_j} \right) - \frac{\partial T}{\partial q_j} = \hat{Q}_j \tag{1}$$

$$\hat{Q}_j = Q_j + \sum_i \left(\dot{m}_i \mathbf{v}_{0i} \cdot \frac{\partial P_i}{\partial q_j} \right) - \frac{1}{2} \sum_i \frac{\partial m_i}{\partial q_j} \mathbf{v}_i^2$$

T is the kinetic energy of the system, q_j and Q_j are generalized coordinates and generalized applied forces and \mathbf{v}_{0i} is the velocity of the mass just before being accreted to (or expelled from) the particle i .

Considering the vertical collapse of the WTC twin towers, Bažant and Verdure (2007), as well as Seffen (2008), introduced three major simplifications and a minor one. The first (easily justifiable) major simplification is to consider the 'intact' upper part of the falling structure as a translating rigid body, smashing the 'lower' part as it falls. The second major hypothesis assumes the existence of a density jump through the avalanche front; i.e., the density of the accreted mass jumps from a 'non compacted' value ($\sigma_{nc} = \sigma_0$) to a 'compacted' value (σ_c) in a continuous impact manner, such that a single compaction parameter $K = \sigma_{nc}/\sigma_c$ can model the mass accretion. This implies a velocity jump as well. The third one considers the whole falling region, composed by the 'intact' falling part accreted by the instantaneously

¹ Actually, in the uncommon cases where mass is explicitly dependent on velocity (not in the relativistic sense), a second extra term appears; see Pesce (2003).

compacted part, as a material system with mass varying explicitly with position. The velocity jumps implies that the whole falling region translates as a rigid body of varying mass, or as an equivalent material point with continuously varying mass, explicitly dependent on position. The minor assumption is to model a sequence of resistive force pulses, which would be imposed to the falling part by the lower intact part, at each collapsing floor, by an equivalent and continuous average value.

As it would be the case in the falling chain problem, by applying both forms of the Lagrange equation, the usual and the extended one, Bažant and Verdure (2007), as well as Seffen (2008), found two distinct equations of motions, differing from each other by a term of the form $\frac{1}{2} y_B^{-1} \dot{y}_B^2$. However, neither Bažant and Verdure (2007) or Seffen (2008) were conclusive on the matter, not stating, clearly, which of the two distinct equations is the proper one.

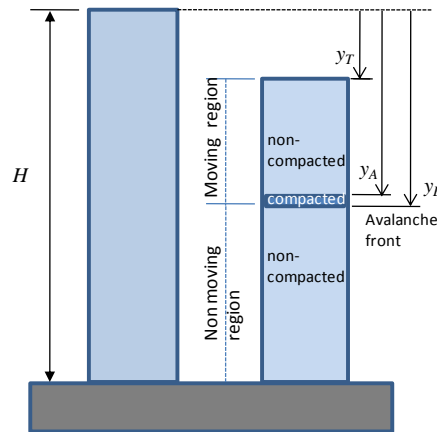


Figure 1 - Schematics of the vertical collapse of buildings; *extracted from* Pesce et al (2011).

In fact, after Casetta (2008), Pesce et al (2011) showed, in a detailed analysis, that *the proper equation of motion*, governing the downward avalanche front propagation may be derived, equivalently from Newtons' law or from the extended Lagrange equation, and written in the nondimensional form,

$$\ddot{y}^* = \frac{1}{(1-K)} \left(1 - \frac{\Phi}{y^*}\right) - \frac{\dot{y}^{*2}}{y^*}, \quad (2)$$

where, $t^* = t\sqrt{g/H}$, $y^* = y_B/H$ and $\Phi = F/(\sigma_{nc}gH) = F/P$ are, respectively, dimensionless variables giving time, position of the avalanche front and resistive force to collapse. This resistive force naturally appears normalized by the whole building weight, $P = Mg = \sigma_{nc}Hg$, where H is the building height. Notice that, if $\Phi \equiv 0$ and $K \equiv 0$, Eq. (2) recovers exactly Cayley's equation of motion, found in the classical falling chain problem.

Instead, if the usual form of Lagrange's equation were applied to the problem, hence missing the $\frac{1}{2}m'(x)\dot{x}^2$ term, the following erroneous equation of motion would be obtained,

$$\ddot{y}^* = \frac{1}{(1-K)} \left(1 - \frac{\Phi}{y^*}\right) - \frac{1}{2} \frac{\dot{y}^{*2}}{y^*}. \quad (3)$$

Both results, the proper form, Eq. (2), and the non proper one, Eq. (3), are shown in Pesce et al (2011) to recover those obtained by Seffen (2008) or by Bažant and Verdure (2007). Moreover, Pesce et al (2011) show that the extra term appearing in the extended form of the Lagrange equation may be related to a Rayleigh-like function of the form $R(x, \dot{x}) = \frac{1}{6} \dot{m} \dot{x}^2 = \frac{1}{6} m'(x) \dot{x}^3$.

Figure 2, extracted from Pesce et al (2011), illustrates some simulation results for the WTC tower 1. A detailed discussion and additional results will be shown during the symposium.

ACKNOWLEDGMENTS

The authors acknowledge CNPq, the Brazilian National Research Council, Research Grant n° 303838/2008-6 and FAPESP, the State of São Paulo Research Foundation, for the PhD scholarship of Leonardo Casetta, n° 04/04611-5.

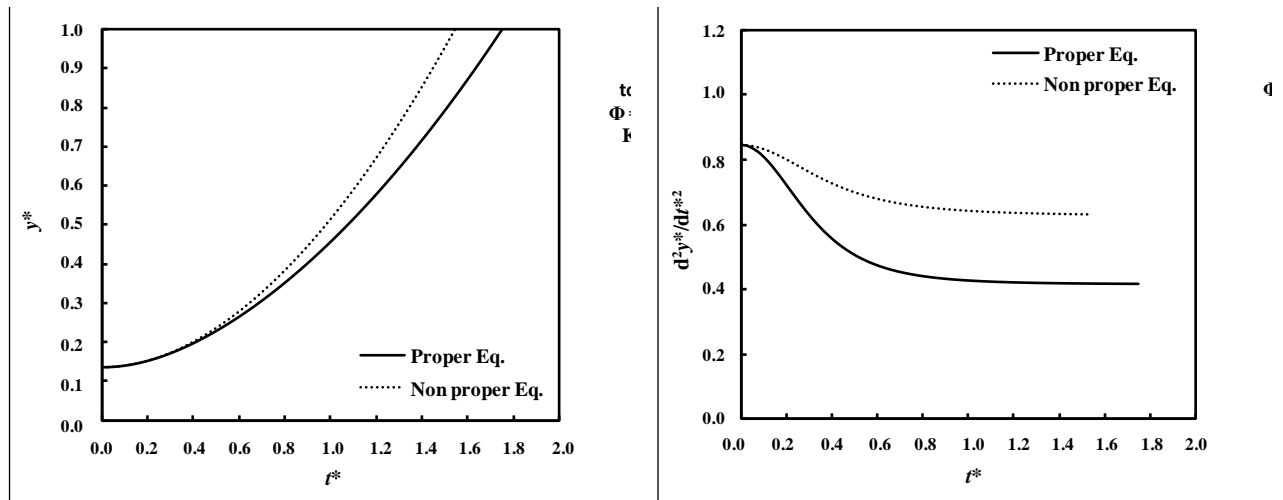


Figure 2 – *Extracted from Pesce et al (2011): simulation of the avalanche front during crush-down. Normalized position and acceleration. Typical values of compaction rate and average resistive force: $K = 0.2, \Phi = 0.044$. WTC: Tower 1: $y^*(0) = h^* = 0.1364$; $\dot{y}^*(0) = 0$.*

REFERENCES

- Bažant, Z. P., Verdure, M., 2007, “Mechanics of progressive collapse: learning from World Trade Center and building demolitions”. *Journal of Engineering Mechanics*, v. 133, n. 3, pp. 308-19.
- Casetta, L., 2008, “Contributions to the mechanics of variable mass systems”, PhD Thesis (in Portuguese), Escola Politécnica, University of São Paulo, 185 p, 2008.
- Cayley, A., 1857, “On a class of dynamical problems”. *Proceedings of the Royal Society of London*, v. 8, pp. 506-11.
- Cvetičanin, L., 1993, “Conservation laws in systems with variable mass”. *Journal of Applied Mechanics*, v. 60, pp. 954-8.
- Pesce, C.P., 2003, “The application of Lagrange equations to mechanical systems with mass explicitly dependent on position”. *Journal of Applied Mechanics*, v. 70, p. 751-6.
- Pesce, C.P., Casetta, L., Santos, F.M., 2011, “On the equation of motion governing the dynamics of vertically collapsing buildings”, submitted.
- Seffen, K. A., 2008, “Progressive collapse of the World Trade Center: simple analysis”. *Journal of Engineering Mechanics*, v. 134, n. 2, p. 125-32.
- Šima, V.; Podolský, J., 2005, “Buquoy’s problem”. *European Journal of Physics*, v. 26, p. 1037-1045.
- Wong, C. W., Yasui, K., 2006, “Falling chains”. *American Journal of Physics*, v. 6, p. 490-496.
- Wong, C. W., Youn, S. H., Yasui, K., 2007, “The falling chain of Hopkins, Tait, Steele and Cayley”. *European Journal of Physics*, v. 28, p. 385-400.

RESPONSIBILITY NOTICE

The authors are the only responsible for the printed material included in this paper.

Comparing Needs of Employers to Learning Outcomes of Engineering Curricula in Europe: Preliminary Results of ECCE Project

Nicolò Bachschmid¹, Federico Cheli¹, Alessio Castelli², Clementina Marinoni²

¹ Dipartimento di Meccanica, Politecnico di Milano, via LaMasa 1, 20158 Milano

² Fondazione Politecnico di Milano, p.za L. da Vinci 32, 201?? Milano

Abstract: An European funded project (ECCE) is trying to understand the changing needs of the industrial employers in the field of engineering in Europe (mainly France, England, Germany, Spain, Italy and Hungary), and to relate the learning outcomes to the required competences. The results of a series of surveys among alumni, interviews with stakeholders, surveys directed to employers and to universities give insight into this rapidly changing scenario. The quality of engineering curricula is evaluated with reference to an European quality framework EQF, and to EUR-ACE formats developed by an international Committee which are used by different accreditation bodies.

Keywords: learning outcomes, engineering curricula, engineering competences and skills

INTRODUCTION

The engineering work place has undergone significant changes in the last decades. A growing number of engineers operate in environments that require intensive cross disciplinary activity, where economic, social and ethic concepts have also to be taken into consideration. Many engineers work in service-oriented businesses rather than in the more traditional product-oriented businesses. Language skills as well as presentation skills are required. And they depend obviously also on networking and computing tools that have appeared on the scene less than twenty years ago. Therefore a re-examination of the preparation that mechanical engineers receive in order accomplish these new requirements seems necessary. At European level also the accomplishment to the so-called Dublin descriptors is required. Many countries have adopted an accreditation system that reflects the needs of the European Higher Education Area, where already accreditation systems and formats in Engineering studies have been developed (as the EUR-ACE system).

In the frame of this process, the Fondazione Politecnico di Milano (Foundation of Politecnico of Milan, FPM) has proposed and is leading a Project, funded by the European Commission, on establishing an “Engineering Observatory on Competences Based Curricula for Job Enhancement” (acronym ECCE), in which the Mechanical Engineering Course (MEC) of the Politecnico is one of the academic partners. Other partners are academics (university of Stuttgart Germany, university of Birmingham UK and university of Budapest Hungary) and professional organizations (like SEFI Société Européenne pour la Formation des Ingenieurs (France), CEFI Comité d’études sur les formations d’ingénieurs (Europe), Associació Catalana d’Enginyers de Telecomunicació in Spain, DEKRA Akademie, biggest training enterprise in Germany).

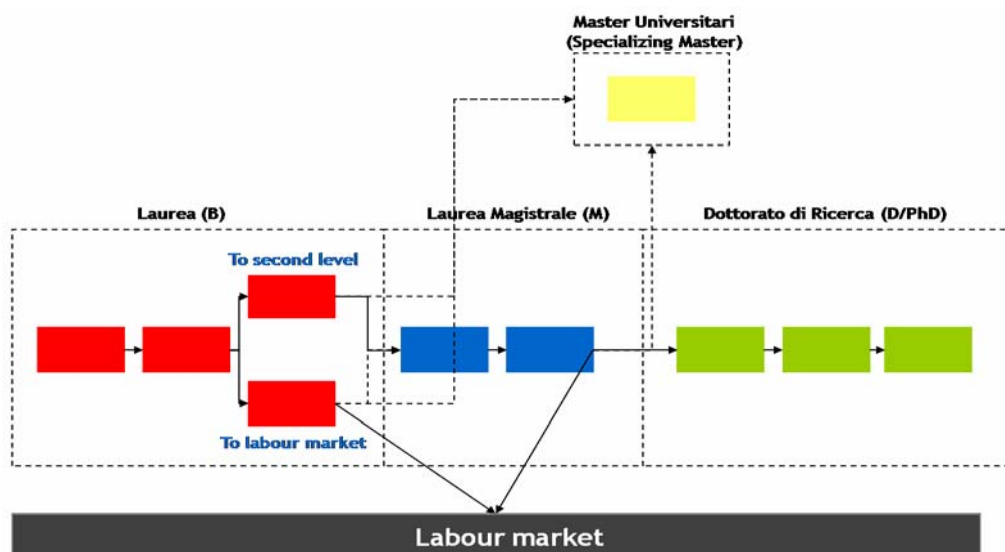


Figure 1 –Actual organization of engineering studies in Italy

The aim of the project is first to define with the aid of professional engineering organisations the expected learning outcomes (LOs) for engineering curricula (mechanical, civil and information technologies) which are suitable for actual engineering professional life. According to the Bologna process the studies in Italy and in many European countries are divided in two levels (bachelor and master), as shown in Fig. 1. The third level (PhD) is not yet considered in the project.

The project will be developed using the level descriptors defined by the European Qualification Framework. The Learning Outcomes (LOs) will be defined using categories of EUR-ACE Framework Standards (see website [1] for more information) for the accreditation of Engineering Programs, and additional specific details for different professional engineering courses (mechanical, civil, telecommunication and information technologies). Further the so defined LOs have to be mapped in the detailed description of the curricula in order to see where and to which extent the development of detailed competences or skills is missing or is instead present in the actual curricula. The necessary changes in the curricula should then be implemented and the results and effects will be monitored by the observatory which should develop a permanent structure. The main objectives, preliminary and expected final results of the project are given in the following (more details can be found in the website [2])

MAIN PROJECT OBJECTIVES

The Higher Education (HE) and the productive world are just facing new and complex challenges. The goals of the Bologna Process and the Lisbon Declaration appear even more important after the 2008' financial crisis, and together with the Communication on "New skills for new jobs" are key points for the EUHEA -European Higher Education Area- and for industry as well. In this scenario, the need of the continuous collaboration between HE institution and enterprises in order to enhance the HE curricula, their transparency and the competences developed is becoming more and more urgent.

Accordingly, the ECCE main objectives are:

- to improve the cooperation among HE institutions and enterprises during the process of definition of the competences to be developed by engineering HE institutions;
- to establish a permanent Observatory, able to regularly provide players and stakeholders with directions and recommendations on skills offer and demand in the engineering context and the ways of aligning and enriching them;
- to develop an easily understandable European model (for Universities and business stakeholders) for the "translation" of engineering higher education courses and curricula into learning outcomes and linking them to the EQF levels (from 6h to 8h).

Thus, the main activities and outputs will be:

- The consultation of business stakeholders and engineers in order to identify the labour market competence needs and the proposal of new competences to be included in curricula;
- The "translation" of several engineering and technical HE curricula into learning outcomes and EQF levels compliant;
- The development of the translation model/language;
- The dissemination of project results through the networks the project partners are involved in;
- The exploitation of results with the involvement of new stakeholders.

It is expected the project will be the reference point for all those actors involved in the process of creation of the European Higher Education Area (EHEA) in Engineering.

A sketch of the proposed process is shown in Fig. 2

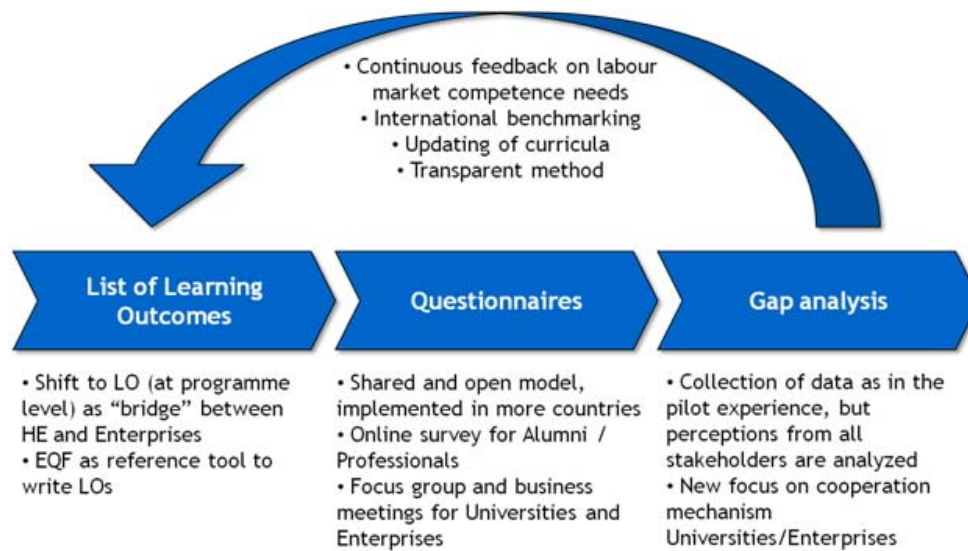


Figure 2 –Sketch of the process designed by ECCE project

DEFINING DESCRIPTORS AND LEVELS FOR LOS

The first activity was to analyze the descriptors defining levels of achievements and abilities acquired at the end of higher education cycles (Bachelor and Master) proposed by the European Qualification Framework (EQF), see [3]. The descriptors provide 3 different types of achievements: *knowledge*, *skills*, and *competence*, where *skills* indicate both cognitive (logical, intuitive and creative thinking) and practical skills, in other words the ability of applying knowledge, and *competence* indicates responsibility and autonomy. As an example the descriptors of level 6 (corresponding to the Bachelor degree) are:

Knowledge advanced knowledge of a field of work or study, involving a critical understanding of theories and principles

Skills advanced skills, demonstrating mastery and innovation, required to solve complex and unpredictable problems in a specialized field of work or study

Competence manage complex technical or professional activities or projects, taking responsibility for decision making in unpredictable work or study contexts. Take responsibility for managing professional development of individuals and groups.

The feeling of the partners of the project was that level 6 (which should be reached in 3 years of university studies) descriptors were too ambitious, at least with regards to the skills and moreover with regards to the competence. Students with bachelor degree have no possibility to train in solving *complex and unpredictable* problems, nor to train any form of *management*.

Also for level 7, corresponding to the master degree, skills and competences seemed overestimated.

Regarding knowledge the university partners were confident that students would reach the required level, sometimes even exceeding it.

Since the levels were defined for any one of the higher education study course, it was necessary to define in a more detailed way the descriptors for the engineering education: this has been done exploiting partly the descriptors provided by the EUR-ACE framework standards for the accreditation of engineering programmes.

EUR-ACE framework define descriptors for following categories: *knowledge and understanding*, *engineering analysis*, *engineering design*, *investigations*, *engineering practice* and *transferable skills*.

For the surveys addressed to alumni, as will be seen in the graphs where the results are reported, the categories have been grouped differently: 1) knowledge and understanding 2) engineering analysis 3) engineering design, investigation and engineering practice 4) management and sustainability 5) soft skills, and for each category different descriptors have been chosen, as the most significant.

More specific descriptors have been defined for different engineering courses: as an example for **mechanical engineering** following descriptors have been chosen:

Knowledge Know and understand the fundamentals of mathematics and physics, and of engineering sciences such as thermodynamics of solids, liquids and gases, statics, kinematics, dynamics and control of mechanical systems, mechanical properties of materials, manufacturing technologies, strength of components, measurements and plant design (lay-out ?).

Engineering analysis Ability to use simple models for mechanical systems (machines or components) for analyzing its behavior, its performance, and the arising stresses and check the strength of components.

Engineering design Ability to develop projects and design mechanical systems able to accomplish given requirements of motion, of performance, of strength and lifetime.

Investigations Ability to investigate by means of bibliographic research, experimental tests and suitable modeling in order to identify the most appropriate solutions in the design of mechanical components, or for improving its performance.

Engineering practice Ability to integrate knowledge of different engineering fields and to use methods and techniques of analysis or synthesis (design) of (complex) mechanical systems.

MAIN RESULTS OF THE SURVEYS ADDRESSED TO ALUMNI

In the first part of the surveys alumni were asked to state their personal data, their employment status and their attained education. In the second part the alumni were asked to define for each one of the above 5 categories, and within each category for each descriptor, the level of mastery required in the actual job, the level acquired at the end of the studies and the level alumni would have desired at the end of studies, scaled between 0 and 4. The graph of the results allows to identify gaps or surplus, and allow to draw interesting remarks. In this presentation we will focus on those categories where gaps between required and acquired levels of mastery appear: these were *Management and Sustainability* and *Soft Skills*, in almost all countries where on-line surveys have been launched. For the other categories generally a good agreement between required and acquired levels has been found, for some descriptors even a surplus of acquired level has resulted.

Significant differences in the results of different countries were not found: this indicates a kind of balanced situation in the European higher education institutes. Some results will be shown in the following figures.

Regarding *Soft skills* figure 3 shows the results obtained in France by SEFI from 211 answers out of the total amount of alumni (1600) that were contacted via e-mail.

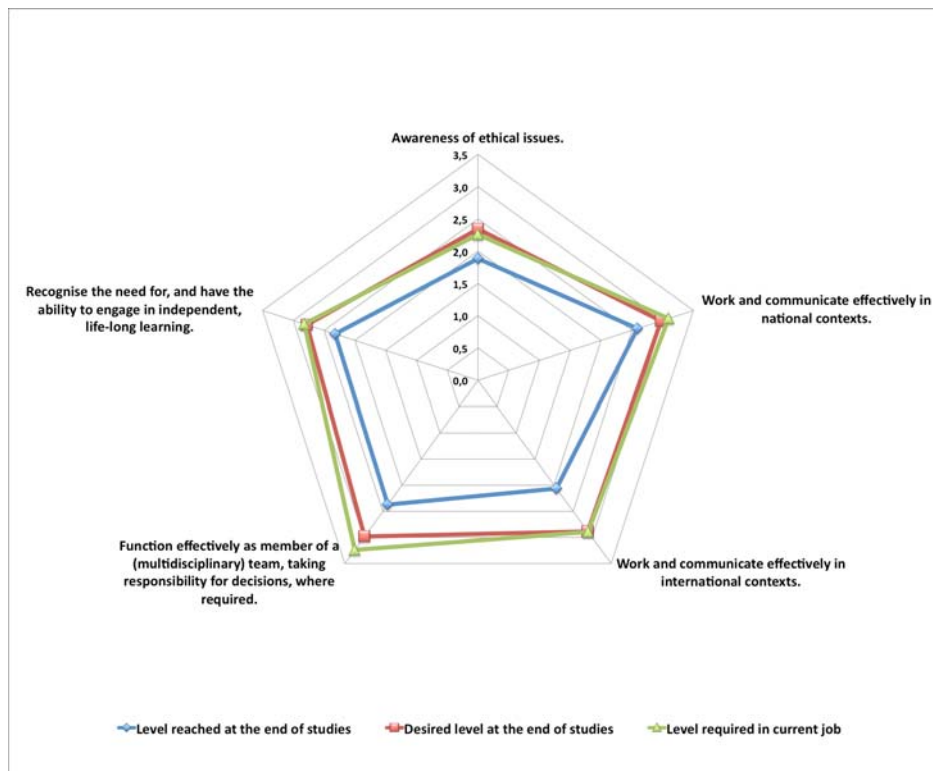


Figure 3 –Levels of mastery in some soft skills as felt by alumni in France

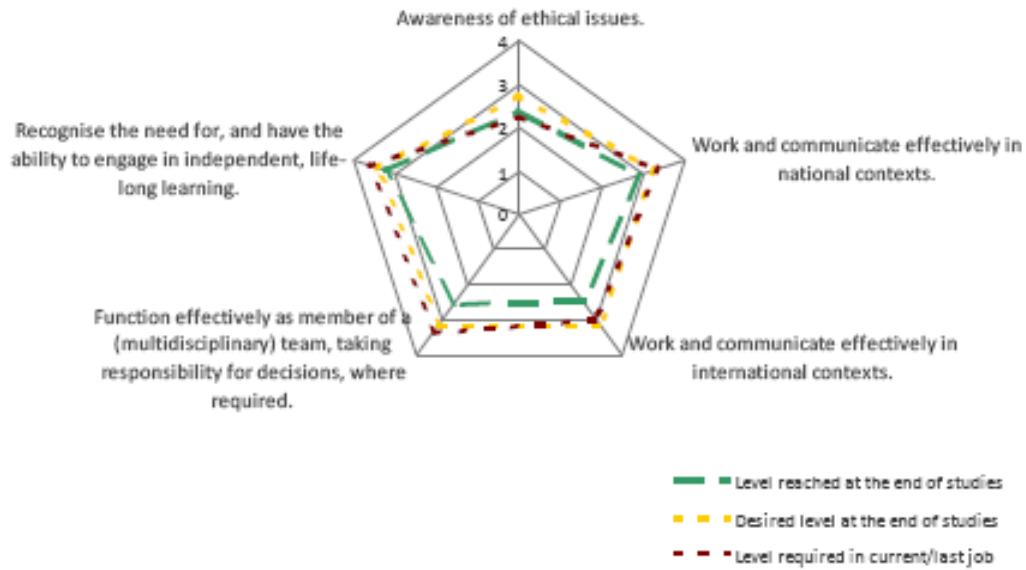


Figure 4 – Levels of mastery in some soft skills as felt by alumni in Stuttgart (Germany)

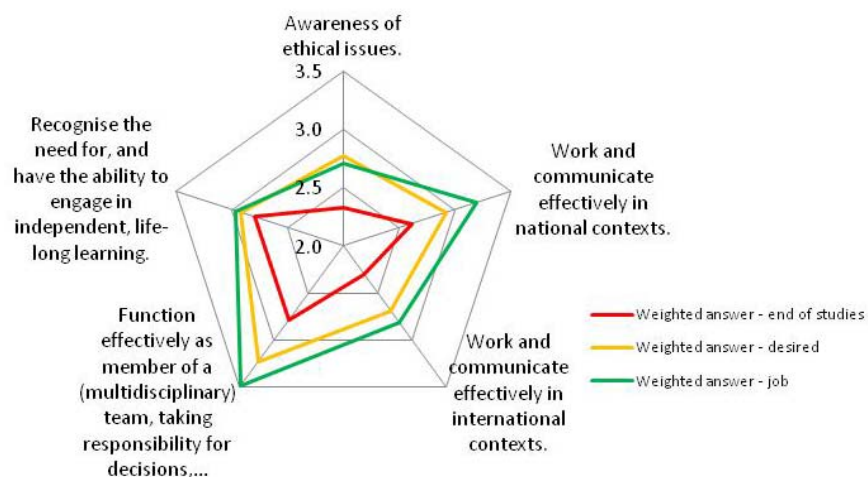


Figure 5 – Levels of mastery in some soft skills as felt by alumni in Birmingham (England)

Fig. 4 shows the results obtained in the same survey by the university of Stuttgart, from 142 answers obtained out of 600 invitations.

Fig. 5 shows the results of the survey launched by the university of Birmingham from 127 answers to 2047 invitations.

The other surveys in Italy (university of Palermo) related to mechanical engineers, in Spain (Association of Telecommunication Engineers ACET of Barcelona) related to telecommunication engineers, and in Hungary (by the Eotvos Lorand university ELTE of Budapest) related to alumni in information technologies, gave in some way similar results.

The question with respect to the soft skills is that the descriptors reflect more personal interests and attitudes than real learning outcomes which can be learned and trained during university courses. Regarding the ability of working and communicating effectively in international contexts, (which is one of the weakest points) this could be trained during periods of studies abroad (Erasmus project) or during stages in industries abroad, but this opportunity is still exploited only by a minority of the student population.

The other weak point where consistent gaps have been found between the required levels at work and the acquired levels in the studies is *Management and Sustainability*, a topic which is generally not the core of engineering studies. With some smaller differences in the descriptors where the maximum gap has been recognized, the responses show clearly that there exists a consistent gap between what is required in the labor market and what has been furnished by the university courses in engineering in the last decades. Again no significant differences have been found in this category between results of surveys in the different European countries.

The question is if the university curricula should include more information about these transverse disciplines, but when something new is included, something old from actual program must be excluded, and it is really difficult to decide which knowledge is not anymore necessary or useful. One should also bear in mind that some basic disciplines help to form culturally the mind of the engineer, even if this knowledge cannot be applied directly in engineering analyses.

The figures from Fig. 6 to Fig. 11 show the results respectively in France, in Stuttgart, in Birmingham, in Barcelona, in Palermo and in Budapest.

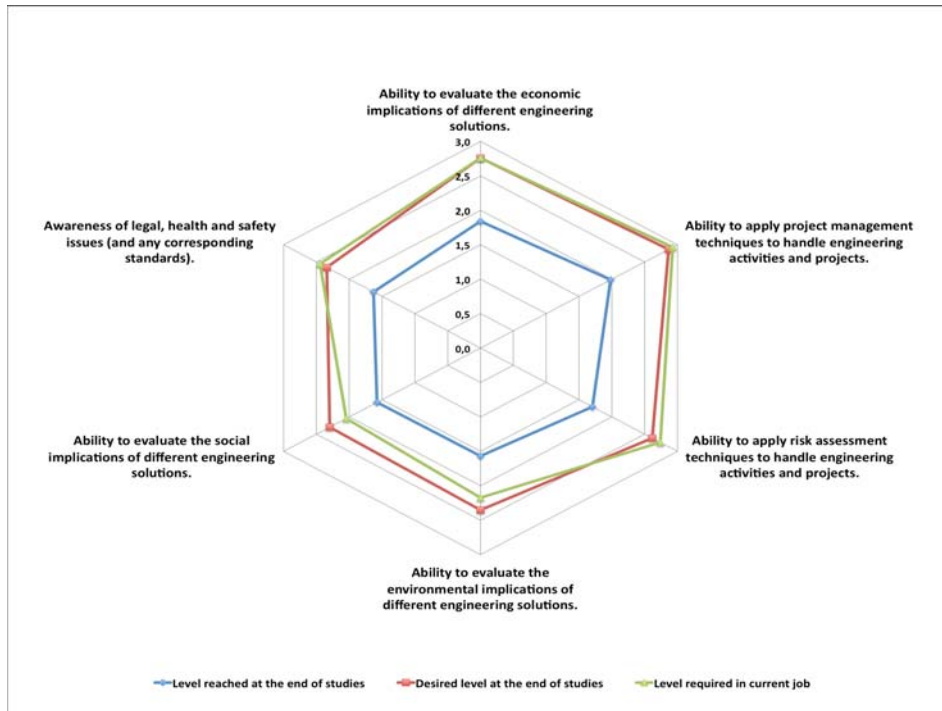


Figure 6 – Levels of mastery in management and sustainability as felt by alumni in France

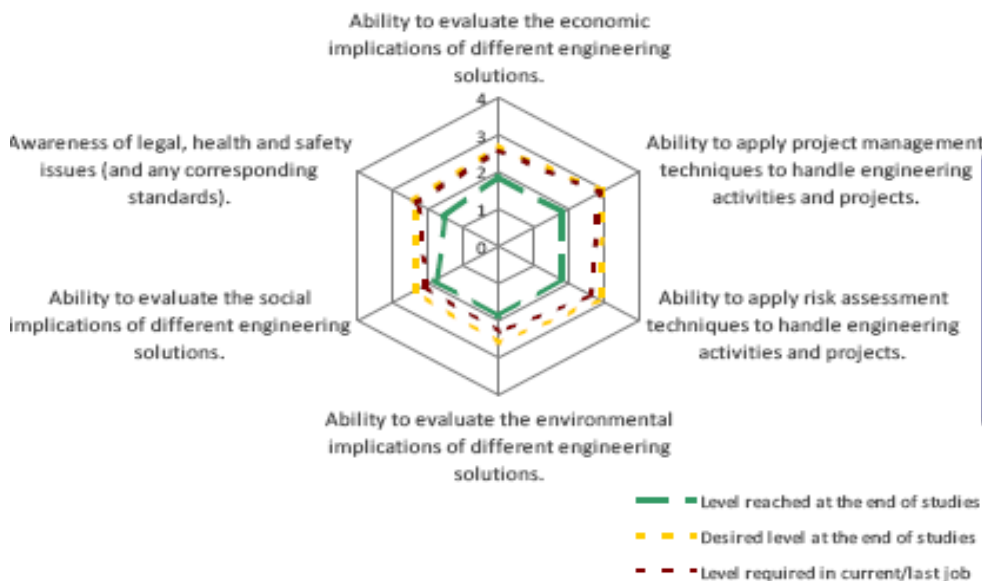


Figure 7 – Levels of mastery in management and sustainability as felt by alumni in Stuttgart (Germany)

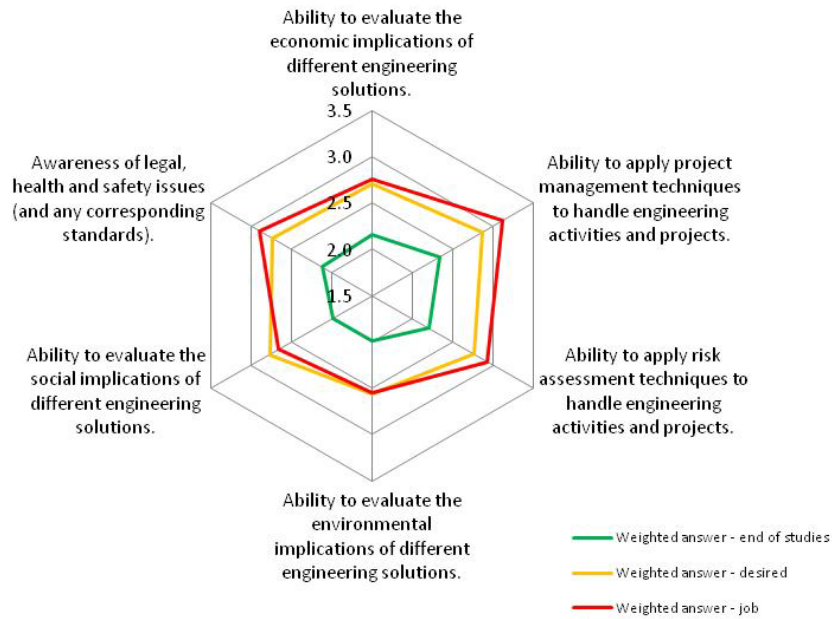


Figure 8 – Levels of mastery in management and sustainability as felt by alumni in Birmingham (England)

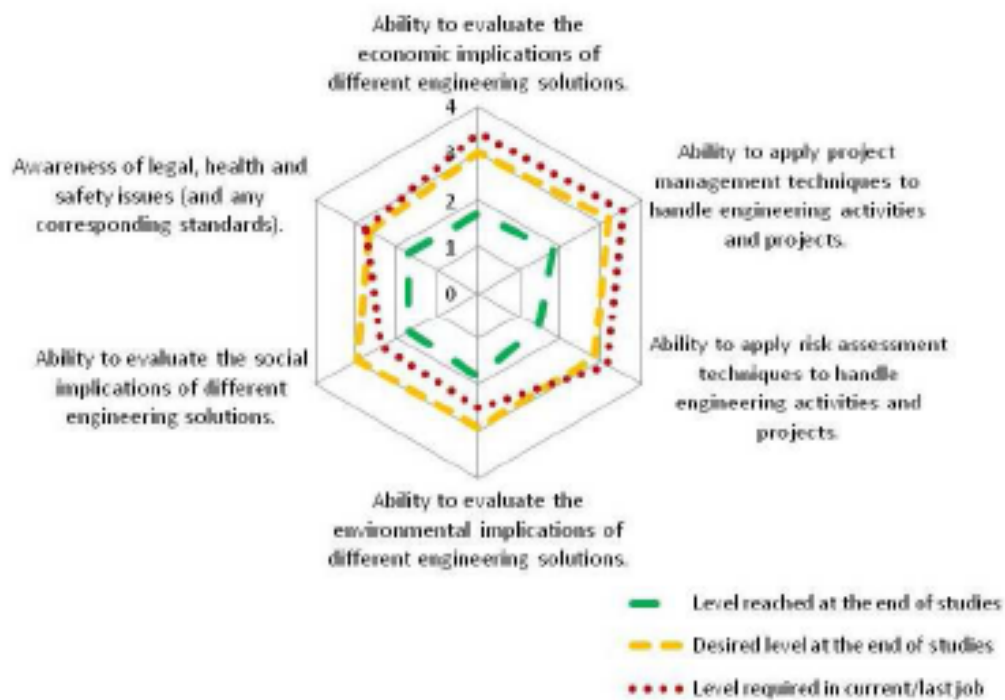


Figure 9 – Levels of mastery in management and sustainability as felt by alumni of Telecommunications in Barcelona (Spain)

Another way to analyze the results is to show which percentage of alumni has experienced a *congruence*, a *deficit* or a *surplus* of the acquired level with respect to the required level. A significant example from France, also related to management and sustainability is shown in Fig. 12. The deficit in the ability of Management and in the awareness of Sustainability is felt by a huge percentage of alumni that ranges from 40% (minimum) to 64% (maximum). Another interesting point is that the only learning outcome for which surplus prevails (for a 54% of cases) is “knowledge and understanding of the scientific and mathematical principles”

Another example of percentage distribution (in this case it is the worst result of the analysis made by Stuttgart university) is given in Fig.13.

For each survey some provisional conclusion has been sought, which were generally invitations to introduce in the curricula the missing topics. A quite general comment about these results (with only few exceptions) is the need to amend programs.

Some universities have already introduced some new topics in the curricula, taking advantage of the reform caused by the application of the Bologna Process, therefore a survey made in a few years would probably yield better results, but the direction in which universities should reform curricula emerges clearly from this analysis.

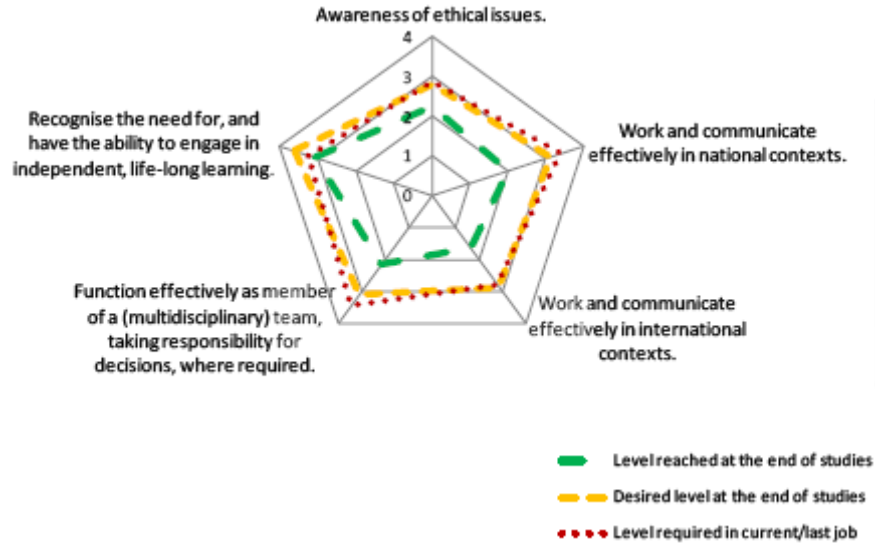


Figure 10 – Levels of mastery in management and sustainability as felt by alumni in Mechanical Engineering in Palermo (Italy)

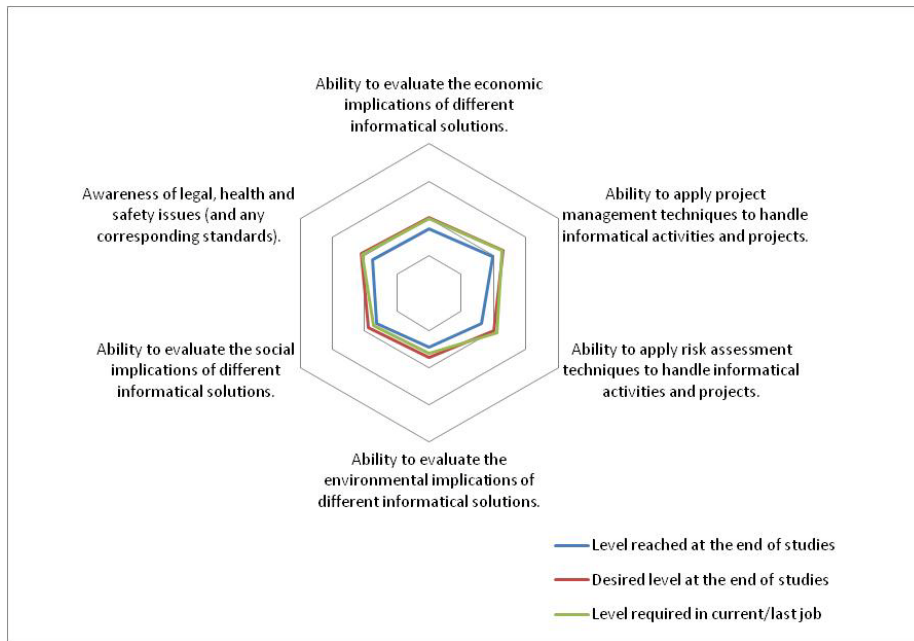


Figure 11 – Levels of mastery in management and sustainability as felt by alumni in Information Technologies in Budapest (Hungary)

But since this survey clarifies the situation perceived by alumni, before stating conclusions it is better to ask employers in the survey directed to enterprises which is being launched at the time this paper is being written. Focus groups with industry stakeholders in France and in Spain and in Germany have already shown a positive background for this further analysis.

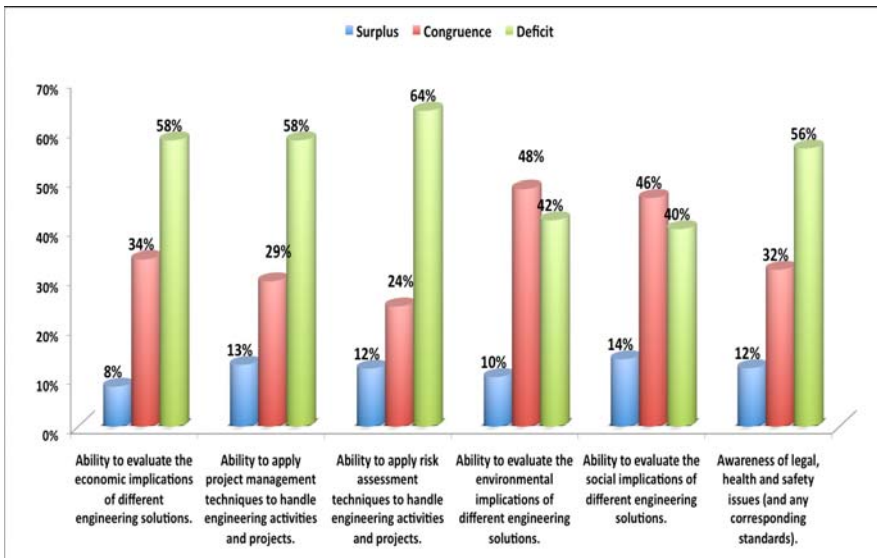


Figure 12 –Surplus/deficit analysis in management and sustainability as felt by alumni in engineering in France

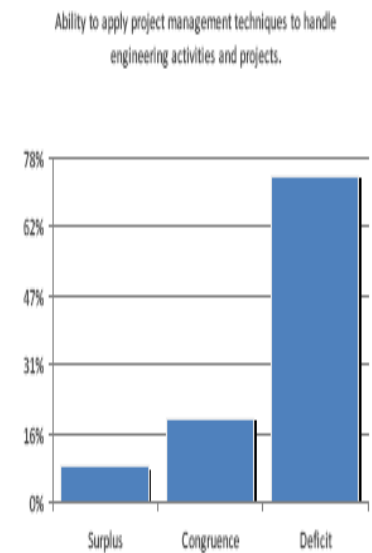


Fig. 13-Deficit of project management felt by Stuttgart alumni

WORK IN PROGRESS TO BE COMPLETED

Two more reviews will be launched : one directed to enterprises, as above specified, and the other addressed to engineering course directors. In the last one course directors will be asked also to declare in which teaching course and in which activity some of the missing abilities are trained, and to give a measure (in terms of credits) of this activity.

Another topic is to map the learning outcomes in the EQF levels, and a table with more detailed description of learning outcomes has been prepared which ranks the LOs in level 6 and 7. Taking account of the results of the surveys some topics will be considered as critical, and consequently its level as LO will be reduced, and recommendation to update curricula will be addressed to the corresponding course directors or related university administration.

There are several other activities in some way related to the objectives of the project, which are performed in Europe. We recall the activity of CEFI, published by his letter “Tendences” which constitutes a kind of observatory in France, and of the European Directorate-General for Education and Culture, which published recently an exhaustive report on “Employers Perception of Graduate Employability” , which can be found in [4].

ACKNOWLEDGMENTS

The authors wish to thank all partners of the project for allowing the publication of the survey results..

REFERENCES

- [1] Website FEANI, European Federation of National Engineering Associations, www.feani.org/webfeani
- [2] Website www.ecceobs.eu
- [3] http://ec.europa.eu/education/lifelong-learning-policy/doc44_en.htm
- [4] http://ec.europa.eu/public_opinion/flash/fl_304_en.pdf

RESPONSIBILITY NOTICE

ECCE project has following ref. n. 504345-LLP-1-2009-1-IT-ERASMUS-ECUE. The project has been funded with support from the European Commission. This publication reflects the views only of the authors, and the Commission cannot be held responsible for any use which may be made of the information contained therein.

THE FEI UNIVERSITY

**Excellence in Management and Technology. A goal for many.
For FEI, it has been a mission for over 60 years.**

The creation of FEI University is linked to the background of the educational institutions which preceded it.

For over six decades, precisely in 1941, during the largest armed conflict ever experienced by humanity, a cultivated, dynamic, and entrepreneurial Jesuit, Priest Roberto Sabóia de Medeiros, founded the ESAN - Escola Superior de Administração de Negócios in São Paulo, Brazil's first higher education Business Management School.

A few years later, in 1946, foreseeing the transformations which would take place in the production processes of the national industry, he also founded the FEI - Faculdade de Engenharia Industrial (School of Industrial Engineering), a pioneering educational institution in its area.

In the 1960s, FEI's engineering degrees were transferred to São Bernardo do Campo, where an ESAN co-branch was also established. Later on, in 1999, FCI - Faculdade de Informática (School of Informatics) was formed, offering a Computer Science degree.

In 2002, FEI, the ESANs and FCI became part of the FEI University, an institution supported by Fundação

Educacional Inaciana Padre Sabóia de Medeiros. To FEI University, quality Human Resources are a serious commitment.

A high-profile teaching staff and course structures strongly focused on theoretical knowledge and experimental and practical activities provide the students with excellent conditions for development in their areas of study.

Besides promoting both technical and scientific education and research development, FEI University is engaged in offering its students an ethical, human and social vision which, combined with intellectual education, helps in the creation of a professional profile at one with the market needs, which are increasingly focused on high technology and innovation.

The FEI University encourages the development of teaching and academic projects by students and professors while providing support and high-quality infrastructure, with a computerized library containing several available databases, in addition to laboratories with high-technology equipment and research and computing centers.

FEI is a non-profit institution interested in offering students a comprehensive academic education focused on technologies, corporate activities, and valuing people.



campus São Bernardo do Campo



campus São Paulo



campus São Bernardo do Campo aerial photo

Undergraduate Courses

FEI courses offer undergraduate students a sound, conceptual and practical education that includes an ethical, social and human vision and results in the expected profile of a critical, creative and proactive professional who is able to study, research, project, and interfere in production and management projects. Students will find, as facilitators of this process, highly qualified and efficient professors and an infrastructure of hi-tech labs for the development of their academic programs or extracurricular-activities. The sum of all these factors turns FEI students into fully educated talents in their fields.

- Business Administration
- Computer Science
- Automation and Control Engineering
- Civil Engineering
- Electrical Engineering
- Mechanical Engineering
- Materials Engineering
- Production Engineering
- Chemical Engineering
- Textile Engineering

Graduation Courses (Lato Sensu)

Our wide experience in lato sensu graduation courses is also part of the educational activities that FEI University offers to the community through the IECAT - Institute for Graduate Studies in Business Administration and Technology. The IECAT took up its activities in 1982 offering lato sensu graduation courses in Administration and Technology. Since then, more than 4,000 students graduated in Technology and another 2,000 students graduated in Business Administration.

The FEI lato sensu courses are aimed at people working in the fields of technology, business and finance. Classes are held by professors who stand out for their professional and academic experience. Courses are offered on our campuses or "In Company".

Master's Degree (Stricto Sensu)

Our master's degree programs follow the excellence and tradition of FEI University to educate highly efficient professionals. A master degree aims at taking students to the frontiers of knowledge in their field, improving their expertise to tackle the main features of any research, development and innovation projects: Principles, Methodology and Contextualization.

Management

Major: Strategic Management of Innovation

Research lines:

- Markets and Consumption
- Organizational Capabilities
- Sustainability

Electric Engineering

Majors:

- Integrated Electronic Devices
- Artificial Intelligence Applied to Automation

Mechanical Engineering

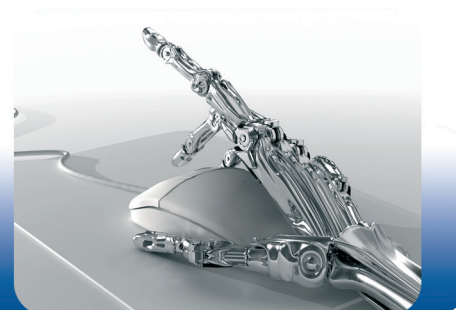
Majors:

- Materials and Processes
 - Processing and Performance of Materials
- Industrial
 - Strategy, Organization and Management of Operations
 - Modeling, Optimization and Control of Processes
- Mobility Systems
 - Propulsion and Energy
 - Dynamics and Control

Doctoral Program

The Doctoral Program in Business Management has concentration area in Innovation Management, with research fields in Sustainability, Markets and Consumption, and Organizational Capacities.

www.fei.edu.br



THE FEI UNIVERSITY

**Excellence in Management and Technology. A goal for many.
For FEI, it has been a mission for over 60 years.**

The creation of FEI University is linked to the background of the educational institutions which preceded it.

For over six decades, precisely in 1941, during the largest armed conflict ever experienced by humanity, a cultivated, dynamic, and entrepreneurial Jesuit, Priest Roberto Sabóia de Medeiros, founded the ESAN - Escola Superior de Administração de Negócios in São Paulo, Brazil's first higher education Business Management School.

A few years later, in 1946, foreseeing the transformations which would take place in the production processes of the national industry, he also founded the FEI - Faculdade de Engenharia Industrial (School of Industrial Engineering), a pioneering educational institution in its area.

In the 1960s, FEI's engineering degrees were transferred to São Bernardo do Campo, where an ESAN co-branch was also established. Later on, in 1999, FCI - Faculdade de Informática (School of Informatics) was formed, offering a Computer Science degree.

In 2002, FEI, the ESANs and FCI became part of the FEI University, an institution supported by Fundação

Educacional Inaciana Padre Sabóia de Medeiros. To FEI University, quality Human Resources are a serious commitment.

A high-profile teaching staff and course structures strongly focused on theoretical knowledge and experimental and practical activities provide the students with excellent conditions for development in their areas of study.

Besides promoting both technical and scientific education and research development, FEI University is engaged in offering its students an ethical, human and social vision which, combined with intellectual education, helps in the creation of a professional profile at one with the market needs, which are increasingly focused on high technology and innovation.

The FEI University encourages the development of teaching and academic projects by students and professors while providing support and high-quality infrastructure, with a computerized library containing several available databases, in addition to laboratories with high-technology equipment and research and computing centers.

FEI is a non-profit institution interested in offering students a comprehensive academic education focused on technologies, corporate activities, and valuing people.



campus São Bernardo do Campo



campus São Paulo



campus São Bernardo do Campo aerial photo

Undergraduate Courses

FEI courses offer undergraduate students a sound, conceptual and practical education that includes an ethical, social and human vision and results in the expected profile of a critical, creative and proactive professional who is able to study, research, project, and interfere in production and management projects. Students will find, as facilitators of this process, highly qualified and efficient professors and an infrastructure of hi-tech labs for the development of their academic programs or extracurricular-activities. The sum of all these factors turns FEI students into fully educated talents in their fields.

- Business Administration
- Computer Science
- Automation and Control Engineering
- Civil Engineering
- Electrical Engineering
- Mechanical Engineering
- Materials Engineering
- Production Engineering
- Chemical Engineering
- Textile Engineering

Graduation Courses (Lato Sensu)

Our wide experience in lato sensu graduation courses is also part of the educational activities that FEI University offers to the community through the IECAT - Institute for Graduate Studies in Business Administration and Technology. The IECAT took up its activities in 1982 offering lato sensu graduation courses in Administration and Technology. Since then, more than 4,000 students graduated in Technology and another 2,000 students graduated in Business Administration.

The FEI lato sensu courses are aimed at people working in the fields of technology, business and finance. Classes are held by professors who stand out for their professional and academic experience. Courses are offered on our campuses or "In Company".

Master's Degree (Stricto Sensu)

Our master's degree programs follow the excellence and tradition of FEI University to educate highly efficient professionals. A master degree aims at taking students to the frontiers of knowledge in their field, improving their expertise to tackle the main features of any research, development and innovation projects: Principles, Methodology and Contextualization.

Management

Major: Strategic Management of Innovation

Research lines:

- Markets and Consumption
- Organizational Capabilities
- Sustainability

Electric Engineering

Majors:

- Integrated Electronic Devices
- Artificial Intelligence Applied to Automation

Mechanical Engineering

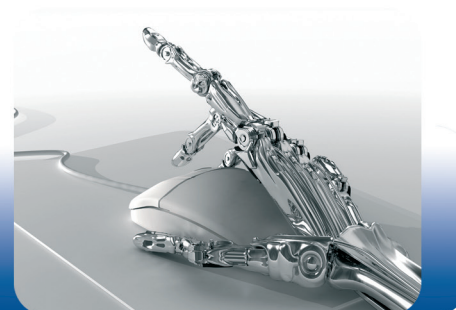
Majors:

- Materials and Processes
 - Processing and Performance of Materials
- Industrial
 - Strategy, Organization and Management of Operations
 - Modeling, Optimization and Control of Processes
- Mobility Systems
 - Propulsion and Energy
 - Dynamics and Control

Doctoral Program

The Doctoral Program in Business Management has concentration area in Innovation Management, with research fields in Sustainability, Markets and Consumption, and Organizational Capacities.

www.fei.edu.br



Organized by



Centro Universitário da **FEI**



UNICAMP

Promoted by



Associação Brasileira de
Engenharia e Ciências Mecânicas

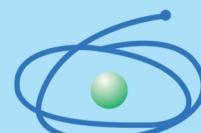
Partnership



Sponsored by



Centro Universitário da **FEI**



C A P E S